ThermaComp2018

# Fifth International Conference on COMPUTATIONAL METHODS FOR THERMAL PROBLEMS

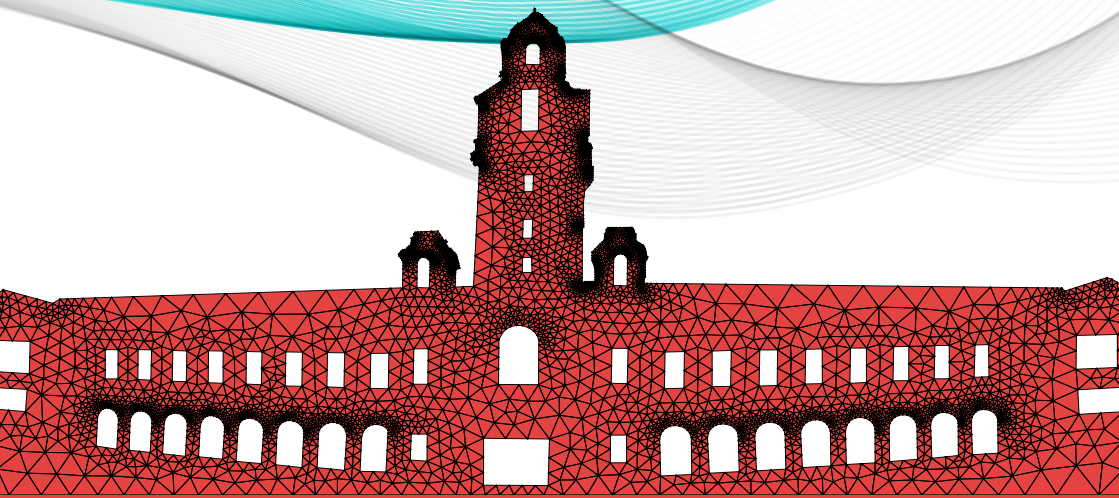

July 9-11, 2018 | J.N. Tata Auditorium, IISc, Bangalore, India

# THERMACOMP2018

## FIFTH INTERNATIONAL CONFERENCE ON COMPUTATIONAL METHODS FOR THERMAL PROBLEMS

JULY 9-11, 2018, IISC, BANGALORE, INDIA

EDITED BY:

**NICOLA MASSAROTTI**
DIPARTIMENTO DI INGEGNERIA
UNIVERSITÀ DEGLI STUDI DI NAPOLI "PARTHENOPE"
NAPOLI, ITALY

**PERUMAL NITHIARASU**
CIVIL AND COMPUTATIONAL ENGINEERING CENTRE
SCHOOL OF ENGINEERING, SWANSEA UNIVERSITY
SWANSEA, UNITED KINGDOM

**PRADIP DUTTA**
DEPARTMENT OF MECHANICAL ENGINEERING
INDIAN INSTITUTE OF SCIENCE
BANGALORE, INDIA

**C RANGANAYAKULU**
AERONAUTICAL DEVELOPMENT AGENCY
BANGALORE, INDIA

WITH THE SUPPORT OF:
**GAURAV TOMAR AND SAGAR KHIVSARA**
INDIAN INSTITUTE OF SCIENCE

**ALESSANDRO MAURO AND SIMONA DI FRAIA**
UNIVERSITÀ DEGLI STUDI DI NAPOLI "PARTHENOPE"

Proceedings of the 5th International Conference on Computational Methods for Thermal Problems, July 9-11 2018, IISc Bangalore, INDIA

Fifth Edition, July 2018


ISSN 2305-6924

# PREFACE

It is indeed our pleasure to welcome all participants of the Fifth International Conference on Computational Methods for Thermal Problems (ThermaComp2018) to Bangalore. This meeting is the continuation of the successful computational thermal problems conference, founded by Professor Roland Lewis in 1979. The aim of the ThermaComp is to bridge the gap between fundamental and applied research in all areas of thermal problems including fluid flow, heat transfer and energy research. The ThermaComp series started in Napoli, Italy in 2009. The conference was then organized in Dalian, China (2011), Lake Bled, Slovenia (2013), and Atlanta, USA (2016). The fifth ThermaComp is hosted by Indian Institute of Science Bangalore (IISc), India. We are indeed grateful that a premier institute in India stepped forward to organize this prestigious meeting. We thank all the organisers and participants and wish them a fruitful ThermaComp2018.

**Professor Nicola Massarotti, Co-Chair, University of Naples 'Parthenope', Italy**
**Professor Perumal Nithiarasu, Co-Chair, Swansea University, UK**
**Professor Pradip Dutta, Co-Chair, Indian Institute of Science, India**
**Dr C. Ranganayakulu, Co-Chair, Aeronautical Development Agency, Bangalore, India**

# MESSAGE FROM THE LOCAL ORGANIZING COMMITTEE

We are pleased to welcome you to the Fifth International Conference on Computational Methods for Thermal Problems (ThermaComp2018) at the Indian Institute of Science, Bangalore.

Over the years ThermaComp has evolved to become surely one of the most important and well attended conference dedicated to numerical techniques in thermal-fluid problems. As in previous years, ThermaComp2018 provides an excellent forum for exchanging information and discussion on the most recent developments and challenges in this field. This meeting represents an interdisciplinary forum of scientists with expertise ranging from heat conduction, convection and radiation to CFD, micro and nano-scale heat transfer.

In order to provide an outstanding technical level for the presentations at the conference, we have invited distinguished experts in thermal-fluid field to deliver 5 keynote and 3 plenary talks. With more than 200 participants from various countries coming together at such a conference, we can once again expect to achieve excellent exchange of knowledge and ideas.

The conference venue is the Indian Institute of Science, a premier institution in India and internationally well known for science and technology research. It is located in Bengaluru, which has always been a major contributor to science and technology at the international stage. In addition to its recent fame as Silicon Valley of India, the city has also emerged as the Research and Development hub of the country, as its hosts several institutions such as the Indian Space Research Organization (ISRO), Defence Research and Development Organisation (DRDO) laboratories, several Indian and multinational corporate R&D organizations, and premier academic institutions.

We are looking forward to meet you in Bangalore during ThermaComp2018 and to sharing a most pleasant, interesting and fruitful conference.

**Pradip Dutta, Conference Co-Chair**
**C.Ranganyakalu, Conference Co-Chair**
**Gaurav Tomar, Convener, Local Organizing Committee**

## SPONSORS






FLOW-3D® and FLOW-3D Cast are registered trademark products of Flow Science Inc., USA

CAMBRIDGE
UNIVERSITY PRESS

# COMMITTEES

***Honorary Chair***
*Professor R.W. Lewis, Swansea University, UK*

***Co-chairs***
*N. Massarotti, Università di Napoli "Parthenope", Italy*
*P. Nithiarasu, Swansea University, UK*
*Pradip Dutta, Indian Institute of Science, India*
*C. Ranganayakulu, Aeronautical Development Agency, India*

***Executive Committee***
*G. Biswas, Indian Institute of Technology Kanpur, India*
*P. Cheng, Shanghai Jiao Tong University, China*
*G. Comini, CISM, Italy*
*M. Ishizuka, Toyama Prefecture University, Japan*
*Y. Jaluria, Rutgers, The State University of New Jersey, USA*
*Y. Joshi, Georgia Institute of Technology, USA*
*X. K. Li, Dalian University of Technology, China*
*J. Murthy, University of California, Los Angeles, USA*
*V. Naso, Università di Napoli Federico II, Italy*
*B. Sarler, University of Nova Gorica & Institute of Metals and Technology, Slovenia*
*K.N. Seetharamu,PES Institute of Technology, India*
*B. Sunden, Lund University, Sweden*
*W.Q. Tao, X'ian Jiatong University, China*
*K. Vafai, University of California, Riverside, USA*

***International Advisory Committee***
*S. Acharya, Memphis State University, USA*
*A. Ambirajan, Indian Institute Space Research Organization, India*
*F. Arpino, Università degli Studi di Cassino e del Lazio Meridionale, Italy*
*B.R. Baliga, McGill University, Canada*
*S.W. Baek, Korea Advanced Institute of Science & Technology, South Korea*
*A. Carotenuto, Università di Napoli "Parthenope", Italy*
*D. Chakraborty, Defense Research and Development Laboratory, India*
*S. Chakraborty, Indian Institute of Technology Kharagpur, India*
*A.J. Chamkha, Public Authority for Applied Education and Training, Kuwait*
*S. Chang, National University of Singapore, Singapore*
*F. Chinesta, Ecole Centrale de Nantes, France*
*R. Codina, Universitat Politècnica de Catalunya, Spain*
*R.M. Cotta, Universidade Federal do Rio de Janeiro, Brazil*
*D. Drikakis, University of Strathclyde, UK*
*G. Dulikravich, Florida International University, USA*
*V. Eswaran, Indian Institute of Technology Hyderabad, India*
*T. Fushinobu, Tokyo Institute of Technology, Japan*
*D. Givoli, Technion - Israel Institute of Technology, Israel*
*D. Gobin, CNRS, France*
*S. Idelsohn, CIMNE - International Center for Numerical Methods in Engineering, Spain*

*A. Kassab, University of Central Florida, USA*
*V. Krishna, PES University, India*
*M. Li, Taiyuan University of Technology, China*
*R. Lohner, George Mason University, USA*
*A.G. Malan, Council for Scientific and Industrial Research, South Africa*
*O. Manca, Seconda Università di Napoli, Italy*
*J.C. Mandal, Indian Institute of Technology Bombay, India*
*A. Mauro, Università di Napoli "Parthenope", Italy*
*C. Nonino, Università di Udine, Italy*
*A.J. Nowak, Silesian Polytechnic University, Poland*
*J. Patterson, University of Sydney, Australia*
*I. Pop, University of Cluj, Romania*
*D. Pradip, Indian Institute of Science, Bangalore, India*
*J. Reese, University of Strathclyde Glasgow, UK*
*W. Shyy, Hong Kong University of Science and Technology, Hong Kong*
*Siraj-ul-Islam, University of Engineering and Technology Peshawar, Pakistan*
*J. Summers, Leeds University, UK*
*T. Sundararajan, Indian Institute of Technology Madras, India*
*K. Sungjin, Korea Advanced Institute of Science and Technology, South Korea*
*V.R. Voller, University of Minnesota, USA*
*I. Vusanovic, University of Montenegro, Montenegro*
*W. Wall, Technische Universität München, Germany*
*L. Xiaobing, Huazong University of Science and Technology, China*

***Local Organising Committee***
*P. Dutta, Indian Institute of Science (IISc), INDIA (Co-chair)*
*C. Ranganayakulu, Aeronautical Development Agency, INDIA (Co-chair)*
*G. Tomar, Indian Institute of Science, INDIA (Convener)*
*N. Balakrishnan, Indian Institute of Science, INDIA (Member)*
*R.V. Ravikrishna, Indian Institute of Science, INDIA (Member)*
*S. Basu, Indian Institute of Science, INDIA (Member)*
*P. Kumar, Indian Institute of Science, INDIA (Member)*
*S. Chaudhuri, Indian Institute of Science, INDIA (Member)*

# PLENARY LECTURES

**Bubble Dynamics in Various Regimes of Boiling**

Gautam Biswas
Department of Mechanical Engineering
Indian Institute of technology Guwahati
Guwahati – 781039, India

## Abstract

The dynamics of vapor bubbles during boiling is a topic of significance considering influence on the heat transfer rate associated with various applications. Depending on the heat flux, the mode of boiling transforms from the nucleate boiling regime to the film boiling regime. In the present investigation, we performed a CLSVOF based direct numerical simulation to predict the bubble generation, growth and its departure during pool boiling. In the film boiling regime, the bubble growth is governed by the instabilities at the liquid-vapor interface instigated by the combined influence of surface tension, buoyancy, heat flux, vapor thrust or any other applied external field (electric field in the present investigation). The dynamical disturbances destabilize the interface which results in bubble formation with the passage of time. The instability mode transforms from Rayleigh-Taylor at the low wall-superheat temperature to Taylor-Helmholtz at the higher superheat values, governing the separation distances between the sites of bubble generation.

The bubble morphology is also observed to be highly dependent on the degree of superheat. The discrete bubbles are seen at the lower range of superheat values while continuous vapor columns are discerned in the case of high superheat values. Bubble growth and departure from the interface follows a regular periodic pattern (both in space and time).

Electric field results in destabilizing the interface and enhancing the bubble growth rate. Through the applied electric force, it was found that the application of electric field normal to the heating surface results in increase of both spatial and temporal frequency of bubble-formation along the heated surface. The dominant wavelength of disturbance decreases which in its turn decreases the separation-distance between adjacent bubbles.

As buoyancy is one of the dominant factors influencing the growth-dynamics of bubbles during boiling, changes in the gravity-level result in a significant variation in boiling characteristics. Analyses have been performed at different levels of gravity to determine the changes in bubble morphology and heat-transfer rate.

The application of electric field compensates for this reduction in the heat transfer rate and recovers the same rate of heat transfer as in normal gravity. The dominance of electric field force

also increases in case of reduced gravity conditions. Both the length and time scales increase appreciably as a result of reduction in the level of gravity. During the initial stage of bubble growth, the interfaces exhibit self-similar profiles, i.e. the bubble interface at different instants of time can be converged on a single profile defined by a fitting function in which the variables are normalized using proper scaling parameters.

Unlike in the film boiling regime, the bubble generation and growth in nucleate boiling is rather intricate. In nucleate boiling, the bubble generation is not instability-dependent but a random process which depends on the heat flux from the surface and the surface-properties. The nucleation starts at cavities as a result of existence of pre-occupied gaseous or vapor phase or due to extreme heat-flux. In this investigation simulations have been performed by incorporating a microlayer model to account for its contribution in the growth of a single bubble. The growth rate is found to be affected by the surface-superheat, the wettability of the surface and the degree of subcooling of the ambient liquid.

Fifth International Conference on Computational Methods for Thermal Problems
THERMACOMP2018, July 9-11, 2018, Indian Institute of Science, Bangalore, INDIA
*N. Massarotti, P. Nithiarasu, Pradip Dutta and C. Ranganayakulu (Eds.)*

# Rib Shape Effects on Heat Transfer Performance in Internal Cooling Passages

**Y. Dai, J. C. Tyacke and P. G. Tucker**
Cambridge University, Trumpington St, Cambridge, UK. E-mail: pgt23@cam.ac.uk

## ABSTRACT

Numerical studies of the flow field and heat transfer in a fully developed ribbed channel have been performed using Large Eddy Simulation (LES). Ten different rib shapes are investigated aiming to improve the heat transfer performance. The triangular rib with increasing height in the flow direction, with the largest recirculation bubble, was found to provide the best heat transfer performance, giving approximately 5% greater heat transfer than the basic square profile. Ribs with larger recirculating zones tend to provide better heat transfer performances. The rounded-corners with the shortest recirculation zones deteriorated the heat transfer performance. Thus when adding round edges to the triangular_up ribs to fit the manufacturing conditions, the heat transfer performance can be reduced by around 12%. An immersed boundary method (IBM) has been implemented for use with LES to solve the challenge of varying complex rigid geometries.

**Key Words:** *Heat Transfer, LES, Turbine, SGS, IBM.*

## 1. INTRODUCTION

Gas turbines have been used extensively to provide power in modern aircrafts and other industrial applications. The high temperature arising in turbines is one of the most critical parameters impacting engine performance, efficiency and blade life. Internal passages with ribs are typically cast into turbine blades to decrease the metal temperature and further, to prevent premature wear. Numerous experiments have been conducted to investigate the effect rib geometries [2-4]. From these experimental results, there is still no certain relation between different rib shapes and heat transfer characteristics. Thus investigations should be further pursued by numerical methods with high fidelity turbulence modelling. However, computational cost has limited most applications of CFD to using the Reynolds averaged Navier-Stokes (RANS) models, which are not reliable for all flow regimes and can lead to poor flow and heat transfer predictions in complex geometries with separated flow [8-10]. In some cases, the differences in heat transfer between RANS models can vary by approximately 100% [10]. Therefore, more reliable turbulence model is required for unsteady flows with high streamline curvature. For this type of flow that is governed by large scales of turbulence, LES is more accurate than RANS [11] and allows greater insight into the physical processes involved. However, when it is used with complex geometries and curved shapes, a complicated grid system needs to be built to fit the computational mesh exactly to the body. Thus, an approach called the immersed boundary method (IBM) has been developed to use with LES in complex rigid geometries. Hence, LES is used in this study to investigate the effects of rib geometry on heat transfer in internal cooling passages. Different rib shapes are investigated with aim being to improve the heat transfer performance. IBM will be used to eliminate the effort for complex grid generation and the overhead of unstructured grids -- this being especially significant for LES.

## 2. NUMERICAL METHODS

### 2.1 Governing equations

The incompressible governing equations for LES are written in the following form:

$$\frac{\partial \bar{u}_j}{\partial x_j} = 0$$

$$\rho \frac{\partial \bar{u}_i}{\partial t} + \rho \frac{\partial \bar{u}_i \bar{u}_j}{\partial x_j} = -\frac{\partial \bar{p}}{\partial x_i} + \frac{\partial}{\partial x_j}[(\mu + \mu_{SGS})\frac{\partial \bar{u}_i}{\partial x_j}] - \rho \frac{\partial \tau_{ij}}{\partial x_j}$$

$$\rho \frac{\partial \bar{T}}{\partial t} + \rho \frac{\partial \bar{u}_j \bar{T}}{\partial x_j} = \frac{\partial}{\partial x_j}[(\frac{\mu}{\mathrm{Pr}} + \frac{\mu_{SGS}}{\mathrm{Pr}})\frac{\partial \bar{T}}{\partial x_j}] - \frac{\partial h_j}{\partial x_j}$$

The governing equations are solved using the NEAT code as presented by Tucker [7]. This is a structured, finite volume, parallel CFD solver. In this work, the Yoshizawa model is used in conjunction with the LANS-α model, creating a mixed nonlinear SGS model [12].

### 2.2 Computational Setup

The computational domain is a straight channel with fully-developed flow over the rib surfaces. The ribs are placed perpendicular to the flow direction at the center of the bottom wall. The settings for the flow parameters were chosen to be consistent with the experiments of Acharya et al. [1]. The baseline geometry and general case set up is similar to that of Tafti [6] and Liu et al. [5]. No slip conditions are imposed at the walls. The solid surface of the rib and the upper wall are assumed to be adiabatic. Fully developed turbulent channel flow is homogeneous in the streamwise and spanwise directions, and periodic boundary conditions are imposed in these directions. A constant heat flux q" boundary condition is applied to the rest of the lower wall.

## 3. RESULTS

The Nusselt number is normally used to measure the convective heat transfer effect. In order to better reflect heat transfer improvement of the ribbed passage, Webb et al. [14] pointed out that the heat transfer performance can be used to evaluate the behavior of an 'enhanced' surface, which considers the heat transfer value as well as the friction factor. The heat transfer performance (η) for evaluating the increased heat transfer is expressed as:

$$\eta = \frac{Nu / Nu_0}{(f / f_0)^{1/3}}$$

where $Nu_0$ and $f_0$ stand for the Nusselt number and friction factor for a smooth duct, respectively.

Although the increased performance of the triangular_up case is not obvious in the Nusselt number profiles, it becomes quite significant when the pressure drop is also taken into consideration, as presented in Figure 1. This finding is consistent with Ahn [2], who proposed that triangular-shaped rib geometry is more efficient for heat transfer than the square-shaped one. The main parameters of the heat transfer results are compared in Table 1.

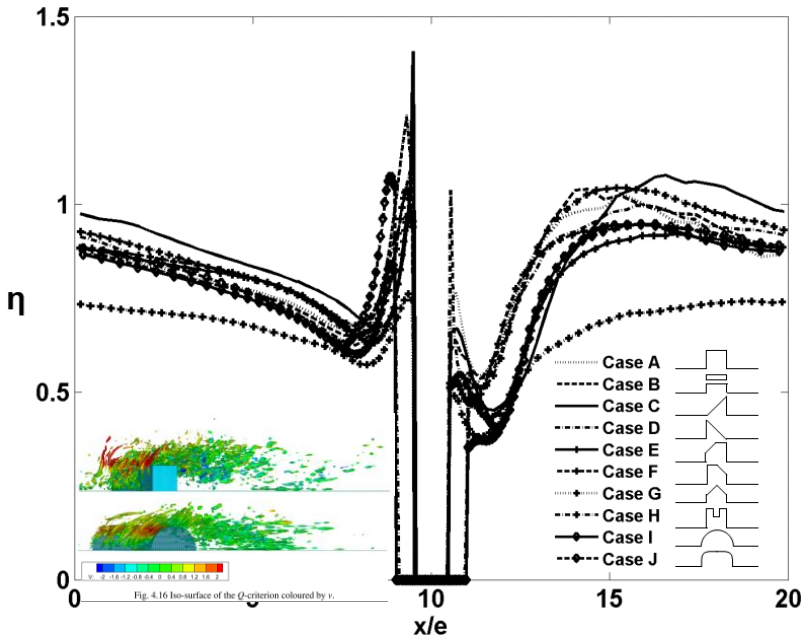


FIGURE 1. Local heat transfer performance distributions

| Case | A | B | C | D | E | F | G | H | I | J |
|---|---|---|---|---|---|---|---|---|---|---|
| Nu | 91.41 | 91.75 | 94.50 | 94.54 | 84.92 | 88.70 | 65.58 | 87.80 | 82.47 | 84.88 |
| $Nu_{max}$ | 139.99 | 139.87 | 149.23 | 125.38 | 106.55 | 113.69 | 77.90 | 114.28 | 103.53 | 117.49 |
| η | 0.81 | 0.81 | 0.85 | 0.81 | 0.78 | 0.81 | 0.60 | 0.80 | 0.75 | 0.77 |
| $η_{max}$ | 1.33 | 1.33 | 1.41 | 1.16 | 1.01 | 1.08 | 0.75 | 1.09 | 0.99 | 1.12 |

TABLE 1. Comparison of main heat transfer parameters

Observation of Figure 1 shows that the local maxima near the backward- and forward-facing corners for the semi-circle and arc rib are also not as sharp as those for the square rib. This illustrates that ribs with round shapes have a low heat transfer rate. This can be expected from the Q-criterion iso-surface. As shown in Table 1, the triangular_up rib provides the best overall performance with a value of η = 0.85, this being 5% higher than the basic square rib. The increase in performance would allow, for example, less fluid to be bled from the compressor in an aeroengine, increasing overall efficiency, or improving durability.

## 4. CONCLUSIONS

Numerical studies of a fully developed channel with ribs have been performed using LES. The square rib was first carried out to validate the accuracy of this LES model -- a nonlinear LANS-α model. Through the velocity field and heat transfer results, LES was found to be able to predict the velocity distribution with good accuracy and obtain the correct Nusselt number trend. IBM is implemented with LES to save the effort of grid generation and enhance speed of CFD solution allowing the rapid exploration of different rib geometries.

The thermal characteristics in terms of heat transfer and friction factor of ten different rib shapes have been investigated. The heat transfer performance was found to strongly depend on the cross-sectional rib shapes. The triangular rib with increasing height in the flow direction, with the largest recirculation bubble, was found to provide the best heat transfer performance, at 5% more than the basic square rib. Ribs with larger recirculating zones tend to provide better heat transfer performances (Case C, Case D, Case F, Case H). Thus, the size of the recirculating zone proved to be a critical factor to determining the heat transfer performance.

## REFERENCES

[1] S. Acharya, S. Dutta, T. Myrum, R. Baker, Periodically developed flow and heat transfer in a ribbed duct, *International Journal of Heat and Mass Transfer* 36 (8) (1993) 2069-2082.

[2] S. Ahn, The effects of roughness types on friction factors and heat transfer in roughened rectangular duct, *International Communications in Heat and Mass Transfer* 28 (7) (2001) 933-942.

[3] P. R. Chandra, M. L. Fontenot, J.-C. Han, Effect of rib profiles on turbulent channel ow heat transfer, *Journal of thermophysics and heat transfer* 12 (1) (1998) 116-118.

[4] T.-M. Liou, J.-J. Hwang, Effect of ridge shapes on turbulent heat transfer and friction in a rectangular channel, *International Journal of Heat and Mass Transfer* 36 (4) (1993) 931-940.

[5] Y. Liu, P. G. Tucker, G. L. Iacono, Comparison of zonal RANS and LES for a non-isothermal ribbed channel flow, *International journal of heat and fluid flow* 27 (3) (2006) 391-401.

[6] D. Tafti, Evaluating the role of subgrid stress modeling in a ribbed duct for the internal cooling of turbine blades, *International Journal of Heat and Fluid Flow* 26 (1) (2005) 92-104.

[7] P. G. Tucker, Computation of unsteady internal flows: fundamental methods with case studies, *Springer Science & Business Media*, 2001.

[8] P. Tucker, S. Eastwood, C. Klostermeier, R. Jefferson-Loveday, J. Tyacke, Y. Liu, Hybrid LES approach for practical turbomachinery flows: part 1hierarchy and example simulations, *ASME Turbo Expo 2010*: Power for Land, Sea, and Air (2010) 997-1009.

[9] P. Tucker, S. Eastwood, C. Klostermeier, H. Xia, P. Ray, J. Tyacke, W. Dawes, Hybrid LES approach for practical turbomachinery flows: part2 further applications, *ASME Turbo Expo 2010*: Power for Land, Sea, and Air (2010) 1055-1067.

[10] J. Tyacke, Low Reynolds number heat transfer prediction employing Large Eddy Simulation for electronics geometries, D.Phil. Thesis, Civil and Computational Engineering Centre, Swansea University.

[11] J. Tyacke, P. Tucker, Large Eddy Simulation of turbine internal cooling ducts, *Computers & Fluids* 114 (2015) 130-140.

[12] J. Tyacke, R. Jefferson-Loveday, P. G. Tucker, Application of LES to labyrinth seals, *Proceedings of the AIAA CFD Conference*, AIAA Paper no. AIAA-2011-3861.

[13] L. Wang, B. Sunden, Experimental investigation of local heat transfer in a square duct with various-shaped ribs, *Heat and Mass Transfer* 43 (8) (2007) 759-766.

[14] R. Webb, E. Eckert, R. Goldstein, Heat transfer and friction in tubes with repeated-rib roughness, *International Journal of Heat and Mass Transfer* 14 (4) (1971) 601-617.

Fifth International Conference on Computational Methods for Thermal Problems
THERMACOMP2018, July 9-11, 2018, Indian Institute of Science, Bangalore, INDIA
*N. Massarotti, P. Nithiarasu, Pradip Dutta and C. Ranganayakulu (Eds.)*

# MITIGATING HOT SPOTS IN 2D AND 3D MICROSYSTEMS USING EMBEDDED MICROFLUIDIC COOLING

**Yuanchen Hu, Daniel Lorenzini, and Yogendra Joshi**

G.W. Woodruff School of Mechanical Engineering

Georgia Institute of Technology

Atlanta, GA 30096, U.S.A.

Yogendra.Joshi@me.gatech.edu

## ABSTRACT

As the dimensional scaling of Silicon microprocessor devices slows, the emergence of heterogeneous integration of multiple functionality chips on 2.5D and 3D platforms is a rapidly emerging trend. This allows for the continued growth of ultra-compact and highly functional microsystems in mobile, and high performance applications. The close placement of multiple chips in such systems poses increasing thermal management challenges, driven by spatially non-uniform heat generation rates and differing allowable temperature limits. The thermal cross-talk via the substrate, and multiple interconnected tiers result in further complexity. We will examine three aspects of microfluidic cooling of 2.5D and 3D systems. The challenges of multi-chip cooling will be illustrated by the thermal design of a 2.5D high performance computing architecture. The need for compact thermal models for thermal-electrical co-design in 3D architectures will be illustrated. Finally, the characteristics of flow boiling in multi-chip architectures will be explored.

**Key Words:** *3D Electronics, 2.5D Electronics, Thermal Management, Hot Spots, Heterogeneous Integration, Microfluidic Cooling.*

## 1. INTRODUCTION

The prediction by Gordon Moore in 1965 about continued reduction in feature sizes and improved performance, known as the Moore's Law, has driven the progress of the microprocessor technology for nearly five decades [1]. In the last decade, this scaling has slowed, and the focus of future microsystems development is shifting to system level performance, instead of just the microprocessor. To enable such More-than-Moore capabilities, new packaging architectures that enable the integration of multiple capabilities such as logic, memory, radio frequency (RF), and micro-electrical-mechanical systems (MEMS) are being developed [2]. Two examples of such approaches, 2.5D and 3D heterogeneous integration, are shown in Fig. 1 [3-5]. Fig. 1(a) shows the 2.5D approach, where an interposer is used to connect multiple laterally and closely placed chips with various functionalities. The reduced length of electrical interconnections permits faster signal transmission for improved performance, and reduced ohmic losses. The interposer material, commonly silicon, is chosen based on multiple requirements, including the ability to allow ultra-fine pitch interconnects. Through silicon vias (TSVs) are used to provide electrical interconnections with the underlying substrate, with larger pitches. Packages based on the 2.5D integration approach are already available commercially. Fig. 1(b) illustrates the 3D stacking of multiple functional chips, e.g. logic and memory. Individual chips can be thinned, and connected vertically using TSVs. This configuration can yield further reduction in interconnection lengths, and even higher performance than 2.5D packaging.

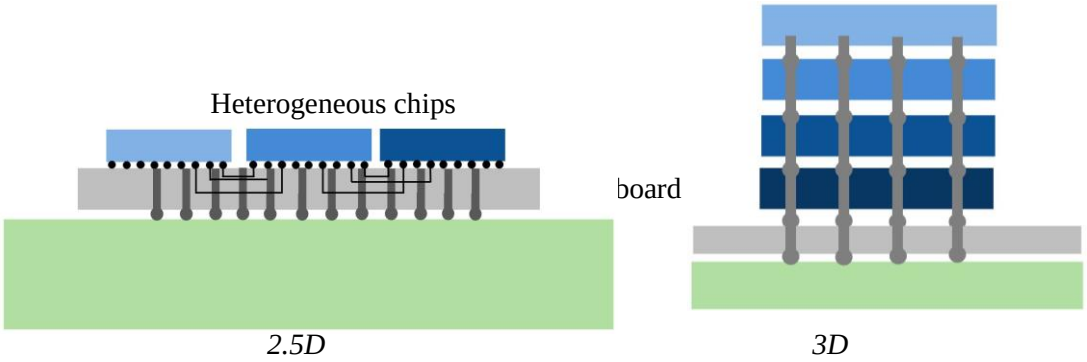


*Fig. 1 Emerging 2.5D and 3D Architectures*

Both 2.5D and 3D architectures pose significant thermal management challenges. Close placement of chips with multiple functionalities results in thermal cross-talk, either via a conducting substrate in 2.5D systems, or directly through contact between the chips in 3D systems. Such integration also results in larger volumetric heat generation rates, and reduced heat transfer surface area per unit volume.

## 2. MAIN BODY

We illustrate the thermal management challenges in 2.5D and 3D systems through the consideration of three examples, illustrated in Fig. 2. Fig. 2(a) shows the 2.5D architecture followed in field programmable gate array (FPGA) based applications in high bandwidth applications, such as 5G networks [6]. Multiple smaller transceiver chips with heat fluxes 10x or larger communicate via a Si interposer with a larger centrally placed FPGA chip. The thermal management of this heterogeneous chip array via single phase microfluidic cooling [7] brings out the need for thermal design parametric studies. Compact thermal modelling of microfluidic cooling in 2.5D and 3D systems is required to perform electrical/thermal co-design.

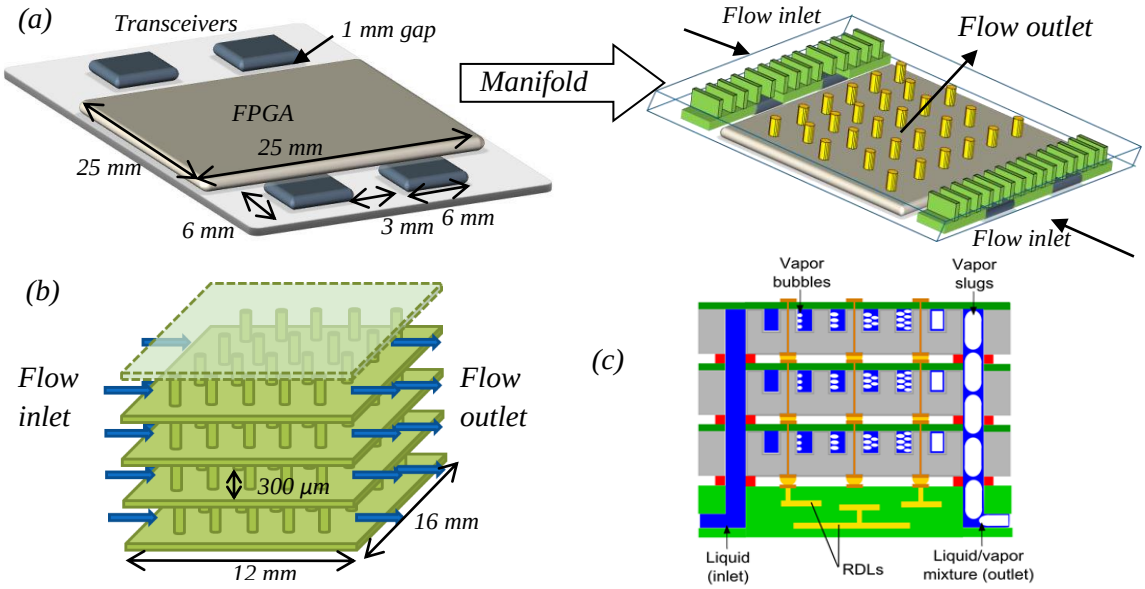


*Fig. 2 Simulated Geometries: (a) 2.5D System with Single FPGA and Four Transceiver Chips, (b) 3D System For Thermal-Electrical C-Design, (c) Flow Boiling in 3D Architecture*

Fig. 2(b) illustrates the 3D configuration with pin fins for enhanced thermal management, and electrical interconnections, considered by Hu [8]. The requirement for the use of dielectric fluids, with inferior thermophysical properties than water has prompted the use of phase change approaches. Fig. 2(c) illustrates the use of flow boiling in pin fin enhanced microgaps, as a possible configuration for 2.5D and 3D microsystems.

## 3. RESULTS

The important role of multi-scale, multi-mode heat transfer modelling in the development of future heterogeneous microsystems is illustrated through three examples.

3.1 Interposer Based Single Phase Cooling for 2.5D Integration: For the configuration in Fig. 2(a) we consider a number of cases for a numerical parametric study, as summarized in Tables 1-3.

| Model number | 1 | 2 |
|---|---|---|
| Transceiver cooling enhancement | Only fins on top | Bridge-wing structures with fins |
| Max T of transceivers (ºC) | **179.6** | **105.4** |
| Max T of FPGA (ºC) | 89.3 | 93.0 |
| Pumping power (W) | 0.05 | 0.22 |

TABLE 1. Parametric Studies of Bridge-wing Structure Cooling Performance in 2.5D System [8]

| Model number | 3 | 4 | 5 | 6 | 7 | 8 |
|---|---|---|---|---|---|---|
| Fin thickness and pitch on transceivers (mm) | 0.18; 0.18 | 0.15; 0.15 | 0.14; 0.14 | 0.12; 0.12 | 0.11; 0.11 | 0.1; 0.1 |
| Transceivers Max T (ºC) | **101.4** | **96.2** | **96.2** | **90.9** | **89.7** | **89.3** |
| Max T of FPGA (ºC) | 92.8 | 93.0 | 93.0 | 93.1 | 93.3 | 93.9 |
| Pumping Power (W) | 0.22 | 0.25 | 0.25 | 0.31 | 0.33 | 0.35 |

TABLE 2. Parametric Studies of Fin Configurations in 2.5D System [8]

| Model number | 9 | 10 | 11 | 12 |
|---|---|---|---|---|
| Outlet numbers, location | 2 at sides | 2 in the center | 1 in the center | 1 in the center |
| Outlet area | 6 x 6 mm | 6 x 6 mm | 6x 6 m | 2 x 2 mm |
| Transceivers max T (ºC) | 89.4 | 89.3 | 89.3 | 89.1 |
| Max T of FPGA (ºC) | **99.2** | **93.9** | **90.4** | **89.2** |
| Pumping power (W) | 0.34 | 0.35 | 0.36 | 0.47 |

TABLE 3. Parametric Studies of Outlet Configurations in 2.5D System [8]

Surface temperature simulations for Models 1 and 12, which display the baseline conditions, and a single flow outlet configuration respectively, are shown in Fig. 3. From these, the temperature non-uniformity due to the varying heat fluxes on the transceiver and FPGA chips is evident.

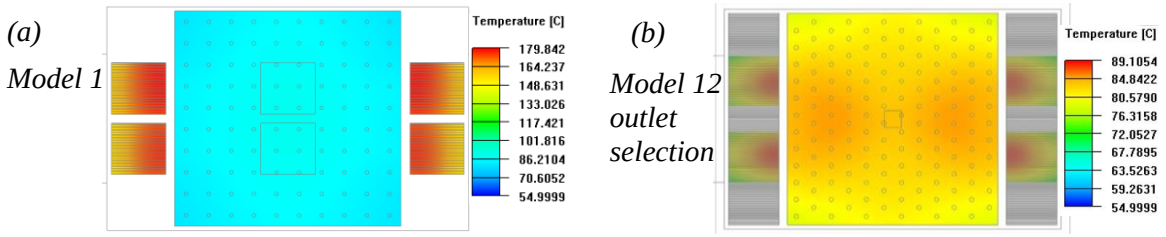


*Fig. 3 Cooling Performance of heterogeneous pin-fin enhanced liquid manifold in 2.5D system [8]*

3.2 Compact Modeling for 3D Electrical-Thermal Co-Design:

The compact model utilized in the configuration in Fig. 2(b) considers in-plane heat conduction within each chip layer, vertical heat conduction between layers through pin-fins, and forced convection of coolant within micro-gaps [8-10]. Based on the spatially and temporally varying power distribution, the model simulates temperature distribution for each layer under both steady state and transient conditions. Based on this distribution, and leakage power and temperature correlation, electrical co-design function provides a more accurate power map by simulating and deducting over-estimated leakage power. This updated power map is applied in the thermal model again to simulate an updated temperature field. These iterative simulations incorporating both electrical and thermal functions, are used to compute the final converged temperatures. Leakage power under these conditions has been obtained.

3.3 Flow Boiling for Multiple Heat Sources:

The effects of placing multiple heat sources as hotspots in a microgap cooling layer, illustrated in Fig. 2(c), are assessed by two-phase numerical simulations of flow boiling. The Coupled Level Set and Volume of Fluid (CLSVOF) method is coupled with a mechanistic phase change model, while also simultaneously solving the heat conduction in the solid domain. Fig. 4 shows the computational domain for the simulations, consisting of a strip taken from a microgap design with three hotspots of 500 µm by 500 µm localized at the inlet, center, and outlet of the domain. The microgap has a height of 200 µm, and the pin fin density is doubled at the hotspot zones in order to allow the dissipation of higher heat fluxes by increasing the surface area. The simulation results will show effects of spreading, temperature field, two-phase flow regimes and pressure drop estimations for different heating ratios, using dielectric fluid HFE-7200 as the coolant.

## 4. CONCLUSIONS

Emerging 2.5D and 2D architectures enabling heterogeneous microsystems pose numerous thermal management challenges. Computational fluid dynamics/heat transfer (CFD/HT) techniques are key to enable the optimized design of these systems. Parametric studies allow for understanding the effects of interactions between multiple non-uniform power density heat sources via conducting substrates. Due to the computationally intensive nature of CFD/HT techniques, compact modelling is needed to enable coupled electrical/thermal co-design. Significant challenges remain in assessing the trade-offs between modelling accuracy and computational effort. Application requirements may require the use of dielectric coolants, which suffer from poorer thermos-physical properties compared to water. To achieve acceptable performance from such fluids, the cooling systems may need to be operated under two-phase conditions. While multiple challenges remain, recent progress in the numerical modelling of such flows presents unique opportunities to design high heat flux cooling solutions for microsystems.

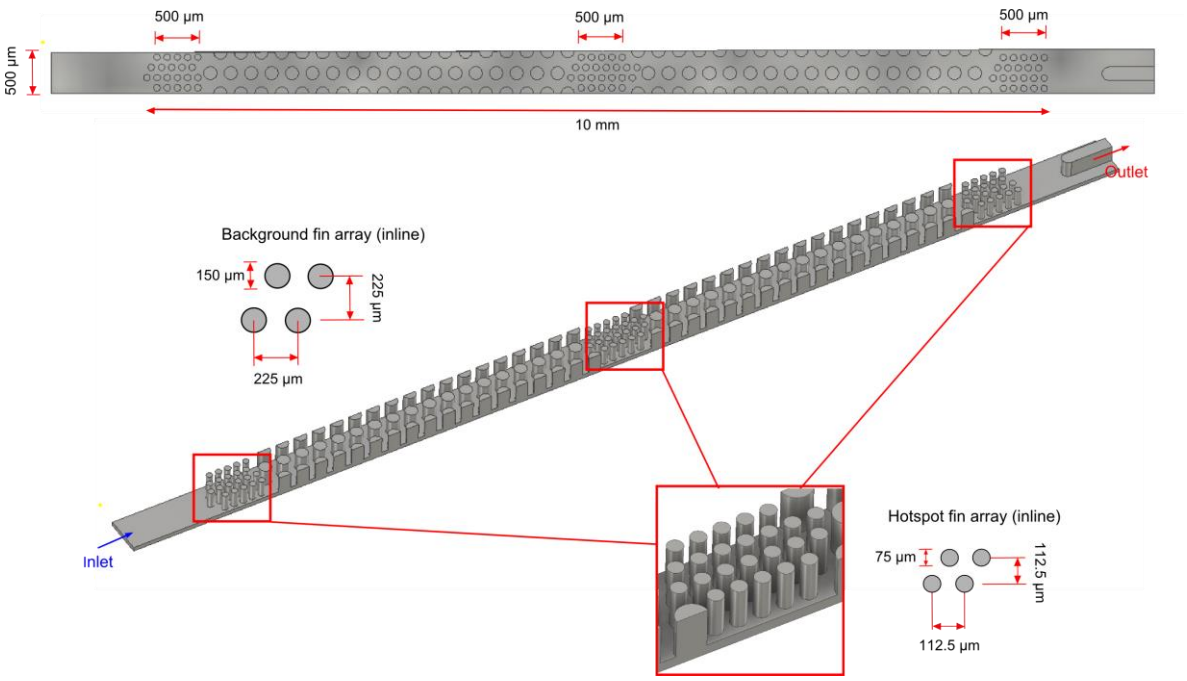


*Fig. 4 Computational domain for the simulation of flow boiling in a silicon microgap with multiple hotspots and variable fin density.*

## REFERENCES

[1] https://www.intel.com/content/www/us/en/silicon-innovations/moores-law-technology.html

[2] W. Arden. M. Brillouët. P. Cogez. M. Graef. B. Huizing. R. Mahnkop, Eds., More-than-Moore White Paper, Downloadable at http://www.itrs2.net/uploads/4/9/7/7/49775221/irc-itrs-mtm-v2_3.pdf, 2010.

[3] C.C. Chi, E.J. Marinissen, S.K. Goel, and C.W. Wu, Post-bond testing of 2.5 D-SICs and 3D-SICs containing a passive silicon interposer base, *In Test Conference (ITC), 2011 IEEE International*, pp. 1-10, 2011.

[4] N.H. Khan, S.M. Alam, and S. Hassoun, System-level comparison of power delivery design for 2D and 3D ICs, *3D System Integration, IEEE International Conference*, pp. 1-7, 2009.

[5] X. Zhang, J.K. Lin, S. Wickramanayaka, S. Zhang, R. Weerasekera, R. Dutta, K.F. Chang, K.J. Chui, H.Y. Li, D.S. Wee Ho, and L. Ding, Heterogeneous 2.5 D integration on through silicon interposer, *Applied Physics Reviews*, 2(2), pp.021308, 2015.

[6] https://www.altera.com/solutions/technology/transceiver/overview.html

[7] Y. Hu, T. Sarvey, M. Bakir, and Y. Joshi, Single phase liquid cooling of hotspots in a heterogeneous pin-fin-enhanced microgap with non-uniform fin array, In 16th IEEE *Thermal and Thermomechanical Phenomena in Electronic Systems (ITherm)*, pp. 500-504, 2017.

[8] Y. Hu, Microfluidic Thermal Management of 2.5D and 3D Microsystems, Ph.D. Dissertation, Georgia Institute of Technology, Atlanta, GA 30332, 2018.

[9] Z. Wan, H. Xiao, Y. Joshi, and S. Yalamanchili, Electrical/Thermal Co-Design of Multi-Core Architectures and Microfluidic Cooling for 3D Stacked ICs", *Proc. of 2013 19th Int. Workshop on Thermal Investigations of ICs and Systems*, pp. 237-242, 2013.

[10] C. Serafy, Z. Yang, A. Srivastava, Y. Hu, and Y. Joshi, Thermoelectric co-design of 3-D CPUs and embedded microfluidic pin-fin heatsinks, *IEEE Design & Test*, 33(2), pp. 40-48, 2016.

# KEYNOTE LECTURES

# Phase-field Modelling and CFD

**Suman Chakraborty**
**Department of Mechanical engineering, Indian institute of Technology Kharagpur, Kharagpur 721302, India**
**E-mail: suman@mech.iitkgp.ac.in**

## Abstract

Phase-field method is a diffuse interface approach which has far-reaching applications in modeling of fluid-fluid interfaces. Not merely restricted to the modelling of simple fluid-fluid interfaces present in multiphase flows, the phase-field method is an important tool for modelling of complex fluid-fluid interfaces such as vesicles and red blood cells. Modelling of fluid-fluid interfaces is challenging due to the moving and deforming nature of the interfaces. The fluid-fluid interfaces can be handled simultaneously with ease and thermodynamic rigour in the paradigm of phase-field method.

Phase-field method replaces the sharp interfaces separating the fluids by a diffuse transition layer where the interfacial forces are smoothly distributed. The diffuse layer in phase-field field method is different from the diffuse layer in VOF or level set method as in the later cases the diffuse layer is an artificial (numerical) transition layer, while the phase-field method introduces diffuse layer from a physical perspective. In sharp contrast to moving mesh methods, the phase-field method automatically captures the fluid-fluid interfaces and thus the explicit tracking of the interfaces and calculation of interface curvature are no longer required. However, one has to solve an extra equation for order parameter. The order parameter is a measure of phase variation which gives the distribution of the participating phases. It is important to note that the order parameter is not arbitrary like the level-set function but can be linked to the physical situation encountered in different phenomena. In sharp contrast to other multiphase methods which uses surface tension forces, the phase-field method is based on free energy of fluids. Phase-field method represents the fluid-fluid interface in terms of a diffuse interface in which the two phases are mixed and store a mixing energy. Simplest form of free energy density for isothermal two-phase system can be constructed by a combination of bulk free energy and gradient free energy. The dynamic evolution of the system (equation for order parameter) can be described by Allen-Cahn or Cahn-Hilliard formulations. Depending on the physical situation, Allen-Cahn or Cahn-Hilliard dynamics can be used to study the following two kinds of problems: (a) Problems related to moving boundary: Phase-field acts as a numerical tool to simulate multiphase flows e.g. Droplet or bubble dynamics. (b) Problems in which the interface profile is of great importance: Phase-field captures microscopic physics on the interface e.g. solidification of alloys, near-critical systems, contact line dynamics. In the later caterogy, the phase-field method gives physically realistic description when the interface width is comparable to the the length scale of the phenomenon. As the phase-field method is based on free energy based formulation, by suitably incorporating different free energies, this method can be used to address biological systems which are inherently driven by gradients of free energies. So, the phase-field method can be effectively used to couple biological systems with transport phenomena.

The lecture will first introduce the speakers to the broad motivation and the fundamental theoretical developments associated with phase field modelling in perspective of CFD applications. Finally, it will aim to outline some typical examples encountered in microfluidics, in order to demonstrate the efficacy of the method.

# Challenges in computation of liquid-metal MHD flow and heat transfer under strong magnetic fields in complex geometries

**Vinayak Eswaran**

Department of Mechanical and Aerospace Engineering, Indian Institute of Technology Hyderabad

Email: eswar@iith.ac.in

Abstract

The talk will be on the experiences of Prof Eswaran's team in developing a numerical code to solve such problems. It will discuss the basic equations and approximations made in liquid metal MHD, the strategies that are used to handle complex geometries, and variable-directional magnetic fields of extremely high strength (Ha ~ 30,000), and finite-thickness walls of variable conductivity, in the context of the design of liquid metal blankets for fusion reactors, as being attempted in the ITER consortium.

Fifth International Conference on Computational Methods for Thermal Problems
THERMACOMP2018, July 9-11, 2018, Indian Institute of Science, Bangalore, INDIA
*N. Massarotti, P. Nithiarasu, Pradip Dutta and C. Ranganyakalu (Eds.)*

# SOLUTION OF INVERSE PROBLEMS FOR THERMAL PROCESSES AND SYSTEMS

**Yogesh Jaluria**
Board of Governors Professor, Mechanical Engineering Department,
Rutgers University, Piscataway, NJ 08854, USA
E-mail: jaluria@jove.rutgers.edu

## ABSTRACT

Inverse problems arise in many practical systems, where the desired result is known but the conditions needed for achieving it are not known. In materials processing, for instance, the temperature cycle to which a component must be subjected in order to obtain desired characteristics through heat treatment is prescribed. However, the boundary and initial conditions are not known and must be determined by solving the inverse problem. The solutions thus obtained are generally non-unique. This paper discusses inverse problems that arise in a variety of practical processes and presents some of the approaches that may be used to obtain results that lie within a small region of uncertainty. Optimization methods that may be used to select locations for experimental data and for reducing the error are presented. A few examples are given to illustrate the applicability of these methods and the challenges that must be addressed in solving inverse problems.

**Key Words:** *Inverse Problems, Unique Solutions, Uncertainty, Practical Systems, Optimization*

## 1. INTRODUCTION

Thermal systems and processes are of considerable interest in a wide variety of important engineering applications, ranging from energy and environment to transportation, heating, cooling and manufacturing. In most problems, the boundary and initial conditions are well defined and the governing equations may be solved by analytical or numerical means to obtain the resulting flow, pressure and temperature distributions from which heat transfer rates may be determined. This is the *forward* or *direct* problem and the literature has extensive results from direct solutions of many different problems of basic or applied interest. However, in many practical situations, the boundary conditions may not be accurately known or defined and the experimental determination of the relevant boundary conditions may be prohibitive in terms of cost and effort. One such circumstance is the optical fiber drawing furnace, where the wall temperature distribution is a critical input to the process, see Figure 1 (a). But this distribution is not easily determined experimentally because of limited access to the furnace and modeling is complicated by the presence of many control and traverse subsystems in the draw furnace. An *inverse* calculation, using the limited temperature data obtained at certain locations may then be employed to determine the wall temperature distribution that gives rise to these data. However, such an inverse calculation generally does not yield unique results and strategies are needed to reduce the uncertainty in the results obtained (Ozisik, 2000).

Similarly, in several thermal processes, the desired result or output is known, but the conditions needed for achieving this are to be determined. This circumstance again leads to an inverse problem. An example of this is the annealing process shown in Figure 1 (b), where the thermal cycle needed to obtain the desired product characteristics are known. But the time-dependent heat input and temperatures are not known and need to be determined by solving the inverse problem. Other processes, such as plastic thermoforming and thermal management of electronic systems, have similar considerations and require an inverse solution to obtain the transport rates that would lead to the desired temperatures within given constraints. The inverse solution is then used to design the appropriate thermal system. This paper discusses the strategies that may be adopted to obtain the

solution to inverse problems with a fairly small region of uncertainty by using optimization techniques.

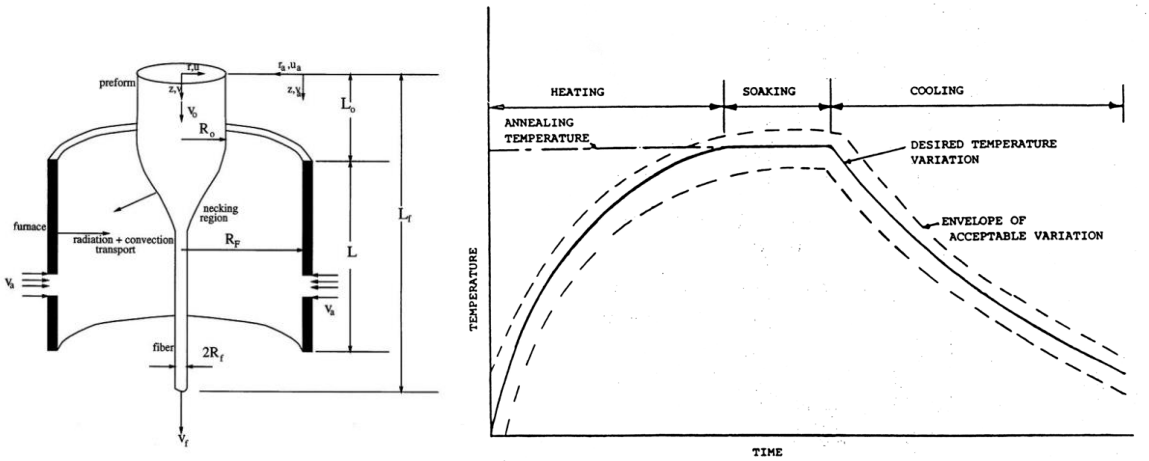


Figure 1. (a) Furnace for optical fiber drawing, indicating the important transport mechanisms; (b) Temperature variation needed for an annealing process

## 2. ANALYSIS

The solution of an inverse problem starts by solving the direct problem at differing parametric values and thus obtaining inverse interpolation functions. These functions are employed to obtain estimates of the missing bounday conditions. Optimization is used to minimize the number of samples or data needed for accurate predictions (Prud'homme and Nguyen, 2001; Orlande, 2012). The optimization process is expected to narrow the domain of uncertainty and ultimately lead to an essentially unique solution of the inverse problem. The basic equations that are used to model the flow and thermal transport in thermal systems are based on the conservation of mass and energy and the force-momentum balance that give rise to the well-known equations for fluid flow and heat transfer. These may be written for a general three-dimensional process as (Burmeister, 1993):

$$\frac{\partial \rho}{\partial t} + \nabla.(\rho \bar{V}) = 0 \tag{1}$$

$$\rho(\frac{\partial \bar{V}}{\partial t} + \bar{V}.\nabla \bar{V}) = \bar{F} - \nabla p + \nabla.[\mu(\nabla \bar{V} + \nabla \bar{V}^{T})] - \frac{2}{3}\nabla(\mu \nabla.\bar{V}) \tag{2}$$

$$\rho C_p(\frac{\partial T}{\partial t} + \bar{V}.\nabla T) = \nabla.(k\nabla T) + \dot{Q} + \mu\Phi + \beta T(\frac{\partial p}{\partial t} + \bar{V}.\nabla p) \tag{3}$$

where $\rho$ is density, $T$ is temperature, $t$ is time, $\bar{V}$ is the velocity vector, $\bar{F}$ is body force, $p$ is pressure, $\mu$ is dynamic viscosity, $C_p$ is specific heat at constant pressure, $\beta$ is coefficient of volumetric thermal expansion, $\mu\Phi$ is viscous dissipation and $\dot{Q}$ is a volumetric heat source. The viscous dissipation and pressure work effects are included in the energy equation, Eq. (3), with the last two terms multiplied by βT representing the pressure effect. The bulk viscosity is taken as zero, giving the second viscosity coefficient λ as – (2/3) μ and Stokes' relationships are used for the viscous forces in the momentum equation, Eq. (2).

These equations can be used to obtain the relevant equations for laminar natural convection induced by a finite heat source over a vertical or horizontal wall, for forced convection from a heat source in a channel and other cases. A turbulence model is required for turbulent flows, which are of interest

in many practical processes such as flow induced by a fire adjacent to a wall or for heat sources and buoyant jets in cross-flow. A wide range of numerical methods are available to solve these equations for different geometries and conditions. A predictor-corrector approach may be adopted to predict the desired conditions and then correct them using an optimization process. Response surfaces and search methods may be used to narrow the domain in which the solution lies.

## 3. RESULTS

Let us first consider the optical fiber drawing furnace shown in Figure 1 (a). An experimental procedure involving axially mounting graphite rods of various diameters and measuring the centerline temperatures is employed. The inverse solution is based on a numerical model for the flow and heat transfer in the furnace and is used to obtain the wall temperature (Issa et al., 1996). Figure 2 (a) shows a sketch of the experimental system. In Figure 2 (b), the measured temperature distribution along the axis of a graphite rod is shown, along with the wall temperature distribution obtained from the solution of the inverse problem. The dashed lines represent the water cooled portion of the furnace cavity. An optimization procedure, based on Lagrange multipliers, is used to narrow the uncertainty in the non-unique solutions and obtain an essentially unique wall temperature distribution. This wall temperature distribution is then used to calculate the graphite rod temperature and a good agreement with the experimental data is observed. The computed maximum heating element temperature was also in good agreement with the furnace control sensor temperature at the hot zone centerline, lending support to the model and the inverse solution.

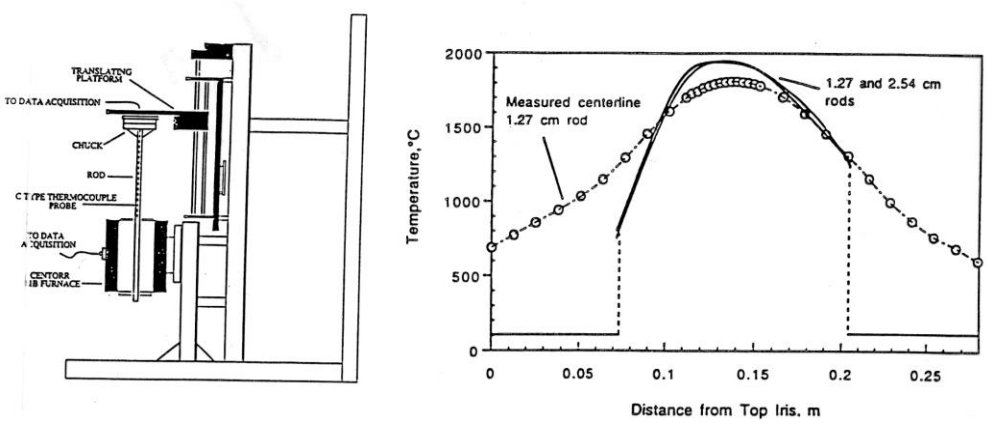


Figure 2. (a) Schematic of an experimental system for measuring the temperature distribution in a rod located axially in an optical fiber drawing furnace; (b) computed furnace wall temperature distributions (solid line) from graphite rod data. Experimental points are for a 1.27 cm diameter rod

A predictor-corrector method is developed to solve the inverse convection problem of a plume or jet in a cross-flow (Vanderveer and Jaluria, 2013, 2015). The inverse problem involves prediction of the strength and location of the heat source by employing a few selected data points downstream. This is accomplished with the help of numerical simulations of the region at differing source strengths and thus obtaining inverse interpolation functions. These functions are employed in the predictor step to determine the source strength. Then, these interpolation functions are used, with adjustments based on the predictor, to determine the source location. Experimental data are then used to determine the strength and location of the source. Optimization of the location of the data points is used to minimize the number of samples needed for accurate predictions. The predictor-corrector method is shown to result in fairly unique solution of the inverse problem. The solution error is found to be less than a few percent. Figure 3 shows comparisons between predicted and actual values for source temperature and jet velocity, indicating good agreement.

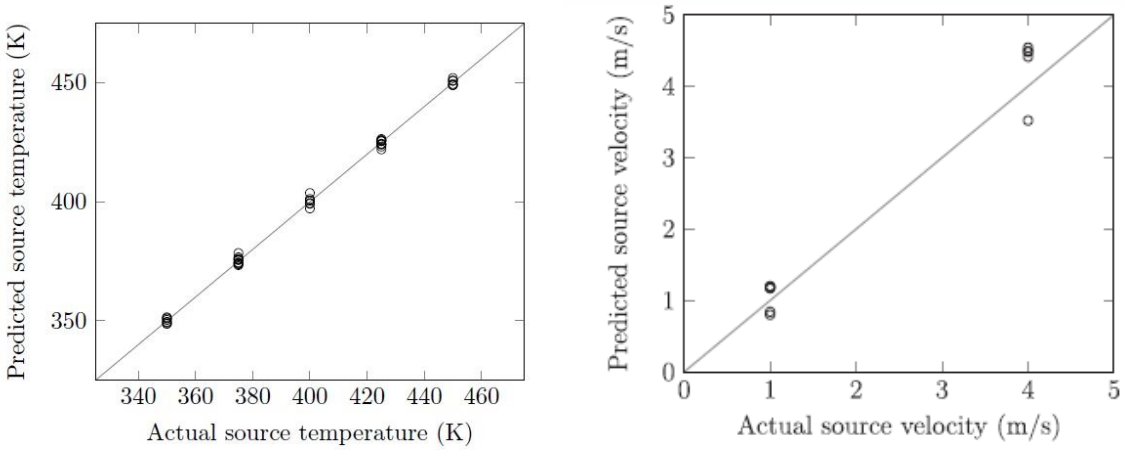


Figure 3. Actual versus predicted source temperature and velocity. (a) heat source; (b) buoyant jet

Similarly, the source and strength of a finite source located on a vertical surface are obtained by an inverse calculation, using data taken downstream of the source. A search based optimization method, particle swarm optimization (PSO), is applied to find the best pair of locations for input of data. The system of equations based on their respective relations is solved to obtain solution to the inverse problem. Figure 4 shows the error resulkting from this inverse calculation.The error in location is found to be greater than that in the source strength, as seen in other cases as well.

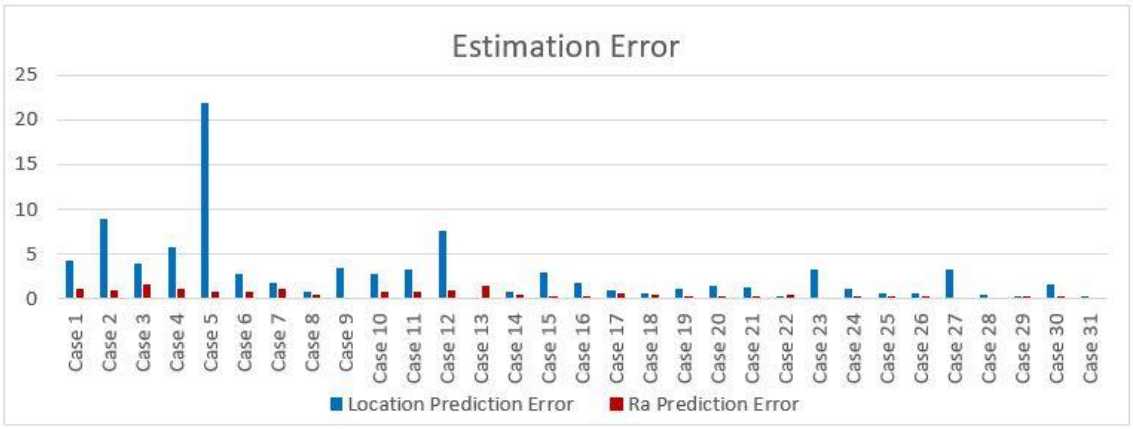


Figure 4. Estimation error diagram for location and source strength, given in terms of the Rayleigh number, Ra

## 4. CONCLUSIONS

The solution of inverse problems, which frequently arise in thermal processes, is discussed. Different strategies to obtain the conditions that lead to a desired result are given. The goal of these approaches is to reduce the uncertainty and obtain essentially unique solutions for different circumstances. The error of the method can be checked against known conditions to see if it is acceptable for the given problem. Several examples are given to illustrate the use of these methods.

## REFERENCES

[1] L.C. Burmeister, Convective Heat Transfer, 2nd Ed., Wiley Interscience, New York, 1993.

[2] J. Issa, Z. Yin, C.E. Polymeropoulos and Y. Jaluria, Temperature distribution in an optical fiber draw tower furnace, *Journal of Materials Processing & Manufacturing Science*, 4, 221-232, 1996.

[3] H.R.B. Orlande, Inverse problems in heat transfer: new trends on solution methodologies and applications, *J. Heat Transfer*, 134, 031011-1-13, 2012.

[4] M. Prud'homme and T.H. Nguyen, Solution of inverse free convection problems by conjugate gradient method: effects of Rayleigh number, *International Journal of Heat And Mass Transfer*, 44, 2011-2027, 2001.

[5] M.N. Ozisik, Inverse Heat Transfer: Fundamentals and Applications, Taylor & Francis, Philadelphia, PA, 2000.

[6] J.R. VanderVeer and Y. Jaluria, Solution of an inverse convection problem by a predictor–corrector approach, *International Journal of Heat and Mass Transfer*, 65, 123-130, 2013.

[7] J.R. VanderVeer and Y. Jaluria, Solution of the inverse jet in a crossflow problem by a predictor–corrector technique, *International Journal of Heat and Mass Transfer*, 89, 929-936, 2015.

Fifth International Conference on Computational Methods for Thermal Problems
THERMACOMP2018, July 9-11, 2018, Indian Institute of Science, Bangalore, INDIA
*N. Massarotti, P. Nithiarasu, Pradip Dutta and C. Ranganyakalu (Eds.)*

# LESSONS FROM ANUPRAVAHA: TOWARDS A GENERAL PURPOSE COMPUTATIONAL FRAMEWORK ON HYBRID UNSTRUCTURED MESHES FOR MULTIPHYSICS APPLICATIONS

**Amaresh Dalal**
Department of Mechanical Engineering, Indian Institute of Technology Guwahati, 781039, India
*Email: amaresh@iitg.ac.in

## ABSTRACT

The indigenous development of a general purpose robust computational fluid dynamics solver, AnuPravaha, has been described for simulations of three-dimensional multiphysics problems. The solver is capable of handling hybrid unstructured meshes in a collocated framework. The pressure-velocity decoupling is avoided using momentum interpolation. The convective terms are calculated using a blend of central and upwind schemes and bounded upwind-biased schemes while the diffusive terms are computed using Green–Gauss reconstruction. The SIMPLE–like algorithm is used to solve the Navier–Stokes equations with a face–based data structure and the momentum, energy and pressure equations are solved using implicit method. The features of the solver have an extensive range to solve complex fluid flows involving turbulence, conjugate heat transfer, species transport, multi-phase flows, electrically charged fluid flows, liquid metal magneto hydro-dynamic flows, radiation in participating medium. The comparison of all test cases with literature is found to be very good. The code with GUI and CGNS format built in has been developed in C++ object oriented language.

The basic solver available with us has the following features.

1. Solves incompressible steady/unsteady flows in two and three dimensions.
2. Laminar and turbulent flows can be simulated. Reynolds-averaged Navier-Stokes equations (RANS) for turbulent flows with different two-equation models namely, κ-ε, κ-ω, Shear Stress Transport (SST) and Lam-Bremhorst models are implemented.
3. Ability to handle arbitrary polyhedral meshes. The solver can handle four types of elements, namely tetrahedrons, pyramids, prisms and hexahedral cells.
4. I/O (Input-Output) operations employ the nearly standardised CGNS file format. This is used both to input grid details into the solver and output the solution from the solver for visualization.
5. Finite volume method with collocated grid arrangement is used to discretize the governing equations with momentum interpolation to avoid pressure-velocity decoupling.
6. The user can solve for velocities, pressure, temperature and miscellaneous scalars.
7. Spatially and temporally varying boundary conditions (Dirichlet, Neumann, Robin and Convective Outflow) with user defined functions are implemented.
8. The user can choose one of the different convective discretization schemes: First order upwind (FOU), Blended scheme between FOU and CDS and bounded upwind-biased schemes (CUBISTA and CUI).
9. Conjugate heat transfer for solving combined heat transfer and fluid flow problems.
10. Natural convective flows at small and large temperature differences using a unified low Mach number algorithm.
11. MHD module with robust approach for high Hartmann numbers.
12. Multiphase flows (Gas-particle, Gas-Gas, Liquid-Liquid) can be simulated for a wide range of density ratios.
13. Radiative heat transfer module with surface-to-surface radiation as well as participating media can be simulated.

14. Depending on the type of problems, the user can choose any one of the four basic algorithms namely, Segregated Fully Implicit Backward Time Central Space Scheme, Coupled Fully Implicit Backward Time Central Space Scheme, Segregated Semi-Implicit Backward Time Central Space Scheme and Coupled Semi-Implicit Backward Time Space Scheme.
15. Efficient solution to linear systems arising from discretized momentum and pressure equations. The user can switch between Gauss-Seidel approach and Krylov solvers implemented via LiS library for this purpose. The latter offers several alternatives and is open source third-party software.
16. User can couple one or more modules to accomplish genuinely multiphysics simulations of interest via UDFs.

Interested readers may refer to the following international journal publications detailing the discussion of specific problems and their numerical simulations using the proposed flow solver.

1. Manik, J., Dalal, A., and Natarajan, G., 2018, "A Parametric Study on the Droplet Detachment Process from the Ceiling Under the Effect of Gravity", Engineering Computations, (In Press).
2. Parmananda, M., Thirumalaisamy, R., Dalal, A., and Natarajan, G., 2018, "Investigations of Turbulence-radiation Interaction in Non-Oberbeck-Boussinesq Buoyancy-driven Flows", International Journal of Thermal Sciences, vol. 134, pp. 298-316.
3. Kotoky, S., Dalal, A., and Natarajan, G., 2018, "Effects of specularity and particle-particle restitution coefficients on the recirculation characteristics of dispersed gas-particle flows through a sudden expansion", Advanced Powder Technology, vol. 29(10), pp. 2463-2475.
4. Parmananda, M., Dalal, A., and Natarajan, G., 2018, "Unified framework for buoyancy induced radiative-convective flow and heat transfer on hybrid unstructured meshes", International Journal of Heat and Mass Transfer, vol. 126, Part B, pp. 908-925.
5. Manik, J., Dalal, A., and Natarajan, G., 2018, "A Generic Algorithm for Three-dimensional Multi-phase Flows on Unstructured Meshes", International Journal of Multiphase Flow, vol. 106, pp. 228-242.
6. Thirumalaisamy, R., Natarajan, G., and Dalal, A., 2018, "A Charge-conservative Approach for Simulating Electrohydrodynamic Two-phase Flows Using Volume-of-fluid", Journal of Computational Physics, vol. 230 (5), pp. 1939-1955.
7. Kotoky, S., Dalal, A., and Natarajan, G., 2018, "A Parametric Study of Dispersed Laminar Gas-Particle Flows Through Vertical and Horizontal Channels", Advanced Powder Technology, vol. 29(5), pp. 1072-1084.
8. Kotoky, S., Dalal, A., and Natarajan, G., 2018, "Effects of Specularity and Particle-particle Restitution Coefficients on the Hydrodynamic Behavior of Dispersed Gas-particle Flows Through Horizontal Channels", Advanced Powder Technology, vol. 29(4), pp. 874-889.
9. Borgohain, P., Choudhary, D., Dalal, A., and Natarajan, G., 2018, "Numerical Investigation of Mixing Enhancement for Multi-species Flows in Wavy Channels", Chemical Engineering & Processing: Process Intensification, vol. 127, pp. 191-205.
10. Parmananda, M., Dalal, A., and Natarajan, G., 2018, "The Influence of Partitions on Predicting Heat Transfer due to the Combined Effects of Convection and Thermal Radiation in Cubical Enclosures", International Journal of Heat and Mass Transfer, vol. 121, pp. 1179-1200.
11. Borgohain, P., Dalal, A., Natarajan, G., and Gadgil, H., 2018, "Numerical assessment of mixing performances in cross-T microchannel with curved ribs", Microsystem Technologies, vol. 24, pp. 1949-1963.
12. Parmananda, M., Khan, S., Dalal, A., and Natarajan, G., 2017, "Critical Assessment of Numerical Algorithms for Convective-Radiative Heat Transfer in Enclosures with Different Geometries", International Journal of Heat and Mass Transfer, vol. 108(11), pp. 627-644.

Fifth International Conference on Computational Methods for Thermal Problems
THERMACOMP2018, July 9-11, 2018, Indian Institute of Science, Bangalore, INDIA
*N. Massarotti, P. Nithiarasu, Pradip Dutta and C. Ranganayakulu (Eds.)*

# MODELLING HEAT TRANSFER IN POWDER BED ADDITIVE MANUFACTURING

**S.G.R. Brown*, A. Giordimaina, A.M. Philo, M.A. Holmes, A.A. Sillars and N.P. Lavery**

Swansea University, College of Engineering, Swansea University Bay Campus, Fabian Way, Swansea, Neath Port Talbot, SA1 8QQ, UK.

* s.g.r.brown@swansea.ac.uk

## ABSTRACT

One of the most important ingredients in a numerical model of Additive Manufacturing (AM) is a heat transfer model. On its own this is challenging enough as conductive, convective and radiative heat transfer mechanisms are all important, coupled with liquid/solid phase changes. For metals and alloys the process is also inherently multiscale – a perennial problem in materials science. Furthermore, heat transfer is only the first step to predict different phenomena of interest including metallurgical microstructure, defects and thermal stresses to name. This paper briefly touches on several of these areas, all of which merit concerted effort by the modelling community.

**Key Words:** *Heat Transfer, Powder Bed Fusion, Additive Manufacturing.*

## 1. INTRODUCTION

For metals both conventional casting and AM processes involve melting and solidification. They share some problems (e.g. porosity, thermal stress, multiscale) but AM brings a new set of problems (e.g. vaporization/keyholing, spatter, much smaller scale fluid flow, powder shape/size distribution or PSD effects). Furthermore, the technology of AM machines is constantly changing; probably more so than casting on top of which specific new alloys for AM will inevitably emerge. Commercial AM codes are still under development. As is the case for casting there is always a play off between accuracy and industrial usefulness. Heat transfer modelling is a key ingredient in these models for prediction of quantities of interest.

## 2. KEY PHENOMENA IN BRIEF

The principal heat transfer effects in AM include conductive (within the melt pool and into the surrounding powder) convective (within the melt pool but also protective gas flows over the bed) and radiative (laser heating of the powder and radiation effects within the powder [1]). Use of incorrect machine settings for laser speed and/or laser power can lead to ‘keyholing’ and vaporisation and spatter or alternatively insufficient melting (Figure 1) [2]. PSD effects, granular flow of powders (Figure 2), thermal stresses and distortion all conspire together to complicate the process further [3-5]. Some representative results are shown below based on Powder Bed Fusion (PBF) of metallic powders using Renishaw AM250, AM400 and AM500 machines.

## 3. SOME RESULTS

Modelling at the powder level can provide fine scale predictions of melting and solidification [3, 6]. Results from such models can then provide a basis for meso structural modelling (i.e. grains) [7]. Experimentation to validate such models can be provided by experiment e.g. a recent crucible experiment design [8] where several crucibles are built, varying powder depth and laser

speed/power (Figure 3), to construct process maps and investigate melting/defect effects (Figures 4 and 5).

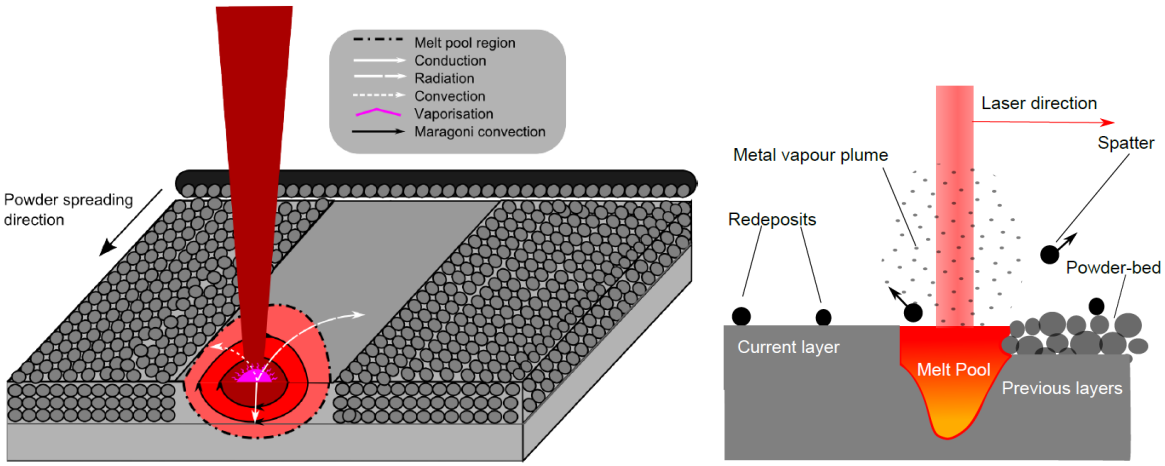


FIGURE 1. Schematic showing Left) physical phenomena inherent within the laser powder bed fusion process and Right) the potential by-products in the PBF process [2].

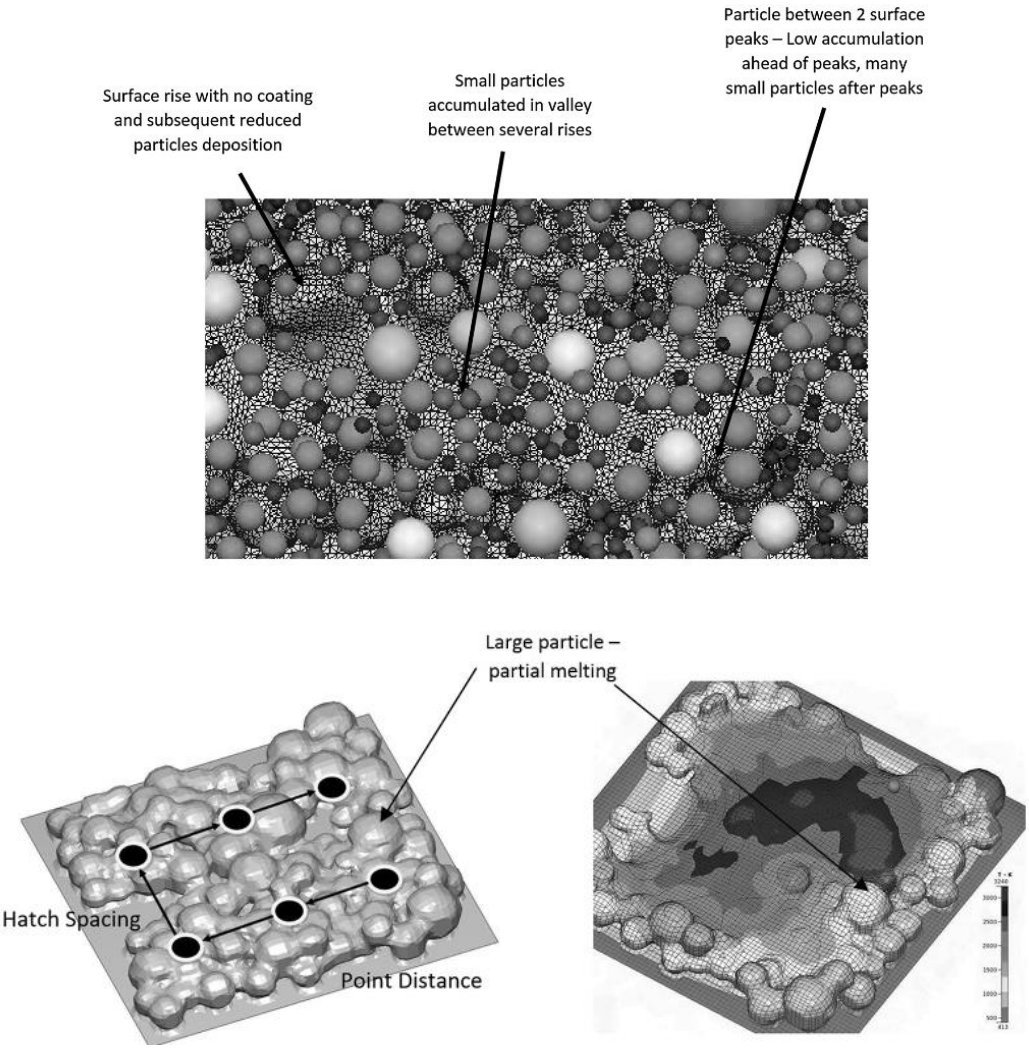


FIGURE 2. Top) Powder layer spread on previously processed surface, Bottom left) laser hatch pattern processing strategy, Bottom right) final surface shape after processing [3].

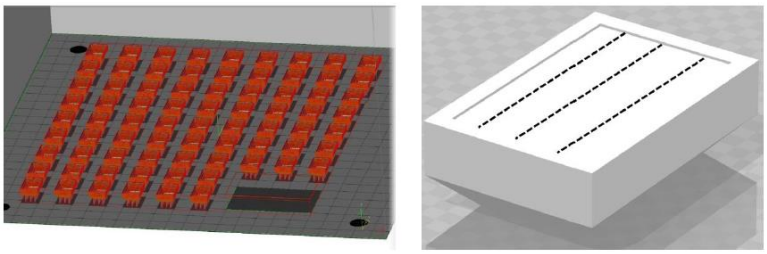

FIGURE 3. Left) CAD drawing of crucibles on base plate used during an experiment, Right) Three single track structures placed at the top of the crucibles [8].

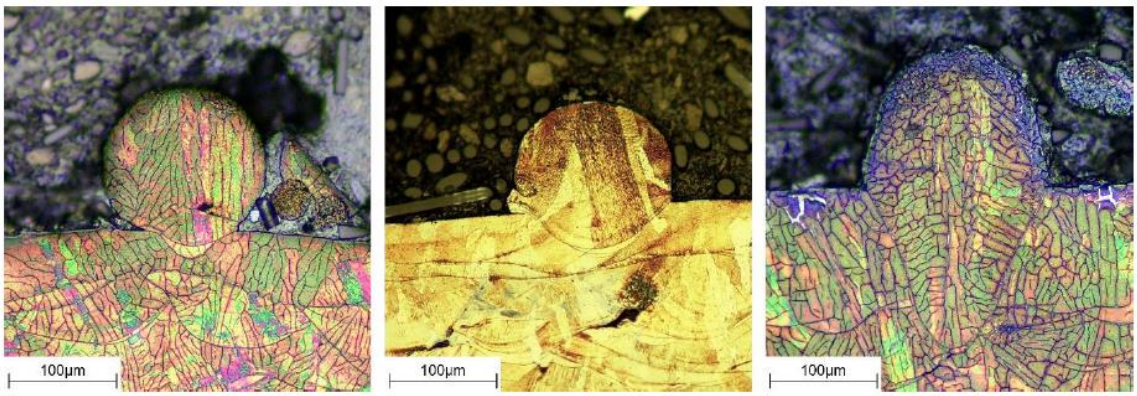


FIGURE 4. Representative results for stainless steel (SS316L) - The three types of tracks formed for laser powers and speeds of Left) insufficient melting 200W, 700mms$^{-1}$, Middle) optimal conduction mode 150W, 300 mms$^{-1}$, Right) keyholing 175W, 200mms$^{-1}$ [8].

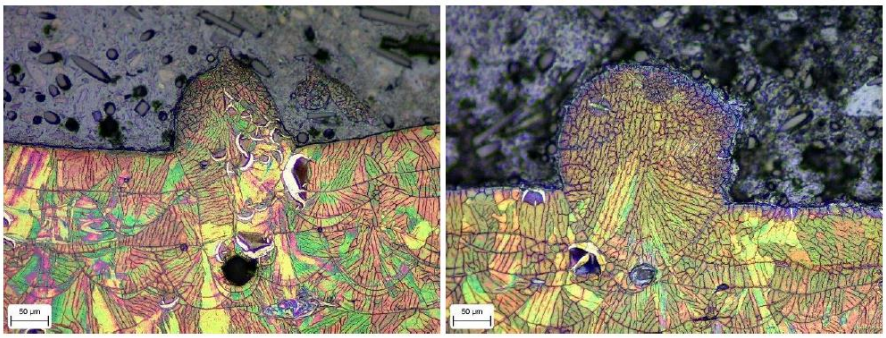

FIGURE 5. (SS316L) – Typical keyhole porosity observed for stainless steel (SS316L) for laser powers and speeds of Left) 200W, 300mms$^{-1}$, Right) 175W, 100mms$^{-1}$ [8].

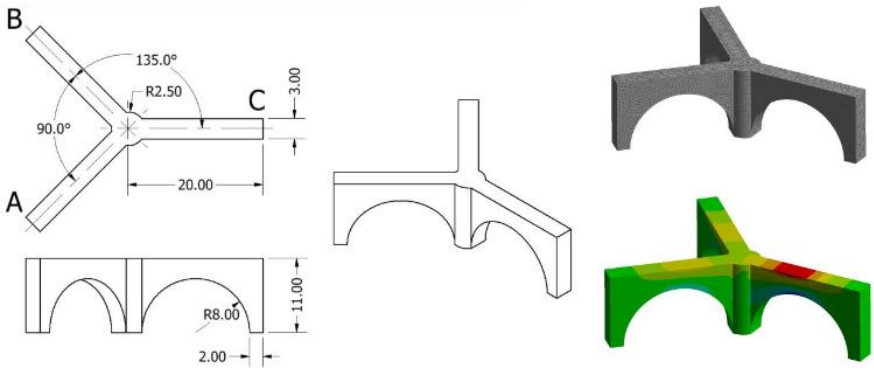


FIGURE 6. Three Prong Method Component Dimensions, Mesh and Stress Analysis [10].

The likelihood of insufficient melting, optimal (conduction mode) melting and unwanted high penetration (keyhole) melting can be determined (Figure 4 left, middle, right respectively). Certain defects (e.g. porosity associated with keyholing) can also be identified (Figure 5) along with grain structures for meso scale grain model validation. However, powder scale models are less useful when dealing with component scale problems such as thermal stress. Simplified macro models are more likely to be useful which exploit continuum approximations to the powder bed [e.g. 2, 9]. Experimental measurement of thermal stresses arising in PBF is also a work in progress for researchers in this field (e.g. Figure 6) [10].

Finally, and returning to the very first sentence, the modelling of casting processes has evolved over several decades [e.g. 11] and yet still engages many researchers in further development. Modelling of AM processes has benefited from this related body of work but is yet to reach the same level of commercial applicability. A predictive capability for microstructure/defect evolution, macro scale thermal stress phenomena, all packaged into a closed-loop control system for AM machines to ensure process optimization and reproducibility, is the ultimate goal [12].

## 4. CONCLUSIONS

There are significant opportunities for the development of new models for additively manufactured components. These components exhibit very different structures from conventionally cast materials and the side-effects of laser processing are many and varied. Numerical models to link processing parameters to material performance are at a fairly early stage of development and are highly dependent on sound thermal models. Realization of such models would significantly enhance future innovation in this rapidly developing field and as such represent a rich field of study for modellers.

## REFERENCES

[1] A. V. Gusarov, I. Yadroitsev, Ph. Bertrand and I. Smurov, J. Heat Transf. (2009) 131(7).

[2] A.M. Philo, *Development of Multi-scale and Multi-physical Models of the ALM Process*, EngD Thesis, Swansea University, UK, 2018.

[3] H.W. Mindt, M. Megahed, N.P. Lavery, M.A. Holmes, and S.G.R. Brown, Metall and Mat Trans A (2016) 47: 3811-3822.

[4] R. Martukanitz, P. Michaleris, T. Palmer, T. DebRoy, Z-K. Liu, R. Otis, T.W. Heo, L-Q. Chen, Addit. Manuf. (2014) 1: 52–63.

[5] M.M. Francois et al, Curr. Opin. Solid State Mater. Sci. (2017) 21: 198-206.

[6] S.A. Khairallah, A.T. Anderson, A. Rubenchik, W.E. King, Acta Mater. (2016) 108: 36-45.

[7] J.A. Koepf, M.R. Gotterbarm, M. Markl and C. Körner, Acta Mater. (2018) 152: 119-126.

[8] A. Giordimaina, *Physical Verification of the Melt Pool in Laser Powder-Bed Fusion for Computational Validation*, EngD Thesis, Swansea University, UK, 2018.

[9] M. Megahed, H.W. Mindt, N. N'Dri, H. Duan and O. Desmaison, Integrating Materials and Manufacturing Innovation, (2016) 5:4, 33 pages.

[10] S.A. Sillars, C.J. Sutcliffe, A.M. Philo, S.G.R. Brown, J. Sienz and N.P. Lavery, Virtual and Physical Prototyping (2017), 13:1, 20-25.

[11] D. Stefanescu, *Science and Engineering of Casting Solidification, Second Edition*, (2009) Springer US.

[12] M. Markl and C. Körner, Annu. Rev. Mater. Res., (2016) 46: 93-123.

# ALL ABSTRACTS

Fifth International Conference on Computational Methods for Thermal Problems
THERMACOMP2018, July 9-11, 2018, Indian Institute of Science, Bangalore, INDIA
*N. Massarotti, P. Nithiarasu, Pradip Dutta and C. Ranganyakalu (Eds.)*

# COOLING PERFORMANCE ANALYSIS OF LOOP HEAT PIPE USING NANOFLUID

**A. Arora, R. C. Gupta**
Department of Mechanical Engineering, Jabalpur Engineering College, Gokalpur, Jabalpur-482011, Madhya Pradesh, India, aroraashish892@gmail.com

**M. S. Lodhi**
Discipline of Mechanical Engineering, PDPM Indian Institute of Information Technology, Design and manufacturing, Dumna Airport Road, Dumna Jabalpur-482005, Madhya Pradesh, India, s.mangal@iiitdmj.ac.in

## ABSTRACT

The paper presents a numerical study to evaluate the cooling performance of Loop Heat Pipe (LHP) using nanofluid. The 3-D numerical model is developed and solved by Volume of Fluid (VOF) model by using commercial software ANSYS FLUENT 16.1. The computation simulation is performed at constant heat flux applied to the evaporator section. The main aim of the study is to predict thermal behaviour of $Al_2O_3$ / *water* nanofluid in Loop Heat Pipe used as a coolant.

**Key Words:** *Cooling performance, Loop Heat Pipe, Nanofluids*

## 1. INTRODUCTION

The heat load of modern electronic devices has increased in recent years, as it becomes small and denser. This induces thermal stresses in such devices, leading to failure in the components and thus require thermal management to improve reliability and prevent premature failure. Loop heat pipes (LHPs), which have exceptionally efficient heat-transfer features, are regarded as one of the promising solutions to this problem [1]. The loop heat pipe comprises a evaporator and a condenser, as in conventional heat pipes, but differ in having separate vapour and liquid lines. As the modern electronic devices are very compact now-a-days, and to dissipate heat from such devices we require a micro dimension heat pipe cooling system. Therefore, in our study we use micro loop heat pipe as a cooling system for such smaller, denser and compact devices. The objective of this work is to study the micro loop heat pipe using ANSYS 16.1. A model is produce for analysis of effect of aluminium oxide nanofluid on micro loop heat pipe regarding temperature and heat flux.

## 2. MATHEMATICAL MODELLING

The computational domain, which is used to simulate the Loop Heat Pipe is shown in Fig. 1.

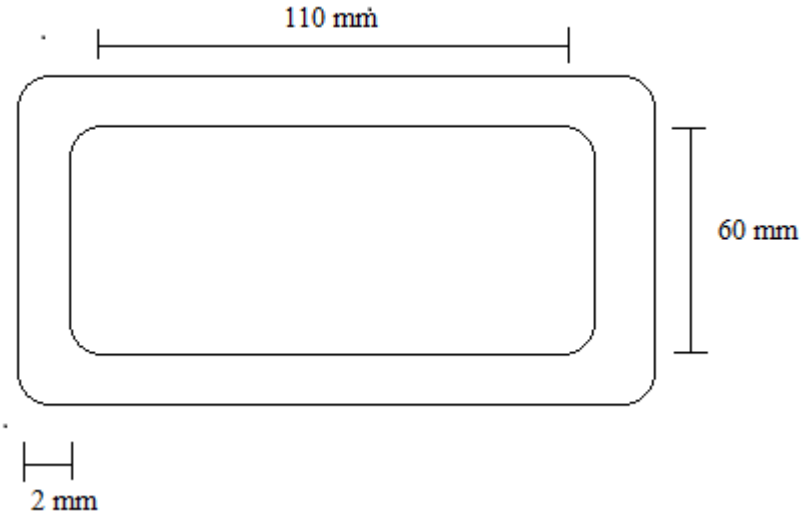


FIGURE 1. Schematic of computational domain

| Specification | Dimension (mm) |
|---|---|
| Evaporator | 60 |
| Liquid Line | 110 |
| Vapour Line | 110 |
| Condenser | 60 |
| Diameter of LHP | 2 |

TABLE 1. Specification of Loop Heat Pipe

## 3. RESULTS AND DISCUSSIONS

The model is analysed by providing heat flux of 20 W at evaporator section. The motion of all phases is modelled by solving a single set of transport equations with appropriate jump boundary conditions at the Interface. The VOF model can model two or more immiscible fluids by solving a single set of momentum equations and tracking the volume fraction of each of the fluids throughout the domain.

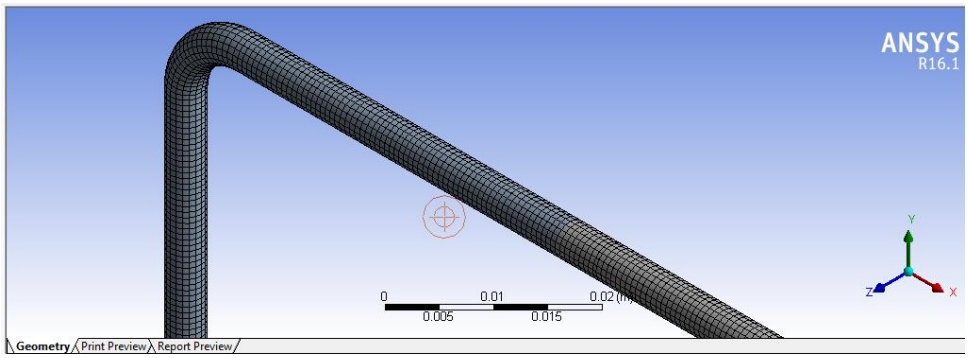


FIGURE 2: A small section of geometry mesh

A mesh is generated as shown in figure above, which is a very fine mesh , helps to analyse our cooling performance characterstics of our model. This is a pre-processing task among three modeling process in CFD software.

After meshing sets up the equations and solves them to compute the flow field. This is the second modeling process which is called as solver, in which we defines the material properties, prescribed boundary conditions such as gives 50000 W/m$^2$ heat flux at evaporator section and ambient temperature of 300 K at condenser section. Also initialize the operating conditions and to calculate our problem, number of time steps provide and iterate the solution at this time steps.

The post-processor is the last part of CFD software, which helps to analyse the results and get useful data. Some of the result that we get as shown below.

For water as working fluid,the below figure 3(a) shows the temperature contour at 50000 w/m$^2$ heat flux:

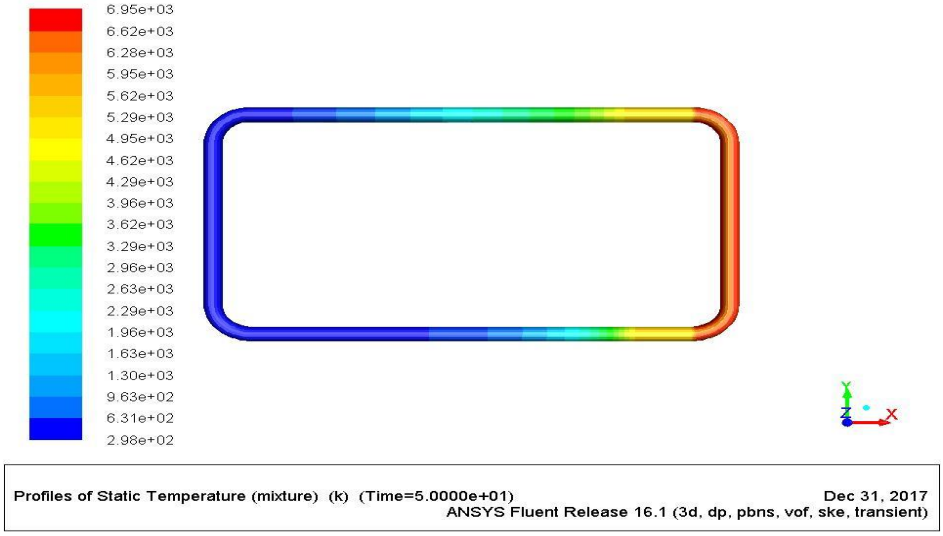


Figure 3(a)

For nanofluid as working fluid,the below figure 3(b) shows the temperature contour at 50000 w/$m^2$ heat flux:

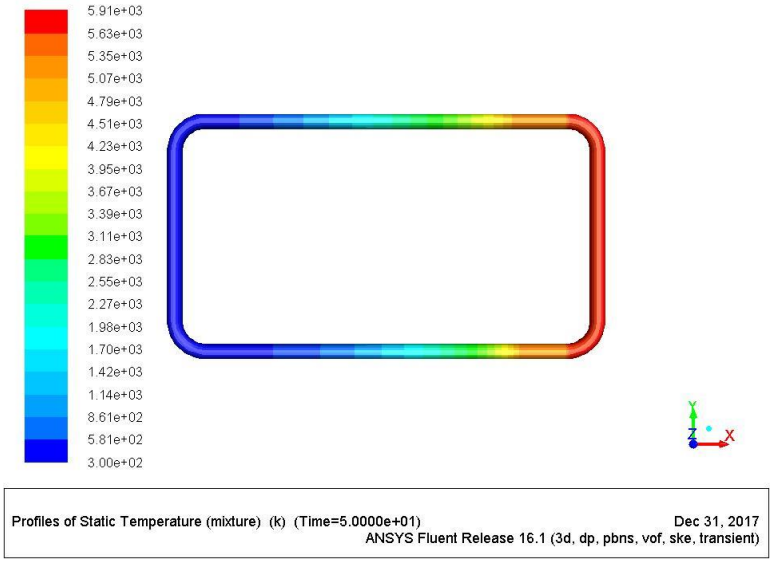


Figure 3(b)

## 4. CONCLUSIONS

From above results we conclude that temperature varies as we use different working fluids which effect the cooling performance of electronic devices.also nanofluid as working fluid gives best result for cooling performance as compare to water as working fluid.

## REFERENCES

[1] Y. F. Maydanik, S.V. Vershinin, M. A. Korukov, J.M. Ochterbeck, Miniature Loop Heat Pipes- A Promising Means for Cooling Electronics, IEEE T Compon Pack T, 28 (2005) 290-296.

[2] Cotter, T. P. " Principles and Prospects of Micro Heat Pipes", Proceedings of the 5th International Heat Pipe Conference, TaTech, Tokyo, 1984, pp. 328-335.

# Flow Passage Design for Thermal management of Li-ion battery

**S. Abdullah, Yasser Rafat**
Department of Mechanical Engineering
ZHCET, AMU, Aligarh, shekhabdullah@zhcet.ac.in

## ABSTRACT

The automotive industry is gradually shifting towards electric and hybrid vehicles which calls for the need of research in Battery Thermal Management System(BTMS). The two main variants of batteries that are of prime importance are Li-ion and Lead-Acid. Former have a higher energy density, which makes them more suitable for portable applications. Furthermore, they offer a 40-50% weight reduction and 20-30% volume reduction. The major obstacle in their usage is large heat generation during operation. Hence, there is a need for an efficacious thermal management system. Present work targets on making the BTMS using air cooling more effective by optimizing the channel shape from which the coolant flows. The numerical simulations were performed using the commercial code Fluent®. The efficacy of different optimized channel shape was studied at different values of Reynolds Number (Re) based on channel inlet length. There was a reduction in maximum temperature of the battery by **1 °C** when Reynolds number was increased from 169 to 338 The optimized channel shapes further brought down the maximum temperature by up to 3°C throughout the length of channel thereby bringing the battery in its favorable working condition.

**Key Words:** *Heat Transfer, PCM, Finite Volume*

## 1. INTRODUCTION

The concern about global warming and its impact is rising. The burning of fossil fuels is responsible for global warming, which results in the emission of CO, NOx, SOx, CO2, and HC. We rely on coal, oil, and gas for over 80% of our current energy needs [1]. The tremendous risk of climate change associated with the use of fossil fuels makes supplying this energy increasingly difficult. These global energy crises drive the adoption of electric vehicle in market. Electric vehicles provide a sustainable solution to avoid the issue of global warming. But electric vehicle energy storage is quite immature due to poor performance and long energy conversion time. Growing demand for advance energy storage (AES) and power management system drives the Li-ion battery market today. The popularity of Li-ion battery has increased due to the fact that they possess higher volumetric and gravimetric energy density. Li-ion batteries have many advantages for electric vehicles but it is very sensitive to temperature. Much research has been done so for forced cooling using different Reynolds number. Xun et al.[2] did numerical modeling regarding cooling capability of cylindrical cell. Increasing Reynolds number lead to decrease of temperature on surface but at very high Reynolds number, a non-uniform temperature distribution was found. K.Yu et al.[3] designed two directional air flow system for enhancing air cooling efficiency in the middle cell. X.M. et al [4] studied heat dissipation performance by forced air. Fan et al. [5] used prismatic cell to study cooling capability using different channel size to optimize its width and they found that optimize channel size was 3mm. The present work uses the same optimized channel size with the use of various obstructions in the channel for the enhancement of the heat transfer. Various post-processing analysis will be done to evaluate the possible mechanism behind the enhancement of heat transfer rate which shall be covered in the final paper.

## 2. VALIDATION AND PROBLEM FORMULATION

To validate the numerical scheme used in the current solver, the three -dimensional domain similar to that used by Fan et al. was simulated under similar boundary conditions. The simulation results clearly showed that the present schemes yielded the solution in close approximation with that of Ref. 5. The same numerical methodology was later used to perform the simulations.

In present study, we have used the rectangular domain whose dimensions are shown in Figure 1.

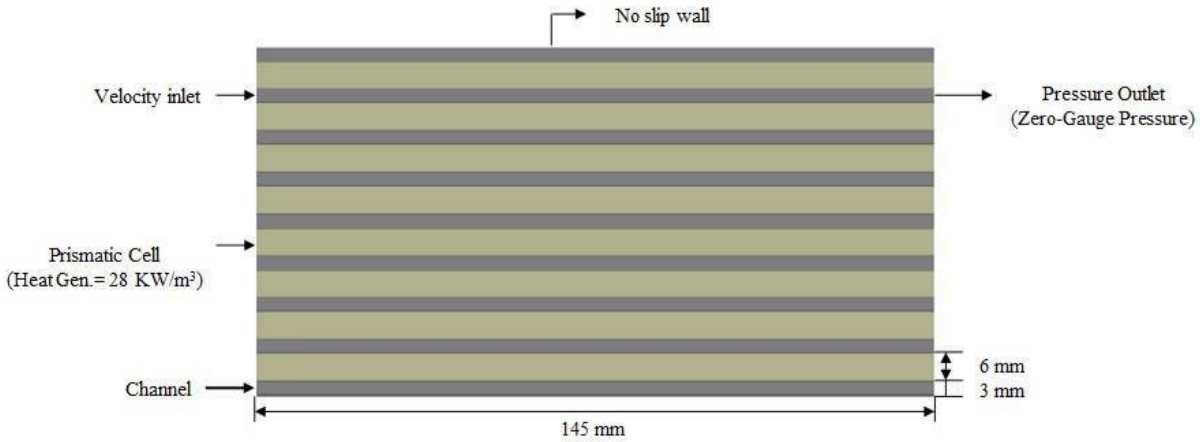


FIGURE 1. Computational domain and boundary conditions

For the purpose of reducing the temperature of the cell, three different cases (where obstructions in the flow passage was introduced) was compared with that of uncontrolled case (Case-1). The cases have been shown as under:

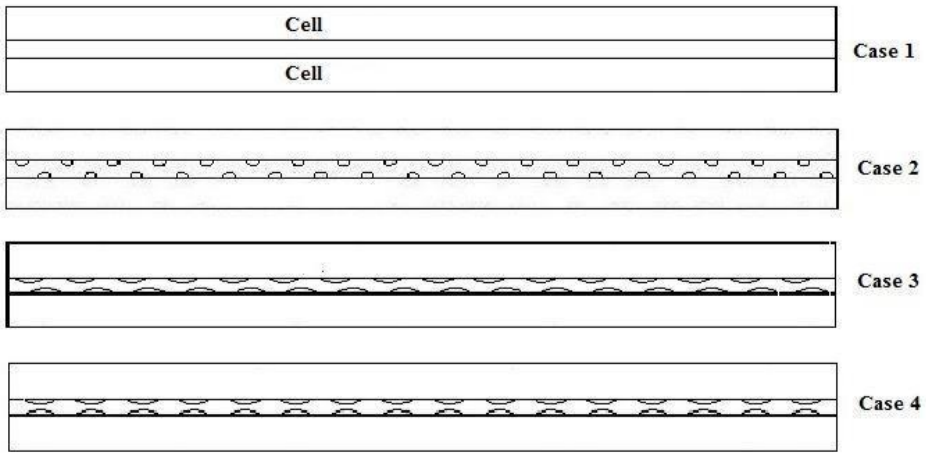


FIGURE 2. Various Case Setup for enhancement of Heat Transfer

## 3. RESULTS

**Spatial variation in temperature**

Figure 3 depicts the variation of temperature of the cell along its axial location (Battery central aixs) at t=1500s for Re=169 and Re=338.

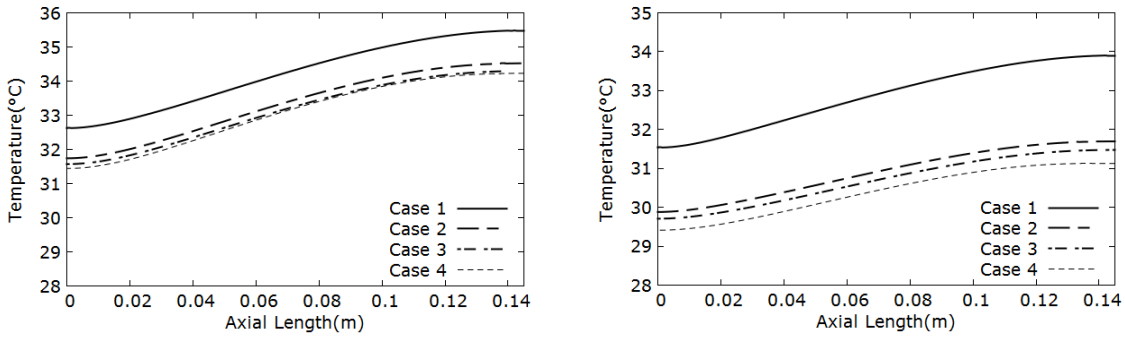


FIGURE 3. Variation of temperature along axial length of central at (a) Re=169 and (b) Re=338

**Temporal variation of temperature**

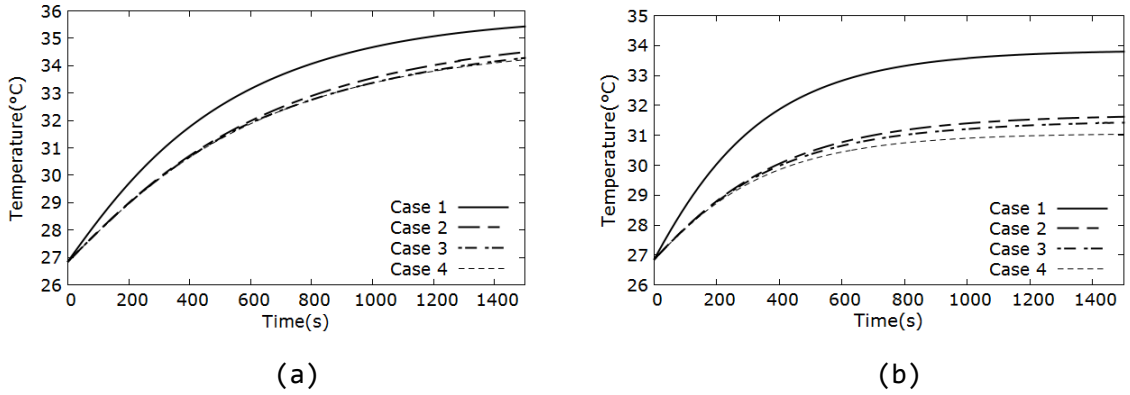


FIGURE 4. Variation of temperature at the central battery surface with time for (a) Re=169 and (b) Re=338

Figure 4 shows that the comparison of temporal variation of maximum cell temperature at outlet. The plots clearly show that the effectiveness of the cases was in order Case 4>Case 3>Case 2>Case1.Figure 4 clearly shows that the temporal difference of temperature was very nominal (<1.5 °C) till the end of 400s. This difference increased to about 3 °C at the end of 1500s hinting at the efficacy of the control strategies for large period of operation. It can be seen that the steady state for the case 1 is achieved by t=1400s, while in case 4 it was already achieved near t=900s.

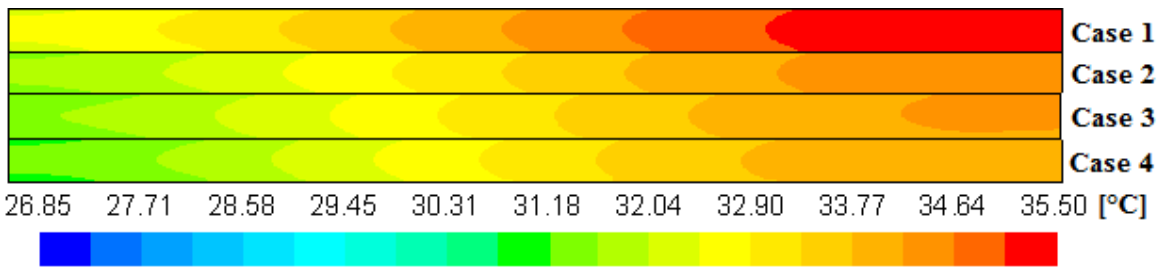


FIGURE 5. Comparison of cell temperature for all cases studied at Re=169 in °C

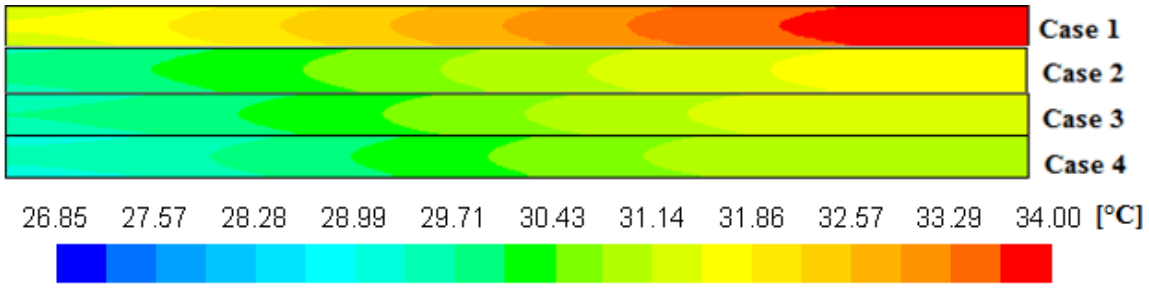


FIGURE 6. Comparison of cell temperature for all cases studied at Re=338 in °C

The temperature contour clearly shows that the maximum temperature attained near the outlet of the cell has reduced substantially with the use of modified passages. The maximum decrease of the peak temperature was in the case 4 as can be seen from figure for Re=169 and Re=338 after 1500s.

## 4. CONCLUSIONS

The present work is aimed at introducing cost effective thermal management systems for the battery of the electric vehicles. The strategy of increasing of Reynolds Number increase was effective but that method caused more of the power of the battery to be used in its cooling. The second strategy was to increase in mixing in flow channel where air as a coolant would flow which will increase convective heat transfer. The initial method used was that of semicircle shaped obstruction. This showed an enhancement of cooling performance. The average temperature of the battery was brought down from 35.14 °C to 33.8 °C and the high temperature regime of cell no 4 which was at central axial location of the channel shifted towards the outlet.

## REFERENCES

[1] John Browne; Proposal - the energy crisis and climate change. Report, 2009.

[2] Jingzhi Xun, Rui Liu, and Kui Jiao. Numerical and analytical modeling of lithium ion battery thermal behaviors with di_erent cooling designs. Journal of Power Sources, 233:47-61, 2013.

[3] Kuahai Yu, Xi Yang, Yongzhou Cheng, and Changhao Li. Thermal analysis and two-directional air ow thermal management for lithium-ion battery pack. Journal of Power Sources, 270:193-200, 2014.

[4] XM Xu and R He. Research on the heat dissipation performance of battery pack based on forced air cooling. Journal of Power Sources, 240:33-41, 2013.

[5] Liwu Fan, JM Khodadadi, and AA Pesaran. A parametric study on thermal management of an air-cooled lithium-ion battery module for plug-in hybrid electric vehicles. Journal of Power Sources, 238:301-312, 2013.

# HYDROGEN JET AUTOIGNITION IN A CO-FLOW AND IN A WAKE OF HEATED AIR

**Abhijit Kalbhor, Arnab Moitro, Swetaprovo Chaudhuri**
Department of Aerospace Engineering, Indian Institute of Science, Bangalore 560012, India
abhijitkalbhoriisc@gmail.com, arnabmoitro@gmail.com, schaudhuri@iisc.ac.in

**Lazar Chitilappilly**
Vikram Sarabhai Space Centre, Indian Space Research Organization, Thiruvananthapuram 695022, India. lt_chitilappilly@vssc.gov.in

## ABSTRACT

Direct Numerical Simulations (DNS) coupled with detailed chemical kinetics are used for a comparative study on the autoignition characteristics of a laminar hydrogen-nitrogen ($H_2$-$N_2$) jet issued into i) co-flow of heated air ii) wake of heated air. Detailed analysis of the autoignition chemistry and the relative roles of certain radical species in the initiation of autoignition process in these non-premixed jets is investigated by tracking the evolution of important chain reactions using a Lagrangian particle tracking approach. The reaction $H_2 + O_2 \rightleftarrows HO_2 + H$ is recognized to be the dominant chain initiation reaction during pre-ignition stage. The autoignition process is found to be marginally accelerated for higher jet velocity ratios in both the non-premixed configurations under the study.

**Key Words:** *Direct Numerical Simulations, Auto-ignition, Hydrogen.*

## 1. INTRODUCTION

In high-speed combustion systems, where non-premixed flame configurations are adopted, the fuel jet mixes with the fast flow of hot oxidizer and auto-ignites forming lifted jet flames or stabilize adjacent to the recirculation zones containing combustion products, in the wake of a flame-holder. Over the past several years, these non-premixed jet flames have been studied towards understanding the inherent mechanisms of auto-ignition and flame stabilization, through experimental and computational approaches. However, the role of large-scale flow structures in imparting molecular level mixing and influencing auto-ignition process in these flames has not been understood effectively and requires further attention. Furthermore, the question of the dominant chain initiation reaction in the auto-ignition of non-premixed hydrogen-air mixtures has not been resolved completely.

In the present work, a comparative study examining ignition dynamics has been conducted in two non-premixed flame configurations i) central fuel jet issued into a co-flowing heated oxidizer ii) central fuel jet injected from the bluff body base into a fully developed wake. Furthermore, to investigate the dominant chain initiation reaction/s in both the configurations, the reaction rate kinetics prior to auto-ignition are examined, using Lagrangian particle tracking approach. Given the importance of mixing triggered by large-scale flow structures, the influence of variation of jet velocity on scalar mixing and ignition behaviour is also studied for the jet in wake configuration.

## 2. COMPUTATIONAL METHODOLOGY

Two basic configurations were studied in a two-dimensional computational domain, extending to $30D_j$ in the streamwise ($x$) and $10D_j$ in the spanwise ($y$) directions with a fuel jet width of $D_j$ = 0.1cm. The fuel stream consisting of $H_2$-$N_2$ (30%-70% by volume), was issued from the central jet, with

velocity $U_j$ = 60 m/s at temperature of $T_j$ = 310 K into surrounding co-flow and into the wake of heated air flowing with velocity $U_c$ = 20 m/s at 1000 K. Figure 1 shows the corresponding schematic of the problem configuration for both the cases. At the inlet boundary, 'hyperbolic tangent' profiles were provided for velocity and reactive scalars (temperature and species mass fractions) to mimic bluff body of dimension ($D = 2D_j$). Direct Numerical Simulations were performed using open source DNS solver PENCIL CODE [1]. Navier-Stokes characteristic boundary conditions were used in the streamwise direction and the Periodic boundary conditions were assigned in spanwise directions. The minimum spatial resolution of 34.7 µm was provided and a solution was advanced at a constant time step of 20 ns. The detailed hydrogen-air kinetic mechanism suggested by Li et al. [2] was used for combustion related computations and the important elementary reactions are specified in Table 1.

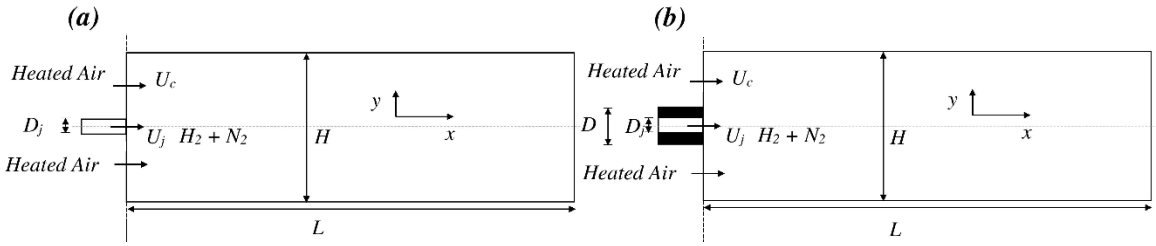


FIGURE 1. Problem configuration with relative dimensions. (a) Jet in a co-flow (b) Jet in a wake

## 3. RESULTS

In Fig. 2, the auto-ignition of hydrogen jet injected into co-flow and into the fully developed wake of hot air is indicated by the development of temperature hotspots. The hot oxidizer mixes with the central fuel jet along the shear layers, and the auto-ignition reactions initiate outside the shear layer at a downstream location. After commencement of ignition, a diffusion flame propagates towards fuel-rich regions while moving upstream along the shear layers. In wake environment, a diffusion flame stabilizes in the close vicinity of the bluff body within the rolled up vortex regions due to strong shear layer interactions. Next, to understand the effects of variation of jet injection velocity on the auto-ignition characteristics, simulations were performed for three different jet velocity values, namely 20 m/s, 40 m/s and 60 m/s. The co-flowing wake velocity and temperature were maintained constant. From the instantaneous temperature contours, as shown in Fig 3, it is indicated that, with the increase in jet velocity, the auto-ignition initiates slightly earlier time.

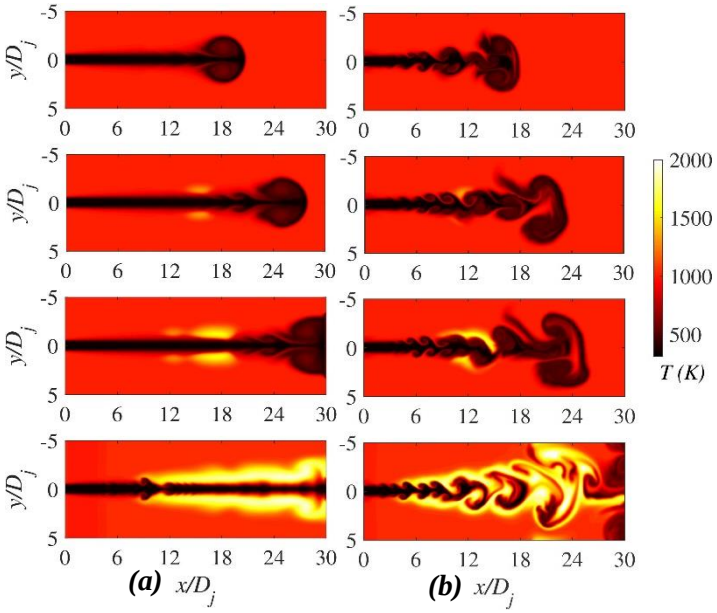


| Reaction | |
|---|---|
| $H + O_2 \leftrightarrow O + OH$ | $(R1)$ |
| $O + H_2 \leftrightarrow H + OH$ | $(R2)$ |
| $OH + H_2 \leftrightarrow H + H_2O$ | $(R3)$ |
| $OH + OH \leftrightarrow O + H_2O$ | $(R4)$ |
| $H_2 + M \leftrightarrow H + H + M$ | $(R5)$ |
| $O_2 + M \leftrightarrow O + O + M$ | $(R6)$ |
| $H + O_2 + M \leftrightarrow HO_2 + M$ | $(R9)$ |
| $H + HO_2 \leftrightarrow H_2 + O_2$ | $(R10)$ |
| $HO_2 + H \leftrightarrow OH + OH$ | $(R11)$ |
| $HO_2 + O \leftrightarrow OH + O_2$ | $(R12)$ |

TABLE 1. Important elementary chemical reactions from Li et al. [2]

FIGURE 2. Instantaneous temperature contours for (a) Jet in a co-flow (b) Jet in a wake taken at interval $t$ = 0.5 ms, 0.675 ms, 0.75 ms, 1.0 ms (from top to bottom respectively)

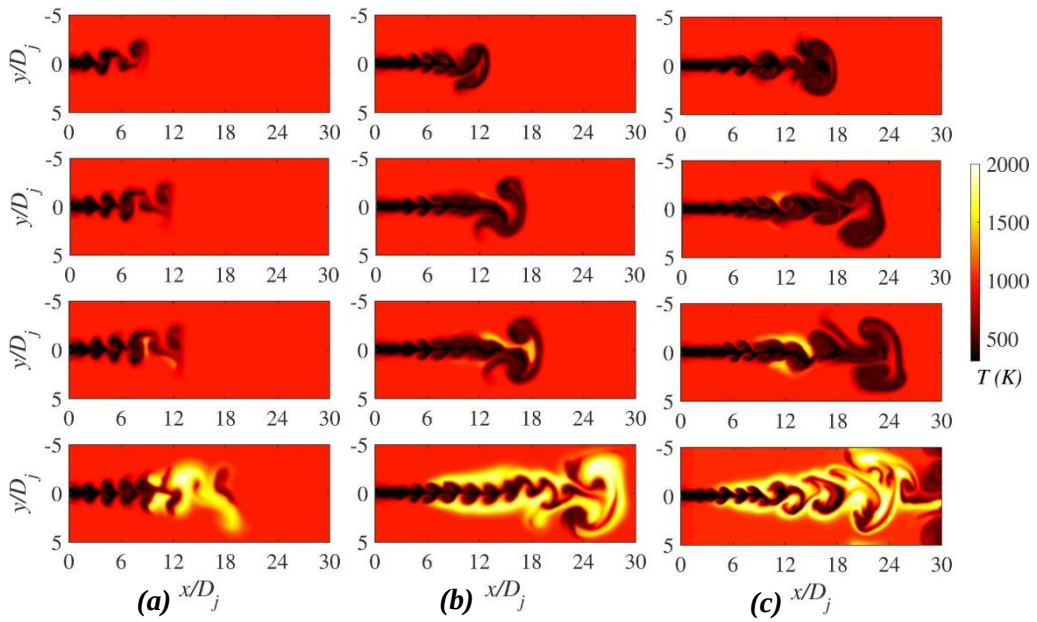


FIGURE 3. Instantaneous temperature contours for variation of jet velocities (a) $U_j$ = 20 m/s, (b) $U_j$ = 40 m/s and (c) $U_j$ = 60 m/s at $t$ = 0.5 ms, 0.675 ms, 0.75 ms, 1.0 ms (from top to bottom)

To examine the behaviour of auto-ignition delay, in Fig. 4a, time series of maximum temperature in the domain is plotted for different cases. Results from one-dimensional unsteady unstrained diffusion flame simulation and from stoichiometric homogeneous mixture simulation are plotted for reference time scales. It is observed that the ignition delay for the jet in the wake is not significantly changed compared to jet in a co-flow and one-dimensional diffusion flame configurations. Also, from Fig. 4b it is observed that, with an increase in jet velocity, the time instants at which maximum temperature starts to rise are also lowered for both the configurations. It suggests that ignition, once initiated, progresses faster in higher jet velocities. However, after initiation of auto-ignition, temporal gradients of maximum temperature are observed to be increased for jet in wake configuration than jet in co-flow. It implies that the ignition delay times are primarily governed by chemical kinetics rather than large-scale mixing characteristics during initial stages prior auto-ignition.

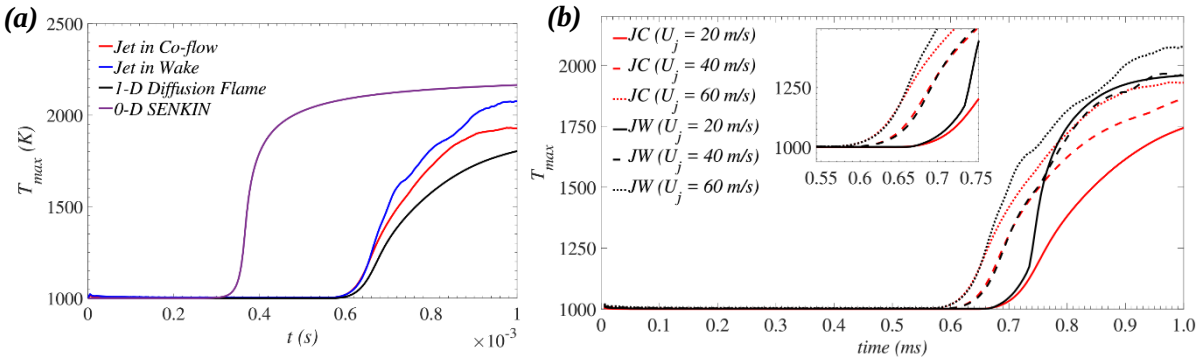


FIGURE 4. Time series of maximum temperature for jet in wake and jet in co-flow simulations a) with 1-D diffusion flame b) with variation in jet velocities. (JC- Jet in Co-flow and JW- Jet in wake)

A Lagrangian particle tracking approach was used to investigate the dominant chain reactions and their temporal statistics in commencing the auto-ignition process. An algorithm proposed by Yeung et al. [3] was used to obtain Lagrangian statistics. In this analysis, 5000 particles were initiated at the inlet boundary within $y = \pm 1.25\ D_j$ at regular interval of 0.1 ms and the minimum crossover temperature of 1200 K was selected as the criteria for identifying ignition. In Fig. 5, as a representative

result, average statistics of temporal evolutions of the elementary reactions contributing to the production/consumption of important radicals is presented only for particles satisfying ignition criterion. From the particle tracking results, it can be observed that the reaction −R10 (refer Table 1) contributes to the production of *H* and $HO_2$ radicals during initial induction period prior auto-ignition. Although the contribution of −R10 is not significant for the production of both the species, its initial contribution in production implies the importance of −R10 in chain initiation. Initially after formation through −R10 reaction, *H* gets consumed with prominent R1 and R9. After initiation, the build-up of $HO_2$ occurs due to termination reaction R9. The *H* radicals required for R9 are mainly supplied from the R3 reaction. R3 consumes the earlier generated *OH* radicals from R1 and R2 during pre-ignition stages. In the course of auto-ignition, $HO_2$ gets consumed immediately through chain branching reaction R11 and R12, which further generates a pool of *OH* radicals and boosts the ignition process.

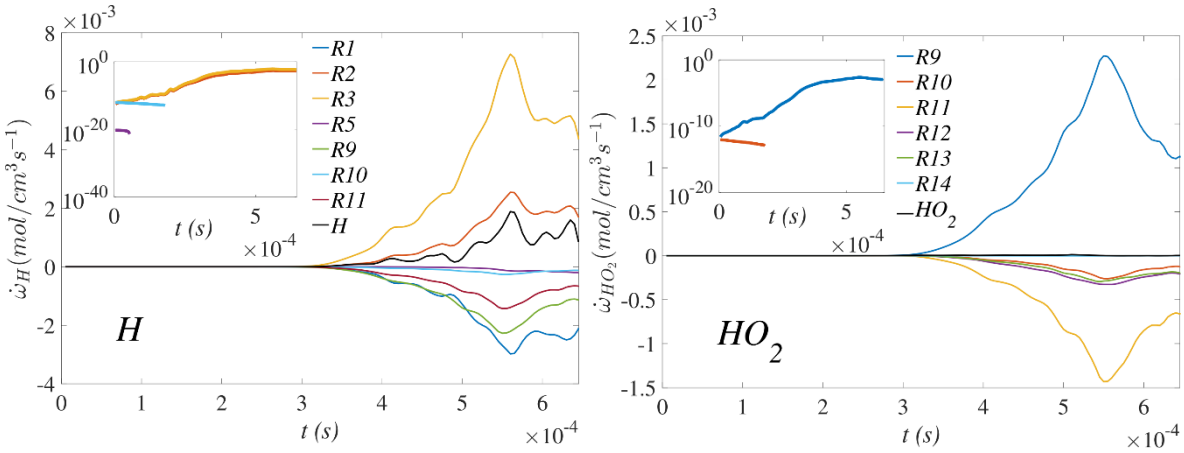


FIGURE 5: Average temporal evolution of contribution of elementary reactions in production of important *H* and $HO_2$ for particle tracking in Jet in a wake case

## 4. CONCLUSIONS

In this work, simulations of one-dimensional diffusion flame, fuel jet in a heated co-flow and fuel jet in wake of heated air show that the initial stages of auto-ignition are primarily governed by chemical kinetics, and large-scale flow characteristics do not have a very significant influence on the overall ignition delay. However, once established, flame propagation and flame stabilization are observed to be highly influenced by the oxidizer flow characteristics. Changes in flow field characteristics, through variation of jet velocity, impact the auto-ignition delay for the jet in wake cases. Reaction rate studies using Lagrangian particle tracking analysis revealed that the reaction −R10 is dominant chain initiation reaction responsible for the generation of *H* radicals during pre-ignition stage.

## REFERENCES

[1] N. Babkovskaia, N. Haugen, A. Brandenburg, A high-order public domain code for direct numerical simulations of turbulent combustion, *Journal of Computational Physics*, 230, 1-12, 2011.

[2] J. Li, Z. Zhao, A. Kazakov, F. L. Dryer, An updated comprehensive kinetic model of hydrogen combustion, *International Journal of Chemical Kinetics*, 36, 566-575, 2004.

[3] P. Yeung, S. Pope, An algorithm for tracking fluid particles in numerical simulations of homogeneous turbulence, *Journal of Computational Physics*, 79, 373-416, 1988.

Fifth International Conference on Computational Methods for Thermal Problems
THERMACOMP2018, July 9-11, 2018, Indian Institute of Science, Bangalore, INDIA
*N. Massarotti, P. Nithiarasu, Pradip Dutta and C. Ranganyakalu (Eds.)*

# EFFECT OF NON-UNIFORM HEATING ON ENTROPY GENERATION FOR THERMALLY DEVELOPING FLOW BETWEEN PARALLEL PLATES

**Abhijit Borah, Nabajit Deka, Sukumar Pati**
Department of Mechanical Engineering, National Institute of Technology, Silchar-788010,
abhijit1d2@gmail.com, njit19@gmail.com, sukumarpati@gmail.com

## ABSTRACT

In this paper, we analyze the effect of non-uniform heating on the entropy generation for thermally developing flow between parallel plates. Several cases of non-uniform heat flux on the walls are considered with a constraint of same rate of heat transfer to find the optimum case for which entropy generation is minimum. Numerical simulations are performed by using finite volume method. Results are presented in the form of temperature distribution, local and total entropy generation rate. The conclusion of this study will make it possible to compare and evaluate merit of non-uniform heating as compared to uniform heating in terms of entropy generation.

**Key Words:** *Entropy minimization, Peak temperature, Heat Transfer.*

## 1. INTRODUCTION

Fundamental insight on minimisation of entropy generation and peak temperature is imperative due to its impact on heat transfer and design of thermal components and systems. The optimisation of thermal systems has been restricted by irreversibility of heat and fluid flow [1]. Other than geometrical factors or the type of fluid, types of thermal boundary conditions also affect the entropy generation. The works pertaining to the study of the effects of thermal boundary conditions on the entropy generation are small in number. Oztop [2] suggested that for laminar flow that the wall heat flux and cross sectional area have substantial effect on entropy generation. Effect of various cross sections of duct on entropy generation is available in the literature [3]. The effect of various wall heat flux boundary condition on entropy generation for a pipe are reported in [4]. Various techniques such as addition of heat source, separating heat source by calculated amount are used to control the peak temperature [5]. Hajmohammadi et al. [6] reported that studied the heat transfer by covering the source of heat generation with a plate of finite thickness.

Study on effect of non-uniform wall heat flux on entropy generation in parallel plate channel is still not found in the literature. The objective of this work is to analyze the entropy generation and maximum temperature due to imposition of different thermal boundary conditions. The thermal boundary conditions for the minimum temperature and entropy generation are identified.

## 2. THEORITICAL FORMULATION

In this paper, laminar, steady and incompressible flow of a Newtonian fluid of high Prandtl number in a parallel plate channel of length 1 m and height 0.025 m is looked upon. Different wall heat flux boundary conditions are applied and analysed for achieving optimum condition which lead to minimization of peak temperature and entropy. The basic configuration i.e. case 1 considered here is uniform heat flux distribution of 5000 $W/m^2$ at both the plates. The rest of the configurations include linearly increasing (case 2) and linearly decreasing (case 3) top wall heat flux keeping the total heat rate constant. The schematic of the three cases are shown in figure 1.

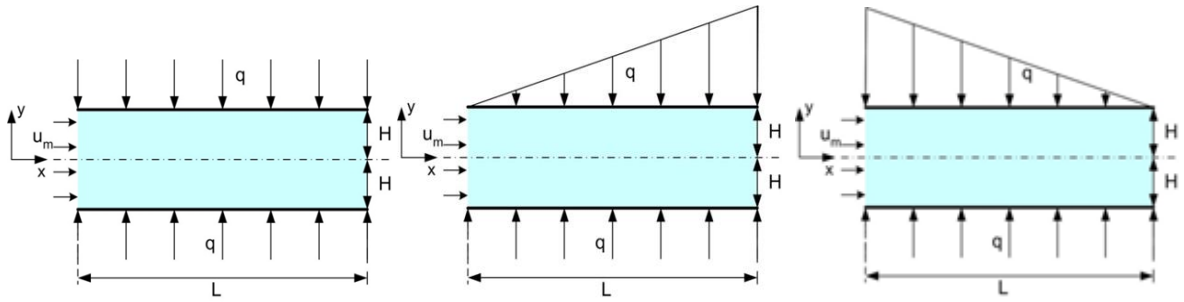


FIGURE 1. Heat flux distribution on the physical model for (a) case 1, (b) case 2 and (c) case 3.

The governing equations in two dimensional Cartesian co-ordinate system are as follows:

Continuity equation

$$\frac{\partial u}{\partial x}+\frac{\partial v}{\partial y}=0 \tag{1}$$

Momentum equation

$$\rho\left(u\frac{\partial u}{\partial x}+v\frac{\partial v}{\partial y}\right)=-\frac{\partial p}{\partial x}+\mu\left(\frac{\partial^2 u}{\partial x^2}+\frac{\partial^2 v}{\partial y^2}\right) \tag{2}$$

Energy equation

$$\rho C_p\left(u\frac{\partial T}{\partial x}+v\frac{\partial T}{\partial y}\right)=k\left(\frac{\partial^2 T}{\partial x^2}+\frac{\partial^2 T}{\partial y^2}\right)+\mu\left\{2\left[\left(\frac{\partial u}{\partial x}\right)^2+\left(\frac{\partial v}{\partial y}\right)^2\right]+\left(\frac{\partial u}{\partial y}+\frac{\partial v}{\partial x}\right)^2\right\} \tag{3}$$

To solve these governing equations, uniform axial inlet velocity, $u_m$ and constant inlet temperature, $T_a$ is chosen. Moreover, heat flux at the walls is taken according to case 1, 2, 3. The total heat rate at the walls is kept constant for all the cases.

The rate of local entropy equation can be found from the following equation

$$S''_{gen}=\frac{k}{T^2}\left(\left(\frac{\partial T}{\partial x}\right)^2+\left(\frac{\partial T}{\partial y}\right)^2\right)+\frac{\mu}{T}\left\{2\left[\left(\frac{\partial u}{\partial x}\right)^2+\left(\frac{\partial v}{\partial y}\right)^2\right]+\left(\frac{\partial u}{\partial y}+\frac{\partial v}{\partial x}\right)^2\right\} \tag{4}$$

## 3. RESULTS

Temperature profiles for five transverse cross sections along the length of the parallel plate channel are shown in Figure 2. For uniform and increasing heat flux boundary condition, maximum temperature is obtained at the channel cross section of x=0.9 m and that for decreasing heat flux is at 0.3m because of high heat flux at respective positions. Another observation from the results is that, among the three cases, the maximum wall temperature is obtained for increasing heat flux condition whereas maximum heat penetration is obtained for decreasing heat flux condition.

Figure 3 which depicts radial entropy generation profiles shows that for decreasing (figure 4(c)) and increasing (figure 4(b)) heat flux condition, maximum entropy generation occurs near the entrance and exit of the channel respectively. This is because of high heat transfer at the beginning for case 3 and at the end for case 2. It is noteworthy that the major portion of entropy generation in flow field is owing to heat transfer. In case 1, entropy generation trend is similar for all the longitudinal

sections. For all sections entropy generation is minimum till the mid of half height and thereafter increases gradually. This is because of low heat penetration to the centre of the channel.

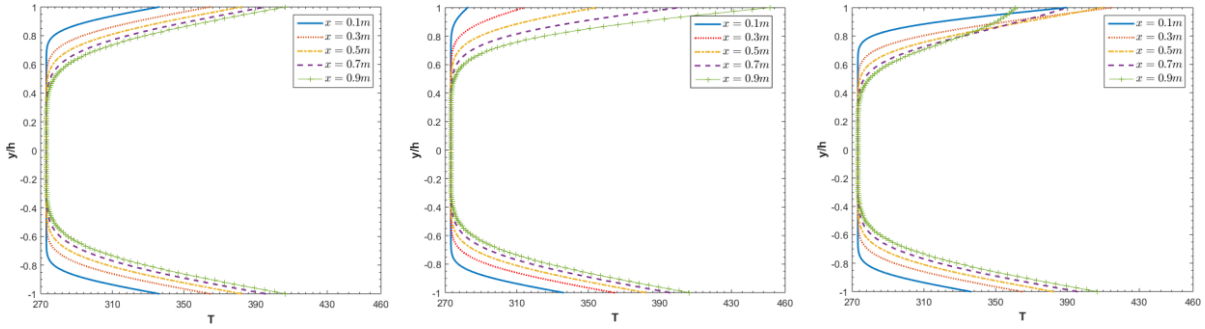


(a) (b) (c)

**FIGURE 2**. Temperature profiles for (a) case 1, (b) case 2 and (c) case 3.

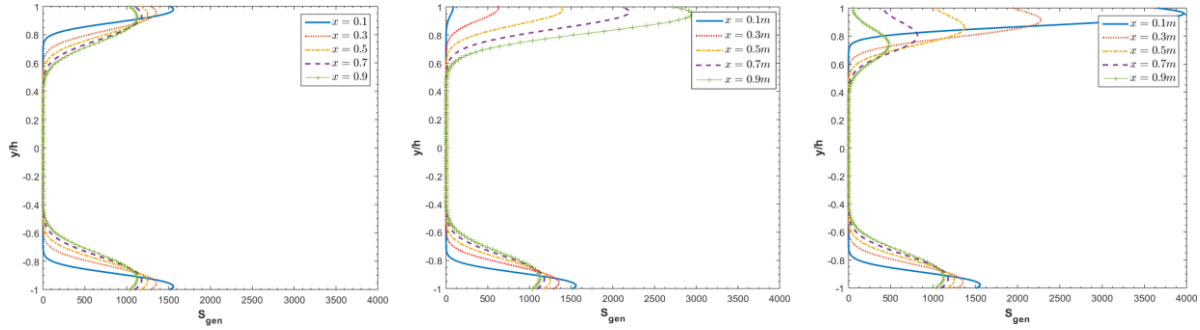


(a) (b) (c)

**FIGURE 3**.Entropy generation profile for (a) case 1, (b) case 2 and (c) case 3.

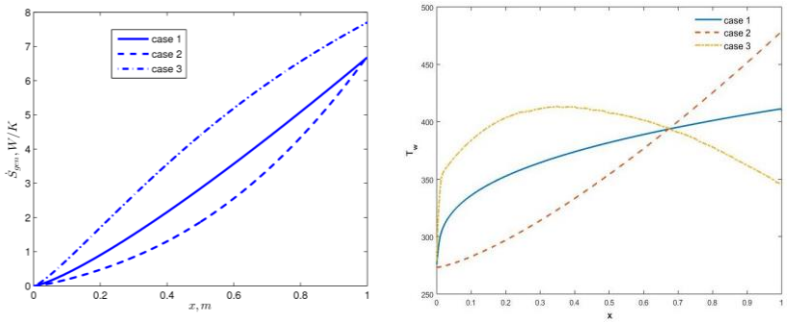


(a) (b)

**FIGURE 4.** (a) Total entropy generation and (b) wall temperature for case 1, case 2 and case 3

The total entropy generation is displayed in figure 4(a) which depicts lowest entropy for case 2. Increasing heat flux results in uniform temperature at the wall which prevents steep increase in entropy. Case 3 on the other hand facilitates steep increase in entropy due to high heat flux initially. In figure 4(b), wall temperature profile for the three cases shows lowest peak temperature for case 3. Since decreasing heat flux condition shows maximum heat penetration (figure 2), so lower peak temperature is observed.

Figure 5 shows the longitudinal entropy generation profile which shows sharp increase in entropy at the entrance followed by gradual decrease for case 1 and 3. This is because of the high heat transfer due to large temperature gradient. Same heat transfer argument attests the gradual increase of

entropy in case 2. At *y/H=0.8* and *-0.8*, owing to the respective wall temperature profile, we see an increasing-decreasing entropy profile for case 3 and only increasing entropy profile for case 2.

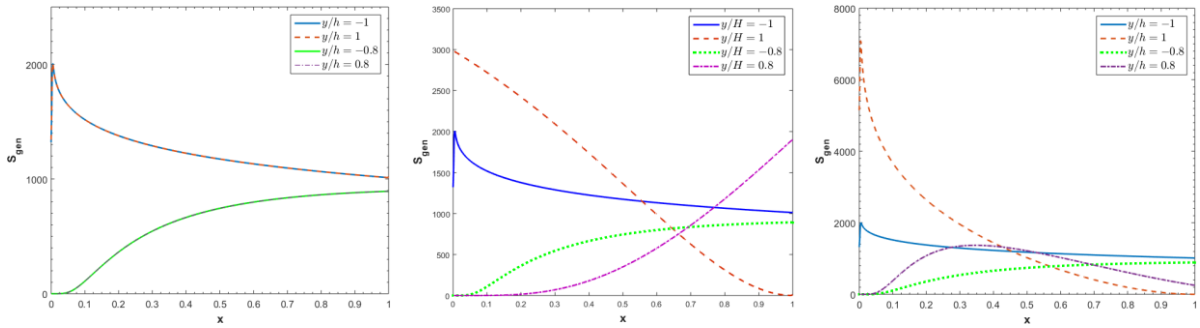


(a) (b) (c)

**FIGURE 5.**Longitudinal entropy generation profile for (a) case 1, (b) case 2 and (c) case 3

## 4. CONCLUSIONS

This paper examines the effect of non-uniform wall heat flux and asymmetric heating in a parallel plate channel. Two non-uniform heat flux boundary condition is compared with uniform wall heat flux condition. All three cases employ same amount of total heat at the walls. Results indicate the existence of a condition which furnishes minimum entropy and minimum peak temperature. In the mentioned physical domain, increasing wall heat flux displays minimum entropy generation for certain optimum set of parameters. From hotspot minimization standpoint, this study signalize that decreasing heat flux boundary condition correspond to lower peak temperature.

## ACKNOWLEDGEMENT

The authors acknowledge TEQUIP-III and the department of Mechanical Engineering, NIT Silchar for supporting the work.

## REFERENCES

[1] A. Bejan, A study of entropy generation in fundamental convective heat transfer, *J. Heat Transfer*, 101(4), 718-725, 2010.

[2] H.Oztop, Effective parameters on second law analysis for semicircular ducts in laminar flow and constant wall heat flux, *Int Commun Heat Mass Transfer*, 32, 266–274, 2005.

[3] I. Dagtekin, H. Oztop, A. Sahin, An analysis of entropy generation through a circular duct with different shaped longitudinal fins for laminar flow. *Int J Heat Mass Transfer*, 48, 171–81, 2005.

[4] J.A. Esfahani, P.B. Shahabi, Effect of non-uniform heating on entropy generation for the laminar developing pipe flow of a high Prandtl number fluid, *Energy Conversion Manage*, 51 2087-2097, 2005.

[5] A. Bejan, E. Sciubba, The optimal spacing for parallel plates cooled by forced convection, *Int. J. Heat Mass Transfer*, 35, 3259-3264, 1992.

[6] M.R. Hajmohammadi, A. Campo, S.S. Nourazar, A.M. Ostad, Improvement of forced convection cooling due to the attachment of heat sources to a conducting thick plate, *J. Heat Transfer*, 135(12), 124504(1-4), 2013.

# INVESTIGATION OF NANOPARTICLE INFUSED TUMOR NECROSIS EMBEDDING LARGE BLOOD VESSELS DURING HYPERTHERMIA TREATMENT

**Abhijit Paul [1], Anup Paul [2*]**

Department of Mechanical Engineering, NIT Arunachal Pradesh, Yupia,79112, India

E-mail addresses: [1] abhijitpaul1501@gmail.com, [2] catchapu@gmail.com* (*Corresponding author)

## ABSTRACT

During Plasmonic photo-thermal therapy the intravenous nanoparticles injection is one of the prominent topographies for complete tumor necrosis. In this therapy the large blood vessels (LBV) performs as a heat sink and therefore takes a vital role. Targeting photo-thermal demolition of targeted tumor, in clinical interference a lot of the safety measures propose the laser irradiation as an alternate method and inclusion of gold nanoparticles to decrease the cooling effect of LBVs. A simulation technique based upon finite element method is applied to calculate the evolution of temperature by solving the equation of bio-heat transmission of Pennes. To replicate the laser heating a Beer-Lambert law based volumetric heat production is applied. In this article a comparative analysis was executed to examine the thermal tissue-tumor history implanted with LBVs for nanoparticles of gold nanosphere and silica-gold nanoshell together with Single vessel transiting tumor (SVTT) and Countercurrent vessel transiting tumor (CVTT) configuration, in order to find out the efficacy of intravenous inoculation of nanoparticles. A surface temperature contour at tumor core is attained for various vascular and bare tissue-tumor replicas along with various types of nanoparticle injections. The computational results propose that the flow of blood through LBVs at the adjacent of the photo-thermally excited tissue can result an ineffective target heating. Also gold nanosphere type of nanoparticles dominates over silica-gold nanoshells in terms of efficacy in complete tumor protein denaturation.

**Key Words:** *Large blood vessels, Tumor necrosis, Nanoparticles, Hyperthermia treatment*

## 1. INTRODUCTION

For a number of decades hyperthermia treatment of cancerous cell by laser heating of targeted tumor turned out to be a vital field of research. For certain kinds of cancers Laser-induced hyperthermia can lead an sovereign technique of treatment, also, it can be applied alongside conventional techniques of cancer therapy as camotherapy and radiotherapy (Niemz, 2007 ; Welch and Gemert, 2010). Such procedure's numerical and simulation modelling helps us to know the biological system's thermo-physical character. For an efficient treatment of laser induced hyperthermia the temperature prediction planning plays a significant role (Das et al., 2003).

## 2. RESULTS

For computational study, 3 dissimilar domains were built with tissue, tumor dimensions of 100 mm × 50 mm × 15 mm and 33 mm × 17 mm × 5 mm in X, Y and Z directions respectively as shown in Fig. 1 (Singh et al., 2014 and Paul et al., 2014). The three geometries were (a) bare tissue-tumor (Fig. 1(a)); (b)

SVTT, where blood vessel center lies at a depth of 2.5 mm from tissue top plane (Fig. 1(b)); and (c) CVTT, at a same depth with 2.5mm away from mid YZ-plane in either side (Fig. 1(c)).

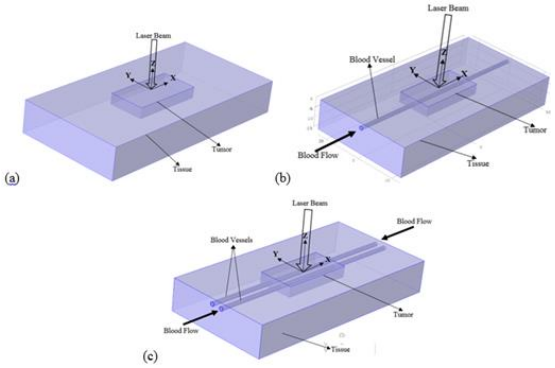


Fig.1 Illustration of Physical Model (a) Bare tissue with tumor, (b) SVTT, (c) CVTT

The laser heat generation equation (Welch, 1984) and governing equations for various domains (Paul et al., 2014) can be written as

$$Q_{laser}(r,z) = \alpha I_0 exp\left\{-\frac{r^2}{2\sigma^2(0)\exp(\beta z)}\right\} exp\{-(\alpha+\beta)z\} \quad (1)$$

$$(\rho C)_t \frac{\partial T_t}{\partial t} = \nabla.(k_t \nabla T_t) + Q_{laser_t} \quad (2)$$

$$(\rho C)_{bv} \frac{\partial T_{bv}}{\partial t} = \nabla.(k_{bv} \nabla T_{bv}) + Q_{laser_{bv}} \quad (3)$$

$$(\rho C)_b \frac{\partial T_b}{\partial t} + (\rho C)_b (V.\nabla T_b) = \nabla.(k_b \nabla T_b) + Q_{laser_b} \quad (4)$$

where, $I_0$ is laser intensity at tissue top surface , $\sigma$ is Gaussian distribution of laser beam, $\alpha$ and $\beta$ are absorption and scattering coefficients respectively. $\rho, \mathrm{C}, k, V, T$ and $t$ are density, specific heat, thermal conductivity, blood velocity, temperature and time respectively. Subscripts *t*, *bv* and *b* represent tissue, blood vessel and blood respectively. The present results show a good agreement with the experimental and numerical outcomes of (Paul.et al, 2014) as depicted in Fig.2 (a). The Maximum surface temperature, beneath the laser spot, variation over time has been considered here for validation purpose.

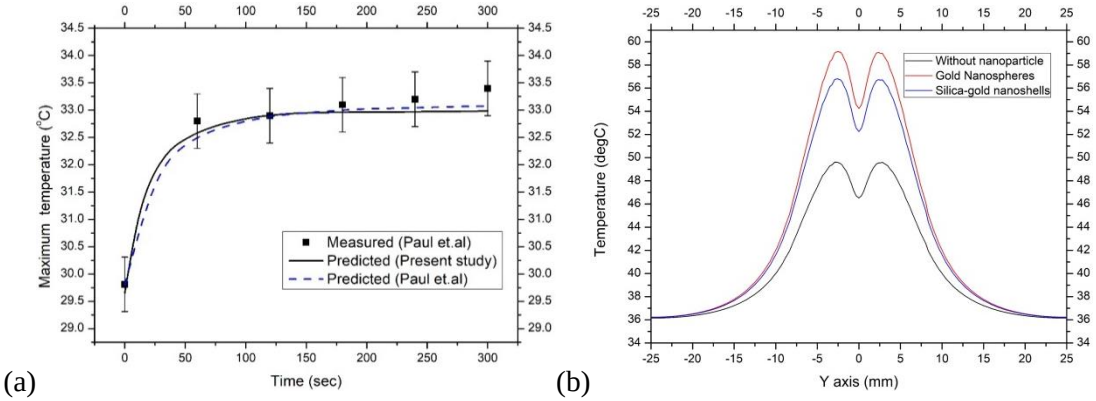


(a) (b)

Fig.2 (a) Comparison of maximum tissue-tumor surface temperature over time for SVTT (power=558mW, spot size=5mm, time=5min) (b) Temperature variation at mid XY plane, z=1.4 mm (time=5min, power=558 mW, spot size=5mm, V=0.1m/s)

To understand the thermal effect of laser heating of tumor infused with nanoparticles, the Pennes bio-heat transfer equation was solved for the approximated computational domain (Fig.1). During hyperthermia treatment the improvement in laser heating of bio-tissues by intravenous nanoparticle injection to the targeted tumor is clearly depicted from present study (as Fig.2 (b)) due to the increase in effective domain optical properties. Also the insignificant heating of the targeted cell due to the heat sink effect of LBV is explored from the study (as Fig. 2(b)). The following figure shows the distribution of temperature at mid XY plane along Y axis at Z =1.4mm. for SVTT. The effective absorption coefficient of tumor with uniform distribution of nanoparticles increases by 3177.2 and 2181.2 for gold nanosphere and silica-gold nanoshell respectively. The resonance wavelength for nanosphere and nanoshell were considered as 521 nm and 843 nm respectively. The maximum temperature observed at the tumor core has been increased with the inclusion of nanoparticles, reaching around $66^0$C from $51^0$C (Fig.3 (a) to (c)) for bare tissue-tumor configuration, suggesting the efficacy of complete tumor necrosis. Also the insignificant heating of targeted tumor due to heat sink effect of LBV is depicted clearly from Fig.3 (d) to (i) as the maximum tumor core temperature reaching to $51^0$C for SVTT and $48^0$C for CVTT, in spite of nanoparticle inclusion. The temperature isotherms analysis justifies the fact that nanoparticles type of gold nanosphere dominates over silica-gold nanoshells regarding complete tumor necrosis (Fig.3) for a certain volumetric concentration (η).

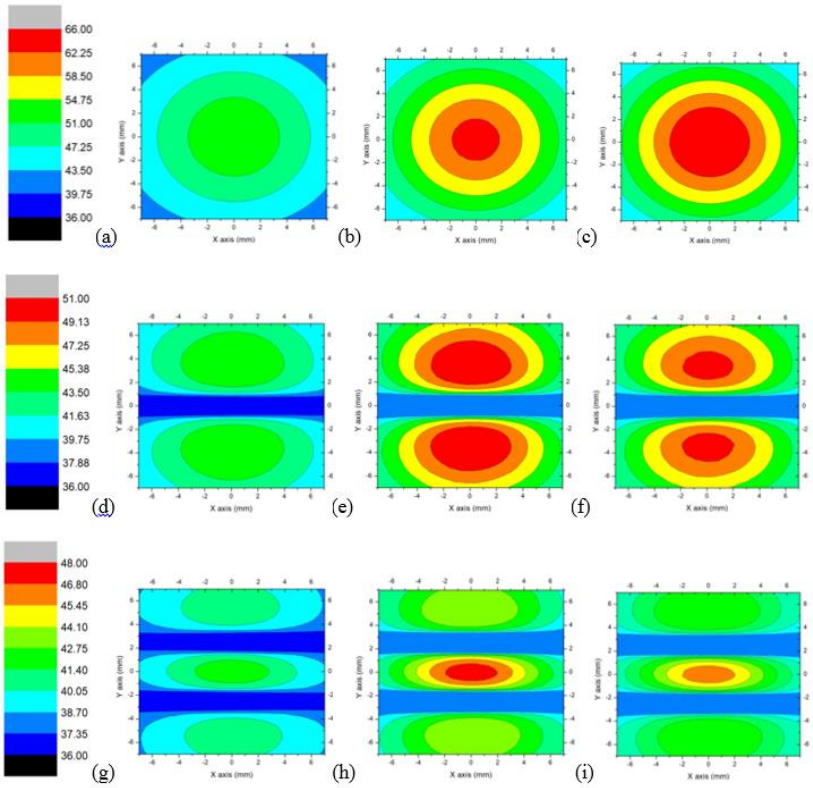

Fig.3 Temperature isotherms in $^0$C at XY-plane (Power=558 mW, $\eta=4.31\times10^{-5}$,time=300s) at tumor core for (a),(b),(c) bare tumor and tissue; (d),(e),(f) SVTT; (g),(h),(i) CVTT; (a),(d),(g) without nanoparticles (b),(e),(h) Gold nanosphere; (c),(f),(i) Silica-gold nanoshell

## 3. CONCLUSIONS

A numerical analysis was executed to inspect the efficacy of laser initiated hyperthermia of a vascular tisssue-tumor infusing gold nanoparticles. A continuous wave type of laser having wavelength of 521 nm and 843 nm was irradiated at the top surface of a 3-D tissue-tumor domain considered. Consequences of usage of different types of nanoparticles having a particular resonance wavelength and different LBV configuration on distribution of temperature contour were examined. The attained results were authenticated with the formerly executed (Paul et al., 2014) simulation and experimental results on replicated tissue-tumor phantom containing LBVs. Study reveals that gold nanosphere dominates over silica-gold nanoshells in terms of efficacy in complete tumor necrosis, as the effective tumor optical properties are comparatively higher in case of gold nanospheres. Result also justifies the fact of insignificant targeted tumor heating due to heat sink effect of LBVs. During hyperthermia treatment the above presented computational analysis plays a key role to understand the mechanism of nanoparticle infused tumor necrosis embedding large blood vessels.

Acknowledgements: Authors would like to acknowledge SERB (DST) sponsored project for supporting this work.

## REFERENCES

1. Niemz, M.H., Laser–Tissue Interactions, Fundamental and Applications, Third edition. Heidelberg,Springer (Chap.3), 2007
2. Welch, A.J., Gemert M.J.V., Optical thermal response of Laser-Irradiated Tissue, Second edition, Springer, New York, (Chap. 12), 2010
3. Das. C., Trivedi, A., Mitra. K., Vo-Dinh, T., Experimental and Numerical analysis of short pulse laser interaction with tissue phantoms containing inhomogenities, Appl: Opt. 42, 5173-5180, 2003
4. Singh, R., Das, K., Mishra, S.C., Laser-induced hyperthermia of nanoshell mediated vascularized tissue-A numerical study, Journal of Thermal Biology, 44, 55-62, 2014.
5. Paul, A., Narasimhan, A., Kahlen, F.J., Das, S.K., Temperature evolution in tissues embedded with large blood vessels during photo-thermal heating, Journal of Thermal Biology, 41, 77-87, 2014.
6. Welch. A.J, The Thermal response of laser irradiated tissue, IEE J. Quantum Electron, 20, 1471-1481, 1984.

Fifth International Conference on Computational Methods for Thermal Problems
THERMACOMP2018, July 9-11, 2018, Indian Institute of Science, Bangalore, INDIA
*N. Massarotti, P. Nithiarasu, Pradip Dutta and C. Ranganyakalu (Eds.)*

# COMBINED EFFECT OF AMBIENT HEAT-IN-LEAK AND LONGITUDINAL WALL CONDUCTION ON THE PERFORMANCE OF THREE-FLUID CROSS-FLOW HEAT EXCHANGER

**Jyothiprakash K H*, Abhimanyu Sharan, Harshith J, V Krishna, K N Seetharamu**
PES University, Bangalore-560085, Karnataka, India, * jprakash@pes.edu

**Y.T.Krishnegowda**
Maharaja Institute of Technology, Professor, Karnataka, India, ytk_gowda@yahoo.com

## ABSTRACT

In this paper the performance of a three-fluid cross-flow heat exchanger, considering the effects of longitudinal wall heat conduction and ambient heat-in-leak is analysed. The governing equations are derived by applying principles of energy conservation and solved for temperature distribution using finite element method. Validation of the present scheme is carried out by comparing its results with results obtained from literature. The objective is identified as cooling of the hot fluid and hence the hot fluid effectiveness is defined to analyse the performance. Several non-dimensional parameters are defined such as heat capacity ratios ($C_{12}$, $C_{32}$), heat conductance ratios ($R_1$, $R_2$, $H_t$, $H_b$) and heat conduction parameters ($\lambda_x$ and $\lambda_y$) and parametric studies are carried out.

**Key Words:** *Heat Transfer, Finite Elements, Cross Flow Heat Exchangers.*

## 1. INTRODUCTION

The performance of multi-fluid heat exchangers is strongly affected by various factors such as inlet flow maldistribution, longitudinal wall heat conduction, heat-in-leak from surroundings and so on. Thermal interaction of a heat exchanger with the surrounding is an unavoidable circumstance. The thermal performance analysis of a multi-fluid cross-flow heat exchanger without considering ambient effect leads to significant error [5]. Yuan [2-3] has investigated the effect of longitudinal wall conduction on the performance of a three-fluid cross-flow heat exchanger while Jyothiprakash [4] has examined the effect of heat-in-leak for the same arrangement. However, the combined effect of heat-in-leak and longitudinal wall conduction on a three-fluid cross-flow heat exchanger's performance has not been examined yet. In this paper the deviation of the heat exchanger performance due to this combined effect is investigated. Principle of energy conservation is used to derive governing equations and solved using finite element method.

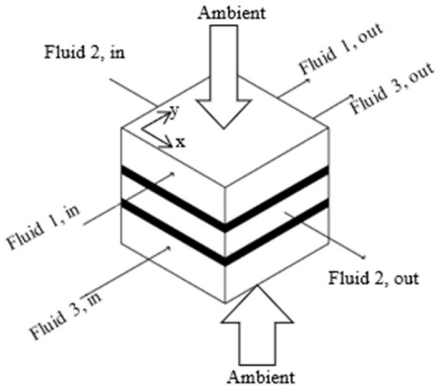


FIGURE 1. Three-Fluid Cross-Flow Heat Exchanger Element

## 2. MATHEMATICAL MODELLING

Figure 1 shows the schematic representation of the arrangement used in this analysis wherein fluids 1 and 3 are in parallel flow while fluid 2 flows between them in cross-flow orientation. Fluid 2 interacts with the two walls separating it from the two cold fluids whereas the two cold fluids interacts with the ambient as well as with the walls separating them from the hot fluid. The ambient temperature $\theta_a$ is considered higher than the two cold fluid temperatures for a cryogenic heat exchanger. In this analysis, it is assumed that ambient heat-in-leak with constant temperature to the heat exchanger is considered from top and bottom surfaces only, while wall heat conduction is considered only in the two walls (w1 and w2) separating the three fluids. Applying principle of energy conversation, the dimensionless governing equations can be written as-

Fluid 1: $$\frac{\partial\theta_1}{\partial\eta}-NTU\,(1+R_1)\,(\theta_{w1}-\theta_1)-H_t\,NTU\,(1+R_1)\,(\theta_a-\theta_1)=0$$

Wall 1: $$C_{12}\,NTU\left(1+\frac{1}{R_1}\right)[(\theta_2-\theta_{w1})+R_1\,(\theta_2-\theta_{w1})]+\lambda_x\frac{d^2\theta_{w1}}{d\xi^2}+\lambda_y\frac{d^2\theta_{w1}}{d\eta^2}=0$$

Fluid 2: $$\frac{\partial\theta_2}{\partial\xi}-C_{12}\,NTU\left(1+\frac{1}{R_1}\right)[(\theta_{w1}-\theta_2)+(\theta_{w2}-\theta_2)]=0$$

Wall 2: $$C_{12}\,NTU\left(1+\frac{1}{R_1}\right)[(\theta_2-\theta_{w2})+R_3\,(\theta_2-\theta_{w2})]+\lambda_x\frac{d^2\theta_{w2}}{d\xi^2}+\lambda_y\frac{d^2\theta_{w2}}{d\eta^2}=0$$

Fluid 3: $$\frac{\partial\theta_3}{\partial\eta}-\frac{C_{12}}{C_{32}}\,NTU\,R_3\left(1+\frac{1}{R_1}\right)(\theta_{w2}-\theta_3)-H_b\,NTU\,\frac{C_{12}}{C_{32}}\,(1+R_1)\,(\theta_a-\theta_3)=0$$

$$\theta=\frac{T-T_{1,in}}{T_{2,in}-T_{1,in}};\ \xi=\frac{x}{L_x};\ \eta=\frac{y}{L_y};\ C_{12}=\frac{(\dot{m}c_p)_1}{(\dot{m}c_p)_2};\ C_{32}=\frac{(\dot{m}c_p)_3}{(\dot{m}c_p)_2};\ R_1=\frac{(hA)_1}{(hA)_2};\ R_3=\frac{(hA)_3}{(hA)_2}$$

$$\lambda_x=\frac{k_x(L_y\delta)}{(\dot{m}c_p)_2L_x};\ \lambda_y=\frac{k_y(L_x\delta)}{(\dot{m}c_p)_2L_y};\ H_t=\frac{(UA)_{1,t}}{(hA)_1};\ H_b=\frac{(UA)_{3,b}}{(hA)_1};\ NTU=\left[(\dot{m}c_p)_1\left(\frac{1}{(hA)_1}+\frac{1}{(hA)_2}\right)\right]^{-1}$$

To apply the finite element method, the heat exchanger is discretized into a number of elements. A linear variation is assumed for the three fluids while a four noded quadrilateral is assumed for the two walls. The temperatures of the fluids $\theta_f$ and the walls $\theta_w$ at any point are given by:

$$\theta_{f1}=(1-\eta)\,\theta_1+\eta\,\theta_2;\ \ \theta_{w1}=(1-\xi)(1-\eta)\,\theta_3+\xi(1-\eta)\,\theta_4+\xi\eta\,\theta_5+(1-\xi)\eta\,\theta_6;\ \ \theta_{f2}=(1-\xi)\,\theta_7+\xi\,\theta_8;$$
$$\theta_{w2}=(1-\xi)(1-\eta)\,\theta_9+\xi(1-\eta)\theta_{10}+\xi\eta\,\theta_{11}+(1-\xi)\eta\,\theta_{12};\ \ \theta_{f3}=(1-\eta)\,\theta_{13}+\eta\,\theta_{14}$$

The finite element analysis is done using Galerkin's mehod where the weighted function is taken as the shape functions. After applying Galerkin's method, the discretized governing equations is converted into matrix form for each element, which is then assembled to form the global matrices, and the boundary conditions are applied as: $\theta_{1\,in}=0$, $\theta_{2\,in}=1$ and $\theta_{3\,in}=$ any intermediate value. The global matrices is solved to determine the temperature distribution along the heat exchanger.

## 3. RESULTS

The validation of the present method, shown in Figure 2, is initially done for no heat-in-leak and no wall conduction conditions by comparing the results of the present numerical scheme with that of the analytical solution [1]. Further validation is done by testing the present scheme for the effects of heat-

in-leak (Figure 3) and longitudinal wall conduction (Table 1) separately and comparing them with numerical results obtained from literature [2-4]. It is seen that the errors are within permissible limits.

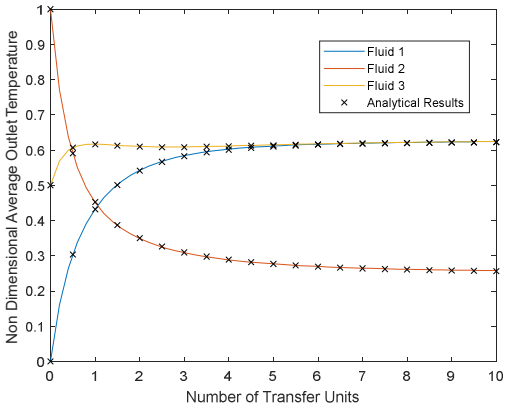


FIGURE 2. Fluid Outlet Temperatures comparison between analytical [1] and present methods with $C_{1,2}= C_{3,2}=R_1=R_3=1$, $H_t= H_b =0$, $\lambda_x=\lambda_y=0$.

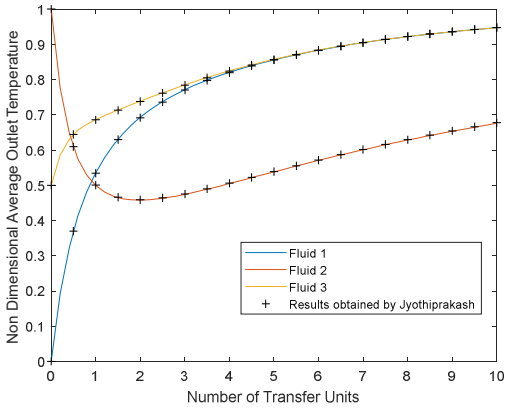


FIGURE 3. Comparison of outlet fluid temperatures for effect of heat-in-leak alone [4] with $C_{1,2}=C_{3,2}=1$, $R_1=R_3=1$, $\theta_{3in}=0.5$, $\theta_a=1$, $\lambda_x=\lambda_y=0$, $H_t= H_b =0.1$

| NTU | Yuan's [2-3] Results | | | Present Scheme Results | | | Deviation (%) | | |
|---|---|---|---|---|---|---|---|---|---|
| | $\tau_1$(%) | $\tau_2$(%) | $\tau_3$(%) | $\tau_1$(%) | $\tau_2$(%) | $\tau_3$(%) | Fluid 1 | Fluid 2 | Fluid 3 |
| 1 | 0.6931 | 0.8939 | 1.3586 | 0.7276 | 0.9086 | 1.3768 | 4.74 | 1.62 | 1.32 |
| 2 | 1.1797 | 1.5583 | 2.6313 | 1.2022 | 1.5958 | 2.6859 | 1.87 | 2.35 | 2.03 |
| 5 | 1.9336 | 2.7598 | 4.8426 | 1.9537 | 2.7696 | 4.8779 | 1.03 | 0.35 | 0.72 |

TABLE 1. Comparison of Deterioration factor ($\tau_i$) defined by Yuan [2] for effect of longitudinal wall conduction alone with $C_{1,2}=C_{3,2}=0.5$, $R_1=R_3=1$, $\theta_{3in}=0.5$, $\theta_a=1$, $H_t= H_b =0$, $\lambda_x=\lambda_y=0$, 0.0125

The results obtained considering combined effect of heat-in-leak and wall heat conduction are shown in figures 4-5 keeping the governing parameters constant with values $C_{1,2}=C_{3,2}=0.5$ and $R_1= R_3= 1$, $\theta_{3in}=0.5$, and $\theta_a=1$. In this paper, the objective identified is cooling of the hot fluid, and hence the hot-fluid effectiveness and degradation factor is defined as follows:

$$\epsilon_2=1-\theta_{2,out}\ ; \quad \tau(\%)= \frac{\epsilon_{2,without\ conduction\ and\ heat\ leak} - \epsilon_{2,with\ conduction\ and\ heat\ leak}}{\epsilon_{2,without\ conduction\ and\ heat\ leak}} *100$$

## 4. CONCLUSIONS

It is seen from figures 4-5 that with increase in ambient heat in leak parameter ($H_t$ and $H_b$), the effectiveness of the heat exchanger decreases considerably (32.67% at NTU=5), while the effect of wall conduction parameter ($\lambda_x$ and $\lambda_y$) on the heat exchanger performance is comparatively much lesser (2.8% at NTU=5). At higher values of $H_t$ and $H_b$, there is minimal effect of varying $\lambda_x$ and $\lambda_y$. Thus, the combined effect of heat-in-leak and longitudinal wall heat conduction (34.27% at NTU=5) is significant and cannot be ignored.

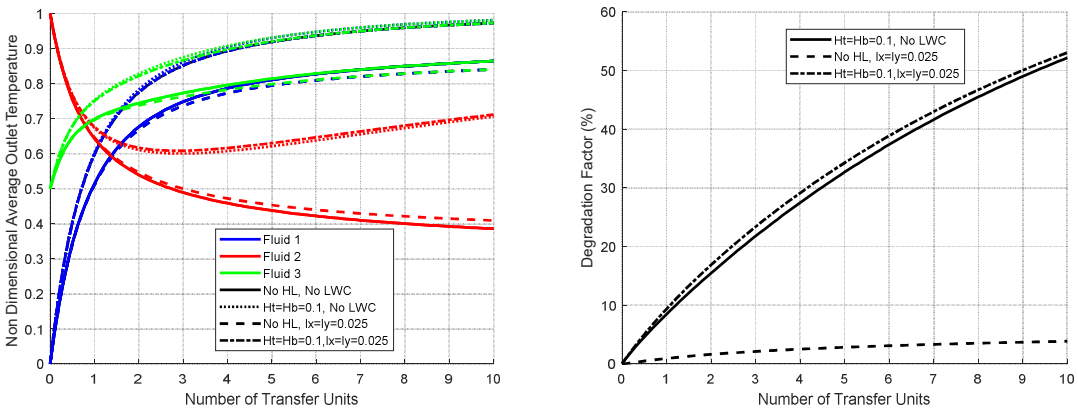


FIGURE 4. Combined effect of heat-in-leak and wall conduction on plot of (a) $\theta_{out}$ vs NTU and (b) τ vs NTU with $C_{12}=C_{32}=0.5$, $R_1=R_3=1$, $\theta_{3in}=0.5$, $\theta_a=1$, $H_t= H_b =0,0.1$ and $\lambda_x=\lambda_y=0,0.025$

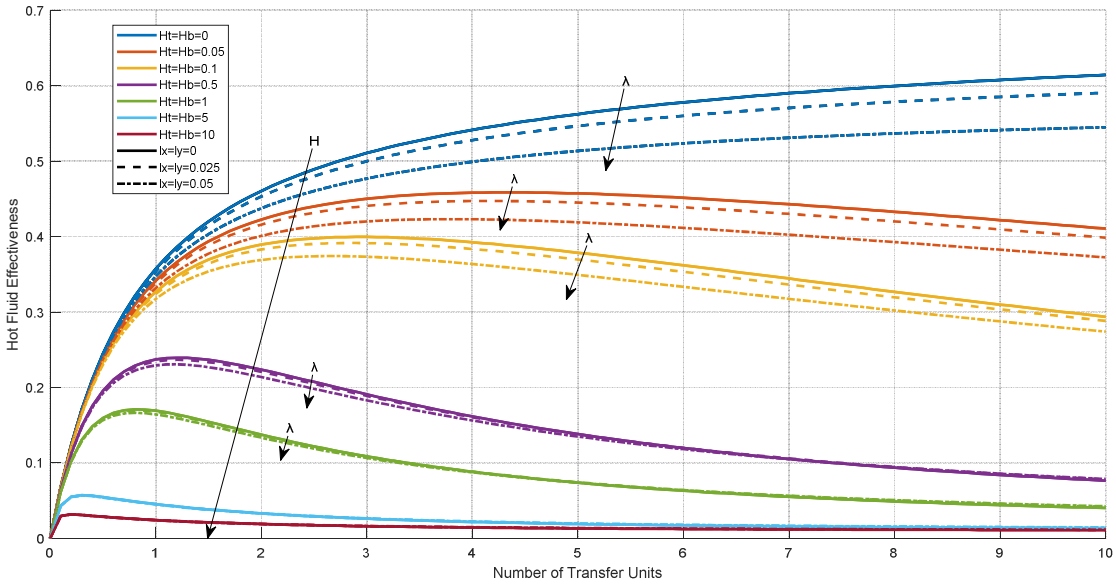


FIGURE 5. Effect of varying $H_t$, $H_b$, $\lambda_x$ and $\lambda_y$ on $\epsilon_2$ with $C_{12}=C_{32}=0.5$, $R_1=R_3=1$, $\theta_{3in}=0.5$, $\theta_a=1$

## REFERENCES

[1] B.S. Bačlić; D.P. Sekulić; D.D. Gvozdenac, "Performances of three-fluid single pass crossflow heat exchanger", In *Heat Transfer,* Vol 6, 167-172, 1982.

[2] Ping Yuan; H.S. Kou, "The comparision of longitudinal wall conduction effect on the crossflow heat exchanger including three-fluid streams with different arrangements", *Applied Thermal Engineering*, 21, 1891-1907, 2001.

[3] Ping Yuan; H.S. Kou, "The effect of longitudinal wall conduction in a three-fluid crossflow heat exchanger", *Numerical Heat Transfer, Part A*, 34, 135-150, 1998.

[4] Jyothiprakash K H; Y.T. Krishnegowda; V. Krishna; K.N. Seetharamu, "Effect of heat-in-leak on the performance of cross-flow heat exchanger", *IJNMHFF*, 2017, Accepted.

[5] Tisha Dixit; Indranil Ghosh, "Two-stream cross flow heat exchangers in thermal communication with the surroundings – A generalized analysis", *IJHMT* 66, 1–9, 2013.

# NUMERICAL MODELLING OF HEAT TRANSFER DURING MULTI-LAYER LASER METAL DEPOSITION PROCESS

**Akash Aggarwal, Arvind Kumar**

Department of Mechanical Engineering, Indian Institute of Technology Kanpur,
Kanpur - 208016, India
akashagg@iitk.ac.in, arvindkr@iitk.ac.in

## ABSTRACT

A three-dimensional model is developed to study heat transfer in the multi-layer Laser Metal Deposion (LMD) process. The deposition of coaxially fed SS316 powder is modelled by a moving computational mesh based on an arbitrary Lagrangian-Eulerian (ALE) formulation. The ALE method enables the motion of the boundary of the computational domain with time by solving partial differential equations for the mesh displacements. The transient energy conservation is solved to simulate the phase change and the associated thermal transport during the single layer and the multi-layer laser metal deposition. Temeprature distrbution and melt pool characteristics, such as melt pool shape and size are described.

**Key Words:** *Laser Metal Deposition, Arbitrary Lagrangian-Eulerian (ALE), Thermal transport.*

## 1. INTRODUCTION

Laser Metal Deposition (LMD) process is an additive manufacturing process that uses a high power laser to melt the metal powder supplied coaxially to the focus of the laser beam through a deposition head. The intense heat generated by the laser beam causes powder particles to melt and to form a melt pool which upon cooling solidifies into a bulk layer of material. This mechanism operates over a predefined path and is repeated for each subsequent layer until the desired product is obtained. LMD process involves interaction of powder material with a high energy beam leading to various physical phenomena such as melting, vaporization, solidification and surface tension driven free surface flow in the melt pool. It is very challenging to study the process experimentally as it involves high energy beam interaction along with high melting and solidification rates. Therefore, alternative strategies, such as computational modelling and simulations are an emerging area to understand deeper insights of the process, effect of the process parameters, and to obtain optimized process conditions. Several computational works ([1], [2]) have been reported in the past to investigate the laser metal deposition process but most of them are limited to single layer deposition process. In this work, an arbitrary Lagrangian-Eulerian method based simulation coupled with the heat transfer physics is developed to investigate the multi-layer coaxially fed deposition of SS316 powder. Results for the melt pool characteristics, such as melt pool geometry and its thermal behavior are presented by taking into account the effect of idle time, mass flow rate, powder catchment efficiency and powder spread radius.

## 2. MODEL DESCRIPTION

Figure 1 shows the schematics of the coaxial laser metal deposition process and the computational domain considered for the finite element simulation. As shown in Fig. 1b, the laser beam traverses from point *a* to point *b* during first layer deposition. After depositing the first layer, the beam is off for a period equal to the ideal time. Then, another layer is deposited on the top of the first layer starting from point *a* to point *b*.

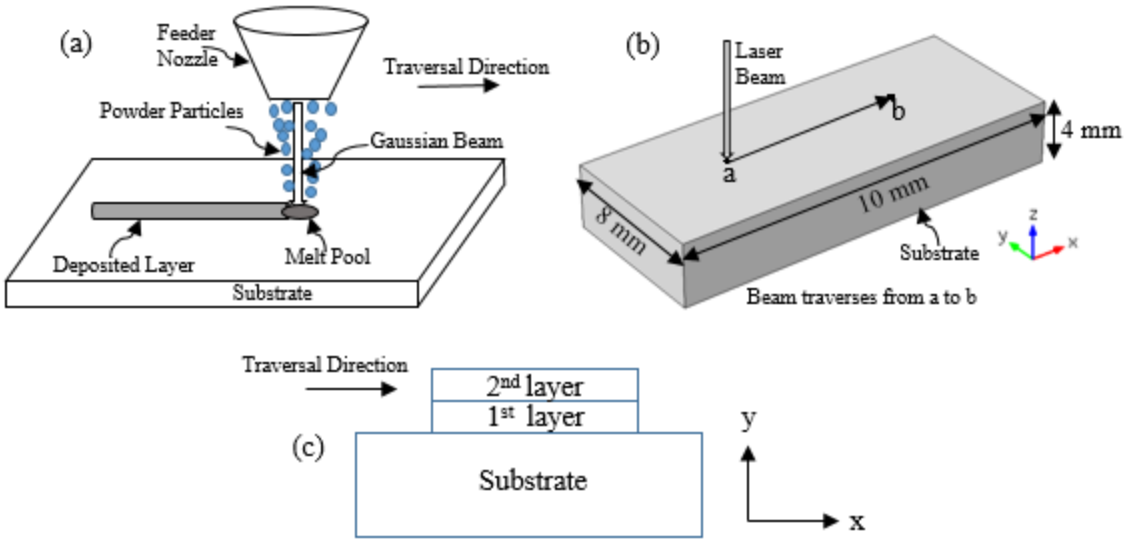


FIGURE 1. Schematic of (a) coaxial LMD process, (b) computational domain, (c) layer deposition

A constant idle time of 0.03 s is considered in the simulation. Dimensions of the computational domain, as given in Table I, are large enough to be considered as infinite. The traversing lengths are kept such that a quasi-steady state in the melt pool shape and size is reached for every case. Parameters considered in the simulations are listed in Table 1 [3]. The hexahedron type mesh structure is used for meshing of the computational domain. The material properties of SS316 are taken from [4].

| Parameter | Value |
|---|---|
| Laser spot size (mm) | 0.45 |
| Mass flow rate (g $min^{-1}$) | 6.2 |
| Laser power (W) | 210 |
| Scanning speed (mm $s^{-1}$) | 12.7 |
| Absorptivity | 0.4 |
| Idle time (s) | 0.03 |
| Domain Size (mm) | 10 × 3.1 × 8 |

TABLE 1. Parameters for simulation

The governing energy conservation equation in the computaional domain is given by

$$\frac{\partial(\rho C_p T)}{\partial t} = \nabla \cdot (k \nabla T) \tag{1}$$

During phase change, the values of $\rho$, $C_p$ and $k$ were determined by the following equations

$$\rho = (1-\beta)\rho_{solid} + \beta\rho_{liquid} \tag{2}$$

$$C_p = \frac{1}{\rho}\left((1-\beta)\rho_{solid} C_{p,solid} + \beta\rho_{liquid} C_{p,liquid}\right) + L\frac{\partial \alpha_m}{\partial T} \tag{3}$$

$$k = (1-\beta)k_{solid} + \beta k_{liquid} \tag{4}$$

$$\beta = \begin{pmatrix} 0 & T < T_{solidus} \\ \dfrac{T - T_{solidus}}{T_{liquidus} - T_{solidus}} & T_{solidus} \le T < T_{liquidus} \\ 1 & T \ge T_{liquidus} \end{pmatrix} \tag{5}$$

where $\beta$, $T_{solidus}$ and $T_{liquidus}$ represent the liquid fraction, solidus and liquidus temperature, respectively. In Eq. (3), $L$ represents the latent heat of fusion and $\alpha_m$ is the mass fraction given as

$$\alpha_m = \frac{1}{2}\ \frac{\beta\rho_{liquid} - (1-\beta)\rho_{solid}}{(1-\beta)\rho_{solid} + \beta\rho_{liquid}} \tag{6}$$

The heat energy from the laser beam can be approximated by a Gaussian distribution and the heat flux (W m$^{-2}$) on the powder bed is given by the following expression

$$q = \frac{2AP}{\pi R^2} e^{((-2(x-Vt)^2 + y^2)/R^2)} \tag{7}$$

where $q$ is the input heat flux, $A$ is the absorptivity, $P$ is the power of laser beam and $R$ is the radial distance in which energy density equals to $e^{-2}$ times that at the centre of the laser spot. The energy balance at the top surface leads to the following boundary equation

$$k\frac{\partial T}{\partial n} = q - h_c(T - T_\infty) - \varepsilon\sigma(T^4 - T_\infty{}^4) \tag{8}$$

Assuming the distribution of falling powder from the coaxially fed nozzle to be of Gaussian profile, the deposition of metal powder is realized by a moving computational mesh based on an arbitrary Lagrangian-Eulerian (ALE) formulation. To incorporate this strategy, the deformed geometry physics in COMSOL Multiphysics™ software has been used. This enables the motion of the boundary of the computational domain with time. This was implemented by solving PDEs for the mesh displacements. The top interface on which the laser beam was focused moves upward with time by a normal velocity $\boldsymbol{V_p}$ [5] given as

$$\vec{V_P} = \frac{2 m_f \eta_m}{\rho_p \pi r_p{}^2} e^{((-2(x-Vt)^2 + y^2)/r_p{}^2)}\ \hat{z} \tag{9}$$

where $m_f$ is the mass flow rate, $\rho_p$ is the density of metal powder, $r_p$ is powder stream radius and $\eta_m$ is powder catchment efficiency.

## 3. RESULTS

In simulations, a laser power of 210 W with scanning speed of 12.7 mm s$^{-1}$ was applied to the top surface of the substrate. Figure 2a shows the temperature distribution in the entire domain after the first layer deposition. In the figure, the substrate, the deposited layer and the melt pool can be clearly seen. After depositing the first layer, the beam is off for a period equal to the ideal time. The temperature field obtained after the first layer deposition is taken as an initial temperature condition for the second layer deposition. Figure 2b shows the temperature distribution during the second layer deposition. From Table 2, it can be clearly seen that the values of maximum temperature in the melt pool, the melt pool width and the melt pool depth during the first layer are significantly lower as compared to the aforementioned values for the second layer. This is due to the already increased temperature of the domain because of the preheating during the first layer deposition. The increased temperature for upper layers during the laser metal deposition leads to complex residual stresses. These stresses are undesirable and have a detrimental effects on material properties. On the contrary, the increased temperature leads to remelting in the previously solidified layer. This remelting will lead to good metallurgical bonding between the layers. Therefore, a balance needs to be maintained by optimizing idle time (for heat dissipation) and reducing power for subsequent upper layers.

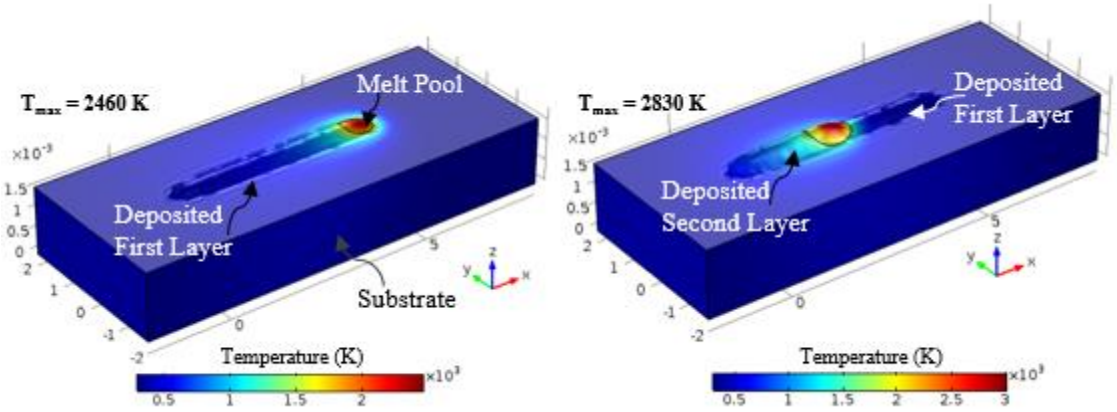


(a) (b)

FIGURE 2. Temperature map during the deposition process for idle time = 0.03 s, (a) First layer deposition, (b) Second layer deposition

| | **First Layer** | **Second Layer** |
|---|---|---|
| Melt pool width (mm) | 0.58 | 0.74 |
| Melt pool depth (mm) | 0.25 | 0.29 |
| Maximum Temperature (K) | 2460 | 2830 |

TABLE 2. Predicted melt pool characteristics

## 4. CONCLUSIONS

In this study, a process scale macroscopic model has been developed for simulating multi-layer laser metal deposition process by coupling transient energy conservation equation with ALE formulation for powder deposition. It was found that the values for maximum temperature, the melt pool width and the melt pool depth for lower layer are less as compared to the subsequent upper layer. This temperature difference influences melting between the successive layers and the generation of residual stresses. As the inter-layer melting governs the metallurgical bonding of the layers, and the residual stresses have a detrimental effects on material properties, further investigation needs to be carried out for finding optimum parameters for the LMD process.

## REFERENCES

[1] L. Han, K. Phatak and F. Liou, Modeling of laser cladding with powder injection, *Metallurgical and Materials Transactions B*, 35, 1139-50, 2004.

[2] S. Wen and Y. C. Shin, Modeling of transport phenomena during the coaxial laser direct deposition process, *Journal of Applied Physics*, 108, 044908, 2010.

[3] V. Manvatkar, A. De and T. Debroy, Heat transfer and material flow during laser assisted multi-layer additive manufacturing, *Journal of Applied Physics*, 116, 0124905, 2014.

[4] K. C. Mills, *Recommended values of Thermophysical Properties for Selected Commercial Alloys*, Cambridge, England, 2002.

[5] Z. Gan, G. Yu, X. He and S. Li, Numerical Simulation of thermal behaviour and multicomponent mass transfer in direct laser deposition of Co-base alloy on steel, *International Journal of Heat and mass Transfer*, 104, 28-38, 2017.

Fifth International Conference on Computational Methods for Thermal Problems
THERMACOMP2018, July 9-11, 2018, Indian Institute of Science, Bangalore, INDIA
*N. Massarotti, P. Nithiarasu, Pradip Dutta and C. Ranganyakalu (Eds.)*

# Prediction of Melting and Solidification Characteristics of Macro-Encapsulated PCM Capsules Using OpenFOAM®

**D. Sachan, A. K. Raj*, S. Jayaraj**
Dept. of Mechanical Engineering, NIT Calicut, Calicut, Kerala – 673 601, India
*Corresponding author: arunkraj03@gmail.com

## ABSTRACT

A transient numerical analysis centred on the aspects of charging and discharging characteristics of an industrial grade paraffin wax was investigated. The main objective of the analysis was to identify an effective macro-encapsulate configuration to be integrated with solar thermal systems (for air/ water as the working fluid). Two configurations: a) cylinder, and 2) rectangle macro-encapsulation of equal volumes has been selected as the computational domain. Enthalpy-based fixed grid method is used to solve the phase change phenomenon. Open source computational tool – OpenFOAM® has been used for simulation and post processing of the generated results. The results obtained inferred that faster charging and discharging occurs within the cylindrical domain than in comparison with rectangular, when subjected to same environmental conditions. The obtained numerical results were validated with the gallium experiment performed by Gau and Viskanta [3].

**Key Words:** *Convection, Encapsulation, Finite volume, Phase change.*

## 1. INTRODUCTION

In general, there are two types of phase change process mostly discussed in literatures, namely, conduction and convection dominated phase transitions. In the former case, during the mathematical formulation of the problem, ignorance of buoyancy effects which results in natural convection of the liquid phase greatly reduce the complications involved during the analysis [1]. Voller [2] formulated an enthalpy-based method to solve phase change problems. Fixed grid enthalpy method was used for the problem formulation. Gau and Viskanta [3] had performed experiments with gallium and presented the results. However, the buoyancy effects are known to play a significant role in dissipation of energy within the melt front. Therefore, neglecting its effect will divert the resulting solution from the actual data. This paper takes into account of buoyant forces during phase transitions for both configurations of macro-encapsulate. In this present numerical approach, rectangular and cylindrical encapsules have been chosen for studying the phase change characteristics of paraffin wax (314K). The volume of melted paraffin wax has been found by considering the volume of melt region. Contours of melt fraction for both configurations obtained during the analysis are presented.

## 2. MAIN BODY

For carrying out the present numerical work, certain assumptions have been taken into account while formulating the mathematical model. The various assumptions are listed out as follows:

• Phase change material is homogeneous and isotropic

• Phase change process in the phase change material is assumed to be non-isothermal

• Thermo-physical properties are different for solid and liquid phases but constant with respect to temperature

• Property degradation and super-cooling are not envisaged in the phase change material

On this basis, the conservative energy equation employed to tackle the phase transition in paraffin wax can be expressed as:

$$\frac{\partial(\rho h)}{\partial t} + div(\rho u h) = div(\lambda . grad(T)) \quad (1)$$

where *h* denotes the specific enthalpy of the PCM and it can be expressed in terms of latent heat as mentioned below:

$$h = h_s + L(T) = \int_{T_{ref}}^{T} c.dT + \gamma L \quad (2)$$

$$\gamma = (T - T_s) / (T_l - T_s) \quad \text{for} \quad T_s < T < T_l \quad (3)$$

However, it must be noted that the energy equation is coupled with the momentum and continuity equation as the convection effects arising in the melt region due to the motion of melt front is taken into account. Momentum conservation equation for the accounted convection effects in melting region can be represented as follows:

$$\frac{\partial(\rho u)}{\partial t} + div(\rho u u) = div(\eta . grad(u)) - \frac{\partial p}{\partial x} \quad (4)$$

$$\frac{\partial(\rho v)}{\partial t} + div(\rho u v) = div(\eta . grad(v)) - \frac{\partial p}{\partial y} + S_b \quad (5)$$

where $S_b$ is the source term in the y-momentum conservation equation and it can expressed as:

$$S_b = \rho g \, . \, [1 - max(\beta \, . \, (T - T_s))] \quad (6)$$

The continuity equation in the incompressible media can be expressed in the form:

$$div(u) = 0 \quad (7)$$

The proposed numerical model was solved by implementing the governing equations as stated and by specifying the boundary conditions into an open source computational tool knwon as OpenFOAM®. A finite volume (FVM) analysis is used for discretization and PIMPLE algorithm is

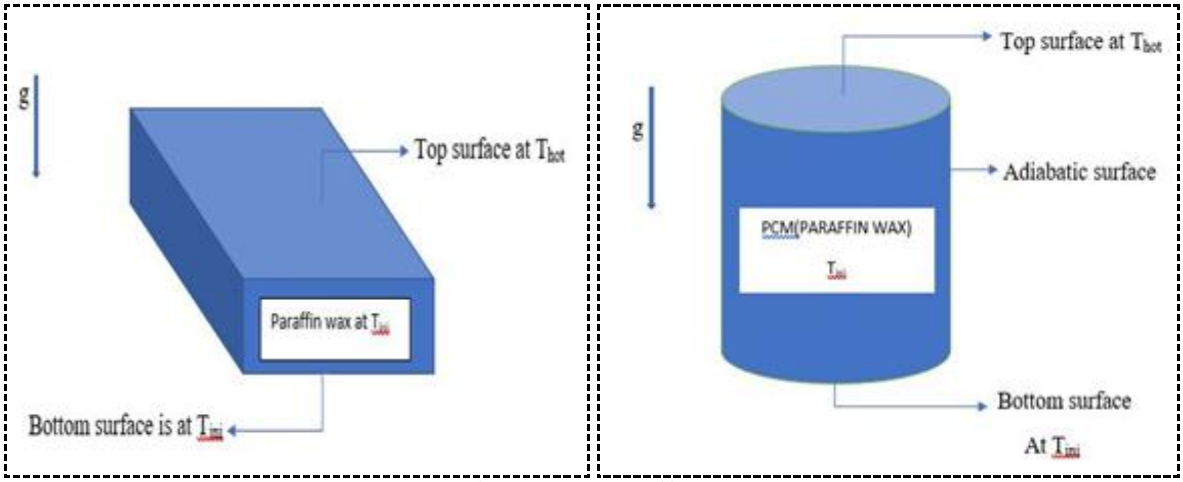


FIGURE 1 a) Rectangle encapsulate filled with paraffin wax, b) cylinder encapsulate containing paraffin wax

| | |
|---|---|
| Density | 820 $kg/m^3$ |
| Thermal conductivity | 0.21 $W/mK$ |
| Melting point | 314K |
| Latent heat of fusion | 141600 $J/kg$ |
| Specific heat capacity(solid) | 1800 $J/kg\ K$ |
| Specific heat capacity(liquid) | 2400 $J/kg\ K$ |
| Dynamic viscosity | 25.34e-03 $kg/m\ s$ |

TABLE 1 Thermophysical properties of paraffin wax

used to solve the pressure-velocity coupling. Two configurations are used for carrying out the present numerical analysis. In the first configuration paraffin wax was filled within a rectangular encapsulate (8×4×17.2cm) while in the second configuration it was filled within a cylindrical encapsulate (*r*: 5cm, *h*: 7cm) as shown in Figures 1(a) and (b). For both configurations, the top face is subjected to temperature greater than all other faces (i.e. $T_{hot} > T_{ini}$). Throughout the analysis, the volume of PCM contained in both the configurations was assumed to be the same. As a result, the surface area available for heat transfer is different for both configurations. The thermo-physical properties of the paraffin wax used for the present analysis is shown in Table 1.

## 3. RESULTS

For postprocessing the simulated results 'Paraview' package in OpenFOAM® has been used. The proposed solver was initially validated with the experimental results of Gau and Viskanta [3] as shown in Figure 3. As stated, gallium was used as the phase change material. From the results obtained it can be concluded that the proposed solver is fairly suitable to predict the phase change characteristics of the encapsulated PCM.

In the present analysis, both charging and discharging aspects of two different macro-encapsulate configurations containing the same amount of PCM is analyzed. Initially for both the configurations, the solid PCM (bluish region corresponds to zero volume fraction) was subjected to a temperature greater than the corresponding melting point of PCM (i.e. $T_{hot} > T_{pcm}$). The results thus obtained showed that during the charging process due to natural convection in the melting region, melting occurs at a faster rate. It was noted that during the initial two hours, the charging process was much faster and later on it gradually slows down due to the dominance of conduction heat transfer in the melt region (reddish region). Yet another aspect which slows down the charging characteristics is the formation of mushy region in between the melt and the solid region. The volume of left over solid PCM in the rectangular configuration after 5 hours of continuous melting process was found to be 2.04e-04cm$^3$. Similarly, for the same applied boundary conditions in cylindrical configuration, the left over solid PCM volume was found to be 2.5e-04cm$^3$. A comparison of the melted region in both configurations showed that about 22% of solid PCM haven't undergone melting in comparison with the rectangular configuration. Figure 4 depicts the melting characteristics of both rectangle and cylinder macro-encapsulates. The percentage increase in charging characteristics in rectangular encapsulate is attributed to its surface area. The heated surface area is 57% more than the cylindrical encapsulate, thereby, more energy is conducted to the solid PCM in case of rectangular encapsulation. Figure 5 describes the contours of discharging of PCM contained in the cylindrical encapsulate. It can be observed that, the discharging is relatively slower than charging process. This is attributed to the fact that, during solidification convection effects are negligible and the only mode of heat transfer is conduction. Moreover, the volumes of solidified paraffin wax after 5 hours was found to be 1.57e-04 cm$^3$ in case of cylinder and 2.06e-04cm$^3$ in case of rectangle macro-encapsulates, respectively.

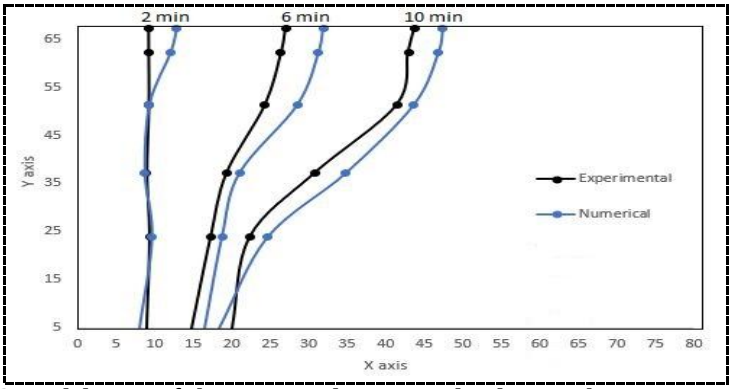


FIGURE 3. Validation of the proposed numerical solver with experimental results

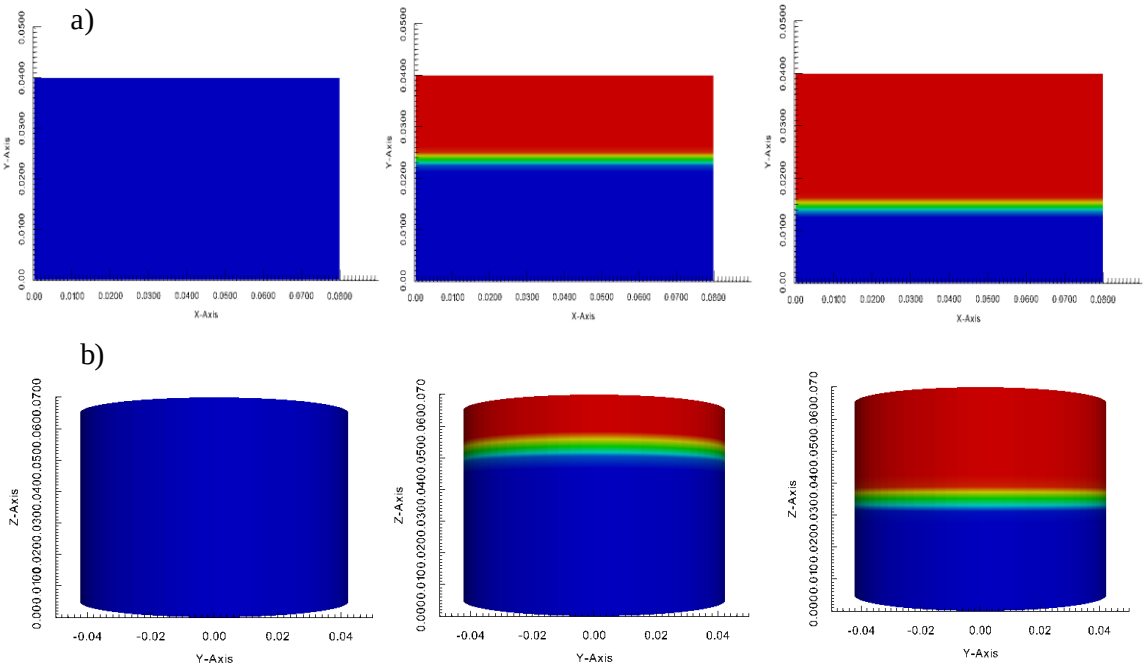


FIGURE 4. Melting of solid PCM at various time intervals for both configurations

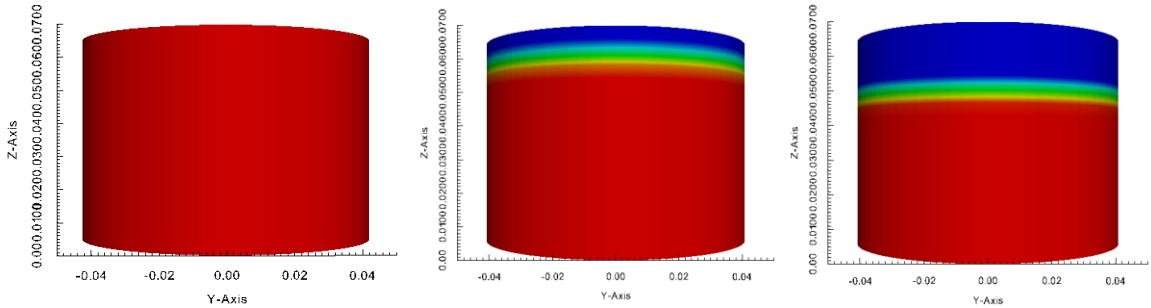


FIGURE 5. Solidification characteristics of melted PCM at various time intervals

## 4. CONCLUSIONS

In this paper both charging and discharging characteristics of a macro-encapsulated PCM has been analysed using the numerical methods. Convection-dominated phase change analysis is performed on two different configurations. The results showed that due to natural convection in the melted region, the charging process was found to be much faster than the discharging process. The numerical analysis was carried out for 5 hours duration. For the same volume, rectangular encapsulation was found to be about 22% more efficient than cylinder during charging. Similarly, solidification was found to be effective in rectangle encapsulate due to its increased surface area.

## REFERENCES

[1] H. Shmueli, G. Ziskind and R. Letan, Melting in a vertical cylindrical tube: numerical investigation and comparison with experiments, *Int. J. Heat Mass Transfer*, 53:4082-4091, 2010.

[2] V. R. Voller, Implicit finite-difference solutions of the enthalpy formulation of Stefan problem, *IMA Journal of Numerical Analysis*, 5,201-214, 1985.

[3] C. Gau and R. Viskanta, Melting and solidification of a pure metal on a vertical wall, *Journal of Heat Transfer*, 108,174-181, 1986.

Fifth International Conference on Computational Methods for Thermal Problems
THERMACOMP2018, July 9-11, 2018, Indian Institute of Science, Bangalore, INDIA
*N. Massarotti, P. Nithiarasu, Pradip Dutta and C. Ranganyakalu (Eds.)*

# MODELING OF THERMAL MANAGEMENT IN AUTOMOTIVE BATTERY MODULES

**Amaresh Dalal*, Amber Gupta, Akshay Gupta**
Department of Mechanical Engineering, Indian Institute of Technology Guwahati, 781039, India
*Email: amaresh@iitg.ernet.in

**Partha P. Mukherjee**
School of Mechanical Engineering, Purdue University, West Lafayette, IN 47907, USA

## ABSTRACT

Li-ion batteries are widely used today due to various advantages associated with them, however a serious problem related to them are finding ways for dissipation of heat generated. To solve this we propose the use of longitudinal vortex generators (winglets) to enhance the heat transfer. In this work CFD simulations of cooling of a battery pack with and without vortex generators are performed. Longitudinal vortices produced behind winglets enhance heat transfer. Various parameters like inlet velocity and positioning of vortex generators are varied to study their effect on cooling. Results are shown in terms of heat transfer coefficient variations.

**Key Words:** *Convection; Thermal management; Vortex generator; Longitudinal vortices.*

## 1. INTRODUCTION

Lithium-ion batteries are growing popular with regard to their wide spread application in the field of electronic goods, aerospace technology and their advantages like lighter weight than other secondary batteries makes them commercially very useful. Chen et al. [1] have accounted for the complex effect of contact layer on heat transfer as it provides extra thermal resistance and heat capacity to the system and contribution of radiation to the overall heat dissipation under natural convection to be about 43-63% suggesting that modifying the surface to enhance the emissivity is an efficient and economical way to improve heat dissipation. The results showed that the extra heat capacity dominates the temperature under natural convection, whereas the extra thermal resistance dominates the temperature under forced convection. Torii et al. [2] were able to augmented heat transfer by 30% to 10% in staggered winglet arrangement, and yet the pressure loss was reduced by 55% to 34% for the Reynolds number ranging from 350 to 2100. In case of in-line tube banks, these were found to be 20% to 10% augmentation, and 15% to 8% reduction, respectively.

Ample research has been done on lithium ion battery analyzing different aspects of heat transfer. Study by Inui et al. [3] on 3D thermal battery models with the same capacity and different cross sectional shapes reveals the effect of laminated cross section on suppression of the temperature rise in comparison with the battery with square cross section to a greater extent but has negligible effect on the suppression of the temperature unevenness. Another battery thermal analysis work by Giuliano et al. [4] on lithium titanate cells used in electric vehicles employs cooling system to improve battery performance and life. Thermo-chromic liquid crystals were implemented to instantaneously measure the entire surface temperature field of the cell.

The present study focuses on the effect of vortices in presence of winglets to the heat transfer rate from the system. They interact with the normal air flow inside the battery, thus generating vortices after flow separation. Evaluation of work performance is done with and without the presence of winglets (vortex generators) and results can be compared based on increase in outlet temperature, increase in heat transfer coefficient inside the battery.

## 2. METHODOLOGY

In the present problem, an attempt has been made to do some modifications for enhancing the cooling rate through air flow. Commercially available A123 Hymotion™ L5 PCM pack assembled with the A123-26650 Li-ion cylindrical cells is used as a reference for geometry of our simplified battery model used for thermal analysis. Model contains 44 heat generating cylindrical cells arranged in 11 columns. Figure 1 shows the dimensions of battery pack. Figure 2 shows the staggered arrangement of the cylindrical cells. In this study

the staggered arrangement of cells has been considered as it gives better performance than the inline arrangement. Modifications are made in model to enhance the heat transfer rate inserting winglets in the base model. We have used delta winglets arranged behind the cylinder as shown in Fig. 3.

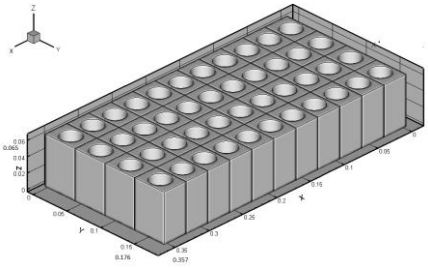

Figure 1. Battery model and its dimensions

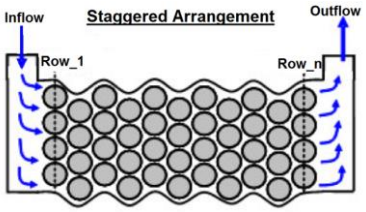


Figure 2. Staggered Arrangement

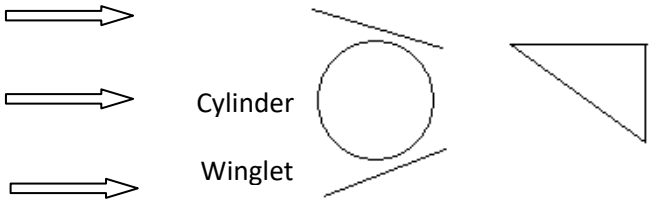


Figure 3. Winglets arrangement

## 3. NUMERICAL SOLVER

The following governing equations are solved for incompressible laminar flows. All simulations in the present study have been performed using ANSYS Fluent. The convergence criteria of $10^{-5}$ were used for all variables.

Continuity equation:

$$\nabla \cdot \mathbf{u} = 0$$

Momentum equation:

$$\nabla \cdot \left( \rho \mathbf{u}\mathbf{u} \right) = -\nabla p + \nabla \cdot \boldsymbol{\tau}_{ij}$$

Energy equation:

$$\nabla \cdot \left( \rho c_p \mathbf{u} T \right) = k \nabla^2 T$$

where **u** represents the velocity vector, $p$ is the pressure, $T$ is the temperature and $\boldsymbol{\tau}_{ij}$ is the deviatoric stress tensor.

## 3. BOUNDARY CONDITION

The boundary conditions for the present problem are considered as follows.

Inlet velocity = 0.4 m/s and 0.8 m/s, inlet temperature = 300 K, cell wall temperature = 318 K, top wall temperature = 323 K, bottom wall temperature = 323 K, side walls heat flux = 0 and outflow boundary condition at outlet.

## 4. RESULTS

The numerical simulation has been carried out for the staggered arrangement of cylindrical cells with and without winglets. Figure 4(a) shows the winglets placement behind first row all cells and Fig. 4(b) shows the winglets placement behind the middle row alternative cells. Another case is also considered as winglets placement behind first row alternative cells.

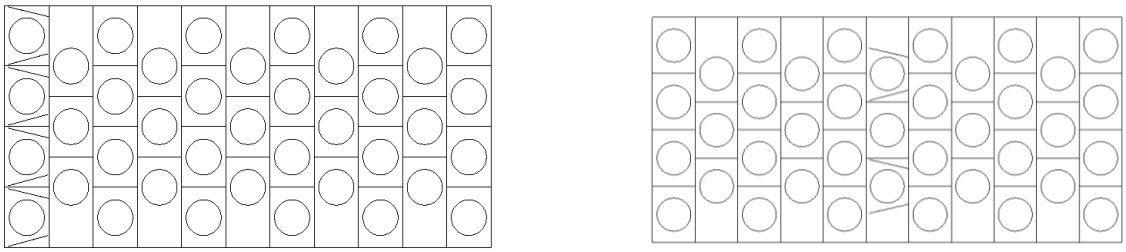

(a) (b)

Figure 4. Top view of staggered arrangement with winglets (a) first row, (b) middle row

From Fig. 5, it is clear that heat transfer coefficient on bottom plane increases by the use of winglets thereby indicating enhancement in cooling. The longitudinal vortices formed due to the placement of winglets increase the heat transfer.

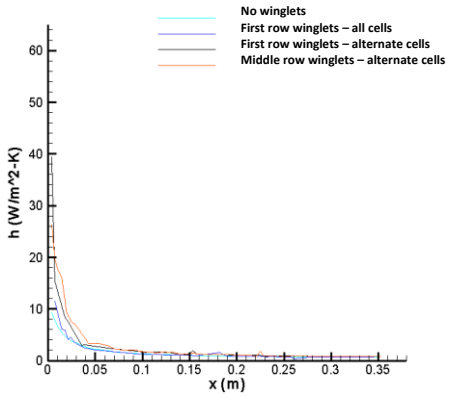


Figure 5. Variation of heat transfer coefficient along $x$ on bottom plane

Table 1 shows the overall heat transfer coefficient for two different inlet velocities. We observe that the heat transfer coefficient increases with the use of winglets which is primarily due to faster heat dissipation by generation of more vortices. The arrangement with winglet placement in first row alternate cells gives the maximum enhancement in heat transfer.

Table 1. Comparison of the heat transfer coefficient placed in alternate cells

| | *v*=0.4 m/s | | | *v*=0.8 m/s | |
|---|---|---|---|---|---|
| | *h* ($W/m^2.K$) | % Increase | | *h* ($W/m^2.K$) | % Increase |
| No slit | 8.69 | - | | 13.42 | - |
| Winglets in first row | 13.85 | 59.38 | | 20.6 | 53.5 |
| Winglets in middle row | 11.42 | 32.44 | | 16.06 | 19.6 |

## 5. CONCLUSIONS

- There is significant increase in heat transfer by use of vortex generators in staggered arrangement of Li-ion cylindrical cells.
- The heat transfer coefficient increases with increase in velocity for all cases studied.
- The winglets placement in first row alternate cells gives the maximum heat transfer coefficient among the cases studied here and upto 50% decrease in pressure drop as compared to base case.

## 6. REFERENCES

[1] Chen S.C.**,** Wan C.C. and Wang Y.Y., 2004, "Thermal analysis of lithium-ion batteries", Journal of Power Sources, 140, 111-124.

[2] Torii K., Kwak K.M, Nishino K., 2002, "Heat transfer enhancement accompanying pressure-loss reduction with winglet-type vortex generators for fin-tube heat exchangers", International Journal of Heat and Mass Transfer, 45, 3795–3801.

[3] Inui Y.**,** Kobayashi Y.**,** Watanabe Y.**,** Watase Y. and Kitamura Y., 2007, "Simulation of temperature distribute on in cylindrical and prismatic lithium ion secondary batteries", Energy Conversion and Management, 48, 2103-2109.

[4] Giuliano M.R., Advani S.G. and Prasad A.K., 2011, "Thermal analysis and management of lithium–titanate batteries", Journal of Power Sources, 196, 6517-6524.

# A Thermal Model for Waste Heat Recovery Using PCM.

**A. Sharma, S.Vasireddy and P. Rath**
School of Mechanical Sciences
Indian Institute of Technology Bhubaneswar
Argul, Jatni, Odisha, India - 752 050

## ABSTRACT

The thermal energy storage ability of PCM plate thermal energy storage (TES) unit for waste heat recovery is investigated numerically. The performance evaluation of TES unit using PCM is studied through a 2-D numerical model to evaluate their suitability for practical usage in household purpose. The heat transfer fluid (HTF) used in this analysis is water and PCM as paraffin wax. Both charging and discharging cycle is included in the model and corresponding results are included here. It is found that almost 12% of energy is stored in PCM TES unit during the charging cycle from the hot inlet HTF and out of which approximately 44% is recovered and given back to cold HTF during discharging cycle. Hence the proposed TES is expected to reduce the power consumption of household appliances such as Dish washer, heater based washing machine etc.

**Key Words:** *PCM, Heat Transfer Fluid, Waste Heat Recovery etc.*

## 1. INTRODUCTION

In the present world scenario of technological development, with the increase in ease of living and living standard, the demand for source of energy also increased simultaneously. One of the solution is to develop energy storage devices, which are as important as developing new sources of energy. Storing the energy in suitable forms, which can conveniently be converted later into the required form, is a current challenge for technological advancement. Hence, the waste heat recovery systems (WHR) have gathered more interest towards the development of new thermal energy storage (TES) technology.Around 20–26% of the total energy consumption in a typical home is consequence of water heating activities [**1-2**]. There are different sources of waste water heat in household applications, i.e.: bath/shower, sink, washing machine or dish-cloth washing machine. For this reason, there is high potential for drain water heat recovery (DWHR) systems in order to save energy used to heat domestic water. A DWHR system recovers heat from a waste water volume, which can be reused for water preheating, the reuse (obtaining heat again) efficiency depends on several factors like type of heat storage i.e. sensible or latent heat storage. The latent heat storage system uses the Phase Change Material (PCM) for storing the energy for its later use. The PCM provides a greater density of energy storage with a smaller temperature difference between storing and releasing heat than the sensible heat storage method. Hence pcm based latent heat storage is more suitable for the purpose of DWHR systems.

## 2. PROBLEM DESCRIPTION AND MATHEMATICAL MODEL

The present problem involves two cycles: the charging and the discharging cycle. During charging cycle, waste hot water which is drained out of a domestic appliance gives part of its thermal energy, which is absorbed by the PCM plates in the form of latent heat and change its phase from solid to liquid. During discharging cycle, the PCM plate releases its thermal energy to preheat the water before its use in the appliance and changes its phase again back to solid. This helps in pre-heating the cold water and also thereby reducing the energy consumption.The physical schematic and the computational domain of the problem are as shown in Fig. 1.

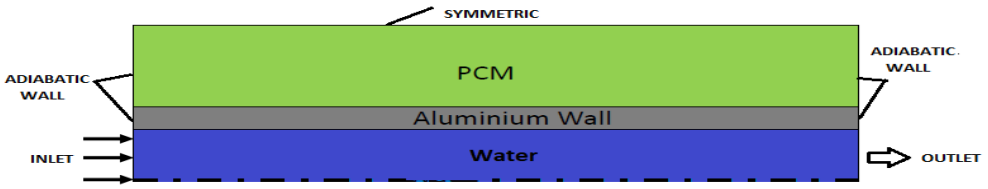


Figure 1. 2-D Model with Boundary Conditions during charging cycle.

HTF (water) flows through the inlet and passes between the PCM plates as shown in Fig. 1. The HTF flows due to forced convection with an inlet velocity of 0.25 cm/s. The opening between the two plates kept as 8 cm. and hence the mass flow rate is 0.15 kg/s. The length of plates are taken as 50 cm. as shown in Fig. 1. Flow of molten pool in the PCM region is due to natural convection which is modeled using the Boussinesq approximation. The thermo physical properties used in numerical analysis are shown in Table 1.

| **Material** | $\rho$ **(kg/m$^3$)** | **K(W/mK)** | $\mu$ **(Ns/m$^2$)** | **$T_m$(K)** | **$L_f$ (kJ/kg)** | **$C_p$ (J/kgK)** | $\beta$ **(1/K)** |
|---|---|---|---|---|---|---|---|
| Paraffin | 853.5 | 0.21 | .007 | 333-337 | 189 | 2230 | .003 |

The governing equations are discretized using the finite volume method [3]. Fully implicit scheme is used for discretizing the transient term. SIMPLER algorithm of Patankar [3] is used to obtain the flow field solutions. The Power law scheme is used to discretize the convection-diffusion terms. A line-by-line Tri-Diagonal-Matrix-Algorithm (TDMA) is used to solve the resulting discrete linear algebraic equations. Multiple sweeping (from all possible directions) algorithm is used to bring in the boundary information quickly into the interior of the domain. This helps in reducing the number of iterations for convergence. The non-linear source terms are linearized using the approach of Patankar [**3**]. The enthalpy –porosity technique of Brent et.al. [**4-5**] is used to model the phase change of PCM in the PCM plate. The governing transport equations for the proposed problem are as given below.

**PCM Region**

**Continuity equation:** $\frac{\partial \rho}{\partial t} + \nabla.(\rho \vec{u}) = 0$

**Momentum equations**

$$\frac{\partial(\rho u)}{\partial t} + \nabla.(\rho \vec{u} u) = \nabla.(\mu(\nabla u)) - \frac{\partial P}{\partial x} + Au$$

$$\frac{\partial(\rho v)}{\partial t} + \nabla.(\rho \vec{u} v) = \nabla.(\mu(\nabla v)) - \frac{\partial P}{\partial x} + Av + \rho g \beta (h - h_{ref}) / C_p$$

where $A = C\frac{(1-\varepsilon)^2}{\varepsilon^3 + b}$ ; ε is the liquid fraction, *C* is mushy zone constant and *b* is a small number to avoid division by zero.

**Energy Equation:** $\frac{\partial(\rho h)}{\partial t} + \nabla.(\rho \vec{u} h) = \nabla.(\alpha(\nabla h)) + S_h$ **;** $h = c_p T$

The governing equations for water, PCM and solid domain are in general form as shown above. The flow field in the solid domain is suppressed by setting $\mu$ to a large value. The mushy source term *A* and the enthalpy source term $S_h$ are applicable only in the PCM region.

## 3. RESULTS

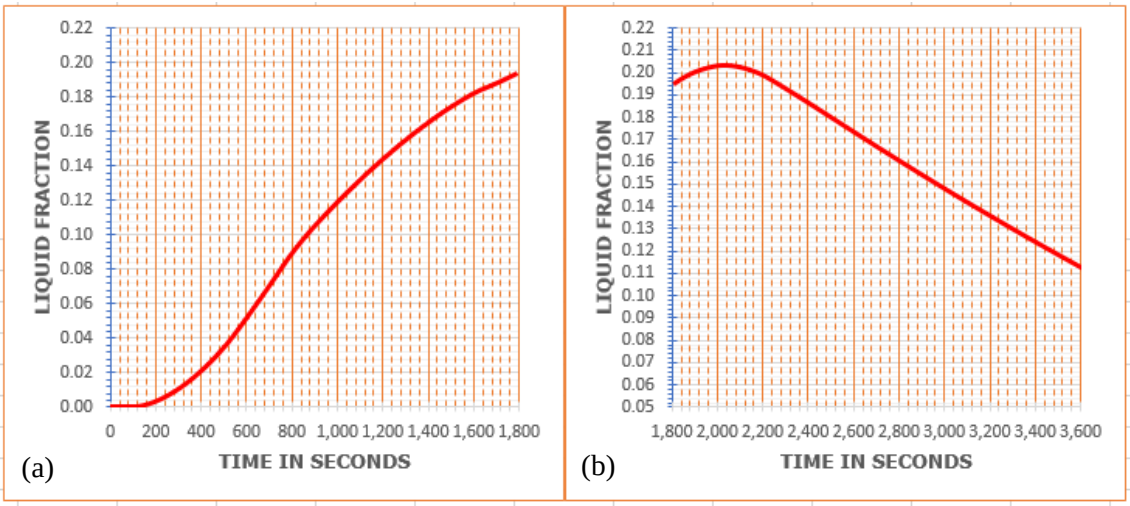


**Fig. 2.** Overall liquid fraction in the PCM region: (a) charging cycle; (b) discharging cycle.

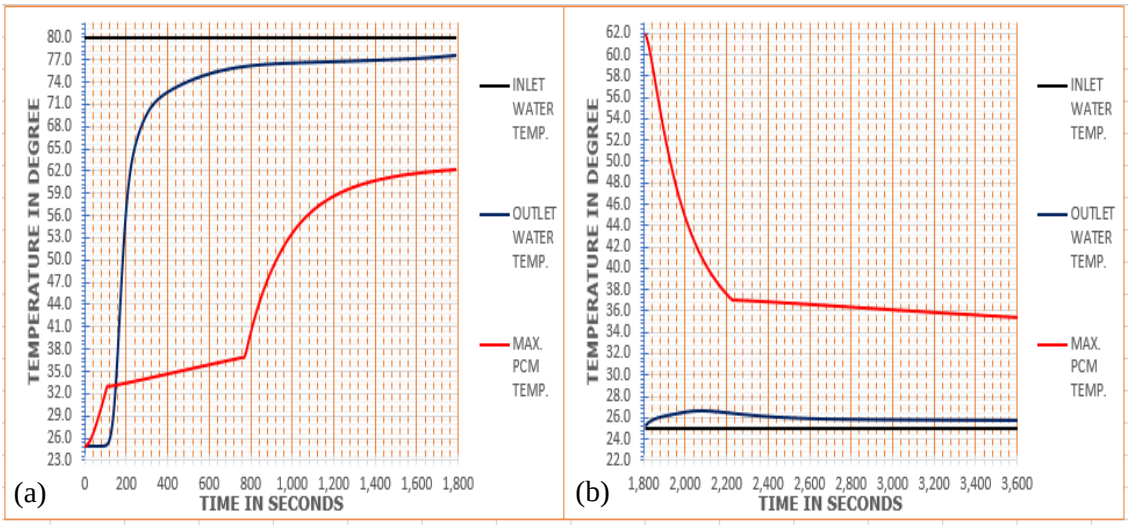


**Fig. 3.** Temperature distribution in the water and PCM region: (a) charging cycle; (b) discharging cycle.

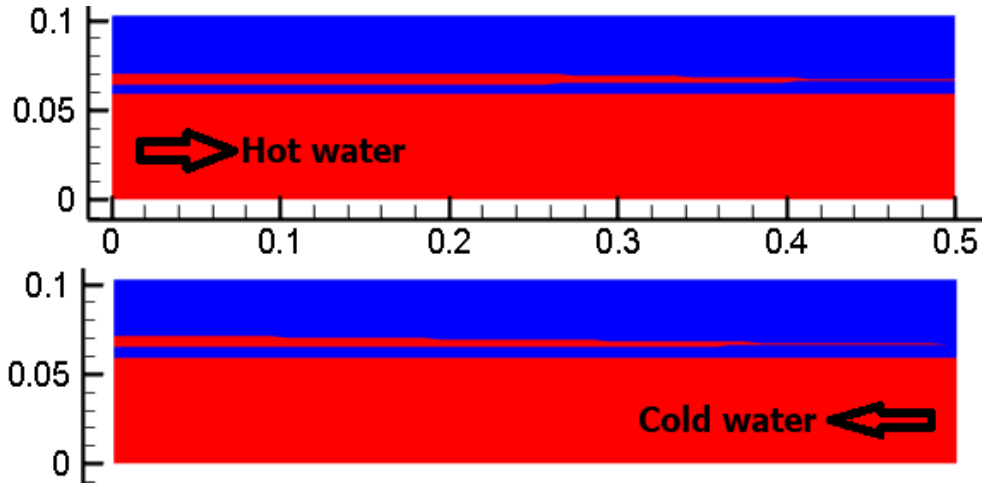


**Fig. 4.** Liquid fraction (filled contour) distribution at the end of charging and discharging cycles.

## 4. RESULTS DISCUSSION

The overall liquid fraction in the PCM region is shown in Fig. 2. For an initial transient period for approximately 200s, sensible heat is absorbed by the PCM during charging cycle and no phase change occurs in PCM with zero liquid fractions. As time progresses further, temperature exceeds the melting temperature of PCM and phase change starts, thereby increase in the liquid fraction with time. Approximately 19% of PCM melts in 1800s during charging cycle. A reverse phenomenon was found during discharging cycle where liquid fraction gradually decreases with time and at the end of 3600s only 11% of liquid PCM left in the PCM region.

Figure 3 shows various transient temperature variations in which temperature range varies from 80°C (Inlet hot water temperature) to 25°C (initial ambient temperature & cold-water inlet temperature). In charging cycle (Fig. 3a) the maximum temperature of PCM is initially increases continuously (around initial 150sec.) due rise in sensible heat, but after some time, it's slop changes as melting (33ºC to 37ºC) in the inlet region gets started. Then again there is change in slop (above 37ºC) because whole PCM near to the inlet region got melted and it starts storing the sensible heat. Similarly, in discharging cycle (Fig. 3b) maximum temperature of PCM first decreases (from 62°C to 37°C) due sensible heat loss by PCM near to the inlet region then there is a change in its slop due solidification of PCM near to the inlet region of cold water.

Figure 4 shows the filled contour of molten PCM in the PCM region at the end of charging and discharging cycles. During charging cycle, hot water enters the unit from left side, hence more melting takes place in the left hand side of the unit due to the absorption of more amount of available thermal energy from the hot water. As water moves downstream (towards right in the figure) its thermal energy content decreases which results in less melting of PCM near to the exit region of hot water. A reverse phenomenon is observed in the discharge cycle, where cold water enters the unit from the right hand side.

Hence by using PCM unit in DWHR system, 12% of energy given by hot water is get stored in the PCM plate unit till 1800s and out of which 44% of total energy which was stored in PCM unit, is given back to cold water during the discharging cycle for next 1800s. This amount of energy is average of 7.29% of the energy required by hot water for next working cycle (charging cycle).

## 5. REFERENCES

1. McNabola, A., and Shields, K., 2013, "Efficient drain water heat recovery in horizontal domestic shower drains", Energy and Buildings, 59, pp. 44-49.
2. S. Morales-Ruiz , J. Rigola , C. Oliet , A. Oliva, "Analysis and design of a drain water heat recovery storage unit based on PCM plates", 2016, Applied Energy, 179, pp. 1006–1019.
3. Patankar, S.V., "Numerical Heat Transfer and Fluid Flow," Hemisphere Publication, New York, NY, 1980.
4. Brent, A.D., Voller, V.R., and Reid, K.J., 1988, "Enthalpy- Porosity Technique for Modelling Convection-diffusion Phase Change: Application to Melting of Pure Metal," Numerical Heat Transfer, Vol. 13, pp.297-318.
5. Sahoo S., Rath P. and Das M., 2016, "numerical study of phase change material based orthotropic heat sink for thermal management of electronics components", international journal of heat and mass transfer, 103, pp. 855-867.

# OPTIMIZATION OF FIN VOLUME FOR PCM BASED HEAT SINK

**Akshay Desai**
Energy Science and Engineering Department, IIT Bombay, Mumbai-400076,
desaiakshay49@gmail.com

**V. K. Singh**
Thermal Engineering Division, Space Applications Centre, ISRO, Ahmedabad-380015,
singhvivek@sac.isro.gov.in

**R. N. Patel**
Thermal Engineering Department, Institute of Technology, Nirma University, Ahmedabad-382481,
rnp@nirmauni.ac.in

## ABSTRACT

Thermal control of space based electronic subsystems is a challenging task due to absence of convective heat transfer in the space environment. In such situation phase change material (PCM) may provide a promising solution wherein heat is absorbed as latent heat of fusion. To improve thermal conductivity of PCM and efficient heat transfer from source to PCM, fins can be used as thermal conductivity enhancer. This paper numerically investigates the effect of thermal conductivity enhancer (fins) on the performance of phase change material based heat sink. The work mainly focuses on the temperature control of electronic subsystem mounted over panel along with PCM based heat sink. Dimethyl sulfoxide is used as a PCM which is having melting temperature of $18^{O}$ C and filled into the heat sink made up of Aluminium 6061. The phase change phenomena is modelled using the effective heat capacity method and pulse heat load conditions are applied at the heat source. Heat generation of electronics subsystem under consideration is 10 W for a period of 12 minutes over a cycle of 100 minutes. As thermal conductivity of PCM is very low, thermal conductivity enhancers have been used in the different volumetric configuration to see the effect on the performance of PCM based heat sink. The volumetric fraction of thermal conductivity enhancers (TCE) are varied from 0% (no fins) to 40% (57 number of fins) of total available volume of PCM cavity. The geometrical dimensions of TCEs are kept constant [2 mm X 2 mm X 18 mm] for all volume fractions. The current study only focuses on the optimization of volume fraction of thermal conductivity enhancers.

**Key Words:** *Phase change material, Thermal conductivity enhancer, Heat sink, Latent heat.*

## 1. INTRODUCTION

Thermal control in space-based subsystems is distinct from those at ground level due to the absence of free convection in space and presence of microgravity condition in space. Certain types of electronics subsystems used in spacecraft payload are subjected to cyclical duty cycle and have large power pulses for a relatively short active period. Humphries & Griggs [1] proposed use of PCM based heat sink for satellite components. Krishnan & Garimella [2] presented numerical investiagrtions of phase change energy storage System for Pulsed Power Dissipation. Humphries & George [3] reported significent effect of presence of microgravity on thermal performnce of PCM capacitors. Himran et al. [4] reported change in thermophysical properties of PCM due to its cyclic operation.

PCM has a big drawback of its low thermal conductivity for efficient conductive heat transfer. To overcome this drawback, several heat transfer enhancement techniques were proposed by the researchers e.g. use of fins [5,6], metal matrices [7], PCM containing Nano particles [8] and micro encapsulation of PCM [9]. Alawadhi et al. [10] modelled phase change phenomena considering only conduction heat transfer for thermal control unit.

In this study, the numerical investigation has been carried out to evaluate the effect of volume fraction of fins on the performance of PCM based heat sink. Volume fraction is varied from 0% (no fin) to 47% under the same heat load [10W for 12 minutes over 100 minutes cycle] and boundary conditions (base plate temperature fixed at $10^0$C). Dimethyl sulfoxide (melting point 18$^o$ C) is used as a PCM. The numerical model is validated with the previously reported experimental results.

## 2. MATHEMATICAL MODEL

PCM based heat sink is studied separately and isolated from the electronic device which reduced the efforts in computations. Several number of numerical simulations are carried out by varying material and height of PCM container to get desired temperature with given heat input. Invar [k=13 W/mK] was selected as container material to avoid heat flow through container and to speed up the heat transfer from heat source to PCM, aluminium [k=167 W/mK] was selected as cover plate material. Schematic of PCM based heat sink is shown in FIGURE **1**. Thermo physical properties of dimethyl sulfoxide (PCM) are given in TABLE **1**.

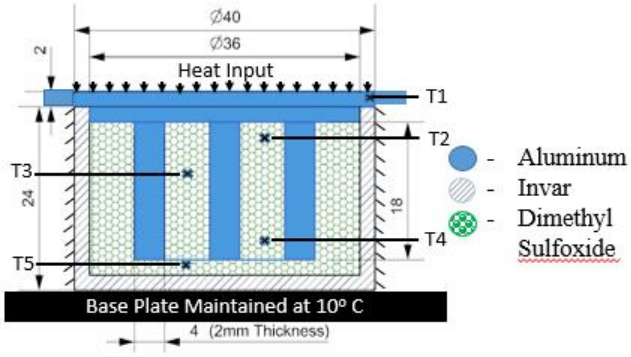


FIGURE 1. Schematic of heat sink

| Properties | Value |
|---|---|
| Density (kg/m$^3$), ρ | 1009 |
| Specific heat (kJ/kg K), $C_p$ | 1.885 |
| Conductivity (W/m K), K | 0.24 |
| Latent heat of fusion (kJ/kg), L | 85.7 |
| Melting temperature (K), $T_m$ | 291 |

TABLE 1. Thermophysical properties of DMS [11]

## 3. NUMERICAL INVESTIGATION

The numerical investigations are carried out with some simplified assumptions and heat equation is discretized by finite element method. In the current study, the phase change phenomena is captured by the effective heat capacity method [10-13]. The heat equation can be written as

$$(\rho C_p)_{eq} \frac{\partial T}{\partial t} = \nabla(k_{eff} \nabla T) \qquad (1)$$

All other thermo physical properties are defined as a function of liquid fraction and modified accordingly. To incorporate the effect of latent heat of fusion during phase change, specific heat $C_p$ should be modified by accounting the latent heat of fusion.

$$C_p(T) = \begin{cases} C_{ps} & ,T < T_m \\ \dfrac{C_{ps} + C_{pl}}{2} + \dfrac{L}{\Delta T} & ,T_m < T < T_m + \Delta T \\ C_{pl} & ,T > T_m + \Delta T \end{cases} \qquad (2)$$

## 4. RESULTS

Numerical simulations are carried out for various volume fraction ranging from 0% (no fins) to 40% (57 fins). During whole cycle, the bottom surface of container is maintained at 10 C of constant temperature. Both charging and discharging phenomena of PCM is shown in FIGURE 2 for various volume fractions. It is seen that initially temperature of heat source decrease with increase in fin volume fraction (up to $46^0$C for 6% volume fraction for current case) and temperature increases further with increase in fin volume fraction due to decrease in mass of PCM. Decrease in mass of PCM lowers the latent heat storage capacity due to which temperature increases.

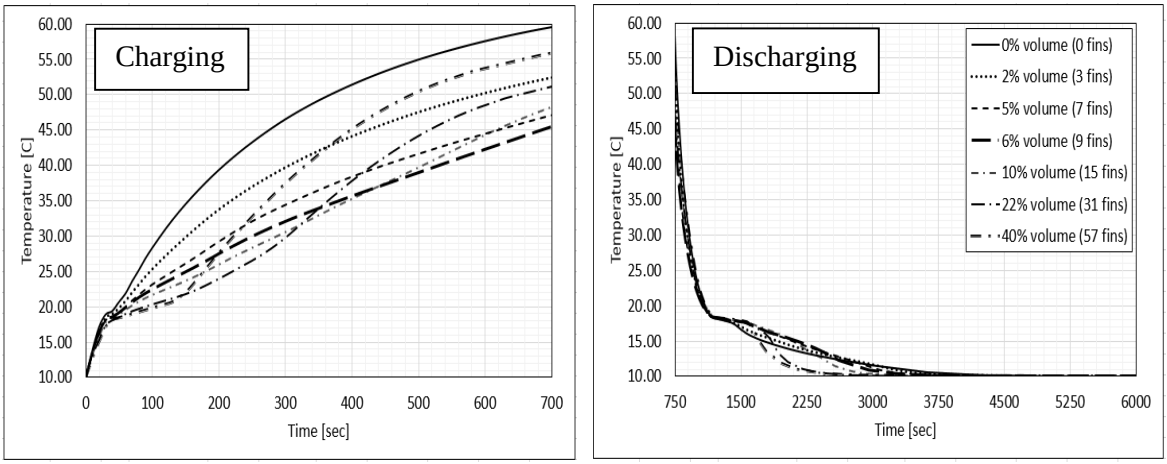


(a) (b)

FIGURE 2. Variation of temperature with time for different fin volume fraction

## 5. CONCLUSIONS

This current study mainly focuses on the effect of thermal conductivity enhancer on the performance of PCM based heat sink. Considerable number of simulations are carried out to obtain the optimum value for volume fraction of TCE. From the optimization study it is found that 6% of total available volume is sufficient to maintain the temperature of electronic subsystem under study. Noticeable temperature difference of $14.5^0$C is observed in fin based PCM heat sink. Increase in fin volume fraction beyond an optimized level increases sensible heat contain of system, which leads to increase in temperature of heat source. Hence, optimization of fin volume is required for design of efficient PCM based heat sinks.

## REFERENCES

[1] W.R. Humphries, E.I. Griggs, A Design Handbook for Phase Change Thermal Control and Energy Storage Devices, 1977.

[2] S. Krishnan, S. V Garimella, Analysis of a Phase Change Energy Storage System for Pulsed Power Dissipation, 27 (2004) 191–199.

[3] R. Humphries, C. George, Performance of Finned Thermal Capacitors, 1974.

[4] S. Himran, A. Suwono, G.A. Mansoori, Characterization of Alkanes and Paraffin Waxes for Application as Phase Change Energy Storage Medium, Energy Sources. 16 (1994) 117–128.

[5] R. Baby, C. Balaji, Thermal optimization of PCM based pin fin heat sinks: An experimental study, Appl. Therm. Eng. 54 (2013) 65–77.

[6] T. Hatakeyama, M. Ishizuka, S. Takakuwa, S. Nakagawa, K. Takagi, Experimental and Thermal Network Study on the Performance of a Pins Studded Phase Change Material in Electronic Device Cooling, J. Therm. Sci. Technol. 6 (2011) 164–177.

[7] R. Baby, C. Balaji, Experimental investigations on thermal performance enhancement and effect of orientation on porous matrix filled PCM based heat sink, Int. Commun. Heat Mass Transf. 46 (2013) 27–30.

[8] J.M. Khodadadi, S.F. Hosseinizadeh, Nanoparticle-enhanced phase change materials (NEPCM) with great potential for improved thermal energy storage, Int. Commun. Heat Mass Transf. 34 (2007) 534–543.

[9] A. Benmansour, M.A. Hamdan, A. Bengeuddach, Experimental and numerical investigation of solid particles thermal energy storage unit, Appl. Therm. Eng. 26 (2006) 513–518.

[10] E.M. Alawadhi, C.H. Amon, Performance analysis of an enhanced PCM thermal control unit, ITHERM 2000. Seventh Intersoc. Conf. Therm. Thermomechanical Phenom. Electron. Syst. (Cat. No.00CH37069). (2000) 283–289.

[11] B. Zalba, J. Marin, L.F. Cabeza, H. Mehling, Review on thermal energy storage with phase change: Materials, heat transfer analysis and applications, 2003.

[12] S. Krishnan, S. V Garimella, Analysis of a Phase Change Energy Storage System for Pulsed Power Dissipation, IEEE Trans. Components Packag. Technol. 27 (2004) 191–199.

[13] N. Bonyadi, S.K. Sömek, C.C. Özalevli, D. Baker, İ. Tarı, Numerical analysis of phase change material characteristics used in a thermal energy storage device, Heat Transf. Eng. 7632 (2017) 0–0.

Fifth International Conference on Computational Methods for Thermal Problems
THERMACOMP2018, July 9-11, 2018, Indian Institute of Science, Bangalore, INDIA
*N. Massarotti, P. Nithiarasu, Pradip Dutta and C. Ranganyakalu (Eds.)*

# NUMERICAL ANALYSIS OF LATENT HEAT THERMAL ENERGY STORAGE (LHTES) PERFORMANCE: A 2-D AXISYMMETRIC APPROACH

**Amit Shrivastava, Dileep Kumar, Prodyut R. Chakraborty**
IIT Jodhpur, Karwad 342037, Jodhpur, India, pchakraborty@iitj.ac.in

## ABSTRACT

The present work focuses on developing a 2-D axisymmetric numerical model to study the dynamic behaviour of charging and discharging cycle for an elementary latent heat storage unit with simple geometry. The domain under consideration consists of a pipe of negligible thickness carrying heat transfer fluid (HTF), while being surrounded by latent heat storage medium or the phase change material (PCM). The PCM domain is considered to be 2-D axisymmetric and heat transfer mechanism is diffusion dominated. On the other hand, 1-D model is considered for the flow of HTF through the pipe. The heat transfer models in the PCM and HTF is coupled through the energy balance at the pipe wall. A fully implicit Finite Volume model is developed to obtain the evolution of temperature in PCM and HTF domain along with extent of melting/solidification in the PCM domain. Simulations are performed for charging and discharging of PCM domain considering pure PCM and PCM-Graphite composite with enhanced thermal conductivity.

**Key Words:** *Latent heat, Storage, Coupling, Solidification, Melting, Charging, Discharging*

## 1. INTRODUCTION

Thermal energy storage (TES) plays the key role for reliable and continuous operation of solar thermal power plants, and the latent heat thermal energy storage (LHTES) is particularly advantageous for is its ability to store (charging) and release (discharging) of thermal energy at near isothermal conditions and high energy density [1, 2]. Studies on LHTES conclude that enhancing thermal conductivity of the storage material can improve charging and discharging dynamics [3, 4]. Multi-tube shell and tube is one of the most commonly used [1-6] design for LHTES. Several modelling approach on LHTES have been performed [1, 2, 5, 6] to analyse heat and fluid flow. However, detailed the coupling method [1, 2] of the PCM and heat transfer fluid (HTF) domain in a storage unit is rarely described. The present work focuses on developing a coupled heat transfer model to describe the heat transfer between the PCM and HTF. Also, parametric study using commercial grade PCM and HTF such as solar salt (60% $NaNO_3$ : 40% $KNO_3$) and Therminol vp -1 is discussed considering pure PCM and PCM graphite composite with enhanced thermal conductivity. The axisymmetric domain under consideration is shown in Fig.1. The model developed uses semi-implicit finite volume scheme [7] for both PCM domain and HTF. Diffusion in the flowing HTF domain and convection in the PCM domain is considered to be negligible. Coupling of the two domains is performed by source term of HTF energy equation and boundary condition of the PCM domain at the pipe wall. Charging/Discharging analyses have been done for PCM with enhanced thermal conductivity by introducing PCM-Graphite composite.

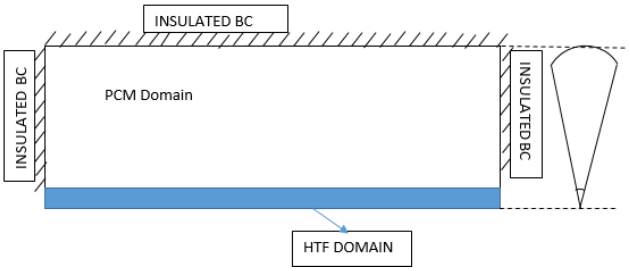


FIGURE 1. Computation Domain

## 2. MATHEMATICAL MODEL

The volume averaged energy conservation equation for the PCM domain with temperature as the primary dependent variable [8], is given in Eq.1.

$$\frac{\partial}{\partial t}\left(\rho c_{ps} T\right) = \nabla.\left(k\nabla T\right) - \frac{\partial}{\partial t}\left(f_l \rho h_{sl}\right) - \frac{\partial}{\partial t}\left[f_l \rho\left(c_{pl} - c_{ps}\right)\left(T - T_m\right)\right] \tag{1}$$

In the present work, specific heat, density and thermal conductivity are assumed to be same for both liquid and solid phases and third term on the RHS of Eq.1 is redundant. In the PCM domain, temperature and solid/liquid fraction ($f_l/f_s$) evolution are captured by using enthalpy updating scheme [8, 9]. On the other hand, The 1- D energy conservation equation for the HTF flowing through the circular pipe is as follows [2]:

$$\rho_f \frac{\partial}{\partial t}\left(C_{Pf} T_f\right) + \dot{G}\frac{\partial}{\partial x}\left(C_{Pf} T_f\right) = \frac{2}{r} h\left(T_{wall} - T_f\right) \tag{2}$$

Where, subscript '$f$' denotes HTF, $\dot{G}$ stands for mass flux (kg/m$^2$ -s), $r$ is the radius of pipe, and $h$ is convective heat transfer coefficient between the pipe wall and HTF. Eq.2 is descritized using Finite Volume Method and considering upwind scheme [7 ].

The computation domain under consideration (Fig.1) consists of a section of PCM and HTF pipe with unit azimuthal angle, radius of the complete domain is 30 mm and length in axial direction is 1.0 m. The Initial conditions of both PCM and HTF domains have been chosen to be: $T_i = T_m - 1$ for the charging process (melting) and $T_i = T_m + 1$ for the discharging process (solidification), where $T_m$ is the melting temperature of PCM. The boundary condition of HTF domain is considered to be $T_{inlet} > T_m$ for case studies associated with charging, and $T_{inlet} < T_m$ for the discharging process. On the other hand similarity condition ($T^{(b)} = T^{(b-1)}$ where, $b$ denotes the nodal location at the outlet) is considered as the outlet condition. Convective heat transfer coefficient $h$ appearing in Eq.4 and 6 is calculated using modified Gnielinski correlation form Nusselt number (Eq.7).

$$Nu = \frac{(F/8)R_e P_r}{1.07 + 12.7(F/8)^{0.5}\left(P_r^{(2/3)} - 1\right)} \tag{7}$$

Where, friction factor $F$ is defined as $F = (0.790 \ln R_e - 1.64)^{-2}$.

The coupling is obtained using the following steps:

1. For a given time-step guess pipe wall temperature $T_w = T_w^*$, solve system of algebraic Eq.5 to obtain HTF temperature distribution $T_f$. A good initial guess for $T_w$ is the wall temperature at the previous time step.
2. Use this $T_f$ to calculate heat flux at the wall from HTF to PCM domain as $q" = h_c(T_f - T_w)$ and use heat flux $q"$ as the boundary condition for the PCM domain to update temperature distribution in the PCM domain and hence obtain the newly updated value of $T_w$.
3. Repeat steps 1 and 2 until temperature distribution in both the domains converge.

## 3. RESULTS

Higher thermal conductivity of the PCM promotes a much faster charging or discharging rate. The temperature distribution of the HTF shown in Fig.2 clearly indicates less heat loss or heat gain of the HTF, with low PCM thermal conductivity. Although, faster charging and discharging might appear to be lucrative, the outlet temperature profile shown in Fig. 3 especially during discharging suggests otherwise, since one of the major objective of installing the storage unit is to attain minimum variation of the HTF outlet temperature for a prolonged period during the discharging process. In fact, an ideal condition would be to attain a fast charging and a slow discharging with a prolonged invariability of HTF outlet temperature. Farther studies are required to obtain such optimal condition by varying different parameters such as mass flow rate, cascaded storage systems, overall length and thickness of PCM domain.

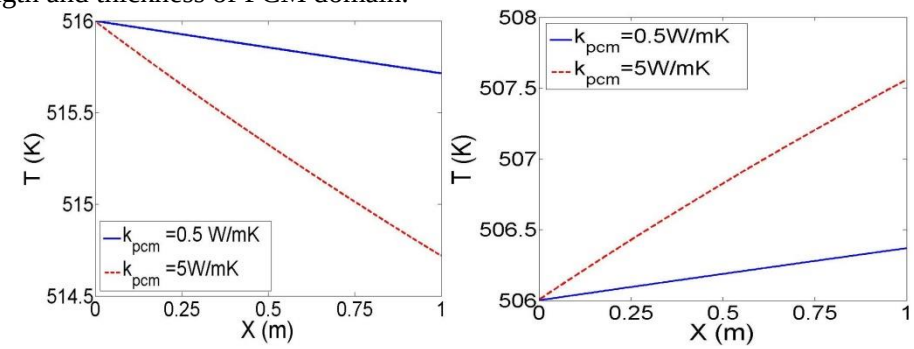


(a) (b)

FIGURE 2. HTF Temperature along the axial direction (a) Charging (b) Discharging

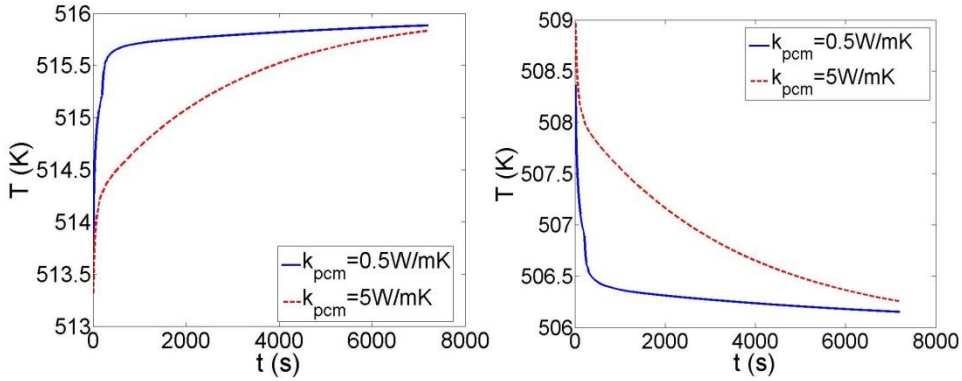


(a) (b)

FIGURE 3. Temperature variation of HTF with respect to time at the exit of the pipe (a) Charging of PCM, (b) Discharging of PCM

## 4. CONCLUSIONS

A coupled model is developed in order to obtain temperature evolution in the PCM domain and HTF for a simple latent heat thermal energy storage unit considering 2-D axisymmetric condition. Heat transfer in the 2-D PCM domain is considered to be diffusion dominated, while a 1-D approach is considered for the heat transfer fluid (HTF) with forced convection being the major contributor in transferring the heat. The developed model is implemented to study the performance analysis of pure PCM and PCM-Graphite composite with enhanced thermal conductivity. Although, enhanced thermal conductivity is found to promote faster charging and discharging rate, low thermal conductivity provided a sustain invariability of HTF outlet temperature for a prolonged period. Farther parametric study is required to obtain ideal situation involving fast charging and sustained invariability of HTF outlet temperature during discharging.

## REFERENCES

[1] Sagar Lakhani, Appasaheb Raul, and sandip K. Saha, Dynamic modelling of ORC- based solar thermal pawer plant integrated with multitube shell and tube latent heat thermal storage system, *Applied thermal engineering,* 123, 458-470, 2017.

[2] Vincent Morisson, Mohamed Rady, Elena Palomo, and Eric Arquis, thermal energy storage system for electricity production using solar energy direct steam generation technology, *Chemical engineering and processing,* 47, 499- 507, 2008.

[3] Yaxue Lin, Yuting Jia, Guruprasad Alwa, and Guiyinn Fang, Review on thermal conductivity enhancement, thermal properties and applications of phase change materials in thermal energy storage, *Renewable and Sustainable Energy Reviews,* 2017.

[4] Francis Agyenim, Philip Eames, and Mervyn Smyth, Heat transfer enhancement in medium temperature thermal energy storage system using a multitube heat transfer array, *Renewable Energy,* 35, 198- 207, 2010.

[5] Imen Jmal, and Mounir Baccar, Numerical study of PCM solidification in a finned tube thermal storage including natural convection, *Applied thermal engineering,* 84, 320- 330, 2015.

[6] Vadim Dubovsky, Gennady Ziskind, and Ruth Letan, Analytical model of a PCM- Air heat exchanger, *Applied thermal engineering,* 31, 3453- 3462. 2011.

[7] S. V. Patankar, Numerical Heat Transfer and Fluid Flow, Hemisphere Publication, Washington, DC, 1980.

[8] Prodyut R. Chakraborty, Enthalpy porosity model for melting and solidification of pure substances with large difference in phase specific heats, *International communications in heat and mass Transfer,* 81, 183- 189, 2017.

[9] A. D. Brent, V. R. Voller, and K. J. Reid, Enthalpy-Porosity technique for modelling convection-diffusion phase change: Application to the melting of a pure metal, *Numerical Heat Transfer: An international journal of computation and methodology,* 13:3, 297-318, 1988.

Fifth International Conference on Computational Methods for Thermal Problems
THERMACOMP2018, July 9-11, 2018, Indian Institute of Science, Bangalore, INDIA
*N. Massarotti, P. Nithiarasu, Pradip Dutta and C. Ranganyakalu (Eds.)*

# DOUBLE DISTRIBUTION FUNCTIONS MRT-LATTICE BOLTZMANN SCHEME FOR THERMAL BENCHMARK FLOWS

**Amitkumar S. Gawas, Dhiraj V. Patil**
Department of Mechanical Engineering, Indian Institute of Technology Dharwad,
Dharwad, KA, 580011, India.

dhiraj@iitdh.ac.in

ABSTRACT

Thermal flows in two-dimensional geometries are analysed using the double distribution functions multiple relaxation time (MRT) Lattice Boltzmann (LB) method. The flow field and temperature field are computed using two different however, coupled distribution functions. The Rayleigh-Bénard Convection (RBC) problem in a square cavity is solved and the method is proposed to be extended to an axisymmetric case for various Rayleigh numbers. Next, the RBC in a cylindrical cavity is analysed and the results are to be compared with the existing results.

**Key Words:** *Lattice Boltzmann method, Rayleigh-Bénard Convection, Mesoscopic method.*

## 1. INTRODUCTION

In industrial applications such as fluid flow and heat transfer through pipes, turbines, as well as various energy equipments thermal flow analysis is important. Many of the industrial cylindrical heaters may be of Rayleigh-Bénard convection (RBC) type. The RBC problem is a classic and various researchers have solved this problem using various numerical approaches. In the last few decades, Lattice Boltzmann (LB) method is developing as useful and easy method to solve these kinds of thermal flows. Recently, multiple relaxation time LB method is proposed to solve the thermal and fluid flow problem and objective of this work is implementation of double distribution functions MRT-LB method with appropriate boundary conditions for various two-dimensional benchmark problems. First, the RBC problem is analysed in a square 2D cavity then axisymmetric RBC in a square cavity problem is proposed for various Rayleigh numbers. The second problem consists of RBC in a cylindrical cavity as axisymmetric problem.

This abstract is arranged as follows, in section 2, MRT-LB method is discussed and preliminary results are discussed for the RBC in a two-dimensional square cavity.

## 2. DOUBLE DISTRIBUTION FUNCTIONS MRT-LB METHOD: THERMAL FLOWS

Two dimensional LB-MRT model with double distribution functions approach is used for thermal fluids. For flow-field, D2Q9 lattice structure (i.e. two dimensional nine velocities model) is used whereas for temprature-field D2Q5 lattice structure (i.e. two dimensional five velocities model) is used. The LB-MRT algorithm [1]–[6] used in this work is explained here and below.

The D2Q9 model for mass and momentum conservations is as,

$$\mathbf{f}(\mathbf{x}_j + \mathbf{c}\delta t, t_n + \delta t) = \mathbf{f}(\mathbf{x}_j, t_n) + \mathbf{S}(\mathbf{x}_j, t_n) + \mathbf{F}(\mathbf{x}_j, t_n)$$

$$\text{where, } \mathbf{S} = -M^{-1} \cdot S \cdot [\mathbf{m}(\mathbf{x}_j, t_n) - \mathbf{m}^{eq}(\mathbf{x}_j, t_n)] \quad (1)$$

$M$ is the matrix which linearly transform the distribution functions $f$ in to velocity moments $m$.

$$m_i = [M] f_i \text{ and } \mathbf{m}^{eq} = (m_0^{eq}, m_1^{eq}, ....m_8^{eq})^t \quad (2)$$

$$M = \begin{bmatrix} 1 & 1 & 1 & 1 & 1 & 1 & 1 & 1 & 1 \\ 0 & 1 & 0 & -1 & 0 & 1 & -1 & -1 & 1 \\ 0 & 0 & 1 & 0 & -1 & 1 & 1 & -1 & -1 \\ -4 & -1 & -1 & -1 & -1 & 2 & 2 & 2 & 2 \\ 0 & 1 & -1 & 1 & -1 & 0 & 0 & 0 & 0 \\ 0 & 0 & 0 & 0 & 0 & 1 & -1 & 1 & -1 \\ 0 & -2 & 0 & 2 & 0 & 1 & -1 & -1 & 1 \\ 0 & 0 & -2 & 0 & 2 & 1 & 1 & -1 & -1 \\ 4 & -2 & -2 & -2 & -2 & 1 & 1 & 1 & 1 \end{bmatrix} \quad (3)$$

In Eq. (2), *t* represents the transpose of equilibrium moments vector. In the equilibrium moments **u** is the flow velocity; $u$ and $v$ are the horizontal and vertical components of flow velocity respectively. The nine equilibrium moments are defined as follows -

$$m_0^{eq} = \delta\rho;\ m_1^{eq} = u;\ m_2^{eq} = v;\quad m_3^{eq} = -2\delta\rho + 3\mathbf{u}.\mathbf{u};\ m_4^{eq} = (u^2 - v^2);$$
$$m_5^{eq} = (uv);\ m_6^{eq} = -(u);\ m_7^{eq} = -(v)\ ;\ m_8^{eq} = \delta\rho - 3\mathbf{u}.\mathbf{u} \quad (4)$$

The diagonal relaxation matrix (S) is as $S = diag(0,1,1,\ S_\nu, S_\nu, S_\nu, S_q, S_q, S_\nu)$;

$$\text{where,}\quad S_\nu = \frac{2}{6\nu + 1};\quad S_q = 8\frac{(2 - S_\nu)}{(8 - S_\nu)} \quad (5)$$

Considering the Boussinesq's approximation, the compression work due to pressure and viscous heat dissipation are neglected so, the forcing term used as buoyancy force as

$$F(\mathbf{x}_j, t_n) = 3\omega_i\alpha(T - T_0)g\mathbf{c}_i \cdot \hat{\mathbf{y}}\ ;\quad \omega_0 = 4/9;\ \ \omega_{1,2,3,4} = 1/9;\ \ \omega_{5,6,7,8} = 1/36 \quad (6)$$

$$\delta\rho = \sum_{i=0}^{8} f_i \quad ;\mathbf{u} = \sum_{i=0}^{8} \mathbf{c}_i f_i \quad (7)$$

The discretized form of LBE for D2Q5 thermal model which is used in this work -

$$\mathbf{g}(\mathbf{x}_j + \mathbf{c}\delta t, t_n + \delta t) = \mathbf{g}(\mathbf{x}_j, t_n) - Q\ \ where,\ Q = N^{-1} \cdot Q \cdot [\mathbf{n}(\mathbf{x}_j, t_n) - \mathbf{n}^{eq}(\mathbf{x}_j, t_n)] \quad (8)$$

Value of *T* at each node is obtained by summation of distribution functions ( $g_i$ ) at corresponding node. The moments in D2Q5 lattice structure is calculated as, $n_i = [N]g_i$. The equilibrium moments ( $n_i^{eq} \mid i = 0,1,2,3,4$ ) corresponding to distribution functions ( $g_i \mid i = 0,1,2,3,4$ ) are defined as; $n_0^{eq} = T;\ n_1^{eq} = uT; n_2^{eq} = vT;\ n_3^{eq} = aT;\ n_4^{eq} = 0$. N is the transformation matrix. The diagonal relaxation matrix is given by $Q = diag(0, \sigma_k, \sigma_k, \sigma_e, \sigma_e)$. The relaxation rates in D2Q5 lattice structure of thermal is $\sigma_e$ and $\sigma_k$. It is calculated as follows-

$$\frac{1}{\sigma_k} = \frac{\sqrt{3}}{6} + \frac{1}{2};\qquad \frac{1}{\sigma_e} = \frac{\sqrt{3}}{3} + \frac{1}{2}$$

$$N = \begin{bmatrix} 1 & 1 & 1 & 1 & 1 \\ 0 & 1 & 0 & -1 & 0 \\ 0 & 0 & 1 & 0 & -1 \\ -4 & 1 & 1 & 1 & 1 \\ 0 & 1 & -1 & 1 & -1 \end{bmatrix} \tag{9}$$

## 3. SIMULATION RESULTS

Fig.1 below shows the results for two-dimensional square cavity RBC problem at different Rayleigh numbers. The first column of the figure indicates streamlines, second column indicates temperature contours, third and fourth column shows $u$ and $v$ velocity contours. Fig. 2 represents the vorticity magnitude contours. It is observed that with the increase in the Ra, the vorticity (velocity-field magnitude) increases. The Table 1, details the quantative information regarding the Nusselt number extracted from the simulation results obtained for various Rayleigh numbers.

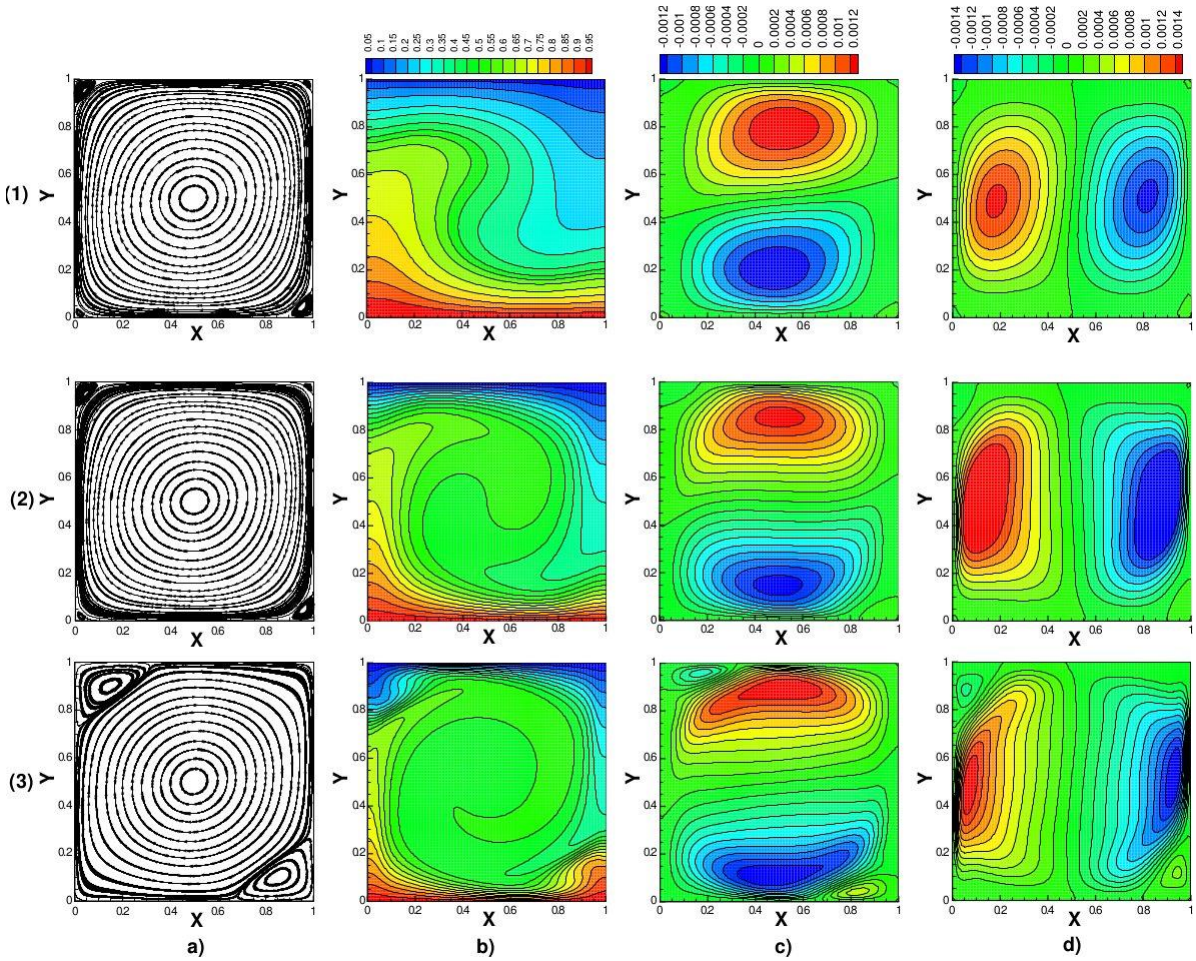


FIGURE 1. Columns: (a) Streamline, (b)Temperature-contours, (c) u- velocity contours, (d) v-velocity contours, for Rows: (1) Ra = $10^4$ (2) Ra = $10^5$ (3) Ra = $10^6$

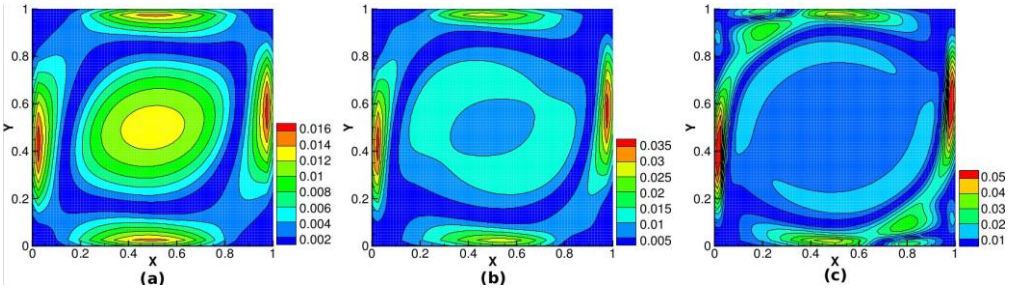


FIGURE 2. Vorticity magnitude contours for (a) Ra = $10^4$, (b) Ra = $10^5$, (c) Ra = $10^6$

| Ra | Grid | $u_{max}$ | y | $v_{max}$ | x | $Nu_{hot}$ |
|---|---|---|---|---|---|---|
| $10^4$ | 81x81 | 20.3336 | 0.8000 | 21.2323 | 0.1875 | 2.1486 |
| $10^5$ | 81x81 | 87.8131 | 0.8625 | 95.9660 | 0.1125 | 3.7925 |
| $10^6$ | 81x81 | 293.2621 | 0.9000 | 321.6431 | 0.0750 | 5.8450 |

TABLE 1. Maximum velocity and Nusselt number

## 4. CONCLUSIONS

In this abstract, double distribution functions MRT-LB method is detailed and applied for the simulations of Rayleigh-Bénard convection in two-dimensional square cavity. The simulations are performed for various Rayleigh numbers. It is proposed to extend the method for axisymmetric thermal flows and simulations of RBC in cylindrical cavity shapes using the 2D axisymmetric formulation.

## REFERENCES

[1] Z. Wang, Y. Liu, H. Wang, and J. Zhang, "A modified double distribution lattice Boltzmann model for axisymmetric thermal flow," *Phys. Lett. A*, vol. 381, no. 13, pp. 1150–1157, 2017.

[2] L. Li, R. Mei, and J. F. Klausner, "Multiple-relaxation-time lattice Boltzmann model for the axisymmetric convection diffusion equation," *Int. J. Heat Mass Transf.*, vol. 67, pp. 338–351, 2013.

[3] L. Wang, Z. Guo, and C. Zheng, "Multi-relaxation-time lattice Boltzmann model for axisymmetric flows," *Comput. Fluids*, vol. 39, no. 9, pp. 1542–1548, 2010.

[4] D. Contrino, P. Lallemand, P. Asinari, and L. S. Luo, "Lattice-Boltzmann simulations of the thermally driven 2D square cavity at high Rayleigh numbers," *J. Comput. Phys.*, vol. 275, pp. 257–272, 2014.

[5] D. D'Humières, I. Ginzburg, M. Krafczyk, P. Lallemand, and L.-S. Luo, "Multiple-relaxation-time lattice Boltzmann models in three dimensions.," *Philos. Trans. A. Math. Phys. Eng. Sci.*, vol. 360, no. 1792, pp. 437–451, 2002.

[6] J. Wang, D. Wang, P. Lallemand, and L. S. Luo, "Lattice Boltzmann simulations of thermal convective flows in two dimensions," *Comput. Math. with Appl.*, vol. 65, no. 2, pp. 262–286, 2013.

# Numerical Analysis of Mixed Convection in a Lid-Driven Cavity with Cu-water nanofluid using Artificial Compressibility Method

**Amogh S Katti**
Department of Mechanical Engineering,
National Institute of Technology Karnataka, Surathkal, Mangalore-575025, India
amoghskatti13@gmail.com

**Ranjith Maniyeri**
Department of Mechanical Engineering,
National Institute of Technology Karnataka, Surathkal, Mangalore-575025, India,
mranji@nitk.edu.in

## ABSTRACT

In this paper, we present a computational model based on an artificial compressibility method to study mixed convection in a lid-driven square cavity containing Cu-water nanofluid for two cases: i) adiabatic vertical walls and horizontal walls kept at constant temperature, and ii) adiabatic horizontal walls and sinusoidal temperature heating along vertical walls. The artificial compressibility method is used to couple pressure and velocity, and solve the momentum and continuity equations. This method is used because of its simplicity in solving steady state incompressible flow problems. The streamlines, isotherms, variation of local Nusselt number at hot walls, and variation of average Nusselt number with change in Cu-nanoparticle concentration are presented. Also, the variation of local Nusselt number with change in Richardson number ($0.1 < Ri < 10$), keeping Grashof number constant (Gr = 100), is obtained. For both cases, it is found that heat transfer increases with increase in Cu-nanoparticle concentration, keeping Richardson number constant, and also with a decrease in Richardson number, keeping Grashof number constant.

**Key Words:** *Heat Transfer, Artificial Compressibility Method, Mixed Convection, Nanofluid.*

## 1. INTRODUCTION

Lid-driven cavity problem is a benchmark problem in the field of computational fluid dynamics and heat transfer. A good amount of literature can be found on natural and mixed convection in a cavity. Tiwari and Das [1] studied mixed convection in a differentially heated square cavity with moving vertical walls. Abu-Nada et al. [2] conducted investigations on mixed convection in a cavity bounded by a wavy wall. To increase the thermal conductivity of the fluid and in turn to enhance heat transfer, some of the above mentioned investigations were carried out with nanofluid as the fluid medium. The enhancement in the thermal conductivity has been studied by Eastman et al. [3] for ethylene glycol-based nano-fluids containing Cu-nanoparticles.

Using finite volume method discretisation, studies have been done on lid-driven cavity with differential heating across horizontal walls by Muthtamilselvan et al. [4] by employing SIMPLE algorithm, also on lid-driven cavity with sinusoidal temperature heating along vertical walls by Arani et al. [5] using SIMPLER algorithm. Motivated by these works, in this paper, we develop a computational model to study mixed convection in a square lid-driven cavity containing Cu-water nanofluid for two cases – i) adiabatic vertical walls and horizontal walls kept at constant temperature, and ii) adiabatic horizontal walls and sinusoidal temperature heating along vertical walls using artificial compressibility method. This method was first proposed by Chorin [6] and has been considered superior to many other similar methods [7]. This method utilises a simple approach

in which an artificial compressibility factor is introduced in the continuity equation by considering an artificial time-derivative of pressure.

## 2. MATHEMATICAL MODELING AND NUMERICAL PROCEDURE

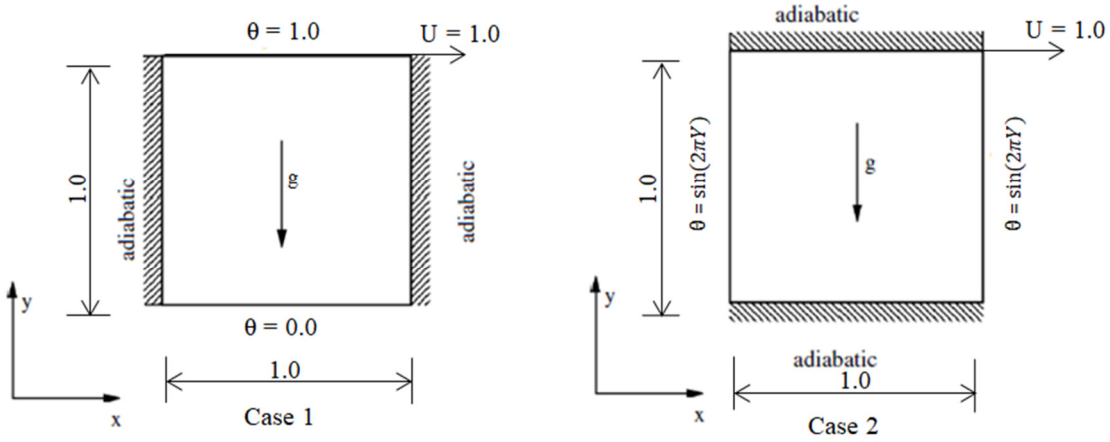


FIGURE 1. A schematic diagram showing the square lid-driven cavity with the boundary conditions

Figure 1 depicts the schematic diagram showing the dimensionless physical domain of the square lid-driven cavity filled with Cu-water nanofluid and the dimensionless boundary conditions for the two cases. We use the non-dimensionalised governing equations and boundary conditions to study mixed convection for the two above mentioned cases. The continuity equation is given as,

$$\delta\frac{\partial P}{\partial \tau}+\frac{\partial U}{\partial X}+\frac{\partial V}{\partial Y}=0 \tag{1}$$

where $\delta$ is the artificial compressibility factor.

The X-momentum and Y-momentum equation are given as,

$$\frac{\partial U}{\partial \tau}+U\frac{\partial U}{\partial X}+V\frac{\partial U}{\partial Y}=-\frac{\partial P}{\partial X}+\frac{1}{Re}\frac{\nu_{nf}}{\nu_f}\left(\frac{\partial^2 U}{\partial X^2}+\frac{\partial^2 U}{\partial Y^2}\right) \tag{2}$$

and

$$\frac{\partial V}{\partial \tau}+U\frac{\partial V}{\partial X}+V\frac{\partial V}{\partial Y}=-\frac{\partial P}{\partial Y}+\frac{1}{Re}\frac{\nu_{nf}}{\nu_f}\left(\frac{\partial^2 V}{\partial X^2}+\frac{\partial^2 V}{\partial Y^2}\right)+\frac{(\rho\beta)_{nf}}{\rho_{nf}\beta_f}Ri\theta \tag{3}$$

The energy equation is given as,

$$\frac{\partial \theta}{\partial \tau}+U\frac{\partial \theta}{\partial X}+V\frac{\partial \theta}{\partial Y}=\frac{\alpha_{nf}}{\alpha_f}\frac{1}{PrRe}\left(\frac{\partial^2 \theta}{\partial X^2}+\frac{\partial^2 \theta}{\partial Y^2}\right) \tag{4}$$

where Re is Reynold's number, Ri is Richardson number, Pr is Prandtl number, and α is the thermal diffusivity. The properties of the nanofluid, density $\rho_{nf}$, heat capacity $(\rho c_p)_{nf}$, and thermal expansion coefficient $(\rho\beta)_{nf}$ are found out from the individual thermophysical properties of water and copper nanoparticles at $25^0$C [4]. The absolute viscosity $\mu_{nf}$ is found out using Brinkman model [8] and the thermal conductivity $k_{nf}$ is found out using Maxwell model [9]. The local value of Nusselt number (Nu) is calculated using the following relation,

$$Nu_l=-\frac{k_{nf}}{k_f}\frac{\partial \theta}{\partial X} \tag{5}$$

The above governing equations are discretized using a staggered grid based finite volume method. The coupling of pressure and velocity is done using artificial compressibility method. The spatial derivatives are discretised using central differencing scheme. The equations are solved by marching in pseudo time. The pseudo time derivatives become zero when a steady state is obtained.

## 3. RESULTS AND DISCUSSION

First of all, the developed code in C is validated for the case of natural convection in a square lid-driven cavity without nanoparticles. The values of average Nu on the hot wall are computed for different Rayleigh numbers using the developed code and are compared with other researcher's results [10,11] and are presented in Table 2. A good agreement is obtained which proves the reliability of our developed code.

| Rayleigh number | Present work | de Vahl[10] | Wan et al[11] |
|---|---|---|---|
| $10^3$ | 1.119 | 1.117 | 1.117 |
| $10^4$ | 2.258 | 2.238 | 2.254 |
| $10^5$ | 4.557 | 4.509 | 4.598 |
| $10^6$ | 8.911 | 8.817 | 8.976 |

TABLE 2. Value of Average Nusselt number on the hot wall

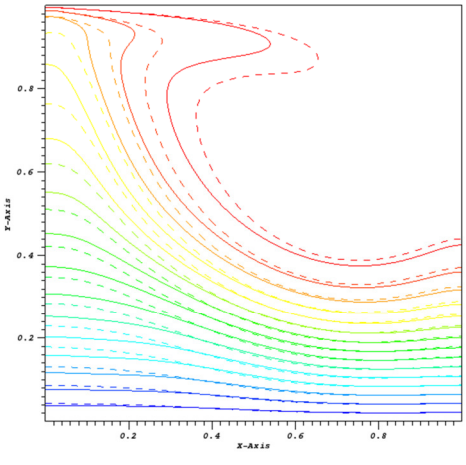


FIGURE 2. Case 1 - Isotherm plot for nanoparticle concentration of 0% (solid line) and of 0.8% (dashed line)

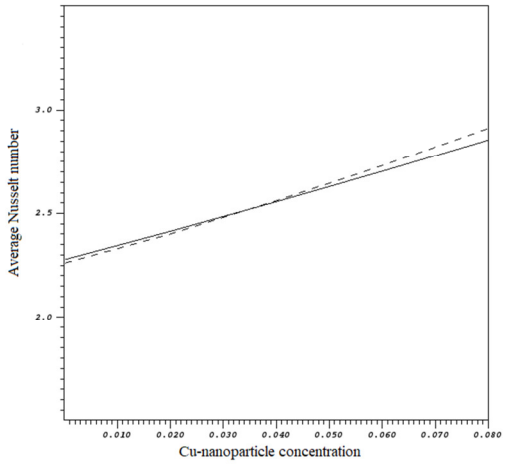


FIGURE 3. Case 1 - Comparison of Average nusselt number, varying with Cu-nanoparticle concentration, from present study (solid line) with Muthtamilselvan et al. (dashed line) [4]

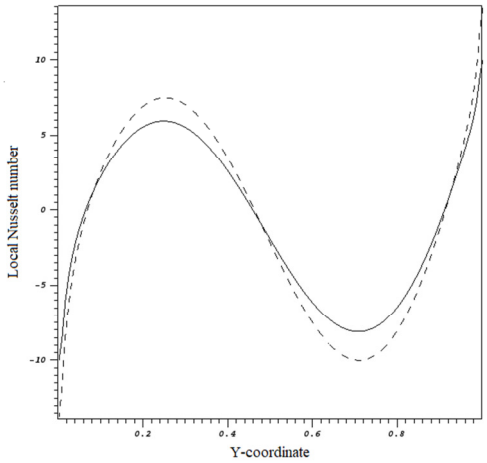


FIGURE 4. Case 2 - Variation of local Nu on the left wall for Cu-nanoparticle concentration 0% (solid line) and 10% (dashed line) for constant Ri = 1.

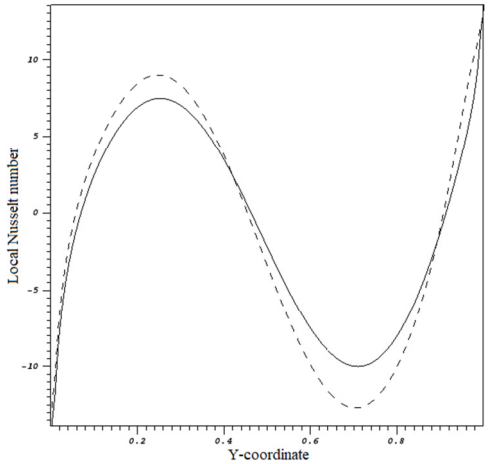


FIGURE 5. Case 2 - Variation of local Nu on the left wall for Ri = 1 (solid line) and Ri = 0.1 (dashed line) for constant Gr = 100, and for constant Cu-nanoparticle concentration = 10%

Figure 2 shows the temperature variation with and without nanoparticles for case 1. Figure 3 illustrates the comparison of variation of average Nu with increasing Cu-nanoparticle concentration, for case 1, between present study (solid line) and that of Muthtamilselvan et al. (dashed line) [4]. It can be observed that the results are in good agreement. Figure 4 shows the variation local Nu on the left wall, in case 2, for Cu-nanoparticle concentration 0% (solid line) and 10% (dashed line) for constant Ri = 1. It is evident that there is an enhancement in heat transfer when the pure water is replaced by nanofluid. Similarly, Figure 5 indicates the enhancement in heat transfer, for case 2, when Ri decreases, keeping Grashof number and Cu-nanoparticle concentration constant. A similar trend was observed by Arani et al. [5]

## 4. CONCLUSION

A two-dimensional computational model is developed to study the mixed convection inside a lid-driven square cavity with Cu-water nanofluid using artificial compressibility method. Two cases are analysed – i) adiabatic vertical walls and horizontal walls kept at constant temperature, and ii) adiabatic horizontal walls and sinusoidal temperature heating along vertical walls. Firstly, the developed code is validated by comparing the results, for the case of natural convection without nanofluid, with de Vahl [10] and Wan et al. [11]. Then, simulations are performed for the above two cases using the developed model. The results from the present work suggest that an increase in nanoparticle concentration enhances the heat transfer. Also, when the Grashof number is kept constant, decrease in Richardson number (or increase in shear force due to moving lid) increases the heat transfer.

## REFERENCES

[1] R.K. Tiwari, M.K. Das, Heat transfer augmentation in a two-sided lid-driven cavity differentially heated square cavity using nanofluids, *International Journal of Heat and Mass Transfer,* 50, 2002-2018, 2007.

[2] Eiyad Abu-Nada, Ali J. Chamkha, Mixed convection flow of a nanofluid in a lid-driven cavity with a wavy wall, *International Communication in Heat and Mass Transfer,* 57, 36-47, 2014.

[3] J.A. Eastman, S.U.S. Choi, S. Li, W. Yu, and L.J. Thompson, Anomalously increased effective thermal conductivities of ethylene glycol-based nano-fluids containing copper nanoparticles, *Applied Physics Letter,* 78, 718-720, 2001.

[4] M. Muthtamilselvan, P. Kandaswamy, and J. Lee, Heat transfer enhancement of copper-water nanofluids in a lid-driven enclosure, *Commun Nonlinear Sci Numer Simulat,* 15, 1501-1510, 2010.

[5] A.A. Abbasian Arani, S. Mazrouei Sebdani, M. Mahmoodi, A. Ardeshiri, M. Aliakbari, Numerical study of mixed convection flow in a lid-driven cavity with sinusoidal heating on side walls using nanofluid, *Superlattices and Microstructures,* 51, 893-911, 2012.

[6] A.J. Chorin, A numerical method for solving incompressible viscous flow problems, *Journal of Computational Physics,* 2, 12-26, 1967.

[7] Y. Tamamidis, G. Zhang, and D.N. Assanis, Comparison of Pressure-Based and Artificial Compressibility Methods for Solving 3D Steady Incompressibe Viscous Flows, *Journal of Computational Physics,* 124, 1-13, 1996.

[8] H.C. Brinkman, The viscosity of concentrated suspensions and solutions, *Journal of Chemical Physics,* 20, 571-581, 1952.

[9] J. Maxwell, A Treatise on electricity and magnetism, II edition, Oxford University Press, Cambridge, UK, 1904.

[10] G. de Vahl Davis, Natural Convection of air in a square cavity: A Benchmark Numerical Solution, *International Journal for Numerical Methods in Fluids,* 3, 249-264, 1983.

[11] D.C. Wan, B.S.V. Patnaik, G.W. Wei, A New Benchmark quality Solution for the Buoyancy-driven cavity by Discrete Singular Convolution, *Numerical Heat Transfer,* 40, 199-228, 2001.

Fifth International Conference on Computational Methods for Thermal Problems
THERMACOMP2018, July 9-11, 2018, Indian Institute of Science, Bangalore, INDIA
*N. Massarotti, P. Nithiarasu, Pradip Dutta and C. Ranganyakalu (Eds.)*

# NOVEL INVERSE HEAT TRANSFER TECHNIQUES FOR ESTIMATION OF UNKNOWN FURNACE MOULD HEAT FLUX

**Ananda S Vaka*, Prabal Talukdar**

**Department of Mechanical Engineering, Indian Institute of Technology, Delhi**
***srivaka@gmail.com**

## ABSTRACT

Many engineering and Industrial applications now a days involve complex processes which require accurate and speedy estimation of important process parameters. The operation and the quality control of various processes occurring in many thermal applications often require accurate knowledge of boundary conditions, such as heat flux. In some situations, measurement of this quantity is very difficult because of unapproachable locations or sluggish measuring techniques. At present, however, the techniques of the inverse heat transfer problem (IHTP) have offered a convenient alternative to estimate the unknown quantities accurately and instantaneously, which significantly reduce the experimental resources. In this work, two such inverse techniques, Ant Colony Optimization (ACO) and Salp Swarm Algorithm (SSA) are used to estimate the spatially varying boundary heat flux of a furnace mould by employing the unique combination of predicting the characteristic profile and estimating the profile parameters. These innovative techniques and the corresponding codes are indigenously developed by the authors. As there are un-measurable and unapproachable locations that exist in the steel melting furnaces which warrant innovative techniques. Inverse heat transfer techniques are best suited for this type of complex problems. There has not been any work done for the furnace applications using these novel inverse heat transfer techniques.

**Key Words:** *Inverse problems, Optimization, IHTP, ACO, SSA.*

## 1. INTRODUCTION

Continuous casting technique is a very predominant process of producing various components using molten metal as raw material. One such application of this process is production of various forms of steel billets and slabs for industrial or structural applications. Non-uniform heating of the mould takes place due to dynamic nature of the process, which gives rise to differential thermal expansion leading to cracks, breakout and the mould distortion. Temperature distribution in the mould depends significantly on heat flux at the hot surface of the mould [1], which provides important information regarding mould performance and product quality. Also, in order to determine the thermal state of this continuous casting mould quickly, so as to improve the operational performance and precision control, accurate calculation of heat flux is necessary. However, this parameter cannot be measured directly because of unapproachable locations or expensive instruments or tedious techniques.

Hence, various empirical and analytical models to estimate the heat flux based on inverse heat transfer techniques [2, 3] are being developed. The inverse heat transfer procedure involves measuring the temperature along the height of the mould using temperature sensors which are fixed at some accessible locations far away from the hot surface to avoid contact with the liquid steel. In order to solve IHTPs, the initial step is to guess the unknown heat flux at the boundary of the surface and find out the predicted temperature using the guessed heat flux near the points where the temperature can be measured and see whether the objective function which is a function of the difference of these two temperatures is within the limits. In order to accurately compute the heat flux variation of a mould, a large number of temperature data is required. However, such provision

of placing a large number of sensors in an actual production setup is difficult and tedious and often, the knowledge of the thermal state of the mould is required within a small amount of time for process control which is very difficult by using traditional IHTP techniques.

To tackle these twin issues simultaneously for efficient operation and quality control, other innovative techniques of combining the prediction of the characteristic profile of the heat flux based on the known theory and experience and using stochastic algorithms of IHTPs such as Ant Colony Optimization (ACO) and Salp Swarm Algorithm (SSA) for accurately predicting the parameters of the profile are used first time in this paper.

## 2. MAIN BODY

This analysis deals with the estimation of the unknown boundary heat flux across the hot surface of a billet mould which is in contact with the molten steel during continuous casting process. Schematic of the problem is shown in Figure 1. A 2D longitudinal section of the mould is considered as a domain of which one side is subjected to a variable heat flux. It is assumed here that the mould is straight unlike the tapered mould in actual conditions. The hot side of the mould below the meniscus is subjected to the high temperature of the molten steel. This boundary heat flux is assumed as a quadratic function with respect to the mould height,' y' in the form, $a1*y^2+a2*y+a3$. Heat loss takes place above the meniscus as shown in Figure 1 by convection. Height of the meniscus is measured as 'H' from the bottom. The total height and width of the mould are $H + H_1$ and L respectively. Outer surface of the mould is cooled by water flowing from bottom. Water enters at a velocity, $U_w$ and at a temperature, $T_{w,in}$ which results in convection heat loss from the cool side. As water flows through the channel, it absorbs heat from the hot mould and its temperature increases. Temperature of the water flowing through the channel is hence a function of the mould height, y.

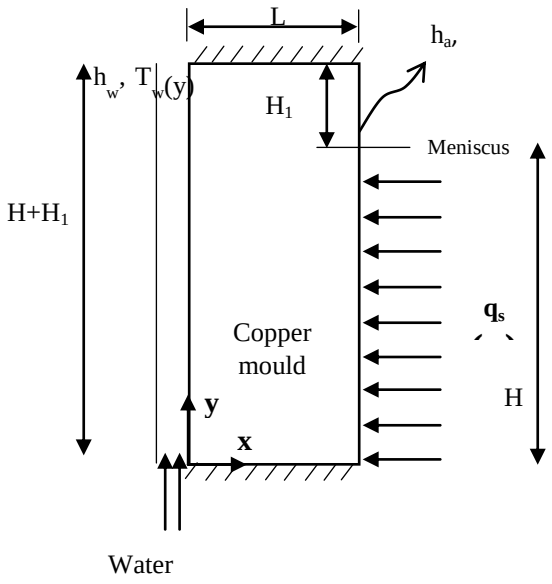


FIGURE 1.Schematic diagram of the mould with applied boundary conditions

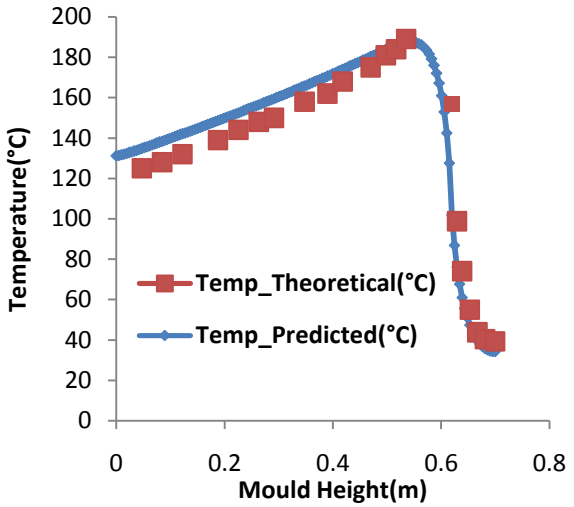


FIGURE 2. Comparison of the Present Technique with that of Literature [1] for Validation

The objective of the present problem is thus to obtain mould hot surface boundary heat flux accurately and rapidly using a novel inverse heat transfer technique. The heat flux is taken from the work of Savage and Pritchard as a theoretical reference [4] which is given below.

$$q_s(y) = 2680 - 335\sqrt{\left[\frac{(H-y)}{U_{casting}}\right]}\ \frac{kW}{m^2} \qquad (1)$$

where, $U_{casting}$ is the casting speed (m/s).

Ant Colony Optimization, ACO [2] works on pheromone evaporation rate which is expressed in terms of narrowing parameter and evaporation rate, which are given as input constants to the algorithm and these ants search the entire domain and find out the food (optimum solution). Similarly, the main inspiration of Salp Swarm Algorithm, SSA [5] is the swarming behaviour of salps when navigating and foraging in oceans. The leader is the salp at the front of the chain, whereas the rest of salps are considered as followers. The position of salps is defined in an *n* - dimensional search space where *n* is the number of variables of a given problem. The leader updates its position with respect to the food source and follower salps follow the leading salp. This process happens iteratively until the satisfaction of an end criterion. The variable heat flux is thus estimated by using the variables as the profile parameters.

The developed direct code is validated against the results available for a mould with a mould height of 700 mm available in the literature [1] as shown in Figure 2. It can be observed from the Figure 2 that both these results agree quiet well. Maximum temperature of the mould is observed near the meniscus in both the cases.

## 3. RESULTS

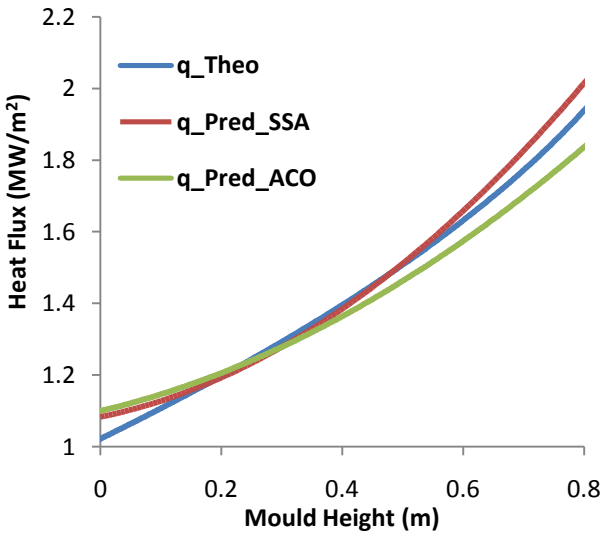


FIGURE 3. Comparison of the Heat Flux predicted using the Present Technique with that of ACO and the Empirical Formula from Literature

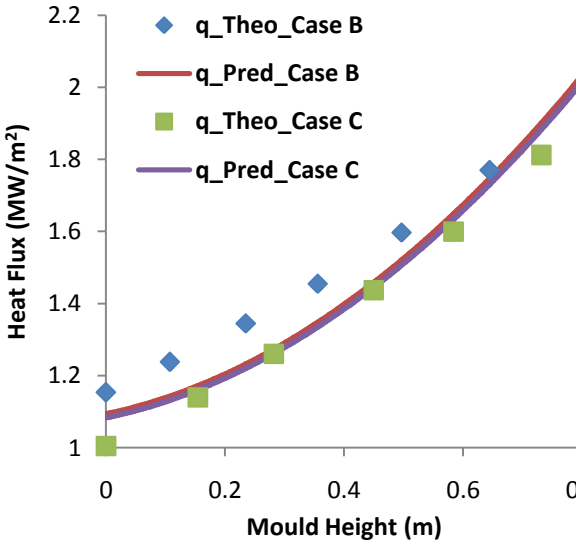


FIGURE 4. Comparison of the Heat Flux predicted using the Present Technique with that of the Empirical Formula from Literature for different casting speeds

After validation of the code, another mould, whose heat flux has to be estimated, is studied using ACO and SSA. In this case, five temperature sensors are mounted along the mould height. Height of the mould is 1 m and sensors are mounted at a distance of 3 mm from the cold side.

Three different cases based on the literature [1] are used to test the results whose casting speeds are 2.45 m/min (Case A), 2.89 m/min (Case B) and 2.4 m/min (Case C).

The unknown heat flux is estimated based on the ACO and SSA techniques for the Case A and it is compared with the theoretical value [4]. The predicted heat flux obtained by SSA is matching more closely with the theoretical value compared to that of ACO which is shown in the Figure 3 in a shorter time. Based on this result, heat flux is predicted for the two other casting speeds (Case B and Case C) using SSA technique and the results are also showing a close match with that of theoretical value [4] which is shown in the Figure 4. It is observed from the Figure 3 and the Figure 4, that the maximum heat flux occurs at the meniscus and the magnitude of the values are matching.

## 4. CONCLUSIONS

A novel and innovative method is proposed in the present study to estimate the spatially varying surface heat flux of a mould. This unique method first predicts the characteristic profile of the unknown heat flux using the already available knowledge from the literature and then, using a few sets of temperature readings, estimates the profile parameters. The Salp Swarm Algorithm, SSA is used which is proven to be one of the accurate and faster optimization technique as compared to that of Ant Colony Optimization, ACO. In industrial casting applications, online temperature measurements using less number of temperature sensors are normally recorded which when used for estimation of the heat flux, do not give the correct results immediately. But, for the process effectiveness, immediate results are sometimes required. Other inverse techniques take exorbitantly more time to predict as heat flux is to be estimated at each and every point of the boundary. And hence, for this type of requirement, the present method is well suited which estimates the heat flux by using a few sets of experimental data.

## REFERENCES

[1] I V Samarasekera and J K Brimacombe. The thermal field in continuous casting moulds. Canadian Metallurgical Quarterly, Vol. 18, pp. 251-266, 1979.

[2] Udayraj, Mulani, K., Talukdar, P., Das, A., and Alagirusamy, R., “Performance Analysis and Feasibility Study of Ant Colony Optimization, Particle Swarm Optimization and Cuckoo Search Algorithms for Inverse Heat Transfer Problems”, *International Journal of Heat and Mass Transfer*, 89, pp. 359-378

[3] Udayraj et al., Estimation of surface heat flux in continuous casting mould with limited measurement of temperature. International Journal of Thermal Sciences 118 (2017) 435-447.

[4] J Savage and W H Pritchard. The problem of rupture of the billet in the continuous casting of steel. Journal of Iron and Steel Institute, Vol. 178 (3), pp. 269-277, 1954.

[5] S Mirjalili et al., Salp Swarm Algorithm: A bio-inspired optimizer for engineering design problems. Advances in Engineering Software 2017: 1–29.

Fifth International Conference on Computational Methods for Thermal Problems
THERMACOMP2018, July 9-11, 2018, Indian Institute of Science, Bangalore, INDIA
*N. Massarotti, P. Nithiarasu, Pradip Dutta and C. Ranganyakalu (Eds.)*

# Numerical Study on Dehumidification Performance of a Cross-Flow Liquid Desiccant Adiabatic Dehumidifier with Various Halide Salt desiccants

**Mrinal Bhowmik, P. Muthukumar**
Centre for Energy, Indian Institute of Technology, Guwahati 781039, India

**R Anandalakshmi**

Department of Chemical Engineering, Indian Institute of Technology, Guwahati 781039, India

## ABSTRACT

To address the significance of liquid desiccant dehumidification systems, this paper discusses a theoretical model of an air–desiccant contact system. Lithium bromide (LiBr), lithium iodide (LiI), and lithium Chloride (LiCl) were considered as potential aqueous desiccant solution. A cross-flow liquid desiccant dehumidifier with celdek packing materials is considered in the present study. Firstly, this model has been validated for operating values available in the literature. Secondly, this established model has been used to predict the thermodynamic properties such as air humidity, air temperature, desiccant temperature, and solution concentration at various inlet concentrations. The prediction results have shown that the lithium iodide also has the significant potentiality that can make it suitable as a desiccant material in the dehumidification systems. It is found that the LiCl has the more moisture removal capacity to dehumidify the air compared with Lithium iodide (LiI) and lithium bromide (LiBr).

**Key Words:** *Liquid desiccant dehumidification systems, Desiccant solutions, Cross-flow Dehumidifier, Thermodynamic properties.*

## 1. INTRODUCTION

The energy resources are essential in all societies to meet basic human requirements and to serve productive processes. As the conventional energy resources depleting very rapidly so their costs also increasing and it further endangered the environment in regards to carbon footprint. Moreover, the increasing demand for human thermal comfort conditions is becoming a major global environmental issue. To meet this demand, an air conditioning device plays a vital role. It has been found that the energy required to supply human thermal comfort conditions is around 50% of building total energy consumption [1]. The International Institute of Refrigeration has estimated that almost 15% of all electricity generated worldwide is used for air-conditioning (ACs) and refrigeration processes of several kinds [2]. Now, in order to reduce the consumption of energy and to reduce the greenhouse emissions, researchers are stimulating their research towards an alternative cooling system and they observed that the desiccant cooling system is promising [3-4].

In conventional vapor compression system, air needs to be cooled below its dew point temperature to maintain the comfortable humidity level that makes more building total energy consumption. This paper essentially focusing on the first stage of desiccant cooling systems in which desiccant agent is used to dehumidifying the ambient air in order to absorb its moisture. And among dehumidifiers, packed bed dehumidifier has been chosen due to its more moisture removal effectiveness [2]. Firstly, a theoretical model for the cross flow packed bed adiabatic dehumidifier fuelled with LiBr as an aqueous solution was solved. Subsequently, thermodynamic properties were predicted for various desiccant solutions (LiBr, LiI and LiCl) for the cross flow packed bed adiabatic dehumidifier.

## 2. MATHEMATICAL MODELLING AND SIMULATION

A three-dimensional cross-flow packed bed dehumidifier model is considered where the air is passing from left to right i.e., in the x-direction and liquid desiccant is in the y-direction, from top to bottom of the dehumidifier are portrayed Figure 1.

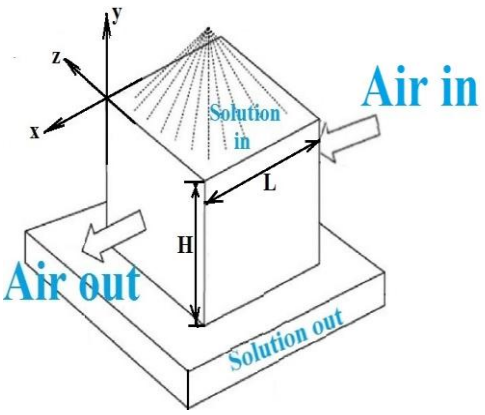


$$\dot{m}_a(h_{a,i+1,j}-h_{a,i,j})=\frac{R}{M}(\dot{m}_{d,i,j}h_{d,i,j}-\dot{m}_{d,i,j+1}h_{d,i,j+1}) \quad (1)$$

$$\dot{m}_a(\omega_{a,i,j}-\omega_{a,i+1,j})=\frac{R}{M}(\dot{m}_{d,i,j+1}-\dot{m}_{d,i,j}) \quad (2)$$

$$\dot{m}_{d,i,j+1}\bullet\xi_{i,j+1}=\dot{m}_{d,i,j}-\dot{m}_{d,i,j}\bullet\xi_{i,j} \quad (3)$$

$$h_{a,i+1,j}-h_{a,i,j}=\frac{NTU}{M}(h_{T_s,sat,i,j}-h_{a,i,j}) \quad (4)$$

$$(\omega_{a,i+1,j}-\omega_{a,i,j})=\frac{NTU}{M}(\omega_{T_s,sat,i,j}-\omega_{a,i,j}) \quad (5)$$

FIGURE 1. Schematic of a cross-flow packed bed dehumidifier.

All the basic balance equations [3-4] are discretized using FDM approach and discretized equations (1-5) are given below. Consequently, discretization of the computational domain is done into M×R number of meshes to implement FDM approach as visualized in Figure 2. The discretized equations are solved using MATLAB with model parameters, which are mentioned in Table 1.

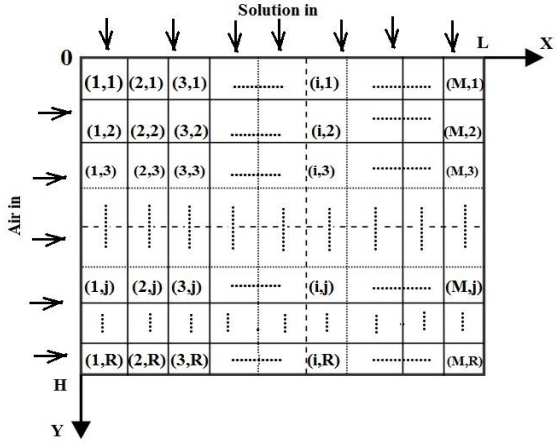


| | |
|---|---|
| Cross-sectional Air mass flow rate, $F_{a,}$ kg/m$^2$-s | 1.97 |
| Cross-sectional desiccant mass flow rate, $F_{d,}$ kg/m$^2$-s | 3.08 |
| Specific heat of salt (LiBr), $C_{P,}$ kj/kg.$^0$C | 2.3 |
| Molality, m | 9.69 |
| Specific surface area of packing material, a, m$^2$/m$^3$ | 396 |
| Vol. of dehumidifier, V, mm$^3$ | 550*400*350 |
| Eff. dia. of the channel $d_e$, mm | 7.85 |
| Number of transfer unit (NTU) | 0.97 |

TABLE 1. Model parameters[3]

FIGURE 2. Discretization of two-dimensional cross-flow dehumidifier domain.

## 3. RESULTS AND DISCUSSION

The simulation result of this theoretical model has shown a good agreement with the experimental results [3] with a maximum deviation of 1.73% that depicted in Figure 3 and tabulated in Table 2.

**3.1. Effect of inlet solution concentration on outlet air specific humidity**: For a given solution temperature, higher the inlet solution concentration, the lower is the vapor pressure of desiccant solution. Hence, the higher difference in vapor pressure between the desiccant surface and the air, increases mass transfer. This causes a gradual change in outlet air specific humidity as shown in Figure 4A. Therefore, higher the concentration, the more moisture will be removed. However, in

case of lithium chloride at 40-45% concentration, it almost showed same humidity and after that, it absorbs less moisture may be for crystallization problem. Hence, the risk of crystallization at normal desiccant temperature is higher at high concentration.

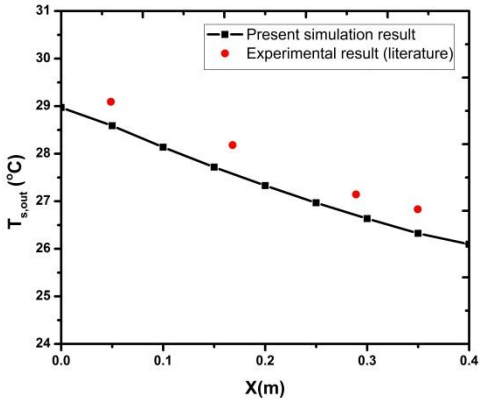


FIGURE 3. Desiccant outlet temperature variation along the length

| | $F_a$ (kg/m$^2$ s) | $T_a$ (°C) | $\omega_a$ (kg/kg) | $F_d$ (kg/m$^2$ s) | $T_d$ (°C) | $\xi$ (%) |
|---|---|---|---|---|---|---|
| Inlet parameters [3] | 1.97 | 31.7 | 0.013 | 3.08 | 22.9 | 45.7 |
| Outlet parameters by experiment[3] | - | 26.9 | 0.0099 | - | 27.8 | 45.7 |
| Present study output simulation | _ | 27.9 | 0.0095 | _ | 27.37 | 45.56 |

TABLE 2. Inlet and outlet parameters of the air-desiccant dehumidifier

**3.2. Effect of inlet solution concentration on air outlet temperature:** In this present study, the air inlet temperature is considered as 31.7$^o$C and there is a significant decrease in the air outlet temperature, with a lower inlet desiccant concentration as shown in Figure 4B. As the dehumidification capacity of air is less in the lower concentration, the mass transfer between the air and desiccant solution also be the less that causes the less release of sorption heat and latent heat of vaporization. In other words, in the lower concentration, the warm humid air has a tendency to release its temperature to desiccant solution during the mass transfer process and in higher concentration of desiccant solution having low vapor pressure that may make not to release air temperature in an effective way to desiccant solution.

**3.3. Effect of inlet solution concentration on desiccant outlet temperature:** Figure 4C shows that there is a significant increment in the solution outlet temperature when the desiccant solution inlet concentration is increased. As the liquid desiccant concentration increases, there is an increase in the mass transfer potential. This high moisture transfer potentiality results in high desiccant temperature since the sorption heat and latent heat of vaporization is released during the mass transfer process.

**3.4. Effect of inlet solution concentration on desiccant outlet concentration:** The mass transfer occurred between the air streams to the desiccant solution due to the vapor pressure difference. And in this present study, the size of the dehumidifier is the 550*400*350 mm where the specific humidity variation is found over the range of concentration and the maximum specific humidity change in that specified range is from 0.013 to 0.0081 that indicates the maximum absorption by the desiccant solution is less compare to the desiccant concentration value. Additionally, the predicted

result for this dehumidifier has shown that the maximum outlet solution concentration varies by 0.52%. So, the Figure 4D has showed almost same at inlet and outlet solution concentration.

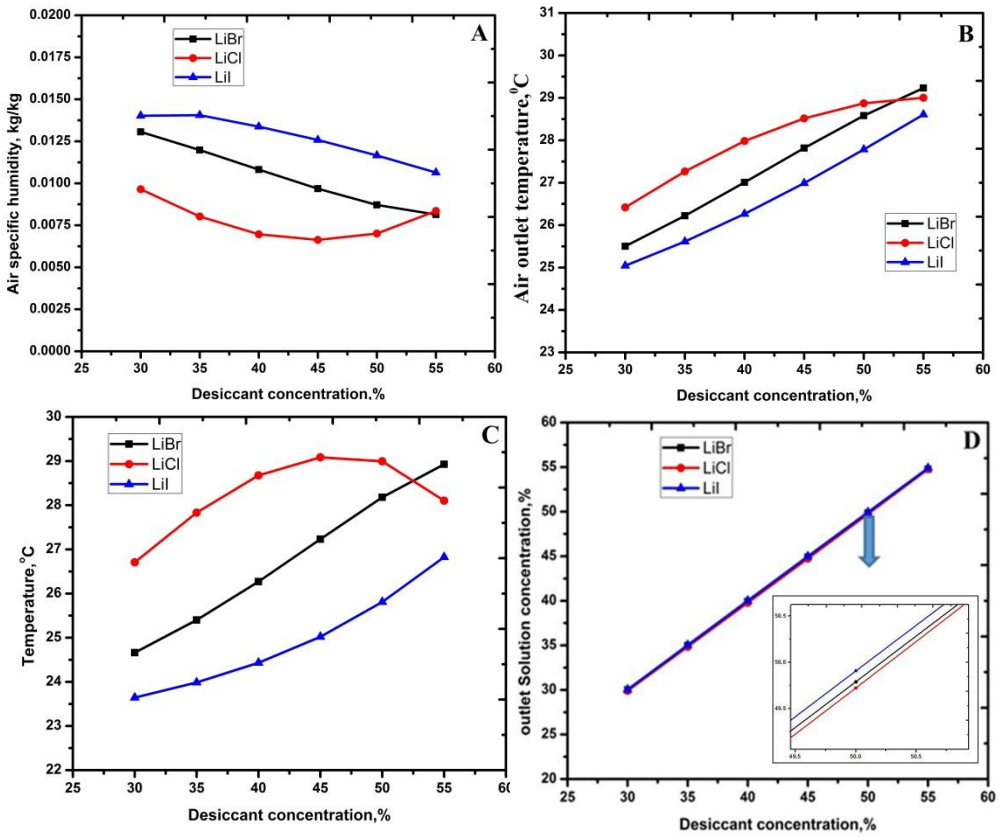


Figure 4. Effect of inlet solution concentration on (A) outlet air specific humidity (B) air outlet temperature (C) desiccant outlet temperature (D) desiccant outlet concentration.

## 4. CONCLUSIONS

The FDM based model empowers a more realistic mapping of the domain of an adiabatic dehumidifier as the predicted results are closer to experimental data. Moreover, the simulation results showed that the inlet concentration differences impact the dehumidification. For this work, the better dehumidification capacity has found for the LiCl solution having the solution inlet concentration is 40-45% and for LiBr is around 50-55% because after that slope of the specific humidity curve not changing too much. LiI can be good desiccant above 55% for deep dehumidification that means the lithium iodide has the potentiality to work as a desiccant martial. Further, both experimental and numerical studies are necessary to validate both modeling methods and confirm their industrial applicability.

## REFERENCES

[1] IEA. Key world energy statistics (2008). "Paris, France: International Energy Agency; 2008.

[2] M. Mujahid Rafique, P. Gandhidasan, Haitham M.S. Bahaidarah, Liquid desiccant materials and dehumidifiers – A review, Renewable and Sustainable Energy Reviews, Volume 56, 2016, Pages 179-195, ISSN 1364-0321.

[3] X.H. Liu, Y. Jiang, K.Y. Qu, Heat and mass transfer model of cross flow liquid desiccant air dehumidifier/regenerator, Energy Conversion and Management, Volume 48, Issue 2, 2007, Pages 546-554, ISSN 0196-8904.

[4] D.I. Stevens, J.E. Braun, S.A. Klein, An effectiveness model of liquid-desiccant system heat/mass exchangers, Solar Energy, Volume 42, Issue 6, 1989, Pages 449-455, ISSN 0038-092X.

# HEAT TRANSFER ANALYSIS FOR GDI DEVELOPMENT

**Andrej Poredos, Simon Gomboc, Marko Tomsic**
AVL-AST d.o.o, SI-2000 Maribor, Slovenia, andrej.poredos@avl.com
AVL-AST d.o.o, SI-2000 Maribor, Slovenia, simon.gomboc@avl.com
AVL-AST d.o.o, SI-2000 Maribor, Slovenia, marko.tomsic@avl.com

## ABSTRACT

More and more stringent environmental legislations push the IC engine development to its limits. "Down-sizing" and "down-speeding" lead to a significant increase of the engine specific power and as a consequence to increased thermal loads of the engine structure. The accurate evaluation of the structural thermal field is of essential importance in order to avoid mechanical failures.
This paper describes an improved methodology for the thermal investigation of a complete engine structure. The improved simulation methodology enables the simultaneous CHT simulation coupled with coolant flow simulation in one single analysis step. The simulation of all structural and fluid parts is performed simultaneously. All important physical phenomena on coolant flow and structural side such as contact resistance, boiling and temperature dependent material properties are considered.
Due to the high importance of friction generated by moving parts like the piston, this method has been refined further. Thermal load distribution due to friction as well as the local distribution of the heat transfer coefficients on the piston skirt and ring contacts are pre-calculated by means of an elasto-hydrodynamics simulation. These loads are applied as thermal coupling conditions in addition to the existing convective boundary conditions to the thermal analysis models of the engine structure and piston group.

**Key Words:** *Thermal Analysis, CFD, combustion, friction analysis*

## 1. INTRODUCTION

Complete GDI engine thermal analysis requires two separated steps. In the first one, the gas side (complete combustion cycle) is simulated by means of CFD. This simulation provides boundary conditions for structural thermal analysis of the complete engine. In the second step, multi-physics and multi-domain thermal investigation of the complete engine, including all structural parts and water jacket, is performed to obtain structural parts temperatures. Heat transfer between the piston and liner is taken into account based on experiences by constant heat transfer coefficients.
Nowadays this approach is insufficient mainly due to two reasons. Firstly because of the missing consideration of piston skirt and ring friction and secondly, because of strong local dependency of the heat transfer on the oil filling and clearance situation. Because of these requirements, a new simulation method has been developed. The thermal load distribution, due to friction as well as the local distribution of the heat transfers at the piston skirt and ring contacts by elasto-hydrodynamics, are pre-calculated. They are applied as thermal coupling conditions in addition to the existing convective boundary conditions to the multi-material models of thermal analysis for block head compound and piston group.

## 2. NEW INTEGRATED METHODOLOGY

Within the classical methods for thermal analysis, normally single component is under investigation. The objective is the determination of the temperature distribution in the piston or the engine block only, in which the thermal boundary conditions (ambient temperatures and heat transfer coefficients) are partially pre-calculated and others are only estimated based on past experience.

In this new approach, all thermal boundary conditions, both convective as well as the ones derived from the contacts are pre-calculated with their local distributions based on physically-based simulation models. In addition, the heat generated by friction is determined. Subsequently, all the thermal boundary conditions are applied together on the entire component group (block, pistons, rings, pins) and the temperature distribution of the whole assembly is determined. The determination of the boundary conditions and the thermal analysis are iterated until a converged temperature distribution is reached, what is usually the case after two iterations.
With the exception of the heat transfer from block to the water jacket, all other thermal boundary conditions are determined cyclic transient. Because the component temperatures, apart from a very thin boundary layer, remain constant within one engine cycle (720 degrees CA), the thermal analysis of structural components is calculated stationary. For this purpose the transient thermal boundary conditions have to be averaged over through whole engine cycle

## 2.1 Gas-side Thermal Boundary Conditions

The major heat source for the block as well as the piston structure comes from the in-cylinder gas. Therefore cylinder inner flow simulation by means of 3D CFD has to be performed. Such complete in-cylinder analysis considers gas exchange, fuel spray injection and combustion simulation and is usually performed only for one cylinder [1,2].

The transient results for near wall gas temperature and the heat transfer coefficient from cylinder inner flow simulation have to be time averaged over one engine cycle and applied as convective boundary conditions to the structure. Predicting that all cylinders have the same time averaged gas temperatures and HTC distributions, the convective boundary conditions of one cylinder are mapped to the surface of all four cylinders (Figure 1) of the structural model.

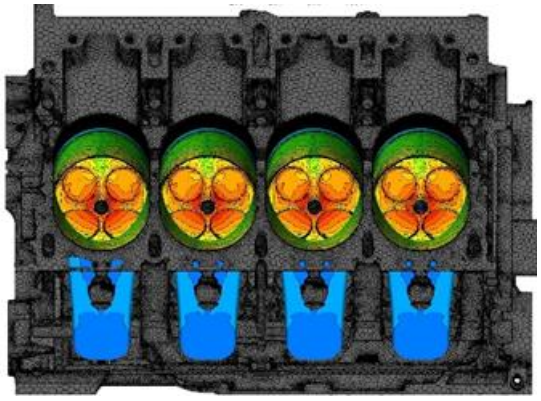

Fig. 1: Gas side thermal boundary conditions – near wall fluid temperature

## 2.2 Friction Power for Piston/Liner Contact

In this context the following contacts are relevant: ring contacts at ring running faces and ring flanks, piston skirt contact at liner and the piston pin bearing contacts. All these contacts are using mixed lubrication conditions. For such contact definition, hydrodynamic and asperity contacts are considered. To evaluate the different friction parts, an accurate definition of gap, oil moistening, contact temperature and surface roughness is important [3]. The contact temperature influences the local viscosity of the oil. The time dependent gap distribution over the contact area is affected by the surface profile (nominal clearance, ovality and convexity, as well as thermal deviation) and the

deformation of the parts under loading conditions. Due to temperature gradients between piston, ring and liner, the heat is transported over the contact areas and structure internally.

The local heat transfer coefficients are dependent on the clearance, oil filling Θ, asperity contact $r_c$ and heat transfer coefficient of oil and structure material $\lambda_{oil}$, $\lambda_{str}$.

With usage of these units, the local and time depending heat transfer coefficient (HTC) for the gap is calculated as following:

$$\alpha_{gap}\left[\frac{W}{m^2K}\right] = (1 - r_c) \cdot \Theta \cdot \frac{\lambda_{oil}}{h_a} + r_c \cdot \frac{\lambda_{str}}{h_a} \qquad (3)$$

For the contacts, an additional consideration of friction between piston, ring and liner is essential, and used in the new calculation method. This method is dividing the heat, which is generated due to friction into two heat flows. The magnitude of the heat flows depends on the heat transfer coefficients.

The time dependent distribution of the heat transfer coefficients, the heat flows and the convective boundary conditions are averaged over one engine cycle (Figure 2). The averaged data are provided to the thermal structural analysis.

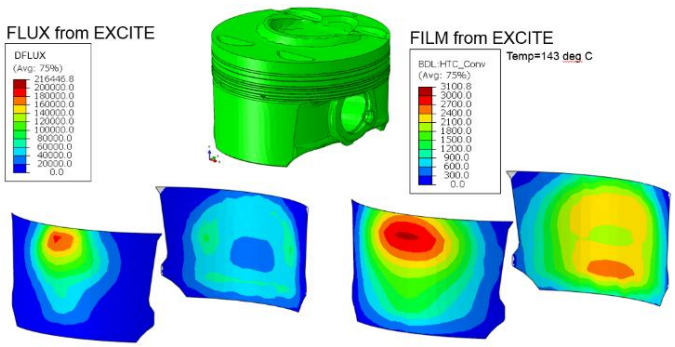


Fig. 2: Thermal Boundary Conditions at Piston Skirt

### 3.3 Thermal Analysis of Cylinder Block and Head

In case of the multi-physics - multi-material approach, the coolant flow simulation is performed simultaneously with the structural thermal analysis.

For the thermal model, temperature dependent material properties, heat contact resistances between different solid materials and nucleate boiling model [7] at the structure to cooling water interface are used.

During the steady state thermal simulation, the fluid simulation provides the convective boundary conditions (near wall fluid temperature and heat transfer coefficients) to the structure and the calculated wall temperature is provided back from the structural thermal analysis to the fluid simulation. For solid domain only, the enthalpy equation is solved in contrast to the fluid domain for which the flow as well as the enthalpy equation has to be solved. Data exchange is ongoing every iteration step of steady state multi-material simulation. This makes the convergence of the temperature fields in the different components extremely fast.

The multi-material CFD approach was applied for four cylinder GDI engine analysis using a polyhedral meshing approach. The friction heat generated at the piston liner contact was applied according to the experience gained from previous simulation projects.

The resulting temperature distribution on the solid surface is presented on Figure 3.

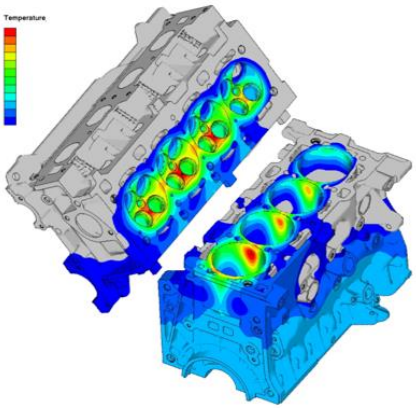


Fig 3: Head and block wall temperature distribution

Inhomogeneous heat transfer and cooling effects can be observed. The thermocouple measurements were performed at different positions in cylinder head (exhaust valve bridges) and in the cylinder block. Comparison between simulation results and measurements in monitoring locations for the cylinder head and the cylinder block is visible in Figure 4. The first simulation (Step 1 curves) was performed considering the contact resistances between valves and valve guides and valves and valve seats. In the second step (Step 2 curves), the contact resistances for all connected solid parts were considered, which significantly improved the agreement between simulation results and measurements. In general, the simulation adequately predicts the temperature trends in the cylinder head and cylinder block domains. The CFD simulation provides predictive values of good quality, especially for the temperatures in the most critical areas, the exhaust valve bridge regions.

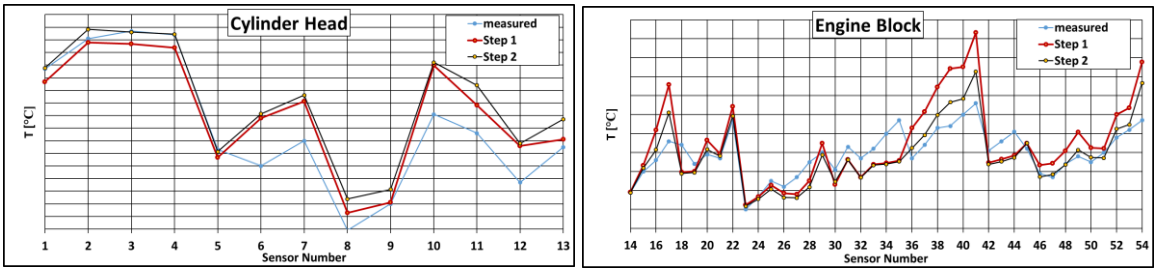


Fig. 4: Comparisons for thermocouple measurement positions in complete engine

In order to show the influence of the friction on the component temperature two calculations where performed. One considering (see paragraph 2.2), and one without considering the friction heat. The results show a significant influence on the additional heat source due to the friction heat. A temperature rise of about 10°C on the anti-thrust side can be seen (Figure 5).

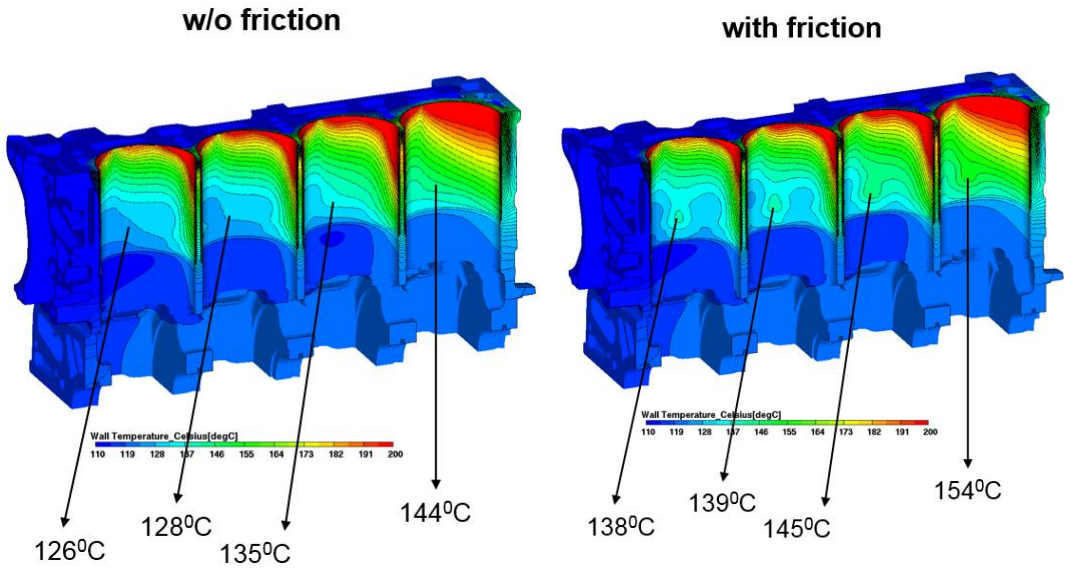


Fig. 5: Temperature distribution on the engine block

## 4. SUMMARY AND CONCLUSIONS

The integrated thermal analysis method provides reliable pre-calculation of the temperature distribution, since it solves both the fluid and solid domains together, using physical approaches for the boundary conditions. It also provides a considerable reduction of simulation time and effort since the entire thermal model is comprised in one computational mesh.
The method has also be extended with success to other highly loaded components of the engine like the piston.

The authors acknowledge the contribution of FCA for providing the engine data.

## 5. REFERENCES

[1] Tibaut P, Poredos A, Multi-Material Heat Transfer Analysis of an Single Cylinder Engine Head, NAFEMS 2014

[2] Tatschl R, Basara B, Schneider J, Hanjalic K, Popovac M, et.al., Advanced turbulent heat transfer modelling for IC-engine applications using AVL FIRE, In: Proceedings of international multidimensional engine modeling user's group meeting, Detroit, MI, 2006

[3] Offner G.: Friction Power Loss Simulation of Internal Combustion Engines Considering Mixed Lubricated Radial Slider, Axial Slider and Piston to Liner Contacts, Tribology Transactions, 2013.

[4] Colin, O., Benkenida, A. and Angelberger, C. "3D Modeling of Mixing, Ig-nition and Combustion Phenomena in Highly Stratified Gasoline Engines", Oil & Gas Science and Technology - Rev IFP, 58(1), 47-62 (2003).

[5] Peters N., The turbulent burning velocity for large scale and small scale turbulence. J. Fluid Mechanics 1999; 384: 107-132.

[6] Hanjalic K., Popovac M., Hadziabdic M. A robust near-wall elliptic-relaxation eddy-viscosity turbulence model for CFD, Int. Journal of Heat and Fluid Flow 25 (2004) 1047-1051, Elsevier, 2004.

[7] Steiner H., Brenn G., Ramstorfer F., Breitschaedel B.: Increased cooling power with nucleate boiling flow in automotive engine applications, New trends and developments in automotive system engineering pp 249-272, 2011.

Fifth International Conference on Computational Methods for Thermal Problems
THERMACOMP2018, July 9-11, 2018, Indian Institute of Science, Bangalore, INDIA
*N. Massarotti, P. Nithiarasu, Pradip Dutta and C. Ranganyakalu (Eds.)*

# Modelling of Microstructure Evolution with Shrinkage Convection

**Anirban Bhattacharya**
School of Mechanical Sciences, IIT Bhubaneswar, Argul, Jatni, Khurda, Odisha – 752050
E-mail: anirban@iitbs.ac.in

## ABSTRACT

This paper presents a numerical model for simulating binary alloy microstructure evolution with shrinkage driven convection. The model involves the modification of enthalpy method to account for volume change during solidification and combines it with a finite volume flow solver for simulating shrinkage driven flow. Important features of microstructure evolution such as grain nucleation, grain orientation and surface tension effects are incorporated. Simulation results show significant influence of shrinkage driven flow on energy transport, solute transport, and grain growth. Simulation of microstructure evolution involving the nucleation and growth of large number of grains show localized regions of high velocity and can be used to predict possible locations of shrinkage voids.

**Key Words:** *Phase change, Microstructure evolution, Equiaxed dendrite, Shrinkage, Convection*

## 1. INTRODUCTION

Convection plays an important role in determining the final microstructure during solidification by influencing the energy and solute transport from the interface. Apart from convection due to thermal and solutal gradients, another important driving force for convection is volume change during solidification. Most engineering alloys have higher densities in the solid phase and thus solidification of such alloys involve a reduction of volume at the interface. This results in generation of flow towards the interface from the bulk liquid. This shrinkage driven flow can significantly change the removal of heat and rejected solute from the interface and thus alter the growth rate of a dendrite beyond that resulting only due to density change. Study of shrinkage driven convection can be used to predict the final morphology of grains during a solidification process as well as to locate potential regions of shrinkage porosity and defects in the microstructure.

In this paper, a microstructure evolution model is presented which incorporates the presence of convection due to shrinkage. The model is based on the enthalpy based dendrite growth model developed previously [1,2] and incorporates additional features to simulate more realistic microstructure such as grain nucleation, individual grain orientation etc. The model is used to simulate large scale microstructure evolution in a square cavity and predict the effect of shrinkage driven convection.

## 2. MODEL DESCRIPTION

The numerical model consists of three main parts: The nucleation model, the solidification model, and the convection model. The nucleation model incorporates a probabilistic calculation of the nucleation rate which is assumed to have a Gaussian distribution [3] as given below

$$\frac{dn}{d(\Delta T)} = \frac{n_{\max}}{\sqrt{2\pi}\Delta T_\sigma} \exp\left[-\frac{1}{2}\left(\frac{\Delta T - \Delta T_n}{\Delta T_\sigma}\right)^2\right] \tag{1}$$

where $\Delta T_n$, $\Delta T_\sigma$, $n_{\max}$ are the mean undercooling, standard deviation undercooling and the maximum nucleation density. Based on the nucleation rate, a critical undercooling value is assigned to each nucleation site and the each nuclei is activated only when it reaches its corresponding critical undercooling. Each nuclei is also assigned a random crystallographic direction.

The solidification model involves the solution of the volume averaged enthalpy and species conservation equations [2]. Due to density difference between solid and liquid phases, all the governing equations are formulated based on two liquid fraction parameters, liquid mass fraction $f_l$ and liquid volume fraction $g_l$. Both of them are related as given below.

$$g_l = \frac{f_l \rho_s}{f_l(\rho_s - \rho_l) + \rho_l} \tag{2}$$

The energy and species conservation equations are solved explicitly based on previous time step temperature and concentration. Subsequently, the temperature, concentration potential and the liquid volume fractions are calculated using an iterative scheme to obtain consistent values based on the temperature-concentration coupling governed by the phase diagram. Anisotropic surface tension is incorporated as an undercooling to calculate the interface temperature. The anisotropy is given with respect to the individual orientation of each grain. This accounts for the anisotropic growth of each dendrite along its own crystallographic axes.

Shrinkage driven convection is simulated by solving the volume averaged continuity and momentum equations. The volume change due to density difference is incorporated using a source term in the pressure and pressure correction equations as per the SIMPLER algorithm [4]. The source term is given by

$$-\left(\frac{\rho^* - \rho^{o*}}{\Delta t^*}\right)\Delta x^* \Delta y^* = \left[\left(g_l{}^o - g_l\right)\left(1 - \frac{\rho_s}{\rho_l}\right)\right]\frac{\Delta x^* \Delta y^*}{\Delta t^*} \tag{3}$$

where $g_l$ is the liquid volume fraction, $\rho_s$ and $\rho_l$ are solid and liquid densities, $\Delta t^*$, $\Delta x^*$ and $\Delta y^*$ are the non-dimensional time step and grid sizes, and superscript $o$ denotes the previous time step value.

## 3. RESULTS

At first, the growth of single dendrite is simulated. It is observed that shrinkage flow occurs from all the sides towards the interface (Figure 1). The effect of shrinkage convection can be clearly observed by comparing the dendrite shapes for three cases – dendrite growth with shrinkage flow, dendrite growth with shrinkage but with the flow switched off, and dendrite growth without shrinkage as shown in Figure 2. As expected, the dendrite growth without shrinkage is fastest as the density of solid is not higher than that of liquid. However, if shrinkage is present, the growth rate is slower if shrinkage flow is also present. The shrinkage flow changes the rate of removal of heat and solute from the interface and acts in the opposite direction to that of diffusion. As a result, the concentration at the interface is higher resulting in lower interface temperature. This leads to lower undercooling and consequently lower growth rate.

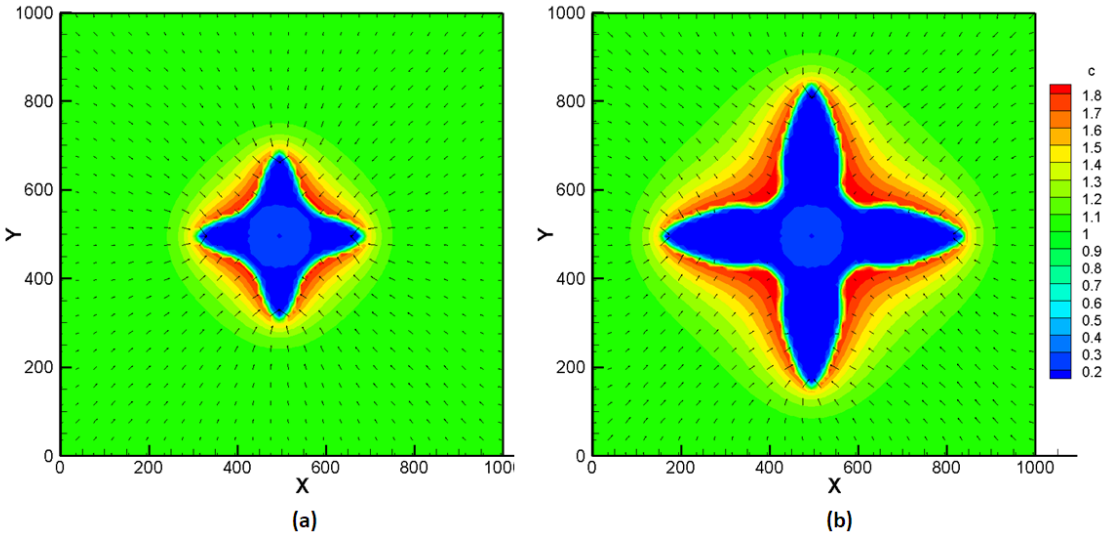


FIGURE 1. Concentration and flow pattern (a) t = 8000 (b) t = 16000

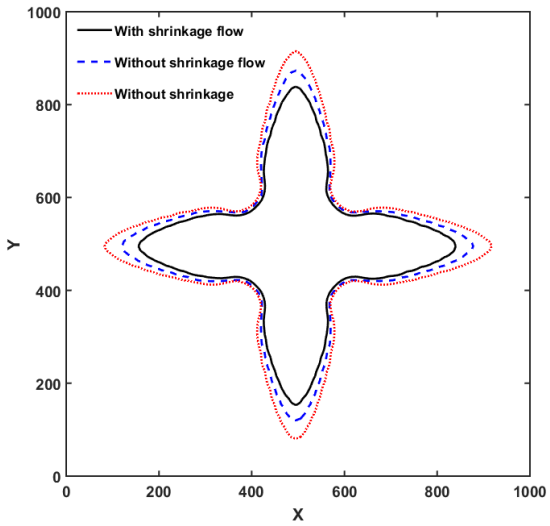


FIGURE 2. Comparison of dendrite shape at t = 16000 for dendrite growth with shrinkage flow, without shrinkage flow but with shrinkage, and without shrinkage.

The model is subsequently applied to simulate large scale microstructure evolution with shrinkage (Figure 3). It is observed that a large of number of dendrites nucleate and grow with different orientation. The partitioning of solute is also seen resulting in localised solute rich regions. Shrinkage flow occurs with a complex pattern with certain regions having a high flow velocity as seen in Figure 3(b) and (c). From the flow pattern, the probable locations for generation of shrinkage voids can be predicted to be the regions where outward flow occurs in almost all directions. The final microstructure depends not only on the nucleation and orientation of grains but also on the effect of shrinkage flow on the evolving thermal and solutal fields.

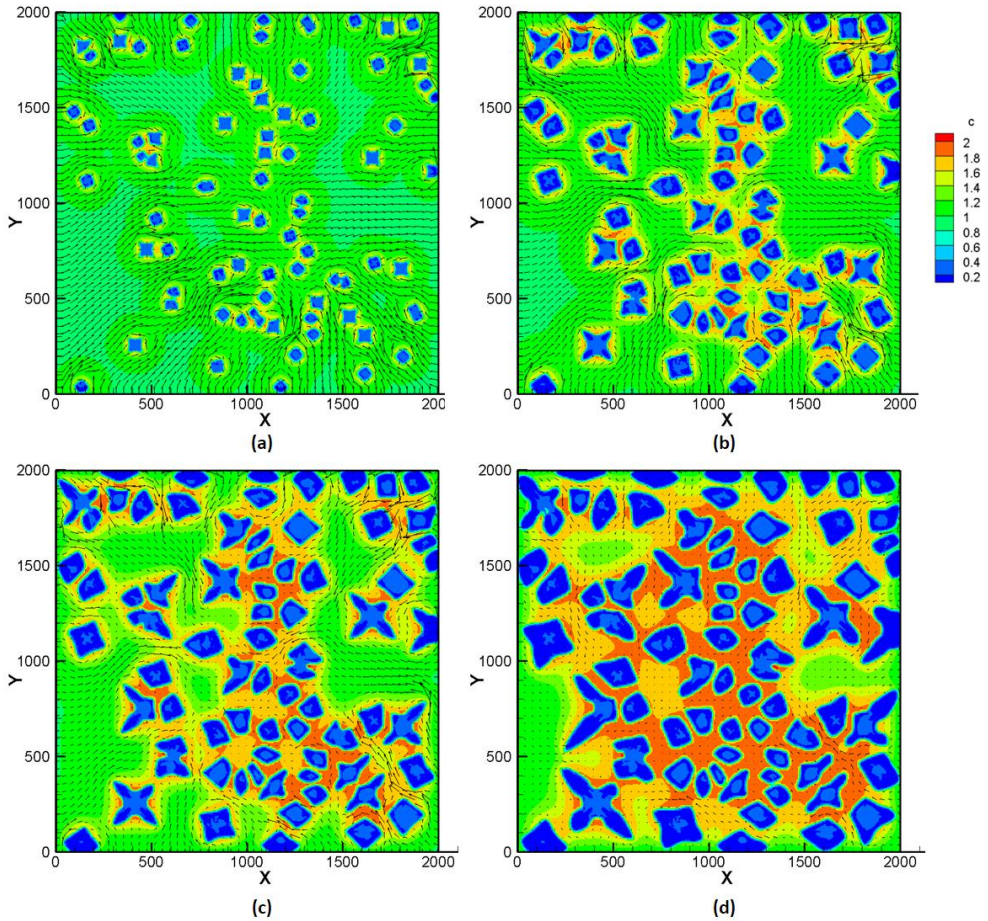


FIGURE 3. Microstructure evolution and shrinkage flow pattern (a) t = 1000 (b) t = 3000 (c) t = 5000 (d) t = 10000

## 4. CONCLUSIONS

A numerical model for simulating large scale dendritic microstructure evolution with shrinkage flow is presented. It is found that shrinkage flow results in significantly slower growth rate due to its transport of solute towards the interface. The final microstructure is influenced by the complex flow pattern generated, particularly, at the regions of high flow rate. The model is also useful for predicting the possible locations of shrinkage porosity during solidification processes.

## REFERENCES

[1] V.R. Voller, An enthalpy method for modeling dendritic growth in a binary alloy, *International Journal of Heat and Mass Transfer*, 51(3), 823-834, 2008.

[2] A. Bhattacharya, and P. Dutta, An enthalpy-based model of dendritic growth in a convecting binary alloy melt, *International Journal of Numerical Methods for Heat & Fluid Flow*, 23, 1121-1135, 2013.

[3] M. Rappaz, and C.A. Gandin, Probabilistic modelling of microstructure formation in solidification processes, *Acta metallurgica et materialia*, 41(2), 345-360, 1993.

[4] S.V. Patankar, *Numerical heat transfer and fluid flow*, CRC Press, Hemisphere, New York, 1980.

Fifth International Conference on Computational Methods for Thermal Problems
THERMACOMP2018, July 9-11, 2018, Indian Institute of Science, Bangalore, INDIA
*N. Massarotti, P. Nithiarasu, Pradip Dutta and C. Ranganyakalu (Eds.)*

# A fourth order compact ADI scheme for N-S equations on non-uniform grids.

**Anirban Chattopadhyay*, Swapan K Pandit***

*Integrated Science Education and Research Centre (ISERC), Visva-Bharati, Santiniketan-731 235
Email: animath81@rediffmail.com

## ABSTRACT

In this work we have proposed a fourth order compact alternating direction implicit (4OC-ADI) scheme for solving two-dimensional (2-D) unsteady Navier-Stokes (N-S) equations on non-uniform grids using streamfunction-vorticity approach. The scheme is second order accurate in time and fourth order accurate in space. The resulting 4OC-ADI scheme in each ADI solution step corresponds to a strictly diagonally dominant tridiagonal matrix equation which can be solved by application of the one-dimensional trigonal Thomas algorithm with a considerable saving in computing time. Our scheme is unconditionally stable which is shown through a discrete Fourier analysis. Results obtained are in excellent agreement with analytical and available numerical results in all test cases, establishing efficiency and accuracy of the proposed scheme.

**Key Words:** *HOC schemes, N-S equations, Non-uniform grid, Reynolds number.*

## 1. INTRODUCTION

The governing equations representing 2-D incompressible viscous flows are the continuity equation and the two momentum equations which in turn using streamfunction and vorticity variables can be written as

$$\frac{\partial^2 \psi}{\partial x^2} + \frac{\partial^2 \psi}{\partial y^2} = -\zeta \quad \text{.....(1)}$$

$$\mathrm{Re}\frac{\partial \zeta}{\partial t} + u\,\mathrm{Re}\frac{\partial \zeta}{\partial x} + v\,\mathrm{Re}\frac{\partial \zeta}{\partial y} = \left(\frac{\partial^2 \zeta}{\partial x^2} + \frac{\partial^2 \zeta}{\partial y^2}\right) \quad \text{.....(2)}$$

Where *Re* is the Reynolds number given by $Re = \frac{Lu_0}{\nu}$, where $L$ is some characteristic length, $u_0$ some characteristic velocity and $\nu$ is the kinematic viscosity, and $u$, $v$ are the velocity components along x-direction and y-direction respectively, and $t$ is the time.

In recent years, HOC methods for simulating flows with irregular geometries have generated renewed interest and a variety of specialized techniques have been developed. A way to obtaining higher order compactness is by using the original differential equation to substitute for the leading T.E. terms of the standard central difference approximation. Kalita et al. [1] developed a class of transient HOC schemes for the solution of unsteady 2D convection-diffusion equations and extend their study to develop HOC schemes on non-uniform grids without transformation. Pandit et al. [2] developed higher order compact schemes for incompressible viscous flows on geometries beyond rectangular using transformation. Karaa et al. [3] and D. You [4] proposed high order ADI schemes on uniform grids for solving 2D convection-diffusion problems.

In the present study we propose a fourth order compact alternating direction implicit (4OC-ADI) scheme for solving two-dimensional (2-D) transient, spatially second order quasi-linear partial

differential equation without the mixed-derivative term. The proposed scheme works equally efficiently on problems described on both rectangular as well as other curvilinear coordinate settings.

## 2. BASIC FORMULATION

Both the equations (1) and (2) can be put under the umbrella of the 2-D time dependent second order equation as

$$l\frac{\partial\varphi}{\partial t}+\alpha\frac{\partial^2\varphi}{\partial x^2}+\beta\frac{\partial^2\varphi}{\partial y^2}+\gamma\frac{\partial\varphi}{\partial x}+\upsilon\frac{\partial\varphi}{\partial y}+2\omega\varphi=\theta \quad \text{.....(3)}$$

We now using a suitable orthogonal transformation

$$x=x(\xi,\eta,t),\ y=y(\xi,\eta,t)$$

from the physical *x-y* plane to the computational $\xi-\eta$ plane which is used to convert a complicated grid into a simple, uniform Cartesian grid. Under this transformation, equation (3) in the physical plane becomes

$$l\frac{\partial\varphi}{\partial t}+a\frac{\partial^2\varphi}{\partial\xi^2}+b\frac{\partial^2\varphi}{\partial\eta^2}+c\frac{\partial\varphi}{\partial\xi}+d\frac{\partial\varphi}{\partial\eta}+2p\varphi=f \quad \text{.....(4)}$$

Using higher order compact consideration with transformation (see [3], [4]) the ADI scheme can be written as

$$\left(L_\xi+\frac{\Delta t}{2l}A_\xi\right)\hat{\varphi}_{ij}^{\ *}=\left(L_\xi-\frac{\Delta t}{2l}A_\xi\right)\left(L_\eta-\frac{\Delta t}{2l}A_\eta\right)\hat{\varphi}_{ij}^{\ n}+\frac{\Delta t}{2l}L_\xi L_\eta(f_{ij}^{\ (n+1)}+f_{ij}^{\ (n)}) \quad \text{.....(5)}$$

$$\left(L_\eta+\frac{\Delta t}{2l}A_\eta\right)\hat{\varphi}_{ij}^{\ (n+1)}=\hat{\varphi}_{ij}^{\ *} \quad \text{.....(6)}$$

where, $A_\xi=A_{ij}\partial_\xi^{\ 2}+B_{ij}\partial_\xi+C_{ij}$, $L_\xi=1+\frac{h^2}{12}(\partial_\xi^{\ 2}+c_{ij}^{\ *}\partial_\xi)$. Similarly for $A_\eta$, $L_\eta$.

## 3. RESULTS

In order to study validity and effectiveness of our proposed scheme, we have applied this scheme to 2D problems namely (i) Diffusion problem having analytical solution, (ii) viscous flow in a lid driven square cavity.

### Problem (i): Diffusion problem having analytical solution:

We have considered a diffusion problem in the unit domain [0, 1] x [0, 1],

$$\frac{\partial\varphi}{\partial t}-\frac{\partial^2\phi}{\partial x^2}-\frac{\partial^2\phi}{\partial y^2}+(x^2+2y)\phi=f$$

The exact solution of this test problem is given by

$$\phi(x,y,t) = e^{-\pi^2 t}\sin(\pi x)\cosh(y)$$

.

The initial and Dirichlet boundary conditions are directly taken from this solution and the source function of this problem is given by

$$f(x,y,t) = (x^2 + 2y - 1)e^{-\pi^2 t}\sin(\pi x)\cosh(y)$$

In figure 1 we have presented the analytical and numerical solutions on a grid size 81 × 81. This figure indicates a very close match of our computed numerical solutions with the exact one.

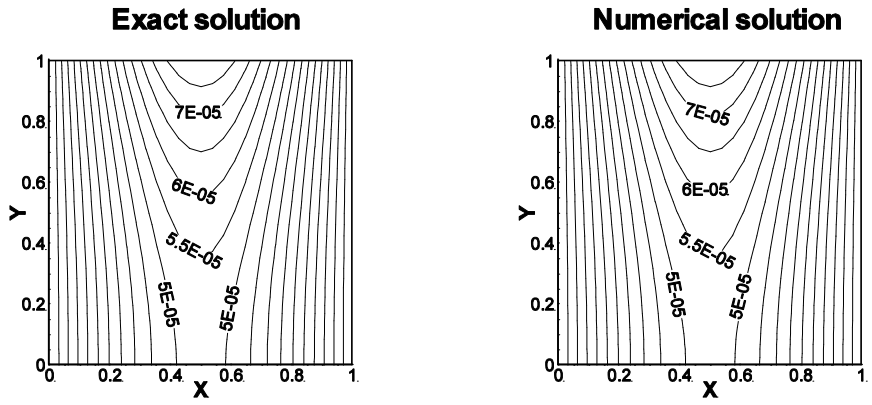


Fig1. Exact and numerical solution of the test problem (i) .

Problem (ii): The lid-driven square cavity problem:

Next we have considered the classical 2D lid-driven square cavity problem. This problem, over the years, has become the most frequently used benchmark problem for the assessment of numerical methods.

Because of the presence of large gradients near the walls, we generate a centro-symmetric grid (see the physical plane in figure 2) with clustering near the walls. In figure 3, we have compared the vertical velocity along the horizontal centreline of a lid-driven square cavity from Re=100 to Re=3200 and compare our data with those of Ghia et al. [5], which were obtained using 129x129 and 257x257 grids, our data is obtained using a 41x41 grid (Re = 100), a 41x41 grid (Re = 400), a 81x81 grid (Re = 1000), 121x121 grid (Re = 3200) .

In each cases, our velocity profiles exhibit a very good matching with Ghia's results.

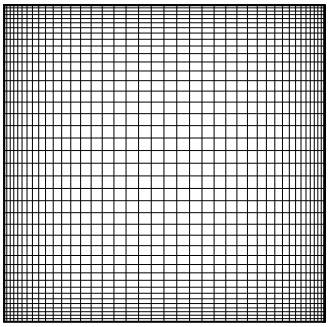

Fig2. The lid-driven square cavity flow problem, a 41 x 41 grid: Physical Plane

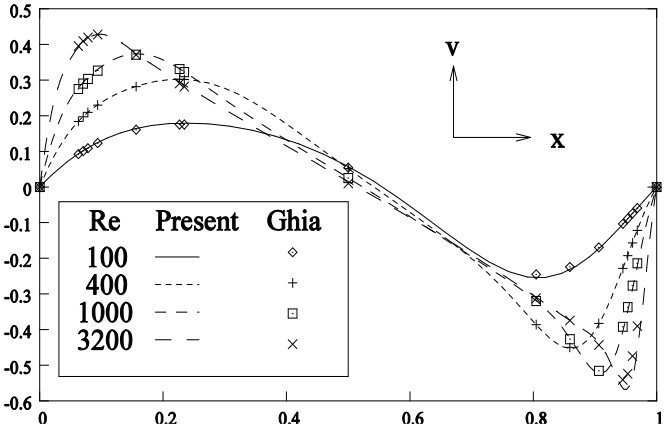


Fig3. The lid-driven square cavity flow problem: Comparison of steady-state vertical velocity along horizontal centreline from Re=100 to Re=3200.

## 4. CONCLUSIONS

In the present work, we introduce a higher order compact ADI formulation for solving unsteady incompressible viscous flow problems in 2D governed by the N-S equations on non-uniform grids. Our proposed method is unconditionally stable, second order accurate in time and fourth order in space. Both Dirichlet and Neumann boundary conditions can easily be implemented in to the scheme. We have addressed several issues relation to the use of HOC schemes on stretched, rectangular and curvilinear meshes. Our scheme can be used in curvilinear coordinates also.

## REFERENCES

[1] J.C.kalita, D.C. Dalal and A.K.Das, A class of higher order compact schemes for the un-steady two dimentional convection-diffutionequation with variable convection coeffcients, *Int. J. Numer: Methods Fluids* 38, 1111-1131, 2002.

[2] S.K. Pandit, J.C. Kalita and D.C. Dalal, A transient higher order compact scheme for incompressible viscous flows on geometries beyond rectangular, *Journal of computational physics*, 225, 1100-1124, 2007.

[3] S. Karra and J. Zhang, High order ADI method for solving unsteady convection-diffusion problems, *Journal of computational physics*, 198,1-9, 2004.

[4] D. You, A high order Pade´ ADI method for unsteady convection-diffusion equations, *Journal of computational physics*, 214, 1-11,2006.

[5] U. Ghia, K.N. Ghia and C.T. Shin, High-*Re* solutions for incompressible Navier-Stokes equation and a multigrid method, *Journal of computational physics*, 48,387-411, 1982.

Fifth International Conference on Computational Methods for Thermal Problems
THERMACOMP2018, July 9-11, 2018, Indian Institute of Science, Bangalore, INDIA
*N. Massarotti, P. Nithiarasu, Pradip Dutta and C. Ranganyakalu (Eds.)*

# Effect of Laser Scan Speed on Melt Pool Evolution during Selective Laser Melting

**Aurabinda Swain, Anirban Bhattacharya**
Indian Institute of Technology Bhubaneswar, Odisha, India-752050, as57@iitbbs.ac.in, anirban@iitbbs.ac.in

**Piru Mohan Khan**

Indian Institute of Technology Kharagpur, West Bengal, India-721302, pmk11@iitbbs.ac.in

## ABSTRACT

In this paper, we present a numerical model for simulating the melting and solidification of a binary alloy during a selective laser melting process. The model is based on the enthalpy-porosity method which has been suitably modified to accommodate for simultaneous melting and solidification. The effect of laser is incorporated by using a moving heat source boundary condition. The model also solves for surface tension driven and buoyancy driven convection which play a prominent part in melt pool evolution. Simulation results show that the model captures the transient melt pool evolution pattern, movement of the melt pool, the nature of convection and the solute segregation and final solute distribution. The model is applied to study the effect of laser scan speed on the melt pool shape and convection pattern.

**Key Words:** *Laser melting, Marangoni convection, Moving melt pool, Scan speed.*

## 1. INTRODUCTION

Additive manufacturing has seen increasing application in recent years for products and models built with polymers and similar materials. Although, metals and alloys are not used as raw materials from a production point of view, lot of research is focussed at present on developing novel techniques for additive manufacturing with metals and alloys. Additive manufacturing of alloy components will significantly improve the feasibility of producing complex parts and reduce the turnaround time for replacing customized components. One of the main techniques for additive manufacturing of alloys is selective laser melting. In selective laser melting, metal or alloy powders are deposited layer by layer and each layer is selectively melted using a laser beam. The molten region subsequently solidifies and the next layer of powder is deposited and selectively melted. This process goes on until the desirable product structure is obtained. The final properties of the produced component depends on process parameters such as laser scan speed, laser power, spot radius, layer thickness, etc. as well as on powder bed characteristics such as particle size distribution & thermophysical properties. It is important to optimize these parameters to obtain desired material properties.

In this paper we present a numerical model for simulating the evolution of a laser driven moving melt pool. The model is developed by making appropriate modifications to the governing equations for momentum, energy and species conservation developed based on the well known enthalpy-porosity technique [1,2] to incorporate the effects of surface tension, moving laser driven heat source and simultaneous melting and solidification. The model is subsequently applied for parametric study of effect of laser scan speed on melt pool shape and convection pattern.

## 2. PROBLEM DESCRIPTION

In the present study, the melting and solidification of Al-5 wt% Cu along a track using a laser source is modelled. It is assumed that, the track is generated over previously solidified tracks. During the melt pool movement, melting occurs from one side of the melt pool while solidification occurs from the other side. Thus, to simulate this phenomena, a model needs to be capable of handling simultaneous melting and solidification. The melt pool evolution model is developed based on the enthalpy-porosity method [1]. The governing equations for continuity, momentum, temperature and species conservation are formulated based on volume averaging principles [1] and solved using a coupled implicit scheme [3]. The main changes to the governing equations for this specific model is outlined below.

To account for laser driven heating, a moving heat flux boundary condition is used for the energy equation which can be defined as

$$S_h = \frac{AP\sqrt{B}}{\sqrt{\pi} r_0} \exp[-B\frac{(x-ut)^2}{r_0^2}] \tag{1}$$

where P is the laser power, u is the scan speed, x and t are the distance along the x coordinate value and time and A and B are constants. This defines the heat source to have a Gaussian distribution where the centre moves at the speed of the laser scanning motion.

One of most important factors for laser melting process is the effect of surface tension. Due to high thermal gradient, the temperature dependent surface tension varies along the melt pool interface resulting in force along the interface. This leads to convection in the melt pool which is known as Marangoni convection. This has been incorporated in the model by using a suitable boundary condition term for the top surface in the U momentum equation as given below [4].

$$\mu\frac{\partial u}{\partial y} = \sigma_0 \gamma_t \frac{\partial T}{\partial t} \text{ where } \gamma_t = -\frac{1}{\sigma_0}\frac{\partial \sigma}{\partial t} \tag{2}$$

To account for simultaneous melting and solidification, the species conservation equation is modified as

$$\frac{\partial(\rho C_{mix})}{\partial t} + \nabla.(\rho \bar{u} C_l) = \nabla.(D\nabla C_l) \tag{3}$$

where the volume averaged concentration $C_{mix} = (1-f_l)C_{s(avg)} + f_l C_l$ during solidification and $C_{mix} = (1-f_l)C_{stored} + f_l C_l$ during melting where $C_{s(avg)}$, $C_l$, $C_{stored}$ are the average solute concentration in the solid, the liquid solute concentration, and the solute concentration preserved in the previously solidified region. This accounts for the stored species in the solid which is available after melting.

The model is applied on a square domain with convective and radiative loss from its left, right and bottom boundaries and Gaussian laser heat source and heat loss at the top surface. The governing equations are solved using an in-house code based on the SIMPLER algorithm and the simulations are continued until the laser moves from one side of the domain to the other side.

## 3. RESULTS

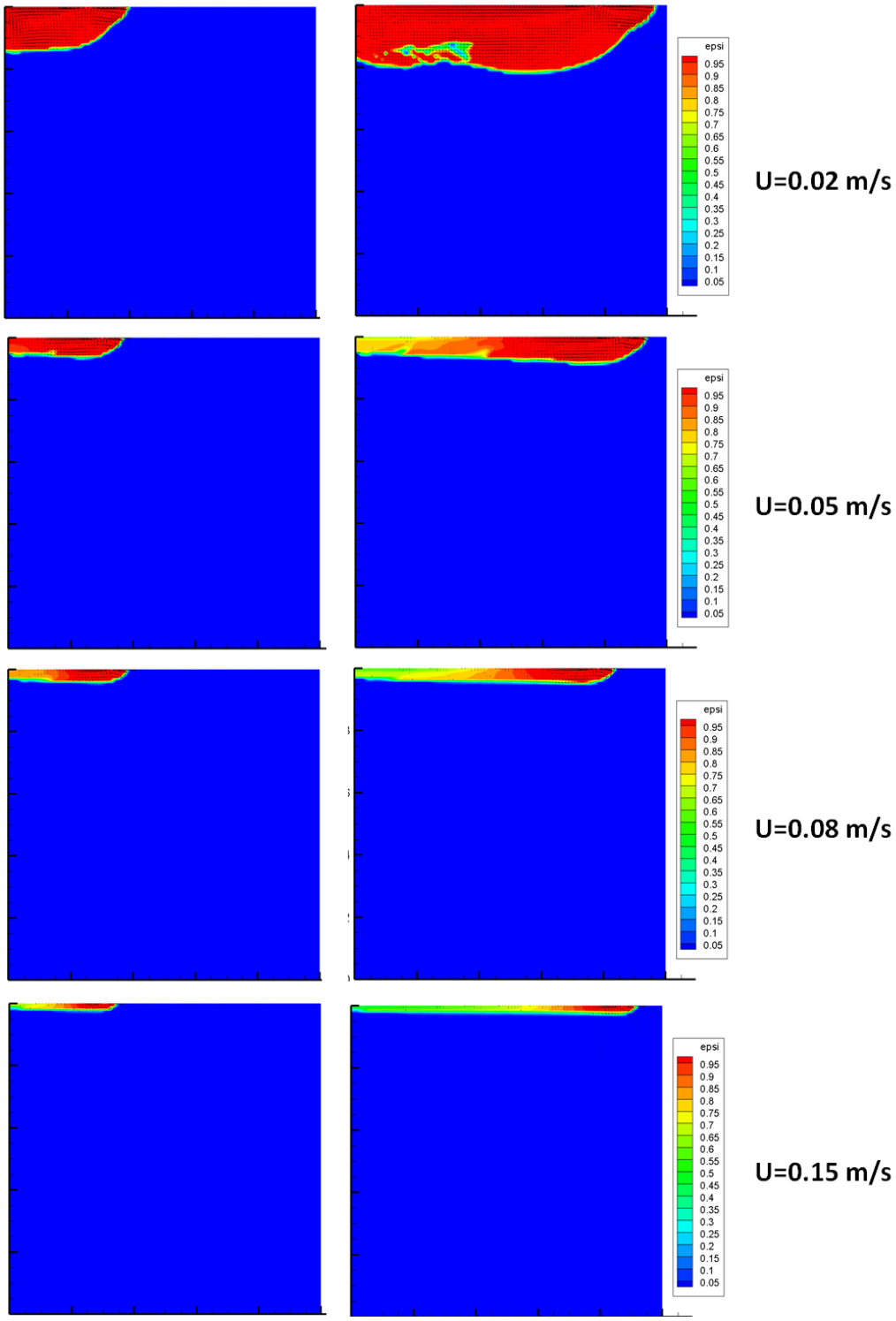


FIGURE 1. Initial and final melt pool shape and convection pattern for different scan speeds

Simulations were performed for laser melting of Al-5 wt%Cu with varying scan speeds ranging from 0.02 m/s to 0.15 m/s by keeping all the other process parameters constant. The effect of different scan speeds on the melt pool pattern is shown in Figure 1. It can be seen that the reduction of scan speed results in much deeper melt pools due to the time available for melting. The

convection pattern shows strong influence of Marangoni effect resulting in flow along the melt pool interface. This results in a shallower and wider melt pool. The study is useful in predicting suitable combinations of laser power and scan speed for a given layer thickness.

## 4. CONCLUSIONS

We have developed a model for simultaneous melting and solidification of binary alloys during selective laser melting process. The model is capable of simulating the evolution and movement of the melt pool, the resultant convection pattern and the final solute distribution. The model can be applied to study the effect of important process parameters such as laser scan speed, laser power, spot radius as well as different alloy compositions. In the present study simulations are performed to observe the effect of laser scan speed on the melt pool evolution and convection pattern. It is observed that the scan speed plays a prominent role on the melt layer thickness and should be chosen appropriately for the given power and layer thickness. The present model will act as a foundation towards the development of a microstructure prediction model for laser based additive manufacturing processes.

## REFERENCES

[1] A. D. Brent, V.R.Voller, and K. J.Reid, The enthalpy porosity technique for modelling convection - diffusion phase change: application to the melting of a pure metal, *Numerical Heat Transfer*, 13, 297-318, 1988

[2] S. Chakraborty, and P. Dutta, A generalized formulation for evaluation of latent heat functions in enthalpy-based macroscopic models for convection-diffusion phase change process, *Metallurgical and Material Transactions* B, 32,562-564, 2001.

[3] S. Patankar, *Numerical heat transfer and fluid flow*, CRC press, 1980.

[4] E. Magyari, and A. J. Chamkha, Exact analytical results for the thermosolutal MHD Marangoni boundary layers, *International Journal of Thermal Sciences*, 47(7), 848-857, 2008.

# FILM COOLING ENHANCEMENT BY INTRODUCTION OF MIST ON A FLAT PLATE

**Anjali Dwivedi, S. Sarkar**
Department of Mechanical Engineering,
Indian Institute of Technology Kanpur,
Kanpur - 208016, India
subra@iitk.ac.in

## ABSTRACT

The protection of blade from hot flue gases is one of the challenges associated with the increasing gas turbine operating temperatures for improved thermal efficiency and power output. The principle objective of the present work is to estimate enhancement of cooling effectiveness by introduction of mist. Euler-Lagrange model is used to investigate the two phase mist flow under the framework of ANSYS 15. Mist introduction in film cooling enhance the film cooling effectiveness by providing small heat sink in the form of droplets in coolant. To characterize the mist film cooling, case study of varying mist concentration and droplet diameter is done, while keeping the other parameters constant. Increase in mist concentration results in enhancement of the film cooling effectiveness. Droplet diameter increase shows complex flow and heat transfer behaviour, depicting that there exists an optimum diameter in which the potential of mist film cooling can be furnished.

**Key Words:** *Heat Transfer, Mist Film Cooling, Two Phase Flow Simulation.*

## 1. INTRODUCTION

Future generation advanced turbine of improved thermal efficiency and higher power output are expected to continue to operate at higher temperatures than the allowable metal temperature of the turbine blade, which demands a sophisticated cooling technique for safe operation. Thus enhanced heat-dissipation technologies development is a vibrant area of research. Film cooling is one of the preferred methods for effective cooling of a gas turbine, in which coolant jets bled from compressors is ejected to form a protective layer between hot flue gases and blade surface. The coolant film and crossflow interaction with the mainstream is highly complex in nature and many studies has been performed experimentally and numerically to understand it. A counter rotating vortex pair (CRVP), jet shear layer vortices, a horseshoe vortex and the upright wake vortices are the prominent flow features observed during jet cross flow interactions. Further the complexity of flow structures increases with the freestream turbulence, wall curvature, rotation and unsteadiness. At present, excessive coolant air is supplied to prevent damage leading to a reduction in efficiency.

Mist cooling as a potential means to enhance the film cooling performance has been introduced in last few years [1-3]. Mist is a two-phase fluid consists of finely dispersed tiny water droplets in coolant air, introduced through plenum chamber. This offers a significant potential for high-heat-flux thermal management owing to the superior thermal properties of mist relative to air. Particularly phase change phenomena dissipate larger heat fluxes than air. It provides steeper temperature gradient near the wall, lower bulk temperature and increased droplet flow mixing induced by JICF flow structures. Continuous evaporation of droplets lasts farther into the downstream region where air film cooling becomes less effective. Few researchers [4-5] have numerically studied the feasibility of mist cooling at the high pressure and temperature. They found that sufficient large diameter (30-40 μm) mist can survive this harsh environment, subjected to experimental investigation. Thus, mist cooling may offer a solution to this problem by providing adequate cooling layer with reduction in excessive amount of coolant air supply. Wang along with few other researchers [2-3,6] tries to simulate the mist cooling for understanding the effects of

curved surface, rotation of blades, different hole geometries, elevated operating conditions on its effectiveness and found that it results in overall increase of cooling effectiveness as a small sink is provided in coolant air in the form of mist. Strong droplet-wall interaction on the pressure side than on suction side results in higher cooling effectiveness on the pressure side [6-7]. Excess mist concentration is also detrimental to corrosion and thermal stresses. Thus to develop an optimized mist ratio which can provide maximum cooling effectiveness for minimum coolant flow, a study of mist concentration and diameter effect on film cooled turbine blade is utmost necessary, which are performed in this study.

## 2. NUMERICAL METHODS AND COMPUTAIONAL DETAILS

Rectangular channel with film cooling hole connected to a plenum chamber same as used by Sarkar and Ranakoti [8] is taken as computation domain. Cartesian structured grid, coordinate system, schematic of computational domain and boundary conditions used in present simulation are described in detail in Fig 1 and Fig 2. Upper boundary, at a distance of 10D, is considered as inviscid wall which is sufficiently away from the bottom wall. Periodic boundary condition is imposed in the span wise direction to mimic a series of holes. All other walls of the computational domain are treated with no slip, no flux and "reflect" boundary condition. A turbulent velocity profile of thickness (δ) of 3.1 mm is imposed at the main stream inlet with fixed temperature 400K. Mist fluid is fed by plenum chamber through the injection hole via cylindrical pipe of 12.7 mm diameter D. Length to diameter ratio L/D, pitch and an inclination angle with the free stream are taken as 1.75, 3D and 35 degree respectively. Uniform velocity at the secondary inlet for blowing ratio (M) = 0.5 and 300K temperature for density ratio (D.R.) =1.2 is applied. Turbulent intensity and length scale are set as 0.2% and 0.01m for both main stream and secondary inlet. All the parameters of mist investigated here are kept constant except its concentration and diameter, which are primary parameters dictating the cooling effectiveness.

Euler-Lagrange model is used here to deal with the complex transport processes and analyse the fluid and thermal phenomena in mist cooling. The Reynolds-averaged Navier–Stokes equations with two equation k–e realizable turbulence model, enhanced wall functions and species transport equations are solved for the continuous phase flow physics using ANSYS 15. Lagrangian approach is used for droplet trajectory tracking in the calculated continuous flow field at specified intervals by stepwise integration. Discrete phase model two-way coupling keeps the qualitative account of interphase exchange between continuous and discrete phase. Detailed validation of the method has already been shown in earlier studies [8, 9].

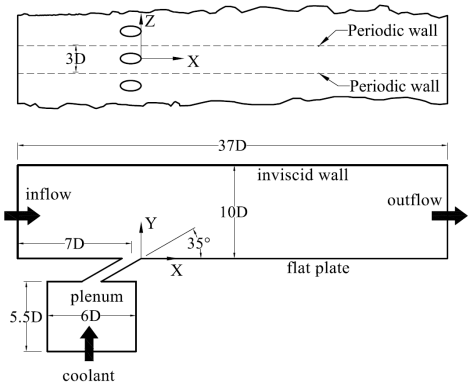


FIG 1. Computational Dimensional detail [8]

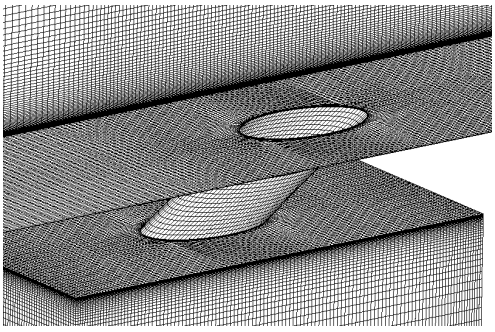

FIG 2. Meshing in 3D computational domain [8]

## 3. RESULTS AND DISCUSSIONS

Trajectory of uniformly distributed 10 micron mist introduced from plenum chamber in coolant show the formation of the coolant envelop in Fig 3. Tiny droplets of mist while flowing downstream work as heat sink, absorbs the heat in coolant layer and provides increased cooling effectiveness. Mist enhances cooling by increasing insulation effect of cooling layer due to convective and latent heat absorption by droplets. Increase of droplet velocity is observed due to drag force induced by mainstream flow. Mist follows the dominant flow feature of JICF, resulting in kidney shaped non-dimensional temperature contour while flowing downstream, Fig 4.

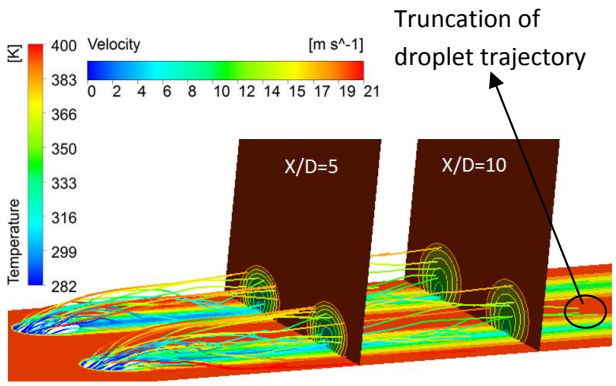


FIG 3. Droplet trajectories along with temperature contour overlaid on cross sectional plane for 3% mist

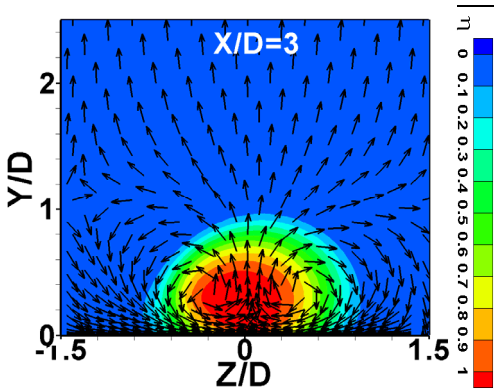


FIG 4. Non-dimensional temperature contour on X/D =3 locations for 5% mist with superimposed velocity vector

Three cases of different mist concentration i.e. no mist, 3%, and 5% have been simulated for 10 micron diameter and analysed. Fig 5 and 6 depicts the film cooling effectiveness $\eta = (T_\infty - T_{aw}/T_\infty - T_C)$ on the bottom wall with and without mist. Surface can be effectively protected for larger length and wider span with increased values of effectiveness for mist cooling. Droplet evaporation and cross flow of hot flue gases downstream the coolant jet take off the coolant from surface results in reduced effectiveness far away from coolant hole. Centreline and span averaged effectiveness plotted in Fig 7 and 8 are the result of complex flow and heat transfer behaviour of mist cooling. Both the span and centreline effectiveness enhance with introduction of mist. Further, drag force increases with increase of mist percentage, more droplets being available. When the droplets percentage is increased from 3 to 5, effectiveness increases downstream as simply the droplets retain their existence. As all droplets evaporate the mist effect gets nullified downstream and no further enhancement $\eta/\eta_0$ is observed ($\eta_0$ is the effectiveness with no mist concentration). Although, effectiveness increases with mist percentage, but it has a tendency of droplet accumulation on surface leading to corrosion. Therefore, the upper limit of mist concentration need to be determined [9].

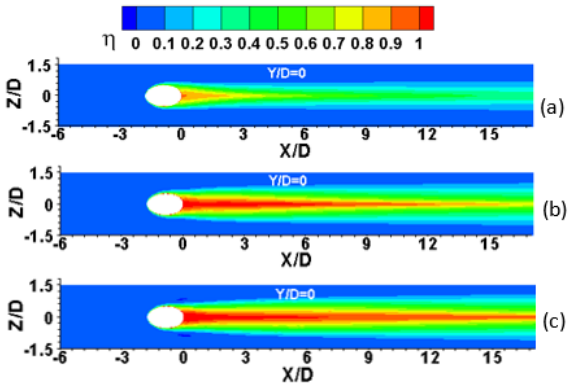


FIG 5. Comparison of adiabatic film cooling effectiveness for (a) 0%, (b) 3% and (c) 5%

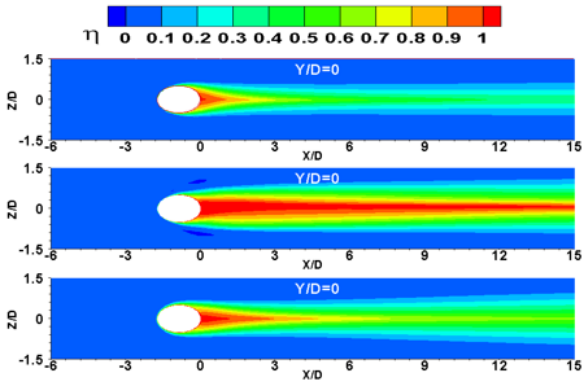


FIG 6. Comparison of adiabatic film cooling effectiveness for (a) 5, (b) 10 and (c) 20 micron

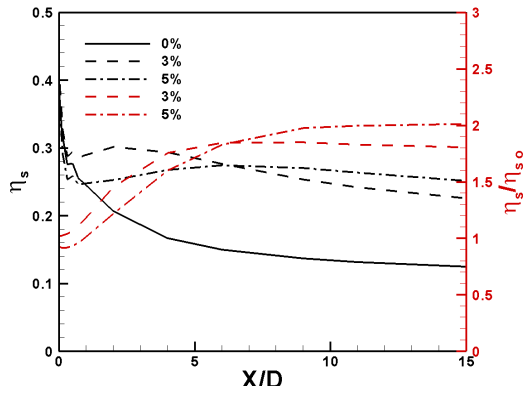


FIG 7. Comparison of span averaged effectiveness

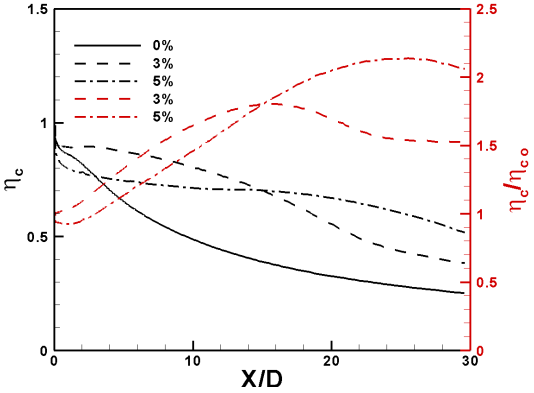


FIG 8. Comparison of centreline effectiveness

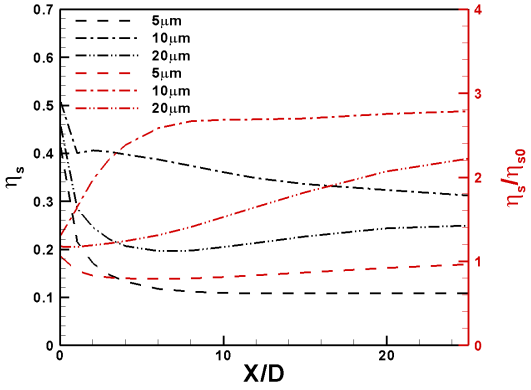


FIG 9. Comparison of span averaged effectiveness

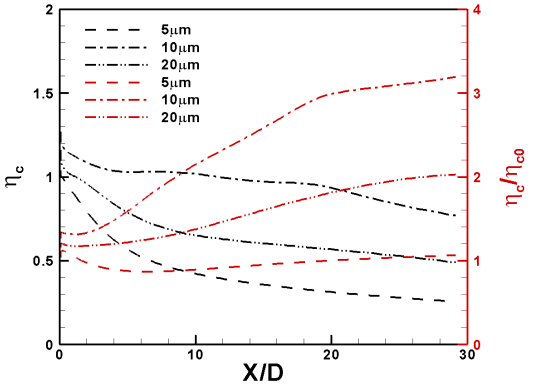


FIG 10. Comparison of centreline effectiveness

To understand the effect of mist droplet diameter three cases are investigated at 5% mist concentration: 5 micron, 10 micron and 20 micron. With same amount of mist percentage small diameter mist provides larger surface area thus evaporates faster while larger diameter droplets sustain for longer distance and effective cooling is provided after travelling some distance. This phenomenon is clearly visible in Fig 6 and its effect on effectiveness is plotted in Fig 9 and 10. Since major content of mist in case of 5 micron diameter, gets evaporated within plenum chamber, it behaves as film cooling with no mist and almost no enhancement is observed in Fig 9 and 10. As the size of droplet increased to 10 micron, droplets sustain in plenum chamber and major part of evaporation takes place from X/D=2, which results in increased slope of enhancement shown in Fig 10. Further increase of diameter to 20 micron is less effective initially as convection mode of heat transfer is dominant than latent heat and droplets may escape from domain without evaporating as shown in Fig 6, 9 and 10. Thus the mist remains underutilized for larger

mist diameter. This suggests that for the given length of plate there exist an optimum diameter of droplet which provides maximum effectiveness as it is 10 micron in this case.

## 4. CONCLUSIONS

Mist film cooling appears very encouraging and maximum increment in centreline effectiveness is found to be 1.80 times at X/D=16 for 3% mist and 2.14 times at X/D=25.5 for 5% mist. While maximum increment in span-average effectiveness is 1.85 times at X/D=9 for 3% mist and 2 times at X/D=15 for 5% mist. There exist an optimum diameter for mist film cooling as it is 10 micron here, where latent heat absorption phenomenon dominates the convective cooling. Maximum increment in centreline effectiveness is 1.12 times at X/D=0.14 for 5 micron, 3.20 times at X/D=29 for 10 micron, and 2.0 times at X/D=29 for 20 micron diameter. While maximum increment in span average effectiveness is 1.07 times at X/D=0 for 5 micron, 2.79 times at X/D=25 for 10 micron, and 2.23 times at X/D=12 for 20 micron diameter. Thus the use of 5 micron mist diameter in the given condition is not encouraging while 10 micron gives the favourable results.

## REFERENCES

[1] Kumari, N., Bahadur, V., Hodes, M., Salamon, T., Kolodner, P., Lyons, A. and Garimella, S, "Analysis of evaporating mist flow for enhanced convective heat transfer". *International Journal of Heat and Mass Transfer*, 53(15-16), pp.3346-3356, 2010.

[2] Li, X. and Wang, T., "Effects of Various Modeling Schemes on Mist Film Cooling Simulation". *Journal of Heat Transfer*, 129(4), p.472, 2007.

[3] Wang, T. and Li, X., "Mist film cooling simulation at gas turbine operating conditions". *International Journal of Heat and Mass Transfer*, 51(21-22), pp.5305-5317, 2008.

[4] Ragab, R., and Wang, T, "An Investigation of Applicability of Transporting Water Mist for Cooling Turbine Vanes". *ASME Paper GT2012-70110. Proceedings of Turbo Expo 2012*, June 11-15, 2012, Copenhagen, Denmark, 2012.

[5] Ragab, R., and Wang, T., "Investigation of Applicability of using Water Mist for Cooling High- Pressure Turbine Components via Rotor Cavity Feed Channels". *ASME Paper HT2013-17150. Proceedings of HT2013 ASME Summer Heat Transfer Conference*, June 14-19, 2013, Minneapolis, MN, USA, 2013.

[6] Dhanasekaran, T. and Wang, T., "Simulation of Mist Film Cooling on Rotating Gas Turbine Blades". *Journal of Heat Transfer*, 134(1), p.011501, 2012.

[7] Yuting J., Zheng Q., Ping D,Hai Z. and Feilong Yu, "Research on heavy-duty gas turbine vane high efficiency cooling performance considering coolant phase transfer". *Applied Thermal Engineering* 73 (2014) 1177-1193

[8] Sarkar, S. and Ranakoti, G., "Effect of Vortex Generators on Film Cooling Effectiveness". *Journal of Turbomachinery*, 139(6), p.061009, 2017.

[9] Anjali Dwivedi, Ankit Verma and S. Sarkar, "Flow and Heat transfer analysis of mist-film cooling on a flat plate". *ASME Paper GTIndia2017-4568. Proceedings of the 2017 Gas Turbine India Conference*, December 7-8, 2017, Bangalore, India.

Fifth International Conference on Computational Methods for Thermal Problems
THERMACOMP2018, July 9-11, 2018, Indian Institute of Science, Bangalore, INDIA
*N. Massarotti, P. Nithiarasu, Pradip Dutta and C. Ranganyakalu (Eds.)*

# THERMO-STRUCTURAL ANALYSIS OF TWO-CHANNEL SIMULTANEOUS DEFORMATION IN I-PHWR UNDER HEATUP

**Ankit Singh,**
Indian Institute of Technology Roorkee, Roorkee, aks13dme@iitr.ac.in

**Pradeep Sahoo**
Botswana International University of Science and Technology, Palapye, Botswana

## ABSTRACT

Loss of Coolant Accident (LOCA), followed by failure of emergency core cooling system (ECCS) in Indian Pressurised Heavy Water Reactor (I-PHWR) lead to Severe Core Damage Accident (SCDA). Due to deteriorating moderator level (heat sink), upper fuel channels in reactor core are exposed to rapid temperature ramp, which leads to deformation of channels under its self-weight and weight of the fuel bundles. Multi-physics coupled field solver by ANSYS v17.2 is used to investigate deformation behaviour of two coolant channels. Coolant channels of Indian PHWR 220MWe reactor are considered. Each channel consists of Pressure Tube (PT), which is placed concentrically inside Calandria Tube (CT). During high temperature transient, PT and CT undergo thermally induced creep. Using available longitudinal creep strain-rate correlations in literature, a subroutine called USERCREEP is written, compiled, and then linked to solver. Objective of this study is the evaluation of channel transient thermal loading on its displacement (sagging). This study also investigate the load transfer from upper channel to the channel below after contact.

**Key Words:** *SCDA, multiphysics creep, coupled element.*

## 1. INTRODUCTION

Indian PHWR 220MWe core consists of 306 horizontal tube channels and each channel consists of two concentric tubes of which inner tube is called as PT while outer tube as CT. Twelve fuel bundles are placed inside PT along length. Core resides in large cylindrical vessel called Calandria vessel, which is submerge with heavy water known as moderator at an atmosphere pressure. Moderator acts as a heat sink under an accident condition. The Calandria vessel lies inside a large shield tank named as the Calandria vault, which contains large volume of light water. Calandria vault acts as an ultimate heat sink under a severe accident condition. Pressurized heavy water coolant flow through PT, which takes heat generated from the fuel bundles, during fission reaction. CT is fixed to a Calandria tube sheets at both ends and PT is placed concentrically with one end fixed while other end as free in an axial direction. Through the annulus of PT-CT, $CO_2$ gas flows, and it acts as a thermal insulator to restrict heat transfer to moderator during normal operating condition [1]. Accident scenario typical to PHWR is one in which moderator system malfunctioned and there is a loss of ECCS. Availability of moderator continuously decreases. This results in reduction of decay heat removal from the channel. Such scenario is termed as severe core damage accidents (SCDA) [2]. If this accident continues, channels may fail at region of high stress levels or channels detach (termed as channel disassembly) and accumulate at bottom of Calandria vessel. These collected channels at the bottom of Calandria, thus form a terminal debris bed.

Objective of this study is the evaluation of transient thermal loading effect on the structural integrity of channels and thus on the transient sagging of channels using multi-physics coupled field solver by ANSYS v17.2 [3]. This study also investigate the load transfer from upper channel to the channel below after contact.

## 2. MODEL DESCRIPTION

Schematic diagram [4] of pressure tube and Calandria tube assembly is shown in Figure 1. Dimensions as shown in schematics are in mm. A 1/3rd scale is considered for the simulation study.

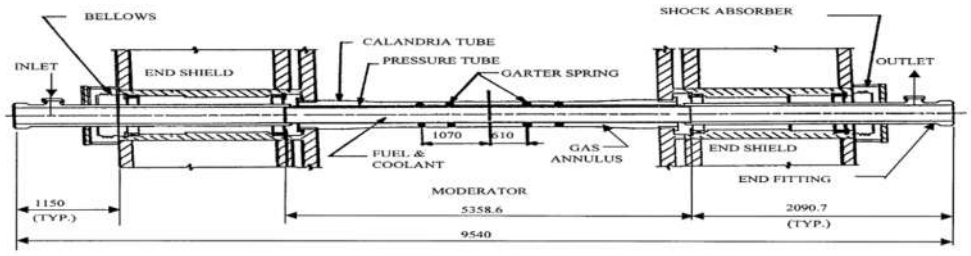


FIGURE 1 Pressure tube and Calandria tube assembly

Direct-coupled field element SOLID226 is used to mesh both PT and CT to understand the coupled effect of thermal and structural response during deformation. SOLID226 is 3-D 20 nodes hex (Brick) element and it can handle geometric non-linearity (large deformation), material non-linearity (creep, plasticity etc.), and surface-to-surface contact problems [5]. Figure 2 shows the schematic diagram of model used in analysis. Length of each CT corresponds to 1/3rd scale of core length as given in Figure 1.

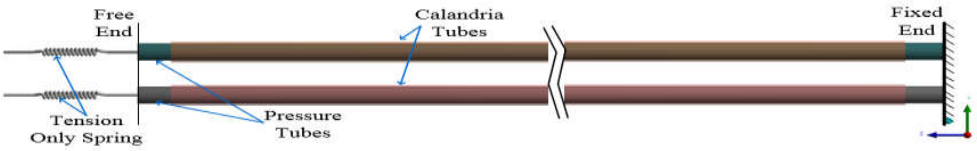


FIGURE 2. Schematic of channels

One end of each PT (z=0mm) is fixed while other end is free to move in axial direction only, but in outward direction from its actual position. Free end condition is achieved by tension only spring. Both ends of CTs are fixed. Total force due to bundles weight is taken as 190.23 N and applied along length and at the bottom of each PT.

Heat-generation rates, for effective powers of 8kW and 6kW, are applied to upper and lower PT respectively as decay heat. Thermal Contact conductance is taken as 8500 W/m$^2$.K [6]. In current study, a constant convective heat transfer coefficient of 10 W/m$^2$.K is considered on outer surfaces of CTs and emissivity of 0.3 is used to model the radiation to ambient with temperature of 100 ˚C. Outer surfaces of extruded portion of PTs are modelled with constant convective heat transfer coefficient of 10 W/m$^2$.K and emissivity of 0.3 is used to model radiation to ambient with temperature of 27 ˚C. Perfect enclosure condition is considered for surface-to-surface radiation heat transfer between the outer surface of PT and the inner surface of CT. Solution is initialized with temperatures of PTs and CTs as 220 ˚C and 100 ˚C respectively. For modelling of longitudinal creep equation [7], Usercreep subroutine is coded in FORTRAN language, which is compiled with supported compiler and link to solver. Material properties are referenced from MATPRO manual [8].

## 3. RESULTS

Figure 3 to Figure 5 show the average temperature profiles of PT and CT at various distances from fixed end. At about 90s, sudden rise in temperature of lower channel is observed. It represents contact of upper channel to below channel, which results in heat transfer due to thermal contact conduction.

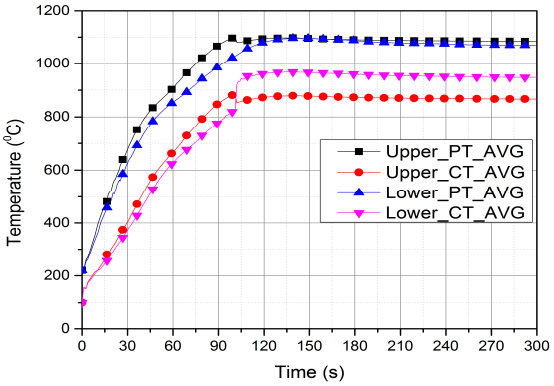


FIGURE 3. Temp. at 900mm

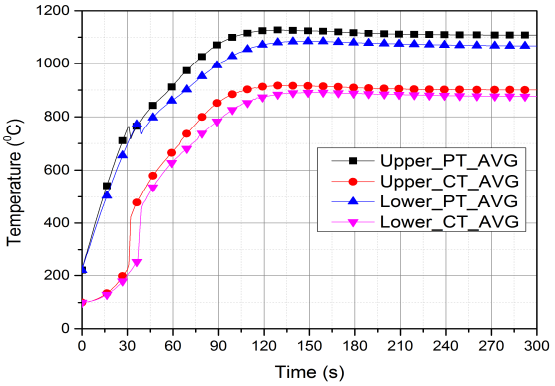


FIGURE 4. Temp. at 1200mm

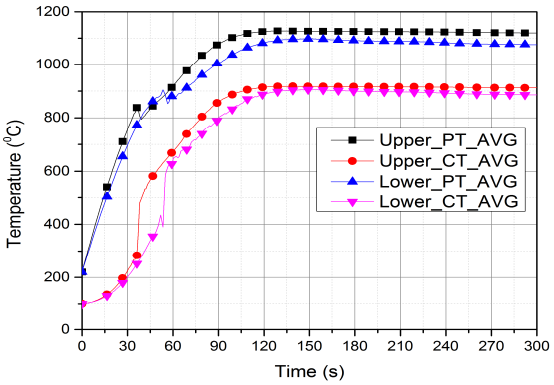


FIGURE 5. Temp. at 1500mm

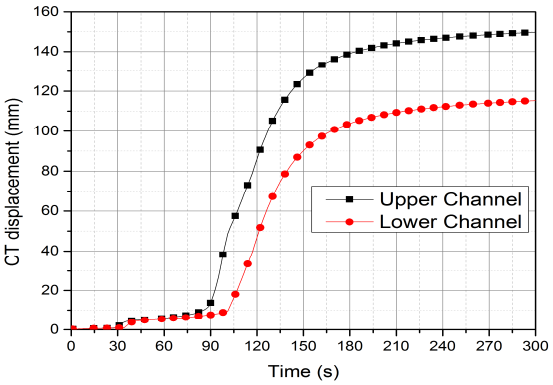


FIGURE 6. Mid-Span vertical displacement

Figure 6 shows vertical displacement of both channels. Observed vertical displacements of both channels are less until 30 s. After 90 s, significant displacements are observed due to creep progression. From Figure 7, it is seen that axial displacement of PT is observed to be increasing from its start position due to thermal expansion, it reaches a maximum and then suddenly decreases to zero. Spring reaction force to keep PTs in its original position is indicated in Figure 8.

Figure 9 delineates the deflection profile at the end of simulation time (300 s). Load transfer due to contact from PT to CT and between channels, are depicted in Figure 10 and Figure 11 respectively. It represents the reaction force that is produced by contact elements during interaction.

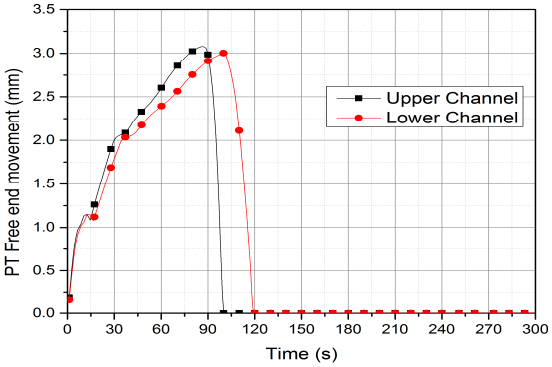


FIGURE 7. Free end displacement

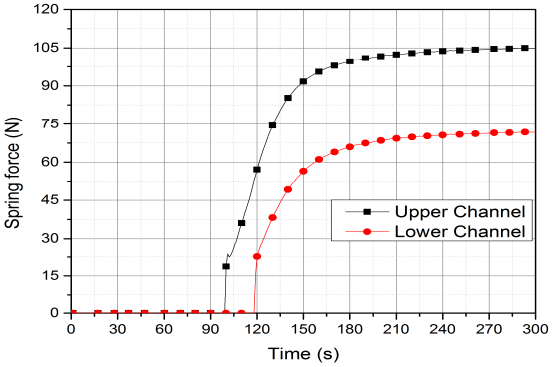


FIGURE 8. Spring reaction force at free ends


FIGURE 9. Deflection profile at the simulation end time

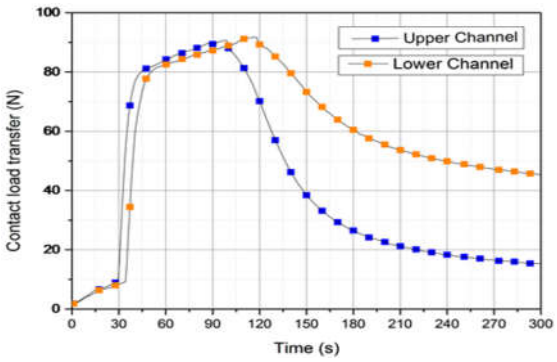


FIGURE 10. Contact load transfer from PT to CT for each channel

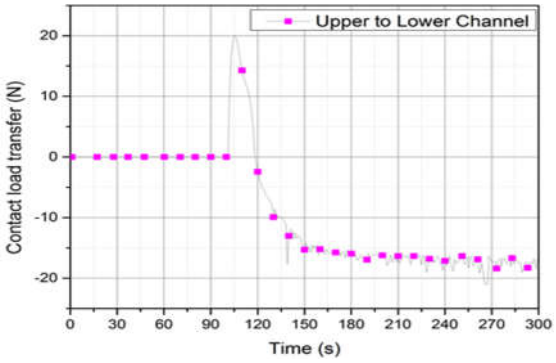


FIGURE 11. Contact load transfer from upper to lower channel

## 4. CONCLUSIONS

Mid-span deflection (sag) increases significantly after the temperatures of the PT and CT reached above 700 ˚C and circumferential temperature variation may have impact on deformation of the PT and CT. Load transfer to below channel depends on its temperature. End load on channels is not enough for its pulling. From results, it is clear that creep is dominant mechanism for channel disassembly progression, and ANSYS solid element model is efficient in prediction of such behaviour during postulated accident progression.

## REFERENCES

[1] S.S. Bajaj, and A.R. Gore, The Indian PHWR, *Nuclear Engineering and Design*, Volume 236, Issues 7–8, Pages 701-722, 2006.

[2] IAEA-TECDOC-1594, Analysis of Severe Accidents in Pressurized Heavy Water Reactors, 2008.

[3] ANSYS Workbench, ANSYS Inc., Version 17.2, 2016.

[4] V.K. Sharma, and V.K. Gupta, A new method for detecting pressure tube failures in Indian PHWRs, *Nuclear Engineering and Design*, Volume 196, Issue 3, Pages 337-351, 2000.

[5] ANSYS Theory Guide, ANSYS Inc., Version 17.2, 2016.

[6] P. Majumdar, B. Chatterjee, H.G. Lele, G. Guillard, and F. Fichot, ASTEC adaptation for PHWR limited core damage accident analysis, *Nuclear Engineering and Design*, Volume 272, Pages 273-286, 2014.

[7] Shewfelt RSW, and Lyall LW, A high temperature longitudinal strain rate equation for Zr – 2.5 wt% Nb pressure tubes. *Journal of Nuclear Material*, Volume 132, Pages 41–6, 1985.

[8] Idaho National Engineering and Environmental Laboratory, SCDAP/RELAP5/MOD3.2 Code Manual Volume IV: MATPRO—a library of materials properties for light-water-reactor accident analysis, NUREG/CR-6150; 1997.

Fifth International Conference on Computational Methods for Thermal Problems
THERMACOMP2018, July 9-11, 2018, Indian Institute of Science, Bangalore, INDIA
*N. Massarotti, P. Nithiarasu, Pradip Dutta and C. Ranganyakalu (Eds.)*

# New Approach in Spherical Discretization to Solve Radiative Transfer Equation by Finite Volume Method

**Ankur Garg[a], G. Chanakya[b] and Pradeep Kumar[c]**
Numerical Experiment Laboratory(Radiation & Fluid Flow Physics)
Indian Institute of Technology Mandi, Kamand, Mandi, H.P.-175005, India
[a]ankur_garg@projects.iitmandi.ac.in, [b]chandrasekhara_pratap@students.iitmandi.ac.in
[c]pradeepkumar@iitmandi.ac.in

ABSTRACT

A new spherical discretization (icosahedral geometry) apporach has been adopted to solve the radiative transfer equation (RTE) by finite volume numerical technique. The code for new discretization has been developed in OpenFOAM (opensource computational fluid dynamics (CFD) package) framework which also has conventional finite volume radiative heat transfer solver (fvRTE). The fvRTE uses spherical coordinates i.e polar, azimuthal like system, to discretize the spherical space. The 3D radiative solver has been used to test new approach with radiative symmetric boundary condition in the third direction. The various two-dimensional cases have been verified with new spherical discretization method and also has been compared with the fvRTE solver of OpenFOAM. The results reveal that new spherical discretization method produce better results than the existing solver in OpenFOAM and comparable results with the existing literature for diffuse radiation cases. The new spherical discretization approach has advantages as it contains uniform elements unlike conventional discretization method and independent of any coordinate system.

**Key Words:** *Radiative Transfer Equation (RTE), Spherical Space, Icosahedron Geometry, Radiative Symmetric Condition*

## 1. INTRODUCTION

In many engineering applications like fire safety equipment, combustion, solar devices, electronic cooling etc. radiation plays an important role. In order to do accurate analysis of those devices, the modeling of radiative heat transfer is absolutely necessary [1]. Radiative heat transfer is governed by an integrodifferential equation [2, 3] whose exact solution is very difficult even in simple situations. Many numerical techniques like P1 approximation, discrete ordinates method, Monte Carlo method etc. [4] have been developed to solve RTE numerically, but finite volume method for RTE (fvRTE) [5, 6, 7] is most applicable and widely used. The fvRTE uses two kinds of discretization (i) domain discretization similar to CFD solutions (ii) Angular space discretization where angular space of $4\pi$ sr is discretized in small solid angles and RTE is solved on these individual solid angles for all domain cells. Mostly, spherical coordinates system is used for angular discretization which gives many numerical issues specially in collimated cases. The new approach for angular discretization promises to mitigate some of the numerical issues, however, in the present study, diffuse radiation cases have been validated.

## 2. RADIATIVE HEAT TRANSFER EQUATION AND BOUNDARY CONDITIONS

In an absorbing and emitting participating medium under thermal equilibrium, the radiation transfer equation is as follow

$$\zeta \frac{\partial I}{\partial x} + \eta \frac{\partial I}{\partial y} + \mu \frac{\partial I}{\partial z} = \kappa I_b - \kappa I \tag{1}$$

where $\zeta$, $\eta$, and $\mu$ are the the direction cosines, $I_b$ is black body radiation intensity, $I$ is radiation intensity and $\kappa$(kappa) is absorption coefficient. The first and second term on the right hand side

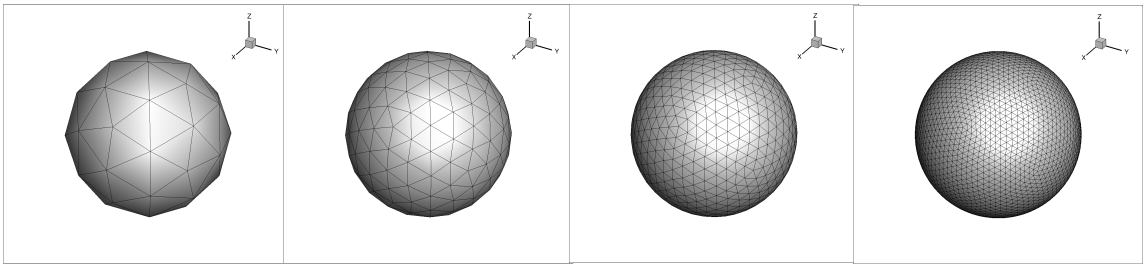

FIGURE 1. Icosphere geometry for recursion levels 2,3,4 and 5.(left to right)

of eq. (1) represent the augmentation and attenuation of radiation by emission and absorption, respectively.

The radiative transfer equation (1) is subjected to the following boundary condition for a diffusely emitting and reflecting wall

$$I(r_w,\hat{s}) = \varepsilon_w I_b(r_w) + \frac{1-\varepsilon_w}{\pi}\int_{\hat{n}\hat{s}>0} I(r_w,\hat{s}) \mid \hat{n}.\hat{s} \mid d\Omega, \qquad \hat{n}.\hat{s} < 0 \tag{2}$$

The two-dimensional radiation cases have also been solved using the 3D solver with radiative symmetric boundary condition in third direction. The detailed description about the solution strategy for two-dimensional cases have been elaborately described by Kumar and Eswaran [8].

## 3. SOLUTION PROCEDURE AND ICOSAHEDRON GEOMETRY

The finite volume formulation of RTE is obtained by double integration of RTE eq. (1) over a control volume and control angle. The set of linear algebraic equations are obtained as

$$\sum_{f=all\,faces} I_f^m A_f D_f^m = (\kappa {I_b}_P{}^m - \kappa I_P^m)\Delta V \Delta\Omega^m \tag{3}$$

where f is face index and P indicates the cell centroid, $D_f^m$ is the directional weight, which is given by

$$D_f^m = \int_{\Delta\Omega^m} (\hat{s}^m.\hat{n}_f) d\Omega \tag{4}$$

where $\hat{n}_f$ is the outward surface normal of a face f, $\hat{s}^m$ is the direction of the radiation and $d\Omega$ is the discrete solid angle attributed to direction m. The directional weight is obtained by constructing regular solid angles on a sphere of unit radius in spherical coordinate system. However, in this way, we obtain mixed faces with very small elements at the pole which causes numerical convergence issue. Instead, we use icosahderon geometry which contain uniform elements for the calculation of direction weights. The icosahedron geometry is obtained by constructing the vertices using the golden ratio as

$$(0,\pm 1,\pm t), \quad (\pm 1,\pm t,0) \quad \text{and} \quad (\pm t,0,\pm 1)$$

where $t$ is golden ratio defined as

$$t = (1.0 + sqrt(5.0))/2.0$$

In this way, we obtain 12 vertices and 20 triangular faces on a sphere of unit radius (icosphere) and this is called recursion level 1. Constructing new vertices between these 12 vertices refines the faces and recursion level 2 is obtained and this process continues to obtain further recursion levels. Icospheres obtained from recursion level 2, 3, 4 and 5 are shown in figure (1).

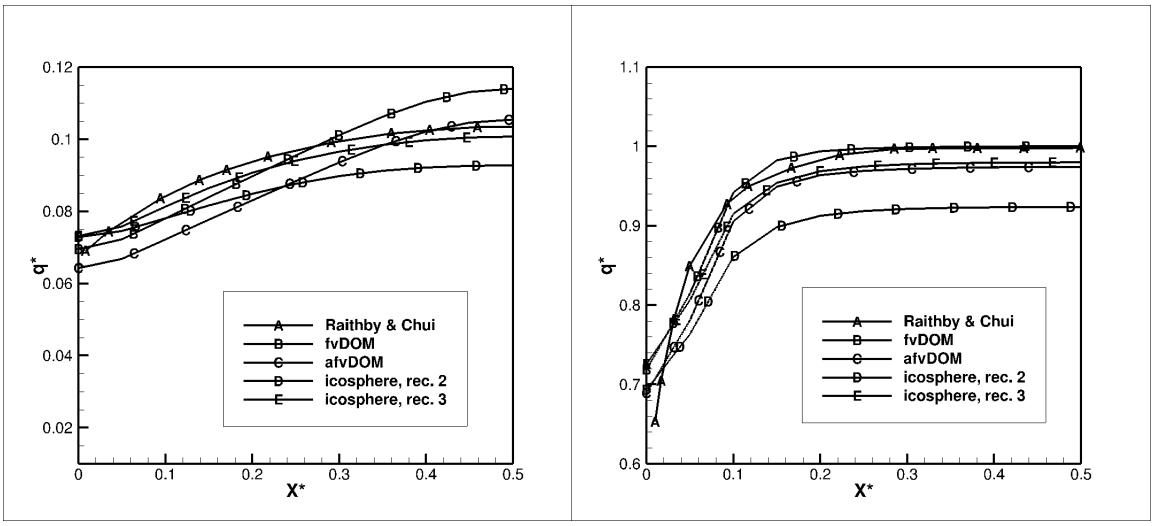


FIGURE 2. Variation of non-dimensional radiative heat flux on bottom wall for $\kappa = 0.1$(left) and $\kappa = 10$(right)

## 4. VALIDATION CASE STUDIES

Square Enclosure:

This 2-D problem has been previously solved by many researchers [5, 6, 7]. The problem is to predict wall radiative heat flux for a 2-D square cavity of unit size filled with absorbing/emitting gas at temperature $T_h$. The walls of enclosure are black and kept at 0K. The domain is discretized uniformly into $20 \times 20$ number of cells. Both, conventional (OpenFOAM implementation) and icosahedron spherical discretization have been used. An alternative to conventional angular discretization (afvDOM) where solid angles are generated with spherical coordinates and 3-D solver is used for 2-D cases. The results have been compared among these approaches and validated with the published results of Raithby and Chui [5]. As the problem is symmetric, the results are shown only for half non-dimensional length.

The comparison results for non-dimensional wall radiative heat flux are shown in figure (2) for the absorption coefficients $\kappa = 0.1$ (left) and $\kappa = 10$ (right). The radiative heat flux at the wall is obtained only due to emission from the gas inside the cavity, since the walls are at 0 K temperature. At the thermal equilibrium, the absorption and emission are the same; it is therefore, higher wall radiative heat flux is obtained for high absorption coefficient. The wall radiaitve heat flux results obtained by alternative way of fvDOM, icosphere with recursion level 3 match well whereas solution by fvDOM and icosphere with recursion level 2 significantly deviate with result by Raith and Chui[5].

Irregular Quadrilateral Enclosure:

Figure 3(left) shows an irregular quadrilateral enclosure (all dimensions are in meter). Similar to the square enclosure case, the absorbing-emitting medium is maintained at $T_g$. The black walls are kept at $0K$.

The non-dimensional radiative heat flux distribution at the bottom wall is shown in figure 3 (right) for absorption coefficient of 1.0. The various spherical discretization methods have been tested and the results have been compared. The RTE solution by afvDOM and spherical discretization by icosphere with recursion level 3 match well with the published result by Chai et al. [7]. The solution of icosphere discretization with recursion level 2 also devites significantly with the published results. The surface area of sphere in the icosphere geometry which recursion level 2 and 3 give 11.66 and 12.33 respectively, whereas exact surface area of sphere is 12.57. Thus, there is an

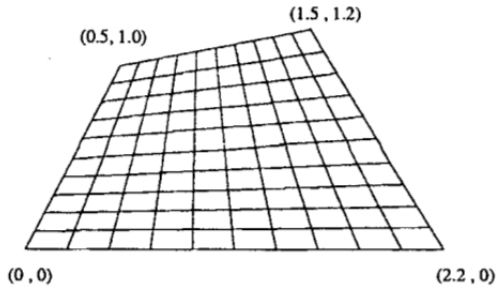


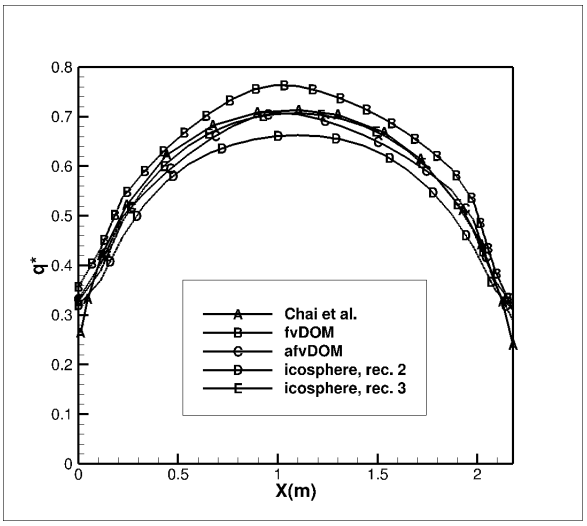


FIGURE 3. Quadrilateral enclosure(left); Non-dimensional heat flux along the bottom wall for $\kappa = 1$(right)

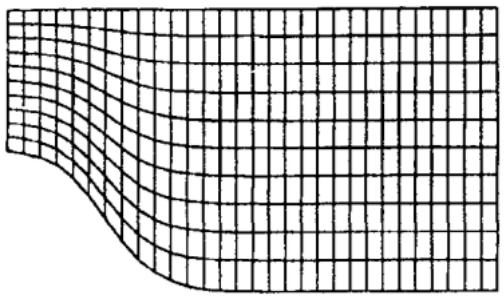

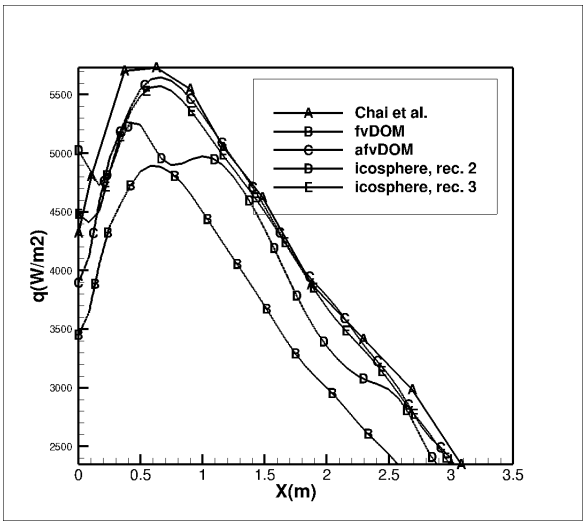


FIGURE 4. Curved geometry(left); Heat flux on top wall for $\kappa = 1.0$(right)

error of 1.83 % in surface $L^2$ norm area of icosphere of level 3. An error of 7.16 % is increased in solution with recursion level 2.

Curved Geometry:

Figure 4(left) shows the schematic of a curved geometry. The top wall is located at y = 1.0 m and the profile of bottom wall is represented according to following equation

$$y = \frac{1}{2}\Big(tanh(2-3x) - tanh(2)\Big), \qquad 0 \leqslant x \leqslant 10/3$$

The bottom wall is black and maintained at 1000K while the other black walls are kept at 0K. The cold (0K) medium absorbs and scatters energy isotropically with an absorption coefficient of $1m^{-1}$. The domain is spatially discretized into 40 x 40 number of cells. Conventional and icosahedral spherical discretization have been used. It is evident from the figure 4(right) that conventional type of angular discretization is unable to produce the correct solution whereas solution by icosahedral discretization with recursion level 3 and afvDOM produces comparable result with Chai et al.[7].

A small difference is observed at the curved section of geometry which may be due to adoption of different solution approach i.e. block-off method by Chai et al.[7]. The icosphere with recusrion level 2 is unable to predict the correct wall heat flux received from curvature zone of lower wall.

## 5. SUMMARY

The summary of the above work are as follows

(i) 3-D radiative solver is used to solve RTE with radiative symmetric boundary condition in the third direction.

(ii) Icosahedral geometry for spherical discretization is tested for variety of 2-D radiation cases.

(iii) The results by icosahedral discretization with recursion level 3 are in comparison to the published results.

(iv) Icosphere with recursion level 2 is unable to produce correct result.

(v) Icosphere geometry result for discretization of spherical space is preferred because it can be generated independently to any coordinate system.

## ACKNOWLEDGEMENT

The authors would like to greatly acknowledge the financial support provided by Science and Engineering Research Board (SERB) (Statutory Body of the Government of India) via grant no ECR/2015/000327 to perform the present work.

## REFERENCES

[1] Mangani, L., "Development and Validation of an Object Oriented CFD Solver for Heat Transfer and Combustion Modeling in Turbomachinery Applications", Ph.D. thesis, UniversitÃă degli Studi di Firenze, Firenze, 2009.

[2] Modest, M.F., Radiative Heat Transfer, Academic Press, San Diego, 2nd edition, 2003.

[3] Siegel, R. and Howell, J.R., Thermal Radiation Heat Transfer, Hemisphere Publishing Corporation, Washington, 3rd edition, 1992.

[4] Pradeep Kumar, "Radiative heat transfer in a participating gray medium and its interaction with fluid flow", Ph.D. thesis, Department of Mechanical Engineering, Indian Institute of Technology Kanpur, 2009.

[5] Raithby G.D. and Chui E.H., "A finite-volume method for predicting a radiant heat transfer in enclosures with participating media", Trans. of the ASME, Journal of Heat Transfer, vol. 112, pp. 415-423, 1990.

[6] Chai J.C., Lee H.S. and Patankar S.V., "Finite volume method for radiation heat transfer", Journal of Thermophysics and Heat Transfer, vol. 8, pp. 419-425, 1994.

[7] Chai J.C., Parthsarthy G., Lee H.S. and Patankar S.V., "Finite volume radiative heat transfer procedure for irregular geometries", Journal of Thermophysics and Heat Transfer, vol. 9(3), pp. 410-415, 1995.

[8] P. Kumar and V. Eswaran, "A Methodology to Solve 2-D and Axisymmetric Radiative Transfer Problems using a General 3-D Solver", Trans. of ASME, Journal of Heat Transfer, vol. 135, pp. 124501-124503, 2013.

Fifth International Conference on Computational Methods for Thermal Problems
THERMACOMP2018, July 9-11, 2018, Indian Institute of Science, Bangalore, INDIA
*N. Massarotti, P. Nithiarasu, Pradip Dutta and C. Ranganyakalu (Eds.)*

# Using Computational Fluid Dynamics for optimizing various configuration of tray driers

**A K Babu, V.Antony Aroul Raj**

Easwari Engineering College, Bharathi Salai, Ramapuram, Chennai 600 089, Tamilnadu, India
ayya_krish_babu@yahoo.com, antonyaroulraj@gmail.com

**G.Kumaresan, R. Velraj**

Institute for Energy Studies, Anna University, Sardar Patel Road, Chennai 600 025, Tamilnadu, India
gkumaresan@annauniv.edu, rvelraj@annauniv.edu

## ABSTRACT

Tray dryers are most suitable dryers for drying leaves. It is desirable to obtain better air distribution for uniform drying in a drier design. Also reduction of pressure drop and increasing the mass transfer rate becomes objective of any mass exchanger. For obtaining this objective in the drier design, Computational fluid dynamics can be used as a tool for designing and testing various configurations of drier theoretically For these objectives, in this work four different geometries of tray dryer for drying Moringa Oleifera were conceived and evaluated theoretically for their performance by using ANSYS FLUENT software. The pressure drop and output of various configurations are checked, evaluated and presented in this work. The best configuration having reduced pressure drop, improved mass transfer and drying efficiency, uniform air flow and uniform temperature distribution is also highlighted. This generalized CFD procedure can be used for checking the performance of any mass exchanger theoretically.

**Key Words:** *Tray dryer; Moringa Oleifera; CFD; Mass exchanger*

## 1. INTRODUCTION

Among the forced convection drying methods, tray dryers are the most suitable dryer used for leaves drying. These dryers are easy to fabricate, and cost effective. Non-uniformity in the moisture content of the end product is an inherent drawback in applying the tray dryer [1]. In the conventional tray dryers, hot and dry air is usually introduced above the first tray (top tray) and passes through the other trays normally. Therefore leaves located on the top trays would receive the maximum possible energy and could be over dried, while the bottom trays may not receive enough energy to be dried due to increase in drying air relative humidity and decrease is air velocity and temperature. Moisture removal rate shows a very strong relationship with drying air temperature, velocity and depth of the tray [2, 3].

Controlling all of these parameters experimentally is very tedious and difficult. Although computational fluid dynamics (CFD) technique cannot replace physical experiments completely but it can significantly reduce the amount of time needed for experimental works [4]. Accuracy of prediction can be strongly improved by including some pertinent physical properties of leaves such as porosity, air flow resistance, and density of moisture in the study. The main objectives of this research were, to investigate the effect of four different geometries of tray dryer on dryer performance for leaves drying and to compare the proposed designs by CFD and to select the best design for having reduced pressure drop, improved mass transfer and drying efficiency, uniform air flow and uniform temperature distribution throughout the dryer. The dryer tested in this work finds application in transit drying. The leaves can be dried during the transportation using waste heat released from transit vehicle.

## 2. CFD ANALYSIS

In conventional tray dryer the hot dry air is completely introduced at the bottom or top of the drying chamber. The drying potential of the hot dry air is gradually diminished as it passes through the upper or bottom trays. In order to reduce the issue of non-uniformity in the air flow distribution in configuration (a), a new design of tray dryer (Configuration b) was introduced. In this design fresh drying air was introduced both to upper and bottom trays to keep the air drying potential high and uniformly distributed within the trays. It is believed that this design change would result in more even air flow distribution and more uniform moisture removal from all the trays simultaneously in the tray dryer.

### (i) Tray configurations

In order to find the most appropriate geometrical shape of tray dryer for achieving more uniform distribution of drying air flow inside the dryer, different designs were analyzed using CFD software. It is obvious that the geometry of drying chamber (air inlet size, distance between the trays, depth of tray, area of the tray) would affect the air flow pattern and moisture removal rate in the drying chamber. Some other important dimensions of dryer could be: air exit size and its location, distance of trays from dryer ceiling. Information about different designs is summarized in Fig.1 and Table.1. Depth of drying chambers is constant and equal to 1 m in all cases.

### (ii) Solver parameters and Simulation

Modelling and analysis of the tray drier is done using ANSYS FLUENT software. The mass, momentum and energy conservation result in the continuity equation, Navier–Stokes equation and energy equation, respectively (Norton and Sun, 2006). The standard k-ε model is a semi-empirical model based on model transport equations for the turbulent kinetic energy (k) and its dissipation rate (ε). To solve the governing equations, initial and boundary condition must be defined around the boundary of the system domain). Since the equations are highly non-linear, they are not solvable by explicit, closed-form analytical methods. The numerical finite volume method as used in ANSYS FLUENT has been used for solving the equations on a PC P i5 3.20 GHz with 8.0 GB RAM. All the geometrical configurations were displayed in Fig.1. They were used to build up a numerical model based on structured three-dimensional mesh by hexahedral cell.

**Table 1**
Geometrical parameters and dimensions of the dryers investigated.

| Geometrical parameters | Design 1 | Design 2 | Design 3 | Design 4 |
|---|---|---|---|---|
| Air inlet size (m) | 0.2 | 0.2 | 0.2 | 0.2 |
| Air outlet size (m) | 0.2 | 0.4 | 0.4 | 0.4 |
| Location of outlet | Bottom | Middle | Middle | Middle |
| Distance of tray from dryer ceiling (m) | 0.2 | 0.2 | 0.2 | 0.2 |

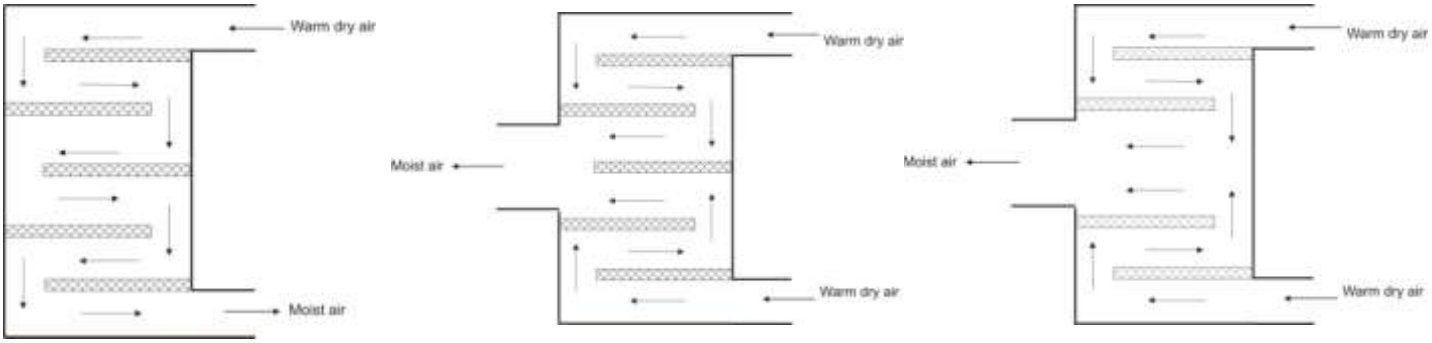


**(a)** **(b)** **(c)**

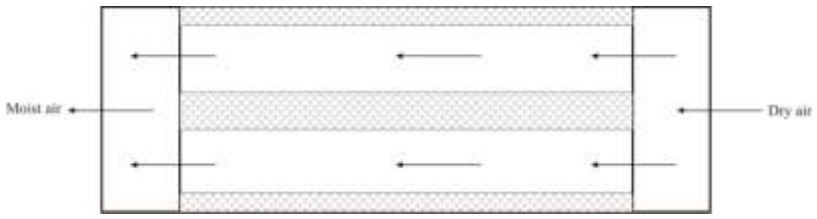


**(d)**

**Fig. 1 Various configurations of tray dryer investigated**

In this study various boundary conditions were defined as following:

- Inlet: inlet velocity of 0.2 m/s and air temperature of 40°C, specific humidity Species fraction, 0.0108 kg/kg of dryer (RH 24.33 % ) were selected. Direction of air flow was normal to the air inlet.
- Outlet: assuming gauge pressure = 0 at the outlet, Fluent extrapolated the required information from the interior of drying chamber.
- Porous media: empirical parameters of pressure drop equation and leaves tray porosity were defined.

To decide about the suitability of the design of the new cabinet dryer, CFD analysis of four proposed plans were carried out. The most feasible design can be assessed by comparing the uniformity of air flow distribution in the drying chamber as done by many other researchers (Amanlou et al., 2010). On the tray dryer design, the configuration shown in the Fig.1 is taken for CFD analysis where the trays are arranged in series and the air flows at taking 180º turn after every tray. The configuration (a) is modelled using pre-processor software as two distinct zones fluid and leaves tray. The moisture generated from the leaves is modeled using user defined function in the source term of the leaf tray domain. The air passing over the tray absorbs the moisture generated from the leaves and exit moisture content increases. Since the moisture generation is a transient process the simulation was carried out by implicit time marching. The exit moisture content is tracked at varying time interval and presented.

For having a common flow and geometric condition, the inlet condition is same for all configurations and volume of leaves tray is same for all configurations. Pressure drop (difference in pressure at inlet and outlet of mass exchanger) was calculated for all configurations. The velocity and pressure plots for the configuration (a) are shown in Fig. 2. Due to turnings in the flow it is observed that the pressure drop in configuration (a) is higher. The mass transfer is tracked for a total time of 100 sec with 20 sec time interval. It can be clearly seen that the mass transfer in the first tray is more compared to the subsequent trays. The mass transfer in the last tray is the least due to smaller concentration gradient between the tray and the air. From this analysis it can be concluded that if the trays are aligned in series the mass transfer rate decreases along the flow path. Drying process will be completed in tray 1 and 2 much before the last trays but the operator has to wait till the last tray gets dried which will be time consuming. Hence it is desirable to have lesser number of trays along the flow path. For this objective configuration (b) was suggested where there are two inlets and single outlet and only trays are the along the flow path conserving the mass. The exit opening is doubled.

For the configuration (b) the pressure drop is reduced compared to previous configuration as the flow path is divided into two. The mass transfer rate is tracked for a period of 100 sec with 20 sec time interval. It is observed that the mass transfer is better in the second configuration but after a long interval of time, the moisture gets released by tray 1 and 2 decreases the mass transfer in tray 3.

Hence it was decided to remove the tray for obtaining uniform drying time and that becomes configuration (c). The pressure drop is reduced compared to configuration (a) and (b). The results of transient mass transfer plots indicate that mass transfer is uniform for this configuration (Fig 3)

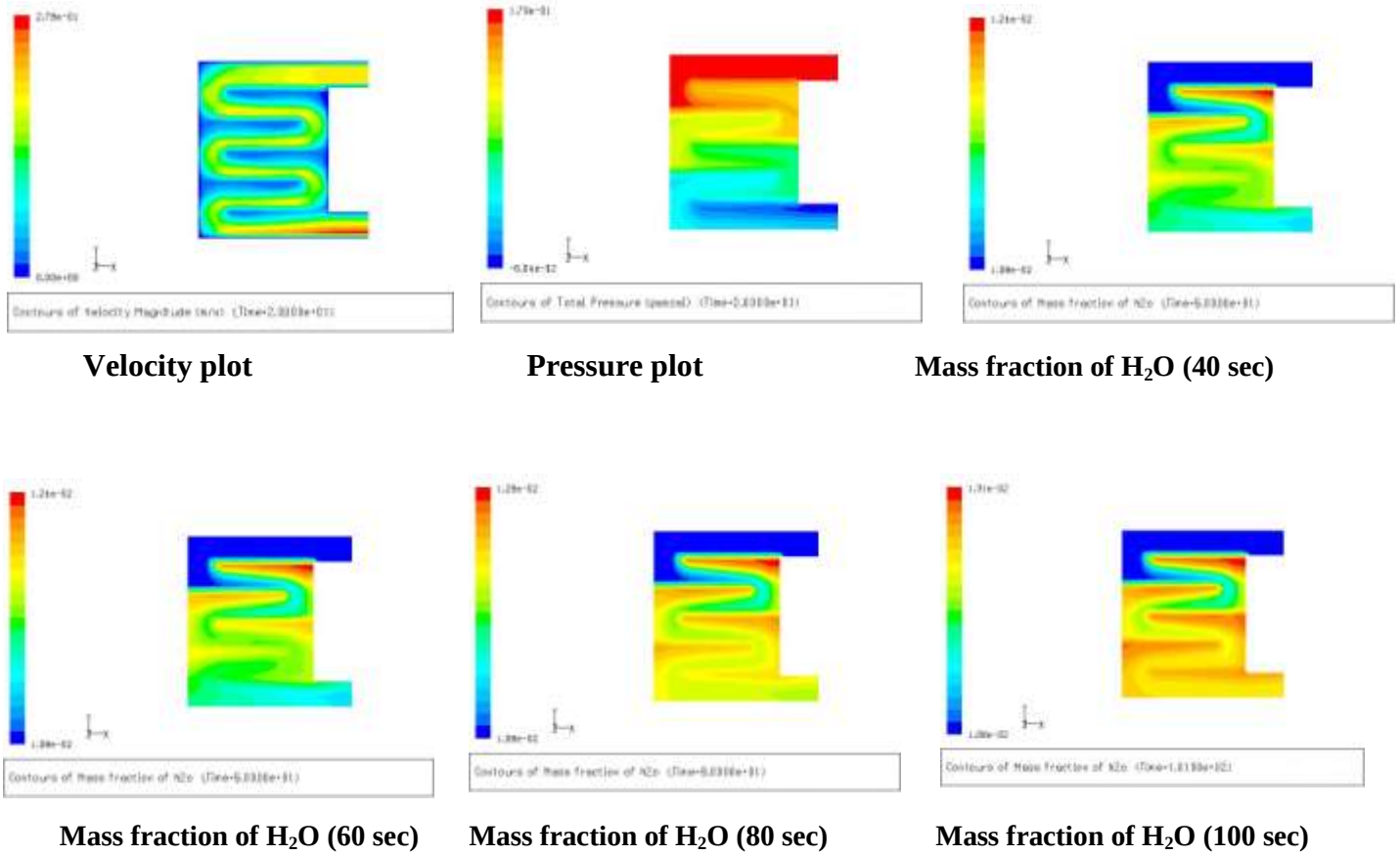

**Velocity plot** **Pressure plot** **Mass fraction of $H_2O$ (40 sec)**

**Mass fraction of $H_2O$ (60 sec)** **Mass fraction of $H_2O$ (80 sec)** **Mass fraction of $H_2O$ (100 sec)**

**Fig 2. Configuration.(a) simulation results**

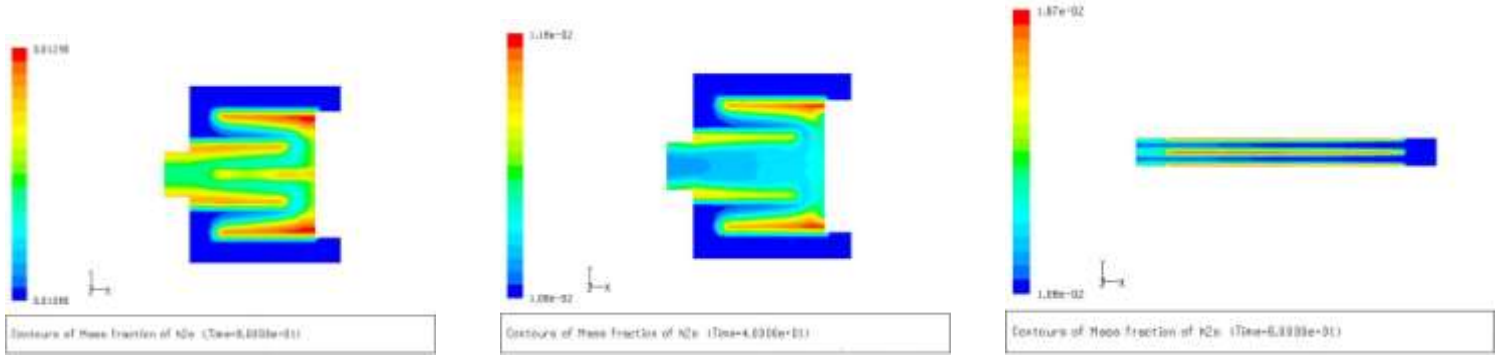

**(b)** **(c)** **(d)**

**Fig. 3. Mass fraction of $H_2O$ (40 sec) for configuration (b), (c) & (d)**

Further it was decided to reduce the pressure drop as well as the flow rate for reducing the capacity of fan used in mass exchanger. For this purpose instead of turning the flow by 180º it was decided to place the trays in series giving configuration (d) where the flow volume is maintained same as configuration (a). The pressure drop is made the least by having straight flow condition. It is found that the mass transfer is more for configuration (d) with lesser pressure drop (Table 2). Hence it is decided to go for this configuration of mass exchanger for transit drying. This methodology can be used as a generalized procedure for testing the performance of tray dryer using CFD.

Table 2 Pressure drop and mass transfer

| | Configuration.(a) | Configuration.(b) | Configuration.(c) | Configuration.(d) |
|---|---|---|---|---|
| Pressure Drop (Δp), Pa | 0.21835 | 0.06712 | 0.06202 | 0.02056 |
| Moisture Removed, kg/s | $2.4991\times10^{-3}$ | $4.3836\times10^{-3}$ | $4.3473\times10^{-3}$ | $3.4566\times10^{-3}$ |

## 4. CONCLUSIONS

- Computational fluid dynamics (CFD) is a very powerful tool for parametric study and optimisation of tray dryer analysis for leaves drying.
- The simulation results of the four different designs of the new cabinet drying chamber were compared with each other and the best design with minimum pressure drop, maximum mass transfer, the most uniform air temperature and air flow distribution for the drying chamber was chosen.
- The trays in series improved dryer's performance. Minimum pressure drop and maximum moisture removal were observed with configuration (d). Hence, configuration (d) will be the best configuration for drying of leaves. Also uniform air temperature and velocity distributions are obtained in this configuration.

## REFERENCES

[1] Xiangyang Lin, Lijing Zhang, Hanwu Lei, Hong Zhang, Yanling Cheng, Rongbi Zhu, and Roger Ruan, Effect of drying technologies on quality of green tea, *International Agricultural Engineering Journal*, Vol.19, No.3, (2010).
[2] Guohua Chen, and Arun S. Mujumdar, Drying of herbal medicines and tea. *Handbook of solar drying*, Taylor & Francis Group, (2006).
[3] S.R. Navale, Upasni Supriya, V.M. Harpale, and K.C. Mohite, Effect of solar drying on the nutritive value of Fenugreek leaves, *International Journal of Engineering and Advanced Technology*, Volume-4, issue-2, (2014).
[4] Armelle de Saint Sauveur, Melanie Broin, Growing and processing moringa leaves, *Moringa news/Moringa Association of Ghana*, (2010).
[5] Donald G.Mercer, *A Basic guide to drying fruits and vegetables*, University of Guelph, (2012).
[6] Y. Amanlou, A. Zomorodian, Applying CFD for designing a new fruit cabinet dryer, Journal of Food Engineering 101, 8-15, (2010).
[7] A. Mulet, A. Berna, M. Borras, F. Pinaga, Effect of air flow rate on carrot drying, *Drying technology*, 5(2), (1987) 245-258.
[8] V.T. Karathanos, V.G. Belessiotis, Sun and artificial air drying kinetics of some agricultural products, *Journal of Food Engineering*, 31(1), (1997) 35-46.
[9] J.D. Anderson, *Computational Fluid Dynamics*, International Edition, McGraw-Hill, New York, (1995).
[10] P.S. Mirade, Prediction of the air velocity field in modern meat dryers using unsteady computational fluid dynamics (CFD) models, *Journal of Food Engineering*, 60, (2003) 41-48.
[11] Suhaimi Misha, Sohif Mat, Mohd Hafidz Ruslan, Kamaruzzaman Sopian, and Elias Salleh, The Prediction of Drying Uniformity in Tray Dryer System using CFD Simulation, *International Journal of Machine Learning and Computing*, Vol.3, No.5, (2013).
[12] E. Mathioulakis, V.T. Karathanos, V.G. Belessiotis, Simulation of air movement in a dryer by computational fluid dynamics: Application for the drying of fruits, *Journal of Food Engineering*, 36, (1998) 183-200.
[13] Donald G.Mercer, "A Basic guide to drying fruits and vegetables", University of Guelph, 2012.
[14] Y. Amanlou, A. Zomorodian, "Applying CFD for designing a new fruit cabinet dryer", Journal of Food Engineering, 101, 8-15, 2010.
[15] A. Mulet, A. Berna, M. Borras, F. Pinaga, "Effect of air flow rate on carrot drying", 5(2), 245-258, 1987.
P.S. Mirade, "Prediction of the air velocity field in modern meat dryers using unsteady computational fluid dynamics (CFD) models", Journal of Food Engineering, 60, 41-48, 2003.

Fifth International Conference on Computational Methods for Thermal Problems
THERMACOMP2018, July 9-11, 2018, Indian Institute of Science, Bangalore, INDIA
*N. Massarotti, P. Nithiarasu, Pradip Dutta and C. Ranganyakalu (Eds.)*

# Electrothermally Actuated Non-Newtonian Binary Fluid Flow Through Microchannel

**Antriksha Vishwakarma**,

Department of Aerospace Engineering, Amrita University, Coimbatore, Tamil Nadu- 641112,
antrikshv96@gmail.com

**Golak Kunti, Suman Chakraborty**

Department of Mechanical Engineering, Indian Institute of Technology Kharagpur, Kharagpur, West Bengal - 721302, India, golakme@gmail.com, suman@mech.iitkgp.ernet.in

## ABSTRACT

We present our work on transporting Newtonian and non-Newtonian binary fluid system through a microgrooved channel by the application of alternating current electrothermal (ACET) forces. One fluid is taken as conducting layer (bottom) and the other fluid is taken as a non-conducting layer (top). The conducting fluid flows due to application of the ACET forces whereas the non-conducting fluid flows due to shear force across the interface. An order parameter based approach was used to track the interface of the two-layer fluid system via Cahn-Hilliard-Navier-Stokes equation. The effectiveness by which the non-conducting fluid gets transported and the necessary conditions which produce maximum throughput were investigated. It is found that higher effectiveness is achieved for non-conducting layer as shear thickening fluid. Highest flow velocities are obtained when the conducting fluids are shear thinning. With the increase in ACET force number and Joule number velocity of the fluids increases. However, the highest velocity was obtained when the conducting fluids are shear thinning.

**Keywords***: Electrothermal, Binary fluid, shear thinning*

## 1. INTRODUCTION

In many biomedical practices, it is required to study the behavior of two immiscible layers of fluid, in which one would be conducting and the other non-conducting. A way to actuate such flows for biomedical applications is through AC Electrothermal forces.

When an AC field is applied across electrodes it results in Joule heating which manifests itself in an inhomogeneous temperature field, this causes local variation of electrical permittivity and electrical conductivity [1]. This produces local charge densities which tend to move due to Coulomb force, thereby helping in exerting a non-zero volume force on the fluid [2]. If there is a binary fluid system with the bottom one being conducting and the top one being non conducting, the movement of the lower fluid generates a shear stress for the upper fluid across the interface. Thus both conducting and non-conducting fluids are transported.

## 2. NUMERICAL MODELLING

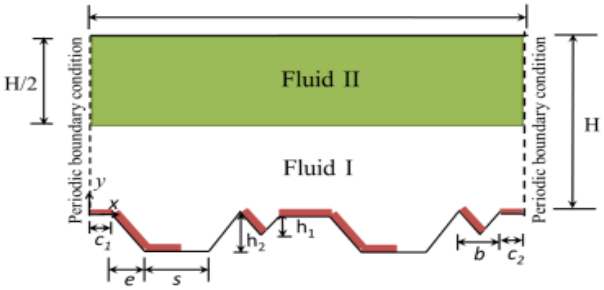


FIGURE 1.Schematic representation of the system. On the floor, electrodes are marked to show their relative position with respect to the wall.

The system analyzed is represented above, it consists of two layers of immiscible fluids confined in a micro-

grooved channel. The y-axis runs along the height of the channel ( $H$ ) and the x-axis runs along the length of the channel ($1.4H$ ). The length scales labeled in the figure have the following values $b = 0.12\ H, c_1 = c_2 = 0.07\ H$, e $= 0.11\ H$, $s = 0.22H$, $h_1 = 0.08\ H$ and $h_2 = 0.15\ H$. Here $h_1$represents the depth of V groove and $h_2$ represents the depth of U groove.

The conducting fluid is referred as fluid I, its properties having the subscript 1 and non-conducting fluid is referred to as fluid II, its properties having the subscript 2. An AC field is applied externally to the thin film electrodes. To simulate conducting and non-conducting fluid we have considered the electrical conductivity of fluid II to be 1/10th of that of fluid I. Moreover we have also ensured that there is no penetration of electric field lines across the interface from fluid I to fluid II, this ascertains the fact that the non-conducting fluid is pumped only via shear forces. We have considered two cases involving two layer binary fluid system: Case 1 in which the conducting fluid is non-Newtonian, whereas the non-conducting fluid is Newtonian and Case 2 in which the conducting fluid is Newtonian and non–conducting fluid is non-Newtonian.

**The phase field formation**

In phase field formulation we would first define an order parameter $\phi$. In the present study $\phi$ is based on diffuse interface framework. The Ginzburg-Landau free energy expression in accordance with the above definition of order parameter for a two layer fluid system is[3]:

$$F = \int_{\forall} \left\{ f(\phi) + \frac{1}{2}\eta\xi|\nabla\phi|^2 \right\} d\forall, \qquad (1)$$

The order parameter $\phi$ is governed by the Cahn Hilliard equation which can be found in Ref. [3]

**Potential and Thermal distribution**

According to the phase field model, the electrical permittivity ($\varepsilon$) and electrical conductivity ($\sigma$) with linear variation in temperature for both fluids can be expressed as in Ref.[4]. Time averaged electro-thermal force $\mathbf{F_E}$ can be written as [1, 2, 5]

$$\mathbf{F_E} = -\frac{1}{2}\left[ \left( \frac{\nabla\sigma}{\sigma} - \frac{\nabla\varepsilon}{\varepsilon} \right) \cdot \mathbf{E} \frac{\varepsilon\mathbf{E}}{1+(\omega\tau)^2} + \frac{1}{2}|\mathbf{E}|^2 \nabla\varepsilon \right]. \quad (2)$$

**Non-dimensionalization**

We have performed our simulation with the help of non dimensionalized governing equations where dimensionless parameters are:

$$u^* = \frac{u}{u_0}, v^* = \frac{v}{u_0}, x^* = \frac{x}{H}, y^* = \frac{y}{H}, t^* = \frac{tu_0}{H}, \theta = \frac{T - T_0}{\Delta T}, \varphi = \frac{\varphi}{\varphi_0}, \rho^* = \frac{\rho}{\rho_0}$$

$$\mu^* = \frac{\mu}{\mu_0}, C_p^* = \frac{C_p}{C_{p0}}, k^* = \frac{k}{k_0}, \varepsilon^* = \frac{\varepsilon}{\varepsilon_0}, \sigma^* = \frac{\sigma}{\sigma_0}, p^* = \frac{pH}{\mu u_0}, \lambda^* = \frac{\lambda}{\eta / H}$$

Where $H$ represents the reference height of the channel, $u_0$ is the reference velocity, ΔT is the difference of maximum temperature in the domain and the reference temperature. All reference properties are denoted with a subscript "0".

**Model Benchmarking**

The numerical methodology was compared with the result of two layer fluid system given in Ref. [6]. We have further benchmarked the phase field model used in our studies with Gao et al. [6] . Benchmarked results show a good agreement with those of Gao et al. [6] .

## 3. RESULTS & DISCUSSIONS

**Effect of Power law index( $n$ )**

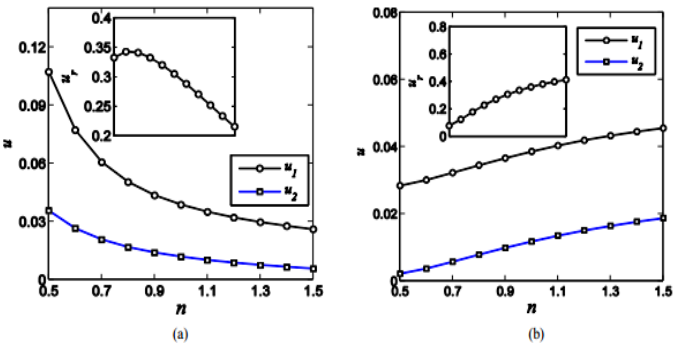


FIGURE 2.(a) represents the variation of velocity with change in flow behavior index ($n$) in case 1.(b) depicts

variation of velocity with change in flow behavior index ($n$) in case 2. Inset figures represent effectiveness.

It is known from power law that if we increase flow behavior index for the same electric potential the velocity would decrease. This is seen in case 1 for the velocities of conducting non-Newtonian fluid. The increase in flow behavior index also increases the effective shear rate; it becomes difficult to move the conducting fluid, which results in a decrease in effectiveness.

In case 2 with increase in flow behavior index in non-Newtonian top layer fluid there is an increase in shear rate. For a Newtonian fluid, the power law takes the form of Newton's law of viscosity. The flow behavior index of a Newtonian fluid is constant. So it transfers the same shear force through the interface across all the values of $n$. This implies that it progressively becomes difficult for the shear force to move the non-Newtonian fluid which is becoming from shear thinning to shear thickening.

A net increase in velocities is observed in case 2 for conducting Newtonian fluid, as there is less resistance from the non-Newtonian to the Newtonian fluid, but this resistance increases as the fluid become more and more shear thickening thereby decreasing the velocity of the bottom layer fluid. $u_2$ of both cases is less than its respective $u_1$ because ACET force gets concentrated near the electrodes where there is a high electric field. This results in higher velocity increase for the conducting fluid. The non-conducting layer gets only the momentum exchange across the interface hence its velocity does not increase as much as the bottom layer fluid. The maximum velocity of case 1 is higher than that of case 2.This can be attributed to the fact that with an increase in effective viscosity in shear thinning fluids the rate of shear deformation decreases whereas when the fluid becomes shear thickening its shear rate increases.

**Effect of ACET number ( ζ )**

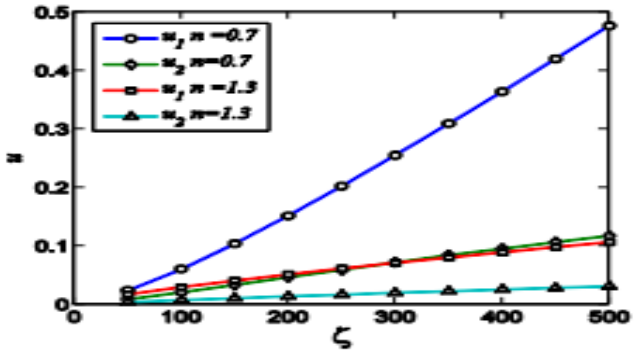


FIGURE 3.(a) represents the variation of velocity with ACET force number (ζ) in case 1.

In case 1 the conducting fluid is non-Newtonian which implies as we increase ACET number the shear rate increases, which means that it requires less force to undergo shear deformation for $n$ = 0.7 (n refers to power law index). It progressively becomes easier to move $n$ = 0.7 fluid with increasing ACET force as it is a shear thinning fluid, leading to a very high increase in its velocities. In this situation no matter how much force we apply, only negligible amount of it is able to transfer across the interface. This is because the conducting fluid is getting sheared so quickly that it is not able to transfer its momentum across the interface. This leads to a low non-conducting fluid velocity. For $n$ = 1.3 it progressively becomes more difficult to flow with increasing ACET force as it is a shear thickening fluid, leading to low velocities. As it is not flowing very rapidly it has enough time to transfer momentum across the interface more effectively. This leads to a less disparate velocities for $u_2$ when compared with $n$ = 0.7

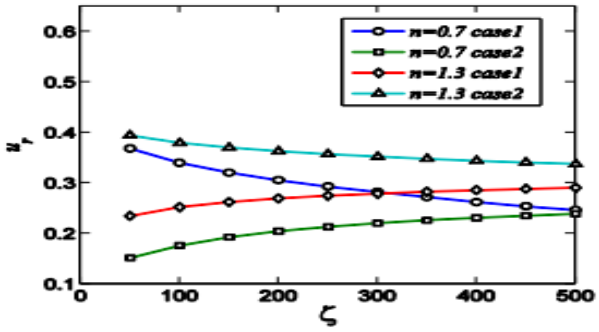


FIGURE 3.(b) ζ vs effectiveness for both cases $n$ = 1.3 case 1 and case 2 and $n$ = 0.7 case 1 and case 2. The

difference between the two velocities keeps on increasing leading to saturation point in this graph.

With the increase in ACET number, the effectiveness of $n$ = 0.7 case 1 reduces whereas that for $n$ = 1.3 case 1 increases. For 0.7 the velocity of conducting fluid was far higher than the velocity of non-conducting fluid due to the ineffective transfer of momentum. This leads to decrease in effectiveness. For 1.3 the velocity of the non-conducting fluid is comparatively much closer to the velocity of conducting fluid. This leads to an increase in effectiveness.

**Effect of Joule Number ( $J$ )**

The relation between non-dimensional number $J$ with dimensional terms is defined as the rate at which heat is produced to the rate at which heat is being conducted across the fluid domain. The velocities of both layers increase with an increase in Joule number. This happens because Joule heating produces steeper temperature gradient which is responsible for generating ACET forces. ACET forces are directly responsible for increasing the velocity of the flow.

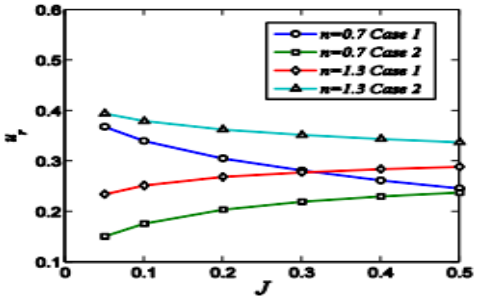


FIGURE 4. shows the effectiveness of velocity with respect to Joule number for $n$ = 0.7 case 1, $n$ = 0.7 case 2, $n$ = 1.3 case 1 and $n$ = 1.3 case 2. All the four curves approach saturation point because the disparity between the velocities keeps on increasing.

The effectiveness of $n$ = 0.7 decreases whereas for $n$ = 1.3 it increases. This happens because of the ineffectiveness in transferring momentum by a shear thinning fluid as compared to the shear thickening fluid, origins of which is the same as stated in the previous paragraphs regarding ACET forces. The shear thickening fluid has a better ability to transfer shear force amongst its layer as compared to shear thinning fluid although some individual layers of shear thinning fluid would have higher velocity.

## 4. CONCLUSION

In this paper, we have come across various ways in which we can improve the flow of binary fluid systems in a micro-channel using AC electrothermal forces. These systems reveal that treating the non-conducting fluid as non-Newtonian has better effectiveness for a shear thickening fluid. Various non-dimensional parameters were studied to reveal the exact conditions required for maximum throughput of these fluid systems through a micro channel. It was found that flow rate depends also on the viscous forces. The flow rate increases with increase in electrothermal forces or rate of heat generation. We believe that the inferences drawn from this paper would contribute in designing efficient ACET hybrid pumps which deal with Newtonian and non-Newtonian binary fluid systems in the field of biotechnology.

## REFERENCES

[1] S. J. Williams, and N.G. Green, Electrothermal pumping with interdigitated electrodes and resistive heaters. *Electrophoresis* 36, 1681–1689, 2015.

[2] E. Du and S. Manoochehri, Enhanced ac electrothermal fluidic pumping in microgrooved channels. *J. Appl. Phys.* 104, 64902, 2008.

[3] D. Jacqmin, Calculation of Two-Phase Navier–Stokes Flows Using Phase-Field Modeling. *J. Comput. Phys.* 155, 96–127, 1999.

[4] G. Kunti, A. Bhattacharya and S. Chakraborty, Alternating current electrothermal modulated moving contact line dynamics of immiscible binary fluids over patterned surfaces. *Soft Matter* 13, 6377–6389, 2017.

[5] H. Morgan and N. G. Green, *AC Electrokinetics: Colloids and Nanoparticles*. Research Studies Press, 2003.

[6] C. Wang *et al.* Interface control of pressure-driven two-fluid flow in microchannels using electroosmosis. *J. Micromechanics Microengineering* 15, 2289–2297, 2005.

Fifth International Conference on Computational Methods for Thermal Problems
THERMACOMP2018, July 9-11, 2018, Indian Institute of Science, Bangalore, INDIA
*N. Massarotti, P. Nithiarasu, Pradip Dutta and C. Ranganyakalu (Eds.)*

# Numerical study of Inclined Air jet impingement cooling of a cylinder

**Anuj Kumar**
M.Tech Scholar
Department of Mechanical Engineering
National Institute of Technology Manipur, India
Email: anujchauhan1793@gmail.com

**Dr. Dushyant Singh**
Assistant Professor
Department of Mechanical Engineering
National Institute of Technology Manipur, India
Email: dushyant@nitmanipur.ac.in

## ABSTRACT
In this present study, numerical analysis of inclined jet impingement was carried out on an isothermal cylinder. A steady state, incompressible, turbulence, three-dimensional model was analyzed with air as working fluid. The distance from nozzle exit to the surface of the heated cylinder is, 7.5 times of the jet diameter. The analysis was done with $Re_d$ = 38,000 using the RNG k-ε, Realizable k-ε, k- ω SST and $v^2$-$f$ turbulence models. The $Re_d$= 38000 was selected for simulation because experimental results are available only for $Re_d$= 38000. The local Nusselt number along with the axis and the circumference was compared with the experimental results of Tawfek [14]. RNG k-ε turbulence model predicted the nature of the local Nusselt number curve better than other turbulence models.

**Key Words:** *Inclined Air jet impingement, heat transfer, turbulence*

## 1. INTRODUCTION
Jet Impingement is a technique by which a large amount of heat can be transferred due to a high local heat transfer coefficient between the target surface and working fluid. At present, there are a lot of applications of jet impingement such as cooling of the workpiece in the manufacturing industry, turbine blades in the power plants and electronic components. There are many experiments conducted on jet impingement cooling on different impinging surfaces such as flat plate and curved surfaces by many researchers.
Jambunathan et al. [1], Hrycak [2], Livingood et al. [3] carried out many studies of the heat transfer along the axis and circumference of the cylinder and established the correlations of the local Nusselt number and average Nusselt number. Singh et al. [4], Mohanty et al. [5], Huang et al. [6], Katti et al. [7], and Baughn et al. [8] has conducted many experimental and numerical studies for the round air jet impingement over an impinging surface, maintained at constant heat flux. From all of these studies, it can be inferred that heat transfer rate in Jet Impingement depends on many factors such as the diameter of Jet, Reynolds number, the angle of impingement and distance between the nozzle and impinging surface.
Gori et al. [9] conducted experiments using the slot air jet impingement for cooling of the cylinder, for Reynolds number ($Re_S$) ranging from 4000 to 20000, were $Re_S$ was calculated based on the cylinder diameter. The diameter of impinging cylinder, D, and slot jet width, S, was 10 mm and 5 mm, respectively. They conducted studies for the different nozzle to surface spacing, h, in the range of 2 to 10. Based on the investigations, they have generated a correlation for local Nusselt Number as a function of impingement angle, h/S ratio, and Reynolds number.
Zuckerman et al. [10] investigated cooling of cylinder numerically, with a different number of slot jet nozzles, varying from 2 to 8, mounted circumferentially above the cylinder. The Reynolds number was ranging from 5000 to 80000 and the diameter of target cylinder was 5 to 10 times of nozzle hydraulic diameter. A correlation was developed between average Nusselt number, the ratio of the nozzle width to target diameter, number of nozzles, Reynolds number and Prandtl number.
Sparrow et al. [11] conducted experiments for cooling of cylinders with circular jet impingement for mass transfer using naphthalene sublimation technique. The range of Reynolds number was from 4000 to 25000 and Reynolds number was based on the diameter of the jet. They conducted various experiments for the different nozzle to surface spacing, h, varying from 5 to 15 times of jet diameter. They have found out relations of Sherwood number and Nusselt numbers based on the analogy of heat and mass transfer for stagnation point.
Singh et al. [12] investigated experimentally and numerically round jet impingement on circular cylinder maintained at constant heat flux. They have conducted experiments for a range of Reynolds number from

10000 to 25000, different nozzle to surface spacing, h, varying from 4 to 16 times of jet diameter and various nozzle diameter to cylinder diameter ratio, d/D, varying from 0.11 to 0.25. They concluded that while h/d ratio decreases, the Nusselt number at stagnation point increases, up to a certain value of d/D = 0.1 in the axial direction of the cylinder.

Tawfek [14] experimentally analyzed the round jet impingement normal to circular cylinder maintained at constant temperature condition. He conducted many experiments for a range of Reynolds number from 3800 to 40000 and different nozzle to surface spacing, h, varying from 7 to 30 times of jet diameter. He also varied the ratio of the nozzle to cylinder diameter (d/D) from 0.06 to 0.14. He concluded that while increasing the axial distance from stagnation point the heat transfer rate is decreasing. From the experimental data, he developed correlations between the average Nusselt number and maximum Nusselt number. Tawfek [13] conducted experiments varying the inclination angle of the nozzle 30 to 90° and other parameters were similar to Tawfek [14].

Although many types of research have been conducted on round jet impingement on cylindrical surfaces, analysis of inclined jet on a cylindrical surface is rare.

## 2. PROBLEM DESCRIPTION AND COMPUTATIONAL DOMAIN

In the present study, the jet diameter and the target cylinder diameter were 7 mm and 54 mm respectively. The inclination angle of air jet from the cylinder surface was taken as 90° and 75°. The nozzle to surface spacing (h) was 7.5d and $Re_d$= 38000. The $Re_d$= 38000 was selected for simulation because experimental results are available only for $Re_d$= 38000. The cylinder surface was maintained at 308 k. The computational domain of the problem is as shown in Fig. 1(a) and (b)

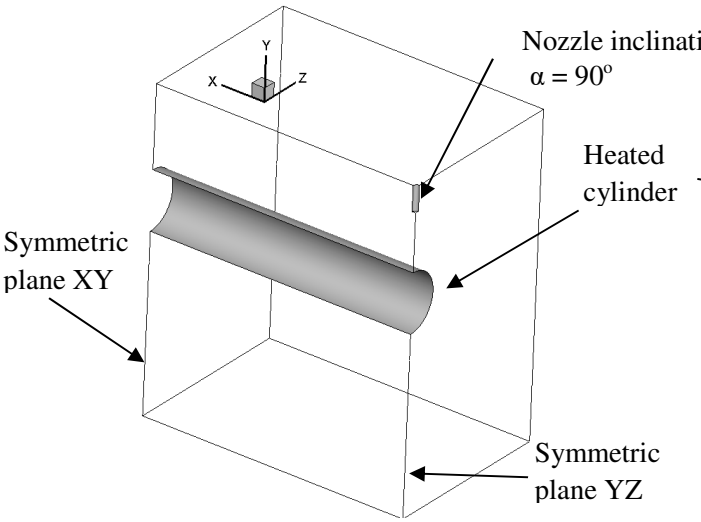


Figure 1(a) Perpendicular nozzle, α = 90°

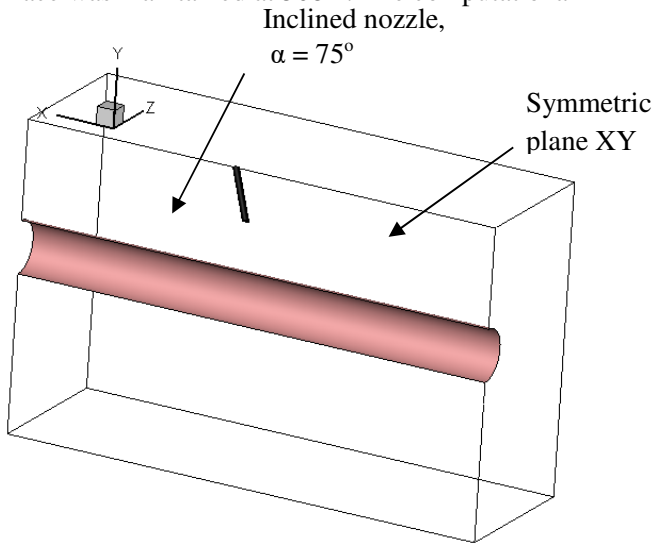


Figure 1(b) Inclined nozzle, α = 75°

The correlations of Reynolds number and Nusselt number used in the study are given as-

$$\mathrm{Re}_d = \frac{ud}{\nu} \text{ And } Nu = \frac{q''D}{(T_w - T_{jet})k_f}$$

## 3. MATHEMATICAL FORMULATION

In this present study, a three dimensional, incompressible, steady state and turbulent flow was considered. The flow was formulated with Reynolds time averaged continuity, momentum and energy equations, as follows.

$$\frac{\partial u_i}{\partial x_i} = 0$$

$$\rho u_j \frac{\partial u_i}{\partial x_j} = -\frac{\partial P}{\partial x_i} + \frac{\partial}{\partial x_j}\left[\mu\left(\frac{\partial u_i}{\partial x_j} + \frac{\partial u_j}{\partial x_i}\right) - \rho\overline{u_i' u_j'}\right]$$

$$\rho u_j \frac{\partial T}{\partial x_j} = \frac{\partial}{\partial x_j}\left[\frac{\mu}{\mathrm{Pr}}\frac{\partial T}{\partial x_j} - \rho\overline{T' u_j'}\right]$$

### 3.1 SOLUTION METHODOLOGY

Commercial software package ANSYS ICEM-CFD was used to create geometry, blocking and meshing while ANSYS Fluent software was used for solving the continuity, momentum, energy and turbulence equations. The turbulence models, RNG k-ε, Realizable k-ε, k-ω SST and $v^2$-$f$ were used in this analysis, in order to find out the best-suited turbulence model for this problem. To solve the pressure and velocity couplings SIMPLE algorithm was used. The boundary conditions are summarized in Table .1

**Table.1** Boundary Conditions

| Boundary Name | Inlet | Heated Cylinder | Symmetry | All Open Domains |
|---|---|---|---|---|
| Boundary Condition | Uniform velocity distribution at 300 k with 5 % turbulent intensity | Isothermally Heated Cylinder at 308 k with no Slip Condition at the cylinder | Symmetry | Pressure inlet and Pressure outlet boundary condition at 300 k |

### 3.2 GRID INDEPENDENCE STUDY

Grid Independence tests were carried out for both problems, at different nozzle inclinations. Four different grids for α = 90°, consists of 1.6 × $10^5$, 3.3 × $10^5$,6.2 × $10^5$, 10.7 × $10^5$ cells each and three different grids for α = 75°, consists of 3.6 × $10^5$, 6.2× $10^5$, 9.7× $10^5$ cells each. The grid independence test results for both cases are shown in fig. 2. For α = 90°, a grid with cells 6.2 × $10^5$ and for α = 75°, a grid with cells 6.2 × $10^5$ were selected for other simulations. The smallest mesh was not selected for other simulations because it is showing small fluctuation near the stagnation point in fig. 2(a).

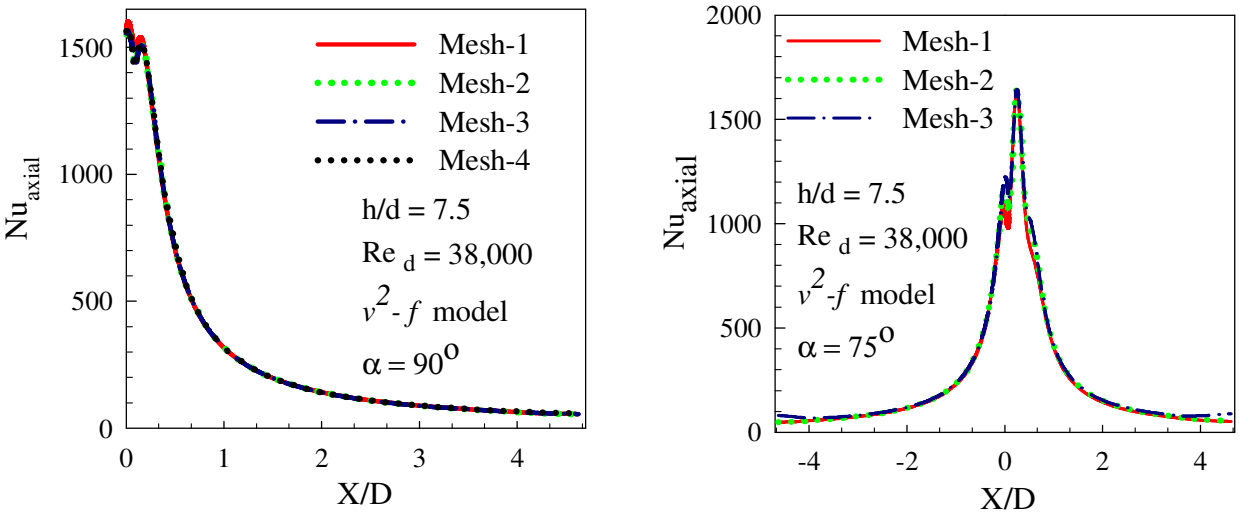


Figure 2 The local Nusselt number distribution along the axis of the heated cylinder (a) for α = 90° (b) for α = 75°

### 4. RESULTS AND DISCUSSIONS

In the present study, the numerical results of h/d = 7.5 for $Re_d$ = 38000 were verified with the experimental data [13] using different turbulence models. As shown in figure 3(a) k-ω SST turbulence model gives the

maximum local Nusselt number value ($Nu_X$ = 2029) at the stagnation point as compared to other turbulence models. The $v^2$-$f$ turbulence model predicts the lower stagnation point Nusselt number value ($Nu_X$ = 1555) than both RNG k-ε ($Nu_X$ = 1577) and Realizable k-ε ($Nu_X$ = 1635) turbulence models. The circumferential distribution of local Nusselt number is shown in fig.3 (b). The $v^2$-$f$ turbulence model shows a secondary peak near the stagnation point.

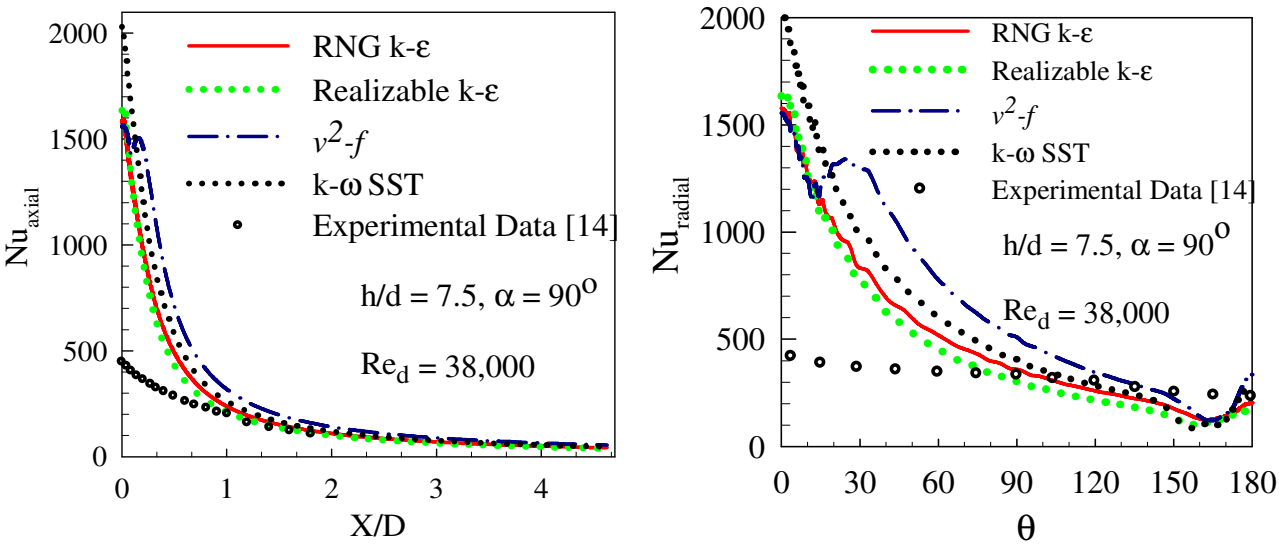


Figure 3 The local Nusselt number distribution along (a) the axis of the cylinder and (b) circumference of the heated cylinder at α = 90° respectively.

As shown in figure 4(a) the stagnation point obtained from the simulation results has shifted towards the forward side from the impinging point. Hence as the impinging angle of the jet reduces, the stagnation point shifts towards the forward side of the impingement point. The $v^2$-$f$ turbulence model predicts the result similar to both RNG k-ε and Realizable k-ε turbulence models. The variation of the Nusselt number along the circumference of the cylinder is as shown in figure 4(b).

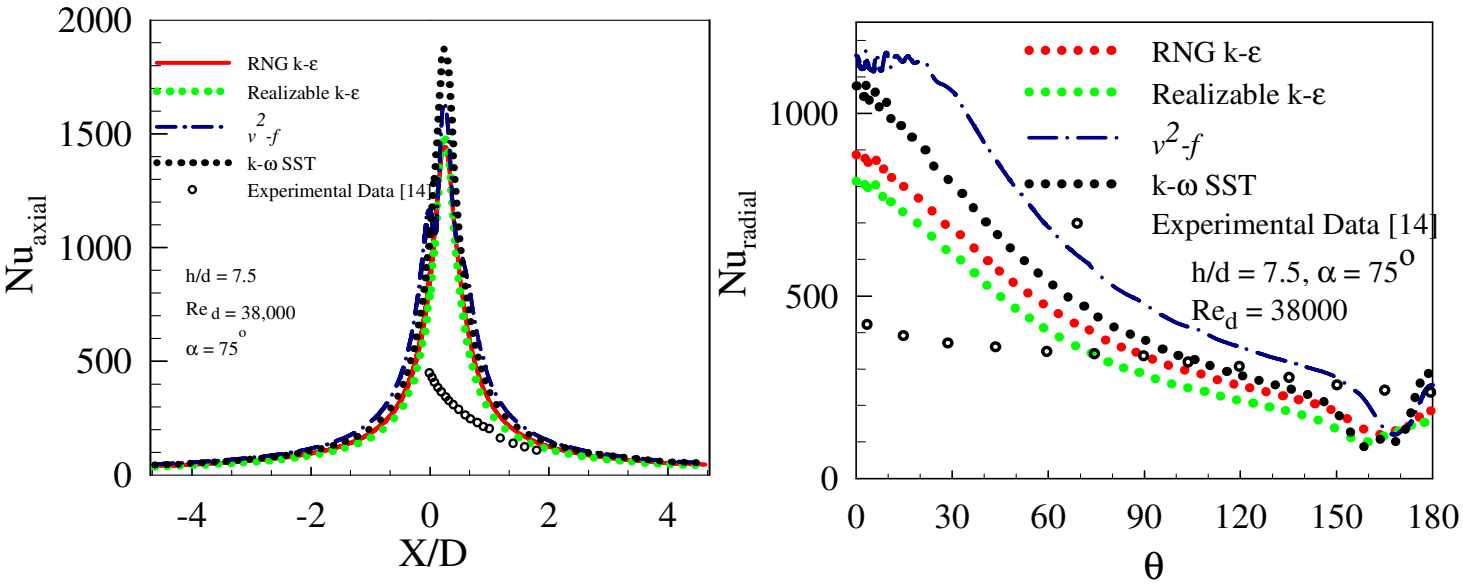


Figure 4 The local Nusselt number distribution along (a) the axis of the cylinder and (b) circumference of the heated cylinder at α = 75° respectively.

In the presented results the Nusselt number value at stagnation point is overpredicted by all turbulence models. For a jet impingement heat transfer, stagnation point Nusselt number is of primary interest. The % increase of the numerical stagnation Nusselt number is around 200 % from the experimental value. The same increase in the % deviation of the numerical stagnation Nusselt number from the experimental value is observed by Singh et al. [4]. The % increase of the predicted numerical stagnation Nusselt number from the experimental value is minimum for RNG k-ε turbulence model as compared to the other turbulence model. The distribution of the numerical local Nusselt number remains almost the same for all the turbulence models. Hence, the RNG k-ε model works very well as compared to the other turbulence models. It is also observed by Singh et al. [4] that the RNG k-ε turbulence model works better as compared to the other turbulence models for a round jet impingement on a circular cylinder.

## 5. CONCLUSION

In this study, the results achieved from the numerical study of different nozzle inclinations on the circular isothermally heated cylinder are presented. RNG k-ε turbulence model gives satisfactory results as compare to other turbulence models. In the inclined nozzle $\alpha = 75°$, the stagnation point was slightly moved far away from the impinging point compared to the stagnation point of the normally inclined nozzle.

## REFERENCES

[1] K. Jambunathan, E. Lai, M.A. Moss, B.L Button, A review of heat transfer data for single circular jet impingement, International Journal of Heat and Fluid Flow 13, 106-115 (1992).
[2] Hrycak, Heat transfer from impinging jets: A literature review, AFWAL-TR 81, 3054(1981).
[3] J.N.B. Livingood, P. Hrycak, Impingement heat transfer from turbulent ait jets to flat plates A literature survey, NASA TM X 2778(1973).
[4] Singh, D., Premachandran, B., and Kohli, S., Numerical simulation of the jet impingement cooling of a circular cylinder. Numerical heat transfer, Part A: Applications: An international journal of computation and methodology 64(2), pp. 153-185 (2013).
[5] Mohanty, A. K., and Tawfek, A., Heat transfer due to a round jet impingement normal to a flat surface, International Journal of Heat and Mass Transfer 36(6), pp. 1639-1647 (1992).
[6] Hung, L., and El-Genk, M., Heat Transfer of an impinging jet on a flat surface, International Journal of Heat and Mass Transfer 37(13), pp. 1915-1923 (1994).
[7] Katti, V., and Prabhu, S. V., Exponential study and theoretical analysis of local heat transfer distribution between the smooth flat surface and impinging air jet from a circular straight pipe nozzle, International Journal of Heat and Mass Transfer, 51(17-18), pp. 4480 - 4495 (2008).
[8] Baughn, J. W., and Shimizu, S., the Heat transfer measurement from a surface with uniform heat flux and an impinging jet, ASME Journal of Heat transfer 111(4), pp. 1096 - 1098 (1989).
[9] F. Gori, L. Bossi, On the cooling effect of an air jet along the surface of a cylinder, International Communication in Heat and Mass Transfer 27, 667-676 (2000).
[10] N. Zuckerman, N. Lior, Radial slot jet impingement flow and heat transfer on a cylindrical target, Journal of Thermophysics and Heat Transfer 21(3), 548-561 (2007).
[11] E. W. Sparrow, C.A.C. Altemani, A. Chaboki, Jet impingement heat transfer for a circular jet impinging in crossflow on a cylinder, ASME Journal of Heat Transfer 106, 570-577 (1984).
[12] D. Singh, B. Premachandran, S. Kohli, Experimental and numerical investigation of jet impingement cooling of a circular cylinder, International Journal of Heat and Mass Transfer 60, 672-688 (2013).
[13] A. A. Tawfek, Heat transfer studies of oblique impingement of round jets on a curved surface, Heat, and Mass Transfer 38, 467-475 (2002).
[14] A. A. Tawfek, Heat transfer due to round impinging normal to a circular cylinder, Heat, and Mass Transfer 35, 327-333 (1999).

## NOMENCLATURE

D – Diameter of cylinder (m)
d – Diameter of nozzle exit (m)
$\alpha$ – Inclination angle of nozzle from cylinder surface (degree)
u – Average velocity of jet (m/s)
$\nu$ - Kinetic viscosity of fluid ($m^2/s$)
h – Distance between nozzle exit to cylinder surface (m)
$T_w$ – Temperature of the cylinder wall (k)
$T_{jet}$ – Temperature of the jet (k)
$K_f$ – Thermal conductivity of fluid (w/m-k)
K – Turbulent kinetic energy ($m^2/s^2$)
$\varepsilon$ – Turbulent dissipation rate ($m^2/s^3$)
$\omega$ – Specific dissipation rate (1/s)
$V^2$ – Velocity variance scale ($m^2/s^2$)
$f$ – Elliptic relaxation function (1/s)

# NUMERICAL SIMULATION OF TURBULENT FLOW OVER A SQUARE CYLINDER USING PARTIALLY AVERAGE NAVIER-STOKES (PANS) METHOD IN OPENFOAM

**Arnab Chakraborty[1], H. V. Warrior[1], Sharath Girimaji[2]**

[1]IIT Kharagpur, West Bengal 721302, junestar66@gmail.com, warrior@naval.iitkgp.ernet.in

[2]Texas A&M University, Texas-77843, U.S.A., girimaji@aero.tamu.edu

## ABSTRACT

In this paper, we have simulated the turbulent flow over a square cylinder using a novel CFD modeling technique, Partially Averaged Navier-Stokes (PANS) [1], the method that bridges RANS with DNS. All normal stresses and Reynolds stresses have been calculated at various locations from the cylinder. It has been shown that this method is capable of capturing the properties of highly unsteady turbulent flows and gives better results than RANS. The PANS results are compared with our simulated RANS results and available experimental results [2] which are good in agreement. The simulation has been performed in 48 parallel processor.

**Key Words:** *Turbulence Modelling, PANS, RANS, Open FOAM.*

## 1. INTRODUCTION

Turbulent flow over a square cylinder is one of the benchmark problems in fluid dynamics. Several attempts have been made to solve these problems using RANS, LES, and DNS etc. which are reported in literatures [7, 8, and 9] but till now, the solution of this problem in Open FOAM [6] by Partially Average Navier-Stokes (PANS) hasn't been reported yet. So, we made an attempt to do this in this paper.

## 2. MATHEMATICAL MODELLING

The starting point of developing PANS model is the incompressible Navier-Stokes equations and continuity equation. Gravitational effects are neglected here. Let V and p represent the full velocity and pressure fields [1, 3, and 5]:

$$\frac{\partial V_i}{\partial x_i} = 0 \qquad (1)$$

$$\frac{\partial V_i}{\partial t} + V_j \frac{\partial V_i}{\partial x_j} = \frac{-\partial p}{\partial x_i} + \nu \frac{\partial^2 V_i}{\partial x_j \partial x_j} \qquad (2)$$

This work focuses on a fixed level of scale resolution. Let, < > represent a generalized homogeneous filter which is fixed in space/time. Let U be the filtered velocity and $u'$ be the sub-filter component:

$$V_i = U_i + u_i', U_i = \langle V_i \rangle, \langle u_i' \rangle \neq 0 \qquad (3)$$

$$p = P + p', P = \langle p \rangle, \langle p' \rangle \neq 0 \qquad (4)$$

Then, it can be shown that the resolved field is governed by the below equations [4]:

$$\frac{\partial U_i}{\partial t} + U_j \frac{\partial U_i}{\partial x_j} = \frac{-\partial \tau(U_i, U_j)}{\partial x_j} - \frac{\partial P}{\partial x_i} + \nu \frac{\partial^2 U_i}{\partial x_j \partial x_j} \qquad (5)$$

$$\tau(U_i, U_j) = \langle U_i U_j \rangle - \langle U_i \rangle \langle U_j \rangle \qquad (6)$$

Wherein $\tau_{ij}$ is the sub-filter stress as a physical expression or generalized central second moment as a mathematical expression. Eq. 5 is *unclosed* due to the presence of the sub-filter stress term $\tau(U_i, U_j)$. It is assumed that the Boussinesq constitutive relation is applicable to PANS:

**Sub-filter stress closure modeling:**

$$\tau_{ij} = \tau(U_i, U_j) = \frac{2}{3} k_u \delta_{ij} - \nu_u \left( \frac{\partial U_i}{\partial x_j} + \frac{\partial U_j}{\partial x_i} \right) \quad (7)$$

$$\nu_u = \frac{k_u}{\omega_u} \quad (8)$$

Here, $k_u$, $\omega_u$ and $\nu_u$ are the unresolved kinetic energy, turbulence frequency and viscosity, respectfully. Besides, the closure of $k_u$ and $\varepsilon_u$ is accomplished with a PANS $k_u - \omega_u$ model that is derived from a parent RANS $k - \omega$ model:

$$\frac{\partial k_u}{\partial t} + U_j \frac{\partial k_u}{\partial x_j} = P_u - \beta^* k_u \omega_u + \frac{\partial}{\partial x_j} \left[ \left( \frac{\nu_u}{\sigma_{ku}} \right) \frac{\partial k_u}{\partial x_j} \right] \quad (9)$$

$$\frac{\partial \omega_u}{\partial t} + U_j \frac{\partial \omega_u}{\partial x_j} = \alpha \frac{\omega_u}{k_u} P_u - \beta' \omega_u^2 + \frac{\partial}{\partial x_j} \left[ \left( \frac{\nu_u}{\sigma_{\omega u}} \right) \frac{\partial \omega_u}{\partial x_j} \right] \quad (10)$$

Where $P_u$the production of is unresolved turbulent kinetic energy, and can be expressed as

$$P_u = \nu_u \frac{\partial U_i}{\partial x_j} \left( \frac{\partial U_i}{\partial x_j} + \frac{\partial U_j}{\partial x_i} \right) = f_k \left( P - \beta^* \frac{k_u \omega_u}{f_\omega f_k} \right) + \beta^* k_u \omega_u \quad (11)$$

Model coefficients are defined as:

$$\beta' = \alpha \beta^* - \alpha \frac{\beta^*}{f_\omega} + \frac{\beta}{f_\omega} \quad (12)$$

$$\sigma_{ku} = \sigma_k \frac{f_k^2}{f_\varepsilon} \quad (13)$$

$$\sigma_{\omega u} = \sigma_\omega \frac{f_k^2}{f_\varepsilon} \quad (14)$$

Moreover, the values of the RANS closure coefficients are:

$\beta^* = 0.09$, $\alpha = 5/9$, $\beta = 0.075$, $\sigma_k = \sigma_\omega = 2.0$. One of the critical steep in PANS is the quantification of resolution in terms of filter width. Girimaji pointed out that the magnitude of unresolved to total kinetic energy ($f_K$) and unresolved to total dissipation ($f_\epsilon$) can best represent the extent of the filtered region relative to the modelled one : $f_k = K_u/K$ & $f_\omega = \omega_u/\omega$. In most practical applications, it is reasonable to assume that all the dissipation occurs in the modeled scales ($f_\epsilon = 1$). Accordingly, $f_\omega = 1/f_k$.

| Settings | Choice |
|---|---|
| Simulation Type | 3D Unsteady |
| Solver | Transient Incompressible (pisoFoam) |
| Temporal Discretization | Backward($2^{nd}$ order accurate) |
| Spatial Discretization | Bounded central- differencing |
| Pressure-Velocity Coupling | PISO |
| Turbulence Model | PANS K-ω |

TABLE1. Simulation set up in Open FOAM for the flow over square cylinder.

**Computational Domain**


Fig.1: Meshing of computational domain

## 3. RESULTS & DISCUSSIONS

**Non-dimensional stream-wise Mean Velocity (U_Mean/U) vs. Y/D:**

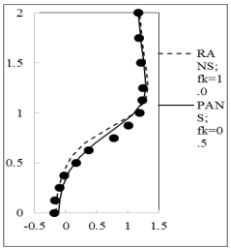


X/D=1

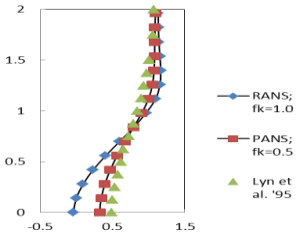


X/D=2.5

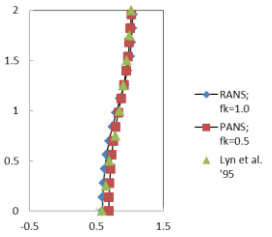


X/D=4

**Non-dimensional wall Normal Velocity (V_Mean/U) vs. Y/D:**

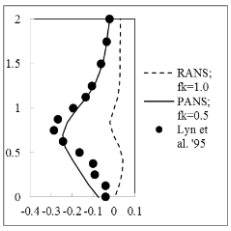


X/D=1

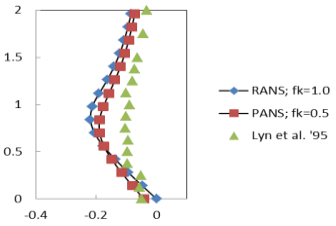


X/D=2.5

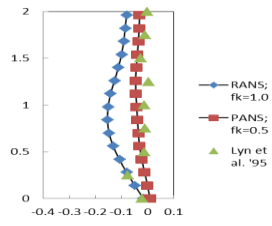


X/D=4

**Non-dimensional Stream-wise normal stress (<uu>/U2) vs. Y/D:**

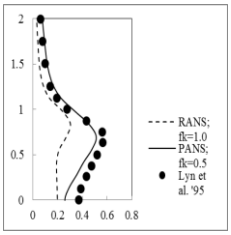


X/D=1

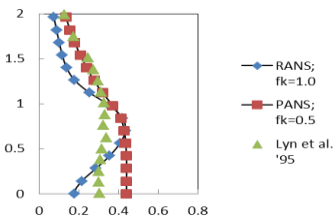


X/D=2.5

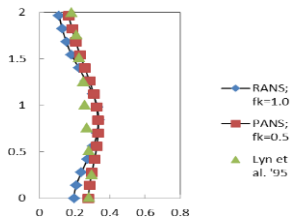


X/D=4

**Non-dimensional Reynolds Stresses (<uv>/U2) vs. Y/D:**

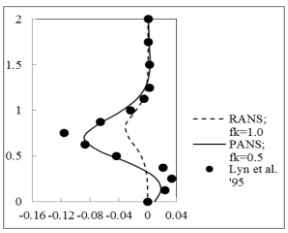


X/D=1

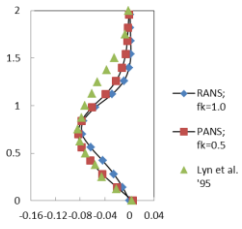


X/D=2.5

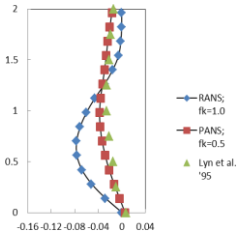


X/D=4

**Non-dimensional wall normal turbulent stress (<vv>/U2) vs. Y/D:**

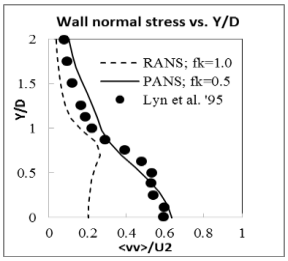


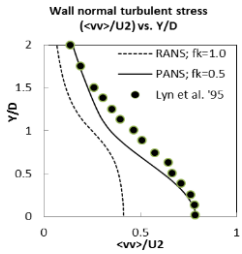


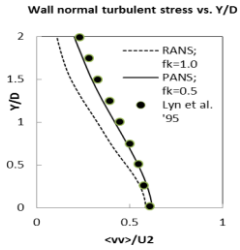


X/D=1 X/D=2.5 X/D=4

**Non-dimensional Turbulent Energy Spectra (TKE) vs. shedding frequency:**

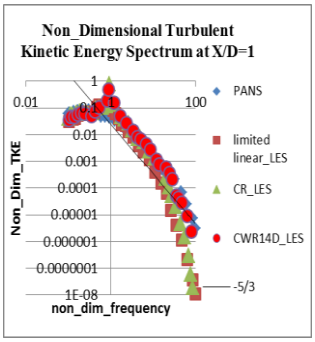


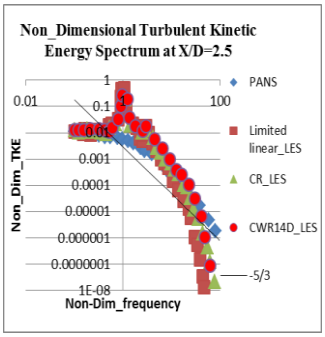


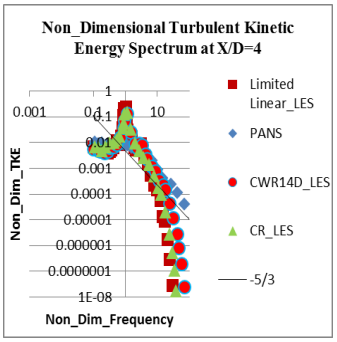


X/D=1 X/D=2.5 X/D=4

As one can see from the above results, the mean stream-wise velocity (U_mean), wall-normal mean velocity (V_mean) have been calculated and normalised by free stream velocity (U), the stream wise turbulent mean stress (<uu>), wall normal mean stress (<vv>), Reynolds stress (<uv>) have been calculed and normalised by suitable scales (U2) **and ploted in X-axis against non-dimensional Y-axis as Y/D.** The results obtained by PANS, and RANS have been compared with the experimental data by Lyn et. *al* [2] which are in good agreement. The turbulent Kinetic Energy (TKE) spectrum have been obtained for three stream-wise point which are obeying the available LES data [10].

## 4. CONCLUSIONS

The mean velocity and turbulent stresses improve substantially with decreasing $f_k$. PANS is capable of capturing 3D complex flow generated in the wake of the cylinder. The higher the physical resolution, the more scales will be liberated and resolved; consequently the prediction of the flow behaviour improves, provided that the grid resolution can afford the implemented physical resolution.

## 5. ACKNOWLEDGEMENT

I am thankful to my thesis guide prof. Hari V. Warrior in my department for his constant motivation and support. I am in debt to prof. S. S. Girimaji, Head of the Department of Ocean Engineering, Texas A&M University, U.S.A. for providing me the high performance computing facilities (HPC) and support throughout the period.

## REFERENCES


[1] Girimaji, S.S., Partially-average Navier-Stokes model for turbulence: A Reynolds –averaged Navier-Stokes to direct numerical simulation bridging method. *Journal of Applied Mechanics*, 3(3), pp.413-421, 2006.

[2] Lyn, D. A., Einav, S., Rodi, W., and Park, J. H., A laser Doppler Velocimetry study of ensemble-averaged Characteristics of the turbulent near wake of a square cylinder. *Journal of Fluid Mechanics*, 304,pp. 285-319, 1995.

[3] Lakshmipathy, S. and Girimaji, **S.S.,** Partially- average Navier-Stokes method for turbulent flows: k-ω model implementation. AIAA paper, 199, pp .2006.

[4] Germano, M., Turbulence: the filtering approach. *Journal of fluid Mechanics*, 238, pp. 325-336, 1992.

[5] Jeong, E. and Girimaji, S.S., Partially Average Navier-Stokes (PANS) method for turbulence simulations-Flow past a square cylinder. *Journal of Fluid Engineering*, 132(12), pp.121-203, 2010.

[6] Jasak, H., Jemcov, A. and Tukovic, Z. Openfoam: A c++ library for complex physics simulations. *International workshop on couple methods in numerical dynamics*, vol. 1000, pp. 1-20, 2007.

[7] Trias, F.X., Gorobets, A. and Oliva, A., Turbulent flow around a square cylinder at Reynolds number 22,000: A DNS study. *Computers & Fluids*, 123, pp.87-98, 2015.

[8] Sohankar, A., and Davison, L., Large Eddy Simulation of flow past a square cylinder: Comparison of different subgrid scaleModels. *ASME Journal of Fluid Engineering*, 122,pp. 39-47, 2000.

[9] Hunt, J.C.R., Wray, A.A., Moin, P**.,** Eddies stream and convergence zones in turbulent flows. In: *Proceeding of the 1998 summer Program (CTR)*, pp. 193-208, 1998.

[10] Yong Cao, Tetsuro Tamura, Large-eddy simulations of flow past a square cylinder using structured and unstructured grids, *Computers and Fluids*, pp. 137, 36–54, 2016.

Fifth International Conference on Computational Methods for Thermal Problems
THERMACOMP2018, July 9-11, 2018, Indian Institute of Science, Bangalore, INDIA
*N. Massarotti, P. Nithiarasu, Pradip Dutta and C. Ranganyakalu (Eds.)*

# Reynolds Average Navier Stokes (RANS) simulation of three dimentional unsteady turbulent channel flow at frictional Reynolds Number ($Re_*$) of 590 using openfoam software

**Arnab Chakraborty, H. V. Warrior**
IIT Kharagpur, West Bengal 721302, junestar66@gmail.com, warrior@naval.iitkgp.ernet.in

**S. S. Girimaji**
Texas A&M University, College Station, Texas- U.S.A, girimaji@tamu.edu

## ABSTRACT

In this paper, we tried to attempt to solve three dimensional unsteady turbulent channel flows in open Foam software using Reynolds Average Navier-Stokes (RANS) model. We have simulated the flow through 4X2X2 channel at frictional Reynolds Number ( $Re_*$) of 590 with six precessions in 48 parallel processor in work station. K-ω model has been used with 50,000 time steps with each of the time stepping of 0.3. Critical care has also been given for maintaining courant Number in between 0.4-0.5 for stability and convergence of the numerical solution. The velocity profile, several normal stress and Reynolds stresses variations with respect to wall have been shown, turbulence energy production, dissipation, their ratios have been compared, individual behaviour of viscous stress, Reynolds stresses and their contribution to total stress have been computed. All computations have been done by high performance parrallel computation (HPC) on 64 processor super computer.

**Key Words:** *Channel Flow, Turbulence modelling, RANS, Open-FOAM*

## 1. INTRODUCTION

Turbulent Channel Flows are very common in every industry and it is one of the benchmark problems in fluid dynamics. Lots of efforts have been made to solve this problem, some of these efforts can be found out in [1, 2, 3, and 4]. But no one reported the solution of this benchmark problem in any of the open source software. So, We attempt to solve this problem in open FOAM as open source software are getting popular day by day and anyone can use these free of cost.

## 2. MATHEMATICAL FORMULATION

Let us consider any quantity with bar in head is instantaneous quantity, the upper case letter denotes it's mean value whereas it's lower case value signifies the fluctuating quantity. Now writing all conservation equations in terms of instantaneous quantities,

Conservation of mass: $\frac{d\tilde{u}_i}{dx_i} = 0$ (1)

Conservation of Momentum:

$$\rho[\frac{\partial \tilde{u}_i}{\partial x_i} + \tilde{u}_j \frac{\partial \tilde{u}_i}{\partial x_j}] = -\frac{\partial \tilde{p}}{\partial x_i} + \frac{\partial \tilde{T}_{ij}}{\partial x_j} \quad (2)$$

Now, any Instantaneous quantity can be decomposing into its mean value and fluctuating value. This is known as Reynolds decomposition theorem.

$$\tilde{u}_i = U_i + u_i \ , \quad \tilde{p} = P + p \ , \quad \tilde{T}_{ij} = T_{ij} + \tau_{ij} \quad (3)$$

Now, putting the above equations (3) into (1) & (2) and taking Average (< >) of the new equations,

Now, the average of any individual fluctuating quantity is zero, i.e. $\langle u_i \rangle = 0$ hence the mean equation satisfies the conservation equation, so the final form of the momentum equation will be,

$$\rho[\frac{\partial U}{\partial x_i} + U_j \frac{\partial U_i}{\partial x_j}] = -\frac{\partial P}{\partial x_i} + \frac{\partial}{\partial x_j}(T_{ij} - \rho\langle u_i u_j \rangle)$$

The above equation is called Reynolds Average Navier Stokes (RANS) equation. The last term in the bracket in the right hand side is known as Reynolds stress which needs to be modelled. Reynolds stresses can be modelled using eddy viscosity model, in which k-ω equations are solved to obtain the turbulent eddy viscosity ($\nu_T$).

$\rho\langle u_i u_j \rangle = \nu_T \frac{\partial U_i}{\partial x_j}$, $\nu_T$ = turbulent kinematic viscosity.

$\nu_T = \frac{k}{\tilde{\omega}}$, $\tilde{\omega} = \max\left\{\omega, C_{lim}\sqrt{\frac{2S_{ij}S_{ij}}{\beta^*}}\right\}, C_{lim} = \frac{7}{8}$, So, it is clear that to evaluate $\nu_T$, we need to solve k equation and $\omega$ equation simultaneously which are given as,

$$\frac{\partial k}{\partial t} + U_j \frac{\partial k}{\partial x_j} = \tau_{ij}\frac{\partial U_i}{\partial x_j} - \beta^* k\omega + \frac{\partial}{\partial x_j}\left[\left(\nu + \sigma^* \frac{k}{\omega}\right)\frac{\partial k}{\partial x_j}\right]$$

$$\frac{\partial \omega}{\partial t} + U_j \frac{\partial \omega}{\partial x_j} = \alpha \frac{\omega}{k}\tau_{ij}\frac{\partial U_i}{\partial x_j} - \beta\omega^2 + \frac{\sigma_d}{\omega}\frac{\partial k}{\partial x_j}\frac{\partial \omega}{\partial x_j} + \frac{\partial}{\partial x_j}\left[\left(\nu + \sigma^* \frac{k}{\omega}\right)\frac{\partial \omega}{\partial x_j}\right]$$

Apart from k, ω, rest of the model coefficients [5] are evaluated as given below,

$$\alpha = \frac{13}{25}, \quad \beta = \beta_0 f_\beta, \quad \beta_0 = 0.0708, \quad f_\beta = \frac{1+85\chi_\omega}{1+100\chi_\omega}, \quad \chi_\omega = \left|\frac{\Omega_{ij}\Omega_{jk}S_{ik}}{(\beta^*\omega)^3}\right|, \quad \beta^* = \frac{9}{100}, \quad \sigma = \frac{1}{2},$$

$$\sigma^* = \frac{3}{5}, \quad \sigma_{do} = \frac{1}{8}, \quad \varepsilon = \beta^*\omega k, \quad l = \frac{k^{\frac{1}{2}}}{\omega}, \quad \Omega_{ij} = \frac{1}{2}\left[\frac{\partial U_i}{\partial x_j} - \frac{\partial U_j}{\partial x_i}\right], \quad S_{ij} = \frac{1}{2}\left[\frac{\partial U_i}{\partial x_j} + \frac{\partial U_j}{\partial x_i}\right],$$

$\tau_{ij} = 2\nu_T S_{ij} - \frac{2}{3}k\delta_{ij}$, $\begin{matrix}\delta_{ij} = 1, i = j \\ \delta_{ij} = 0, i \neq j\end{matrix}$, $\delta_{ij}$ = Kronecker delta=1 only for diagonal elements.

$\sigma_d = 0, \frac{\partial k}{\partial x_j}\frac{\partial \omega}{\partial x_j} \leq 0$ , $\sigma_d = \sigma_{do}, \frac{\partial k}{\partial x_j}\frac{\partial \omega}{\partial x_j} > 0$

| | |
|---|---|
| Solver | PISOFOAMChannel590 |
| Total Time Steps | 50,000 |
| Each Time Step | 0.3 |
| Turbulence Model | K-ω |
| Transport Model | Newtonian |
| Reference kinematic viscosity | 1e-05 |
| Time Discretization | Backward Euler |
| Gradient of Pressure | Gauss Linear |
| Divergence of Velocity | Gauss Linear |
| Divergence of Kinetic Energy | Gauss Limited Linear1 |

| | |
|---|---|
| Divergence of Vorticity | Gauss Limited Linear1 |
| Divergence of Kinematic viscosity | Gauss Limited Linear1 |
| Laplacian Evolution scheme | Gauss Linear Corrected |
| Interpolation Scheme | Linear |

TABLE 1. Details of solver specification in Open FOAM

Boundary Conditions: The wall boundary conditions are imposed on top and bottom wall, cyclic boundary conditions are imposed on the other boundaries.

## 3. RESULTS

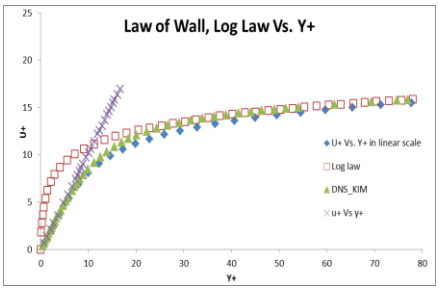


FIGURE 1. Velocity Vs.Y+ in linear scale

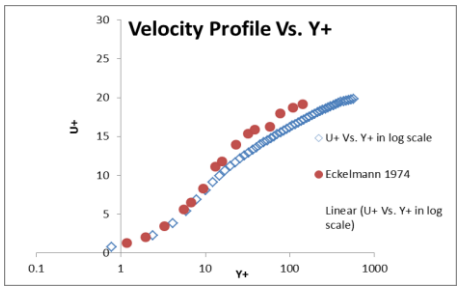


FIGURE 2. Velocity Vs.Y+ in Log scale

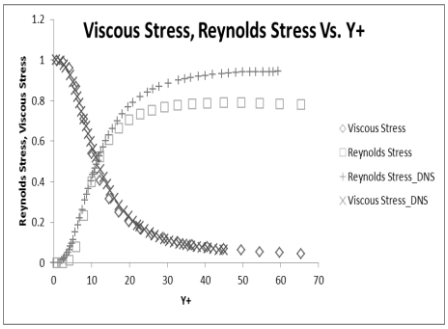


FIGURE 3. Contribution of Stresses

To total stress Vs. Y+

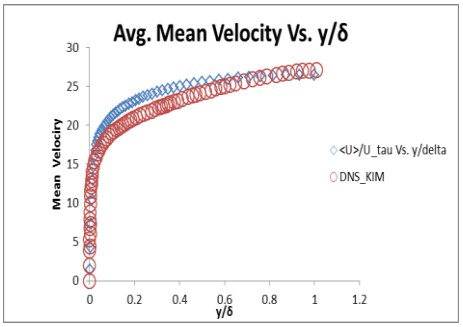


FIGURE 4. Average Mean Velocity Vs. Y+

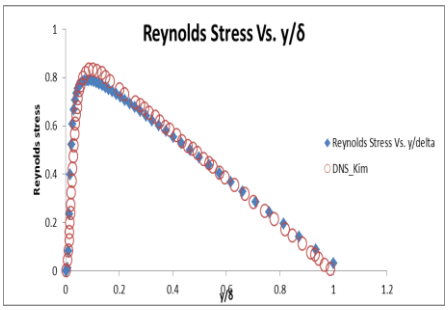


FIGURE 5. Reynolds Stress vs. y/δ

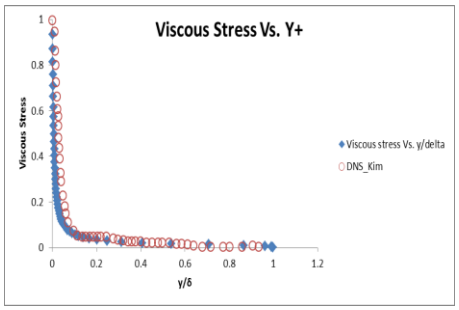


FIGURE 6. Viscous Stress vs. y/δ

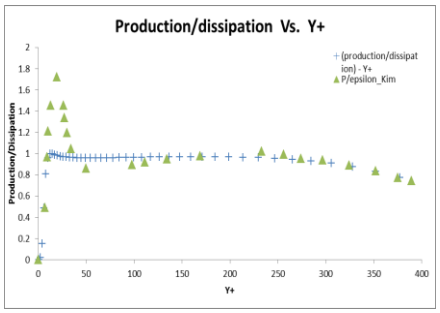


FIGURE 7. Production/Dissipation vs. Y+

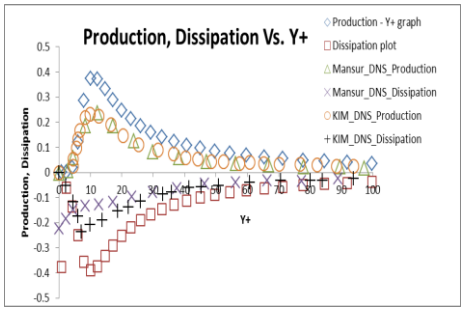


FIGURE 8. Production, Dissipation vs. Y+

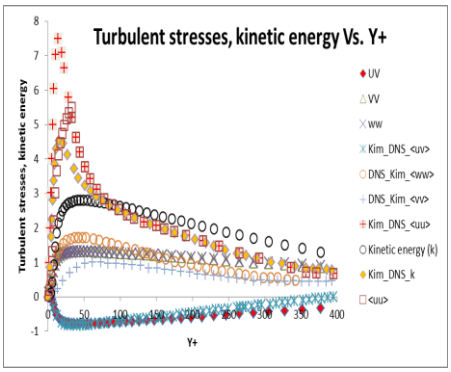


FIGURE 9. TKE, Stresses vs. Y+

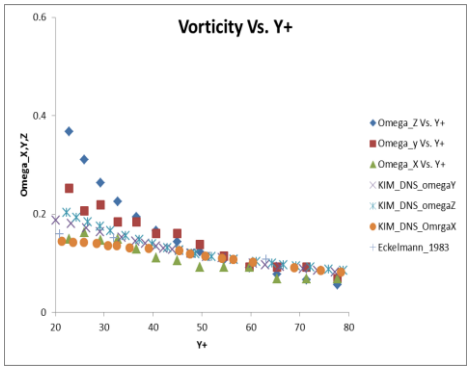


FIGURE 10. Vorticity vs. Y+

FIGURE 1& 2 depict the normalised stream-wise velocity profile with respect to (w.r.t) wall units so it is very evident from the figures that the law of wall is satisfied upto wall units (Y+) between 10 to 12 which is viscous sublayer region, then it follows the log law after wall units (Y+) of 30 which is known as log-layer and the region in between 12-30 of Y+ is known as buffer layer. FIGURE 3, 5, 6 shows that, shows that in near wall region, the viscous stress is maximum due the presence of wall and the conjugate effect of kinematic viscosity and no slip boundary conditions due to which the Reynolds stress is eventually dried out. But as one move further from the wall, the effect of wall is getting weak hence the continuous decay of viscous effect and continuous increase of Reynolds stress is observed up to the central line where the total stress which is the conjugate effect of viscous and Reynolds stress is getting constant. In the FIGURE 7, 8, the turbulent production is exactly equal to dessipation in the viscous sublayer zone, i.e. the turbulent energy is purely dissipated into smaller to smallest eddies due to the kinematic viscosity then the rate of production is getting dried out after some distance from the wall and becomes constant. In FIGURE 9, the turbulent kinetic energy (TKE), Reynolds stress (<uv>), streamwise stress (<uu>), wall normal stress (<vv>), spanwise stress (<ww>) have been ploted where we can observed that all peaks come near the wall, hence turbulence is near wall phenomena. And as RANS couldn't capture the near wall zone physics accurately so there are slight mismatches in results upto Y+=12 then they are in good agreement with DNS results. In FIGURE 10, all vorticity components are ploted and compared with existing results which show that our results are in good match with existing results apart from near wall zone as RANS couldn't resolved eddies but as the Reynolds number is not so high, so all other results are agreeing with DNS in the flow field apart from near wall zone, interestingly vorticity peaks again are in near wall zone due to high strain rate caused by combined effect of viscosity and inertia then they are getting faded out w.r.t the wall unit.

## 4. CONCLUSIONS

In this paper, we investigate the Law of Wall, Logarithmic Law, the contribution of viscous stress and Reynolds stress to the total stress. We investigate the ratio of production to dissipation variations and their individual variation, variation of TKE, several turbulent stresses and vorticity components are examined. All of these variations have been plotted with respect to wall units (Y+) or sometimes with respect to y/δ, where δ is the half width of the channel. All the computed data have been compared with the available data in literature and these comparisons show that our computed data are in quite good agreement with the reported data in literature in all over the flow domain except in the near wall region. This mismatch is due to the fact that RANS only models the mean flow and couldn't resolve any of the eddies, so it couldn't capture the rapid formation of eddies or their destruction or the wake region where the turbulent length scales are very low, i.e. near wall region (up to Y+=20), after that the results are in good match with DNS results [2]. So, It also get verified that researchers can proceed with open source software for solving these kind of engineering problems as these software are free and anyone can access from anywhere and they don't need license.

## REFERENCES

[1] Robert D. Moser, John Kim, Nagi N. Mansour, Direct numerical simulation of turbulent channel flow up to $Re_\tau$=590, *PHYSICS OF FLUIDS,* 11(4), 1070-6631, 1999.

[2] John Kim, Parviz Moin, Robert Moser, Turbulence statistics in fully developed channel flow at Low Reynolds number, *Journal of Fluid Mechanics, vol.* 177, *pp.* 133-166, 1987.

[3] H. Eckelmann, The structure of the viscous sublayer and the adjacent wall region in a turbulent channel flow, *Journal of Fluid Mechanics,* vol. 65(3), *pp.* 439-459, 1974.

[4] S. B. Pope, Introduction to Turbulence, *Cambridge University Press,* 2000.

[5] DC Wilcox, Turbulence modeling for CFD, *DCW Industries*, 1994.

Fifth International Conference on Computational Methods for Thermal Problems
THERMACOMP2018, July 9-11, 2018, Indian Institute of Science, Bangalore, INDIA
*N. Massarotti, P. Nithiarasu, Pradip Dutta and C. Ranganyakalu (Eds.)*

# NUMERICAL SIMULATION OF MICROGAP BASED FOCAL BRAIN COOLING BIOIMPLANTS FOR TREATMENT OF EPILEPSY

Narendran G., Amit Kumar, Gnanasekaran N., Arumuga perumal D*
Dept. of Mechanical Engineering, National Institute of Technology Karnataka, Surathkal, Mangalore - 575025**, E-mail:** Perumal.iit@gmail.com

## ABSTRACT

Epilepsy is most common neurological disorder that affects people of all ages and around 30% of the patients do not recover because of existing treatment like medication therapy and surgery. Due to imprudent neuronal activities, excessive heat is observed at epileptic focus and to cool this focal cerebral cooling system is used. Our aim of this study is to enhance the existing design of focal cerebral cooling system by adding constructional structures there by creating micro gaps throughout the cooling device. In this study computational model is developed to perform transient analysis on flow hydrodynamics and heat transfer using commercial package ANSYS FLUENT 15.0.

**Key Words:** *Epilepsy, Seizure, Focal cerebral Cooling, Epileptic Focus.*

## 1. INTRODUCTION

Recent findings report that out of 40 million patients suffering from epilepsy 30% of them do not recover from the existing treatment in which some patients risk to premature death due to intensive chronic epilepsy. However, existing passive therapy like drug intake and surgical treatments do not make patients seizure free [1, 2]. Fujii et al. [3] proposed a concept of Focal brain cooling device which is used to get seizure free. Yang and Rothman [4] concluded that the surface tepreature of brain should lie between 10-20°C and this limit depends upon epileptic focus location. Oku et al. [5] concluded that due to contact between implanted cooling devices with brain surface no after effect was reported. They also reported that focal brain cooling have a withholding effect on electric discharges form due to epilepsy. Peltier device [6] is also a new approach for brain focal cooling but it takes a lot of space for its operation for placing instrument like pump, heat sinks, battery and power management which may result in unwearable cooling devices for patients.

So, our main aim of this study is focused on optimum design of implantable focal cerebral cooling device and contact surface temperature analysis so that a patient can wear this cooling device with ease. The current article employs the experimental details of Inoue et al. [7] as the base case and further design modifications been introduced to examine the flow hydrodynamics in the seizure implant.

## 2. PROBLEM CONSIDERED

Since in the base case the inlet and outlet of the device are parallel present near the side walls, so as fluid enters through the inlet of the device, it gets circulated only through the side walls because of continuous motion and picking heat only from sides of the heat exchanger and so central zone of the heat exchanger is left with the high temperature shown in Figure 1(a). Further, during simulation it is noticed that the fluid which is coming from outlet brings some of the low temperature inlet fluid results in ineffective heat transfer shown in Figure 1(b). Figure 1(c) demonstrates the majority of the fluid interacting on the top wall of the heat sink which is seen throughout the simulated duration developing the region near to inlet temperature. Due to this the top surface of the heat sink experiences maximum cooling but neighboring zones remains

unaffected due to less contact between fluid and reduced velocity at far end zone of heat sink. Also, more irreversible losses are occurring inside cooling device results in decrease of effectiveness of cooling device.

## 3. NUMERICAL METHODOLOGY

A laminar forced convection in a rectangular microchannel is considered for the present study by using commercial CFD software ANSYS FLUENT 15.0. The schematic diagram of the computational base model and modified domains are shown in Figure 2(a) and Figure 2 (b) to (d). The computational model comprises two domains namely fluid and solid that corresponds to Saline water and Titanium plate. The model involves conjugate heat transfer and hence, momentum and energy equations are solved under transient condition. The governing equations are presented below.

$$\nabla . u = 0$$

$$\rho\left[\frac{\partial u}{\partial t} + u.\nabla u\right] = -\nabla p + \nabla .\left[\mu\left(\nabla u + (\nabla u)^T\right)\right]$$

$$\nabla .(\rho u h) = \nabla .(k \nabla T) + \phi; \quad = \tau_{ij} \frac{\partial u_i}{\partial x_j}$$

The fluid is considered as single phase, incompressible laminar without viscous dissipation of energy. Laminar fully developed flow and uniform zero pressure is assumed at the outlet.

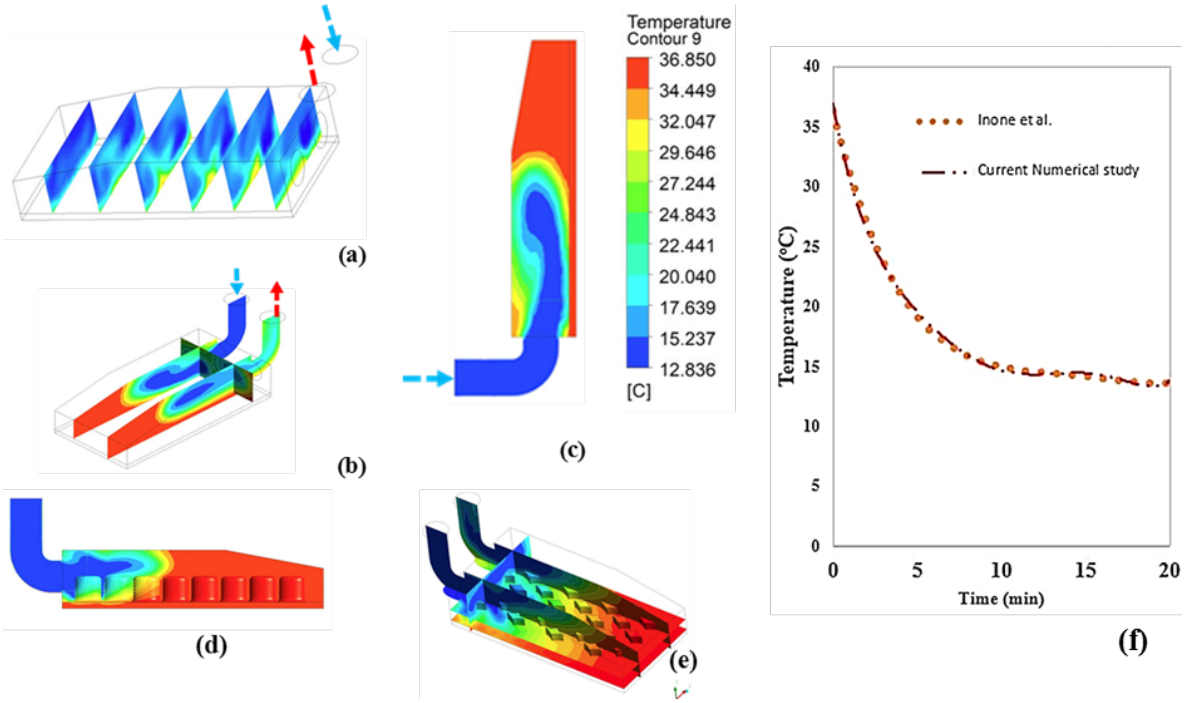


FIGURE 1. Temperature contour in Base model. (a) Temperature of heat sink along the length (b) Inlet and outlet temperature of Base model (c) Temperature contour of inlet interaction with top wall (d) Ellipse structure, (e) Diamond structure and (f) Validation plot.

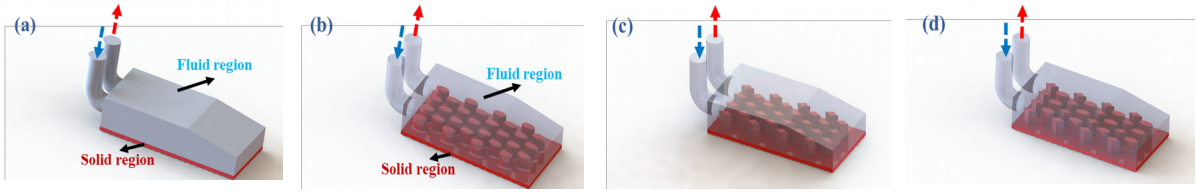


FIGURE 2. Computational domains of various heat sinks. (a) Base model, (b) Ellipse structures, (c) Diamond structure and (d) Mixed structure

## 3. RESULTS

The temperature distribution in the heat sinks for transient time steps are shown in Figure 3. The outlet temperature of the base model is found comparatively higher which is shown in Figure 3(a). Since the fluid hits directly to the ceiling of the sink the initial cooling happens at the top portion of the domain which is seen in Figure 3(b,c). This trend is not observed in the heat sink with structures which is shown in Figure 3(d-f). Inclusion of the structures diverts the fluid flow direction and moreover additional surface area of the structures provides the enhancement in heat transfer.

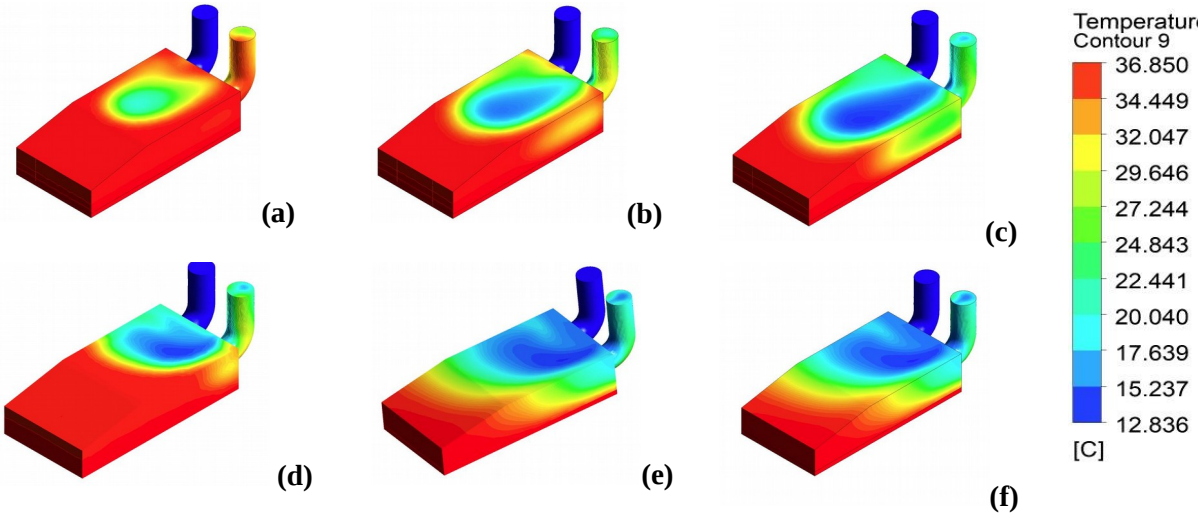


FIGURE 3. Temperature variation for increased time. (a-c) Base model and (d-f) diamond structured heat sink.

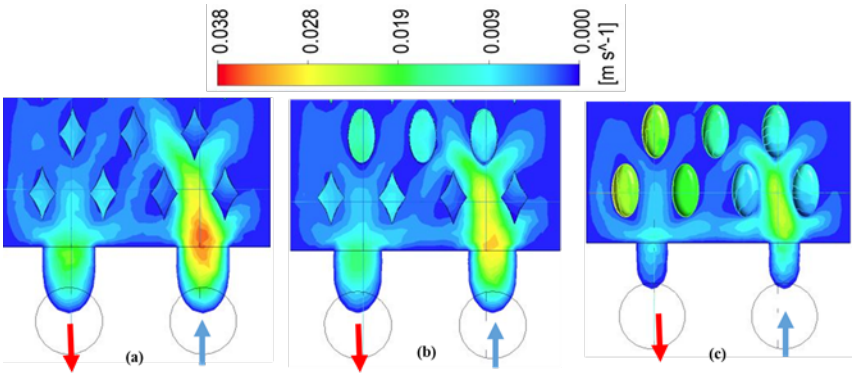


FIGURE 4. Velocity flow fields for different cross section shapes. (a) Diamond shape, (b) Mixed and (c) Ellipse shape.

Figure 5 demonstrates the temperature values along the length of the heat sink for both the base model heat sink shown in Figure 5(a). The maximum temperature of the sink throughout the sink is maintained for 37ºC (310 K) but 5ºC (278 K) temperature drop was noticed near the inlet and outlet regions of the base model. A maximum outlet temperature of 32ºC (305 K) was achieved in base model but in ellipse structured model is found lower seen in Figure 5(b).

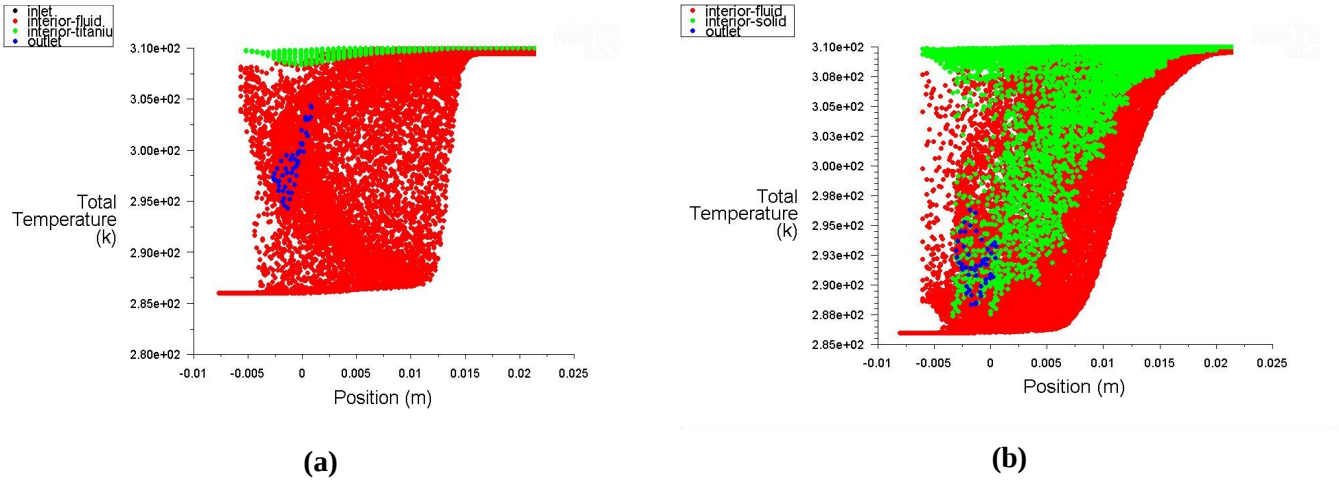


**(a)** **(b)**

FIGURE 5. Temperature distribution along the heat sink. (a) Base model and (b) Ellipse structured heat sink.

## 4. CONCLUSIONS

The effects of heat transfer and fluid hydrodynamics on focal brain cooling devices has been numerically investigated with different structures. It is observed that by adding effective structural array in cooling devices enhance the heat transfer rate. Further results were obtained and found micro gaps increases the distribution of the inlet fluid. The results highly recommend the use of diamond shape constructional structures for implementation in bio implant cooling applications.

## ACKNOWLEDGEMENTS

Authors acknowledges the Goverment of india for its financial support through SERB/ECR/2017/000387 fund.

## REFERENCES

[1] J. W. Sander, The epidemiology of epilepsy revisited, *Current Opinion in Neurology*, 16, 165-170, 2003.

[2] B. Litt and J. Echauz, Prediction of epileptic seizures, *The Lancet Neurology*, 1, 22-30, 2002.

[3] M. Fujii, H. Fujioka, T. Oku, et al., Application of Focal Cerebral Cooling for the treatment of Intractable Epilepsy, *Neurologia Medico-Chirugica*, 50, 839-844, 2010.

[4] X-F. Yang and S. M. Rothman, Focal cooling rapidly terminates experimental neocortical seizures, *Annals of Neurology*, 49, 721-726, 2001.

[5] T. Oku, M. Fujii, N. Tanaka, et al., The influence of focal brain cooling on neurophysiopathology: Validation for clinical application, *Journal of Neurosurgery*, 110, 1209-1217, 2009.

[6] H. Dinis, J. Fernandes, V. Silva, et al., Thermal modeling of an implantable brain focal cooling device, *IEEE Bioengineering (ENBENG)*, 5, 283-286, 2017.

[7] T. Inoue, M. Fujii, H. Kida, T. Yamakawa, et al., Epidural Focal brain cooling abolishes neocortical seizures in cats and non-human primates, *Neuroscience Research*, 122, 35-44, 2017.

Fifth International Conference on Computational Methods for Thermal Problems
THERMACOMP2018, July 9-11, 2018, Indian Institute of Science, Bangalore, INDIA
*N. Massarotti, P. Nithiarasu, Pradip Dutta and C. Ranganyakalu (Eds.)*

# MOLECULAR DYNAMICS STUDY OF FLUID SOLID INTERFACIAL SLIP AND ITS EFFECT ON HEAT TRANSFER

**Asef Mohammed[1], Jeetu S Babu[2]**
Department of Mechanical Engineering, Amrita Vishwa Vidyapeetham, Amritapuri, India,
E-mail:[1]asefmohammed3@gmail.com, [2]jeetusbabu@am.amrita.edu

## ABSTRACT

Interfacial hydrodynamic slippage plays a key role in the field of nanofluidics with immense applications in various domains including heat transfer. It is commonly believed that the heat transfer removal rate could be increased by increasing the flow rate. Investigations have found that the large enhancement in flow rate can be achieved by employing a channel with high slip length. The slippage of liquid was found to depend on the physical structure and chemical composition of the surface. This points to the fact that the chemical composition of the surface plays a major role in determining the surface heat removal rate in nanoscale channels. As a way to study this phenomenon, we have tried to connect the effect of the physical structure and chemical composition of the surface on the surface heat removal rate by connecting the fluid solid interfacial slip with the interfacial thermal resistance (ITR). The slip lengths associated with the flow is measured by extrapolating the velocity profile obtained by performing molecular dynamics (MD) simulations of reduced Lenard-Jones (LJ) surface. Different slip lengths were obtained by varying the fluid-solid interaction energy andalso by tuning the elastic behavior of the wall. This paper studies the variation of ITR for varying contact angles and also gives an explanation why ITR should also be considered while designing flow through nanochannels.

**Key Words:** *Fluid-solid interfacial slip, Interfacial thermal resistance, Molecular dynamics, Nanochannels.*

## 1. INTRODUCTION

Recent studies in the literature have shown that the rate of fluid flow through nanochannels can be controlled by tuning the solid-fluid interfacial parameters [1]. Various experimental studies have been conducted which tries to connect the effect of chemical property and the physical structure of the surface on the interfacial slippage of water. One such example is the Tunable wettability in surface-modified ZnO-based hierarchical nanostructures [2]. In which they found that, as the cap size of the nanonails monotonically increases, a modulation of the static contact angles were observed. This behavior can be explained due to the presence of surface roughness which reduces the slip length. Mohammed and Babu have done a MD study on fluid solid interfacial slip and its effects on aerodynamics drag [3]. The manipulation of slip was made, and it was found to have considerable effect on aerodynamic drag. The slip was varied by creating surface asperities of square and cylindrical shape. Babu et al. had proposed a method based on Eyring theory for the calculation of slip length and demonstrated the size dependent changes in the slip length using this [4]. Thekkethala and Sathian had performed MD simulations to investigate the thermal transport properties at the solid–liquid interface when graphene layers are introduced inside copper nanochannels [5]. These works propose various methods to manipulate the fluid solid interfacial friction and thus act as a guidance to design systems according to our need. For example,

manipulation of fluid solid interfacial friction can help in tuning the ITR which can have immense application in waste heat removal in integrated chips etc.

The objective of our paper is to investigate the effect of variation of slip length on the ITR with the help of MD simulations. The manipulation of the slip length was made possible by changing the fluid solid interaction where the fluid was made philic to phobic and also by applying elastic property to the lower wall.

## 2. MAIN BODY

The MD simulation is implemented using LAMMPS open source library package [6] and the visualisation of the same is done using OVITO [7] which is also an open source software. The simulation system consist of a channel of height 1nm bounded by rigid solid as shown in Fig. 1. Argon atoms are used as fluid and platinum atoms for wall. The system is designed for couette flow so that the upper plate is made moving with a small velocity V and the lower plate is kept stationary.

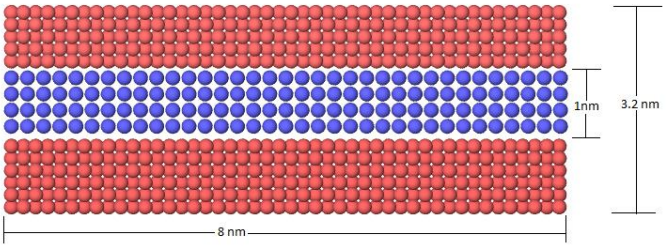


FIGURE 1. Couette flow simulation system

Lenard Jones (LJ) interaction potential is used to model the wall-wall, fluid-fluid and wall-fluid interactions [3]. Wall-fluid interaction is varied to change the contact angle. The second part of the work is done by providing elastic behaviour to the wall, by assigning spring like behaviour to the wall atoms. Slip length is calculated by extrapolating the velocity profile, obtained from MD simulation of couette flow, to meet the velocity of the wall. The calculation of ITR from the temperature profile.

## 3. RESULTS

In this study we have investigated the effect of varying slip length on ITR. As normally expected the heat transfer removal rate would increase as the flow rate through the channel increases i.e as the slip length increases. But, the results obtained in our study were in counter agreement with the above statement. The ITR was found to be increasing as the slip length increased, which means that the Heat transfer removal rate will be less from the actual value predicted. The details of which are as shown below. All the values obtained are represented with respect to the values obtained for a wall fluid interaction of 0.169 kcal/mole.

As shown in Fig. 2 when the wall fluid interaction energy reduces the slip length is found to increase, this is because as the interaction energy reduces the fluid becomes more phobic and as a result the flow rate will increase. This phenomena can be explained by looking into the interaction energy. As the fluid solid interaction energy increases, slip length decreases indicating an increase in energy and momentum transfer between the fluid and solid. As shown in Fig**. 3** when the interaction energy reduces, ITR is found to increase, this is also due to increased momentum and energy transfer which is more dominant in nanoscale than the effect of flow rate and hence the ITR is found to increase while slip length increases.

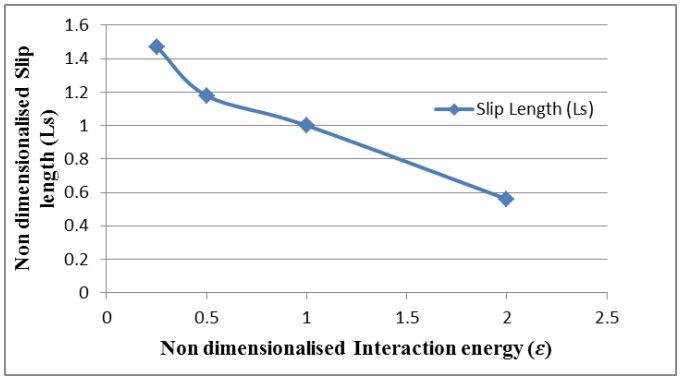


FIGURE 2. Variation of slip length with respect to wall-fluid interaction energy

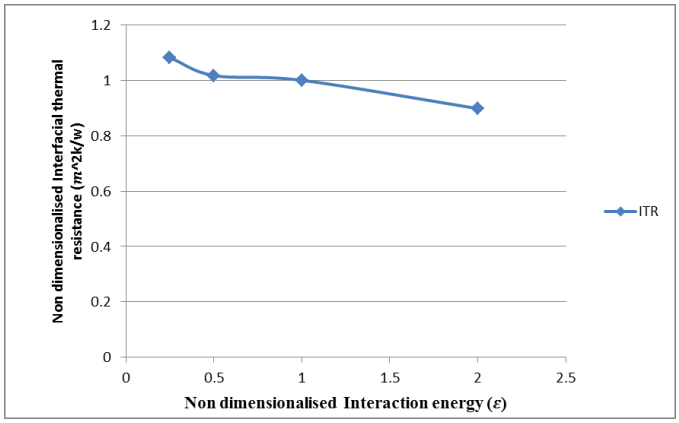


FIGURE 3. Variation of interfacial thermal resistance with respect to wall fluid interaction energy

When the spring constant decreases, the wall becomes less rigid and more energy transfer occurs between the wall and the fluid thus decreasing both sliplength and ITR. The results obtained for the same is shown in Figure 4 and Figure 5. A further reduction in slip length as well as ITR was found from rigid channels due to the reduction in spring constant i.e. by making the wall more elastic.

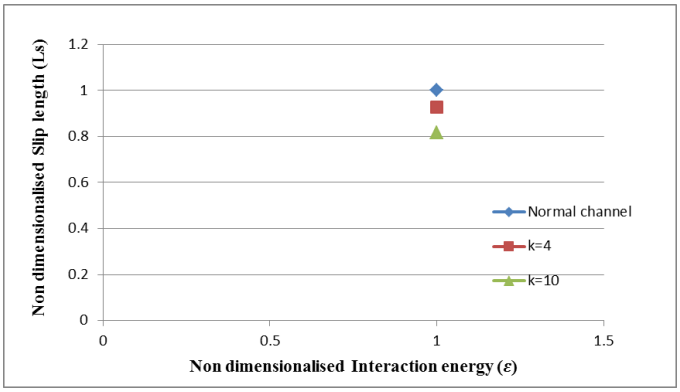


FIGURE 4. Variation of slip length with respect to wall-fluid interaction energy (♦), change in spring constant K [■, ▲]

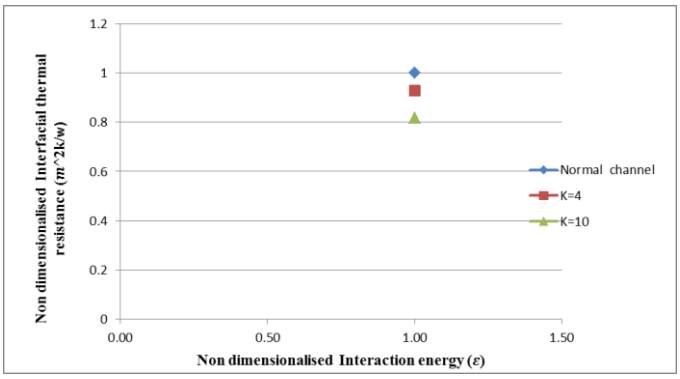


FIGURE 5. Variation of interfacial thermal resistance with respect to wall fluid interaction energy (♦), change in spring constant K [■, ▲]

## 4. CONCLUSIONS

By performing molecular dynamics simulation over reduced Lenard-Jones surface, the slip length as well as ITR for varying contact angles were studied. The variation in contact angles were achieved by changing the surface fluid interaction energy and also by employing elastic behavior to the wall. As normally expected the heat transfer removal rate should be more when the channel is subjected to high flow rate but the results obtained from our work is in counter agreement with the above statement, here the effect of interaction energy is dominant over the effect of flow rate and hence the ITR is found to increase while slip length increases. To summarize, while considering nanochannels as a potential candidate for heat transfer applications, the effect of slip length on ITR should also be taken into consideration. This work also demonstrates a practically feasible methodology to tune ITR that could have immense applications in modern MEMS/NEMS

## REFERENCES

[1] C. Bakli, and A. Misra, On the Comparability of Chemical Structure and Roughness of Nanochannels in Altering Fluid Slippage, arXiv :1605.02479, 2016.
[2] G. Li, T. chen, B. Yan, Y. Ma, Z. Zhang, T. Yu, Z. Shen, H. Chen and T. Wu, Tunable wettability in surface modified Zno-based hierarchical nanostructures, *Applied Physics Letters* 92, 173104, 2008.
[3] A. Mohammed and J. S. Babu, Molecular Dynamics study of fluid solid interfacial slip and its effect on aerodynamic drag, *2nd International conference on Mechanical, Material and Aerospace engineering*, 2017.
[4] J.S. Babu, S. Uday, S. Sekhar and S.P. Sathian, Physicochemical Analysis of Slip flow phenomina in liquids under nanoscale confinements, *European Physical Journal E*, 38,109, 2015.
[5] J.F. Thekketala and S.P. Sathian, The effect of graphane layers on interfacial thermal resistance in composite nanochannels with flow, *Microfluid Nanofluid* 18, 637-648, 2014.
[6] S. Plimpton, Fast parallel algorithems for Short-Range Molecular Dynamics, *J Comp Phys*, 117,19, 1995.
[7] A. Stukowski, Visualization and analysis of atomistic simulation data with OVITO - the Open Visualization Tool, *Modelling Simul. Mater. Sci. Eng*. 18, 015012, 2010.

Fifth International Conference on Computational Methods for Thermal Problems
THERMACOMP2018, July 9-11, 2018, Indian Institute of Science, Bangalore, INDIA
*N. Massarotti, P. Nithiarasu, Pradip Dutta and C. Ranganyakalu (Eds.)*

# Hybrid RANS/PDF simulations of the Adelaide jet-in-hot-coflow burner using 3D FGM tabulated chemistry

**Ashoke De, Bharat Bhatia**
Department of Aerospace Engineering, Indian Institute of Technology Kanpur, Kanpur, 208016, India; Email: ashoke@iitka.an.in

**Gerasimos Sarras, Dirk Roekaerts**
Department of Process and Energy, Delft University of Technology, Leeghwaterstraat 44, 2628 CA Delft, NL; Email: D.J.E.M.Roekaerts@tudelft.nl

## ABSTRACT

A probability density function (PDF) based combustion modeling approach for RANS is used in the simulation of a jet issuing into a hot and diluted coflow. A tabulated chemistry based model, i.e. Flamelet Generated Manifold (FGM), is adopted in the PDF method. The manifolds are constructed using igniting counter-flow diffusion flamelets with different coflow composition. To handle the inhomogeneity of the coflow and the entrainment of the ambient air, a second mixture fraction is defined to quantify the mixing of a representative coflow composition with the ambient air. The chemistry is then parameterized as a function of two mixture fractions and a reaction progress variable. Two flames, namely HM1 and HM3, having different oxygen mass concentration in the hot coflow, 3% and 9% O2 respectively, have been simulated for Reynolds number (Re) =10000. The mean oxygen concentration and temperature profiles are well predicted showing the capability of the tabulated chemistry. Profiles of mean mixture fraction and major species are also accurately captured by the model.

**Key Words:** *Hybrid RANS/PDF, FGM, Jet-in-Hot-Coflow.*

## 1. INTRODUCTION

The need to avoid pollutant emission has resulted in the development of new combustion techniques. These techniques include High-Temperature Air Combustion (HiTAC), Flameless Oxidation combustion (FLOX), and Moderate and Intense Low oxygen Dilution (MILD) combustion which falls under the category of 'clean combustion techniques'. One of the features of the MILD combustion is the high re-circulation ratio. The hot gas re-circulation serves the combustion process in two ways; first, it raises the reactant temperature, providing the heat needed for stable ignition. Secondly, it reduces the oxygen concentration of the mixture which reduces the flame temperature and the thermal $NO_x$ emissions. Other features of the MILD combustion include flat temperature field, low turbulence fluctuations, smooth radiation flux, barely visible and audible flame [1-3].

Dally et al. [4] of the Adelaide University designed a jet-in-hot-coflow burner and carried out experiments producing detailed profiles of major as well as minor species. The experiments performed on this burner provided a detailed database which has been used in the present study. Various numerical studies [3-12] have also been carried out using these databases to evaluate the performance of different turbulence and combustion models. There have been various RANS based modeling studies carried out in the context of the Adelaide burner most notable among them being the ones carried out by Christo et al. [5]. The major finding was that the SKE turbulence model with a modified dissipation constant ($C_{\varepsilon 1}$=1.6) produced the best agreement with the experimental results. Other notable RANS based modeling studies include the ones carried out by De et al. [3],

Frassoldati et al. [6], Mardani et al. [7, 8] and Aminian et al. [9]. All of these studies used different chemical mechanisms in order to study the flame structure and the effects of molecular diffusion on flame characteristics in the MILD regime. Kim et al. [10] simulated the JHC flames using the Conditional Moment Closure (CMC) with the primary goal of understanding the flame structure and NO formation in the MILD regime. Ihme et al. [11, 12] studied the JHC flames using LES with the Flamelet/Progress Variable (FPV) approach. They considered the burner as a three stream mixing problem by introducing an additional conserved scalar (second mixture fraction) to identify flamelets of different mixture composition and showed that the coflow composition can not be adequately represented by a single mixture fraction. From this review, it is evident that a major problem while modeling these flames is the non-linear interaction between fluid mixing and finite rate chemistry in the MILD regime. The transported probability density function (PDF) method is suited to handle this problem. It allows to include the effects of turbulence-chemistry interaction in the Reynolds Averaged Navier Stokes (RANS) framework [13].

The objective of this work is to explore the predictive capability of Flamelet Generated Manifold (FGM) chemistry in a RANS/PDF framework. This study is attempted to extend the FGM with a second mixture fraction to account for coflow in-homogeneity and air entrainment in predicting Adelaide JHC flames. The numerical predictions obtained using this model is compared with experimental measurements.

## 2. NUMERICAL DETAILS

Two different flames with different oxygen content in the hot coflow have been simulated, namely HM1 (3% $O_2$) and HM3 (9% $O_2$) at Re=10000. A 2D axisymmetric grid has been used in the simulations. The computational domain starts 4 mm downstream of the jet exit and extends for 300 mm in the axial direction and 80 mm in the radial direction. The grid consists of 200x120 cells in the axial and radial direction, respectively (stretched in both directions). At the end of the computational domain, the boundary condition is set to outflow. For the fuel jet inlet, the velocity profiles are used from a detailed separate simulation whereas at the hot coflow inlets the velocity boundary conditions are set to 3.2 m/s and at the cold air 3.3 m/s. Here the turbulent intensities at the hot coflow and cold air have been set to 5% and to 7% at the fuel jet inlet as reported in literature [5, 6]. The radial profiles of the mean temperature and mean species mass fraction with experimental values at *x=4* mm have been used to create the FGM tables with a resolution of Z x Y = 201x201 points. The PDF transport equation is solved using the Lagrangian Monte Carlo approach initialized with approximately 30 particles per cell. The IEM micro-mixing model [13] is employed with a mixing constant $C_\phi = 2$.

## 3. RESULTS

The simulation results are presented for two flames, i.e. HM1 & HM3. The profiles of mean temperature and major species are reported and compared. We have considered the progress variable ($PV\ (c) = Y_{CO} + Y_{CO2} + Y_{H2O} + Y_{H2}$) as reported by Ihme et al. [11] in order to make a comparison of our predictions. Initially, we have checked the mixture fraction profiles, which are well predicted in the whole domain for both the flames (not shown). From the $O_2$ profiles (not shown), it is observed that the 3D-FGM table is able to capture the inhomogeneity of the coflow. However, at X=60mm and 120mm, the simulation consistently under-predicts the experimental results, which suggests the air entrainment is more important for the upper part of the flame. In general, the temperature profiles are in good agreement with the experimental data except a slight under-prediction in the inner shear layer (between jet and coflow) for HM1 flame. The predictions in the outer shear layer (between the coflow and the surrounding air) are excellent for both the cases. Comparing the results of Ihme et al. [11], both the LES/FPV approach and the present approach exhibit similar behavior in predicting the ignition peaks as well as the profiles in the outer

shear layer region (r >5 mm) at the downstream locations for both the flames. In this work, even though the turbulence model is of RANS type, the turbulence-chemistry interaction is treated accurately making it possible to capture the ignition peaks correctly. Radial profiles of $H_2O$ mass fraction are depicted in Fig. 1. For both the flames, there is a consistent under-prediction of the mass fraction of $H_2O$ in the shear layer between the fuel and the hot coflow. While looking at the profiles of $CO_2$, a slight over-prediction is observed for HM3 case while the HM1 compares reasonably well with the measurements. However, both the profiles in the outer shear layer (r>20 mm) are nicely captured at all the radial locations for these flames. While comparing with the published results of [11], our predictions show opposite trend, i.e. under-prediction in r<20 mm and well captured at r>20 mm. For CO, the simulations predict the correct peak location for both the flames at X=30 mm. At further downstream locations, the peak values are under-predicted for the HM1 case. This can be attributed to the under-predicted oxygen concentration at these locations. With increasing $O_2$ concentration, the CO-results show better agreement, i.e. for flame HM3. Also, it was reported [11] that the main CO conversion to $CO_2$ is through the propagation reaction of $OH+CO \Leftrightarrow H+CO_2$. In the present work, the possible reason for the differences of $CO_2$ predictions can primarily be attributed to the over-prediction of OH radicals (not shown), where higher OH values lead to the higher $CO_2$ formation, especially for the higher $O_2$ case, i.e. HM3.

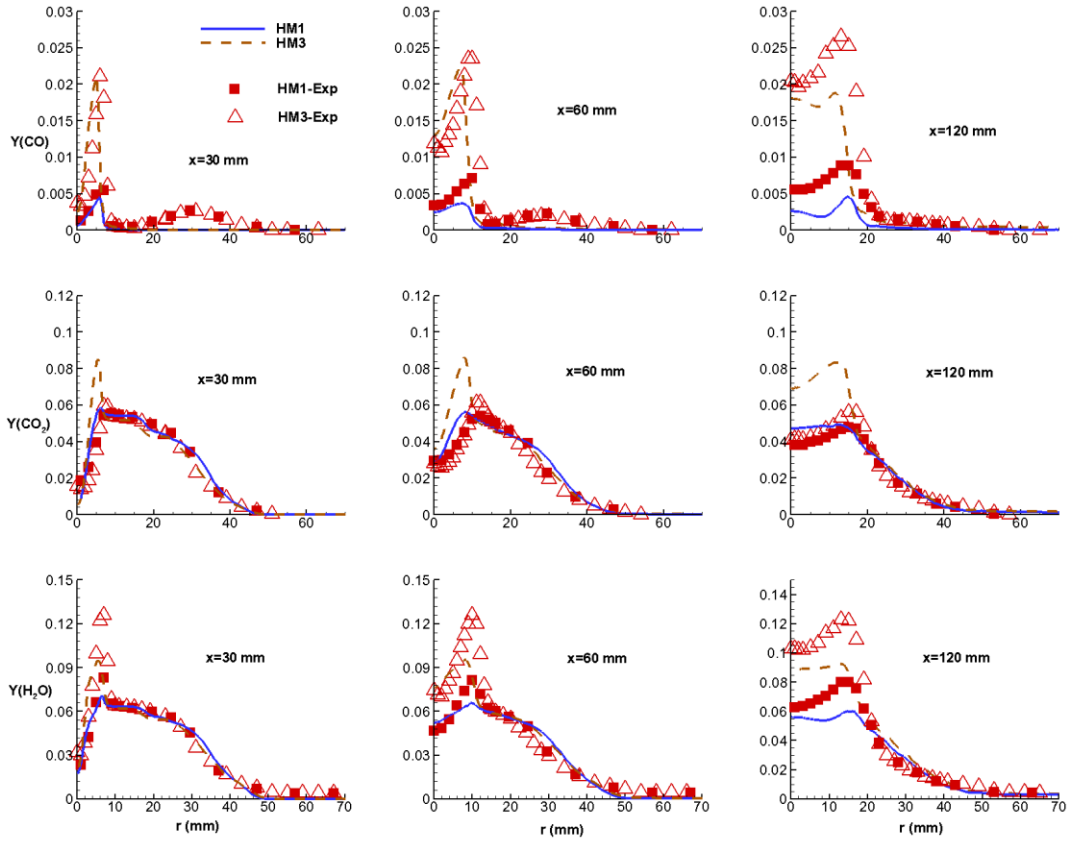


Figure 1: Radial profiles of mean CO, CO2, H2O mass fraction: symbols are measurements and lines are predictions.

## 4. CONCLUSIONS

The performance of hybrid RANS/PDF method including tabulated chemical kinetics to predict the JHC flames is presented. A 3D FGM table based on two mixture fractions and a reaction progress variable has been constructed to account for the inhomogeneity of the coflow and the entrainment of the ambient air. Igniting counter-flow diffusion flamelets are created for different coflow compositions quantified by the second mixture fraction. Two flames, namely HM1 and HM3, have been simulated and compared. Temperature and $O_2$ predictions are in excellent agreement, showing the proper ignition peaks for both the flames. However, the CO predictions appear to be in excellent agreement at the upstream locations and show under-predictions at the downstream locations for the flames studied herein. Furthermore, $CO_2$ predictions are good for HM1 case but exhibit over-predictions for HM3 case. Whereas, $H_2O$ profiles are under-predicted in the inner shear layer while nicely captured in the outer shear layer at all the radial locations. These discrepancies need further investigation and can be the part of the future studies.

## REFERENCES

[1] A. De, E. Oldenhof, P. Sathiah, D.J.E.M. Roekaerts, Numerical simulation of Delft-Jet-in-Hot-Coflow (DJHC) flames using Eddy Dissipation Concept (EDC) model for turbulence-chemistry interaction, *Flow, Turbulence and Combustion*, 87(4), 537-567, 2011.

[2] A. De, A. Dongre, R. Yadav, Numerical investigation of Delft-Jet-in-Hot-Coflow (DJHC) burner using Probability Density Function (PDF) transport modelling, *ASME Turbo Expo*, ASME paper GT2013-95390, 2012.

[3] A. De, A. Dongre, Assessment of turbulence-chemistry interaction models in MILD combustion regime, *Flow, Turbulence and Combustion*, 94, 439-478, 2015.

[4] B.B. Dally, A.N. Karpetis, R.S. Barlow, Structure of turbulent non-premixed jet flames in a diluted hot coflow, *Proceedings of the Combustion Institute*, 29, 1147-1154, 2002.

[5] F.C. Christo, B.B. Dally, Modelling turbulent reacting jets issuing into a hot and diluted coflow, *Combustion and Flame*, 142, 117-129, 2005.

[6] A.F. Frassoldati, P. Sharma, A. Cuoci, T. Faravelli, E. Rangi, Kinetic and fluid dynamics modeling of methane/hydrogen jet flames in diluted coflow, *Applied Thermal Engineering*, 30, 376-383, 2010.

[7] A. Mardani, S. Tabejamaat, M. Ghamari, Numerical study of influence of molecular diffusion in the Mild combustion regime, *Combustion Theory and Modeling*, 14(5), 747-774, 2010.

[8] A. Mardani, S. Tabejamaat, M. Ghamari, Numerical study of effect of turbulence on rate of reactions in the MILD combustion regime, *Combustion Theory and Modelling*, 15(6), 753-772, 2011.

[9] J. Aminian, C. Galletti, S. Shahhosseini, L. Tognotti, Numerical investigation of a MILD combustion burner: Analysis of Mixing field, Chemical kinetics, and Turbulence-Chemistry interaction, *Flow Turbulence and Combustion*, 88, 597-623, 2012.

[10] S.H. Kim, K.Y. Huh, B.B. Dally, Conditional moment closure modeling of turbulent non-premixed combustion in diluted hot coflow, *Proceedings of the Combustion Institute*,30, 751-757, 2005.

[11] M. Ihme, Y.S. See, LES flamelet modelling of three-stream MILD combustor: Analysis of flame sensitivity to scalar inflow conditions, *Proceedings of Combustion Institute*, 33, 1309-1317, 2011.

[12] M. Ihme, J. Zhang, G. He, B.B. Dally, LES of a Jet-in-Hot-Coflow burner operating in the oxygen-diluted combustion regime, *Flow, Turbulence, and Combustion*, 89, 449-464, 2012.

[13] D.C. Haworth, Progress in probability density function methods for turbulent reacting flows, *Progress in Energy and Combustion Science*, 36, 168-259, 2010.

Fifth International Conference on Computational Methods for Thermal Problems
THERMACOMP2018, July 9-11, 2018, Indian Institute of Science, Bangalore, INDIA
*N. Massarotti, P. Nithiarasu, Pradip Dutta and C. Ranganyakalu (Eds.)*

# Investigation of NO in pilot stabilized flames using Eddy Dissipation Concept model

**Rohit Saini, Bharat Bhatia, Ashoke De**
Department of Aerospace Engineering, Indian Institute of Technology Kanpur, Kanpur, 208016, India; Email: ashoke@iitka.an.in

## ABSTRACT

The present study investigates the NO formation using Eddy Dissipation Concept (EDC) model with detailed chemistry, where the simulations are carried out in the OpenFOAM framework. The EDC model is based on Perfectly Stirred Reactor (PSR) concept which is considered as constant pressure and adiabatic homogeneous reactors. The Sandia (D-F) flame series is considered for assessment as they vary from a simple diffusion flame (Sandia D) to strong extinction dependent (Flame E and F), especially in the same geometric configuration. Two chemical mechanisms, such as GRI 3.0 with 53 species and a reduced mechanism with 30 species, are invoked to investigate the effect of species on flame characteristics and NO formation. In the EDC model, the stiff ODE's for reaction rates are integrated using a robust implicit Runge-Kutta method (RADAU5), while the fvDOM model is used to compute the radiant fraction. The absorption coefficient is modeled using the Weighted-Sum-Gray-Gases model (WSGGM). The predictions of the scalar quantities and species are compared with the experimental measurements of Barlow and Frank (1998) for assessment. Further, the effect of chemical kinetics in all the flames (D, E and F) is assessed as the flame F moves towards the blow-out regime.

**Key Words:** *EDC, Sandia flames, NO.*

## 1. INTRODUCTION

The advanced combustion systems need to enhance the efficiency and reduce pollutant emissions, namely soot, nitrogen oxides, and carbon monoxides (in the order of decreasing chemical time scale). The reason behind almost frozen chemistry associated with NO formation is due to the action of nitrogen, oxygen, and hydrocarbons at high temperatures. This brownish gas plays a vital role in the atmospheric reactions and produces smog in hot summer days leading to acidic rain. According to the United States Environmental Protection Agency (EPA), half of such substantial anthropogenic emissions are produced from the mobile sources such as diesel engines, gas turbines, reciprocating spark ignition engines, etc.[1]. Hence, the stringent laws are unavoidable to control NO emissions in the foreseeable future. To meet these stringent rules of NO emission, a thorough understanding of the behavior of these pollutant species in conjunction with turbulence-chemistry and turbulence-radiation interaction is highly required.

In the last three decades, various sophisticated NOx predictions models have been developed that include various numbers of NOx formation pathways in the flame. The notable studies include the studies by Ihme and Pitsch [2] (used FPV approach with LES), Nanduri et al. [3] (used EDC+ reduced chemistry with RANS), Monaghan et al. [4] (used EDC+reduced chemistry with RANS), Liu et al. [5] (used Lagrangian PDF with RANS). Some of the studies included the effect of radiation in their simulations too.

In order to account for the effect of intermittencies occurring due to a number of species and expenses of computations involved, Ren et al. [6] used partitioned GRI 1.2 mechanism and GRI-Mech 3.0 [7] and found reduced description configuration agrees well with the full description and

incurs less than 5% error in NO predictions. Karalus et al. [8] developed a skeletal mechanism for methane-lean premixed combustion, consisting of 30 species and 177 reactions (termed as Red_30), derived from a GRI-Mech 3.0 and validated the mechanism using a single jet stirred reactor configuration. Further to reduce computational expenses and to gain significant CPU time, Stefanidis et al. [9] investigated the systematic reduction of the detailed combustion chemistry using quasi-steady state (QSS) approximation resulting from several reduced mechanisms ranging from 7 steps to 12 steps, skeletally derived from the detailed GRI-Mech 3.0.

The purpose of the present study is to assess the effect of chemical kinetics on the NO formation pathways using finite rate chemistry based turbulence-chemistry interaction model. Further, radiation-chemistry interaction is included to quantify the reduction in NO formation in the presence of radiative heat transfer losses. For this purpose, Sandia D-F series flames [10] from Turbulent Non-Premixed (TNF) workshop have been chosen for the wide range of availability of numerical as well as the experimental database.

## 2. NUMERICAL DETAILS

The turbulence-chemistry interaction is modeled using Eddy Dissipation Concept model [11]. In the current study, we employed a finite volume discrete ordinate (fvDOM) radiation model which is coupled with the gas solver to reflect the effect of radiation, while the absorption coefficient is modeled through the weighted sum of gray gas method (WSGGM). The solver based on rhoPisoFOAM, for compressible URANS modeling, is used in the current study [12]. Two chemical mechanisms with a varying number of species and reactions have been investigated, i.e. GRI-Mech 3.0 [7] and Red_30 [8]. The turbulence field is provided using a two-equation standard $k-\varepsilon$ model with defaults constants. Proper grid is chosen after carrying out the grid independence test. The fuel jet, pilot, and co-flow compositions and flow field conditions are specified from the experimental conditions [10, 13].

## 3. RESULTS

We have analyzed both the center line as well as the radial distribution of temperature, axial velocity, and mixture fraction for all the flames, but only a few plots are presented here due to space limitation. Overall, predictions are found to be in good agreement with the measurements. Figures 1 & 2 show the centerline distribution of NO mass fractions along with the comparison of previously published results for flames D & F only (flame E is not shown). Present EDC predictions are in reasonable agreement with all the results. Interestingly, GRI3.0 doesn't show any variation in distribution with the inclusion of radiation effect whereas significant effect can be seen in the case of Red_30. The inclusion of reduction results in a reduction of peak concentration by a factor of 3.2. However, the reduction in NO formation due to the account of radiation is enormous in the case of Red_30, but a marginal effect is noticed with GRI3.0, while the maximum peak concentration is accurately captured in the computations. One of the possible reasons for this effect may due to the optically thin assumption used in the current study, as this assumption was found to be inappropriate for partially premixed flames [12].

A dominance of the prompt mechanism can be seen in the concentration predictions from the Fig. 1. The inclusion of radiation depicts 60% and 40% change in the concentration of HCN and NCO species, respectively, in the case of Red_30. Whereas the similar phenomenon is significantly seen in the predictions with GRI3.0, showing only 16% and 40% change in the concentration of HCN and NCO species, respectively. However, the concentration of NCO species is predicted to be on the scale of the order of 8, which is 3 order lesser as compared to the concentration scale of HCN. Nitric oxides are mostly formed under fuel-lean and high-pressure conditions. $N_2O$ is formed significantly in the shear layer between fuel and oxidizer, resulting into consumption zone in the core of the flame. The inclusion of radiation shows the reverse effect on the concentration of $N_2O$

species by increasing the peak amount to 15% and 20% in GRI3.0 and Red_30, respectively. This discrepancy can be attributed to the radiation modeling with optically thin assumption.

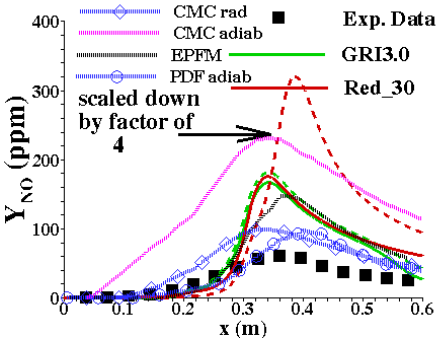


Figure 1: Fame D: Centerline distribution of NO mass fraction, peak species concentration contributing towards different NO. Solid lines with radiation and dashed lines without radiation.

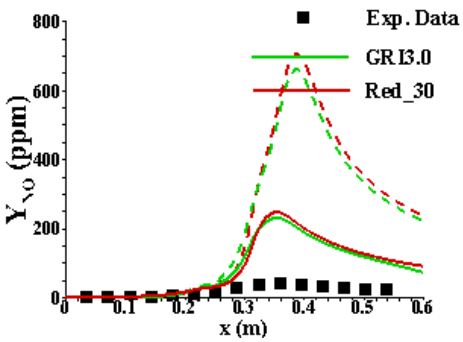


Figure 2: Fame F: Centerline distribution of NO mass fraction, peak species concentration contributing towards different NO. Solid lines with radiation and dashed lines without radiation.

For flame F, the predominant effect of HCN, as observed previously in flame D is inevitable (Fig. 2). However, the increase in concentration is not enormous, as previously observed in flame D. The concentration of HCN is increased by 9% and 6% with GRI3.0 and Red_30, respectively. Whereas NCO concentration increased by 50% and 30% with GRI3.0 and Red_30, respectively, depicting the dominant prompt mechanism in the NO formation pathways. The nitric oxide route remains unchanged as compared to the predictions of flame D. In this case, the significant increase in NNH route is noticed, i.e. 40% and 50% increase in NH concentration with GRI3.0 and Red_30 mechanism, respectively; and 22% and 18% increase in observed in NNH concentration with GRI3.0 and Red_30, respectively. This shows that of the total NO produced by Sandia Series D-F flames, the prompt mechanism is the driving mechanism of NO formation and the Red_30 mechanism is very sensitive towards radiation modeling and yields similar predictions as compared to detailed GRI3.0.

## 4. CONCLUSIONS

This study presents RANS modeling of Sandia series D-F flames using EDC combustion model combined with PSRs methodology implemented in OpenFOAM toolbox. The detailed mechanism (GRI3.0) containing 53 species and reduced mechanism (Red_30) containing 30 species have been

used to investigate the effect of chemistry on NO formation. The effect of radiation has been quantified and its effect on species leading to NO formation pathways has been discussed. Interestingly for Sandia D and E flame, the enormous effect of HCN and NCO can be seen after the inclusion of radiation. Whereas the similar effect in flame F is not dominant, leading to a marginal increase in the concentration of species involved in the prompt mechanism. The role of predominant HCN concentration is explored in all of three flames. Further, Red_30 mechanism shows extreme sensitivity towards radiation effect in all the three flames.

## REFERENCES

[1] https://www3.epa.gov/

[2] M. Ihme M and H. Pitsch, Modeling of radiation and nitric oxide formation in turbulent nonpremixed flames using a flamelet/progress variable formulation, *Physics of Fluids*, 20(5), 055110, 2008.

[3] J.R. Nanduri, D.R. Parsons, S.L. Yilmaz, I.B. Celik, P. A. Strakey, Assessment of RANS-based turbulent combustion models for prediction of emissions from lean premixed combustion of methane, *Combustion Science and Technology*, 182(7), 794-821, 2010.

[4] R.F. Monaghan, R. Tahir, A. Cuoci, G. Bourque, M. Füri, R.L. Gordon, T. Faravelli, A. Frassoldati, H.J. Curran, Detailed multi-dimensional study of pollutant formation in a methane diffusion flame, *Energy & fuels*, 26(3), 1598-1611, 2012.

[5] X. Liu, H. Zheng, Y. Li, H. He, PDF Calculation of Emission NO in Turbulent Diffusion Flame With Gas and Soot Radiation Thermal Effect, *ASME Power Conference*, POWER2013-98102, 2013.

[6] Z. Ren, G.M. Goldin, V. Hiremath, S.B. Pope, Simulations of a turbulent non-premixed flame using combined dimension reduction and tabulation for combustion chemistry, *Fuel*, 105, 636-644, 2013.

[7] G.P. Smith, D.M. Golden, M. Frenklach, N.W. Moriarty, B. Eiteneer, M. Goldenberg, C.T. Bowman, R.K. Hanson, S. Song, Jr. W.C. Gardiner, V.V. Lissianski, GRI-Mech 3.0. (1999) 51-55

[8] M.F. Karalus, K.B. Fackler, I.V. Novosselov, J.C. Kramlich, P.C. Malte, A skeletal mechanism for the reactive flow simulation of methane combustion, *ASME Turbo Expo*, GT2013-95904, 2013

[9] G.D. Stefanidis, G.J. Heynderickx, G.B. Marin, Development of reduced combustion mechanisms for premixed flame modeling in steam cracking furnaces with emphasis on NO emission, *Energy & fuels*, 20(1), 103-113, 2006.

[10] R.S. Barlow, S.B. Pope, A.R. Masri, In Workshop Proceedings, http://www.sandia.gov/TNF/9thWorkshop/TNF9, 2002.

[11] I.S. Ertesvåg, B.F. Magnussen, The eddy dissipation turbulence energy cascade model, *Combustion science and technology*, 159(1), 213-235, 2000.

[12] D.A. Lysenko, I.S. Ertesvåg, K.E. Rian, Numerical simulations of the sandia flame D using the eddy dissipation concept, *Flow, Turbulence and Combustion*, 93(4), 665-687, 2014.

[13] R.S. Barlow, J.H. Frank, Effects of turbulence on species mass fractions in methane/air jet flames, *Proceedings of the Combustion Institute*, 27(1), 1087-1095, 1998.

# DATA CENTER RACK ANALYSIS USING DETACHED EDDY SIMULATIONS

**Anashusen Saiyad, Yogesh Fulpagare, Atul Bhargav**
Indian Institute of Technology Gandhinagar, Palaj, Gujarat, India, atul.bhargav@iitgn.ac.in

## ABSTRACT

In this study, the secondary flow field and the recirculation zones inside the Cold aisle of a 3-Rack system are investigated using the detached eddy simulation (DES) consisting of the elliptic blended κ-ε model. The secondary flow fields inside the cold aisle can result in reduced air flow through the servers and ultimately, localized heating of the servers above the prescribed temperature limits. DES is selected for analysis as it incorporates both the Large Eddy Simulation (LES) in the near-wall region and Unsteady Reynold Averaged Navier-Stokes (URANS) simulation away from the wall. Hence, DES can resolve complex flow structures relatively better than LES, while using reduced computational resources. The distribution of turbulent kinetic energy (TKE) and mean velocity magnitudes inside the cold aisle are examined. We find that there are relatively lower inlet velocities near the bottom of the server rack, thereby causing inlet temperatures to rise. We believe that these results would be useful in designing better, more energy efficient cooling approaches.

**Key Words:** *Data Center, Detached Eddy Simulation, Turbulent Kinetic Energy.*

## 1. INTRODUCTION

Data centers house Information technology (IT) equipment, Computer Room Air Conditioning units (CRAC), Chiller plants and various other infrastructure facilities. Due to rapid growth and increased demand in the IT sector, the power consumption and subsequent heat generation have increased on a tremendous scale inside the Data centers. In 2014 in the US, around 1.8 % of the total electricity consumption was consumed by data centers [1]. Out of the total energy consumption within the data center, a large part of it is consumed by the cooling unit [2]. The reduction of the overall energy consumption of the data center is a great challenge and can be optimized by efficient cooling strategies. The air flow inside the data center is complex and dynamic due to dynamic loading on servers and the cold-hot aisle arrangements. To analyze the behavior and effects of the various parameters like cold air inlet and hot air outlet temperatures, rack inlet-outlet temperatures, etc. computational fluid dynamics (CFD) simulations can be carried out [3]–[6]. Major research carried out by researchers is based upon the CFD turbulence modeling using Unsteady Reynolds Averaged Navier-Stokes (URANS) based κ-ε model [3]–[5]. The κ-ε model is an Eddy viscosity model which uses Reynolds Averaged Navier-Stokes (RANS) equation in conjunction with the assumptions of isotropy and is based on mean flow properties. It is used widely due to its low computational expense and better numerical stability [7]. Due to Cold-Hot aisle arrangement, Large server room and objects present in the Data center, the fluid domain is complex in nature involving recirculation and localized hot spot generation inside the Server room. This localized temperature rise may increase the temperature of the servers above the allowed working temperatures by the ASHRAE guidelines and may lead to failure of the system [8]. Thus, to resolve the eddies and complex turbulent structures inside the fluid domain of the Server room, the Detached Eddy Simulation (DES) can be employed. The DES employs the Large Eddy Simulation (LES) in away from the wall region and URANS based turbulent model in the near-to-wall region [7]. The LES was used to investigate the secondary flow structures and the flow field inside the square duct by Madabhushi and Vanka [9] and J. Yao et al. [10]. Similarly, Liang and Xue [11] investigated the formulation of the wing-tip vortex in the near field of a NACA0015 airfoil using DES and concluded that DES model could simulate the flow

characteristics in the tip vortex effectively, whereas the RANS model underpredicted the vorticity in the tip vortex by 40% with the same grid as DES. Kumar and Joshi [12] experimentally investigated the server air distribution in the same lab with similar experimental facilities as considered in this research using the Particle Image Velocimetry (PIV) technique. The data obtained by the PIV technique predicted the low-pressure zone at the inlet of the bottom servers in comparison with that of the upper servers of the racks due to high-velocity jets emanating from the perforated tiles at the cold aisle inlet. This in turns resulted into rack air recirculation and ultimately rise in the temperatures of the bottom servers. Hence, to identify the recirculation and complex flow field in the cold aisle, the DES of the Data center server room is studied in this paper.

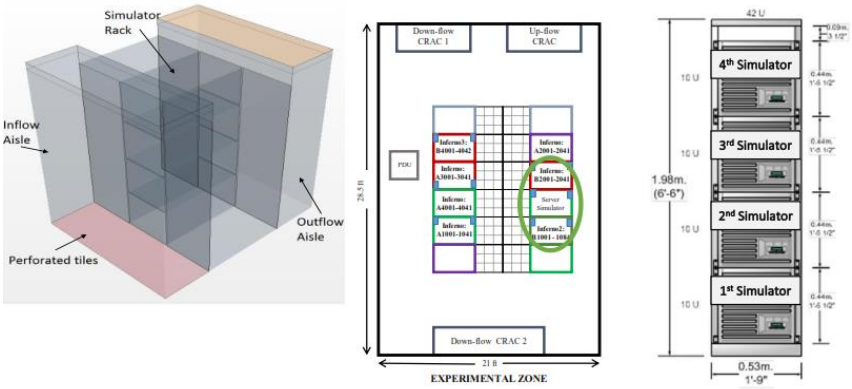


FIGURE 1. Selected experimental section of the lab that includes the server simulator rack and the CAD drawing to highlight the specific experimental domain [13], [14]

## 2. NUMERICAL MODELLING AND BOUNDARY CONDITIONS

A 3 Rack server configuration having Raised floor plenum data center room as shown in Figure 1 [13], [14] was considered in the analysis. Each rack is of height 42U (1U = 4.45 cm). Middle rack houses four server simulators each having a height of 10U whereas the racks at both sides house real-time operating live servers. Each server simulator in the middle rack has four fans mounted on a plate and dial settings to adjust the desired flow rates through the server and the rear side of the servers was modeled using the server fan curve provided by the manufacturer [15]. The fan speeds are kept constant throughout the simulation and fan swirl effects are neglected. The similar rack has been used for the analysis previously by Arghode et al. [16]. The Cold aisle is having physical dimensions of 72" ×24" ×91" (l × b × h). The rack walls were treated with the no-slip boundary condition, the tile flow rate at the bottom of the cold aisle was set to average velocity inlet of 1.53 m/s and the top surface of the hot aisle was modeled as exhaust with zero-gauge pressure. All four server simulators were modeled as having 85% porosity and the inertial and viscous resistance of the porous media were adopted from [13] and [16]. A total heat of 10 kW was assigned to each rack which contributes to 2500 W heat source to each server rack. The air inside the domain was treated as an ideal gas and the analysis was carried out using the commercial CFD tool STAR-CCM+. The hexahedral mesh with total cell count around 0.31 million was used for the study due to the limitation of available computational resources. The simulations were carried out using the Elliptic blended DES (EB-DES) model [17]. The DES simulation utilized a segregated flow solver with a Hybrid bounded-central difference (Hybrid-BCD) convection scheme. The temporal discretization was selected as Implicit Unsteady with the Convective Courant no. nearby 0.33. The WALE sub-grid scale model was selected for the closure of the filtered Navier Stokes equations. A time step of 0.01s was chosen against the large eddy turnover time of 0.4 s for the DES simulation. As the Turbulent Kinetic Energy (TKE) represents the mean kinetic energy per unit mass in the fluctuating velocity field [7], the areas of recirculation and complex flow physics can be well-identified based upon the TKE values. Hence, the TKE was selected as the indicating parameter in this study.

## 3. RESULTS

The velocity streamlines and temperature contour plot inside the 3 Rack system are shown in the fig. 2 (a) and (b) respectively. From the streamlines, it can be seen that there exists a recirculation zone in the top portion of the Cold aisle. From the temperature plot, the average rack inlet temperatures for the Server simulator rack are within the range of 1.7$^{o}$C and the average rack outlet temperatures are within 4$^{o}$C of experimental data [13], [14] obtained by the co-authors. The temperature inside the bottom servers is higher than that of the top servers. This can be an effect of the lesser amount of cooling air entering into bottom servers as compared to top servers due to the momentum of the air near the floor at the inlet of the Cold aisle (Cold aisle entrainment) which tends to move upward due to high velocity. A similar pattern of cooling air flow inside the cold aisle was observed by Kumar and Joshi [12]. This can also be observed from the mean velocity profile of air inside the cold aisle along vertical (Z) direction as shown by the fig. 3 (a). Similarly, from TKE variation profiles along the vertical (Z) direction fig. 3 (b), the TKE energy at the inlet of the middle rack is lower as compared to that for the surrounding racks due to recirculation at the inlet of the remaining servers. From the contour plot of the mean velocity magnitude in the plane passing through the top servers in fig. 4 (a), the low-velocity regions can be observed at the inlet of both the extreme servers in comparison of the middle server and the same recirculation can be observed in the velocity vector scene upon the same plane in the fig. 4 (b). Accordingly, variation in the TKE i.e., a lower value in front of the middle server due to recirculation at the inlet of the remaining servers along the longitudinal direction (X) in fig. 3 (c) can be observed. Here, the TKE at the near wall regions at the mid-height (z/h = 0.56) is higher compared to the central region due to recirculation nearby the corners as shown in the vector plot. Similarly, for the TKE along the width (Y) has higher magnitude away from the server inlet in front of the top-middle server as shown in the fig. 3 (d).

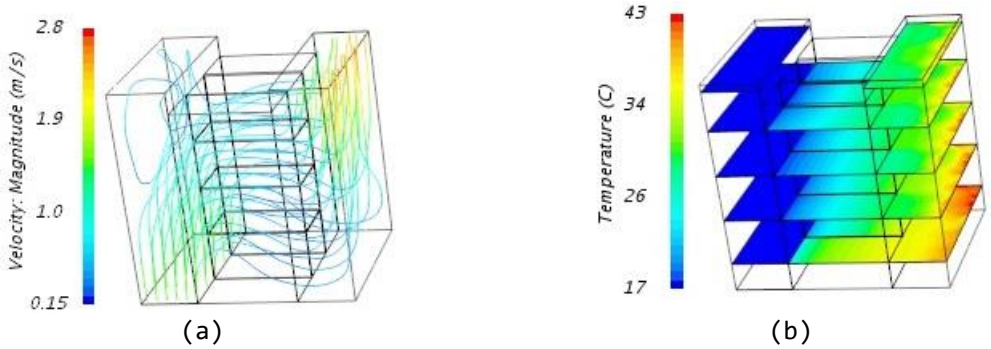


FIGURE 2. Velocity streamlines and Temperature scalar scene respectively inside the 3 Rack system

## 4. CONCLUSIONS

In this study, the DES simulation has been carried for a 3 Rack system to examine the flow field inside the Cold aisle at the Rack level. The recirculation zones near the corners and at the top of the Cold aisle are identified. The low-velocity magnitudes of the cold air at the inlet of the bottom servers are clearly identified which lead to a rise in the temperature of the bottom servers. Due to the limitation of computational resources, the number of cell count used for this study was lower. The fan swirl effects and the variation in the fan speeds with the server temperatures should be taken into consideration to mimic the actual flow field more precisely. To maintain the temperatures in the bottom servers within the specified limit, either placement of larger capacity fan for the bottom servers or allocation of lower workload to the bottom servers in comparison with that of the top servers can be suggested. Detailed analysis of the whole domain with finer mesh size and smaller time step can result in more accurate data.

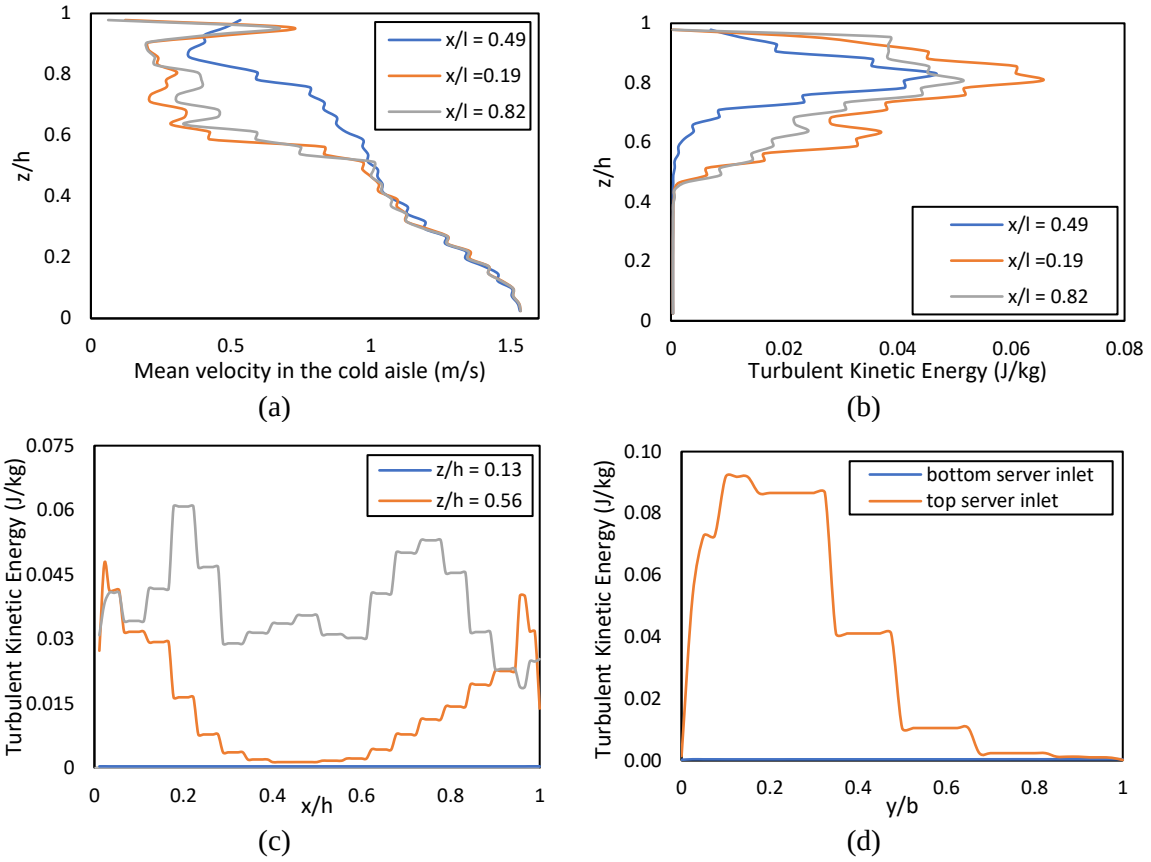


FIGURE 3. Mean inlet velocity and Turbulent kinetic energy variations inside the Cold aisle

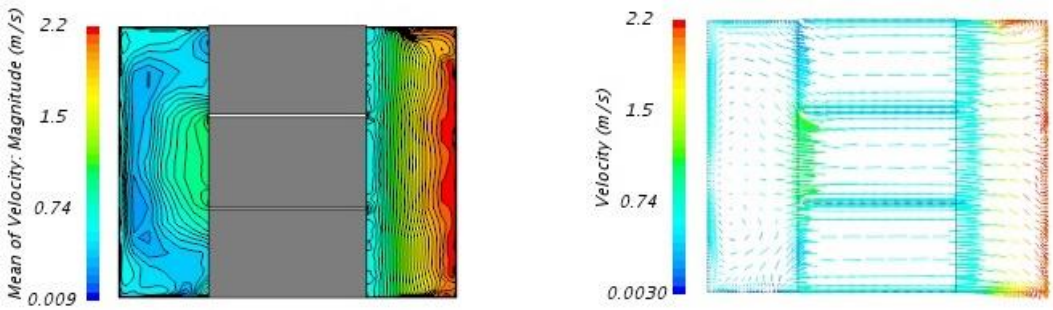


FIGURE 4. Mean velocity contour plot and Velocity vector scene respectively along the horizontal plane passing through mid of the top servers

## REFERENCES

[1] A. Shehabi *et al.*, "United States Data Center Energy Usage Report," Lawrence Berkeley National Laboratory, Berkeley, CA, USA, 2016.

[2] J. Koomey, "Growth in Data Center Electricity use 2005 to 2010," Analytics Press, Oakland, CA, USA, 2011.

[3] Y. Fulpagare and A. Bhargav, "Advances in data center thermal management," *Renew.*

*Sustain. Energy Rev.*, vol. 43, pp. 981–996, 2015.

[4] Y. Fulpagare, G. Mahamuni, and A. Bhargav, "Effect of plenum chamber obstructions on data center performance," *Appl. Therm. Eng.*, vol. 80, pp. 187–195, 2015.

[5] Y. Fulpagare, Y. Joshi, and A. Bhargav, "Rack level transient CFD modeling of Data center," in *Fourth International Conference on Computational Methods for Thermal Problems, THERMACOMP2016*, Atlanta, GA, USA, 2016.

[6] J. D. Rambo and Y. K. Joshi, "Multi-Scale Modeling of High Power Density Data Centers," in *ASME 2003 International Electronic Packaging Technical Conference and Exhibition*, pp. 521–527, Maui, Hawaii, USA, 2003.

[7] S. B. Pope, *Turbulent Flows*. Cambridge: Cambridge University Press, 2000.

[8] ASHRAE TC 9.9, "2011 Thermal Guidelines for Data Processing Environments – Expanded Data Center Classes and Usage Guidance," Atlanta, GA, USA, 2011.

[9] R. K. Madabhushi and S. P. Vanka, "Large eddy simulation of turbulence-driven secondary flow in a square duct," *Phys. Fluids A Fluid Dyn.*, vol. 3, no. 11, pp. 2734–2745, 1991.

[10] J. Yao, Y. Zhao, and M. Fairweather, "Numerical simulation of turbulent flow through a straight square duct," *Appl. Therm. Eng.*, vol. 91, pp. 800–811, 2015.

[11] Z. C. Liang and L. P. Xue, "Detached-eddy simulation of wing-tip vortex in the near field of NACA 0015 airfoil," *J. Hydrodyn.*, vol. 26, no. 2, pp. 199–206, 2014.

[12] P. Kumar and Y. Joshi, "Experimental investigations on the effect of perforated tile air jet velocity on server air distribution in a high density data center," in *2010 12th IEEE Intersociety Conference on Thermal and Thermomechanical Phenomena in Electronic Systems*, pp. 1–7, Las Vegas, NV, USA, 2010.

[13] Y. Fulpagare, Y. Joshi, and A. Bhargav, "Rack level forecasting model of Data center," in *2017 16th IEEE Intersociety Conference on Thermal and Thermomechanical Phenomena in Electronic Systems (ITherm)*, pp. 824–829, Orlando, FL, USA, 2017.

[14] Y. Fulpagare, Y. Joshi, and A. Bhargav, "Rack level transient CFD modeling of data center," *Int. J. Numer. Methods Heat Fluid Flow*, vol. 28, no. 2, pp. 381–394, 2018.

[15] G. Nelson, "Development of an experimentally-validated compact model of a server rack," Georgia Institute of Technology, Atlanta, GA, USA, 2007.

[16] V. K. Arghode, P. Kumar, Y. Joshi, T. Weiss, and G. Meyer, "Rack Level Modeling of Air Flow Through Perforated Tile in a Data Center," *J. Electron. Packag.*, vol. 135, no. 3, p. 30902, 2013.

[17] CD-adapco, *STAR-CCM+ Users Manual*.

# NATURAL CONVECTION OF CARREAU NANOFLUID FLOW PAST VERTICAL FLAT PLATE WITH PERIODIC VARIATION OF TEMPERATURE AND CONCENTRATION

**B Vasu and Atul Kumar Ray***
Department of Mathematics, Motilal Nehru National Institute of Technology, Allahabad, India
**Email:** bvasu@mnnit.ac.in, rma0215@mnnit.ac.in

## ABSTRACT

In this paper, natural convection flow of Carreau nanofluid from a vertical plate with the periodic variations of temperature of surface as well as the nanofluids volume fraction of species is studied. The governing equations are first reduced to non-dimensionalized form by using suitable transformation. These non-dimensionalized equations are further reduced to non-similar form by using stream function formulations and then solved by Homotopy Analysis Method. Computations are done for various values of the Prandtl number, Schmidt number, and Weissenberg number, thermophoresis parameter, Brownian motion parameter and buoyancy ratio parameter. The obtained results explore that the velocity of shear thinning fluid is raised by increasing the Weissenberg number while contrary response is seen for the shear thickening fluid. The temperature and thermal boundary layer thickness expands with the increase in thermophoresis and Brownian motion parameter.

**Key Words:** *Natural Convection, Homotopy Analysis Method, Carreau nanofluid.*

## 1. INTRODUCTION

The existence of thermal and concentration gradients give rise to buoyancy induced forces and flows which are responsible for many transport process in our living environment. Natural convectional heat transfer [1] has been a popular research topic because of its wide applications in many engineering, industry and geophysical fields. A number of literatures [2-5] are available for different types of geometries, various conditions, and for Newtonian and non-Newtonian fluids. The power-law viscosity model [6] is the simplest generalized Newtonian fluid model. But this model has certain restrictions that it cannot estimate the viscosity for small/large shear rates. Spriggs fluid model [7] overcomes the limitation of power law model in small shear rates but it cannot estimate the viscosity for large shear rates. To overcome the limitation of power law fluid and Spriggs fluid models, one can consider another generalized Newtonian fluid model, namely Carreau fluid model [8, 9] which has ability to estimate the viscosity for both small and large shear rates. To enhance the heat transfer rate of base fluid, a nano sized solid particle is suspended in the heat transfer fluids, resultant fluids are known as nanofluids [10-12]. In the present paper, the behaviour of natural convection flow of Carreau nanofluid from a vertical plate with the sinusoidal variations of surface temperature and nanofluids volume fraction is discussed.

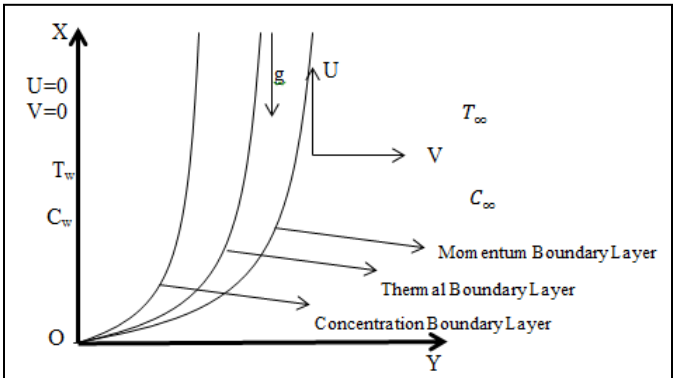

FIGURE 1. Schematic diagram of the problem

## 2. MATHEMATICAL FORMULATION

A two-dimensional natural convection incompressible Carreau nanofluid flow along a vertical flat is studied. Here it is assume that temperature of surface and the nanofluids volume fraction of surface species display little oscillations in the distance along the surface from the leading edge. The schematic diagram of the problem is shown in FIGURE. 1. The constitutive relation for a Carreau fluid [8] is describe as

$$\tau = \left[ \eta_\infty + (\eta_0 - \eta_\infty)(1 + (\lambda\dot{\gamma})^2)^{\frac{n-1}{2}} \right] \dot{\gamma} \tag{1}$$

where the parameters used in above relation are $\tau$ - extra stress tensor, $\lambda$ - time constant, $n$ - dimensionless power law index number, $\eta_0$ - zero shear rate viscosity, $\eta_\infty$ - infinite shear rate viscosity and $\dot{\gamma}$ is defined as

$$\dot{\gamma} = \sqrt{\frac{1}{2}\sum_i \sum_j \dot{\gamma}_{ij}\dot{\gamma}_{ji}} = \sqrt{\frac{1}{2}\Pi} \tag{2}$$

$\Pi$ is known as second invariant of strain rate tensor. In many practical cases, we take $\eta_0 >> \eta_\infty$ so that $\eta_\infty = 0$, thus, (1) reduces to

$$\tau = \eta_0 (1 + (\lambda\dot{\gamma})^2)^{\frac{n-1}{2}} \dot{\gamma} \tag{3}$$

The non-dimensional form of basic conservation equations of momentum, energy and nanoparticle with boundary layer approximation as follows:

$$f''' + \frac{3}{4} f f'' - \frac{1}{2}(f')^2 + \frac{3}{4}(n-1)We\xi^{1/2} f'''(f'')^2 + g - Nrh = \xi\left( f' \frac{\partial f'}{\partial \xi} - f'' \frac{\partial f}{\partial \xi} \right) \tag{4}$$

$$\frac{1}{\Pr} g'' + \frac{3}{4} f g' + Nb g' h' + Nt (g')^2 = \xi\left( f' \frac{\partial g}{\partial \xi} - g' \frac{\partial f}{\partial \xi} \right) \tag{5}$$

$$\frac{1}{Sc} h'' + \frac{3}{4} f h' + \frac{Nt}{Nb} g'' = \xi\left( f' \frac{\partial h}{\partial \xi} - h' \frac{\partial f}{\partial \xi} \right) \tag{6}$$

and associated boundary conditions becomes,

$$f(\xi,0) = 0,\ f'(\xi,0) = 0\ \ g(\xi,0) = 1 + a\,\mathrm{Sin}\,\pi\xi\ ,\ h(\xi,0) = 1 + a\,\mathrm{Sin}\,\pi\xi$$
$$f'(\xi,\infty) = 0,\ g(\xi,\infty) = 0,\ \ h(\xi,\infty) = 0 \tag{7}$$

where prime denotes differentiation with respect to $\eta$, and material fluid parameter is represented by $We$, where $\Pr = \frac{\upsilon}{\alpha}$, $\tau = \frac{(\rho c_p)_p}{(\rho c_p)_f}$ $We = \frac{\upsilon^2}{L^4} Gr^{3/2}\Gamma^2$, $Nr = \frac{(\rho_p - \rho_f)(C_w - C_\infty)}{(1 - C_\infty)\rho_f \beta (T_w - T_\infty)}$, $Nb = \frac{\tau D_B (C_w - C_\infty)}{\upsilon}$ and $Nt = \frac{\tau D_T (T_w - T_\infty)}{\upsilon T_\infty}$ are respectively Prandtl number, Weissenberg number, buoyancy ratio parameter, Brownian motion parameter and thermophoresis parameter.

Governing equations are transformed to non-dimensionalized equation using following transformation

$$x = \frac{X}{L},\ y = \frac{Y}{L} Gr^{1/4},\ U = \frac{\upsilon}{L} Gr^{1/2} u,\ V = \frac{\upsilon}{L} Gr^{1/4} v,\ \frac{T - T_\infty}{T_w - T_\infty} = \theta,\ \frac{C - C_\infty}{C_w - C_\infty} = \phi \tag{8}$$

Here, $Gr = \frac{(1 - C_\infty) g \beta (T - T_\infty) L^3}{\upsilon^2}$ is Grashof number. Transformed equations then undergoes the following stream function formulation,

$$\psi = \xi^{3/4} f(\xi,\eta),\ \eta = \frac{y}{\xi^{1/4}},\ \xi = x,\ \theta = g(\xi,\eta),\ \phi = h(\xi,\eta) \tag{9}$$

where $\psi$ is stream function for which $u = \partial\psi/\partial y$, $v = -\partial\psi/\partial x$.Hence continuity equation is satisfied and the transformation (8) and stream function formulation (9) leads governing equations to (4)-(7).

## 3. RESULTS

Table 1 reveals that velocity of shear thinning fluid increases whereas velocity for shear thickening fluid decreases by increasing We. FIGURE 2 and FIGURE 3 explore the effect of We and Sc over coefficient of surface of shear stress. The Schmidt number, Sc, are taken to represent the species, like, Hydrogen (Sc = 0.22), water vapour (Sc = 0.60) and Ethyl benzene (Sc = 2.01). FIGURE 4 shows velocity profile for different $\xi$, while FIGURE 5 indicates that increases in thermophoresis leads to grow in thermal boundary layer. FIGURE 6 and FIGURE 7 describes that increases in brownian motion parameter leads to increase in thermal boundary layer while decrease in nanoparticle volume fraction.

| | *n=0.5* | | | *n=1.5* | | |
|---|---|---|---|---|---|---|
| $\eta$ | We=1 | We=15 | We=50 | We=1 | We=15 | We=50 |
| 0.5 | 0.045835 | 0.045847 | 0.045876 | 0.045833 | 0.045822 | 0.045792 |
| 2 | 0.034207 | 0.03421 | 0.034217 | 0.034207 | 0.034204 | 0.034197 |
| 3.5 | 0.013948 | 0.013949 | 0.013951 | 0.013948 | 0.013947 | 0.013944 |
| 5 | -0.00057 | -0.00057 | -0.00057 | -0.00057 | -0.00057 | -0.00057 |

TABLE 1. Effect of We on velocity for shear thinning and thickening fluid

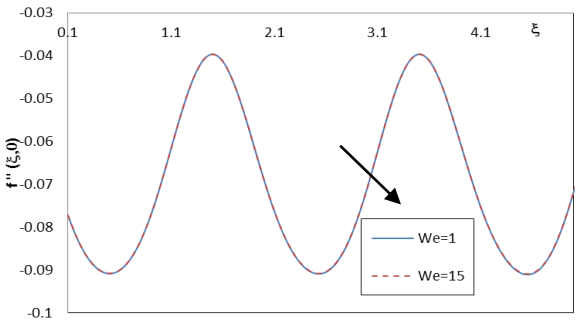


FIGURE 2. Varition of coefficient of surface of shear stress

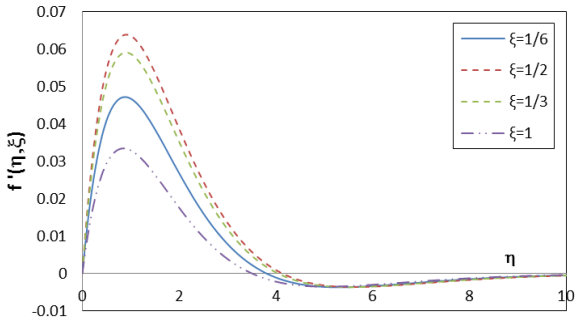


FIGURE 4. Effect of distance along the plate over velocity profile

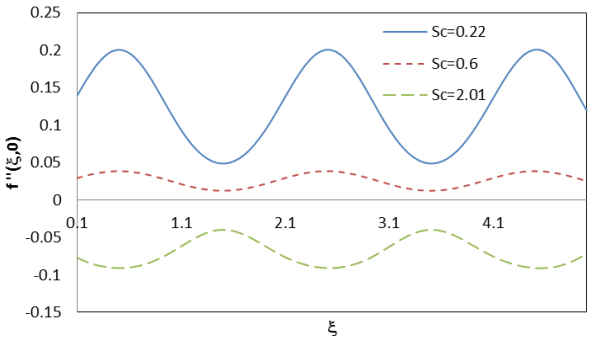


FIGURE 3. Effect of Sc over coefficient of surface shear stress

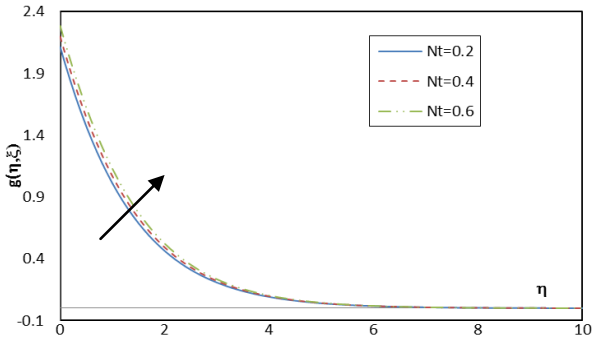


FIGURE 5. Effect of thermophoresis over tempreture

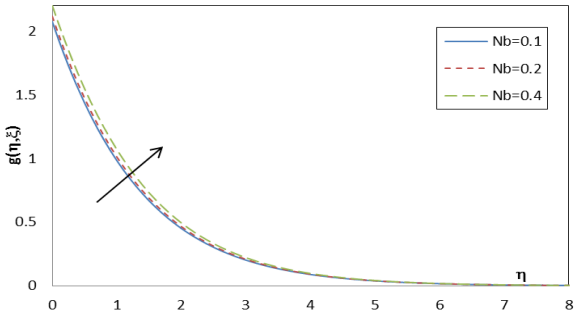


FIGURE 6. Effect of Brownian motion paramter over tempreture

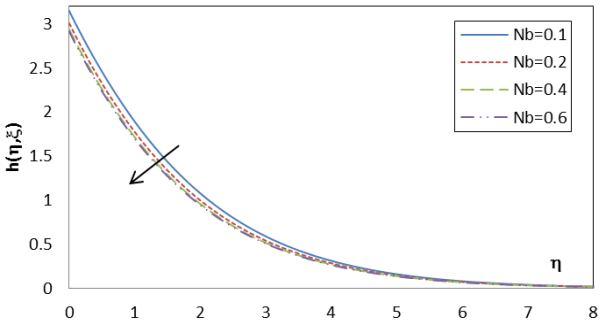


FIGURE 7. Effect of Brownian motion paramter over nanoparticle volume fraction

## 4. CONCLUSIONS

The appropriate transformations are implemented to reduce the governing equations into non-similar ordinary differential equations. From the derived equations, one can retrieve the equations for Newtonian fluid which is as a limiting case of the present problem. The HAM was used to solve these systems of equations. It is found that as Sc increases, the coefficient of surface shear stress decreases. With the increase in the Weissenberg number $We$, velocity decreases for shear thinning while increase for shear thickening fluid. Increment in thermophoresis $Nt$ and Brownian motion parameter $Nb$ shows expansion to the temperature and thermal boundary layer thickness while we obtained reduction in nanoparticle volume fraction for Brownian motion parameter.

## REFERENCES

[1] Theodore L. Bergman and Frank P. Incropera, *Fundamentals of heat and mass transfer*, seventh ed., John Wiley & Sons, 2011

[2] Ostrach, S., Laminar Flows with Body Forces, *Theory of Laminar Flows, High-Speed Aerodynamics and Jet Propulsion*, Vol. 4, edited by F. K. Moore, Princeton, 28, 1964.

[3] Gebhart, B., "External Natural Convection Flows, *Applied Mechanics Reviews*, 22, 691, 1969.

[4] Blasius H. Grenzschichten in Flussigkeiten mit kleiner Reibung. *Z Mathematik Physik*, 56, 1–37, 1908.

[5] V. Ramachandra Prasad, , B. Vasu, and O. Anwar Bég. "Thermo-diffusion and diffusion-thermo effects on MHD free convection flow past a vertical porous plate embedded in a non-Darcian porous medium." *Chemical Engineering* Journal, 173(2), 598-606 2011.

[6] Abhijit Guha, Kaustav Pradhan, Natural convection of non-Newtonian power-law fluids on a horizontal plate, *International Journal of Heat and Mass Transfer* 70, 930-938, 2014.

[7] A. K. Ray and B. Vasu, Hydrodynamics Of Non-Newtonian Spriggs Fluid Flow Past An Impulsively Moving Plate, *Applications of Fluid Dynamics: Proceedings of ICAFD* 2016, 95, 2017.

[8] B.R. Bird, R.C. Amstrong, O. Hassager, Dynamics of Polymeric Liquids, second ed., *John Wiley and Sons Inc., New York*, 1987.

[9] Hayat, T., Waqas, M., Shehzad, S. A., & Alsaedi, A., Stretched flow of Carreau nanofluid with convective boundary condition, *Pramana*, 86(1), 3-17, 2016.

[10] U.S. Choi, Enhancing Thermal Conductivity of Fluids with Nanoparticles, Developments and Application of Non-Newtonian Flows. *ASME Journal of Heat Transfer*, 66, 99-105, 1995.

[11] J. Buongiorno, Convective transport in nanofluids, *ASME Journal of Heat Transfer*, 128, 240–250, 2006.

[12] Sh.M. Vanaki, P. Ganesan, H.A. Mohammed, Numerical Study of convective heat transfer of nanofluids: A Review, *Renewable and Sustainable Energy Reviews*, 54, 1212-1239, 2016.

Fifth International Conference on Computational Methods for Thermal Problems
THERMACOMP2018, July9-11, 2018, Indian Institute of Science, Bangalore, INDIA
*N.Massarotti, P.Nithiarasu, Pradip Duttaand C. Ranganyakalu (Eds.)*

# NUMERICAL ANALYSIS OF NUKIYAMA'S EXPERIMENT AROUND A THIN WIRE

**Avik Saha, Chandan Swaroop Meena, Arup Kumar Das,**
Department of Mechanical and Industrial Engineering, IIT Roorkee, 247667, India,
aviksaha129@gmail.com, chandanswaroop2008@gmail.com, akdasfme@iitr.ac.in

## ABSTRACT

Present paper deals with numerical simulation of boiling heat transfer around a heated wire. It reports nucleation of bubble, thickening of film and as a whole breaking and making of interfaces. Volume of fluid based finite volume discretization is adapted for modelling mass, momentum and energy equations. Similar to Nukiyama's experiment a cylindrical wire has been taken as source of heat. Liquid water at normal atmospheric pressure is considered as working fluid in the simulations. Continuous supply of heat from constant temperature wire caused film boiling and nucleation after sufficient growth of film thickness. In absence of nucleation site, generated bubbles are formed randomly from the upper surface of the wire. Complete life cycle of the bubble and formation of bubble cloud over the wire has been observed. From simulation, it has been observed that with increase in heat flux bubble release rate increases. Similar has been also concluded by Nukiyama in his famous boiling experiment.

**Key Words:** *Boiling Heat Transfer, Volume of Fluid, Bubble Dynamics, Film Boiling.*

## 1. INTRODUCTION

Boiling is an example of phase transition and can be initiated by raising the temperature of a liquid above its saturation temperature. Two most common ways of accomplishing boiling are by applying an external heat flux to a solid surface in contact with a liquid or by reducing the pressure in the surrounding environment. Former one is more popular and well used in industrial applications. There are three distinct regimes that characterize boiling induced by a heated surface namely, nucleation, transition, and film formation. Boiling regime and interfacial mode depends on the excess temperature and the magnitude of the applied heat flux to the surface. The excess temperature is defined as the difference between the temperature of the solid surface and the saturation temperature of the liquid at given pressure. In this regard, experiment by Nukiyama (1934) to observe different modes of boiling around a heated wire is quite famous and can be treated as pioneer in the field. It proposes a boiling curve and establishes link between nucleation and film formation. Following Nukiyama's (1934) effort multiple researchers tried to understand basic boiling modes from analytical, experimental and numerical viewpoints. A brief idea about these works on boiling heat transfer can be found in review of Dhir (1998). But it can be found from literature that majority of the studies in boiling heat transfer are experimental in nature. Very few groups targeted modeling all modes of boiling heat transfer numerically. Son and Dhir (2008) used level set method to numerically investigate the nucleate boiling with high heat fluxes. They have also simulated three-dimensional film boiling situation on a horizontal cylinder. But the basic understanding of physics behind the different modes of boiling heat transfer is still due. Complexity increases when the bubbles are forming and they are departing from the nucleation sites. But due to non-intuitive and counter-intuitive nature of two phase interfacial behavior, prediction of bubble behavior is not yet fully understood. Present effort targets simulation of boiling heat transfer around a heated wire and understand full phase change framework. In the next section, methodology for simulation has been described followed by results of numerical simulation.

## 2. DOMAIN DESCRIPTION AND MODEL FORMULATION

Numerical simulation of bubble formation is performed by using the finite volume based OpenFoam 2.2.0 solver. The geometry and initial conditions for obtaining boiling situations are shown in Figure 1. To study boiling around a heated wire a domain of 110 mm × 20 mm × 50 mm has been taken and a wire of diameter 2 mm and length of 100 mm is placed in the domain at a height of 10 mm from the bottom as shown in the Figure 1. While initializing the simulation a thin vapor film of 0.5 mm has been considered to avoid numerical singularity. All the external boundaries other than the top boundary has been considered as wall and all the walls are kept constant at saturated temperature 373.15 K at normal atmospheric pressure. All the walls including the wire surface are subjected to zero slip condition. The top boundary is kept at constant pressure outlet of 1 bar. A range of constant temperature (ΔT = 110 °C, 120°C and 130°C) is supplied to observe the bubble dynamics around wire.

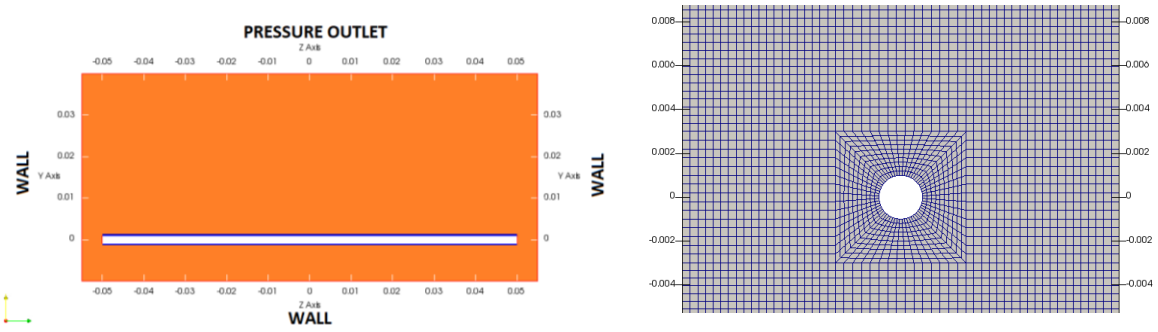


(a) (b)

Figure. 1 (a) Domain description and boundary conditions (b) Cross-sectional view of the mesh near the wire

For simulation of two phase flow with the phase change, the governing equations for mass momentum and energy conservation are casted in one-fluid framework. In boiling, mass transfer from one phase to the other is a local phenomenon and it does not change the global conservation equations. The surface tension in momentum equation is accounted by continuum surface force model (CSF) without the density averaging proposed by Brackbill et al. (1992). As both phases are assumed to be incompressible, the equation for pressure is derived from continuity and momentum equations. For modelling boiling heat transfer following energy equation is solved with source term for mass transfer from liquid to gas.

$$\frac{\partial}{\partial t}(T) + \nabla.(\mathrm{UT}) - \nabla.(\mathrm{D_k}\nabla \mathrm{T}) = -\mathrm{D_c m^m} \times (\mathrm{H_{LG}} + \dot{(}\mathrm{C_L} - \mathrm{C_G})\mathrm{T_{sat}}) \tag{1}$$

In order to keep the numerical stability $D_k$ and $D_c$ are linked up with phase fraction, density, thermal conductivity and specific heats. The transport equation for interface is derived from continuity equation as:

$$\frac{\partial \alpha_L}{\partial t} + \vec{U}.\nabla\alpha_L + \nabla.(\alpha_L(1-\alpha_L)\vec{U_C}) = -\dot{m}'''\left[\frac{1}{\rho_L} - \alpha_L\left(\frac{1}{\rho_L} - \frac{1}{\rho_G}\right)\right] \tag{2}$$

where $\alpha_L$ is the VOF function, having non-zero value near the interface. As there is no interface reconstruction in present study, interface is diffused in a region between two to three cells, Therefore, iso-contour $\alpha_L$ = 0.5 represents interface position. The thermophysical properties of two immiscible fluids such as viscosity (μ), density (ρ) and thermal conductivity (k) are calculated using a weighted average of phase fraction. In present study phase change model proposed by Tanasawa (1991) is employed. The volumetric transferred mass (kg/m$^3$ s) at the liquid–vapor interface is given by:

$$\dot{m}''' = \frac{2\gamma}{2-\gamma}\sqrt{\frac{1.0}{2\pi R}}\frac{\rho_G H_{LG}(T-T_{sat})}{T_{sat}^{(3/2)}}\nabla\alpha_L \tag{3}$$

where $T_{Sat}(P)$ is local saturation temperature, and γ is the fraction of molecules transferred from one phase to the other during phase change.

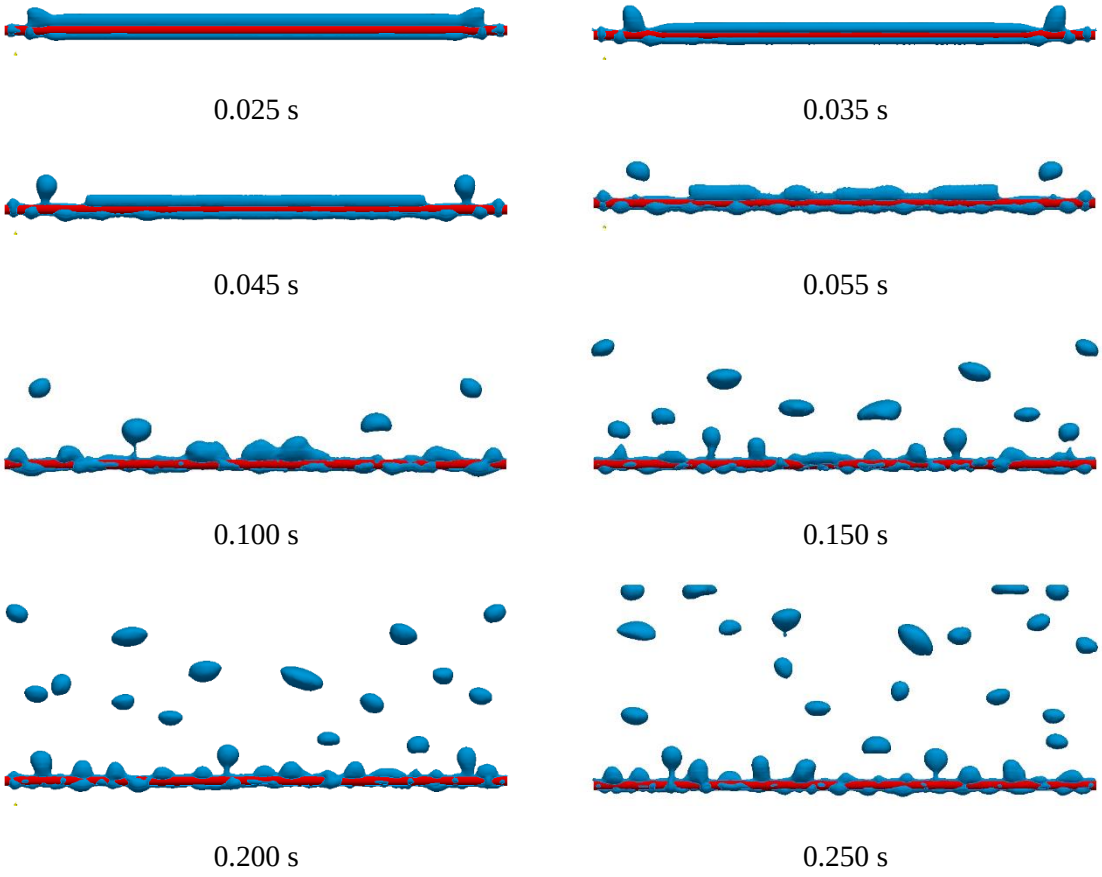


Figure 2. Temporal progress of boiling phenomenon around heated wire; film growth, nucleation, pinch off and free rise of bubble

## 3. RESULTS AND DISCUSSION

From the results of the simulation, bubble dynamics around the wire has been visualized using phase contour of $\alpha_L = 0.5$. It has been observed that at the beginning by virtue of surface tension, film grows radially and it tries to contract longitudinally to form a bulge at both the ends, as shown in Figure 2. This growth subsequently gives rise the nucleation of first bubbles from the corners. Subsequently, the film gets destabilized and shows wave in the periphery. At the peak of the wave the growth of the film continues to produce nucleation site for the bubbles. It can be also noticed that the film is not azimuthally symmetric and thickens at the top. Once the bubbles get bigger in size, neck formation is observed before pinch off from the site. Later on it moves up due to buoyancy in the neighborhood of surrounding bubble. This makes a population of bubble on top of the wire.

Parametric variation is also tried to observe the effect of degree of superheat on the density of bubble population formed from the surface. It has been observed that pinch off of first bubble is independent of degree of superheat (0.05 s). But later on, more and more bubbles are formed around the wire which makes a denser bubble population around the wire. It can be clearly seen from comparative view of two different superheats (10 and 30˚) in Figure 3. It reports the bubble cluster at 0.25 s after the simulation. One can also see that not only concentration of bubbles is increasing but average bubble size is also increasing with temperature. It also observed that with increase in temperature the wire is gradually getting covered with a vapor film which will affect the heat transfer coefficient.

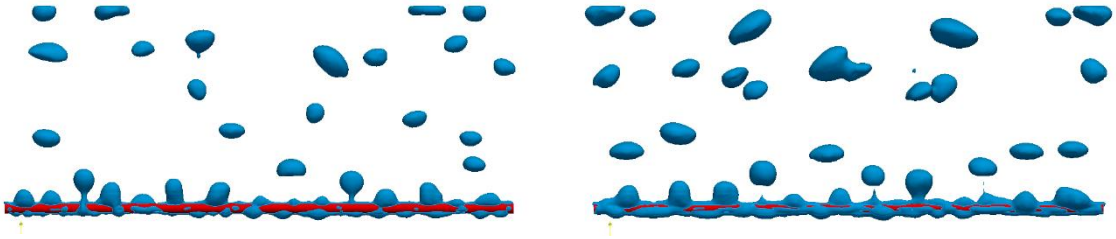

ΔT = 10°C ΔT = 30°C

Figure 3. Comparison of bubble population for different degree of superheat at 0.25 sec

## 4. CONCLUSION

Numerically, Nukiyama's experiment has been revisited and similar features of film and nucleate boiling has been observed. Finite volume-based simulation showed asymmetric growth of film around the wire, nucleation, mass injection in the bubbles, pinch off and free uprise around the wire. Comparative simulations at different wire temperature showed generation of more and more bubbles at high degree of superheat. Along with increase in number, one can see from the simulations that the bubble sizes increase with increase in degree of superheat. Present numerical simulation numerically verifies the experimental observations of Nukiyama (1934) and extends the findings for different degree of superheats.

## REFERENCES

[1]. S. Nukiyama, Maximum and minimum values of heat q transmitted from metal to boiling water under atmospheric pressure [J], *Society of Mechanical Engineering Japan*, 37, 53-54, 367-374, 1934.

[2]. V. K. Dhir, Boiling heat transfer, *Annular Review of Fluid Mechanics*, 30, 365-401, 1998.

[3]. G. Son, V. K. Dhir, Numerical simulation of nucleate boiling on a horizontal surface at high heat fluxes, *International Journal of Heat and Mass Transfer*, 51, 2566–2582, 2008

[4]. J. U. Brackbill, D. B. Kothe, C. Zemach, A continuum method for modeling surface tension, *Journal of Computational Physics*, 100, 335–354, 1992.

[5]. I. Tanasawa, Advances in condensation heat transfer, *Advances in heat transfer*, 21, 55–139, 1991.

Fifth International Conference on Computational Methods for Thermal Problems
THERMACOMP2018, July 9-11, 2018, Indian Institute of Science, Bangalore, INDIA
*N. Massarotti, P. Nithiarasu, Pradip Dutta and C. Ranganyakalu (Eds.)*

# Design and analysis of scroll expander using $N_s$-$D_s$ diagram

**Avinash Dash, Pardeep Garg, Pradip Dutta**

Department of Mechanical Engg., Indian Institute of Science, Bangalore, India

dash.avinash@gmail.com

pardeep_1127@yahoo.com

pradip@mecheng.iisc.ernet.in

## ABSTRACT

Various studies on scroll expander available in literature have proven it to be an attractive choice for micro-scale (< 20 kWe) ORC application. These studies comprise of modifying the scroll compressor to be used in the expander mode followed by the development of semi-empirical models to determine the scroll performance. These models can provide the guidelines to design scroll expanders for a specific ORC application. This paper generates a number of scroll expander geometries and optimizes them for the best cycle efficiency for a 10 kWe R134a ORC cycle using the above mentioned models. Conventionally, the scroll expanders have been studied by plotting their performance indicators against the cycle operating parameters such as temperature, pressure and volume ratio. In this paper, we analyze these scroll expander geometries on the classical $N_s$-$D_s$ diagram along with other expanders. It is observed that scroll expander occupies a domain of low $N_s$ and high $D_s$, away from conventional turbine type expanders but closer to other positive displacement devices such as rotary and reciprocating type of expanders. This unique domain of scroll expanders $N_s$-$D_s$ plot also signifies existence of other potential applications.

**Key Words:** Organic Rankine cycles, volumetric expander, scroll expander, semi-empirical model, scroll geometry, $N_s$-$D_s$ diagram.

## 1. INTRODUCTION

In recent years, the growing concern about pollution from fossil fuels has resulted in an increased effort for utilization of low-grade heat sources such as industrial waste heat, solar and other renewable sources. Various thermodynamic cycles have been proposed and studied for conversion of low-grade heat sources into electricity. Among these options, ORCs are reported to be more efficient and commercially implemented in many projects for all the applications mentioned above. However, choice of expander becomes crucial at scales below 50 kWe as the turbine type of expanders tend to exhibit high rotational speeds. Positive displacement device such as the scroll expander has been proposed as a potential candidate for such applications.

Scroll devices have traditionally been used as compressors and have recently been explored as expanders for power generation in small scale ORCs. In the absence of any commercially available scroll expanders, scroll compressors have been modified to operate in the expansion mode and generate expander characteristics. Based on these experimental data, semi-empirical and simulation based models have been developed to extrapolate the expander characteristics. For example, Lemort et al. [1] developed a deterministic model for the scroll expander performance with the experimental data generated from their studies with R245fa as the working fluid in the ORC. Similarly, the modeling tool for simulating the non-uniform wall thickness scroll expanders has been developed by Orosz et al [5]. However, there exist very little guidelines for designing a scroll

expander in a broader perspective, highlighting the consequence of scaling various design parameters. Classical dimensionless techniques like the specific speed *vs* specific diameter diagram ($N_s$-$D_s$ diagram) have been pivotal in understanding of general behavior of the conventional turbomachinery. Use of $N_s$-$D_s$ diagrams helps in the rapid screening of efficient turbine geometries, which are subsequently analyzed in detail using higher order simulation based models. Such a performance analysis of scroll expanders on the $N_s$-$D_s$ diagram has not been done yet in the literature.

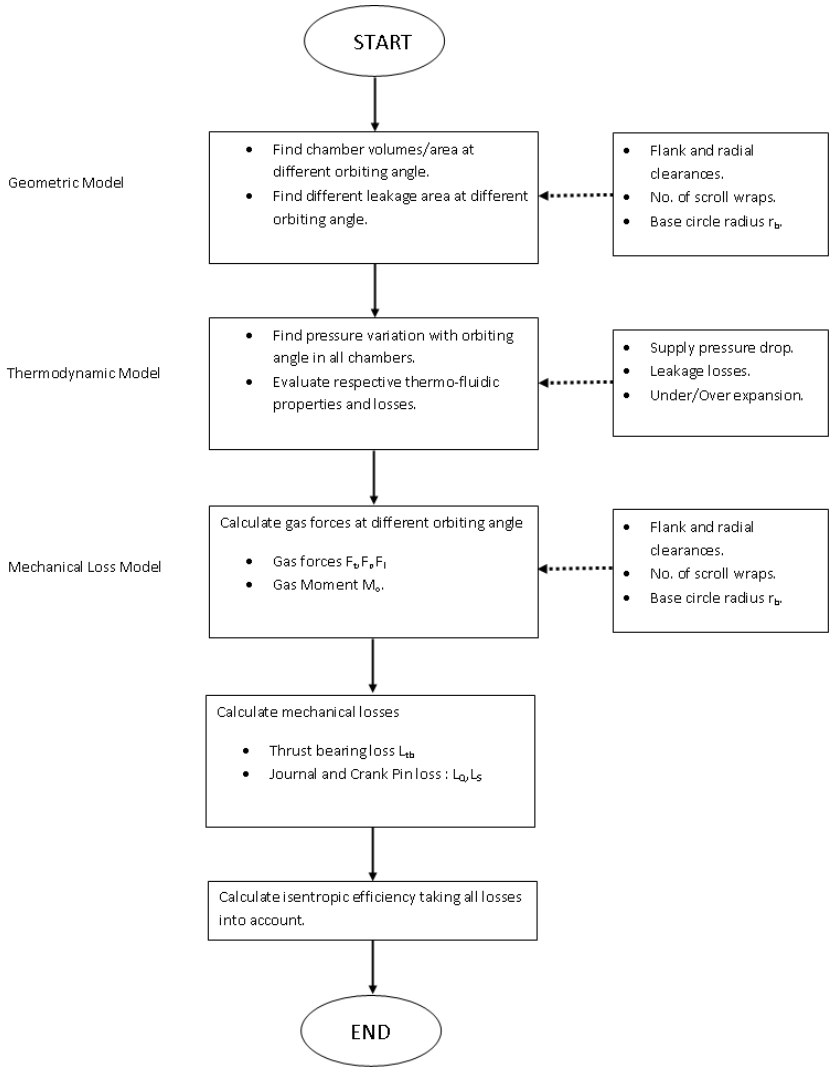


Fig.1. Algorithm of scroll expander's semi-empirical model.

## 2. $N_s$-$D_s$ diagram from semi-empirical model

In this paper, we have relooked at the design of scroll expander using the $N_s$-$D_s$ diagram. To obtain $N_s$-$D_s$ diagram for scroll expander a state of art semi-empirical model has been used, whose logic is shown in flowchart above (Fig. 1). Initially, the scroll is studied in the context of ORC using various iso-curves and best efficiency curve, to understand the causes and consequence of scaling various design parameters. The scroll expander was found to occupy a unique domain in the $N_s$-$D_s$ space, thus signifying potential application in unexplored domain. One such application could be

super critical $CO_2$ cycle, but extensive laboratory and field testing is recommended for conclusively proving such application of scroll expander.

## 3. RESULTS

1) Contours of iso-efficiency lines are superimposed on $N_s$-$D_s$ diagram; this will help rapid selection of an efficient expander for a specific application.

2) Scroll expander's $N_s$-$D_s$ curves are superimposed on those of other turbines/expanders. The unique domain of scroll expander shows its application in domains where conventional turbines haven't found their place.

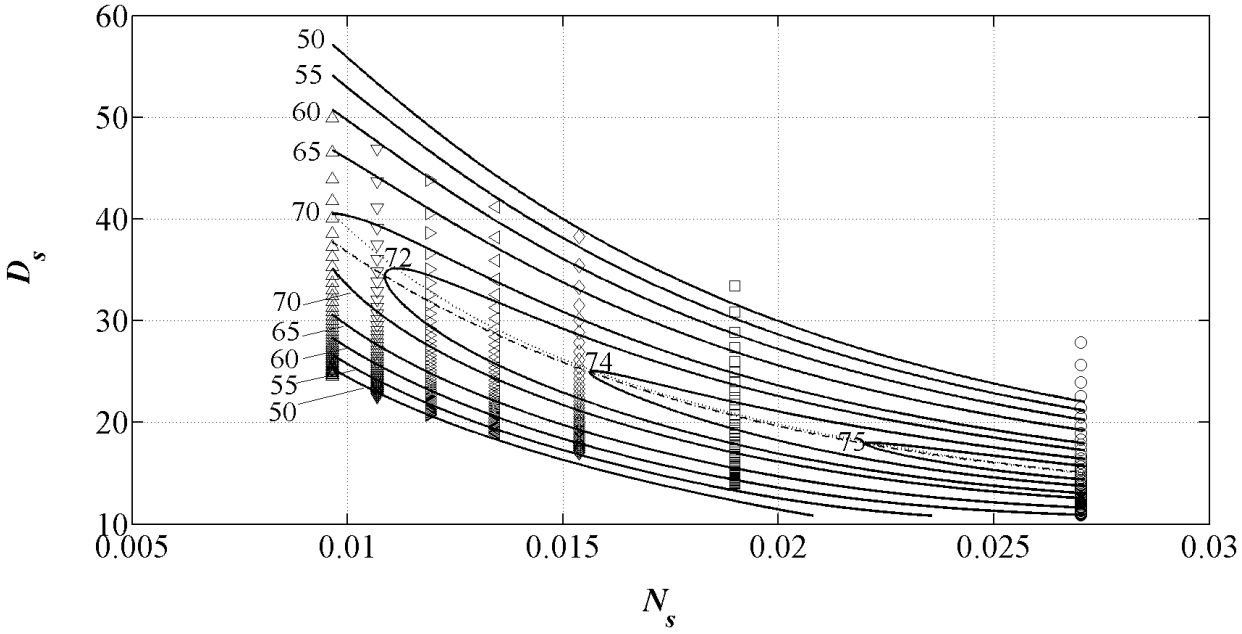


Fig. 2. Contours of iso-efficiency ratio lines on $N_s$-$D_s$ plot for R134a as a working fluid in ORC. Legend: ○ $T_{3'}$ = 89 °C, □ $T_{3'}$ = 100 °C, ◊ $T_{3'}$ = 110 °C, ◁ $T_{3'}$ = 120 °C, ▷ $T_{3'}$ = 130 °C, ▽ $T_{3'}$ = 140 °C, Δ $T_{3'}$ = 150 °C.

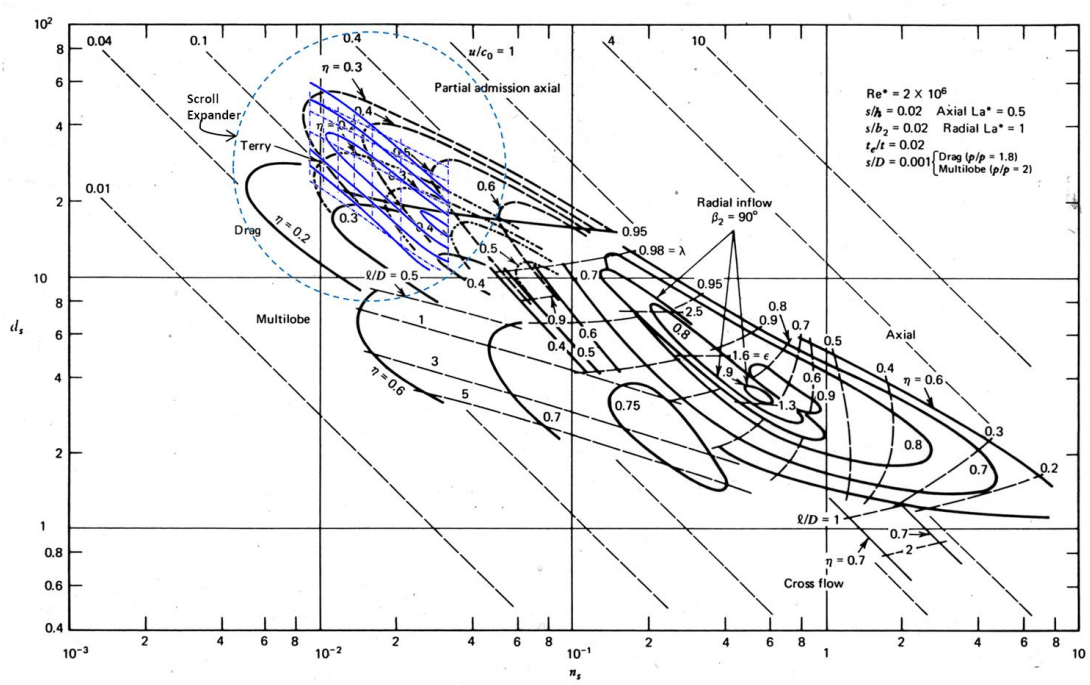


Fig. 3. Scroll expander on $N_s$-$D_s$ diagram along with other type of expanders.

## 4. CONCLUSIONS

In this study, scroll expander has been analyzed on $N_s$-$D_s$ diagram, where a number iso-curves are constructed using a semi-empirical model for a 10 kWe ORC with R134a as working fluid. This technique gives designer a broader perspective, highlighting the causes and consequences of scaling various design parameters. The scroll expander is found to occupy a distinct domain in the $N_s$-$D_s$ space making it a better choice compared to the conventional turbines for small scale applications, thus reconfirming earlier literature work. The unique niche of scroll expander in the $N_s$-$D_s$ domain away from conventional turbines, suggests that it can be applied in unexplored applications.

## REFERENCES

1) V. Lemort, S. Quoilin, C. Cuevas, J. Lebrun, Testing and modeling a scroll expanderintegrated into an Organic Rankine Cycle, Appl. Therm. Eng. 29 (2009) 3094–3102.

2) H.J. Kim, J.M. Ahn, S.O. Cho, K.R. Cho, Numerical simulation on scroll expander–compressor unit for CO2 trans-critical cycles, Appl. Therm. Eng. 28 (2008) 1654–1661.

3) Y. Chen, N.P. Halm, E. a. Groll, J.E. Braun, Mathematical modeling of scroll compressors—part I: compression process modeling, Int. J. Refrig. 25 (2002) 731–750.

4) P. Song, M. Wei, L. Shi, S.N. Danish, C. Ma, A review of scroll expanders for organic Rankine cycle systems, Appl. Therm. Eng. 75 (2015) 54–64.

5) M.S. Orosz, A. V. Mueller, B.J. Dechesne, H.F. Hemond, Geometric Design of Scroll Expanders Optimized for Small Organic Rankine Cycles, J. Eng. Gas Turbines Power. 135 (2013).

Fifth International Conference on Computational Methods for Thermal Problems
THERMACOMP2018, July 9-11, 2018, Indian Institute of Science, Bangalore, INDIA
*N. Massarotti, P. Nithiarasu, Pradip Dutta and C. Ranganyakalu (Eds.)*

# EXPERIMENTAL STUDY OF ROTATING CONVECTION IN A NOVEL CONFIGURATION

**Ayan Kumar Banerjee, Amitabh Bhattacharya, Sridhar Balasubramanian**
Department of Mechanical Engineering, IIT Bombay

## ABSTRACT

Novel laboratory experiments were configured to study convective dynamics and heat transport characteristics in a non-homogeneously heated rotating annulus. The non-homogeneous heating was obtained by imposing a tandem radial and vertical temperature gradient ($\Delta T$). ANSYS-Fluent simulations were also carried out in a 2D axisymmetric plan to mimic one r-z plane of the real experimental set up of the above mentioned configuration.. The parameter range for simulation was $Ra=2.43\times10^8$-$1.2\times10^9$, and Ta= 0-$2.7\times10^9$. The working fluid was water with a Prandtl number, Pr=7. Temperature time series was acquired for varying Ta (i.e. rotation rates, $\Omega$) for two fixed Ra (i.e. $\Delta T$). Vertical temperature profiles showed decreasing impact of thermal forcing with increasing elevation. ANSYS-Fluent simulation combined with experimentally obtained thermal results indicate coexistence and interplay of thermal plumes and baroclinic waves for the present configuration.

**Key Words:** *Heat Transfer, Finite Elements, Natural Convection.*

## 1. INTRODUCTION

Atmospheric general circulation which is an example of rotating convection, is instrumental in understanding large-scale synoptic weather pattern. However, it is difficult to study in the real atmospheric situations due to the fact that in real atmospheric situation, different atmospheric parameters (e.g. temperature, pressure, density etc.) could vary randomly and hence can not be studied in a controlled manner. But these large-scale atmospheric flow phenomena can be studied in laboratory conditions controlling the governing physical parameters. The differentially heated rotating cylindrical annulus of fluid, generally known as Hide-Mason configuration, is generally appreciated as an exquisite experimental setup for studying baroclinic instability mechanism, which is responsible for heat and momentum transport in mid latitude. However, mutual feedback and interaction between the fully developed baroclinic instabilities and background stratification can't be studied in Hide-Mason configuration due to intense boundary layer dominated overturning circulation. Hence, a new system is proposed consisting of a inhomogeneously heated fluid annulus where the inner wall is maintained at a constant colder temperature and the periphery is heated on the bottom using a 'thin' Al strip. Therefore, this new configuration is subjected to differential heating on bottom like horizontal convection system and simultaneously a radial gradient is imposed on a similar fashion to Hide-Mason configuration. This system will provide a better understanding of the heat transport from the strong convection near the tropics to the stably-stratified mid-latitude.

## 2. . ANSYS-FLUENT SIMULATION RESULTS

ANSYS Fluent was used to simulate the flow dynamics in a 2D axisymmetric plane as geometry of the cylindrical annulus is symmetric with respect to the axis of rotation. The plane for simulation mimics *r-z* plane in the experimental set up whose vertical edges (left and right) represent the outer and inner radiuses respectively of the cylindrical annulus used in lab experiment (Figure 6). Simulations were done for $Ra = 2.43\times10^8$ - $1.2\times10^9$ and $Ta = 0$ - $2.7\times10^9$. Different *Ra* and *Ta* were achieved by keeping $\Delta T = 15$ K (288 K in inner cylinder and 303 K in outer periphery) and $\Delta T = 10$ K (293 K in inner cylinder and 303 K in outer periphery) and $\Omega$=0.141-0.289 rps. All the boundaries were kept at no-slip and isothermal condition (except right vertical edge and small narrow part on bottom). Aspect ratio for the simulation was 1 similar to experiment. All the simulations were done using laminar-simulation option owing to the fact that Reynold number (*Re*) in the present configuration is very small (of the order 40-400). Therefore, no schemes for analyzing turbulence works well enough at that limit.

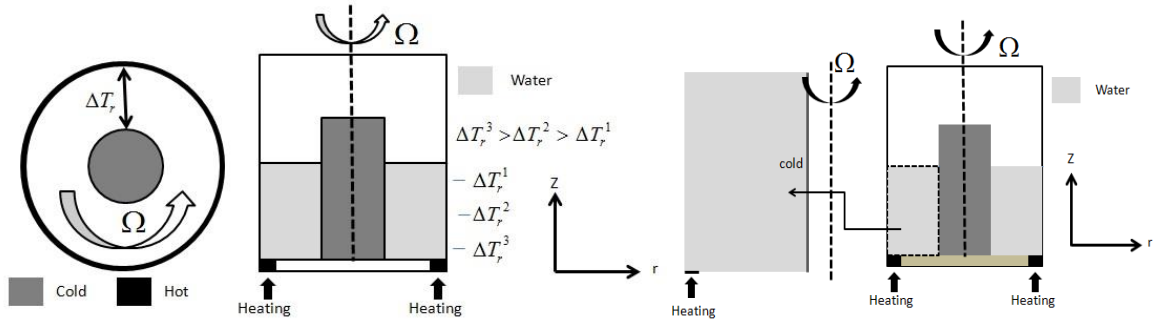


(a) (b)

Figure 1. (a) SCHEMATIC OF EXPERIMENTAL SET UP ([19-20]) (b) VERTICAL PLANE FOR SIMULATION

Various contour plots (velocity, temperature fields) were simulated of , which plots for $Ra = 3.66 \times 10^8$ and various *Ta* are shown below:

*1. Relative axial velocity:*

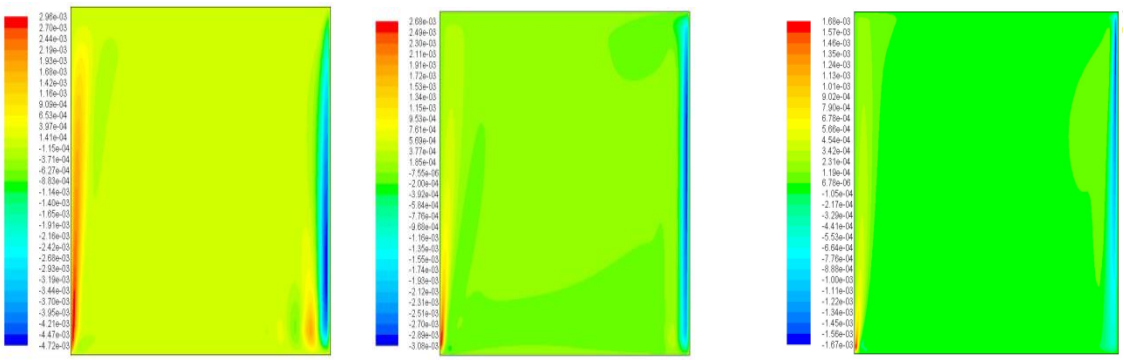

(a) (b) (c)

Figure 2. (a) $Ta=0$, (c) $Ta=2\times 10^7$, (e) $Ta=6.45\times 10^8$

In most of the cases buoyancy driven upward flow (convective plume) is found to have existed near outer periphery and sinking downward motion exists near cold inner wall. Bulk flow field in between inner and outer wall has near zero downward velocity. However, axial velocity contour turns up to be chaotic for very high *Ta.*

*2. Relative radial velocity:*

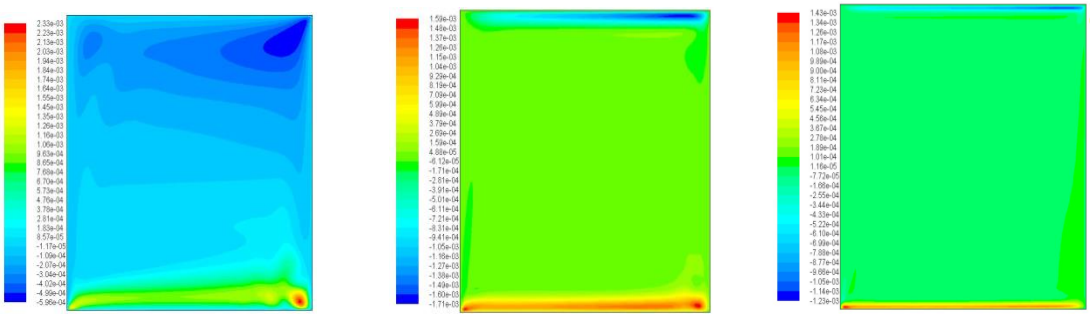

(a) (b)

Figure 3. (a) $Ta$=0, (b) $Ta$=2× $10^7$, (c) $Ta$=6.45× $10^8$

In general, relative radial velocities exist only near boundary (towards inner wall on bottom and towards outer wall on top) for rotating cases. However, relative radial velocity contour turns up to be chaotic for very high *Ta.* Bulk flow field in between inner and outer wall has near zero relative radial velocity.

*5.Static temperature:*

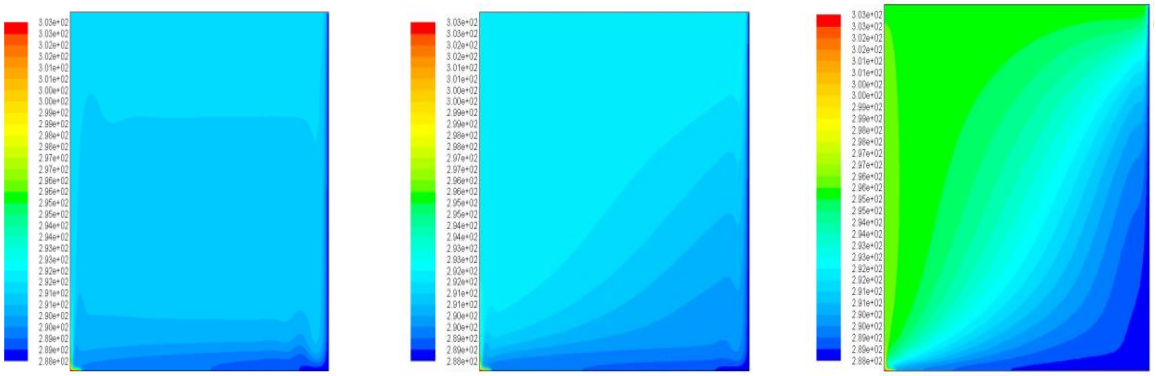

(a) (b)

Figure 5. (a) $Ta$=0, (c) $Ta$=2× $10^7$, (e) $Ta$=6.45× $10^8$

Static temperature contour is very interesting. Slant isotherms are due to baroclinicity. It is also found that temperature between outer and inner radius tend to be homogeneous very slowly as time elapses indicating that the heat transfer process is very slow in the present configuration. It shows that impact of heating decreases with elevation as was also found from temperature time series data.

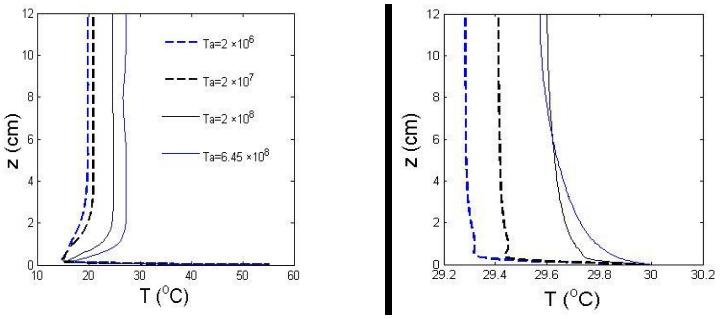


(a) (b)

Figure 6. *T* vs *z* for (a) Ra=3.66× $10^8$ and (b) Ra=2.44× $10^7$

Based on simulation data, *T* vs *z* near outer wall, at Ra=6.45× $10^8$ for two different *Ta* are plotted in Figure 13. It is evident that simulated *T* vs *z* matches qualitatively well with *T* vs *z* obtained experimentally. Similar to experimentally obtained plot, Figure 13a also shows decrease in *T* occurs approximately up to z=1 cm, then increases approximately up to z=3 cm and then onwards it remains fairly constant along the vertical height. Whereas for very small $\Delta T$, therefore for small *Ra*=2.44× $10^7$, decrease in *T* occurs approximately up to *z*=1 cm, then onwards it remains fairly constant along the vertical height due to decreasing bottom heating influences over the vertical height. However, quantitative mismatch is expected due to 2D nature of the simulation which constrains secondary flow structures in azimuthal direction.

## 4. CONCLUSIONS

Rotating convection in a new configuration with localized bottom heating and central cooling is studied by simulation . The present paper primarily focuses on vertical distribution of instantaneous temperature near outer wall and different contour plots (temperature, relative velocity) from 2D axisymmetric Ansys-Fluent simulation. Relative axial velocity contour plots shows existence of thermal plume (near outer wall) and experimental visualization on horizontal plane shows wandering baroclinic waves, thereby hinting at coexistance of convective plume and baroclinic waves (in bulk). Different modes of heat transport for rotating and non-rotating convection was also implied from it. Vertical distribution of instantaneous temperature data at steady state implies existence of two different layers, one near boundary layer and the other outside the boundary layer in a geostrophic balance.

## REFERENCES

[1] Banerjee. A. K, Tirodkar. S, Bhattacharya. A, and Balasubramanian. S, 2016 , Convection in rotating flows with simultaneous imposition of radial and vertical temperature gradients, arXiv preprint arXiv:1611.00807

[2] Banerjee. A. K, Bhattacharya. A, and Balasubramanian. S, 2018, Study of rotating convection in the presence of combined radial and vertical thermal gradient, *Phy Fluids*, **(Submitted)**

[3] Y.G.Park and J.A.Whitehead,(1998). Rotating Convection Driven by Differential Bottom Heating," *J. phy. Oceanography*,vol. 19.

[4] Hignett et. al,On rotating thermal convection driven by non uniform heating from below. *J. Fluid Mech.*, vol. 109, pp. 161-187, 1981.

Fifth International Conference on Computational Methods for Thermal Problems
THERMACOMP2018, July 9-11, 2018, Indian Institute of Science, Bangalore, INDIA
*N. Massarotti, P. Nithiarasu, Pradip Dutta and C. Ranganyakalu (Eds.)*

# NUMERICAL INVESTIGATIONS OF CONJUGATE NATURAL CONVECTION IN A SQUARE CAVITY FILLED WITH NANOFLUID WITH TEMPERATURE VARIATIONS ONHORIZONTAL WALLS

**Balesh Babali[1], Aswatha[2], and K.N. Seetharamu[3]**

[1] Department of Mechanical Engineering, PES University, Bangalore–560085,
balesh39@gmail.com
[2] Department of Mechanical Engineering, Bangalore Institute of Technology, Bangalore–560 004,
aswath_bit@yahoo.co.in
[3] Professor, Department of Mechanical Engineering, PES University, Bangalore–560085,
knseetharamu@yahoo.com

## ABSTRACT

The problem of conjugate natural convection in a square cavity filled with a nanofluid with sinusoidal temperature variations on both horizontal walls is visualized by streamlines and isotherms. Water-based nanofluids with Ag, Cu, $Al_2O_3$, nanoparticles are chosen for investigation. The governing equations together with the specified boundary conditions are solved numerically using the finite difference method over a wide range of Rayleigh number ($10^3 < Ra < 10^7$), wall to nanofluid thermal conductivity ratios (0.5 Kr 1) and wall thickness to height ratios varied. Comparisons with previously published work verify good agreement with the proposed method. Detailed computational results for the influence of the various parameters on streamlines, isotherms, and the overall heat transfer are shown graphically. It is found that the heat transfer rate is significantly enhanced by incrementing the solid wall thickness. Different values of the thermal conductivity ratio are shown to depict a variety of enhancements for the heat transfer rate.

***Key Words:*** *Conjugate natural convection, Nanofluid, Sinusoidal conditions, Finite difference method.*

## 1. INTRODUCTION

Conjugate natural convection heat transfer is an important phenomenon in engineering systems because of its wide range of applications in electronic cooling, heat exchangers, and double pane windows. Conjugate natural convection heat transfer occurs in cavities and is caused by temperature differences and buoyancy forces. It can be analysed by using cavities filled with a clear fluid or nanofluid. The low thermal conductivity of conventional heat transfer fluids such as water and oils is a primary limitation to enhancing the performance and compactness of many electronic engineering devices. Solids typically have a higher thermal conductivity than liquids. For example, copper (Cu) has a thermal conductivity 700 times greater than water and 3000 times greater than engine oil. A new innovative technique to enhancing heat transfer is by using solid nanoparticles with diameters of 10–50 nm in a base fluid (i.e. nanofluids). Because of the small size and very large specific surface area of the nanoparticles, nanofluids have superior properties such as high thermal conductivity, minimal clogging of flow passages, long term stability, and homogeneity. Thus, nanofluids have a wide range of potential electronic, automotive, and nuclear applications where improved heat transfer or efficient heat dissipation is required. An early study considered heat transfer enhancement in a differentially heated cavity by using the finite volume method. The suspended nanoparticles were found to substantially increase the heat transfer for all of the given Rayleigh number.

## 2. MAIN BODY

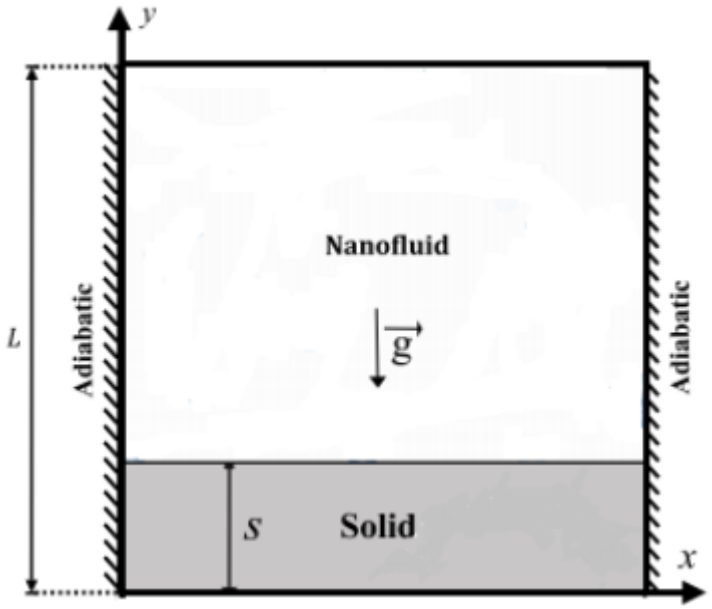


Consider two-dimensionalsteady natural convection in a square cavity with length L, as illustrated in Fig. 1. The top and bottom horizontal walls of the cavity have varying sinusoidal temperature distributions, while the left and right vertical walls thermally insulated. The boundaries of the annulus are assumed to be impermeable; the fluid within the cavity is a water-based nanofluids having Ag, Cu or $Al_2O_3$ nanoparticles. The Boussinesq approximation is applicable; the nanofluid physical properties are constantexcept for the density.

## 3. RESULTS

| Heating type | Aspect ratio (*AR*) | Rayleigh number range | Bottom Wall | | | Side Wall | | |
|---|---|---|---|---|---|---|---|---|
| | | | Correlation | $R^2$ | % Error | Correlation | $R^2$ | % Error |
| Sinusoidal temperature | 0.5 | $10^4$ to $10^7$ | $Nu_{avg} = 0.121Ra^{0.247}$ | 0.999 | < 1.5 | $Nu_{avg} = 0.240Ra^{0.246}$ | 0.999 | < 1.5 |
| | 1 | $2x10^4$ to $10^5$ | $Nu_{avg} = 0.298Ra^{0.249}$ | 0.999 | < 1.0 | $Nu_{avg} = 0.154Ra^{0.242}$ | 0.999 | < 1.0 |
| | | $10^5$ to $10^7$ | $Nu_{avg} = 0.272Ra^{0.261}$ | 0.998 | < 2.0 | $Nu_{avg} = 0.072Ra^{0.305}$ | 0.999 | < 2.0 |
| | | $2x10^4$ to $10^7$ | $Nu_{avg} = 0.248Ra^{0.267}$ | 0.999 | < 2.9 | $Nu_{avg} = 0.088Ra^{0.292}$ | 0.998 | < 3.0 |
| Linearly varying temperature | 0.5 | $10^4$ to $10^7$ | $Nu_{avg} = 0.288Ra^{0.181}$ | 0.997 | < 2.0 | $Nu_{avg} = 1.553Ra^{0.133}$ | 0.998 | < 1.5 |
| | 1 | $10^5$ to $10^7$ | $Nu_{avg} = 0.374Ra^{0.213}$ | 0.998 | < 3.0 | $Nu_{avg} = 0.050Ra^{0.287}$ | 0.998 | < 3.0 |
| | | $2x10^4$ to $10^7$ | $Nu_{avg} = 0.378Ra^{0.212}$ | 0.997 | < 3.0 | $Nu_{avg} = 0.053Ra^{0.284}$ | 0.998 | < 3.0 |

**Table 1 Correlation of Nusselt number with Rayleigh number**

Correlations of average Nusselt number with Rayleigh number

Case (a) sinusoidal temperature;

The correlations presented in the table 1 for sinusoidal temperature variation at bottom wall is very close to that of reference with a maximum error of 1%. However the error increases to a maximum of 3% when Ra ranges from $2x10^4$ to $10^7$.

Case (b) linearly varying temperature;

The correlation presented in the table 1 for linearly varying temperature at bottom wall in the range of Ra $10^5$ to $10^7$ exhibits a maximum error of 3%. It is also observed that when the range of Ra is from Ra $2x10^4$ to $10^7$ the maximum error is 3% for the bottom wall. However for the side wall the maximum error is seen to be 3.5.

## 4. CONCLUSIONS

This study considered the visualization of temperature and stream function on conjugate natural convection in a square cavity filled with nanofluid with sinusoidal temperature variations on both horizontal walls. The finite difference method was applied to solve the non-dimensional governing equations together with the specified boundary conditions.

- Phase deviation increment significantly affects flow behavior and temperature distribution within the cavity. This is due to the difference of the sinusoidal temperature variations on the horizontal walls.
- Significant enhancement of streamlines and temperature profiles occur with increasing solid wall thickness. At low thickness, a second streamline cell occurs in the anticlockwise direction at the top right corner of the cavity. Streamline flow circulation maximum strength increases whereas the minimum decreases with insertion of the solid wall, due to the resistance of the solid wall.
- The local Nusselt number shows that convection heat transfer is significantly enhanced with sinusoidal temperature variations both horizontal walls.
- The average Nusselt number significantly increases with increasing nanoparticle volume fractions, due to the higher thermal conductivity of the nanoparticles. Significant increment of convection heat transfer occurs for increasing phase deviation.

## 5. REFERENCES

[1] S. Ostrach, "Natural convection in enclosures", J. Heat Transfer 110 (1988) 1175 1190.

[2] J. Eastman, S. Choi, S. Li, W. Yu, L. Thompson, anomalously increased effective thermal conductivities of ethylene glycol-based nanofluids containing copper nanoparticles, Appl. Phys. Lett.78 (2001) 718–720.

[3] H.F. Oztop, E. Abu-Nada, "Numerical study of natural convection in partially heated rectangular enclosures filled with nanofluids", Int. J. Heat Fluid Flow 29(2008) 1326–1336.

[5] K. Khanafer, K. Vafai, M. Lightstone, "Buoyancy-driven heat transfer enhancement in a two-dimensional enclosure utilizing nanofluids", Int. J. Heat Mass Transfer 46 (2003) 3639–3653

[6] R.Y. Jou, S.C. Tzeng, "Numerical research of nature convective heat transfer enhancement filled with nanofluids in rectangular enclosures", Int. Commun. Heat Mass Transfer 33 (2006) 727–736.

[7] R.K. Tiwari, M.K. Das, "Heat transfer augmentation in a two-sided lid-driven differentially heated square cavity utilizing nanofluids", Int. J. Heat Mass Transfer 50 (2007) 2002–2018.

[8] Z. Alloui, P. Vasseur, M. Reggio, "Natural convection of nanofluids in a shallow cavity heated from below", Int. J. Therm. Sci. 50 (2011) 385–393.

[9] H.F. Oztop, M. Mobedi, E. Abu-Nada, I. Pop, "A heat line analysis of natural convection in a square inclined enclosure filled with a CuO nanofluid under non-uniform wall heating condition" Int. J. Heat Mass Transfer 55 (2012) 5076–5086.

[10] D. Kaminski, C. Prakash, "Conjugate natural convection in a square enclosure: effect of conduction in one of the vertical walls", Int. J. Heat Mass Transfer 29(1986) 1979–1988.

Fifth International Conference on Computational Methods for Thermal Problems
THERMACOMP2018, July 9-11, 2018, Indian Institute of Science, Bangalore, INDIA
*N. Massarotti, P. Nithiarasu, Pradip Dutta and C. Ranganyakalu (Eds.)*

# PREDICTION OF HEAT TRANSFER WITH DISCRETE HEAT SOURCES IN A VERTICAL CHANNEL FILLED WITH HIGH POROSITY METAL FOAM

**Banjara Kotresha, N Gnanasekaran**
Department of Mechanical Engineering, National Institute of Technology Karnataka, Surathkal, Mangaluru-57502, bkotresha@gmail.com, gnanasekaran@nitk.edu.in

## ABSTRACT

This paper discusses about the numerical prediction of isothermal condition with discrete heat sources in a vertical channel filled with high porosity metal foams. The problem considered consists of a vertical channel in which discrete heat source assembly is placed at the centre and high porosity metal foams are placed on either side of the aluminium plates to enhance the heat transfer. The flow through the metal foam porous medium is predicted by using Darcy Extended Forchheimer model and Local thermal non-equilibrium model as well as local thermal equilibrium model is used for heat transfer prediction. The results are presented in terms of temperature excess over the ambient for both empty and metal foam filled channel. Finally, the heat input through the discrete heat sources is varied to obtain an isothermal condition on all the heat sources at a constant inlet velocity.

**Key Words:** *Heat Transfer, Discrete heat sources, metal foam, vertical channel, LTE, LTNE.*

## 1. INTRODUCTION

Metal foams are receiving considerable attention in thermal applications because of its distinct properties such as high surface area density, ability to increase turbulence, interconnected voids etc. Hotta et al. [1] experimentally determined the optimal distribution and configurations of heat sources on a substrate under natural convection. They studied the effect of surface radiation for determining optimal configuration and developed correlations for the same. Thermal transport in high porous metal foams has been reviewed by Zhao [2]. The review mainly focuses on forced convection of single phase, flow boiling and pool boiling heat transfer and thermal radiation in high porosity cellular metal foams. Calmidi and Mahajan [3] analyzed different pore density aluminum metal foams of varying porosity ranging from 0.89 to 0.97. They reported that the thermal dispersion is negligible in the foam – air combination due to high thermal conductivity of the solid matrix of metal foams. Lu et al. [4] carried out analytical studies on forced convection through horizontal plate channel partly filled with metal foams. They predicted the velocity distribution and temperature profile for the entire domain for different pore densities and also examined for different porosities of the metal foam. Sener et al. [5] carried out experimental study on aluminum metal foam filled in a rectangular channel for calculating pressure drop and heat transfer. They concluded that heat transfer in the channel increases with increasing filling rate of the foam. Yu and Joshi [6] experimentally studied the heat transfer enhancement in a pin fin heat sinks in horizontal and vertical orientations from enclosed discrete components for closed and vented enclosures. They concluded that the completely closed enclosures have lower thermal resistance compared to the vertical orientation. Kamath et al. [7] carried out experiments on high porosity aluminum metal foams filled in a vertical channel. They identified the mixed and forced convection regions based on Reynolds and Richardson numbers of the flow. Many researchers [8-9] perfomed optimization studies on discrete heat sources involving porous medium.

Based on the above literature it is has been identified that the numerical studies on discrete heat sources are inadequate. Therefore, the objective of the present study is to predict the isothermal

condition on all the heat sources by varying the heat inputs at a constant inlet velocity in a vertical channel filled with aluminum and copper metal foams.

## 2. Physical and Computational domain

The physical domain considered for the present study consists of vertical channel in which discrete heat source assembly is placed at the centre of a channel and high porosity metal foams are placed on either side heater assembly to enhance the heat transfer. The size of the aluminium strips is 20 x 250 x 3 (all in mm), Bakelite strips are 22.5 x 250 x 7 and the metal foam has a size of 150 x 250 x 20 (all in mm). The physical geometry considered in the present simulation is shown in Figure 1. Since the domain is symmetrical about the Y axis, only a two dimensional computational domain is considered for the computations which consists of one side discrete heater plate assembly, one side metal foam, upstream and downstream of the channel as shown in Figure 2. The boundary conditions used for the computational domain are also shown in Figure 2. The metal foam characteristics used for the heat transfer enhancement in the present study are listed in Table 1.

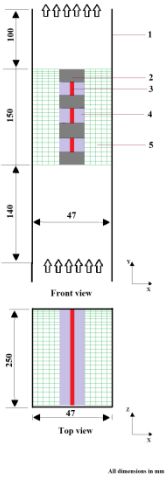


FIGURE 1. Physical domain considered for the present study 1) Wall 2) Bakelite 3) heater 4) Aluminium strip 5) metal foam

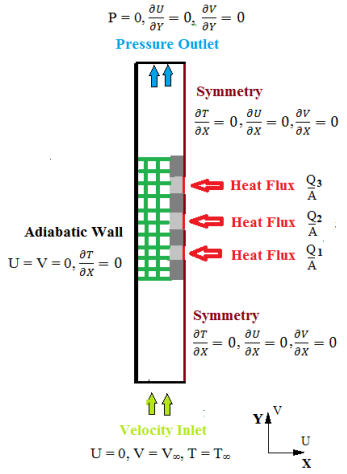


FIGURE 2. Computational domain with boundary condition

| Material 10PPI | Porosity | Diameter (mm) | | Permeability (K, x $10^{-7}$ $m^2$) | Form drag coefficient (C) | Surface area density ($a_{sf}$, $m^{-1}$) |
|---|---|---|---|---|---|---|
| | | Pore | Fibre | | | |
| Aluminum | 0.94 | 4.982 | 0.526 | 6.706 | 167.56 | 440.25 |
| Copper | 0.86 | 4.732 | 0.703 | 4.779 | 225.48 | 824.72 |

TABLE 1. Metal foam characteristics

## 3. RESULTS

The two dimensional numerical simulation is carried out by using commercially available ANSYS FLUENT software. The metal foam region in the computations is considered as an isotropic

homogeneous porous medium. The Darcy Extended Forchheimer model is used to predict the flow characteristics through the metal foam region. The heat transfer through the metal foams which are beside the Bakelite strips are predicted with LTE thermal model and metal foams which are adjacent to the discrete heat sources are calculated with LTNE thermal model. Air is considered as the working fluid which is flowing through open region as well as metal foam region and the properties of the air is taken at an inlet temperature of $30^0$ C. For the purpose of validation, the results of the pressure drop and the excess temperature obtained for 10PPI aluminium metal foam filled in the vertical channel with single full length heater are compared with the experimental results of Kamath et al. [7] and are shown in Figure 3. From the plots of pressure drop and temperature difference, it is clear that the numerical results obtained are in good agreement with the experimental results.


(a) (b)

FIGURE 3. Comparison of present simulation results with experimental benchmarks for (a) pressure drop (b) temperature difference

Figure 4 shows the excess temperature variation with respect to the inlet velocity for an equal heat input of 9.2W for all the three heaters for an empty channel. From the plot it is clear that the bottom heater is able to take more heat compared to middle and top heaters. In the second case a total input of 70W is supplied to all the heaters in such a way that the bottom heater is supplied with 40W, middle heater is supplied with 20W and top heater supplied with 10W. The excess temperature variation for unequal heat input for both with and without metal foam is presented in Figure 5. It is clear from the plot that the metal foams significantly enhance the heat transfer.

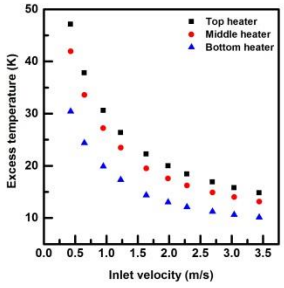


FIGURE 4. Temperature excess variation for equal heat input for empty channel

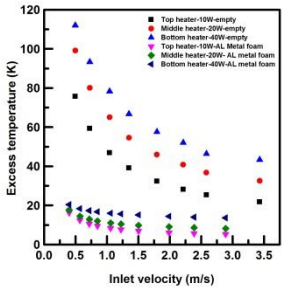


FIGURE 5. Temperature excess variation for unequal heat input for empty channel and aluminium metal foam

To get an optimal heat input condition on all the heaters, a fixed inlet velocity of 0.54 m/s is considered and the heat inputs are varied. Figure 6 shows the isothermal condition obtained by using aluminium and copper metal foams. The optimal design condition for aluminium metal foam is 32W for bottom heater, 22W for middle heater and 16W for top heater. Similarly with the use of

copper metal foam the optimal condition is 34W for bottom heater, 21W for middle heater and 15W for top heater.


(a) (b)

FIGURE 6. Aluminium strip surface temperature for optimal heat input (a) aluminium metal foam (b) copper metal foam

## 4. CONCLUSIONS

The numerical simulation of heat transfer through high porosity metal foams with discrete heat sources is carried out using commercially available FLUENT software. The use of metal foams significantly improves the heat transfer in the range of velocities studied. The aluminium and copper metal foams are used for the prediction of isothermality condition on all aluminium strips at a constant inlet velocity of 0.54 m/s. The aluminium metal foam gives an optimal design for the heat input of $Q_1$=32W, $Q_2$=22W and $Q_3$=16W and copper metal foam predicted at $Q_1$=34W, $Q_2$=21W and $Q_3$=15W.

## REFERENCES

[1] T. K. Hotta, P. Muvvala and S. P. Venkateshan, Effect of surface radiation heat transfer on the optimal distribution of discrete heat sources under natural convection, Heat and Mass Transfer, 49, 207-217, 2013.

[2] C.Y. Zhao, "Review on thermal transport in high porosity cellular metal foams with open cells", International Journal of Heat and Mass Transfer, 55, pp. 3618–3632, 2012.

[3] V. Calmidi and R. Mahajan, Forced convection in high porosity metal foams, ASME Journal Heat Transfer, 122, 557–565, 2000.

[4] W. Lu, T. Zhang and M. Yang, Analytical solution of forced convection heat transfer in parallel-plate channel partially filled with metallic foams, International Journal of Heat and Mass Transfer, 100,718-727, 2016.

[5] M. Sener, A. Yataganbaba and I Kurtbas, Forchheimer forced convection in a rectangular channel partially filled with aluminum foam, Experimental Thermal and Fluid Sciences, 75, 162-172, 2016.

[6] E. Yu and Y. Joshi, Heat transfer enhancement from enclosed discrete components using pin-fin heat sinks, International Journal of Heat and Mass Transfer, 45(25), 4957-4966, 2002.

[7] P. M. Kamath, C. Balaji, S. P. Venkateshan, Experimental investigation of flow assisted mixed convection in high porosity foams in vertical channels, International Journal of Heat and Mass Transfer, 54, 5231-5241, 2011.

[8] G. Kumar, C. Rao, Interaction of surface radiation with conjugate mixed convection from a vertical plate with multiple nonidentical discrete heat sources, Chemical. Engineering Communication, 198 (5), 692–710, 2011.

[9] A.K. da Silva, S. Lorente, A. Bejan, Optimal distribution of discrete heat sources on a wall with natural convection, Int. J. Heat Mass Transf. 47 (2), 203–214, 2004.

Fifth International Conference on Computational Methods for Thermal Problems
THERMACOMP2018, July 9-11, 2018, Indian Institute of Science, Bangalore, INDIA
*N. Massarotti, P. Nithiarasu, Pradip Dutta and C. Ranganyakalu (Eds.)*

# VORTEX TUBE BASED EXPANSION DEVICE FOR VAPOUR COMPRESSION REFRIGERATION SYSTEM

**Irwin O. Toppo, Vishal Singh, Bhajneet Singh**
Department of Mechanical and Automation Engineering, GB Pant Government Engineering College, Okhla-III, New Delhi-110020, India

irwinosmond@gmail.com, vishal.singh.1404@gmail.com, singh84b@gmail.com

## ABSTRACT

An experimental and numerical investigation into the possibility of using counter flow vortex tube as a substitute to throttling valve in vapour compression refrigeration system with air as a refrigerant has been carried out. The output characteristics like cold outlet temperature, hot outlet temperature and cold fraction were studied by varying input parameters.

**Key Words:** *Vortex tube, Vapour compression refrigeration (VCR), Expansion device.*

## 1. INTRODUCTION

The Ranque-Hilsch vortex tube is a device without any moving parts that separates a compressed gas stream into a low temperature stream and a high temperature stream due to expansion of rapidly moving gas vortex [1]. The flow is internally separated in layers rotating at different radii. The flow along the periphery becomes hotter as kinetic energy is converted into heat energy due to viscous dissipation and the axially flowing stream looses its energy to the outer flowing stream thus cooling down.

Vortex tube is utilized in machine cooling, injection mould cooling, etc. as an independent refrigeration system due to its simplicity, durability, compactness, safety, robustness but its low COP and high cost makes is less preferable for other applications [1][2]. However, with some design modifications its cost can be reduced drastically and it can be utilized as a replacement to throttling valve in VCR system providing an expansion device that can withstand high pressure as well as maintain subcritical cycle for $CO_2$ [3].

## 2. DESIGN

The high cost of the commercial vortex tube overshadows the performance improvement of the vapour compression refrigeration system. Thus, a counter flow tube was redesigned with economic considerations using relative design parameters available in the literature. For instance, the length to inlet diameter ratio should be around 30:1 to 50:1 for optimum results [4]. Similarly, smaller cross-section area of cold outlet is necessary for the occurrence of secondary cold stream and a diameter of 6mm is optimum for reaching the minimum cold gas temperature [5].

AISI 1080 was used to keep the cost low and the tube was designed in five different parts for the ease of manufacturing. The inlet enclosure provides the casing to the vortex generator and acts as a reservoir for the compressed gas. The vortex generator swirls the incoming gas which is carried through the main tube towards the hot outlet while a part of the gas returns axially along the divergent tube to exit at the cold end. At the hot outlet, a control knob was fixed to adjust the mass fraction leaving the hot end which will eventually affect the temperature difference between the hot and cold stream.

(a) Inlet enclosure (b) Vortex generator (c) Divergent tube

FIGURE 1. Components of vortex tube

The individual components manufactured by machining (see Figure 1) were welded together to complete the assembly. The experimental setup comprised of the vortex tube, air compressor, pressure gauges and thermostat. Some crucial dimensions of the vortex tube are as follows:

- Diameter of the inlet = 15 mm
- Length of the main tube = 620 mm
- Number of inlets of Vortex Generator = 4
- Diameter of the inlet of vortex generator = 6 mm
- Diameter of the hot outlet = 26 mm
- Diameter of the cold outlet = 8 mm

## 3. RESULTS

The vortex tube was tested experimentally by varying inlet pressure and corresponding changes in cold outlet temperature, hot outlet temperature and cold fraction were recorded. Also, 3-D transient numerical analysis was conducted using mesh shown in Figure 2. Standard k-epsilon model was used for modelling turbulence.

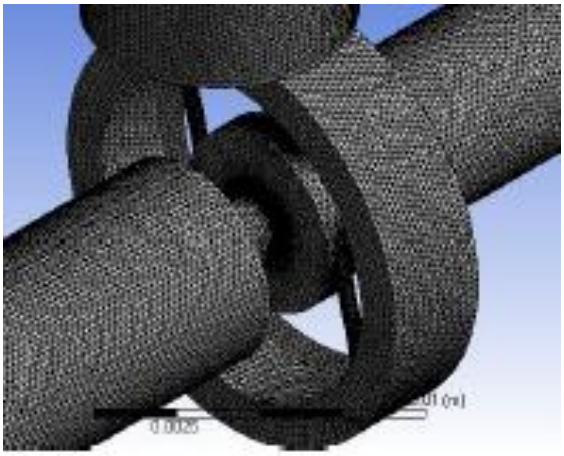

FIGURE 2. Computational mesh near vortex generator

The obtained experimental and numerical results were validated with the existing literature [6]. Figure 3 shows the static pressure at cold and hot exit for different values of cold fraction. The results obtained for cold exit pressure are in close agreement with those reported in the literature [6]. In contrast, the values of hot exit pressure differ significantly from the results available in

literature which can be due to difference in the dimensions of the vortex tube that has been used for the present study.

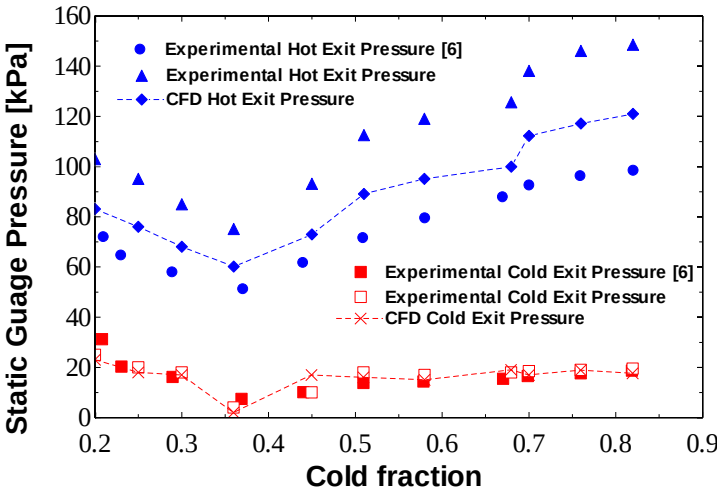


FIGURE 3. Cold exit and hot exit pressure at various cold fraction

The variation of cold and hot temperature separation with respect to cold fraction is shown in Figure 4. The experimental and CFD results of the present study show the same trend as obtained by the experimental results reported in the literature [6] but both the experimental and CFD values are much higher due to the change in the dimensions of the vortex tube.

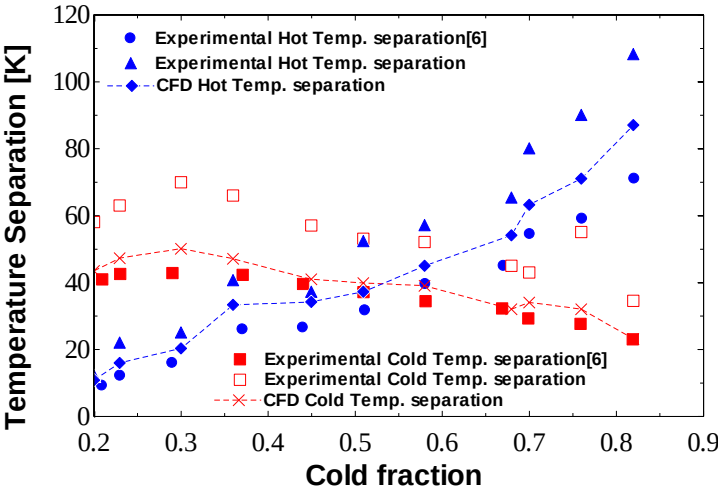


FIGURE 4. Cold temperature and hot temperature separation at various cold fractions

## 4. CONCLUSIONS

In the present study, experimental and CFD analysis of counter flow vortex tube as an expansion device for a vapour compression system has been done. The locally manufactured low cost vortex tube has been used instead of commercially available vortex tube. Static pressure and temperature separation were recorded at different cold fraction and the trend has been similar with the results obtained for commercially available vortex tube. In future, the device will be tested for suitability with other refrigerants and the effect on the COP of the system will be studied.

## REFERENCES

[1] Hilsch, R., The use of the expansion of gases in a centrifugal field as cooling process, *Review of Scientific Instruments*, 18(2), 108-113, 1947.

[2] Ahmad-Yazid, A., & Almanar, I. P., A review of cryogenic cooling in high speed machining (HSM) of mold and die steels, *Scientific Research and Essays*, 5(5), 412-427, 2010.

[3] Li, D., Baek, J.S., Groll, E., & Lawless, P.B., Thermodynamic analysis of vortex tube and expansion work output devices for the transcritical carbon dioxide cycle, *Science et technique du froid*, 463-470, 2001.

[4] Kargaran, M., & Farzaneh-Gord, M., Experimental Investigation the effects of Orifice Diameter and Tube Length on a Vortex Tube Performance, *International Journal of Recent Advances in Mechanical Engineering*, 2(3), 1-8, 2013.

[5] Behera, U., Paul, P.J., Kasthurirengan, S., Karunanithi, R., Ram, S.N., Dinesh, K., & Jacob, S., CFD analysis and experimental investigations towards optimizing the parameters of Ranque–Hilsch vortex tube, *International Journal of Heat and Mass Transfer*, 48(10), 1961-73, 2005.

[6] Skye, H. M., Nellis, G. F., & Klein, S. A., Comparison of CFD analysis to empirical data in a commercial vortex tube, *International Journal of Refrigeration*, 29(1), 71-80, 2006.

**Computational Methods for Thermal Problems**
**ThermComp 2018**
**9-11 July 2018, IISc Bangalore**
**India**

# AXIAL LOAD ESTIMATION OVER IMPELLER OF CENTRIFUGAL PUMP FOR AERO ENGINES

**TV Yogesh**
yogesh_tv@gtre.drdo.in

**Navin Anand**
nanand@gtre.drdo.in

**Poornima N**
Poornima4777@gmail.com

**Vimala Narayanan**
vimala@gtre.drdo.in

**Kishore Prasad**
kishore_d@gtre.drdo.in

Gas Turbine Research Establishment, CV Raman Nagar, Bangalore, Karnataka, India

## ABSTRACT

Centrifugal pump is a rotating machine in which flow and pressure are generated dynamically. The disciplined one dimensioned thinking and analysis enables one to deduce pump operational characteristics at both the optimum/design conditions and off design conditions. This enables the designer or user to judge whether the pump and the fluid system in which it is installed will operate smoothly or with instabilities. The design of the centrifugal pump is taken up to supply metered fuel to combustion chamber of a gas turbine engine at all operating conditions based on the flow demand set by the engine controller. The Computational fluid flow analysis of centrifugal pump is carried out to predict axial loading on the blade during design and off design conditions.

This paper discusses about the axial load estimation for different rib sizes and different gap between blade and casing of the centrifugal pump using CFD code Ansys Fluent 16.0. The code is validated with one set of measured data and reported the margin between CFD and experimental.

Further the performance characteristics at various operating points have been analysed and will be covered in the full paper along with the conclusions and references. Figure 1-3 are listed below which shows the fluid model, performance characteristics and contour plots of static and total pressure.

**Keywords:** Impeller, Ribs, CFD, axial load

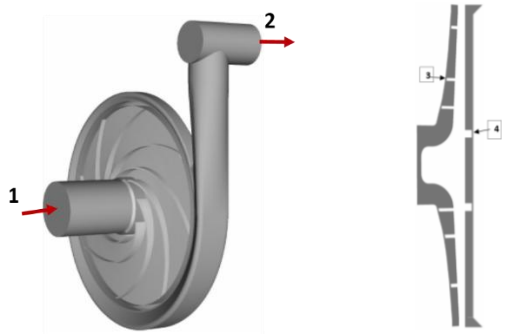


Figure 1: Geometry model of centrifugal pump

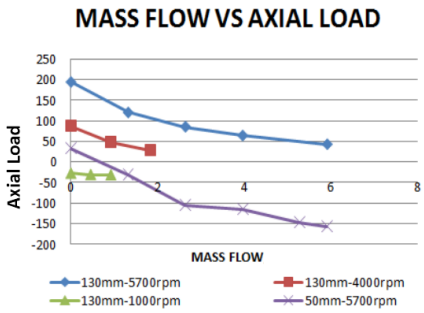


Figure 2: Plot of mass flow with axial load

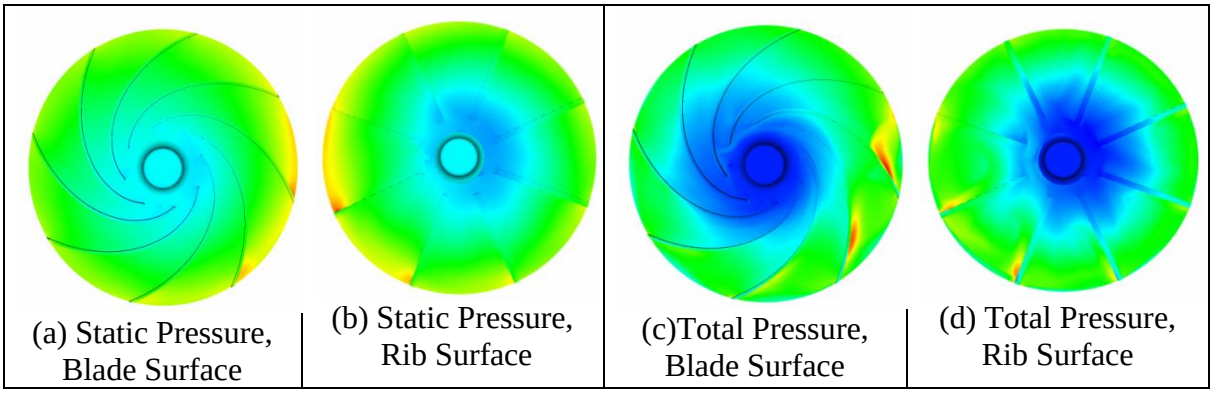


Figure 3: Contour plots of Static pressure and Total pressure on Blade surface and Rib surface

**REFERENCE**

[1] Daniel O Baun and Ronald D Flack,
'Radial Impeller Forces Using CFD'ASME TURBO EXPO 2002, June 2002, GT-2002-30378.

[2] Ashfaq C M, Shiva Kumar U, Lingamoorthy K, Anbuchezian S, Girish KD ' Design & Performance evaluation of areo engine booster Pump ASME 2015,December-2015 GTINDIA2015-1322.

[3] Karassik I.J, Messina, J.P, Cooper, P Heald, C.C, 2001," Pump Hand book ", McGraw-Hill, New York.

[4] Gulich. JF. 2008, "Centrifugal Pumps". Springer Verlag Berlin.

[5] Raghavendra S Muttalli , Shweta Agrawal , Harshla Warudkar CFD Simulation of Centrifugal Pump Impeller
Using ANSYS-CFX, IJIRSET, August-2014, ISSN: 2319-8753

[6] [ P.Gurupranesh, R.C Radha, N Karthikeyan IOSR Journal of mechanical and civil Engineering PP 33-41

[7] Jaydeep G. Chaudhari, A.S Dandiwala, A.V Doshi IJSRD, Vol. 2 Issue 09,2014

[8] Ansys Fluent manual

# Inverse Design of Thermal Barrier Coatings for IC Engines Applications

**Chandra Pratap Singh,**
Department of Mechanical Engineering, Indian Institute of Technology Bombay, Mumbai, Maharashtra, India,
chandrapratap07@iitb.ac.in
**Arif Taibani**
Cummins Technologies India Pvt. Limited, Pune, Maharashtra, India
arif.taibani@cummins.com
**Alankar Alankar**
Department of Mechanical Engineering, Indian Institute of Technology Bombay, Mumbai, Maharashtra, India,
alankar.alankar@iitb.ac.in
**Milan Visaria**
Cummins Technologies India Pvt. Limited, Pune, Maharashtra, India
milan.visaria@cummins.com
**Shankar Krishnan**
Department of Mechanical Engineering, Indian Institute of Technology Bombay, Mumbai, Maharashtra, India,
kshankar@iitb.ac.in (Corresponding Author)

## ABSTRACT

This paper reports on a combined inverse method and IC engines performance simulation, to design near "optimal" thermal barrier coatings (TBC). Using GT suite, ideal piston surface temperature profile that maximizes I.C. engine thermal as well as volumetric efficiency is obtained. Ideal temperatures are used as inputs for an inverse heat conduction parameter estimation problem. Thermal conductivity and volumetric heat capacity of TBCs are simultaneously obtained. A set of possible permutations of structures are obtained when the estimated thermophysical properties are combined with geometric parameters. Generic models based on topology and porosity are used to arrive at the effective thermophysical properties. A simple protocol to arrive at realizable geometry is obtained when manufacturing and reliability constraints are imposed. To showcase the performance improvement, the generated porous TBC material is modelled on FLUENT, commercial CFD software, with instantaneous combustion gas temperature and heat transfer coefficients at rated speed full load condition to quantify the heat insulation and temperature "swing" characteristics.

**Key Words:** *Thermal Barrier Coating (TBC), temperature swing, parametric study.*

## 1. INTRODUCTION

Nowadays several research programs, in automotive industries, are being carried out to decrease engine fuel consumption and pollution. Normally, in diesel engines about 19-22 percent of fuel energy is rejected to coolant fluid. TBCs can reduce this heat loss and lead to better thermal efficiency [1]. Interest in design and development of thermal barrier coating (TBC) is increasing due to increase in fuel costs and due to decrease in high quality fuel production. The concept of TBC for diesel engines began in 1980s. The primary function of the TBC is to reduce the rate of heat transfer from the working gas of the combustion chamber to the metallic wall of the IC engine. Thin TBC of low thermal conductivity and low heat capacity gives high thermal efficiency [2]. Thin coatings can help prevent intake air heating with effective resistance during the combustion. However, fundamental relationships between thermal/volumetric efficiency and thermophysical properties, structure and durability of TBC is not known.

Variable thermal properties of the coat can improve the thermal efficiency and volumetric efficiency [3]. Time varying thermal properties such as thermal diffusivity and thermal effusivity can improve the thermal efficiency and reduce the major heat loss during the power stroke [4]. Thermal diffusivity ($\alpha = k/\rho c$) and thermal effusivity ($e = \sqrt{k\rho c}$) depends on the thermal conductivity 'k' and heat capacity per unit volume 'ρc' of the material. In our prior work [4] we showed that a TBC material should possess high thermal diffusivity during intake stroke while lower thermal effusivity during power stroke.
In this work, we report on an "inverse" method to arrive at required TBC properties from ideal performance thermal profiles. When combined with generic models for effective properties using known manufacturable topologies then realizable TBC structures are obtained. Further, this work establishes an optimization framework, to obtain near optimal TBCs.

## 2. PROBLEM FORMULATION

In this problem, heat transfer in TBC depends on many parameter such as thermal conductivity, density and heat capacity of material. Parameter estimation methodology adopted to understand the behaviour of TBC for optimum performance. In parameter estimation, model studied repeatedly for different parameter values. [5,6]

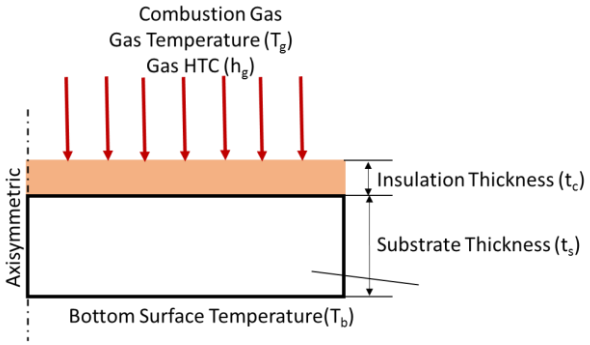


Figure 1. Thermal Barrier Coating with Substrate Material

An axisymmetric, one-dimensional insulated piston substrate geometry is assumed for the numerical model as shown in Figure1. Instantaneous boundary conditions throughout the engine cycle, which includes gas temperature, surface temperature and heat transfer coefficients (HTC) calculated from initial GT Suite engine cycle simulation.
In the first part of study, The thermal conductivity 'k' are considered unknown with known value of heat capacity per unit volume, C=ρc. Where ρ is density and c is specific heat of the material. A pulse heat flux boundary condition at x = 0 and an initial temperature ($T_{ini}$) condition are applied. The amount of heat flux (q) is considered known. The governing differential equation for the TBC

$$\frac{\partial}{\partial x}\left(k\frac{\partial T}{\partial x}\right) = \rho c \frac{\partial T}{\partial t}$$

$$-k\left.\frac{\partial T}{\partial x}\right|_{x=0} = q$$

$$T = T_c$$

$$T_{(x,t_o)} = T_{init}$$

Using sequential parameter estimation method, the thermal conductivity 'k' and heat capacity per unit volume 'ρc' are determined [5].

## 3. ANALYSIS AND RESULTS

A one-dimensional transient heat conduction analysis was conducted to predict the surface temperature profile. Instantaneous combustion gas temperature and heat transfer coefficients calculated from initial GT Suite engine cycle simulations at rated speed full load condition were used as convective boundary conditions on the gas side and the constant wall temperature boundary condition was assumed on the other side. The detail of engine operating conditions listed in Table 1. Various hypothetical insulation materials were studied by scaling the thermal properties (thermal conductivity and volumetric specific heat) and the case which shown best thermal swing characteristics and the optimum engine performance (the one with lower thickness, lowest effussivity and higher diffusivity), was selected for analytical work to predict the time varying thermal properties such as thermal conductivity. A detailed methodology is shown in Figure2.


Figure 2. Simulation Methodology

| | |
|---|---|
| Engine Type | Turbocharged, Air Cooled 6 cylinder inline engine |
| Stroke | 159 mm |
| Bore | 159 mm |
| Compression Ratio | 14.7 |
| Engine Speed | 1200rpm, 1500rpm and 1900rpm |
| Load | Part Load and Full load |
| Fuel | Diesel |

Table 1: Engine Operating Conditions

Figure 3 shows the variation of thermal conductivity as a function of crank angle (one cycle) for different thickness of TBC. Two different TBC thicknesses are plotted in Figure 3. Owing to high temperature gradients, 0.3 mm thickness TBC may incur higher thermal stresses. Hence, higher thickness material may be preferable.

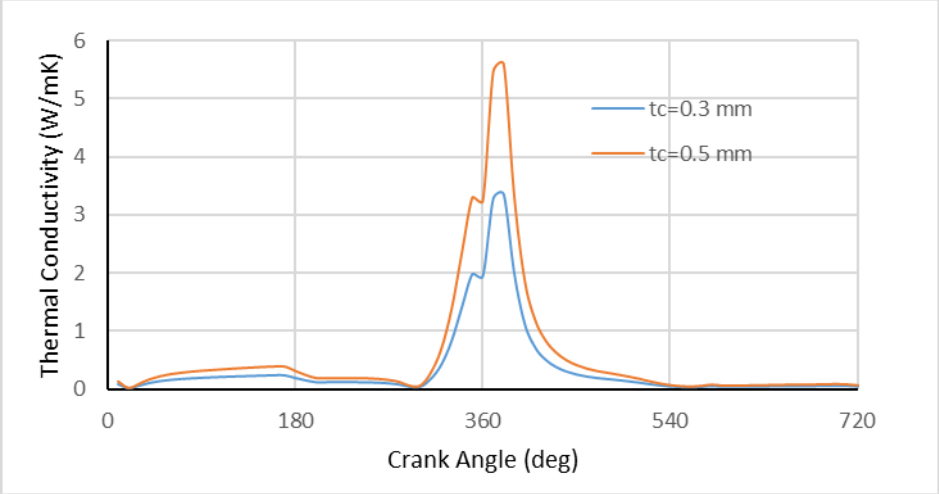


Figure 3.Thermal Conductivity of TBC for different thickness ($t_c$=0.3mm and 0.5mm)

## . 4. CONCLUSIONS

Inverse heat conduction method coupled with the GT Suite-ANSYS FLUENT software has been used to design near optimal TBC. Ideal piston's surface temperature profile was used as input in an inverse heat conduction problem to simultaneously predict the thermal conductivity and volumetric heat capacity of the TBC. Results indicate that thin TBC showed less heat loss in the power stroke due to its lower effective thermal conductivity (keff). However, thin TBCs may incur high thermal stresses and hence there is a need to optimize TBC thickness for durabilty. Knowledge of thermal conductivity and volumetric heat capacity of TBCs can provide valuable design guidelines for optimum engine performance.

## ACKNOWLEDGEMENT

The authors wish to thank MHRD Uchhatar Avishkar Yojana and Cummins Technologies India Private Limited for providing the financial support for this work.

## REFERENCES

1. M. Azadi, M. Baloo, G. Farrahi, and S. Mirsalim, "Paper: A Review Of Thermal Barrier Coating Effects On Diesel Engine Performance And Components Lifetime," International Journal of Automotive Engineering, vol. 3, no. 1, pp. 305–317, 2013
2. Wong, V., Bauer, W., Kamo, R., Bryzik, W. et al., "Assessment of Thin Thermal Barrier Coatings for I.C. Engines," SAE Technical Paper 950980, 1995, doi: 10.4271/950980.
3. H. Kosaka, Y. Wakisaka, Y. Nomura, Y. Hotta, M. Koike, K. Nakakita, and A. Kawaguchi, "Concept of 'Temperature Swing Heat Insulation' in Combustion Chamber Walls, and Appropriate Thermo-Physical Properties for Heat Insulation Coat," SAE Int. J. Engines, vol. 6, no. 1, pp. 142–149, 2013
4. Arif Taibani, Milan Visaria, Shankar Krishnan "Analysis of Temperature Swing Thermal Insulation on the Performance of Diesel Engines" Proceedings of the 24th National and 2nd International ISHMT-ASTFE, Heat and Mass Transfer Conference (IHMTC-2017)
5. Beck, J. V. and Arnold, K. J., Parameter Estimation in Engineering and Science,Wiley, New York, 1977.
6. J.V Beck, B. Blackwell, Ch.R.St. Clair, Inverse heat conduction, Ill posed Problems, Wiley Interscience Publication, New York, 1985

# THERMAL PERFORMANCE INTENSIFICATION OF CAM SHAPED TUBES IN STAGGERED LAYOUT

**Chidanand K. Mangrulkar, Ashwinkumar S. Dhoble, Tushar M. Sathe**
Department of Mechanical Engineering, Visvesvaraya National Institute of Technology (V.N.I.T.), Nagpur, India. cmangrulkar@gmail.com

**Sunil Chamoli**
Department of Mechanical Engineering, DIT University, Dehradun, Uttarakhand, India.

**Arunkumar H S**
Department of Mechanical Engineering, Manipal Institute of Technology, Manipal University, Manipal, Udupi, Karnataka, India.

## ABSTRACT

The passive mode of heat transfer enhancement is most frequently used in the process heat transfer applications. The cross-flow heat exchanger prominently uses the circular tubes in forming an array of tube bank. however, the development of wake and high-pressure drop lowers the thermal performance of the heat exchanger. In this study the numerical analysis is performed over the cam-shaped tube to investigate the thermal performance of the system. The CFD results indicates that cam-shaped tube results in slight lower heat transfer rate over circular due to reduction in frontal area, but pressure drop is also significantly very low. This leads to the overall improvement in the thermal performance of the tubes. The results are also compared with the experimental finding with overall deviation was found to be less than 10%.

**Key Words:** *Heat Transfer, friction factor, thermal performance.*

## 1. INTRODUCTION

The heat transfer augmentation with the passive mode of enhancement is being widely used across the globe since decades. The passive mode of enhancement is mostly preferred as it requires no additional secondary energy source. The heat exchangers commission in process industry are often involved gas-liquid interface for energy transfer. The parallel and counter flow heat exchangers are cannot be used due to the large difference in the heat capacity of the two fluids. So the cross flow heat exchangers are considered to be the best possible option in many industries. The cross-flow heat exchangers are associated with the two fluids in orthogonal flow directions. The cross-flow heat exchanger comprises of tubes carrying hot fluid and cold fluid flows over the tube surface. The layout of the tubes can be in-line or staggered configuration. The most commonly used tube profile is circular tubes as used since initial work reported by Roshko [1]. However, the circular section are bluff bodies and hence flow experience large pressure drop along with the wake and large eddies at the tube downstream. Hence research involves in reducing the wake and pressure drop across the circular tubes. The possible way is to control the tube profile which reduced the wake and pressure drop across the tubes. So us of non-circular tubes are being used to control the flow characteristics.

Ota et al.[2] make use of the elliptic tube section in tube bank and suggests the improvement in the thermal performance with attack angle. Aiba et al. [3] investigated the Nusselt number for staggered tubes at different tube pitch ratio. The high heat transfer with increased turbulence is reported at large pitch ratio. Talaat et al. [4] investigated the thermal performance at different pitch ratio and attack angle in case of the elliptic tubes. The results report the better thermal performance is found at a lower attack angle of tubes. Similarly, other section as wing profile is investigated by Ahmed et al. [5] and reported that the pressure coefficient increases with

the increased attack angle of air. Toolthaisong et al. [6] investigated the performance of tubular tubes in tube bank with different attack angle in the estimation of heat transfer and friction factor for the tube bank array. As most of the above profiles are being used since last few decades there is a need for a new profile which can enhance the thermal performance eve more. So Lavasani et al. investigated the thermal performance for cam shaped tubes at pitch ratio of 1.5, and 2.0 and reported the improve performance than circular tubes. As the cam profile is the latest development in the new tube profile the better insight is necessary for the exact application. hence the present study reported the three-dimensional numerical simulation for cam shaped tubes in a staggered configuration with the comparison over the experimental data for the wide range of Reynolds number. The present study highlights the numerical contours for the heat and fluid flow characteristics for the flow over the cam-shaped tubes in a staggered configuration, as no such study is performed in recent times.

## 2. GRID DEVELOPMENT AND NUMERICAL ANALYSIS

The numerical simulation is performed by considering the experimental study performed by lavasani et al. [7]. The ambient air is being allowed to pass over the staggered layout of cam tubes aas shown in fig. 1. The three-dimensional numerical grid is generated using commercial software ANSYS ICEM CFD 16.0. The mesh domain is indicated in fig 2.

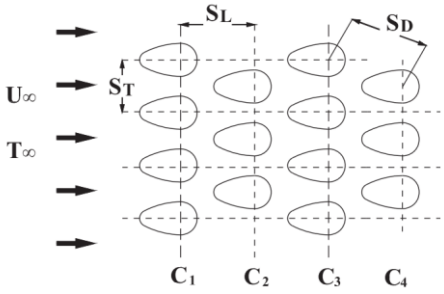


Figure 1. tubes arrangement

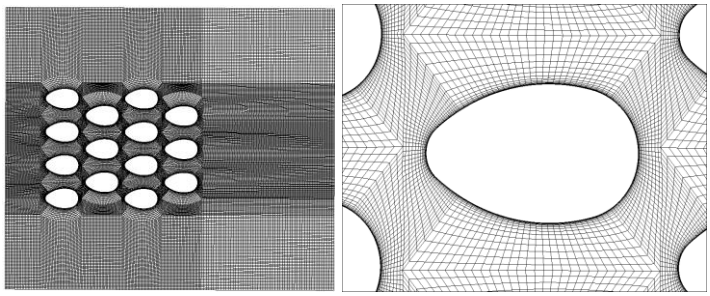

Figure 2. structured mesh over domain

The structured uniform mesh is generated with the dimensionless y plus as 1.0, so effects of the boundary layer can be considered while estimation the heat transfer. The mesh quality is maintained as 0.85 and above with aspect ratio of 1.12. The very fine mesh is created near the wall surface of the cam-shaped tubes.

The numerical analysis is performed in solver FLUENT 16.0, with pressure-velocity coupling by SIMPLE algorithm. The tubes surface is maintained at constant temperature of 353K, while the ambient air flows across the tube surface. The Reynolds number for the flow is maintained from 27000 to 42500. The flow is assumed to be steady and convective losses from the wall are negligible. The residuals are converged to the order of $10^{-5}$ and $10^{-8}$ for the mass continuity and energy equation. The RNG k-ε turbulence model with enhanced wall function is most suited in case of the staggered orientation of the tube surface.

The mean Nusselt number is determined as $$Nu=\frac{h.D_{eq}}{k} \quad \text{(i)}$$

friction factor across the tube bank is estimated as, $$f=\frac{2.\Delta P}{\rho.N_L.U_{max}^2} \quad \text{(ii)}$$

where $D_{eq}$ is the equivalent diameter of the cam-shaped tube, k is the thermal conductivity of the fluid, $\Delta P$ is the pressure drop across the tube array, $N_L$ is the number of tubes in the longitudinal direction, $U_{max}$ is the maximum flow velocity, and $\rho$ is the fluid density.

## 3. RESULTS

The flow characteristics across the tube bank can be studied by the temperature and streamline contours which is derived numerically.

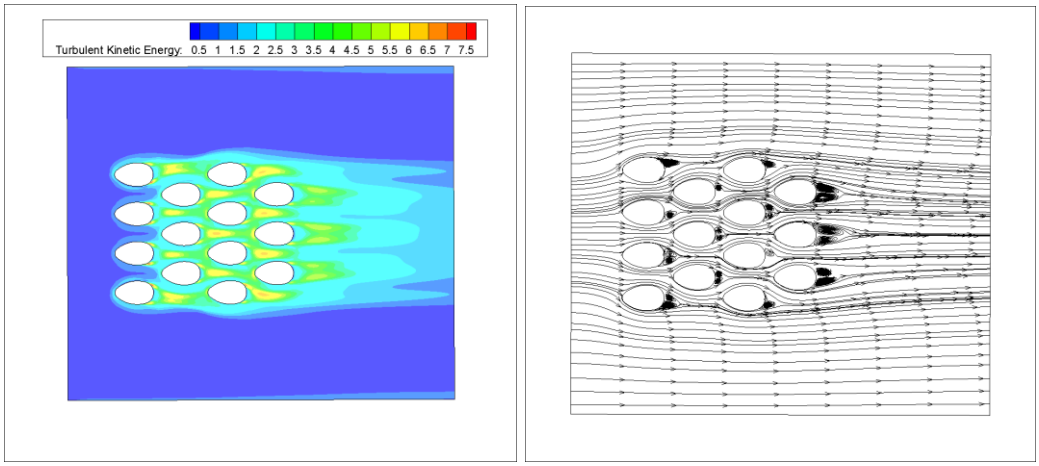


Figure 3 Turbulent kinetic energy contour and streamline contours

The turbulent kinetic energy and streamline contours are represented in the fig. 3. The intensity of turbulence increases with the number of the tube along the flow direction. The peak intensity is observed at a point close to the downstream of the tube indicating the point of separation of the fluid. In a similar way, for streamline contours, the vortex formation at the downstream is of a smaller size indicating the delay separation as compared to the conventional circular tubes. The vortex at the last row of tubes are relatively of large size due to a reduction in the flow velocity of the fluid. As the separation is delayed the fluid remain in contact with the tube surface for the longer duration thereby transferring more energy to the cross fluid.

Heat transfer and friction factor:- The average Nusselt number and friction factor for cam shaped tubes are represented in figure 4. The thermal performance is governed by both the parameters.

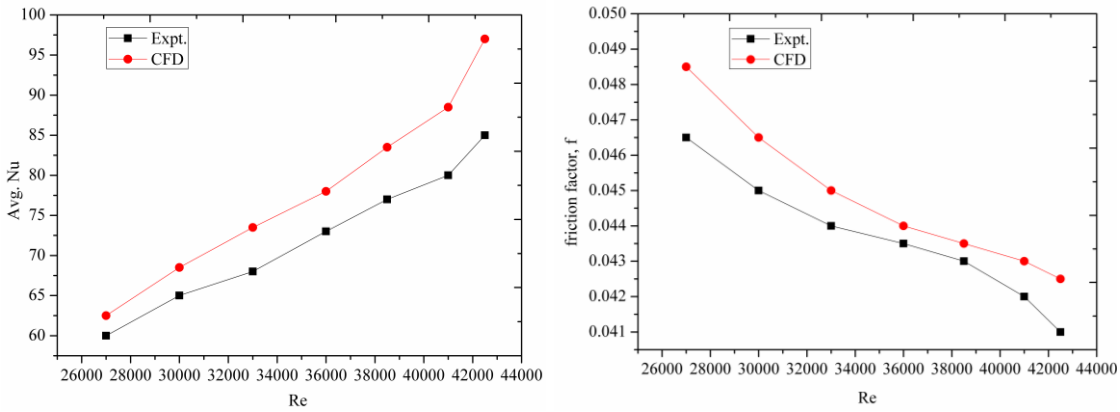


Figure 4 Average Nusselt number and friction factor for cam shaped tubes

The Nusselt number increases with increase in the flow Reynolds number. The CFD results are close to that of the experimental data of Lavasani et al. [7]. The variation in

the experimental and CFD results are of the order of 6-9%. However, the deviation is slightly higher at high Reynolds number as convective losses increase with increased flow Reynolds number. In case of the friction factor, there is a drastic reduction in the pressure drop for the cam-shaped tubes due to the streamline section of the tubes. Furthermore, due to a reduction in the frontal area of the tube, the pressure drop reduces even more. In the conventional circular cylinder, the separation occurs at mid-way for high flow Reynolds number which contributes to high-pressure drop. So by considering the combined effect of heat and friction factor the overall thermal performance is improved. In case of staggered layout the pressure drop is very high for the circular tube bank, hence friction factor significantly controls the overall thermal performance.

## 4. CONCLUSIONS

The numerical simulation is performed on the staggered configuration of cam-shaped tubes. The numerical analysis is being compared with the experimental finding [7] with the following aspects;

- The numerical results are in close proximity with the experimental data generated by Lavasani et al. [7]. The Nusselt number increases with increase in the flow rate.
- The average Nusselt number is less than that of the circular tube due to a reduction in the flow projected area, but the pressure drop is reduced substantially for cam shaped tubes. This leads to the improved thermal performance of cam shaped tubes over the circular tubes for entire range of Reynolds number. The overall thermal performance is improved by four times over circular tubes.
- The vortex formation is reduced at the cylinder downstream due to the delayed separation of the boundary layer. This leads to reduced turbulence within tube bank over circular tubes. So friction factor is significantly low even for staggered layout thereby promoting superior overall thermal performance for the entire range of Reynolds number. The overall reduction in the friction factor was found to be around 70% over circular tubes.

## REFERENCES

[1] A. Roshko, Experiments on the flow past a circular cylinder at very high reynolds number, Journal of Fluid Mechanics. 10 (1961) 345–356. doi:http://dx.doi.org/10.1017/S0022112061000950.

[2] O. Terukazu, N. Hideya, T. Yukiyasu, Heat transfer and flow around an elliptic cylinder, International Journal of Heat and Mass Transfer. 27 (1984) 1771–1779. doi:10.1016/0017-9310(84)90159-5.

[3] S. Aiba, H. Tsuchida, O. Terukazu, Heat Transfer around Tubes in Staggered Tube Banks, Bulletin of the JSME. 25 (1982) 927–933.

[4] T.A. Ibrahim, A. Gomaa, Thermal performance criteria of elliptic tube bundle in crossflow, International Journal of Thermal Sciences. 48 (2009) 2148–2158. doi:10.1016/j.ijthermalsci.2009.03.011.

[5] S.A.E. Sayed Ahmed, O.M. Mesalhy, M.A. Abdelatief, Effect of Longitudinal-External-Fins on Fluid Flow Characteristics for Wing-Shaped Tubes Bundle in Crossflow, Journal of Thermodynamics. 2015 (2015). doi:10.1155/2015/542405.

[6] S. Toolthaisong, N. Kasayapanand, Effect of Attack Angles on Air Side Thermal and Pressure Drop of the Cross Flow Heat Exchangers with Staggered Tube Arrangement, Energy Procedia. 34 (2013) 417–429. doi:10.1016/j.egypro.2013.06.770.

[7] H. Bayat, A.M. Lavasani, T. Maarefdoost, Experimental study of thermal-hydraulic performance of cam-shaped tube bundle with staggered arrangement, Energy Conversion and Management. 85 (2014) 470–476. doi:10.1016/j.enconman.2014.06.009.

# STUDY ON THE EFFECTS OF PARTICLE SHAPE IN FREE MOLECULAR REGIME

**Arun Kumar Chinnappan, Rakesh Kumar**

Department of Aerospace Engineering,
Indian Institute of Technology Kanpur, India
E-mail: arun@iitk.ac.in, rkm@iitk.ac.in

**Abstract**

Shape effects of particle in free molecular regime is investigated using an in-house, three dimensional direct simulation Monte-Carlo (DSMC) solver. The solver is validated for typical shape i.e sphere with available analytical results and compared with practical particle shape i.e ellipsoidal. The sensitivity of particle shape is discussed using surface properties such as drag and heat transfer. Moreover, the variation of surface properties with respect to angle of attack is discussed.

**KEY WORDS ::** DSMC, GAS-SOLID FLOW, NON-SPHERICAL, FREE MOLECULAR REGIME

## 1 Introduction

Multiphase flows considering gas-solid have many applications in industries such as cyclone separators, sand blasting, sand storm, pollution control systems, etc. Numerous studies had been done in several years to study the gas-solid flow behavior, however it is limited to low-speed and continuum regime. Even though not many research found in high speed and free molecular regimes considering gas-solid flows, it is important to study in order to address several practical situations such as unburned fuel in solid propellant rocket nozzles, dust dispersion in lunar/planetary landings, etc. Experimental studies are quite expensive in order to mimic the low density environments as well as high speed flows. Moreover, the conventional Navier-Stokes solver is not suitable to study because of continuum failure at free molecular/transitional regime, where the characteristic length is comparable to the mean free path of the molecule. Some researchers proposed theoretical approaches to study gas-solid flows at free molecular regime notably: Gallis *et al.* [1] proposed a theoretical relation using Greens function approach to calculate drag and heat flux experienced by a particle moving in free molecular regime for monatomic gas. This approach was used to study effects of unburned solid propellants in rocket nozzle [2], predict dust emission mechanism of lunar sand particles due to plume impingement from the nozzle[3], etc. Saucer [4] derived a analytical relation to determine total heat transfer experienced by a particle in free molecular regime.

All the aforesaid research had considered particles as perfect spheres which are very convenient to model whereas, particles are non-spherical in reality. Non-spherical particle-gas flow behavior have been studied by some researchers in continuum regimes[5, 6] and addressed the complexity dealing with it. A single characteristic value (diameter) is enough to describe the behavior for spheres whereas at least two parameters are required to study even for regular non-spherical particles such as ellipsoid. Moreover, the pitching torque and lift force need to be considered if the angle of attack is non-zero.

The present work aims to study the importance of particle shape consideration in free molecular regime in aerodynamic as well as heat transfer aspects. In this work, we have used a kinetic-particle based Direct Simulation Monte-Carlo (DSMC) solver to study particle behavior in free molecular regime. This paper is arranged as follows: the brief description about DSMC method is given in Sec. 2, the numerical parameters are presented in Sec. 3. This is followed by results and discussion in Sec. 4 and conclusions in Sec. 5.

## 2 Computational Model :: The DSMC Method

The Direct Simulation Monte Carlo method (DSMC) is a particle based method proposed by G.A. Bird for the simulation of non-equilibrium gas flows [7]. This method deals with simulated molecules, each of which represents a large number of real molecules. This method governs the physics through molecular movements and collisions. Every molecule is moved with respect to their velocities and given time step. Molecular collisions are modeled probabilistically. The macroscopic parameters are calculated by time averaging the sampled data. The DSMC method does not produce direct solution to Boltzmann equation

but it evaluates the same physics as the Boltzmann equation and it has been demonstrated that this method approaches to solution of the Boltzmann equation in the limit of vanishing cell size and time step [7]. The detailed explanation about the method can be found in the references [7, 8]. The parallel in-house DSMC solver named NFS used in this work is already validated with several experimental and simulation results[9, 10]. In our solver, the Variable Hard Sphere (VHS) model is used for elastic collisions. The quantum and continuous versions of Larsen Borgnakke model are employed to model inelastic collisions.

To study this problem, the three dimensional NFS solver is used in this study with some modifications to reduce computational cost. In free molecular flows, gas-surface collision is more dominant mechanism governing the physics than gas-gas collision because the mean free path of the molecule is greater than the characteristic length (particle diameter in this case). To ensure that gas molecules are not affected by the presence of body, we have made a small modification in gas-surface interaction step in DSMC algorithm. Once a molecule hits the particle surface, the molecule velocity is unchanged instead its position will be changed randomly inside the domain. In other words, gas is not affected by the presence of body and it is quite valid in free molecular regime. However, the incident and reflected momentum/energy during gas-surface collision is sampled to calculate forces, moments and heat flux experienced by the particles. Therefore, the actual gas-surface interaction is modeled but post-reflection velocities are not assigned to the gas molecules to ensure gas properties are constant throughout the simulation.

# 3 Numerical Parameters

A 3D cubical domain is considered with a particle at the center. Argon is used as gas species. The gas density and temperature are $1.989 \times 10^{-5}\ Kg/m^3$ and 500 $K$, respectively. The bulk velocity of gas is varied based on speed ratio. Particle volume is taken as $5.236 \times 10^{-19}\ m^3$ represents a sphere of having a diameter 1 $\mu m$ and mass of the particle is $9.94 \times 10^{-16}\ Kg$. The time step is taken as $1 \times 10^{-9}\ s$, which is much smaller than the mean collision time of the gas. Periodic boundary condition is employed at all the six sides of the domain. CLL model [11] is used for gas-surface interaction with accommodation coefficient of unity.

# 4 Results and Discusion

## 4.1 Spherical Particle In Free Molecular Regime

It was found by several researchers that the particle drag and heat flux depend only on the molecular speed ratio $S$ [12, 13] in free molecular regime, where $S$ is the ratio of particle speed to the mean molecular speed of gas ($S = \frac{U}{\sqrt{2RT}}$). The analytical relation for heat transfer experienced by a spherical particle[4] is expressed in terms of thermal recovery factor $r'$ and modified Stanton number $St'$ as:

$$r' = \frac{(2S^2+1)[1+\frac{ierfc(S)}{S}] + \frac{2S^2-1}{2S^2} erf(S)}{S^2[1+\frac{ierfc(S)}{S}] + \frac{erf(S)}{2S^2}} \tag{1}$$

$$St' = \frac{S^2 + S\ ierfc(S) + \frac{erf(S)}{2}}{8S^2} \tag{2}$$

where $ierfc(S)$ is the integrated complementary error function. The analytical relation for drag coefficient of a spherical particle in the free molecular limit[12] is given by:

$$C_D = \frac{e^{S^{1/2}}}{\sqrt{\pi}S^2}(1+2S^2) + \frac{4S^4+4S^2-1}{2S^4}\ erf(S) + \frac{2\sqrt{\pi}}{3S} \tag{3}$$

In DSMC simulation, the modified Stanton number is derived from heat flux $Q$ and is given by:

$$St' = \frac{Q}{A\rho U c_p (T_r - T_w)} \frac{\gamma}{\gamma+1} \tag{4}$$

The variation of drag coefficient and modified Stanton number with respect to speed ratio for a spherical particle is plotted and compared with analytical results given by Eq. 2,3. The results obtained from 3D DSMC solver is agree well with the analytical result in all speed ratios.

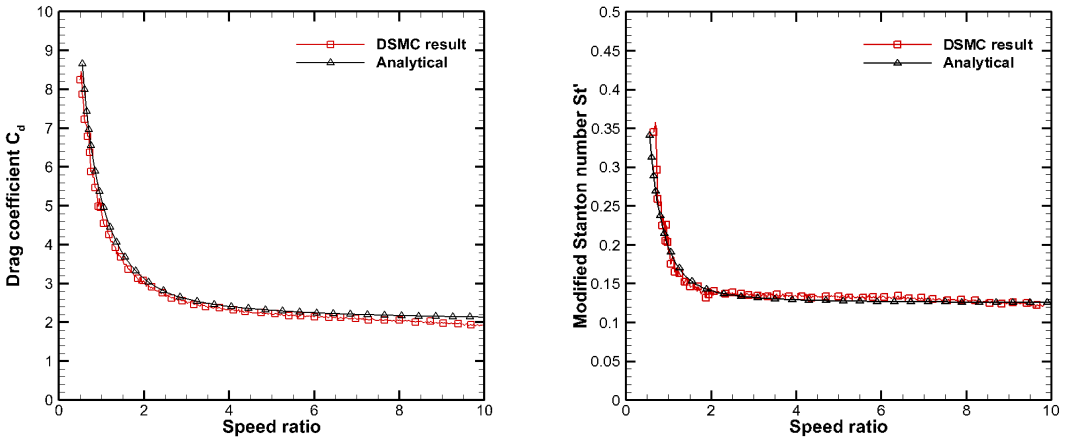


Figure 1: Comparison of DSMC results with analytical a) Drag coefficient (left) and b) Modified Stanton number (right)

## 4.2 Ellipsoidal Particle In Free Molecular Regime

To study the shape effects, we have considered an ellipsoidal particle having volume as same as sphere. In this study, there are three different ellipsoidal shapes considered having eccentricity of 0.7,0.8 and 0.9. In the first phase, the angle of attack is considered to be zero to avoid pitching torque, which arises due to particle shape. The drag coefficient and Stanton number are plotted against molecular speed ratios as shown in Fig.2. As eccentricity increases, the particle shape deviates from spherical and closes to flat plate. In other words, the contact surface area decreases as eccentricity increases since the angle of attack is zero. Therefore, less number of gas-surface collision occurs as eccentricity increases, which makes less momentum and energy imparted to the surface. This is the reason for decreasing drag coefficient and Stanton number observed in DSMC simulations as shown in Fig.2.

The difference in drag/heat flux between spherical and ellipsoidal cases is large at high speed ratios. It is observed that the variation is in the order of 50% between sphere and ellipsoidal case of eccentricity 0.9 after speed ratio 2. Similarly, the difference in Stanton number is also in the order of 50% after speed ratio 2. In our second study, we have considered ellipsoidal particle of eccentricity 0.7 and simulated for

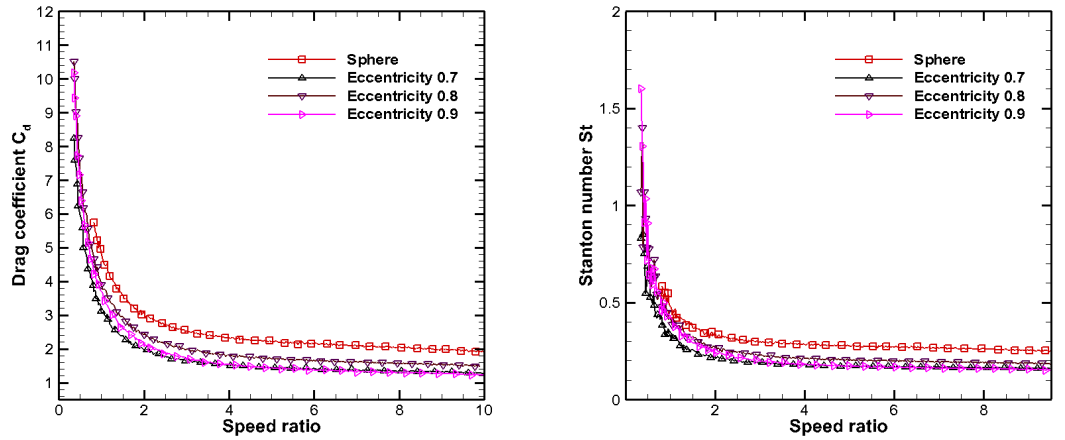


Figure 2: Comparison of spherical particle results with ellipsoidal a) Drag coefficient (left) and b) Modified Stanton number (right)

different angle of attacks as shown in Fig. 3. As angle of attack increases, the frequency of gas-granular collision increases and this leads to an increase in drag and heat flux. From the above results, we conclude that the surface properties very sensitive to the shape and its orientation to the flow.

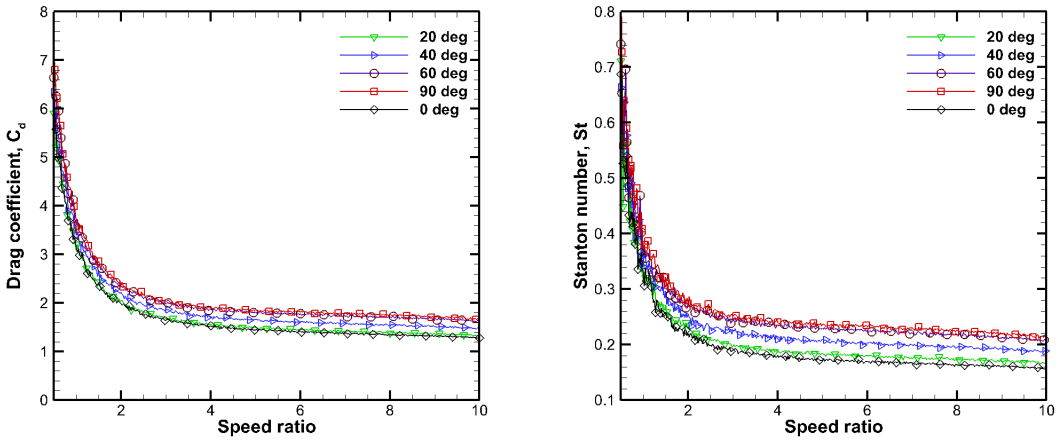


Figure 3: Variation of a) Drag coefficient (left) and b) Modified Stanton number (right) with respect to speed ratio for different angle of attack

# 5 Conclusions

Aerodynamic and heat transfer characteristics of different shaped/sized particles were studied in the DSMC framework. There was huge variation in drag and heat flux have been observed for spherical and ellipsoidal particles. Moreover, the sensitivity of angle of attack was studied in terms of drag and heat transfer. It was found that particle shape and its orientation play an important role in determining the dynamics of gas-solid flows. Furthermore studies need to be done by considering particle rotation.

## References

[1] Gallis *et al.* "An approach for simulating the transport of spherical particles in a rarefied gas flow via the direct simulation Monte Carlo method." Physics of Fluids 13.11 (2001): 3482-3492.

[2] Burt, J. M. (2006). "Monte carlo simulation of solid rocket exhaust plumes at high altitude" (Doctoral dissertation, The University of Michigan).

[3] Morris*et al.* "Approach for modeling rocket plume impingement and dust dispersal on the moon." Journal of Spacecraft and Rockets Vol. 52, No. 2 (2015), pp. 362-374

[4] Saucer *et al.* "Convective heat transfer from spheres in a free-molecule flow." Journal of the Aeronautical Sciences 18-353 (1952).

[5] Zastawny *et al.* "Derivation of drag and lift force and torque coefficients for non-spherical particles in flows." International Journal of Multiphase Flow 39 (2012): 227-239.

[6] Ouchene *et al.*"Drag, lift and torque coefficients for ellipsoidal particles: From low to moderate particle Reynolds numbers." Computers & Fluids 113 (2015): 53-64.

[7] Bird GA. "Molecular Gas Dynamics and Direct Simulation of Gas Flows." Clarendon Press, Oxford, 1994, 508.

[8] Prasanth *et al.* "Direct simulation Monte Carlo (DSMC): A numerical method for transition-regime flows-A review." Journal of the Indian Institute of Science 86.3 (2013): 169.

[9] Kumar *et al.*. "Development of a multi-species, parallel, 3D Direct Simulation Monte-Carlo solver for rarefied gas flows." Computers & Fluids 159 (2017): 204-216.

[10] Chinnappan *et al.* "Insights into flow and heat transfer aspects of hypersonic rarefied flow over a blunt body with aerospike using direct simulation Monte-Carlo approach." Aerospace Science and Technology 66 (2017): 119-128.

[11] Padilla, Jose F., and Iain D. Boyd. "Assessment of Gas-Surface Interaction Models for Computation of Rarefied Hypersonic Flow," Journal of Thermophysics and Heat Transfer 23.1 (2009): 96-105.

[12] Schaaf, S. A., & Chambr, P. L. (1961). "Flow of rarefied gases." Princeton University Press. 1962.

[13] A. K. Oppenheim, "Generalized theory of convective heat transfer in a free-molecule flow." Journal of Aeronautical Science 20-49 (1953)

# Effect of Joule-Thomson pressure drop on the thermal performance of a three fluid heat exchanger with three communications, for cryogenic applications using finite element method

**Chodankar Vishnudas Alias Vipul Luvu**
Department of Automobile Engineering, Saraswati College of Engineering, Navi Mumbai-410210, India, c.vishnudas282@gmail.com

**Aswatha**
Department of Mechanical Engineering, Bangalore Institute of technology, Bangalore-560 004, Karnataka, India, dr.aswath999@gmail.com

**V. Krishna, K. N. Seetharamu**
Department of Mechanical Engineering, P.E.S Institute of technology, Bangalore-560 085, Karnataka, vkrishna@pes.edu, seetharamukn@yahoo.com

## ABSTRACT

Pressure drop effects are neglected in most cryogenic applications, as its effects are negligible. However when the heat exchanger requirements are strict, the examination of the pressure effects is a must. In this study the thermal aspect of pressure loss is investigated, which is different from most previous researches were they examined the hydraulic aspects. The study is carried out using Finite Element Method by considering seven non-dimesional parameters of which one includes Joule-Thomson pressure loss parameter. The results reveals the indirect effect of pressure loss on the thermal performance of heat exchanger.

**Key Words:** *Pressure loss, Heat Exchangers, Finite element methods.*

## 1. INTRODUCTION

Three fluid heat exchanger are widely used in several fields of applications such as power plant, gas liquefaction process, refrigeration systems including cryocooler, air conditioning and so on [1]. Ideally a heat exchanger is assumed to have infinite heat transfer conductance and implicate no pressure loss. However the pressure loss is indispensably developed with the increase in heat transfer conductance. Therefore a proper heat exchanger design is mainly to make a compromise between hydraulic aspect (pressure loss) and thermal one (heat transfer conductance).

The finite element model for a three fluid heat exchanger with three communications with ambient heat in leak and longitudinal conduction through walls was developed by V. Krishna et al. [2, 3]. In their research they studied the effect of seven non dimensional parameters on temperature profile, effectiveness and degradation factor. Results revealed the degradation of heat exchanger performance with an introduction of ambient heat in leak and longitudinal conduction. Veerabhadrappa et al. [4] developed a transient model of three fluid heat exchanger with three communications. They studied the effects of step change in inlet temperature of fluids on time to reach steady state, outlet temperature of fluids and effectiveness. This investigation concluded that the time to reach the steady state is independent of the amplitude of step change in the inlet temperature of fluids. Hwang and Jeong [5] developed the first analytical model of two fluid recuperative heat exchanger with Joule-Thomson(J-T) pressure loss. These analysis presented that the effect of pressure drop depends on NTU and heat capacity ratio. As per the author's knowledge, no work is carried on the performance of three fluid heat exchanger in context to J-T pressure drop.

## 2. MODEL FORMULATION

A three fluid, single pass, parallel flow heat exchanger involving thermal communication between all the three fluids – hot, intermediate and cold are considered. Each of these fluids is in thermal communication with the other two fluids. Along with the fluid thermal interactions during the flow, there is continuous pressure drop. The pipe cross-sectional view for the heat exchanger (HX) along with the flow arrangement for this study is as depicted in Figure 1, where cold and intermediate flows in one direction while the hot fluid flows in counter direction to them.

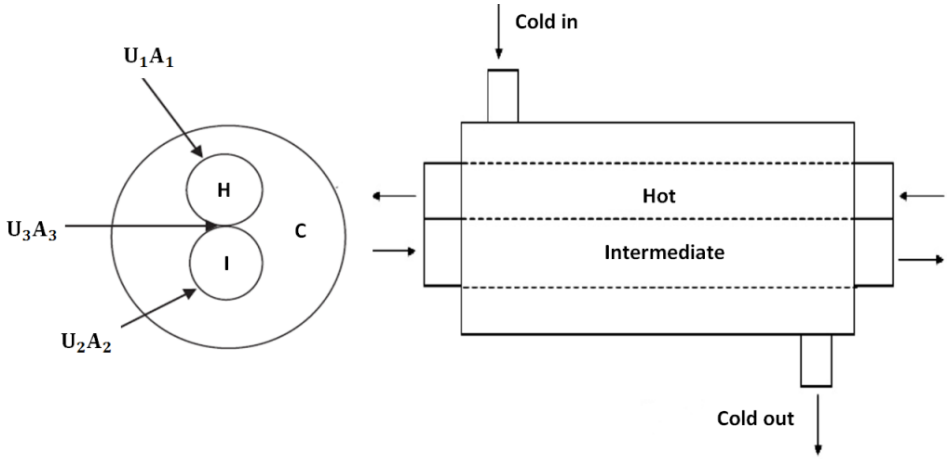


FIGURE 1. Tubular arrangement and flow directions of the three fluid heat exchanger.

The governing equations for hot, cold and intermediate fluids obtained by energy balance are as follows.

Hot Fluid:

$$\frac{d\theta_h}{dX} + \omega_h * \left(\frac{d\theta_h}{dX} - \frac{d\theta_c}{dX} - \frac{d\theta_i}{dX}\right) = \frac{NTU}{R_2}(\theta_h - \theta_c) + \frac{NTU * H_2}{R_2}(\theta_h - \theta_i) \quad (1)$$

Cold fluid:

$$\frac{d\theta_c}{dX} - \omega_c * \left(\frac{d\theta_h}{dX} - \frac{d\theta_c}{dX} - \frac{d\theta_i}{dX}\right) = NTU * (\theta_h - \theta_i) + NTU * H_1 (\theta_i - \theta_c) \quad (2)$$

Intermediate fluid:

$$\frac{d\theta_I}{dX} - \omega_i * \left(\frac{d\theta_h}{dX} - \frac{d\theta_c}{dX} - \frac{d\theta_i}{dX}\right) = \frac{NTU * R_1 * H_2}{R_2}(\theta_h - \theta_i) - \frac{NTU * R_1 * H_1}{R_2}(\theta_i - \theta_c) \quad (3)$$

The different non-dimensional terms used in the analysis are defined as below:

$$NTU = \frac{U_1 P_1 L_e}{C_c}, \; H_1 = \frac{U_2 P_2}{U_1 P_1}, \; H_2 = \frac{U_3 P_3}{U_1 P_1} \quad (4)$$

$$R_1 = \frac{C_h}{C_i}, \; R_2 = \frac{C_h}{C_c}, \; \theta = \frac{T - T_{c,in}}{T_{h,in} - T_{c,in}}, \; \omega = \frac{d\theta_{JT}}{d(\theta_h - \theta_c)}, \; X = \frac{x}{L_e} \quad (5)$$

## 4. FINITE ELEMENT METHOD

The heat exchanger is discretized into a number of elements. A linear variation is assumed for the hot, cold and intermediate fluids in a single element. Using the Galerkin's method of minimizing

the weighted residual (Lewis et al. [6]), the governing equations are reduced to a set of algebraic equations. The discretized governing equations are written in the matrix form for each element as:

$$[K]\{\theta\} = \{f\} \tag{6}$$

where [K] is a stiffness matrix, $\{\theta\}$ is the non-dimensional temperature vector and $\{f\}$ gives the loading terms. The stiffness matrix is assembled for all the elements in the solution domain to get the global stiffness matrix. The boundary conditions are applied and the system of equations is solved by MATLAB to obtain the dimensionless temperatures along the heat exchanger.

## 5. EFFECTIVENESS

Cooling of hot fluid is identified as the core objective of three fluid heat exchanger(V. Krishna et al. [2]). So along with the cooling of hot fluid the pressure drop effect are also introduced. Hence the effectiveness is redefined as:

$$\varepsilon = \begin{cases} \left(1 - \theta_{h,out}\right) + \omega_h\left\{\left(\theta_{h,out} + \theta_{c,out} + \theta_{i,out}\right) - \left(\theta_{i,in} + 1\right)\right\} & (C_h \le C_c, C_i) \\ \dfrac{\left(1 - \theta_{h,out}\right) + \omega_h\left\{\left(\theta_{h,out} + \theta_{c,out} + \theta_{i,out}\right) - \left(\theta_{i,in} + 1\right)\right\}}{\frac{1}{R_2} + \frac{1 - \theta_{i,in}}{R_1}} & (C_h > C_c, C_i) \end{cases} \tag{7}$$

## 6. PERFORMANCE CHANGE

Performance change is the measure of increase or decrease in performance with the change in pressure drops. It is defined as the ratio of the heat exchanger effectiveness with pressure loss to the one without pressure loss(Hwang and Jeong [5]), as given below.

$$r = \frac{\text{actual heat transfer rate with pressure loss effect } (\varepsilon)}{\text{actual heat transfer rate without pressure loss effect } (\varepsilon_{\omega=0})} \tag{8}$$

## 7. RESULTS

According to the defination of NTU, an increase in NTU leads to decrease in heat transfer resistance between hot and cold fluid and/or decrease in thermal capacity of the cold fluid. As the values of $H_1$ and $H_2$ are fixed, the increase in NTU will not result in any change in the thermal resistance between the hot and cold fluid. This will only result in decrease in thermal capacity of cold fluid. As the specific heat of cold fluid is constant, hence it results in decrease in mass flow rate of cold fluid with the increase of NTU. The effect of NTU and Joule-Thomson pressure drop on the hot fluid effectiveness is shown in Figure 2. The effectiveness increases rapidly for the initial values of NTU from 0 to 3, further increase in NTU shows marginal change in effectiveness. The positive pressure drop on the hot fluid shows an decrease in effectiveness. For cold and intermediate fluids the positive pressure drop shows an increase in effectiveness until value NTU=4 and reduces eventually. In similar way the negative pressure drop on hot fluid side shows increased effectiveness. And negative pressure drops at cold and intermediate fluid shows reduced effectiveness upto NTU value of 4 and increases for higher values of NTU.

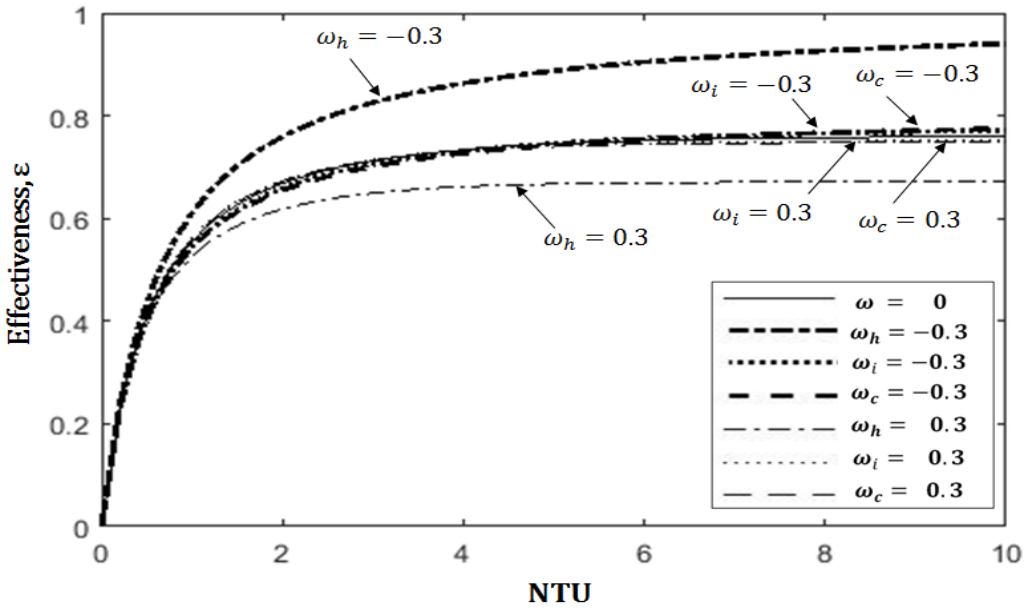


FIGURE 2. Effect of NTU on the hot fluid performance for a three fluid HX with Joule-Thomsons pressure drops, values of other non-dimensional parameters: $H_1$ = 1.5, $H_2$ = 2, $R_1$ = 2, $R_2$ = 1.25, $\theta_{h,in}$ = 1, $\theta_{i,in}$ = 0.4, $\theta_{c,in}$ = 0.

## 6. CONCLUSIONS

The idea of this paper is to put forth the effect of Joule -Thomson pressure drops on the performance of heat exchanger. It also originates with a suggestion that the numerator of the effectiveness, which is 'actual heat transfer rate', should be defined not only by temperature difference but also by pressure difference (i.e. the enthalpy difference) if the pressure drop occurs inevitably.

## REFERENCES

[1] Ramesh KS, Dusan PS, *Fundamentals of heat exchanger design*, John Wiley & Sons, 2003.

[2] V. Krishna, Pradeep G. Hegde, N.Subramanian, K.N. Seethramu, Effect of ambient heat-in-leak on the performance of a three fluid heat exchanger, for cryogenic applications, using finite element method, *International Journal of Heat and Mass transfer*, 55, 5459-5470, 2012.

[3] V. Krishna, S. Spoorthi, Pradeep G. Hegde, K.N. Seethramu, Effect of longitudinal wall conduction on the performance of a three fluid cryogenic heat exchanger with three thermal communications, *International Journal of Heat and Mass transfer*, 62, 567-577, 2013.

[4] Kavadiki Veerabhadrappa, Gulabal Vinayakaraddy, K.N. Seetharamu , Pradeep G. Hegde, V. Krishna, Transient behavior of three-fluid heat exchanger with three thermal Communications under step change in inlet temperature of fluids Using finite element method, *Applied Thermal Engineering*, 108, 1390–1400, 2016.

[5] Gyuwan Hwang, Sangkwon Jeong, Pressure loss effect on recuperative heat exchanger and its thermal performance, *Cryogenics*, 50, 13–17, 2010.

[6] Roland W. Lewis, Perumal Nithiarasu, Kankanhalli N. Seetharamu, *Fundamentals of Finite Element Method for Heat and Fluid Flow*, John Wiley and Sons, 2004.

# NATURAL CONVECTION IN SQUARE POROUS ENCLOSURE WITH DIATHERMAL PARTITION WALL

**Chordiya Jayesh Subhash**[1]
Research Scholar, NIT Jamshedpur-831014, Jharkhand, jayesh.subhash@gmail.com
**Ram Vinoy Sharma**[2]
Professor, NIT Jamshedpur-831014, Jharkhand, rvsharma.me@nitjsr.ac.in

## ABSTRACT

Heat transfer in an unsteady natural convection within a fluid-saturated square porous enclosure having vertical diathermal partition wall is studied for different partition ratio in this paper. The primary objective is to curtail the heat transfer rate across a differentially heated porous enclosure by aligning the diathermal partition vertically and to manifest the effect of its position within the enclosure. Governing equations are developed using Darcy's model and solved numerically by Successive Accelerated Replacement scheme and explicit scheme. Partition ratio, which is the ratio of partition position from hot wall to the length of enclosure, is varied from 0 to 1. Fluid flow is analysed by observing streamlines and isotherms while heat transfer is evaluated by calculating average Nusselt number. Numerical analysis is carried out for modified Rayleigh number 100, 500 and 1000. It is found that employing the diathermal partition attenuates the heat transfer rate considerably. Also, Nusselt number is the least when partition is in the center of enclosure. The drop in Nusselt number is sudden and larger for higher modified Rayleigh number while for lower value of Ra the drop in Nu is gradual and comparatively smaller.

**Key Words:** *Porous Media, Partition, Natural Convection.*

## 1. INTRODUCTION

Most materials in engineering applications like insulation, cork, cement, ceramics, desalination equipment's, rocks, wood, nuclear fuels etc. are porous in nature. Anderson and Bejan [1] worked on vertical impermeable wall and found that Insertion of one vertical partition in the middle of a vertical porous layer drastically reduces the net heat transfer through the layer. The current work is based on attenuating the heat transfer rate through a fluid saturated porous medium within a square enclosure. The objective is to investigate the effect of partition ratio on heat transfer in a fluid-saturated square porous enclosure with vertical diathermal partition wall.

## 2. MATHEMATICAL FORMULATION

Consider an incompressible, laminar, two dimensional, unsteady natural convection flow in a square porous enclosure of length L. Figure 1 shows the physical model with vertical partition. Initially, complete enclosure is at a lower temperature $T_c$. For $\tau > 0$, the left wall is subjected to a higher uniform temperature $T_h$, while the bottom and top wall are insulated. The outer boundaries are considered impermeable and Boussinesq approximation is applied. The solid matrix of the porous media is assumed rigid; porous bed is assumed homogenous, isotropic, and saturated with incompressible fluid. Moreover, the partition under study is assumed to be diathermal, impermeable, rigid and thin.
The conservation equations for momentum and energy equations for Darcy flow model in non-dimensional form are shown below. X (= x/L), Y (= y/L) are non-dimensional x and y coordinates, $\psi$ and $\theta$ are non-dimensioanl stream function and temperature ($T-T_c/T_h-T_c$), $r_p$ is partition ratio (d/L), Ra is modified Rayleigh number ($Kg\beta\Delta TL/\alpha\nu$) and $\tau$ is non-dimensioanl time ($\alpha t/L^2$).

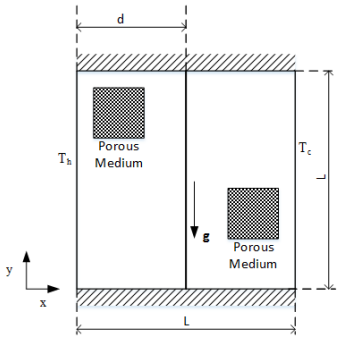


FIGURE 1. Physical model of square porous enclosure with vertical partition

$$\frac{\partial^2\psi}{\partial X^2}+\frac{\partial^2\psi}{\partial Y^2}+\mathrm{Ra}\frac{\partial\theta}{\partial X}=0 \tag{1}$$

$$\frac{\partial\theta}{\partial\tau}+\frac{\partial\psi}{\partial Y}\cdot\frac{\partial\theta}{\partial X}-\frac{\partial\psi}{\partial X}\cdot\frac{\partial\theta}{\partial Y}=\frac{\partial^2\theta}{\partial X^2}+\frac{\partial^2\theta}{\partial Y^2} \tag{2}$$

Subjected to initial and boundary conditions,

$$\theta=0,\quad \psi=0 \quad \text{at} \quad \tau=0$$

$$\theta=1,\quad \psi=0 \quad \text{at} \quad X=0,\quad \tau>0$$

$$\theta=0,\quad \psi=0, \quad \text{at} \quad X=1,\quad \tau>0$$

$$\frac{\partial\theta}{\partial Y}=0,\quad \psi=0, \quad \text{at} \quad Y=0,\ 1\ ,\ \tau>0 \tag{3}$$

The suitable condition at vertical partition is,

$$X=0.5,\quad \psi=0,\quad \frac{\partial\theta^-}{\partial X}=\frac{\partial\theta^+}{\partial X} \tag{4}$$

Average Nusselt number is calculated as shown below. AR is aspect ratio given by H/L.

$$\overline{Nu}=\int_0^1 \mathrm{Nu_h}(Y)dY=\int_0^1 \mathrm{Nu_c}(Y)dY \tag{5}$$

Eq. (1, 2) along with boundary conditions in Eq. (3) and suitable condition at partition in Eq. (4) were numerically solved using Successive Acceleration Replacement (SAR) scheme. For discretization of equations, Finite Difference Method (FDM) with second-order accuracy in central difference was used while a second order forward and backward difference was used at the wall boundaries. Unsteady term was dealt using explicit scheme. The stream function and temperature were solved using this technique for all grid points until the convergence was achieved.

## 3. RESULTS

The effect of vertical partition and partition ratio ($r_p$) was studied by noting the transient effects of streamlines and isotherms for modified Ra = 100, 500 and 1000 and $0 \le r_p \le 1$. A numerical code was developed to solve the algebraic equations resulted from FDM scheme. In view of both computational cost and precision, the results obtained with the 41 x 41 mesh was considered acceptable. Exception occurs for higher Rayleigh number where 61x61 mesh is preferred. For validation, the values of average Nusselt number were compared with similar works in literature for porous enclosure with no partition i.e., $r_p = 0$ which are shown in Table 1.

| **AUTHORS/ Ra** | **10** | **100** | **1000** |
|---|---|---|---|
| BEJAN [2] | | 4.2 | 15.8 |
| BAYTAS & POP [3] | 1.079 | 3.160 | 14.060 |
| TREVISAN & BEJAN [4] | 1.080 | 3.270 | 18.380 |
| *PRESENT STUDY* | 1.081 | 3.309 | 16.950 |

TABLE 1. Validation of present work with similar works in literature

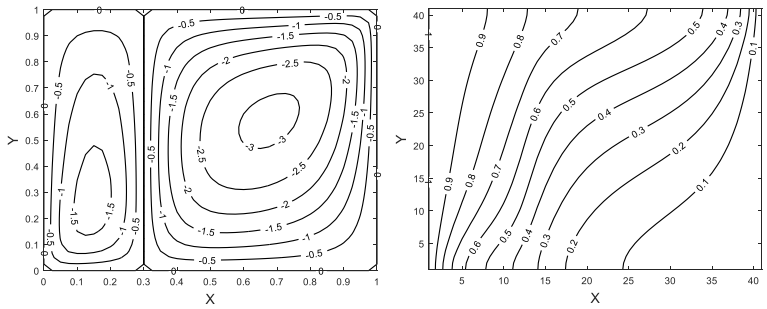

(a)

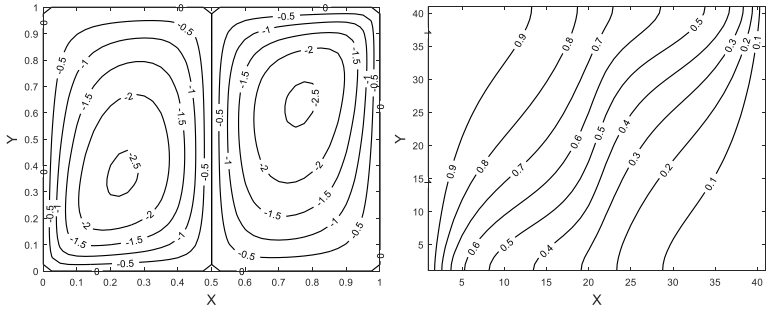

(b)

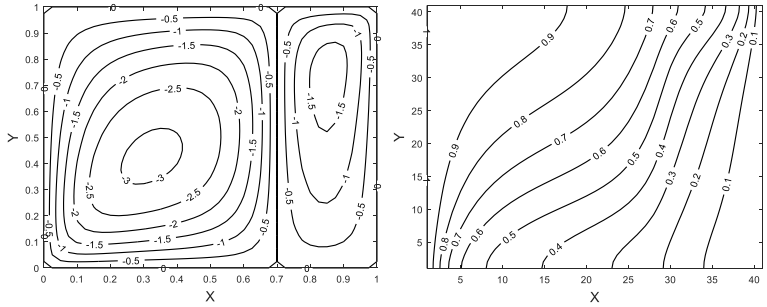

(c)

FIGURE 2. Streamlines (left) & isotherms (right) at steady state for enclosure with partition ratio: (a) $r_p = 0.3$; (b) $r_p = 0.5$; (c) $r_p = 0.7$

Based on above validation, it can be concluded that the current work shows a good agreement with the works in literature and thus, present computational code can be used with greater assurance to study the problem stated in this paper. Fig 2 shows streamlines and isotherms for enclosure with vertical partition for modified Rayleigh number 100 and $r_p$ 0.3, 0.5 and 0.7 at steady state. When $r_p$ = 0.3 as shown in Fig. 2a, the partition is near the hot wall. Hence in initial stages, there is a larger

temperature difference in the first porous block of enclosure wall. Thus convection which is set up in the first block heats up the partition and this gradually sets off convection in second block. As the distance of partition increases, as can be seen in Fig 2b the temperature difference across the first block in initial stages decreases which in turn slows the convection strength and hence the heat transfer rate. As and when partition approaches the cold wall as in Fig. 2c, the temperature difference across the second porous block in the latter stage increases, which aids in a comparatively faster convection in second porous block. More insight of this phenomena can be taken from Fig. 3 which shows variation of average Nusselt number with entire range of partition ratio. It is clear from the figure that Nusselt number decreases as $r_p$ approaches the centre of enclosure and after which it starts increasing again. However, for higher values of Ra the decrease in Nu is more prominent.

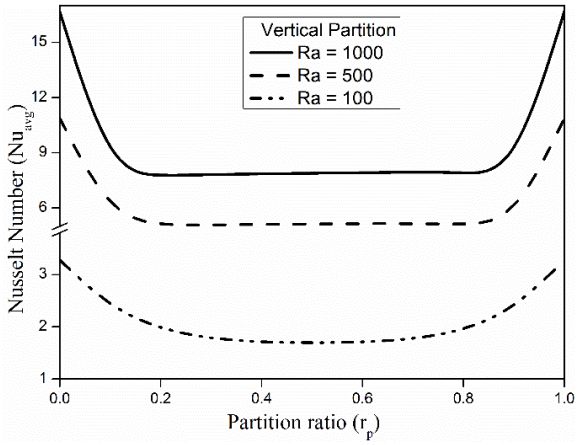


FIGURE 3. Variation of average Nusselt number with partiton ratio at steady state

## 4. CONCLUSIONS

Numerical analysis of square porous enclosure with vertical diathermal partition for varying partition ratio has been carried out in this paper. It is found that employing vertical diathermal partition decreases the Nusselt number considerably. Nusselt number shows a maximum drop when partition is at the center of enclosure. The decrease in Nusselt number is sudden and larger for higher modified Rayleigh number while for lower value of Ra the drop in Nu is gradual and comparatively smaller.

## REFERENCES

[1] Anderson Ren and Bejan Adrian, Heat transfer across a vertical impermeable partition imbedded in porous medium, Int. J. Heat Mass Transfer, Vol. 24, No. 7, pp. 1237-1245, 1981.

[2] Bejan A., On the boundary layer regime in a vertical enclosure filled with a porous medium. Lett.Heat Mass Transf., vol.6, pp. 93–102, 1979.

[3] Baytas A.C., Pop I., Free convection in oblique enclosures filled with a porous medium. Int. J. Heat Mass Transf., vol. 42, pp. 1047–1057, 1999

[4] Trevisan Osvair V. and Bejan Adrian, Natural convection with combined heat and mass transfer buoyancy effects in a porous medium, Int. J. Heat Mass Transfer. Vol. 28, no. 8, pp. 1597-161, 1985.

# Towards a comprehensive bio-heat transfer model for the human body including ageing effects

**Alberto Coccarelli, Neeraj Kavan Chakshu and Perumal Nithiarasu**
ZCCE, Swansea University, Swansea, UK, p.nithiarasu@swansea.ac.uk

## ABSTRACT

With this work we introduce a bio-heat transfer framework for the human body, which accounts for ageing effects. This is carried out by introducing new features into a pre-existing bio-heat transfer model recently proposed by the authors. Blood variables are computed by employing a morphologically detailed arterial tree, including a realistic heart model. Age condition is simulated for the flow system by modifying respectively heart function, arterial stiffness and terminal resistance. Aortic and brachial pressure waveforms were computed for different ages and showed a good agreement with experimental data and other simulated results. This represents a key step towards the development of an aged human body bio-heat transfer model.

**Key Words:** Bio-heat transfer, ageing, arterial flow

## 1. INTRODUCTION

Ageing is a process that can be defined as an i*ntrinsic deterioration of the homoeostatic capabilities of an organism, leading to a constantly increasing risk of death* [1]. The accumulation of defective mitochondria represents one of the most accredited factor causing ageing [2, 3, 4, 5]. At tissue level such irreversible cellular degradation leads to changes in organs' functionalities, physical properties and volumes. Ageing effects on the human body may also be influenced by the lifestyle and the environmental conditions which the subject is exposed to. Due to a less efficient immune system, elderly individuals are more vulnerable to pathogens than young adults. Furthermore, ageing affects also the capacity of the body to react to changes of either internal or external conditions, such as physical workload, food digestion and thermal stress exposure. The energy balance of the body depends on different physiological and anatomical components such as cardiac output, tissue volumes and thermal properties, metabolic production, and may be extremely sensitive to any of these factors' variation. Elderly people generally present significant alterations of such components with respect to the younger individuals, which may involve completely different thermal responses for the same external conditions. The difference of patterns becomes more evident whether the environmental exposure is extreme, like in case of heat waves or hypothermic conditions. However, due to their limited sensory perception, elderly people are at risk also when they are exposed to mild environmental conditions for long times. When the subject is exposed to a hot stress environment, the body temperature increase is contrasted by the action of thermoregulatory system, which tries to keep the core temperature within the thermo-neutrality range (assumed to be 36.8-37.5 o C) by using different mechanisms such as sweating and vasodilation. If, the regulatory mechanisms are not able to level off the thermal energy income with the cooling losses, the thermal balance remains impaired, causing a further temperature rise. Every time that the body core temperature is out from the thermos-neutrality range, cellular physiological processes start gradually to change, up to impair organs' functions and regulatory functions. If this situation is prolonged, the person may experience, in order, heat exhaustion first and then heatstroke, which is considered a life-threatening illness. This scenario is quite rare for young people but it is more likely to happen for aged people, because their thermal resistance may be much lower and thus such processes may occur much faster, without letting the subject to take adequate countermeasures. The prediction of the temperature distribution in an aged body under thermal stress may therefore provide insightful

indications for preventing the onset of such pathological conditions. Furthermore, modelling heat transfer in aged human body may also be useful for other applications, such as temperature controlled surgeries, and ageing related diseases, like Alzheimer. For studying heat transport in the human body, several different bio-heat transfer models were proposed in the recent past [6, 7, 8, 9, 10, 11], ranging from simple lumped models to more complex realistic 3D representations of the body. Although most of these works present very comprehensive modelling methodologies, ageing effects on the body energy balance are not generally taken into account. To the best of the author's knowledge, a limited number of works were carried out on this topic. In this work age-variations in cardiac output and tissues volumes are not included, but they assumed that sweating losses are affected by ageing. Also in this case, the predicted results agreed well with the experimental data obtained for different age categories. With regard to the ageing effects on the arterial system circulation, relevant contributions were given by the works of Maksuti et al. [15] and Pagoulatou and Stergiopulos [16]. In these works the left ventricle thickening, and thus the contractility, is changed by the age-related arterial stiffening, which represents a bigger resistance for the pumped flow. The modelling of such components was carried out according to experimental data and the global methodology were proved to give excellent simulating results with respect the measurements. With the current work, we believe that, by including all the major features above mentioned, we can obtain the most comprehensive approach possible for representing heat transfer in a elderly person body. The current methodology is based on the framework proposed in [11].

## 2. AN AGE-DEPENDENT HUMAN THERMAL MODEL

The proposed model is based on the methodology developed in [11], which can be subdivided into 3 major sub-components, that are the arterial systemic circulation, the solid tissues and the thermo-regulatory system.

### 2.1 Systemic circulation

The larger arterial system is realized according with what proposed by Low et al. [18]: it is a branching characterized by bifurcations and cross-sections discontinuities. Reflections due to network singularities and terminals are also accounted for. The whole network is composed of 91 segments (28 tapering vessels), 6288 elements and 6379 nodes. Full details about the parameters and dimensions of the network are given in [18].

### 2.2 Solid conduction

The tissue model consists of fourteen cylindrical elements representing head, neck, shoulders, thorax, abdomen, thighs, legs, arms and forearms. The segments representing shoulders, legs, thighs, arms and forearms are constituted by four layers of materials with different properties; from inside to outside there are bone, muscle, fat tissues and skin. For head, thorax and abdomen, inner organs are included, which are respectively brain, lung and viscera. In addition, cylinders are not considered to be deformable by temperature gradients. For the geometrical, thermos-physical and basal physiological properties of tissue materials and the body features, we use those proposed by Fiala et al. [7].

### 2.3 Age related modifications

For representing arterial stiffening we adopted 2 different strategies: i) *uniform* augmentation, in which wall elasticity is linearly increased with age (doubling from 20 to 80 years), ii) *specific* augmentation, where the pulse wave velocity is linked to the diameter of the artery via the age-related relationships proposed in [16]. For representing the left ventricle thickening we used changed the elastance coefficients (Emin, Emax) according to [15]. The terminals were tapered in order to obtain a final cardiac output between the range 6-7 l/min. In the next future it will also be necessary including age-modifications for the tissues, such as the ones indicated in [17].

## 3. PRELIMINARY RESULTS AND CONCLUSIONS

In such section we present arterial pressure waveforms computed for 4 different ages (30, 40, 60,80 yr). The left column reports results for beta coefficient uniformly augmented, while the central column shows results obtained by using the relationship from [16]. Both approaches have results that are in good agreement with the computational results from [16].

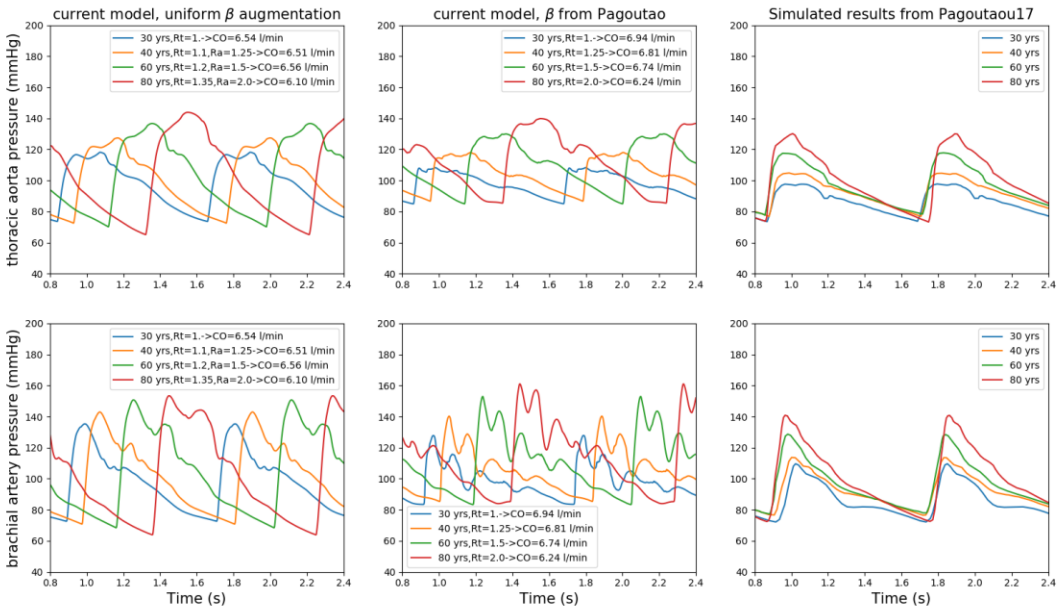


Figure 1. Pressure waveform along arterial tree for different ages.

Such comparison demonstrates also that uniform stiffening hypothesis (beta augmented with a uniform coefficient) along the arterial network may also give accurate results. In the case of uniform stiffness augmentation, the pressure amplitude is bigger than the specific. This may be due to the fact that such a method does not take into account the type of vessel, and is globally applied to each vessel of the network, regardless the diameter size. On the other hand, this strategy has the advantage that no extrapolation from measurements is necessary. Modelling flow age-related changes represents the first step towards modelling ageing effects on heat transfer occurring within the entire human body.

## REFERENCES

[1] Kowald A., Dawson M., and Kirkwood T. B. L. Mitochondrial mutations and ageing: Can mitochondrial deletion mutants accumulate via a size based replication advantage? Journal of Theoretical Biology, 340:111–118, 2014.

[2] Miquel J., Economos A. C., Fleming J., and Johnson J. E. Jr. Mitochondrial role in cell aging. Experimental Gerontology, 15:575âĂŞ591, 1980.

[3] Harman D. Free radical theory of aging: consequences of mitochondrial aging. Age, 6:86–94, 1983.

[4] Richter C. Do mitochondrial dna fragments promote cancer and aging? 241:1–5, 1988. FEBS Letters.

[5] Linnane A. W., Marzuki S., Ozawa T., and Tanaka M. Mitochondrial dna mutations as an important contributor to ageing and degenerative diseases. Lancet, 1:642âĂŞ645, 1989.

[6] C. Smith. A transient, Three Dimensional Model of the Human Thermal System. PhD thesis, Kansas State University, 1991.

[7] D. Fiala, K.J. Lomas, and M. Stohrer. Computer prediction of human thermoregulatory and temperature response to a wide range of environmental conditions. International Journal of Biometeorology, 45:143–159, 2001.

[8] M. Salloum, N. Ghaddar, and K. Ghali. A new transient bioheat model of the human body and its integration to clothing model. International Journal of Thermal Sciences, 46:371–384, 2007.

[9] W. Karaki, N. Ghaddar, K. Ghali, K. Kalev, I. Holmer, and L.L. Vanguard. Human thermal response with improved ava modeling of the digits. Int J Therm Sci, 67:41–52, 2013.

[10] M. Rida, W. Karaki, N. Ghaddar, K. Ghali, and J. Hoballah. A new mathematical model to simulate ava cold-induced vasodilation reaction to local cooling. Int. J. Biometeorol., 58:1905–1918, 2014.

[11] A. Coccarelli, E. Boileau, D. Parthimos, and P. Nithiarasu. An advanced computational bio heat transfer model for a human body with an embedded systemic circulation. Biomechanics and Modeling in Mechanobiology, 15(5)(DOI: 10.1007/s10237-015-0751-4):1173–1190, 2016.

[12] Novieto D. T. Adapting a human thermoregulation model for predicting the thermal response of older persons. PhD thesis, Montfort University, 2013.

[13] Rida M., Ghaddar N., Ghali K., and Hoballah J. Elderly bioheat modeling: changes in physiology, thermoregulation, and blood flow circulation. Int. J. Biometeorol., 58:1825–43, 2014.

[14] Hirata A., Nomura T., and Laakso I. Computational estimation of body temperature and sweating in the aged during passive heat exposure. International Journal of Thermal Sciences, 89:154–163, 2015.

[15] Maksuti E., Westerhof N., Westerhof B. E. et al. Contribution of the arterial system and the heart to blood pressure during normal aging - a simulation study. PLoS ONE, 11(6):e0157493, 2016.

[16] Pagoulatou S. and Stergiopulos N. Evolution of aortic pressure during normal ageing: A model-based study. PLoS ONE, 12(7):e0182173, 2017.

[17] Chen H., Zhou X., Fujita H., Onozuka M., 3, and Kubo K.-Y. Age-related changes in trabeular and cortical bone microstructure. International Journal of Endocrinology, 2013:ArticleID 213234, 9 pages, 2013.

[18] K. Low, R. van Loon, I. Sazonov, R. L. T. Bevan, and P. Nithiarasu. An improved baseline model for a human arterial network to study the impact of aneurysms on pressure-flow wave-forms. International Journal for Numerical Methods in Biomedical Engineering, 28:1224–1246, 2012.

Fifth International Conference on Computational Methods for Thermal Problems
THERMACOMP2018, July 9-11, 2018, Indian Institute of Science, Bangalore, INDIA
*N. Massarotti, P. Nithiarasu, Pradip Dutta and C. Ranganyakalu (Eds.)*

# POROUS MEDIA MODELING OF COMPRESSIBLE FLOW IN MICRO HEAT EXCHANGERS

**Coppola M.A., Croce G., D'Agaro P.**
University of Udine, via delle Scienze 206, 33100 Udine
Giulio.croce@uniud.it

## ABSTRACT

An efficient equivalent porous media model designed to simulate the heat and fluid flow in a gas-gas micro heat exchanger is presented. Although similar models are common in macroscale environment, the present implementation takes into account several issues typical of microscale applications. In particular, three coupled solutions provide the hot fluid temperature, cold fluid temperature, and solid temperature, thus including conjugate heat transfer effects. Proper source terms incorporate the pressure loss effects and provide the coupling among the domains via the mutual heat transfer computation. Furthermore, since for gaseous, compressible flows no fully developed flow is attained, specific local based microscale correlations are used for the determination of heat transfer coefficients and friction factors, using only local values and properly taking into account both rarefaction and compressibility effects.

**Key Words:** *Micro Heat Exchanger, Porous Model, compressible, rarefaction.*

## 1. INTRODUCTION

Micro-heat exchangers typically include tens, if not hundreds, of micro-channels, and often are component of more complex devices. The flow details within each of the micro-channel actually are of much smaller scale than the whole device: thus, despite the high efficiency of current CFD tools, the detailed simulations of the whole device geometry is not practical as standard design tool.
Modelling of the whole device via a homogeneous porous media representation reduces the computational effort, offering an interesting compromise between accuracy and efficiency: the computational domain for both operating fluids covers the whole device, and the single control volume includes both fluids and solid sections. The solid must be modelled, too, since the relatively thick walls may well have an effect on heat transfer rate [1]. A porous resistance introduces the wall effect in the momentum equations, as commonly done also in most commercial CFD tools. The same approach is applied to the energy balance defining, at each control volume, three different temperatures (hot fluid, cold fluid, wall) and three different energy equations. The heat transfer between solid and fluids provides the coupling among the domains and is computed via Nusselt correlation. For gaseous, compressible, rarefied micro flows, no fully developed flow occurs, and thus the correlations have to be based on local parameters, and have to take into account both compressibility and rarefaction. Here, we exploit a fully local correlation developed by the authors in a recent paper [2] in order to simulate the flow in a micro heat exchanger in presence of relevant rarefaction and compressibility effects. The correlation is defined in terms of a proper temperature parameter designed to take into account the relative importance of heat transfer and conversion of thermal into kinetic energy, typical of highly compressible regime.

## 2. MATHEMATICAL MODEL

The main idea is to discard the geometrical details of the single heat exchanger tube or channel, introducing proper source terms in order to mimic their average effect on the bulk flow. In particular, we have to model a source term to introduce the average effect of wall friction in the

momentum equation, assuming some correlation for the friction factor *f*, and a source term for the energy equation in order to take into account the energy exchange between the hot and cold stream. For each stream, a porosity coefficient $\xi$ defines the geometrical obstruction due to the solid walls and the other fluid passage.

This distributed approach, or porous media description of the device, has been commonly used for a while in heat exchanger applications [3]. Commercial CFD codes usually implement a similar kind of porous media model for the momentum equation, including the proper source terms and porosity definitions, while the energy equation takes into account the solid only as a kind of passive element, affecting the average effective conductivity and thermal capacity in the computational domain.

If the subscript *i* identify identifies either the hot or the cold stream (*i*=*h*,*c*) and the subscript *s* refers to the solid, the governing equations, in steady state, assume the following form:

$$\nabla\cdot\left(\xi_i\rho_i\mathbf{u}_i\right)=0$$

$$\nabla\cdot\left(\xi_i\rho_i\mathbf{u}_i\mathbf{u}_i\right)+\nabla\cdot\left(\xi_i p_i\right)-\nabla\left(\xi_i\boldsymbol{\tau}\right)=-C_{Mi}\frac{1}{2}\rho_i\mathbf{u}_i\cdot\mathbf{u}_i$$

$$\nabla\cdot\left[\xi_i\rho_i\mathbf{u}_i\left(E_i+p_i\right)\right]-\nabla\cdot\left(\xi_i\lambda_i\nabla T_i\right)=C_{Ti}\frac{1}{2}\left(T_s-T_i^0\right)$$

$$\nabla\cdot\left(\xi_s\lambda_s\nabla T_s\right)=\sum_i C_{Ti}\frac{1}{2}\left(T_s-T_i^0\right)$$

These equations correspond to nine scalar equations for a 2D problem, and eleven scalar equations for the 3D case. Fully compressible flow form is retained, since at microscale we can have significant density variation and possibly high Mach numbers [4,5]. Thermal conductivities are anisotropic, to take into account specific channel geometries. Furthermore, the energy source term is function of the stagnation temperature $T^0$ (i.e., the temperature attained after an adiabatic stop), which is a measure of the actual total energy content of the fluid, including the kinetic component. Finally, the coefficients $C_M$ and $C_T$ are related to the friction coefficient *f* and Nusselt number *Nu*:

$$C_{Mi}=f_i\frac{1}{D_h\xi_i^2}\qquad\qquad C_{Ti}=Nu_i\frac{\lambda_i}{D_h}\frac{A}{V\xi_i}$$

## 3. GEOMETRY AND CORRELATIONS

As a preliminary validation, a simple configuration is considered, allowing for validation with previous full CFD computations [6]. In particular, let us focus on an infinite array of planar channel, with hot and cold streams running in a counter current arrangement. The resulting 2D geometry was analysed in [6] for a wide range of pressure ratios, Maranzana axial parameter [1] and rarefaction levels within the slip flow regime. The operating fluid on both sides is air, and each channel has a height *H* of 10μm. The microchannels are separated by a solid wall of 5μm thickness, with a solid/fluid conductivity ratio of 100. Boundary conditions for both full CFD solution and the current porous media approach follow usual compressible flow approach: fixed stagnation temperature and pressure (i.e., upstream plenum values) at the inlets, fixed static pressure at the outlet, symmetry on the remaining domain boundaries.

The governing equations may be solved with any kind of CFD solver. Here, we used Fluent code coupled with proper user defined functions for the fluid simulations, and an in-house finite difference code for the conduction problem. Correlations for microscale gas flows are not yet well established, due to the complex superimposition of different effects: slip flow at the wall, compressibility effects, strong axial conduction due to the relevant relative thickness of solid walls, often of the same order of magnitude of the hydraulic diameter $D_h$. In [2] it was found that the main reason for discrepancies between heat transfer values at gaseous, compressible, microscale conditions and geometry, and the standard macroscale incompressible flow is due to the competition between two independent

phenomena that affect the temperature: the actual convective heat transfer, and conversion between internal and kinetic energy. In particular, following [2,6] we define the Nusselt number using bulk stagnation temperature $T_b^0$, since it is a direct measure of the flow energy content. Nusselt was found to be, in most conditions, in nice correlation with the parameter ϕ:

$$\phi = \frac{T_b^0 - T_w}{T_b^0 - T_b}$$

The numerator, difference between the bulk stagnation temperature and wall temperature, measures the total convective heat transferred in the process; the denominator, difference between the flow bulk stagnation temperature and flow bulk temperature, relates to the amount of energy transported by the flow as kinetic energy. The correlation derived in [2] will be adopted here, and offers:

$$Nu^0 = 7.54 - \frac{3\gamma}{2\phi|\phi|^{\frac{1}{5}}} \ .$$

Note that eq.(11) implies Nusselt higher than the incompressible values if the flow is cooled, and lower if the flow is heated; furthermore, the equation admits negative values for *Nu*. This is reasonable, since at low heat transfer rate and high compressibility effect (i.e. small $\phi$) we may have a hot fluid bulk total temperature still higher than the wall temperature despite a static temperature always lower than the wall one. Finally, by post-processing and fitting the same data base used to derive the Nu, the following expression is used for the Poiseuille number or the friction factor *f*:

Commented [P.D'A.1]: ????

$$Po = f \cdot \mathrm{Re} = \frac{96}{1+12Kn}\left(1 + 4.21Ma^2 + 92.18Ma^4\right)$$

The correlation prediction, validated in [7], combines the evaluation of compressible and rarefaction effects, via the Knudsen number, ratio between mean free path and hydraulic diameter. Minor entrance loss are included via an additional, zero-thickness porous screen at inlet section.

## 4. RESULTS AND DISCUSSION

An array of short channels, with an aspect ratio height to length of 20, with an inlet total pressure of $3 \cdot 10^6$ Pa and an outlet pressure of $10^6$ Pa is considered leading to a significant exit Mach number (Fig.1, left). Pressure profile are no longer linear (Fig.1, right). Hot flow enters at 333 K, cold one at 285 K. In contrast with the uncompressible case, Fig.2 shows that the wall temperature is clearly closer to the cold fluid, due to the cooling related to the conversion of internal energy into kinetic one. It is worth to notice that the exit bulk static temperature for the hot fluid is actually lower than the wall temperature (275 K vs. 280), yielding to the abrupt change of slope of the temperature near the hot flow exit (x=0.0002). Comparisons with the full CFD results from [6] looks fully satisfying, and even the thermal efficiency $\varepsilon = \left(T_h^{0inlet} - T_c^{0exit}\right) / \left(T_h^{0inlet} - T_c^{0inlet}\right)$ of the device is well predicted, with a 5% accuracy. Finally, Fig.3 offers the static temperature contours for the cold stream in a cross-flow arrangement. Both convective heating and conversion between internal and kinetic energy affects the contour shape: the latter provides the temperature reduction at the left side of the domain (cold flow exit), the former the temperature reduction from the top left corner (hot side inlet, cold side exit) and the bottom right corner (hot side exit, cold side inlet).

## 5. CONCLUSIONS

A porous media modelization for the simulation of microscale heat exchangers is applied to compressible flow regime. The results and the comparison with full CFD results show that the combination of the porous model and of a set of correlation taking into account the conversion of internal to kinetic energy due to compressible flow acceleration, is able to fully predict the unusual conditions that can be found in short microchannels.

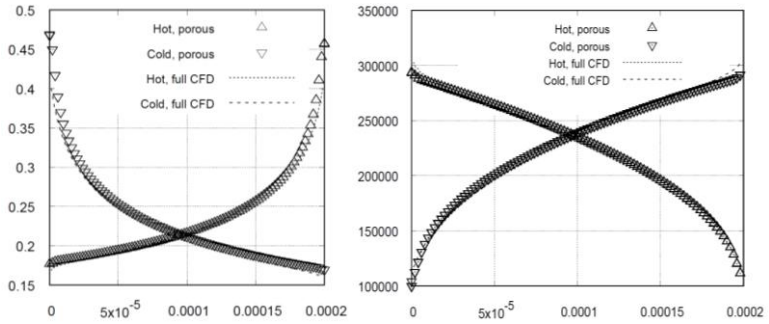


FIGURE 1. Validation: Mach (left) and pressure (right, [Pa]) profile along streamwise direction [m]

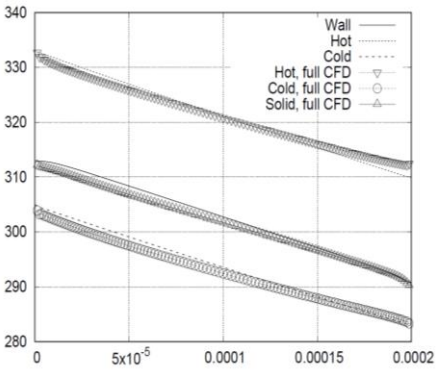


FIGURE 2. Validation: fluid stagnation and wall temperature [K] along streamwise direction [m]

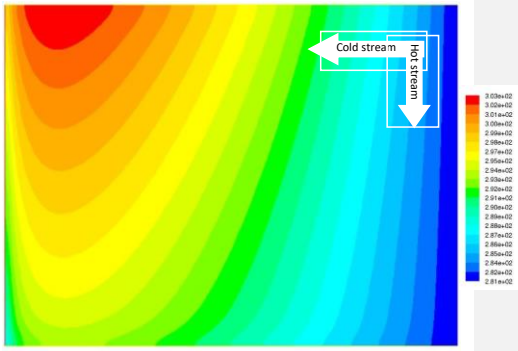


FIGURE 3. Static temperature contours, cross flow arrangement, exit Ma=0.5, cold stream [K]

## REFERENCES

[1] Maranzana, G., Perry, I., Maillet, D., Mini and micro-channels: influence of axial conduction in the walls, *Int. J. Heat Mass Transfer*, 47, 3993-4004., 2004

[2] Coppola M. A. and Croce G., Heat Transfer Correlations for compressible flow in Micro Heat Exchangers, *Journal of Physics: Conference Series*, 745, 2016

[3] Prithiviraj M. and Andrews M.J., Three-dimensional numerical simulation of shell-and-tube heat exchangers. Part I: Foundation and fluid mechanics, *Num. Heat Trans. Part A, Applications*, 33/8, 799-816, 1998

[4] Yang, Y.H., Morini, G.L., Brandner, J., Experimental analysis of the influence of wall axial conduction on gas-to-gas micro heat exchanger effectiveness, *Int. J. Heat Mass Transfer*, 69, 17-25, 2014

[5] Yang Y.H., Hong C.P., Morini G.L., Asako Y, *Int. J. Heat Mass Transfer*, 78, 732-740, 2014

[6] Croce, G., Coppola, M.A., Conjugate Heat Transfer simulation in gaseous flow Micro Heat Exchanger, ASME paper, ICNMM 2015, San Francisco, 2015

[7] Croce, G., Coppola, M.A., D'Agaro P., Porous Media modelization of Micro Scale, Gas-Gas Heat Exchanger, proc. CHT17, Neaples 2017

# Towards modeling of combustion dynamics in solid rocket motors

**Debasis Chakraborty, Kalyana Chakravarthy**
Defence Research & Development Laboratory, Kanchanbagh, Hyderabad-500058, India
debasis_cfd@drdl.drdo.in, v_kalyana_chakravarthy@yahoo.co.in

## ABSTRACT

Large eddy simulation of flow in a rectangular duct with transpiring walls is performed to capture transition to turbulence and associated increase in friction coefficient. The constant mass flux condition at the walls in current simulation replaced with a pyrolysis law along with addition of solid phase heat condution and a gas phase flame model is expected to result in a predictive model for combustion is solid rocket motors. As the flow transitions, increased convective heat transfer and pyrolysis would lead to erosive burning.

**Key Words:** *Turbulence, Transition, Heat transfer, solid propellant combustion.*

## 1. INTRODUCTION

Turbulence may play a key role in internal flow and combustion dynamics of solid propellant rocket motors. Flow starts out laminar at the head end of the motor and if the lenth-to-diameter ratio and burn rate are high enough, there would be transition and possibly fully turbulent flow at the nozzle end of the motor. As in case of any solid fuel based combustion, the flame in solid rocket motors stands away from the fuel surface. The heat transfer from the flame to the surface leads to pyrolysis generates gaseous species that burn within the flame. Accurate modeling of this heat transfer is key to capturing the flow effects on combustion.

Accurate predictions of convective heat transfer rates to or from solid boundaries are routinely done in case of both laminar and turbulent boundary layers. For turbulent boundary layers, the computational cost associated with resolving all the near wall dynamics is circumvented by using scaling laws for near wall regions in Reynolds averaged Navier-Stokes equations (RANS) based simulations. The scaling laws adjusted to account for transpiration are available [1] but their use in RANS approaches, if any, is not common knowledge.

The additional difficulty in modeling heat transfer in rocket motors is associated with transition. RANS based transition approaches are mostly phenomenological with adjustable constants. Besides, they are mostly used for external flows. Even those that may work for internal flows may need to be adjusted for transpiration boundary conditions and the fact that the transpiration makes the mass flux vary in space (unlike in case of confined flows with solid walls).

Large eddy simulation (LES) methods which resolve the wall layer dynamics and are more predictive for transitional flows offer a tractable computational platform for modeling flow and combustion dynamics in solid rocket motors. For Reynolds numbers typical of even small rocket motors, direct numerical simulation approaches which seek to resolve all the length and time scales of relevance still remain impossible even with the computing power that parallel computers of today offer.

Two relatively inexpensive LES approaches are possible for modeling flow/flame dynamics in rocket motors. First is a two-dimensional simulation with accurate modeling of conjugate heat transfer and flame using multispecies transport equations. The very small time step required for integrating chemical kinetics make three-dimensional simulations very expensive as explained in our earlier work [2]. The present work lays the foundation for an alternative three-dimensional

approach where a level set approach using a single scalar equation called the G-equation is used for modeling the flame. This obviates the need for integrating reaction kinetics and is therefore quite suitable for three-dimensional simulations. The results of the three-dimensional and previous two-dimensional simulations are compared here.

## 2. MAIN BODY

The experiment of Traineau et al. [3], which emulates flow in a solid rocket motors is considered for validation here. The sideview of the domain is shown in Figure 1. The width of channel is 4cm. Use of solid walls on the sides as in the experiment would require near-wall grid clustering. Use of a mesh that is uniform in spanwise direction would reduce the number of grid points and the overall computational cost. This can be done by using periodic boundary conditions provided side walls effects localised to boundary that are very thin compared to spanwise width of 4cm. One of the past LES studies [4] used side walls but the other made this simplification and used periodic boundary conditions [5]. A comparison suggests that periodic boundary conditions does not affect the overall predictions which compare very well with measurements in the middle core region of the flow. The same is done here.

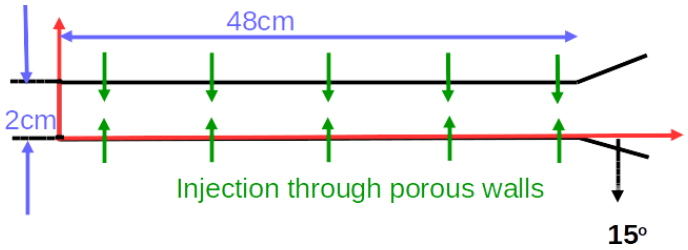


Figure *1*: Side view of the flow setup

The mass flux and the temperature at the walls are fixed at 13.0 kgm/s2 and 260K respectively. Additional white noise is added to the inflow velocity to mimic the noise in the experiment that induces transition. The details of the numerical method are provided elsewhere [6] and are left out here. A 512x64x32 mesh that is clustered near the transpiring walls in used for the simulation.

## 3. RESULTS

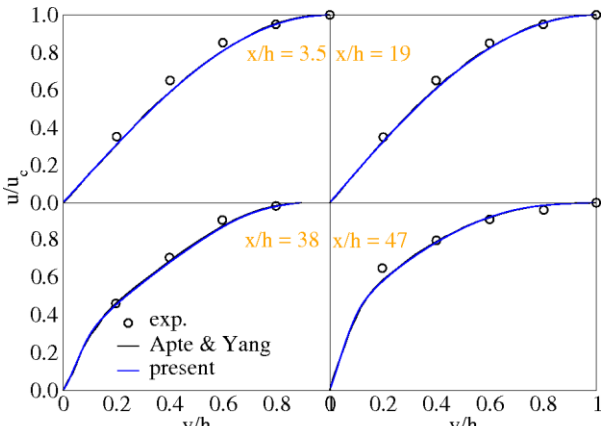


The mean streamwise velocity profiles at various axial locatons are plotted in Figure 2. Results from a previous three-dimenional LES [4] are included for comparison. Transition from a near parabolic laminar profile to flatter at the center turbulent profile is well captured in the simulations. In fact, mean velocity profiles can accurately be captured even with two-dimensional simulations as

noted in past studies. It is in second order statistics predictionwhere they fall short. The two simulations predict similar profiles indicating an insignificant confinement effect and negligible effect of the periodic spanwise boundary conditions.

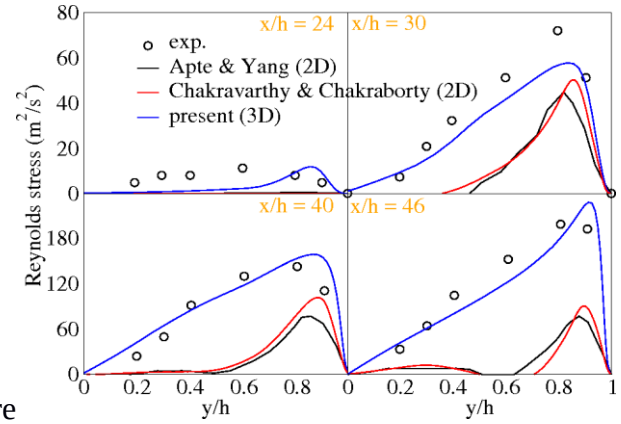


Figure *3*:

The flow in the upstream half of the domain is mostly steady with low level noise resulting from white noise superimposed at the inflow. Coherent structures resulting from hydrodynamic instabilities start to appear around the mid-point of the domain. In addition to primary shear instability which creates Tollmien-Schlichting waves, the transpiration boundary condition leads to so called parietal vortex shedding. The parietal vortex shedding has a single characteristic frequency and in this sense, the parietal vortices are more regular. The two-dimensional structures resulting from the two instabilities by first twisting into lambda-vortices and then into hairpin vortices breakdown and generate three-dimensional turbulence. The generation of Reynolds stress is integral to this process. In two-dimensions, however, the lack of vortex stretching keeps the two-dimensional structures in tact and Reynolds stress levels are subdued. This is evident from the comparison of the predictions from two [2,7] and three-dimensional simulations along with corresponding experimental data in Figure 3. The profiles and levels predicted in the present three-dimensional simulation, like in some of past three-dimensional simulations, are almost similar to those in experiments.

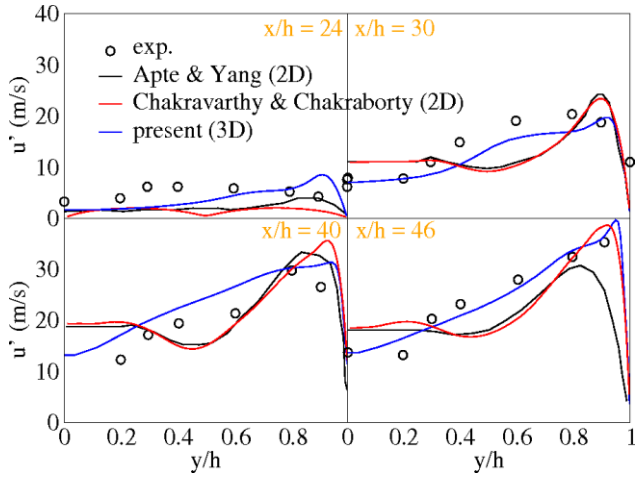


Figure *4*: Turbulent intensities profiles at various axial locations

The profiles of turbulent intensity at various axial locations are shown in Figure 4. At any location, though the levels of turbulence in two-dimensional simulations are nearly the same as in the experiment, the profiles shapes are clearly incorrect. The unsteady kinetic energy in these simulations is associated with chaotic dynamics of two-dimensional vortices as compared to three-dimensional turbulence in the experiments. The migration of such large scale two-dimensional structures in two-dimensional simulations leads to overprediction of unsteadiness in the core region towards the downstream end of the flow.

## 4. CONCLUSIONS

The three-dimensional predictions here and in past studies are closer to experiments than the two-dimensional predictions. The increased accuracy comes at a computational cost that is an order of magnitude higher but not prohibitive. While the turbulence intensities in the near wall regions are well predicted in two-dimensional simulations, the nature of the constituent eddies could be different when compared to the experiment. How the three-dimensional fluctuations affect the flame depends of how close it is to the wall. If the time scales associated with spanwise fluctuations are too small, the flame may not respond to them. Use of a simplified flame tracking model using the G-equation in a three-dimensional simulation is proposed as the next step. This when compared to a similar two-dimensional simulation may help bring out the three-dimensional effects. This seems to be a more pragmatic approach than using multispecies transport equations based flame simulations.

## REFERENCES

[1] H. Tennekes. Similarity laws for turbulent boundary layers with suction or injection, *Journal of Fluid Mechanics*, 21 (4), 689–703, 1965.

[2] K. Chakravarthy and D. Chakraborty, Vortex pairing and reverse cascade in a simulated two-dimensional rocket motor-like flow field, Physics of Fluids, 29, 075104, 2017.

[3] J. C. Traineau, P. Hervat, and P. Kuentzmann, Cold-flow simulation of a two-dimensional nozzleless solid-rocket motor, *AIAA Paper No*. 86-1447, 1986.

[4] S. V. Apte and V. Yang, A large-eddy simulation study of transition and flow instability in a porous-walled chamber with mass injection, *Journal of Fluid Mechanics*, 477, 215-225, 2003.

[5] B. Wasistho and R. Moser, Simulation strategy of turbulent internal flow in solid rocket motor, Journal of Propulsion and Power, 21(2), 251-263, 2005.

[6] V. Kalyana Chakravarthy, K. Arora and D. Chakraborty, A simple hybrid finite volume solver for compressible turbulence, International Journal For Numerical Methods in Fluids, 77 (12), 707-731.

[7] S. Apte and V. Yang, Unsteady flow evolution is porous chamber with surface mass injection. Part I: Free oscillations, *AIAA Journal*, 39(8), 1577-1586, 2001.

# Influence of Nano-Silicon Carbide and Alumina Reinforced Aluminum Fins for Natural Convective Heat Transfer

D.Deepa[1], R.Thanigaivelan[2*]

[1]Department of Mechanical Engineering, Muthayammal Engineering College (Autonomous), Rasipuram-637408,India.Email: d.deepadev.deepa1@gmail.com,
[2]Department of Mechanical Engineering, Mahendra Engineering College (Autonomous), Mallasamudram-637503, India.Email: tvelan10@gmail.com

## ABSTRACT

The need for low weight, high efficiency and low cost heat transfer system contributes for new development of fin materials which finds major application in electronics industries. Keeping this requirement and new micro-fin material is developed with different composition of nano sized reinforcement. Nano sized reinforcement such as silicon carbide (SiC) and alumina is considered for the study with different composition such as 2, 4 and 6 gms respectively. The thermal conductivity of the different composition micro-fin is evaluated. Among the various composition of alumina nano powder, the weight of 6gms reinforcement produces stable and higher convective heat transfer co-efficient. Aluminium with,6grams of alumina test piece produces increased convective heat transfer coefficient compared to aluminium with 2,4,6grms of SiC. Increased convective heat transfer coefficient of 23.07% is obtained after 4 hours of heating for aluminium with alumina test piece compared to aluminium with 6gms of SiC test piece.

**Keywords** *: Nano reinforcement,free convection, Buoyancy force,viscous force,metal matrix composite(MMC)*

## INTRODUCTION

Recent requirements for the low volume and high performance devices add for the development of micro-technologies in the last decades. Fields such as power electronics, photovoltaic's cells and Light Emitting Devices requires micro-fins for micro-cooling application [1]. Progressive research on thermal behaviour of micro-fin under natural convective conditions is extensively carried out by the researchers. Kim et al (2008) studied the natural convective heat transfer around the micro-fin. The micro-fin array with fin height of 100 µm shows better result compared with one with fin height of 200 µm. Mahmoud et al. (2011) experimentally investigated the effects of micro-fin dimensions on convective heat transfer coefficient for a horizontally mounted heat sink. Their study revealed that the convective heat transfer coefficient decrease with increase in fin height and the highest convective heat transfer coefficient value is recorded as 8 $Wm^{-2}K^{-1}$. Yu et al. (2011) investigated the natural convective heat transfer of radial heat sink. They propose to optimise both thermal performance and heat sink mass simultaneously and suggested that the simultaneous optimization of both the characteristics is impossible. Zhou et al. (2012) have developed 3D graphene growth for thermal management on porous $Al_2O_3$ ceramics heat sink using chemical vapour deposition technology. They found that this type of heat sink is suitable for electronic applications. Micheli et al. (2015) have studied the thermal behaviour of pin micro-fins and plate micro-fins. Based on the investigation the pin micro-fins show the better thermal performance compared to plate micro-fins. Taha et al. (2016) modified the surface of the nickel wire using carbon nano fibre to improve the heat transfer performance characteristics. The dense carbon nano fibre distribution resulted in 34 % increased heat transfer performance compared to samples made at 500ºC. The highly conductive surface, rough surface and surface area contributes for increased performance. Primeaux et al. 2016 moulded the 1D and 2D micro-fin array on an aluminium sheet metal. They suggested a new and low cost fabrication method for micro fin arrays. Zhuang et al. 2016 developed a micro fin with composite metal and polymer and studied the heat transfer performance. The study reveals that the highest heat transfer

coefficient of 23.7 W/$m^2$ K was obtained at the lowest fin height of 0.1 mm and the greatest spacing of 0.5 mm. Thanigaivelan and Deepa (2017) have fabricated the aluminium and copper micro-fin with different orientation and improved the heat transfer coefficient by applying aluminium paint coating on each test piece. It is evident from the above literatures that the research on micro-fin is witnessed in recent years there is still a lack of knowledge on the thermal behaviour of composite micro-fin under natural convective conditions. Moreover in the view of improving the overall efficiency, weight, cost and size of the heat transfer system a new micro-fin material is proposed. In this research a micro-fin arrays are fabricated with aluminium reinforced with nano SiC[5] and nano alumina [1].Three different composition of nano-reinforcement is proposed for preparing the micro-fin materials[7]. Among these compositions, low and medium shows good response for the convective heat transfer.

## EXPERIMENTAL SET-UP

The MMC casting is prepared through stir casting process in which aluminium 8090 series of weight 150gm is melted up to the temperature 740º C for 20 minutes. Ball milled preheated SiC and alumina nano powder is added to the aluminium matrix, stirred and cooled for some time in order to make a perfect casting. Three different compositions such as 2, 4 and 6 grams of SiC and alumina nano powder were added to the aluminium matrix. The prepared casting was surface finished using milling process and surface grinding[8]. The finally micro-fin array[2] ,[6]with dimension of 4.5 x4.5 x 0.5 cm is generated on the test specimen. Total 6 test pieces with same dimensions of height 0.25 mm and spacing of 5 mm with thickness of 5 mm is fabricated [9] and heated with 12 Watts supply for 4 hours. To evaluate the thermal conductivity of the test pieces it is covered with fibre glass box and further covered with styropor block. The specimen was heated by supplying AC voltage using step down transformer. The experiments are carried out with the help of auto transformer, ammeter, voltmeter and heating element as shown on figure 1. Heating element is kept at the bottom of the test pieces and constant 15 Watts power supply was given to the specimen and readings were taken for every one hour. The specimen is totally covered with insulating material and heat will be added from the bottom side of the test piece. Since the temperature researches to stable at the top of the specimen the heating was done.The thermal conductivity of the test specimen is calculated by using equation 1 [12]. The thermalconductivity for AlSic(150gms+2,4,6gms) increases by 11.85w/mk,6.44w/mk,37.036w/mk. For Al +$Al_2$ $O_3$ (150gms+2,4,6gms) decreases by 32.92w/mk,49.38w/mk,12.88w/mk

$$K = q^* d / T_1 - T_2 \qquad [1]$$

$q^*$ - Quantity of heat passing through a unit area of the sample in unit time (W / $m^2$)
$q^* = (Q / A)$
d - Distance between two sides of the sample (in meters)
$T_1$ - Temperature of warmer side of sample (K)
$T_2$ - Temperature of colder side of sample (K)
Q - Quantity of heat passing through a base area of the sample (W)
A - Base area of the sample ($m^2$) .

Convective heat transfer was calculated by ,

$Nu = 1.18 [ Ra ( r/H )^4 ( r / L )^4 ]^{0.147}$ [6]
$Nu = h_c r / k$ [11]
$Ra = g ß ( T_w - T_a ) r^3 / v α$
$r = 2 HS/2H+ S$ [3]
$h_c$ - convective heat transfer coefficient
H - Height of fin
K - Thermal conductivity W/mk
$T_w$ - Surface temperature in Kelvin
$T_a$ - Air temperature in Kelvin
υ - Kinematic viscosity $m^2$ / sec
α - Thermal Diffusivity $m^2$ / sec

## RESULT AND DISCUSSION

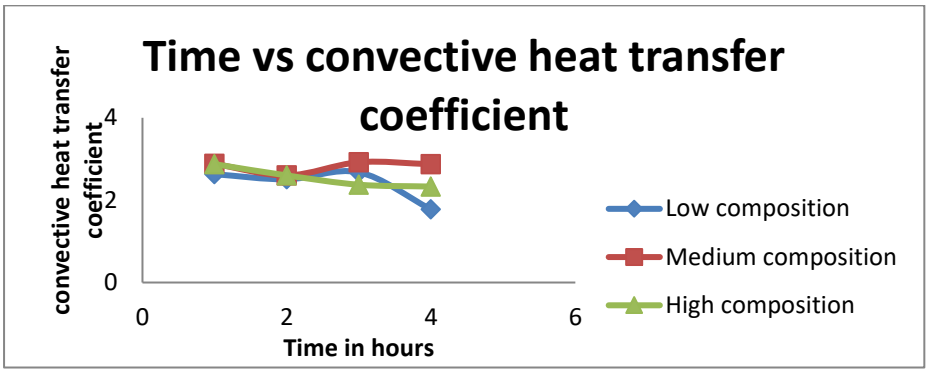


Fig 3 (Al+2,4,6 grams of sic )

The above graph is plotted between time and convective heat transfer coefficient.In high composition the heat convection decreases by 18.92% when compared to low composition.The reason is ,heat conduction is essentially the transmission of energy by molecular motion. Thermal conduction in solids is due to the two effects.i)motion of free electrons ii). Molecular vibrations. For metals the Increase in temperature abstruct the flow of free electrons and and reducing the thermal conductivity . In case of non metals,there are no free electrons,so only the molecular vibrations are responsible for conduction of heat and hence for non metals the conductivity increases with increase in temperature And also when conduction increases, the convective heat transfer co efficient decreases. Sic is having the ability to store much amount of heat only the conductivity increases.

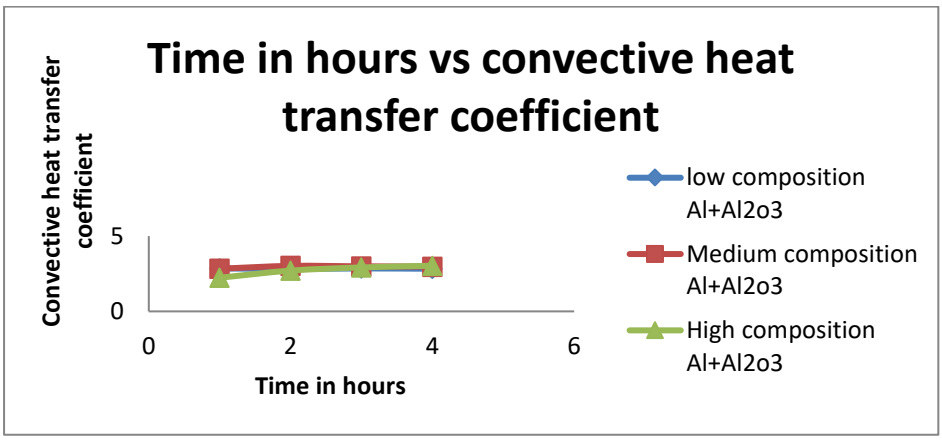


Fig 3 (Al+2,4,6 grams of $Al_2O_3$ )

In case of (aluminium+ alumina ) the conductivity decrease by 60.87%. The reason is aluminium and its alloy is having the ability to loss its heat at high temperature.So the conductivity decreases and convection increases [4],[12]

## CONCLUSION

In the view of reducing the weight and cost of the heat transfer system a new micro-fin material is developed with different composition of nano- reinforcement. Nano-reinforcement such as SiC and alumina is considered for the study with different composition such as 2, 4 and 6 gms.

1. The thermal conductivity for 2, 4, and 6 gms of SiC reinforced test piece was found to be 11.85W/m K 6.44 W/m K and 37.06 W/m K respectively.
2. The thermal conductivity for 2, 4, and 6 gms of alumina reinforced test piece was found to be 32.92,49.38,12.88w/mk respectively.

3. The convective heat transfer coefficient was found to be in higher side for aluminium with alumina reinforcement [10]
4. Among the various composition of alumina nano-powder, the weight of 6 gms reinforcement produces stable and higher convective heat transfer co-efficient over a period of time.
5. Aluminium with 6 gms of alumina test piece produces 23.30% increased convective heat transfer coefficient compared to aluminium with 6 gms of SiC at four hours of heating.

## REFERENCE

[1].Aslan Farjam, Yannick Cormier, Philippe Dupuis, Bertrand Jodoin, and Antoine Corbeil, Influence of Alumina Addition to Aluminum Fins for Compact Heat Exchangers Produced by Cold Spray Additive Manufacturing, Journal of Thermal Spray Technology, DOI: 10.1007/s11666-015-0305-4.

[2]J.S.Kim,B.K.Park & J.S.Lee(2008) Natural convection heat transfer around microfin arrays, Experimental Heat Transfer: A Journal of Thermal Energy Generation, Transport, Storage, and Conversion, 21:1, 55-72, DOI: 10.1080/08916150701647835.

[3]S.Mahmound et al.(2011) Effect of micro fin geometry on natural convection heat transfer of horizontal micro structures, Applied Thermal Engineering, 31 ,627-633.

**[4]**Seung-Hwan Yu et.al(2010) .Natural convection around a radial heat sink, Internternational journal of Heat and Mass Transfer Volume 53, Issues13-14, Pages 2935-2938.

[5]Mi Zhou, and Tianquan Lin (2012) Highly Conductive Porous Graphene/Ceramic Composites for Heat Transfer and Thermal Energy Storage, Advanced Functional Materials, 23(18), pp. 2263-2269.
[6]J.Leonardo Micheli et.al(2015)General correlations among geometry, orientation and thermal performance of natural convective micro-finned heat sinks,International Journal of Heat and Mass Transfer,Volume 91, Pages 711-724.

[7]T.J. Taha et.al(2016) Effect of carbon nanofiber surface morphology on convective heat transfer from cylindrical surface: Synthesis, characterization and heat transfer measurement, International Journal of Thermal Sciences 105 , 13-21.

[8]Philip A Primeaux1 et.al.(2017) Aluminum-based one- and two-dimensional micro fin array structures: high-throughput fabrication and heat transfer testing. J. Micromech. Microeng. 27 , 025012 (9pp).

[9]Jian Zhuang. et.al (2016) Influence of factors on heat dissipation performance of composite metal–polymer heat exchanger with rectangular microstructure, Applied Thermal Engineering 102 ,1473–1480.

[10]Thanigaivelan R and Deepa D (2016) Heat transfer enhancement by coated fins in the microscale domain,Thermal science, doi.org/10.2298/TSCI160901089T.

[11]U.S Kim et.al(2008) Natural Convection Heat Transfer around microfin arrays.Explaimetal heat transfer,21: 55-72.
[12]Yunus A.Cengel.,(2007) 3rd d edition ,Heat and Mass Transfer-A practical approach, New Delhi: Tata McGraw-Hill Education Pvt Ltd, chapter- 12, p.388-389.

Fifth International Conference on Computational Methods for Thermal Problems
THERMACOMP2018, July9-11, 2018, Indian Institute of Science, Bangalore, INDIA
*N.Massarotti, P.Nithiarasu, Pradip Duttaand C. Ranganyakalu(Eds.)*

# AERODYNAMIC BEHAVIOUR OF A LINEAR SUBSONIC COMPRESSOR CASCADE IN A DROPLET LADEN FLOW

**Deepak narayanan[1],Anand S[1], S Anish[1]**
Department of Mechanical Engineering, National Institute of Technology Karnataka, Surathkal, Mangalore - 575025, *Email: anish@nitk.edu.in,*

## ABSTRACT

In the present investigation a computational study of droplet laden flow in a linear compressor cascade has been carried out. Simulations have been carried out at different incidence angles in order to understand the effect of water droplets in the separated flow regions. The study reveals significant flow modifications in the separated flow region by the presence of water droplets and the total loss coefficient reduces at the downstream side of the compressor significantly at positive incidence angles. Particular emphasis has been given to study the effect of water injection on the blade loading and analyze pressure distribution over the blade at negative and positive incidence angles. It has been noted that pressure distribution over blade is almost uniform at higher incidence angles. At smaller incidence angles the blade suction side pressure values are non-uniform in the axial direction due to the increased droplet wall interactions. As a result, the pressure contours are highly non-uniform in the suction surface. On the contrary at higher incidence angles a smoother pressure contours are observed at the suction side .

**Key Words:** *Wet compression, Incidence angle, Linear compressor cascade,Over spray,*

## 1. INTRODUCTION

The consequences for the operation of gas turbines equipped with a water injection system have been investigated and the possibility to augment the power output has been confirmed by many researchers [1-8]. However, development of the theory and explanation of the phenomena associated with overspray are not always consistent and are sometimes misleading and incorrect. The detailed aerodynamic effects on the compressor's blades imposed by the presence of liquid droplets in the compressor flow have not been fully understood. This knowledge is essential to be able to match the blade geometry to fully utilize the potential of the overspray technique. The presence of water droplets can alter the local recirculation zone and compressor stage matching inside a multistage compressor. Hence a detailed understanding of the blade loading with the overspray under various operating conditions is extremely important. The present study is aimed towards that direction.

## 2. METHODOLOGY

A linear compressor cascade available at the Turbo machinery Laboratory, NITK has been chosen for the present study. It is a low speed linear cascade and the blades are designed such that they have aerodynamic similarity to real machines rather than geometrical similarity. It operates at a Reynolds number several times lower than a real compressor. The cascade tunnel is of blown down type with an axial flow fan. For the numerical study a single compressor blade passage is modeled using ICEM CFD. The inlet of the fluid domain is 1.5 times the axial chord distance ($C_{ax}$) away from the leading edge of the blade, whereas the outlet plane is kept at a distance of 1.25 times the axial chord distance away from the trailing edge of the blade. Entire span of the blade is modeled and along the transverse direction, translational periodicity is set at one pitch length. The computational domain is filled with structured hexahedral elements (Fig. 1). Large Eddy

simulations using Smagorinsky model is used for the computations. ANSYS CFX is used for solving as well as post processing . The values of the total pressure and total temperature prescribed at compressor inlet are 220 Pa and 303 K respectively. Outlet boundary is defined with a mass flow rate of 0.157 kg/s. No slip and adiabatic conditions are specified on the hub, shroud and blade surfaces. Boundary condition chosen for the periodic surface is conservative interface flux.

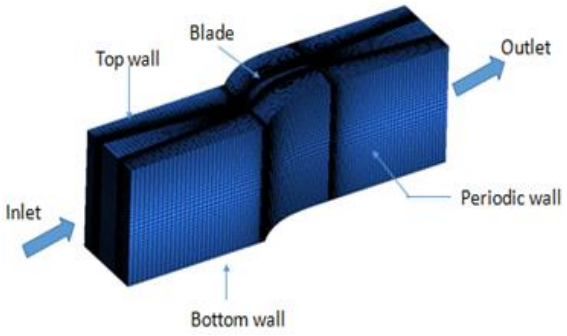


FIGURE 1. Computational domain filled with hexahedral elements

For simulations with water injection, air is the continuous fluid and water droplets is set as the Lagrangian fluid. Water injection at the compressor inlet assumed to be in accordance with the Rosin-Rammler distribution. Droplets are specified as fully coupled to continuous fluid. Wall film formation due to the droplet interaction with the blade surface is considered for this study. Accordingly, Elsaesser model is chosen for the droplet wall interaction. Primarily six incidence angle has been considered other than the nominal incidence angle; these are -5deg. -10deg. -15deg. +5deg. +10deg. and +15deg. If the flow leaning towards the pressure surface, it is regarded as a positive incidence. The wall static pressure distribution of the simulated results (without water injection) is compared with the experimentally measured values. In fact, the static pressure values are normalized with inlet dynamic pressure and is plotted in the form of contours for a blade passage. The comparison with the experimental results reveals that the low pressure regions near the pressure surface and in the middle of the blade passage have been accurately captured with the present numerical simulations.

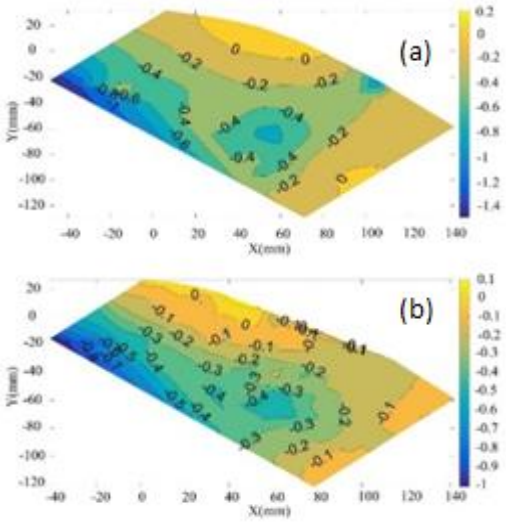


FIGURE 2. Comparison of normalized static pressure distribution (a) computed values (b) experimental

## 4. RESULTS

The effect of incidence angle on compressor cascade performance can be directly analyzed from the variation of total pressure along the blade passage. Hence the mass average total pressure loss coefficient ($C_{p0}$) is calculated along the axial chord and is shown in Fig. 3a. This has been carried out without any water injection at the inlet. As expected the increasing positive incidence angles enhances the flow separation at the suction side whereas the negative incidence angles tries to suppress it. In order to understand the effect of water injection one percent (by mass) of water droplets with a mean diameter of 20 microns is injected at the inlet and simulations are carried out for negative as well as positive incidence angles. Figure 3b shows the loss coefficient values for 15 deg. incidence angles (positive and negative). It is observed that with the introduction of 1% water droplets the loss coefficient values are reduced significantly for positive incidence angles, whereas the losses are enhanced for negative incidence angles.

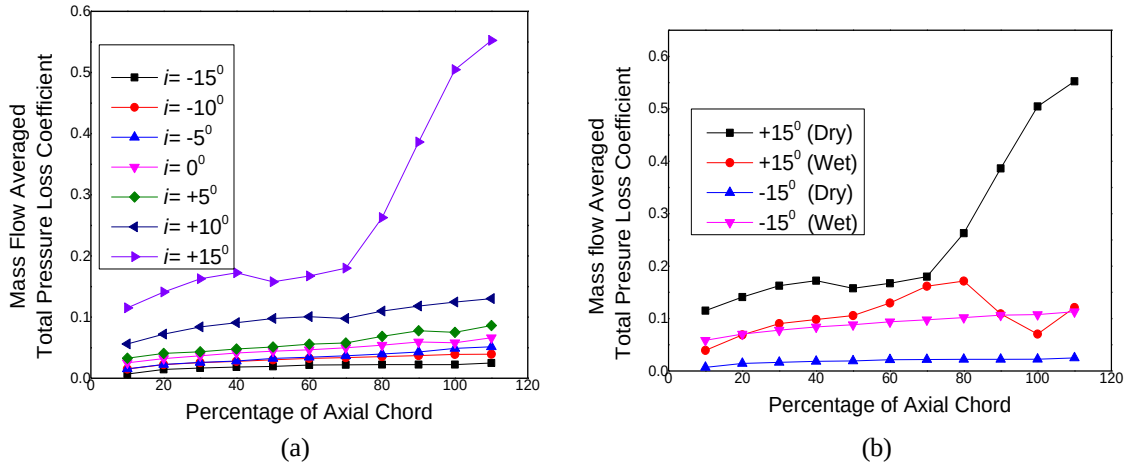


FIGURE 3. (a) Mass flow averaged total pressure loss coefficient at different incidence angle for dry air (b) Comparison of loss coefficient for dry (without water injection) and wet (with water injection) cases

Velocity contours are plotted for +15 deg. incidence angle at 5% span and is shown in Fig.4. The flow is much more detached from the suction surface in the dry case in comparison with wet case. The disturbances are high in the flow passage as well as in the downstream region, particularly near the trailing edge, for dry case. The separated flow region causes significant blockage in the blade passage. With the injection of water droplets, the blockage in the blade passage is brought down (Fig.4b). However, the circumferential mixing of the fluid streams from pressure surface and suction surface are diminishes at the downstream side after the trailing edge. This establishes one favorable and another unfavorable outcome at the downstream side. The lower circumferential mixing accounts for a smaller mixing loss in the downstream region, which results in smaller total pressure loss coefficient. The unpropitious outcome of the weaker mixing is that it results in a higher circumferential non uniformity at exit. Hence it can be concluded that the point of separation and the separated flow regions within the blade passage are almost similar in both wet and dry cases, but the mixing at the downstream side of the blade is affected by the presence of water droplets.

As there is not much variation in the point of separation from the blade surface, the overall blade loading also remains similar for cases with and without water droplets. Figures 5a-d shows the blade loading for 5 deg. and 15 deg. incidence angles. For 5 deg. incidence angles the area enclosed by the curves are almost similar for both wet and dry cases. However smaller differences are noted at larger incidence angles. At 5 deg. incidence angles the blade suction side pressure values are no

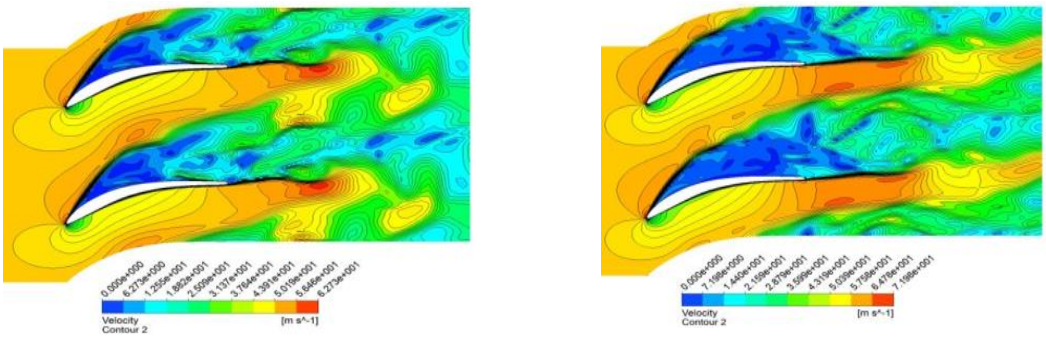


(a) (b)

FIGURE 4. Axial velocity contour at 5% of span (a) dry case (b) wet case

uniform in the axial direction due to the increased droplet wall interactions. As a result, the pressure contours are highly non-uniform in the suction surface. On the contrary at higher incidence angles a smoother pressure contours are observed at the suction side due to lower droplet-wall interactions.

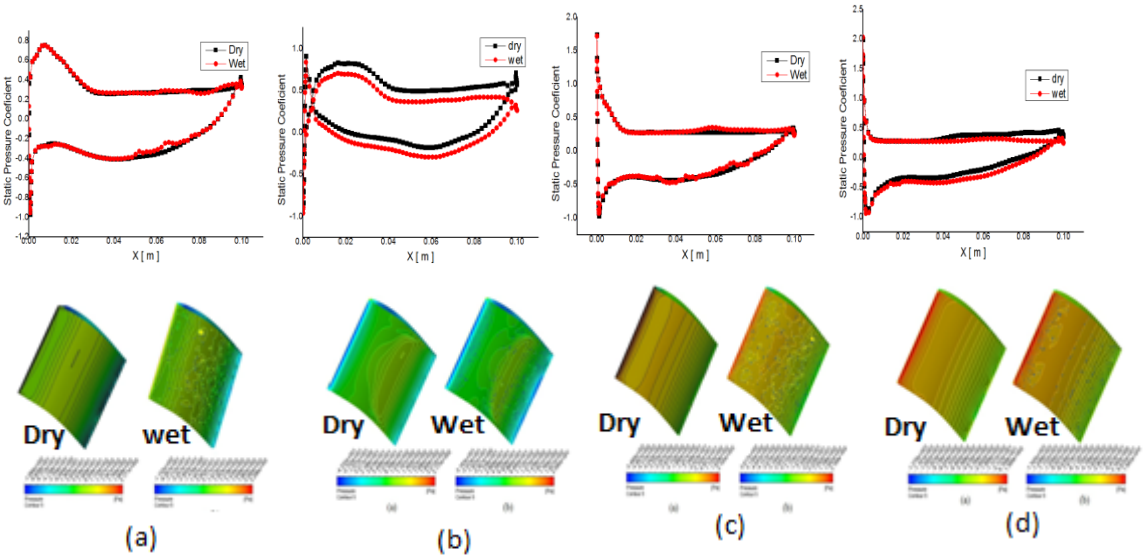


FIGURE 5. blade loading and pressure distribution over the blade (a) -5 deg.(b)-15deg.(c) +5deg.(d)+15 deg.

## 5. CONCLUSIONS

A computational investigation is carried out to understand the effect of water injection on the separated flow regions in a compressor cascade at different incidence angles. The major findings of this investigation are detailed below.The water injection produces two contrasting results at positive and negative incidence angles. With increase in the positive incidence angles the water injection helps to reduce the loss coefficients inside the blade passage by controlling the separated flow regions. Whereas for negative incidence angles, presence of water droplets enhances the loss generation inside the blade passage. It is also observed that the mixing of the jet and wake fluid streams at the downstream of the blade is diminished with the water injection. The overall blade loading is not significantly affected by the droplet-wall interactions. However small perturbations are observed on the suction surface of the blade. As a result, the pressure gradient in the transverse direction is affected.

## REFERENCES

1. Kang, J. S., Cha, B. J., and Yang, S. S., 2006, "Thermodynamic and Aerodynamic Meanline Analysis of Wet Compression in a Centrifugal Compressor." Journal of Mechanical Sci. and Tech., 20, pp. 1475-1482.
2. Meher-Homji, C.B., and Mee III, T. R., 2000, "Inlet Fogging of Gas Turbine Engines: Part A- Theory, Psychrometrics And Fog Generation," ASME paper no. 2000-GT-0307.
3. Bhargava, R., and Meher-Homji, C.B., 2005, "Parametric Analysis Of Existing Gas Turbines With Inlet Evaporative And Overspray Fogging," ASME J. Eng. Gas Turb. Power, 127, pp. 145-158.
4. Zhang , W., Chen, L., and Sun, F., 2009, "Performance Optimization For An Open-Cycle Gas Turbine Power Plant With A Refrigeration Cycle For Compressor Inlet Air Cooling. Part 2: Power and Efficiency Optimization," Proc. Instn. Mech. Engrs., Part A: J. of Power and Energy, 223, pp. 515-522.
5. Sun, L., Zheng, Q., Li, Y., and Bhargava, R., 2011, "Understanding Effects of Wet Compression on Separated Flow Behavior in an Axial Compressor Stage Using CFD Analysis," ASME J. Turbomach., 133, pp. 1-14.
6. Sun, L., Zheng, Q., Luo, M., Li, Y., and Bhargava R.K., 2011, “On the Behavior of Water Droplets When Moving Onto Blade Surface in a Wet Compression Transonic Compressor,” ASME . J. Eng. Gas Turbines Power, 133, pp. 82001-10.
7. White, A. J., and Meacock, A. J., 2004, "An Evaluation of the Effects of Water Injection on Compressor Performance," ASME J. Eng. Gas Turb. Power, 1269, pp.748–754. 17.
8. Roumeliotis, I., and Mathioudakis, K., 2006, "Water Injection Effects on Compressor Stage Operation," ASME J. Eng. Gas Turb. Power, 129, pp.778–798.

# STUDIES ON HEAT AND MASS TRANSFER FOR GELDART B PARTICLES USING BATCH FLUIDIZED BED DRYER

**D Yogendrasasidhar, Y Pydi Setty***
Department of chemical engineering, National Institute of Technology Warangal, Warangal-506004, India, sasidhar811@gmail.com, psetty@nitw.ac.in

## ABSTRACT

The major advantage of fluidized bed dryer is that it gives high heat and mass transfer rates. Due to fluidization of bed particles in hot gas, high heat and mass transfer rates between solid and gas are observed. The heat and mass transfer rates vary with material properties and dryer conditions. In the present study, Nusselt number and Sherwood number of Geldart B particles using batch fluidized bed dryer are estimated and reported.

**Key Words:** *Heat transfer coefficient, Mass transfer coefficient, Geldart B particles*

**Nomenclature**

| | | | |
|---|---|---|---|
| d | diameter of particle, m | δ | bubble fraction in bed |
| u | velocity of air, m/s | **Subscripts** | |
| μ | viscosity of air, kg /m.s | g | gas |
| ρ | density, kg/m$^3$ | p | particle |
| **Greek symbols** | | s | solids |
| Ɛ | voidage | m | minimum fluidization velocity |
| Ø | Sphercity | f | fluidization |

## 1. INTRODUCTION

Drying is the mechanism of removing moisture due to transfer of heat energy to wet material. Several industries use different types of dryers based on product requirements. The type of dryer can be classified based on supplied heat transfer. Heat and mass transfer plays important role in any drying process. Fluidized bed dryers are very efficient and economical for different food and pharmaceutical industries. Main advantages of these dryers are high heat and mass transfer and good gas solid mixing. Heat and mass transfer rates depend on several parameters like material characteristics and operating conditions of dryer [1]. Generally, bed materials used in fluidized bed dryers are solids of different sizes. According to Geldart classification, the solid particles are classified into four types such as C, A, B and D based on their fluidization behavior. Most of the bed materials used in industries come under Geldart B and Geldart D particles. Comparatively, both have different fluidization behavior [2]. Peishi and David (1984) have studied on fluid to particle heat transfer of ferric oxide particles in fluidized bed and developed a correlation [3]. Mohideen et al. (2012) have conducted heat transfer studies on Geldart D particles of diameter 3.56 mm in swirling fluidized bed and reported heat transfer coefficient at different heights [4]. Zhang and Koksal (2006) have studied on heat transfer from surface to Geldart B bed of particles at different flow pulsation in pulsed fluidized bed [5]. Several authors have conducted heat and mass transfer studies in different ways and correlated the results. Recently Ndukwu et al. (2017) conducted studies on heat and mass transfer of cocoyam slice in oven drying [6]. In the present study the Nusselt number and Sherwood number of Geldart B particles of 0.4 mm and 0.6 mm using batch fluidized bed dryer are estimated using the present experimental data from the equations reported in literature.

## 2. EXPERIMENTAL SETUP AND PROCEDURE

In present experimental set up, fluidized bed dryer consists of fluidization column with a height of 1 m and diameter of 8.3 cm. Calming section of 1 m height has been used for uniform distribution of air. Air is drawn from the compressor and passed through calming section, followed by the fluidized bed drying zone. The air flow rate was controlled using a bypass valve and measured using rotameter. The inlet air temperature is maintained through air heater. The temperature of bed and air were measured with the help of thermocouples and indicator. In the present study, material used is sand with density 2600 kg/m$^3$. Figure 1 shows the experimental setup. Sand particles of Geldart Type B of diameter, dp: 0.4, 0.6 mm have been used in the present study. Known amount of solids with a particular initial moisture content has been used inside the fluidized bed dryer.Initially air flow has been initiated with required temperature for experimentation and the samples were collected at the top of the bed at regular intervals. The collected samples were weighed and dried to obtain the moisture content of solids.

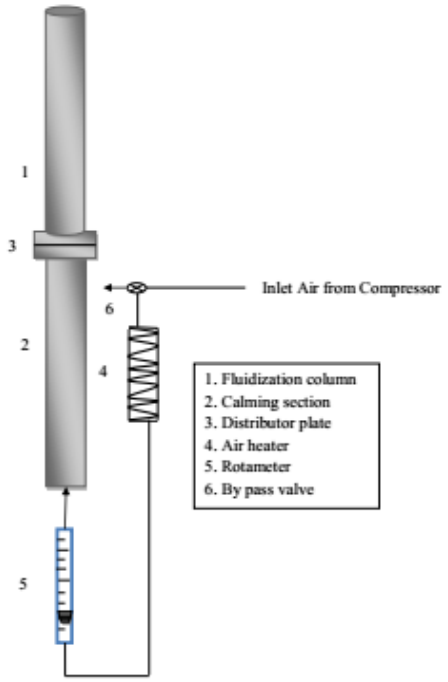


FIGURE 1.Batch fluidized bed dryer

## 3. RESULTS AND DISCUSSION

Generally in any dryer, heat transfer between gas and particle plays major role on drying characteristics of bed material. In fluidized bed dryer, the heat transfer rate between gas to particle and particle to particle shows impact on moisture removal rate of particle. Experiments were carried out for Geldart B particles (0.4 and 0.6 mm) varying air velocity and keeping remaining parameters constant. From Figure.2, it can be observed that drying rate of particles increased with increasing air velocity. Reynolds number of particles at different air velocity was determined using Equation.1 and presented in Figure.3. In fluidized bed dryer bed porosity also shows impact on heat and mass transfer rate. Nusselt number and Sherwood number of particles considering bed porosity in emulsion phase were calculated using Equation 2 to 7(Gunn 1978) [7, 8]. From Figure 4, it can be observed that heat transfer coefficient of Geldart B particles increased with air velocity. From Figure 5, it can be observed that mass transfer coefficient increased with increasing air velocity and air temperature.

$$Re_p = \frac{d_p u \rho}{\mu} \tag{1}$$

$$\frac{d_p u_{mf} \rho_g}{\mu} = \left[(28.7)^2 + 0.0494\left(\frac{d_p^3 \rho_g (\rho_s - \rho_g) g}{\mu^2}\right)\right]^{1/2} - 28.7 \tag{2}$$

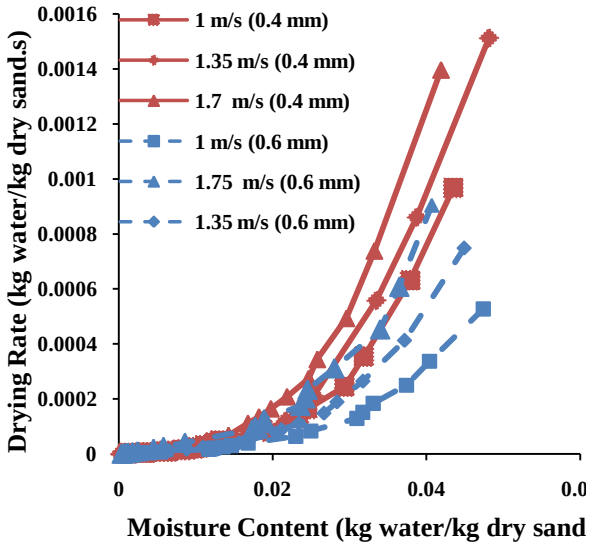


FIGURE 2.Drying characteristics of Geldart B particles at different air velocities

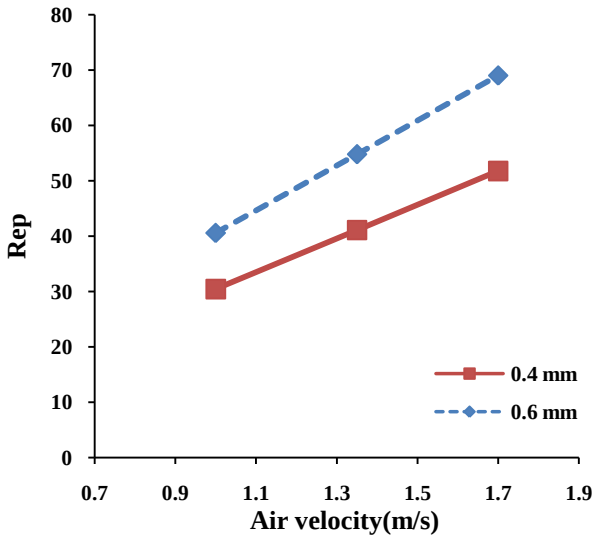


FIGURE 3.Reynolds number of Geldart B particles at different air velocities

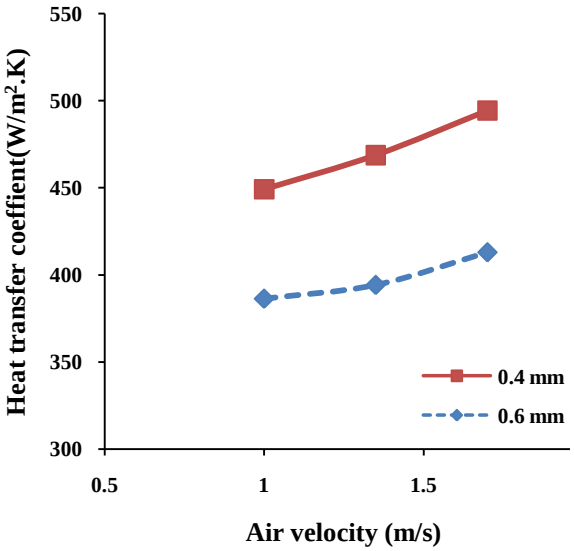


FIGURE 4.Heat transfer coefficient of Geldart B particles

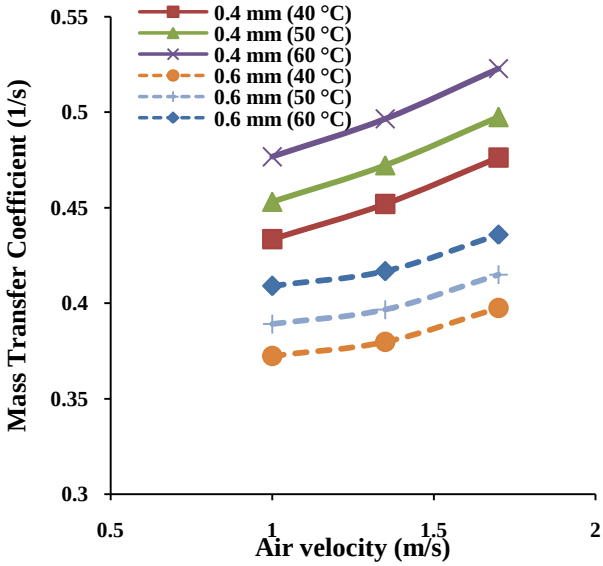


FIGURE 5.Mass transfer coefficient of Geldart B particles

$$\varepsilon_{mf} = 0.586 \times (\emptyset^{-0.72}) \times \left[\frac{\mu^2}{\rho_s(\rho_s-\rho_g)g d_p^3}\right]^{0.029} \left(\frac{\rho_g}{\rho_s}\right)^{0.021} \quad (3)$$

$$\delta = 0.534 - 0.534 \times exp\left(-\frac{u_0-u_{mf}}{0.413}\right) \quad (4)$$

$$\varepsilon_f = \delta + (1-\delta)\,\varepsilon_{mf} \quad (5)$$

$$\mathrm{Nu} = \left(7 - 10\varepsilon_f + 5{\varepsilon_f}^2\right)\left(1 + 0.7 Re_p^{0.2} Pr^{1/3}\right) + \left(1.33 - 2.4\varepsilon_f + 1.2{\varepsilon_f}^2\right)\mathrm{Re_p^{0.7}Pr^{1/3}} \quad (6)$$

$$\mathrm{Sh} = \left(7 - 10\varepsilon_f + 5{\varepsilon_f}^2\right)\left(1 + 0.7 Re_p^{0.2} Sc^{1/3}\right) + \left(1.33 - 2.4\varepsilon_f + 1.2{\varepsilon_f}^2\right)\mathrm{Re_p^{0.7}Sc^{1/3}} \quad (7)$$

## 4. CONCLUSIONS

Experiments were carried out with Geldart B particle (0.4 and 0.6 mm) using batch fluidized bed dryer. Reynolds number, Nusselt number and Sherwood number of Geldart B particles at different experimental conditions were estimated from the correlations reported in the literature using present experimental data on heat and mass transfer studies in a batch fluidized bed dryer. From the results, it can be observed that heat transfer coefficients increased with increasing air velocity and mass transfer coefficient increased with increasing air velocity and air temperature.

## REFERENCES

[1] A. S. Mujumdar, *Handbook of Industrial Drying*, New York, Marcel Dekker, 2014.

[2] D. Kunii and O. Levenspiel, *Fluidization Engineering*, 2 nd Edition, Boston, Butterworth Heinemann, 1991.

[3] P. Chen and D. C. T. Pei, Particle Heat Transfer in Fluidized Beds of Mixed-Sized Particles, *Can. J. Chem. Eng.*, 62 , 1984.

[4] M. F. Mohideen, B. Sreenivasan, S. A. Sulaiman, and V. R. Raghavan, Heat transfer in a swirling fluidized bed with geldart type-D particles, *Korean J. Chem. Eng*, 29, 862–867, 2012.

[5] D. Zhang and M. Koksal, Heat transfer in a pulsed bubbling fluidized bed, *Powder Technol.*, 168, 21–31, 2006.

[6] M. C. Ndukwu, C. Dirioha, F. I. Abam, and V. E. Ihediwa, Heat and mass transfer parameters in the drying of cocoyam slice, *Case Stud. Therm. Eng.*, 9, 62–71, 2017.

[7] D. J. Gunn, Transfer of heat or mass to particles in fixed and fluidised beds, *Int. J. Heat Mass Transf.*, 21, 467–476, 1978.

[8] G. Srinivas and Y. P. Setty, Heat and mass transfer studies in a batch fluidized bed dryer using Geldart group D particles, *Heat Mass Transfer*, 50, 1535-1542, 2014.

Fifth International Conference on Computational Methods for Thermal Problems
THERMACOMP2018, July 9-11, 2018, Indian Institute of Science, Bangalore, INDIA
*N. Massarotti, P. Nithiarasu, Pradip Dutta and C. Ranganyakalu (Eds.)*

# Large eddy simulation of counter rotating Taylor-Couette flow at high Reynolds numbers

**Dhaval Paghdar, Kameswararao Anupindi**
Department of Mechanical Engineering, Indian Institute of Technology-Madras, Chennai,
Tamilnadu-600 036, India. kanupindi@iitm.ac.in .

## ABSTRACT

Flow between differentially rotating cylinders, also known as counter rotating Taylor-Couette (CRTC) system exhibit a wide variety of flow states comprising of separate laminar and turbulent regions as well as flow states with co-existence of both of them. In the present work we focus on simulating incompressible turbulent flow in a CRTC system using large eddy simulation(LES) turbulence model available in OpenFOAM. The statistical features of the flow field such as time-averaged mean field and the root means square velocity fluctuations are computed for different Reynolds numbers and are validated from literature. The dynamical features of the flow such as instantaneous iso-surfaces of $\lambda_2$ are computed from the simulations. Overall, the results obtained demonstrate the capability of LES to simulate strongly rotating wall bounded flows.

**Key Words:** Finite volume, LES, Turbulent flow, PISO, Reynolds stress, CRTC, subgrid scale.

## 1. INTRODUCTION

Rotating turbulent flows are omnipresent in science and engineering applications. Examples of such flows include atmospheric and ocean flows and flows in the wake of ship propellers, jet engines, and wind turbines. Rotating turbulent flows exhibit a number of features that are not present in turbulent flows without rotation.

Previously Direct Numerical Simulation(DNS) was performed by Dong [1] for this CRTC systems at a range of Reynolds numbers varying from $Re_i = -Re_o = 500,1500,2500$ and 4000, a detailed study of the statistical and dynamical features were reported. In the present simulation we focus only on a k-equation model for all the simulations. Also validating the results with the DNS study of CRTC system, we study the physics of the flows at high Reynolds numbers by using LES.

## 2. MAIN BODY

### Governing Equations

In LES, the large scales which contain the most of the energy, which are affected strongly by the boundary conditions and do the most of the energy transport are resolved while the small scales are represented by using a model. To saperate small scale from large scale filtering process used, in present case it happens itself by grid size filter.

In LES, any flow F variable can be composed of a large scale $\bar{F}$ (resolved/filtered component) and a small scale f (residual/SGS part f) contribution as follows: $F = \bar{F} + f$

The governing equations are the filtered incompressible Navier-Stokes equations, assuming that the filter commutes with differentiation we can write these equations as follows:

**1. Continuty Equation :** $$\frac{\partial \bar{U}_i}{\partial x_i} = 0$$

**2. Momentum Equation :** $$\frac{\partial \bar{U}_i}{\partial t} + \bar{U}_j \frac{\partial \bar{U}_i}{\partial x_i} = -\frac{1}{\rho}\frac{\partial \bar{p}}{\partial x_i} + \nu \frac{\partial^2 \bar{U}_i}{\partial x_i^2} - \frac{\partial \tau_{ij}^{SGS}}{\partial x_j}$$

In the above equations the term $\tau_{ij}^{SGS}$ the residual-stress tensor/SGS stress tensor and the isotropic part has been absorbed into the filtered pressure term. Like the Raynolds Average Navier-Stokes(RANS) equations for $\bar{U}$ , the filtered equations for U are unclosed. Closure is achieved by modeling the residual (or SGS) stress tensor $\tau_{ij}^{SGS}$ as,

$$\tau_{ij}^{SGS} = \overline{U_i U_j} + \overline{U_i}\,\overline{U_j}$$

**Geometry and mesh details**

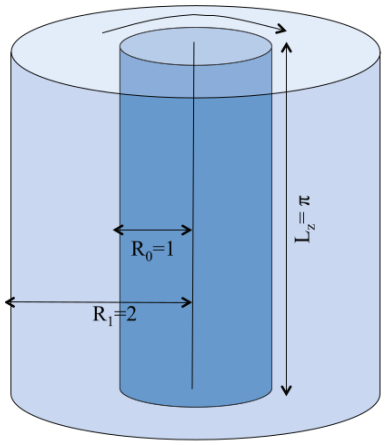


***Figure 1:*** *Geometry of the counter rotating Taylor-Couette flow*

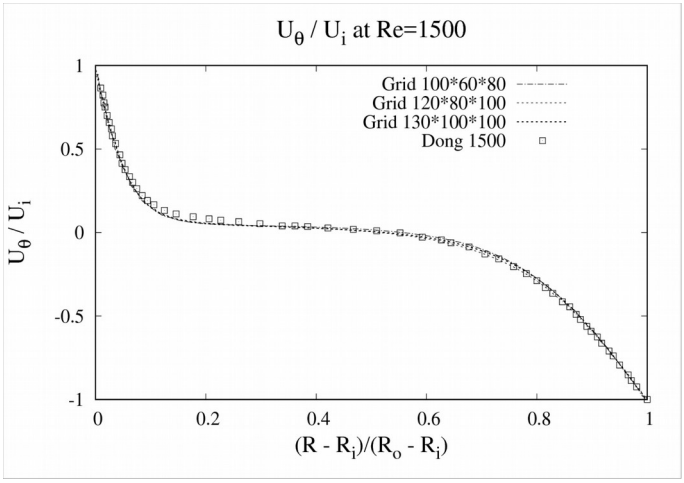


***Figure** 2: Validation of mean azimuthal velocity across the cylinder using different grids.*

The geometry of the domain consists of two circular cylinder with inner and outer radius $R_i = 1$, $R_o = 2$ and the length of the domain in the axial direction is taken as $L_z = \pi$. Both the inner and outer cylinders act as impermeable no-slip walls and in the axial direction periodic boundary conditions are used in order to simulate infinitely long cylinders. Only a quarter of domain was used in the azimuthal direction to save computational time. Finite volume method with PISO (Pressure Implicit with Splitting of Operators) algorithm is used for the pressure velocity coupling and second order accurate schemes are used in space and time.

The mesh was generated, contains a total of 0.96 million cells, with $\Delta r$=2.22e-03, $\Delta\theta$ = 0.0196 and $\Delta z$ =0.0314 with this grid maximum $\mathbf{r^+}$ ,$\boldsymbol{\theta^+}$ **and** $\mathbf{z^+}$ are **0.607, 5.36 and 8.58** respectively for a Reynolds number 8000. Velocity of the both cylinders maintained in such that $\mathbf{Re_i = -Re_o}$. Reynolds number of the system calculated as $\mathbf{Re = Re_i - Re_o}$. Grid convergence of the system is varified with the three cases, a course mesh (100 × 60 × 80) with 0.48 million cells, a medium mesh (120 × 80 × 100) with 0.96 million cells and a fine mesh (130 × 100 × 100) with 1.3 million cells. Azimuthal velocity profile at $Re_i = -Re_o = 1500$ plotted in Fig. 2 and compared with DNS study for the same Reynold number.

## 3. RESULTS

All the cases were run using k-equation as the SGS model in LES and they have been run upto a time t= 500 with a time step of $\Delta t$ = 1e-03. Simulations were performed using OpenFOAM in parallel mode with Message Passing Interface as the parallelization technique and domain decomposition method. A total of 16 processors were utilized for running the solver and each of the simulations have taken a total wall clock time of 42 hrs.

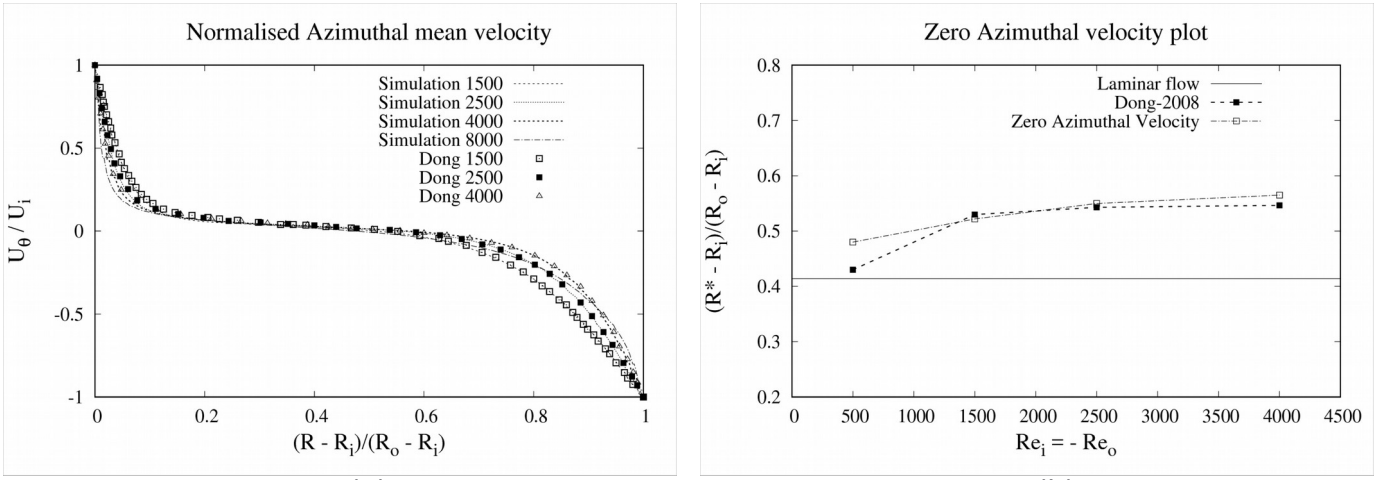


***Figure 3:*** *(a) Normalised mean azimuthal velocity profiles at different Reynolds numbers averaged along z-θ plane and the result from DNS (b) radial coordinate of the zero velocity surface as a function of Reynolds number. $U_\theta$ is the azimuthal velocity and $R^*$ is the radius of zero-velocity surface.*

In order to validate the results obtained, we first compare the variation of mean azimuthal velocity profiles averaged over the z-θ plane at different Reynolds numbers as shown in Fig. 3(a), with corresponding results from DNS study of Dong [1]. The results obtained from the present calculations seem to be matching to that of the DNS results. As the Reynolds number increases from 1500 to 8000 we can see in Fig. 3(a) that mean azimuthal velocity profiles have become steeper with a wider zero azimuthal region in the central portion away from both the walls. Unlike the plane Couette flow the mean velocity profiles are not symmetric and the profile seems to be closer to the inner wall more than it does at the outer wall rendering the asymmetry. $R^*$ is the coordinate where zero azimuthal velocity is attained. In Fig. 3(b) normalized $R^*$ is plotted as function of the Reynolds number, together with the location of the zero-velocity surface in a laminar circular Couette flow with $Re_i = -Re_o$ and Ri/Ro=0.5 plotted as a horizontal line, which is $(R^* - R_i)/(R_o - R_i) = \sqrt{2} - 1$. As the Reynolds number increases, the zero-velocity surface moves outward, and its radius appears to approach a limiting value is about $(R^* - R_i)/(R_o - R_i) \sim 0.55$.

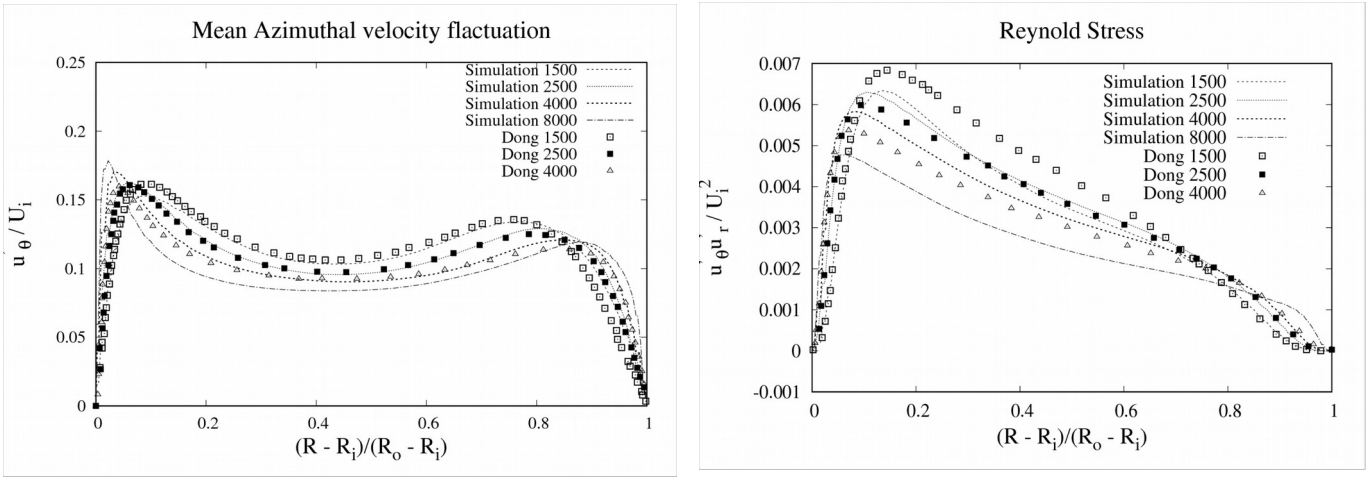


***Figure 4:*** *Comparison of profiles of mean azimuthal velocity flactuations and Reynold stress at different Reynold number averaged over the z-θ plane*

From Fig. 4(a) showing the validation of azimuthal velocity fluctuations, we see two peaks closer to the wall and the fluctuations reaching a minimum value in the central portion of the annulus. As the Reynolds number increased from 1500 to 8000 the peaks move closer to the walls indicating the presence of more near wall vortices and fluctuations. Also, the Reynolds stress normalized by $\mathbf{U_i * U_i}$ are plotted in Fig. 4(b). From this plot we can see that Reynolds stresses are very small for the case of low Reynolds number indicating very little turbulence in this case. As the Reynolds number increases we see that peak moves closer to the inner wall indicating more intense fluctuations and near wall vortices. Whereas at the outer wall all the plots seem to be closing in a tail like fashion. In core region the Reynolds stress become more and more flat as Reynolds numbers increses which shows that Reynolds stress becoming constant in core region as the Re tends to infinity. Throughout in all the case we observe a positive Reynolds stress distribution.

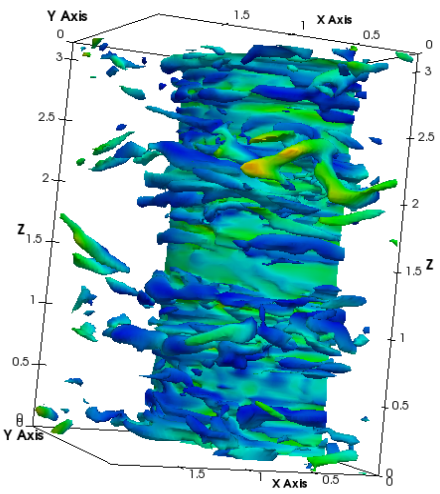


***Figure 5:*** *Iso-surface of instantaneous* $\lambda_2$*= -21 at* $Re_i = -Re_o = 4000$.

In the present to analyse the vortical structures in turbulent flow, we used $\boldsymbol{\lambda_2}$ criteria the second eigen value in the tensor $\mathbf{S \cdot S + \Omega \cdot \Omega}$, where S and Ω are the symmetric and anti-symmetric parts of the velocity gradient tensor. Plotting of these $\lambda_2$ surfaces as discussed in Jeong & Hussain helps us to visualize and explore the structural characteristics of the small-scale vortices in the turbulent CRTC system. Isosurfaces for $\lambda_2$=-21 is plotted in Fig. 5. Many azimuthal vortices seem to be originating from the inner and outer walls and convecting into the central portion of the annulus. In the present CRTC system the vortices seem to be elongated in azimuthal direction rather than hairpin-like as seen in the turbulent channels and flat-plate boundary layers.

## 4. CONCLUSIONS

In the present work the dynamical and statistical features of the turbulent flow between counter-rotating concentric cylinders are investigated employing detailed three-dimensional large eddy simulation. The study is for a radius ratio $R_i/R_o$=0.5 at inner/outer cylinder Reynolds numbers ranging from 500 to 8000 while the condition $Re_i$=−$Re_o$ is maintained.

LES with k-equation model as the SGS model is used to simulate a CRTC system at different Reynolds number and the results seem to be matching with reference DNS data. Also, the turbulent statistics and the vortical structures obtained are similar to the DNS results. The results obtained demonstrate the capability of LES to simulate strongly rotating wall bounded flows.

## REFERENCES

[1] S. Dong. Turbulent flow between counter-rotating concentric cylinders: a direct numerical simulation. Study Journal of Computational Physics, 229:3402–3414, 2010.

[2] Y. Bazilevs and I. Akkerman. les of turbulent taylor-couette flow using isogeometric analysis and the residual based variational multiscale method. Journal of Computational Physics, 229:3402–3414, 2010.

[3] S. B. Pope. Turbulent Flows. Cambridge University Press, 2000.

[4] J. Jeong and F. Hussain. On the identification of a vortex. J. Fluid Mech., 285:69–64, 1995.

Fifth International Conference on Computational Methods for Thermal Problems
THERMACOMP2018, July 9-11, 2018, Indian Institute of Science, Bangalore, INDIA
*N. Massarotti, P. Nithiarasu, Pradip Dutta and C. Ranganyakalu (Eds.)*

# EFFECT OF POROUS MEDIA ON HAEMODYNAMIC PERFORMANCE OF THE FONTAN CONNECTION

**Dhayananth K, Arunn Narasimhan**
Heat Transfer and Thermal Power Laboratory, Department of Mechanical Engineering, Indian Institute of Technology Madras, Chennai- 600036, India. E-mail: arunn@iitm.ac.in

ABSTRACT

The haemodynamics of the Fontan connection is studied both numerically and experimentally by placing porous media across the connection. The 1D-offset total cavopulmonary connection (TCPC) configuration is considered for the present study with steady, laminar and newtonian assumptions. The inlet caval flow rates are varied by increasing the total cardiac output from 2LPM to 6LPM. The TCPC with porous media provides 7% reduction in pressure drop penalty, compared with no-porous medium case. Hence the introduction of porous media helps in improving the hydraulic efficiency by curtailing the recirculation zones across the connection.

**Key Words:** *Fontan surgery, Porous media, Pressure drop*

## 1. INTRODUCTION

The babies born with congenital heart disease (CHD) such as tricuspid atresia, and hypoplastic heart syndrome, have heart chambers which are connected in parallel fashion. This results in mixing of venous return and pulmonary blood which lead to cyanosis and detrimental to the life expectancy of the patients. The palliative surgical procedure for tricuspid atresia was performed by Fontan et al. [1] through the cavo-pulmonary anastomosis. This physiological correction restores the pulmonary blood flow and suppresses the mixing of the right and left blood. Since its inception, Fontan procedure undergoes various modifications and adopted for the management of various CHDs. The improved form of Fontan connection called total cavo-pulmonary connection (TCPC) [2] which gained importance due to the reduced flow resistance across the configuration. Several in-vitro and in-vivo investigations are performed to make the flow pathway energy efficient by streamlining the Fontan geometry. Of these Sharma et al. [3] evaluated the effect of offsetting the vena cava and found that energy loss reduced by 50% for 1D and 1.5D offset cases compared to zero offset case. The recent improvement in TCPC design includes Optiflo TCPC model [4], Y- shaped graft to connect IVC to PA [5] and flow divider (triangular insert) [6] in the IVC baffle helps in reduction of power loss across the connection. The major traits for the pressure loss in the connection are flow recirculation, stagnation zone, flow separation and vortices across the junction. It has been shown that use of porous media at appropriate locations can reduce the overall pressure drop by 20% in near-compact heat exchanger configuration [7]. The present study investigates the TCPC with suitable porous medium design to perform with reduced pressure drop when compared to existing TCPC design with recirculation loss.

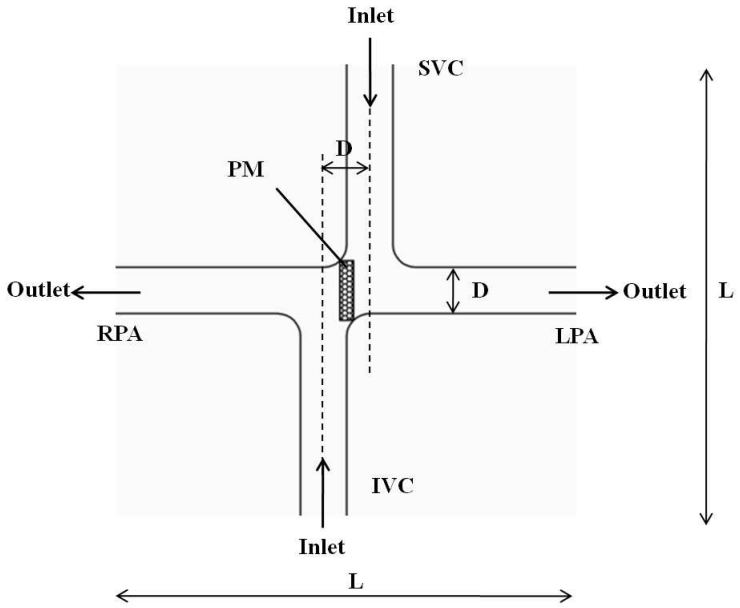


Figure 1: TCPC configuration. IVC-Inferior Vena Cava, SVC-Superior Vena Cava, LPA-Left Pulmonary Artery, RPA-Right Pulmonary Artery

## 2. METHODOLOGY

### 2.1 Model description:

The present study is performed in one diameter offset TCPC model as shown in Figure 1. The diameter (D) and length (L) of the blood vessel are 13.34 mm and 140 mm respectively. The porous medium (PM) is employed at the junction of both pulmonary arteries and vena cava. The three-dimensional geometry is constructed and meshed using ICEM CFD. The blood flow across the connection is simulated by solving conservation equations for clear fluid and porous media domain using ANSYS Fluent 14.5. The flow is considered to be steady, newtonian, laminar and incompressible. The total cardiac output is varied from 2LPM to 6LPM. It is assumed that 40% of the cardiac output flows through SVC and the remaining 60% flow through IVC. The flow split condition of LPA:RPA = 40:60 is maintained throughout the study. The uniform velocity boundary condition is applied at each inlet. The outlets are extended to ensure fully developed flow at the exit to prevent false diffusion errors. The porous medium properties used in this study are shown in Table 1. The properties are used to simulate the viscous and form drag effects in the porous domain.

### 2.2 Pressure drop calculation:

The pressure drop is a major source of energy loss which determines the Fontan efficiency of the connection. Therefore total pressure drop across the TCPC connection is calculated using

static pressure data of each blood vessel and it is given by,

$$\Delta P = \Delta P_{s,IVC} + \Delta P_{s,SVC} - \Delta P_{s,LPA} - \Delta P_{s,RPA} \tag{1}$$

| Material | Porosity | Permeability $(m^2)$ | Form-coefficient $(m^{-1})$ |
|---|---|---|---|
| ABS | 0.72 | 1.18E-07 | 59 |

Table 1: Porous medium properties

## 3. RESULTS AND DISCUSSIONS

### 3.1 Numerical investigation:

The hydraulic efficiency of the TCPC configuration depends on the local flow dynamics across the geometry. The TCPC with porous media placed at the centre is modelled and simulated to investigate the performance of the connection. Figure 2 shows the variation of pressure drop for different total cardiac outputs. The insertion of PM at the center of the TCPC connection helps in on average of 7% reduction in pressure drop when compared with clear fluid (CF) case. Hence, placing the PM at the TCPC junction arrests the recirculation zones which in-turn helps in improving the overall performance.

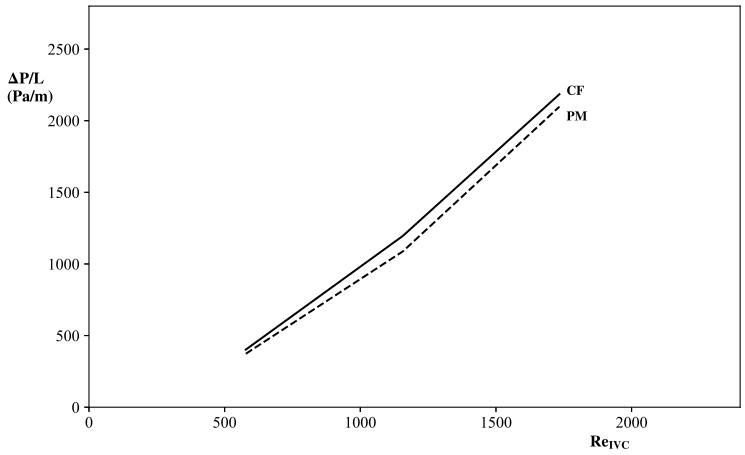


Figure 2: Effect of PM on the pressure drop of TCPC configuration for different $Re_{IVC}$. CF denotes the no-porous medium case.

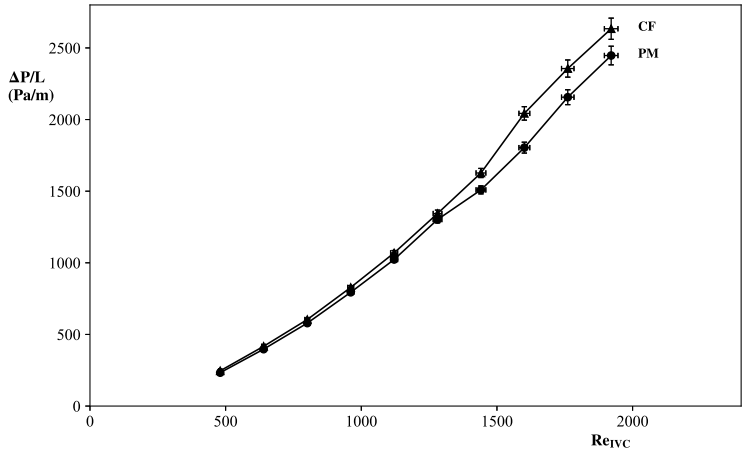


Figure 3: Variation of pressure drop with $Re_{IVC}$ for TCPC configuration with PM placed at the junction. CF denotes the no-porous medium case.

### 3.2 Experimental investigation:

The present numerical study is validated by performing experiments on in-vitro glass Fontan model. The blood mimicking fluid, water-glycerine mixture solution is used as a working fluid with a viscosity of 3.65 mPas. The static pressure across the connection is measured using differential pressure transmitter. Using the pressure data, the total pressure drop is determined using equation (1). The flow rates are measured using variable area flow meters and controlled by ball valves. Figure 3 shows the effect of PM on the pressure drop of the TCPC configuration. An average of 6% reduction in pressure drop is observed for PM placed at the centre of the junction. The presence of porous media curtails the recirculation region at the TCPC junction which results in the gain in efficiency of the connection. The greater amount of reduction in pressure drop is observed at higher flow rates.

The present study is performed by changing the total cardiac output from 2LPM to 6LPM. The lower cardiac output and higher cardiac output corresponds to diseased and exercised condition of the heart. From the study, latter condition shows greater improvement in performance for the TCPC configuration with PM .

## 4. CONCLUSIONS

Three-dimensional computational model of TCPC with porous medium (PM) has been developed and numerical simulations are performed to determine the hydraulic efficiency of the connection. The current numerical study is validated with experiments. Placing the porous medium at the centre of the TCPC connection helps in 7% reduction of overall pressure drop. Hence the presence of porous media influences the hydraulic performance of the TCPC connection.

## References

[1] Fontan, F., and Baudet, E., Surgical repair of tricuspid atresia, *Thorax*, 26(3), 240-248, 1971.

[2] de Leval, M. R., Kilner, P., Gewillig, M., and Bull, C., Total cavopulmonary connection: a logical alternative to atriopulmonary connection for complex Fontan operations. Experimental studies and early clinical experience, *The Journal of thoracic and cardiovascular surgery*, 96(5), 682-95, 1988.

[3] Sharma, S., Goudy, S., Walker, P., Panchal, S., Ensley, A., Kanter, K., Tam, V., Fyfe, D., and Yoganathan, A., In vitro flow experiments for determination of optimal geometry of total cavopulmonary connection for surgical repair of children with functional single ventricle, *Journal of the American College of Cardiology*, 27(5), 1264-1269, 1996.

[4] Soerensen, D. D., Pekkan, K., de Zelicourt, D., Sharma, S., Kanter, K., Fogel, M., and Yoganathan, A. P., Introduction of a new optimized total cavopulmonary connection, *The Annals of thoracic surgery*, 83, 2182-2190, 2007.

[5] Marsden, A. L., Bernstein, A. J., Reddy, V. M., Shadden, S. C., Spilker, R. L., Chan, F. P., Taylor, C. A., and Feinstein, J. A., Evaluation of a novel Yshaped extracardiac Fontan baffle using computational fluid dynamics, *Journal of Thoracic and Cardiovascular Surgery*, 137(2), 394-403, 2009.

[6] Desai, K., Haggerty, C. M., Kanter, K. R., Rossignac, J., Spray, T. L., Fogel, M. A., and Yoganathan, A. P., Haemodynamic comparison of a novel flow-divider Optiflo geometry and a traditional total cavopulmonary connection, *Interactive CardioVascular and Thoracic Surgery*, 17(1), 1-7, 2013.

[7] Raju, S.K. and Narasimhan, A., Porous medium interconnector effects on the thermohydraulics of near-compact heat exchangers treated as porous media, *Trans. ASME: Journal of Heat Transfer*, 129, 273-81, 2007.

# Thermodynamic analysis of a biomass based solid oxide fuel cell (SOFC) integrated combined heat and power (CHP) system

**Dibyendu Roy**
PhD Scholar, Department of Mechanical Engineering, Indian Institute of Engineering Science and Technology, Shibpur, Howrah 711103, West Bengal, India
**Samiran Samanta**
Assistant Professor, School of Mechanical Engineering, Kalinga Institute of Industrial Technology, Deemed to be University, Bhubaneswar-24, Orissa, India
**Sudip Ghosh**
Associate Professor, Department of Mechanical Engineering, Indian Institute of Engineering Science and Technology, Shibpur, Howrah 711103, West Bengal, India

## ABSTRACT

In this study, a biomass gasification based solid oxide fuel cell (SOFC) integrated advanced heating cogeneration system has been modeled and analyzed thermodynamically. The proposed integrated system includes a biomass gasifier, a SOFC module and a heat recovery steam generator (HRSG) for the heating process. As SOFC is the power production component of the system, the influence of major variables on the performance of integrated heating co-generation system has been analyzed. Performance of the co-generation system is expressed in terms of net electrical power output, useful heat, exergy efficiency and fuel energy saving ratio (FESR).

**Key Words:** *Solid Oxide Fuel Cell, Gas Turbine, Exergy, Fuel Energy Saving Ratio*

## 1. INTRODUCTION

Developing clean and energy efficient power generation system is a concern specially with ever increasing energy demand and steady depletion of fossil fuels. Unlike fossil fuels, biomass is considered as renewable energy sources. Carbon neutrality and renewability are the two major benefits of typically utilized biomass fuels. On the other hand, solid oxide fuel cell technology is an attractive technology because of its high efficiency.

In this study, an advanced heating co-generation system comprises a SOFC unit for power generation, and a HRSG unit for the heating process has been modeled and analyzed thermodynamically. Performance of the proposed co-generation system is measured in terms of fuel energy saving ratio (FESR) and heating to power ratio (HTPR). As SOFC is the power production component of the system, the influence of it major variables on the performance of integrated heating co-generation system has been deeply analyzed. This study differs from other SOFC integrated studies as in this research three technologies viz. gasification, SOFC and HRSG have been incorporated in an unique system.

## 2. SYSTEM DESCRIPTION

The proposed system is shown in Figure 1. Proposed heating co-generation system is a combination of a SOFC module, and a HRSG for heating process. Schematic representation of the proposed plant is depicted in Figure 1. Air is compressed by a primary air compressor (AC1) and fed to the biomass gasifier for the gasification of the woody biomass. Syngas from the gasifier exit is supplied to the anode inlet of the SOFC after cleaning the gas in the gas cleaning equipment (GCE) unit. GCE unit is similar to the model of Jia et al.(2015). Heat is supplied to the secondary air compressor (AC2) fed compressed air. Preheated compressed air is fed to the cathode inlet of the SOFC. Unutilized fuel from the anode channel exit of SOFC is completely burned in the after

burner (AB) by using unutilized air coming out from cathode exit. HRSG module produces steam utilizing waste heat coming out from the exhaust of HEX.

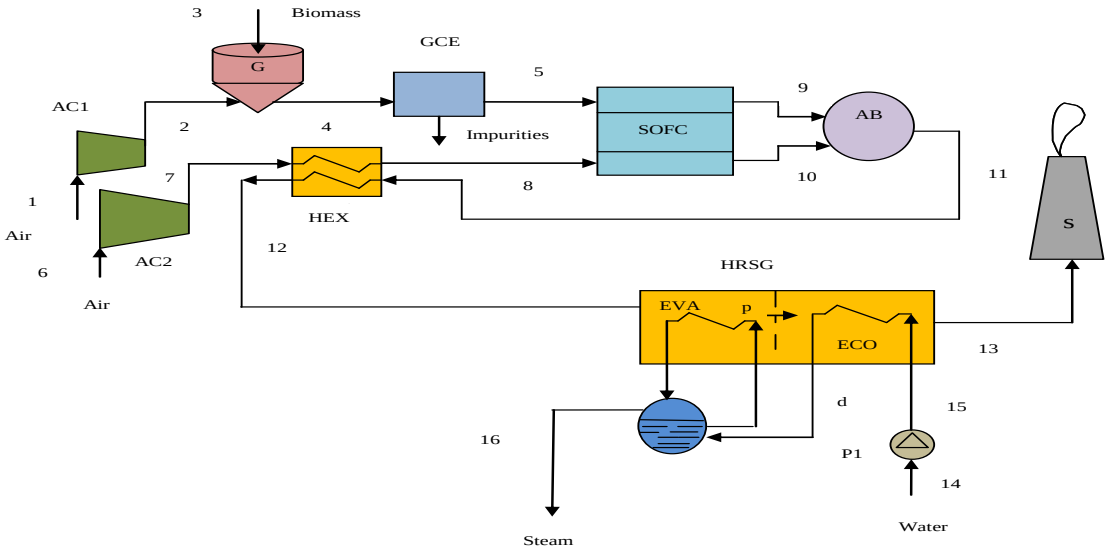


FIGURE 1. Schematic of proposed heating co-generation system

## 3. RESULTS

The effects of changing fuel utilization factor ($u_f$) on the performance of co-generation system have been shown in Figures 2 & 3. In these figures, performance of the system on fuel utilization factor from 0.55 to 0.90 are investigated. Figure 2 depicts the variations in $W_{net}$ and Q with changing fuel utilization factor of SOFC for three different operating temperatures of SOFC. Figure 2 shows, as the $u_f$ increases net power output also increases whereas Q decreases. It is due to higher consumption of fuel in SOFC stack at elevated fuel utilization factor, which results in a lower molar fraction of fuel at the SOFC exhausts. It is also observed that rising cell temperature negatively affects the $W_{net}$, at higher fuel utilization factors.

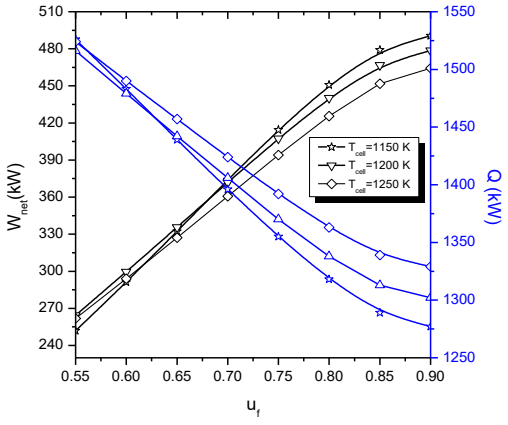


FIGURE 2. Variations of $W_{net}$ and Q with fuel utilization ratio at different cell temperatures ($P_{cell}$=106.5 kPa, j=0.2 A/cm$^2$)

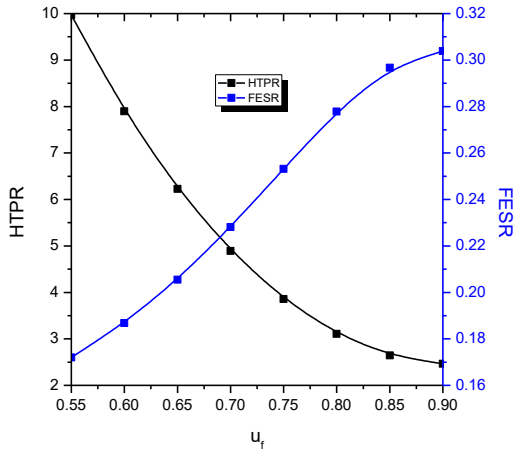


FIGURE 3. Effect of fuel utilization factor on HTPR and FESR ($T_{cell}$=1050 K,$P_{cell}$=106.5 kPa, j=0.2 A/cm$^2$)

Figure 3 depicts the effect of fuel utilization factor ($u_f$) on heating to power ratio (HTPR) and fuel energy saving ratio (FESR) at $T_{cell}$=1050 K,$P_{cell}$=106.5 kPa, j=0.2 A/cm$^2$. With rising fuel utilization factor, net work output increases whereas heat output decreases as shown in Figure 2. Thus, HTPR decreases with rising fuel utilization factor. It is also seen from Figure 3, FESR increases with increasing $u_f$. It is due to increase of $W_{net}$ as the fuel utilization factor increases. Component-based exergy destruction of the heating co-generation system has been inspected in this paper. Useful exergy, total exergy destruction and stack loss of the system in terms of fuel input have been depicted in Figure 4. The useful exergy and total exergy destruction of the proposed system found to be 40.72% and 55.34% respectively. Exergy destruction for individual components with respect to total exergy destruction have been shown in Fig.5. It is found that highest exergy destruction taking place at gasifier (38.94%) followed by HRSG (23.66%). Other components such as HEX , AB and SOFC also contributes higher exergy destruction.

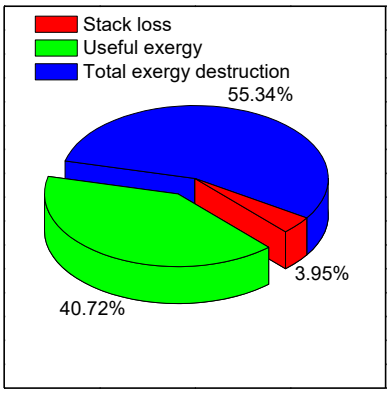


FIGURE 4. Stack loss, useful exergy and exergy destruction of system ($T_{cell}$=1050 K, $P_{cell}$=106.5 kPa, j=0.2 A/cm$^2$)

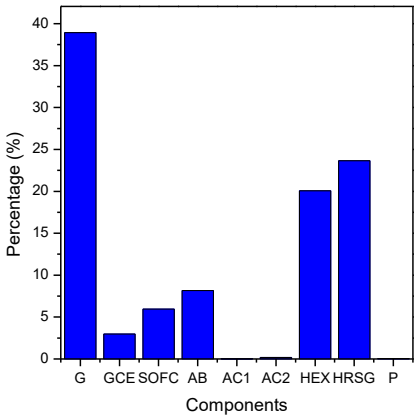


FIGURE 5. Exergy destruction of system components in terms of total exergy destruction

## 4. CONCLUSIONS

In this study, biomass gasifier coupled with an internal reforming type SOFC driven heating co-generation system has been modeled and analyzed. Energy and exergy analyses of the proposed system have been conducted. It is found that FESR increases with increasing $u_f$. The useful exergy and total exergy destruction of the proposed system found to be 40.72% and 55.34%, respectively. It is found that highest exergy destruction taking place at gasifier (38.94%) followed by HRSG (23.66%). Highest FESR of the cogeneration system found to be 30.02%.

## REFERENCES

[1] J. Jia, A. Abudula, L. Wei, B. Sun, and Y. Shi, Thermodynamic modeling of an integrated biomass gasi fi cation and solid oxide fuel cell system, *Renewable Energy*, vol. 81, pp. 400–410, 2015.

[2]F. Ranjbar, A. Chitsaz, S. M. S. Mahmoudi, S. Khalilarya, and M. A. Rosen, “Energy and exergy assessments of a novel trigeneration system based on a solid oxide fuel cell,” *Energy Conversion and Management*, vol. 87, pp. 318–327, 2014.

Fifth International Conference on Computational Methods for Thermal Problems
THERMACOMP2018, July 9-11, 2018, Indian Institute of Science, Bangalore, INDIA
*N. Massarotti, P. Nithiarasu, Pradip Dutta and C. Ranganyakalu (Eds.)*

# Numerical and experimental analysis of a real Operating Theater with LAF system

**Nicola Massarotti, Alessandro Mauro, Gabriella Paderni, Domenico Sainas**
Dipartimento di Ingegneria, Università degli Studi di Napoli "Parthenope", Isola C4, Centro Direzionale di Napoli, 80143 Napoli, Italy, massarotti@uniparthenope.it, alessandro.mauro@uniparthenope.it, gabriella.paderni@uniparthenope.it, domenico.sainas@uniparthenope.it.

## ABSTRACT

Ventilation is essential in all occupied premises and assumes a crucial role for the efficiency of an operating theater. It controls the thermo-hygrometer comfort level and the airborne contaminant level, in order to minimize the risk of post-operative infections for patients. For this reason, the design of ventilation systems in operating rooms is of fundamental importance. The aim of this work is to perform an experimental and numerical activity to reproduce the air distribution and thermal comfort in an actual operating theater.

**Key Words:** *Airflow, Operating room, Thermal field*

## 1. INTRODUCTION

The operating theater is the environment inside of hospitals that requires the greatest deal of attention in the choice of the devices for air supply, diffusion and recovery. The design of Heating Ventilation and Air Conditioning (HVAC) systems dedicated to these environments plays a crucial role, in order to drastically reduce the risk of infections for patients, in addition to the maintenance of adequate thermo-hygrometric comfort conditions for the medical team.

Nowadays, the air quality in an operating theater is one of the key factor for reducing the post-operative infection rates of surgical procedures. It has been reported that 80-90% of bacterial contamination observed in an open wound comes from the ambient air [1]. Therefore, a lower risk of sepsis has been reported thanks to a cleaner air injection in operating rooms. Several guidelines are available for a correct design of HVAC systems for operating rooms, depending on the country legislations.

The obtained numerical results have proven that the numerical modelling approach can be successfully applied to the simulation of the real performance of an operating theater in terms of air velocity and temperature distributions, after validation against experimental data.

## 2. CASE STUDY

Experimental investigation was conducted in a real operating theater of the Hospital of Aversa "G. Moscati" (Italy). The layout of the operating theatre considered in this work is reported in Figure 1. The net height of the room is 2.8m and its area is 36.6m$^2$. The operating theater is provided with a vertical laminar airflow (LAF) system composed of 6 terminal HEPA H14 filters (of which 4 with dimension 610x900mm and 2 with dimension 610x610mm) installed in a plenum of 2400x2400mm. At each corner of the operating theater, two extraction grilles are installed, as shown in Figure 1. In order to respect the limitations in terms of air quality and contamination control, 3200 m$^3$/h (or 30 Air Changes per Hour – ACH) of air is injected from the ceiling filters. In order to avoid the risk of contaminant infiltrations from adjacent environments, an overpressure of 15Pa is maintained in the operating theater by extracting 90% of air. The supply air at the ceiling filters has a design set-point temperature of 23°C and 50% relative humidity.

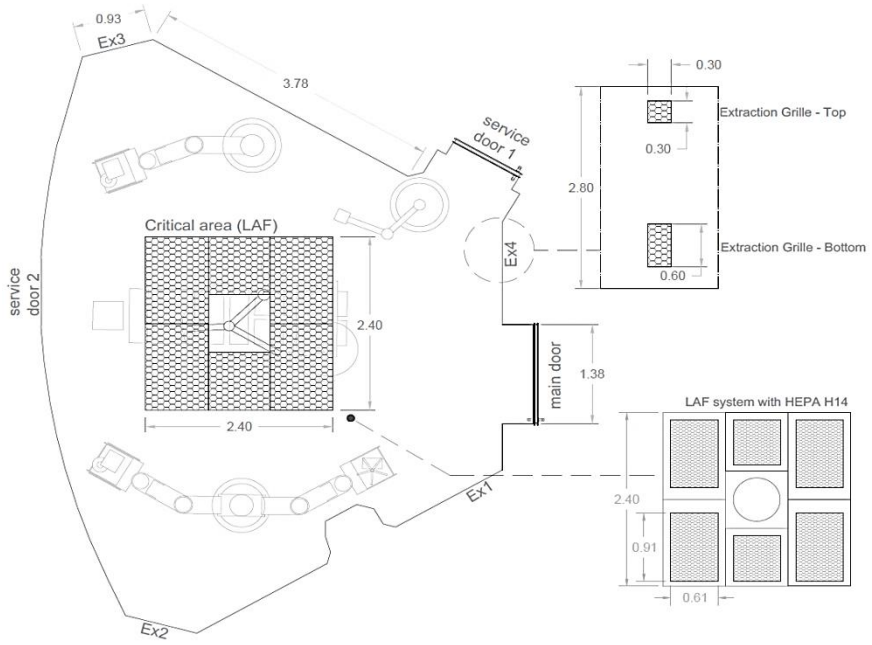


Figure 1. Layout of the operating theatre and detail of the H14 filters installed in the ceiling.

## 3. GOVERNING EQUATIONS AND BOUNDARY CONDITIONS

The numerical model is based on the partial differential equations reported in reference [2], and is based on the RANS (Reynolds Averaged Navier-Stokes) approach, and on realizable k-ε turbulence model, which has already proven to be appropriate for calculating airflow and heat transfer phenomena in indoor environments [3]. The air is modelled as a Newtonian incompressible fluid, under steady state conditions. The fluid properties have been referred to dry air, since the difference with the values corresponding to humid air can be considered negligible.

The boundary conditions, reported in Table 1 have been determined during an experimental campaign in the operating room or taken from the available literature.

| **Objects** | **Boundary conditions** | **Value** | **Source** |
|---|---|---|---|
| Inlet | Velocity inlet | 0.3 m/s | Measured |
| Outlet | Pressure outlet | 0 Pa | Measured |
| Walls | No slip velocity and wall functions | - | - |
| Surgical light (glass) | Temperature | 27.5°C | Measured |
| Surgical light (cover) | Temperature | 29.2°C | Measured |
| Monitor | Heat flux | 400 W/m$^2$ | From literature |
| Brain and Body | Temperature | 36°C | From literature |
| Neck | | 36.4°C | |
| Leg | | 32°C | |
| Foot | | 29.3°C | |
| Chest | | 33.9°C | |
| Thigh and Arm | | 32.9°C | |
| Abdomen | | 33.2°C | |
| Hand | | 29.9°C | |
| Temperature (Inlet and Outlet) | Temperature | 23°C | Measured |

Table 1. Boundary conditions employed.

## 4. RESULTS

The numerical model has been validated against the experimental data collected during the on-field activity. Figure 2 shows the comparison between experimental and numerical results, in terms of vertical velocity. The velocity values are referred to a height of 2.25m, under the ceiling filters, as reported on the rigth side of Figure 2. As concerns the measured values, the authors report both the average values and the expanded combined uncertainties, calculated combining type A and type B uncertainties and by using a coverage factor k=2, implying a 95% confidence interval [4].

The results reported in Figure 2 are in good agreement with the experiments. In fact, the maximum difference between the numerical results and the experimental data is approximately equal to 6.6%, and this value is smaller than the minimum measurement uncertainty value, equal to 8.7%.

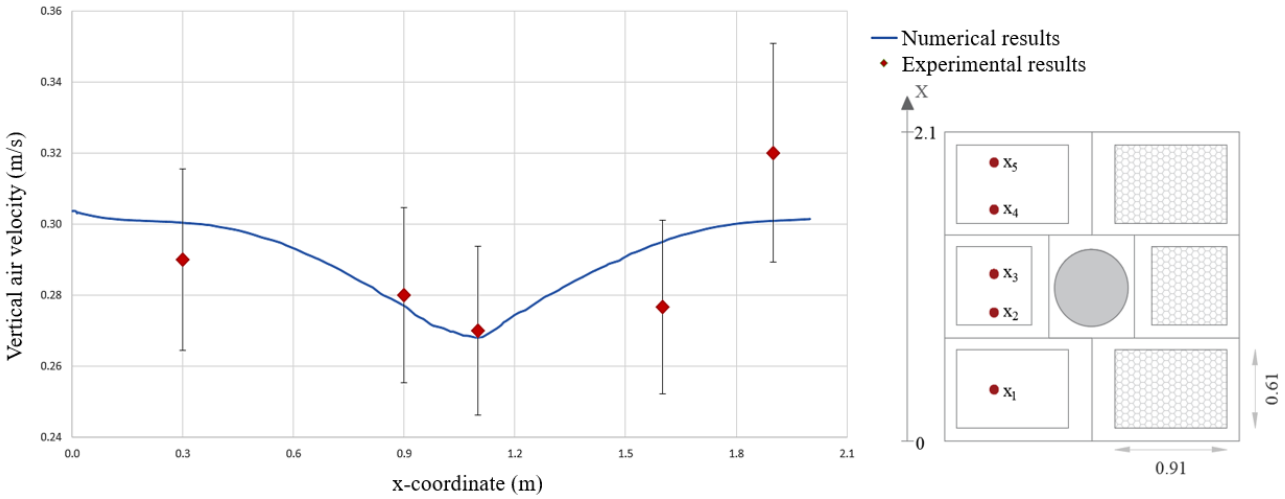


Figure 2. Comparison between experimental and numerical results at a height of 2.25m, under the ceiling filters.

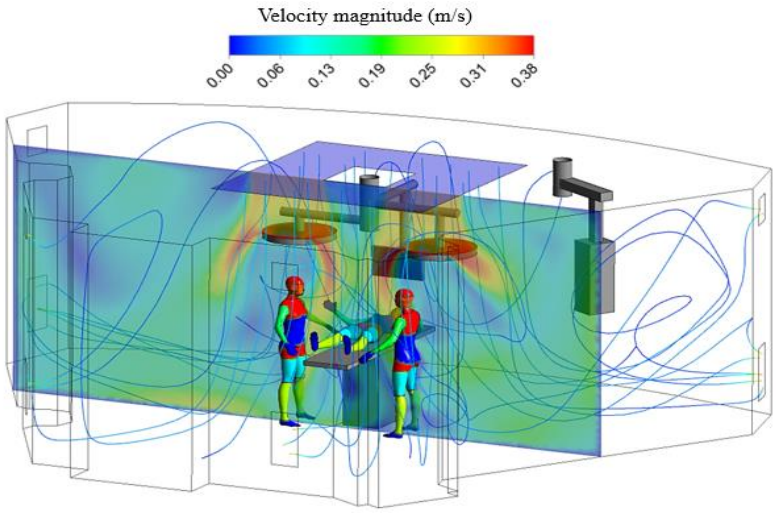


Figure 3. Velocity field and path lines in the middle plane of the operating theatre.

Figure 3 reports the velocity field calculated in the middle plane of the operating theatre. Near the wound site, the air velocity is lower than 0.15 m/s, even if the air velocity field is slightly deformed by the thermal effect due to the presence of the surgical lights. In order to reduce this effect, it is possible to tilt the lamps, with a consequent increase of the comfort conditions for the medical staff. In fact, higher velocity close to neck and face should be avoided (this is a common problem in operating theatres, if the HVAC system is not well design and regulated). The ceiling filters generate an unidirectional airflow over the operating table, ensuring a good

flushing in the critical area. However, there are small areas of air stagnation close to the walls of the operating theatre, where no extraction grilles are installed.

Figure 4 reports the temperature field on a horizontal plane, at a height of 1.1m. The authors have chosen to report the results at this height in order to involve the surgical table. The thermal field inside the room is locally modified due to the presence of the medical staff, patient and surgical light. However, the air temperature in the critical area is less than 23.5°C, and the ventilation system installed in the real operating theatre ensures of temperature distribution uniformity.

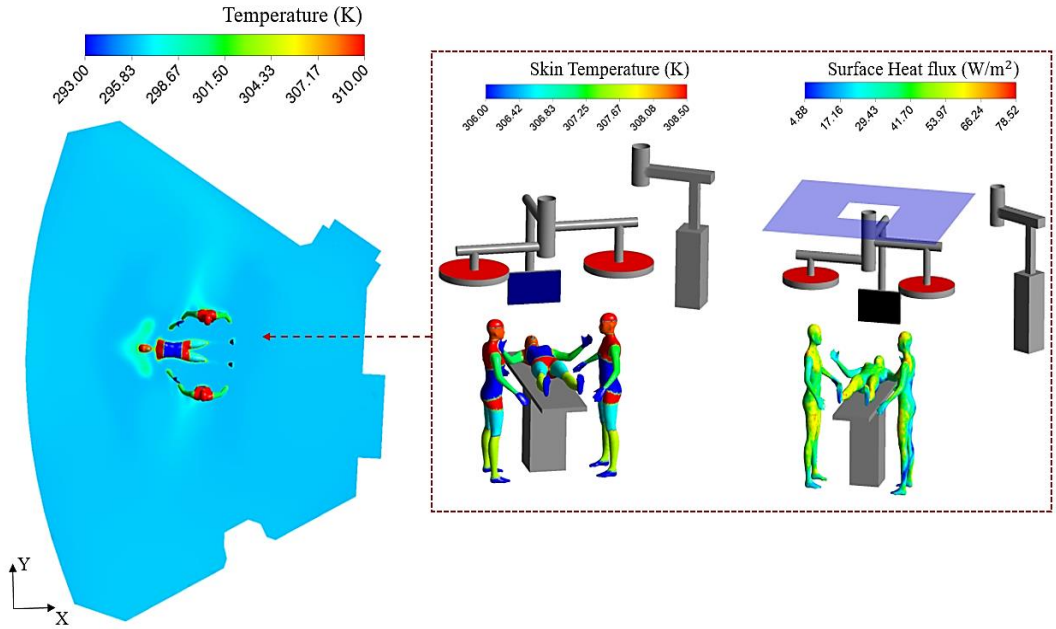


Figure 4. Temperature distribution at the horizontal plane 1.1m above the floor and details of the temperature profile and heat flux on human bodies.

## 5. SUMMARY

A numerical model to reproduce the airflow and thermal field inside a real operating theatre, provided with a vertical laminar airflow (LAF) system, has been developed. The authors have carried out an experimental campaign, in order to acquire data to be used both for boundary conditions and for validation purposes. An analysis of the measurement uncertainties has been also carried out.

After validation, the model has been used to reproduce the air distribution and thermal field inside the operating room. The present model allows to produce useful results to improve the comfort conditions for the medical staff. The numerical data can be also used as practical indications for the operation of the room, for example to avoid undesired stagnation areas.

## REFERENCES

[1] J.P. Nelson, The operating room environment and its influence on deep wound infection in the hip, *Proceedings of the 5th Scientific Meetings of Hip Society*. C.V. Mosby, St. Louis, 1977.

[2] P. Nithiarasu, C.B. Liu, N. Massarotti, Laminar and turbulent flow calculations through a model human upper airway using unstructured meshes, *Communications in Numerical Methods in Engineering*, 23, 1057-1069, 2007.

[3] J. Screbic, V. Vukovic, G. He, X. Yang, CFD boundary conditions for contaminant dispersion, heat transfer and air flow simulations around human occupants in indoor environments, *Building and Environment*, 43, 294-303, 2008.

[4] F. Arpino, N. Massarotti, A. Mauro, L. Vanoli, Metrological Analysis of the Measurement System for a Micro-Cogenerative SOFC Module, *International Journal of Hydrogen Energy*, 36, 10228-10234, 2011.

Fifth International Conference on Computational Methods for Thermal Problems
THERMACOMP2018, July 9-11, 2018, Indian Institute of Science, Bangalore, INDIA
*N. Massarotti, P. Nithiarasu, Pradip Dutta and C. Ranganyakalu (Eds.)*

# OXYGEN TRANSPORT PREDICTION IN THE ELECTROLYTE MEMBRANE OF PEMFC BY USING MOLECULAR DYNAMICS SIMULATION

**Akihiro Kimura[1], Mahiro Kato[1], Hong Duc Doan[2], Kazuyoshi Fushinobu[1]**
[1]Tokyo Institute of Technology, Tokyo 152-8550 Japan, fushinobu.k.aa@m.titech.ac.jp
[2]VNU at Hanoi, University of Engineering and Technology, Hanoi Vietnam

## ABSTRACT

Effect of force field selection and the parameters are investigated on the prediction of molecular transport of oxygen in the electrolyte membrane of PEMFC (proton exchange membrane fuel cell.) Simulation has been conducted by using GROMACS. Various force fields are examined to compare the calculated density to choose the AMBERGS with parameter adjustment. The results predict the density within 5% or relative error to the experimental value, and the value of $D$ (relative diffusion coefficient of oxygen to the humidified electrolyte membrane) within about 20% of relative error to the experiment in the range of $\lambda$ (water content) between 2.5 to 7.5. The results also predict the decreasing trend of $D$ with increasing $T$ (temperature of the membrane) within the range of 80 ˚C to 30 ˚C. Comparison between calculated and experimentally obtained values of $E_a$ (activation energy obtained from the Arrhenius plot of $D$) with various $\lambda$ are also disccussed to show that the calculated values are relatively smaller than the values in membrane and closer to the value in bulk water. The results can be due to the domain size. Further study is needed to simulate much larger computational domain to see the effect on the data prediction.

**Key Words:** *Molecular dynamics simulation, Force field, PEMFC.*

## 1. INTRODUCTION

PEMFC (Proton exchange membrane fuel cell,) or PEFC (polymer electrolyte fuel cell,) can be an alternative energy conversion device option for the applications, such as automobile, co-generation systems, emergency power supplies, and UAVs (unmanned aerial vehicles,) considering the variety of primary energy sources, local clean nature, and its relatively high thermal efficiency. Fuel cell-based co-generation systems for households have been commercially available since 2009 in Japan, and the cumulative market sales exceeded 200,000 units in 2017. Fuel cell vehicles have also been commercially available since 2014 with over 100 hydrogen stations including the planned sites.

One of the issues for the PEMFC is its durability. Previous studies have revealed cell degradation due to gas molecules cross-leaking [1]. The polymer electrolyte membrane, which is supposed to have gas barrier function, in fact has a very tiny amount of permeation of oxygen and hydrogen gas molecules during its operation. This cross-leaking of gas molecules results in the formation of hydrogen peroxide in the membrane under certain condition to degrade the membrane as well as degrading the cell performance.

Authors have experimentally measured the diffusion coefficient of oxygen and hydrogen in electrolyte membrane under operation conditions [2]. Limiting current technique is applied to measure the overall gas transport resistance along the thickness-wise direction of the membrane by using microprobe technique. The resistance is then analyzed to obtain the diffusion coefficient in the membrane by plotting the resistance versus thickness-wise position of the microprobe. The results showed the increasing trend of the diffusion coefficient of both oxygen and hydrogen with increasing membrane water uptake and with other parameters, as well as other unique trends. Further understanding of the behavior however encounters fundamental problem; one cannot see

what is happening at molecular level to analyze the phenomena. The authors [3] therefore used MD (molecular dynamics) simulation by using commonly used free software, LAMMPS, to simulate the oxygen in the humidified membrane to reveal the molecular structure and the resulting diffusion coefficient trend. MD simulation is so powerful to visualize the molecular structure in order to explain the trend of bulk transport property. Next step is to enlarge the computational domain to improve the statistical accuracy. In this sense, MD software for high performance computing capability on TSUBAME, the super computer of our institution, is a better choice for us.

In this work, we have conducted a molecular dynamics simulation of oxygen molecules in humidified PFSA (perfluorosulfonate acid) membrane by using MD software called GROMACS. As the first step for simulation, force field selection and the parameter adjustment have been conducted, followed by the evaluation of calculated diffusion coefficient in comparison with the experimental values.

## 2. NUMERICAL METHOD

Figure 1 shows the chemical formula of PFSA membrane simulated in calculation where $x = 7$, $y = 1$, $n = 10$ are chosen as the parameter set to simulate Nafion® membrane [4], NR-211 and NR212 with EW = 1100 g/eq, that are used in experiment [2]. Protons are considered to bond with water molecules, and SPC/E model is used for water molecules.

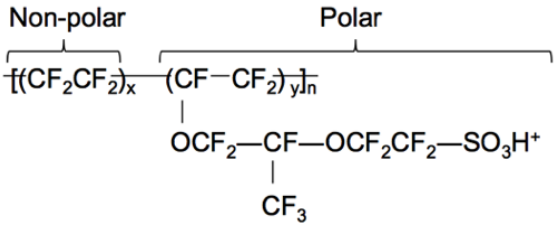


FIGURE 1. Chemical formula of PFSA (perfluorosulfonic acid)

Free and open source software, GROMACS [5], is used for simulation. Three types of force fields, GROMOS53a6, AMBER99, and AMBERGS are examined since they can handle both fluorine atoms and hydrogen bond. Initial configuration consists of 24 PFSA chains with water molecules, ranging $\lambda = 3$ to 20, and three oxygen molecules. Annealing is conducted by swinging both the pressure and temperature for four times under NPT ensemble. The system is then held under NVT ensemble to obtain the final structure.

## 3. RESULTS

Figure 2 shows the comparison of the effect of the force fields. Calculated density becomes 25% lower for GROMOS53a6 and 11% lower for both AMBER99 and AMBERGS than the experiment [6]. Since the molecular structure is reported to have strong influence on the transport properties [7-8], torsion and angle parameters are further modified by following the idea of previous work [9] where the authors adjusted the parameters in potential field to fit the density. AMBERGS, that is more sensitive to the angle and torsion parameter adjustment, get the density values of 1864 g/L for $\lambda = 3$, 1815 g/L for $\lambda = 5$, and 1743 g/L for $\lambda = 8$ at both torsion and angle parameter of 1/8 of their original values. The calculated density values lie within the range of 5% relative error to the experimental value. Density value is then compared by repeating the annealing process to see the change after 3rd and 4th cycles to find that the relative error of the 4th cycle to the 3rd is within 1% to confirm the convergence.

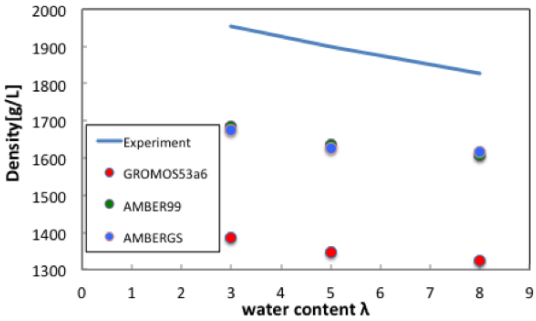


FIGURE 2. Effect of force field and parameter on density prediction

Figure 4 shows the calculated $D$ as a function of $\lambda$ at various temperature in comparison with the experiment at 80 ˚C [2]. Calculated results agree well with the experiment at 80 ˚C. The increasing trend of $D$ with increasing $T$ also agree with the well-known trend in polymers [2].

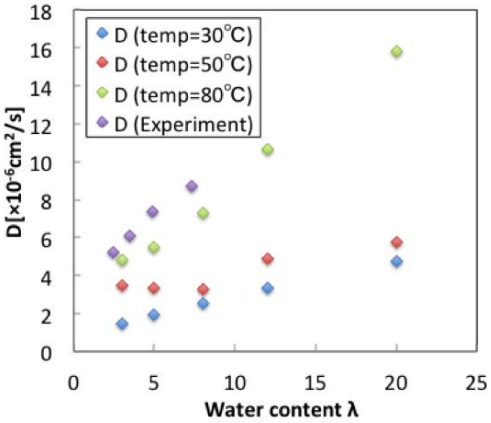


FIGURE 3. Calculated and experimental diffusion coefficient

Figure 4 shows the Arrhenius plot of $D$. The plot is then used to obtain the value of activation energy, $E_a$.

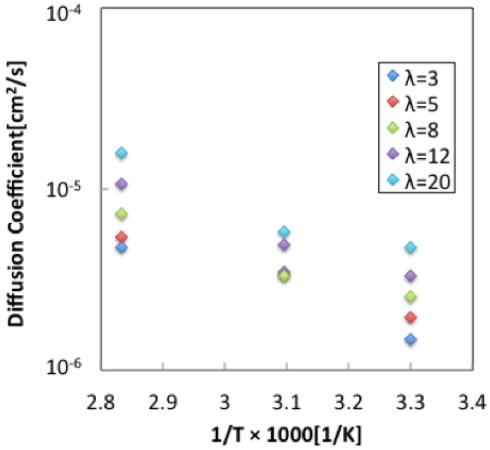


FIGURE 4. Arrhenius plot of diffusion coefficient

Table 1 shows the calculated value of $E_a$, and Table 2 shows the reference values of $E_a$. Calculated results show relatively smaller values compared with the values in membrane that lies between 23 to 50 kJ/mol and are closer to the value in bulk water, indicating that the calculation domain needs to be enlarged to obtain statistically reliable data to avoid localization of the molecules.

| $\lambda$ | 3 | 5 | 9 | 12 | 20 |
|---|---|---|---|---|---|
| $E_a$, kJ/mol | 20.5 | 18.2 | 18.9 | 20.9 | 21.9 |

TABLE 1. Calculated activation energy

| $\lambda$ | In membrane w/ 0% RH gas | In membrane w/ 100% RH gas | In water |
|---|---|---|---|
| $E_a$, kJ/mol | 50 | 23 | 18 |

TABLE 2. Apparent activation energy of gas diffusion [2]

## 4. CONCLUSIONS

MD simulation of oxygen molecule behaviour in PFSA membrane has been conducted by using GROMACS in order to predict the diffusion coefficient. Further study is needed to enlarge the computational domain to see the dependence on the domain size.

## ACKNOWLEDGEMENT

Part of this work has been conducted under the support of JFE 21st Century Foundation.

## REFERENCES

[1] A. Ohma, S. Suga, S. Yamamoto, and K. Shinohara, Membrane Degradation Behavior during Open-Circuit Voltage Hold Test, *J. Electrochemical Society*, 154, B757-B760, 2007.

[2] M. Ohishi, Y. Ono, and K. Fushinobu, Measurement of Gas Transport Characteristics in PEFC Electrolyte Membrane by Using Microprobes, *Nanoscale and Microscale Thermophysical Engineering*, 17, 69-78, 2013.

[3] M. Kato, A. Henry, S. Graham, H.D. Doan, and K. Fushinobu, Molecular dynamics simulation of oxygen transport characteristics in the electrolyte membrane of PEMFC, *International Journal of Numerical Methods for Heat and Fluid Flow*, in press.

[4] S.S. Jang, V. Molinero, T. Cagin, and W.A. Goddard, Nanophase-Segregation and Transport in Nafion 117 from Molecular Dynamics Simulations: Effect of Monomeric Sequence, *Journal of Physical Chemistry B*, 108, 3149-3157, 2004.

[5] GROMACS, www.gromacs,org.

[6] D. R. Morris, and X. Sun, Water-sorption and transport properties of Nafion 117 H, *Journal of Applied Polymer Science*, 50, 1445-1452, 1993.

[7] J. S. Vrentas, and J. L. Duda, Diffusion in polymer—solvent systems. I. Reexamination of the free-volume theory, *Journal of Polymer Science B: Polymer Physics*, 15, 403-416, 1977.

[8] John M. Zielinski, and J. L. Duda, Predicting polymer/solvent diffusion coefficients using free-volume theory, *AIChE Journal*, 38, 405-415, 1992.

[9] T. Mabuchia, and T. Tokumasu, Molecular Simulation of Proton and Water Transport in Hydrated Nafion Membrane, *ECS Transactions*, 50, 175-181, 2012.

Fifth International Conference on Computational Methods for Thermal Problems
THERMACOMP2018, July 9-11, 2018, Indian Institute of Science, Bangalore, INDIA
*N. Massarotti, P. Nithiarasu, Pradip Dutta and C. Ranganyakalu (Eds.)*

# NUMERICAL INVESTIGATION OF BOUNDARY LAYER EFFECT IN A FLOW THROUGH A CIRCULAR PIPE

**Prasad G, Rajasekar K, Ramesh M, Vadivelu P**
Department of Aeronautical Engineering , Bannari amman Institute of Technology,
sathyamangalam, India -638401
prasad@bitsathy.ac.in[1], rajasekark@bitsathy.ac.in[2],rameshm@bitsathy.ac.in[3]
vadivelup@bitsathy.ac.in[4]

## ABSTRACT

In this article, the boundary layer flow and heat transfer of steady flow in a circular pipe under different temperature boundary condition effects are investigated numerically. The velocity profiles are obtained in various station of pipe in order to predict the internal flow velocity profile. This work depicts the thermal fluid interaction, utilizing Computational Fluid Dynamics (CFD), which is the area to be considered in real world problems. In addition, the presented method reduces the solution of the problem to the solution of a system of governing equations. The numerical results are reported to show the accuracy and efficiency of the novel proposed computational procedure. Comparisons of present results are made with those obtained by previous works and show excellent agreement.

**Key Words:** *boundary layer, thermal fluid interaction, computational fluid dynamics.*

Fifth International Conference on Computational Methods for Thermal Problems
THERMACOMP2018, July 9-11, 2018, Indian Institute of Science, Bangalore, INDIA
*N. Massarotti, P. Nithiarasu, Pradip Dutta and C. Ranganyakalu (Eds.)*

# A Sharp-Interface Immersed Boundary based Solver for Conjugate Heat Transfer with Moving Boundary

**Hemanshul Garg**
Department of Mechanical Engineering IIT Bombay, Mumbai 400076
Email: hemanshul.garg@gmail.com

**Rajneesh Bhardwaj**
Department of Mechanical Engineering IIT Bombay, Mumbai 400076
Email: Rajneesh.bhardwaj@iitb.ac.in

## ABSTRACT

We extend a sharp-interface immersed boundary method (IBM) based in-house fluid-structure interface (FSI) solver to tackle the conjugate heat transfer (CHT) problems. The governing equations of fluid flow and heat transfer within the fluid region are discretized on the non-staggered uniform/non-uniform Cartesian grid using finite difference method. The energy equation within the structure is solved by utilizing Galerkin finite element method. The immersed structure is represented by the unstructured triangular element. The Dirichlet-Neumann coupling is used at the fluid-structure interface to achieve the perfect thermal contact. We verify the results obtained from our CHT-IBM solver by comparing with the analytical and published results.

**Key Words:** *Immersed boundary method, Conjugate heat transfer*.

## 1. INTRODUCTION

The development of conjugate heat transfer (CHT) solver along with immersed boundary method (IBM) based incompressible viscous flow solver has a great advantage to tackle a large class of problems. The implementation of CHT using IBM scheme was successfully accomplished by Iaccarino and Moreau [1]. In the past, the coupled CHT-IBM solver based on the curvilinear grid was proposed by Nagendra et al. [2]. The advantage of using the IBM is that it doesn't require the body-conformal grid, which eliminates the complexities (re-gridding and/or grid deformation at every time step) arising due to body-conformal grid method. In the IBM the body is "immersed" in a background grid and at the immersed structure boundary special treatments are required to apply boundary conditions. The CHT solver to handle flow past a heated cylinder in cross-flow has been developed by Laskowski et al. [3] which is CHT-RANS (Reynolds-averaged Navier-Stokes) solver. In the more recent steady Marinis et al. [4] has proposed improved conjugate heat transfer (CHT) immersed boundary method (IBM) to tackle flow past the air-cooled C3X turbine guide vane. Nearly all the experimental or computational conjugate heat transfer studies both focus on the turbulent flows and flow past the air-cooled turbines.

The objective of present work is to extend in-house solver to tackle CHT problems for stationary and moving structures. Already existing sharp-interface immersed boundary method based flow solver has the capabilities to handle incompressible, viscous flow over complex stationary, moving and/or deformable structures. The energy equation to get temperature field inside the structure is discretized using Galerkin finite element method. The solver capable to simulate the heat transfer inside the structure is coupled with the existing flow solver, but to get the perfect thermal contact at fluid-structure interface a combination of Dirichlet-Neumann boundary condition is used. The CHT-IBM solver is verified with the analytical solutions of Barletta et al. [5].

## 2. Computational Model

The governing equations of fluid flow and heat transfer for unsteady incompressible viscous fluid, as well as the energy equation to get the temperature field within the structure, are given as follows:

$$\frac{\partial u_j}{\partial x_j} = 0\,, \tag{1}$$

$$\frac{\partial u_j}{\partial \tau} + \frac{\partial u_j u_i}{\partial x_i} = -\frac{\partial P}{\partial x_j} + \frac{1}{\mathrm{Re}}\frac{\partial}{\partial x_i}\left(\frac{\partial u_j}{\partial x_i}\right), \tag{2}$$

$$\frac{\partial \theta_f}{\partial \tau} + u_i \frac{\partial \theta_f}{\partial x_i} = \frac{1}{\mathrm{Re}\,\mathrm{Pr}}\left(\frac{\partial^2 \theta_f}{\partial x_j^2}\right), \tag{3}$$

$$\frac{\partial \theta_s}{\partial \tau} = \frac{\alpha_s}{\alpha_f}\frac{1}{\mathrm{Re}\,\mathrm{Pr}}\left(\frac{\partial^2 \theta_s}{\partial x_j^2}\right) + Q\,, \tag{4}$$

Where $u_j$ ($j$ = 1,2) are components of non-dimensional velocity vector in $x(x_1)$ and $y(x_2)$ directions, respectively. *Re* and *Pr* are Reynolds number ($u_{ref} L_{ref} / \nu$) and Prandtl number ($\nu / \alpha$), respectively, where $\nu$ and $\alpha$ are kinematic viscosity and thermal diffusivity, respectively. $\theta$ is non-dimensional temperature. $Q$ is the non-dimensional volumetric heat generation. The Eqs. (1-3) are discretized using finite difference method on Cartesian uniform/non-uniform collocated (non-staggered) grids. To satisfy the boundary conditions on immersed boundary ghost-cell based method is employed [6]. For time integration the fractional step method is used. To get intermediate velocity components Crank-Nicolson scheme is used for convective and diffusion terms of momentum equations, given by eq. (2). The second order central difference scheme is used for both convective and diffusion terms. Eq. (4), the energy equation to get the temperature field within the structure, is discretized by using Galerkin finite element method (GFEM) on unstructured triangular grid.

- **Summary of the Strongly Coupled Algorithm**
  1. First, we obtain the flow field using in-house flow solver.
  2. Obtain temperature field within the structure by utilizing the GFEM based structure solver. Dirichlet boundary condition is applied at the structure boundary as the temperature is available at the interface from fluid.
  $$\theta_s = \theta_f \quad at\ \Gamma_b \tag{5}$$
  3. Calculate and transfer the heat flux at the interface from structure to fluid. Before that provide some under-relaxation to the evaluate temperature within the structure as mentioned below
  $$\theta_s^n = (1-\omega)\theta_s^{n-1} + \omega\theta_s^n \tag{6}$$
  $$k_f\left(\frac{\partial\theta}{\partial n}\right)_f = k_s\left(\frac{\partial\theta}{\partial n}\right)_s \ at\ \Gamma_b \tag{7}$$
  4. Now solve the energy equation within fluid region. The boundary condition at the fluid-structure interface to solve this equation is the heat flux (Neumann boundary condition) obtained for fluid at the interface.
  5. Repeat steps 1-4 till the convergence of temperature in the whole domain is reached.

## 3. RESULTS

First we verify the CHT-IBM solver with the published results. Second we present a simple problem in which uniform flow over a stationary cylinder (with volumetric heat generation, $Q$ = 1) at *Re* = 100, to demonstrate the developed CHT-IBM solver capability.

### 3.1 Verification of CHT-IBM solver

We verify CHT-IBM solver with the analytical results of Barletta et al. [5]. Fig. 1(a) is the schematic of the problem taken by Barletta et al. [5], it has two parallel infinite plates with wall thickness 1.2*H*, where *H* is the height of the channel as shown in. The fully developed velocity boundary condition is implemented at the inlet of the channel with a sinusoidal temperature distribution in the longitudinal direction at the channel walls is taken. The analytical solution is determined with the assumption of negligible heat conduction in the longitudinal direction along with no viscous dissipation. The channel length in our numerical model is taken as long enough to take care of these assumptions. The parameter *B* is defined as $Pe\beta y_o$, where $y_o = H/2$ and *Pe* is Peclet number signifies the convective to conductive heat transfer within the fluid.

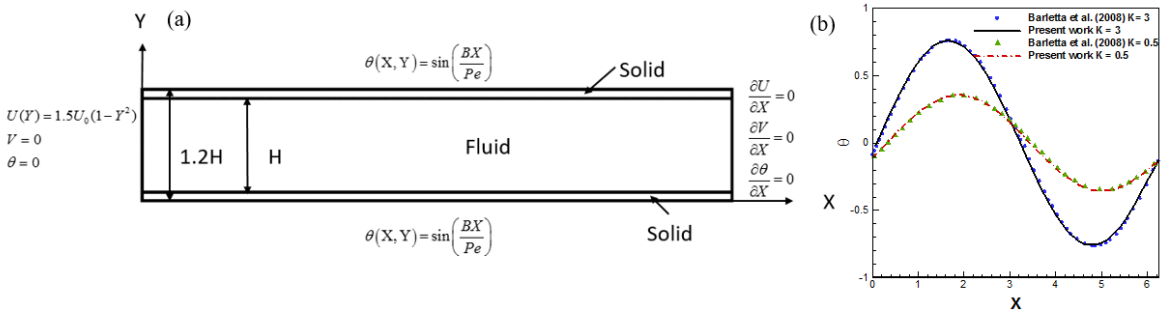


Figure 1: (a) The schematic of two infinite-parallel plates with sinusoidal longitudinal temperature boundary condition, (b) the steady state non-dimensional interface temperature for different conductivity ratio *K*.

The non-dimensional interface temperature is compared for two cases with the structure to fluid conductivity ratio is taken as 0.5 and 3. The parameters *B* and *Pe* are taken 100 for both the cases. The domain is taken as 2.4×12.6 with uniform mesh in both direction with $\Delta x_{min}$ and $\Delta y_{min}$ = 0.02, 630×120 grid points for the fluid region and for the structure triangular unstructured mesh is used for both the walls (i.e. top & bottom walls of the channel) with 8777 nodes & 16276 elements each. The results are time marched with uniform time stepping as $\Delta t$ = 0.005. Also, the effect of conductivity can be observed in non-dimensional interface temperature as shown in fig. 1(b). There is a spatial shift in interface temperature in both the cases in the forward direction compared to the sinusoidal longitudinal boundary condition, for lower conductivity ratio *K* = 0.5 the shift is larger than the larger conductivity ratio *K* = 3.0.

### 3.2 Flow over cylinder with heat generation

We present the problem in which the CHT-IBM solver is utilized to solve the flow over a cylinder with a volumetric heat source. The computational domain is taken as 30*D*×50*D* (where *D* is the cylinder diameter), with uniform mesh in both direction with $\Delta x_{min}$ and $\Delta y_{min}$ = 0.02, 384×384 grid points for the fluid region and for the cylinder triangular unstructured mesh is used with 5563 nodes & 10809 elements. The cylinder is kept in the uniform flow field with the centre located at 8*D*×15*D*. The Neumann boundary condition for velocity and temperature is imposed at the top, bottom and right boundaries of the computational domain. At the left boundary which is considered as the inlet, the velocity and the temperature are specified as $u_1$ = 1.0 and $\theta = 0$, respectively. The cylinder to fluid conductivity ratio is taken as $K(k_s/k_f)$ = 1. The cylinder has the volumetric heat source *Q* = 1.0. The numerical experiment is performed at *Re* = 100 and *Pr* = 0.71 (corresponding to air). In figs. 2(a),

(b) and (c), the temperature field, vorticity field and interface temperature are shown, respectively, at the time instant $t$ = 100.

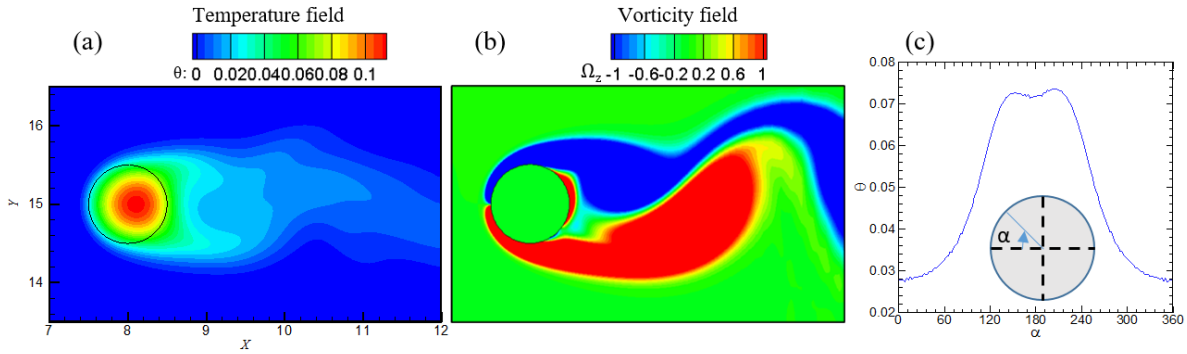


Figure 2: (a) The temperature field for the flow over cylinder with volumetric heat generation $Q$ = 1, (b) the vorticity field and (c) the interface temperature at time instant $t$ = 100 for $Re$ = 100.

## 4. CONCLUSIONS

The in-house IBM based FSI solver is further developed to tackle the problems involving conjugate heat transfer. To account for the perfect thermal contact, the Dirichlet-Neumann coupling is used at the fluid-structure interface. The CHT-IBM solver is verified with the published results. A simple problem in which the uniform flow over a cylinder with the heat source is considered to demonstrate the CHT-IBM capability. In future, the more numerical experiments need to be performed to account for the moving boundary CHT problems.

## REFERENCES

1. Iaccarino, G. and S. Moreau, *Natural and forced conjugate heat transfer in complex geometries on cartesian adapted grids.* Journal of fluids engineering, 2006. **128**(4): p. 838-846.
2. Nagendra, K., D.K. Tafti, and K. Viswanath, *A new approach for conjugate heat transfer problems using immersed boundary method for curvilinear grid based solvers.* Journal of Computational Physics, 2014. **267**: p. 225-246.
3. Laskowski, G., et al., *Mixed convection heat transfer to and from a horizontal cylinder in cross-flow with heating from below.* International journal of heat and fluid flow, 2007. **28**(3): p. 454-468.
4. De Marinis, D., et al., *Improving a conjugate-heat-transfer immersed-boundary method.* International Journal of Numerical Methods for Heat & Fluid Flow, 2016. **26**(3/4): p. 1272-1288.
5. Barletta, A., et al., *Conjugate forced convection heat transfer in a plane channel: Longitudinally periodic regime.* International Journal of Thermal Sciences, 2008. **47**(1): p. 43-51.
6. Mittal, R., et al., *A versatile sharp interface immersed boundary method for incompressible flows with complex boundaries.* Journal of Computational Physics, 2008. **227**(10): p. 4825-4852.

Fifth International Conference on Computational Methods for Thermal Problems
THERMACOMP2018, July 9-11, 2018, Indian Institute of Science, Bangalore, INDIA
*N. Massarotti, P. Nithiarasu, Pradip Dutta and C. Ranganyakalu (Eds.)*

# THERMAL TRACKING OF ABLATION BEHAVIOUR IN VVER CORE CATCHER

**Kumar Gaurav*,**
NPCIL, Mumbai-400094, krgaurav@npcil.co.in

**Sitesh Sil**
NPCIL, Mumbai-400094, ssil@npcil.co.in

**Abhishek Kumar,**
NPCIL, Mumbai-400094,kabhishek@npcil.co.in

**Sandeep M. Saxena ,**
NPCIL, Mumbai-400094,smsaxena@npcil.co.in

**Y.K.Pandey,**
NPCIL, Mumbai-400094, ypandey@npcil.co.in

**Gautam Biswas,**
NPCIL, Mumbai-400094, gbiswas@npcil.co.in

## ABSTRACT

Modern NPP designs require a device for core melt localization within the containment, a key element of Severe Accident Management (SAM). Several concepts of molten core immobilization have been developed and implemented such as in-vessel corium retention (IVR), crucible-type core-catcher developed for Russian VVER-1000 reactors and Catcher with melt spreading developed for the European EPR reactor. A Finite volume method (FVM) based Computer code for analysing the phenomena inside core-catcher of KK NPP has been developed in-house. Detailed modelling and simulation of interaction of molten corium with sacrificial material which includes thermal tracking of melt and associated heat transfer, chemical reactions and metallurgy associated with this phenomena has been carried out. This is a first of a kind (FOAK) work being done in India.

The modelling involves dynamic geometrical behaviour of molten corium having different components and having dispersed melting and solidification on solidus and liquidus lines. Simultaneous chemical reactions occurring and all three modes of heat transfer have been taken into account along with crust formation dynamics. Cumulative hydrogen generation due to melt- water interaction is also estimated.

**Key Words:** *Severe Accident Management , Finite volume, Natural Convection, core catcher.*

## 1. INTRODUCTION

Severe accident is defined as an accident involving the melting or breakdown of a substantial portion of the fuel rods in the core of a nuclear reactor. The main objective of severe accident management is to keep the containment building intact.

A core melt accident could occur if multiple safety systems fail to transfer the decay heat out of the fuel after reactor is shutdown. Such a situation could only be developed if the initiating event, for example a large break LOCA or a total loss of electricity, is combined with major loss of plant safety systems. So, modern NPP designs require a device for core melt localization within the containment as a key element of severe accident management.

This paper describes the modelling and simulation of molten corium and sacrificial material interaction inside KKNPP core catcher. After giving a brief description of KKNPP core catcher, function of sacrificial material and phenomenon related to crucible type core catcher, detailed modelling of interaction of molten corium and sacrificial material have been described. The simulation results are discussed subsequently.

## 2. MAIN BODY

KKNPP core catcher is basically a cylindrical vessel and the distribution of Sacrificial Material (SM) in core catcher is axi-symmetric. The outer wall core catcher consists of three layers.

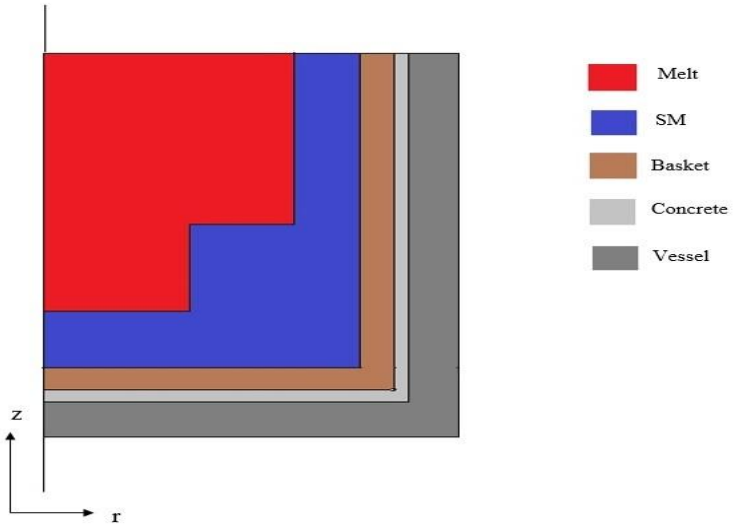


FIGURE 1. Schematic of VVER core catcher

After relocation of molten corium inside core catcher, ablation of sacrificial material takes place in radial and axial direction. To capture the ablation behaviour of SM inside the core catcher an axi-symmetric model is developed. The rate of sacrificial material ablation is controlled by heat transfer from melt to molten corium

Since, conduction is a dominant mode of heat transfer in molten corium and SM, the governing energy equation becomes as below for axi-symmetric treatment

$$\frac{1}{r}\frac{d}{dr}\left(rk\frac{dT}{dr}\right)+\frac{d}{dz}\left(k\frac{dT}{dz}\right)+q'''=\rho c_p\frac{dT}{Dt}$$

Where r and z are radial and axial directions respectively

Finite Volume Method (FVM) is adopted for converting the governing energy equation from PDE (partial differential equation) form to a set of algebraic equations and grids are generated to discretise the axi-symmetrical computational plane. An implicit scheme is used for time-marching for this unsteady-state problem. The resulting algebraic system is solved using line-by-line TDMA (Tri-diagonal Matrix Algorithm) method.

$$\int_t^{t+dt}\int_{dV}\frac{1}{r}\frac{d}{dr}\left(rk\frac{dT}{dr}\right)dVdt+\int_t^{t+dt}\int_{dV}\frac{d}{dz}\left(k\frac{dT}{dz}\right)dVdt+\int_t^{t+dt}\int_{dV}q'''dVdt$$
$$=\int_t^{t+dt}\int_{dV}\rho c_p\frac{dT}{dt}dVdt \qquad (3.1)$$

Radiative boundary condition is employed at the top surface. To compute the heat transfer from the side walls of core catcher, an equivalent thermal resistance is calculated by considering conductive resistance of composite wall and convective resistance (natural convection) of surrounding water. As the natural convection current inside the heat generating molten pool is not modelled, empirical correlations for Nusselt number at the boundary of natural convective was implemented to simulate

the heat transfer at melt-SM interface. These correlations are based on modified Rayleigh number of the heat-generating pool.
Among numerous reactions, both at the top of melt and melt-SM interfac, the following exothermic reactions dominates the resulting thermal behaviour of the system and reaction enthalpy is added to the heat source term in the govering equation.

$$2H_2O + Zr \longrightarrow ZrO_2 + 2H_2 + Q$$

$$Fe_2O_3 + 1.5\,Zr \longrightarrow 1.5ZrO_2 + 2Fe + Q$$

The kinetics of 1st equation is modelled using parabolic Urbanic model which is based on Arrhenious equations and the 2nd reaction the rate of reaction is assumed to be infinite.

The thermal abalion of SM is modelled using decomposition temperature of SM and the abalated SM is instantaneously mixed with molten pool by assuming infinite mass diffusivity.

## RESULTS

Initially when the corium relocates in the core catcher, sacrificial material is present in core catcher at the containment ambient temperature. As time progress molten corium in the core catcher melts the sacrificial material. Figure 4.10 to Figure 4.19 shows the progression of corium penetration inside core catcher.

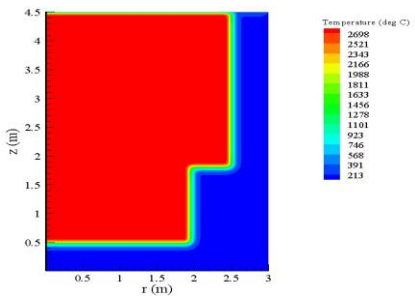


FIGURE 2.1 after 1 hour

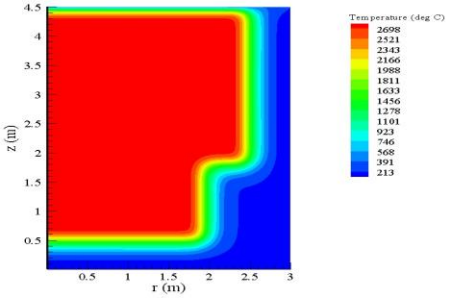


FIGURE 2.2 after 10 hour

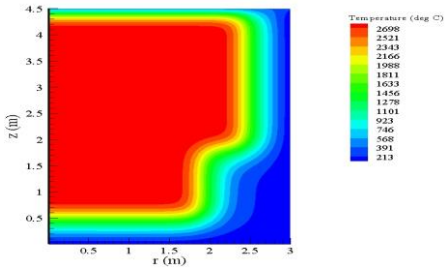


FIGURE 2.3 after 30 hour

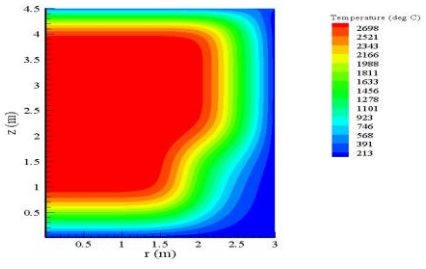


FIGURE 2.4 after 100 hour

FIGURE 2. Temperature contour at different time instant

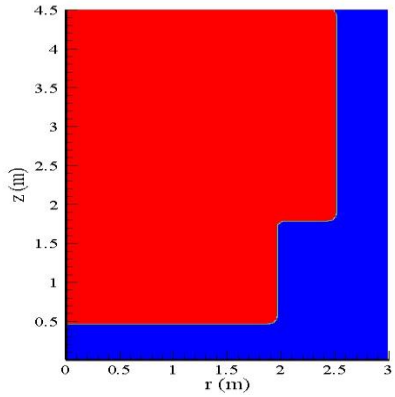


FIGURE 3.1 after 1 hour

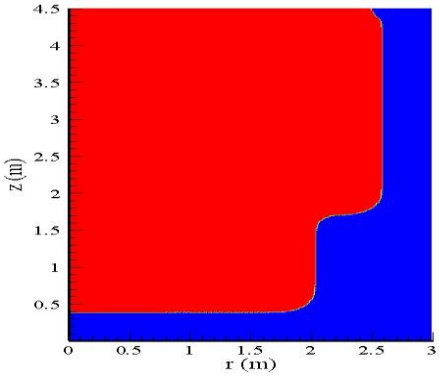


FIGURE 3.2 after 10 hour

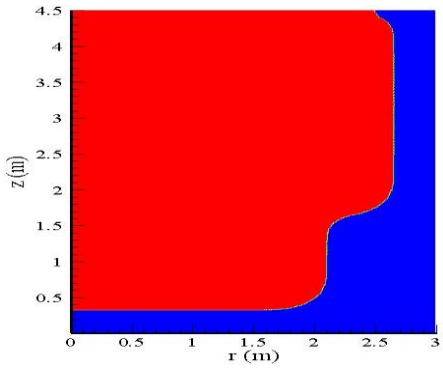


FIGURE 3.3 after 30 hour

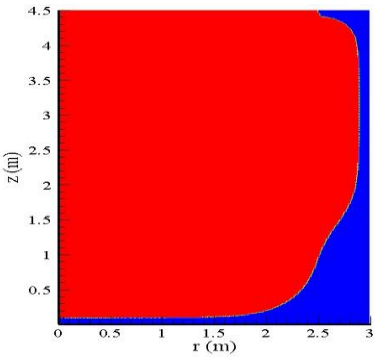


FIGURE 3.4 after 100 hour

FIGURE 3. Melt front propagation at different time instant

## 4. CONCLUSIONS

Natural convection in melt plays an important role in heat transfer from melt to SM. SM material plays a vital role in preconditioning of melt inside core catcher.

## REFERENCES

[[1] Vladimir Benzianovich Khabensky, Vladimir Semenovich Granovsky, Sevostian Victorovich Bechta and Victor Vladimirovich Gusarov. *Severe accident management concept of the vver-1000 and the justification of corium retention in a crucible-type core catcher.* Alexandrov Scientific Research Institute of Technology (NITI), Sosnovy Bor, Russia.

[2] V. G. Asmolov ,A. A. Sulatskii, S. V. Beshta, V. S. Granovskii, V. B. Khabenskii, E. V. Krushinov, S. A. Vitol, V. I. Almyashev, V. V. Gusarov, and V. F. Strizhov. "*The Interaction of Nuclear Reactor Core Melt with Oxide Sacrificial Material of Localization Device for a Nuclear Power Plant with Water-Moderated Water-Cooled Power Reactor*". Thermophysical propertiesof materials (2007).

Fifth International Conference on Computational Methods for Thermal Problems
THERMACOMP2018, July 9-11, 2018, Indian Institute of Science, Bangalore, INDIA
*N. Massarotti, P. Nithiarasu, Pradip Dutta and C. Ranganyakalu (Eds.)*

# STUDY OF HEAT TRANSFER IN MICROCHANNELS USING DIRECT SIMULATION MONTE CARLO METHOD

**Abhimanyu Gavasane, Amit Agrawal, U. V. Bhandarkar**
Indian Institute of Technology Bombay, Powai, Mumbai, India – 400076,

abhimanyug@iitb.ac.in, amit.agrawal@iitb.ac.in, bhandarkar@iitb.ac.in,

## ABSTRACT

The aim of this paper is to study heat transfer characteristics of Poiseuille flow through a microchannel. The variation of the local heat flux and Nusselt number is studied for a range of Knudsen number varying from 0.01 to 1. The pressure ratio is 3 and aspect ratio is 10. The velocity slip and temperature jump increase with an increase in rarefaction. The heat flux and Nusselt number (Nu) decrease with increase in Kn. The local Nusselt number varies from 19.81 at the inlet to nearly zero at the outlet for Kn = 0.01 whereas it varies from 0.195 to nearly zero for Kn = 1. The Peclet number (Pe) is less than 10 and Brickman number (Br) is greater than 1 that makes viscous dissipation and axial conduction effects significant.

**Key Words:** *Heat Transfer, microchannel, DSMC.*

## 1. INTRODUCTION

The flow in a microchannel is rarefied and compressible even at atmospheric conditions on account of the small characteristic dimension. The rarefaction induces velocity slip and temperature jump at the walls and compressibility leads to a non-linear pressure variation. This changes the fluid flow and heat transfer characteristics of a micro flow compared to macro flow. The rarefaction is quantified in terms of Knudsen number (Kn) which is the ratio of the mean free path of gas to the characteristic length. Based on Kn, flow is divided into four regimes namely, continuum (Kn < 0.001), slip (0.001 < Kn < 0.1), transition (0.1 < Kn < 10) and the free molecular (Kn > 10). The flow in a microchannel falls in the slip and transition regimes where the Navier-Stokes equations do not give accurate answers.

Conventionally, the rate of heat transfer is estimated in terms of Nusselt number (Nu). Sparrow and Lin [1] discussed the effect of rarefaction on heat transfer in tubes. It was found that Nu decreases with an increase in rarefaction. The velocity slip tends to decrease the temperature difference between wall and flow whereas temperature jump tends to increase this difference. This results in an increase in Nu with an increase in the velocity slip and a decrease in Nu with an increase in the temperature jump. Aydın and Avcı [2] studied the effect of viscous dissipation on heat transfer for rarefied gas flow between parallel plates. For the heated wall case, viscous dissipation increases the bulk temperature near the wall. This results in a decrease in the difference between the wall and flow temperatures and ultimately Nu. In both these studies, it was assumed that the flow is incompressible. Demsis et al. [3] experimentally studied heat transfer for rarefied gas flows and obtained Nu three orders lower than the continuum value. Yan and Farouk [4] studied heat transfer for rarefied gas flows using the Direct Simulation Monte Carlo method for constant wall temperature boundary condition. The aspect ratio of the heated portion was 4. It was observed that average Nu decreases with an increase in rarefaction. A correlation for Nu was derived in terms of Peclet number (Pe) and Kn. It was concluded that the effect of Pe is more pronounced than the effect of Kn. Balaj et al. [5] studied heat transfer in a microchannel using DSMC for constant wall heat flux condition.

The analytical studies for rarefied gas flow employs incompressible flow assumption while available DSMC study used small aspect ratio channel for constant wall temperature boundary condition. The objectives of this paper are to discuss the effect of rarefaction on the local heat flux

and local Nu and to discuss the effect of viscous dissipation and axial conduction on the local Nu for constant wall temperature boundary condition.

## 2. Numerical Methodology

The heat transfer in a 2-D micro Poiseuille flow is studied using DSMC in this work. The DSMC method was devised by Bird [6] in 1960 and it is used for solving rarefied gas problems. DSMC is a particle simulation method. The algorithm of DSMC consists of movement, indexing, collision, and sampling of particles. The flow domain is divided into cells and subcells. The cell width is selected such that it is less than the mean free path. The simulated molecules are distributed into cells and velocities are assigned according to the Maxwellian distribution function. Each simulated molecule represents a large number of actual molecules. The molecular movement and intermolecular collisions are separated by a small time step. The time step should be lesser than the mean collision time. The molecules are moved and their interactions with the wall are calculated. The molecules are indexed into cells and collision pairs are selected from a subcell on a probabilistic basis. The macroscopic properties are calculated by sampling over long time. An in-house 2-D OPEN-MPI parallel DSMC code was developed that was also used earlier to study temperature drop in microchannels [7]. The code validation and simulation details are given in [7].

The geometry of the microchannel is shown in figure 1. The working fluid is Argon gas. The length of the microchannel (L) is 10 μm and height (H) is 1 μm. The inlet gas flow temperature ($T_{in}$) is 300 K and wall temperature ($T_w$) is 500 K. The pressure ratio across the microchannel is kept as 3. The inlet Kn numbers are 0.01, 0.05, 0.1, 0.5 and 1.

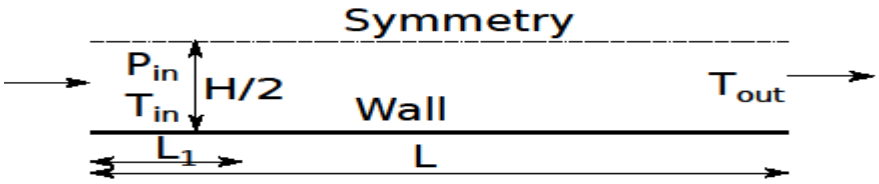


FIGURE 1. Geometry of the 2-D microchannel

## 3. RESULTS

The general characteristics of the 2-D microchannel flow with wall temperature higher than inlet flow temperature are discussed initially. The pressure variation is non-linear along the length of the microchannel and nonlinearity decreases with an increase in the rarefaction. The streamwise velocity increases along the length of the microchannel and it decreases with increase in the rarefaction. The flow slips at the wall and the slip velocity increases along the length of the microchannel. The slip velocity increases with increase in the rarefaction.

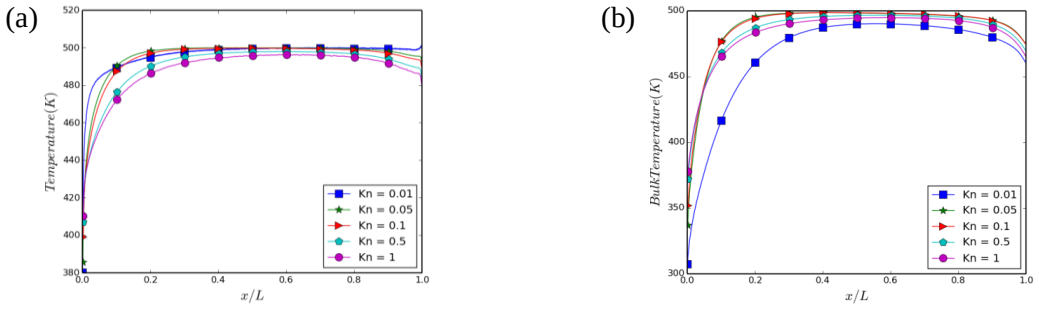


FIGURE 2. Variation of the (a) flow temperature near wall and (b) bulk temperature along the length of the microchannel for different Kn.

Figure 2 (a) shows the variation of fluid temperature next to wall along the length of the microchannel for different Kn numbers. The temperature starts to increase along the length of the microchannel and achieves a constant value after a certain length ($L_1$). The temperature in the middle portion of the microchannel is constant and nearly equal to the wall temperature. The temperature decreases towards the exit of the microchannel. The difference between the wall temperature and fluid temperature next to wall is defined as the temperature jump. The temperature jump increases with increase in Kn up to length $L_1$. The temperature jump is nearly zero for low Kn and a small temperature jump is observed for higher Kn after $L_1$ distance. Figure 2 (b) shows the variation of the bulk temperature along the length. The variation of the bulk temperature is similar to that of fluid temperature next to the wall. However, bulk temperature is lesser than the wall temperature for Kn = 0.01, 0.5 and 1.

The heat flux ( $q_x = \frac{\sum E^i - E^r}{A_s \Delta t}$) at the wall is defined as the difference of energies of the incident and reflected molecules. Figure 3 (a) shows the variation of heat flux along the length of the microchannel. The maximum heat exchange is observed at the inlet and it decreases rapidly along the length and becomes zero after distance $L_1$. The heat flux is maximum for Kn = 0.01 and the heat exchange process is observed up to x/L = 0.4. The heat flux decreases with an increase in Kn and the length over which heat exchange happens also decreases. A similar trend of heat flux was observed by Yan and Farouk [4].

Figure 3 (b) shows the variation of local Nu ($Nu = \frac{q_x H}{A_s K (T_b - T_w)}$) along the length of the microchannel. The local Nu is maximum at inlet and decreases along the length and becomes nearly zero towards the exit of the microchannel. Similar behaviour of Nu was observed by Hemadri et al. [8] in the experimental studies. The Nu decreases with an increase in the inlet Kn. It should be noted that Nu becomes negative for Kn = 0.05 and Kn = 0.1 in the middle section. This is because the heat flux is positive in the middle section for these Kn. However, the magnitude of this heat flux is small compared to the inlet heat flux. Yan and Farouk [4] did not observe Nu = 0 towards exit as their aspect ratio was small (=4).

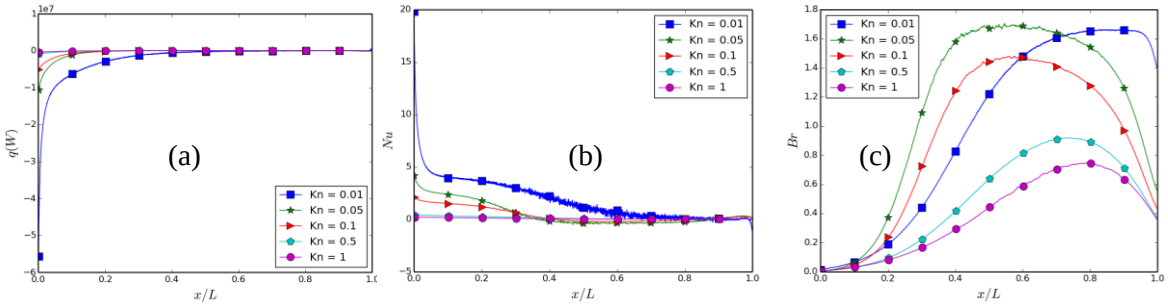


FIGURE 3. Variation of the (a) heat flux and (b) Nu (c) Br along the length of the microchannel for different Kn.

The viscous dissipation is defined in terms of Brickman number ($Br = \frac{\mu U^2}{K (T_b - T_w)}$ ). Figure 3 (c) shows the variation of local Br along the length of the microchannel. The Br number increases along the length sharply achieve a peak and decreases towards the exit. The Br number decreases with an increase in Kn. However, Br for Kn = 0.01 and Kn = 0.05 are of the same magnitude.

## 4. DISCUSSIONS

The variation of bulk temperature and heat flux can be explained through Pe. Pe is defined as the ratio of advective transport rate to the diffusive transport rate. The highest Pe is 9.8 for Kn = 0.01 among all cases considered here. Instead of advecting the heat along the length of the channel (stream

velocity increases along the length), most heat is diffused in all directions. This causes heat exchange in the initial part of the microchannel and flow attains the wall temperature after that. The length over which heat is exchanges decreased with increase in Kn due to further decrease in Pe. In the same fashion, Nu varies. The Nu number is maximum at inlet and decreases rapidly and becomes zero in the middle part of the microchannel. The Nu number decreases with increase in Kn due to rarefaction and decrease in Re. A similar behavior was observed for earlier studies[1,2,3,4]. For Kn = 0.05 and Kn = 0.1, the Br is maximum in the middle part of microchannel where positive heat flux and negative Nu is observed. The viscous dissipation acts like a heat source near the wall. For the middle part of the microchannel, the temperature is already equal to the wall temperature, viscous dissipation increases temperature slightly higher than wall temperature and this result in positive heat flux and negative Nu.

## 5. CONCLUSIONS

The heat transfer in a 2-D microchannel with constant wall temperature is studied for slip and transition regime flows. The velocity slip and temperature jump increase with an increase in rarefaction. The heat exchange occurs in the initial part of the microchannel and no heat exchange occurs in the middle section due to small Pe. The diffusive heat transport mechanism (small Pe) is dominant for microchannel flows. The Nu number decreases along the length rapidly and asymptotes to nearly zero after the midsection. The Nu decreases by two orders of magnitude for high Kn. The effect of the viscous dissipation is seen in the midsection of the channel for Kn = 0.05 and Kn = 0.1.

## REFERENCES

[1] Sparrow, E. M., and S. H. Lin. "Laminar heat transfer in tubes under slip-flow conditions." *Journal of Heat Transfer* 84, no. 4 (1962): 363-369.

[2] Aydın, O. and Avcı, M., 2007. Analysis of laminar heat transfer in micro-Poiseuille flow. *International Journal of Thermal Sciences*, *46*(1), pp.30-37.

[3] Demsis, A., Verma, B., Prabhu, S.V. and Agrawal, A., 2009. Experimental determination of heat transfer coefficient in the slip regime and its anomalously low value. *Physical Review E*, *80*(1), p.016311.

[4] Yan, F. and Farouk, B., 2002. Computations of low pressure fluid flow and heat transfer in ducts using the direct simulation Monte Carlo method. *Journal of Heat Transfer*, *124*(4),pp.609-616.

[5] Balaj, M., Roohi, E., Akhlaghi, H. and Myong, R.S., 2014. Investigation of convective heat transfer through constant wall heat flux micro/nano channels using DSMC. *International Journal of Heat and Mass Transfer*, *71*, pp.633-638.

[6] Bird, G.A., 1994. Molecular gas dynamics and the direct simulation monte carlo of gas flows. *Clarendon, Oxford*, *508*.

[7] Gavasane, A., Agrawal, A., Pradeep, A.M. and Bhandarkar, U., 2017. Simulation of a temperature drop for the flow of rarefied gases in microchannels. *Numerical Heat Transfer, Part A: Applications*, *71*(10), pp.1066-1079.

[8] Hemadri, V., Briadar, G. S., Shah, N., Garg, R., Bhandarkar, U., and Agrawal, A., 2017. Experimental study of heat transfer in rarefied gas flow in a circular tube with constant wall temperature. *Experimental Thermal and Fluid Science, Accepted.*

Fifth International Conference on Computational Methods for Thermal Problems
THERMACOMP2018, July 9-11, 2018, Indian Institute of Science, Bangalore, INDIA
*N. Massarotti, P. Nithiarasu, Pradip Dutta and C. Ranganyakalu (Eds.)*

# EFFECT OF VARIABLE THERMAL CONDUCTIVITY ON HEAT TRANSFER CHARACTERISTICS OF A NUCLEAR FUEL ELEMENT

**G. Jilani, T.K. Favas**
National Institute of Technology Calicut, Kerala, India 673601, jilani@nitc.ac.in, favastk@gmail.com

## ABSTRACT

The prime objective of this study is to examine the effect of temperature dependent thermal conductivity on heat transfer characteristics of a rectangular fuel element dissipating heat into a stream of liquid sodium. Accordingly, equation governing the thermal field in the solid domain is solved numerically along with equations governing the flow and thermal fields in the fluid domain. Taking Prandtl number as constant at 0.005, numerical results are presented and discussed for wide range of values of thermo-geometric parameters. Finally, it is concluded that unrealistic assumption of constant thermal conductivity results in significant under prediction of maximum temperature in the fuel element.

**Key Words:** *Nuclear Fuel Element, Variable Thermal Conductivity, Finite Difference Method.*

## 1. INTRODUCTION

Plate with volumetric energy generation finds many applications in thermal systems such as nuclear reactors and electronic equipments [1,2]. In such cases, energy generated within the plate is to be dissipated to a coolant so as to keep its maximum temperature below its allowable limit [3]. As the thermal conductivity of a material such as uranium dioxide, which is commonly used material of a nuclear fuel element, generally varies with temperature [3], many investigators have paid their attention to the heat transfer characteristics of an energy generating plate having temperature dependent thermal conductivity. Ghasemi et al. [4] analytically obtained steady, one-dimensional thermal field in an energy generating plate with variable thermal conductivity. Employing a semi-analytical method and considering the dependence of thermal conductivity on temperature, Mosayebidorcheh et al.[5] studied transient one-dimensional heat conduction problem in an energy generating plate. Using semi-analytical method and considering variable thermal conductivity, Torabi and Zhang [2] obtained heat transfer and thermodynamic performances of a heat generating composite wall. Using finite difference method, Sobamowo [6] analyzed heat transfer characteristics of an energy generating plate having variable thermal conductivity. The preceding review of the literature reveals that all previous studies are based on one-dimensional heat conduction in a plate and on unrealistic assumption of average heat transfer co-efficient over its heat dissipating surfaces. Deriving motivation from these shortcomings, the present numerical study examines the effect of temperature dependent thermal conductivity on the variation of maximum temperature in a rectangular nuclear fuel element with vital thermo-geometric parameters by including the effect of axial conduction in the fuel element and by imposing conditions of continuity of temperature and heat flux at solid-fluid interface.

## 2. MATHEMATICAL MODEL AND ITS NUMERICAL SOLUTION

Figure 1 depicts a rectangular fuel element of a nuclear reactor of height $H$ and thickness $2W$ dissipating heat into a laminar, incmpressible and viscous stream of liquid sodium. The volumetric energy generation $q'''$ in the fuel element is considered to vary along its axial direction [1]. Thermal

conductivity $k_s$ of the material of the fuel element is assumed to vary as $k_s = \frac{1}{a_1 + a_2 T_s}$ [3]. Under steady state conditions, energy generated in the fuel element is first conducted within it and ultimately dissipated to the stream of liquid sodium. Due to existence of flow and thermal symmetry, half of the solution domain can be taken as the computational domain as shown in Fig. 2 with relevant boundary conditions indicated thereon. The non-linear equation governing steady, two-dimensional temperature field in the solid domain in its linearized form can be obtained as:

$$a_3 \frac{\partial^2 \theta_s}{\partial X^2} + a_4 \frac{\partial^2 \theta_s}{\partial {Y_s}^2} + a_{12} \frac{\partial \theta_s}{\partial X} + a_{13} \frac{\partial \theta_s}{\partial Y_s} + Q = 0\,; \qquad Q = Q_{max} cos\pi \left(\frac{1}{2} - X\right) \tag{1}$$

Where, $a_3 = a_7 a_8\,;\ a_7 = \dfrac{1}{a_1 + a_2(\theta_s\, \Delta T_c + T_\infty)};\ a_8 = \dfrac{a_9}{C}\,;\ a_9 = \dfrac{1}{k_\infty};\ C = 4Ar^2;\ a_4 = a_7 a_9;$

$a_5 = a_8 a_{10} a_{11};\ a_{10} = -a_2\, \Delta T_c;\ a_{11} = {a_7}^2;\ a_6 = a_9 a_{10} a_{11};\ a_{12} = a_5 \left(\dfrac{\partial \theta_s}{\partial X}\right); a_{13} = a_6 \left(\dfrac{\partial \theta_s}{\partial Y_s}\right)$

$a_1 = 0.0533; \qquad a_2 = 0.000235\,;\ \Delta T_c = T_0 - T_\infty$

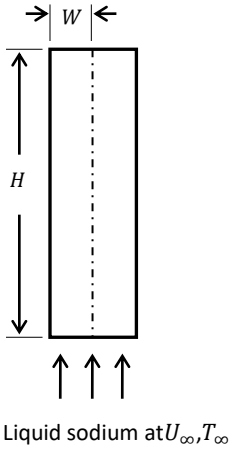


FIGURE 1. Physical model

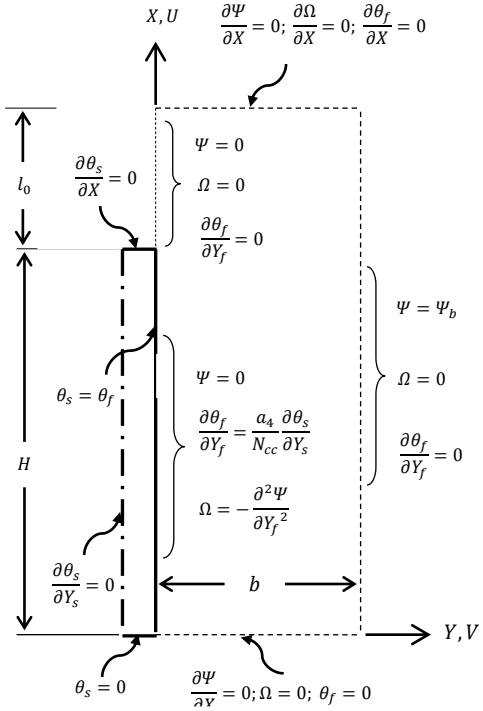


FIGURE 2. Computational domain

Stream function, vorticity transport and energy equations governing the flow and thermal fields in the fluid domain can be transformed into their dimensionless forms as given below:

$$\frac{\partial^2 \Psi}{\partial X^2} + \frac{\partial^2 \Psi}{\partial {Y_f}^2} = -\Omega \qquad (2a); \quad U \frac{\partial \Omega}{\partial X} + V \frac{\partial \Omega}{\partial Y_f} = \frac{1}{Re_H} \left(\frac{\partial^2 \Omega}{\partial X^2} + \frac{\partial^2 \Omega}{\partial {Y_f}^2}\right) \tag{2b}$$

$$U \frac{\partial \theta_f}{\partial X} + V \frac{\partial \theta_f}{\partial Y_f} = \frac{1}{Re_H Pr} \left(\frac{\partial^2 \theta_f}{\partial X^2} + \frac{\partial^2 \theta_f}{\partial {Y_f}^2}\right) \tag{3}$$

The dimensionless variables and parameters used in the preceding equations are defined as:

$$X = \frac{x}{H};\ Y_s = \frac{y}{W};\ Y_f = \frac{y}{H};\ U = \frac{u}{U_\infty};\ V = \frac{v}{U_\infty};\ \theta = \frac{T - T_\infty}{\Delta T_c};\ A_r = \frac{H}{2W}\,; Pr = \frac{\mu_f c_p}{k_f};$$

$$N_{cc} = \frac{k_f}{k_\infty}\left(\frac{W}{H}\right); Q = \frac{q''' W^2}{k_\infty\, \Delta T_c}\,; Q_t = \frac{2}{\pi} Q_{max};\ Re_H = \frac{\rho_f U_\infty H}{\mu_f}$$

Equations (1) and (2a) are discretized using second-order accurate finite difference schemes and the resulting system of equations is solved using Gauss-Siedel iterative solution procedure, while pseudo-transient form of Eqs. (2b) and (3) are discretized using Alternating Direction Implicit (ADI) scheme and resulting system of equations is solved using Thomas Algorithm. The numerical results are generated using an indigenously developed and validated computer code [7], the details of which and grid convergence test performed are not presented here for the sake of brevity.

## 3. RESULTS AND DISCUSSION

The prime objective of the present numerical study is to examine the effect of temperature dependent thermal conductivity on variation of maximum temperature $\theta_{max}$ in the fuel element with conduction-convection parameter $N_{cc}$, total energy generation parameter $Q_t$ and Reynolds number $Re_H$ while aspect ratio $A_r$ of the fuel element, free stream temperature of the coolant $T_\infty$, allowable temperature in the fuel element $T_o$ and Prandtl number of the coolant $Pr$ are kept constant at 10, 673 K, 2354 K and 0.005 respectively. These numerical results obtained are presented and discussed as follows:

Figure 3 depicts the variation of $\theta_{max}$ with $N_{cc}$ for both constant and variable $k_s$. As expected, it is abundantly clear from this figure as well that for both constant and variable $k_s$, $\theta_{max}$ monotonically decreases with increase in $N_{cc}$. Further, it is important to note that assumption of constant $k_s$ results in significant under prediction of $\theta_{max}$ for entire range of values of $N_{cc}$. It is also worth noticing that the magnitude of under prediction is higher at lower values of $N_{cc}$ as compared to its higher values.

Figure 4 illustrates the variation of $\theta_{max}$ with $Q_t$ for both constant and variable $k_s$. It is very much clear from this figure that for both constant and variable $k_s$, $\theta_{max}$ keeps on increasing with increase in $Q_t$ which is in conformity with the physics of the problem. Further, it is worth noticing that irrespective of the value of $Q_t$, assumption of constant $k_s$ significantly under predicts $\theta_{max}$ which becomes more predominant with increase in $Q_t$.

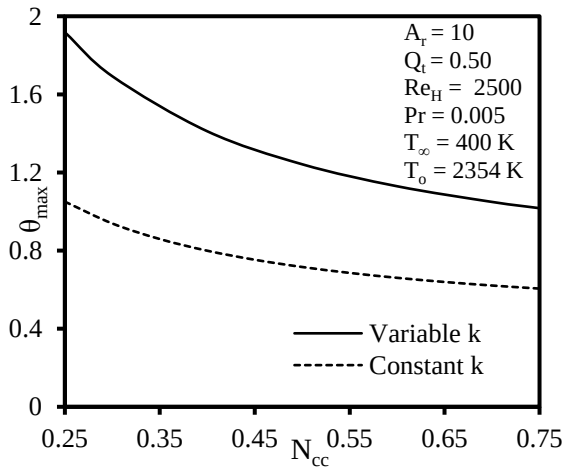


FIGURE 3. Variation of $\theta_{max}$ with $N_{cc}$

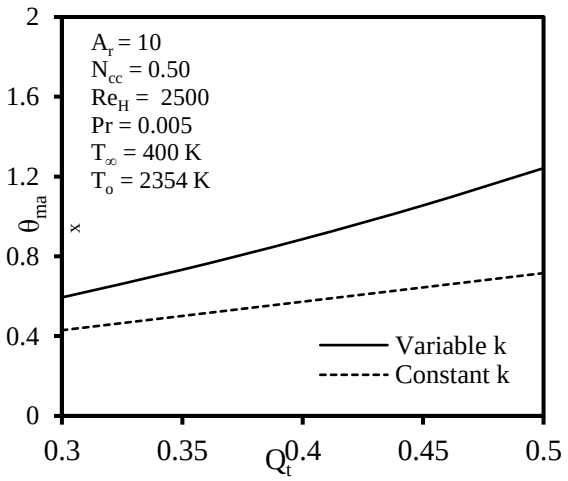


FIGURE 4. Variation of $\theta_{max}$ with $Q_t$

Figure 5 shows the variation of $\theta_{max}$ with $Re_H$ for both constant and variable $k_s$. Since $N_{cc}$ and $Q_t$ are being kept constant, $\theta_{max}$ is expected to decrease with increase in $Re_H$ which is very much evident from this figure. Further, it is very much obvious from this figure that irrespective of the value of $Re_H$, assumption of constant $k_s$ results in considerable under prediction of $\theta_{max}$ which is somewhat more significant at lower values of $Re_H$ as compared to its higher values.

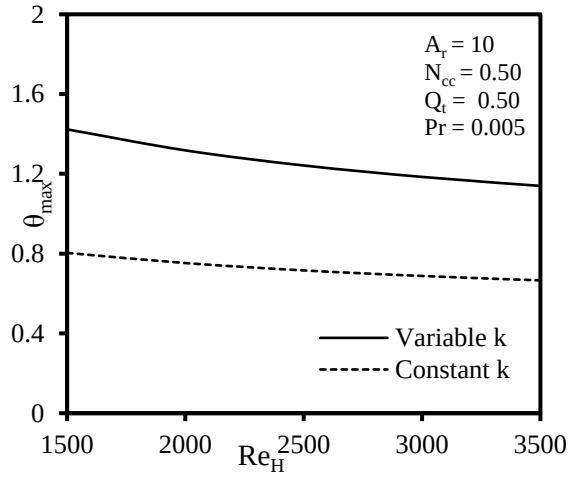


FIGURE 5. Variation of $\theta_{max}$ with $Re_H$

## 4. CONCLUSIONS

The foremost objective of the present numerical study is to examine the effect of temperature dependent thermal conductivity on variation of maximum temperature in a rectangular nuclear fuel element with involved thermo-geometric parameters. From the discussion of numerical results presented in the preceding section, it is concluded that unrealistic assumption of constant thermal conductivity results in significant under prediction of maximum temperature in the fuel element.

## REFERENCES

[1] M.M. El-Wakil, *Nuclear Power Engineering*, McGraw Hill Book Company,New York, 1962.
[2] M. Torabi, and K. Zhang K, Heat transfer and thermodynamic performance of convective-radiative double layer walls with temperature-dependent thermal conductivity and internal heat generation, *Energy Conversion and Management*, 89, 12-23, 2015.
[3] R.H.S. Winterton, *Thermal Design of Nuclear Reactors*, Pergamon Press, 1981.
[4] S.E. Ghasemi, M. Hatami, and D.D. Ganji, Thermal analysis of convective fin with temperature-dependent thermal conductivity and heat generation, *Case Studies in Thermal Engineering*, 4, 1-8, 2014.
[5] S. Mosayebidorcheh, M. Farzinpoor, and D.D. Ganji, Transient thermal analysis of longitudinal fins with internal heat generation considering temperature-dependent properties and different fin profiles, *Energy Convesion and Management*, 86, 365-370, 2014.
[6] M.G. Sobamowo, Analysis of convective longitudinal fin with temperature-dependent thermal conductivity and internal heat generation, *Alexandria Engineering Journal*, 56, 1-11, 2017.
[7] T.K. Favas, and G. Jilani, The effect of non-uniform energy generation on entropy generation in a plate being cooled in a fluid medium, *Heat and Mass Transfer Research Journal*, 1(1), 35-47, 2017.

# A CRITICAL REVIEW OF CONDENSATION HEAT TRANSFER COEFFICIENT CORRELATIONS

**BhavaniSankar G**
Research Scholar, JNTUA Ananthapuramu, gbspro@gmail.com

**Ranganayakulu Ch.**
Scientist 'H', ADA Bengaluru, ranganayakulu@jetmail.ada.gov.in

## ABSTRACT

Two-phase heat transfer due to its higher heat transfer efficiencies is being applied in many applications. Prediction of refrigerant condensation heat transfer coefficient is important for design of compact heat exchangers in aerospace environmental control system design and development. A fundamental understanding of heat transfer involving boiling and condensing of refrigerants in mini channels is important as the hydraulic diameters involved are around 1mm. There is a vast amount of literature available on the two-phase flow in mini channels and many correlations are developed for the heat transfer coefficients. This paper does a critical review of these correlations for condensation heat transfer. The effect of heat flux, mass flux and the quality of refrigerant on the heat transfer coefficient are compared through a parametric study using MATLAB. The results are plotted and conclusions are drawn.

**Key Words:** *Compact Heat Exchangers, Correlations, Refrigerant (R134a), Condensation*

## 1. INTRODUCTION

Design of a compact heat exchanger (CHE) for phase change applications is a challenging part in the aircraft Environmental Control System development [1]. Especially so in systems based on vapor compression refrigeration cycle system consisting of a Compressor, a Condenser, and Expansion Valve and an Evaporator. The amount of power input required for compressor is fully dependent on condensation process. The vapor refrigerant discharged from the compressor is generally cooled and condensed in a condenser via heat transfer to a secondary heat transfer fluid such as air. An inefficient condenser that does not dissipate the heat well requires a higher discharge pressure resulting in an increase in compressor power demand. The way of increasing the condenser effectiveness by increasing the size of the condenser is not a solution for the aerospace applications. It is in this context, the study and availability of data to understand the two-phase heat transfer in these CHE is important.

The flow passages in CHE are complicated with the use of different fins and there is not much data available to understand the two-phase phenomenon to arrive at heat transfer coefficients that are required in designing and optimising this equipment. However, there is literature available to understand the heat transfer phenomenon for mini and micro channels [2] which is relevant due to the small hydraulic diameters that are involved. In addition to the refrigerant properties and the geometrical parameters of the CHE, the heat flux, mass flux and vapour quality also affect theheat transfer coefficients [3]. In this paper correlations for the heat transfer coefficients for condensation are studied from various sources. Those studies that are close to the practical applications of the CHE are studied further. A MATLAB code is developed, to compare the effect of heat flux, mass flux and the quality of refrigerant on the heat transfer coefficient with different parameters. The results are given a graphical representation.

## 2. MAIN BODY

Abundant literature is available on the heat transfer mechanism and the correlations developed for two phase flow in mini channels [4]–[12]. There are many studies done to arrive at correlations for heat transfer during condensation [10]–[18]. Alejandro López Belchí thesis [19] gives a good survey of the literature citing 141 references that were available up to 2013. In addition to these references, papers from 2013 to 2017 are supplemented in this study [20]–[25].

## 3. LITERATURE

TABLE 1 below gives the year wise studies done on condensation heat transfer in channels with the R134a refrigerant. The hydraulic diameter of the channels and the mass flux range are captured in this table.

| No. | Correlation | Year | Hyd. Dia mm | Mass Flux ($kg/m^3/s$) | Ref. | Remarks |
|---|---|---|---|---|---|---|
| 1. | Dobson et. Al. | 1994 | 4.57 | 75 – 500 | [2] | Updated later with other Hyd. Dia. |
| 2. | Haraguchi | 1994 | 8.4 | 90 – 400 | [2][19] [26][27] | Heat Flux of 3 – 33 $kW/m^2$ Annular Flow |
| 3. | Singh et al. | 1996 | 11 | 50 – 300 | [2][28] | Experimental & Analytical |
| 4. | Vardhan & Dunn | 1997 | 1.494 | 400 – 1100 | [19][29] | Experimental & Model |
| 5. | Yang & Webb | 1997 | 1.41, 1.56 | 400, 1400 | [2][19] [30] | Model |
| 6. | Dobson & Chato | 1998 | 3.14, 4.6, 7.04 | 25 – 800 | [2][19] [31][32] | Experimental Annual & Stratified-Wavy Flows |
| 7. | Moser et. al. | 1998 | 3.14<br>4.57<br>7.04<br>8 | 300-650<br>148-678<br>151-665<br>121-407 | [2][19] [31][33] | Equivalent Re Model Annular Flow |
| 8. | Yu & Koyama | 1998 | 8.78 | 100,200,300 | [31][34] | Model Gravity & Shear Flows |
| 9. | Webb & Zhang | 1998 | 2.13, 3.25 | 200 – 1000 | [2][35] | Experimental |
| 10. | Hurlburt & Newell | 1999 | 3 – 10 | 200 – 650 | [19] | Scaling Equations Annular Flow |
| 11. | Wang | 1999 | 1.46 | 200 – 600 | [19][10] | Annular, Wavy and Slug Flows |
| 12. | Garimella & Bandhauer | 2001 | 0.4 – 4.91 | 150 – 750 | [2][19] | Intermittent, Annular and Mist Flows |
| 13. | Tabatabai & Faghri | 2001 | 4.8 – 15.88 | | [2][36] | Flow Regime Studies |
| 14. | Webb & Kemel | 2001 | 0.44, 0.611, 1.33,1.564 | 300 – 1000 | [2] | Experimental |

| No. | Correlation | Year | Hyd. Dia mm | Mass Flux ($kg/m^3/s$) | Ref. | Remarks |
|---|---|---|---|---|---|---|
| 15. | Cavallini | 2002 | 8 | 100 – 750 | [2][31] | Annualar, Annular-Stratified & Stratified-Slug Flows |
| 16. | Wang et al. | 2002 | 1.46 | 75 - 750 | [2][19] [10] | Annular, Wavy & Slug Flows |
| 17. | El Hajal et. al. | 2003 | 3.14 – 21.4 | 16 – 1532 | [2][37] | Flow Regime Studies |
| 18. | Koyama et al. | 2003 | 0.8 - 1.114 | 100 - 700 | [2][19] [38][39] | Experimental |
| 19. | Thome | 2003 | 3.14 – 21.4 | 24 – 1022 | [2][31] [40] | Flow pattern based Heat Transfer Model Annular, Stratified-Wavy & Wavy Flows |
| 20. | Wilson et. al. | 2003 | 1.84, 4.4, 6.37, 7.79 | 75 – 400 | [2][41] | Experiments with progressively Flattened tubes |
| 21. | Wang et. al. | 2004 | 0.577 | 100 – 1300 | [2][42] [43] | Theoretical Model |
| 22. | Shin & Kim | 2005 | 0.5 – 1 | 100 – 600 | [2][19] [44] | Experiments with circular and square channels |
| 23. | Cavallini | 2005 | 1.4 | 200 – 1000 | [2][19] [45][46] [47] | Experimental with reduced pressures inside multi-port multi channel tubes |
| 24. | Bandhauer et al. | 2006 | 0.506 – 1.524 | 150 – 750 | [19][48] | Measurements and Model |
| 25. | Cavallini | 2006 | 8 | 50 – 800 | [19][31] [49] | $\Delta T$-dependent & $\Delta T$-independent Flows |
| 26. | Mèdèric et al. | 2006 | 0.56 | 3.4 – 13.85 | [19][50] | Experimental study Annular and Bubbly Flows |
| 27. | Cavallini | 2008 | 0.96 | 200, 400 & 600 | [19][51] | Experiments at medium and high pressures |
| 28. | Cavallini | 2009 | 0.5 – 3.2 | > 150 | [19][52] | Experiments at reduced pressure and a Model Annular, Annular-Mist & Mist Flows |
| 29. | Matkovic et al. | 2009 | 0.96 | 100 – 1200 | [19][53] | Experimental study |
| 30. | Agarwal et al. | 2010 | 0.424 – 0.839 | 150 – 750 | [19][54] | Experimental and Model for non circular microchannels |
| 31. | Cascales et al. | 2010 | 0.96 | 200 | [19][13] | Model |
| 32. | Bohdal et al. | 2011 | 0.31 – 3.3 | 100 – 1300 | [19][55] | Experimental and Model |
| 33. | Park et al. | 2011 | 1.45 | 50 – 260 | [19][56] | Experimental and Model |
| 34. | Del Col et al. | 2011 | 1.23 | 200 – 800 | [19][57] | Experimental with square shape minichannel |

| No. | Correlation | Year | Hyd. Dia mm | Mass Flux ($kg/m^3/s$) | Ref. | Remarks |
|---|---|---|---|---|---|---|
| 35. | Jige et al. | 2011 | 0.85 | 100 – 400 | [19] | Experimental with multi port tube and a Model |
| 36. | Derby et al. | 2011 | 1 | 75 – 450 | [19][58] | Experimental study on square, triangular & semicircular multiple parallel minichannels |
| 37. | Goss Jr & Passos | 2013 | 0.77 | 230 – 445 | [19][59] | Experimental Study at 7.3 to 9.7 bar pressure and 17 to 53 $kW/m^2$ heat flux |
| 38. | Al-Hajri et al. | 2013 | 0.7 | 50 – 500 | [19][60] | Experimental study in a single micro channel |
| 39. | Sakamapatan | 2013 | 1.1 & 1.2 | 340 – 680 | [19][61] | Experimental study at 15, 20 & 25 $kW/m^2$ heat flux |
| 40. | Arslan | 2014 | 7.52 | 20 – 175 | [20] | Experimental study at 5.8 & 7 bar pressure |
| 41. | Meyer et al. | 2014 | 8.38 | 100 – 400 | [21] | Experimental study at inclination angles from $-90^o$ to $+90^o$ |
| 42. | Ewim et al. | 2015 | 8.67 | 300 – 400 | [62] | Experimental study with an enhanced tube of 60 fins of 0.22 mm spiraled at an angle of $37^o$ |
| 43. | Aroonrat | 2016 | 8.1 | 300 – 500 | [23] | Experimental study with dimpled tube at 10, 15 & 20 $kW/m^2$ heat fluxes |
| 44. | Ewim et al. | 2016 | 8.38 | 20 – 100 | [22] | Experimental study in a smooth horizontal tube |
| 45. | Kaew-On et al. | 2016 | 3.51 | 350 – 900 | [24] | Experimental study with circular and flattened tubes at a pressure of 8 to 12 bar for a heat flux of 10 to 50 $kW/m^2$ |
| 46. | Qingpu Li | 2017 | - | 400 – 1100 | [63] | Experimental Study in smooth and micro fin tubes |
| 47. | Wang | 2017 | 0.3016 | 60 – 250 | [25] | Experimental Study in oval micro channels. Film Wavy, Corner Wavy, Slug & Bubbly Flow |

TABLE 1 HEAT TRANSFER STUDIES FOR R134A CONDENSATION IN CHANNELS

## 4. MODELS CONSIDERED

The hydraulic diameter of the fins used in the aerospace CHEs is around 1mm. From the data available as of date the correlations of Koyama ($0.8\text{-}1.114D_h$), Cavalini ($1.4D_h$), Bhanduer ($0.506\text{-}1.524D_h$) and Wang ($1.46D_h$) which are from the experimental data of about 1mm hydraulic

diameter, along with the classical Akers [64] and Nusselt are taken to study and compare the effects of heat flux, mass flux and the quality of the refrigerant on the heat transfer coefficient during condensation refrigerant (R134a). For the purpose of comparison of the correlations approximately typical conditions have been used.

Koyama et al. [38], [39] studied the R134a condensation local characteristics of pressure drop and heat transfer in aluminium tubes of about 1mm $D_h$. They have also developed a new correlation of HTC by modifying the effect of diameter in the correlation of Haraguchi et. al. [27] which takes into account the convection forces, free convection and surface tension effects. Cavallini [45]–[47] studied the condensation under huge range of reduced pressures and proposed a correlation for the HTC. Bandhauer et al. [48] studied the R134a condensation in horizontal minichannels and proposed a correlation for the HTC. Wang et al. [10] studied R134a condensation and proposed an expression for HTC combining the annular and stratified flow regions. Akers [64] presented the model through their equivalent Reynolds number model. The model predicts HTC during ransition from gravity controlled region to forced convection condensation at higher mass fluxes. Nusselt presented the model to predict the heat transfer coefficient during the transition from gravity controlled laminar region at lower mass fluxes.

## 5. PARAMETRIC STUDY

The analysis has been done on available correlations to exercise the Parameters listed in the TABLE 2 on the heat transfer coefficient, the mass flux and the quality. The CHE understudy is constructed of Wavy and Lance-Offset fins. The hydraulic diameter is 1.345mm.

| No. | Dimensions (mm) | Mass Flow Rate (kg/s) | Heat (kW) |
|---|---|---|---|
| 1. | 150 X 75 | | |
| 2. | 150 X 100 | | |
| 3. | 150 X 125 | 0.08 | 10 |
| 4. | 150 X 150 | | |
| 5. | 150 X 200 | | |

TABLE 2 PARAMETRIC STUDY

### 3.1. Effects of Saturation Temperature and mass flux

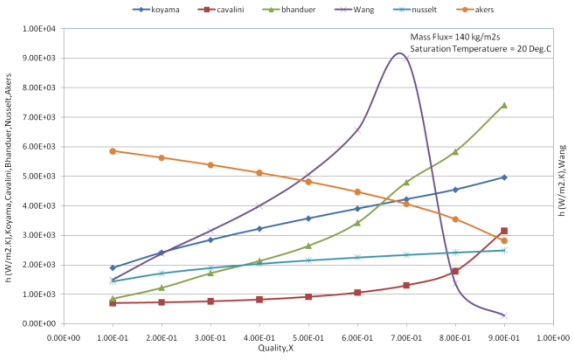


FIGURE 1 : QUALITY VS. HEAT TRANSFER COEFFICIENT (MASS FLUX=140 KG/M2S,TS=20)

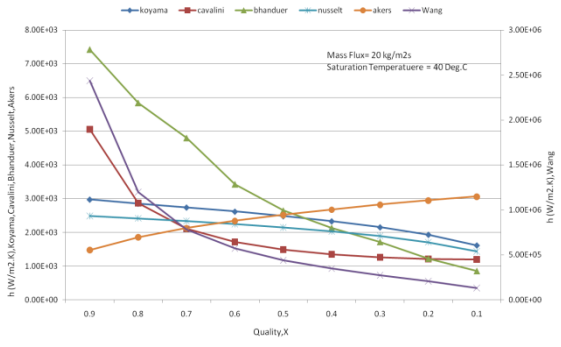


FIGURE 2: QUALITY VS. HEAT TRANSFER COEFFICIENT (MASS FLUX=20 KG/M2S,TS=40)

All the correlations show similar trend in Figure 2, except the Akers, for the variation of h wrt x. At low quality, the correlations of Bhanduer & Cavalini & Wang give higher values of h, however from 0.6 of x onwards, all of them come to a close range except the correlation of Wang

### 3.2. Effects of Saturation Temperature and Quality

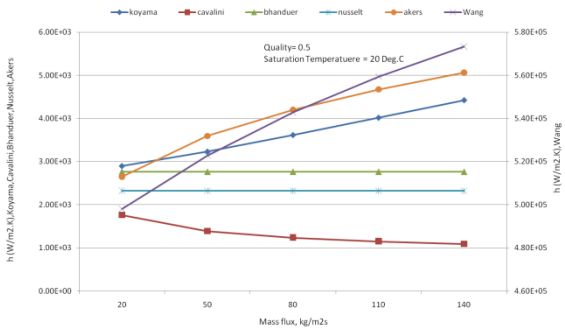


FIGURE 3: MASS FLUX VS. HEAT TRANSFER COEFFICIENT (QUALITY=0.5, TS= 20)

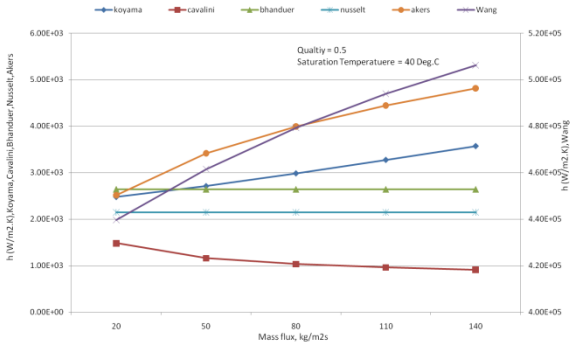


FIGURE 4: MASS FLUX VS. HEAT TRANSFER COEFFICIENT (QUALITY=0.5, TS= 40)

### 3.3. Effect of saturation temperature

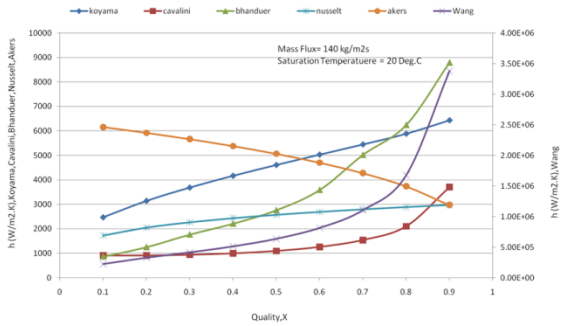


FIGURE 5: QUALITY VS. HEAT TRANSFER COEFFICIENT ( MASS FLUX=140 KG/M2S,TS=20)

## 6. CONCLUSIONS

In this paper different correlations to study the phase change heat transfer in CHE is presented. The comparison of various correlations in a parametric study are graphically shown to bring out the dissimilarities with respect to the assessment of the heat transfer coefficient vis-à-vis the heat flux, mass flux and the quality of the refrigerant.

As the flow stratifies and filmwise Nusselt condensation dominates at low mass flux or low quality there is insensitivity to quality in correlations that are based on annular film forms. These correlations show significant dependence on quality and mass flow as the forced convection becomes dominant.

## REFERENCES

[1] G. Bhavanisankar and C. Ranganayakulu, “Emerging Trends in Aircraft Environmental Control System,” in *National Conference on Emerging Trends in Mechanical Engineering (e-TIME ’16)*, 2016.

[2] S. G. Kandlikar, S. Garimella, D. Li, C. Stephane, and M. R. King, *Heat transfer and fluid flow in minichannels and microchannels*, First edit. Elsevier Ltd, 2006.

[3] R. Chennu and S. KN, *Compact Heat Exchangers - Analysis, Design and Optimization using FEM and CFD approach*. John Wiley & Sons Ltd. & ASME Press, 2018.

[4] W. Sjölin, "Two-phase modeling in a heat exchanger with focus on condensation," 2012.
[5] S. C. Palmer, W. V. Payne II, and P. A. Domanski, "Evaporation and condensation heat transfer performance of flammable refrigerants in a brazed plate heat exchanger," US Department of Commerce, Gaithersburg MD 20899.
[6] T. Bohdal, H. Charun, and M. Sikora, "Heat transfer during condensation of refrigerants in tubular minichannels," *Arch. Thermodyn.*, vol. 33, no. 2, pp. 3–22, 2012.
[7] S. Garimella, "Condensation Flow Mechanisms in Microchannels : Basis for Pressure Drop and Heat Transfer Models," *Heat Transf. Eng.*, vol. 25, no. 3, pp. 104–116, 2004.
[8] R. Sánta, "The Analysis of Two-Phase Condensation Heat Transfer Models Based on the Comparison of the Boundary Condition," *Acta Ploytechnica Hungarica*, vol. 9, no. 6, pp. 167–180, 2012.
[9] A. S. Dalkilic, S. Wongwises, T. Division, F. Mechanics, and T. Thonburi, "Two-Phase Heat Transfer Coefficients of R134a Condensation in Vertical Downward Flow at High Mass Flux," in *Heat Transfer - Theoretical Analysis, Experimental Investigations and Industrial Systems*, A. Belmiloudi, Ed. InTech, 2011.
[10] W. W. Wang, T. D. Radcliff, and R. N. Christensen, "A condensation heat transfer correlation for millimeter-scale tubing with flow regime transition," *Exp. Therm. Fluid Sci.*, vol. 26, pp. 473–485, 2002.
[11] M. Balcilar, A. S. Dalkiliç, B. Bolat, and S. Wongwises, "Investigation of empirical correlations on the determination of condensation heat transfer characteristics during downward annular flow of R134a inside a vertical smooth tube using artificial intelligence algorithms," *J. Mech. Sci. Technol.*, vol. 25, no. 10, pp. 2683–2701, 2011.
[12] G. a. Longo, "Refrigerant R134a condensation heat transfer and pressure drop inside a small brazed plate heat exchanger," *Int. J. Refrig.*, vol. 31, no. 5, pp. 780–789, 2008.
[13] J. R. García-Cascales, F. Vera-García, J. Gonzálvez-Maciá, J. M. Corberán-Salvador, M. W. Johnson, and G. T. Kohler, "Compact heat exchangers modeling: Condensation," *Int. J. Refrig.*, vol. 33, no. 1, pp. 135–147, 2010.
[14] H. J. Kang, C. X. Lin, and M. a. Ebadian, "Condensation of R134a flowing inside helicoidal pipe," *Int. J. Heat Mass Transf.*, vol. 43, no. 14, pp. 2553–2564, 2000.
[15] J. R. García-Cascales, F. Vera-García, J. M. Corberán-Salvador, and J. Gonzálvez-Maciá, "Assessment of boiling and condensation heat transfer correlations in the modelling of plate heat exchangers," *Int. J. Refrig.*, vol. 30, no. 6, pp. 1029–1041, 2007.
[16] G. a. Longo, a. Gasparella, and R. Sartori, "Experimental heat transfer coefficients during refrigerant vaporisation and condensation inside herringbone-type plate heat exchangers with enhanced surfaces," *Int. J. Heat Mass Transf.*, vol. 47, no. 19–20, pp. 4125–4136, 2004.
[17] R. Krayiannis, Tassos; Al-Dadah and J. W. Rose, "Two-phase Heat Transfer in Small Passages and Microfinned Surfaces – Fundamentals and Applications .," in *Proceeding of the Institute of Refrigeration*, 2006.
[18] W. Wang and X. Wang, "Experiments of Condensation Heat Transfer in Micro Channel Heat Exchanger," in *International Refrigeration and Air conditioning*, 2010.
[19] A. L. D. Belchí, "Characterisation of Heat Transfer and Pressure Drop in Condensation Processes Within Mini - Channel Tubes With Last Generation of Refrigerant Fluids," Universidad Politécnica de Cartagena, 2014.
[20] G. Arslan and N. Eskin, "Heat transfer characteristics for condensation of R134a in a vertical smooth tube," *Exp. Heat Transf.*, vol. 28, no. 5, pp. 430–445, 2015.
[21] J. P. Meyer, J. Dirker, and A. O. Adelaja, "Condensation heat transfer in smooth inclined tubes for R134a at different saturation temperatures," *Int. J. Heat Mass Transf.*, vol. 70, pp. 515–525, 2014.
[22] D. R. . Ewim, R. Kombo, and J. P. Meyer, "Flow pattern and Experimental Investigation of heat transfer coefficients during the Condensation of R134A at low mass fluxes in a smooth horizontal tube," in *12th International Conference on Heat Transfer, Fluid Mechanics and*

*Thermodynamics*, 2016.

[23] K. Aroonrat and S. Wongwises, "Experimental study on two-phase condensation heat transfer and pressure drop of R-134a flowing in a dimpled tube," *Int. J. Heat Mass Transf.*, vol. 106, pp. 437–448, 2017.

[24] J. Kaew-On, N. Naphattharanun, R. Binmud, and S. Wongwises, "Condensation heat transfer characteristics of R134a flowing inside mini circular and flattened tubes," *Int. J. Heat Mass Transf.*, vol. 102, pp. 83–97, 2016.

[25] J. Wang, J. Wang, and J. M. Li, "R134a condensation flow regime and pressure drop in horizontal microchannals cooled symmetrically and asymmetrically," *Int. J. Heat Mass Transf.*, vol. 115, pp. 1091–1102, 2017.

[26] H. Haraguchi, S. Koyama, and T. Fujii, "Condensation of Refrigerants HCFC 22, HFC 134a and HCFC 123 in a Horizontal Smooth Tube (1st Report, Proposals of Emperical Expressions for the Local Frictional Pressure Drop)," *Transac. JSME*, vol. 60, pp. 239–244, 1994.

[27] H. Haraguchi, S. Koyama, and T. Fujii, "Condensation of refrigerants HCFC 22, HFC 134a and HCFC 123 in a horizontal smooth tube (2nd report, proposals of empirical expressions for local heat transfer coefficient)," *Trans. Japan Soc. Mech. Eng. Part B*, vol. 60, no. 574, pp. 245–252, 1994.

[28] A. Singh, M. M. Ohadi, and S. V. Dessiatoun, "Empirical modeling of stratified-wavy flow condensation heat transfer in smooth horizontal tubes," in *ASHRAE Transactions*, 1996, vol. 102, no. 2, pp. 596–603.

[29] A. Vardhan and W. E. Dunn, "Heat Transfer and Pressure Drop Characteristics of R-22 , R-134A and R-407C in Microchannel Tubes," 1997.

[30] C.-Y. Yang and R. L. Webb, "A Predictive Model for Condensation in Small Hydraulic Diameter Tubes Having Axial Micro-Fins," *J. Heat Transfer*, vol. 119, no. 4, p. 776, 1997.

[31] W. Li, K. Alabi, and F. Ladeinde, "Comparison of 30 Boiling and Condensation Correlations for Two- Phase Flows in Compact Plate-Fin Heat Exchangers," in *ASME Summer Heat Transfer Conference (SHTC 2017)*, 2017, pp. 1–12.

[32] M. K. Dobson and J. C. Chato, "Condensation in Smooth Horizontal Tubes," *J. Heat Transfer*, vol. 120, no. 1, p. 193, 1998.

[33] K. W. Moser, R. L. Webb, and B. Na, "A New Equivalent Reynolds Number Model for Condensation in Smooth Tubes," *J. Heat Transfer*, vol. 120, no. 2, p. 410, 1998.

[34] J. Yu and S. Koyama, "Condensation heat transfer of pure refrigerants in microfin tubes," in *International Refrigeration and Air conditioning*, 1998.

[35] R. L. Webb and M. Zhang, "Heat Transfer and Friction in Small Diameter Channels," *Microscale Thermophys. Eng.*, vol. 2, no. 3, pp. 189–202, 1998.

[36] A. Tabatabai and A. Faghri, "A New Two-Phase Flow Map and Transition Boundary Accounting for Surface Tension Effects in Horizontal Miniature and Micro Tubes," *J. Heat Transfer*, vol. 123, no. 5, p. 958, 2001.

[37] J. El Hajal, J. R. Thome, and A. Cavallini, "Condensation in horizontal tubes, part 1: Two-phase flow pattern map," *Int. J. Heat Mass Transf.*, vol. 46, no. 18, pp. 3349–3363, 2003.

[38] S. Koyama, K. Kuwahara, and K. Nakashita, "Condensation of refrigerant in a multi-port channel," *ASME 2003 1st Int. Conf. Microchannels Minichannels*, pp. 193–205, 2003.

[39] S. Koyama, K. Kuwahara, K. Nakashita, and K. Yamamoto, "An experimental study on condensation of refrigerant R134a in multi-port extruded tube," *Int. J. Refrig.*, vol. 26, no. 4, pp. 425–432, 2003.

[40] J. R. Thome, J. El Hajal, and A. Cavallini, "Condensation in horizontal tubes, part 2: New heat transfer model based on flow regimes," *Int. J. Heat Mass Transf.*, vol. 46, no. 18, pp. 3365–3387, 2003.

[41] M. J. Wilson, T. A. Newell, J. C. Chato, and C. A. Infante Ferreira, "Refrigerant charge, pressure drop, and condensation heat transfer in flattened tubes," *Int. J. Refrig.*, vol. 26, no. 4, pp. 442–451, 2003.

[42] H. Wang and J. W. Rose, "Film Condensation in a Horizontal Triangular section Microchannels: A Theoretical Model," in *The 2nd International Conference on Microchannels and Minichannels*, 2004.
[43] H. S. Wang, J. W. Rose, and H. Honda, "A theoretical model of film condensation in square section horizontal microchannels," *Chem. Eng. Res. Des.*, vol. 82, no. 4, pp. 430–434, 2004.
[44] J. S. Shin and M. H. Kim, "An experimental study of flow condensation heat transfer inside circular and rectangular mini-channels," *Heat Transf. Eng.*, vol. 26, no. 3, pp. 36–44, 2005.
[45] A. Cavallini, D. Del Col, L. Doretti, M. Matkovic, L. Rossetto, and C. Zilio, "Condensation heat transfer and pressure gradient inside multiport minichannels," *Heat Transf. Eng.*, vol. 26, no. 3, pp. 45–55, 2005.
[46] A. Cavallini, L. Doretti, L. Rossetto, and C. Zilio, "A Model for Condensation inside Minichannels," in *2005 ASME Summer Heat Transfer Conference*, 2005.
[47] A. Cavallini, L. Doretti, M. Matkovic, and L. Rossetto, "Update on condensation heat transfer and pressure drop inside minichannels," *Heat Transf. Eng.*, vol. 27, no. 4, pp. 74–87, 2006.
[48] T. M. Bandhauer, A. Agarwal, and S. Garimella, "Measurement and Modeling of Condensation Heat Transfer Coefficients in Circular Microchannels," *J. Heat Transfer*, vol. 128, no. 10, p. 1050, 2006.
[49] A. Cavallini *et al.*, "Condensation in horizontal smooth tubes: A new heat transfer model for heat exchanger design," *Heat Transf. Eng.*, vol. 27, no. 8, pp. 31–38, 2006.
[50] B. Médéric, P. Lavieille, and M. Miscevic, "Heat transfer analysis according to condensation flow structures in a minichannel," *Exp. Therm. Fluid Sci.*, vol. 30, no. 8, pp. 785–793, 2006.
[51] A. Cavallini, S. Bortolin, D. Del Col, and L. Rossetto, "Condensation and Vaporization of Halogenated Refrigerants Inside a Circular Minichannel," 2008.
[52] A. Cavallini, D. Del Col, M. Matkovic, and L. Rossetto, "Pressure Drop During Two-Phase Flow of R134a and R32 in a Single Minichannel," *J. Heat Transfer*, vol. 131, no. 3, p. 33107, 2009.
[53] M. Matkovic, A. Cavallini, D. Del Col, and L. Rossetto, "Experimental study on condensation heat transfer inside a single circular minichannel," *Int. J. Heat Mass Transf.*, vol. 52, no. 9–10, pp. 2311–2323, 2009.
[54] A. Agarwal, T. M. Bandhauer, and S. Garimella, "Measurement and modeling of condensation heat transfer in non-circular microchannels," *Int. J. Refrig.*, vol. 33, no. 6, pp. 1169–1179, 2010.
[55] T. Bohdal, H. Charun, and M. Sikora, "Comparative investigations of the condensation of R134a and R404A refrigerants in pipe minichannels," *Int. J. Heat Mass Transf.*, vol. 54, no. 9–10, pp. 1963–1974, 2011.
[56] J. E. Park, F. Vakili-Farahani, L. Consolini, and J. R. Thome, "Experimental study on condensation heat transfer in vertical minichannels for new refrigerant R1234ze(E) versus R134a and R236fa," *Exp. Therm. Fluid Sci.*, vol. 35, no. 3, pp. 442–454, 2011.
[57] D. Del Col, S. Bortolin, A. Cavallini, and M. Matkovic, "Effect of cross sectional shape during condensation in a single square minichannel," *Int. J. Heat Mass Transf.*, vol. 54, no. 17–18, pp. 3909–3920, 2011.
[58] M. Derby, H. J. Lee, Y. Peles, and M. K. Jensen, "Condensation heat transfer in square, triangular, and semi-circular mini-channels," *Int. J. Heat Mass Transf.*, vol. 55, no. 1–3, pp. 187–197, 2012.
[59] G. Goss and J. C. Passos, "Heat transfer during the condensation of R134a inside eight parallel microchannels," *Int. J. Heat Mass Transf.*, vol. 59, no. 1, pp. 9–19, 2013.
[60] E. Al-Hajri, A. H. Shooshtari, S. Dessiatoun, and M. M. Ohadi, "Performance characterization of R134a and R245fa in a high aspect ratio microchannel condenser," *Int. J. Refrig.*, vol. 36, no. 2, pp. 588–600, 2013.
[61] K. Sakamatapan, J. Kaew-On, A. S. Dalkilic, O. Mahian, and S. Wongwises, "Condensation heat transfer characteristics of R-134a flowing inside the multiport minichannels," *Int. J.*

*Heat Mass Transf.*, vol. 64, pp. 976–985, 2013.

[62] D. R. . Ewim and J. P. Meyer, "Condensation Heat Transfer Coefficients of Enhanced Tumes," in *Third Aouth African Solar Energy Conference*, 2015, no. 11–13 May, pp. 230–235.

[63] Q. Li, L. Tao, L. Li, Y. Hu, and S. Wu, "Experimental Investigation of the Condensation Heat Transfer Coefficient of R134a inside Horizontal Smooth and Micro-Fin Tubes," *Energies*, vol. 10, no. 9, p. 1280, 2017.

[64] W. W. Akers, H. A. Deans, and O. K. Crosser, "Condensing heat transfer within horizontal tubes," *Chem.Eng.Progr.*, vol. 54, pp. 89–90, 1958.

# Mixed convection in a nanofluid filled double lid driven porous enclosure with discrete heat sources

**Krishno Das Goswami[1], Swapan K. Pandit[2]**
**Integrated Science Education & Research Centre (ISERC), Visva-Bharati, Santiniketan-731 235, India.** kris6890@gmail.com [1], swapankumar.pandit@visva-bharati.ac.in [2]

**ABSTRACT:** The present work has been carried out to investigate the fluid flow and heat transfer enhancement of mixed convection in a double lid driven porous enclosure filled with copper-water Nanofluid. The flow is influenced by two discrete heat sources along the bottom wall of the enclosure. The governing equations including the conservation of mass, conservation of linear momentum and conservation of energy are solved numerically using the finite difference method. The effects of governing non-dimensional parameters such as Richardson number ($0.1 \leq Ri \leq 10$), Darcy number ($10^{-2} \leq Da \leq 10^{-1}$), Reynolds number ($10 \leq Re \leq 1000$) and nanoparticle volume fraction (0.0-0.1) with fixed Prandtl number ($Pr$) = 6.2 are examined. It is found that the average heat transfer increases with increasing the nanoparticle volume fraction, whereas on decreasing the Darcy number the average heat transfer increases.

**Key Words:** *Fourth-Order Accurate Compact Scheme, Mixed Convection, Nanofluid, Porous Medium.*

## 1. INTRODUCTION:

Mixed convection in a double lid driven cavity has large scale applications such as cooling of electronic devices, nuclear reactors, coating, solidification, food processing and solar power. The main objective in the study of heat transfer is to empower the enhancement of the cooling performances in an enclosure. Nanoparticle suspended in a base fluid is more efficient to increase the thermal conductivity compared to low conductivity of conventional fluids like water, ethylene glycol etc. Due to the efficiency of high thermal conductivity, nanofluid has a great role as coolant in many heat transfer systems.

To the best of authors knowledge, Choi [1] first introduced the "nanofluid" in the form of a mixture of nanoparticle and base fluid. Continuing from the last few years researchers have a keen interest to study the heat transfer by utilizing nanofluid. Various experimental as well as numerical studies have been carried out on the basis of thermal conductivity of nanofluid till date. Eastman et al. [2] in their experimental work pointed out that the effective thermal conductivity is increased up to 40% as compared to pure ethylene glycol by using 0.3% volume fraction of copper nanoparticles of size ≤10 nm. Moumni et al. [3] examined the heat transfer characteristics for various nanofluids in a vertical lid driven enclosure in the discrete heat sources on the bottom wall. Studies are available in the literature on the subject of mixed convection nanofluid flow in porous medium [4-6].

The main motivation of the present work is due to the insufficient study related to the discrete heating in a double lid driven porous enclosure containing nanofluid. On the basis of the literature review and to the best of our knowledge, it appears that the present work was not reported so far.

## 2. MAIN BODY

The schematic diagram of the physical configeration is represented in Fig. 1 is a two dimensional square enclosure of length L, filled with a Cu-water nanofluid saturated with a porous medium. Two discrete heat sources under uniform heating are placed on bottom wall of length L/4 while the remaining portion of the bottom wall are assumed to be thermally insulated. Both the vertical walls are maintened at constant cold temperature and the top wall is thermally insulated. The vertical walls are moving upward direction with uniform velocity.

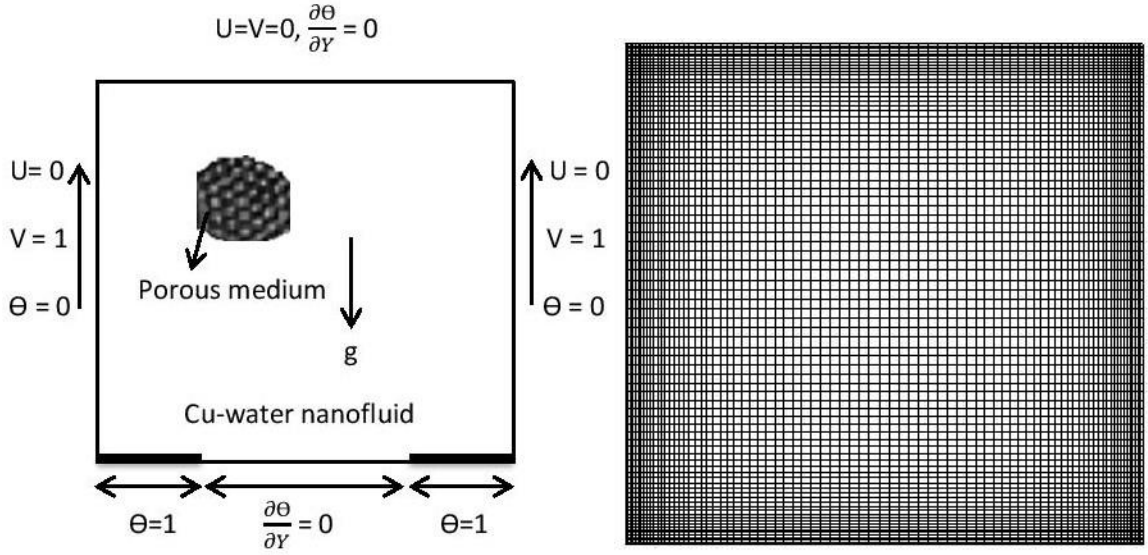


(a) (b)

FIGURE. 1. (a) Physical configuration of the problem and (b) grid structure.

The governing equations describing the steady, incompressible viscous flows in a two-dimensional lid-driven square cavity filled with a Cu-water nanofluid and saturated with porous medium is in non-dimensional stream function (Ψ) - vorticity (ζ) formulation is as follows:

$$-\left(\frac{\partial^2 \Psi}{\partial X^2}+\frac{\partial^2 \Psi}{\partial Y^2}\right)=\zeta \tag{1}$$

$$-\frac{\rho_f}{\rho_{nf}\,(1-\phi)^{2.5}}\frac{\partial^2 \zeta}{\partial X^2}-\frac{\rho_f}{\rho_{nf}\,(1-\phi)^{2.5}}\frac{\partial^2 \zeta}{\partial Y^2}+URe\frac{\partial \zeta}{\partial X}+VRe\frac{\partial \zeta}{\partial Y}+\frac{\rho_f}{\rho_{nf}\,(1-\phi)^{2.5}}\,\frac{\zeta}{Da}=\frac{(\rho\beta)_{nf}}{\rho_{nf}\beta_f}RiRe\frac{\partial \theta}{\partial X} \tag{2}$$

$$-\frac{\alpha_{nf}}{\alpha_f}\frac{\partial^2 \Theta}{\partial X^2}-\frac{\alpha_{nf}}{\alpha_f}\frac{\partial^2 \Theta}{\partial X^2}+URePr\frac{\partial \theta}{\partial X}+VRePr\frac{\partial \theta}{\partial Y}=0 \tag{3}$$

The relavent non-dimensional boundary conditions along the cavity walls are as follows:

U=V=0, $\frac{\partial \theta}{\partial Y}$ = 0, at Y=1, 0≤X≤1, U=0, V=1, θ = 0, at X=0, 0<Y<1, U=0, V=1, θ = 0, at X=1, 0<Y<1,

U=V=0, $\theta = \theta_b$. at Y=0, 0≤X≤1 where $\theta_b = \begin{cases} \theta = 1, & \text{if } X \in \left[0,\frac{1}{4}\right) \cup \left(\frac{3}{4},\ 1\right]. \\ \frac{\partial \theta}{\partial Y} = 0, & elsewhere. \end{cases}$ (4)

The local Nusselt number ($Nu$) and the average Nusselt number ($Nu_m$) along the heated surface are computated as: $Nu_X = -\frac{k_{nf}}{k_f}\left(\frac{\partial \theta}{\partial Y}\right)_{\text{hot wall}}$, $Nu_{m_{s_i}} = \frac{\int_{hot\ wall} Nu_X dX}{\int_{hot\ wall} dX}$ (5)

The overall surface average Nusselt number $(Nu_m) = \frac{Nu_{m_{s_1}} + Nu_{m_{s_2}}}{2}$, where $s_1$ and $s_2$ represent the left and right hot section of the bottom wall. Now using a fourth-order accurate compact scheme as proposed in [7], we have discretized the governing equations on nonuniform grids.

## 3. RESULTS

The present code is validated against Ghasemi et al. [8]. Fig. 2 and Table 1 show a very good agreement between present work and Ghasemi et al. [8] for zero Hartmann number.

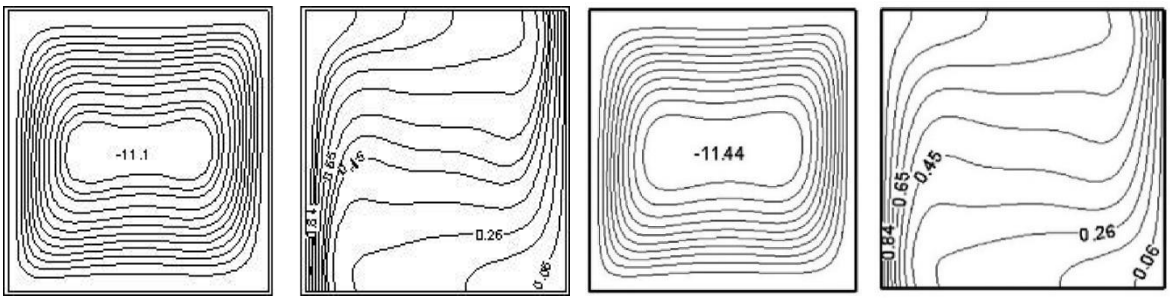


FIGURE 2**.** Comparision of Streamlines (a,c) and Isotherms (b,d) for Ra=$10^5$ and $\phi$ = 0.03 on a grid size 41X41. Present work (a,b), Ghasemi et al. [8] (c,d).

| Solid volume fraction ($\phi$) | Present work | | Ghasemi et al. [8] | |
|---|---|---|---|---|
| | $Nu_m$ | $\lvert\Psi\rvert_{max}$ | $Nu_m$ | $\lvert\Psi\rvert_{max}$ |
| $\phi$ = 0.0 | 4.679 | 11.369 | 4.738 | 11.053 |
| $\phi$ = 0.02 | 4.756 | 11.585 | 4.820 | 11.313 |
| $\phi$ = 0.04 | 4.831 | 11.833 | 4.896 | 11.561 |
| $\phi$ = 0.06 | 4.9 | 12.072 | 4.968 | 11.801 |

TABLE 1. Comparison of the average Nusselt number ($Nu_m$) and maximum stream function ($|\Psi|_{max}$) for Ra=$10^5$ on a grid size 61X61.

Fig. [3,4] represent the streamline and isotherm distribution for various volume fraction ($\phi$), which show that the fluid flow and the temperature distribution are symmetric about the vertical centreline.

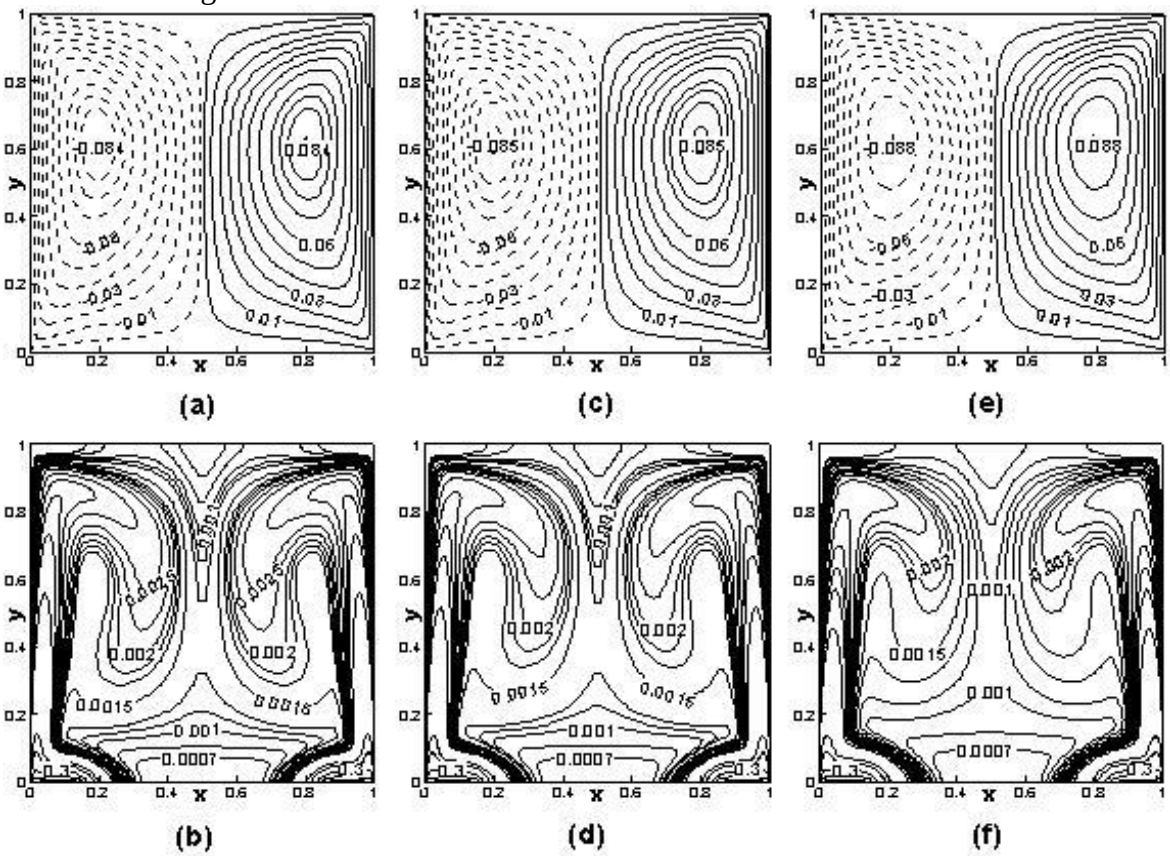


FIGURE 3. Streamlines (a, c, e) and Isotherms (b, d, f) for Re=100, Ri=1, Da=$10^{-1}$ and $\phi$ = 0.0 (a, b), $\phi$ = 0.03 (c, d) and $\phi$ = 0.1 (e,f).

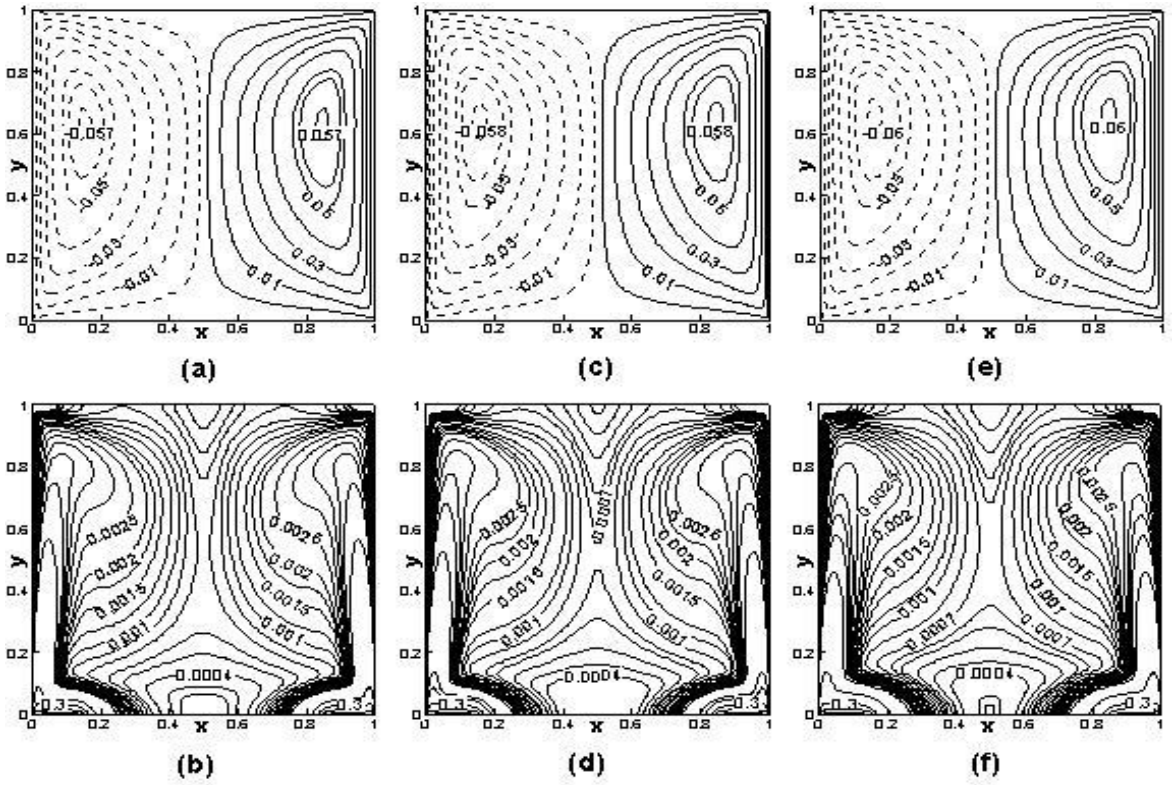


FIGURE 4. Streamlines (a, c, e) and Isotherms (b, d, f) for Re=100, Ri=1, Da=$10^{-2}$ and $\phi = 0.0$ (a, b), $\phi = 0.03$ (c, d) and $\phi = 0.1$ (e, f).

## 4. CONCLUSIONS

The fluid flow and thermal distribution are analysed using the streamlines and isotherms. The heat transfer characteristics are examined by the illustration of Nusselt number. The present study indicates that the Darcy number and the nanoparticle solid volume fraction have influential role on the flow phenomenon and the heat transfer characteristics.

## REFERENCES

[1] S.U.S. Choi, Enhancing thermal conductivity of fluids with nanoparticles, ASME-Publications-Fed 231, 99–106, 1995.

[2] J.A. Eastman, S.U.S Choi, S. Li, W. Yu and L.J. Thompson, Anomalously increased effective thermal conductivities of ethylene glycol-based nanofluids containing copper nanoparticles, Appl. Phys. Lett. 78 (6), 718–20, 2001.

[3] H. Moumni, H. Welhezi, R. Djebali and E. Sediki, Accurate finite volume investigation of nano fluid mixed convection in sided Lid Driven Cavity Including Discrete Heat Sources, Appl. Math. Model. 39(14,15), 4164-79, 2015.

[4] F. Talebi, A.H. Mahmoudi and M. Shahi, Numerical study of mixed convection flows in a square lid driven cavity utilizing nanofluid, Int. Comm. Heat mass Transfer 37, 79-90, 2010.

[5] M.A. Mansour and S. E. Ahmed, A numerical study on natural convection in porous media filled an inclined triangular enclosure with heat sources using nanofluid in the presence of heat generation effect, Eng. Sci. Technol., Int. J. 18(3), 485–95, 2015.

[6] A. J. Chamka and E. Abu-Nada, Mixed convection flow in single- and double-lid driven square cavities filled with water-$Al_2O_3$ nanofluid: Effect of viscosity models, Eur. J. Mech. B/Fluids, 36, 82-96, 2012.

[7] S.K. Pandit and A. Chattopadhyay, A robust higher order compact scheme for solving general second order partial differential equation with derivative source terms on nonuniform curvilinear meshes, Computers & Mathematics with Applications, 74-(6), 1414-34, 2017.

[8] B. Ghasemi, S.M. aminossadati and A. Raisi, Magnetic field effect on natural convection in a nanofluid-filled square enclosure, Int. J. Thermal Sci. 50 , 1748-56, 2011.

Fifth International Conference on Computational Methods for Thermal Problems
THERMACOMP2018, July 9-11, 2018, Indian Institute of Science, Bangalore, INDIA
*N. Massarotti, P. Nithiarasu, Pradip Dutta and C. Ranganyakalu (Eds.)*

# CONVECTIVE HEAT TRANSFER OF A NANOFLUID OVER A STRETCHING SHEET WITH VARIABLE VISCOSITY AND HALL EFFECT

**G. Sreedevi[a], A. J. Chamkha[b] and D. R. V. Prasada Rao[c]**
[a]Department of Mathematics, K.L. University, Green Fields, Vaddeswaram, Guntur 522502, AP, India, sreedeviahari2007@gmail.com
[b]Mechanical Engineering Department, Prince Mohammad Bin Fahd University (PMU), Al-Khobar 31952, Saudi Arabia; achamkha@pmu.edu.sa
[c]Department of Mathematics, S.K. University, Anantapur 515003, AP, India; drv_atp@yahoo.in

## ABSTRACT

This paper presents a numerical study of Hall current effect and variable viscosity in a convective heat transfer flow over a stretching sheet. A fifth-order Runge-Kutta-Fehlberg method with shooting technique was employed for solving governing non-linear boundary layer equations for two types of nanoparticles, namely copper (Cu) and alumina ($Al_2O_3$) in the base fluid ($H_2O$). The effects of velocity, temperature, skin friction and Nusselt number are discussed and analysed through graphs. Comparison of numerical results is made with published literature under limiting cases. *(Comparison table will be provided in the full length paper).*

**Key Words:** *Heat Transfer, Stretching Sheet, Nanofluids, Hall Current, Variable Viscosity.*

## 1. INTRODUCTION

Owing to enhanced thermal conductivity properties, the study of nanofluids (homogeneous mixture of nanoscale particles of 1-100 nm size), initiated by Choi [1], gained momentum in recent decades resulting in wider industrial and scientific applications.

A numerical solution employing similarity transformation of a steady heat flow on a moving continuous flat surface was considered by Sakiadis [2]. Watanabe and Pop [3] examined the influence of Hall currents on MHD boundary layer flow over a moving flat plate in a viscous incompressible electrically conducting fluid. Makinde et al. [4] studied MHD flow of a variable viscosity nanofluid over a radially stretching convective surface with radiative heat. Sreedevi et al. [5] studied the combined influence of radiation absorption and Hall current effects on MHD double-diffusive free convective flow over a stretching sheet. Tripathi et al. [6] studied Double diffusive flow of a hydromagnetic nanofluid in a rotating channel with Hall effect and viscous dissipation. *(Complete introduction will be provided in the full length paper)*

The objective of this paper is to study the effects of Hall current and variable viscosity over a stretching sheet in Cu and $Al_2O_3$-water based nanofluids. The theoretical study in this paper is hoped to be a useful guide for experimentalist to study in free convective viscous flow filled with Cu and $Al_2O_3$ water based nanofluids to increase the rate of heat transfer.

## 2. FORMULATION OF THE PROBLEM

Consider steady free convective flow of nanofluid over a stretching sheet in a porous medium. A uniform magnetic field of strength $B_0$ is applied normal to the sheet at Y axis and the sheet is stretched with a velocity proportional to the distance from a fixed origin O. Figure1 demonstrates

the problem under consideration and the coordinate system. The problem is modeled mathematically based on the following assumptions:

- it is considered that the there is no applied voltage which implies that an electric field is absent.
- taking Hall effects into account, the generalized Ohm's law provided in the following form $\vec{J} = \frac{\sigma}{1+m^2}(\vec{E} + \vec{V} * + \vec{B} - \frac{1}{en_e}\vec{f} * \vec{B})$, where $m = \frac{\sigma B_0}{en_c}$ is defined as the Hall current parameter. Hall current gives rise to a force in the z-direction which in turn produces a cross-flow velocity in this direction and then the flow becomes three-dimensional.
- the temperature is maintained at prescribed constant value $T_w$ at the sheet and $T_\infty$ is the fixed value far away from the sheet.
- the fluid viscosity μ is assumed to vary as a reciprocal of a linear function of temperature given by $\frac{1}{\mu} = \frac{1}{\mu_\infty}[1 + \gamma_0(T - T_\infty)]$ , $\frac{1}{\mu_\infty} = a(T - T_\infty)$ where $a = \frac{\gamma_0}{\mu_\infty}$, $T_r = T_\infty - \frac{1}{\gamma_0}$, both $a$ and $T_r$ are constants, and their values depend on the thermal property of the fluid $\gamma_0$. In general, $a > 0$ represent for liquids, whereas for gases $a < 0$.

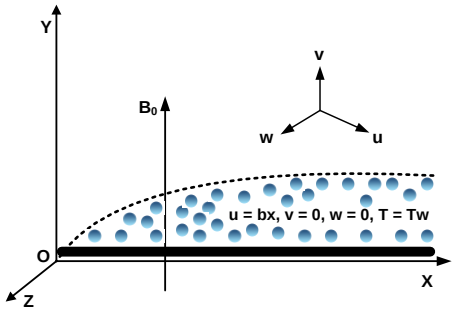


FIGURE 1. Formulation of the Problem

Considering the above assumptions, the generalized Ohm's law with Hall effect are governed by the following system of equations

$$\frac{\partial u}{\partial x} + \frac{\partial v}{\partial y} = 0 \tag{1}$$

$$\rho_{nf}\left(u\frac{\partial u}{\partial x} + v\frac{\partial u}{\partial y}\right) = \mu_{nf}\frac{\partial^2 u}{\partial y^2} + (\rho\beta)_{nf}\, g\left(T - T_\infty\right) - \frac{\sigma_{nf}B_0^2}{1+m^2}(u + mw) \tag{2}$$

$$\rho_{nf}\left(u\frac{\partial w}{\partial x} + v\frac{\partial w}{\partial y}\right) = \mu_{nf}\frac{\partial^2 u}{\partial y^2} + \frac{\sigma_{nf}B_0^2}{1+m^2}(mu - w) \tag{3}$$

$$(\rho_m C_p)_{nf}\left(u\frac{\partial T}{\partial x} + v\frac{\partial T}{\partial y}\right) = k_{nf}\frac{\partial^2 T}{\partial y^2} - Q\left(T - T_\infty\right) \tag{4}$$

where ($u$, $v$, $w$) are the velocity components along the ($x$, $y$, $z$) directions respectively. $C_p$ is the specific heat at constant pressure and $T_m$ is the mean fluid temperature. The boundary conditions are

$$u = bx, v = w = 0, T = T_w \text{ at } y = 0; \qquad u \to 0, w \to 0, T \to T_\infty \text{ at } y \to \infty \tag{5}$$

where $b$ (> 0) being stretching rate of the sheet. The boundary conditions on velocity in Equation (5) are the no-slip condition at the surface $y = 0$, while the boundary conditions on velocity at $y \to \infty$ follow from the fact that there is no flow far away from the stretching surface.

To examine the flow regime adjacent to the sheet, the following transformations are invoked

$$u = bxf'(\eta); v = -\sqrt{bv}\, f(\eta); w = bxg(\eta);\ \ \eta = \sqrt{\frac{b}{v}}\, y; \theta(\eta) = \frac{T - T_\infty}{T_w - T_\infty}; \tag{6}$$

where $f$ is a dimensionless stream function, $\eta$ is the similarity space variable and θ is the dimensionless temperature respectively. Clearly, the continuity Equation (1) is satisfied by $u$ and $v$ defined in Equation (5). Substituting Equation (6) the Equations (2) - (4) reduce to

$$\left(\frac{\theta-\theta_r}{\theta_r}\right)(f' - f\ f'') + \left(\frac{1}{A_1A_3}\right)f''' - \left(\frac{\theta'}{\theta-\theta_r}\right)f'' - \left(\frac{\theta-\theta_r}{\theta_r}\right)\left(\frac{A_4}{A_3}\right)G(\theta) + \frac{A_6}{A_3}M^2\left(\frac{\theta'-\theta_r}{\theta_r}\right)\left(\frac{f'+mg}{1+m^2}\right) = 0 \tag{7}$$

$$\left(\frac{\theta-\theta_r}{\theta_r}\right)(f'g - fg') + \left(\frac{1}{A_1A_3}\right)g'' - \left(\frac{\theta'}{\theta-\theta_r}\right)g' - \frac{A_6}{A_3}M^2\left(\frac{\theta-\theta_r}{\theta_r}\right)\left(\frac{mf'+g}{1+m^2}\right) = 0 \tag{8}$$

$$\left(\frac{1}{A_5}\right)\theta'' + \Pr\lambda\theta + \frac{A_6M^2}{A_5(1+m^2)}(f'^2 + g^2) = 0 \tag{9}$$

where

$$A_1 = (1-\varphi)^{2.5}; A_2 = \frac{k_{nf}}{k_f}; A_3 = 1-\varphi+\varphi\left(\frac{\rho_s}{\rho_f}\right); A_4 = 1-\varphi+\varphi\left(\frac{(\rho\beta)_s}{(\rho\beta)_f}\right); A_5 = 1-\varphi+\varphi\frac{(\rho C_P)_s}{(\rho C_P)_f}; A_6 = \left(1+\frac{3(1-\sigma)\phi}{(\sigma+2)}\right), \sigma = \frac{\sigma_s}{\sigma_f}$$

Similarly, the transformed boundary conditions are given by

$$f'(\eta) = 1, f(\eta) = 0, g(\eta) = 0, \theta(\eta) = 1 \ \text{at}\ \eta = 0;\ \ f'(\eta) \to 0,\ g(\eta) \to 0,\ \theta(\eta) \to 0 \ \text{at}\ \eta \to \infty \tag{10}$$

where a prime denotes the differentiation with respect to η only and the dimensionless parameters appearing in the Equations (7)-(10) are respectively defined as $\theta_r = \frac{T_r - T_\infty}{T_w - T_\infty} = -\left[\frac{1}{\gamma_0(T_w - T_\infty)}\right]$ the viscosity parameter, $M = \frac{\sigma B_0^2}{P_\infty b}$ the magnetic parameter, $P_r = \frac{\rho C_p \nu}{k}$ the Prandtl number, $G = \frac{g_0\beta_T(T_w - T_\infty)}{b^2 x}$ the local Grashof number, $\lambda = \frac{Q}{\rho_\infty C_p b}$ is defined as the heat source. Other variables in the present study are skin friction coefficient $C_f$ and Nusselt number Nu which are defined as

$$C_f = \frac{\tau_w}{\mu bx\sqrt{\frac{b}{v}}} = f''(0) \ \text{where}\ \tau_w = \mu\left(\frac{\partial T}{\partial y}\right)_{y=0} = \mu b x\sqrt{\frac{b}{v}}\, f''(0) \tag{11}$$

$$Nu = \frac{\dot{q}_w}{k\sqrt{\frac{b}{v}}(T_w - T_\infty)} \ \text{where}\ q_w = -k\left(\frac{\partial T}{\partial y}\right)_{y=0} = -k\sqrt{\frac{b}{v}}(T_w - T_\infty)\theta'(0) \tag{12}$$

## 3. NUMERICAL APPROACH

The coupled ODEs (7)-(10) are solved and reduced into system of simultaneous equations. By using fifth-order Runge-Kutta-Fehlberg integration scheme with automatic grid generation, simultaneous equations convergence at a faster rate. The value of $\eta_\infty$ greatly depends on the set of the physical parameters such as Hall current, magnetic parameter, strength of heat source and Prandtl number so that, no numerical oscillations would occur. During the computation, the shooting error was controlled by keeping at less than $10^{-6}$. *(Complete approach will be provided in the full length paper)*

## 4. RESULTS AND DISCUSSIONS

Figure 2 explains that the axial velocity $f'(\eta)$ increases with increase in Hall parameter m. This is because as m increases, the Lorentz force opposes the fluid flow and leads to the degeneration of the fluid motion. Figure 3 displays that the cross flow velocity $g(\eta)$ decelerates with rise in variable viscosity parameter $\theta r$. Figure 4 depicts that the temperature reduces with increase in $\phi$. This may be attributed that an increase in $\phi$ decreases the thickness of the thermal boundary layer. An increase the m enhances $\tau_x$ in $Al_2O_3$-water and reduces in Cu-water and for higher $m \geq 2.5$, it is opposite. Nu enhances with increase in $\phi \leq 0.1$, in both types of nanofluids. *(Total 12 graphs and complete discussion will be provided in the full length paper)*

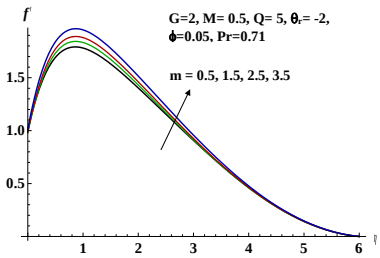


FIGURE 2. Variation of $f'$ with m

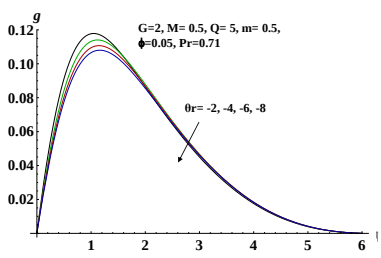


FIGURE 3. Variation of $g$ with $\theta r$

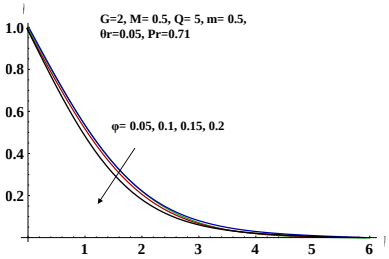


FIGURE 4. Variation of $\theta$ with $\varphi$

## 5. CONCLUSIONS

It is found that the Hall current (m) has a tendency to enhance the axial velocity and temperature but reduces the cross flow velocity $g(\eta)$ over stretching sheet. It is noted that with increase in m, skin friction parameter $\tau_x$ reduces in Cu-water and enhances in $Al_2O_3$-water nanofluids. The axial and cross flow velocity increases with the increase in the viscosity parameter $\theta r$. $g(\eta)$ decelerates the momentum boundary layer with increase in the viscosity. It is observed that with the increase in $\theta r$ the temperature enhances in the boundary layer. The velocities enhance and temperature reduces in the boundary layer with increase in the nanoparticle concentration($\phi$). Nusselt number decreases in Cu-water and enhances in $Al_2O_3$-water by increasing the Hall current parameter.

## REFERENCES

[1] S.U.S. Choi, Enhancing thermal conductivity of fluids with nanoparticles, in developments and applications of non-Newtonian flows, D.A. Siginer, H.P. Wang eds. New York: *The American Society of Mechanical* Engineers, FED–231/MD–66, 99-105, 1995.

[2] B.C. Sakiadis, Boundary layer behaviour on continuous solid surfaces, *The American Institute of Chemical Engineers Journal*, 7(2), 221-225, 1961.

[3] T. Watanabe, I. Pop, Hall effects on magneto-hydrodynamic boundary layer flow over a continuous moving flat plate, *Acta Mechanica*, 108, 35-47, 1995.

[4] O.D. Makinde, F. Mabood, W.A. Khan and M.S. Tshehla, MHD flow of a variable viscosity nanofluid over a radially stretching convective surface with radiative heat, *Journal of Molecular Liquids*, 219, 624-630, 2016.

[5] G. Sreedevi, R.R. Rao, D.R.V. Prasada Rao and A.J. Chamkha, Combined influence of radiation absorption and Hall current effects on MHD double-diffusive free convective flow past a stretching sheet, *Ain Shams Engineering Journal*, 7, 383-397, 2016.

[6] R. Tripathi, G.S. Seth and M.K. Mishra, Double diffusive flow of a hydromagnetic nanofluid in a rotating channel with Hall effect and viscous dissipation: active and passive control of nanoparticles, *Advanced Powder Technology*, 28(10), 2630-2641, 2017.

*(Complete references will be provided in the full length paper).*

# Numerical Studies using CFD on Pulsed continuous Detonation in a Tube with shock propagation Shchelkin Spiral blockages using different Air-Fuel mixtures.

**Mukul Batra, Nikhil Sharma**
BTech Aerospace, UPES University
batra.mukul1996@gmail.com, nikhil.niksharma15@gmail.com
**Velidi V S S Gurunadh, Sudhir Joshi**
UPES University
GVSSVELIDI@ddn.upes.ac.in

## ABSTRACT

Pulse Detonation Engine (PDE) is the future of Propulsion system for air-vehicles. The Idea behind this paper is to reduce transition distance and time of deflagration to detonation using Shchelkin Spiral. For doing this numerical analysis we will use computational fluid dynamics solver to analyze flow characteristics of the detonation process. The Hydrogen- Oxygen and Kerosene – Oxygen mixture with rich mixtures will be analyzed for the simple tube configuration with Shchelkin Spiral with one end open and other end closed and compare it with simple tube with same length and tube diameter. At first the method used to start the detonation is by creating a region of pressure and temperature at inlet of the tube using the combustion process, and hence shock will be produced. The shock wave propagation will be channelized using blockages in the tube for obtaining higher Mach number, which will greatly contribute for obtaining higher Thrust. Fuel - Oxygen are injected at calculated mass flow rates and certain inlet velocity leading to produce high pressure and shock wave is induced which travels towards open end inside the tube.

**Key Words:** *Pulse Detonation Engine, Shchelkin spiral, Deflagration, Detonation, Combustion, Shock Wave.*

## 1. INTRODUCTION

Pulse detonation engines are based on similar pattern as pulse-jet engines which genrates the thurst by combusting in pulses. Deflagration is process in which the fuel is combusted with heat generated with the reaction of oxidiser and fuel whereas as PDEs detonate in which the reaction is vigorous and much more rapid than simple deflagration.The current propuslive systems which are being used have some disadvantages which can be overcome by using PDE and this paper introduces these applications of PDE. PDE can be broadly divided into 3 different types namely, Pure PDE, Combined-Cycle PDE and Hybrid PDE. Pure PDE engines depends on totaly on detonation. Combined-cycle PDE engines combine various other propulsive cycles along with detonation to generate thrust. Turbojet engines and turbofan engines are also used with attached PDEs and this combination is Hybrid PDE. Deflagrations are good means of combustion but less efficient then detonation as means of combustion of fuel and oxidizer. Detonation has an ability to conitnously combust once initiated without any external heat application and produces results of combustion process at mach greater than 1.3.Comparing both the process, it has been found out that detonation process has more efficiency and produces high pressure values and velcities during combustion. PDE is initiated idea in recent research on propulsion systems in which we use continuous detonations to get thrust or power. Rather than using constant pressure process which are being used in many conventional engines, PDE uses a Constant volume cycle process to produce thrust and power which lead various advantages over other engines. In our PDE model combustion of fuel is carried as a shock wave or detonation wave and this wave travels through the length of the tube containing Shckelkin spirals along its length. The efficiency and performance calculations can be done using in Computational Fluid Dynamics (CFD) analysis as our PDE model is having simple geometry. Predefined size of geometry and obstacles is being used for processing of this CFD studies. In PDE Obstacles are having major in propagation of shock wave along tube length but from previous studies Shchelkin spiral shape gives more efficiency and performance as compared to other geometry obstacles used.

## 2. MAIN BODY

From previous studies and researches conducted it has been found out that the CFD analysis gives accurate and reliable results in pulse detonation engines. Air-Fuel mixture is stimulated from inlet at one end of the model and other end is kept open. From closed end air-fuel mixture is combusted and a shock wave is propagated resulting in detonation. Near to the closed end the shock is produced and travel towards the open end in a period of micro-seconds causing detonation and the process is repeated several multiple times in small intervals of time. Various studies of CHIPING LI and K. KAILASANATH “Detonation Transmission and Transition in Channels of Different Sizes” [1] and Another study by KAILASANATH and G. PATNAIK [2] performed various simulations on PDE to find performance, efficiency and other thurst parameters.

### 2.1 ZND Theory

ZND Theory of Zeldovich (1940), von Neumann (1942) and Doering (1943) for detonation proposed 1D detonation wave structure and hydrodynamic Euler equations along finite rate chemical reactions is solved by this model. The induction region and reaction region following the detonation shock wave is depicted in Figure 2.1, and these regions travel at detonation velocity at same instance.

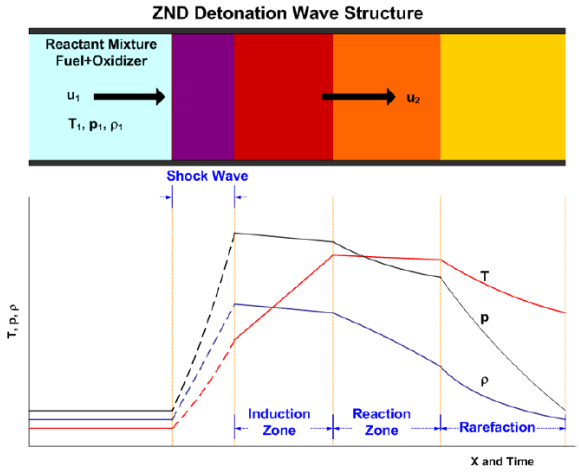


Figure 1: Diagram illustrating the pressure, temperature and density profiles of a ZND theory model [4].

## 2.2 3-D Structure of Detonation Waves & Cell Dimensions

The Wave Front due to detonation is actually a 3D rather than 2D in real. The Dynamic interaction of advancing wave horizontal reflected wave and Mach branches makes a variable structure causing various triple points to arise[3] [4]. Tracing the triple points form diamond shapes known as detonation cells, as shown in Figure 2.2. A detailed diamond formation is illustrated in Figure 2.3. As seen in Figure 2.2, **λ** is denoted as cell width or cell size. Using various values of λ for different air-fuel mixtures at stoichiometric condition from previous researches. As the equivalence ratio varies the cell size also changes for particular air-fuel combination and at an equivalence ratio ranging from 1 to 1.1 this size reduces to its minimum value and this size increases as there is decrease or increase of equivalence ratio forming a curve in U-Shape. Theoretically it is seen that liquid fuels like kerosene and jet fuels have identical cell width as that of propane-air mixtures.

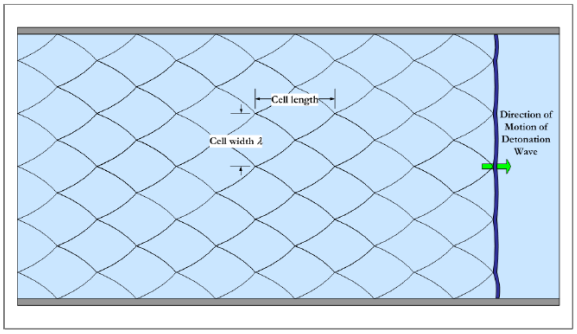


Figure 2: Schematic of detonation cells formed within a tube as the detonation wave travels down its length [4].

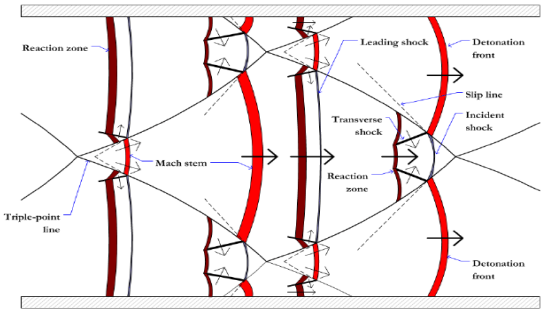


Figure 3: Complete illustration of formation of the diamond shapes [4].

## 2.3 Deflagration to Detonation Transition (DDT)

With an effective tube size deflagration can be converted to detonation with increase in pressure and temperature. This transition can be fasten up by increased wall roughness and turbulence. Practically this was verified by use of Shchelkin spiral as these spirals increases the wall friction and also flame front is accelerated due to hot spots formed in the flow. Streamlined flame front interact with obstacles forming hot burning gases cavities and compression waves which along with flame front merge with shock. The self-sustaining CJ detonation is formed due coupling of flame front accelerated due to high pressure with shock. Experimentally successful movement of shock wave can be found out by means of cell dimensions of mixture used and diameter of tube can be estimated as greater than $\lambda / \pi$.

## 3. RESULTS

### 3.1 Calculations

From above formulae, graphs and figures we calculated the cell width of Hydrogen-air mixture as 10.9mm at stoichiometric conditions and for kerosene-air mixtures as 51.3mm and computing the minimum diameter of tube using $\lambda / \pi$ we get minimum diameter for hydrogen-air mixture as 3.469mm and for kerosene-air mixture as 16.329mm. We have taken the blockage ratio to be 0.5. Doing various calculations we take main tube diameter to be 35mm and Shchelkin Spiral diameter comes to be 17.5mm and 45mm to be the pitch of the spiral and tube length is taken as 500mm.

### 3.2 Results

Post Simulation we have found values of pressure, temperature and velocity and to check the credibility of the values these results are compared with various visual results from previous researches or theoretically using flow properties across shockwaves.

**Meshing**

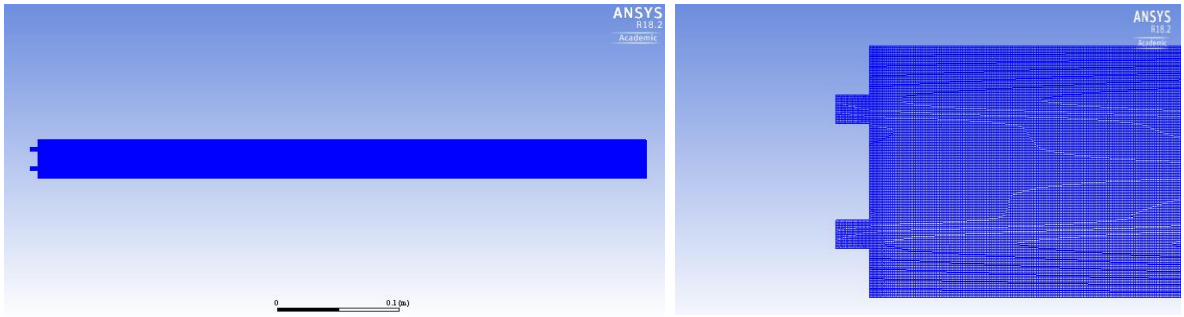


Figure 4: Simple Tube

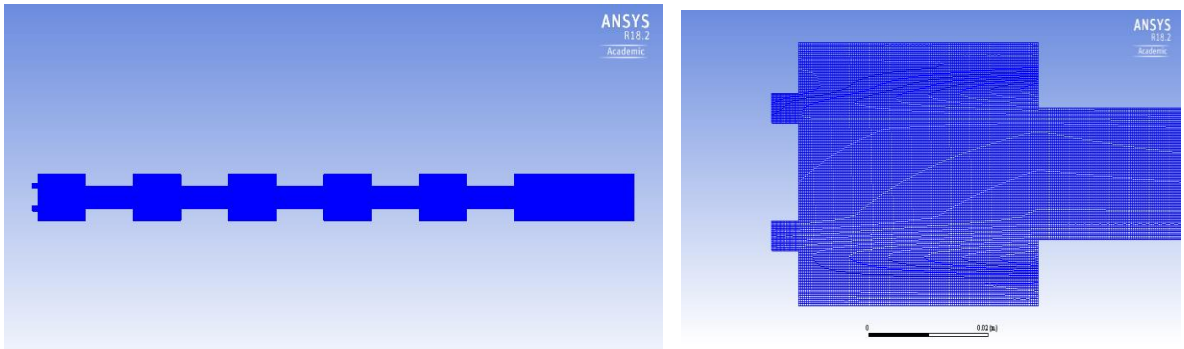


Figure 5: Shchelkin spiral Tube

**Mach Contours**

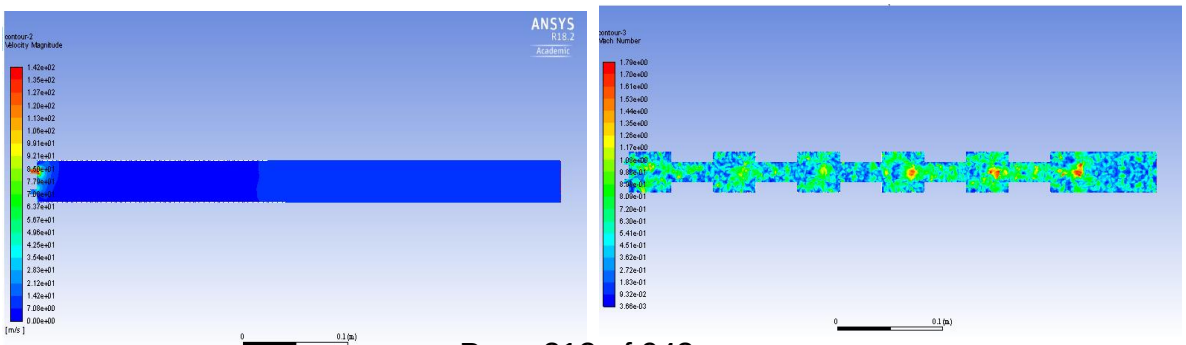

After studying the above Mach number contours we can deduce that Mach values obtained for Shchelkin spiral detonation tube is maximum and twice the values obtained for simple tube.

**Velocity Graphs**

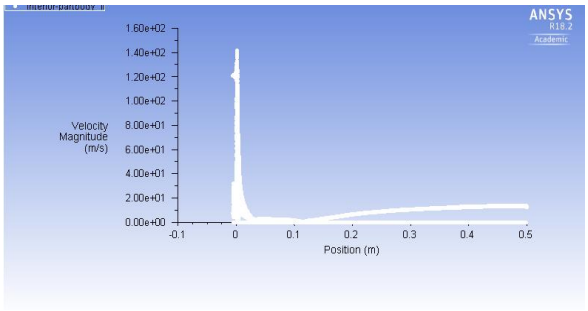


Figure 7:Velocity Graph for Shchelkin spiral Tube

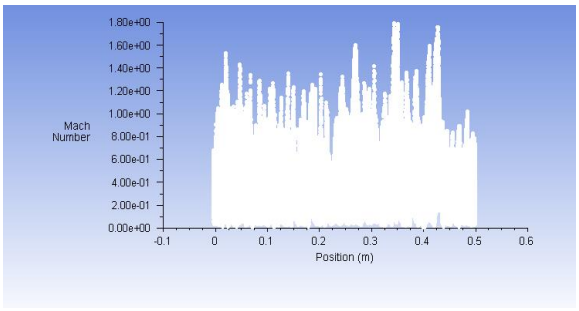


Figure 6: Velocity Graph for Simple Tube

The variation of velocity across the length of the tubes is shown in above graphs which tells us the formation of shockwaves and DDT transitions being carried out in PDE.

## 4. CONCLUSIONS

PDE works on a simple principle by detonating air-fuel mixture in combustion chamber of engine instead of deflagrating it. CFD Analysis have been done for a simple straight tube and Shchelkin spiral tube with 35 mm and 17.5 mm main tube diameters respectively. Potential of using Shchelkin spiral is seen through obtained values of velocity and Mach number. Also it is seen to be effective in achieving detonation rapidly.

## REFERENCES

[1] CHIPING LI and K. KAILASANATH "Detonation Transmission and Transition in Channels of Different Sizes" paper on proceedings of the combustion Institute, Volume 28, 2000/pp. 603–609.

[2] K. KAILASANATH and G. PATNAIK "PERFORMANCE ESTIMATES OF PULSED DETONATION ENGINES" paper on proceedings of the combustion Institute, Volume 28, 2000/pp. 595–601

[3] FICKETT W. and DAVIS, W.C, "Detonation Theory and Experiment", Dover Publications Inc., Mineola, New York, 1979; Fickett-Davis cycle: pp. 35-38.

[4] KUO, K.K, "Principles of Combustion," 2nd Ed., John Wiley and Sons, Inc., 2005.

[5] Li, J., LAI, W.H. and CHUNG, K., "Tube Diameter Effect on Deflagration to Detonation Transition of Propane-Oxygen Mixtures," Shock Waves, Vol. 16, No. 2, Dec. 2006, pp. 109-117.

[6] KANESHIGE, M. and SHEPHERD, J.E., "Detonation Database. Technical Report FM97-8," GALCIT, Jul. 1997. See also the electronic hypertext version at http://www.galcit.caltech.edu/detn_db/html/, accessed May 2008.

# Effect of eccentricity on the charging of a multi tube Latent Heat Storage System

**Gurpreet Singh Sodhi, P Muthukumar**
Department of Mechanical Engineering
Indian Institute of Technology, Guwahati, India
g.sodhi@iitg.ernet.in, pmkumar@iitg.ernet.in

## ABSTRACT

A numerical study has been conducted for investgating the effect of natural convection on the charging process of a high temperature latent heat storage system. A finite element method based simulation has been performed with the help of simulation tool COMSOL Multiphysics 4.3a. The phase change material (PCM) chosen for the study is $NaNO_3$ (melting temperature - 306 $^oC$), which is suitable for high temperature storage systems. Two dimensional simulations are performed for analyzing the effect of natural convection on the charging characteristics of the PCM and a comparison between concentric tube, eccentric tube and eccentric tube square shell configurations is made. It is observed that time required for melting the PCM is strongly dependent on the natural convection effect, which is found to improve by shifting the heat transfer fluid supply tubes of a multi tube square shell model, vertically downward. An improvement of charging time of 48 % is reported over the symmetric multi tube model.

**Key Words:** *Natural Convection; Phase Change Material; Effective Heat Capacity.*

## 1. INTRODUCTION

Thermal energy storage is one of the most effective solutions to overcome the problem of intermittant nature of solar energy. The solar energy extracted during the peak intensity of sunlight can be stored and will be utilised during night and overcast conditions. Thermal energy can be stored by three means namely: sensible, latent and thermochemical storage. Latent heat storage systems utilize the phase change of a material to store the energy. Generally, PCM's have a low thermal conductivity and therefore, to overcome the poor heat transfer rate during the phase change process in PCM, various heat transfer enhancement techniques have been explored. Although, significant amount of works has been carried out on heat transfer enhancement techniques like finned models (Rahimi et.al. [1]), adding high thermal conductivity metals to PCM (Cabeza et.al. [2]), multi-PCM (Yang et.al. [3]) and increasing number of tubes in multi tube LHSS (Niyas et.al. [4]), limited research works have been reported on focussing the effect of orientation of tubes on natural convection inside the PCM. In the present work, the effect of eccentricity in tube arrangement of multi tube systems on natural convection during the melting of PCM is studied and a multi tube heat exchanger design for latent heat storage is developed. More emphasis is laid on enhancement of heat transfer during melting. A 2-D simulation is performed to demonstrate the role of natural convection in the concentric tube, eccentric tube and eccentric tube square shell models. The results are later used to analyse the performance of a multi tube model. A new design with eccentricity in the bundle of tubes is proposed with improvements in natural convection for charging of Sodium Nitrate.

## 2. NUMERICAL MODELLING

A finite element method based simulation tool COMSOL Multiphysics 4.3a has been used to build the numerical model. The effective heat capacity method is used for incorporating the latent heat in the model. Time stepping is done by Euler Backward Difference formula and free tetrahedral mesh is used. A comparative analysis is done to study the effect of eccentricity on PCM melting in a tube-in-tube, eccentric tube and eccentric tube square shell models. The model dimensions are described in Fig. 1. The ratio of PCM volume to the total system volume is maintained as 0.8 in all three

configurations. The heat transfer during phase change occurs mostly due to natural convection and is weekly dominated by conduction.

### *2.1 Geometrical Configuration:*

The basic geometrical model is a tube in tube configuration with outer tube of diameter D = 50 mm. The other two models with their dimensions are also shown in Fig 1. Here $d_i$ =18.92 mm, $d_o$ = 22.23 mm, $D_1$ = 44.31 mm and e = 7.14 mm. The inner tube is of copper and the outer part is PCM. The natural convection is symmetric about vertical axes.

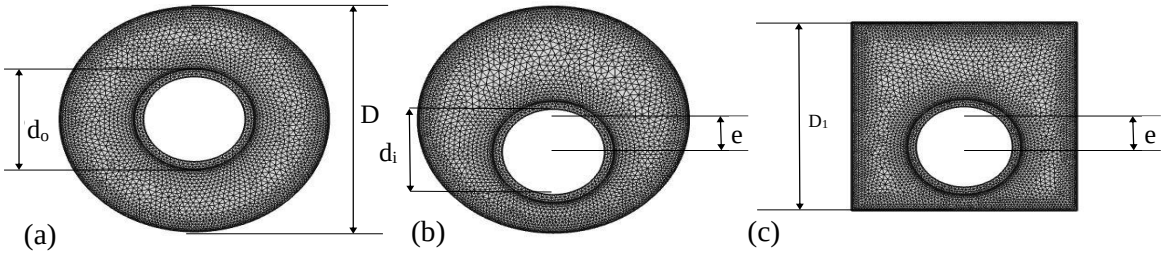


Figure 1. Three different configurations, (a) Concentric tube model, (b) Eccentric tube model and (c) Square shell eccentric tube model employed in the analysis.

Boundary Conditions: $T_{initial}$ = 559.15 K, $T_{wall}$ = 599.15 K (given at inner wall of the copper tube).

Basic assumptions considered for numerical modelling are as follows:

- PCM is considered to be Newtonian fluid in liquid phase.
- Fluid flow in the PCM is incompressible and laminar.
- Density variation during phase change is taken into account by using Boussinesq approximation

### *2.2 Governing Equations:*

Continuity equation - $$\nabla \cdot \vec{V} = 0 \qquad (2.1)$$

Momentum Equation - $$\frac{D\vec{V}}{Dt} + \vec{V}.\nabla\vec{V} = \frac{1}{\rho_f}(-\nabla p + \mu\nabla^2\vec{V} + \rho\vec{g}\beta(T - T_m)) + \vec{S} \qquad (2.2)$$

Energy Equation - $$\rho_f C_{pf}\frac{DT}{Dt} = \nabla\cdot\left(k_f \nabla T\right) \qquad (2.3)$$

$$\vec{S} = \frac{-(1-\theta)^2}{\theta^3 + \varepsilon} A_{mush}\vec{V} \qquad (2.4)$$

Where $\vec{S}$ is the source term added to modify the momentum equation in the mushy zone. Here $A_{mush}$ is the mushy zone constant and its value is set to $10^5$. $\varepsilon$ is a small constant with value 0.001 to avoid the division by 0 and $\theta$ is the melt fraction varying from 0 to 1 within the melting range. The modelling is done with the help of effective heat capacity method, wherein, modified heat capacity ($C_{p,eff}$) formula shown in Eq. 2.5 is considered for phase change. It is included in order to incorporate the effect of latent heat during a constant temperature process.

$$C_{p,pcm} = \begin{Bmatrix} C_{ps},\ for\, T < T_1 \\ C_{p,eff},\ for\, T_1 \le T \le T_2 \\ C_{pl},\ T > T_2 \end{Bmatrix} \qquad (2.5)$$

$$C_{p,eff} = \frac{C_{ps,pcm} + C_{pl,pcm}}{2} + \frac{H_{fg}}{\Delta T_m} \qquad (2.6)$$

where $C_{ps}$ and $C_{pl}$ are the heat capacity values in the solid state and the liquid state.

## 3. RESULTS AND DISCUSSIONS

After carefully visualizing the melt fraction contours at different time intervals for the three different configurations shown in Fig. 2, it is seen that the melting takes place in a similar fashion for the eccentric tube cylindrical and square shell models, such that it is independent of the outer

| Table 1. Thermophysical properties of PCM [5] | |
|---|---|
| Latent Heat (kJ/kg) | 178 |
| Thermal Conductivity (W/m/K) | 0.5(Solid),0.514(Liquid) |
| Melting Point ($^oC$) | 306 |
| Density (kg/m$^3$) | 2260(Solid),1908(Liquid) |
| Specific Heat (kJ/kg/K) | 1.5(Solid),1.7(Liquid) |

| Table 2. Model specifications | |
|---|---|
| Number of tubes | 16 |
| Tube inner diameter(mm) | 8.5 |
| Tube outer diameter(mm) | 12.7 |
| PCM S.A./Total S.A. | 0.947 |
| Square Container height(mm) | 198.7 |

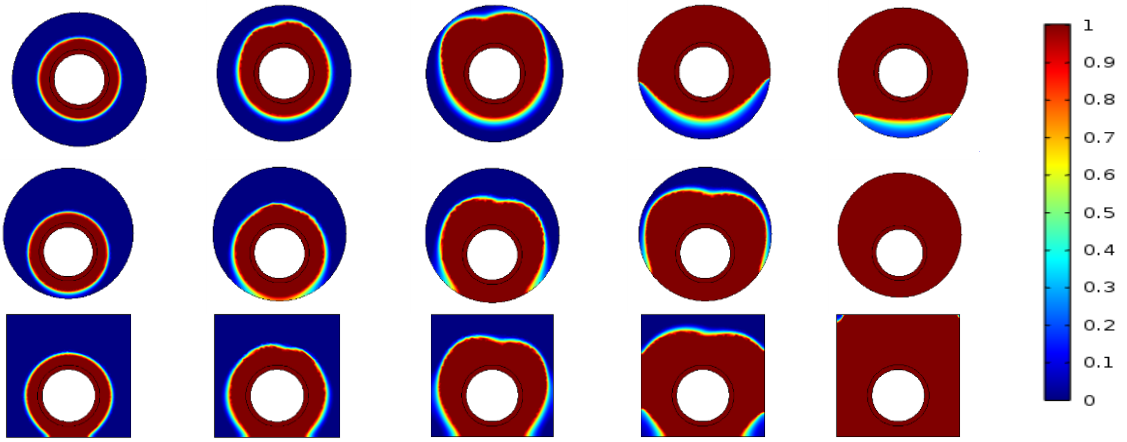


Figure 2: Comparison of melt fraction contours for three configurations after 10,20,30,40 and 60 min.

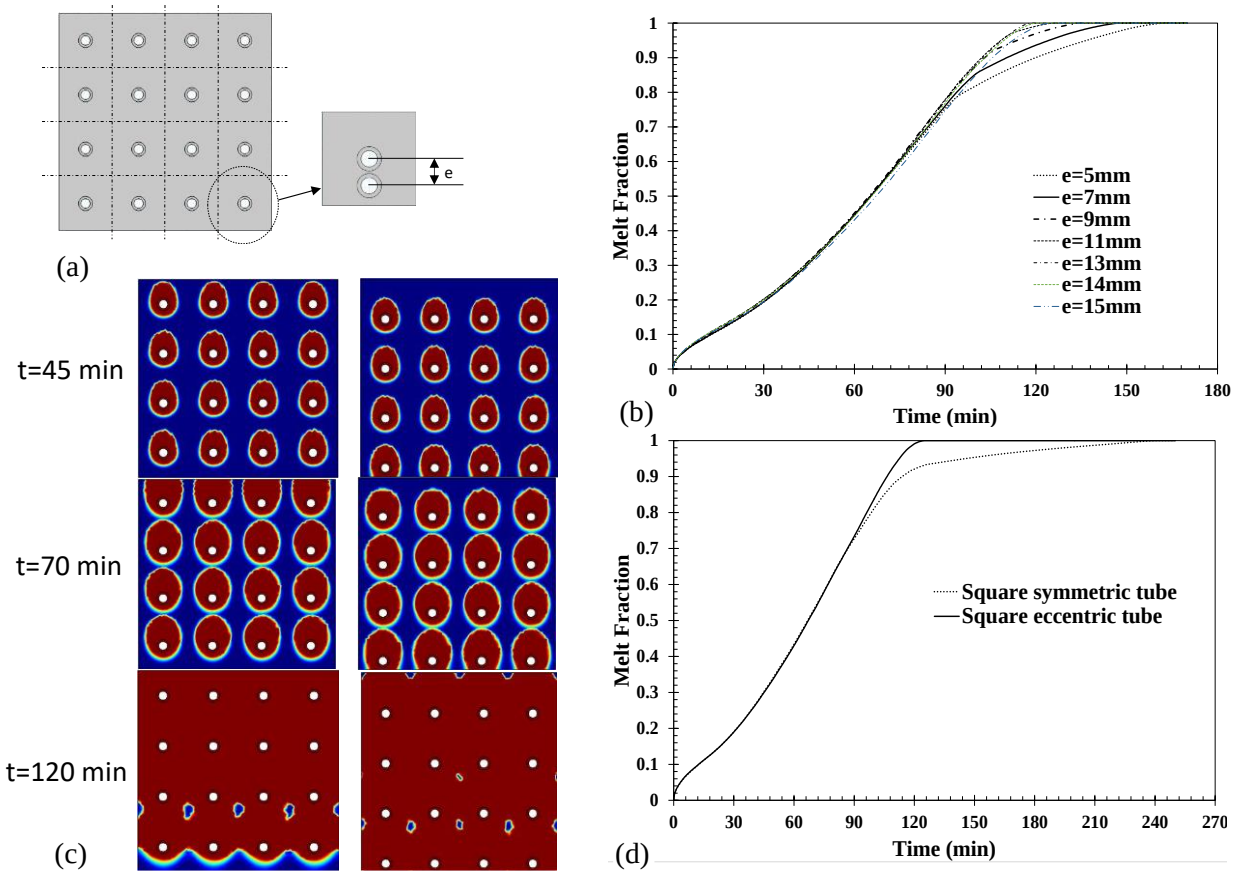


Figure 3: (a)2D 16 tube square shell model, (b)effect of eccentricity in single tube, (c) Melting contours comparison and (d) Melt fraction variation with time for concentric and eccentric 16 tube square shell models

container shape. Initially, natural convection heat transfer emerging from tube surfaces can be seen in all three configurations. At t = 60 min, some solid PCM is left at the bottom part of the concentric tube model, where the melt fraction is approximately 0.8. Whereas, in both the inner eccentric tube models, there is no solid PCM left at the bottom portion at this time and PCM is found to be melted completely. This happens because both upper and bottom portions of the model are melted simultaneously due to eccentricity. The similar results are observed for a multi tube model.

A 16 tube square shell model shown in Fig. 3 (a) is designed for a storage capacity of 10 MJ. The thermophysical properties of PCM and the model specifications for the 16 tube model are described in Tables 1 and 2. The eccentricity in tubes is decided by considering 16 equal domains in the multi tube model. Since the corner domains are surrounded by walls on two sides (which is at initial temperature of $T_{initial}$ = 559.15 K) , they have least probability for heat transfer. The effect of eccentricity of tube on melt fraction and heat transfer in a corner domain is shown in Fig. 3(b). The optimized value of eccentricity with e = 13.5 mm is chosen. The melting contours and variation in melt fraction with time for the symmetrical tube and eccentric tube square shell models are shown in Fig. 3(c) and Fig. 3(d). It can be observed that in the symmetric 16 tube model, the melting of PCM is very slow at the end (after approximately 80% of melting) due to conduction phenomenon alone. Whereas, in the eccentric 16 tube model, both conduction and natural convection occur simultaneously from the starting of charging and therefore, there is overall enhancement in heat transfer in the PCM domain which melts the PCM faster and the overall charging time for the PCM reduces.

## 4. CONCLUSIONS

A 2-D thermal model to observe the behavior of natural convection during melting is presented and a multi tube latent heat storage model is developed based on this study. The following conclusions are drawn from the present study:

- Charging is slower in concentric tube model due to delay in heat transfer at the bottom part of the model because of conduction heat tranfer at the end, whereas simultaneous melting in bottom and top portions of eccentric tube models lead to enhanced heat transfer and faster melting.
- Charging is natural convection dominated. Therefore, in order to reduce the melting time, natural convection has to be utilized completely.
- The symmetric and eccentric 16 tube square shell models are melted completely in 126 min and 243 min, respectively with an overall reduction of 48% in charging time.

The present study provides useful guidelines for the design and development of large scale latent heat stroage systems with enhanced heat transfer characteristics.

## REFERENCES

[1] M. Rahimi, A. A. Ranjbar, D. D. Ganji, K. Sedighi, M. J. Hosseini, and R. Bahrampoury, "Analysis of geometrical and operational parameters of PCM in a fin and tube heat exchanger," *Int. Commun. Heat Mass Transf.*, vol. 53, pp. 109–115, 2014.

[2] L. F. Cabeza, H. Mehling, S. Hiebler, and F. Ziegler, "Heat transfer enhancement in water when used as PCM in thermal energy storage," *Appl. Therm. Eng.*, vol. 22, no. 10, pp. 1141–1151, 2002.

[3] L. Yang, X. Zhang, and G. Xu, "Thermal performance of a solar storage packed bed using spherical capsules filled with PCM having different melting points," *Energy Build.*, vol. 68, no. PART B, pp. 639–646, 2014.

[4] Niyas H, Prasad S, and Muthukumar P, "Performance investigation of a lab – scale latent heat storage prototype – Numerical results," *Energy Convers. Manag.*, vol. 135, pp. 188–199, 2017.

[5] Tao Y.B, Lin C.H and He Y.L,"Preparation and thermal properties characterization of carbonate salt/carbon nanomaterial composite PCM," vol. 97, pp.103–110, 2015.

Fifth International Conference on Computational Methods for Thermal Problems
THERMACOMP2018, July 9-11, 2018, Indian Institute of Science, Bangalore, INDIA
*N. Massarotti, P. Nithiarasu, Pradip Dutta and C. Ranganyakalu (Eds.)*

# Double Diffusive Mixed Convection in a Partially Heated Square Cavity with Various Wall Speed Ratios

**Samrat Hansda[1], Swapan K Pandit[2]**

Integrated Science Education & Research Centre (ISERC), Visva-bharati, Santiniketan-731 235, India,
Email: samrathansda143@gmail.com [1], swapankumar.pandit@visva-bharati.ac.in [2]

## ABSTRACT

In this paper, we have numerically simulated double diffusive mixed convection in a double lid-driven with partially heated square cavity. A portion of the two vertical walls are considered as hot zone while the rest portions of the vertical walls are considered to be adiabatic and impermeable. Both the top and bottom walls of the cavity are maintained at constant cold temperature and concentration. The bottom and top walls of the cavity can move in the same or opposite directions with speed ratio $\lambda$. The governing Navier-Stokes (N-S) equations in stream function-vorticity form with energy and the concentration equations representing incompressible viscous flows are solved by adopting a compact scheme. The numerical results are reported for the effect of Richardson number ( $Ri$ ), Lewis number ( $Le$ ), walls speed ratio ( $\lambda$ ), buoyancy ratio ( $N$ ) and Grashof number ( $Gr$ ).

**Key Words:** *Double Diffusion, Mixed Convection, Heat and Mass Transfer, Wall Speed Ratios, Partial Heating.*

## 1. INTRODUCTION

Over the last few decades, double diffusive mixed convection has been studied in rectangular cavity to observe mass transfer with heat transfer and fluid flow topology. Fluid flows generated by combining thermal and solutal buoyancy forces are known as double diffusive convection. It occurs in a very wide range of fields such as oceanography, astrophysics, geology, biology, and chemical processes, as well as in many engineering applications such as solar ponds, natural gas storage tanks, crystal manufacturing, electronic equipment cooling, solar energy collectors, and nuclear reactors, solar technologies, safety aspects of gas cooled reactors, crystal growth in liquids and food processing and metal solidification processes. Heat and fluid flows due to shear force is a fundamental problem in heat transfer and fluid mechanics. Nithyadevi and Yang [1] simulated double diffusive natural convection of water filled in a partially heated square enclosure with Soret and Dufour. They found that the increase in the thermal Rayleigh number leads to increase in heat and mass transfer rate irrespective of the thermal source section. Arbin et al. [2] studied the double diffusive natural convection in an open top square cavity, partially heated and salted from the side, via the heatline approach. They have concluded that the heat and mass transfer mechanisms are strongly influenced by the heater segment length. Higher values of $Le$ will decrease the heat transfer rates but will enhance the mass transfer rates for both flows (opposing and aiding) through the cavity. Very recently, the wall speed ratio in a both sided lid-driven cavity, achieves the higher heat transfer rate [3]. To the best of our knowledge, double diffusive convection (ddc) with different wall speed ratios has not been studied so far. Our aim is to study numerically ddc depending on the different location of heat sources.

## 2. MAIN BODY

The physical domain under investigation, is a two-dimensional (2D) partially heated lid-driven square cavity. A portion of length $H$ of both the vertical walls are thermally and solutally active, while remaining portions of vertical walls are taken to be adiabatic and impermeable as shown in Figure 1. The top and bottom walls of the cavity are maintained at constant cold temperature and low concentration. These walls of the cavity can slide in the same or opposite direction with various velocity ratio $\lambda$. The left and right walls are kept stationary. Two different cases are considered depending on the locations of heat and concentration sources as shown in Figure 1.

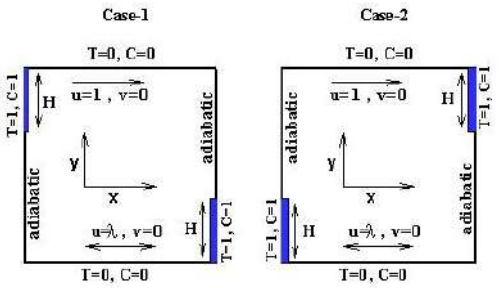


FIGURE 1: Physical configuration and coordinate system

The governing equations describing the incompressible viscous flows in a two-sided lid-driven cavity are in non-dimensional streamfunction $(\psi)$, vorticity $(\varsigma)$, temperature and concentration as follows:

$$-\left(\frac{\partial^2\psi}{\partial x^2}+\frac{\partial^2\psi}{\partial y^2}\right)=\varsigma \quad (1)$$

$$\frac{\partial\varsigma}{\partial t}-\frac{\partial^2\varsigma}{\partial x^2}-\frac{\partial^2\varsigma}{\partial y^2}+u\,\mathrm{Re}\frac{\partial\varsigma}{\partial x}+v\,\mathrm{Re}\frac{\partial\varsigma}{\partial y}=\mathrm{Re}\,Ri\left(\frac{\partial T}{\partial x}+N\frac{\partial C}{\partial x}\right) \quad (2)$$

$$\frac{\partial T}{\partial t}-\frac{\partial^2 T}{\partial x^2}-\frac{\partial^2 T}{\partial y^2}+u\,\mathrm{Re}\,\mathrm{Pr}\frac{\partial T}{\partial x}+v\,\mathrm{Re}\,\mathrm{Pr}\frac{\partial T}{\partial y}=0 \quad (3)$$

$$\frac{\partial C}{\partial t}-\frac{\partial^2 C}{\partial x^2}-\frac{\partial^2 C}{\partial y^2}+\mathrm{Re}\,\mathrm{Pr}\,Le\frac{\partial C}{\partial x}+\mathrm{Re}\,\mathrm{Pr}\,Le\frac{\partial C}{\partial y}=0 \quad (4)$$

where $u,v$ are the velocity components along $x$ & $y$ directions, $Le\left(=\frac{\alpha}{D}\right)$ is the Lewis number, with $D$ being the solutal (concentration) diffusivity, $Re\left(=\frac{V_0 L}{\nu}\right)$ is the Reynolds number, with $\nu$ being the kinematic viscosity and $V_0$ being reference velocity , Pr is the Prandtl number, Gr is the Grashof number, Ri is the Richardson number defined as $Ri\left(=\frac{Gr}{Re^2}\right)$, N being Buoyancy ratio number.

The dimensionless boundary conditions are as follows:

Case-1:

$u=1, v=0$ and $T=0, C=0$ for $y=1$ and $0\le x\le 1$,

$u=\lambda, v=0$ and $T=0, C=0$ for $y=0$ and $0\le x\le 1$,

$u=0=v$ and $\frac{\partial T}{\partial x}=0=\frac{\partial C}{\partial x}$ for $x=0$ and $0\le y\le 1-H$ and $T=1=C$ for $x=0$ and $1-H\le x\le 1$,

$u=0=v$ and $T=1=C$ for $x=1$ and $0\le y\le H$ and $\frac{\partial T}{\partial x}=0=\frac{\partial C}{\partial x}$ for $x=1$ and $H\le y\le 1$.

Case-2:

$u=1, v=0$ and $T=0, C=0$ for $y=1$ and $0\le x\le 1$,

$u=\lambda, v=0$ and $T=0, C=0$ for $y=0$ and $0\le x\le 1$,

$u=0=v$ and $T=1=C$ for $x=0$ and $0\le y\le H$, $\frac{\partial T}{\partial x}=0=\frac{\partial C}{\partial x}$ for $x=0$ and $H\le y\le 1$,

$u=0=v$ and $\frac{\partial T}{\partial x}=0=\frac{\partial C}{\partial x}$ for $x=1$ and $0\le y\le 1-H$, $T=1=C$ for $x=1$ and $1-H\le x\le 1$.

| $\lambda$ | -2.0 | -1.0 | -0.5 | 0.5 | 1.0 | 2.0 |
|---|---|---|---|---|---|---|
| Jmai et al [5] | 0.051 | 0.061 | 0.066 | 0.077 | 0.091 | 0.16 |
| Present study | 0.052 | 0.061 | 0.066 | 0.076 | 0.089 | 0.16 |

TABLE 1: Comparison of maximum value of the streamfunction between the Jmai et al. [3] and present study for $Ri=100$.

## 3. RESULTS

To validate the numerical accuracy of our inhouse computer code, we have computed the results of the problem described as Jmai *et. al.* [3]. The comparison is made using the following dimensionless parameters $\mathrm{Pr}=6.2$, $Ri=100$, $Ra=10^4$. The maximum values of the streamfunction are presented in Table 1. These results clearly show a good agreement between Jmai et al. [3] and our computed result. The working fluid is chosen with Prandtl number Pr =0.71 and is fixed throughout the study. In the present study, Grashof number is fixed at Gr =$10^4$. We

have discretized the governing equations by adopting the compact scheme proposed in [4, 5]. The resultant algebraic equations are solved using BiCGStab solver.

In figure 2, we have computed the numerical result for case-1 at $Ri = 0.1$ and $10$ respectively. In the upper half, the shear force and the buoyancy force are in the same direction while in the lower half these two forces act in the same direction for $\lambda < 0$ and act in the opposite direction for $\lambda > 0$ .

.

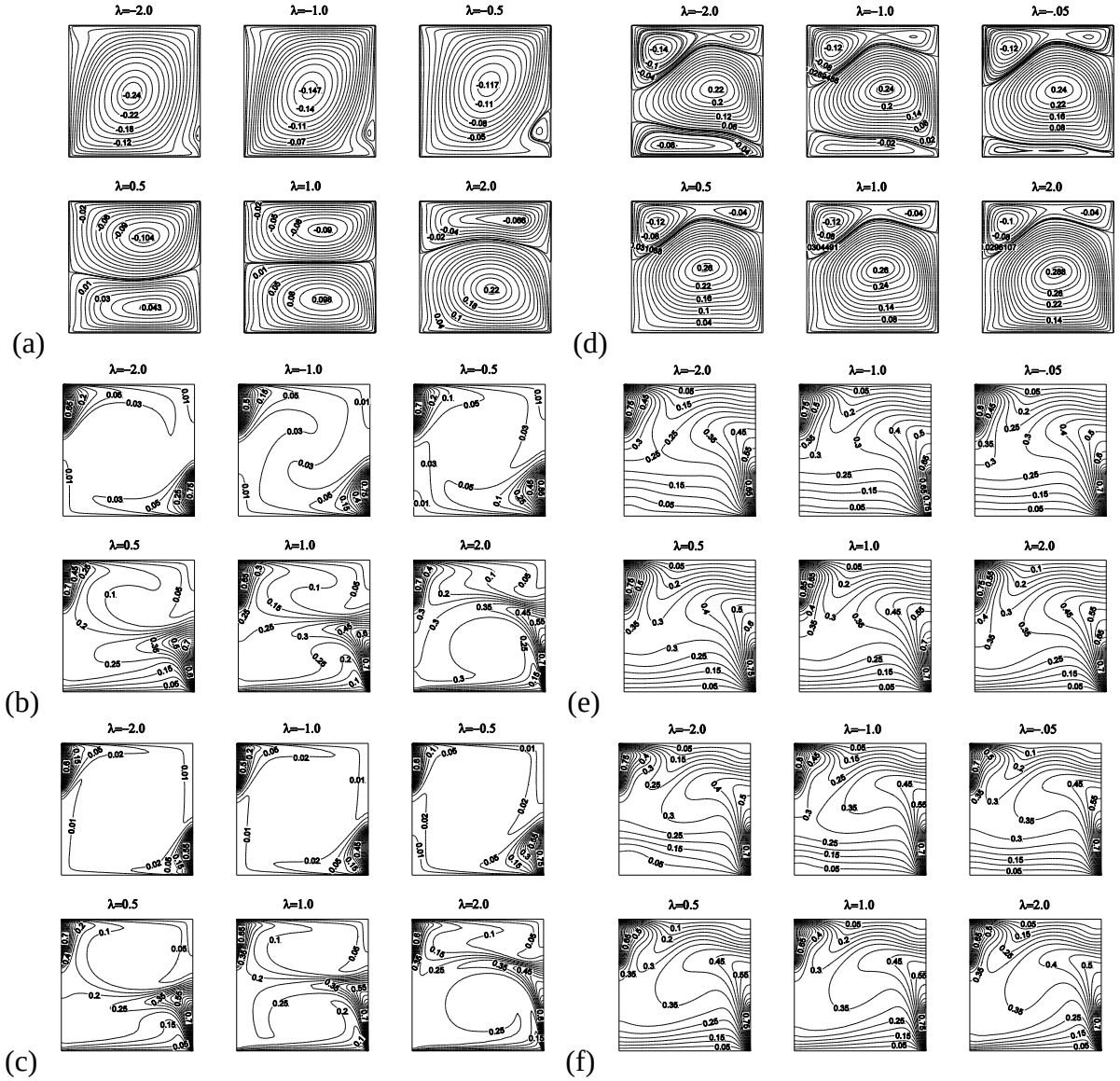


FIGURE 2. Case-1: Streamline (a,d), temperature (b,e) and concentration (c,f) contours for different wall speed ratios with $Gr = 10^4,\ Le = 2,\ N = 5$ and for Ri=0.1 and 10.0.

It is seen that at $Ri = 0.1$ for opposite motion of the bottom and top wall, a large clockwise circulating vortex occupying almost the whole part of the cavity is generated. The centre of the vortex is at the geometric centre of the cavity. As in the lid driven cavity the streamline are perturbed in the top left corner and bottom right corner of the cavity. As $\lambda$ is increasing, the size of the bottom right corner increases. For lid motion, in the same direction, it is seen that two counter rotating vortices are formed. The shape and size of the vortices are very sensitive to the change of the parameters $Ri$ and $\lambda$. It is also seen that the temperature and concentration contours are uniformly distributed throughout the cavity. In figure 3 for case-2, we have considered the physical domain as the mirror image of case-1. It is seen that the flow features are not mirror image of case-1. In the upper half of the cavity, the shear force and the buoyancy force are acting on the opposite direction while in lower half of the cavity for $\lambda > 0$ both the shear and the buoyancy forces are acting in same direction, while for $\lambda < 0$, they are in the opposite direction. In this case also flow patterns are sensitive to the variation of the parameters $\lambda$ and $Ri$.

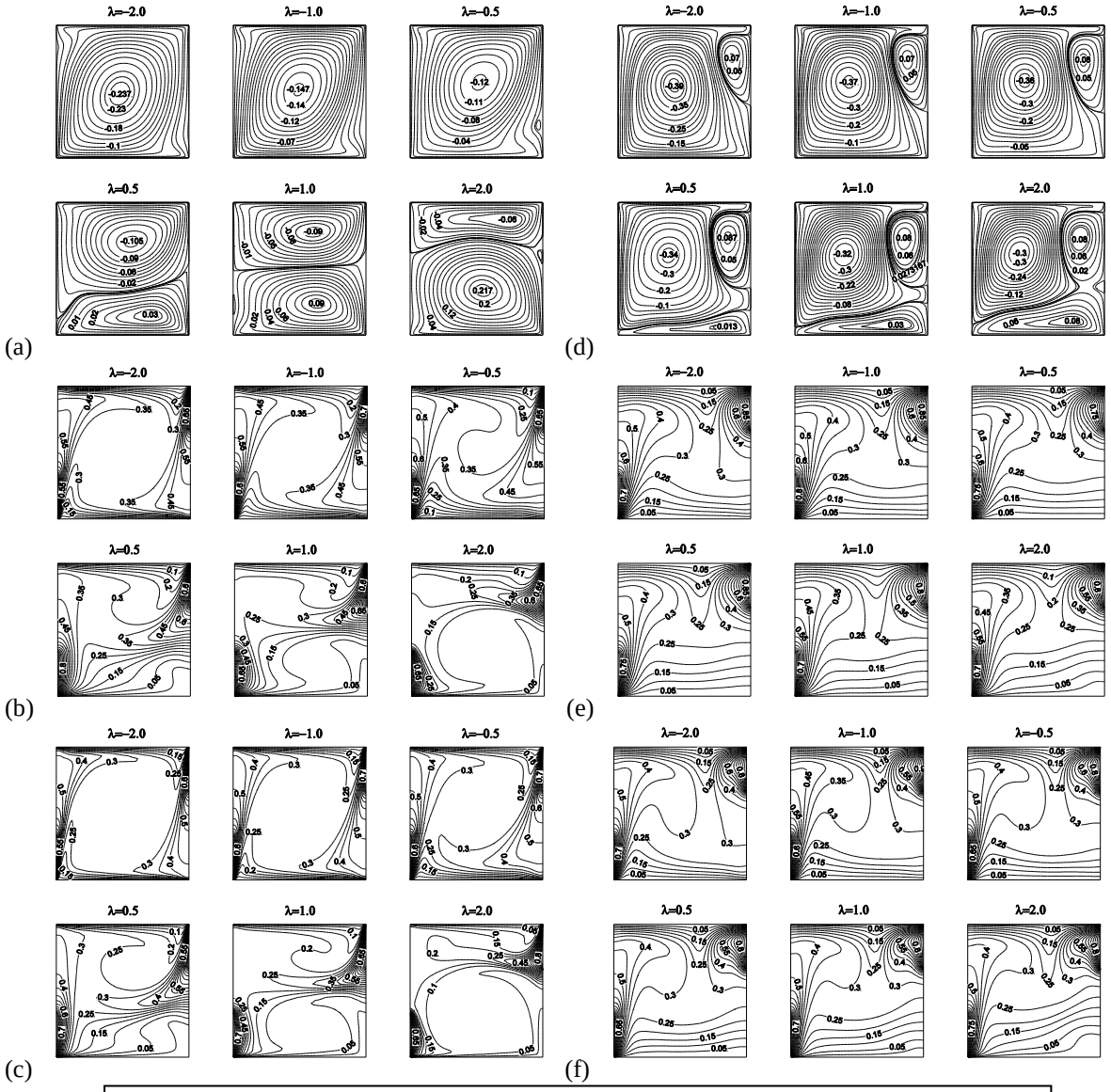


FIGURE 3. Case-2: Streamline (a,d), temperature (b,e) and concentration (c,f) contours for different wall speed ratios with $Gr = 10^4$, $Le = 2$, $N = 5$ and for Ri=0.1 and 10.0.

## 4. CONCLUSIONS

In this paper, we have carried out numerical simulation of double diffusive mixed convection in a double lid-driven with partially heated square cavity. The speed ratio λ influences significantly the fluid flow as well as the temperature distribution and also concentration distribution within the cavity. The results shows that *Ri* and λ play a significant role in the heat and mass transfer for both the cases.

## REFERENCES

[1] N. Nithyadevi and R. Yang, Double diffusive natural convection in a partially heated enclosure with Soret and Dufour effects, Int. J.Heat Fluid Flow, 30, 902-910, 2009.
[2] N. Arbin, H. Saleh, I. Hashim and A. J. Chamkha, Numerical investigation of double-diffusive convection in an open cavity with partially heated wall via heat line approach, Int. J. Therm. Sci., 100, 169-184, 2016.
[3] R. Jmai, B. Ben-Beya and T. Lili, Numerical analysis of mixed convection at various walls speed ratios in two-sided lid-driven cavity partially heated and filled with nanofluid, J. Mol. Liq., 221, 691-713, 2016.
[4] S. K. Pandit, J. C. Kalita and D. C. Dalal, A transient higher order compact schemes for incompressible viscous flows on geometries beyond rectangular, J. Comput. Phys., 225, 1100-1124, 2007.
[5] S. K. Pandit and A. Chattopadhyay, A robust higher order compact scheme for solving general second order partial differential equation with derivative source terms on nonuniform curvilinear meshes, Computers & Mathematics with Applications, 74(6), 1414-1434, 2016.

Fifth International Conference on Computational Methods for Thermal Problems
THERMACOMP2018, July 9-11, 2018, Indian Institute of Science, Bangalore, INDIA
*N. Massarotti, P. Nithiarasu, Pradip Dutta and C. Ranganyakalu (Eds.)*

# HEAT TRANSFER OF GASEOUS FLOW THROUGH MICRO-ANNULUS IN SLIP REGIME

**Hari Mohan Kushwaha, Amit Agrawal**
Indian Institute of Technology Bombay, Powai-400076, Mumbai, Maharashtra,
hmkushwaha@gmail.com, amit.agrawal@iitb.ac.in

## ABSTRACT

In this paper, an analytical investigation on convection heat transfer for hydrodynamically and thermally fully developed flow through a micro-annulus, is presented. The effect of velocity slip, temperature jump at the wall and viscous dissipation are considered. The case of uniform heat flux at the outer wall and adiabatic inner wall case is considered. Here, closed form expressions are obtained for the non-dimensional temperature field and Nusselt number as a function of Knudsen number and Brinkman number.

**Key Words:** *Brinkman number, Knudsen number, Nusselt number, Temperature jump, Velocity slip.*

## 1. INTRODUCTION

The recent technological advancements in microdevices that ensure the ease of everyday life enhance the significance of heat transfer analysis in such microdevices. Micron size mechanical devices are today encountered both commercial and scientific applications. Design and fabrication has increased the need of accurately understanding the flow physics and heat transfer characteristics in such microdevices. At the microscale, the ratio of surface area to volume is much larger as compared to the macroscale. Microscale flows are usually characterized based on a non-dimensional parameter, Knudsen number ($Kn$), defined as the ratio of mean free path ($\lambda$) to the characteristic dimension ($D_h$) of the microdevice. Generally, the Knudsen number encountered in classic microdevices is between $10^{-3}$ and $10^{-1}$, which is the range of slip flow regime. Various studies have been carried out to model the fluid flow in microdevices and include effects such as: rarefaction, viscous dissipation, axial conduction, roughness, and shear work at the wall. Avci and Aydin [1] reported analytical solution for non-dimensional temperature distribution and Nusselt number for a concentric annular duct with different thermal boundary conditions. In another study, Avci and Aydin [2] analytically studied forced convection heat transfer in hydrodynamically and thermally fully developed flow of viscous dissipating gas in an annular micro-duct between two concentric micro-cylinders. The aim of the present study is to analytically investigate the convective heat transfer in a micro-annulus in the fully developed region by employing uniform heat flux at the outer wall and inner wall adiabatic. The combined effect of rarefaction and viscous dissipation on the bulk temperature and Nusselt number are also studied. Closed form expressions for the non-dimensional temperature distribution and Nusselt number are obtained.

## 2. THEORETICAL ANALYSIS

The fluid flow is assumed to be laminar, steady, Newtonian, incompressible, fully developed both hydrodynamically and thermally. Thermophysical properties are assumed to be constant. Axial conduction is assumed to be negligible both in the fluid and wall.

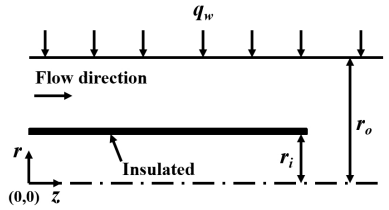


FIGURE 1. Schematic of the flow domain

*Governing equations and boundary conditions*

Under the above assumptions the momentum and energy equations can be written as

$$\frac{1}{r}\frac{d}{dr}\left(r\frac{du}{dr}\right)=\frac{1}{\mu}\frac{dp}{dz}=\text{const} \tag{1}$$

$$u\frac{\partial T}{\partial z}=\frac{\alpha}{r}\frac{\partial}{\partial r}\left(r\frac{\partial T}{\partial r}\right)+\frac{\nu}{c_p}\left(\frac{du}{dr}\right)^2 \tag{2}$$

$$(i)\ r=r_i,\ u=u_s=\lambda\left(\frac{du}{dr}\right)_{r=r_i} \quad (ii)\ r=r_o,\ u=u_s=-\lambda\left(\frac{du}{dr}\right)_{r=r_o} \tag{3}$$

The velocity slip and temperature jump boundary conditions at the wall are

$$(i)\ u_s=-\frac{2-\sigma_v}{\sigma_v}\lambda\left.\frac{du}{dr}\right|_{r=r_o} \quad \text{(ii)}\ T_s-T_w=-\frac{2-\sigma_T}{\sigma_T}\frac{2\gamma}{\gamma+1}\frac{\lambda}{\text{Pr}}\left.\frac{\partial T}{\partial r}\right|_{r=r_o} \tag{4}$$

The non-dimensional parameters are: $R=\frac{r}{r_o},\ r^*=\frac{r_i}{r_o},\ U=\frac{u}{u_m},\ \theta=\frac{T-T_s}{q_w r_o/k},\ \theta_m=\frac{T_m-T_w}{q_w r_o/k}$ (5)

From Eqns. (1), (3) and (5) the velocity distribution is obtained as [2]: $U=2\left[\frac{1-R^2+2r_m^{*2}\ln R+A}{B}\right]$ (6)

Where, $A=4Kn\left(1-r^*\right)\left(1-r_m^{*2}\right)$ and $B=\left(1-r^{*2}-4r_m^{*2}\left(\frac{1}{2}+\frac{r^{*2}}{1-r^{*2}}\ln r^*\right)+8Kn\left(1-r^*\right)\left(1-r_m^{*2}\right)\right)$

Here, $Kn$ is Knudsen number and $r_m^*$ designates the dimensionless radius where the maximum velocity occurs at $\left(\frac{du}{dr}\right)=0$ and is given as [2]: $r_m^*=\frac{r_m}{r_o}=\left(\frac{\left(1-r^{*2}\right)\left(1+4Kn\right)}{2\ln\left(\frac{1}{r^*}\right)-4Kn\left(\frac{r^{*2}-1}{r^*}\right)}\right)^{1/2}$ (7)

The second term in the right hand side of Eq. (2) is the viscous dissipation term. A constant heat flux condition is applied at the wall, which states that $k\left.\frac{\partial T}{\partial r}\right|_{r=r_o}=q_w$ (8)

Where, $q_w$ is positive when its direction is to the fluid (heated case), otherwise it is negative. For the uniform wall heat flux case, the first term in the left side of Eq. (2) is given by [1, 2]

$$\frac{\partial T}{\partial z}=\frac{dT_w}{dz}=\frac{dT_s}{dz} \tag{9}$$

Using Eqns. (5), (6), (8) and (9), Eq. (2) in non-dimensional form can be expressed as [1, 2]

$$\frac{1}{R}\frac{d}{dR}\left(R\frac{d\theta}{dR}\right)=aU-Br\left(\frac{dU}{dR}\right)^2 \tag{10}$$

where, $a=\left(\frac{u_m k r_o}{\alpha q_w}\frac{dT_s}{dz}\right)$ and $Br\left(=\frac{\mu u_m^2}{q_w r_o}\right)$ is the Brinkman number.

The non-dimensional thermal boundary conditions are given by

$$(i)\ \theta = 0 \text{ at } R = 1 \quad (ii)\ \frac{d\theta}{dR} = 1 \text{ at } R = 1 \text{ and } (iii)\ \frac{d\theta}{dR} = 1 \text{ at } R = r^* \quad (11)$$

The solution of Eq. (10) by using the boundary conditions (Eq. 11), is obtained as:

$$\theta(R) = \frac{T - T_s}{q_w r_o / k} = \frac{a}{2B}\left[-\frac{3}{4} - A + 2r_m^{*2} + R^2\left(1 + A - 2r_m^{*2} - \frac{R^2}{4}\right) - \ln R\left(\left(1 + 2A - 2r_m^{*2}\left(1 + R^2\right)\right)\right)\right]$$

$$+\frac{Br}{B^2}\left[\left(1 - R^2\right)\left(1 + R^2 - 8r_m^{*2}\right) + 4\ln R\left(1 - 4r_m^{*2}\right) - 8r_m^{*4}\left(\ln R\right)^2\right] + \ln R \quad (12)$$

$$\text{where, } a = \left[\frac{-2B^2 + 8Br\left(r^{*2} - 1\right)\left(1 + r^{*2} - 4r_m^{*2}\right) + 32Brr_m^{*4}\ln r^*}{B\left(\left(1 + 2A - 2r_m^{*2} - r^{*2}\right)\left(r^{*2} - 1\right) + 4r_m^{*2}r^{*2}\ln r^*\right)}\right] \quad (13)$$

The non-dimensional temperature distribution with temperature jump at the wall is given by

$$\theta^*(R) = \frac{T - T_s}{q_w r_o / k} = \frac{a}{2B}\left[-\frac{3}{4} - A + 2r_m^{*2} + R^2\left(1 + A - 2r_m^{*2} - \frac{R^2}{4}\right) - \ln R\left(\left(1 + 2A - 2r_m^{*2}\left(1 + R^2\right)\right)\right)\right]$$

$$+\frac{Br}{B^2}\left[\left(1 - R^2\right)\left(1 + R^2 - 8r_m^{*2}\right) + 4\ln R\left(1 - 4r_m^{*2}\right) - 8r_m^{*4}\left(\ln R\right)^2\right] + \ln R - \frac{4\gamma}{\gamma + 1}\frac{Kn}{\Pr}\left(1 - r^*\right) \quad (14)$$

The bulk mean temperature is defined as: $T_m = \dfrac{\int_{A_c} \rho c_p u T dA}{\int_{A_c} \rho c_p u dA}$ (15)

$$\theta_m^* = \frac{4\left(p_1 + p_2 + p_3\right)}{\left(1 + A - 2r_m^{*2}\right)} - \frac{4Kn\gamma}{\Pr\left(\gamma + 1\right)}\left(1 - r^*\right) \quad (16)$$

Where,

$$p_1 = \frac{a}{2B}\left(\frac{(1+2A-2r_m^{*2})(-3-4A+8r_m^{*2})}{8} + \frac{(1+A-2r_m^{*2})(4+12A-6r_m^{*2})}{48} - \frac{(3+12A-4r_m^{*2})}{288} - \frac{2r_m^{*2}(-10-18A+18r_m^{*2})}{288}\right)$$

$$p_2 = \frac{Br}{B^2}\left(\frac{(1-8r_m^{*2})(1+2A-2r_m^{*2})}{4} - \frac{(3+12A-4r_m^{*2})}{72} + \frac{24r_m^{*2}(2+6A-3r_m^{*2})}{72} + \frac{(1-4r_m^{*2})(-3-4A+8r_m^{*2})}{4} - \frac{r_m^{*4}(7+8A-24r_m^{*2})}{4}\right)$$

$$p_3 = \frac{(-3-4A+8r_m^{*2})}{16}$$

The Nusselt number is defined as: $Nu = \dfrac{q_w D_h}{k\left(T_w - T_m\right)} = -\dfrac{2}{\theta_m^*}\left(1 - r^*\right)$ (17)

## 3. RESULTS

Figure 2 describes the non-dimensional velocity profiles for different values of Knudsen number. Figure 3 shows the variation of $r_m^*$ with aspect ratio ($r^*$) for different *Kn*. For $r^* < 0.5$, $r_m^*$ decreases with *Kn*, which dictates that the maximum dimensionless velocity occurs near to the inner wall. While for $r^* > 0.5$, *Kn* has minimal effect on $r_m^*$, which shows that the point of the maximum dimensional velocity remains almost the same. Figure 4 shows that an increase in *Kn* results in a decrease in non-dimensional temperature profile. Figure 5 illustrates that *Nu* decreases with *Kn* due to the temperature jump at the wall. Also, viscous dissipation increases the bulk fluid temperature especially near the wall due to the highest shear rate in this region. Hence, it decreases the temperature difference between the wall and the bulk fluid, which is the main driving mechanism

for the heat transfer from wall to fluid. The influence of *Br* is more pronounced on *Nu* for lower values of *Kn* as compared to the higher values of *Kn*.

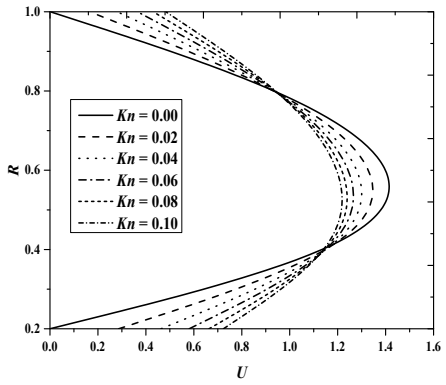


FIGURE 2. Dimensionless velocity profile at different values of *Kn*

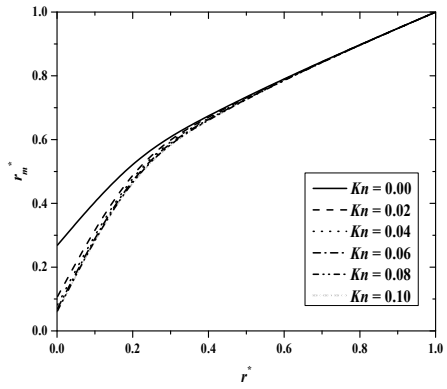


FIGURE 3. The variation of $r_m^*$ with aspect ratio at different values of *Kn*

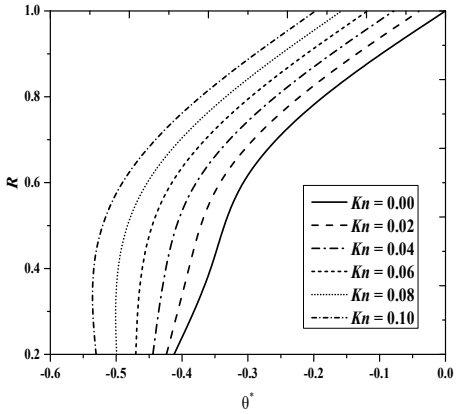


FIGURE 4. Non-dimensional temperature distribution at different values of *Kn* at $r^* = 0.4$

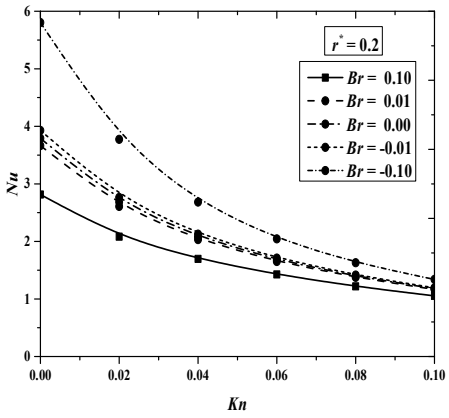


FIGURE 5. The variation of *Nu* with *Kn* for different values of *Br*

## 4. CONCLUSIONS

In the present study, closed form expressions are derived for the non-dimensional temperature distribution and the Nusselt number as a function of various modeling parameters. The limiting value of the Nusselt number is obtained by substituting $Kn = 0$ in the derived expression, which is exactly same as the continuum value. The Nusselt number is found to decrease with *Kn*.

## REFERENCES

[1] M. Avci, O. Aydin, Laminar forced convection with viscous dissipation in a concentric annular duct, *C. R. Mecanique,* 334, 164–169, 2006.

[2] M. Avci, O. Aydin, Laminar forced convection slip-flow in a micro-annulus between two concentric cylinders, *International Journal of Heat and Mass Transfer* 51, 3460–3467, 2008.

# Comparison of CFD implementation of empirical correlations for subcooled nucleate boiling

**Hemant Punekar, Vinay Kumar Gupta**
ANSYS Software Pvt. Ltd., 34/1, Pune Infotech Park, Hinjewadi, Pune-411057,
Hemant.Punekar@ansys.com, Vinaykumar.Gupta@ansys.com

## ABSTRACT

In modern cooling systems, the requirement of higher performance demands highest possible heat transfer rates, which can be achieved by controlled nucleate boiling. To simulate subcooled nucleate boiling for such boiling based cooling systems, semi-mechanistic wall boiling models that use empirical correlations of boiling are popular. Such models are simple to implement yet robust, provide reasonable accuracy in overall heat transfer prediction, moreover can be used for the geometrically complex cooling channel. However, the accuracy of those reduced order CFD model depends on the choice of empirical correlation derived from simple geometry. Two of the most widely used correlations are due to Rohsenow and Chen. In the present work, these two correlations are adapted in 3D CFD environment, the results are presented and the pros and cons of each correlation are discussed. Chen correlation is found to be better suited for CFD adaptation for flow boiling.

**Key Words:** *Heat Transfer, Cooling System, Nucleate boiling, Chen, Rohsenow*

## 1. INTRODUCTION

Cooling plays an important role in several engineering applications, commonly encountered in automotive industries, electronics industries, chemical & process industries, power industries etc. One of the ways to increase cooling rate is by employing sub-cooled nucleate boiling. It is known to the engine design community that coolant undergoes boiling in certain hot regions of IC Engine cooling jackets, which happen to be close to the cylinder, fire deck or the exhaust port. Nucleate boiling is desirable as it increases the heat transfer coefficient significantly, however, the vapour stratification and stagnation is highly undesirable as it reduces the area available for heat transfer. To allow controlled nucleate boiling, designers are using various tools for modelling and CFD is one of the most widely used tool. Semi mechanistic boiling models that use 1D empirical correlation are increasingly used to model boiling. These models adapt 1D correlation in 3D CFD environment. Bo [1] employed Rohsenow correlation [2] for flow boiling calculation. Srinivasan [3] used similar approach for boiling of water, but for evaporative heat transfer coefficient Chen correlation [4] was used. In our previous work [5 & 9], a modified Chen correlation was employed to model subcooled nucleate boiling. In the present work both the correlations are implemented in ANSYS Fluent and results are presented.

The empirical correlations for boiling divide the total wall heat flux into two parts as follows.

$$q_{total} = q_{s.p.} + q_{nuc.} \tag{1}$$

where, $q_{s.p.}$ is Single phase heat flux to liquid and $q_{nuc.}$ is the additional heat flux due to nucleate boiling.

Different correlations propose different ways of modeling these two fluxes. ANSYS Fluent calculates heat transfer to the in the near wall cells based on the turbulent wall functions, so $q_{s.p.}$ is

readily available and hence directly used in the present work. Further discussion is limited to modeling of $q_{nuc.}$

Rohsenow [2] proposed a correlation for pool boiling situation, in which the nucleate boiling heat flux is modelled as follows.

$$q_{nuc.} = \mu_{sat.l} L \sqrt{\frac{g(\rho_{sat.l} - \rho_{sat.v})}{\sigma}} \left( \frac{C_{pl} \Delta T_{sup}}{C_{sf} L \, Pr_{sat.l}^{n}} \right)^{3} \tag{2}$$

where, subscripts $l, v \,\&\, sat.$ refer to liquid, vapor and saturation, $\mu$ is viscosity, $L$ is Latent heat, $g$ is gravitational acceleration, $\rho$ is density, $\sigma$ is Surface tension, $C_p$ is specific heat, $\Delta T_{sup} = (T_{wall} - T_{sat.})$ is wall superheat, $Pr$ is liquid Prandtl number and $C_{sf}$ & $n$ are empirical constants that depend on the combination of wall and liquid materials and also on the surface properties like roughness. For the present study, values of $C_{sf}$ and $n$ are chosen as 0.007 and 1.0 in accordance with the experimental conditions from [6].

Some researchers tune these consants to get better agreement with the experimental data, however, it makes the validity of model questionable especially for different operating conditions.

Chen [4] proposed a correlation for flow boiling conditions, in which the nucleate boiling heat flux is modelled as follows.

$$q_{nuc.} = h_{nuc.} \Delta T_{sup} \tag{3}$$

where, $h_{nuc.}$ is the nucleate boiling heat transfer coefficient defined as follows.

$$h_{nuc.} = S \times 0.00122 \times \left[ \frac{\mathrm{k}_{\mathrm{l}}^{0.79} C_{pl}^{0.45} \rho_l^{0.49}}{\sigma^{0.5} \mu_l^{0.29} \left( L \rho_g \right)^{0.24}} \right] \times \Delta T_{\mathrm{sup.}}^{0.24} \left( P_{wall} - P_{sat.} \right)^{0.75} \tag{4}$$

where, $P_{wall}$ and $P_{sat.}$ indicate saturation pressure corresponding to $T_{wall}$ and $T_{sat.}$. S is the suppression factor ranging from 0 to 1, originally presented with a graph by Chen and later suggested with a best fit curve by Collier, J.G. [6] as follows.

$$S = \frac{1}{1 + 0.12 (Re \times 10^{-4})^{0.14}} \tag{5}$$

Inclusion of this factor to account for suppression of nucleate boiling due to increase in flow velocity makes Chen correlation more mechanistic than a mere curve fit to the experimental data.

As evident from the formulation of this model, there are no empirical constants in this model that requires tuning.

## 3. CFD IMPLEMENTATION

To model subcooled nucleate boiling accurately, it is necessary to simulate two phase fluid flow, account for the heat transfer augmentation at the wall and model the mass transfer between the liquid and vapor phase. The present wall boiling model is developed using the mixture multiphase model [7] available with CFD solver ANSYS FLUENT. To model turbulence, RNG k-epsilon model was employed. Heat transfer augmentation during subcooled boiling is modelled using both Rohsenow [2] and Chen [4] correlation modified for 3-D CFD environment. In-built evaporation-

condensation [7] mass transfer model is used to capture the phase change process. The details of numerical implementation can be found in [9].

## 4. RESULTS AND DISCUSSION

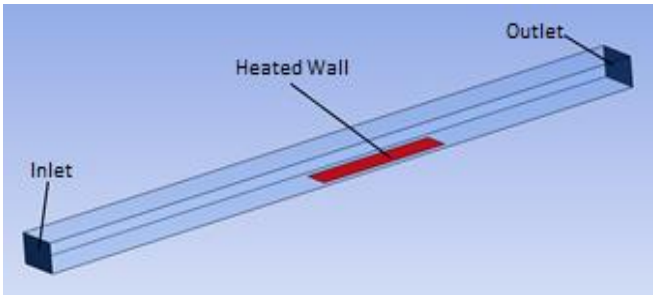


FIGURE 1. Computational domain to replicate Robinson's experimental work [8]

The experimental data from Robinson's work [8] is used to validate the current approach for the variation of wall heat flux versus the changes of the wall temperature under different pressures, flow velocities and degree of inlet sub-cooling. Typical anti-freeze coolant mixture, 50% aqueous ethylene glycol is used. Both surface finish and surface fluid combination are important parameter for boiling, so in the test case to replicate the boiling similar to engine jacket, cast from an aluminum alloy is used. In Figure 1 computational domain is shown, which is created to mimic the experimental set up. The main flow channel is horizontal, 241 mm long and has a rectangular cross section of 16x10 mm2. The heating surface is at the bottom of the flow channel, 10x50 mm2, and located 76 mm downstream from the entrance of the channel. Inlet velocity of 0.25 m/s is chosen for the validation study, in which operating pressure is varied from 1 bar to 3 bar and wall temperature is varied from 90C to 170C. Outlet boundary is set as pressure outlet with zero gauge pressure. All the walls are set as adiabatic expect for the heated wall, which has the specified temperature boundary condition.

For 'liquid phase' temperature varying properties are taken from NIST data base and Robinson's work [8]. For 'vapor phase' saturated steam properties (at corresponding pressure) are taken, considering the fact that the boiling point of water is lesser than both the antifreeze mixture and pure ethylene glycol, so the generated vapour for the mixture is water vapour only [8].

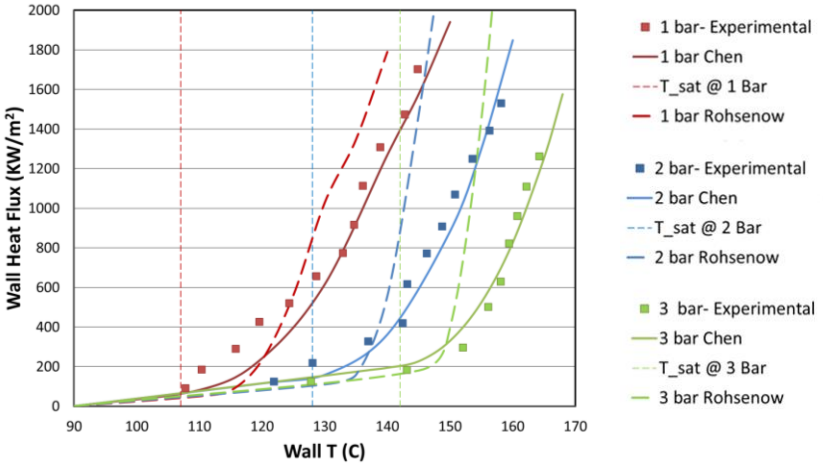


FIGURE 2. Comparison of total heat flux predicted by the model against the experimental data for inlet velocity = 0.25 m/s, inlet temperature = 90 C, pressure = 1bar, 2 bar and 3 bar .Vertical dashed lines are indicating the saturating temperature for respective operating pressure

As shown in Fig. 2, Chen correlation provides accurate results over wider range of the wall superheat as compared to Rohsenow, which significantly over predicts the heat flux for high wall superheat. This behaviour can be attributed to the fact that the flow tends to suppress boiling, which is taken care of through a suppression factor in Chen correlation, however, not taken into account in Rohsenow correlation.

At low wall superheat, both the models under predict the heat transfer rates, especially at low operating pressures, i.e. 1 and 2 bar conditions.

For Rohsenow correlation, it is also worth noting that the heat transfer rate is extremely sensitive to the values of liquid viscosity, latent heat & $C_{sf}$. This can also be deduced from the sensitivity analysis of equation (2), which suggests that for 1% variation in the value of liquid viscosity, latent heat value and $C_{sf}$ results in 4.1%, 2% and 3% variation of $q_{nuc.}$ respectively. As compared to this, Chen correlation seems to be less sensitive to such properties because 1% change in any such properties does not result in a change of more than 1% in the $q_{nuc.}$ value.

## 5. CONCLUSIONS

1D empirical correlation due to Rohsenow and Chen are implemented in 3D CFD environment and the results are compared with the experiments. Chen correlation is found to provide reasonable accuracy over the wide range of wall superheat. With Rohsenow correlation, an over prediction of wall heat flux is observed at high wall superheat. Also, as compared to Chen correlation, Rohsenow correlation is found to be more sensitive to the material properties and model constants.

## REFERENCES

[1] Bo, T., “CFD Homogeneous Mixing Flow Modelling to Simulate Subcooled Nucleate Boiling Flow”, SAE International 2004-01-1512, 2004.

[2] Rohsenow, W.M.,“A Method of Correlating Heat Transfer Data for Surface Boiling of Liquid”, Trans. ASME, 74, 969, 1952.

[3] Srinivasan, V., “Numerical simulation of flow boiling of binary mixtures using multi-fluid modeling approach”, Proceedings of IMECE 2011, ASME International Mechanical Engineering Congress and Exposition November 11-16, 2011.

[4] Chen, J.C., “Correlation for boiling heat transfer to saturated fluids in convective flow”, Ind. & Eng. Chem. –Process Design and Development, Vol 5 no 3, 322-329, 1966.

[5] Punekar H. & Das S. “Numerical Simulation of Subcooled Nucleate Boiling in Cooling Jacket of IC Engine”, Paper no. 2013-01-1651, SAE 2013 World Congress & Exhibition, April 16, 2013, Detroit, Michigan, United States.

[6] Jabardo, J. M. S., Silva, E. F., Barros, S. F. “Evaluation of the Rohsenow correlation through experimental pool boiling of halocarbon refrigerants on cylindrical surfaces, J. Braz. Soc. Mech. Sci. & Eng., Vol. XXVI, n-2, pp.218, 2004.

[7] Theory Guide, ANSYS FLUENT 14.0 Documentation, 2011.

[8] Robinson, K., Hawley, J.G. and N.A.F., “Experimental and modeling aspects of flow boiling heat transfer for application to internal combustion engines,” Proc. Instn Mech. Engrs Vol. 217 Part D : Automobile Engineering, 2004.

[9] Das S, Punekar H. On Development of a Semimechanistic Wall Boiling Model. ASME. J. Heat Transfer. 2016;138(6):061501-061501-10.

Fifth International Conference on Computational Methods for Thermal Problems
THERMACOMP2018, July 9-11, 2018, Indian Institute of Science, Bangalore, INDIA
*N. Massarotti, P. Nithiarasu, Pradip Dutta and C. Ranganyakalu (Eds.)*

# GENESIS AND EVOLUTION OF PREMIXED FLAMES IN TURBULENCE

**Himanshu L. Dave, Abinesh M., Swetaprovo Chaudhuri**
Indian Institute of Science, CV Raman Road, Bangalore, schaudhuri@iisc.ac.in

## ABSTRACT

Direct Numerical Simulation (DNS) of $H_2$-air premixed flames is combined with a newly developed computational tool called the Backward Flame Particle Tracking (BFPT) algorithm. Flame particles are points that move with isoscalar surfaces in a premixed flame. The DNS-BFPT framework helps us to address: from where and how do the complex topology and physico-chemical state of a fully developed turbulent premixed flame generate and evolve in time. It is found that flame surfaces at time $t_f$ evolve from multiple leading regions from an earlier time $t_i$ ($t_i < t_f$). Flow-flame properties like flow velocity, stretch-rate, and pair-dispersion statistics are also evaluated revealing important insights into the dynamics of turbulent premixed flames.

**Key Words:** *Turbulent premixed flames, Lagrangian tracking, flame particles, leading points.*

## 1. INTRODUCTION

Investigating the multi-scale, nonlinear turbulence-flame interactions is essential for understanding many practically relevant and naturally occurring flows. A premixed flame, in particular, could be considered as an ensemble of propagating isoscalar surfaces, say isotherms, separating the unburnt reactants from products. Tracking points on such surfaces as they evolve provides us with the time history of specific portions and associated properties of the flame, which is crucial in understanding numerous phenomena like flame extinction. This methodology of tracking points on isoscalar surfaces is called the Flame Particle Tracking (FPT) algorithm [1]. It has been developed as a post-processing computational tool based on the rigourous foundations developed by Pope [2]. This Lagrangian-type tracking of points on isoscalar surfaces offers a new paradigm of investigating turbulence-flame interactions. The equation governing the evolution of a flame particle position is $\partial \boldsymbol{x}^F/\partial t = \boldsymbol{v}^F = \boldsymbol{u}^F + S_d^F \boldsymbol{n}^F$. Here, $\boldsymbol{x}$ is position vector, $\boldsymbol{u}$ is local fluid velocity, $S_d$ is local flame displacement speed relative to $\boldsymbol{u}$, and $\boldsymbol{n}$ is local normal to the isoscalar surface. The superscript $F$ indicates that all the properties in the equation are Lagrangian in nature. They are obtained by interpolation from the corresponding Eulerian fields which in-turn are obtained from the DNS.

When turbulence interacts with a premixed flame it wrinkles, stretches, and folds the flame at multitude of length- and time-scales. These interactions cause certain regions of the flame to annihilate. But, for burning reactants continuously the flame surfaces should generate as well. However, the locations that would generate new surface elements are not known *a priori*. The above mentioned FPT algorithm tracks the flame particles with time progressing from $t_i$ to $t_f$ ($t_i < t_f$). But, when a uniform distribution of flame particles is tracked using FPT, they cluster in the increasingly concave (w.r.t unburnt reactants) regions of the flame surface following which they annihilate. Therefore, to investigate where the new flame surface elements generate, flame particle must be tracked backward in time, i.e., from $t_f$ to $t_i$. While backtracking, the governing transport equations are not solved again, but the saved Eulerian fields from the DNS are read backwards, like a movie played in reverse. This backward flame particle tracking (BFPT) algorithm was developed by modifying the back-tracking algorithm for fluid particles developed by Nahum & Seifert [3] to suit it for back-tracking flame particles. With the help of BFPT simulations, we addressed important specific questions concerning the dynamics of turbulent premixed flames.

## 2. COMPUTATIONAL DETAILS

### 2.1 Direct Numerical Simulation (DNS) Databases

Two cases: Case-1 and Case-2, were obtained by DNS of $H_2$-air premixed flame at an equivalence ratio $\phi = 0.81$ and pressure $P = 1$ atm. The DNS were performed using an open-source solver called the Pencil code. The code uses explicit, central finite difference scheme for spatial discretization and 2N-RK3 scheme for temporal integration. The resultant Eulerian fields are 6th order accurate in space and 3rd order accurate in time. The DNS is performed in two steps. First, homogeneous isotropic turbulent flow field of unburnt reactants at temperature $T_u = 310$ K is simulated in a cube with periodic boundary condition on all 6 faces. In the 2nd step, this turbulent flow field is issued with a mean velocity from the inlet YZ plane into a cuboid. The cuboid has periodic boundary condition along Y and Z directions and NSCBC [4] boundary condition along X direction. The traversing turbulent field then interacts with a premixed, planar laminar flame which is initialized at some distance downstream of the inlet YZ plane. The thermal thickness $\delta_L = 0.0361$cm and laminar flame speed $S_L = 184$ cm/s. Following this interaction, a turbulent premixed flame is realized which is allowed to reach a statistically stationary state. Afterwards, the Eulerian fields from the DNS are saved onto a hard-disk at very fine time-intervals $\Delta t$. These Eulerian fields are then used in the BFPT simulation. Table 1 presents the DNS simulation parameters.

| Case | $L_x$ | $L_y$ | $N_x$ | $N_y$ | $k_{\max}\eta$ | $\delta_L/\Delta x$ | $\tau_\eta/\Delta t$ | $T/\tau_\eta$ | $u'/S_L$ |
|---|---|---|---|---|---|---|---|---|---|
| 1 | 1.918 | 0.48 | 960 | 240 | 2.5 | 18 | 1/12 | 21 | 4.3 |
| 2 | 1.2 | 0.40 | 384 | 128 | 1.5 | 14 | 1/5 | 17 | 4.4 |

TABLE 1. Simulation parameters of the DNS cases: Case-1 and Case-2

$L_x$ is the length (in cm) of the domain along X direction, $L_y = L_z$ are lengths along lateral directions. $N_x$ and $N_y = N_z$ are the corresponding grid points. $u'$ is the rms of turbulent fluctuations. $k_{\max}\eta \geq 1.5$ indicates that the spatial resolution of the turbulent flow field is sufficient. $k_{\max} = \pi/\Delta x$ is the maximum resolvable wavenumber. $\eta$ is the Kolmogorov length scale. $\Delta x$ is the mesh spacing. $\delta_L/\Delta x$ is a measure of the resolution of the flame. $\tau_\eta/\Delta t$ indicates that the Eulerian snapshots are saved at a factor less than the smallest time-scales in the flow, the Kolmogorov time-scales $\tau_\eta$. $T$ is the BFPT simulation time.

### 2.2 Backward Flame Particle Tracking (BFPT) Algorithm

The BFPT algorithm is implemented in 2 stages: estimation and correlation. While numerically solving for the flame particle position, the discretized equation is implicit. This is demonstrated below by using a 1st order accurate discretization.

$$\frac{\boldsymbol{x}^F(t) - \boldsymbol{x}^F(t-\Delta t)}{\Delta t} = \boldsymbol{v}^F(t-\Delta t)$$

Back-tracking progresses from $t$ to $t-\Delta t$ to calculate $\boldsymbol{x}^F(t-\Delta t)$; the quantities at $t$ are known while at $t-\Delta t$ are unknown. In the *estimation stage*, this issue is circumvented by approximating $\boldsymbol{v}^F(t-\Delta t)$ with $\boldsymbol{v}^F(t)$ as a first guess. The equation is then solved using the triangle–ray intersection algorithm as used in the FPT [1] for an estimate $\boldsymbol{x}^{F*}$ of the flame particle position. $\boldsymbol{x}^{F*}$ is then corrected in the correlation stage. In the *correlation stage*, the local neighbourhood in the vicinity of $\boldsymbol{x}^{F*}$ is refined by defining lots of "dummy" flame particles, say $\boldsymbol{g}_i$. Then, two arrays of velocities are defined for each neighbourhood. Array

$A$ contains the "available" velocities obtained by interpolating $\boldsymbol{v}$ onto the dummy points. Array $B$ contains the "required" velocities given by $\boldsymbol{B}_i = (\boldsymbol{x}^F(t) - \boldsymbol{g}_i)/\Delta t$. Finally, we compute a correlation parameter $D_i = \boldsymbol{A}_i.\boldsymbol{B}_i/\max\{|\boldsymbol{A}_i|, |\boldsymbol{B}_i|\}^2$, where $D_i \in [-1, 1]$. The "dummy" flame particle from the neighbourhood with $D_i$ closest to 1 is $\boldsymbol{x}^F(t - \Delta t)$. The actual implementation of BFPT algorithm is however 2nd order accurate in time.

## 3. RESULTS

BFPT simulation starts at $t_f$ with a uniform distribution of flame particles on an isotherm. It was performed for isotherms with isovalue $T_0 = 350\text{K}$, 500K, 800K, and 1100K for Case-1 and $T_0 = 350\text{K}$ for Case-2. For each simulation 2000 flame particles were used. Simulation with 4000 flame particles show that the results are not sensitive to the number of flame particles. It is observed that the flame particles, at the end of BFPT (time $t_i$), form multiple clusters in the predominantly positively curved (convex w.r.t unburnt reactants) leading regions of the corresponding isotherms. Therefore, it can be said that the new surface elements of a fully developed turbulent flame originate from such leading clusters. This observation is in partial consonance with Zeldovich's conjecture of a singular leading point [5]. Figure 1 shows how the flame particle clusters at time $t_i$ expand to span the complete isotherms at time $t_f$ through some intermediate time $t_c$ $(t_i < t_c < t_f)$ for Case-1. Thus, the DNS-BFPT framework facilitates identifying the source locations of a flame surface.

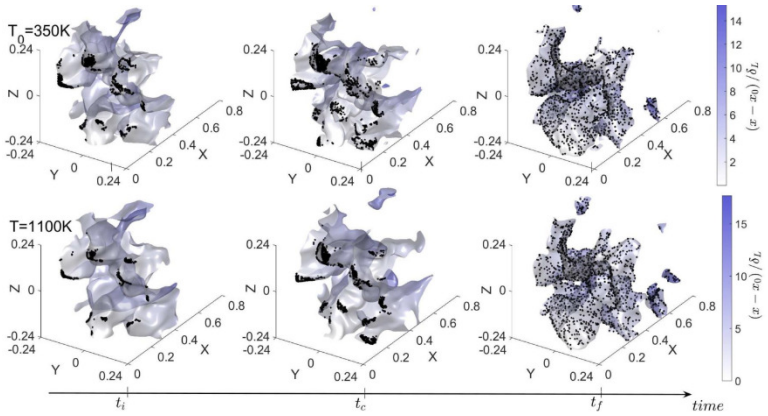


FIGURE 1. Snapshots of isotherms with flame particles (black dots) at $t_i, t_c,$ and $t_f$ for Case-1.

Figure 2 shows the probability density functions (PDFs) of important flow-flame properties evaluated at the leading surface, $T_0 = 350\text{K}$ isotherm, and the corresponding flame particles at time instants $t_i, t_c$, and $t_f$ for Case-1. It is observed that the flame particles at time $t_i$ occupy leading regions (most advanced into the unburnt reactants) which are predominantly positively curved. $x_0$ is the X-component of the most-leading point on the surface. These leading flame particles also have low $\boldsymbol{u}^F$. It is because of this remarkable similarity between these flame particles and the leading points defined elsewhere in the literature [5] we call these flame particles as the *leading points*. Figure 2 also shows the PDFs of the quantities which govern the rate at which the area of flame surface elements change. At $t_f$, the PDFs of the leading points approximate the PDFs of the leading surface.

Finally, the separation distances of pairs of leading points $\Delta^F$ in the range $50\eta - L_0$ were tracked in time. Figure 3 shows the dispersion statistics for Case-1. $L_0$ is the large length scale in turbulence. They are found to exhibit a modified Batchelor dispersion law $\langle|\Delta^F - \Delta_0^F|^2\rangle = 11/3\, C_G(\Delta_0^F \epsilon_T)^{2/3} t^2$. Here, $\Delta_0^F$ is the initial separation, $C_G$ is constant for pairs on an isotherm, but varies with $T_0$. A pair dispersion study for flame particle pairs tracked in forward time using FPT [6] exhibited a similar dispersion law given by $\langle|\Delta^F - \Delta_0^F|^2\rangle = 11/3\, C_D(\Delta_0^F \epsilon_T)^{2/3} t^2$. The constant, however, was given by $C_D$. The ratio of time-scales $\tau_G$ and $\tau_D$ for particle pairs to grow from $50\eta$ to $L_0$ during generation

and to shrink from $L_0$ to $50\eta$ during annihilation respectively, is given by $\tau_G/\tau_D \sim Re_{L_0}^{1/4}$. $Re_{L_0}$ is the large scale Reynolds number. This scaling relationship tells that statistically a flame surface should take more time to generate than to annihilate. This has implications on the oscillations of the turbulent flame speed $S_T$, which is a global quantity of central importance.

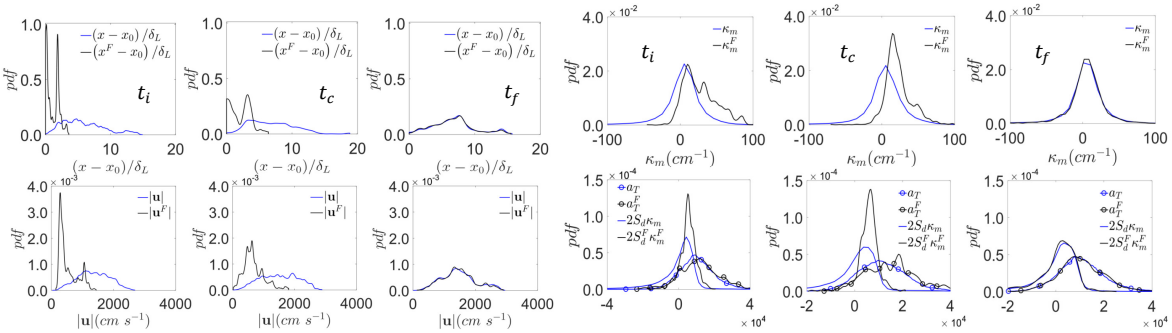


FIGURE 2. PDFs of flow-flame properties on leading surface and leading points at $t_i, t_c$, and $t_f$.

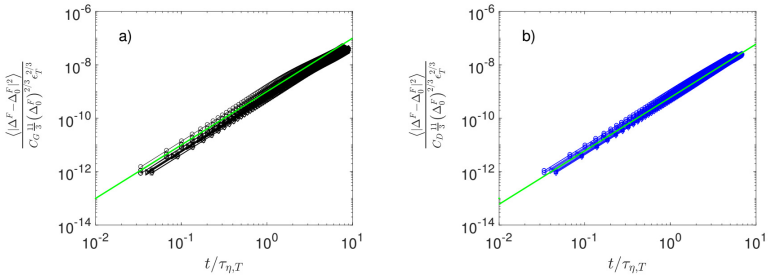


FIGURE 3. Pair-dispersion statistics of flame particles during a) generation, b) annihilation. The green solid line shows exact $t^2$ behaviour.

## CONCLUSIONS

The DNS-BFPT computational framework has enabled identification of source locations of a fully developed turbulent premixed flame. The BFPT algorithm has two stages: estimation and correlation. The PDFs of the leading points indicate that the source locations have low fluid speeds and are most advanced into the unburnt reactants. The distance between pairs of leading points scales with $t^2$ and was used to identify that a flame surface takes more time to generate than to annihilate.

## REFERENCES

[1] S. Chaudhuri, Life of flame particles embedded in premixed flames interacting with near-isotropic turbulence, *Proceedings of the Combustion Institute*, 35, 1305-1312, 2015.

[2] S. B. Pope, The evolution of surfaces in turbulence, *International Journal of Engineering Science*, 26, 445-469, 1988.

[3] A. Nahum and A. Seifert, Technique for backward particle tracking in a flow field, *Physical Review E,* 74 016701, 2006.

[4] T. J. Poinsot and S. K. Lele, Boundary conditions for direct simulations of compressible viscous flows, *Journal of Computational Physics*, 101(1), 104-129, 1992.

[5] A. Lipatnikov, Fundamentals of premixed turbulent combustion, CRC Press, London, 2012.

[6] S. Chaudhuri, Pair dispersion of turbulent premixed flame elements, *Physical Review E*, 91, 021001(R), 2015.

# THERMAL MODELING OF NATURAL CIRCULATING RISER-DOWNCOMER CIRCUIT FOR STEAM GENERATION

**Md Naim Hossain, Koushik Ghosh, Nirmal K. Manna**

Department of Mechanical Engineering, Jadavpur University, Kolkata-700032, India
naimhossain6@gmail.com, kghoshjdvu@gmail.com, nirmalkmannaju@gmail.com

## ABSTRACT

The naturally circulating thermosyphon circuit finds widespread utility in many industrial applications such as in boilers of power generating plants, solar collectors etc. The present paper analyses the variation of mass flux rate and exit steam quality through a typical riser downcomer circuit systematically by varying the diameter and length of the riser tube, and the applied heat-flux. For this work, a novel model has been developed introducing an arbitrarily chosen slip to the usual homogeneous flow model. The model takes care of appropriate friction factor multiplier of two-phase flow and a nonlinear equation for mass flux through the riser tube. The developed model is validated with the existing experimental result. The mass flux through riser downcomer circuit is evaluated by solving the developed nonlinear algebraic equation using MATLAB.

**Key Words:** *Riser Downcomer circuit, Natural Circulation, Mass flow rate, Dryness fraction*

## 1. INTRODUCTION

Naturally circulated thermosyphon system is used in boiler of conventional steam power plant and solar water heater etc. In naturally circulating riser-downcomer circuit, the fluid flows on the principle of thermosyphon without any external aid. Density difference of flowing fluid creates the driving pressure head for establishment of flow. Literature survey shows some research findings on thermosyphon devices both from numerical and experimental studies, which mainly focuses on the mass flow rate or mass flux. But these studies do not address the detailed thermal modeling of the riser-downcomer circuit for mass flux calculation on the basis of geometrical and thermo-physical parameters. In present work, an attempt has been made on thermal modeling of a boiler riser-downcomer circuit with subcooled or saturated liquid at entry to the riser tube. The case of two-phase flow is analyzed with the help of proper two phase multiplier for frictional pressure drop. In addition, appropriate slip ratio between liquid and vapor has been considered.

## 2. MAIN BODY

A simplified form of the riser downcomer circuit of the actual boiler of steam power plant is considered and shown schematically in Figure 1(a) and 1(b) .

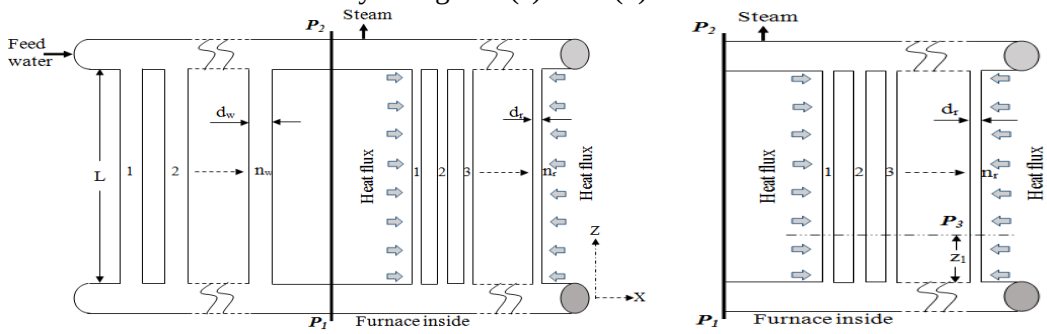


FIGURE 1: Schematic of riser downcomer circuit with (a) saturated liquid (b) subcooled liquid.

For this present work it is considered that, both the riser and downcomer tubes are of same length with constant cross sectional area and $n_r$ number of riser tubes and $n_w$ number of downcomer tubes have been taken. By heating, the liquid is transformed to vapor through evaporative phase change, and their mixture is moving upward in the riser tube. For subcooled downcomer liquid flow case (Figure 1 (b)), the water incoming into riser tube, first gains heat and becomes saturated (at point $P_3$) then phase change starts. But for saturated downcomer liquid flow case (Figure 1 (a)), the saturated water directly enters into the riser tube and phase change occurs starting from the entrance. For this present study a model has been developed following homogeneous slip flow assumption. The model takes care of appropriate two-phase flow friction factor multiplier and a nonlinear equation for mass flux through the riser tube. Integrating the momentum equation over riser downcomer circuit, we obtain (through rigorous algebra) the basic mass flux rate equation for homogeneous flow with slip approach as,

$$C^H_{F_{downcomer}} G^{F^H_{downcomer}} - C^H_{G_{downcomer}} + C^H_{F_{riser.upto.saturation}} G^{F^H_{riser.upto.saturation}} + C^H_{G_{riser.upto.saturation}} G + C^H_{F_{riser.after.saturation}} G^{F^H_{riser.after.saturation}} \left[ \begin{array}{l} \left( \frac{NL}{G} + 1 \right)^{3/4} (-4GH + 7GN + 3HNL) - \\ (NR_1 + 1)^{3/4} (-4GH + 7GN + 3HNR_1) \end{array} \right] + G^2 \left[ \frac{AC_1 G + L(1-A)}{EC_1 G + L(\rho_g - E)} - \frac{AC_1 + R_1(1-A)}{EC_1 + R_1(\rho_g - E)} \right] + C^H_{G_{riser.after.saturation}} G \left[ \ln \frac{1 + R_2 \frac{L}{G}}{1 + R_2 R_1} \right] = 0 \quad (1)$$

Where,

$$C^H_{G_{riser.after.saturation}} = \frac{g h_{fg} d_r}{4\varphi \nu_{fg}}, C^H_{G_{downcomer}} = \rho_f g L, C^H_{G_{riser.upto.saturation}} = \rho_f g R_1, R_2 = \frac{4\varphi \nu_{fg}}{h_{fg} d_r \nu_f}, H = \left( \frac{\rho_f}{\rho_g} - 1 \right) \frac{4\varphi}{h_{fg} d_r},$$

$$N = \left( \frac{\mu_f}{\mu_g} - 1 \right) \frac{4\varphi}{h_{fg} d_r}, A = \left( \frac{\rho_g}{\rho_f} \right) \left( \frac{\mu_f}{\mu_g} \right), C_1 = \frac{h_{fg} d_r}{4\varphi}, E = A\rho_f, \text{ and } R_1 = \frac{C_{pf} d_r (T_{sat} - T_a)}{4\varphi}$$

And the values of the coefficients of the above equation for different cases are expressed below,

| Models | Values of coefficients |
|---|---|
| Subcooled Turbulent Case | $C^H_{F_{downcomer}} = \frac{0.158 \mu_f^{1/4} \nu_f L}{d_r^{5/4} f^{19/4} n^{7/4}}, C^H_{F_{riser.upto.saturation}} = \frac{0.158 R_1 \nu_f \mu_f^{1/4}}{d_r^{5/4}}, C^H_{F_{riser.after.saturation}} = \frac{0.632 \nu_f \mu_f^{1/4}}{21 d_r^{5/4} N^2},$ $F^H_{riser.upto.saturation} = 11/4, F^H_{downcomer} = 7/4, F^H_{riser.after.saturation} = 7/4,$ |
| Subcooled Laminar Case | $C^H_{F_{downcomer}} = \frac{128 \mu_f \nu_f L}{d_r^2 f^4 n}, C^H_{F_{riser.upto.saturation}} = \frac{128 R_1 \nu_f \mu_f}{d_r^2}, C^H_{F_{riser.after.saturation}} = \frac{512 \nu_f \mu_f}{21 d_r^2 N^2},$ $F^H_{downcomer} = 1, F^H_{riser.upto.saturation} = 2, F^H_{riser.after.saturation} = 1$ |
| Saturated Turbulent Case | $C^H_{F_{riser.upto.saturation}} = 0, C^H_{G_{riser.upto.saturation}} = 0, F^H_{riser.upto.saturation} = 0, F^H_{riser.after.saturation} = 7/4, R_1 = 0,$ $F^H_{downcomer} = 7/4, C^H_{F_{downcomer}} = \frac{0.158 \mu_f^{1/4} \nu_f L}{d_r^{5/4} f^{19/4} n^{7/4}}, C^H_{F_{riser.after.saturation}} = \frac{0.632 \nu_f \mu_f^{1/4}}{21 d_r^{5/4} N^2}$ |
| Saturated Laminar Case | $F^H_{downcomer} = 1, F^H_{riser.upto.saturation} = 0, C^H_{F_{riser.upto.saturation}} = 0, C^H_{G_{riser.upto.saturation}} = 0, F^H_{riser.after.saturation} = 1, R_1 = 0,$ $C^H_{F_{downcomer}} = \frac{128 \mu_f \nu_f L}{d_r^2 f^4 n}, C^H_{F_{riser.after.saturation}} = \frac{512 \nu_f \mu_f}{21 d_r^2 N^2}$ |

Equation for exit steam quality for saturated case is (derived from energy equation) expressed as, $x_e = \frac{4\varphi L}{G d_r h_{fg}}$ (2), And for subcooled case is expressed as, $x_e = \frac{4\varphi L}{G d_r h_{fg}} - \frac{C_{pf}}{h_{fg}} (T_{sat} - T_a)$ (3)

The mass flow through riser downcomer circuit and exit steam quality is evaluated by solving the nonlinear algebraic equation 1 and equation 2 respectively, using MATLAB.

## 3. RESULTS

For validation purpose, present model is tested against the experimental results of thermosyphon reboiler reported by Ali and Alam [7] as shown in Figure 2. The experiment was carried out by a single tube natural circulation loop for water. The experimental scattered data are shown along with the predictions by the present model that falls within the experimental data range. The variation observed may be due to mismatch of subcooling temperature data between the experiment and numerical studies. The predicted curve by the present model, in general, is consistent with experimental results.

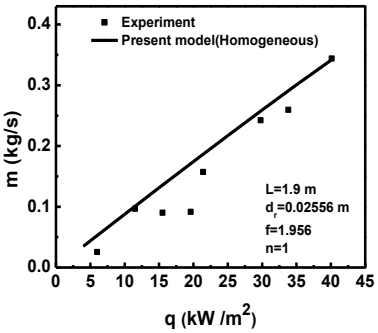


FIGURE 2. Mass flow rate vs. heat flux

For the analysis of present naturally circulating thermosyphon model, the operating pressure is taken 20 bar and water as working fluid. For this case study, diameter ratio (1.4), number of riser tubes (200) and number of downcomer tubes (20) are considered as fixed parameters. The main objective of all these parametric studies is to find out the trend of variation of mass flux rate and exit steam quality against the pertinent parameters. Various degree of subcooling is taken in the analysis to investigate its effect on the mass flux rate and exit steam quality variations.

The mass flux rate increases nonlinearly with the riser diameter (Figure 3 (a)) without showing any peak point due to progressively reduced frictional resistance for saturated and lower degree of subcooled cases. But mass flux initially increases and later decreases following a peak point value for higher degree of subcooled case due to initial buoyancy and later friction effect domination.

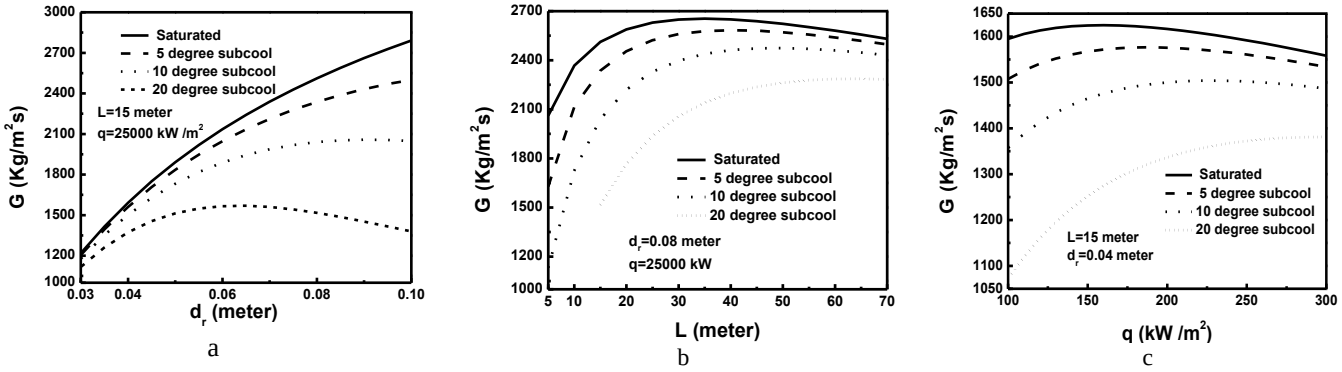


a b c

FIGURE 3. Mass flow rate vs. (a) riser diameter (b) riser length (c) applied heat flux

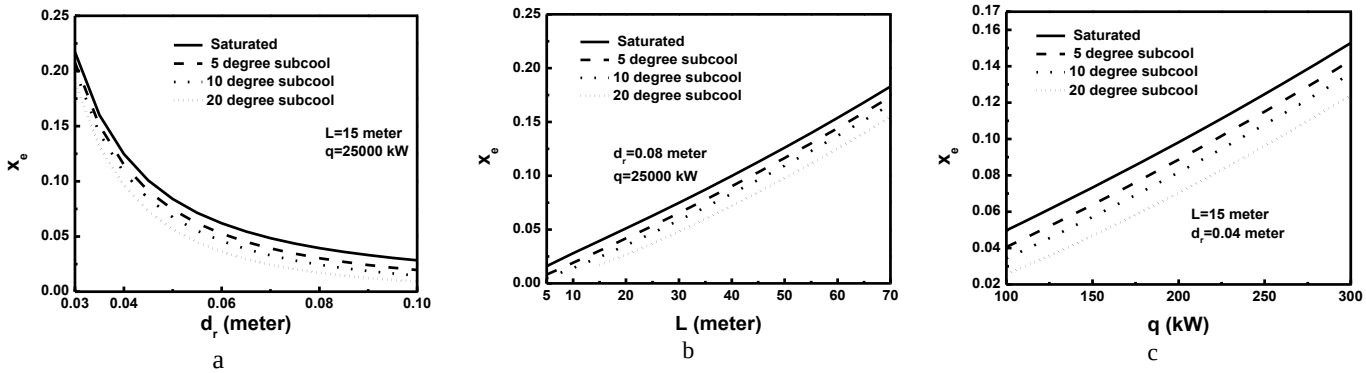


a b c

FIGURE 4. Exit steam quality vs. (a) riser diameter (b) riser length (c) applied heat flux

Mass flux initially increases and later decreases following a peak point value with both the riser length (Figure 3(b)) and applied heat flux (Figure 3(c)) due to initial buoyancy domination and later friction domination. Exit steam quality decreasing nonlinearly with increasing riser diameter (Figure 4 (a)) because of increased mass flow rate that does not allow the water to be heated sufficiently to convert into steam. Exit steam quality increases nonlinearly with riser length (Figure

4 (b)) and heat flux (Figure 4 (c)). For higher degree of subcooling, lower quality is visible for all the cases.

## 4. CONCLUSIONS

The present work addresses mainly the numerical investigation of mass flux rate (along with exit steam quality) of two-phase mixture flow inside the riser tube. Form the detailed parametric study, it is found that the mass flux rate shows a peak-forming variation with riser diameter for higher degree of subcooling and wider variation for saturated and lower degree of subcooling. Mass flux rate shows initially increasing and later decreasing variation followed by a peak point with riser length and applied heat flux at furnace. At lower riser diameter, mass flux rate variation shows lower dependency on subcooling, but at higher diameter subcooling effect is prominent. On the other hand, at lower riser length and with applied heat-flux, mass-flux rate variation shows higher dependency on subcooling. But, at higher riser length and with applied heat-flux, the subcooling effect is reduced which is opposite trend of the diameter variation case. Exit steam quality decreases nonlinearly with the riser diameter and increases nonlinearly with varying slope with the riser length and applied heat flux. With increasing degree of subcooling, the exit steam quality decreases.

## REFERENCES

[1] H. Bieliński, and J. Mikielewicz, A two phase thermosyphon loop with minichannels heated from the vertical side and cooled from the horizontal one. *Chemical and Process Engineering*, 31, 535-551, 2010.

[2] A.K. Nayaka, P. Dubey, D.N. Chavan, Vijayan, P.K., Study on the stability behaviour of two-phase natural circulation systems using a four-Eq. drift flux model. *Nuclear Engineering and Design*, 237, 386-398, 2007.

[3] Franco, A. and Filippeschi, S., *Closed Loop Two-Phase Thermosyphon of Small Dimensions: a Review of the Experimental Results.* Microgravity Science Technology, 2012. 24: p. 165-179.

[4] F. Visentin, and B. Baudouy, Helium Two-Phase Flow in a Thermosiphon Open Loop, *Proceedings of the COMSOL Conference* Milan, 2009.

[5] N.Z. Aung, and S. Li, Numerical investigation on effect of riser diameter and inclination on system parameters in a two-phase closed loop thermosyphon solar water heater. *Energy Conversion and Management*,. 75, 25-35, 2013.

[6] H. Ali, and S.S. Alam, Circulation rates in thermosiphon reboiler. *Int. J. Heat and Fluid Flow*, 13, 86-92, 1992.

[7] A, M. Woldesemayat and A.J Ghajar, Comparison of void fraction correlations for different flow patterns in horizontal and upward inclined pipes. *International Journal of Multiphase Flow*, 33, 347-370, 2007.

## NOMENCLATURE

| | | | | | | | |
|---|---|---|---|---|---|---|---|
| $C_{pf}$ | Specific heat of water | $h_{fg}$ | Latent heat $=(h_g - h_f)$ | $q$ | Heat flux | $x_e$ | Exit steam quality |
| $d_r$ | Diameter of the riser tube | $L$ | Length of riser/downcomer tube | $T_{sat}$ | Saturation Temperature of water | ***Greek Letter*** | |
| $d_w$ | Diameter of the downcomer tube | $m$ | Mass Flow rate | $T_a$ | Atmospheric Temperature | $\mu_f$ $\mu_g$ | Viscosity of water, Viscosity of steam |
| $f$ | Diameter ratio $(d_r/d_w)$ | $n_1$ | Number of riser tubes | $v_f$ | Specific volume of water | $\rho_f$ , $\rho_g$ | Density of water, Density of steam |
| $g$ | Gravitational acceleration | $n_2$ | Number of downcomer tubes | $v_g$ | Specific volume of steam | $\varphi$ | Heat flux |
| $G$ | Mass flux rate inside riser | $n$ | Tube ratio $=(n_2/n_1)$ | $v_{fg}$ | $=v_g - v_f$ | | |

# MESOSCOPIC SIMULATION OF NON-NEWTONIAN NATURAL CONVECTION IN A STENOTIC ARTERY

**Ignatius Fernandes**

Rosary College, Navelim, Goa, ignatius4u@gmail.

## ABSTRACT

Lattice Boltzmann method is used to simulate natural convection in blood flow through stenotic artery. The problem of natural convection in stenotic artery is considered and the influence of elevated temperature and material properties is studied on the flow properties. A porous like square stenotic medium in a human artery with fluid (blood) at the left wall of the geometry and the north wall kept to a normalized temperature of 1.0 is considered. The flow properties like velocity profiles, streamlines, temperature profiles and the rate of heat transfer are then studied with respect to the material properties like porosity and permeability and flow parameters like Rayleigh number and power law index.

**Key Words:** *Lattice Boltzmann method, porous media, non-Newtonian, blood flow, natural convection, Carreau-Yasuda model.*

## 1. INTRODUCTION

Numerical simulation has a potential ability to assist developments in medical research by providing a reliable alternative for decision making by not only providing a low cost decision making tool but by helping to plan for a medical procedure for future advances. This paper considers a porous like square stenotic medium in a human artery with fluid (blood) at the left wall of the geometry and the north wall kept to a normalized temperature of 1.0. The flow properties like velocity profiles, streamlines, temperature profiles and the rate of heat transfer are then studied with respect to the material properties and flow parameters like Rayleigh number and power law index. Porosity is varied from 0.1 to 0.7 whereas Darcy number is fixed at $10^{-3}$. The power law index is varied from 0.5 to 1 to consider shear-thinning behaviour of blood and the Pr is taken as 4, while Ra is varied from $10^3$ to $10^5$. The aim is to understand the localized behaviour of blood in the parts affected in the blood vessels so as to plan a general or an individual based treatment procedure. In case of a stenosis, the path of the blood flow is abnormally blocked by accumulation of substances that grows on the walls of the artery. Elevated temperatures can be used to influence convection in these porous like substance so that the accumulated particles are forced to flow along with the blood. This can be achieved by subjecting the affected part to a temperature difference or treatments like hydrotherapy. A temperature difference will influence a buoyancy effect resulting in a natural convection phenomenon within the porous media. Elevated temperatures are also considered to be an effective way of managing pain and recovery process enhancing tool. That is because heat promotes a faster recovery by increasing blood flow to the pain affected area and increasing natural metabolic rate.

## 2. NUMERICAL METHOD AND IMPLEMENTATION

### 2.1. GOVERNING EQUATIONS

The mathematical model for natural convection in porous media can be expressed by the continuity equation, the Brinkman–Forchheimer equation, and the energy equation [1-4]. The fluid is modeled by a single-particle distribution function $f_i(x,t)$ governed by a lattice Boltzmann equation [5-7]

$$f_i(x+e_i dt, t+dt) - f_i(x,t) = \frac{f_i^{eq}(x,t) - f_i(x,t)}{\tau} + dtF_i \quad (1)$$

Second order bounce back rule for non-equilibrium distribution function is used to determine velocity on the four walls. For energy distribution function, second order extrapolation rule is used on the right wall and the energy distribution function at all other walls were determined the boundary conditions for all other walls were defined as [8]. Carreau-Yasuda model is used to represent non-Newtonian fluids given by [9]

$$\mu = \mu_0 + (\mu_0 - \mu_\infty) \Big/ \left(1 + a\left(\dot{\gamma}\right)^b\right)^{\frac{n-1}{b}} \quad (2)$$

## 3. RESULTS

For non-Newtonian fluids, Darcy's law for fluid flowing through a porous media is given by [10]. Thus, validity of the numerical procedure for non-Newtonian numerical simulation can be established by verifying that the plot of $q$ and $\nabla p = grad(p)$ is linear with slope $1/n$ as given in Table1.

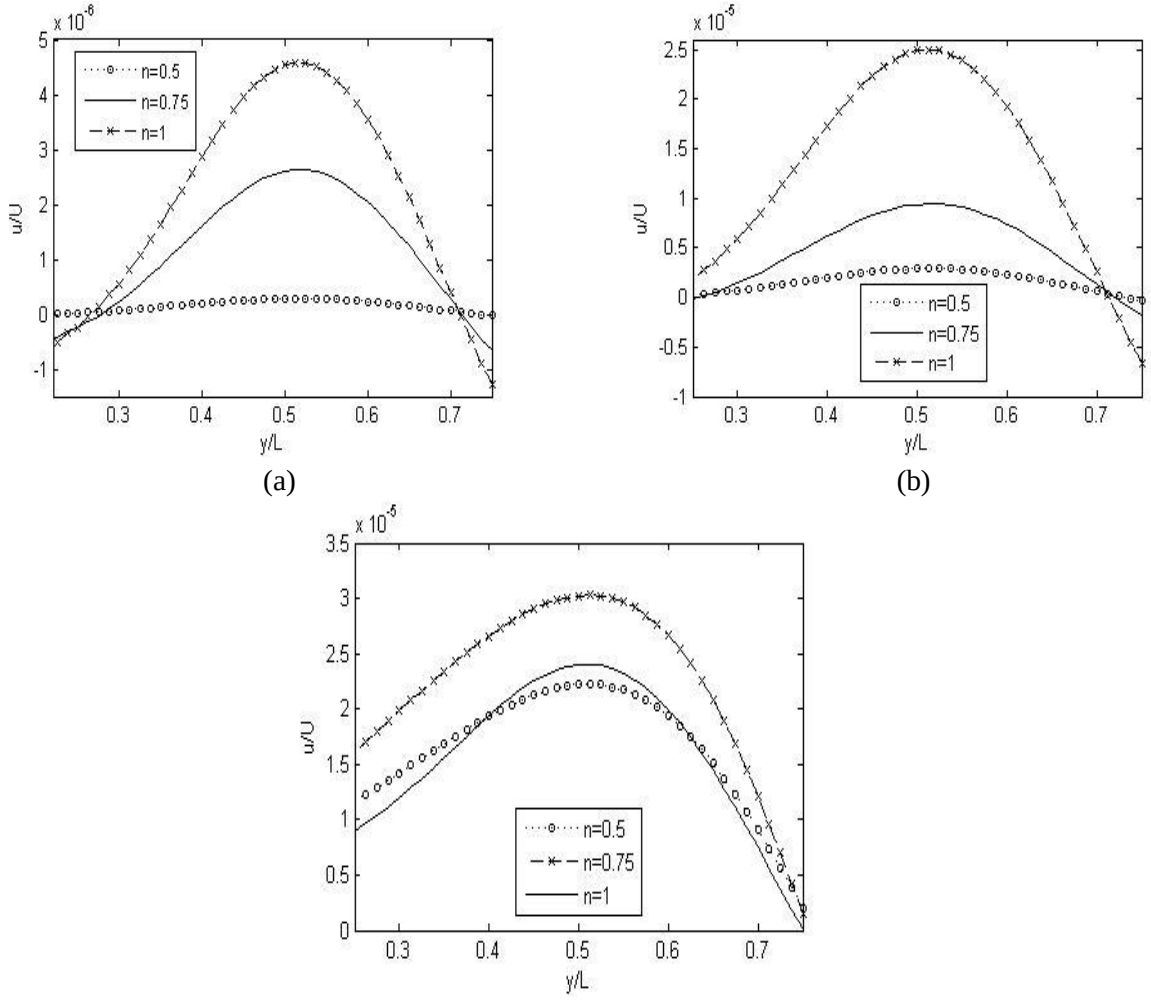


FIGURE 1. u-velocity profiles for $eps = 0.4$ at various values of $n$ (a) $Ra = 10^3$ (b) $Ra = 10^4$ (c) $Ra = 10^5$.

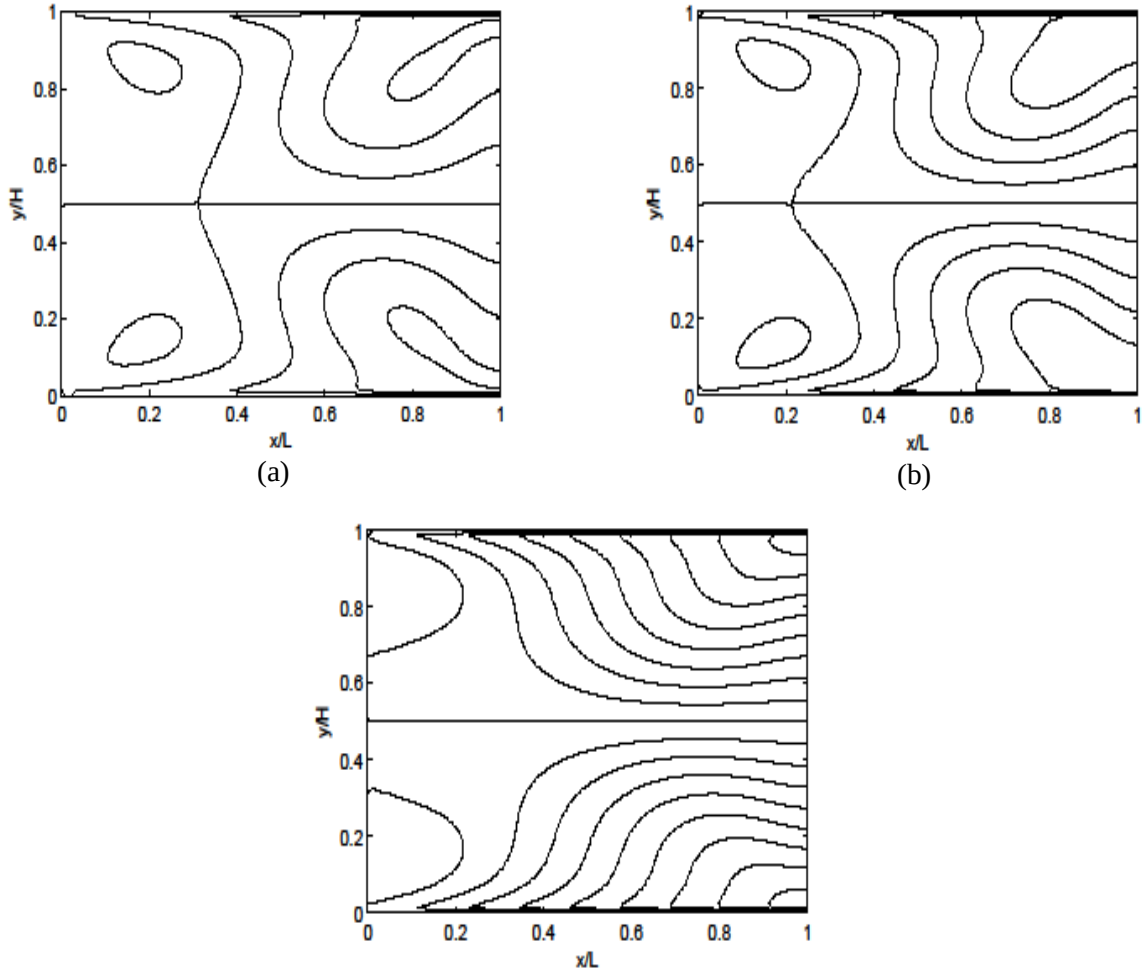


(a) (b)

(c)

FIGURE 2. Streamline plots for $a = 0.5$ and $eps = 0.4$ (a) $Ra = 10^3$ (b) $Ra = 10^4$ (c) $Ra = 10^5$

The values of parameter $\mu_0$ for values 0.5, 0.75 and 1 of $n$ were identified as 0.1, 0.06 and 0.02, respectively, while $\mu_\infty$ was fixed at 0.001. Parameters $a$ and $b$ were taken as 2 and 0.64, respectively. Boundary conditions based on non-equilibrium parts were implemented on velocity distribution function, while the unknown energy distribution functions were determined as [8].

The temperature difference between top wall and the fluid induces fluid flow inside the geometry which results in heat transfer. Various flow properties are recorded to quantify the influence of natural convection on these parameters. The u-velocity profiles in Fig 1 presents the variation in u-velocities with respect to $n$ for fixed values of $\varepsilon$ and Ra at the center half of the cavity. The profiles show a sinusoidal behavior with the highest velocity magnitude at geometric center of the cavity. The u-velocities were observed to increase in magnitude with $n$, although the basic trend remains the same. Influence of $\varepsilon$ and Ra is also observed on velocity profiles as $\varepsilon$ is increased from 0.4 to 0.7 and Ra form $10^3$ to $10^5$, with a similar behavior as in Fig 1. These results indicate that an induced flow can help in transporting the saturated particles within the stenosis to move out from the infected part. Plots in Fig 2 show the influence of these various flow parameters on streamlines. Streamlines are symmetric as required for natural convection in a differentially heated geometry. At higher Ra values, flow strength is stronger as compared to lower values. Also, as $n$ increases from

0.5 to 1, circulation is observed to shift towards the left wall of the cavity. Formation of vortices can be observed for lower values of Ra implicating the flow circulation due to dominance of conduction over conduction. As the influence of convection start dominating, flow field expands to major part of the geometry. For lower values of Ra, vortices on the left of the geometry tend to occupy bigger space. However, these vortices shift towards left and disappear as flow is influenced by buoyancy effect for higher values of Ra. As $n$ increases from 0.5 to 1, flow field due to convection increases which is relevant form expansion of flow field from right to left.

| $n$ | $\varepsilon = 0.4$ | | | $\varepsilon = 0.7$ | | |
|---|---|---|---|---|---|---|
| | Ra | | | Ra | | |
| | $10^3$ | $10^4$ | $10^5$ | $10^3$ | $10^4$ | $10^5$ |
| 0.5 | 1.3154 | 1.3169 | 1.3357 | 1.3179 | 1.3205 | 1.3391 |
| 0.75 | 1.3104 | 1.3157 | 1.3274 | 1.3132 | 1.3168 | 1.3299 |
| 1 | 1.3029 | 1.3140 | 1.3261 | 1.3039 | 1.3144 | 1.3264 |

TABLE 1. Nu at hot wall for various values of $n$, $\varepsilon$ and Ra

## 4. CONCLUSIONS

The rate of heat transfer increases with an increase in porosity and decreases with an increase power law index. The process of increasing rate of heat transfer can be used in pain relief by influencing blood flow in any injured part of the body. At higher Ra values, flow strength is stronger as compared to lower values.

## REFERENCES

1. Merrill W. Edward, Rheology of blood, *Physiological Reviews*, Vol. 40, No. 4, 1969.
2. Wang Chen-Hao, Ho Jeng-Rong, A lattice Boltzmann approach for the non-Newtonian effect in the blood flow, *Computers and Mathematics with Applications*, 62 75–86, 2011.
3. Gijsen F.J.H., van de Vosse F.N., Janssen J.D., The influence of the non-Newtonian properties of blood on the flow in large arteries: steady flow in a carotid bifurcation model, *Journal of Biomechanics* 32, 601-608, 1999.
4. Seta Takeshi, Takegoshi Eishun, Okui Kenichi, "Lattice Boltzmann simulation of natural convectionin porous media", *Mathematics and Computers in Simulation* 72, 195–200, 2006.
5. Guo Zhaoli, Zhao T.S., "Lattice Boltzmann model for incompressible flows through porous media", *Physical Review E* 66, 036304, 2002.
6. Shiyi Chen, Gary D. Doolen, "Lattice Boltzmann method for fluid flows", *Annu. Rev. Fluid Mech.* 30, 329-364, 1998.
7. Ashrafizaadeh Mahmud, Bakhshaei Hani, A comparison of non-Newtonian models for lattice Boltzmann blood flow simulations, *Computers and Mathematics with Applications*, 58, 1045-1054, 2009.
8. Zou Qisu, He Xiaoyi, On pressure and velocity boundary conditions for the lattice Boltzmann BGK meodel, *Phys. Fluids* 9 (6), 1997.
9. Sochi Taha, Non-Newtonian flow in porous media, *Polymer*, 51, 5007-5023, 2010.
10. Sullivan S.P., Gladden L. F., Johns M. L., Simulation of power-law flow through porous media using lattice Boltzmann techniques, *J. Non-Newtonian Fluid Mech.* 133, 91-98, 2006.

# GENERALIZED ONSAGER'S EQUATION SYSTEM AS MATHEMATICAL MODEL OF HEAT AND MASS TRANSFER IN MICROGRAVITY

**Iuliia V. Brazaluk, Dmytro V. Yevdokymov**
Mechanical and Mathematical Faculty, Oles Honchar Dnipro National University, Gagarin ave. 72, Dnipro, 49010, Ukraine, E-mail addresses: brazaluk_jv@ukr.net, devd@ykr.net

## ABSTRACT

Generalized Onsager's equation system is considered as an mathematical model of heat and mass transfer in microgravity conditions assuming that the forced convection is absent in the system and the free convection is quite small. Onsager's equation system is transformed into system of heat conduction equations, which can be solved by any relevant numerical method. It is shown that the generalized Onsager's equation system can be transformed by similar way.

**Key Words:** *Onsager's Equation System, Microgravity, Boundary Element Method.*

## 1. INTRODUCTION

Constantly growing interest to space exploration and fast development of space technologies during last two decades require a development of mathematical models and calculation methods for quantitative analysis of physical and chemical processes in space, in particular, in microgravity conditions. The main difference between heat and mass transfer in microgravity condition and in terrestrial condition is, of course, absence of natural convection. Beside of that, the process is mainly determined by heat conduction phenomena, but influence of several other effects can be sufficient too. However to consider the process, beside the mentioned heat conduction, effects of diffusion, thermodiffusion and coupled diffusion (for multicomponent systems) must be taken into account too. From the mathematical point of view the problem is Onsager's equation system for temperature and concentrations in domain with possibly moving boundary by result of phase transition. Methods of analytical and numerical solution of Onsager's equation system and generalized Onsager's equation system are developed in the present work. It is proposed to use preliminary transformation of Onsager's equation system to heat conduction equation system. The last system can be solved by any relevant numerical method usually using for solution of heat conduction equation. The similar algorithm is developed for generalized Onsager's equation system. Computational potential theory is better for numerical calculation of the considered class of boundary-value problems, than finite difference or finite element method, because the problem is linear, it is formulated in domain of complex shape and there are possible moving boundaries.

## 2. MAIN BODY

### Governing equations

Let us consider an Onsager's equation system

$$\frac{\partial u_i}{\partial \tau} = \alpha_{ij} \Delta u_j, \tag{1}$$

where $u_i$ are unknown fields, which must be determined, $\tau$ is time, matrix $\alpha_{ij}$ is called Onsager's matrix. Repeating indexes in the right hand side of equation system (1) indicate that a sum of correspondent terms is assumed. An Onsager's rule takes place

$$\alpha_{ij} = \alpha_{ji,} \tag{2}$$

thus the Onsager's matrix is symmetrical. From the physical meaning of Onsager's coefficients it is evident that

$$\alpha_{ii} > \alpha_{ij}, \qquad i \neq j. \tag{3}$$

Last inequality (3) leads to all above-mentioned difficulties in numerical solution of Onsager's equation system. Boundary and initial conditions for the system (1) are prescribed by conventional way, as conditions of first, second or third kind well-known in heat and mass transfer theory. To finish the formulation of the problem it is necessary to note that all coefficients in the equations are assumed constant.

**Transformation of Onsager's equation system**

The main idea of Onsager's equation system transformation is replacement of every equation by linear combination of all equations so, that the same heat conduction operator acts on every unknown variable in every obtained equation. Thermal diffusivities in the obtained operators are correspondent eigenvalues of Onsager's matrix, what is evident from following relation

$$\frac{\gamma_{mi}\,\alpha_{i1}}{\gamma_{m1}} = \ldots = \frac{\gamma_{mi}\,\alpha_{ik}}{\gamma_{mk}} = \ldots = \frac{\gamma_{mi}\,\alpha_{iN}}{\gamma_{mN}}, \tag{4}$$

because the relation (4) coincides with definition of eigenvalue. It is easy to see that $\gamma_{mi}$ are components of eigenvector of Onsager's matrix correspondent to eigenvalue $\alpha_m$. Thus new vector of unknown variables $w$ can be introduce by following way

$$w_i = \gamma_{ik}\,u_{k,} \tag{5}$$

and therefore the system (1) can be replaced by the following system

$$\frac{\partial w_i}{\partial \tau} = a_i\,\Delta w_i. \tag{6}$$

There isn't summation in the right hand side of (6). Boundary and initial conditions are transformed by similar way.

**Generalized Onsager's equation system**

There may be sorption, chemical reactions, radioactive decay and other similar phenomena. They lead to generalized Onsager's equation system

$$\frac{\partial u_i}{\partial \tau} + (\vec{V}\,\nabla)\,u_i = \alpha_{ij}\,\Delta u_j + \beta_{ij}\,u_j, \tag{7}$$

where $\nabla$ is Hamilton's operator, $\vec{V}$ is fluid velocity vector.

To build a transformation of generalized Onsager's equation system like described above, let us consider an intermediate system

$$\frac{D u_i}{\partial \tau} = \alpha_{ij} \Delta u_j + \sigma_i u_i, \tag{8}$$

where $\sigma_i$ are some real constants and there is not summation in the last term in (8). Well-known substitution

$$u_i = u_i^* e^{\sigma_i \tau}, \tag{9}$$

transforms the system (8) into new system

$$\frac{D u_i^*}{\partial \tau} = \alpha_{ij}^* \Delta u_j^*, \tag{10}$$

where

$$\alpha_{ij}^* = \alpha_{ij} e^{(\sigma_j - \sigma_i)\tau}. \tag{11}$$

The system (10) formally coincides with Onsager's equation system (1), except properties of matrix $\alpha^*$. However it is shown that their eigenvalues coincide. Then the transformation like (5), (6) can be proposed for the generalized Onsager's equation system

$$v_i = \chi_{ij} u_j, \tag{12}$$

where $\chi_{ij}$ is matrix formed from eigenvectors of matrix $\beta$. It transforms the initial system (7) into system like (8)

$$\frac{D v_i}{\partial \tau} = \alpha'_{ij} \Delta v_j + b_i v_i, \tag{13}$$

where $b_i$ are eigenvalues of matrix $\beta$ and

$$\alpha' = \chi \alpha. \tag{14}$$

After substitution $v_i = v_i^* e^{b_i \tau}$ the system (13) is reduced to the system like Onsager's equation system

$$\frac{D v_i^*}{\partial \tau} = \alpha'^*_{ij} \Delta v_j^*, \tag{15}$$

and the following transformation into system of heat conduction equation $w_i^* = \gamma'_{ik} v_k^*$, is completely similar to previous one, here $\gamma'_{ik}$ is matrix formed from eigenvectors of matrix $\alpha'^*_{ij}$. The final system

$$\frac{D w_i^*}{\partial \tau} = a'_i \Delta w_i^*, \tag{16}$$

is similar to the system (6). In the case of $\vec{V} = 0$ equation system (16) formally coincides with (6). The restricted size of the present paper doesn't give an opportunity to describe methods of numerical solution of formulated problems. However any proper numerical method for heat conduction equation can be used in this case. In particular, boundary element method is used in the present work because of reasons described above.

## 3. RESULTS

To illustrate the proposed approach let us shortly describe several examples. The first one is drying of soil. The soil is considered as semi-infinite homogeneous porous media with constant properties. The process is described by system (1). Moisture content, temperature and pressure on the soil surface are assumed known. Then the system (1) can be transformed into three independent boundary-value problems for new variables with first kind boundary conditions. Beside of that, due to the simplest shape of the solution domain every obtained problem can be solved analytically by Green's function method. For example, in three-dimensional case

$$\begin{aligned} w_i(x_0, y_0, z_0, \tau) = & \int_{\tau_0}^{\tau} \int_{-\infty}^{\infty} \int_{-\infty}^{\infty} w_{ie}(\tau, y, z) \big(\varphi_i(x_0, 0, y_0, y, z_0, z, \tau, \tau_0) - \\ & - \varphi_i(-x_0, 0, y_0, y, z_0, z, \tau, \tau_0)\big) d\tau\, dy\, dz + \\ & + \int_{0}^{\infty} \int_{-\infty}^{\infty} \int_{-\infty}^{\infty} w_{i0}(x, y, z) \big(\varphi_i(x_0, x, y_0, y, z_0, z, \tau, \tau_0) - \\ & - \varphi_i(-x_0, x, y_0, y, z_0, z, \tau, \tau_0)\big) dx\, dy\, dz, \end{aligned} \tag{17}$$

here the well known fundamental solution of three-dimensional heat conduction equation is used in the solution (17).

## 4. CONCLUSIONS

The following conclusion can be made as a result of the present consideration: 1. The proposed transformations give an opportunity to develop enough accurate method for numerical solution of Onsager's equation system and generalized Onsager's equation system. 2. Potential theory and boundary element method application to the considered problems is convenient because it gives an opportunity to obtain numerical and analytical solutions. 3. Nevertheless sufficient achievements in mathematical description of the considered problems, they are rather model problems, because a lot of difficulties remain in theoretical and experimental evaluations of non-diagonal elements of Onsager's matrix and coefficients of source terms in generalized Onsager's equation system. It is an additional reason to develop potential theory and boundary element method in this field, because they are suitable for inverse problems.

# Pressure-driven Plane Poiseuille Flow by Onsager-Burnett Equations

**Ravi Sudam Jadhav, Abhimanyu Gavasane, Amit Agrawal**

Indian Institute of Technology, Bombay, Powai, Mumbai, India-400076

E-mail addresses: rave169@gmail.com, abhimanyu.gavasane@gmail.com, amit.agrawal@iitb.ac.in

## ABSTRACT

In the present study, pressure-driven plane Poiseuille flow is numerically investigated using the Onsager-Burnett equations. The functional dependency of pressure on two space coordinates (x and y) renders this flow problem difficult to solve in one-dimensional framework by the conventional Burnett equations. However, the constitutive relationships for stress tensor obtained in O-Burnett equations contains only cross single order derivatives of velocity with no gradient terms of temperature, density and pressure. This unique feature of these equations allows us to obtain solution for equilibrium variables in pressure driven plane Poiseuille flow. The results for the equilibrium variables, pressure, velocity and temperature, are presented for three Knudsen numbers, Kn = 0.013, 0.05 and 0.12. The Knudsen number range studied, covers the entire slip and early transition regime. These results are validated by comparing it with the stochastic mesoscopic DSMC simulation results. It is observed that the O-Burnett equations are able to capture the non-constant pressure profile in the cross stream direction, a non-equilibrium phenomenon evident in the rarefied micro-scale gas flows.

**Key Words:** *Pressure driven plane Poiseuille flow, O-Burnett equations, Lateral pressure variation.*

## 1. INTRODUCTION

The accurate modelling of non-equilibrium phenomena in rarefied gas flows presents a tough challenge in fluid dynamics. These rarefied gas flows resemble flow situations which are far from equilibrium. As a result, the linear constitutive relationships of classical Navier-Stokes-Fourier (NSF) equations are no longer valid in these extreme flow conditions. In order to overcome these serious limitations of the NSF equations, second order accurate Burnett equations [1] were derived using the Chapman-Enskog expansion method. However, these equations require more number of boundary conditions and are unstable for transient processes. Grad's moment method [2] offer an alternative option to describe rarefied gas flows. However, these equations fail to capture the physics of shock waves beyond Mach number 1.65. Combining the advantages of Chapman-Enskog method and Grad's moment method, regularized 13 (R13) moment equations [3] were developed recently. These equations have proved to be successful in predicting several rarefied gas phenomena. The Burnett equations as well as R13 moment equations have mostly ignored the fundamental principles of non-equilibrium thermodynamics such as positive entropy production and Onsager's reciprocity principle. Our group recently derived the Burnett-type higher order continuum equations, termed as O-Burnett equations [4], which satisfy the fundamental principles of non-equilibrium thermodynamics. Unlike the conventional Burnett equations, O-Burnett equations were proved to be unconditionally stable [4]. Moreover, these equations require same number of boundary conditions as that of NSF equations. These equations are the most generalized set of higher order Burnett-type equations applicable to any kind of molecule. In the present work, we apply these equations to a benchmark flow problem – pressure-driven plane Poiseuille flow.

## 2. ONSAGER-BURNETT EQUATIONS

In the derivation of O-Burnett equations, the phase density function was represented in terms of thermodynamic forces and fluxes. The employed phase density function satisfied the linearized Boltzmann equation and collision invariance property without breaking the Onsager's symmetry principle. This form of phase density function was then utilized to evaluate the constitutive

relationships for stress tensor and heat flux vector. The derivation of Onsager-Burnett equations is given in [4]. Here, the final set of conservation equations for mass, momentum and energy along with the constitutive relationships for the stress tensor and heat flux vector is presented.

$$\frac{\partial \rho}{\partial t}+\frac{\partial \rho u_k}{\partial x_k}=0, \quad (1) \qquad \rho\frac{\partial u_i}{\partial t}+\rho u_k\frac{\partial u_i}{\partial x_k}+\frac{\partial p}{\partial x_i}+\frac{\partial \sigma_{ik}}{\partial x_k}=\rho G_i, \quad (2)$$

$$\rho\frac{\partial \epsilon}{\partial t}+\rho u_k\frac{\partial \epsilon}{\partial x_k}+\frac{\partial q_k}{\partial x_k}+p\frac{\partial u_k}{\partial x_k}+\sigma_{ij}\frac{\partial u_i}{\partial x_j}=0, \quad (3)$$

where constitutive relationships for stress tensor and heat flux vector are obtained by adding the corresponding Navier-Stokes-Fourier terms and Burnett terms.

$$\sigma_{11}=\sigma_{11}^{NS}+\sigma_{11}^{B}=\mu\delta_1 u_x+\mu\delta_2 v_y+\mu\delta_2 w_z+4\frac{\mu^2\beta}{\rho}[\alpha_1 u_x^2+\alpha_2 u_y^2+\alpha_3 u_z^2+\alpha_4 u_y v_x+\alpha_5 u_z w_x$$
$$+\alpha_6 w_x^2+\alpha_7 v_x^2+\alpha_8 u_x v_y+\alpha_9 v_y^2+\alpha_{10} w_z^2+\alpha_{11} v_y w_z+\alpha_{12} u_x w_z+\alpha_{13} v_z w_y+\alpha_{14} w_y^2+\alpha_{15} v_z^2], \quad (4)$$

$$\sigma_{12}=\sigma_{12}^{NS}+\sigma_{12}^{B}=\mu\delta_3 u_y+\mu\delta_3 v_x+4\frac{\mu^2\beta}{\rho}[\beta_1 u_x u_y+\beta_2 v_x v_y+\beta_3 u_z v_z+\beta_4 u_x v_x+\beta_5 u_y v_y$$
$$+\beta_6 w_x w_y\,\beta_7 v_z w_x+\beta_8 u_z w_y+\beta_9 u_y w_z+\beta_{10} v_x], \quad (5)$$

$$q_1=q_1^{NS}+q_1^{B}=\delta_4\kappa\frac{\beta_x}{2R\beta^2}+4\frac{\mu^2\beta}{\rho}[\gamma_1\frac{g_x u_x}{\beta}+\gamma_2\frac{\beta_x v_y}{\beta^2}+\gamma_3\frac{\beta_x w_z}{\beta^2}+\gamma_4\frac{1}{\beta}g_y u_y+\gamma_5\frac{1}{\beta}g_y v_x+\gamma_6\frac{1}{\beta}g_z w_x$$
$$+\gamma_7\frac{\beta_x u_x}{\beta^2}+\gamma_8\frac{1}{\beta^2}\beta_y u_y+\gamma_9\frac{1}{\beta^2}\beta_z u_z+\gamma_{10}\frac{1}{\beta^2}\beta_y v_x+\gamma_{11}\frac{1}{\beta^2}\beta_z w_x+\gamma_{12}\frac{g_x v_y}{\beta}+\gamma_{13}\frac{g_x w_z}{\beta}]$$
$$+\left(\frac{2\kappa(\gamma-1)}{R\gamma}\right)^2\frac{1}{\rho\beta}[\gamma_{14}\beta_y v_x+\gamma_{15}\beta_z w_x+\gamma_{16}\beta_x u_x+\gamma_{17}\beta_y u_y+\gamma_{18}\beta_z u_z+\gamma_{19}\beta_x v_y+\gamma_{20}\beta_x w_z], \quad (6)$$

Note that subscripts represents derivative with respect to that variable. Also, $\beta = 1/(2RT)$ and $g = \log(\rho/\beta)$. The coefficients ($\alpha$'s, $\beta$'s, $\gamma$'s and $\delta$'s) are functions of the type of gas and the interaction potential between the molecules. The values of these coefficients are given in Singh et al. [4].

## 3. PROBLEM STATEMENT

In the present study, we consider a steady state flow confined between two infinite and stationary plane parallel walls located at $y = \pm H/2$. The velocity normal to the walls ($v$) and third component of velocity ($w$) are both taken as zero. All the physical quantities except pressure are functions of $y$-coordinate only. Unlike the conventional Burnett equations, the constitutive relationships for stress tensor contain cross single order derivatives of velocity with no gradient terms of pressure, density and temperature. This unique structure of these equations allows us to obtain solution for equilibrium variables in the pressure driven plane Poiseuille flow. With the assumptions listed above and using the constitutive relationships for stress tensor and heat flux vector, final set of conservation equations for momentum and energy reduce to:

$$\frac{\partial p}{\partial x}-\mu\frac{d^2u}{dy^2}=0, \quad (7); \quad \frac{\partial p}{\partial y}+2\mu^2\alpha_7\frac{\partial}{\partial y}\left[\frac{1}{p}\left(\frac{du}{dy}\right)^2\right]=0, \quad (8); \quad u\frac{\partial p}{\partial x}+k\frac{d^2T}{dy^2}+\mu\left(\frac{du}{dy}\right)^2=0. \quad (9)$$

where $\alpha_7 = -3/5$. We assume that pressure gradient in the $x$-direction to be a constant. The variables in the above equations are non-dimensionalized as follows:

$$y'=\frac{y}{H}, \qquad x'=\frac{x}{H}, \qquad u'=\frac{u}{\sqrt{RT_o}},\ T'=\frac{T}{T_o}, p'=\frac{p}{p_o}, \qquad (10)$$

where the subscript '*o*' represents the variables in the reference centreline state. After non-dimensionalization, the governing equations become (primes are removed for better readability),

$$\frac{d^2u}{dy^2} = \frac{1}{Kn_o}\frac{\partial p}{\partial x}, \quad (11); \quad \frac{\partial p}{\partial y} = \frac{\left[-4Kn_o^2\alpha_7 \frac{1}{p}\frac{du}{dy}\frac{d^2u}{dy^2}\right]}{\left[1 - 2Kn_o^2\alpha_7 \frac{1}{p^2}\left(\frac{du}{dy}\right)^2\right]}, \quad (12); \quad \frac{d^2T}{dy^2} = -Pr\frac{(\gamma-1)}{\gamma}\left[\left(\frac{du}{dy}\right)^2 + \frac{1}{Kn_o}u\frac{\partial p}{\partial x}\right], \quad (13)$$

where, Pr is Prandtl number and $\mathrm{Kn_o} = \frac{\mu_o}{\rho_o\sqrt{\mathrm{RT_o}}\mathrm{H}}$ is the reference Knudsen number defined with reference variables. The x-momentum equation is second order ordinary differential equation; hence we need to specify two boundary conditions. Making use of the inherent symmetry in the problem, we already have, $\frac{\mathrm{du}}{\mathrm{dy}}|_{\mathrm{y=0}} = 0$, $\frac{\mathrm{dT}}{\mathrm{dy}}|_{\mathrm{y=0}} = 0$. Rather than worrying for the velocity slip and temperature jump boundary conditions, the current problem is solved as an initial value problem. For this purpose, we make use of the centreline profile values measured in the DSMC simulations. Equations [11-13] are solved numerically in Matlab using inbuilt function ode45.

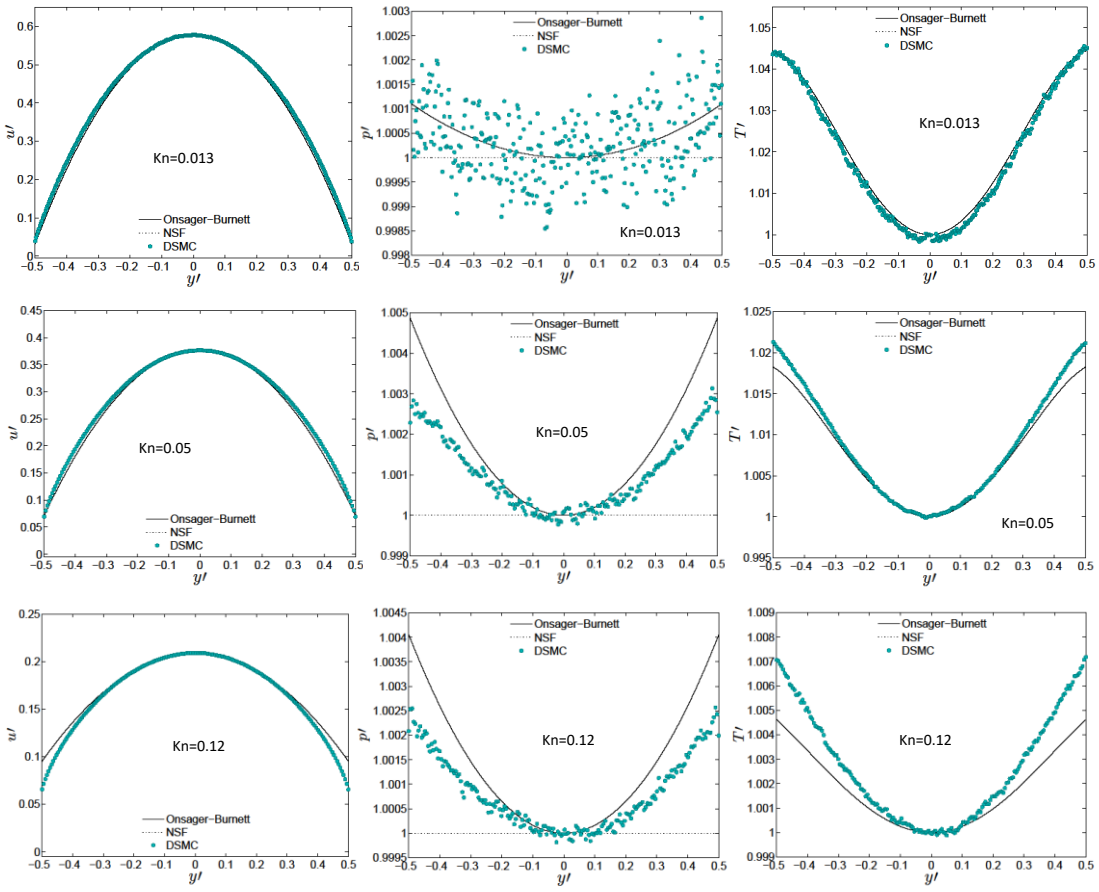


FIGURE 1: Dimensionless profiles across the channel for pressure-driven flow

## 4. RESULTS

The numerical results of O-Burnett equations are compared with the direct simulation Monte Carlo (DSMC) results at Kn = 0.013, 0.05 and 0.12 for argon gas molecule. An in-house DSMC code developed by Gavasane et al. [5] is used to carry out the simulations. The aspect ratio *L/H* considered in the DSMC simulations is 10, where *L* is the micro-channel length and *H* is the micro-channel height. The reason for maintaining high aspect ratio is to minimize the entrance and exit

effects and to make sure that fully developed flow conditions prevail along the length of the micro-channel. A pressure gradient is imposed along the length of micro-channel that drives the flow. The wall temperature and the inlet gas temperature are set at 300 K. The simulations are carried out at a pressure ratio, $P_i/P_o$ equal to 3, where $P_i$ is inlet pressure and $P_o$ is exit pressure. The comparison of dimensionless profiles according to O-Burnett equations against the DSMC results is shown in Fig. (1). At very low Knudsen number, i.e. in the continuum regime, it is well known that constant pressure profile with no pressure gradient is observed in the normal direction. However, in the early slip flow regime at Kn = 0.013, it is evident that there is variation in the pressure in the normal direction with a minimum at the centre of the channel. This non-constant pressure profile can be established when we closely look at the y-momentum equation. Within the NSF framework, the normal stress $\sigma_{22}$ is exactly zero resulting in constant pressure profile. However, the non-zero Burnett order contribution is the ultimate source for the non-constant pressure profile. This is one of the many non-equilibrium phenomena that appear in the case of pressure driven plane Poiseuille flow which classical NSF equations fail to capture. At Kn = 0.05, the velocity results of O-Burnett equations are again found to be in excellent agreement with the DSMC simulation results. However, in case of temperature and pressure, discrepancy is observed near the wall region with reasonable agreement in the bulk region. As we move into the transition regime, i.e., at Kn = 0.12, the discrepancy between the O-Burnett results and the DSMC simulation results at the boundaries becomes higher. As the degree of rarefaction increases i.e. at higher Knudsen numbers, the curvature in the pressure profile becomes much more apparent. It is worth mentioning here, that the present analysis is carried out for constant thermo-physical properties, thereby excluding some of the non-linear effects. This may be the reason for differences in the numerical and DSMC results, especially at the boundaries.

## 5. CONCLUSIONS

In the present study, pressure-driven plane Poiseuille flow is numerically investigated using Onsager-Burnett equations. The absence of temperature, density and pressure gradient terms in the constitutive relationship for stress tensor allows us to obtain solution for equilibrium variables in this flow problem which is difficult with conventional Burnett equations. The results for equilibrium variables are presented for Kn = 0.013, 0.05 and 0.12, covering the entire slip and early transition regime. These results are validated against the DSMC simulation results. It is observed that the Onsager-Burnett equations are able to capture the non-constant pressure profile in the transverse direction. The results for velocity and temperature are in excellent agreement with the DSMC simulation results at lower Knudsen numbers. However, in the transition regime, at Kn = 0.12, discrepancy in results, especially at walls, is observed. This discrepancy can be attributed to assumption of constant thermo-physical properties which excludes certain non-linear effects. Nevertheless, the results of Onsager-Burnett equations for equilibrium variables are encouraging and the results for non-equilibrium variables will be duly reported in the future works.

## REFERENCES

1. Burnett, D. (1935). The Distribution of Velocities in a Slightly Non-Uniform Gas. *Proceedings of the London Mathematical Society, 2*(1), 385-430.
2 Grad, H. (1949). On the kinetic theory of rarefied gases. *Communications on Pure and Applied Mathematics, 2*(4), 331-407.
3. Struchtrup, H., & Torrilhon, M. (2003). Regularization of Grad's 13 moment equations: Derivation and linear analysis. *Physics of Fluids, 15*(9), 2668-2680.
4. Singh, N., Jadhav, R. S., & Agrawal, A. (2017). Derivation of stable Burnett equations for rarefied gas flows. *Physical Review E,* 96(1), 013106.
5. Gavasane, A., Sachdev, S. S., Mittal, B. K., Bhandarkar, U. V., & Agrawal, A. (2011). A critical assessment of the Maxwell slip boundary condition for rarified wall bounded flows. *International Journal of Micro-Nano Scale Transport, 2*, 109-116.

Fifth International Conference on Computational Methods for Thermal Problems
THERMACOMP2018, July 9-11, 2018, Indian Institute of Science, Bangalore, INDIA
*N. Massarotti, P. Nithiarasu, Pradip Dutta and C. Ranganyakalu (Eds.)*

# Numerical investigation for ammonia based axial grooved heat pipe for space application

**Jayesh Mahitkar [1], V.K.Singh*[2], S. S. Kachhwaha[3]**
[1], [3] Department of Mechanical Engineering, Pandit Deendayal Petroleum University, Gandhinagar, India-382007
[2] Thermal Engineering Division, Space Applications Centre, ISRO, Ahmedabad, India-380015
*singhvivek@sac.isro.gov.in

## ABSTRACT

Heat pipe is two-phase passive device having evaporator and condenser to transport relatively large amount of heat from one end to another end with very low temperature difference. Axial grooved heat pipes (AGHP) are widely used in spacecraft panels to transfer heat genearted by various subssyemts mounted over it. This paper deals with detailed numerical investigations to understand the behaviour of axial grooved heat pipe with ammonia as working fluid. Young's lapalace equation is used to predict variation of meniscus radius inside the groove, liquid and vapor pressure drop along the length. Variation of meniscus radius is used to determine liquid film thickness variation along length. Mass conservation is applied to determine liquid and vapour velocity variation along length. Detailed thermal resistance network is constructed to determine effect of various geometrical parameters, thermophysical properties of working fluid and operating conditions. Results of mathematical model is presented for constant condenser temperature at 20˚C and different two heat input i.e. 60 W and 120 W. Mathematical model is extensively validated with experimentation but not reported in present paper.

**Key Words:** *Axial grooved, Ammonia, Heat transfer, modelling*

## 1. INTRODUCTION

AGHPs are passive heat transfer device to transport large amounts of heat over comparatively long distance (1m -5m), without any external means by using latent heat of vaporization and condensation of working fluid sealed inside metallic container. Axial grooves serves the purpose of wick to return condensed fluid to evaporator. As ammonia required high ammount of heat for liquid to vapor conversion restricting phase change, only small mass flow rate required for transport of adequate heat and also temperature differnce across ends of HP is small [1]. AGHPs are usually fabricated from extrusion process leads reduced fabrication costing as well as grooved wick is mechanically resistant and have flexibility in design. For spacecraft thermal control, axial grooved heat pipes are used as a part of honeycomb structural panels and act as an isothermaliser, Kim et al. [2] developed analytical model for operational characteristic of miniature groove heat pipe considering the effect of shear stress at liquid vapor interface and fluid inventory. Using analytical model of Kim et al. [2], Arab et al. developed a model based approach for analysis of working fluid in heat pipe [3]. Peterson et al. developed mathematical model for maximum heat transportation capacity and temperature gradient in '**Ω**' artery wick structure heat pipe.

A detailed resistance network is constructed to determine thermal resistance of trapazoidal shaped axial groove heat pipe. All resistances are computed numerically instead of using imperical relations for liquid vapour interface resistance for evaporator and condenser section. Performace of a typical axial grooved heat pipe is predicted at two typical heat loads (60W and 120W). Mathematical model is validated with experimentation but not reported in current paper.

## 2. NUMERICAL MODELING OF AGHP

In present study, ammonia charged aluminium axial groove heat pipe having trapezoidal grooves is used for numerical performance prediction using partial-analytical hydraulic approach. Ammonia is chosen as working fluid because of higher merit number and good compatibility with the aluminium [1]. Detailed view of single groove cross section of heat pipe chosen for study is schematically shown in Figure 1. It has 28 number of grooves (N) and total length of heat pipe is 1.0 m. Inner diameter of heat pipe (Di) is 10.5 mm, height of groove (hg) is 1.3 mm, groove inclination angle (2γ) is 87˚, evaporator ($L_e$) and condenser ($L_c$) length is 300 mm respectively. Numerical investigations are carried out for constant condenser temperature at 20˚C and two different two heat loads at evaporator section.

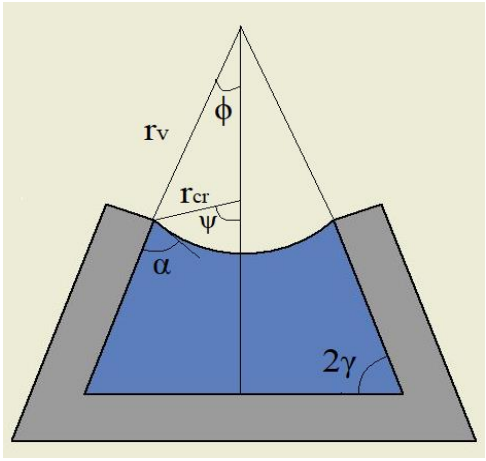


FIGURE 1 Groove cross section of AGHP

Initially Young – Laplace equation (1) is solved with assumption of very large axial meniscus radius($r_{ca}$) as compared to radial meniscus radius($r_{cr}$). With this assumption and taking derivative of equation (1) reduces to eq. (2), which relate variation of liquid and vapor pressure and meniscus radius along length. Variation of vapor and liquid pressure drop along length is given by eq. (3) and (4) respectively.

$$P_C = P_v - P_l = \sigma\left(\frac{1}{r_{ca}} + \frac{1}{r_{cr}}\right) \quad (1) \qquad \frac{dp_v}{dz} - \frac{dp_l}{dz} = -\frac{\sigma}{r_{cr(z)}^2}\left(\frac{dr_{cr}(z)}{dz}\right) \quad (2)$$

$$\frac{dP_v}{dz} = -\frac{2\mu_v C f_v Re_v \dot{m}_v(z)}{{D_{v,h}}^2 A_{v,h}\rho_v} \quad (3) \qquad \frac{dP_l}{dz} = -\frac{2\mu_l f_l Re_l \dot{m}_l(z)}{{D_{l,h}}^2 N A_{l,h}\rho_l} \quad (4)$$

The heat pipe is converted into detailed resistance network [equations (5)-(9)]. Detailed definition of these resistances can be found in Arab & Abbas [3]. Variation of liquid film thickness is determined using $\left(\frac{6\mu_l\omega_{fin}Q_{mic}\bar{r}_{cr}}{LN_g\sigma\rho_l h_{fg}}\right)^{\frac{1}{3}}$ and same is used to compute $R_3$ and $R_6$ which are resistance through liquid film region for evaporator and condenser section respectively [5]. $R_e = \frac{(R_1+R_2+R_3)(R_4+R_5)}{L_e N_g(R_1+R_2+R_3+2(R_4+R_5))}$ (5) $\qquad R_c = \frac{(R_6+R_7+R_8)(R_9+R_{10})}{L_c N_g(R_6+R_7+R_8+2(R_9+R_{10}))}$ (6)

$$R_a = \frac{T_{v,e}T_{v,c}R\ log\left(\frac{P_v\ at\ z=0}{P_v\ at\ z=L}\right)}{h_{fg}Q_{in}} \quad (7) \qquad R_{tot} = R_e + R_a + R_c \quad (8)$$

$$\Delta T = Q_{in}R_{tot} \quad (9)$$

Where,

A, Area ($m^2$); L, Length (m); C, Coefficient of Poiseuille number; D, Diameter (m); fRe, Poiseuille number; z, Length (m); $\dot{m}$, Mass flow rate ($Kgs^{-1}$); N, Number; P, Pressure (Pa); Q, Heat (W); R, Thermal resistance ($CW^{-1}$); R, Gas constant ($JKg^{-1}K^{-1}$), Re, Reynolds number; σ, Surface tension ($Ns^{-1}$) ; α, Contact angle (˚); ρ, Density (Kg$m^{-3}$ ); Ψ, Meniscus radios angle (˚); Φ, Vapor Channel radios angle (˚); μ, Viscosity (Pa. s)

Subscripts

a, adiabatic section; c, capillary/ condenser section; ca, capillary axial; cr, capillary radial, e, evaporator section; f, working fluid; g, groove; h, hydraulic; in, input; l, liquid; v, vapor mic, micro region; tot, total

## 3. RESULTS & DISCUSSION

Variation of various parameters, which governs the performance of AGHP is given in Figures 2-12. Figure 2 shows the heat input along the length which is indicated by 60 W and 120 W. The mass flow rate along liquid line i.e. grooved channels and vapour line i.e. inner core of heat pipe is shown by Figure 3, in which negative sign remarks the vapour flow in reverse direction. Velocity inside the liquid line is negligible compared to vapour line because of difference in cross section area and liquid and vapour density. Variation in pressure drop across liquid (Figure 6) and vapor line (Figure 7) in evaporator region is significant for 60W and 120W heat loads because of heat addition within specified region and same for condenser region is almost negligible because of heat is rejected. In meniscus radius (Figure 8) is increasing along the length and it is reduced with same trend with increase in heat input at evaporator section. Also meniscus radius angle shown in Figure 9 is less for high power input and vice versa. Contact angle (α) (Figure 10) is increasing from evaporator end to condenser end while liquid film thickness (Figure 11) also increases because of condensation of liquid shows its effect. Variation of thermal resistance with heat load is shown in Figure 12.
By increasing the heat load, liquid film thickness is increased which reduces the condenser resistance which ultimately lead to reduction in total thermal resistance. Thus we can say that as heat load increases thermal resistance decreases.

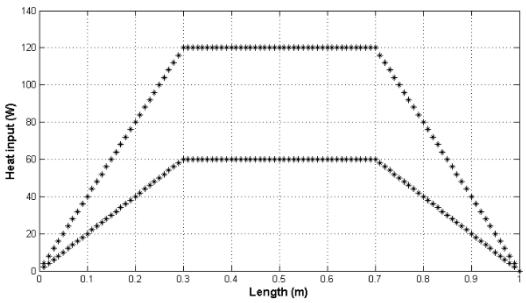


FIGURE 2 Heat flow along length

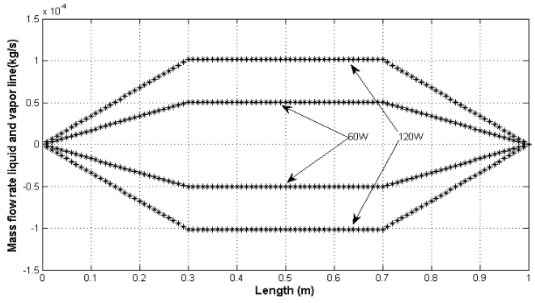


FIGURE 3 Mass flow rate along liquid and vapor line

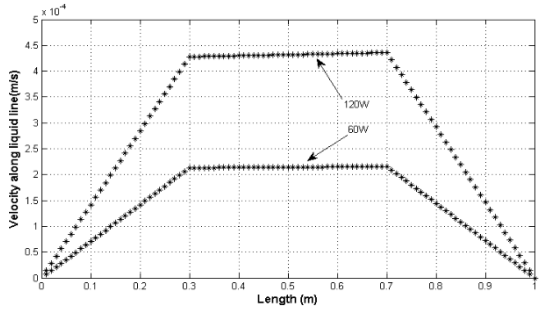


FIGURE 4 Velocity along liquid line

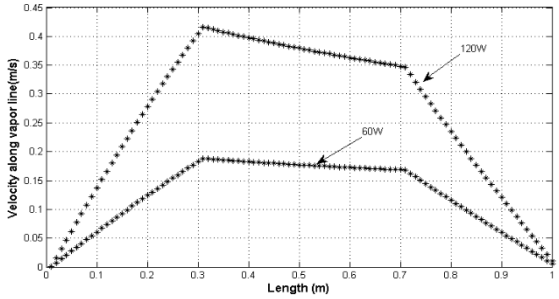


FIGURE 5 Velocity along vapor line

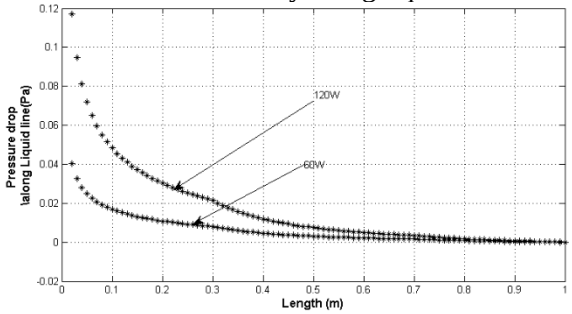


FIGURE 6 Pressure drop along liquid line

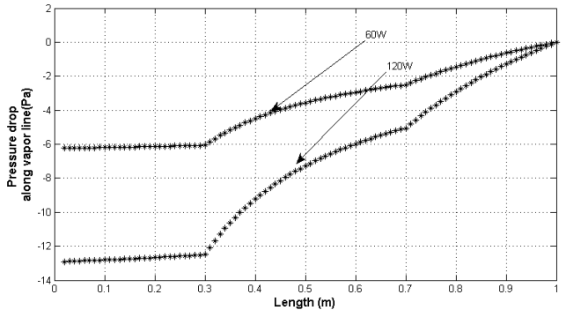


FIGURE 7 Pressure drop along vapor line

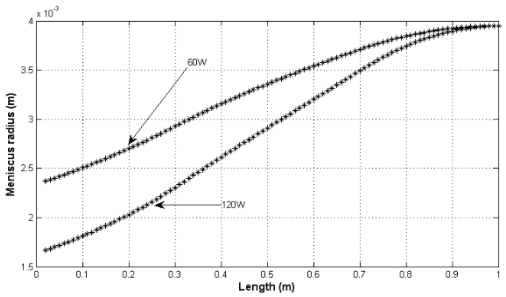


FIGURE 8 Meniscus radius along length of HP

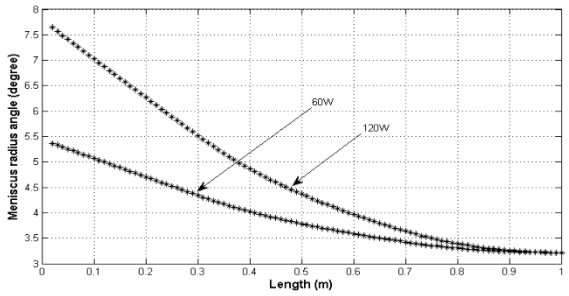


FIGURE 9 Meniscus radius angle along HP

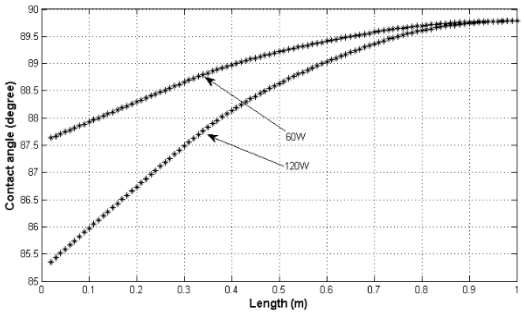


FIGURE 10 Contact angle along HP

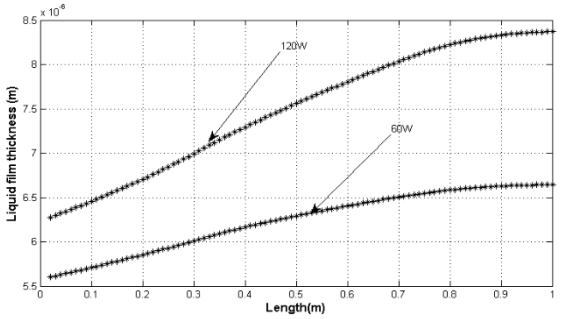


FIGURE 11 Liquid film thickness along length

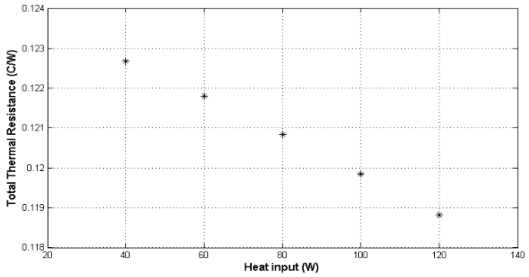


FIGURE 12 Total thermal resistance along heat input

## 4. CONCLUSION

Detailed numerical investigations are carried out for determination of variation of various parameters governing performance of AGHP. Current mathematical model gives better insight of physical phenomena happening inside AGHP. This can be used for optimizing groove geometry. Effect of variation of geometrical parameters of groove, working fluids on thermal performance need to be studied in detail. Mathematical model can be extended for determination of maximum heat transport capacity.

## REFERENCES

[1] G. P. Peterson, An introduction to heat pipes modeling, testing and applications, New York, *USA: John Wiley & Sons*, 1994.

[2] Kim et. al., "Analytical and experimental investigation on the operational characteristics and the thermal optimization of a miniature heat pipe with a grooved wick structure," *International Journal of Heat and Mass Transfer*, vol. 46, no. 11, pp. 2051-2063, 2003.

[3] M. Arab. and A. Abbas, "A model-based approach for analysis of working fluids in heat pipes," *Applied Thermal Engineering*, vol. 73, pp. 749-761, 2014.

[4] Anand et. al., "Analytical and experimental investigations on axially grooved aluminium-ethane heat pipe," *Heat Transfer Engine*, vol. 29, no. 4, p. 410–416, 2008.

[5] A.J. Jiao, R. Riegler, H.B. Ma, G.P. Peterson, Thin film evaporation effect on heat transport capability in a grooved heat pipe, *Microfluidics and Nanofluidics*, 1 (2005) 227-233.

Fifth International Conference on Computational Methods for Thermal Problems
THERMACOMP2018, July 9-11, 2018, Indian Institute of Science, Bangalore, INDIA
*N. Massarotti, P. Nithiarasu, Pradip Dutta and C. Ranganyakalu (Eds.)*

# NUMERICAL COMPARISON OF CHILLDOWN THROUGH STRAIGHT AND HELICAL CRYOGENIC TRANSFER LINES

**Jesna Mohammed**
Assistant Professor, TKM College of Engineering, Kollam, Kerala, India,
jesnamohammed@tkmce.ac.in

**Pranav Shyam Praveen, Godwin J Philip,** PG Student, TKM College of Engineering, Kollam, Kerala, India,

**Rizwan Rasheed , Reby Roy K.E,** Assistant Professor, TKM College of Engineering, Kollam, Kerala, India, rebyroy@tkmce.ac.in

## ABSTRACT

Cryogenics is a new rising technology which is being used in almost all scenarios from food processing, transportation etc. The main disadvantage of the system is that they need to be chilldown before operation and this process uses a large amount of cryogen which are wasted. Production of cryogens are energy intensive and chilldown process leads to wastage of these energy intensive resource. Therefore, by reducing the cryogen wasted can bring down the cost and thus this new emerging technology can be more commercialised.

This numerical analysis aims at developing a CFD model of the cryogenic chilldown procedure and in analysing the continuous and pulsed flow in helical coiled tubes and comparing with similar flow conditions in straight tubes. The test section is modelled using Ansys Design Modeller and the computational analysis was carried out using Ansys Fluent 15.0. The studies use nitrogen as the working fluid and different square wave pulse flow strategies are examined.

**Key Words:** *Chilldown, Helical coil, Pulsed flow, CFD or Computational Fluid Dynamics.*

## 1. INTRODUCTION

Cryogenics is the study of production and effects of temperatures below -150 °C. As contrasted to low temperature physics, cryogenic engineering primarily involves the practical use of low temperature phenomena rather than basic research. Cryogenic fluids find wide applications in many areas, ranging from space propellants, space life support systems, cryogenic hardening of metals to increase hardness and durability, cooling superconducting magnets such as those used in MRI, cryo-preservation of blood and biological materials, cryosurgery, and other chilling and freezing applications.

One application that is continuously getting attention has been the use of cryogenic propellants for rocket propulsion. This interest is sparked by the fact that cryogenic propellants yield more energy, when compared to non-cryogenic propellants and the storage systems for these cryogenic propellants are lighter than those required for their non-cryogenic counterparts. Cryogens such as hydrogen and oxygen are often stored in liquid form due to their high ratio of weight to volume leading to efficient storage. Therefore, the efficient and safe transport and storage of cryogenic fluids are important design considerations in space applications. The introduction of the cryogenic fluid in a transfer line that is in thermal equilibrium with environment results in voracious boiling within the line. Thus, the operation of a cryogenic system requires cooling of transfer line before establishing a steady flow of cryogenic fluid between various system components. The process of cooling down the equipment with cryogenic fluid is known as a cryogenic chilldown process.

The chilldown process is a complex phenomenon with a combination of both thermal and fluid flow transients. A precise understanding of the chilling time, flow rate and fluid quality is important to arrive at proper cryogenic operation sequence in ground and space conditions. The amount of liquid cryogen required to chilldown lines, tanks, turbo pumps, etc. from room temperature is often of significant importance. The physical phenomena involved can be complex, including film boiling and transition boiling, and two-phase pressure drops. Pressure surges can also be experienced due to sudden vaporisation of liquid which can reduce the fluid flow and even reverse the flow. Therefore, feedline should be chilled close to the fluid temperature to achieve a steady smooth flow. Chilling should be carried out for sufficient duration to achieve the wall temperature in the adequate range and to ensure the further operations in the safe condition. In cryogenic rocket engines, insufficient chilling of feedline leads to improper flow of cryogenic fluid in to the combustion chamber that could affect the ignition. It is therefore essential that the chilling procedure and the wall temperature achieved are accurately known to ensure satisfactory performance of the system. A reduction in chill down time and chill down rate will save a metered quantity of cryogen.

Helical flow passages/tubes are very commonly found in many cryogenic regenerative cooling systems. They are used as transfer lines connecting external cryogenic storage vessels and the cryogenic liquid storage tanks in space vehicles. Helically coiled tubes are used widely in heat exchangers, steam generators, food and chemical plants, etc. Helically coiled pipes have many benefits than straight pipes, because of their real-world importance, ease of manufacture and arrangement, higher efficiency in heat transfer and compactness in structure. As compared to straight tube, helically coiled tube shows higher heat transfer coefficient and friction factor due to the enhanced turbulence caused by constantly varying flow direction. The centrifugal forces induce in a coiled tube give rise to secondary flow pattern because of this swirl flow, which consists of two vertices perpendicular to the axial flow direction. Therefore, the heat transfer takes place by diffusion in the radial direction and as well as by convection. The contribution of such secondary convective transport influence the overall process and significantly increases the heat transfer rate per unit length of the tube in comparison with a straight tube of equal length. The extremely complex flow and heat transfer structure present in the channels necessitates exhaustive studies of the problem.

## 2. VALIDATION

The chilldown model is based on experiment study conducted by Reid Shaeffer, Hong Hu and Chung J.N. The results obtained by computational analysis and experimental results were proven to be similar.

## 3. BOUNDARY CONDITIONS APPLIED

The inlet velocity is given to be 0.13m/s for all flow conditions and a fluid temperature of 77K is assumed at inlet. For pulsed flow velocity at inlet varies according to the pulse period and duty cycle which is obtained by using user defined functions in Ansys Fluent. Pulsed flows are represented using a specific nomenclature using pulse period and percentage of duty cycle. (Pulse period in seconds). For e.g. a pulse flow represented as 4s 50 denotes a pulse cycle with a period of 4 seconds and 50% duty cycle. Two such pulsed flows 4s 50 and 10s 50 are analysed in this work. A turbulent intensity of 1% and Hydraulic diameter of 0.0102m is given for each case.

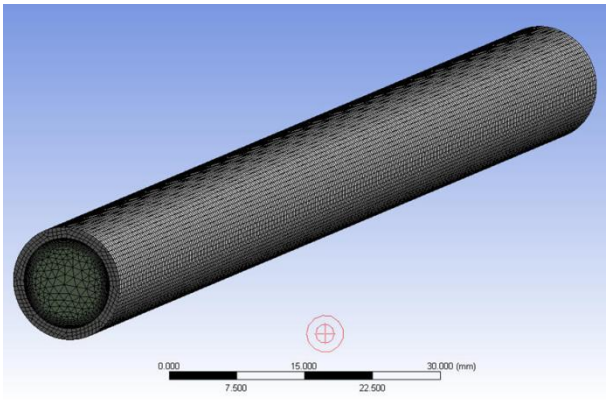

**Figure 1: Mesh in straight pipe**

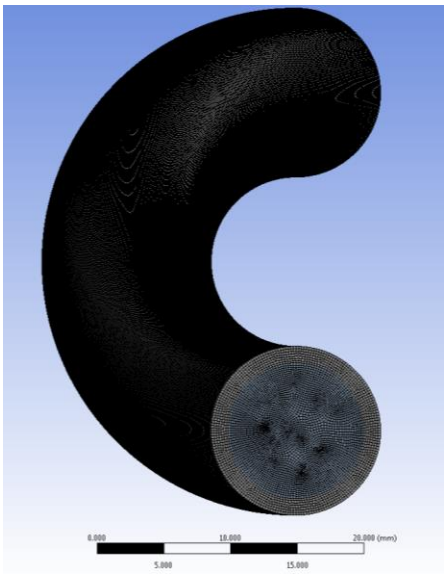

**Figure 2: Mesh in helical pipe**

Meshing is done for both straight as well as helical pipe as shown in Figure 1 and 2 with relevance centre as fine, a relevance of 100 and a curvature normal angle of 10˚. Since the heat flux is given on the wall, the interface between the solid and liquid domain is of utmost importance. So the mesh has to be finer near the boundary layer. For that purpose small face sizing mesh of 0.20mm is applied. A growth rate of 1.10 is given.

## 4. RESULTS

The chilldown time is determined from the temperature plots with time. The total mass of cryogen required for complete chilldown is calculated using the density of liquid nitrogen, inlet velocity, cross sectional area of tube and chill down time. The percentage increase in chilldown time and percentage reduction in mass of the cryogen required for pulsed flow compared to continuous flow is also determined. The data thus obtained are tabulated in the following **Error! Reference source not found.**. A comparison of mass of cryogen required for different type of flow is shown in figure 4.

| Section | Type of Flow | Chilldown Time | % Increase in Chilldown Time | Total Mass Required | % Reduction in Mass |
|---|---|---|---|---|---|
| **Straight Tube** | Continuous | 56.3 | | 0.4839 | |
| | 4s 50 | 68.1 | 20.96% | 0.2931 | 39.43% |
| | 10s 50 | 82.3 | 46.18% | 0.3636 | 24.86% |
| **Helical Tube** | Continuous | 54.3 | | 0.467 | |
| | 4s 50 | 74 | 36.28% | 0.3268 | 30.02% |
| | 10s 50 | 81.7 | 50.46% | 0.3586 | 23.21% |

**TABLE 1.Chilldown time and mass requirement for various cases**

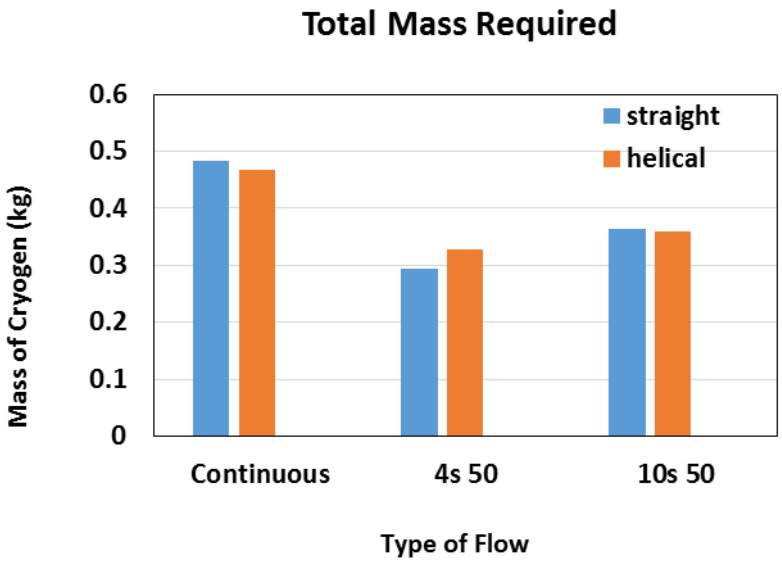


**Figure 4: Comparison of Mass of cryogen requred for different types of flow.**

## 4. CONCLUSIONS

From the simulation results it can be concluded that for continuous flow, the helical coils are more advantageous than straight tubes considering both mass saving and time saving. This might be due to the introduction of secondary flow in the helical coil which increases the heat transfer rate and thus improves chilldown process. When the pulse time is small the straight tube shows better chilldown time and chilldown efficiency compared to helical tube. When helical coil is used instead of a straight tube, due to increased discontinuity, the effect of secondary flow will be very inferior compared to the increased thermal mass of the tube. When the pulse time period increases the helical coil shows better characteristics towards chilldown. This effect is due to the longer ON- time creates time for the creation of secondary flow, but the following longer OFF- period causes the momentum loss of the fluid, therefore the increasing the loss. This loss shadows the favourable effects of the secondary flow created with ON-period. Thus reducing the overall advantage using the pulse with longer time period. Thereby adopting pulsed flow with longer ON period compared to OFF period may provide a favourable effect towards chilldown time reduction.

## REFERENCES

[1] N. Massarotti, F. Arpino, R.W. Lewis, and P. Nithiarasu, Fully explicit and semi-implicit CBS procedures for incompressible flows, *International Journal for Numerical Methods in Engineering*, 66, 1618-40, 2006.

[2] O.C. Zienkiewicz and R.C. Taylor, *The Finite Element Method*, 4th Edition, Vol. I, McGraw Hill, 1989, Vol. II, 1991.

[1] .Reid Shaeffer, Honghu, Chung J.N., (2013), “an experimental study on liquid nitrogen pipe chilldown and heat transfer with pulse flows”, university of Florida, science direct, (954-958)

[2] Jelliffe Kevin Jackson, (2006), “cryogenic two-phase flow during chilldown: flow transition and nucleate boiling heat transfer”, university of Florida.

[3] N.T.VanDresar and J.D.Siegwarth, “*Cryogenic transfer line chilldown”*, NASA Glenn research center

[4] Burke, J.C., Bynles, W.R., Post**,** A. H., and Ruccia, F.E., (1960), "P*ressurized cooldown of cryogenic transfer lines",*A*dvances in Cryogenic engineering,* vol. 4, plenum press, New York, pp. 378-394.

[5] Steward, W. G., Smith, R. V., And Brennan, J. A., (1970), "*Cooldown Transients in Cryogenic Transfer Lines*," *Advances In Cryogenic Engineering,* Vol. 15, Plenum Press, New York, Pp. 354-363.

[6] Cheng-Feng tai, (2008),"*cryogenic two-phase flow and phase-change heat transfer in microgravity",* university of Florida, dissertation

[7] Alok Majumdar, S.S. Ravindran, (2011) "*Numerical prediction of conjugate heat transfer in fluid network*", Journal of propulsion and power Vol 27, No-3

[8] K. Yuan, Y. Ji, J.N. Chung, W. Shyy, (2008) "*Cryogenic boiling and two-phase flow during pipe chilldown in earth and reduced gravity*", J. Low Temp. Phys. 150 101–122.

[9] V.V. Klimenko, M.V. Fyodorov, Y.A. Fomichyov, (1989) "*Channel orientation and geometry influence on heat transfer with two-phase forced flow of nitrogen*" , Cryogenics 29 (1) 31–36

[10] O. Kawanami, T. Nishida, I. Honda, Y. Kawashima, H. Ohta, (2007) "*Flow and heat transfer on cryogenic flow boiling during tube quenching under upward and downward flow, microgravity*", Sci. Technol. 19 (3–4) 137–138.

[11] Jacobs,R.B., (1963) "*Liquid requirements for the Cool-down of Cryogenic Equipment*" in "*Advances in Cryogenic Engineering*, edited by K.D. Timmerhaus, Plenum Press, New York, 8 529-535,
12. Flynn, T.M., (1996), *Cryogenic Engineering*, Marcel Decker, New York, pp. 67-69

[12] D. G. Prabhanjan, G. S. V. Ragbavan and T. J. Kennic, "*comparison of heat transfer rates between a straight tube heat exchanger and a helically coiled heat exchanger*", ,Int. Comm. Heat and Mass transfer,vol. 29. No. 2. Pp. 185-191

[13] M.V. Krishnamurthy et al., (1996) Experimental studies on cool-down and mass flow characteristics of a demountable liquid nitrogen transfer line, Cryogenics, Volume 36, Issue 6, June, Pages 435–441

# FLOW TRANSIENTS DURING VALVE OPERATION IN CRYOGENIC FEED SYSTEM

**Jeswin Joseph, Gagan Agrawal, Deepak K Agrawal, J. C. Pisharady and S Sunil Kumar**
Liquid Propulsion Systems Centre, ISRO, Trivandrum, Kerala, India
jeswinj.90@gmail.com

## ABSTRACT

A transient, thermodynamic, two-phase flow model of a cryogenic feed line is developed to simulate pressure oscillations in cryogenic fluid occurring due to sudden opening. The effects of dead segments volumes, line chilling and flow rate changes on amplitude and frequency of these oscillations are investigated using numerical analysis. The model is validated with in-house experimental data and literature based on MOC solution for valve operation. Current study is significant for understanding pressure oscillations during valve operation in launch vehicle cryogenic engine. Pressure oscillations can cause fluctuations in propellant flow rate, resulting in undesirable variations in thrust output from the engine. Trapped vapour volumes in dead segments, which are not a part of flow line, can affect the oscillation parameters. Computational analysis shows significant reduction in oscillation frequency when trapped vapour volumes are used. Analysis for valve opening operation in unchilled line shows pressure surge due to evaporation is significant.

**Key Words:** *feed line, valve opening, trapped volume.*

## 1. INTRODUCTION

The study analyzes methods to control the amplitude and frequency of the oscillations occurred due to valve opening during engine operation. A detailed analysis of valve operation is needed as pressure oscillation may lead to system failure. Very low pressures attained due to fluid-hammer oscillation could lead to reduction in pump inlet pressure below saturation level. This may cause pump cavitation during engine operation. Pressure oscillations also cause fluctuations in propellant flow rate, resulting in undesirable variations in thrust output from the engine. These phenomena are more vital in case of cryogenic feed system due to high volatility of cryogenic fluid. Dead segments containing vapour pockets and degree of feedline chilling can alter the nature of these oscillations and the effect of these parameters is analyzed here.

Cryogenic feedlines are subject to large differential pressure when sudden opening of a valve in the line takes place, typically during initiation of test sequence or start-up of cryogenic engine in launch vehicles. Valve opening operations induce fluid hammer by the force at valve outlet due to sudden change in fluid momentum. This causes fluid pressure oscillations leading to fluctuating flow of cryogenic fluid into the engine chamber, resulting in adverse transients in outputs.

## 2. SOLUTION METHODOLOGY

Current study focuses on developing a transient, two-phase, thermodynamic flow model [1]-[4] of a typical cryogenic feed line to simulate feed line pressure oscillations due to sudden opening of valve. Detailed schematic of analytical model is shown in Fig. 1

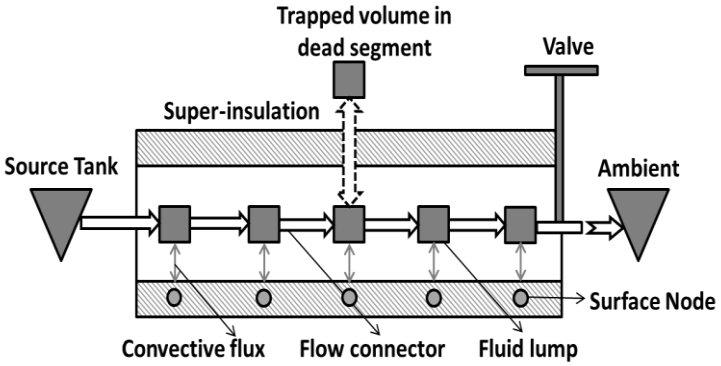


FIGURE 1: SCHEMATIC OF COMPUTATIONAL MODEL FOR STUDYING FLUID-HAMMER PHENOMENON

## 3. SALIENT RESULTS

The model captures the amplitude and frequency of pressure oscillation caused due to sudden opening of liquid hydrogen injection valve at the start of cryogenic engine operation. The model is validated with literature [5] and in-house experimental data using LOX and LH2 as flow media, respectively. Comparison of pressure oscillation in experiment of engine operation and simulations are shown in Fig.2.

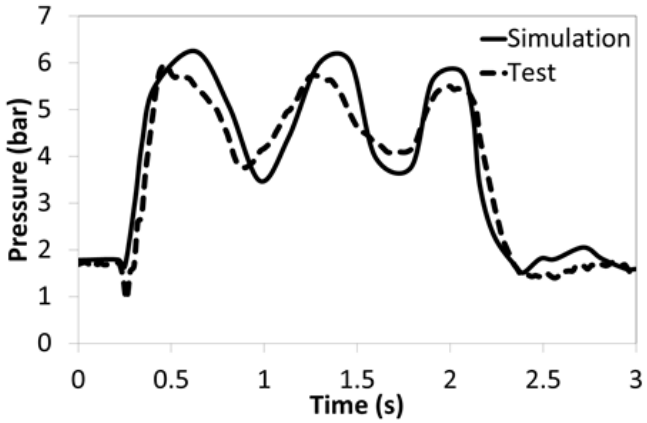


FIGURE 2: VALIDATION OF COMPUTATIONAL MODEL USING

IN-HOUSE TEST RESULTS

The effects of dead segments volumes and unchilled feedline on amplitude and frequency of fluid-hammer induced pressure oscillations are investigated. Computational analysis shows high oscillation and peak amplitude of pressure in unchilled feed system as shown in Fig 3. Analysis also shows significant reduction in oscillation frequency when dead segment volumes are included in the feed system.

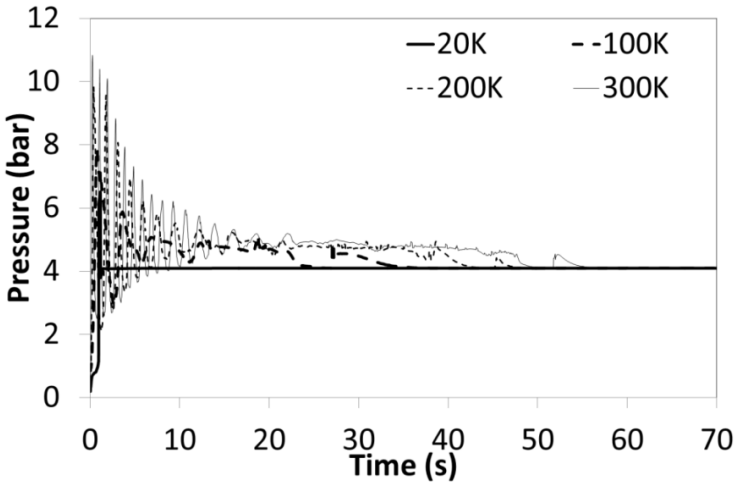


FIGURE 3: PRESSURE PROFILE SIMULATED AT ORIFICE INLET LOCATION DURING VALVE OPENING OPERATION USING DIFFERENT INITIAL TEMPERATURE OF FEEDLINE FOR A DURATION OF 70S (DURATION TO REACH STEADY PRESSURE LEVEL)

## 4. CONCLUSIONS

Analysis is carried out to study the pressure oscillation pattern occurring due to sudden valve opening which admits the cryogenic fluid to feedline at various degrees of chilling. Following are the important conclusions from the analyses:

- Pressure oscillation in valve opening scenario dampens faster compared to valve closing scenario in fully chilled line due to continuous flow of fluid taking place after valve opening. Oscillation frequency reduces with time due to line chilldown.
- Pressure transients in unchilled lines are mainly due to liquid evaporation and subsequent vapour generation. Pressure transients due to fluid-hammer effect while opening of valve in unchilled lines are found insignificant compared to the transients due to thermal effect.
- Presence of trapped vapour volume is found disadvantageous when used in unchilled line configuration during valve opening scenario.

## REFERENCES

[1] Mostafa Ghiaasiaan S, 2008 *Two-Phase Flow, Boiling and Condensation in Conventional and Miniature Systems,* Cambridge University Press, Cambridge, UK, Chap. 10 and 13. ISBN: 978-0-521-88276-7.

[2] Lochkhart R W, and Martinelli, R C, 1949 *Proposed Correlations of Data for Isothermal Two Phase Two Component Flow in Pipes,* Chemical Eng., Prog.45, pp. 39-48.

[3] Incropera F P, Dewitt D P, 2009 *Fundamentals of Heat and Mass Transfer,* John Wiley and Sons, Chap. 8, ISBN: 978-81-265-1261-4.

[4] Van Dresar N T, Siegwarth J D, and Hasan M M, 2002 *Convective Heat Transfer Coefficient for Near-Horizontal Two-Phase Flow of Nitrogen and Hydrogen at Low Mass and Heat Flux,* Cryogenics Vol. 41, pp.805-81.

[5] Majumdar A 2003, *Numerical Modeling of Unsteady Thermofluid Dynamics in Cryogenic Systems*, 14th Annual Thermal & Fluid Analysis Workshop.

# CFD ANALYSIS AND OPTIMIZATION OF THE ULTRASONIC TREATMENT OF MG ALLOY MELT

**Jigar Desai, Shyamprasad Karagadde, Atul Sharma**
Department of Mechanical Engineering, Indian Institute of Technology, Bombay-400076, India
desai.jigar117@gmail.com, s.karagadde@iitb.ac.in , atulsharma@iitb.ac.in

## ABSTRACT

The effect of ultrasonic treatment on the melts is mainly due to the ultrasonic streaming and cavitation. In this paper, the influence of different process parameters and geometrical parameters i.e. ultrasonic frequency, ultrasonic probe depth and ultrasonic probe diameter on the streaming in Mg alloy melt is numerically simulated. Firstly, the results are validated by comparing them with the available literature and then the effect of different parameters on the flow field of Mg alloy melt are investigated using ANSYS Fluent 16.2 solver. It is found that for a given set of geometrical parameters (ultrasonic reactor size, ultrasonic probe diameter and probe depth in melt) and material properties, there is a critical frequency at which the velocity flow field and thus streaming effect is desirable for uniform and homogeneous distribution of the nanoparticles in MMCs..

**Key Words:** *Ultrasonic streaming, Melt convection, CFD.*

## 1. INTRODUCTION

Magnesium based metal matrix composites (MMCs) have been extensively studied and widely used in the aerospace, automotive and military industries due to their high strength-to-weight ratios and enhanced mechanical and thermal properties including specific modulus, superior strength, stiffness, good wear resistance, fatigue resistance and improved thermal stability [1–3]. However, the particles commonly used are micron-sized which has a counterpart that the ductility of the MMCs deteriorates with high ceramic particle concentration [4]. Consequently, more attention has been drawn to metal matrix nano composites (MMNCs), since the properties of metallic alloys reinforced by ceramic nanoparticles (with dimensions less than 100 nm) would be enhanced considerably while the ductility of the matrix is retained [5–12]. However, it is extremely difficult to obtain uniform dispersion of nano sized ceramic particles in liquid metals due to high viscosity, poor wettability in the metal matrix, and a large surface-to-volume ratio, which results in agglomeration and clustering of the particles [4]. Currently, several fabrication technologies including high-energy ball milling [9,12], in situ synthesis [8], electroplating [13], and ultrasonic technology (UST) [4–6] are most commonly used, among which UST is supposed to be more reliable and cost effective. To study the effect of ultrasonic treatment on melt, many researchers carried out experiments with different processing and geometrical parameters. They compared the microstructures of particular material with and without ultrasonic treatment and they found that the material with ultrasonic treatment exhibits more desirable properties i.e. smaller grain size, increased yield strength, more uniform distribution of nanoparticles.

Extensive experimental work has been carried out related to ultrasonic treatment of the melts. However, there is a little information available to develop an optimized process map. In this paper, a parametric investigation of ultrasonic treatment of the Mg alloy melt is reported by varying the probe size and position (schematic shown in Fig. 1). The numerical modelling framework and approach are discussed, followed by the results and discussion.

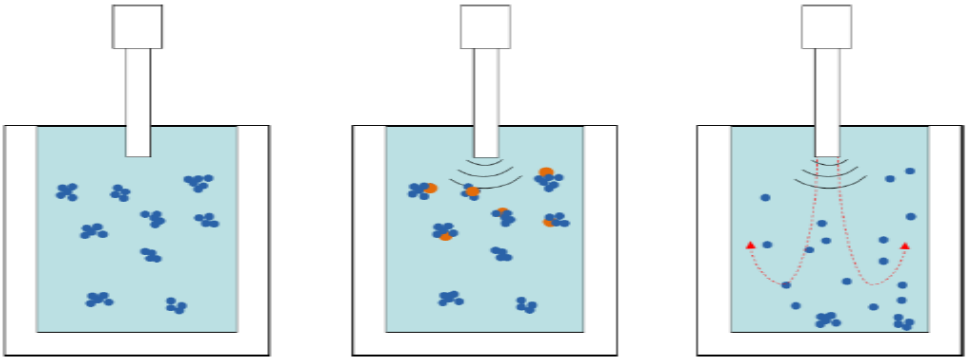

FIGURE 1. Basic principle of ultrasonic treatment

## 2. NUMERICAL SIMULATION

### 2.1 Numerical Simulation Model and Parameters

The numerical simulation in Mg melt is carried out by ANSYS Fluent 16.2 solver. The geometry used in the CFD calculation is shown in Fig. 4. The model is two dimensional and axi-symmetrical, and one half is selected for simulation. The ultrasonic probe of diameter 20 mm is immersed vertically into the melt 25 mm deep in a container of 150 mm × 100 mm. The ultrasound with three different frequencies 15 kHz, 20 kHz and 25 kHz is introduced into the Mg alloy melt. Density of Mg alloy melt is 1820 kg/m$^3$ and viscosity is $1.12\times10^{-3}$ Pa.s. The geometry and mesh are shown in figures 2 and 3 respectively.

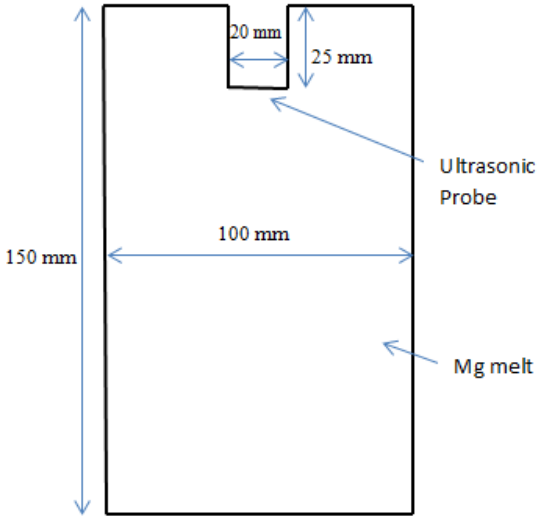


FIGURE 2. Geometry

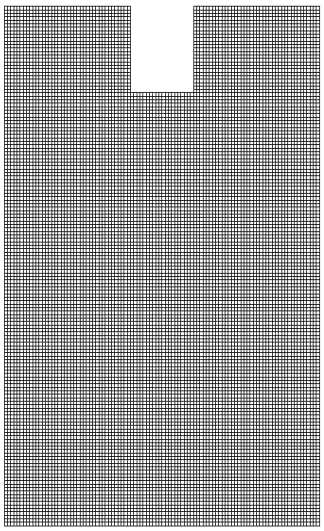

FIGURE 3. Mesh used for simulation

### 2.2 Governing Equations

Continuity and Momentum (N-S) euations are solved. k–Ɛ turbulence model is used for tubulent flow at ultrasonic frequencies.

### 2.3 Boundary Conditions

(1) Pressure Inlet: The boundary of the ultrasonic probe from which ultrasound is introduced into the melt is set to be the pressure-inlet boundary. The pressure varies with time according to the sine law at the frequency of the ultrasonic probe. The pressure inlet condition is defined by UDF ([13] User Defined Function, ANSYS, Inc., US) files. The expression of pressure variation is as follows:

$$P = Pa * \sin(2\pi ft) \quad (1)$$

where $Pa$ = pressure amplitude = 2 Mpa, $f$ = ultrasonic frequency, $t$=time

(2) Pressure Outlet: The interface between Mg melt and air is set as pressure outlet.

(3) Symmetry: For reducing computational time, only half of the domain is simulated. Hence symmetry boundary condition is applied at center axis.

(4) Walls: The boundaries except pressure-inlet, pressure-outlet and symmetry axis are set to be wall boundary, and the heat transfer between wall boundary and environment is ignored.

## 3. RESULTS AND DISCUSSION

The probe size and location are varied to see the flow profiles. In Fig. 4(b-c), two zones with zero velocity can be observed which represents vortices/recirculation. These zones are not present in the other cases (Fig. 4&5). In the case of MMNCs, where nanoparticles are introduced in melt in order to increase desirable properties, uniform and homogeneous distribution is desirable. Nanoparticles may get entrapped or accumulated in these low velocity regions. These regions also indicate that the temperature of the melt is not homogeneous due to the absense of convection.

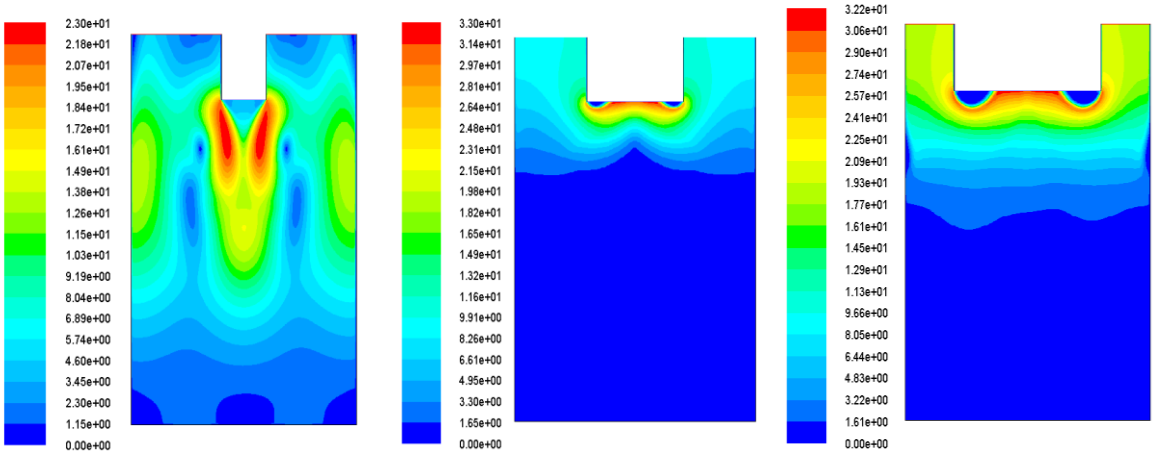


(a) (b) (c)

FIGURE 4. Velocity distribution at t = 1 s, f = 20 kHz and ultrasonic probe diameter
(a) d=20 mm (b) d=40 mm (c) d=60 mm

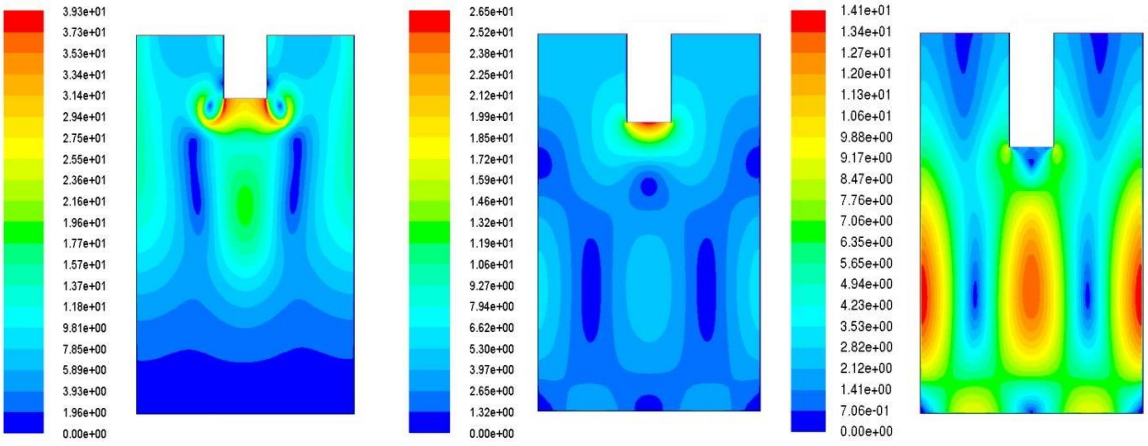


(a) (b) (c)

FIGURE 5. Velocity distribution at t = 1 s, f = 20 kHz and ultrasonic probe depth
(a) h=25 mm (b) h=35 mm (c) h=50 mm

From Fig. 4, it can be observed that d=20 mm case will give favourable velocity field for nano particle distribution. With the increase in ultrasonic probe depth, velocity magnitude and intensity increases as shown in Fig. 6. With h=25 mm and h=35 mm case, the melt in the bottom part of reactor is unaffected, whereas it is not the case for h = 50 mm case.

## 4. CONCLUSIONS

The ultrasonic streaming in Mg melt was investigated by CFD numerical simulation, and the results were validated with the available literature. CFD simulations were carried out different probe diameters and depths to study their effect on velocity field and thus on nanoparticle distribution. As the ultrasonic probe diameter increases, its effect on flow field confined to the flow field nearer to probe. As the ultrasonic probe depth increases, its effect tends to penetrate towards the bottom part of the reactor, which helps in homogeneous distribution of nanoparticles. The low velocity regions also indicate negligible convective heat transfer, and thus are likely to develop hot spots.

Acknowledgements: Authors acknowledge the funding from the Department of Science and Technology's Advanced Manufacturing Technology grant, SMART FOUNDRY 2020.

## REFERENCES

[1] JW Kaczmar, K Pietrzak, W. Wlosinski, "The production and application of metal matrixcomposite materials", J Mater Process Technology 2000; 106:58–67.
[2] K. Durisinova, J. Durisin, M.Orolinova, "Effect of particle additions on microstructure evolutionof aluminium matrix composite", J Alloys Compd 2012; 525:137–42.
[3] CH. William, "Commercial processing of metal matrix composites", Mater Sci Eng. A 1998;244(1):75–9.
[4] Yang, J. Lan, Li X, " Study on bulk aluminium matrix nano-composite fabricated by ultrasonic dispersion of nano-sized SiC particles in molten aluminium alloy", Mater Sci Eng. A 2004;380:378–83.
[5] Li X, Yang, Weiss, "Ultrasonic cavitation based dispersion of nanoparticles in aluminium meltsfor solidification processing of bulk aluminium matrix nano composite: theoretical study, fabrication and characterization", AFS Transactions. Schaumburg, IL, USA: American Foundry Society; 2007.
[6] G.Cao, H. Konishi, X.Li, "Mechanical properties and microstructure of SiC-reinforced Mg-Al 1Si Nano composites fabricated by ultrasonic cavitation based solidification processing", Mater Sci Eng. A 2008; 486:357–62.
[7] JH. Shin, HJ Choi, MK. Cho, DH. Bae, "Effect of the inter face layer on the mechanical behaviour of TiO2 nanoparticle reinforced aluminium matrix composites", J Compos Mater 2014; 48(1):99–106.
[8] B. Dikici, M. Gavgali, "Synthesis of in situ TiC nanoparticles in liquid aluminium: the effect of sintering temperature", J Compos Mater 2010; 45(8):895–900.
[9] AA El-Daly, M. Abdelhameed, M. Hashish, WM. Daoush, "Fabrication of silicon carbide reinforced aluminium matrix Nano composites and characterization of its mechanical properties using non-destructive technique", Mater Sci Eng. A 2013; 559:384–93.
[10] X. Jiang, M. Galano, F. Audebert, "Extrusion textures in Al, 6061 alloy and 6061/Si Nano composites" Mater Charact 2014;88:111–8.
[11] JH. Shin, DH Bae, "Effect of the TiO2 nanoparticle size on the decomposition behaviours in aluminium matrix composites", Mater Chem Phys 2014; 143:1423–30.
[12] C. Borgohain, K. Acharyya,S. Sarma, KK Senapati, KC Sarma, P. Phukan, "A new aluminium-based metal matrix composite reinforced with cobalt ferrite magnetic nanoparticle", J Mater Sci 2013; 48:162–71.
[13] ANSYS Fluent Solver Theory guide. ANSYS Inc., Canonsburg, PA, Release 17, 2016

Fifth International Conference on Computational Methods for Thermal Problems
THERMACOMP2018, July 9-11, 2018, Indian Institute of Science, Bangalore, INDIA
*N. Massarotti, P. Nithiarasu, Pradip Dutta and C. Ranganyakalu (Eds.)*

# POROUS MEDIUM MODELING OF GESTAIONAL AGE DEPENDENT FETAL DRUG EXPOSURE

**Ajith Joseph[1] and Arunn Narasimhan[2]**
[1]Research Scholar, HTTP Laboratory, Department of Mechanical Engineering, Indian Institute of Technology, Madras, Chennai, India 600036, *Email:ajith.jsph@gmail.com*
[2]Professor, HTTP Laboratory, Department of Mechanical Engineering, Indian Institute of Technology, Madras, Chennai, India 600036, *Email:arunn@iitm.ac.in*

## ABSTRACT

A numerical model for evaluating fetal exposure of maternally administered drugs has been developed. A single repeating functional unit cell of placenta has been modelled as a porous medium species exchanger between mother and fetus. The model is capable of predicting fetal drug concentration with respect to maternal one at any point of perfusion time for any gestational age ranging from 20$^{th}$ week to term pregnancy. It also predicts the possible drug absorption in to chorionic and basal plate tissue.

**Key Words:** *Transplacental, porous medium, species transport, numerical*

## 1. INTRODUCTION

Many of the compounds that are administered for maternal treatment may cross the placenta and elicit harmful effects in fetal tissues and organs [1]. It can affect the fetus causing damage, abnormal development (leading to birth defects), or death. Fetal exposure can be expressed classically as the ratio (FM) of fetal drug concentration ($C_f$) to maternal drug concentration ($C_m$). But, for ethical and technical reasons, clinical studies in pregnant women are very rare. Therefore, to evaluate fetal drug exposure *via* placenta, researchers have to gather the information from a series of alternative models that imitate the materno-fetal interface. The currently employed approaches include *in vitro* models of cell cultures derived from human placental tissue, *ex vivo* perfused human placenta or *in situ* perfused animal placenta and in vivo transgenic animals [2].

Among these methods, only e*x vivo* perfused human placenta provides the opportunity to investigate transplacental drug transfer directly in the human placenta [3]. Though, it is the best known method for validating transfer of substances to the fetus, cells in perfused placentae remains viable only for up to 48 h limiting its maximum perfusion time period. The model is also incapable of representing pre-term placenta as it undergoes constant development during the pregnancy period. Since placenta is a very complex organ, none of the above mentioned models can exactly reflect the fetal drug exposure *in vivo.*

In this paper we introduce a new model for placental drug transfer and thereby fetal drug exposure which can overcome the above mentioned drawbacks. Here, the repeating functional unit cell of placenta, a placentone has been mapped as a porous medium species exchanger. Flow and species transport properties were assumed to be dependent on gestational age. The model was found to be effectively predicting the fetal drug exposure within the range of 20-40 weeks of gestation.

## 2. MATHEMATICAL MODELING

The computational domain, as shown in Figure 1 represents the single functional species exchange unit cell (placentone) of a healthy term placenta. The domain mainly consist of three regions, namely the Intervillious space (IVS), fetal capillary (FC) and placental barrier (PB) separating both. The drug diffuses from the maternal blood in IVS in to fetal blood in fetal capillary chamber through the placental barrier. The drug is assumed to be lipophilic and its molecular size is less than the critical size for trans-placental transfer. The species transport process of the drug across the placental barrier is assumed to be according to Ficks' law for unsteady passive diffusion process.

The impermeable regions, the basal plate and the chorionic plate mark the top and bottom boundaries of a placentone. While the intervillious space and fetal cappiliary are treated as porous media, the placental barrier is solid continuum through which only diffusion happens.

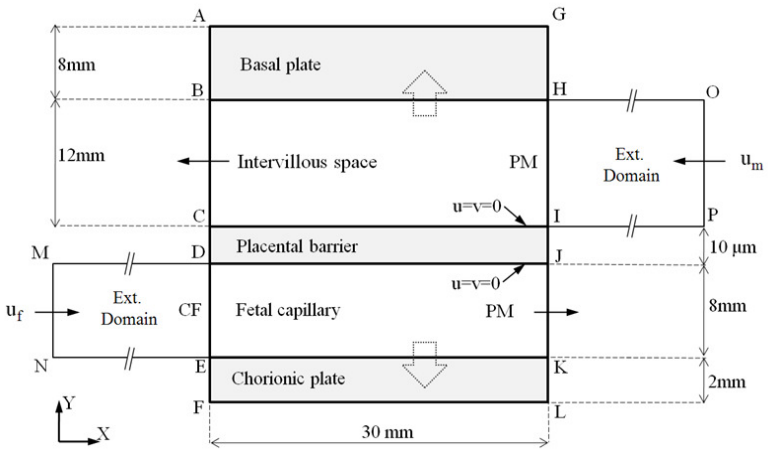


FIGURE 1:Representative computational domain

The extended domains used at the inlet of IVS and FC ensure the total amount of fluid required in the maternal and fetal circulations as per the standards of perfusion experiment. The lengths of these extended domains were chosen such that the relative amount of blood flowing through the IVS and FC matches the standard recalculating perfusent volume [3].

TABLE 1 : Diffusion boundary conditions

| Boundary | Boundary Condition |
|---|---|
| OP, BC | $C'_{OP} = C'_{BC}$ , $C_{OP} = C_{BC}$ |
| MN, JK | $C'_{MN} = C'_{JK}$ , $C_{MN} = C_{JK}$ |
| HI, DE | $C'_{+} = C'_{-}$ , $C_{+} = C_{-}$ |
| BH, EK, CI, DJ | $(DC')_{+} = (DC')_{-}$ |

TABLE 2 : Flow boundary conditions

| Boundary | Boundary Condition |
|---|---|
| OP | $u = -u_m$ , $P = 10 \times 10^3$ Pa |
| BC | $P = 0$ Pa |
| MN | $u = u_f$ , $P = 4 \times 10^3$ Pa |
| JK | $P = 0$ Pa |
| HI, DE | $u_{+} = u_{-}$ |

The porous media and the continuous fluid regions were assumed to be saturated with blood of viscosity $\mu=3.5\times10^{-3}$ *Pa.s* and density $\rho=1.05\times1^{-3}$ *kg/m*$^3$. The diffusivity *D* of drug in blood and tissue (basal plate and chorionic plate) are $4\times10^{-10}$ *m*$^2$*/s* and $1\times10^{-12}$ *m*$^2$*/s* respectively [4]. Different boundary conditions used in the study are summarized in Table 1 and 2.

TABLE 3 : Gestational age dependent variables

| Gestational age | $u_m$ $(m/s)$ | $u_f$ $(m/s)$ | $D_{PB}$ $(m^2/s)$ | $L_{PB}$ (µm) |
|---|---|---|---|---|
| 20 weeks | $0.38\times 10^{-2}$ | $0.4\times 10^{-2}$ | $4.4\times 10^{-11}$ | 2 |
| 40 weeks | $0.38\times 10^{-1}$ | $0.4\times 10^{-1}$ | $4.4\times 10^{-10}$ | 10 |

The properties of flow and species transport which vary depending upon the gestational age are included in this model as given in the Table 3. Initial conditions, $C=1$ *mol/m*$^3$ within IVS and its extended domain, $C=0$ *mol/m*$^3$ everywhere else, was being used.

The equations governing diffusion through porous medium are,

In IVS, FC and their attached extended domains,

$$\frac{\partial C}{\partial t} + (U \cdot \nabla C) = \nabla \cdot (D \nabla C) \quad (1)$$

In basal plate, chorionic plate and placental barrier,

$$\frac{\partial C}{\partial t} = \nabla \cdot (D \nabla C) \quad (2)$$

Here, C is the drug concentration and U is the flow velocity vector. The effective diffusivity is taken according to $D = \epsilon\tau D_F$ . Where $\varepsilon$ is the porosity and $\tau$ denotes the tortuosity factor of the porous medium. $D_F$ represents the diffusivity of the fluid phase (blood) filling the porous structures of IVS and FC.

In IVS and FC, PM flow is governed by the equations,

$$\frac{\rho}{\epsilon}.\frac{1}{\epsilon}(U.\nabla U) = -\nabla P + \mu\,\nabla^2 U + \frac{\mu}{K}U \tag{3}$$

In extended domains, viscous free flow is defined by,

$$\rho(U.\nabla U) = -\nabla P + \mu\,\nabla^2 U \tag{4}$$

Everywhere in domain except placental tissue and placental barrier,

$$\nabla \cdot U = 0 \tag{5}$$

*K* is the macroscopic permeability of blood through the porous structure of IVS and FC with porosity values 0.7 and 0.17 respectively [4]. A commercially available software, COMSOL [5], was used to solve the discretized governing equations by finite element method. Implicit time stepping, which uses the backward differentiation formula (BDF), was chosen while solving the equations. Simulations were carried out using the gestational age dependent parameters as shown in Table 3

## 3. RESULTS AND DISCUSSION

The Figure 2 shows 3 separate pairs of maternal and fetal blood concentrations for 40th week, 28th week and 20th week respectively. For the 40th week case, the drug concentrations equilibrate between maternal and fetal circulations in less than 12 hours. While for 20th week, the same takes more than 2 days (48hours).

As the pregnancy progresses, the diffusion distance across the placental barrier decreases and blood flow rates in both maternal and fetal compartments increases. Consequently, both the convection and diffusion transfer of species speeds up. The effects are directly reflected as the reduced time for attaining concentration equilibrium between maternal and fetal blood streams. Maternal and fetal concentration profiles or all gestational ages follow exponential decay and growth patterns respectively. Cases for gestational ages between 20th and 40th week also follows the same trend and their materno-fetal concentration pairs falls within these two curve pairs which marks the boundaries of the present model's valid range.

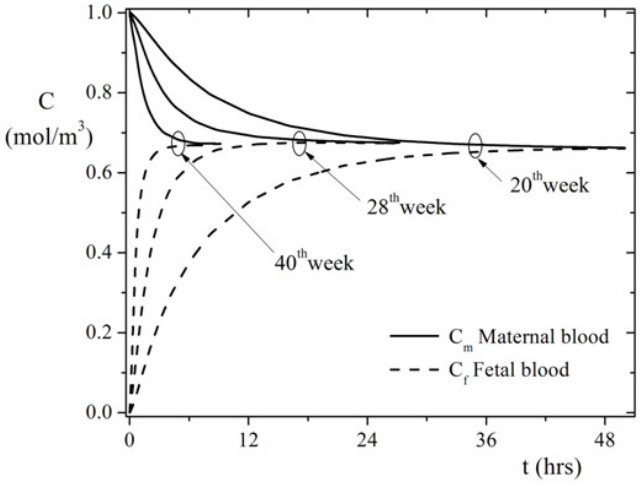


FIGURE 2: Drug concentrations (C) in maternal and fetal blood

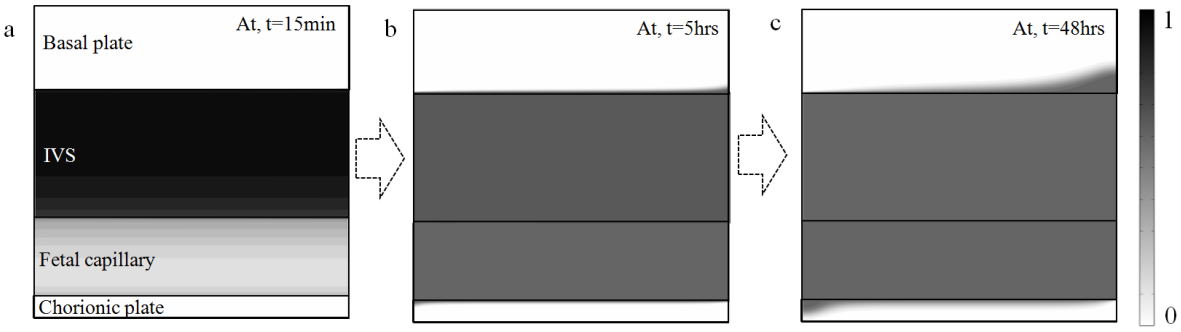


FIGURE 3: Variation of drug concentraion with time for different regions placentone at term

This indicates that the time available for taking counter measures after mother is exposed to harmful chemicals is very less towards term pregnancy. Whereas in early stages of gestation, there is more time to plan and act with the counter measures. Meanwhile, it is also to be considered that the low body weight of the fetus during early stages of pregnancy can elicit toxicity much earlier than in the case of near term. To understand the minute details of variation of drug concentration in each region of placentone, a time sequence of the concentration contours at term (40th week), as shown in Figure 3, was analysed for up to a period of 48 hours. After 5 hours, the two blood streams equilibrate completely and no further trans-barrier transfer occurs. But another diffusion zone develops within the basal and chorionic plates where the blood comes into contact with their surface. This indicates the possible absorption of drug into tissue regions which can act as a dummy source of drug even after the blood streams are cleared of drug.

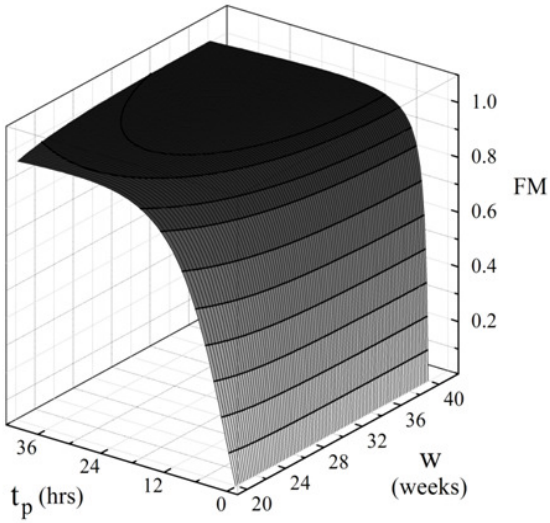


FIGURE 4: Drug concentrations charecteristics represented as 3D surface

The overall results of the study ranging from 20th week to 40th week of gestational age has been summarized as a 3D Rational-Taylor surface as shown in Figure 4. Any point on the surface predicts the non-dimensional fetal blood concentration at the corresponding perfusion time with an accuracy of 98% of the actual simulation results.

## 3. CONCLUSION

The numerical model developed in this work treats placenta as a dynamic porous medium species exchanger. Flow and diffusion properties of placenta which are gestational age dependent have been included. The model effectively predicts the fetal exposure level of maternally ingested drug for any gestational age between $20^{th}$ week and $40^{th}$ week. It has been observed that during pre-term pregnancy period, the fetal exposure level was much lower compared to that of a term placenta for same perfusion time. Even after transplacental drug transfer stops, diffusion zones which were active for much longer period were observed to exist in placental tissue of both chorion and basal plate. These diffusion zones could act as dummy reservoirs even after the drug has been cleared from the blood by active or passive elimination methods.

## REFERENCES

[1] Jacqz-Aigrain, E., and Gideon Koren. "Effects of drugs on the fetus." *Seminars in Fetal and Neonatal Medicine*. Vol. 10. No. 2. WB Saunders, 2005.

[2] Vähäkangas K. Chemical Exposure as Etiology in Developmental Origin of Adult Onset Human Cancer. *Frontiers in Pharmacology*. 2011;2:62. doi:10.3389/fphar.2011.00062.

[3] Karttunen, V., et al. "Criteria and challenges of the human placental perfusion–Data from a large series of perfusions." *Toxicology in Vitro* 29.7 (2015): 1482-1491.

[4] Vijayaratnam, Pujith RS, et al. "The impact of blood rheology on drug transport in stented arteries: Steady simulations." *PloS one* 10.6 (2015): e0128178.

[5] Multiphysics, C. O. M. S. O. L. "Comsol multiphysics user guide (version 4.3 a)." *COMSOL, AB* (2012): 39-40.

Fifth International Conference on Computational Methods for Thermal Problems
THERMACOMP2018, July 9-11, 2018, Indian Institute of Science, Bangalore, INDIA
*N. Massarotti, P. Nithiarasu, Pradip Dutta and C. Ranganyakalu (Eds.)*

# NUMERICAL STUDY ON SLOT JET IMPINGEMENT USING OPENFOAM AND ANSYS FLUENT

**Joseph Issac**
PG student
Department of Mechanical Engineering
National Institute of Technology, Manipur
**Email**: ebuissac@gmail.com

**Dr. Dushyant Singh**
Assistant Professor
Department of Mechanical Engineering
National Institute of Technology, Manipur
**Email**: dushyant@nitmanipur.ac.in

## Abstract

In this present study, the slot jet impingement of air on heated flat plate is numerically analysed by using two different solvers namely, ANSYS Fluent and OpenFOAM. The present study considered two dimensional, incompressible, turbulence and steady state for nozzle to plate spacing h/S = 4 and $Re_s$ = 2750 using k-ω SST and $v^2 - f$ turbulence models. The local Nusselt number results were compared with the experimental results of Gardon et al. [1].The variation of turbulent kinetic energy at different locations of the domain were studied for both the turbulence models. The simulation results obtained using OpenFOAM predicts the secondary peak of the curve in k-ω SST turbulence model while the stagnation point was captured more accurately by ANSYS Fluent.

**Key Words:** *Heat Transfer, Air Jet Impingement, Turbulence*

## 1. Introduction

Jet impingement heat transfer has always been a topic of interest in many industrial applications such as heating, cooling and drying. Constant intensive researches are done to gain more insight in this field. Jet impingement is an inevitable part of heat transfer due to its varied advantages like immediate and selective cooling. Gardon et al. [1] has experimentally concluded the relationship of various factors, like Reynolds number, nozzle to plate spacing and how it affects heat transfer coefficient. They have found out that the lateral variation of heat transfer coefficient forms a bell shaped curve for nozzle to plate spacing greater than 14 slot width. The dependence of heat transfer coefficient at stagnation point has been investigated by many researchers and they unanimously agree that higher the Reynolds number higher will be the heat transfer coefficient at stagnation point [1 - 3]. For fixed Re the Nusselt number increases for decreasing values of nozzle to surface spacing [9 - 11]. Ashforth et al. [3] has found experimentally about the effect of semi-confinement at stagnation point heat transfer and concluded that heat transfer reduces up to 10% at stagnation point due to semi-confinement.They have also found out that the highest heat transfer is obtained when the plate is kept at the end of the potential core of the impinging jet.

These experimental problems can be numerically simulated using CFD codes which enables the use of various turbulence models to predict the velocity variations and heat transfer behaviour. Various models like K- ε and k-ω are commonly used two equation models. The $v^2 - f$ turbulence model proposed by Durbin [5] and modified by Lars Davidson et al. [6] has done a great deal in predicting the velocity variations in different problems. His study concluded that for both massive and smooth separations, the near wall treatment of $v^2 - f$ system of equations is in good agreement with the experimental results. The velocity fluctuations were experimentally analysed by many researchers in order to study the turbulence effects of the flow [2 & 12]. However the selection of turbulence model depends upon the nature of the problem. Dutta et al. [4] have conducted studies on various turbulence models and closeness of its prediction to the experimental results and concluded that k-ω model predicts the nature of the heat transfer curve better for flat plate slot jet impingement.

Though the various turbulence models were studied, the comparative study done on this, based on different CFD software namely ANSYS Fluent and OpenFOAM is not very common. The variance of velocity fluctuations and how precise the same model, in predicting various behaviours of the flow when run in different software are the key factor of interest in this present study.

## 2. Problem Statement

In this present study, slot jet impingement of incompressible air on an isothermal flat plate is investigated numerically. The Nozzle to plate spacing, h/S = 4, for a flow of $Re_S$ = 2750 impinging on a flat plate is considered for the present numerical study [1]. The slot width of the nozzle S is 0.0015875 m and the side of the plate is 0.1524 m in length. The computational domain is as shown in Fig. 1.

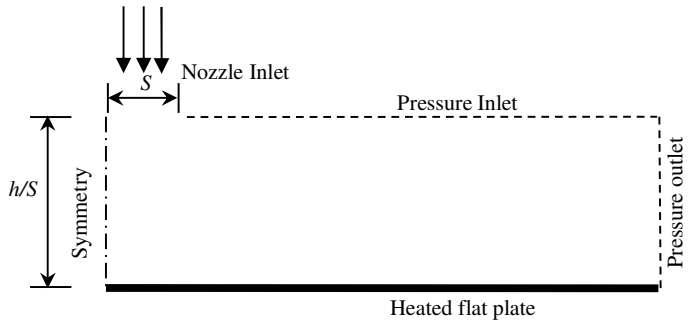


**Figure 1**: Domain geometry used for numerical study

The Reynolds number and Nusselt number are defined based on slot width,S of the nozzle

$$\mathrm{Re}_S = \frac{uS}{\nu} \text{ and } Nu = \frac{q''S}{(T_w - T_j)k_f}$$

## 3. Governing Equations

The Reynolds time averaged governing equation for continuity, momentum and energy of an incompressible fluid are given as follows

$$\frac{\partial u_i}{\partial x_i} = 0$$

$$\rho u_j \frac{\partial u_i}{\partial x_j} = -\frac{\partial P}{\partial x_i} + \frac{\partial}{\partial x_j}\left[\mu\left(\frac{\partial u_i}{\partial x_j} + \frac{\partial u_j}{\partial x_i}\right) - \rho\overline{u_i' u_j'}\right]$$

$$\rho u_j \frac{\partial T}{\partial x_j} = \frac{\partial}{\partial x_j}\left[\frac{\mu}{\mathrm{Pr}}\frac{\partial T}{\partial x_j} - \rho\overline{T' u_j'}\right]$$

### 3.1 Numerical Methodology

In this present study, the numerical simulations were carried out using two CFD software packages, ANSYS Fluent and OpenFOAM. The simulation is done for incompressible, steady state, symmetric, turbulent slot jet impingement problem, giving exact same inputs in both the software. $K-\omega$ SST and $v^2-f$ models were used to model the turbulence. For setting up the cases in OpenFOAM [7] and ANSYS Fluent [8] their respective user guides were followed. SIMPLE algorithm was used for pressure and velocity coupling. Second order upwind scheme was used for spatial discretization of convective terms.

### 3.2 Boundary Conditions

- **Inlet** – Uniform velocity distribution is considered at 300 K. The turbulent intensities were varied between 2 to 4 percentage and the turbulent viscosity ratio was varied from 1 to 5 percentages. The initial values of turbulent kinetic energy, turbulent dissipation rate and specific dissipation rate were calculated from the following equations.

$$K = \frac{3}{2}(uI)^2,\ \varepsilon = C_\mu \frac{\rho K^2}{\mu}(\mu_t/\mu)^{-1},\ \omega = \frac{\rho K}{\mu}(\mu_t/\mu)^{-1} \text{ and } v^2 = \frac{2}{3}K$$

- **Heated Plate** – Isothermal heated plate at 350 K with no slip condition is considered.
- **Symmetry** – Symmetry boundary condition is applied.

- **All Open Domains** – Both Pressure inlet and pressure outlet are open sides of the domain with zero initial gauge pressure as shown in Fig. 1.

### 3.3 Grid Independence Test

Grid independence test was done for both the software using three different mesh dimensions (*x,y*): 225× 100, 280×150, 340× 200. For OpenFOAM only a slight variation was observed at the secondary peak region and for ANSYS Fluent all the curves overlapped as shown in Fig. 2. Hence the grid 280 × 150 was chosen for further studies. Grid is made sufficiently fine so as to ensure a $Y^+$ below unity.

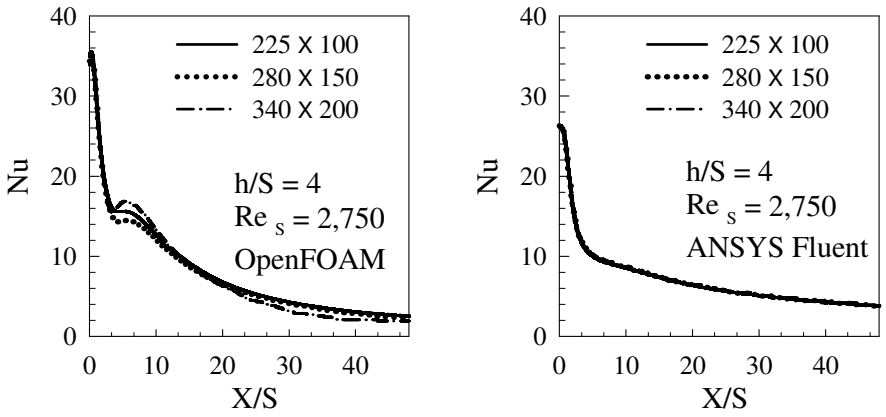


**Figure 2**: Grid independence test result with $K-\omega$ SST turbulence model.

## 4. Results and Discussions

For OpenFOAM simulations, the stagnation point Nusselt number was over predicted and is almost same for both turbulence models. But the phenomena of secondary peak was captured by $K-\omega$ SST turbulence model only. The variation of turbulent intensity and eddy viscosity ratio varies the nature of Nusselt number curve but the stagnation point Nusselt number is not varied much.

The stagnation Nusselt number for both turbulence models simulated by ANSYS Fluent matches with that of the experimental result but it failed to predict the secondary peak as shown in Fig. 3. The Nusselt number curve of $v^2-f$ model in ANSYS Fluent over predicts the behaviour of the curve after secondary peak, but $v^2-f$ model prediction in OpenFOAM matches with experimental curve after secondary peak. The assumption of initial turbulent intensity of 4 % and turbulent viscosity ratio of 1% was able to give better fit with the experimental result when using k-ω SST model while the $v^2-f$ model predicted the result at 2 % turbulent intensity and 5 % turbulent viscosity.

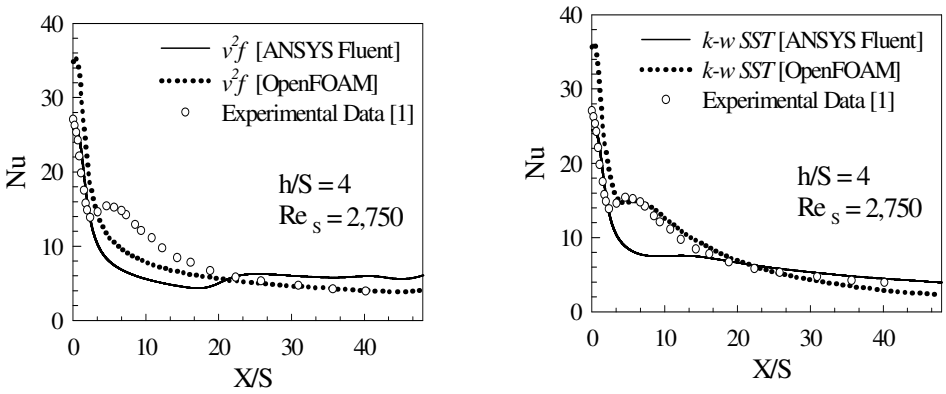


**Figure 3**: Comparison of numerical results of $v^2-f$ and k-ω SST models with the experimental results.

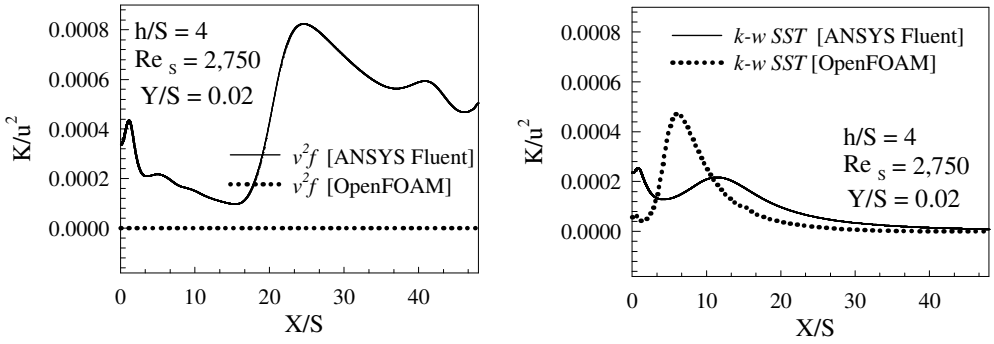


**Figure 4**: Non dimensional value of turbulent kinetic energy at near wall Y/S = 0.02.

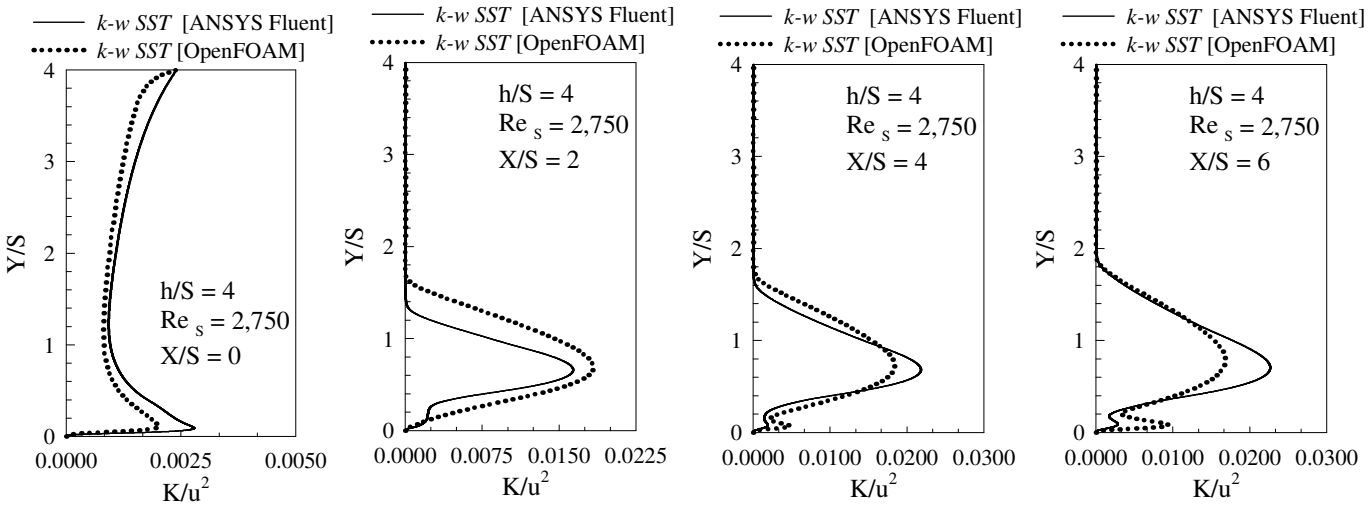


**Figure 5**: The variation of turbulent kinetic energy at different locations with k-ω SST turbulence model.

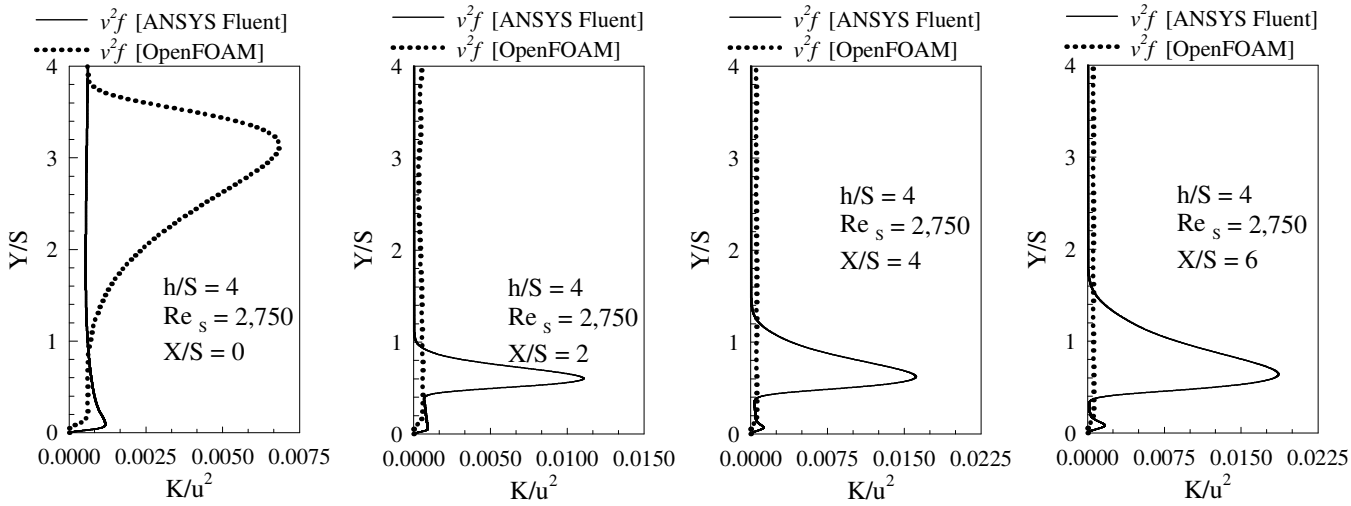


**Figure 6**: The variation of turbulent kinetic energy at different locations with $v^2 - f$ turbulence model.

The variation in predictions occur due to the variations in capturing the fluctuating velocity components of the flow at different points. Figure 4 shows the predictions of near wall turbulent kinetic energy at Y/S = 0.02, for both turbulence models when solved with OpenFOAM and ANSYS Fluent. From Fig. 3 the secondary peak of Nusselt number curve of k-ω SST model in OpenFOAM, occurs at X/S = 6. From Fig. 4 it

is evident that at X/S = 6, the turbulent kinetic energy curve of k-ω SST model in OpenFOAM has a peak compared to ANSYS Fluent result. This variation helps k-ω SST model in OpenFOAM to capture the secondary peak in Nusselt number. It has been experimentally studied that near wall turbulence and correlated motion in outer region causes the rise in heat transfer coefficient creating a secondary peak [2]. The turbulent kinetic energy at various X/S ratios for k-ω SST turbulence model differ slightly for both the software as shown in Fig. 5. The variation of turbulent kinetic energy for $v^2 - f$ model using ANSYS Fluent and OpenFOAM shows considerable amount of differences at different locations of the domain as shown in Fig. 6.

## 5. Conclusion

1) The stagnation Nusselt number was better predicted by both the turbulence model in ANSYS Fluent.
2) The phenomenon of secondary peak was captured only by k-ω SST turbulence model while running in OpenFOAM.
3) The variation of near wall turbulent kinetic energy is the main reason for changes in predictions of the secondary peak by k-ω SST model in different software.

## References

[1] Robert Gardon, J. CahitAkfirat, Heat Transfer Characteristics of impinging two dimensional jets,Transactions of the ASME, February (1966).
[2] V. Narayanan a, J. Seyed-Yagoobi, R.H. Page, An experimental study of fluid mechanics and heat transfer in an impinging slot jet flow, Int. Journal of Heat and Mass Transfer 47 (2004) 1827–1845.
[3] S Ashforth-Frost, K Jambunathan, Effect of nozzle geometry and semi-confinement on the potential core of a turbulent axisymmetric free jet, Int. Comm. Heat Mass Transfer, VoL 23(2), pp. 155-162, (1996).
[4] Rabijit Dutta, Anupam Dewan, Balaji Srinivasan, Comparison of various integration to wall (ITW) RANS models for predicting turbulent slot jet impingement heat transfer, Int. Journal of Heat and Mass Transfer 65 (2013) 750–764.
[5] P A Durbin, Separated Flow Computations with the K-ε-$v^2$ model. AIAA Journal, Vol.33, No. 4, April 1995.
[6] Lars Davidson, Peter V. Nielsen and Andreas Sveningsson, Modifications of the $v^2 - f$ Model for Computing the Flow in a 3D Wall Jet, Turbulence, Heat and Mass Transfer 4, 577-584 (2003).
[7] OpenFOAM User Guide version 5.0 (2017).
[8] Fluent INC (2015). FLUENT 15.6 user's guide. Fluent Documentation.
[9] Dushyant Singh, B. Premachandran, and Sangeeta Kohli, Numerical Simulation Of The Jet Impingement Cooling Of A Circular Cylinder, Numerical Heat Transfer, Part A, 64: 153–185, (2013).
[10] Dushyant Singh, B. Premachandran, Sangeeta Kohli, Experimental and numerical investigation of jet impingement cooling of a circular cylinder, Int. Journal of Heat and Mass Transfer 60 (2013) 672–688.
[11] Dushyant Singh, B. Premachandran, Sangeeta Kohli, Double circular air jet impingement cooling of a heated circular cylinder, Int. Journal of Heat and Mass Transfer 109 (2017) 619–646.
[12] Jiang Zhe, Vijay Modi, Near Wall Measurements for a Turbulent Impinging Slot Jet, Transactions of the ASME, Vol. 123, MARCH 2001.

## Nomenclature

S – Width of slot nozzle (m)
h – Nozzle to plate spacing (m)
u – Average Velocity (m/s)
I – Turbulent Intensity
$\frac{\mu_t}{\mu}$ - Eddy Viscosity Ratio
$\nu$ - Kinematic Viscosity
$q''$ - Heat Flux
$T_w$ - Wall Temperature
$T_j$ - Jet exit Temperature
$k_f$ - Thermal Conductivity of the fluid
K - Turbulent Kinetic Energy
$\varepsilon$ - Turbulent Dissipation Rate
$\omega$ – Specific Dissipation Rate
$C_\mu$ – Model Constant 0.09
$\rho$ – Density
$\mu$ – Dynamic Viscosity

Fifth International Conference on Computational Methods for Thermal Problems
THERMACOMP2018, July 9-11, 2018, Indian Institute of Science, Bangalore, INDIA
*N. Massarotti, P. Nithiarasu, Pradip Dutta and C. Ranganyakalu (Eds.)*

# Thermal characterization of shock-induced separation in hypersonic flows

**Aniruddha A. Kane, Ravi K. Peetala**

Department of Mechanical Engineering, Visvesvaraya National Institute of Technology (VNIT), Nagpur-440010, India, aniruddha.kane74@gmail.com, ravipeetala@gmail.com

ABSTRACT

The focus of the present investigation is to understand one of the important phenomenon in high speed flows called shock wave boundary layer interaction (SWBLI). Present study initially considers laminar and turbulent flows to understand the variation of wall skin friction coefficient, heat flux and coefficient of pressure distribution during hypersonic flow and after comparison with the standard results, laminar flow is considered for remaining work. The effect of variation of wall temperature, total flow enthalpy and Mach number on shock-induced separation is carried out in this study. The length of separation bubble is considered as a comparison parameter for skin friction coefficient calculations and it is found that length of the bubble is shorter in the turbulent case than laminar while it has increasing trend for increasing wall temperature, reducing trend for both increasing total energy content and increasing Mach number. In case of the heat flux calculations turbulent case gives higher values than laminar while reducing trend is obtained for increasing wall temperatures. Heat flux has an increasing trend for increasing total enthalpy as well as Mach number.

**Key Words:** *Hypersonic flows, shock wave boundary layer interaction, separation bubble.*

## 1. INTRODUCTION

Hypersonic flow is one of the sought after topics of research. The phenomena particular to this flow regime which make designing and analysis of hypersonic vehicles critical are shocks, shockwave boundary layer interactions (SWBLI) and shock-induced separation. Higher heating loads and chemical reactions are some of the consequences of SWBLI[1]. Scramjet engine inlets, ramp-like surfaces on the aircraft's body actually experience such phenomena[2]. SWBLI does not always have a negative impact. It helps in the mixing of air and fuel in case of engine inlets[2]. But other than this SWBLI has adverse effects on the body of the aircraft. So it is necessary to control the occurrence of SWBLI and hence proper understanding of the issue, parameters on which it depends and effects developed by it are required. Wall temperature, Total enthalpy of flow and Mach number are some important factors on which SWBLI depends[3]. These parameters cause variation of skin friction coefficient, heat flux, pressure distribution near the location of interaction. These issues are crucial for analysis and developing co-relations[4]. So the focus of the current study is on the thermal characterization of shock-induced separation caused by SWBLI in hypersonic flows.

## 2. MATHEMATICAL MODELING AND SOLUTION STRATEGY

The integral cartesian form of compressible Navier-Stokes equations is used in order to capture the physics involved in the present investigation. The equations are given below.

$$\frac{\partial}{\partial t}\int W dV + \oint [F - G].dA = \int H dV$$

where $F = \begin{Bmatrix} \rho v \\ \rho v u + p\hat{\imath} \\ \rho v v + p\hat{\jmath} \\ \rho v E + pv \end{Bmatrix}$ $G = \begin{Bmatrix} 0 \\ \tau_{xi} \\ \tau_{yi} \\ \tau_{ij} v_{ij} + q \end{Bmatrix}$ $W = \begin{Bmatrix} \rho \\ \rho u \\ \rho v \\ \rho E \end{Bmatrix}$ and vector $H$ contains source terms such as body forces and energy sources. $\rho$, $v$, $E$, $p$ are density, velocity, total energy per unit mass and pressure of the fluid respectively. $\tau$ is the viscous stress tensor and $q$ is the heat flux. Total energy ($E$) and total enthalpy ($H_o$) are related as $E = H_o - p/\rho$ while $H_o = h + |v|^2/2$ where $h$ is enthalpy of fluid.

For the present study, a two-dimensional single wedge geometry is considered as a computational domain. The density-based solver with implicit formulation is utilized to get the steady-state solution. The flow of air is modeled by perfect gas law while Sutherland's model is considered to calculate the viscosity and constant Prandtl number of 0.7 are considered. The calculation of convective fluxes is carried out by AUSM scheme while the second-order upwind scheme is considered for spatial discretization.

## 3. RESULTS AND DISCUSSIONS

The present study is carried out by considering hypersonic flow over a two-dimensional single wedge surface as discussed in [3], [5].Computational domain consists of a 0.05m flat plate with a wedge of the angle of 15$^o$ attached to it as shown in Fig.1. Grids are clustered near the 'No-slip' surfaces and at the junction of flat plate and ramp for capturing the boundary layer and SWBLI induced separation. Grid independence test is carried out by considering grid sizes of 180x60, 180x90, 240x120, 300x150 cells. It is found that 180x90 cells give grid independent solution. The grid with 180x90 cells and appropriate boundary conditions is shown in Fig.2. The free stream conditions employed in the investigation are M=6, Re= $8x10^{-5}$ $m^{-1}$, wall temperature of 300 K and free stream stagnation enthalpy of 1.08 MJ/kg for laminar and turbulent flow considerations. The coefficient of pressure ($C_p$) and wall heat flux are used as comparison parameters. From Fig.3 and 4 it seems that the laminar flow consideration is in good agreement with the experimental as well as numerical results and hence it is used for further parametric studies. The high-speed flow with M=6 reaches the compression ramp and there is a formation of an oblique shock. The shock interacts with the boundary layer and submits it to the adverse pressure gradient and causes flow reversal which ultimately produces a separation bubble which is seen in Fig.5. The wall shear stress and ultimately skin friction coefficient ($C_f$) becomes negative where the flow separation starts and again attains positive value at reattachment point. The length of the separation bubble is the length between separation and reattachment points. The plot of skin friction coefficient is compared for both the cases of laminar and turbulent flows as shown in Fig.6. It can be understood from the plot that due to turbulence nature or eddies in the flow the separation bubble length is shorter as compared to the laminar separation bubble length and it comes out to be 14.6 mm for the turbulent case while 19 mm for the laminar case. In the separated zone, both velocity and thermal gradients reduce and thus it is evident from the Fig.4 and 6 that both $C_f$ and heat flux reduces in the separation zone.

3.1 Effect of Wall Temperature: Now the effect of wall temperature on some parameters such as skin friction coefficient, the heat flux is analyzed. It is quite evident from the Fig.7 that as the wall temperature has increased the point of separation and reattachment moves away which means the length of separation bubble increases. And it attains maxima in case of adiabatic wall condition when the maximum temperature of 1190 K is attained. The reason behind that is increased wall temperature increases the viscosity of the near wall fluid which means thicker boundary layer. Thus the chances of the separation increases and it gives rise to the enhanced length of separation bubble. Reduced heat flux as shown in Fig.8 is also observed for higher wall temperatures as increased wall temperature causes the reduction in near-wall thermal gradient.

3.2 Effect of Total Enthalpy: Now the combined effect of the wall temperature and the total temperature is studied by considering two wall temperature values 300 K and 500 K for two enthalpy values that are low enthalpy for 1.08 MJ/kg and high enthalpy for 1.8 MJ/kg. As the enthalpy of the flow is increased keeping the same wall temperature there is a reduction in the separation bubble size as seen in Fig.9. It is also observed that the plots of low enthalpy flow-300 K wall temperature and high enthalpy flow-500 K wall temperature follows the identical path. Here for both these cases wall temperature to total temperature ratio i.e. $T_w/T_o$ is same thus it is important to note that this ratio $T_w/T_o$ is a crucial parameter for skin friction coefficient calculations rather than considering $T_w$ and $T_o$ individually. Higher enthalpy flows mean higher flow velocities and which ultimately creates more resistance for separation. Also because of increased free stream temperatures in higher enthalpy flows temperature gradient in the near-wall region is increased and hence higher values of heat flux are observed as shown in Fig.10.

3.3 Effect of Mach number: Three cases M=5, 6 and 7 are considered to study the effect of Mach number on SWBLI. It is observed from the Fig.11 that as the Mach number is increased point of separation and reattachment move towards each other. In other words, the length of separation bubble reduces by an increment in Mach number. This is because the kinetic energy of the flow enhances as Mach number increases and it hinders the process of shock-induced separation. Further, when higher kinetic energy fluid is decelerated because of shock its temperature will rise. And the corresponding rise in thermal gradient will cause higher heat flux values which can be seen in the Fig.12.

## 4. CONCLUSION

Investigations are carried out in order to study the effect of some crucial parameters on SWBLI using commercial code. Important trends of skin friction coefficient, heat flux, and coefficient of pressure necessary

to develop a correct understanding of SWBLI are obtained. The skin friction coefficient trend is used to quantify the separation bubble size. It can be concluded that separation bubble length is lower in case of turbulent flows than laminar case while it increases with increase in wall temperature. It is also found that separation bubble length increases with a decrease in total enthalpy and Mach number. It emerges from the study that ratio of wall temperature to total temperature is an important parameter for shear stress calculations. The trend of heat flux is an important parameter for design procedure. It can be noted that heat flux increases with decreasing wall temperatures, increasing total enthalpy and increasing Mach numbers.

## REFERENCES

[1] J.D.Anderson, *Hypersonic and high-temperature gas dynamics*. 2006.

[2] J. Délery and J. P. Dussauge, "Some physical aspects of shock wave/boundary layer interactions," *Shock Waves*, vol. 19, no. 6, pp. 453–468, 2009.

[3] B. John, V. N. Kulkarni, and G. Natarajan, "Shockwave boundary layer interactions in hypersonic flows," *Int. J. Heat Mass Transf.*, vol. 70, pp. 81–90, 2014.

[4] B. John and V. Kulkarni, "Numerical assessment of correlations for shock wave boundary layer interaction," *Comput. Fluids*, vol. 90, pp. 42–50, 2014.

[5] M. Marini, "Effects of Flow And Geometry Parameters On shock-wave boundary-layer interaction phenomena," *Am. Inst. Aeronaut. Astronaut.*, vol. 98, no. 1570, pp. 319–329, 1998

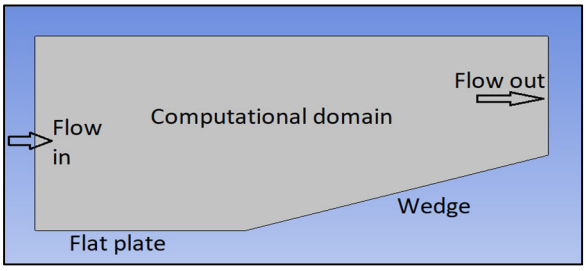


FIGURE 1. Computational domain

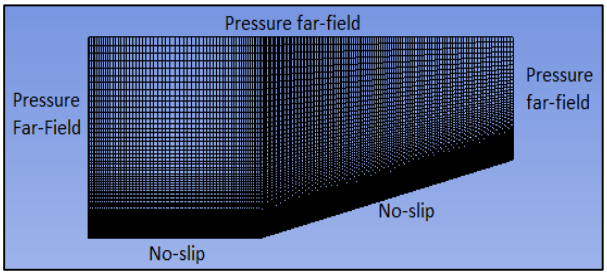


FIGURE 2. Mesh with appropriate boundary conditions

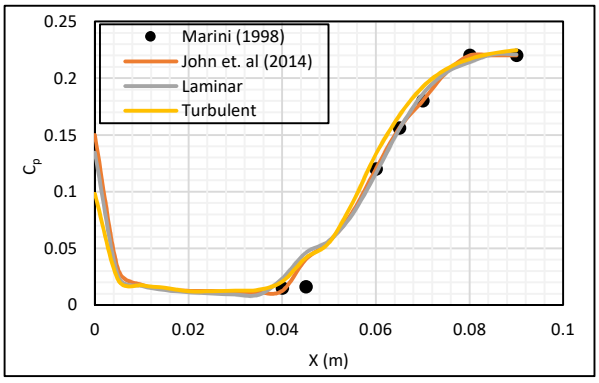


FIGURE 3. Comparison of $C_p$ for various studies

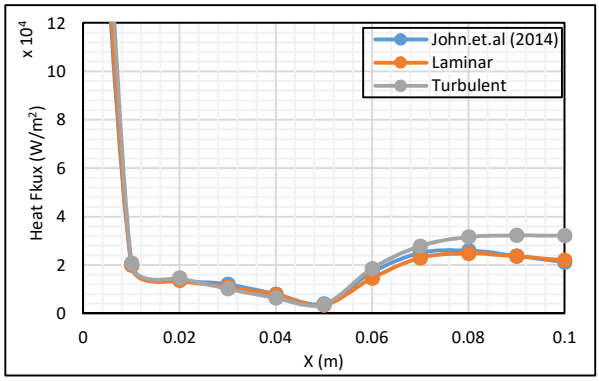


FIGURE 4. Comparison of heat flux for various studies

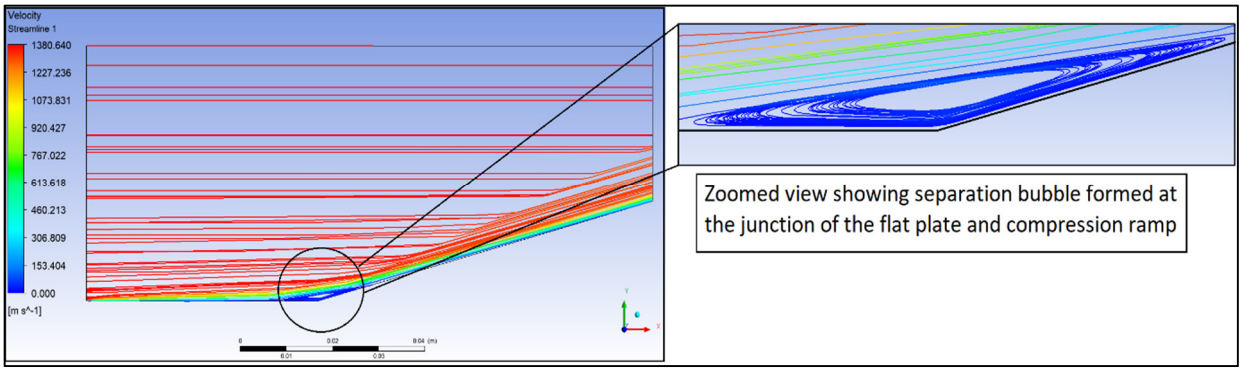


FIGURE 5. Shock-induced separation bubble indicated by streamlines

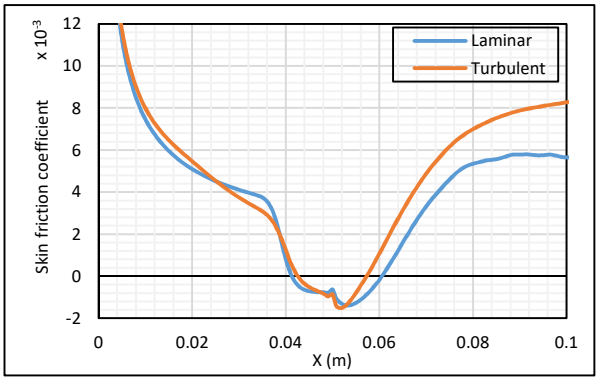


FIGURE 6. Comparison of skin friction coefficient for laminar and turbulent flows

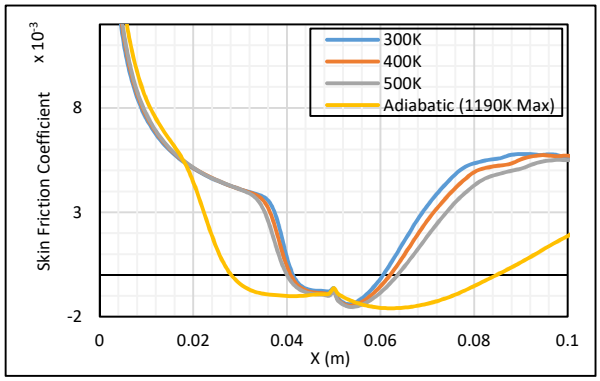


FIGURE 7. Effect of wall temperature on $C_f$

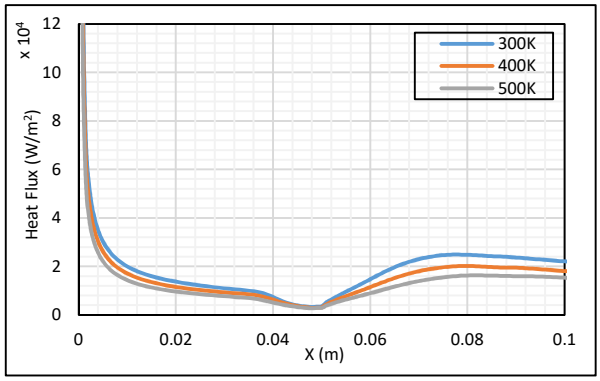


FIGURE 8. Effect of wall temperature on heat flux

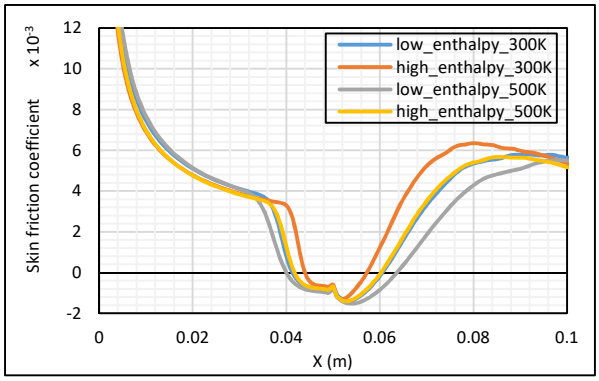


FIGURE 9. Effect of total enthalpy of flow on $C_f$

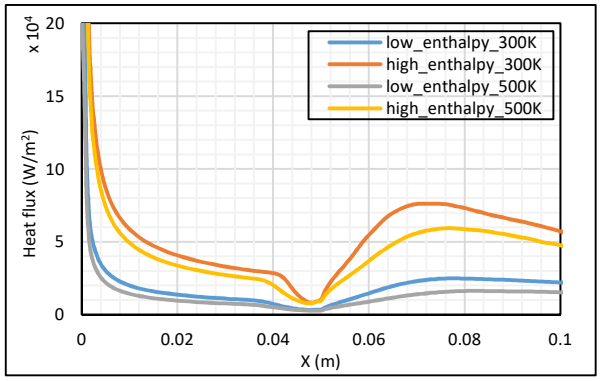


FIGURE 10. Effect of total flow enthalpy on heat flux

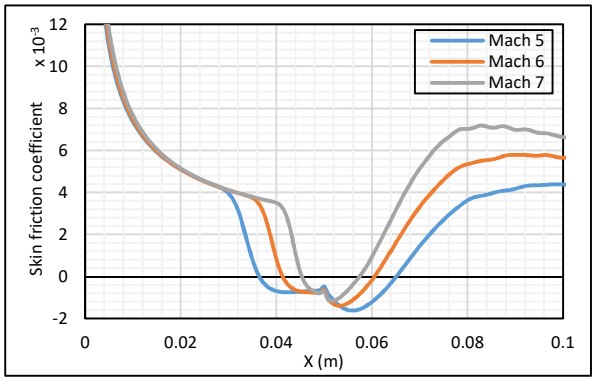


FIGURE 11. Effect of Mach number on $C_f$

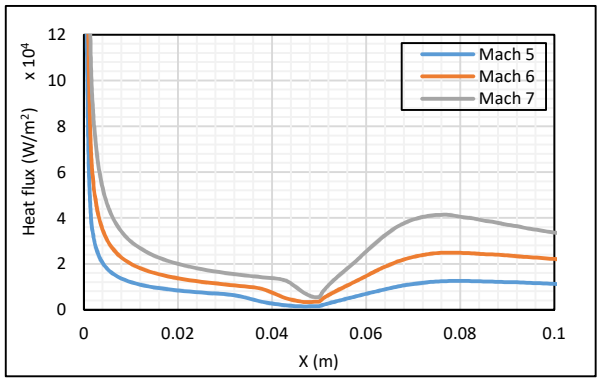


FIGURE 12. Effect of Mach number on heat flux

# THERMAL PERFORMANCE OF DIRECT ABSORPTION SOLAR COLLECTOR BASED SINGLE STAGE FLASHING DESALINATION SYSTEM

**Kapil Garg, Swapnil S. Salvi, Vishal Bhalla**
School of Mechanical, Materials and Energy Engineering
Indian Institute of Technology Ropar
Rupnagar, Punjab, India
kapil.garg@iitrpr.ac.in, swapnil.salvi@iitrpr.ac.in, vishal.bhalla@iitrpr.ac.in

**Vikrant Khullar**
Mechanical Engineering Department
Thapar University
vikrant.khullar@thapar.edu

**Sarit K. Das**
School of Mechanical, Materials and Energy Engineering
Indian Institute of Technology Ropar
skdas@iitrpr.ac.in

**Himanshu Tyagi**
School of Mechanical, Materials and Energy Engineering
Indian Institute of Technology Ropar
himanshu.tyagi@iitrpr.ac.in

## ABSTRACT

Water scarcity is becoming one of the serious global challenges due to increasing population, industrialization and contamination of existing water resources. To increase the supply of fresh water in order to meet its growing demand, desalination has been practiced worldwide from many years. In the present paper a single stage flashing (SSF) desalination system coupled with the nano-fluid based direct absorption solar collector (DASC) with the help of a counter-flow heat exchanger has been studied numerically. The thermal performance of the entire system is measured in terms of gained output ratio (GOR).The effect of various influencing parameters such as height ($H$) and length ($L$) of the collector, particle volume fraction ($f_v$) of nanoparticles and incident flux ($q$) on gained output ratio (GOR) and top brine temperature ($T_o$) is studied numerically.

**Key Words:** direct *absorption solar collector, flash desalination, nano-particles, solar energy, gained output ratio*

## 1. INTRODUCTION

In order to meet the growing demands of fresh water, desalination is the reliable method and there are various methods used for desalination such as multi-stage flash desalination (MSF), multi-effect distillation (MED) and vapor compression (VC) which are basically phase change processes and requires a heat source [1]. Solar energy can be used as a heat source for thermal (phase change) desalination systems which is also a clean source of energy. In flashing desalination system which is one of the simplest method, the seawater is heated to a saturation temperature by any heat source and it then enters into a flash chamber which is maintained at a pressure lower than the saturation pressure of the heated seawater. Vapors of fresh water are obtained due to sudden reduction in pressure (flashing) which are then condensed in a condenser through which the cold saline water is flowing and in this way latent heat of vaporization of vapors produced is used to preheat the cold saline water[2]. The flashing chamber can be maintained at any temperature lower than the satuation temperature of heated

seawater so that flashing of the heated seawater takes place. The remaining seawater which is called brine is rejected out of the system. In the present study, a nano-fluid based direct absorption solar collector (DASC) is coupled with the single stage flash (SSF) desalination unit with the help of a counter flow heat exchanger. The incident solar energy is absorbed by the nanofluid inside the collector which is used to supply the required energy to preheated saline water in a counterflow heat exchanger. The output of the system is measured in the form of gained output ratio (GOR) and the effect of various parameters related to collector such as height ($H$), length ($L$), particle volume fraction ($f_v$) of nanoparticles inside the base fluid and incident solar radiation ($q$) on the gained output ratio (GOR) and top brine temperature ($T_o$) is studied numerically.

## 2. MODELING OF DASC BASED SSF DESALINATION SYSTEM

The DASC based single stage flashing desalination system is shown in Fig.1. Modelling of the DASC system is done with the following assumptions. Nanofluid flows through the enclosed space of DASC at a very low and constant velocity. The bottom surface of DASC is highly insulating and transparent. Top surface of the container is a glass cover with transmissivity value of 0.95. The incident solar radiation on DASC is absorbed by the nanofluid flowing inside the collector. The variation of incident intensity along $y$ direction is calculated using the radiative transport equation (RTE) which is given by Eq. (1)[3]:

$$\frac{\partial I_\lambda}{\partial y} = -\left(K_{a\lambda_{basefluid}} + K_{e\lambda_{\text{nanoparticles}}}\right) I_\lambda = -K_{e\lambda_{nanofluid}} I_\lambda , \tag{1}$$

where $K_{a\lambda}$ ,$K_{s\lambda}$ and $K_{e\lambda}$ are spectral absorption coefficient, spectral scattering coefficient and spectral extinction coefficient and their equations are obtained from[3] and relation for spectral intensity ($I_\lambda$) is obtained from[4]. After obtaining the intensity distribution, the heat transfer model for DASC which is steady state and two-dimensional, is solved using the finite difference implicit method (FDM). The following governing equation is employed[3]:

$$k\frac{\partial^2 T}{\partial y^2} - \frac{\partial q_r}{\partial y} = \rho C_p U \frac{\partial T}{\partial x}, \tag{2}$$

where $k$ is the thermal conductivity of the nanofluid, $\rho$ is the density, $C_p$ is the specific heat. The radiative flux absorbed by the nanofluid is given by Eqn. (3) which is as follows[3]:

$$q_r = \iint I_\lambda d\phi d\lambda , \tag{3}$$

where $d\phi$ is the solid angle between the sun and the earth. In order to solve the model numerically, Eq. (1) is discretized into the uniform spectral nodes of 0.1 μm in the wavelength range of 0.1-3 μm (incident solar spectrum) and Eq. (2) is desctrezied into the uniform nodes of finite differences and such 1000 nodes are taken in both $x$ and $y$-directions. The value of incident solar flux is taken to be 1000W/m$^2$ [3].

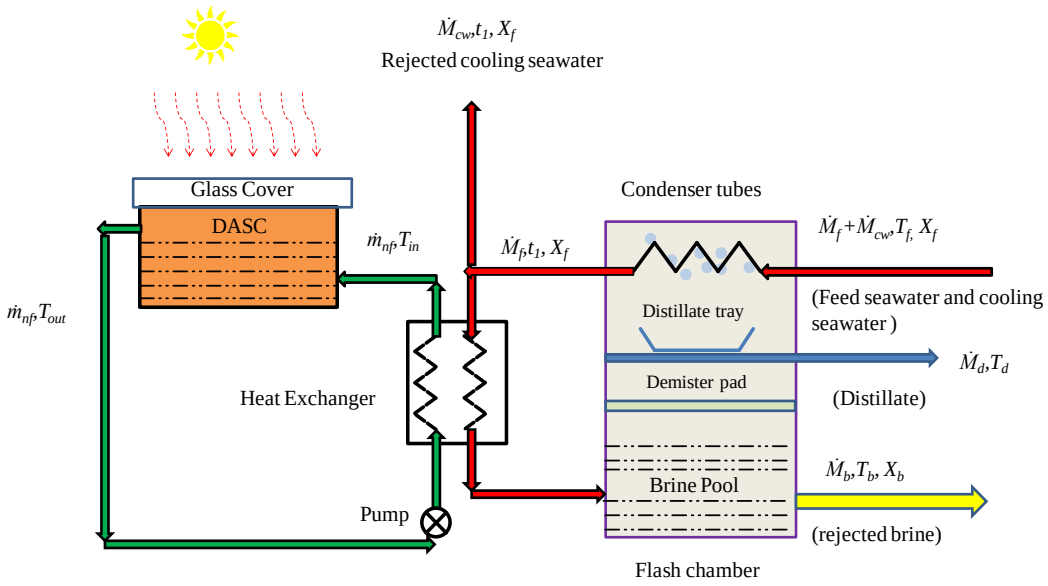


FIGURE 1. Schematic of single stage flashing (SSF) desalination unit coupled with the nano-fluid based direct absorption solar collector (DASC) through a counter-flow heat exchanger.

The mathematical model is prepared for SSF unit which consists of a flash chamber and a heat exchanger.The mathematical model for single stage flash unit is quite simple and it includes total mass and salt balances. The total mass and salt balance equations are[5]:

$$\dot{M}_f = \dot{M}_b + \dot{M}_d, \tag{4}$$

$$\dot{M}_f X_f = \dot{M}_b X_b, \tag{5}$$

where $\dot{M}_f$, $\dot{M}_b$ and $\dot{M}_d$ are mass flow rates of feed seawater, rejected brine and distillate. The salinity of rejected brine and feed seawater are denoted as $X_b$ and $X_f$ respectively. The mass flow rate of the distillate produced is calculated by the following expression[2]:

$$\dot{M}_d = \frac{\dot{M}_f C_p T_{st}}{h_{fg\,avg}}, \tag{6}$$

where $\dot{M}_f$ is the mass flow rate of feed seawater having salinity $X_f$ ,$C_p$ is the specific heat capacity of the feed seawater, $T_{st}$ is temperature drop of feed seawater during flashing and $h_{fgavg}$ is the average enthalpy of vaporization of distillate formed taken at the average temperature which is ($T_{avg}$ = ($T_o$+$T_b$ )/2). The temperature drop of seawater in the flashing chamber, $T_{st}$, is given by[2]:

$$T_{st} = T_o - T_b, \tag{7}$$

where $T_o$ is the top brine temperature, i.e. temperature of the feed seawater at the entry to the flashing chamber and $T_b$ is the temperature of brine at the exit of the flashing chamber which is taken as 30ºC. The main output of the system i.e. gained output ratio (GOR) is calculated by the following expression[1]:

$$GOR = \frac{\dot{M}_d \, h_{fg_{avg}}}{Q_{abs}}, \tag{8}$$

where $Q_{abs}$ is the rate of heat transfer between the preheated feed seawater and heated nanofluid in the heat exchanger and is calculated by the following equation:

$$Q_{abs} = \dot{M}_f \, C_p (T_o - t_1), \tag{9}$$

where $t_1$ is the temperature of feed seawater at the exit of the flashing chamber.

## 3. RESULTS AND DISCUSSIONS

In this section, the variation of gained output ratio (GOR) and top brine temperature ($T_o$) as a function of various influencing parameters related to collector is shown. The values of the various parameters used in the numerical study are as follows. Inlet temperature of feed seawater ($T_f$) = 25°C, effectivess of the heat exchanger (Ɛ) = 0.8, mass flow rate of nanofluid ($\dot{m}_{nf}$) and feed seawater are 0.1 and 0.05 kg/s respectively. The copper nanoparticles are used to prepare the nanofluid.

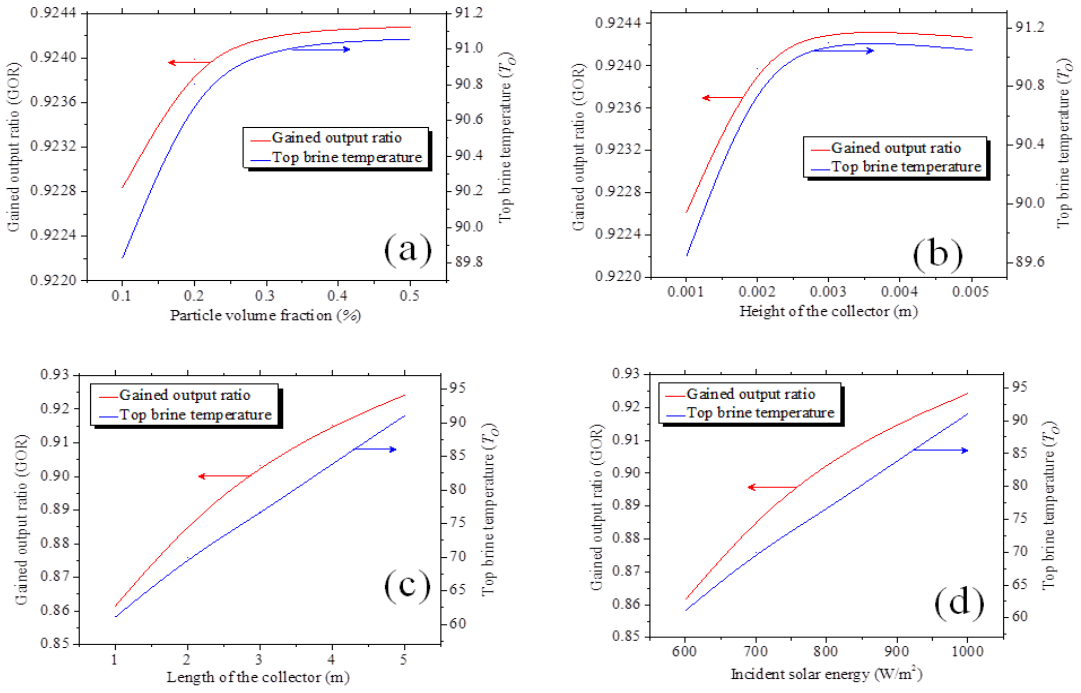


FIGURE 2. Variation of gained output ratio and top brine temperature as (a) function of particle volume fraction ($f_v$), (b) height of the collector ($H$), (c) lenght of the collector ($L$) and (d) incident flux on the collector ($q$).

Figure ( 2a) shows the effect of particle volume fraction on the GOR and $T_o$ for $H$ = 4mm. As particle volume fraction increases, outlet temperature of nanofluid ($T_{out}$) increases due to higher absorption of incident energy by the nanofluid due to which top brine temperature increases due to higher rate of heat trasnsfer in heat exchanger and hence mass flow rate of distillate ($\dot{M}_d$) and GOR. Figure (2b) shows the effect of height ($H$) of the collector on the top brine temperature and gained output ratio for $f_v$ = 0.5%. As height of the collector increases, the absorption of incident energy by the nanofluid increases due to which outlet temperature of nanofluid increases which leads to higher top brine temperature and gained output ratio as explained above. Figure (2c) shows the effect of length ($L$) of the collector on the top brine temperature and gained output ratio for $f_v$ = 0.5% and $H$ = 4mm . As length of the collector increases, outlet temperature of nanofluid increases as nanofluid remains under the sunlight for the greater time and absorbs more amount of radiation and increase in outlet temperature leads to increase in top brine temperature and ultimately gained output ratio. Figure (2d) shows the effect of incident solar radiation on the top brine temperature and gained output ratio for $H$ = 4mm and $f_v$ = 0.5%. As intensity of incident radiation increases, nanofluid absorbs more amount of radiation which increases the outlet temperature of nanofluid which ultimately increases the top brine temperature and gained output ratio.

## 4. CONCLUSION

The single stage flashing desalination system has been coupled with the nanofluid based direct absorption solar collector using a counter flow heat exchanger. The parameters related to collector such as height ($H$) and length ($L$) of the collector, particle volume fraction ($f_v$) and incident solar radiation ($q$) affects the outlet temperature of the nanoluid which ultimately affects the top brine temperature and hence gained output ratio (GOR). Gained output ratio of the system presented is lower than 1 which indicates that the system needs further improvements.

## 5. ACKNOWLEDGEMENTS

The support provided by the School of Mechanical, Materials and Energy Engineering at IIT Ropar and Mechanical Engineering Department at Thapar University, Patiala is gratefully acknowledged.

## REFERENCES

[1] Narayan, G. P., Sharqawy, M. H., Summers, E. K., Lienhard, J. H., Zubair, S. M., and Antar, M. A., 2010, "The Potential of Solar-Driven Humidification-Dehumidification Desalination for Small-Scale Decentralized Water Production," Renew. Sustain. Energy Rev., 14 (4), pp. 1187–1201.

[2] El-Dessouky, H. T., and Ettouney, H. M., 2002, Fundamentals of Salt Water Desalination.

[3] Tyagi, H., Phelan, P., and Prasher, R., 2009, "Predicted Efficiency of a Low-Temperature Nanofluid-Based Direct Absorption Solar Collector," J. Sol. Energy Eng., 131(4), p. 41004.

[4] Cengel, Y. A., and Ghajar, A. J., 2007, Heat & Mass Transfer: A Practical Approach, McGraw-Hill Education (India) Pvt Limited.

[5] Al-Wazzan, Y., and Al-Modaf, F., 2001, "Seawater Desalination in Kuwait Using Multistage Flash Evaporation Technology Historical Overview," Desalination, 134 (November 2000), pp. 257–267.

# Biharmonic Approach for Solving Navier-Stokes Equations on Nonuniform Grids

**Hemanta Karmakar[1], Swapan K Pandit[2]**
Integrated Science Education & Research Centre (ISERC)
Visva-Bharati, Santiniketan, West Bengal-731235, India
E-mail: 1987hemanta@gmail.com[1], swapankumar.pandit@visva-bharati.ac.in[2]

## ABSTRACT

In this paper, an implicit unconditionally stable 5- point compact formulation has been developed for solving the two dimensional unsteady incompressible viscous flows governed by Navier-Stokes equation on nonuniform and nonorthogonal grids. This formulation is the continuation from uniform to nonuniform grids of our previous formulation presented in [1]. We have introduced discretization techniques for the mixed derivative terms to handle the flow problems on nonuniform and nonorthogonal grids. The compact scheme is based on 5-point stencil of streamfunction formulation and is found to be second-order spatially and temporally accurate. Depending on the wave number analysis we have chosen proper forms of discretization for mixed derivative terms. Accuracy, effectiveness and stability of the proposed compact method have been seen by analyzing the analytical and numerical results.

**Key Words:** *Semilinear streamfunction equation, Biharmonic formulation, 5-point and9-point stencils, Benchmark problems.*

## 1. INTRODUCTION

The construction of compact schemes to solve fluid flow problems governed by unsteady Navier-Stokes (N-S) equations using biharmonic approach is fairly recent [2]. Even the compact schemes have brought about a renewed interest towards the finite difference approach using optimized stencil. Very recently, Tian and Yu[3] proposed a steady biharmonic formulation of a compact scheme based on 5-point stencil on uniform grids. But this approach could not fully exploit the advantages associated with using unsteady term and nonuniform grids. This motivates us to concentrate on optimized nonuniform stencil. In the present study, we have considered the Navier-Stokes equations as generalized second order partial differential equations including mixed derivative andreaction terms. In addition, we have constructed the biharmonic formulation on nonuniform grids using 5-point compact stencils. The details of the literature survey on nonuniform grids in the biharmonic formulation have been given in [1]. In this paper a new formulation is developed by reducing the role of gradient of $\psi$ and concentrating on the unsteady compact streamfunction-velocity approach for solving biharmonic formulation of N-S equations. It is based on 5-point as well as 9-point compact stencil [4] on nonuniform grids. Our proposedscheme works equally efficiently on problems described on both rectangular aswell as other curvilinear coordinate settings. It handles both Dirichlet and Neumann boundary conditions with ease. The performance of the proposed methodis investigated by considering well-studied benchmark problems such as classicall id-driven cavity flow. We compare our numerical results with both analytical and establishednumerical results, and excellent match is obtained in all the cases.

## 2. GOVERNING EUATIONS

In the context of fluid flow problems, the two-dimensional (2-D) incompressible viscous flows governed by N-S equations in cartesian coordinates in the traditional streamfunction ($\psi$) vorticity ($\zeta$) formulation include a convection-diffusion equation for vorticity and a Poisson equation for the streamfunction which are written in a bounded, simply connected domain $\Omega \subseteq \mathbb{R}^2$with smooth boundary $\partial\Omega$ as follows:

$$-\frac{\partial^2\psi}{\partial x^2}-\frac{\partial^2\psi}{\partial y^2}=\zeta \qquad (1)$$

$$Re\frac{\partial\zeta}{\partial t}-\frac{\partial^2\zeta}{\partial x^2}-\frac{\partial^2\zeta}{\partial y^2}+uRe\frac{\partial\zeta}{\partial x}+vRe\frac{\partial\zeta}{\partial y}=0\,. \qquad (2)$$

Where $Re$ are the Reynolds number and $u, v$ are the velocity components along $x$ and $y$ directions respectively and the streamfunction is related with the velocity component as

$$u = \frac{\partial \psi}{\partial y}, v = -\frac{\partial \psi}{\partial x}. \quad (3)$$

By substituting equation (1) in equation (2), we have a biharmonic equation in streamfunction. The streamfunction-velocity or the purely streamfunction formulation based methodology has been developed for the solution of the 2D incompressible fluid flows governed by Navier-Stokes equations. By considering the transformation techniques the discretized form can be written as:

$$\begin{aligned}
&\{a_{i,j}\delta_\xi^2\delta_t^+\psi_{i,j}^n + g_{i,j}\delta_t^+\left(D_{I_{i,j}}^{*n}\right) + b_{i,j}\delta_\eta^2\delta_t^+\psi_{i,j}^n + c_{i,j}\delta_\xi\delta_t^+\psi_{i,j}^n + d_{i,j}\delta_\eta\delta_t^+\psi_{i,j}^n + p_{i,j}\delta_t^+\psi_{i,j}^n \\
&\quad + \mu\left[\frac{12}{h^2}A_{i,j}\left(-\delta_\xi^2\psi_{i,j}^{n+1} + \delta_\xi U_{i,j}^{n+1}\right) + \Gamma_{i,j}\delta_\xi^2\delta_\eta U_{i,j}^{n+1} + B_{i,j}\left(D_{IV_{i,j}}^{*n+1}\right)\right. \\
&\quad + \Lambda_{i,j}\delta_\xi\delta_\eta^2 V_{i,j}^{n+1} + \frac{12}{k^2}C_{i,j}\left(-\delta_\eta^2\psi_{i,j}^{n+1} + \delta_\eta V_{i,j}^{n+1}\right) + D_{i,j}\delta_\xi^2 U_{i,j}^{n+1} + E_{i,j}\left(D_{III_{i,j}}^{*n+1}\right) \\
&\quad + F_{i,j}\left(D_{II_{i,j}}^{*n+1}\right) + G_{i,j}\delta_\xi^2 V_{i,j}^{n+1} + L_{i,j}\delta_\xi^2\psi_{i,j}^{n+1} + M_{i,j}\left(D_{I_{i,j}}^{*n+1}\right) + N_{i,j}\delta_\eta^2\psi_{i,j}^{n+1} \\
&\quad \left. + X_{i,j}\delta_\xi\psi_{i,j}^{n+1} + Y_{i,j}\delta_\eta\psi_{i,j}^{n+1} + Z_{i,j}\psi_{i,j}^{n+1}\right] \\
&\quad + (1-\mu)\left[\frac{12}{h^2}A_{i,j}\left(-\delta_\xi^2\psi_{i,j}^n + \delta_\xi U_{i,j}^n\right) + \Gamma_{i,j}\delta_\xi^2\delta_\eta U_{i,j}^n + B_{i,j}\left(D_{IV_{i,j}}^{*n}\right) + \Lambda_{i,j}\delta_\xi\delta_\eta^2 V_{i,j}^n\right. \\
&\quad + \frac{12}{k^2}C_{i,j}\left(-\delta_\eta^2\psi_{i,j}^n + \delta_\eta V_{i,j}^n\right) + D_{i,j}\delta_\xi^2 U_{i,j}^n + D_{i,j}\left(D_{III_{i,j}}^{*n}\right) + F_{i,j}\left(D_{II_{i,j}}^{*n}\right) + G_{i,j}\delta_\xi^2 V_{i,j}^n \\
&\quad \left. + L_{i,j}\delta_\xi^2\psi_{i,j}^n + M_{i,j}\left(D_{I_{i,j}}^{*n}\right) + N_{i,j}\delta_\eta^2\psi_{i,j}^n + X_{i,j}\delta_\xi\psi_{i,j}^n + Y_{i,j}\delta_\eta\psi_{i,j}^n + Z_{i,j}\psi_{i,j}^n\right] \\
&\quad = O((\Delta t)^s h^2 k^2,
\end{aligned}$$

where $D_{I_{i,j}}^*, D_{II_{i,j}}^*, D_{III_{i,j}}^*$ and $D_{IV_{i,j}}^*$ are the appropriate choices of the mixed derivative terms $\frac{\partial^2\psi}{\partial\xi\partial\eta}, \frac{\partial^2\psi}{\partial\xi^2\partial\eta}, \frac{\partial^2\psi}{\partial\xi\partial\eta^2}$ and $\frac{\partial^2\psi}{\partial\xi^2\partial\eta^2}$ are shown in figure presented in the form of wavenumber analysis.

## 3. RESULTS AND DISCUSSIONS

The resolution and diffusion properties of the proposed scheme are observed by the Fourier analysis technique. The difference between approximation and exact results are concerned with the resolution characteristics. In the present section, the Fourier analysis of the second ($\psi_{\xi\eta}$), third ($\psi_{\xi\xi\eta}$, $\psi_{\xi\eta\eta}$) and fourth ($\psi_{\xi\xi\eta\eta}$) order mixed derivatives is performed using the discretization of the elements in their sets. We begin by considering the trial function $\psi = e^{I(k_\xi\xi + k_\eta\eta)}$, $I = \sqrt{-1}$ where wavenumbers $k_\xi, k_\eta$ are in the $\xi$ and $\eta$ directions respectively. The non-dimensional characteristics of the above mentioned derivatives as afunctionof $k_\xi h$ corresponding to values of $k_\eta k = 0.5$ have been shown in Fig. 1 and 2 From the resolution characteristics it is seen that $\delta_\eta\psi_\xi$ and $\delta_\eta^2\psi_\xi$ are giving better spectral resolution in comparison to second order and even third order wide molecule central difference schemes for $\psi_{\xi\eta}$ and $\psi_{\xi\xi\eta}$ respectively. In addition from Fig. 3, it is seen that $\delta_\xi^2\delta_\eta^2\psi$ is giving better performance over other formulations, but to restrict our formulations in5-pt stencils in (n+1)$^{th}$ level, we have chosen $\delta_\xi^2\delta_\eta\psi_\eta$. This concludes that the present compact scheme has much smaller dissipative error. The abovediscussion suggests that the compact algorithm developed here possesses better resolution properties and may be best suited for high Reynolds number flow computation.

Taylor Green decaying vortices problem is extensively used as a model problem for analyzing accuracy ofthe newly developed scheme designed for time dependent problem.The governing equations are the equations (1)-(2) which will be solved in the square domain $D = \{(x, y): 0 \leq x, y \leq \pi\}$. In biharmonic formulations, the exact expression for $\psi$is $\cos(x)\cos(y)e^{\frac{-2t}{Re}}$. The initial

and boundary conditions for this biharmonic formulation can be easily derived from the exact solution. Fig. 4 shows the numerical and analytical streamline contours for *Re* = 1000 on a 41x41 grid. This indicates a very close match of the numerical solutions with the exact ones.

We have considered here also the problem of two-dimensional lid-driven square cavity flow which is extensively used as a benchmark for code validation of the incompressible N-S equations. In Fig. 5, we have compared the horizontal velocities along the vertical centerline of the square cavity for Reynolds numbers ranging from 100 to 5000 and compare our computed data with those of Ghia et al. [5].

## 4. CONCLUSIONS

In this paper, we proposed an implicit, unconditionally stable compact scheme on nonuniform and nonorthogonal grids for solving the fourth order streamfunction equations for unsteady N-S equations for incompressible viscous fluid flows. The results for all the test cases are in excellent agreement with the established experimental and numerical results

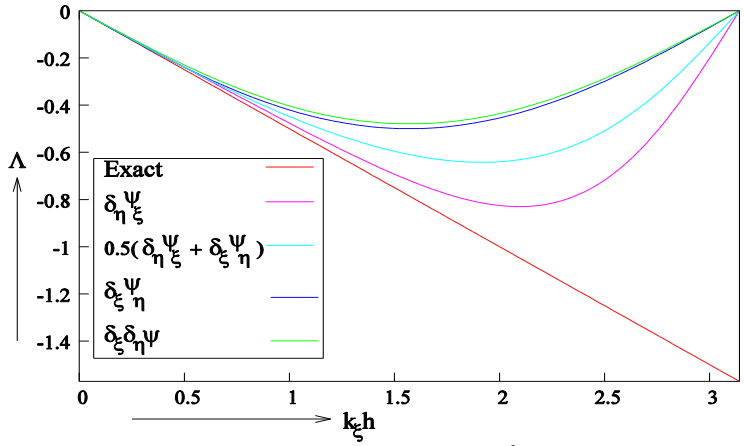


Fig.1. Comparison of nondimensional characteristics for 2nd order mixed derivative for $k_\eta k = 0.5$

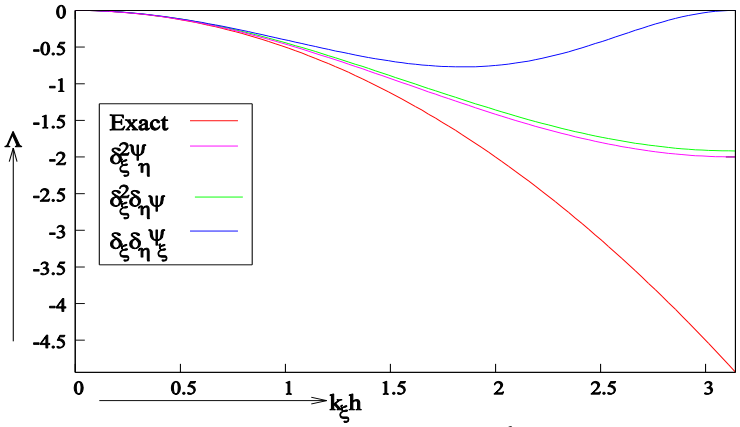


Fig.2. Comparison of nondimensional characteristics for 3rd order mixed derivative for $k_\eta k = 0.5$.

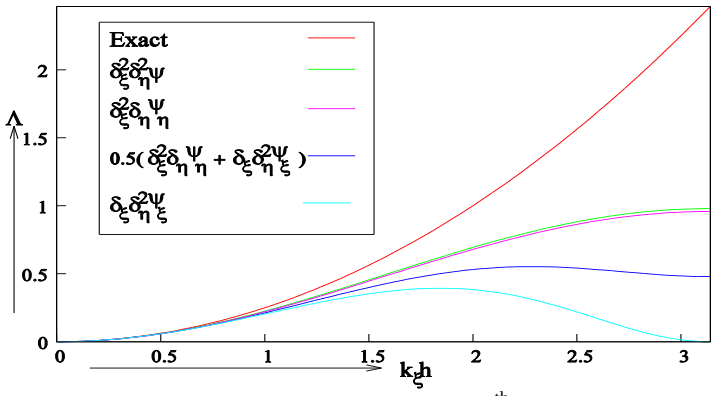


Fig.3. Comparison of nondimensional characteristics for 4th order mixedderivative for $k_\eta k = 0.5$

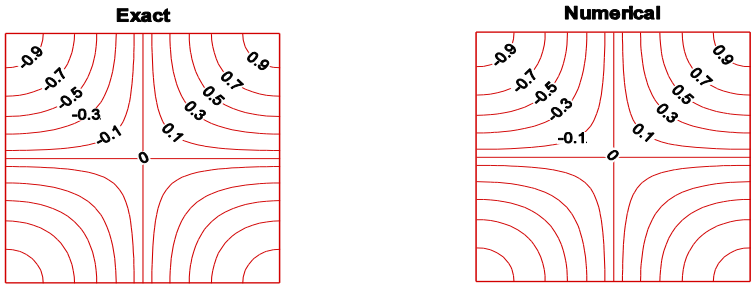


Fig.4. Streamfunction contour for Re=1000 at t=0.5 for the exact and numerical result.

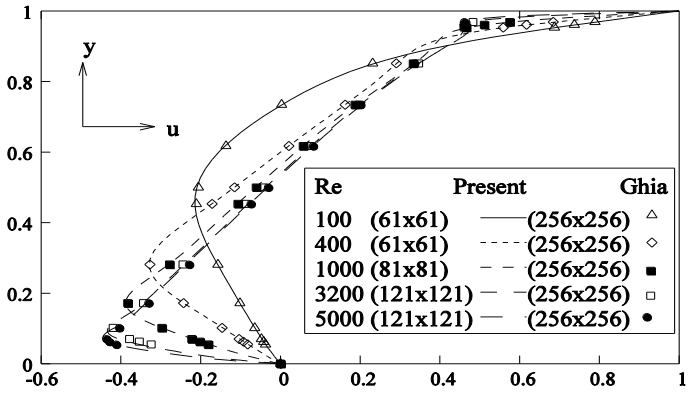


Fig.5. Comparision of horizontal velocity along the vertical centreline for Re 100 to 5000.

## 5. REFERENCES

[1] S.K. Pandit and H. Karmaka, Higher order compact computations of transient natural convection in a deep cavity with porous medium. Journal of Scientific Computing, 68(2), 653-688, 2015.

[2] J.C. Kalita and M.M. Gupta, A new paradigm for solving Navier-Stokes equation: streamfunction-velocity formulations, J. Comput. Phys. 207, 52-68,2005.

[3] Z.F. Tian and P.X. Yu, An efficient compact finite difference scheme for solving the streamfunction formulation of the incompressible Navier-Stokes equation, J. Comput. Phys. 230, 6404-6419, 2011.

[4] S.K. Pandit,On the Use of Compact Streamfunction-Velocity Formulation of Steady Navier-Stokes Equations on Geometries beyond Rectangular, J. of Sci.Computing.36,219-242, 2008.

[5] U. Ghia,K.N. Ghia. andC.T. Shin, High Re-solution for incompressible Navier-Stokes equation and a multigrid method, J. Comput. Physics. 48, 387-411, 1982.

Fifth International Conference on Computational Methods for Thermal Problems
THERMACOMP2018, July 9-11, 2018, Indian Institute of Science, Bangalore, INDIA
*N. Massarotti, P. Nithiarasu, Pradip Dutta and C. Ranganyakalu (Eds.)*

# LATTICE BOLTZMANN COMPUTATION OF NATURAL CONVECTION IN A SQUARE POROUS CAVITY WITH DIFFERENT THERMAL BOUNDARY CONDITIONS

**Dhrubajyoti Kashyap* and Anoop K. Dass**
Department of Mechanical Engineering, Indian Institute of Technology Guwahati, India-781039
*Email: k.dhrubajyoti@iitg.ernet.in

## ABSTRACT

The present work deals with the effect of four different thermal boundary conditions on fluid flow and thermal behavior during natural convection in a closed square porous cavity. The generalized lattice Boltzmann method is used to simulate the flow through the porous cavity. Four different heating arrangements are made at the hot left wall of the cavity by adopting isothermal, sinusoidal and two different linear temperature distributions respectively while the right wall is maintained isothermally cold with the thermally insulated horizontal walls. Numerical solutions are obtained in terms of stream functions, Nusselt number ($Nu$) and entropy generation due to both heat transfer ($S_\theta$) and fluid friction irreversibilities ($S_\psi$) for the range of Rayleigh number ($Ra$) $10^3$ - $10^5$ and Darcy number ($Da$) $10^{-1}$ - $10^{-6}$ with porosity ($\varepsilon$) at 0.5. The comparison is carried out with existing published results to lend legitimacy to the findings. The entropy generation minimization (EGM) approach based on heat transfer rate and entropy generation is implemented to make a judicious choice of boundary condition in terms of energy efficiency. The results indicate that the selection of optimum boundary condition depends on the values of *Ra* and *Da*. The uniform and bottom to top linear heating are found to be energy efficient.

**Key Words:** *Thermal lattice Boltzmann method, Porous medium, Non-uniform temperature, EGM.*

## 1. INTRODUCTION

Natural convection in a porous structure has always been a topic of interest for researchers as it is encountered in various natural and practical applications such as infiltration of molten metals, gas drying and transport process, geothermal operation, separation process, thermal reservoir, etc. Many experimental and numerical studies have been carried out to investigate different flow problems with a porous medium to study different aspects of porous medium based thermal systems. The current work deals with different thermal boundary conditions including non-uniform temperature distributions at the walls which can be found in various practical applications like microwave heating of food materials, air conditioning in a room, cooling of electronic equipment, solar collector, etc. So, it is crucial to identify the optimal boundary condition at which maximum heat transfer rate and minimum entropy generation prevail for a thermal system subjected to different boundary conditions. Recently, the use of EGM technique as a thermodynamic optimization tool has been significantly increased for different thermal systems such as natural convection in porous cavities [1].

A perusal of literature suggests that few studies have been made concerning the effect of thermal boundary conditions on entropy generation during natural convection in fluid-saturated porous media. Besides that, studies made by using LBM are very limited. Hence, the objective of the current study is to exploit thermal lattice Boltzmann method (TLBM) to analyze the effect of four different thermal boundary conditions on entropy generation and heat transfer in a water-saturated porous cavity.

## 2. PROBLEM FORMULATION AND METHOD OF ANALYSIS

The physical system considered for current problem consists of a closed fluid-saturated porous square cavity with side *L*. Four different configurations of heating condition are considered at the left vertical

wall by applying uniform, sinusoidal and linear temperature distributions respectively. For all four cases, the right vertical wall is uniformly cooled while keeping the top and bottom walls thermally insulated as shown in Figure 1. At all four walls, a no-slip impermeable velocity boundary condition is used. In the schematic diagram of the present computational model (Figure 1), the boundary conditions for four different cases are presented in a dimensional form.

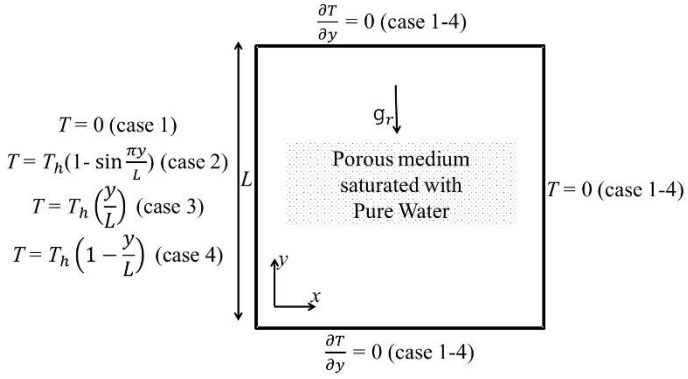


FIGURE 1. Schematic diagram of computational model.

In this work, Guo and Zhao's generalized lattice Boltzmann model based on Brinkman–Forchheimer extended Darcy model [2] is adopted to simulate the flow through the porous medium at representative elementary volume (REV) scale. This approach uses a modified equilibrium distribution function (EDF) and a force term to incorporate the porosity term into the basic LBE and thus takes into account the linear and nonlinear drag forces of the porous media. To model heat transfer phenomenon, double-distribution-function (DDF) [2] is adopted with slight modifications to incorporate the effect of the porous medium. The D2Q9 lattice structure [2] is used to simulate 2D flow problems, where D and Q stand for a number of dimensions and particle velocities respectively.

## 3. CODE VALIDATION

We have investigated natural-convection in a differentially heated square porous cavity to check the validity of code in simulating porous thermal flow while comparing the results with published works of Nithiarasu et al. [3] and Nguyen et al. [4]. Table 1 depicts a good concordance between the results in terms of the average Nusselt number ($\overline{Nu}$) along hot wall of the cavity for different *Ra* and *Da* at *Pr* fixed at 1.0, which gives the confidence to carry out the present problem using our code.

| *Ra* | *Da* | $\overline{Nu}$ | | | | | | | | |
|---|---|---|---|---|---|---|---|---|---|---|
| | | $\varepsilon$ = 0.4 | | | $\varepsilon$ = 0.6 | | | $\varepsilon$ = 0.9 | | |
| | | Present work | Nithiarasu et al. | Nguyen et al. | Present work | Nithiarasu et al. | Nguyen et al. | Present work | Nithiarasu et al. | Nguyen et al. |
| $10^3$ | $10^{-2}$ | 0.998 | 1.01 | 1.005 | 1.003 | 1.015 | 1.010 | 1.008 | 1.023 | 1.015 |
| $10^4$ | $10^{-2}$ | 1.341 | 1.408 | 1.404 | 1.468 | 1.530 | 1.533 | 1.605 | 1.64 | 1.667 |
| $10^5$ | $10^{-4}$ | 1.056 | 1.067 | 1.062 | 1.059 | 1.071 | 1.065 | 1.061 | 1.072 | 1.066 |
| $10^6$ | $10^{-4}$ | 2.546 | 2.55 | 2.702 | 2.650 | 2.725 | 2.764 | 2.731 | 2.740 | 2.817 |

TABLE 1. Comparison of present results for $\overline{Nu}$ with Nithiarasu et al. [3] and Nguyen et al. [4].

## 4. RESULTS AND DISCUSSION

For the current investigation, the grid size of 151×151 for *Ra* = $10^3$, 201×201 for *Ra* = $10^4$ and 301×301 for *Ra* = $10^5$ are found to be suitable for all computations. The solutions for current

simulations are assumed to be converged if their relative $L_1$-error norms are less than $10^{-8}$. Simulations are carried out for the range of Rayleigh number ($Ra$) $10^3$-$10^5$ and Darcy number ($Da$) $10^{-1}$-$10^{-5}$ while keeping the porosity ($\varepsilon$) at 0.5 and Prandtl number ($Pr$) at 6.2.

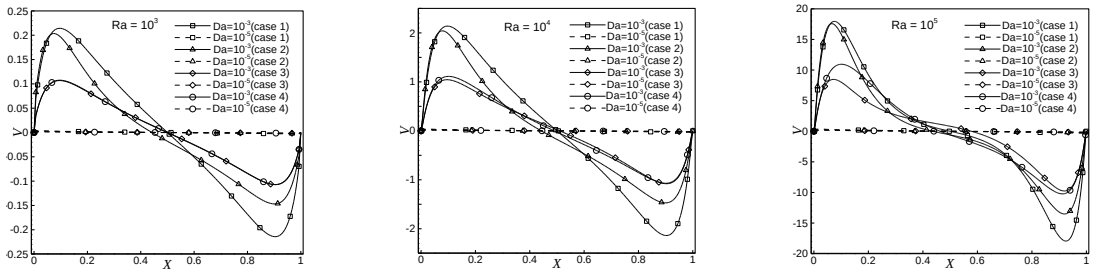


FIGURE 2. Comparison of vertical velocity $V$ in the horizontal midline of the cavity at $Ra$'s of $10^3$, $10^4$ and $10^5$ respectively with $Da$ = $10^{-3}$ and $10^{-5}$.

It is found from Figure 2 that for all values of $Ra$, the flow rate diminishes and velocity approaches zero when $Da$ reaches a very low value of about $10^{-5}$. The flow velocity increases with $Ra$ values for all four cases and position of maximum velocity comes close to the vertical walls of the cavity. Both the cases of linear heating have similar velocity profile at $Ra$ = $10^3$ and $10^4$ irrespective of $Da$ and have lower magnitudes than the other two cases.

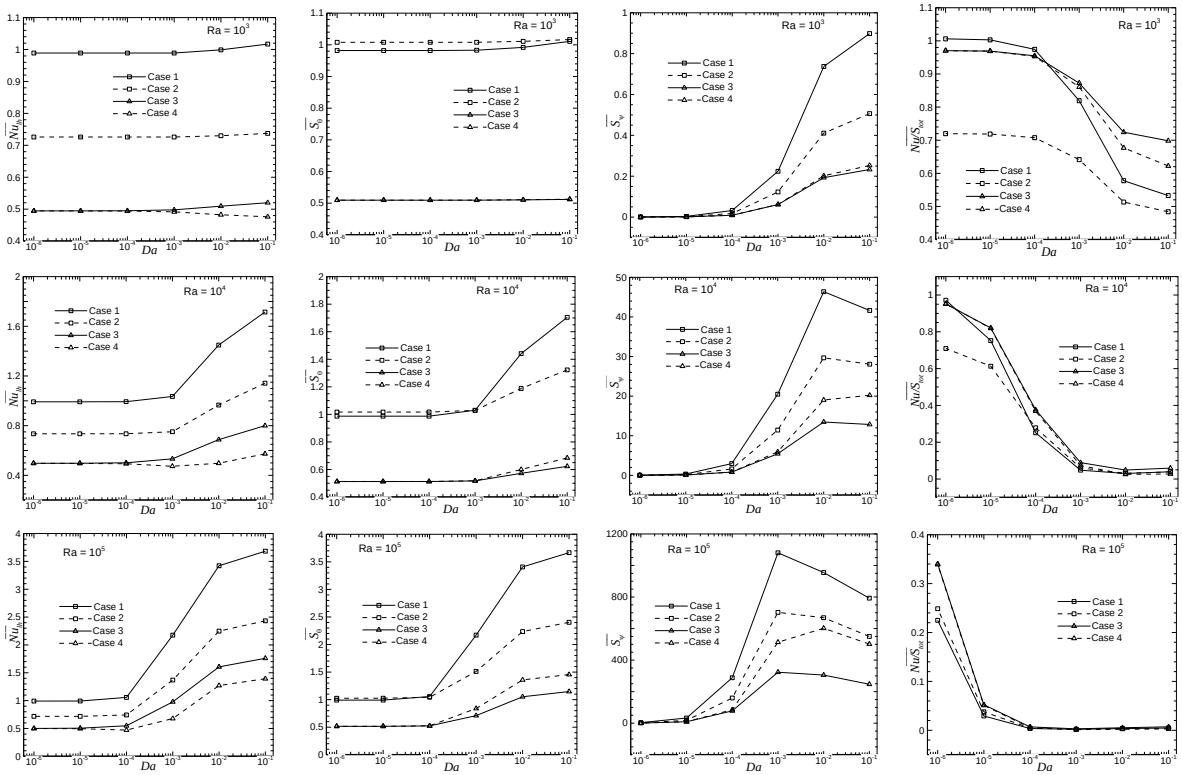


FIGURE 3. variations of $\overline{Nu_{lh}}$, $\overline{S_\theta}$, $\overline{S_\psi}$ and $\overline{Nu}/\overline{S_{tot}}$ with $Da$ varying from $10^{-1}$ to $10^{-6}$ at three different $Ra$'s of $10^3$ (top panel), $10^4$ (mid panel) and $10^5$ (bottom panel) for four cases respectively.

Figure 3 shows that the variation of average Nusselt number ($\overline{Nu_{lh}}$) along the left hot wall of the cavity with $Da$ is found to be insignificant at $Ra$ = $10^3$. However, $\overline{Nu}$ slightly decreases with the increase in $Da$ at $Ra$ = $10^3$ for the top to bottom linear heating where the flow is mainly dominated by conduction mode of heat transfer. It is observed that the $\overline{Nu}$ increases with $Da$ at $Ra$ = $10^4$ and $10^5$

as the effect of convective heat transfer augments. The maximum and minimum $\overline{Nu}$ are attained for the case of uniform heating and top to bottom linear heating respectively. The augmentation of average entropy generation due to heat transfer ($\overline{S_\theta}$) and viscous effect ($\overline{S_\psi}$) throughout the cavity with increase in *Da* value is noticed for *Ra* = $10^3$, $10^4$ and $10^5$ with minimal variation of $\overline{S_\theta}$ for *Ra* = $10^3$. However, $\overline{S_\psi}$ first increases and then decreases with increase in *Da* for all cases at *Ra* = $10^4$ and $10^5$ due to the enhancement of convective flow velocity. At all studied values of *Ra* and *Da*, $\overline{S_\theta}$ and $\overline{S_\psi}$ are found to be maximum for uniform heating and minimum for the case of bottom to top linear heating. It is seen that at low *Da* values for *Ra* = $10^3$ and $10^4$, the effect of $\overline{S_\psi}$ is trivial and the entropy generation is mainly contributed by heat transfer irreversibility. The ratio between the $\overline{Nu}$ and the $\overline{S_{tot}}$ (= $\overline{S_\theta}$+$\overline{S_\psi}$ )is calculated to make a comparison among the boundary conditions in terms of energy efficiency. $\overline{Nu}/\overline{S_{tot}}$ is found to be higher for both linear heating compared to other two cases at lower values of Darcy-Rayleigh number, $Ra_m$ = 10 and $10^2$ at *Ra* = $10^3$ and $10^4$ and for very low *Da* = $10^{-5}$ and $10^{-6}$ at *Ra* = $10^5$ as the heat transfer is controlled by conduction. However, the uniform heating has a higher value of $\overline{Nu}/\overline{S_{tot}}$ at higher $Ra_m$ = $10^3$ and $10^4$ for *Ra* = $10^4$ and $10^5$ and at low $Ra_m$ = 10 and $10^2$ for higher *Ra* = $10^5$ where flow field is dominated by convection.

## 5. CONCLUSIONS

The present study exploits a double-population thermal lattice Boltzmann method to make a detailed analysis of the effect of four different thermal boundary conditions in closed square porous cavities on the fluid flow and thermal behavior during natural convection which has not been considered yet by other researchers. The current investigation deals with a number of non-dimensional parameters like *Ra* = $10^3$-$10^5$, *Da* = $10^{-1}$-$10^{-6}$ with porosity at 0.5. It is observed that the boundary conditions and different values of *Ra* and *Da* have a profound influence on heat transfer rate, entropy generation (due to both heat transfer and fluid friction irreversibilities). Sinusoidal heating is found to be the least energy efficient among the four cases due to its low $\overline{Nu}/\overline{S_{tot}}$. Between the two cases of linear heating, bottom to top linear heating is found to be energy efficient due to higher heat transfer rate and lower entropy generation. At very low values of *Da* = $10^{-5}$ and $10^{-6}$ for all *Ra*s, $\overline{Nu}/\overline{S_{tot}}$ is higher for all four configurations as the conduction mode of heat transfer characteristics prevails. The uniform heating is found to be more suitable for higher $Ra_m$ = $10^3$ and $10^4$ for *Ra* = $10^4$ and $10^5$ and at low $Ra_m$ = 10 and $10^2$ for higher *Ra* = $10^5$ whereas, bottom to top linear heating can be an effective and alternative heating condition for low Darcy-Rayleigh number, $Ra_m$ = 10 and $10^2$ at *Ra* = $10^3$ and $10^4$ and for very low *Da* = $10^{-5}$ and $10^{-6}$ at *Ra* = $10^5$. As the LBM code has been validated by replicating reliable published results, the current results presented in this article enjoy a good credibility.

## REFERENCES

[1] P. Biswal, and T. Basak, Entropy generation vs energy efficiency for natural convection based energy flow in enclosures and various applications: A review, *Renewable and Sustainable Energy Reviews,* 80, 1412-1457, 2017.

[2] Z. Guo, and T. S. Zhao, A lattice Boltzmann model for convection heat transfer in porous media, *Numerical Heat Transfer B*, 47, 157-177, 2005.

[3] P. Nithiarasu, K.N. Seetharamu, and T. Sundararajan, Natural convective heat transfer in a fluid saturated variable porosity medium, *Int. J. Heat Mass Transfer*, 40, 3955–3967, 1997.

[4] M.T. Nguyen, A.M. Aly, and S.W. Lee, Natural convection in a non-Darcy porous cavity filled with Cu-water nanofluid using the characteristic-based split procedure in finite-element method, *Numer. Heat Transfer A*, 67, 224–247, 2015.

Fifth International Conference on Computational Methods for Thermal Problems
THERMACOMP2018, July 9-11, 2018, Indian Institute of Science, Bangalore, INDIA
*N. Massarotti, P. Nithiarasu, Pradip Dutta and C. Ranganyakalu (Eds.)*

# EFFECT OF SWIRL DEVICE ON THE HEAT TRANSFER CHARACTERISTICS IN A DECAYING LAMINAR SWIRLING FLOW THROUGH A PIPE

**C M Pranav[1], Anmol Kathail[2], P Kaushik[3]**

Department of Mechanical Engineering, Ramaiah Institute of Technology, Bengaluru - 560054

Emails: pranavcm@gmail.com[1], anmolkathail@gmail.com[2], kaushik.engg@gmail.com[3]

## ABSTRACT

The effect of a swirl-device on the heat transfer characteristics in a decaying laminar swirling flow was studied numerically using Ansys Fluent. The taper angle of the swirl-device was varied from 15° to 45° for different inlet gap widths. We showed the variation of the Nusselt number along with the axial direction for each of these cases and observed that the effect of the taper angle of the swirl-device has an important role to play in affecting the heat transfer characteristics of the flow close to the inlet. We found that higher values of the taper angle gave more heat transfer enhancement irrespective of the inlet gap width. These results could be of important use when designing swirl-devices for heat transfer enhancement.

**Key Words:** *Heat Transfer, Hydrocyclone, Swirling flow, Swirl Decay.*

## 1. INTRODUCTION

The use of swirl flows are broad which include combustion chambers and in heat transfer enhancement applications[1], cyclone separators[1] and mixers[2]. Inducing of a swirling motion at the inlet is one of the ways to actuate swirl. This swirl may decay along the length of the channel. Study of decaying swirling flow in a pipe was conducted by Yao and Fang[3] using analytical method and Ayinde[3] by numerical method. Swirl decay studies for flows with interfacial slip have also been conducted [4], [5]. In a more recent study, the effect of a tapered swirl device at inlet has also been considered[1]. Studies have found that heat transfer has been enhanced when swirl is induced at the inlet[6]. Although some studies on the heat transfer effects of decaying swirling laminar pipe flow are found in literature, they have not addressed the effect of tapered swirl device at the inlet. Therefore, in order to have a better design of the tapered part of the inlet swirl device, we attempt a numerical study to show the effect of the angle of taper of the inlet swirl device on the heat transfer effect as reflected by the Nusselt number. We assume the taper of the inlet swirl device to be adiabatic and perform our analysis using the commercial CFD package Ansys Fluent.

## 2. MODELING

The computational domain is as shown in Fig. 1. We assume the swirl velocity to be invariant in the azimuthal direction and hence choose a two-dimensional axis-symmetric domain. The swirl device causes the flow to enter into the pipe with a swirling velocity superimposed over the axial velocity.

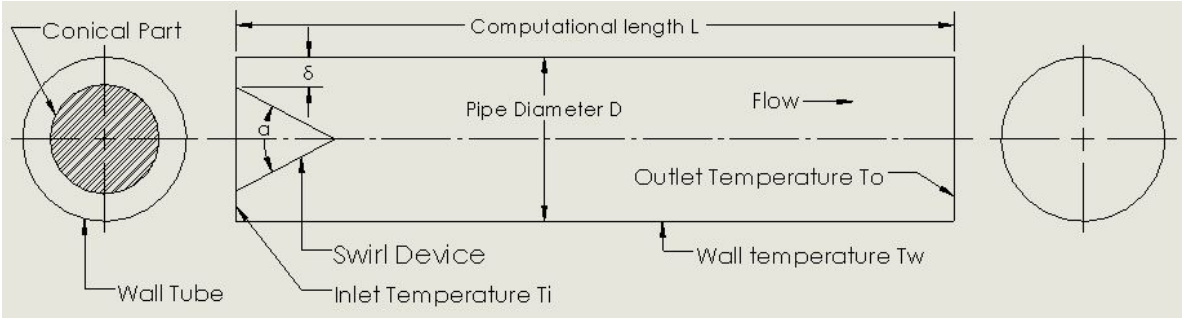


FIGURE 1. Schematic diagram of the computational domain.

We use the half-domain of the pipe for our study. The fluid at entry is assumed to be isothermal with a temperature $T_i$ and the wall of the pipe is assumed to be isothermal with a temperature $T_w$. The equations governing the flow with their usual symbols are as follows[4], [5]:

$$\frac{1}{r}\frac{\partial}{\partial r}\left(rv_r\right)+\frac{\partial v_z}{\partial z}=0 \tag{1}$$

$$\rho\left(v_r\frac{\partial v_z}{\partial r}+v_z\frac{\partial v_z}{\partial z}\right)=-\frac{\partial p}{\partial z}+\mu\left[\frac{1}{r}\frac{\partial}{\partial r}\left(r\frac{\partial v_z}{\partial r}\right)+\frac{\partial^2 v_z}{\partial z^2}\right] \tag{2}$$

$$\rho\left(v_r\frac{\partial v_r}{\partial r}+v_z\frac{\partial v_r}{\partial z}-\frac{v_\theta^2}{r}\right)=-\frac{\partial p}{\partial r}+\mu\left[\frac{1}{r}\frac{\partial}{\partial r}\left(r\frac{\partial v_r}{\partial r}\right)+\frac{\partial^2 v_r}{\partial z^2}-\frac{v_r}{r^2}\right] \tag{3}$$

$$\rho\left(v_r\frac{\partial v_\theta}{\partial r}+v_z\frac{\partial v_\theta}{\partial z}-\frac{v_\theta v_r}{r}\right)=\mu\left[\frac{1}{r}\frac{\partial}{\partial r}\left(r\frac{\partial v_\theta}{\partial r}\right)+\frac{\partial^2 v_\theta}{\partial z^2}-\frac{v_\theta}{r^2}\right] \tag{4}$$

$$\rho C_p\left(v_r\frac{\partial T}{\partial r}+v_z\frac{\partial T}{\partial z}\right)=\kappa\left[\frac{1}{r}\frac{\partial}{\partial r}\left(r\frac{\partial T}{\partial r}\right)+\frac{\partial^2 T}{\partial z^2}\right] \tag{5}$$

The boundary conditions used for solving the above equations are as follows:

$$\text{At inlet, } v_z=U_{zi}, v_\theta=U_{\theta i}, v_r=0, T=T_i$$

$$\text{At outlet, } \frac{\partial v_z}{\partial z}=0, \frac{\partial v_\theta}{\partial z}=0, v_r=0, \frac{\partial}{\partial z}\left[\frac{T-T_w}{T_m-T_w}\right]=0$$

$$\text{At wall, } v_z=0, v_\theta=0, v_r=0, T=T_w$$

Where, $T_m$ is the mean temperature.

## 3. METHODOLOGY

In order to generate the results, we use the following definitions to aid our representation: The Reynolds number is defined as $Re = \frac{\rho v_z D}{\mu}$, where $D$ is the diameter of the pipe. Nusselt number at each section is calculated using $Nu = \frac{hD}{\kappa}$, where $h = \frac{q_w}{(T_w - T_m)}$ and $q_w$ is the heat flux at the wall of the tube. Grid independence tests were carried out and 29565 elements were used in the computational domain.

## 4. RESULTS

The computational domain for the pipe's geometry with the computational length of 5000mm and a diameter of 50mm was chosen. A non-uniform grid was created with the mesh more refined at the wall, inlet, and the tapered section. The grid independence test was carried out by successively increasing the number of mesh elements until further grid refinement did not change the results significantly. It was found that 29565 elements gave the desired grid-independence. To study the heat transfer characteristics, the fluid inlet temperature was set at a steady value of 300K, while the wall was chosen to be isothermal at a temperature of 310K. The tapered section of the swirl device was assumed to be adiabatic. The fluid used to run the simulation was water.

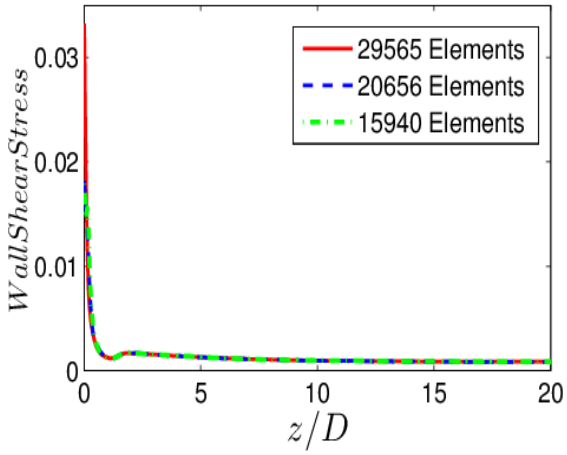


FIGURE 2. Plot of wall shear stress with the dimensionless axial coordinate for different grids for $Re = 250$. We observe that grid becomes independent for 29565 elements and choose 29565 elements throughout the present study.

Numerical simulations were performed for different taper angle of the swirl-device α (15º, 30º, 45º) taken at different inlet gap width δ (5mm and 10mm) values. The Nusselt number was then calculated at each section of the pipe in the grid using the above formulas and plotted in the axial direction. It is found that for higher values of α, the Nusselt number close to the inlet is higher (See Fig.3). However, for the same α, a lower δ produces higher Nusselt numbers towards the inlet. It was also found that irrespective of the value of δ, Nu closer to the inlet is higher for higher value of α as seen from Fig. 3(a) and 3(b). Use of larger taper angle of the swirl-device would help in increasing the heat transfer closer to the inlet in decaying laminar swirling flow through a pipe.

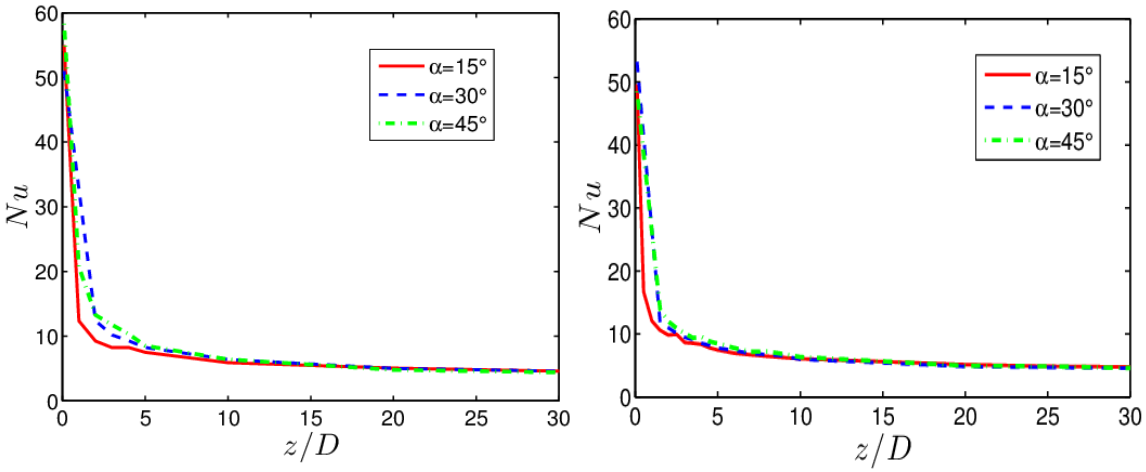


FIGURE 3. Plot of Nusselt number with the dimensionless axial coordinate for different values of taper angle of the swirl device $\alpha$ with (a) $\delta = 5mm$ and (b) $\delta = 10mm$ for $Re = 250$.

.

## 4. CONCLUSIONS

The effect of a swirl-device on the heat transfer characteristics in a decaying laminar swirling flow was studied. It was seen that the effect of the taper angle of the swirl-device has an important role to play in affecting the heat transfer characteristics of the flow close to the inlet as described by the change in Nusselt number. It was observed that higher values of the taper angle gave more heat transfer enhancement irrespective of the inlet gap width. These results could be of important use when designing swirl-devices for heat transfer enhancement.

## REFERENCES

[1] A. D. Rocha, A. C. Bannwart, and M. M. Ganzarolli, "Effects of inlet boundary conditions in an axial hydrocyclone," *Journal of the Brazilian Society of Mechanical Sciences and Engineering*, vol. 39, no. 9, pp. 3425–3437, 2017.

[2] S. Jin, Y. Liu, W. Wang, Z. Cao, and H. S. Koyama, "Numerical evaluation of two-fluid mixing in a swirl micro-mixer," *Journal of Hydrodynamics, Ser. B*, vol. 18, no. 5, pp. 542–546, Oct. 2006.

[3] S. Yao and T. Fang, "Analytical solutions of laminar swirl decay in a straight pipe," *Communications in Nonlinear Science and Numerical Simulation*, vol. 17, no. 8, pp. 3235–3246, 2012.

[4] P. Kaushik, S. Pati, S. K. Som, and S. Chakraborty, "Hydrodynamic Swirl Decay in Microtubes with Interfacial Slip," *Nanoscale and Microscale Thermophysical Engineering*, vol. 16, no. 2, pp. 133–143, Apr. 2012.

[5] P. Kaushik, S. Pati, S. K. Som, and S. Chakraborty, "Hydrodynamic and thermal transport characteristics of swirling flows through microchannels with interfacial slip," *International Journal of Heat and Mass Transfer*, vol. 55, no. 15–16, pp. 4359–4365, Jul. 2012.

[6] A. H. Algifri, R. K. Bhardwaj, and Y. V. N. Rao, "Heat transfer in turbulent decaying swirl flow in a circular pipe," *International journal of heat and mass transfer*, vol. 31, no. 8, pp. 1563–1568, 1988.

Fifth International Conference on Computational Methods for Thermal Problems
THERMACOMP2018, July 9-11, 2018, Indian Institute of Science, Bangalore, INDIA
*N. Massarotti, P. Nithiarasu, Pradip Dutta and C. Ranganyakalu (Eds.)*

# HEAT TRANSFER CHARACTERISTICS OF A VISCOELASTIC FLUID SQUEEZED AND EXTRUDED BETWEEN TWO PARALLEL PLATES

**P Kaushik**
Department of Mechanical Engineering, National Institute of Technology, Tiruchirappalli 620015, Tamilnadu, India

Email: kaushik.engg@gmail.com

## ABSTRACT

We study the effect of viscous dissipation on the heat transfer characteristics of a viscoelastic fluid undergoing simultaneous squeezing and extrusion between two parallel plates. Viscous dissipation becomes important for certain non-Newtonian fluids because of increase in shear stresses. We use the Oldroyd-B model for modelling the dynamics of the viscoelastic fluid. Our study shows an intricate coupling between the fluid rheology and Nusselt number. Our study finds importance when designing equipment handling the simultaneous squeezing and extrusion of viscoelastic fluids, especially with respect to the heating and the removal heat.

**Key Words:** *Squeezed, Extruded, Nusselt number, Oldroyd-B, Viscoelastic Fluid*

## 1. INTRODUCTION

Common industrial applications such as reactive extrusion, blending, compounding and stamping processes involve simultaneous squeezing and extrusion of soft materials and fluids. Processes such as hot extrusion and stamping may also involve heating of the fluid during the simultaneous squeezing and extrusion process. The complex interplay of the time scales of squeezing and extrusion on the fluid flow and heat transfer time scales is of prime importance to researchers in order characterize the flow physics and thermal transport properties of such processes via theory and experiments[1], [2]. The fluid rheology decides the time scale of the fluid and is an important consideration when studying the heat transfer effect of non-Newtonian liquids squeezed and extruded between two parallel plates [3]. Some studies have been reported in literature for the simultaneous squeezing and extrusion of Newtonian as well as power-law fluids between two parallel plates[3], [4]. These studies have clearly shown that the effect of viscous dissipation is of utmost importance when dealing with such flows[3]. The combined effect of squeezing and extrusion was examined on the flow properties of a viscoelastic fluid [4], however, no report of the heat transfer and thermodynamic characteristics was made. This discussion therefore essentially shows that there has been no reported study describing the heat transfer properties of a viscoelastic fluid being squeezed and extruded between two plates, despite being of relevance in many applications.

## 2. MAIN BODY

Let us consider the unsteady flow of a viscoelastic fluid between two parallel plates of length $L$ at a distance $H$ apart (see Fig.1). The coordinate system is chosen in such a way that the $x$-axis is parallel to the plates and the $y$-axis is along the perpendicular direction of the plates as shown in Fig. 1. We assume that the plates are isothermal with both the plates at the same temperature. The motion in the fluid, which is at rest initially, is triggered by the simultaneous motion of the bottom plate along the positive $x$-direction with an uniform velocity $U$ and the top plate along the negative $y$-direction with an uniform velocity $V$ (as shown in Fig. 1). The viscoleastic fluid is

initially assumed to be in thermal equilibrium with the walls, the flow of the fluid is incompressible and laminar, the distance between the two plates is much smaller compared to the length of the plates, the fluid properties do not depend on the temperature and the fluid is free of any stresses initially, internal heat generation is not there except through viscous dissipation, lubrication approximation is valid [5], squeezing velocity is considered to be very small, the distance separating the plates remains approximately constant owing to a very small squeezing velocity of the top plate [1], leading to a quasi-steady process.

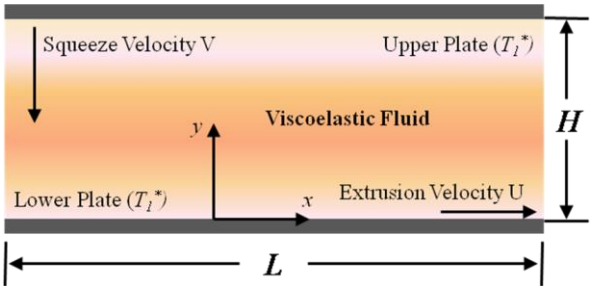


Fig. 1. Schematic diagram describing the problem

The governing dimensionless equations for the flow and heat transfer of a viscoelastic fluid squeezed and extruded between two parallel plates may be written as:

$$\frac{\partial u}{\partial x}+\frac{\partial v}{\partial y}=0 \qquad \tau_{xx}+\frac{Wi}{\Omega\omega}\frac{\partial \tau_{xx}}{\partial t}-2Wi\tau_{xy}\frac{\partial u}{\partial y}=0$$

$$\frac{\partial u}{\partial t}+\omega v\frac{\partial u}{\partial y}=\frac{\partial \tau_{xy}}{\partial y}+\beta\frac{\partial^2 u}{\partial y^2} \qquad \tau_{xy}+\frac{Wi}{\Omega\omega}\frac{\partial \tau_{xy}}{\partial t}-Wi\tau_{yy}\frac{\partial u}{\partial y}=(1-\beta)\frac{\partial u}{\partial y}$$

$$\frac{\partial v}{\partial t}+\omega v\frac{\partial v}{\partial y}=\Omega\frac{\partial \tau_{yy}}{\partial y}+\beta\frac{\partial^2 v}{\partial y^2} \qquad \tau_{yy}+\frac{Wi}{\Omega\omega}\frac{\partial \tau_{yy}}{\partial t}=2\omega(1-\beta)\frac{\partial v}{\partial y}$$

$$\left[\frac{\partial \theta}{\partial t}+\omega v\frac{\partial \theta}{\partial y}\right]=\frac{1}{\mathrm{Pr}}\frac{\partial^2 \theta}{\partial y^2}+\Phi$$

where $\Phi=\frac{2\beta\,\mathrm{Ec}}{\Omega^2}\left(\frac{\partial v}{\partial y}\right)^2+\beta\,\mathrm{Ec}\left(\frac{\partial u}{\partial y}\right)^2+\mathrm{Ec}\,\tau_{xy}\frac{\partial u}{\partial y}+\frac{\mathrm{Ec}}{\Omega}\tau_{yy}\frac{\partial v}{\partial y}$. The equations have been non-dimensionalized using the following parameters:

$$u=\frac{u^*}{U},\ v=\frac{v^*}{V},\quad x=\frac{x^*}{L},\quad y=\frac{y^*}{H},\quad t=t^*\Big/\frac{\rho H^2}{\eta},\quad p=\frac{p^*}{\rho V^2},\quad \theta=\left(T^*-T_1^*\right)\Big/\left(\Delta T^*\right).$$

The dimensionless numbers appearing in the above equations are defined as: Prandtl number $\mathrm{Pr}=\eta C_P/\kappa$, Eckert number $\mathrm{Ec}=U^2/C_P\left(\Delta T^*\right)$, $\Omega=U/V$, Weissenberg number $Wi=\lambda_1 U/H$, $\beta=\lambda_2/\lambda_1$ and $\omega=\rho VH/\eta$. It is important to mention here that the parameters

$\Omega$ and $\omega$ are called the extrusion parameter and squeezing parameter respectively[4]. The initial and boundary conditions employed for the solution of above equations are as follows:
for $t \le 0,\ u = 0,\ v = 0,\ \theta = 0,\ \tau_{xx} = 0,\ \tau_{xy} = 0,\ \tau_{yy} = 0\ \forall$ y ,
for $t > 0,$ At $y = 0,\ u = 1,\ v = 0,\ \theta = 0$ and for $t > 0,$ At $y = 1,\ u = 0,\ v = -1,\ \theta = 0$

The Nusselt number at the wall is evaluated using $\mathrm{Nu}(t) = \left|\partial\theta/\partial y\right|$ at $y = 0$ from the solution of the temperature field.

## 3. RESULTS

We assume a fully forced convection and solve the dimensionless velocity equations before solving for the non-dimensional temperature . Second order central difference scheme is used for all the spatial discretization [6] and a fully implicit first order scheme is used for progressing in time. After conducting a grid independence and convergence test, a uniform grid of $\Delta y = 0.01$ and a dimensionless time step size of $\Delta t = 10^{-4}$ was chosen for our study. In order to validate our study, we match our results for a Newtonian fluid with Duwairi et al [1] and find a good match.

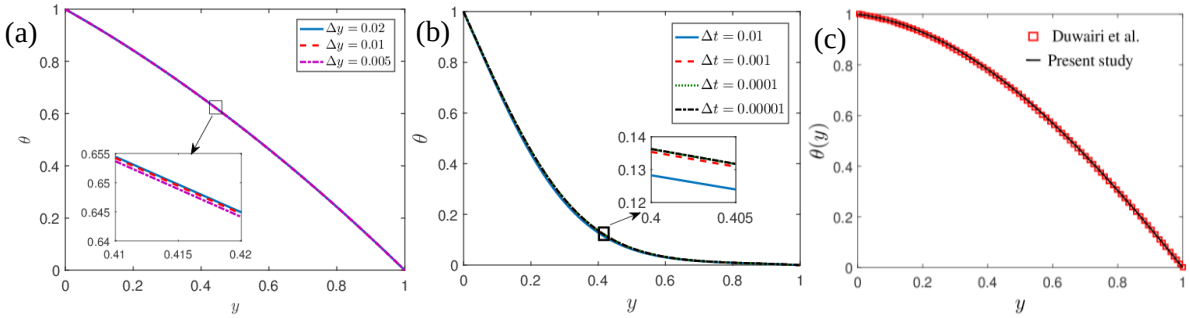


Fig 2. (a) Grid independence test: Plot of $\theta$ vs $y$ for various numbers of grid points for $\Omega = 10$, $Ec = 0.1$, $\omega = 0.01$, $\Omega = 10$, $Pr = 10$, $Wi = 1.0$, $\beta = 0.8$ and $\Delta t = 10^{-4}$ at quasi-steady state and (b) Convergence test: Plot of $\theta$ vs $y$ for various time step for $\Omega = 10$, $Ec = 0.1$, $Pr = 10$, $\omega = 0.01$, $Wi = 1.0$, $\beta = 0.8$ at $t = 0.3$. (c) ***Model Validation***: Plot showing the variation of dimensionless temperature $\theta(y)$ vs $y$ at quasi-steady state obtained for two different values of $\Omega = 15$. The other parameters considered are $Ec = 0.01$, $Pr = 0.72$, $\omega = 0.5$, $Wi = 0$ and $\beta = 1$. The value of the dimensionless temperature $\theta$ obtained from the present study shows an excellent match with the results found in Duwairi et al [1].

We plot the temporal variation of Nusselt number for two different viscoelastic parameters namely Weissenberg number $(Wi)$ and $\beta$. Weissenberg number is the ratio of the relaxation time scale of the fluid to the advective time scale of the flow, while $\beta$ is the ratio of the retardation time scale to the relaxation time scale. We observe that the Nu is significantly higher for smaller values of $Wi$ and larger values of $\beta$, indicating that the viscous dissipation is higher for Newtonian fluids as compared to viscoelastic fluids. This is because of energy absorbing capability of viscoelastic fluid as compared to a Newtonian fluid because of the presence of the elastic nature within it. We also observe that as the value of $Wi$ increases and the value of $\beta$ decreases, the value of overall value of Nu is decreases. We also observe that value of Nu value has significant difference during transience as compared to steady state and is because of the effect of the elastic traction terms being

more prominent during early transience. Due to the presence of residual stresses, the value of Nu at steady state is different for different values of the various parameters.

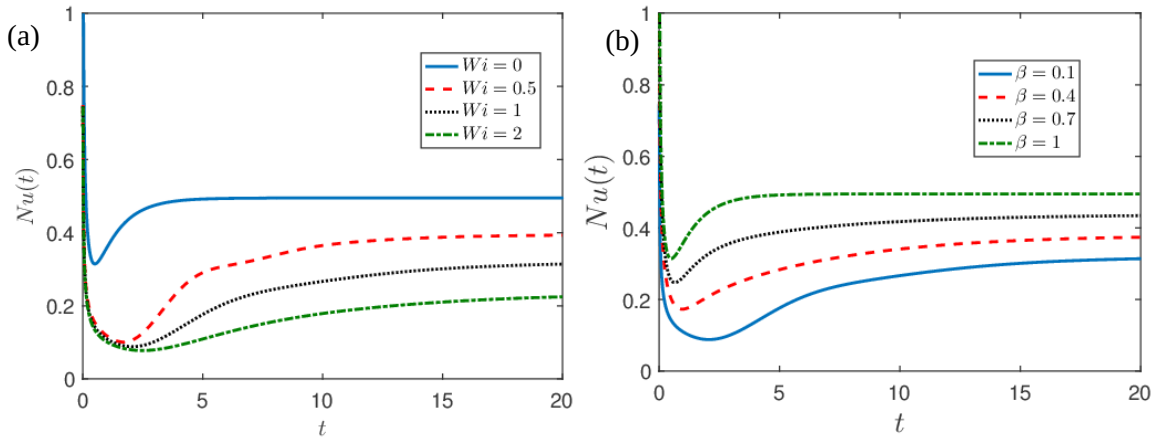


Fig 3. Plot of $Nu(t)$ vs. $t$ for various (a) $Wi$ with $\beta = 0.1$ and (b) $\beta$ with $Wi = 1$ for $\Omega = 10$, $\omega = 0.01$, $\Omega = 10$, $Ec = 0.1$, $Pr = 10$.

## 4. CONCLUSIONS

An unsteady heat transfer characteristics study of a viscoelastic liquid, squeezed and extruded between two parallel plates is studied. The major conclusions drawn from the present study are as follows:

• Nu increases for increase in $Wi$ and decrease in $\beta$ .

• Viscous heating is more in case of Newtonian fluids as compared to viscoelastic fluids because of inability of Newtonian fluids to absorb energy.

• Nusselt number at steady state varies with $Wi$ and $\beta$ because of existence of residual stresses.

## REFERENCES

[1] H. M. Duwairi, B. Tashtoush, and R. Damseh, "On heat transfer effects of a viscous fluid squeezed and extruded between two parallel plates," *Heat and Mass Transfer*, Aug. 2004.

[2] A. Lawal and D. M. Kalyon, "Nonisothermal extrusion flow of viscoplastic fluids with wall slip," *International Journal of Heat and Mass Transfer*, vol. 40, no. 16, pp. 3883–3897, Oct. 1997.

[3] P. Kaushik, P. K. Mondal, S. Pati, and S. Chakraborty, "Heat Transfer and Entropy Generation Characteristics of a Non-Newtonian Fluid Squeezed and Extruded Between Two Parallel Plates," *Journal of Heat Transfer*, vol. 139, no. 2, pp. 22004–22009, Nov. 2016.

[4] P. Kaushik, P. K. Mondal, and S. Chakraborty, "Flow dynamics of a viscoelastic fluid squeezed and extruded between two parallel plates," *Journal of Non-Newtonian Fluid Mechanics*, vol. 227, pp. 56–64, 2016.

[5] L. G. Leal, *Advanced Transport Phenomena: Fluid Mechanics and Convective Transport Processes*. Cambridge University Press, 1989.

[6] J. Anderson, *Computational Fluid Dynamics*. McGraw-Hill Education, 1995.

Fifth International Conference on Computational Methods for Thermal Problems
THERMACOMP2018, July 9-11, 2018, Indian Institute of Science, Bangalore, INDIA
*N. Massarotti, P. Nithiarasu, Pradip Dutta and C. Ranganyakalu (Eds.)*

# ASSESSMENT OF PREMIXED CMC MODEL USING DIRECT NUMERICAL SIMULATION

**Kedar G. Bhide, S. Sreedhara**
Indian Institute of Technology Bombay, Mumbai, India

kedarbhide@iitb.ac.in, sreedhara.s@iitb.ac.in

## ABSTRACT

Conditional Moment Closure (CMC) model has been applied to turbulent premixed combustion only recently. Three- dimensional Direct Numerical Simulation (3D DNS) of growth of an ignition kernel in homogeneous and iso-tropic turbulence was performed to assess the accuracy of premixed CMC model. Variation of turbulent intensity was considered in this study and flames belonged to the thin reaction zones regime of turbulent premixed combustion. Premixed CMC model correctly predicted the variation of conditional scalars across the flame. Also, predictions of CMC model were found to be accurate at different stages of growth of an ignition kernel.

**Key Words:** *DNS, CMC, Premixed Combustion*

## 1. INTRODUCTION

Conditional Moment Closure (CMC) is an emerging modelling strategy for turbulent premixed combustion. CMC was independently proposed by Klimenko [1] and Bilger [2]. Underlying assumption of CMC model is as follows: fluctuations in variables like temperature, mass fractions can be associated with the fluctuations of a single property. Also, deviation of variables from the mean is smaller when conditioned on such a single property. Though CMC model does not make a-priori assumption of combustion being premixed or non-premixed, application of CMC model to premixed combustion is relatively new. Premixed CMC (PCMC) model and its advancement, Tabulated PCMC (TPCMC) will be discussed in the Section 2. Validation of TPCMC model using the data obtained by Direct Numerical Simulation (DNS) of ignition kernel growth will be discussed in the subsequent sections.

## 2. PREMIXED CMC MODEL

Reaction Progress Variable (RPV), denoted by $c$, is used as a conditioning variable in the PCMC. Conditional average is denoted by $\langle Y \mid c=\eta \rangle$ or simply $\langle Y \mid c \rangle$. Condition for averaging is given to the right of vertical line. $\langle\ \rangle$ indicates averaging operation. Here, $Y$ can be any scalar (for example, fuel mass fraction). η is a sample space of RPV. In the CMC, $Q_i$ is used to denote averaged quantity and $Q_i(\eta;x,t)=\langle Y(x,t) \mid c=\eta \rangle$. Martin *et al.* [3] and Velez *et al.* [4,5] have given governing equation for $Q_i$ in a turbulent premixed medium (Eq. 1). Governing equations for all such $Q_i$ are solved in the CMC. $\dot{\omega}$ is a reaction rate term in Eq. 1. $N$ denotes scalar dissipation rate and it is defined by Eq. 2. Conditional average of reaction rate (T1) and conditional scalar dissipation rate (T2) are used in Eq. 1. Single and double dashes over $Q_i$ in Eq. 1 denote first and second derivative of $Q_i$ in RPV, i.e., $c$ space. $c$ is a reactive scalar and hence, the third term, $S_c$ (T3), appears in the equation of $Q_i$. $Q_i$ is converted into unconditional value in the physical space by using a suitable probability density function (PDF). The β-PDF of $c$ is constructed using favre averaged value of c ($\tilde{c}$) and variance of $c$ ($\widetilde{c''^2}$), as given by Klimenko and Bilger [6].

$$\underbrace{\langle(\dot{\omega}_i/\rho)\mid c\rangle}_{\text{T1}}+\underbrace{\langle N\mid c\rangle Q_i''}_{\text{T2}}-\underbrace{\langle S_c\mid c\rangle Q_i'}_{\text{T3}}=0 \tag{1}$$

$$N = D(\nabla c)^2 \tag{2}$$

It may be noted that the value of scalar dissipation rate obtained from a CFD solver is an unconditioned value and this value should be converted to a conditional average of scalar dissipation rate. Solving Eq. 1 requires this conditionally averaged value of scalar dissipation rate.

Velez *et al.* [4,5] used a value at each cell in the domain to choose a solution of $Q_i$ useful at that cell in the domain. In order to obtain a conditioned value of $N$, Eq. 3 was used by Velez *et al.* [4,5]. $N_0$ is the unconditional value of scalar dissipation rate obtained from a CFD solver and used to choose a solution of $Q_i$.

$$\langle N \mid c \rangle = 4N_0\{c(1-c)\} \tag{3}$$

The flowchart for TPCMC model is shown in Fig. 1(a). In the TPCMC method, equations for $Q_i$ are solved offline for different values of scalar dissipation rate [4,5]. Scalar dissipation rate is also calculated at every cell in the physical domain. This value of scalar dissipation rate is used to choose a correct solution of Eq. (1). Solving equations offline reduces the time required for simulation. Eq. (1) was solved for number of values of $N$ using Two-point boundary value solver [7]. GRI-1.2 mechanism of methane-air combustion was used obtain the solutions [8]. Influence of $N$ on solution of Eq. (1) may be observed in Fig. 2(b) for methane mass fraction. Values at the boundary are fixed and serve as boundary conditions to Eq. (1). Between $c$ = 0 and $c$ = 1, solution is affected by $N$.

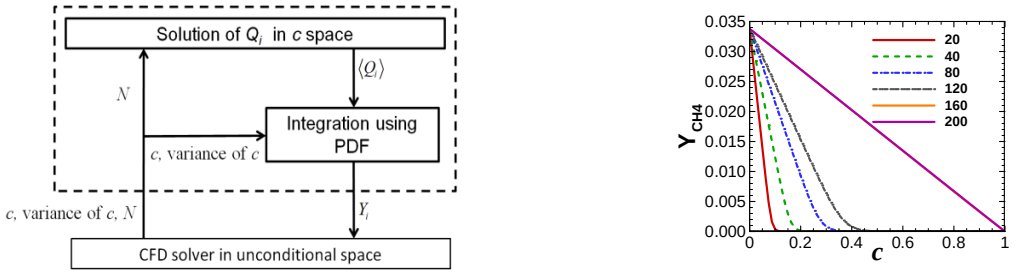


(a) (b)

Figure 1: (a) Flow-chart for TPCMC model [5], and (b) Influence of $N$ on the solution of Eq. (1) for mass fraction of $CH_4$.

In the present study, accuracy of TPCMC model was tested using the data obtained from Direct Numerical Simulation (DNS) of growth of ignition kernel. Favre averaged value of scalar dissipation rate ($\tilde{N}$), $\tilde{c}$, and $\widetilde{c''^2}$ was obtained from DNS. Based on the value of $\tilde{N}$, appropriate solution of Eq. (1) was chosen. It was integrated using PDF constructed based on $\tilde{c}$ and $\widetilde{c''^2}$ to obtain the values in physical space.

## 3. DIRECT NUMERICAL SIMULATION

DNS of ignition kernel growth was performed using PENCIL code. PENCIL code is an open-source DNS code capable of solving multi-step chemistry [9]. Three-step irreversible chemistry of methane-air combustion was used [10]. Initial ignition kernel, containing products of combustion, was created in the form of a sphere of diameter 0.25 *cm* at a temperature of 1660 *K*, which is same as the adiabatic flame temperature at equivalence ratio φ = 0.6. Chemical time-scale ($\tau_c = \delta_L / S_L$) is 6.01 *ms*. Periodic boundary conditions were applied on all the boundaries. Parameters of the two cases are given in Table 1. Intensity of turbulence is denoted by $u'$ and integral scale is denoted by $l_t$ in Table 1. Karlovitz number of both cases is also given in Table 1. Both flames belong to the thin reaction zones regime. Simulations were run for a total of 6 *ms*, which is equal to $\tau_c$. RPV has been

defined using mass fraction of $CH_4$ as given in Eq. 4. Subscripts *b* and *u* denote mass fractions in burned and unburned states of fuel-air mixture respectively.

| | | | |
|---|---|---|---|
| Laminar flame speed ($S_L$) | 13.8 *cm/s* | Flame thickness ($\delta_{th}$) | 0.083 *cm* |
| Unburned gas temperature | 300 *K* | Initial pressure | 1.01 *bar* |
| Domain size | 4 × 4 × 4 *cm* | Grid size | 256 × 256 × 256 |

| | $u'$ (*cm/s*) | $l_t$ (*cm*) | $\tau_f$ (*ms*) | $Da = \tau_f / \tau_c$ | *Ka* |
|---|---|---|---|---|---|
| Case 1 | 50 | 0.15 | 3 | 0.5 | 5.13 |
| Case 2 | 69 | 0.15 | 2.17 | 0.361 | 8.31 |

Table 1: Parameters of simulation

$$c = 1 - \frac{Y_{CH_4}}{Y_{CH_4 u}} \tag{4}$$

## 4. RESULTS AND DISCUSSIONS

Data obtained from DNS was favre averaged on the surfaces of constant radius. Radius was calculated from the centre of mass of the flame. Methane mass fraction and temperature were chosen to compare the predictions of DNS and TPCMC. Figure 2 shows comparison of DNS and TPCMC predictions for methane mass fraction and temperature for both cases. Data shown in Fig. 2 was obtained at 6*ms*. For both cases, predictions of TPCMC are in close agreement with the DNS for both scalars.

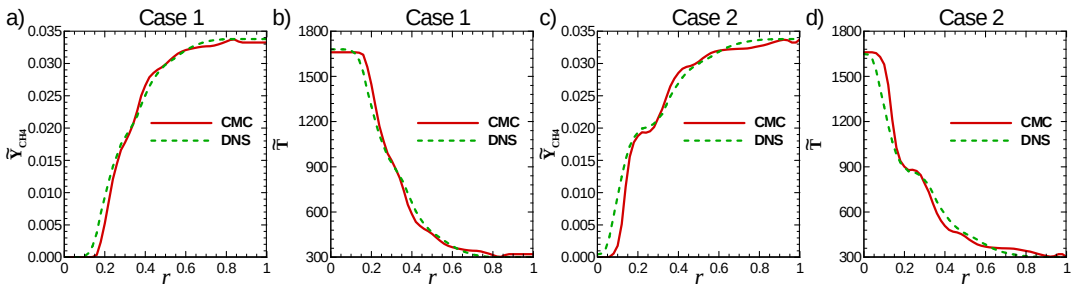


Figure 2: Comparison of DNS and TPCMC predictions for (a,c) methane mass fraction and (b,d) temperature.

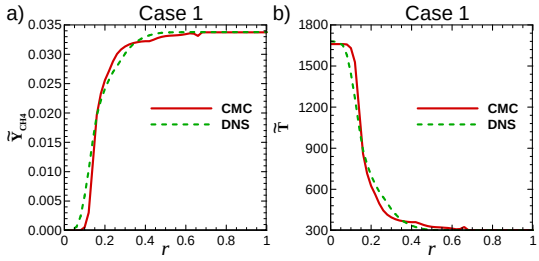


Figure 3: Comparison of DNS and CMC predictions for (a) methane mass fraction and (b) temperature at 3.2 *ms*.

In order to test the accuracy of TPCMC in predicting the values at an earlier stage of growth of ignition kernel, TPCMC predictions at 3.2 *ms* were compared with DNS predictions for case 1.

Figure 3 shows the results for comparison at 3.2 *ms*. Agreement between CMC and DNS is equally good at this earlier stage in the growth of ignition kernel.

## 5. CONCLUSIONS

Direct Numerical Simulation of growth of an ignition kernel was performed. Data obtained from the DNS was used to assess the accuracy of TPCMC model. Predictions of TPCMC was tested with the data obtained from DNS at different time instances. TPCMC was found to predict variation of methane mass fraction and temperature accurately at different stages of growth of an ignition kernel. Also, the accuracy TPCMC model was unaffected by variation of *u'*, though limited parametric range was considered in this study. TPCMC equation considered in this study does not contain an unsteady term, whereas problem of ignition kernel considered here is purely unsteady in nature. Predictions of TPCMC were found to be accurate for this unsteady problem as well. Also, different chemical mechanisms were used in DNS and CMC. This did not affect the accuracy of TPCMC model. DNS with detailed chemistry and over a larger parametric range may be performed to further judge the accuracy of TPCMC.

## 6. REFERENCES

[1] Klimenko, A. Y., Multicomponent Diffusion of Various Admixtures in Turbulent Flow, *Fluid Dynamics*, 25(3), 327–334,1990.

[2] Bilger, R. W., Conditional Moment Closure for Turbulent Reacting Flow, *Physics of Fluids A: Fluid Dynamics*, 5(2), 436–444,1993

[3] Martin, S. M., Kramlich, J. C., Kosály, G., and Riley, J. J., The Premixed Conditional Moment Closure Method Applied to Idealized Lean Premixed Gas Turbine Combustors, *Journal of Engineering for Gas Turbines and Power*, 125(4), 895–900, 2003.

[4] Velez, C., MArtin, S., Jemcov, A., and Vasu, S., LES Simulation of an Enclosed Turbulent Reacting Methane Jet With the Tabulated Premixed CMC Method, *Proceedings of ASME Turbo Expo 2015*,1–13, 2015.

[5] Velez, C. A., Martin, S. M., and Vasu, S. S., Reacting Unsteady Reynolds-Averaged Navier–Stokes with the Tabulated Premixed Conditional Moment Closure Method,*Journal of Propulstion and Power*, 1–15, 2016.

[6] Klimenko, A. ., and Bilger, R. W., Conditional Moment Closure for Turbulent Combustion, *Progress in Energy and Combustion Science*, 25(1999), pp. 595–688,1999.

[7] Grcar. J.F., The Twopnt Program for Boundary Value Problems, *Sandia National Laboratories Report SAND91-8230,*1992,

[8] Frenklach, M. *et al*., GRI-Mech-1.2, An Optimized Detailed Chemical Reaction Mechanism for Methane Combustion, 1995

[9] Babkovskaia, N., Haugen, N. E. L., and Brandenburg, A., A High-Order Public Domain Code for Direct Numerical Simulations of Turbulent Combustion, *Journal of Computational Physics*, 230(1), 1–12, 2011.

[10] Bibrzycki, J., and Poinsot, T., , Reduced Chemical Kinetic Mechanisms for Methane Combustion in O2/N2 and O2 /CO 2 Atmosphere, *Work. note ECCOMET WN/CFD/10/17, CERFACS*, 2010.

# NUMERICAL INVESTIGATION ON AIR SLOT JET IMPINGEMENT COOLING OVER A CYLINDER

**Ketan A. Ganatra and Dushyant Singh**
Department of Mechanical Engineering
National Institute of Technology Manipur, India
ketanganatra0@gmail.com and dushyant@nitmanipur.ac.in

**Abstract**
In the present study, a numerical investigation is carried out for a slot air jet impingement from a heatred circular cylinder. The flow is assumed to be two-dimensional incompressible, steady and turbulance.The non-dimensional pressure coefficient and the Nusselt number have been evaluated for the validation of the fluid flow and heat transfer characteristics. The results obtained from numerical work are compared with the experimental work [1-2]. The numerical investigation has been carried out using four different turbulence models such as, Realizable k-ε, RNG k-ε, SST k-ω and $v^2f$. The numerical results are obtained for the case of H/S = 8, S/D = 0.25 and $Re_D$ = 20,000.
**Key Words:** *Slot air jet impingement, Fluid flow, Heat transfer, Turbulence models*

## 1. Introduction

Impinging jets are widely used in many industrial applications such as heating, cooling or drying a surface because of the characteristics of immediate and selective cooling for a heated surface.It has the advantages of low cost and simple in construction. It is widely used for tempering of glass, drying of textiles, paper, photographic films and painted surfaces, cooling of metal sheets and turbine blades and thermal control of electronic equipments. The number of researchers have presented the review for the jet impingement heat transfer on a flat surface. The availability of the literature for the jet impingement heat transfer with the curved surfaces is very few.Present study focuses the literature mainly on the cylindrical (curved) target surface with a slot air jet impining.Brahma et al. [1] has investigated the flow characteristics experimentally for a circular cylinder with an impinging slot air jet. The non-dimensional pressure coefficient have been calculatedon a circularcylinder. With the increase in Reynolds number, the stagnation pressure increases and the stagnation zone decreases. F.Gori&L.Bossi [2] have investigated for air slot jet impingement heat transfer from heated cylinder. They have studied the effect of non-dimensional distance between the slot jet and the cylinder (H/S) in the range of 2-10 and reported that the maximum value of mean nusselt number is at H/S = 6 and developed a heat transfer correlation for average Nusselt number ($Nu_{avg.}$).The same authors [3]have made an experimental work with different slot size with D/S = 1,2 and 4. The maximum value of average Nusselt number is found to be at H/S = 8 for Re 4,000to 22,000. Pachpute & Premchandran [4] have studied both experimental as well as numerical work of air slot jet impingement cooling of a circular cylinder with and without a bottom opening semi-circular confinement. The numerical simulation has been carried out using the $v^2f$ turbulence model. They reported the maximum deviation for the stagnation Nusselt number to be 14% by comparing the experimental and numerical results.They have also suggested that the effect of flow confinement is significant at H/S = 2. The same authors [5] have made a numerical analysis with and without a top confinement by the $v^2f$ turbulence model. The numerical results are compared with the experimental data for the flat plate and the cylinder. They reported the effect of confinement is significant for H/S ≤ 4 and $L_{conf}/D \leq 6$. They also measured the deviation for the stagnation Nusselt number to be 16% by comparing the experimental results.

The present study focuses mainly on the air slot jet impingement heat transfer with the target surface as cylinder. The numerical simulation is carried out with the four different turbulence models. Hence, the objective of the present study is to select a turbulene model for the fluid flow and heat transfer characteristics.

## 2. Problem Statement

Figure. 1 shows the computational domain for the present study. The different parameters considered are non-dimensional jet to heated cylinder spacing (H/S), jet width to diameter ratio (S/D) and Reynolds number based on the diameter of the cylinder ($Re_D$).

$$\mathrm{Re}_D = \frac{\rho V D}{\mu}$$

The Nusselt number defined based on the diameter of the cylinder as,

$$Nu_\theta = \frac{q''}{(T_w - T_{jet})}\frac{D}{k_f}$$

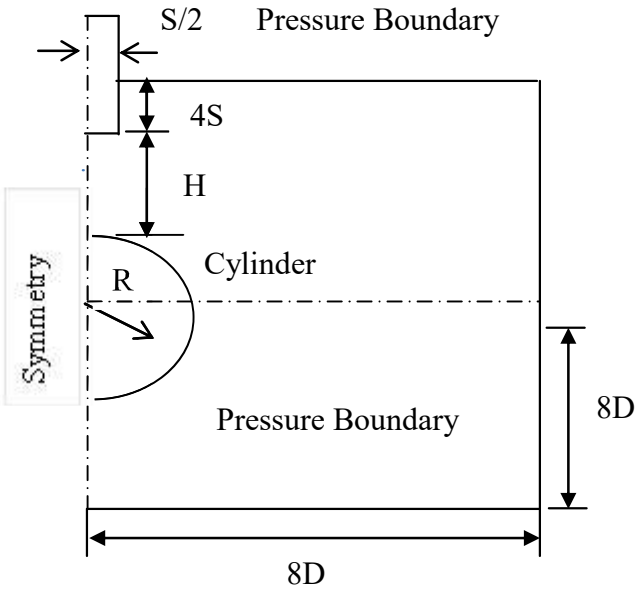


Figure.1 Computational domain used for the present study

## 3. Numerical Method

The flow is assumed steady, incompressible and turbulent, the Reynolds time averaged Navier-Stokes equations are used for the numerical simulation. The continuity, momentum and energy equations are as follows,

$$\frac{\partial u_i}{\partial x_i} = 0$$

$$\rho u_j \frac{\partial u_i}{\partial x_j} = -\frac{\partial P}{\partial x_i} + \frac{\partial}{\partial x_j}\left[\mu\left(\frac{\partial u_i}{\partial x_j} + \frac{\partial u_j}{\partial x_i}\right) - \rho\overline{u_i' u_j'}\right]$$

$$\rho u_j \frac{\partial T}{\partial x_j} = \frac{\partial}{\partial x_j}\left[\frac{\mu}{\mathrm{Pr}}\frac{\partial T}{\partial x_j} - \rho\overline{T' u_j'}\right]$$

The numerical simulation is carried out with the open source CFD solver OpenFOAM.The different turbulence models used are Realizable k-ε, RNG k-ε, SST k-ω and $v^2f$. SIMPLE algorithm is usedfor the pressure and velocity coupling. The convective and turbulence terms are discretised using Gauss upwind method. The convergence is assumed to be reached when the residuals for all the convective and turbulence terms are less than $10^{-6}$.

A constant magnitude of velocity of air is imposed at the Nozzle inlet. The flow is assumed to be fully developed at the exit of the Nozzle.

**Numerical bounadry condition**

- **Nozzle Inlet-** A uniform velocity profile is imposed at the nozzle inlet.The temperature of the air is assumed to be 300 K. The turbulent intensity and the viscosity ratio are fixed as 5% and 5 for all the cases.
- **Nozzle wall -** The nozzle wall is assumed to be adiabatic with no-slip.
- **Cylindrical wall –**The constant heat flux of 1000 W/m$^2$ is imposed at the cylinder wall with a no-slip boundary condition for the velocity of the air.

- **Pressure boundary -** The pressure boundary is assumed to be the entrainment boundary where the atmospheric air interacts with the inlet air. The total temperature at the boundary is assumed to be 300 K.

Table 1. Parametric boundary conditions at different locations

| **Parameter** | Bounadry names | | | |
|---|---|---|---|---|
| | **Nozzle Inlet** | **Nozzle Wall** | **Heated Cylinder** | **Entrainment** |
| U | FixedValue | FixedValue uniform (0 0 0) | FixedValue uniform (0 0 0) | PressureInletOutlet Velocity uniform (0 0 0) |
| T | FixedValue 300 K | Adiabatic | HeatFlux 1000 W/m$^2$ | Total Temperature 300 K |
| k | FixedValue | kqRWallFunction | kqRWallFunction | ZeroGradient |
| Ɛ | FixedValue | epsilonWallFunction | epsilonWallFunction | ZeroGradient |
| f | ZeroGradient | *f*WallFunction | fWallFunction | ZeroGradient |
| $v^2$ | FixedValue | $v^2$WallFunction | $v^2$WallFunction | ZeroGradient |
| p_rgh | ZeroGradient | ZeroGradient | zeroGradient | Total Pressure uniform 0 |

### 3.2 Grid independence test

A grid independence study is carried out with the four different grid sizes having 5548, 8265, 12889 and 20578 quadrilateral cells. The grid test is carried out with the $v^2f$ turbulence model for H/S = 8, $Re_D$ = 4500 and S/D = 4 as shown in Fig. 2.. All the grids near the walls are made in such a way that y+ value remains below unity. The grid having the least number of quadrilateral cells is selected for the further analysis.

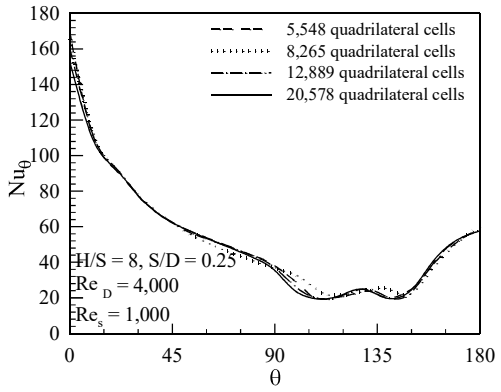


Figure 2 Grid independence study with different number of quadrilateral cells.

## 4. Results and Discussion

Numerical simulations are carried out to understand the fluid flow and heat transfer characteristics for air slot jet impingement heat transfer on cylinder. The local distribution of non-dimensional pressure coefficient and Nusselt number are reported.

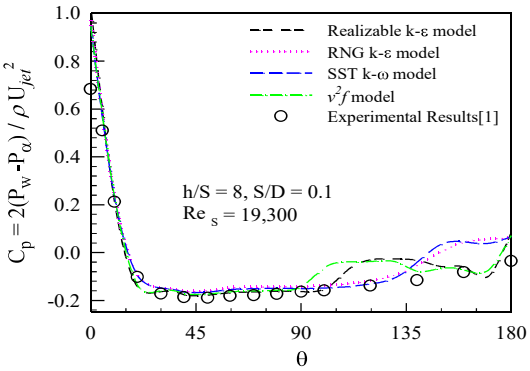


Figure.3 Comparison of numerical non-dimensional pressure coefficient results with the experimental results [1]

Figure 3 shows the non-dimensional pressure distribution around the circumferential direction of the cylinder. The non-dimensional pressure is maximum at stagnation point. After it decreases upto around $40^0$ from the stagnation point. It remains unaltered upto around $125^0$and then after a slight increase in pressure is observed experimentally.The same trend is observed by RNG k-Ɛ and SST k-ω turbulence model. This shows that the RNG k-Ɛ and SST k-ω model predict the fluid flow characteristics well as compared to other models.

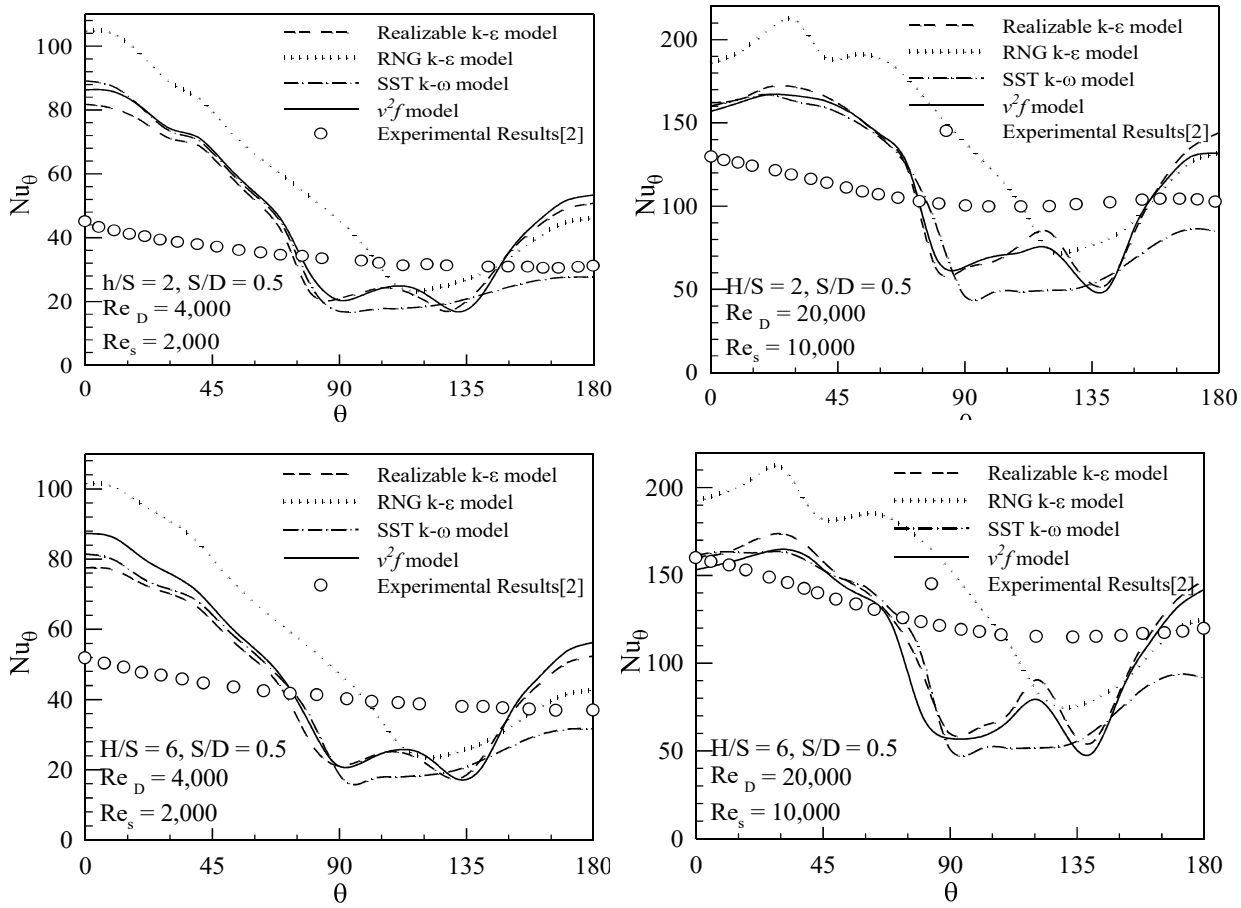


Figure.4 Comparison of numerical local Nusselt number results with the experimental results [2]

Figure 4 shows the local distribution of Nusselt number for H/S = 2 and 6, S/D = 0.5 and $Re_D$ = 4,000 and 20,000. The experimental results show that the value of the nusselt number is maximum at the stagnation point.It observed that from numerical resuts, all turbulance models trend similar from at stangation piont 0° to 180° except RNG k-ε turbulance model. It also found that the RNG k-Ɛ model capatre the secondary peak at around 40°.

## 5. Conclusion

The following conclusions are drawn from the numerical analysis

1. For the fluid flow characteristics of the slot jet impingement heat transfer, RNG k-Ɛ and SST k-ω turbulance models are better as compared to other models.
2. For the heat transfer characteristics, no turbulence models predict at stagnation region Nusselt number well
3. The RNG k-Ɛ model predicts the secondary peak on circumferential at $\theta = 40^o$

## 6. References

[1]Brahma et al., Experimental investigation of mean flow characteristics of slot jet impingement on a cylinder, Springer-Verlag, Vol. 26, (1991), 257-263
[2]F.Gori & L.Bossi, on the cooling effect of an air jet along the surface of a cylinder, Int. Comm. Heat Mass Transfer, Vol. 27, No. 5 (2000), pp. 667~76
[3]F.Gori & L.Bossi, Optimal slot height in the jet cooling of a circular cylinder, Applied Thermal Engineering 23 (2003) 859–870
[4]Sharad Pachpute & B.Premachandran, Experimental and numerical investigations of slot jet impingement with and without a semi-circular bottom confinement, International Journal of Heat and Mass Transfer 114 (2017) 866–890
[5]Sharad Pachpute & B.Premachandran, Slot air jet impingement cooling over a heated circular cylinder with and without a flow confinement, Applied thermal engineering 132 (2018) 352-367
[6] S.A.Nada, Slot/slots air jet impinging cooling of a cylinder for different jets–cylinder configurations, Heat Mass Transfer (2006) 43: 135–148
[7]F.Gori & I.Petracci, On the effect of the slot height in the cooling of a circular cylinder with a rectangular jet, International Communications in Heat and Mass Transfer 48 (2013) 8–14
[8]N.Chauchat & E.Schall, Cooling of a heating cylinder by confined impacting air jets, International Journal of Numerical Methods for Heat & Fluid Flow, Vol. 26, No. 7, 2016
[9]Neil Zuckerman & Noam Lior, Radial Slot Jet Impingement Flow and Heat Transfer on a Cylindrical Target, journal of thermo physics and heat transfer, Vol. 21, No. 3, July–September 2007
[10] E.E.M. Olsson et al., Heat transfer from a slot air jet impinging on a circular cylinder, Journal of Food Engineering 63 (2004) 393–401
[11] N. NITIN et al., conjugate heat transfer associated with a turbulent hot air jet impinging on a cylindrical object, Journal of Food Process Engineering 29 (2006) 386–399
[12] C.Gau & C.M.Chung, Surface Curvature Effect on Slot Air-Jet Impingement Cooling Flow and Heat Transfer Process, JOURNAL OF HEAT TRANSFER, ASME (1991)
[13] T.L.Chan et al., Heat Transfer Characteristics of a Slot Jet Impinging on a Semi Circular Convex Surface, International Journal of Heat and Mass Transfer 45 (2002) 993-1006
[14] Zeyi Jiang et al., Numerical Simulation of Flow and Heat Transfer from Slot Jets Impinging on a Cylindrical Convex Surface, Journal of Thermal Science Vol.20, No.5 (2011) 460-466
[15] Dae Hee Lee et al., Heat Transfer with Fully Developed Slot Jets Impinging on Confined Concave and Convex Surfaces, International Journal of Heat and Mass Transfer 88 (2015) 218-223
[16]S.K.Singh & R.Paul Singh, Air impingement cooling of cylindrical objects using slot jets, springer food engineering 89-104

**Nomenclature**

D – Based on the diameter of the cylinder
k – Turbulent kinetic energy ( $m^2/s^2$ )
$v^2$ – Velocity fluctuations normal to the streamlines ( $m^2/s^2$ )
f – Elliptic relaxation function (1/s)
H – Distance between the nozzle exit and the cylinder (m)
S – Slot width of the jet (m)
D – Diameter of the cylinder (m)
Re – Reynolds number, dimensionless
V – Magnitude of the velocity of the air (m/s)
Nu – Nusselt number, dimensionless
q'' – Heat flux (W/ $m^2$ )
$T_W$ – Cylinder wall temperature (K)
$T_{jet}$ – Jet temperature or nozzle exit temperature (K)
$k_f$ – Thermal conductivity of the air (W/mK)
L– Length of the confinement (m)

**Greek**

ε – Turbulent dissipation rate ( $m^2/s^3$ )
ω – Turbulence specific dissipation rate (1/s)
μ - Dynamic Viscosity of the air (kg/ms)
ρ – Density of the air (kg/ $m^3$ )

# NOVEL APPROACH FOR PREDICTING THE PERFORMANCE OF THE EVACUATED U – TUBE SOLAR COLLECTOR INTEGRATED WITH PARABOLIC REFLECTOR

**B. Kiran Naik, P. Muthukumar***
Department of Mechanical Engineering, IIT Guwahati, Assam – 781039, India.
*Email: pmkumar@iitg.ernet.in ; pmkumariitg@gmail.com

ABSTRACT

In this paper, the experimental and numerical analyses on evacuated U – tube solar collector integrated with parabolic reflector are presented. Experimental facilities for testing the thermal performance of the evacuated U – tube solar collector integrated with parabolic reflector has been fabricated. A novel three dimensional numerical model on a U – tube solar collector is developed using finite element based CFD package – COMSOL Multiphysics 5.0. The numerical results obtained from the developed model are compared with the experimental data and a good agreement is found between them. Thermal efficiency of the solar collector is estimated at various solar intensities and working fluid temperatures. It is observed that the collector efficiency increases with increase in solar intensity and decrease in working fluid temperature. Further, the rise in working fluid temperature and variation in pressure drop along the U – tube are predicted numerically.

**Key Words:** *Evacuated U – tube solar collector; Parabolic reflector; Thermal modeling; Solar collector efficiency.*

## 1. INTRODUCTION

The evacuated U – tube solar collector is a crucial component for effective utilization of solar thermal energy [1]. Nowadays, this type of collector is being used in several practical applications due to their higher operating temperatures and lower investment cost. It is basically a heat exchanger which transfers the solar radiation from the Sun to the working fluid. The solar radiation incident on the outer glass surface of the evacuated tube is transferred to the inner glass through radiative heat transfer and then it is absorbed by the U – tube due to conduction (Fig. 1(a) – (b)). Finally, the energy collected by the U – tube is exchanged to the working fluid by means of convective heat transfer. The experimental setup fabricated at IIT Guwahati shown in Fig. 1(a) – (b), additionally consists of parabolic reflector along with evacuated U – tube solar collector. This reflector reflects the solar radiation to the evacuated tube received from the Sun, which provides additional heat to the solar collector and also, improves the collector performance.

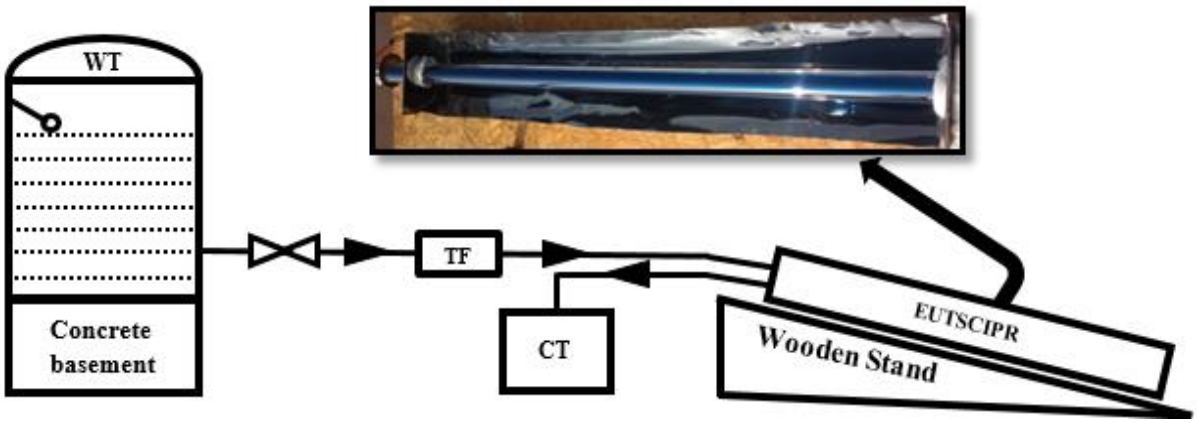


(a) schematic view

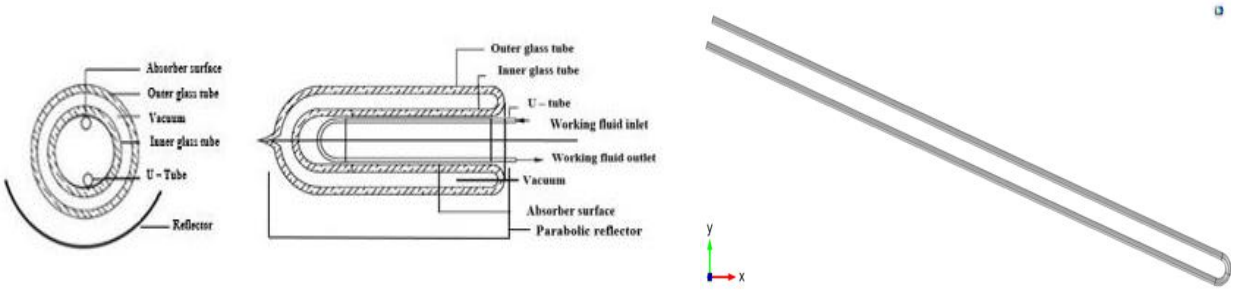


(b) cross sectional view (c) U – tube solar collector model

FIGURE 1. Evacuated U – tube solar collector integrated with parabolic reflector.

Very few experimental studies have been carried out for analysing the performance of the evacuated tube solar collector integrated with parabolic reflector and there is no profound numerical and experimental analyses on evacuated U – tube solar collector integrated with parabolic reflector reported in the literature [2]. Therefore, this paper focuses on developing a novel numerical model for analysing the heat transfer characteristics of the evacuated U – tube solar collector and the numerically predicted thermal efficiency and pressure drop of the solar collector are compared with the experimental data.

## 2. EXPERIMENTAL APPARATUS AND TEST PROCEDURE

The schematic and cross-sectional views of the experimental setup and evacuated U – tube solar collector integrated with parabolic reflector (*EUTSCIPR*) are shown in Fig. 1(a) & 1(b). The main components of this setup are evacuated tube, copper U – tube, parabolic reflector, data acquisition system, pyranometer and turbine type flow meter (TF). The cold water is passed into the U – tube through a control valve from the cold water storage tank situated at an elevated height of 1.3 m from the ground level using a flexible plastic pipe (Fig.1 (a)). The control value is used for regulating the flow rate. In order to monitor the flow rate, the turbine type flow meter (TF) (accuracy ±3%) is fitted just after the control value. The capacity of the storage tank is about 500 lit and the water level in the storage tank is maintained constant using a float ball valve. A mercury in glass thermometer (accuracy ±0.5 $^{o}$C) is placed at the top of the storage tank to measure the cold water temperature.

TABLE 1. Dimensions, surface properties and operating parameters chosen for experimental and numerical analysis of the evacuated U – tube solar collector integrated with parabolic reflector.

| TABLE 1(a). Dimensions | |
|---|---|
| Outer glass tube outer diameter (cm) | 5.8 |
| Outer glass tube thickness (cm) | 0.2 |
| Inner glass tube outer diameter (cm) | 4.7 |
| Inner glass tube thickness (cm) | 0.2 |
| Air gap (cm) | 0.1 |
| U – tube outer diameter (cm) | 0.1 |
| U – tube inner diameter (cm) | 0.95 |
| Collector tube length (m) | 1.8 |
| Parabolic reflector length (m) | 1.6 |
| Focal point (cm) | 3.8 |

| TABLE 1(b). Thermo – physical properties | |
|---|---|
| Glass tube transmittance | 0.9 |
| Absorptivity of coating material | 0.9 |
| Reflectivity of parabolic reflector | 0.9 |
| Water density (g/cm$^3$) | 1 |
| Cp of water (kJ/kg – K) | 4.2 |
| Copper conductivity (W/m – K) | 307 |
| TABLE 1(c). Operating range | |
| Ambient temperature ($^{o}$C) | 26 – 34 |
| Solar intensity (kW/m$^2$) | 0.52 – 1.08 |
| Water inlet temperature ($^{o}$C) | 23 – 38 |
| Water flow rate (g/s) | 6 – 24 |
| Reynolds number (Re) | 792 – 3700 |

The heat gained by the evacuated tube due to the reflection of solar radiation from the parabolic reflector and the direct emission of solar radiation from the Sun, is transferred to the cold water entering into the solar collector through copper U – tube (surface to surface heat exchange). Thus, the hot water coming out of the solar collector is collected in a hot water collection tank (CT). A pyranometer is placed adjacent to the evacuated U – tube solar collector integrated with the parabolic reflector for measuring the solar radiation incident on the evacuated tube outer glass surface. K – Type thermocouples (accuracy ± 0.5 $^{o}$C) are placed at the exit of the copper U – tube and to the open atmosphere for measuring the hot water and the ambient temperatures respectively. Data acquisition system is used for acquiring the outputs of thermocouples and pyranometer. The wooden support is used for maintaining

the inclination angle. The solar collector inclination angle is chosen based on maximum solar radiation that can be incident on the U – tube solar collector and according to Guwahati climatic solar irradiance data, this angle has been fixed at 150° along the negative X – direction from the origin [3]. Stainless steel sheet is used for designing the parabolic reflector and the parabolic shape is fabricated by calculating the focal point. The dimensions, the thermo – physical properties and the operating conditions of the evacuated U – tube solar collector integrated with parabolic reflector are listed in Table 1. The uncertainties involved in the estimation of dependent parameters such as pressure drop, useful heat gain and thermal efficiency are calculated using Kline and McClintock method [4] and they are estimated as ± 3%, ± 2% and ± 3%, respectively.

## 3. NUMERICAL MODELLING

To develop a numerical model, COMSOL Multiphysics 5.0 is chosen. Fig. 1(c) shows the cross – sectional view of the three dimensional U – tube solar collector model containing working fluid inside the U – tube. Copper and water are used as the U – tube material and the working fluid, respectively. Following assumptions are considered for solving the developed model numerically,

- Working fluid is incompressible and Newtonian.
- Buoyancy effect is quantified using the Boussinesq approximation.
- Fluid flow is stationary along the U – tube.
- In between the evacuated tube and the U – tube, heat transferred by the process air is negligible.

### *3.1 Governing equations*

Continuity equation: $\nabla\vec{V} = 0$ (1)

Momentum equation: $\left(\vec{V}.\nabla\right)\vec{V} = \nu\nabla^2\vec{V} - \frac{1}{\rho}\nabla P - g\beta\Delta T$ (2)

Energy equation: $\rho C_p\left(\vec{V}.\nabla T\right) = k\nabla^2 T$ (3)

where ρ, V, $C_p$ and β are the density (kg/m$^3$), velocity, specific heat (kJ/kg – K) and volumetric thermal expansion coefficient (1/K) of the working fluid.

### *3.2 Boundary conditions*

- The mass flow rate of the working fluid (ṁ) and the atmospheric pressure (P = $P_{atm}$ =1.013 kPa) are imposed as the boundary conditions for the entrance and exit of the U – tube respectively.
- Constant heat flux ($\phi_q$) along the upper surface of the U – tube i.e. $\phi_q = \tau_{g,o}\tau_{g,i}\alpha_c I(1+\rho_r)$, where $\phi_q$ is the heat absorbed from the evacuated tube (W/m$^2$), I is the solar intensity (W/m$^2$), $\tau_{g,o}$ and $\tau_{g,i}$ are the transmissivity of the inner and outer glass surface respectively, I is the solar intensity, $\alpha_c$ is the absorptivity of the coating material and $\rho_r$ is the reflectivity of the parabolic reflector.

### *3.3 Mesh generation and Grid independence test*

The domains and boundaries of the U – tube are meshed using free unstructured tetragonal and triangular meshes. These type of meshes are chosen to ensure the discretization of relatively smaller sections of the U – tube i.e. the entrance and the exit of the U – tube. Finer mesh sizes are applied at working fluid inlet/outlets and working fluid boundary layer and 'U' bend. Grid independence test is performed for the developed model and found that the total grid elements of about 4, 68,437 are suitable for the present model.

### *3.4 Performance parameters*

(a) Experimental pressure drop: $\Delta P = \frac{f L_u \rho V^2}{2 D_u}$ (Darcy–Weisbach Eq.); (4)

Friction factor, f = $\frac{64}{\mathrm{Re}}$ for Re < 2300 & $f = 0.079\,\mathrm{Re}^{-0.25}$ for 2300 < Re < $10^5$ (Blasius Eq.)

(b) Collector thermal efficiency: $\eta_c = \frac{\dot{m} C_p (T_{w,o} - T_{w,i})}{2\phi_q \pi D_a L_a}$ (5)

where $T_{w,o}$/$T_{w,i}$ and ṁ are the working fluid inlet/outlet temperatures (°C) and flow rate (kg/s), $D_u$ and $L_u$ are the U – tube diameter (m) and length (m) ($L_t = L_{eq}$ : equivalent length along the 'U' bend + $L_a$ :U – tube length along the absorber tube) and $D_a$ and $L_a$ are the absorber tube diameter (m) and length (m), respectively.

## 4. RESULTS AND DISCUSSIONS

The variation of solar collector thermal efficiency with the normalized heat loss ($(T_m - T_a)/I$) and the effect of mass flow rate on the pressure drop are presented in Fig. 2(a) & 2(b). It is observed that the numerical predictions are match well with the experimental data and the maximum deviation between them is $\pm$5.8%. From Fig. 2(a), it is also observed that with increase in normalized heat gain, the collector thermal efficiency decreases. This indicates that, the thermal losses across the U – tube solar collector increases with increase in working fluid temperature. From Fig. 2(b), it is also found that with increase in working fluid flow rate, the pressure drop along the U – tube increases. This happens because as the flow rate increases, frictional losses due to increase in fluid viscosity and velocity and dynamic losses due to change in flow direction along the 'U' bend increases. As a consequence, the pressure drop along the U – tube increases.

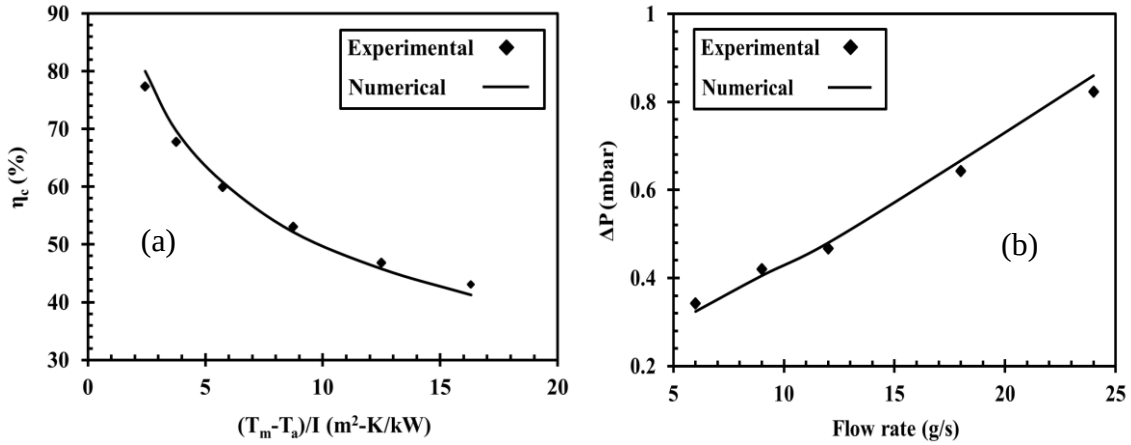


FIGURE 2. Performance analysis of the fabricated solar collector.

## 5. CONCLUSIONS

A novel numerical model for evacuated U – tube solar collector integrated with parabolic reflector has been developed. The numerical results obtained from the developed model were compared with the experimental data of the designed setup and observed good agreement between them with a maximum deviation of $\pm$ 5.8%. The performance of the solar collector has been predicted numerically and also compared with experimental values. From these analysis, following key points are observed.

- During peak and non – peak solar intensities i.e. at I = 1080 W/m$^2$ and I = 520 W/m$^2$, the maximum and minimum collector thermal efficiencies were observed as 77% and 43%, respectively.
- The collector thermal efficiency increases by 44%, with decrease in normalized heat loss from 16.3 (m$^2$ – K/kW) to 2.5 (m$^2$ – K/kW).
- For the given operating conditions, with increase in working fluid flow rate from 6 kg/s to 24 kg/s, increases the pressure drop by 58%.

Present study simplifies the approach for analysing the heat transfer fluid flow variations along the U – tube and the thermal performance of the evacuated U – tube solar collector integrated with parabolic reflector.

## 6. REFERENCES

[1] V. Dabra and A. Yadav, Parametric study of a concentric coaxial glass tube solar air collector: a theoretical approach, *Heat and Mass Transfer*, 1 – 13, 2017.

[2] B. Kiran Naik, A. Varshney, P. Muthukumar and C. Somayaji (2016) Modelling and performance analysis of U – type evacuated tube solar collector using different working fluids, *Energy Procedia*, 90, 227–237, 2016.

[3] M. Boxwell, *Solar electricity handbook: A simple, practical guide to solar energy – designing and installing solar photovoltaic systems*, 3rd Edition, 2017.

[4] S.J. Kline and F.C. Mc – Clintock, Describing uncertainties in single – sample experiments, *Journal of Mechanical Engineering*, 3 – 12, 1953.

# Study of Atomic Interactions in the Oxidation of Silicon Carbide using Molecular Dynamics Simulations

**Punit Kumar Suman, Kishore Kumar Kammara, Srujan Kumar Naspoori, Rakesh Kumar**
Indian Institute of Technology Kanpur, Department of Aerospace Engineering, IIT Kanpur, Kanpur-208016, punits@iitk.ac.in, kkkumar@iitk.ac.in, srujann@iitk.ac.in, rkm@iitk.ac.in

## ABSTRACT

Molecular dynamics simulations are carried out on oxidation of SiC to study chemical interactions between constituent atoms. Simulation of the oxidation process is performed using ReaxFF based molecular dynamics method. A system of SiC slab and oxygen molecules are created in LAMMPS software which uses ReaxFF potential to model the breaking and formation of bonds. The simulation is carried out in three stages, increasing the temperature of the system from 100 K - 3000 K. A post-processing code is developed to calculate the number of bonds formed between each pair of atoms at each time step during the entire simulation. This code also calculates the total number of various types of bonds that are being formed and the rate of change of forming/breaking of various bonds during the simulation.

**Key Words:** Oxidation, Molecular Dynamics, ReaxFF, LAMMPS

## 1. INTRODUCTION

During re-entry of space vehicles in the earth's atmosphere, very high temperature and pressure is generated at the surface of the vehicle. To withstand such extreme conditions, a thermal coating is coated on the shuttle which will act as Thermal Protection System (TPS). Materials used for TPS have to withstand a very high temperature. A more fundamental understanding of the behavior of these materials when exposed to very high temperatures and pressures, especially the degradation pattern, is required in order to develop a more efficient thermal protection system. One of the most widely used materials used in TPS design is Silicon Carbide (SiC). During the oxidation of SiC, oxide of silica is formed. SiC can go through the process of either passive oxidation or active oxidation [1].

In passive oxidation, the partial pressure of the oxidizing agent is high and a protective layer of oxide of silica is formed which prevents further oxidation. Whereas, in active oxidation, the partial pressure of oxidizing agent is low and no protective layer of oxide of silica is formed. Instead, SiO is formed which is in a gaseous state.

For active oxidation, oxidation reaction occurs in the following form as shown in equation 1

$$SiC(s) + O_2(g) \rightarrow SiO(g) + CO(g) \qquad \ldots \text{Equation 1}$$

While for passive oxidation, the following equation 3 is the way the constituents react.

$$SiC(s) + 3/2O_2(g) \rightarrow SiO_2(s) + CO(g) \qquad \ldots \text{Equation 2}$$

The passive-to-active transition occurs when $SiO_2$ begins to react with the SiC substrate in the following way,

$$SiC(s) + 2SiO_2(s) \rightarrow 3SiO(g) + CO(g) \quad \text{… Equation 3}$$

$$SiC(s) + SiO_2(s) \rightarrow 2SiO(g) + C(s) \quad \text{… Equation 4}$$

With initial temperature, pressure and number of atoms set, the reactions occur naturally with time. Performing reactive dynamics simulations is perhaps a better way to study a chemically reacting system. This reacting system can be studied most accurately via Molecular Dynamics (MD) methods.

In MD method, the atoms and molecules are allowed to interact, giving a dynamic view of the evolution of the system. The trajectories of atoms and molecules are determined by numerically solving Newton's equations of motion for a system of interacting particles, where forces between the particles and their potential energies are calculated using interatomic potentials. A sophisticated bond-order based force field, ReaxFF[2] is used, which is capable of handling bond-breaking and bond-making. ReaxFF favors working with bond-order over bonds themselves. The ReaxFF method is unique among reactive force field approaches in that it obtains better accuracy for both reaction energies and reaction barriers.

In this project, we carry out the oxidation of SiC using ReaxFF MD simulations at 3000 K temperature. The type of bonds being formed at each timestep is then calculated to understand the various reactions in the initial stages at the high temperature oxidation. This data can further be utilized to outline the rate constants and rate equations.

## 2. SIMULATION DETAILS

ReaxFF potential used in the simulation here was developed at Pennsylvania State University for studying the oxidation of SiC[3]. The simulation was carried out using LAMPPS program. LAMMPS includes the ReaxFF potentials for soft and solid-state materials and coarse-grain systems.

### 2.1. STRUCTURAL SETUP

A periodic domain of cell-size (15x12x50) Å was defined in which the atoms were created. For creating SiC structure we used repeating lattice of SiC with a lattice constant of 4.35 Å. In the space above and below the slab of SiC, oxygen molecules were created as shown in Figure 1 (a).

### 2.2 SIMULATION SETUP

Simulation was done in Canonical ensemble (NVT). A timestep of $2.5 \times 10^{-4}$ ps was used.

The simulation was carried out in three stages:

(a) The atoms were created and the system was maintained at 100 K. (Timesteps: 100000)
(b) The temperature was increased linearly from 100 K to 3000 K. (Timesteps: 1000000)
(c) The system was maintained at 3000 K (Timesteps: 5000000)

The temperature of system is maintained constant using Nosé-Hoover thermostat[4].

### 2.3 PROCESSING DATA

The data which we obtained from the simulation had information about each atoms regarding their coordinates at each timestep, the neighbor list, and their bond order with each neighboring atoms. A code was written in C language to process this data. This code considers atoms' neighbor list and

coordinates as input and calculate the bond-length of each of the atoms with its neighboring atoms at each time step. This calculated bond-length was then compared with the theoretical bond-lengths for the pair of atoms to identify whether the pair is forming a bond or not.

## 3. RESULTS

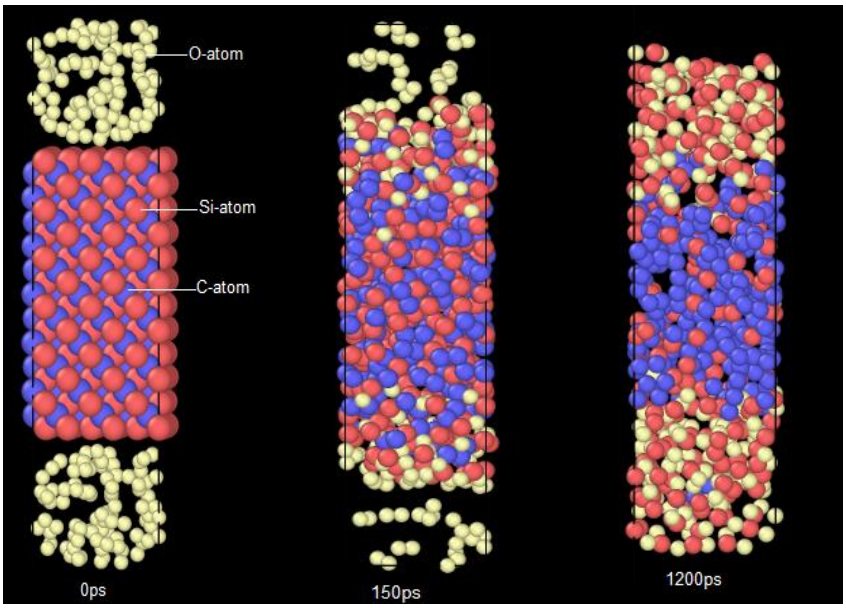


(a) (b) (c)

Figure 1. Structures from ReaxFF MD simulations at three different stages.

Figure 1 shows the snapshots of simulation at three different time instants. In Figure 1, leftmost image (a) corresponds to the initial timestep; middle snapshot (b), shows the intermediate timestep where we observe that the oxygen molecules are moving into the SiC to form various bonds, and the last image (c), shows that the entire SiC structure is disturbed and different molecules like SiO, C-C, etc., are formed.

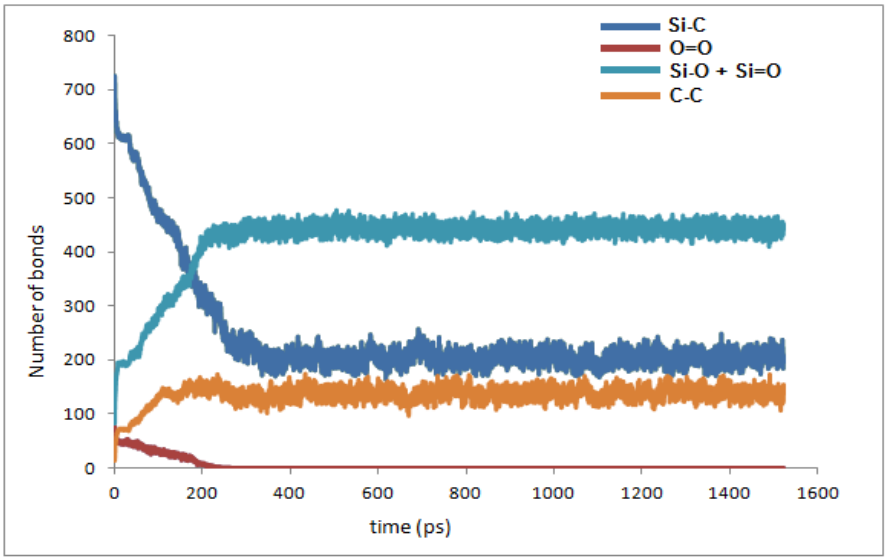


Figure 2. Formation and breaking of bonds for all three stages.

Using the post-processing code, we now calculated the number of bonds that are formed during the simulation. Figure 2, shows the forming and breaking of the different bonds. The reaction started in the first stage and it continued till the last stage until the system has reached equilibrium. This is evident from the dissociation of Si-C bonds and $O_2$ molecule at very early timesteps and the increase in interaction between silicon and oxygen as well. In the first 200 ps itself silicon oxide is formed and the system reaches equilibrium. The temperature at that instant was around 2500 K.

A more important observation was made regarding the Carbon atoms. From the stoichiometric oxidation of silicon carbide, carbon monoxide was expected to be formed. But, we can see in Figure 2 that there is a negligible interaction between carbon and oxygen atoms. Melting point of silicon is around 1500 K, whereas melting point of carbon is around 3500 K. As the temperature of the system is increased, SiC undergoes a slow phase-separation resulting in formation of amorphous silica slab and a separated carbon structure. This shows that silica started to show melting behavior. The formation of solid carbon chunk is also evident from the increased number of C-C single bonds in Figure 3 which also equilibrated at around 200 ps. Upon further analysis of the system it was observed that although there was no significant change in the formation of new bonds, but, there was a clear phase separation, showing the separation of carbon from silicon oxide at 3000 K.

Simulations by varying temperature are being carried out and will be updated during the presentation. This variation would help us understand the formation of various products that can be formed. To improve fuel characteristics, simulations consisting of water molecules during oxidation are required and these simulations will also be considered.

## 4. CONCLUSION

In this work, bond-formation and bond-breaking trends for different pairs of atoms during oxidation of SiC at 3000 K temperature is presented. The simulation was carried out using the ReaxFF based molecular dynamics simulations. A solid slab of SiC was created to interact with gaseous oxygen molecules. From the results, we conclude that along with the formation of silicon oxides, a chunk of carbon is also being formed. From stoichiometric equation we know that silicon carbide when reacts with oxygen gives silicon oxide and carbon monoxide. But, in our analysis, there is no trace of interaction of carbon with oxygen atoms even when the system attains equilibrium. So, we can conclude that all the oxygen atoms are interacting with silicon and the number of oxygen atoms used in the simulations are less than required to interact with carbon atoms. Further more insight into the dynamics of reactions will be provided after completion of ongoing simulations.
The above reaction happening can be summed up as,

$$SiC(s) + O_2 \rightarrow SiO_x + C(s) \quad ; \text{where } x = 1, 2.$$

## REFERENCES

1. Harder, B., Jacobson, N., Myers, D. “Oxidation Transitions for SiC Part II. Passive-to-Active Transitions”. Journal of the American Ceramic Society, 2013, 96 (2), pp 331-664. doi:10.1111/jace.12104
2. Van Duin, A.C.T., Dasgupta, S., Lorant, F., Goddard, W.A. “ReaxFF: A Reactive Force Field for Hydrocarbons”. Journal of Phys. Chem. A., 2001, 105 (41), pp 9396–9409. doi:10.1021/jp004368u

3. Newsome, D.A., Sengupta, D., Foroutan, H., Russo, M.F., van Duin, A.C.T. “Oxidation of Silicon Carbide by $O_2$ and $H_2O$: A ReaxFF Reactive molecular Dynamics Study, Part I. J. Phys. Chem. C., 2012, 116 (30), pp 16111–16121. doi:10.1021/jp306391p
4. Nosé, S. "A unified formulation of the constant temperature molecular-dynamics methods". Journal of Chemical Physics, 1984, 81 (1): pp 511–519. doi:10.1063/1.447334

# Numerical study of entropy generation in a doubly stratified fluid saturated Darcy porous enclosure in the presence of Soret and Dufour effects under the influence of MHD forces

**Vinay Kumar [1], S. V. S. S. N. V. G. Krishna Murthy [2,*]**

Department of Applied Mathematics, Defence Institute of Advanced Technology,
Deemed to be University, Pune - 411025, India,
[1]Email:vkmchoudhary@gmail.com, [2,*]Email: sgkmurthy@gmail.com, skmurthy@diat.ac.in

**B. V. Rathish Kumar [3]**

Department of Mathematics and Statistics, Indian Institute of Technology, Kanpur -208016, India, Email: bvrk@iitk.ac.in

## ABSTRACT

In this present investigation, entropy generation for combined free convective heat and mass transfer in doubly stratified fluid saturated square porous cavity under the multiple interacting force is reported. The left wall of the cavity is maintained at uniform temperature and concentration and right wall is assumed at stratified temperature and concentrations whereas the top and bottom walls are kept adiabatic. A viscous dissipation mathematical model is developed for the thermal and mass stratified fluid flow in porous media and implemented to the application of the entropy generation concept to optimize the free convective heat and mass transport. Further, the non-linear partial differential equations governing the study are solved numerically by using Galerkin Finite Element Method (FEM). Obtained results are compared with those from literature and are found to be in good agreement. In order to evince the characteristics and inherent structures of irreversibility in fluid flow, the obtained numerical results are demonstrated graphically by plotting the entropy generation due to velocity fields, heat transfer, mass transfer and total entropy generation plots for various values of parameters involved in the problem like: Magnetic parameter ($M_g$), Thermal ($S_T$) and Mass ($S_C$) stratification, Buoyancy ratio ($B$), Rayleigh number ($Ra$), Lewis number ($Le$), Soret ($S_r$) and Dufour ($D_f$) numbers.

Key Words: *Free convection, Porous medium, MHD, Stratification, Entropy, Finite Element Method.*

## 1. INTRODUCTION

In many of the engineering applications such as metallurgical, chemical and nuclear process, crystal growth, MRI of mass transport process, NMR to petroleum exploration and production, nuclear waste management, microwave heating, nuclear magnetic resonance imaging, reactive polymer flows in heterogeneous porous media, electrochemical generation of elemental bromine in porous electrode systems, electronic cooling, a detailed study of the MHD free convective heat and mass transfer in fluid-saturated porous media is required [2, 3, 4, 5]. In this proposed work, the numerical study of free convective heat and mass transfer process in doubly stratified fluid saturated porous enclosure with considering the Soret and Dufour effects under the influence of magnetic forces is projected. Detailed numerical simulations are carried out by using Galerkin Finite Element Method for a wide range of parameters such as Magnetic parameter ($M_g$), Thermal ($S_T$) and Mass ($S_C$) stratification, Buoyancy ratio ($B$), Rayleigh number ($Ra$), Lewis number ($Le$), Soret ($S_r$) and Dufour ($D_f$) numbers. In order to enhance the visualization of heat and mass transport, heatline and massline plots are depicted in addition to tracing streamlines, isotherms and iso-concentrations curves.

So far, there has not been reported much work on free convective heat and mass transfer process in thermal and mass stratified fluid saturated porous enclosure by considering viscous dissipation. Particularly, entropy generation in the free convective heat and mass transfer within the porous enclosure under the interaction of MHD forces and thermal/mass stratification forces, which becomes very relevant in the context of designing the

prototype of thermal devices, packed bed thermal energy storage systems [6], urban ponds [7], solar hot water storage tanks [8], environmental chamber for bacterial culture preservation etc., have not been considered so far.

## 2. MAIN BODY

In the present investigation, a study of entropy generation in free convective heat and mass transfer process within the doubly stratified fluid saturated square porous cavity of length ($\ell$) is carried out. As per the physical model, a uniform magnetic field of strength $m_d$ is imposed in the horizontal direction normal to the plane i.e. in the Y-direction. Here, the bottom edge of the left vertical wall is considered at the origin of the coordinate system and the X-axis is measured along it. The left vertical wall of the cavity is maintained at the uniform temperature ($t_w$) and concentration ($c_w$) of some constituent of fluid and it is higher than the ambient temperature and concentration respectively. Moreover, the bottom and top wall of the cavity are kept adiabatic. Whereas, the right wall of the cavity considered at the ambient stratified temperature ($t_{\infty,x}$) and concentration ($c_{\infty,x}$). The porous medium is considered homogeneous and isotropic. The fluid and the square porous matrix within the cavity are maintained everywhere in local thermal equilibrium and Boussinesq approximation is valid. Under the action of above-mentioned assumptions, the non-dimensional form of the equations governing the flow, heat and mass transport in a fluid-saturated porous media can be written as follows:

$$\frac{\partial^2\Psi}{\partial X^2}+\left(1+M_g\right)\frac{\partial^2\Psi}{\partial Y^2}=Ra\left(\frac{\partial T}{\partial Y}+B\frac{\partial C}{\partial Y}\right)$$

$$\frac{\partial\Psi}{\partial Y}\frac{\partial T}{\partial X}+S_T\frac{\partial\Psi}{\partial Y}-\frac{\partial\Psi}{\partial X}\frac{\partial T}{\partial Y}=\left(\frac{\partial^2 T}{\partial X^2}+\frac{\partial^2 T}{\partial Y^2}\right)+D_f\left(\frac{\partial^2 C}{\partial X^2}+\frac{\partial^2 C}{\partial Y^2}\right)$$
$$+\frac{Ge}{Ra}\left(\left(\frac{\partial\Psi}{\partial X}\right)^2+\left(\frac{\partial\Psi}{\partial Y}\right)^2\right)+\frac{Ge\cdot M_g}{Ra}\left(\frac{\partial\Psi}{\partial Y}\right)^2$$

$$\frac{\partial\Psi}{\partial Y}\frac{\partial C}{\partial X}+S_C\frac{\partial\Psi}{\partial Y}-\frac{\partial\Psi}{\partial X}\frac{\partial C}{\partial Y}=\frac{1}{Le}\left(\frac{\partial^2 C}{\partial X^2}+\frac{\partial^2 C}{\partial Y^2}\right)+S_r\left(\frac{\partial^2 T}{\partial X^2}+\frac{\partial^2 T}{\partial Y^2}\right)$$

The associated boundary conditions in non-dimensional form are established as:

$$\Psi=0, T=1-S_T X, C=1-S_C X \quad \text{on } Y=0, \quad 0\le X\le 1,$$

$$\frac{\partial\Psi}{\partial Y}=0, T=0, C=0 \qquad \text{on } Y=1, \quad 0\le X\le 1,$$

$$\Psi=0, \frac{\partial T}{\partial X}=0, \frac{\partial C}{\partial X}=0 \qquad \text{at } X=0,\ X=1, \quad 0\le Y\le 1.$$

## 3. ENTROPY GENERATION

The overall entropy generation due the combined heat and mass transfer in a porous cavity is calculated by the addition of entropy due to viscous dissipation ($E_{\psi,i}$), entropy generation due heat transfer ($E_{T,i}$) and entropy generation due to coupled heat and mass transfer ($E_{C,i}$).

$$E_{\psi,i}=N_\mu\left\{\left(\frac{\partial\Psi}{\partial X}\right)^2+\left(\frac{\partial\Psi}{\partial Y}\right)^2\right\}+N_\mu\left\{M_g\left(\frac{\partial\Psi}{\partial Y}\right)^2\right\}$$

$$E_{T,i}=\left\{\left(\frac{\partial T}{\partial X}+S_T\right)^2+\left(\frac{\partial T}{\partial Y}\right)^2\right\}$$

$$E_{C,i}=N_C\left\{\left(\frac{\partial C}{\partial X}+S_C\right)^2+\left(\frac{\partial C}{\partial Y}\right)^2\right\}+N_{TC}\left\{\left(\frac{\partial T}{\partial X}+S_T\right)\left(\frac{\partial C}{\partial X}+S_C\right)+\left(\frac{\partial T}{\partial Y}\right)\left(\frac{\partial C}{\partial Y}\right)\right\}$$

$$E_{gen,i}=E_{\psi,i}+E_{T,i}+E_{C,i}$$

$$E_{\text{gen},i} = \left\{\left(\frac{\partial T}{\partial X} + S_T\right)^2 + \left(\frac{\partial T}{\partial Y}\right)^2\right\} + N_C\left\{\left(\frac{\partial C}{\partial X} + S_C\right)^2 + \left(\frac{\partial C}{\partial Y}\right)^2\right\}$$

$$+ N_{TC}\left\{\left(\frac{\partial T}{\partial X} + S_T\right)\left(\frac{\partial C}{\partial X} + S_T\right) + \left(\frac{\partial T}{\partial Y}\right)\left(\frac{\partial C}{\partial Y}\right)\right\} + N_\mu\left\{\left(\frac{\partial \Psi}{\partial X}\right)^2 + \left(\frac{\partial \Psi}{\partial Y}\right)^2 + M_g\left(\frac{\partial \Psi}{\partial Y}\right)^2\right\}$$

$$E_{Total} = \int_0^1\int_0^1 E_{\text{gen},i}\, dXdY$$

$$N_\mu = \frac{\mu\, t_{\infty,0}}{k}\left\{\frac{\alpha^2}{K\left(\Delta t\right)^2}\right\},\ N_C = \frac{RD\, t_{\infty,0}^2}{k\, c_{\infty,0}}\left(\frac{\Delta c}{\Delta t}\right)^2,\ N_{TC} = \frac{RD\, t_{\infty,0}}{k}\left(\frac{\Delta c}{\Delta t}\right);$$

## 4. RESULTS

The above non-dimensional of governing equations (1-3) with boundary conditions (4) have been solved using Galerkin Finite Element Method. At the very first instance, results are ensured independent of grid size. So that computations are done on various grid systems of 80 × 80, 90 × 90, 100 × 100, and 110 × 110. Where, it is observed that there is only a marginal variation of Nusselt number as one moves from 100 × 100 grid system to 110 × 110 grid system so that 100 × 100 is chosen for further simulations. Before executing the extensive numerical computations, the code has been validated by comparing the results with those available in the literature [1]. Detailed numerical simulations have been carried out for associated parameters to investigate the impact of coupled MHD forces and thermal/mass stratification of fluid on entropy generations in the heat and mass transfer process in a porous square enclosure.

In the Fig 1, total entropy generation curves have been plotted for Magnetic parameter ($M_g$), Thermal ($S_T$) and Mass ($S_C$) stratification, Buoyancy ratio ($B$) and Rayleigh number ($Ra$) while fixing other parameters. Where it is observed that for $M_g = 0$, entropy generation curves at the left bottom and right top corner of the cavity are alike parabola whereas at the core of domain entropy generation patterns are embedded ellipses having major axis in horizontal direction. As the $M_g$ is raised, these curves started stretching in the vertical direction with reducing the value of entropy. Where the reduction in maximum value of entropy ($E_{\max}$) is noted 57.88% by increasing the magnetic parameter from $M_g = 0$ to $M_g = 1$ and it reaches to 98.93% for $M_g = 50$. Moreover, while increasing the thermal ($S_T$) and mass ($S_C$) stratification, for the case '$0 \le S_T, S_C \le 1$', it decreases the maximum value of entropy generation but influence is vice-versa for '$1 \le S_T, S_C$'. On the other hand, increasing the buoyancy ratio ($B$) lead to enhance the magnitudes of '$E_{\max}$' and for the negative value of the buoyancy ratio ($B$), '$E_{\text{gen}}$' curves are found mirror images of '$E_{\text{gen}}$' patterns while ($B \ge 0$) at line '$X = 1$'. Additionally, for lower values of Rayleigh number ($Ra$), entropy generation curves look like set of two rectangular hyperbola families. While '$Ra$' is increased, such patterns turns into embedded ellipses (in the core of domain) having horizontal major axis for higher values of '$Ra$' and magnitudes of '$E_{\text{gen}}$' are elevated.

## 5. CONCLUSIONS

The aim of the present study is entropy generation analysis on natural convection in doubly stratified fluid saturated porous enclosure under multiple interacting forces. The mathematical model has been solved by using Galerkin Finite Element Method and simulations have been carried out for various parameters influencing the model. Present investigation shows that, the entropy generation reduces locally when rising the magnetic forces. Whereas increasing levels of thermal and mass stratification raise the entropy for '$0 \le S_T, S_C \le 1$' and it is reverse in case when '$1 \le S_T, S_C$'. Additionally, rising the Buoyancy ratio ($B$) and Rayleigh number ($Ra$) increased the entropy of the system. The maximum magnitudes of total entropy are found at the left bottom and right top portion of the cavity.

## REFERENCES

[1] A. C. Baytas,, "Entropy generation for natural convection in an inclined porous cavity," *International Journal of Heat and Mass Transfer*, vol. 43, no. 12, pp. 2089–2099, 2000.

[2] D. A. Nield and A. Bejan, *Convection in porous media*. Springer Science & Business Media, 2006.
[3] D. B. Ingham and I. Pop, *Transport Phenomena in Porous Media*, vol. 3. Elsevier, Oxford, UK, 2005.
[4] K. Vafai, *Handbook of porous media*. CRC Press, 3rd ed., 2015.
[5] V. Kumar, S. K. Murthy, and B. R. Kumar, "Influence of MHD forces on Bejan's heatlines and masslines in a doubly stratified fluid saturated Darcy porous enclosure in the presence of Soret and Dufour effects–a numerical study," *International Journal of Heat and Mass Transfer*, vol. 117, pp. 1041–1062, 2018.
[6] E. Oro´, A. Castell, J. Chiu, V. Martin, and L. F. Cabeza, "Stratification analysis in packed bed thermal energy storage systems," *Applied energy*, vol. 109, pp. 476–487, 2013.
[7] K. Song, M. A. Xenopoulos, J. M. Buttle, J. Marsalek, N. D. Wagner, F. R. Pick, and P. C. Frost, "Thermal stratification patterns in urban ponds and their relationships with vertical nutrient gradients," *Journal of environmental management*, vol. 127, pp. 317–323, 2013.
[8] T. Bouhal, S. Fertahi, Y. Agrouaz, T. El Rhafiki, T. Kousksou, and A. Jamil, "Numerical modeling and optimization of thermal stratification in solar hot water storage tanks for domestic applications: CFD study," *Solar Energy*, vol. 157, pp. 441–455, 2017.

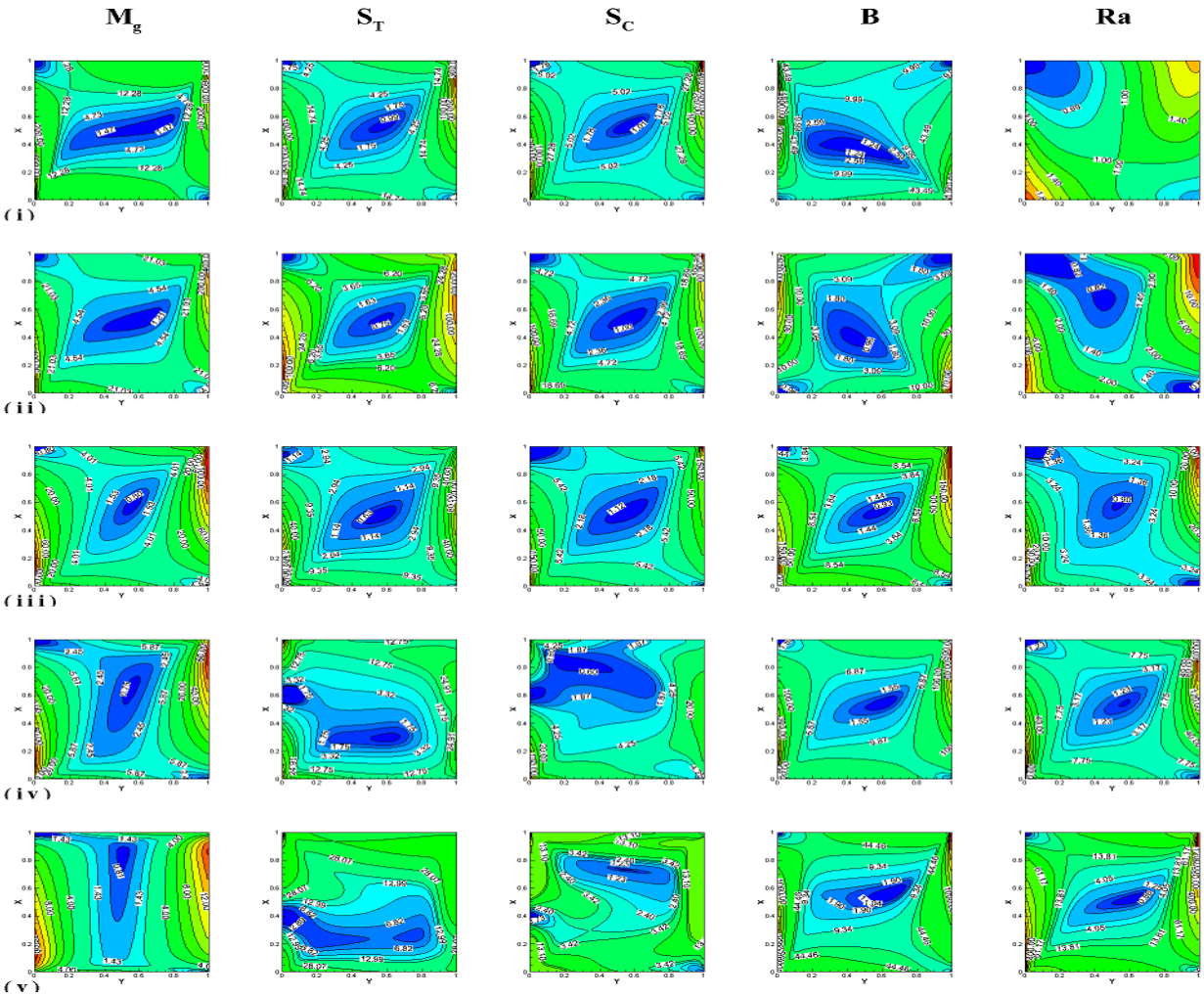


FIGURE 1. Contour plots of entropy generation for Magnetic field parameter ($M_g$) as (i) $M_g = 0$, (ii) $M_g = 1$, (iii) $M_g = 5$, (iv) $M_g = 10$, (v) $M_g = 50$, similarly for Thermal ( $S_T = 0, 0.5, 1, 3, 5$ ) and Mass ( $S_C = 0, 0.5, 1, 3, 5$ ) stratification, Buoyancy ratio ( $B = -5, -2, 1, 2, 5$ ) and Rayleigh number ( $Ra = 10, 50, 100, 200, 500$ ).

Fifth International Conference on Computational Methods for Thermal Problems
THERMACOMP2018, July 9-11, 2018, Indian Institute of Science, Bangalore, INDIA
*N. Massarotti, P. Nithiarasu, Pradip Dutta and C. Ranganyakalu (Eds.)*

# Design and CFD Analysis to Visualize the Flow Pattern Inside Air Turbine: A Component of Turboexpander

**Dravida Krishnatreya*, M. Kumar, S. K. Behera, R. K. Sahoo**

Department of Mechanical Engineering, NIT, Rourkela, Odisha, India, 769008,

E-mail:- getdravida@gmail.com, manojbeg526@gmail.com

## ABSTRACT

In this paper, CFD investigation has been done to visualize the flow pattern of air through a radial Inflow Cryogenic Turbine for the liquefaction of air. The mean-line design and three dimensional model of turbine blade and fluid passage (Hub, Shroud, Inflow, Periodic side, outblock etc.) is obtained using Blade-Gen. The computational grid is created using in ICEM-CFD software. Three-dimensional numerical simulation is performed using k-w model with shear stress transport (SST) turbulence model in Fluent© 18.1. Pressure, velocity, turbulence parameters etc. are visualized inside the fluid domain. It is observed that the pressure will be varied from 5 bar at the inlet to approximately 2.1 bar at the outlet. It is interesting to observe that the vortex forms at the trailing edge which is minimize by refining the blade profile.

**Key Words:** Radial turbine, Flow pattern, Turbo-expander, Air.

## 1. INTRODUCTION

The concept of using an expansion turbine in a cycle for the liquefaction of gasses was first introduced by Lord Rayleigh in a letter to 'Nature' in June 1898. He emphasized that the refrigeration produced would be the most important function of the turbine rather than the power recovered. Edgar C. Thrupp patented a liquefying machine using an expansion turbine [1]. Turbo-expander has wide application in various industrial processes as sources of refrigeration. The various applications of turbo-expanders include extracting hydrocarbon liquids from natural gas, refrigeration systems, power generation, power recovery in fluid catalytic cracker, etc. The turbo expansion turbines can be called as the heart of the modern cryogenic and refrigeration systems. With the efficiency and reliability of small scale turbines, the use of reciprocating expanders is being slowly phased out.

The design of centrifugal turbo-expander was perfected by a Russian physicist Pyotr Kapitsa in 1939 [2]. Using a 8 cm Monel wheel with straight blades And operating at 40000 rpm, he claimed that his turbine could achieve an efficiency of 83%. A high speed turbine expander was developed as a part of a cold moderator refrigerator for the Argonne National Laboratory (ANL) by Voth et. al [3]. In 1964, the first commercial turbine using helium was operated in a refrigerator that produced 73 W at 3 K for the Rutherford helium bubble chamber [4].

The use of modern technology, such as computer numerical control technology, CFD software and Holographic techniques during turboexpander design process to further improve the turboexpander efficiency performance has been explained by Agahi et. Al [5]. Improvements in analytical techniques and design features have made turboexpanders to be designed and operated at more favorable conditions such as higher rotational speeds.

Kiyarash et. al. [6] developed an effective method for improving the efficiency of a small scale radial inflow turbine (RIT). 1-D modeling was very effectively used for preliminary design and performance study of the turbine based on input design parameters. With 3-D CFD analysis they could achieve a better model of the 3-D fluid flow behavior, hence enabling a better turbine design. With the aid of CFD modeling they were able to attain a turbine efficiency of 84.5% instead of 81.3% attained by the 1-D modeling.

K.G.Nitesh et. al. [7] designed a RIT using working fluid R-22 for a closed loop ocean thermal energy conversion plant of 2 kW capacity running at a speed of 34000 rpm with inlet and outlet temperatures of 24.5 degree C and 14 degree C respectively. Their input parameters were blade width at rotor inlet and outlet (6mm and 11mm respectively), rotor tip and shroud radii (24mm and 19mm respectively), axial length of 17.5mm and diffuser length of 62mm, 1-D modelling of the turbine is done using relations. Then 3-D simulation is carried out using ANSYS-CFX. They found that as number of nozzle and rotor blades increases, the maximum efficiency point shifts towards the lower mass flow rate. Stagger angle too was found to have a prominent effect on the maximum efficiency.

The steady state analysis of high-speed micro-turbine to predict the flow pattern of the helium in between the two blades using CFX. The numerical study visualizes the flow behavior, high pressure zone, heat transfer characteristics, vortex formation etc. of fluid in the flow passage as well as to mitigate these losses by refining the geometry [8, 9].

In this paper, the steady state analysis of high-speed micro-turbine to predict the flow pattern of the air in between the two blades using ANSYS Fluent©. The CFD study visualize the flow behavior, pressure, velocity, high pressure zone, vortex formation etc. of fluid in the flow passage as well as to mitigate these losses by refining the geometry. k-w with shear stress transport turbulence model is used to predict the flow field inside the domain.

## 2. COMPUTATIONAL DOMAIN AND GOVERNING EQUATUIONS

The one dimensional mean-line design and geometry has been created thereafter the basic parameters for the turbine blade, blade angles etc. is generated using ANSYS Blade-Gen®. The geometry is exported to ICEM software for generation of mesh. Mesh is generated by first creating o-grid blocks. Tetra-Quad mixed mesh is created by taking global element seed size of 2 and a global element scale factor of 2. Twelve mapped blocks is created with 22811 nodes and 136189 elements which is shown in Fig. [1]. The generated mesh is than simulated for 3-D analysis in FLUENT. The simulation is done by selecting k-w SST turbulence model. Air is used as the working fluid. The boundary conditions are taken as 500 kPa inlet pressure and 100 K inlet temperature. At the outlet the pressure is taken as 200 kPa.

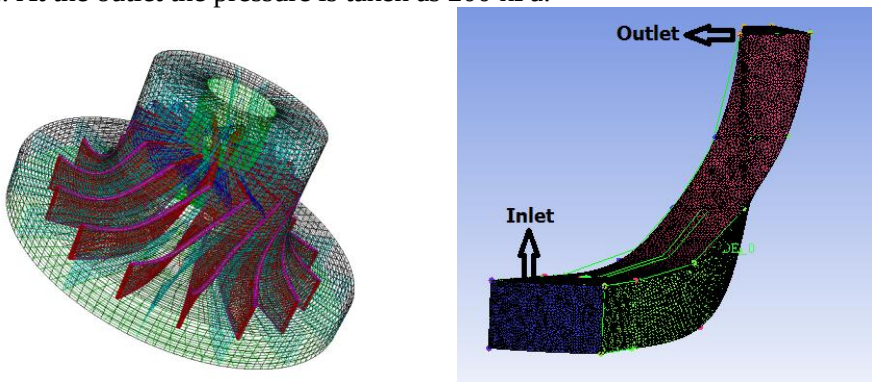


(a) (b)

Fig. 1. (a) Rotor as Generated in BladeGen (b) Mesh over the Entire Blade Profile.

The governing equations which is used to solve the computational domain in Fluent© are as follows.

Continuity Equation:

$$\frac{\partial \rho}{\partial t} + \nabla.(\rho U) = 0$$

Momentum Equations:

$$\frac{\partial(\rho U)}{\partial t}+\nabla.(\rho U\otimes U)=-\nabla p+\nabla.\tau+S_M$$

Total Energy Equation:

$$\frac{\partial(\rho h_{tot})}{\partial t}-\frac{\partial p}{\partial t}+\nabla.(\rho U h_{tot})=\nabla.(\lambda\nabla T)+\nabla.(U.\tau)+U.S_M+S_E$$

## 3. RESULTS

Fig. [2 , 3] shows the variation of pressure, velocity, vorticity and turbulent kinetic energy from inlet to outlet. In pressure contour diagram, it is clearly shown that the static pressure varies between 5 bar at the inlet to 2.1 bar at the outlet. With maximum pressure at the inlet, the pressure falls to a minimum value near the mid span of the blade at the shroud end.

Velocity contour shows that the maximum velocity along the fluid path is 816.775 m/s while the minimum velocity along the walls is 0 m/s due to no slip boundary condition at the turbine wall. The maximum velocity occurs near the trailing edge of the blade, though at the surface of the blade the velocity is zero due to no slip condition at the walls.

From the vorticity contour diagram and the turbulence contour diagram along with the turbulence vector diagram we see that even though some turbulence is present along the mid span of the blade profile, turbulence is highest at the trailing edge of the blade. Also from the velocity vector and vorticity vector diagrams it can be seen that flow separation takes place at the trailing edge of the blade which is a major source of energy loss.

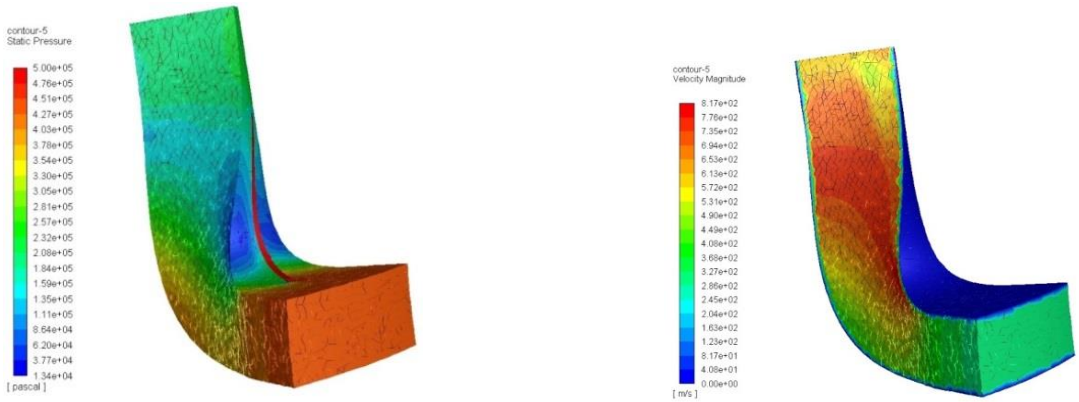


(a) (b)

Fig. 2. (a) Pressure Contour Diagram (b) Velocity Contour Diagram

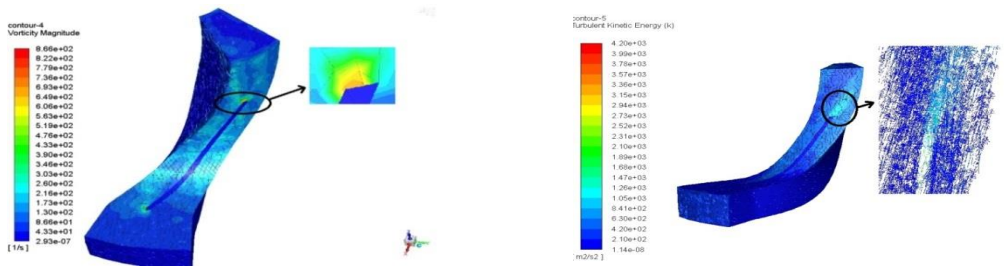


(a) (b)

Fig. 3. (a) Vorticity Contour Diagram (b) Turbulence Kinetic Energy Contour

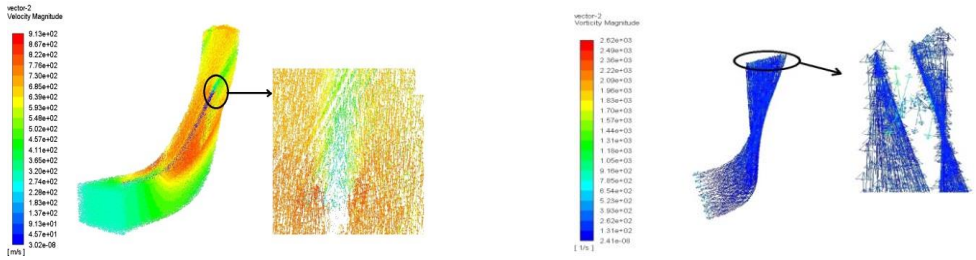

(a) (b)

Fig. 4. (a) Velocity Vector Diagram (b) Vorticity Vector Diagram along the Blade

## 4. CONCLUSIONS

This study proposed a systemic methodology to design a turbine and analyses the flow pattern. The variation of pressure, velocity, vorticity, TKE etc. of cryogenic radial turbine for air has been simulated. The loss of energy takes place at the trailing edge the blade, further investigation at the trailing edge is required to ascertain the exact nature of turbulence which in turn will help us to minimize the energy loss as the fluid flows through the turbine. A systematic study of the turbulence and entropy generation would help us design a blade profile with minimum loss and hence in designing of a better efficient turbo-expander. The shape of rotor blade, blade angle and thickness variation and number of blades was modified to improve the compactness of turbo-expander.

## REFERENCES

[1] Collins, S.C. and Cannaday, R.L. Expansion Machines for Low Temperature Processes Oxford University Press (1958).

[2] Swearingen, J. S. Turbo-expanders Trans AIChE (1947), 43 (2), 85-90.

[3] Voth, R. O., Norton, M. T. and Wilson, W. A. A cold modulator refrigerator incorporating a high speed turbine expander Advances in Cryogenic Engineering (1966) , V11, 127-138.

[4] Clarke, M. E. A decade of involvement with small gas lubricated turbine & Advances in Cryogenic Engineering (1974), V19, 200-208.

[5] Agahi,R.R., Lin,M.C. and Ershaghi,B. Improvements of the efficiency of the turboexpanders in cryogenic applications. Advances in Cryogenic Engineering(1996), V41,933-940.

[6] Rahbar, Kiyarash,Mahmoud,Saad, Al-Dadah,Raya K.,Moazami,Nima, Mirhadizadeh,Seyed, A Development and experimental study of a small-scale compressed air radial inflow turbine for distributed power generation. Applied Thermal Engineering 116(2017) 549-583.

[7] Nithesh,K.G., Chatterjee,Dhiman, Oh,Cheol, Lee,Young-Ho. Design and Performance analysis of radial-inflow turboexpander for OTEC application. Renewable Energy 85(2016) 834-843.

[8] M. Kumar, S. K. Behera, A. Kumar, A Numerical Analysis of Predicting Flow Pattern Inside a Turbo-expander, Proceedings of the 6th International and 43rd National Conference on Fluid Mechanics and Fluid Power, December 15-17, 2016, MNNITA, Allahabad, U.P., India

[9] M. Kumar, R. K. Sahoo, Development and Numerical Analysis to Visualize the Flow Pattern of Cryogenic Radial Turbine for Helium Gas, Proceedings of the 24th National and 2nd International ISHMT-ASTFE Heat and Mass Transfer Conference (IHMTC-2017), December 27-30, 2017, BITS-Pilani, Hyderabad, India

Fifth International Conference on Computational Methods for Thermal Problems
THERMACOMP2018, July 9-11, 2018, Indian Institute of Science, Bangalore, INDIA
*N. Massarotti, P. Nithiarasu, Pradip Dutta and C. Ranganyakalu (Eds.)*

# AERO THERMAL ANALYSIS OF WING LEADING EDGE OF RE-USABLE LAUNCH VEHICLE

**K S Lakshmi, Anoop P**
Scientist/Engineer-SD, VSSC, ISRO, lakshmi_kota@vssc.gov.in, Scientist/Engineer-SF, VSSC, ISRO, p_anoop@vssc.gov.in

**Sundar B, M J Chacko**
Scientist/Engineer-G, VSSC, ISRO, b_sundar@vssc.gov.in, Scientist/Engineer-H, VSSC, ISRO, mj_chacko@vssc.gov.in

## ABSTRACT

ISRO has successfully demonstrated Reusable Launch Vehicle Technology Demonstrator (RLV-TD) to cater the future re-entry missions with a lifting entry configuration. RLV-TD is a winged body mounted on solid booster. Its atmospheric flight includes ascent as well as re-entry into atmosphere which will encounter severe thermal environment. The vehicle should be able to withstand this thermal load. Thermal environments were estimated for RLV-TD and hot structures like wing leading edge was designed as hot structures.

A design code has been developed for the computation of heat transfer rates over a re-entry winged body and its thermal response along a trajectory is estimated. Beckwith & Gallagher correlation is used for the wing stagnation point and is treated as infinite swept cylinder for the flows with an angle of incidence. This code has been validated for heat flux obtained for similar configurations. Temperature measurements were made on RLV- TD to verify the design. Post flight analysis was carried out and measured temperatures are compared with predicted temperatures. Fairly good comparison is seen between estimated and measured temperatures validating the thermal design methodology.

This paper briefly describes the methodology of heat flux estimation and thermal design of wing leading edge of RLV-TD and validation with flight measurements.

**Key Words:** *Wing leading edge, RLV-TD, Beckwith & Gallagher.*

## NOMENCLATURE

| | | | |
|---|---|---|---|
| [C] | Capacitance matrix | α | Velocity gradient |
| $C_H$ | Stanton number | λ | Sweep back angle (deg) |
| dt | Time step (s) | ρ | Density (kg/m$^3$) |
| [F] | Load vector | μ | Coefficient of dynamic viscosity (Ns/m$^2$) |
| h | Heat transfer coefficient (W/m$^2$K) | ν | Coefficient of kinematic viscosity (m$^2$/s) |
| H | Enthalpy (J/kg) | **Superscripts** | |
| k | Thermal conductivity (W/mK) | * | Eckert's Reference temperature conditions |
| [K] | Conductivity matrix | **Subscripts** | |
| l | Reference length (m) | e | Edge of boundary layer |
| M | Mach number | rec | Recovery conditions |
| $N_{Pr}$ | Prandtl number | s | Value at stagnation line |
| P | Pressure (N/m$^2$) | w | Wall conditions |
| $r_N$ | Nose radius (m) | ∞ | Free stream conditions |
| T | Temperature (K) | | |
| u | Velocity (m/s) | | |
| $u_R$ | Chordwise velocity (m/s) | | |

| | | | |
|---|---|---|---|
| 0 | Free stream stagnation conditions | 01 | Post shock stagnation conditions |

## 1. INTRODUCTION

ISRO's Reusable Launch Vehicle – Technology Demonstrator (RLV-TD) was successfully flight tested on 23rd May 2016.

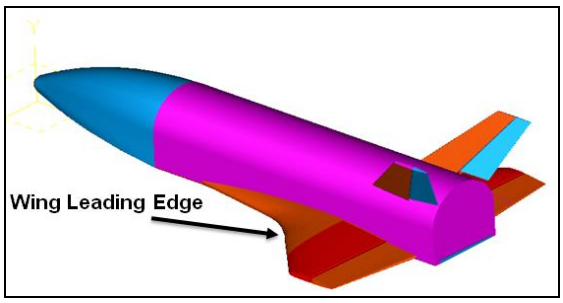


FIGURE 1: Configuration of RLV-TD

Figure 1 shows the schematic of RLV-TD with fuselage (body), nose cap, double delta wings and twin vertical tails. During the ascent phase of flight it is propelled by HS9 booster and re-entry from an altitude of 65km as an autonomous aircraft. Some of the major objectives of RLV-TD are hypersonic aerothermal characterization of a winged body and thermal protection system characterization.

During vehicle's re-entry kinetic energy is converted to thermal energy. Aerodynamic heating is due to forced convection which depends on the viscous interactions of the atmosphere with vehicle surface. The severity of aerodynamic heating depends on flight trajectory, atmosphere, vehicle geometry and external pressure distribution over the vehicle. Heating rates encountered during descent phase are much higher compared to ascent phase.

Wing leading edge experiences high temperatures. Ablative TPS materials cannot be used over the wing leading edges since the configuration/shape change of the lifting/ control surfaces effects the vehicle's stability.

Hot structures have a capability to maintain aerodynamic characteristics during high temperatures and hence can be used in wing leading edge regions. Hot structures protect vehicle via heat sink and radiative mechanisms.

This paper describes about the hot structure design and thermal analysis of RLV-TD wing leading edge. This design is validated with thermal measurements of flight data.

## 2. CONFIGURATION

Profile of the Wing leading edge is divided into two regions based on sweep back angle ($\lambda$) of $45^o$ and $80^o$ as shown in Figure 1. For $\lambda=80^o$ sector, a constant round off radius is considered and for $\lambda = 45^o$ sector variation of round off radius in spanwise direction is considered.

## 3. DESIGN METHODOLOGY FOR HEAT FLUX ESTIMATION

Based on the trajectory as shown in Figure 2, the altitude and velocity of the re-entry body at any instant of time are known. Free stream properties like temperature, pressure and density are evaluated based on altitude data from standard atmospheric model. Free stream conditions are considered with Mach number normal to the leading edge. Post shock conditions are computed by

solving one-dimensional mass, momentum and energy equations using normal shock equations. High temperature equilibrium air properties are estimated using Hansen tables **[3]**.

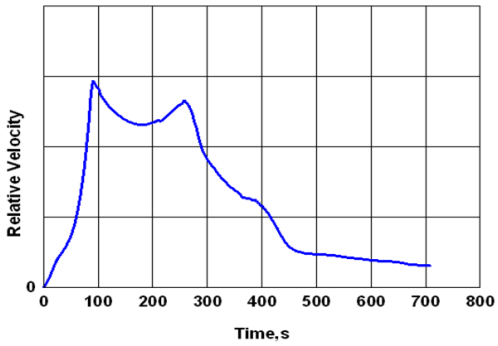


FIGURE 2: RLV-TD flight trajectory

Based on these inputs, an inhouse software code has been developed to estimate aerodynamic heat flux on the wing leading edge.

At the stagnation point of the wing leading edge heat flux is estimated using Beckwith and Gallagher method **[1]**. In this method the body is treated as infinite swept cylinder for the flows with angle of incidence.

For the conservative estimate turbulent heating rates are considered which is given by the correlation.

$$\frac{hl}{k_\infty} = N_{Pr}^{\frac{1}{3}} \left[\frac{u_{R\infty} l}{\nu_\infty}\right]^{\frac{n}{1+n}} \left(a \frac{P_s}{P_\infty} \frac{\mu_w}{\mu_o} \frac{T_\infty}{T_w}\right)^{\frac{n}{1+n}} (sin\lambda)^{\frac{n-1}{n+1}} \left(\frac{49}{376} \frac{\mu_o}{\mu_\infty} cos\lambda \frac{l}{u_\infty} \left(\frac{du}{dx}\right)_s\right)^{\frac{1}{1+n}} \quad (1)$$

Where n = 4 and a=0.0228 (constants from Blasius skin friction)
where α - velocity gradient for cylinder which is given by

$$\alpha = \left(\frac{du}{ds}\right)_{s=0} \rightarrow (2) \quad \alpha = \left(\frac{u_\infty}{D}\right)(4 - 1.66M_\infty^2) \text{ (for } M_\infty < 1) \text{ and } \alpha = \frac{1}{r_N}\sqrt{2\frac{(P_{01} - P_\infty)}{\rho_{01}}} \text{ (for } M_\infty > 1) \rightarrow (3)$$

where D = 2rN

$$T_{rec} = T_0 \left[0.9\left(1 - \frac{T_{01}}{T_0}\right) + \frac{T_{01}}{T_0}\right] \quad (4)$$

Heat flux is computed from the correlation (5)

$$Q = h(T_{rec} - T_w) \quad (5)$$

Eckert's **[2]** method is used for heat flux estimation at other locations of the wing leading edge using the correlation (6).

$$\dot{Q} = \rho^* u_e C_H (H_{rec} - H_w) \quad (6)$$

Figure 3 shows the computed non-dimensional heat flux history at wing leading edge stagnation point using flight trajectory. Heat flux is non-dimensionalized with respect to nose cap stagnation heat flux.

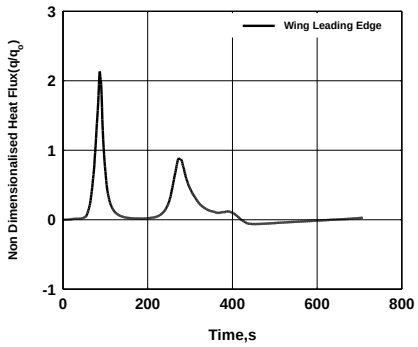


FIGURE 3: Computed flight heat flux history at stagnation point

## 4. NUMERICAL MODELLING

In finite element formulation, temperature distribution over element 'e' is assumed as

$$T^e(x,y,z) = \sum_{i=1}^{n} N_i(x,y)T_i(t) \tag{7}$$

where T is temperature, x,y,z are coordinates, t – time, Substituting in the variational form and minimizing it with respect to all the nodes

$$[K](T)^e + [C]^e\left(\frac{dT}{dt}\right)^e = (F)^e \tag{8}$$

The elements are assembled into global matrices and the final system of equations obtained is

$$[K](T) + [C]\left(\frac{dT}{dt}\right) = (F) \tag{9}$$

Where [K] is the conductivity matrix, [C] is the capacitance matrix and [F] is the load vector. Finite element model is generated using ANSYS **[4]** which solves equations with Pre condition Conjugate Gradient (PCG) solver. This solver starts with element matrix formulation and assembles the full global stiffness matrix and calculates the degree of freedom solution by iterating to convergence.

## 5. THERMAL RESPONSE ANALYSIS

Three-dimensional finite element model of a typical section of wing leading edge is shown in Figure 4.

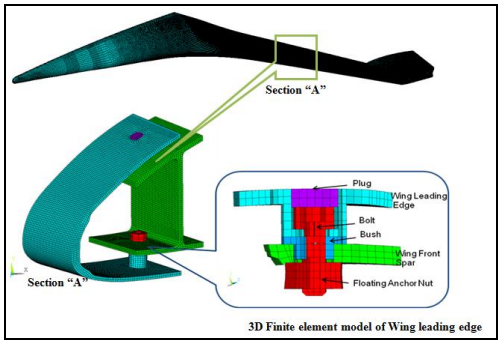


FIGURE 4: Finite element model of RLV-TD wing leading edge

Model consists of wing leading edge, plug, bolts, bush, anchor nut, spar. Wing leading edge is attached to spar with attachments plug, bolts, bush and anchor nut. Spar is made of Aluminium alloy where as other components are made of 15CDV6 steel.

For the finite element model shown in Figure 4 transient thermal response analysis is carried out using finite element software ANSYS. Table 1 shows thermo physical properties of materials used for analysis. Initial temperature of 313K was taken by considering worst case launch pad environment.

| Material | Density (kg/m$^3$) | | Specific heat (J/kg K) | | Conductivity (W/m K) | |
|---|---|---|---|---|---|---|
| | T (K) | ρ | T (K) | $C_P$ | T(K) | k |
| 15CDV6 Steel | 273 | 7850 | 253 | 442 | 253 | 42 |
| | 573 | 7790 | 400 | 492 | 600 | 39.1 |
| | 673 | 7720 | 600 | 575 | 800 | 34.4 |
| | 873 | 7650 | 800 | 688 | 1000 | 27.4 |
| | 1000 | 7650 | 1000 | 969 | | |
| Aluminium alloy | 2800 | | 963 | | 121 | |

TABLE 1: Thermo physical properties

## 6. RESULTS AND DISCUSSIONS:

For the 3D model, thermal analysis is carried out and temperature contour of wing leading edge is shown in Figure 5. Temperature measurement sensors are mounted at different locations of wing leading edge. Fairly good comparison is seen between flight measured and computed temperature histories which is given in Figure 6.

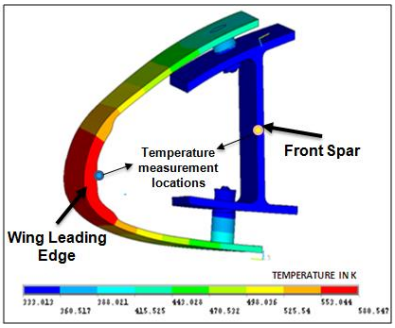


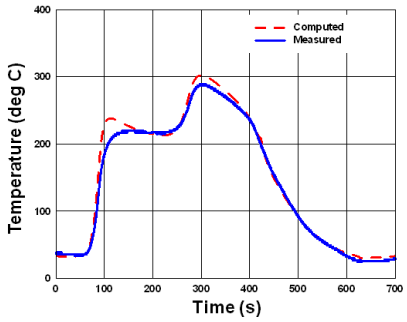


FIGURE 5: Temperature contour of wing leading edge, FIGURE 6: Comparison between maximum measured and computed temperature histories of wing leading edge

Maximum computed temperature on wing leading edge is 301$^o$C compared to flight measured temperature of 289$^o$C.

Figure 7 shows comparison between computed and measured temperature history on front spar. Maximum measured temperature on spar is 80$^o$C which is well below the constraint of 120$^o$C. The small difference between computed and measured temperatures can be attributed to the assumption of perfect contact between the structures.

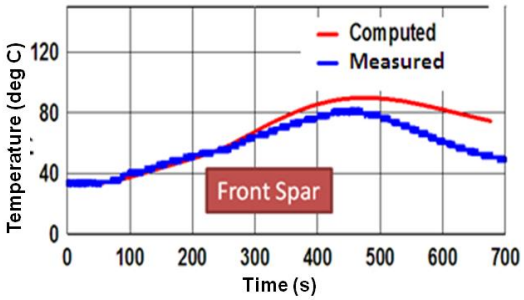


FIGURE 7: Comparison between maximum measured and computed temperature histories of front spar

All the measured temperatures are well within their temperature constraints.

## 7. CONCLUSIONS

- Aero thermal analysis is carried out for RLV –TD metallic wing leading edge.
- A design code has been developed for the computation of heat transfer rates over a re-entry winged body and its thermal response along a given trajectory.
- Post Flight analysis was carried out for the temperature measurements made on RLV-TD wing leading edge.
- Maximum computed temperature on wing leading edge is 301$^{o}$C compared to flight measured temperature of 289$^{o}$C.
- All the measured temperatures are well with in their temperature constraints and hence validating the thermal design methodology.

## 8. REFERENCES

[1] Ivan E Beckwith and Gallagher, Local heat transfer and recovery temperatures on Yawed cylinder at Mach number of 4.15 and high Reynolds numbers, *NASA TR R-104, 1962*

[2] E R G Eckert, Engineering relations for heat transfer and friction in high velocity laminar and turbulent boundary layer flow over surfaces with constant pressure and temperature, *Journal of Applied Mechanics, Transactions of ASME, Vol 78,* August 1956, pg 1273-1283

[3] CF Hansen, Approximations for the thermodynamic and transport properties of high temperature air, *NASA TR R-50,* 1959.

[4] ANSYS 12.0 User manual

Fifth International Conference on Computational Methods for Thermal Problems
THERMACOMP2018, July 9-11, 2018, Indian Institute of Science, Bangalore, INDIA
*N. Massarotti, P. Nithiarasu, Pradip Dutta and C. Ranganyakalu (Eds.)*

# A NUMERICAL FRAMEWORK FOR LINEAR STABILITY ANALYSIS OF TWO-DIMENSIONAL STEADY FLOWS

**Nitin Kumar**
Department of Applied Mechanics, Indian Institute of Technology, Hauz Khas, New Delhi, INDIA.
Email: nitinbali100@gmail.com
**Nipun Arora, Amit Gupta**
Department of Mechanical Engineering, Indian Institute of Technology, Hauz Khas, New Delhi, INDIA. Email: nipunarora088@gmail.com, agupta@mech.iitd.ac.in
**Sanjeev Sanghi**
Department of Applied Mechanics, Indian Institute of Technology, Hauz Khas, New Delhi, INDIA.
Email: sanghi@am.iitd.ac.in

## ABSTRACT

A novel numerical framework for conducting linear stability analysis of two-dimensional steady laminar flows is presented. Using two case studies involving analysis of thermal and laminar flows, stability of laminar flows in the numerical sense is addressed. The two-dimensional base flow is computed by using the lattice Boltzmann method for various values of the controlling parameter (Reynolds number for flow past a square cylinder and Rayleigh number for double-glazing problem). Subsequently, the perturbed equations with two-dimensional disturbances are linearized and form a set of partial differential equations that govern the evolution of these perturbations. Using normal mode analysis, the eigenvalues of the resultant equation are used to determine the stablilty of the base flow.

**Key Words:** *linear stability analysis, lattice Boltzmann, laminar flow, eigenvalue problem.*

## 1. INTRODUCTION

The role of hydrodynamic stability in fluid mechanics, which focuses on the evolution with time of small disturbance of base flow, is of prime importance to understand many natural phenomena as well as in the analysis and design of many engineering systems. For example, it is pursued in civil aviation to design modern lifting surface with drag reduced by passive means. In these circumstances, keeping the flow stable over a wing to as large an extent possible is the ultimate goal. The fundamental ideas of linear stability analysis have been documented in the classical works of Chandrasekhar [1] and Drazen [2]. The primary objective of earlier studies was to analytically calculate the critical flow parameters responsible for hydrodynamic instability on simple fluid flow problems such as Couette and Poiseuille flows by reducing the problem to one dimension using the Orr-Sommerfeld equation [3]. In the present study, we wish to examine the suitability of performing linear stability analysis of steady state solutions in the numerical sense.

## 2. MAIN BODY

The numerical methods are outlined here which are used to compute the base flow, formulation of eigenvalue problem for the determination of critical state and solution of the eigenvalue problem. The lattice Boltzmann BGK two-dimensional nine velocity (D2Q9) model is used as a direct numerical solver for computing the base flow. The finite differences method is used as a

discretization for the fourth order partial differential equations for formulation of an eigenvalue problem. Simultaneous iterative method is used as a solution of the eigenvalue problem

## 3. RESULTS

To analyze the performance of the discrete linear stability framework, numerical simulations are performed for some standard fluid mechanics and heat transfer problems described below.

Flow past a square cylinder

At very low Reynolds number $(\mathrm{Re} < 1)$, no separation takes place at bluff body surface because viscous forces dominate. Further, on increasing the Reynolds number, flow separation starts to takes place with symmetrical vortex formation. The transition of vortex shedding from symmetric to asymmetric wake pattern occurs at a critical Reynolds number, defined as $\mathrm{Re}_{crit}$. When this critical Reynolds number is exceeded, the well-known von Karman vortex street is formed with a periodic vortex shed behind the cylinder. The flow around bluff bodies is studied by many researchers which primarily focused on circular cylinder under free flow conditions. In the present study, the focus is using linear stability analysis to predict the critical Reynolds number for onset of vortex shedding behind a square cylinder that will lead to unsteadiness in flow and to locate the point of bifurcation.

There is a wide range of critical Reynolds number that are reported in literature. These critical value also define on the blockage ratio, defined as the ratio of the cross-stream projection of the square (characteristic dimension of the cylinder) to the domain width. Okajima [4] specified an upper limit of critical Reynolds number at 70. Kelkar and Patankar [5] determined $\mathrm{Re} = 53$ based on numerical linear stability analysis of the steady flow by using initial value problem at a blockage of 14.2%, while Norberg et al. [6] found experimentally the critical value of Reynolds number within the range of $47 \pm 2$ at a 0.25% blockage. Sohankar et al. [7] determine the critical value of Reynolds number at $51.2 \pm 1.0$ at a 5% blockage based on numerical simulations by using linearized Stuart-Landau equation and found that critical Reynolds number increases with increasing blockage.

The layout of the computational domain along with the location of the fixed square cylinder and imposed boundary conditions is shown in Figure 1 with incompressible flow and constant fluid properties being considered. The Reynolds number is defined as $\mathrm{Re} = aU_\infty/\nu$, where $a$ is the side of cylinder, $\nu$ is kinematic viscosity of fluid and $\mathrm{U}_\infty$ is freestream velocity.

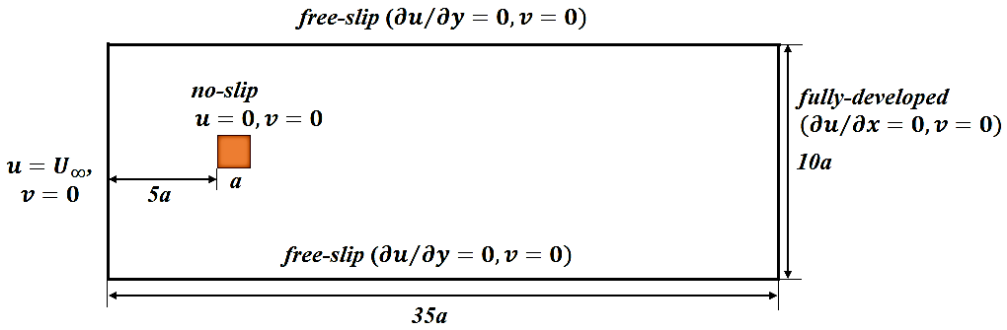


FIGURE 1. Layout of the computational domain with the imposed boundary conditions.

For computational efficiency, we used coarser grids for the discretization of eigenvalue problem than the base flow. The grids for both the base flow and eigenvalue problems are uniform but the number of grid is half in the eigenvalue problem. The number of grid points (N) used for computation of eigenvalues ranged from 80000 to 50000, giving the eigenvalue problem with 160000 to 100000 degree of freedom. In Table 1 the eigenvalues determined on different number of grid points for flow past a square cylinder at $\mathrm{Re} = 45$ and at $\mathrm{Re}_{crit} = 52$ are shown. It found that 70000 grid points are adequate for obtaining grid invariant results.

TABLE 1. Eigenvalues for flow past a Square cylinder for $\mathrm{Re} = 45.0$ and $\mathrm{Re}_{crit}$ =52

| Re | Mesh | $500\Delta x \times 200\Delta y$ | $600\Delta x \times 200\Delta y$ | $700\Delta x \times 200\Delta y$ | $800\Delta x \times 200\Delta y$ |
|---|---|---|---|---|---|
| 45 | *N* | 50000 | 60000 | 70000 | 80000 |
| | Real Part | 0.031988 | 0.032989 | 0.031386 | 0.029957 |
| | Imaginary Part | 0.008822 | 0.027010 | 0.018353 | 0.012117 |
| 52 | Real Part | | | -0.010300 | |
| | Imaginary Part | | | ±0.020037 | |

Double glazing problem

The "double glazing" or a two-dimensional air filled rectangular cavity with constant thermal conductivity along with the Boussinesq approximation is chosen as the second case study for characterization of thermal instability since it is increasingly difficult to obtain accurate solutions for high Rayleigh number flows. Winters [9] studied the stability of this problem with differentially heated sidewalls and adiabatic horizontal surface by computing the eigenvalues of the Jacobian matrix of the corresponding steady flow and determined the point of Hopf bifurcation. This work concentrated on verification of the experimental results published by Briggs and Jones [8], who had conducted similar experiments on the "double-glazing" problem by maintaining the vertical sidewalls at fixed temperatures. A pictorial representation of geometry and boundary conditions is shown in Figure 2.

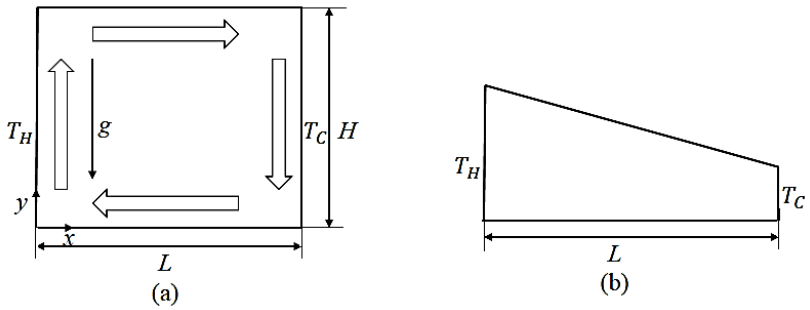


FIGURE 2. (a) Enclosure geometry and boundary condition, (b) Boundary condition at the bottom and top walls.

The base temperature distribution for this problem at a particular Rayleigh number and at different time instants is found by using Temperature lattice Boltzmann equation (TLBE). The grids for both the base flow and eigenvalue problems are same and uniform. The number of grid points (N) used

for computation of eigenvalues ranged from 2601 to 961, giving the eigenvalue problem with 7803 to 2883 degree of freedom. In Table 2 the eigenvalues determined on different grid points (N) for double glazing problem at $Ra = 1\times10^6$ and at critical Rayleigh number ($Ra_{crit} = 2.04\times10^6$) are shown.

TABLE 2. Eigenvalues for Double glazing problem for $Ra = 1\times10^6$ and $Ra_{crit} = 2.04\times10^6$

| Ra | Mesh | $31\Delta x\times31\Delta y$ | $41\Delta x\times41\Delta y$ | $51\Delta x\times51\Delta y$ |
|---|---|---|---|---|
| $1\times10^6$ | N | 961 | 1681 | 2601 |
| | Real part | 0.063017 | 0.06184 | 0.061072 |
| $2.04\times10^6$ | Real part | | -0.0073 | |

## 4. CONCLUSIONS

A discrete linear stability analysis framework for two-dimensional laminar flow is applied for locating Hopf bifurcation in the cases of flow past a square cylinder and double glazing problem. The results indicate that in the case of flow past a square cylinder the onset of two-dimensional vortex shedding is found at Re=52 which is reasonable in agreement with Sohankar et al. [6] and Kelkar and Patankar [5]. In the case of double glazing problem onset of stability is found at $Ra = 2.04\times10^6$ which is very well in consistance with Winters [9].

## REFERENCES

[1] Chandrasekhar, S. (1961). *Hydrodynamic and Hydrodynamic stability*. OUP.

[2] Drazin, P. G., & Reid, W. H. (2004). *Hydrodynamic Stability*. Cambridge University Press.

[3] Fortin, A., Jardak, M., Gervais, J. J., & Pierre, R. (1994). Old and new results on the two-dimensional Poiseuille flow. *Journal of Computational Physics*, *115*(2), 455-469.

[4] Okajima, A. (1990). Numerical simulation of flow around rectangular cylinders. *Journal of Wind Engineering and Industrial Aerodynamics*, *33*(1-2), 171-180.

[5] Kelkar, K. M., & Patankar, S. V. (1992). Numerical prediction of vortex shedding behind a square cylinder. *International Journal for Numerical Methods in Fluids*, *14*(3), 327-341.

[6] Sohankar, A., Norberg, C., & Davidson, L. (1998). Low-Reynolds-number flow around a square cylinder at incidence: study of blockage, onset of vortex shedding and outlet boundary condition. *International journal for numerical methods in fluids*, *26*(1), 39-56.

[7] Sohankar, A., Norbergb, C., & Davidson, L. (1997). Numerical simulation of unsteady low-Reynolds number flow around rectangular cylinders at incidence. *Journal of Wind Engineering and Industrial Aerodynamics*, *69*, 189-201.

[8] Briggs, D. G., & Jones, D. N. (1985). Two-dimensional periodic natural convection in a rectangular enclosure of aspect ratio one. *Journal of Heat Transfer*, *107*(4), 850-854.

[9] Winters, K. H. (1987). Hopf bifurcation in the double-glazing problem with conducting boundaries. *Journal of Heat Transfer*, *109*(4), 894-898.

# MODELING OF SOLIDIFICATION OF WATER DROPLET IMPACT ON A SUBSTRATE WITH UNDERCOOLING EFFECT

**Digvijay Singh, Jaiprakash Kumawat, Alok Kumar, Arvind Kumar***
Dept. of Mechanical Engineering, Indian Institute of Technology Kanpur, Kanpur – 208016, India,
*arvindkr@iitk.ac.in

## ABSTRACT

Solidification with undercooling effect during water droplet impact on a stainless steel substrate is studied by using CFD simulation and experiment. HS imaging is used to capture the droplet spreading on the substrate and the evolution of the solid-liquid interface. A numerical model is developed for the non-equilibrium solidification by considering the undercooling effect. The governing equations are numerically solved using the SIMPLE algorithm and the free surface of the liquid droplet is tracked by using the THINC/WLIC (VOF) method. The model is validated with the experimental result on droplet spreading factor. Consideration of non-equilibrium solidification in the model significantly influences the predictions of interface position, temperature history and droplet spreading. The non-equilibrium solidification is an important factor and should be considered during freezing of droplet impacting on substrates.

**Key Words:** *Droplet impact, Solidification, Undercooling, Free surface, HS imaging.*

## 1. INTRODUCTION

Droplet impact on a cold solid surface is relevant for many applications in natural, agricultural and industrial processes. Roisman et al. [1] had proposed different models for the maximum spreading ratio for droplet impact and spreading process. The freezing characteristics of a droplet on cold surfaces have been widely studied experimentally [2-3]. When a droplet impacts onto a cold substrate, it might experience undercooling because of small solidified thickness and high rate of heat transfer between the liquid and the substrate, which leads to a high rate of solidification near the substrate [4]. In literature, the models of rapid solidification during droplet impact on surfaces assume simplified assumptions, like one-dimensional treatment and consideration of only conduction heat transfer, as if freezing in the droplet starts once it was spread and flattened completely on the surface (stagnant splat). In this way, the role of spreading, free surface evolution, convection and multi-dimensionality were completely ignored on the rapid solidification kinetics. For example, Zhang et al. [5] reported a simplified one-dimensional conduction model for the splat formation where they considered undercooling, nucleation and non-equilibrium solidification. In reality, droplet impact on surfaces involves complexities, such as free surface evolution, multi-dimensional heat transfer, convection along with the characteristics of rapid solidification (undercooling, nucleation and recalescence). In this study, the rapid solidification during droplet impact on a cold stainless steel substrate is studied using a computational model considering the above-mentioned aspects. The influence of non-equilibrium solidification on droplet spreading behaviour, the evolution of the solid-liquid interface (solidified thickness) and temperature history are described by comparing the predictions using the conventional equilibrium and the presented non-equilibrium solidification models. Also, an experimental study of droplet impact is performed using HS imaging to capture the droplet spreading on the substrate and the evolution of the solid-liquid interface. The model prediction of droplet spreading factor is validated with the experimental result.

## 2. MODEL

A water droplet ($D_0$ = 4.8 mm, $T_{drop}$ = 300 K, $V_{impact}$ = 3.5 m/s) is impacting on the stainless steel substrate ($T_{subs}$ = 248 K) at atmoshpheric pressure. Figure 1 shows the schematic of the computational domain for the equilibrium and non- equilibrium solidification. At all walls, no slip boundary condition is used. For heat transfer at all walls and at pressure outlets adiabatic conditions are used The variation of material properties is considered as independent of the temperature. The thermal contact resistance ($2.4\times10^{-4}$ $m^2$-K/W)[6] and contact angle (100º) is assumed constant for the entire simulation. The governing equations of the numerical model are shown in table 1.

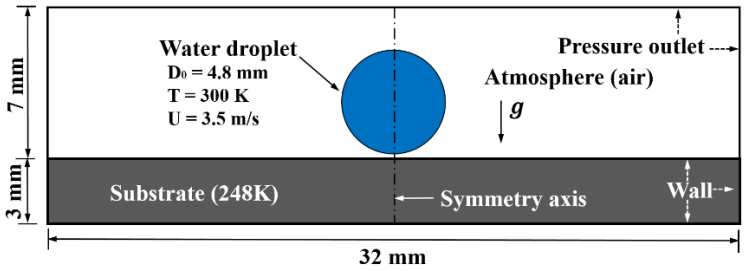


FIGURE 1: Computational domain

| | | |
|---|---|---|
| VOF equation | $\frac{\partial F}{\partial t} + \nabla \cdot \vec{u}F = 0$ | (1) |
| Definition of mixture quantities for a cell in the mushy state | $f_s + f_l = 1,\ c_{eff} = F\,c_d + (1-F)c_{air}, \rho = F\rho_d + (1-F)\rho_{air}$<br>$k_{eff} = F\,k_d + (1-F)k_{air}, k_d = f_l k_l + (1-f_l)k_s, \mu = F\,\mu_d + (1-F)\mu_{air}$ | (2) |
| Continuity equation | $\nabla \cdot \vec{u} = 0$ | (3) |
| Momentum conservation equation [7-8] | $\frac{\partial}{\partial t}(\rho\vec{u}) + \nabla\cdot(\rho\vec{u}\vec{u}) = -\nabla p + \nabla\cdot[\mu(\nabla\vec{u} + \nabla\vec{u}^T)] + \rho\vec{g} + F_{vol} - S\vec{u}$<br>$S\vec{u} = \begin{cases} \left[C\frac{(1-f_l)^2}{f_l^3+e}\right]\vec{u} & F = 1 \\ 0 & F < 1 \end{cases}, \quad F_{vol} = \sigma\kappa(\vec{x})\frac{\rho}{\rho_d+\rho_{air}}\nabla F$ | (4) |
| Energy conservation equation | $\frac{\partial}{\partial t}(\rho c_{eff}T) + \nabla\cdot(\rho\vec{u}c_{eff}T) = \nabla\cdot(k_{eff}\nabla T) + S_h$<br>$S_h = \begin{cases} -L\left[\frac{\partial}{\partial t}(\rho f_l)\right] & F = 1 \\ 0 & F < 1 \end{cases}$ | (5) |
| Substrate: Conduction heat transfer equation | $\frac{\partial}{\partial t}(\rho_{subs}c_{subs}T) = \nabla\cdot(k_{subs}\nabla T)$ | (6) |
| Equilibrium solidification model [9] | $[\Delta H_p]_{n+1} = [\Delta H_p]_n + \frac{a_p}{a_p^0}\lambda\left[\{h_p\}_n - G^{-1}\{\Delta H_p\}_n\right],\ a_p^0 = \rho\Delta V/\Delta t$<br>$f_l = \frac{\Delta H}{L} \quad G^{-1}[\Delta H] = c_d T_m, \quad \lambda - \text{Relaxation factor}$ | (7) |
| Non-equilibrium solidification model [10] | $V_i = a\,\Delta T^b, \quad \Delta T = T_m - T_i\ , \quad a = 2.8\times10^{-3}\ \text{ms}^{-1}\text{K}^{-1.8}, \quad b = 1.8$<br>$f_s^{n+1} = f_s^n + \frac{V_{ix}\Delta t}{\Delta X} + \frac{V_{iy}\Delta t}{\Delta Y}$ | (8) |

Symbols

| | | | | | |
|---|---|---|---|---|---|
| $c$ | Specific heat capacity | $\vec{u}$ | Continuum velocity vector | ρ | Density |
| $C$ | Constant related to Darcy source term | $\Delta t$ | Timestep | *Subscripts* | |
| $f$ | Weight fraction | $\Delta H$ | Latent heat content of a control volume | *air* | Air |
| $F$ | Volume of fluid function | $\Delta X$ | Cell width in x-direction | *d* | Droplet |
| $F_{vol}$ | Continuum surface tension force | $\Delta Y$ | Cell width in y-direction | *eff* | Effective |
| $\vec{g}$ | Acceleration due to gravity vector | $G^{-1}[\Delta H]$ | Inverse of latent heat function | *i* | Interface |
| $k$ | Thermal conductivity | *Greek symbols* | | *l* | Liquid |
| $L$ | Latent heat of fusion | α | Thermal diffusivity | *m* | Melting |
| $T$ | Temperature | μ | Dynamic viscosity | *s* | Solid |
| | | $\kappa$ | Local mean curvature | *subs* | Substrate |

TABLE 1: Governing equations

## 2. RESULTS AND DISCUSSIONS

Experimental result of a water droplet ($D_0$ = 4.8 mm, $T_{drop}$ = 300 K, $V_{impact}$ = 3.5 m/s) impact and spreading on a stainless steel substrate ($T_{subs}$ = 248 K) is shown in Fig. 2. The evolution of solid-liquid interface in the solidifying droplet is identified in the snapshots captured using HS imaging (see the marked arrow in F at *t* = 12.25 ms and the contrast difference in E, F, G). The droplet spreads after its impact on the surface and the spreading ratio (defined as local spread diameter to droplet initial diameter) initially increases (A-D) governed by inertia. The maximum spreading was observed at 5.25 ms (D). Afterward, the spreading ratio decreases slightly (E-G) due to recoiling governed by surface tension up to 12.25 ms (F). The droplet solidified completely as a splat at 75 ms (I).

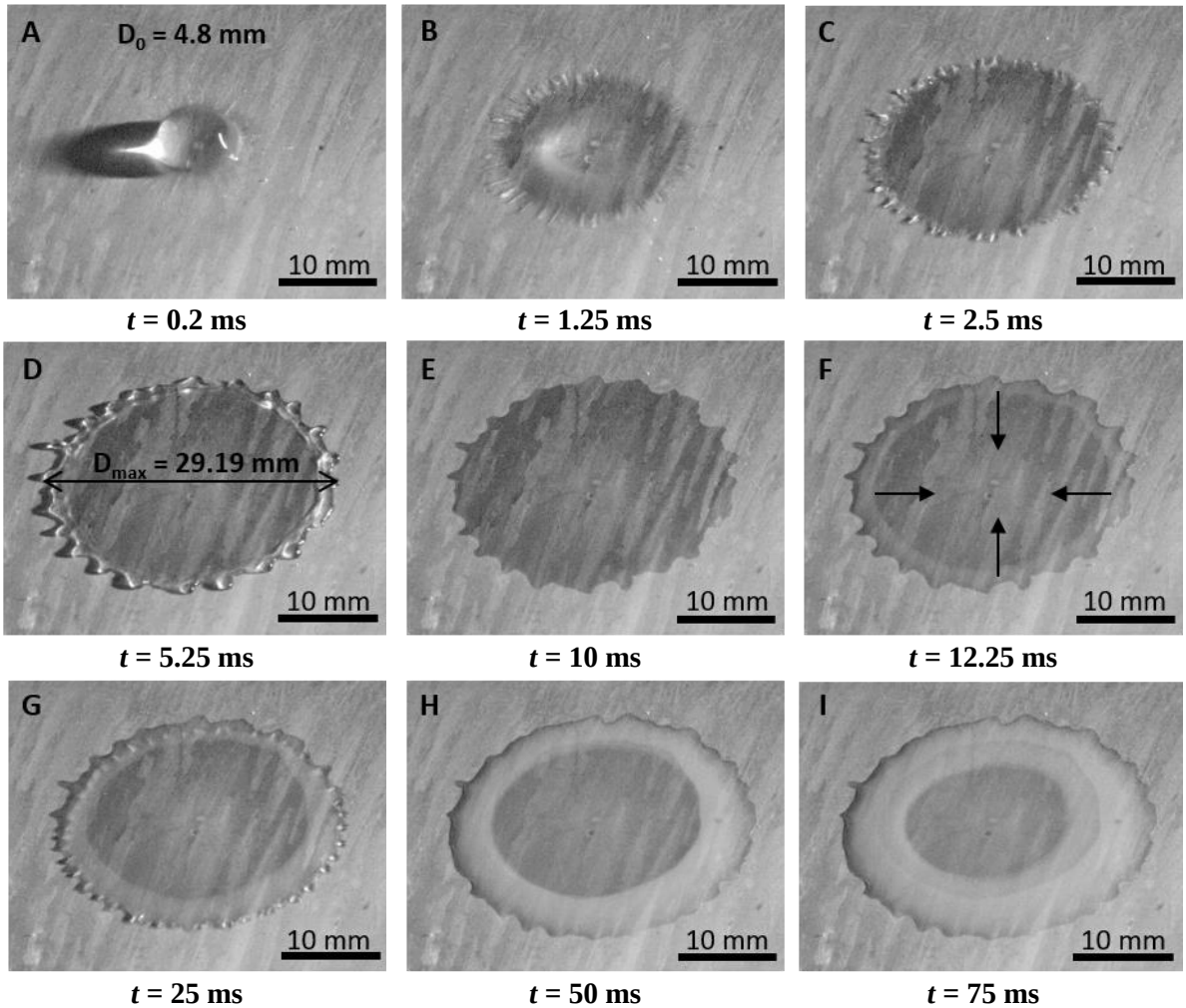


FIGURE 2: Experimental results captured using HS imaging showing droplet spreading and evolution of solid-liquid interface in the droplet (top view)

Numerical results the droplet impact and speeding at a different time is shown in Fig. 3. The liquid fraction distribution for both the equilibrium and the non-equilibrium solidification model is shown. It is observed that solidification in the case of equilibrium solidification model starts earlier ( *t* = 5.41 ms) than the non-equilibrium solidification model. In the non-equilibrium solidification model, it is required to reach the nucleation temperature (which is below the melting temperature) to initiate solidification. This causes a delay in initiation of solidification in the case of non- equilibrium solidification model. As temperature difference is low, the differences between the predicted

geometries by the equilibrium and the non-equilibrium model cannot be easily identified, however, the difference is quantified in figs 4-6.

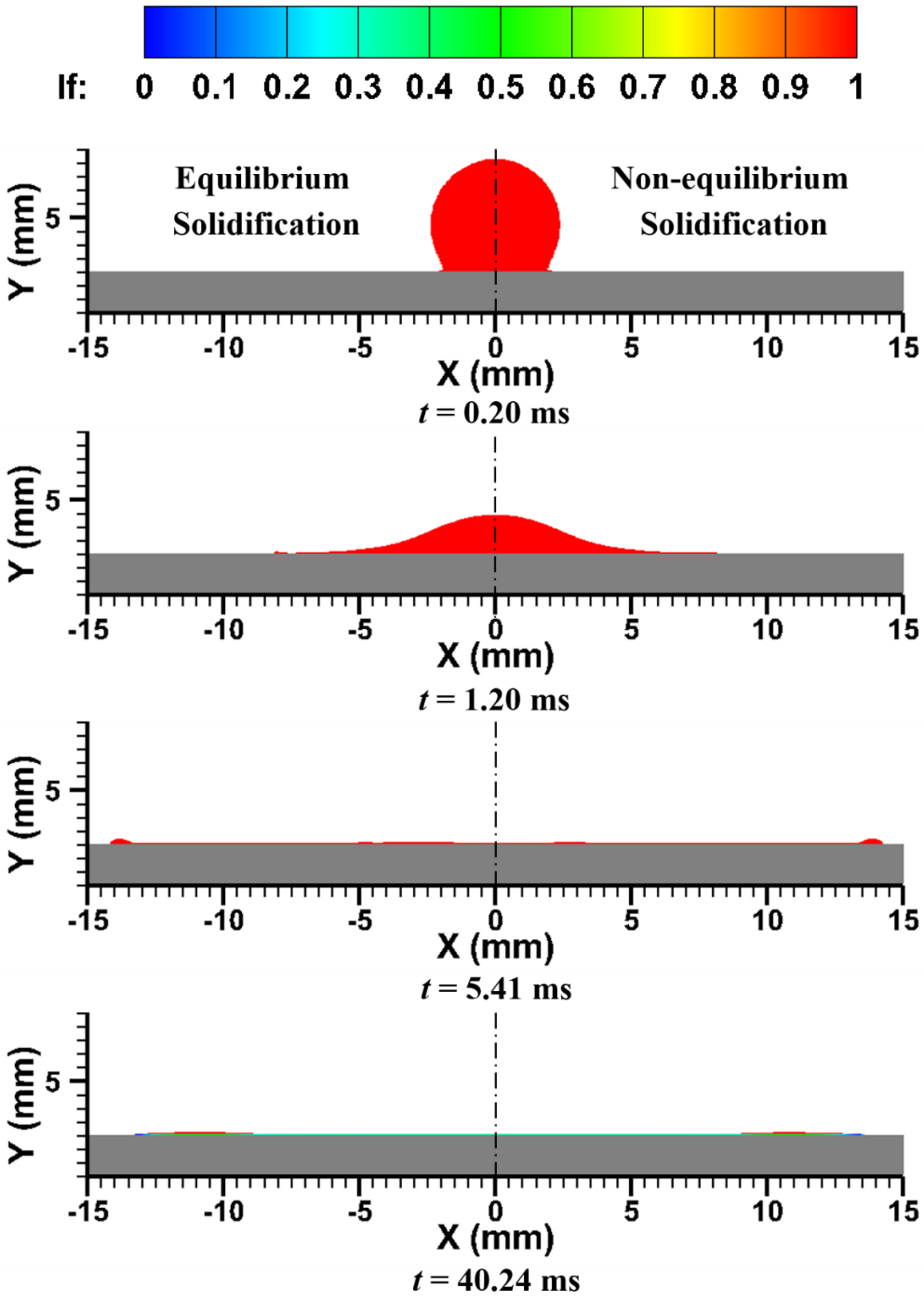


FIGURE 3: Liquid fraction distribution for equilibrium and non-equilibrium solidification

Figure 4 shows the comparison of the predicted evolution of droplet spreading ratio for equilibrium and non-equilibrium solidification model with the experimental results. It is noticed that the droplet reaches its maximum spread at 5.41 ms then surface tension pulls the edges of the droplet inwards and the spreading stabilizes when the droplet mainly solidifies. Droplet spreading is more in non-equilibrium solidification because of undercooling effect at the initial stage of solidification which

delays the solidification and spreading continues for a longer time. The spreading ratio in the non-equilibrium solidification is found to be closer to the experimentally measured value. Figure 5 shows the comparison of temperature history just above the substrate-droplet contact point (at the central axis) as predicted by equilibrium and non-equilibrium solidification model. In the case of equilibrium solidification, the temperature first decreases and then remain constant ($T_M$ ) during the progress of the phase change. However, in the case of non-equilibrium solidification, initially, the temperature decreases up to the nucleation temperature ($T_N$) and then solidification initiates. This stage is undercooling. With progress in solidification, temperature increases up to the melting temperature ($T_M$). This is due to the rapid evolution of latent heat during solidification. This stage is recalescence. Once the temperature reaches the melting temperature ($T_M$) further solidification progresses at this temperature. During this stage, it is observed that in between this stage there is a slight increase in temperature (A′) for a short time interval due to recoiling of warm water from the periphery towards the center caused by the surface tension effect. The equilibrium model also showed this behaviour (A). Figure 6 shows, the evolution of solidified thickness (position of solid-liquid interface form the substrate). In case of the non-equilibrium model, the solidified thickness is lower as compared to the equilibrium solidification as the initiation of solidification is delayed due to undercooling effect. The delay in initiation of solidification in the case non-equilibrium model can be clearly seen in fig. 6 from the solidified thickness versus time plot.

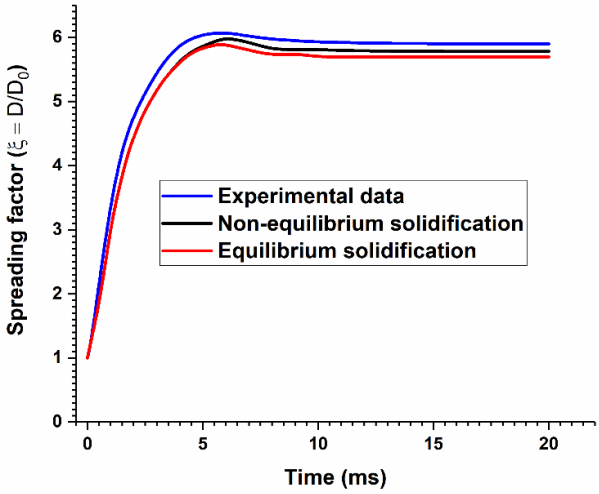


FIGURE 4: Comparison of spreading factor

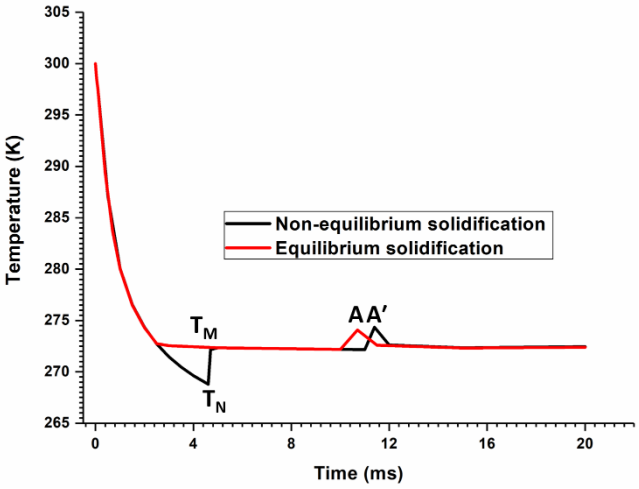


FIGURE 5: Temperature history at just above the contact point

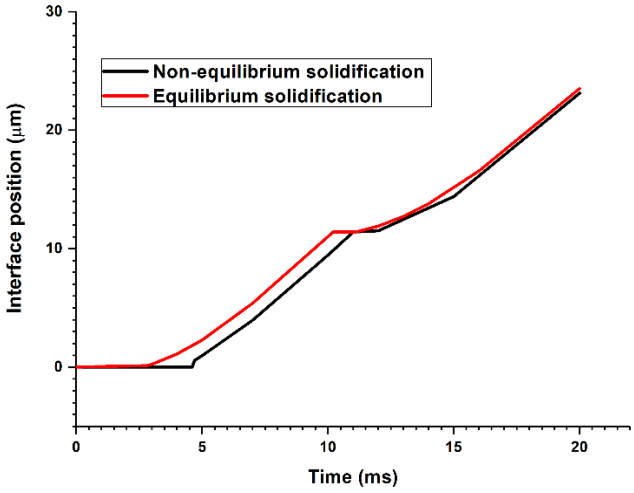


FIGURE 6: Interface position from the substrate with time

## 4. CONCLUSIONS

The effect of equilibrium and non-equilibrium solidification on solidified thickness evolution, temperature history and droplet spreading are investigated and compared to a water droplet impact and spreading on a substrate. Droplet spreading is observed to be more in the non-equilibrium solidification as compared to the equilibrium solidification and it is in closer agreement to the experimental data. In the non-equilibrium solidification case, the initiation of solidification is delayed and the solidified thickness evolves slowly than the equilibrium solidification case. As compare to the equilibrium solidification, temperature history in the non-equilibrium solidification evolves dynamically during the phase change, nucleation, undercooling and recalescence are successfully captured.

## REFERENCES

[1] V. Roisman, R. Rioboo, C. Tropea, Normal impact of a liquid drop on a dry surface: model for spreading and receding, *Proc. R. Soc. Lon,* A 458, 1411-1430, 2022.

[2] L. Zheng, Z. Li, S. Bourdo, K.R. Khedir, M.V. Bahadur, L. Mishchenko, B. Hatton, J.A. Taylor, J. Aizenberg, T. Krupenkin, Exceptional superhydrophobicity and low velocity impact icephobicity of acetone-functionalized carbon nanotube films, *Langmuir,* 27, 14143-14150, 2011.

[3] J. Hua, K. Xua, Y. Wub, B. Lana, X. Jianga, L. Shua, The freezing process of continuously sprayed water droplets on the superhydrophobic silicone acrylate resin coating surface, *Applied Surface Science*, 317, 534-544, 2014.

[4] R. K. Shukla, V. Patel, A. Kumar, Modeling of rapid solidification with undercooling effect during droplet flattening on a substrate in coating formation, *Journal of Thermal Spray Technology*, https://doi.org/10.1007/s11666-017-0666-y, 1-19, 2017.

[5] H. Zhang, X.Y. Wang, L.L. Zheng, S. Sampath, Numerical simulation of nucleation, solidification, and microstructure formation in thermal spraying, *Int. J. Heat Mass Transf.,* 47, 2191-2203, 2004.

[6] G. Chaudhary R. Li, Freezing of water droplets on solid surfaces: An experimental and numerical study, *Experimental Thermal and Fluid Science*, 57, 86–93, 2014.

[7] J.U. Brackbill, D.B. Kothe, C. Zemach, A continuum method for modeling surface tension, *J. Comput. Phys*. 100, 335-354, 1992.

[8] A. Kumar, S. Gu, H. Tabbara, S. Kamnis, Study of impingement of hollow ZrO2 droplets onto a substrate, *Surf. Coatings Technol*. 220, 164-169, 2013.

[9] N. Pathak, A. Kumar, A. Yadav, P. Dutta, Effects of mould filling on evolution of the solid-liquid interface during solidification, *Appl. Therm. Eng*., 29, 3669-3678, 2009.

[10] J.B. Cohen, Dendrite growth velocity in undercooled nickel melts, *Acta Metallurgica,* 10, 895-897, 1962.

Fifth International Conference on Computational Methods for Thermal Problems
THERMACOMP2018, July 9-11, 2018, Indian Institute of Science, Bangalore, INDIA
*N. Massarotti, P. Nithiarasu, Pradip Dutta and C. Ranganyakalu (Eds.)*

# Prediction of Thermal Characteristics of Double Pass Solar Air Heater (DPSAH) Using Artificial Neural Network (ANN) and Validated by Analytical Method

**G.Kunal[a], A.K.Raj and S.Jayaraj**

Department of Mechanical EngineeringNIT Calicut-673601, INDIA [a]kunalgarud1@gmail.com

## ABSTRACT

This paper represents prediction of performance parameters of counter flow double pass solar air heater (DPSAH) using artificial neural network (ANN) model along with validation of developed model and experimental results by analytical method. Experiments were conducted at solar energy centre of NIT Calicut (11.15°N, 75.49°E) India in the month of March and April, 2017 from 09:00 to 17:00 hrs under clear sky conditions. Experimental data was used to develop ANN model with Feed Forward Back Propagation (FFBP) learning algorithm with its LM (Lavenberg Marguardt) variant by using two transfer functions Tan-sigmoidal and Logistic-sigmoidal having 10 hidden neurons. Results shows that developed ANN model with both transfer function and same training algorithm predicts closer results to the experimental results having R=0.99. Experimental results were validated by analytical method by developing code in C (by gauss seidel iterative method) having average error of 6-8%.

**Keywords:** *Solar energy, DPSAH, ANN*

## 1. INTRODUCTION

Applications of artificial intelligence techniques have been increased drastically in last two decades to predict performance of renewable energy systems due to uncertain relation between performance parameters of such systems and factors affecting these parameters. A theoretical model was developed by Ong [1] for estimation of performance of four different configuration of flat plate solar collectors. Naphon et al [2] have compared performance of double pass solar air heaters with and without porous media by their developed mathematical model. Neural network with LM learning algorithm with 20 hidden neurons was developed by Caner et al. [3] accurately predict the thermal characteristics of solar collectors.

## 2. METHODOLOGY

### 2.1 ANN Model:

Experiments were conducted from 09:00 to 17:00 and temperatures of glazing cover, both channel passages, absorber plate and bottom plate were measured at every 10 minutes interval. Hence we have 49 data points for each temperature. For ANN model based on this experimental data we have taken insolation (I) and ambient temperature ($T_a$) as input parameters because they are the most significant factors that affect the performance parameters those are glass cover temperature ($T_g$), air temperature in channel 1 and 2 ($T_{f1}$ and $T_{f2}$), absorber plate temperature ($T_p$), bottom plate temperature ($T_b$) and efficiency ($\eta$) of air heater which were taken as output parameters. With these input and output parameters ANN model was trained by back propagation algorithm, LM variant with tan-sigmoidal and log-sigmoidal transfer functions having 10 hidden neurons.

Input and output from the experiments were taken as input and target of the ANN model. With these inputs and target, network was trained by two combination of algorithms till predicted output approaches to target. This can be done by adjusting the weights between the layers. Neural network with proper combination of algorithm and hidden neurons which shows minimum error was taken as optimal configuration for performance prediction. Fig. 1 shows ANN model with its three layers and number of neurons (parameters) in each layer for DPSAH.

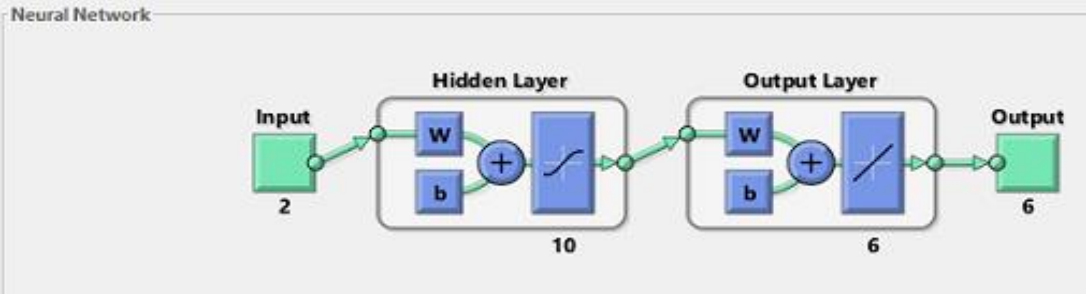


**Fig. 1 Structure of ANN model developed for DPSAH**

2.2 Analytical Solution:

Temperatures at various locations of air heater were obtained analytically by applying energy balance for each part of air heater. By applying energy balance for glass cover, both the channels, absorber and bottom plate, we have obtained following 5 equations. These equations were solved by gauss-seidel iterative method.

(1) Energy balance for glass cover

$$I\alpha_g = h_{(g-a)} (T_g - T_a) + h_{r,(g-sky)} (T_g - T_{sky}) + h_{(g-f1)} (T_g - T_{f1}) + h_{r,(g-p)} (T_g - T_p) \ldots\ldots \quad (1)$$

(2) Energy Balance for channel 1

$$m\, c \frac{dT_{f_1}}{dx} = h_{(f1-g)} A_g (T_g - T_{f1}) + h_{(f1-p)} A_p (T_p - T_{f1}) \ldots\ldots \quad (2)$$

(3) Energy balance for absorber plate

$$I\, \alpha_p\, \tau_g = h_{(f1-p)} (T_p - T_{f1}) + h_{(p-f2)} (T_p - T_{f2}) + h_{r,(p-g)} (T_p - T_g) + h_{r,(p-b)} (T_p - T_b) \ldots\ldots (3)$$

(4) Energy Balance for Channel 2

$$m\, c \frac{dT_{f_2}}{dx} = h_{(f2-p)} A_p (T_p - T_{f2}) + h_{(f2-b)} A_b (T_b - T_{f2}) \ldots\ldots (4)$$

(5) Energy Balance for Bottom plate

$$h_{(f2-b)} (T_b - T_{f2}) + h_{r,(b-p)} (T_b - T_p) = 0 \ldots\ldots (5)$$

Where h is the heat transfer coefficient, A is surface area, α is the absorptivity, τ is the transmissivity $T_{sky}$ is the sky temperature, m is the mass of fluid and suffix r, g, f1, p, f2, and b indicate radiative, glass cover, fluid in channel 1, absorber plate, fluid in channel 2 and bottom respectively.

For solving equations (2) and (4) we have taken boundary conditions as,

At x=0 $T_{f1} = T_a$

At x=L $T_{f1} = T_{f2}$

Calculation of heat transfer coefficient, sky temperature and mass of fluid were done based on various correlation obtained from reference [1]. For obtaining solution of these equations we have assumed steady state condition.

## 3. RESULTS

We have 49 data points for each parameter which is divided in to two part: one part having 40 data points were used to train the neural network with LM algorithm and two transfer functions having 10 hidden neurons. Trained neural network for 40 data points with this algorithm shows overall accuracy R (correlation coefficient) = 0.99 for both the transfer functions as shown in Fig 2(a) and 2(b). Now this trained ANN model is validated by predicting output for remaining 9 data points for which we have only entered their input parameter values. Output predicted by both the algorithm shows closer agreement with the experimental results as shown in Figs. 3(a) to 3(f).

Experimental results were validated by solving 5 energy balance equations which predict the temperatures at various locations of air heater. Equations were solved by gauss seidel iterative method by developing c code. Temperatures were obtained by solving these equations show very good accuracy with the experimental results as shown in Fig. 3(a) to 3(f). Average error in $T_g$, $T_{f1}$, $T_p$, $T_{f2}$ and $T_b$ were calculated as 0.66%, 3.66%, 8.42%, 7.97% and 8.77% respectively.

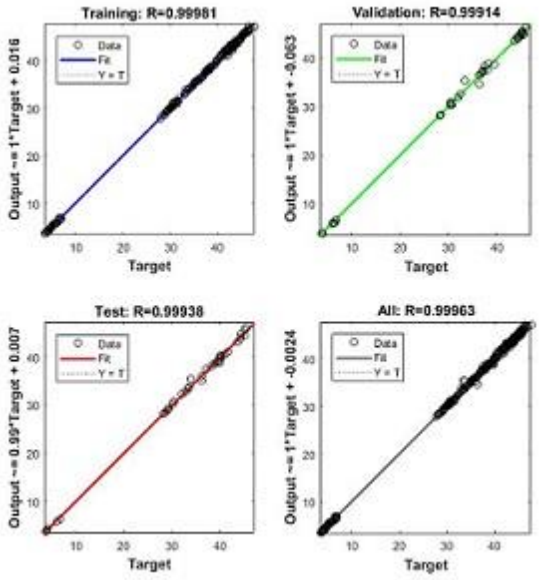


**Fig. 2 (a)**

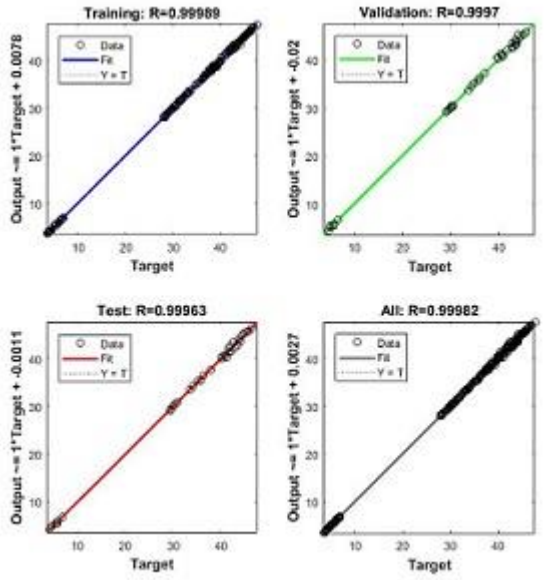


**Fig. 2 (b)**

**Fig. 2(a) and 2(b) Accuracy of trained ANN by tan-sigmoidal and Log-sigmoidal respectively**

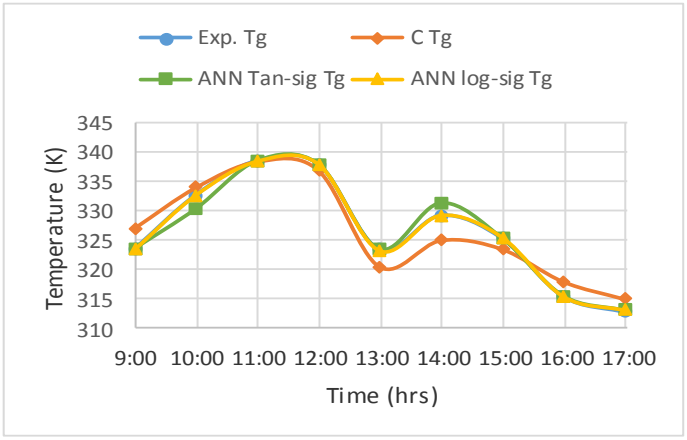


**Fig. 3 (a)**

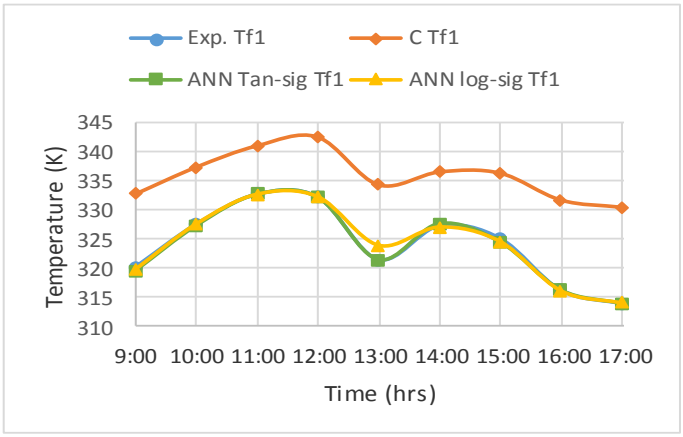


**Fig. 3 (b)**

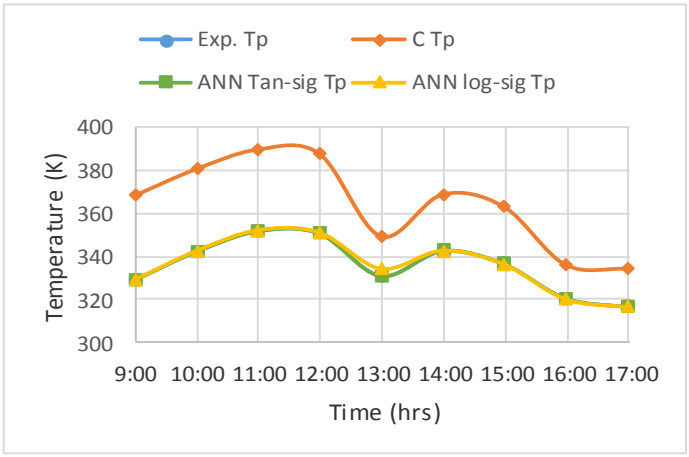


**Fig. 3 (c)**

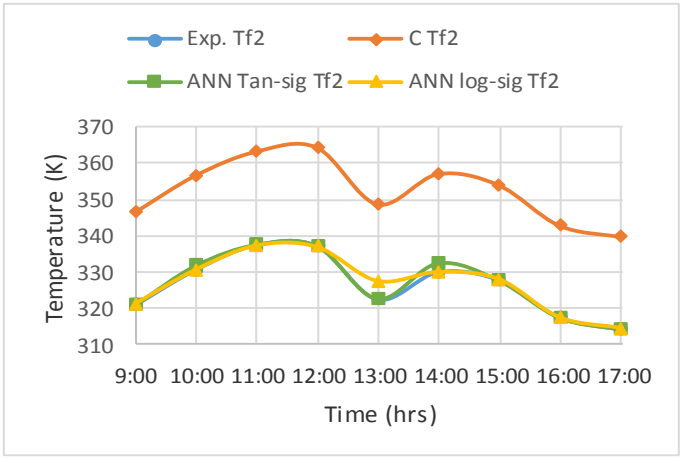


**Fig. 3 (d)**

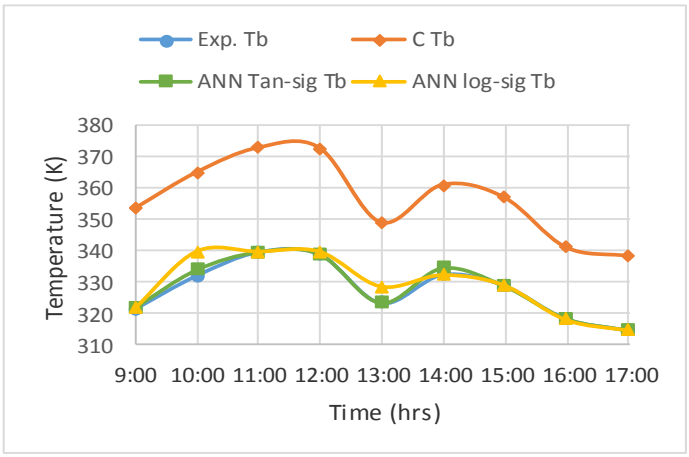


**Fig. 3 (e)**

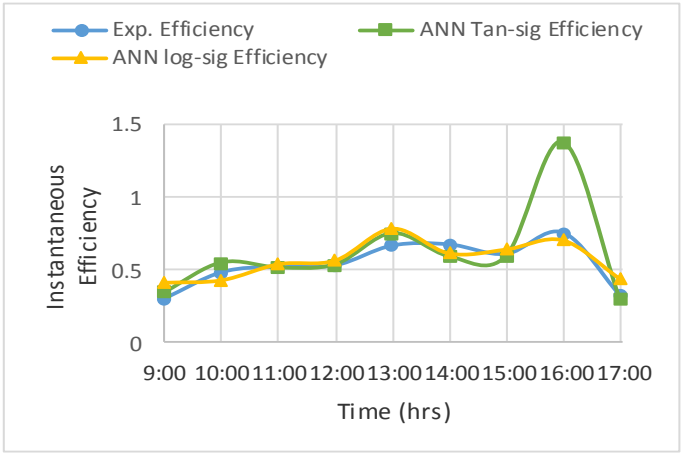


**Fig. 3 (f)**

**Figs. 3(a) to 3(f) Comparison of Experimental, C code and ANN for various parameters**

## 4. CONCLUSIONS

ANN model was developed based on experimental results of DPSAH. From the experiments we found that insolation and ambient temperature are the most important factors that affect the performance of air heater. Hence we have only considered these two parameters as input parameters of ANN. ANN model was trained by using feed forward back propagation (FFBP) algorithm with LM variant and two transfer functions (Tan-sig and Log-sig) having 10 hidden neurons. Developed ANN model with same variant and different transfer functions show very good agreement (R=0.99) with the experimental results. But as we compared results of both the transfer functions, they show almost similar accuracy for all the parameters except efficiency. For efficiency log-sigmoidal shows more accurate results than tan-sigmpidal. From efficiency graph we can observe that efficiency is maximum at 16:00 hrs because at this time insolation was very low and absorber contains some heat from previous hrs high insolation hence absorber was capable to transfer heat to the air even though insolation was very low. So according to definition of instantaneous efficiency ratio of heat gain by air to heat absorbed by collector increases. This means because of supply of heat from collector to air at very low insolation, the quantity heat gain becomes higher than absorbed energy of collector.

Hence this point has maximum value of efficiency. Experimental results of air heater was validated analytically by solving energy balance equations by Gauss Seidel method with C code. Analytical solution by C code shows closer agreement with the experimental results having average error for all the parameters is equal to 6-8%.

## REFERENCES

1. Ong, K. S. (1995). Thermal performance of solar air heaters—Experimental correlation. *Solar Energy*, *55*(3), 209-220.
2. Naphon, P. (2005). Effect of porous media on the performance of the double-pass flat plate solar air heater. *International communications in heat and mass transfer*, *32*(1-2), 140-150.
3. Caner, M., Gedik, E., & Keçebaş, A. (2011). Investigation on thermal performance calculation of two type solar air collectors using artificial neural network. *Expert Systems with Applications*, *38*(3), 1668-1674.

Fifth International Conference on Computational Methods for Thermal Problems
THERMACOMP2018, July 9-11, 2018, Indian Institute of Science, Bangalore, INDIA
*N. Massarotti, P. Nithiarasu, Pradip Dutta and C. Ranganyakalu (Eds.)*

# Estimation of Approximate Temperature Distribution in Annular Fins of Hyperbolic Profile by Power Series Method and Comparison of it with Exact Solution by Modified Bessel Function

**G.Kunal[a], A.K.Raj and S.Jayaraj**

Department of mechanical engineering, NIT Calicut-673601, INDIA [a]kunalgarud1@gmail.com

## ABSTRACT

This paper elaborates comparison of approximate analytical solution of temperature distribution by power series method of various order with the exact solution by modified Bessel equation in annular fin of hyperbolic profile. Solution of differential equation that governs heat transfer in a fin was obtained by power series (Frobenious) method with different order (3 and 5) of series and Modified Bessel function (2nd order 2nd kind). Temperature distribution were obtained by solving differential equation of both the methods with the code developed in Matlab 2017a. Comparison of both the methods were done for different values of enlarged biot number and radius ratio. From the results obtained, we can conclude that temperature distribution solution by power series method (approximate solution) approaches to Modified Bessel (exact) solution as we increase the order of power series, higher order of the series gives more closer results to exact solution.

**Keywords:** *Annular fins, Modified Bessel function, Power series method, Temperature*

## 1. INTRODUCTION

Annular fins of hyperbolic profile has higher rate of heat transfer than other type (straight and parabolic profile) of fins because according to geometrical configuration it has maximum area nearer to its centre axis and from centre to edge it is reducing, hence its effective area to transfer the heat is more compare to other type of fins. Hence heat transfer rate and temperature distribution of such a fins has significant important to estimate. Many literatures have been found out for estimation of performance of such a fins. Campo et al. [1] have found out approximate temperature distribution in straight annular fins by power series method and compared it with exact solution by modified Bessel function which they have solved using maple (Mathematica). Arauzo et al. [2] have estimated temperature distribution and efficiency of annular fins of hyperbolic profile with their power series solution of order 5 and 10 and compared it with exact solution with different combination of enlarged biot number and radius ratio.

## NOMENCLATURE:

| | | | |
|---|---|---|---|
| C | normalized radius ratio = $r_1/r_2$ | | |
| h | convective heat transfer coefficient | | |
| $I_0$ | Modified Bessel function of first kind zero order | | |
| $K_0$ | Modified Bessel function of second kind zero order | $r_1$ | inner radius |
| K | Thermal conductivity | $r_2$ | outer radius |
| M | enlarged biot number = $\frac{h\, r_2^3}{k}$ | T | temperature |
| R | dimensionless parameter = $r/r_2$ | $T_\infty$ | fluid temperature |

## 2. MATHEMATICAL MODELLING

Assumptions:

- Steady state condition.
- Thermal conductivity k independent of temperature T.
- Only radial conduction (one dimensional conduction).
- No internal heat generation.
- Heat loss from the tip is negligible.
- Profile $y(r) = \frac{1}{r}$

### 2.1 Modified Bessel Function:

Heat Balance:

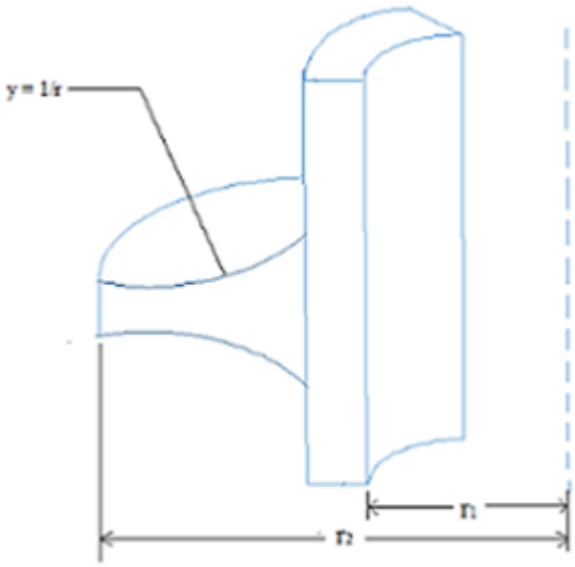


**Fig.1 Section view of hyperbolic fin**

$Q_r = Q_{r+\Delta r} + Q_{convection}$

$Q_r = Q_r + \frac{d(Q_r)}{dr}dr + Q_{convection}$

$\frac{d(Q_r)}{dr}\,dr + Q_{convection} = 0$ …… (a)

$\frac{d}{dr}(-k2\Pi r y(r)\frac{dT}{dr})\,dr + h\,(2\Pi r ds)(T-T_\infty) = 0$

$\frac{d}{dr}(r\,y(r)\frac{dT}{dr}) - \frac{h\,r}{k}(T-T_\infty) = 0$

$\frac{d^2\Theta}{dr^2} - \frac{h\,r}{k}\Theta = 0$

$\frac{d^2\Theta}{dR^2} - \frac{h\,r_2^3}{k}R\,\Theta = 0$

$\frac{d^2\Theta}{dR^2} - M^2 R\,\Theta = 0$ ……. (b)

Solution of this equation is given by,

$\Theta(R) = \frac{1}{3}R^{1/2}[C_1 I_{-(1/3)}(\frac{2}{3}MR^{\frac{3}{2}}) - C_2 I_{(1/3)}(\frac{2}{3}MR^{\frac{3}{2}})]$ …….. (c)

Boundary conditions

At R = C, Θ = 1

$1 = \frac{1}{3}C^{1/2}[C_1 I_{-(1/3)}(\frac{2}{3}MC^{\frac{3}{2}}) - C_2 I_{(1/3)}(\frac{2}{3}MC^{\frac{3}{2}})]$ ……. (d)

At R = 1, $\frac{d\Theta}{dR} = 0$ {Here we used properties of Bessel function as

$\Theta(1) = \frac{1}{3}[C_1 I_{-(1/3)}(\frac{2}{3}M) - C_2 I_{(1/3)}(\frac{2}{3}M)]$ $\frac{d[x^{-n}J_n(x)]}{dx} = x^{-n}J_{n+1}(x)$

$\frac{d\Theta}{dR} = \frac{1}{3}[C_1 I_{(2/3)}(\frac{2}{3}M) - C_2 I_{(-2/3)}(\frac{2}{3}M)]$ $\frac{d[x^{n}J_n(x)]}{dx} = x^{n}J_{n-1}(x)$ [3]}

$\frac{1}{3}[C_1 I_{(2/3)}(\frac{2}{3}M) - C_2 I_{(-2/3)}(\frac{2}{3}M)] = 0$ …… (e)

Solve the equation (d) and (e)

$$\Theta = (\frac{R}{C})^{1/2}[\frac{I_{(1/3)}(\frac{2}{3}MR^{\frac{3}{2}})I_{(2/3)}(\frac{2}{3}M) - I_{(-1/3)}(\frac{2}{3}MR^{\frac{3}{2}})I_{(-2/3)}(\frac{2}{3}M)}{I_{(1/3)}(\frac{2}{3}MC^{\frac{3}{2}})I_{(2/3)}(\frac{2}{3}M) - I_{(-1/3)}(\frac{2}{3}MC^{\frac{3}{2}})I_{(-2/3)}(\frac{2}{3}M)}] \text{ ……. (1)}$$

Equation (1) is the exact Solution by using Bessel function.

2.2. Power series method:

$\frac{d^2\Theta}{dR^2} - M^2 R\,\Theta = 0$

Series solution of this equation is given by,

$\Theta = \sum_{r=0}^{\infty} C_n R^n$…….. (f)

$\Theta' = \sum_{r=1}^{\infty} C_n n\, R^{n-1}$

$\Theta'' = \sum_{r=2}^{\infty} C_n n\,(n-1) R^{n-2}$

Put above values in governing equation

We get,

$C_{n+2} = \frac{M^2(C_{n-1}+C_n)}{(n+1)(n+2)}$ [Put n=0, 1, 2, 3, 4]

$C_2 = \frac{M^2}{2}C_0$, $C_3 = \frac{M^2}{6}C_0$, $C_4 = \frac{M^4}{24}C_0$, $C_5 = \frac{M^4}{120}C_0$

$\Theta = C_0 + C_1R + C_2R^2 + C_3R^3 + C_4R^4 + C_5R^5$ [for order 5]

$\Theta = C_0 + C_2(R-1)^2 + C_3(R-1)^3 + C_4(R-1)^4 + C_5(R-1)^5$ [take 1 as a centre point]

At R = 1, $\frac{d\Theta}{dR} = 0$ hence $C_1 = 0$

At R = C, Θ = 1

$1 = C_0 + \frac{M^2}{2}C_0(C-1)^2 + \frac{M^2}{6}C_0(C-1)^3 + \frac{M^4}{24}C_0(C-1)^4 + \frac{M^4}{120}C_0(C-1)^5$

$1 = C_0[1 + \frac{M^2}{2}(C-1)^2 + \frac{M^2}{6}(C-1)^3 + \frac{M^4}{24}(C-1)^4 + \frac{M^4}{120}(C-1)^5]$ …… (g)

Take, $M^2 = 5$ and C = 0.2 in equation (g)

$$1 = C_0\left[1 + \frac{5}{2}(0.8)^2 - \frac{5}{6}(0.8)^3 + \frac{25}{24}(0.8)^4 - \frac{25}{120}(0.8)^5\right]$$

$$C_0 = 0.4175, \quad C_2 = 1.04375, \quad C_3 = 0.3479, \quad C_4 = 0.4348, \quad C_5 = 0.26093$$

Series solution of order 5 is given by,

$$\Theta(5) = 0.4175 + 1.04375(R-1)^2 + 0.3479(R-1)^3 + 0.4348(R-1)^4 + 0.26093(R-1)^5 \quad ..(2)$$

Same way series solution of order 3 is given by,

$$\Theta(3) = 0.46 + 1.15(R-1)^2 + 0.38(R-1)^3 \quad ..... (3)$$

From equation (1) [Put $M^2 = 5$ and C = 0.2]

$$\Theta = \left(\frac{R}{0.2}\right)^{1/2}\left[\frac{I_{(1/3)}\left(\frac{2}{3}\sqrt{5}R^{\frac{3}{2}}\right)I_{(2/3)}\left(\frac{2}{3}\sqrt{5}\right) - I_{\left(-\frac{1}{3}\right)}\left(\frac{2}{3}\sqrt{5}R^{\frac{3}{2}}\right)I_{\left(-\frac{2}{3}\right)}\left(\frac{2}{3}\sqrt{5}\right)}{I_{(1/3)}(0.133)I_{(2/3)}(1.49) - I_{\left(-\frac{1}{3}\right)}(0.133)I_{\left(-\frac{2}{3}\right)}(1.49)}\right] \quad ..... (4)$$

## 3. RESULTS:

Matlab code is developed to solve equation (2), (3) and (4). Comparison of temperature solution by modified Bessel function and power series of order 3 and 5 are shown in Fig. 2. From figure we can conclude that as we increase order of series solution will approach to exact solution. This comparison was done for $M^2 = 5$ and C = 0.2. If we take different values of radius ratio c= 0.4, 0.6, 0.8, 1 and same biot number, power series solution of order 5 approaches to exact solution with very good accuracy.

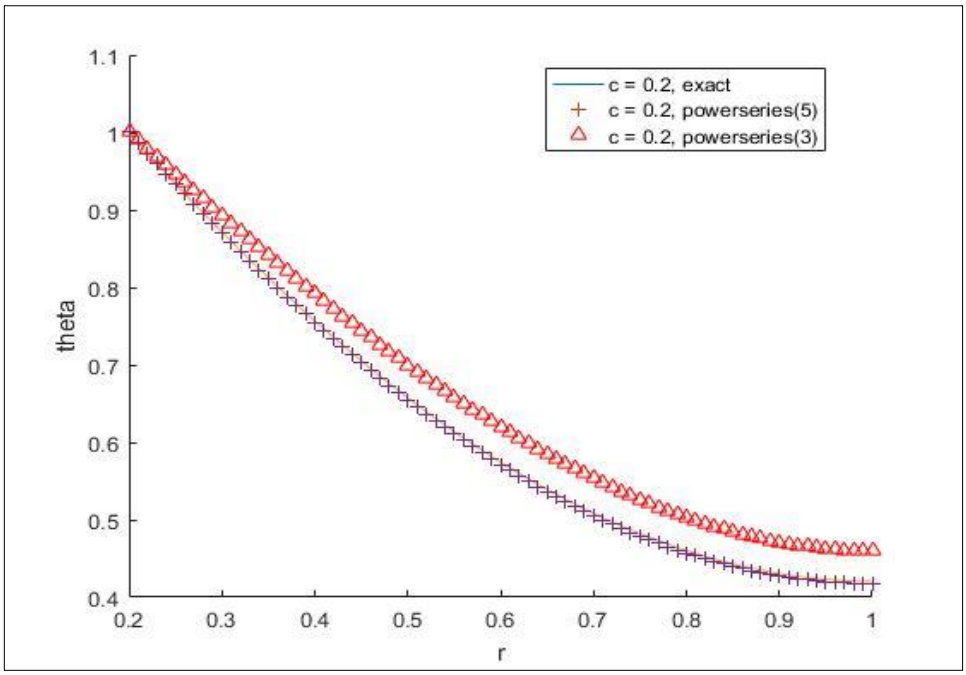


**Fig. 2 Comparison of power series solution of order 3 and 5 with exact solution for C=0.2**

## 4. CONCLUSIONS

Solution of ordinary differential equations with variable coefficients (modified Bessel function) which represents heat transfer from annular fins are complex. This paper represents solution of such a problem by using power series method of different order and comparing it with exact solution. From the results obtained, we can conclude that increase in the order of power series solution leads to more accurate results and it almost approaches to exact solution at higher order. Exact solution of temperature distribution in annular fin of hyperbolic profile by modified Bessel function was compared to power series solution of order 3 and 5 in this paper. Power series solution of order 5 shows more closely results to exact one for all the values of radius ratio (C).

## REFERENCES

1. Campo, A., & Rodrfguez, F. (1998). Approximate analytic temperature solution for uniform annular fins by adapting the power series method. *International communications in heat and mass transfer*, *25*(6), 809-818.
2. Arauzo, I., Campo, A., & Cortés, C. (2005). Quick estimate of the heat transfer characteristics of annular fins of hyperbolic profile with the power series method. *Applied thermal engineering*, *25*(4), 623-634.
3. Grewal, B. S. (1996). Higher engineering mathematics. *2002, Khanna Publishers, New Delhi*.

# Exergy performance of a low-tech PhotoVoltaic/Thermal (PVT) collector with and without thermal insulation

**Francesco Calise**

Department of Industrial Engineering, University of Naples Federico II P.le Tecchio 80, 80125, Naples, Italy, frcalise@unina.it

**Rafal Damian Figaj**

Department of Engineering, University of Naples Parthenope, Centro Direzionale IS.C4, 80143, Naples, Italy, rafal.figaj@uniparthenope.it

**Laura Vanoli**

Department of Civil and Mechanical Engineering, University of Cassino and Southern Lazio, V. Di Biasio 43, Cassino, 03043, Italy, vanoli@unicas.it

Department of Engineering, University of Naples Parthenope, Centro Direzionale IS.C4, 80143, Naples, Italy

## ABSTRACT

This paper presents a one-dimensional finite-volume model of an unglazed and not insulated photovoltaic/thermal solar collector. The type of collector consists of a conventional PV collector including a roll bond heat exchanger. The unit was discretized along the longitudinal direction of the cogenerative collector. This paper is based on previous works, where the PVT collector without any back insulation is experimentally and numerically analysed. In the present study, different insulation materials and thicknesses are analysed numerically as a possible integration of back insulation layer. In particular, the exergy performance is analysed with and without insulation. The experimental data are used in order to simulate the operation of the collector with different back insulation configurations. The analysis of the performance is performed along the discretization direction for all considered configurations.

**Key Words:** *PVT Collector, Finite Volume, Exergy Analysis.*

## 1. INTRODUCTION

The actual trends show that solar energy is one of the most sustainable renewable energy sources. Traditionally, thermal and electrical energy are produced separately with solar thermal collectors and photovoltaic panels, respectively. On the contrary, hybrid PhotoVoltaic/Thermal collector (PVT) technology allows one to produce simultaneously thermal and electrical energy using the available solar radiation [1]. Such configuration has the advantages of the cooling of the photovoltaic module coupled with the production of thermal energy [2]. Although numerical and experimental investigations of PVT collectors have been widely discussed in scientific literature, there is a scarce focus on the investigation of low cost/tech PVT units. For such reason, this paper presents a detailed finite-volume model of a commercially available photovoltaic/thermal solar collector, manufactured by the Italian Company AV Project (Figure 1). The unit has been previously investigated from both energy and exergy points of view [3, 4], along with a possible energy performance increase achievable with the integration of a back-side insulation [5]. Here, the exergy performance is numerically analysed considering different insulation materials and thicknesses. In particular, the experimental data collected for the unit without insulation are used in order to simulate the operation of the collector with different back insulation configurations. The performance is also analysed along the discretization direction for all the considered configurations.

## 2. COLLECTOR DESCRIPTION AND NUMERICAL MODEL

The collector includes a roll bond heat exchanger and a conventional PV panel (Figure 1). The photovoltaic module was a high efficiency polycrystalline silicon panel and the aluminium roll bond heat exchanger was equipped with a separated double circuit in order to distribute the cooling fluid across the channels. The photovoltaic module and the heat exchanger were bonded with a butyl resin. The collector configuration does not include any glass cover or back and insulation. The operating fluid, flowing inside the channels of the absorber, was water. The collector was 1644 mm high and 992 mm wide, with a useful area of the photovoltaic module of 1.44 $m^2$. The absorber plate was equipped with 48 channels.

FIGURE 1. JANUS PVT COLLECTOR

A 1-dimensional finite-volume model has been developed (Figure 2).

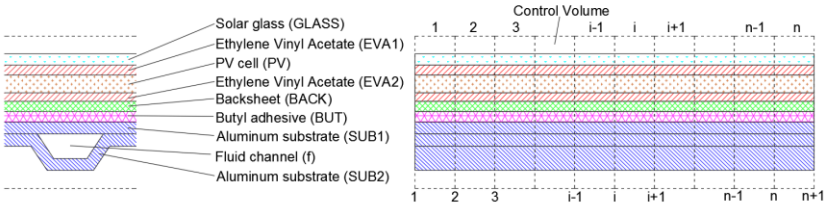


FIGURE 2. DISCRETIZATION OF THE COMPUTATIONAL DOMAIN

The model calculates the thermodynamic parameters, heat flows, electrical powers and exergy parameters along the direction of the heat transfer fluid passing through the PVT collector. Mass, energy and exergy balance equations have been implemented for each computational domain element using Engineering Equation Solver (EES) software. The collector was divided in several parts, as outlined in Figure 2. The following assumption were considered:

- thermodynamic equilibrium and steady state conditions;
- negligible kinetic and gravitational terms in the energy balances;
- uniform distribution and absorption of the solar radiation;
- constant thermal conductivity of solid materials;
- uniform temperature distribution in each solid material of the computational domain element;
- linear variation of the fluid temperature between the inlet and outlet of the domain element.

The collector was discretized along its longitudinal axis in n elementary slices, thus, n+1 nodes of the computational domain were considered. For such domain, the inlet and outlet thermodynamic conditions for slice 1 and n, respectively, were the boundary conditions used for the simulation of the PVT collector. In order to reduce the error of the linearization of the temperature profile, a number of 20 elements was adopted during the simulation. Finally, the model parameters were accurately selected according to the manufacturer's data.

The analytical model of the collector without and with back-side insulation is reported in Ref. [3, 5], thus only the global exergy balance is reported here sake of brevity:

$$A_{PVT,i} I_{tot,i} (1-\rho_{GLASS}) \left(1-\frac{T_0}{T_{sun}}\right) = m\left(ex_{ph,f,out} - ex_{ph,f,in}\right) + A_{PVT,i} I_{tot,i} \eta_{PV,i} + h_{GLASS,i} A_{PVT,i} (T_{GLASS,i} - T_{AIR}) \left(1-\frac{T_0}{T_{GLASS,i}}\right) +$$
$$+\varepsilon_{GLASS} \sigma A_{PVT,i} \left(T^4_{GLASS,i} - T^4_{AIR}\right) \left(1-\frac{T_0}{T_{GLASS,i}}\right) + \varepsilon_{SUB2} \sigma A_{SUB2,i} \left(T^4_{SUB2,i} - \varepsilon_{GROUND} T^4_{GROUND,i}\right) \left(1-\frac{T_0}{T_{SUB2,i}}\right) + \quad (1)$$
$$+h_{SUB2,i} A_{SUB2,i} (T_{SUB2,i} - T_{AIR}) \left(1-\frac{T_0}{T_{SUB2,i}}\right) + Ex_{d,i}$$

## 3. RESULTS

In this study, previously collected experimental data were used. Total solar radiation, air and ground temperature, PVT inlet/outlet water temperature, PVT bottom side temperature and water flow rate were sampled with a 1.00 minute time period (Figure 3). The flow was set to 5.00 l/min, thus, to 1.25 l/min per each collector. The details of the experimental set-up is reported in Ref. [3]

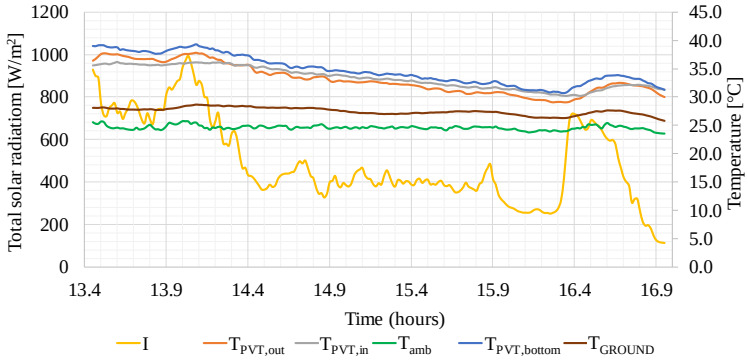


FIGURE 3.EXPERIMENTAL DATA MEASURED FOR THE NOT INSULATED COLLECTOR [3].

The numerical results carried out by the developed model were compared with the experimental one, showing good agreement [3, 4].
Rock wool, polyester and polyurethane foam with different thicknesses (3.0, 5.0 and 7.0 cm) are used in order to perform the comparison. In particular, thermal conductivity of 0.018, 0.030 and 0.035 W/(m K) was adopted for the polyurethane foam, polyester and rock wool, respectively.
In this paper, only some results of the exergy analysis are reported for sake of brevity. The difference of the exergy product between insulated and not insulated PVT unit for an insulation thickness of 5.0 cm is reported in Figure 4.

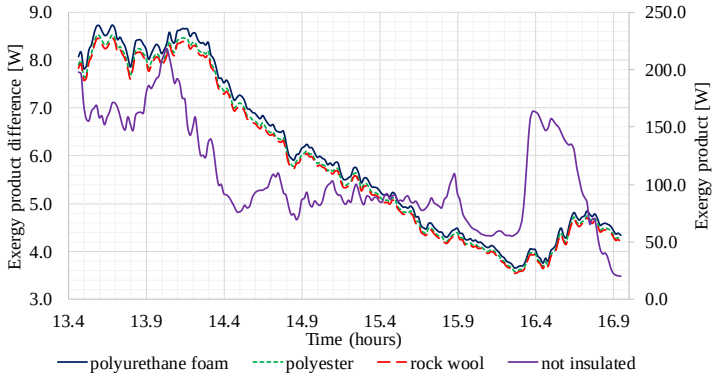


FIGURE 4. EXERGY PRODUCT DIFFERENCE BETWEEN INSULATED AND NOT INSULATED PVT UNIT, INSULATION THICKNESS 5.0 CM.

As expected, the exergy product in case of polyurethane foam is the highest, while for the other two insulation materials this increase is lower. This is achieved because the thermal conductivity of polyester and rock wool is higher compared to the polyurethane foam. Thus, lower exergy losses and a higher exergy product are achieved. The exergy product increase ranges between 3.5 and 8.7 W. It is worth noting that higher differences are achieved in case of higher solar radiation. For the other thicknesses, a similar increase is achieved.

In Figure 5, the destroyed exergy and exergy efficiency differences are reported along the computational domain for a thickness of 5.0 cm. The destroyed exergy of insulated units decreases along the fluid direction. In fact, the fluid temperature increases along x axis, and this increase is higher in case of thermal insulation. However, the difference among the insulation materials is negligible, as outlined by the overlapping trends. A higher fluid temperature allows one to achieve a higher exergy efficiency along the fluid flow direction, since the negative effect of a higher operating temperature on the electrical power is scarce. The exergy efficiency increase ranges between 0.14 and 0.22 %. The analysis revealed that the variations are similar in case of other thicknesses.

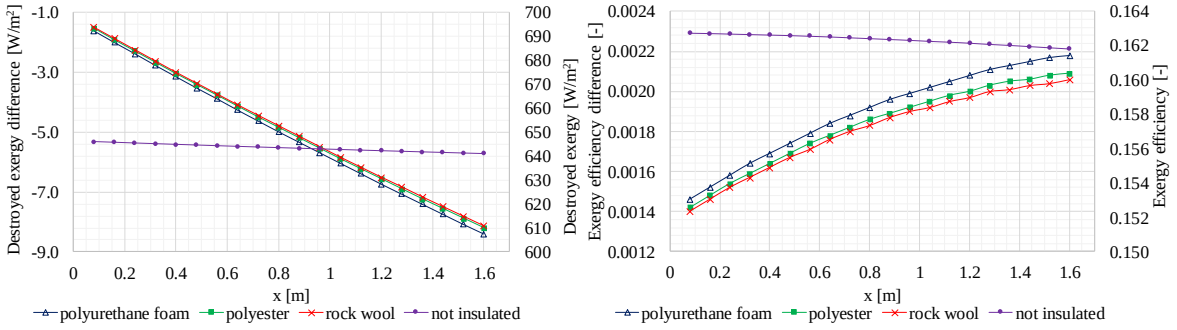


FIGURE 5. DESTROYED EXERGY DIFFERENCE (LEFT) AND EXERGY EFFICIENCY DIFFERENCE (RIGHT) BETWEEN INSULATED AND NOT INSULATED PVT UNIT, INSULATION THICKNESS 5.0 CM.

## 4. CONCLUSIONS

Although an increase of the thermal output of the unit due to insulation, the exergy performance slightly increases for all the selected cases. This increase does not significantly affect the electrical output of the unit, due to the limited operating temperature increase. Future developments will include a sensitivity analysis as a function of the main operating/design parameters.

## REFERENCES

[1] Zondag HA, Flat-plate PV-Thermal collectors and systems: A review. *Renewable and Sustainable Energy Reviews*,12, 891-5.2008.

[2] Chow TT, A review on photovoltaic/thermal hybrid solar technology, *Applied Energy*, 87, 365-79, 2010.

[3] Calise F., Figaj RD., Vanoli L., Experimental and numerical analyses of a flat plate photovoltaic/thermal solar collector. *Energies*, 10(4), 491, 2017.

[4] Calise F., Figaj RD., Vanoli L., One-dimensional exergy analysis of an unglazed low-cost PhotoVoltaic/Thermal solar collector', Int. J. Exergy, in press.

[5] Calise F., Figaj RD., Vanoli L., Energetic performance of a low-cost PhotoVoltaic/Thermal (PVT) collector with and without thermal insulation, Proceedings of International Conference on the Sustainable Energy and Environmental Development, SEED17, 14-17 November 2017, Cracow, Poland

Fifth International Conference on Computational Methods for Thermal Problems
THERMACOMP2018, July 9-11, 2018, Indian Institute of Science, Bangalore, INDIA
*N. Massarotti, P. Nithiarasu, Pradip Dutta and C. Ranganyakalu (Eds.)*

# NUMERICAL STUDIES OF MULTIPLE SQUARE JET ARRAY IMPINGING ON A FLAT PLATE

**Leena R, M. Jose Prakash**

Department of Mechanical Engineering, TKM college of Engineering, Kollam, India
leenakalidas@gmail.com, jpmmech@yahoo.co.in

## ABSTRACT

This paper presents flow and heat transfer prediction of multiple slot air jets impinging on a flat plate. Numerical simulations were performed using CFD software package ANSYS FLUENT. The influence of injection parameters, such as injection distance, jet to jet spacing, jet velocity are investigated. The results obtained are validated with the experimental data available in the literature. The Reynolds number is varied from 2000 to 10000. The stagnation Nusselt number is maximum when the nozzle-to-plate distance is 9. The flow characteristics and the heat transfer distribution are found to be dependent on the parameters such as jet to jet spacing, nozzle to plate distance and Reynolds number.

**Key Words:** *Multiple square jet, Heat transfer enhancement, Computational Fluid Dynamics*

## 1. INTRODUCTION

Impinging jets have received considerable attention due to their inherent characteristics of high rates of heat transfer.They are used in a wide variety of applications such as cooling of electronics and turbine blades, and in the heating, cooling, or drying of pulp, paper and textile. The ability to control heat transfer from the surface by varying flow parameters such as jet exit velocity and geometrical parameters such as jet exit opening, jet-to-plate spacing, and nozzle-to-nozzle spacing in arrays are some of the key factors that have lead to the sustained and widespread use of jet impingement technologies. Jet impingement is an effective mechanism for achieving high localized transport rates.

Puneet Gulati et al. [1] studied the effect of jet-to plate spacing and Reynolds number on the local heat transfer distribution to normally impinging submerged circular air jet on a smooth and flat surface. Ozmen[2]found that the interaction between the twin jets decrease with the increase of nozzle-to-plate distance and jet-to jet spacing. San and Lai [3] studied the effect of jet to jet and jet to wall distances to optimize the heat transfer in stagnation point and obtained a correlation as a function of Reynolds number, s/d and H/d ratios. Heyerichs and Pollard [4] assessed the performance of turbulent models k–ω and several versions of the k– ε by considering both separating and impinging turbulent flows with heat transfer.

Vadiraj V.Katti et al [5] observed that at lower Reynolds numbers, the effect of jet to plate distances covered during the study on the stagnation point Nusselt numbers is minimum. Lytle and Webb [6] examined experimentally using infrared thermal imaging technique that the local heat transfer characteristics of air jet impingement at nozzle-plate spacings of less than one nozzle diameter and focused their study on low nozzle-to-plate spacing. K. Chougule et al. [7] has studied the numerical simulation of the 4x4 pin fin heat sink with single jet and 3x3 multi air jet impingement. Lance Fisher [8] conducted a numerical study to investigate the heat transfer to an axisymmetric circular impinging air jet using the k-ϵ turbulence model. Gardon and Akfirat [9] studied the effect of turbulence on the heat transfer between two-dimensional jet and flat plate.

## 2. NUMERICAL ANALYSIS

The simulation were performed using Computational Fluid Dynamics (CFD) code Ansys Fluent that solves equations of continuity, momentum end energy using the Reynolds-Averaged Navier-Stokes approach. The turbulence model used is k-ϵ model which is found to work the best for this flow configuration and is also chosen due to its simplicity, computational economy and wide acceptability. The schematic diagram of the computational domain and temperature contour is shown in Fig.1.

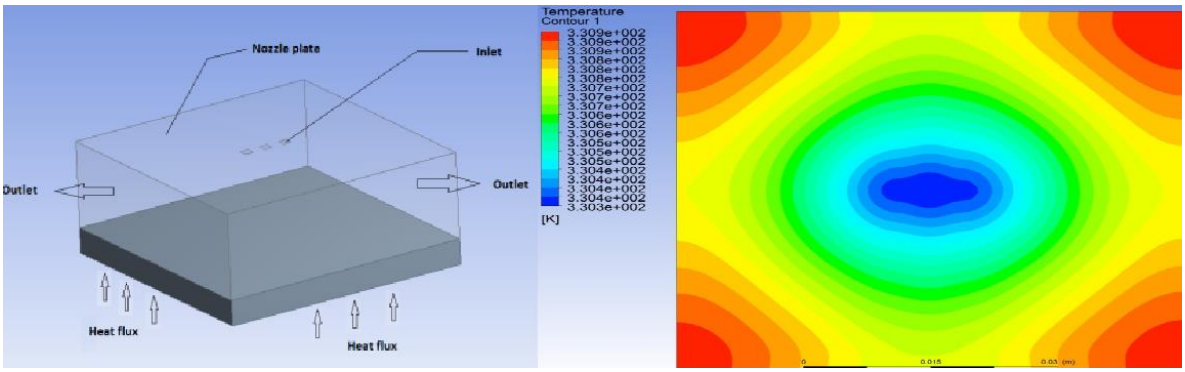


FIGURE.1 The computational domain and temperature contour

## 3. RESULTS

### *A. Validation of Numerical Results*

Numerical simulation was validated using the experimental results obtained from the previous work done by reference[1] is shown in Fig.2.The numerical results are in good agreement with the experimental results

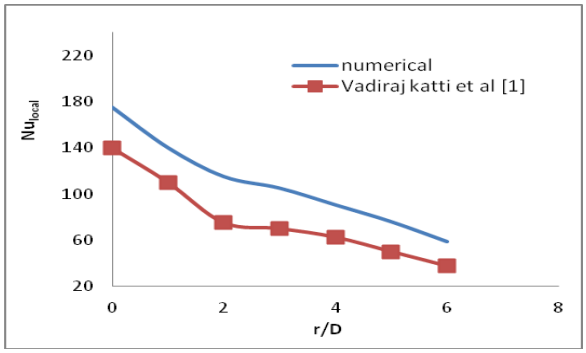


FIGURE.2 Variation of Local Nusselt number with radial distance for Re=15000, Z/D=4

### *B. Effect of nozzle-to-plate distance on stagnation Nusselt number*

Fig. 3 shows the stream wise distribution of the stagnation Nusselt numbers with nozzle-to-plate distance for a Reynolds number of 6000. The heat transfer rate depends on the turbulence intensity of the jet nearer to the impingement surface and the turbulence intensity in turn depends on the velocity of jet.

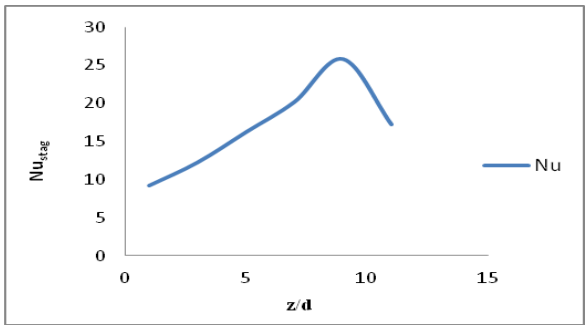


FIGURE.3 Variation of stagnation Nusselt number with Z/d for Re=6000

*C. Effect of nozzle-to-plate distance on Local Nusselt number*

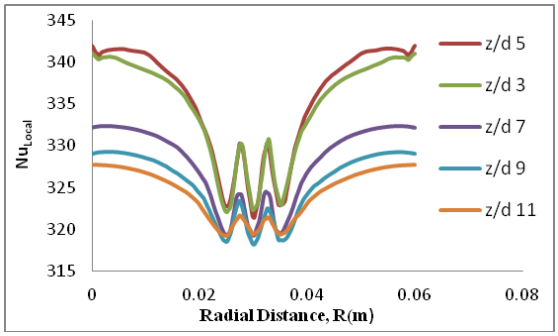


FIGURE.4 Variation of local Nusselt number with in radial direction for Re=6000

Fig. 4 shows the stream wise distribution of the local Nusselt numbers corresponding to different nozzle-to-plate distance for a constant Reynolds number of 6000. At very low nozzle-to-plate distance, the spreading of jet before impingement is quite less.

*D. Effect of pitch variation on local nusselt number*

Fig.5 shows the effect of jet-to-jet interaction depends on the nozzle-to-plate distance and jet-to-jet spacing. This interaction between the jets increases with the increase of nozzle-to-plate distance and decreases with the increase of jet-to-jet spacing(p).

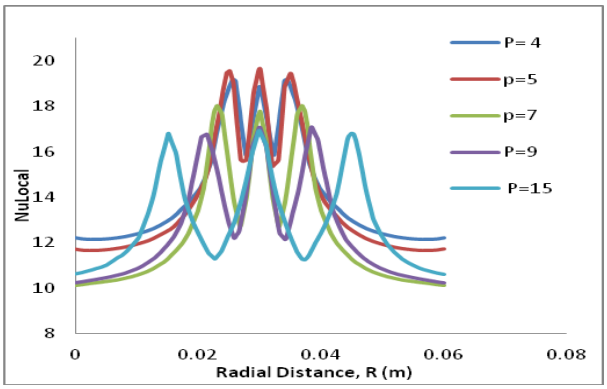


FIGURE.5 Stream wise distribution of Local Nusselt number variation with Z/D=9 and Re=6000

*E. Effect of Reynolds Number*

Fig.6 indicates the effect of Reynolds number on Nusselt number. The local Nusselt number at all points increases with the increase in Reynolds number and this is due to the better mixing of the jets at high Reynolds number.

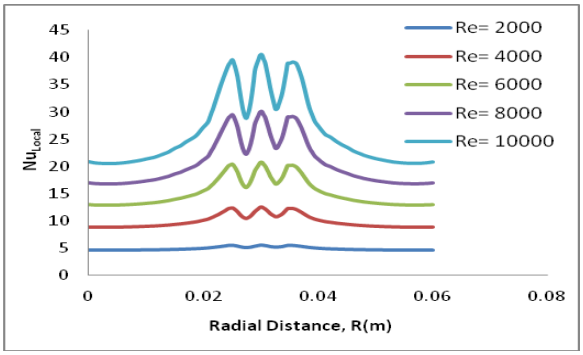


FIGURE.6 Streamwise distribution of Nusselt number for various Reynolds number

## 4. CONCLUSION

Heat transfer characteristics of multiple square jet is investigated by varying Reynolds number, Z/D ratio and pitch. Numerical results reveal that the stagnation Nusselt number attains its maximum value when the nozzle-to-plate distance is 9. The heat transfer rate is a strong function of the jet Reynolds number, nozzle-to-plate distance and jet-to jet spacing. This interaction between the jets depends strongly on the nozzle-to-plate distance and jet-to-jet spacing. The effect of jet interaction decreases with decrease of nozzle-to-plate distance and increases with decrease of jet-to- jet spacing. The optimum value of jet to jet spacing was found to be 5.

## REFERENCES

1. Puneet Gulati,Vadiraj Katti, and S.V.Prabhu,. Influence on the shape of the nozzle on local heat transfer distribution between smooth flat surface and Impingement Air Jet, *International Journal of Thermal Sciences*,48, 602-617, 2009.
2. Y Ozmen, Confined impinging twin air jets at high Reynolds numbers, *Experimental thermal and fluid science*,35, 355-363, 2011.
3. San, J.-Y. and M.-D. Lai, Optimum jet-to-jet spacing of heat transfer for staggered arrays of impinging air jets, *International Journal of Heat and Mass Transfer* ,44,3997-4007,2001.
4. K. Heyerichs and A. Pollard, Heat transfer in separated and impinging turbulent flows, *International Journal of Heat and Mass Transfer*,39 ,2385–2400,1996.
5. Vadiraj V.Katti,S.Nagesh Yasaswy and S.V. Prabhu, Local Heat Transfer Distribution Between Smooth and Flat Surface and Impinging Air Jet from a Circular Nozzle at Low Reynolds Numbers, *International Journal of Heat and Mass Transfer*, 47, 237-244,2011.
6. Lytle, D and Webb, B.W, Air jet impingement heat transfer at low nozzle plate spacing, *International Journal of Heat and Mass Transfer* ,37, 1687– 1697,1994.
7. N.K.Chougule, G.V.Parishwad and C.M.Sewatkar, Numerical Analysis of Pin Fin Heat Sink with a Single and Multi Air Jet Impingement Condition, *International Journal of Engineering and Innovative Technology*,3, 44-50, 2012.
8. Lance Fisher, A Numerical Investigation of Jet Impingement on a Heated Flat Plate, *The Pennsylvania State University ME* ,513-16, 2001.
9. Robert Gardon, J and Cahit Akfirat, The Role Turbulence in Determining the Heat Transfer Characteristics of Impinging Jets, *International Journal of Heat and Mass Transfer* ,8,1261-1272,1965.

Fifth International Conference on Computational Methods for Thermal Problems
THERMACOMP2018, July 9-11, 2018, Indian Institute of Science, Bangalore, INDIA
*N. Massarotti, P. Nithiarasu, Pradip Dutta and C. Ranganyakalu (Eds.)*

# MULTIPLE TIME SCALE APPROACH FOR HIGH PRANDTL NUMBERS IN LATTICE BOLTZMANN METHOD

**M. Jithin, Malay K Das**
Energy Conversion and Storage Laboratory, Department of Mechanical Engineering, Indian Institute of Technology Kanpur, Kanpur, jithinm@iitk.ac.in , mkdas@iitk.ac.in

**Ashoke De**

Department of Aerospace Engineering, Indian Institute of Technology Kanpur, Kanpur, ashoke@iitk.ac.in

## ABSTRACT

Lattice Boltzmann method faces the limitation of instability or inaccuracy while dealing with systems of high diffusion coefficient ratios such as Prandtl number, Schmidt number or Lewis number, in spite of the use of multiple relaxation times for collision of different modes. In the present work, a new multiple time scale based approach is proposed to circumvent the limitation. In the proposed approach, the time step for the solution of each transport equation is selected based on the corresponding diffusion time scale. Then the solution of each equation is coordinated based on the ratio of the diffusion coefficients. The new approach successfully captured steady and transient results for systems with wide range of Prandtl numbers. The authors believe that the new method is capable of handling systems with regions of different transport coefficient values, like systems with both porous and clear media.

**Key Words:** *Multiple Time Scales Approach, Lattice Boltzmann Method, Prandtl Number, Coupled Heat and Mass Transfer.*

## 1. INTRODUCTION

Lattice Boltzmann method (LBM) has been derived from its predecessor, the lattice gas automata (LGA), with improvements to overcome some of its major limitations. LGA faced with the problem of Galilean invariance due to density dependent convection term and the velocity dependent equation of state [1,2], in addition to the inaccurate representation of the transport coefficients. In LBM, the choice of the appropriate equilibrium distribution function and collision term eliminates the Galilean invariance and facilitates the more accurate representation of the transport coefficients.

The simplest of the collision models is the linearized one with the assumption that all modes relaxes to equilibrium at the same rate. This collision model is called the single relaxation time (SRT) collision. Under this assumption, the same relaxation parameter is used for all the modes which forces the Prandtl number of the fluid to unity. To overcome this, a generalized LBM model was proposed in which the collision is conducted in the moment space. As each moment is related to physical quantities and their fluxes, relaxation to equilibrium of each of the moments being controlled individually, confirm independence among the different transport coefficients. However, even with the use of multiple relaxation times (MRT), simulation of fluid flow and heat transport using LBM faces issues of stability as the values of relaxation times for the momentum transport and the energy transport is dependent on the transport coefficients.

Under situations of very different momentum diffusion rates and thermal diffusion rates, the diffusion coefficient ratio namely the Prandtl number will have values far away from unity. Attempt towards simulation of the two transport phenomena with LBM using same time steps makes it impossible to obtain a solution as the values of the relaxation parameters are limited by stability criteria. The present work proposes an alternate approach in which the transport of momentum and heat are solved using different time steps values and the validity and applicability is analyzed using

a test problem. The simulations are conducted using the MRT approach as discussed in [3] which is not repeated here due to the constraint of available space.

## 2. VALIDATION OF THE SOLVER

Cases of flow induced due to natural convection in a square cavity with heated walls are simulated for different Rayleigh and Prandtl numbers. The geometry and parameters used are similar to that used by Roy, Basak [4]. In the square cavity, the bottom and left vertical walls are heated, whereas, the right wall is kept at a lower temperature while the top wall is insulated. Plots of local Nusselt number distribution along the heated walls is plotted and compared with results of [4] as shown in figures 1.

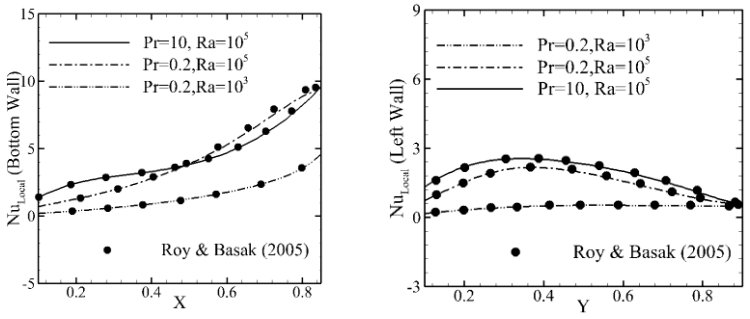


FIGURE 1. Comparison of flow and heat transfer results with Roy and Basak [4]- Nusselt number distribution along heated walls of a square cavity with natural convection induced flow.

## 4. RESULTS AND DISCUSSIONS

To discuss the newly proposed approach, an example of flow and heat transfer in a lid driven square cavity is simulated for a range of Prandtl numbers. The cavity considered has the top wall moving with a constant velocity while all the other walls are stationary. The top and bottom walls are insulated to heat transfer while the left and right walls are kept at constant high and low temperatures, respectively. At the start of the simulation, fluid is at rest and at uniform temperature same as that of the right wall. The average Nusselt number is calculated as the integral, over the entire height, of the non-dimensional temperature gradient at the wall divided by the surface area. The numerical parameters used are given in the table 1. The transient state values of Nu on the right and left walls till it reaches the steady state are plotted in figure 2(a) for Re=10 for different Pr.

| | |
|---|---|
| Domain =100×100 $lsu^2$ | Relaxation time (tau) =0.68 |
| Lattice space unit ($lsu$)=$10^{-4}$ m | Kinematic viscosity (nu) =0.06 $lsu^2/ltu$ |
| Lattice time unit ($ltu$)=$10^{-6}$ s | Velocity of top lid ($U_{lid}$) =0.006 $lsu/ltu$ |

TABLE 1. Parameters used for simulation

In LBM, the transport coefficients are related to the relaxation time, which are calculated as:

$\frac{3\nu}{\Delta t} = \tau - 0.5$ and $b = \frac{60\alpha}{\sqrt{3}} - 4$ where, $\nu$ and $\alpha$ are kinematic viscosity and thermal diffusivity respectively and $\tau$ and $b$ are relaxation parameters for momentum and heat transport respectively.

Consider that for the present problem, the lattice units and physical units are related as: 1 Lattice space unit ($lsu$)= $10^{-4}$ meters and 1 Lattice time unit ($ltu$)= $10^{-6}$ seconds. Hence the conversion of transport coefficients from physical to lattice units can be done as:

$D_{lu} = D_{pu}\frac{m^2}{s} = D_{pu}\times\left(\frac{lsu}{10^{-4}}\right)^2\times\left(\frac{10^{-6}}{ltu}\right) = D_{pu}\times 10^2\frac{lsu^2}{ltu}$ .Here $D_{lu}$ and $D_{pu}$ are transport coefficients in lattice units and physical units respectively. The relaxation time is calculated based on $D_{lu}$ . In the numerical method, discussed in the present paper, $\tau$ and $b$ starts showing instability as their value approaches 0.5 and -4.0, respectively, which are their respective minimum possible values. Also, values greater than 1 usually shows larger numerical errors showing lose in accuracy. Hence for Pr values away from unity, use of same $ltu$ for kinematic viscosity and thermal diffusivity will result in either or both of these relaxation factors having values outside this stable range. The values of the relaxation factors for different Pr are shown in table 2. It can be seen that the relaxation factor for heat transport equation is having values in the unstable range for Pr~0.1 and lower and Pr~100 and higher. Hence we propose the use of different time scales for the two equations. Physically this can be justified as use of larger time steps for the quantity with slower temporal variations and vice versa.

| Pr | ltu (s) | $\tau$ | a |
|---|---|---|---|
| 0.01 | 1.00E-006 | 0.68 | 203.8461 |
| 0.1 | 1.00E-006 | 0.68 | 16.78461 |
| 1 | 1.00E-006 | 0.68 | -1.921539 |
| 10 | 1.00E-006 | 0.68 | -3.792154 |
| 100 | 1.00E-006 | 0.68 | -3.979215 |

TABLE 2. Relaxation parameter values for different Pr for same time scale approach

In this approach, the fluid flow equation is discretized with $ltu_1$ and the temperature equation with $ltu_2$ . The values of $ltu_1$ and $ltu_2$ are selected such that, the relaxation times of both the equations will be within their stable range. However, for the solutions of both equation to be marching in time at the same rate, for each time stepping of the flow equation, the temperature solution has to be stepped by $n$ times, where $n = ltu_1/ltu_2$ . The calculation of values of relaxation times for flow and heat transport for different Pr using different time scale approach can be seen from table 3. Calculation using these time scales resulted in values of both relaxation times ( $\tau$ and $b$ ) in the stable range.

| Pr | $ltu_1$ (s) | $ltu_2$ (s) | n ($dt_1/dt_2$) | tau | a ($dt_2$) | $U_1$ ($dx/dt_1$) |
|---|---|---|---|---|---|---|
| 0.0001 | 1.00E-006 | 2.00E-010 | 5000 | 0.68 | 0.156921938 | 0.1 |
| 0.001 | 1.00E-006 | 2.00E-009 | 500 | 0.68 | 0.156921938 | 0.1 |
| 0.01 | 1.00E-006 | 2.00E-008 | 50 | 0.68 | 0.156921938 | 0.1 |
| 0.1 | 1.00E-006 | 2.00E-007 | 5 | 0.68 | 0.156921938 | 0.1 |
| 1 | 1.00E-006 | 1.00E-006 | 1 | 0.68 | -1.921539031 | 0.1 |
| 10 | 1.00E-006 | 2.00E-006 | 0.5 | 0.68 | -3.584307806 | 0.1 |
| 100 | 1.00E-006 | 2.00E-005 | 0.05 | 0.68 | -3.584307806 | 0.01 |
| 1000 | 1.00E-006 | 2.00E-004 | 0.005 | 0.68 | -3.584307806 | 0.001 |
| 10000 | 1.00E-006 | 2.00E-003 | 0.0005 | 0.68 | -3.584307806 | 0.0001 |

TABLE 3. Relaxation prameter values for different Pr for different time scale approach

The unit of velocity calculated from the flow solution will be $lsu/ltu_1$ . Hence the velocity used in the temperature equation should be the velocity from flow equation solution divided by $n$ . As higher values of velocity gives rise to compressibility error in LBM, care should be taken that the

maximum value of $velocity/n$ will be lower than $0.2\,lsu/ltu$. For reducing the velocity values without altering Re, it is, therefore, required to select appropriate $lsu$. To represent this, figure 2(b) is added showing the maximum possible value of $lsu$ to be used for simulating the present problem of lid driven cavity for different Pr.

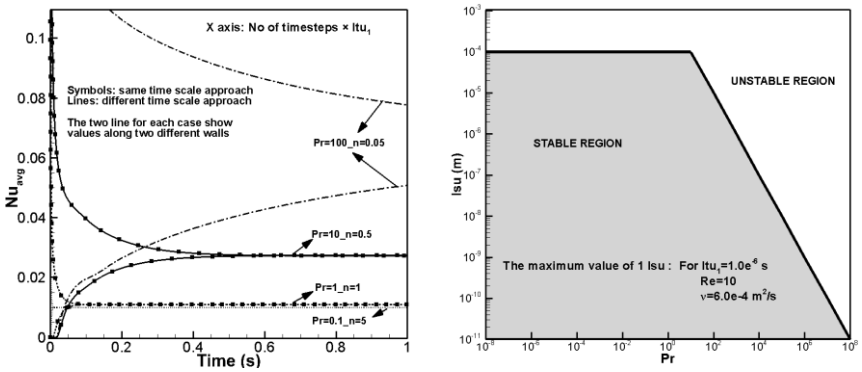


FIGURE 2. (a) Multiple time scale approach and same time scale approach (b)Pr dependence of grid size showing the maximum value of $lsu$ that can be used

Using the same time scale for flow and heat transport, only Pr=1 and 10 could be simulated, whereas the new approach gave results for larger and smaller values of Pr as shown in figure 2(a). The results of the two approaches for Pr=1 and 10 are also compared for validation and the results match perfectly. The different time scale method captured even the transient results accurately. This shows that the use of larger time stepping for the quantity with slower transport does not cause serious compromise in terms of accuracy.The new method, in addition to being very easy in implementation in any existing LBM code, showcases additional advantages. It completely eliminates the restriction caused due to instability associated with the transport coefficient values. As can be seen from figure 2(a), results of cases of Pr ranging from 100 to 0.1 are shown. Likewise, any value of Pr can be dealt with, just by changing the value of $n$. The approach can also be extended to the use of different time scales in different regions of the computational domain.

## 4. CONCLUSIONS

1. In spite of using MRT collision, the use of LBM is limited to cases of Pr close to unity. Results for fluids having Pr values far away from 1 will either face instability or inaccuracy.
2. A new multiple time sale approach is proposed wherein the limitation of Pr value is overcome. Transport of different quantities is solved using different time steps based on the value of the diffusion coefficient. Results for cases with very high and very low Pr has been successfully generated without loss in accuracy. Even transient results are successfully captured.
3. The proposed approach is extendable to coupled solution of momentum, heat and solute transport in both clear and porous media. The approach enables use of different time scales in different domains such as in systems with both clear and porous media. However, special treatment might be required at the interface.

## REFERENCES

[1] Chen, H., Chen, S., Matthaeus, W. H., 1992. "Recovery of the Navier-Stokes equations using a lattice-gas Boltzmann method". Physical Review A 45 (8)R5339

[2] Lallemand, P., Luo, L.-S., 2000. "Theory of the lattice Boltzmann method: Dispersion, dissipation, isotropy, Galilean invariance, and stability". Physical Review E 61 (6)6546

[3] Guo, Z., Zhao, T., 2005. "A lattice Boltzmann model for convection heat transfer in porous media". Numerical Heat Transfer, Part B 47 (2)157-177

[4] Roy, S., Basak, T., 2005. "Finite element analysis of natural convection flows in a square cavity with non-uniformly heated wall (s)". International Journal of Engineering Science 43 (8)668-680

Fifth International Conference on Computational Methods for Thermal Problems
THERMACOMP2018, July 9-11, 2018, Indian Institute of Science, Bangalore, INDIA
*N. Massarotti, P. Nithiarasu, Pradip Dutta and C. Ranganyakalu (Eds.)*

# HEAT TRANSFER IN THE COOLING WHEEL DURING PLANAR FLOW MELT SPINNING PROCESS

**Sowjanya Madireddi**
CVR College of Engineering, Hyderabad,501510, India, madireddisowjanya@gmail.com

## ABSTRACT

Planar Flow Melt Spinning is a rapid solidification process to manufacture amorphous ribbons for transformer core applications. The process involves heat transfer between the melt and the rotating cooling wheel to produce a thin layer of melt in the form of a ribbon. The amorphous or crystalline structure of the end product depends on the heat transfer from the molten alloy to the cooling wheel. This in turn depends on the dissipation of heat from the cooling wheel to the cooling fluid circulated inside the wheel and surrounding atmosphere. To obtain ribbons of amorphous structure, it is important to maintain the wheel at low temperatures throughout the production. The present work compares the heat transfer in various designs of the cooling wheel. The wheel is observed to dissipate more heat and maintain at lower temperatures for I-Section design of 20 mm thick than wheel with 5 mm thickness.

**Key Words:** *Heat Transfer, Finite volume, Conduction, Convection, Fluid-structure interaction.*

## 1. INTRODUCTION

Core losses of distribution transformers can be reduced by replacing the silicon graded core with amorphous material. Amorphous metal core consists of laminations made of few microns thickness having amorphous structure. This helps to reduce eddy current and hysteresis losses by 75% [1]. Planar flow melt spinning (PFMS) is a widely used process to obtain an amorphous ribbon by rapid solidification technique. Fig. 1 shows the schematic of the PFMS process. Critical process parameters are ejection pressure (P) and temperature (T) of the melt, speed of rotation of the wheel (U), gap between the crucible-nozzle and wheel surface (G), and the slit width of the nozzle (w). Crucible holding the molten alloy is brought down near to the pre-set distance from the rotating wheel. Molten metal is ejected by gas pressure on to the wheel surface through a slit nozzle. A small melt puddle is formed on the wheel surface between the nozzle-wheel gap. A thin layer of melt which is in contact with wheel surface under the puddle, transforms to amorphous at its glass transition temperature due to rapid cooling. This thin layer is dragged out of the puddle in the form of a ribbon due to wheel rotation. The end product obtained must have a defect free surface with amorphous structure to use it as core material. The ribbons obtained by some investigators show amorphous structure for thickness less than 40 μm [2]. But the study was based on the ribbons obtained out of few milligrams in a very less processing time. However, in realistic conditions, the time of production is continuous. Present author studied [3] the heat transfer in the cooling wheel under these production conditions using a numerical model. The ribbons obtained were of discontinuous and broken with increase in wheel temperature with increase in processing time. The portion of wheel coming back under the puddle after every rotation is observed to be hotter with time. If this temperature is reduced by enhancing the heat transfer rate from the wheel to the cooling water, amorphous structure can be obtained throughout the production. The present work is to compare the heat transfer in the cooling wheel of thickness 20 mm, 5 mm and 20 mm as I section. Enhanced numerical models can be of great use to estimate the heat transfer phenomenon as experimental investigation is expensive and time consuming. Some investigators employed a part of the wheel of 12.7 mm thickness [4]. Melt wheel contact to ribbon detachment is considered in the computations and observed that the wheel expansion due to increase in temperature leads to

defective ribbon. Few others included complete wheel for computations [5,6]. The investigation shows that poor thermal conductivity of wheel material may also increase wheel temperature, because of lower heat dissipation rates. Hence, Cu-Be alloy was suggested as the wheel material and thickness not less than 2 mm [7] to avoid thermal stresses. Present author also employed full wheel in the computations, including convection from the surface of the wheel to the atmosphere [3]. Convective heat transfer coefficient is calculated using the Nusselt number equation for a rotating cylinder in a fluid [8]. In the present work the wheel surface is redesigned to enhance the heat transfer rate.

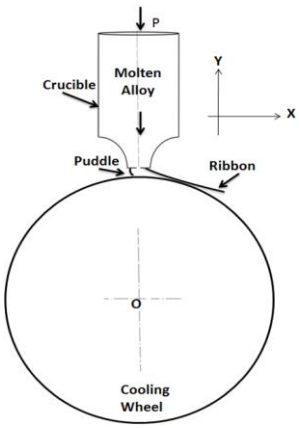


FIGURE 1. Schematic of Planar Flow Melt Spinning Process

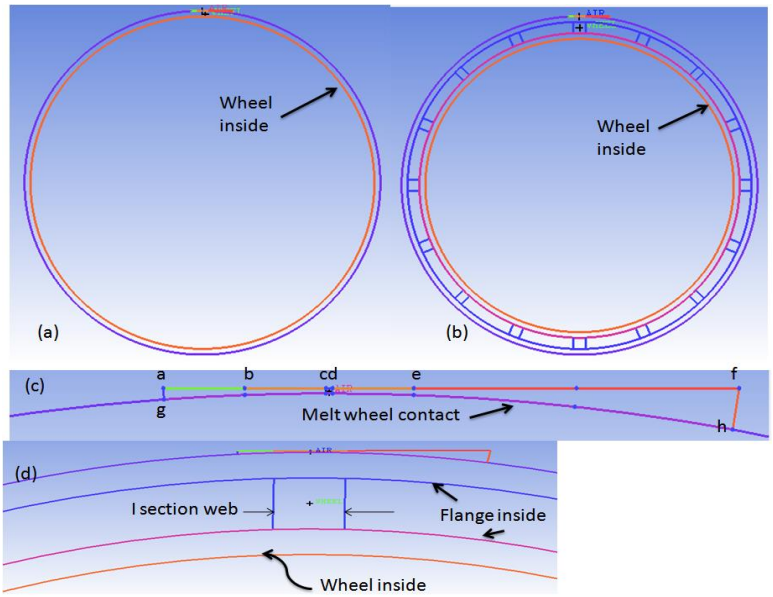


FIGURE 2. (a) Wheel with 5 mm thick (b) Wheel with I-Section (c) Air domain coupled with solid wheel domain (d) Portion of wheel showing I-Section

## 2. NUMERICAL

Numerical model includes the whole wheel and the nozzle-wheel gap in the computations. The domain is extended on both sides of the nozzle wall to include the surrounding atmosphere. Fig. 2(a) and (b) shows, numerical model of the wheel with 5 mm thickness and 20 mm thickness of I – section. Fig.2(c) shows the air domain near to the wheel surface. This is the computational domain between the nozzle-wheel gap when the crucible is brought down near the wheel surface. The air and wheel domains are coupled at the melt wheel contact region. Mass, momentum, energy equations are solved [3] including the temperature dependent viscosity equation. Volume of fluid equation employed in the simulations help to show the boundaries of melt flowing in the air domain up on ejection. Properties of the material ($Fe_{78}Si_9B_{13}$) except viscosity are temperature independent. The assumption are similar to the earlier model [3]. For the new designs shown in Fig. 2(a) and 2(b) the boundary conditions are: (i) Nozzle walls bc and de are stationery with no heat flux and made of quartz material (ii) Melt inlet ‘cd’ is pressure inlet with specified superheat temperature(iii) Melt wheel contact ‘gh’ is rotating with a specified speed (iv) boundaries ‘ab’, ‘ag’, ‘ef’ are pressure inlet representing surrounding atmosphere and condition at ‘hf’ is pressure out let (v) Solid wheel domain is rotating and air domain is stationary (vi) Wheel inside is maintained at 300 K (vii)Wheel I-section surface and outside surfaces dissipate heat with convection. The material for wheel is taken as copper. Ribbon formation is due to rapid cooling of melt to glass transition temperature by heat dissipation to cooling wheel. The thickness of the ribbon is the thickness of the thin layer of melt below the glass transition temperature of the alloy at the intersection of melt, air and ribbon [8].

## 3. RESULTS

The process parameters considered for the simulations are: P=13.789 kPa, T=1553 K, U=1250 rpm, G=0.3 mm and w=0.4 mm. The heat transfer coefficient from the wheel outside surface is taken as 219.5 W/m$^2$ [3]. Cooling water is sent into the wheel to absorb the heat and drawn out continuously using a pump. Experimental investigators presumed that the water maintains the wheel at constant temperature. Hence, the inside wheel temperature is assumed as constant at 300 K. Fig. 3 shows a raise in temperature of the wheel of 20 mm thickness. The part of the wheel which comes back under the puddle after every rotation is to be at the same temperature to produce a ribbon of uniform quality. Quality of the product includes both surface topography as well as thickness. However, increase in wheel temperature leads to decrease in cooling rate or extending the ribbon formation much away from the puddle. Former problem leads to crystalline structure and later one leads to winding of the ribbon around the wheel. Both cases are to be avoided. Hence, to improve the heat transfer rate first the thickness of the wheel is reduced to 5 mm. The model is developed using commercial software I-CEMCFD. The mesh obtained is of unstructured Quad mesh of high quality. Simulations are performed with 1e-6 time step up to 1 second. As stable puddle formation takes 10 to 15 milliseconds [9], the time of computations is considered reasonable. Moreover, the wheel completes 20 rotations in 1 second. For a 20 mm thick wall, the wheel enters the air domain zone at 1034 K which is higher than the glass transition temperature of the alloy (873 K). This clearly shows the in-sufficient heat dissipation from the wheel of 20 mm thick. Fig.3 (b) shows the isotherms at similar conditions for a wheel of 5 mm thickness. The temperature of the wheel near to the air domain is 951 K. However, the isotherms near the ribbon ejection zone are of 311 K. For wheel of 20 mm thick, high temperatures in the wheel extended beyond the air domain in the direction of wheel rotation. This clearly shows the reduction in temperature with reduction in wheel thickness. Comparing the above results it is understood that the heat transfer rate can be enhanced by changing the wheel thickness. But the wheel of 5 mm thick may not be structurally stable. Hence, Wheel of 20 mm with I section is considered to obtain enhanced heat transfer rate.

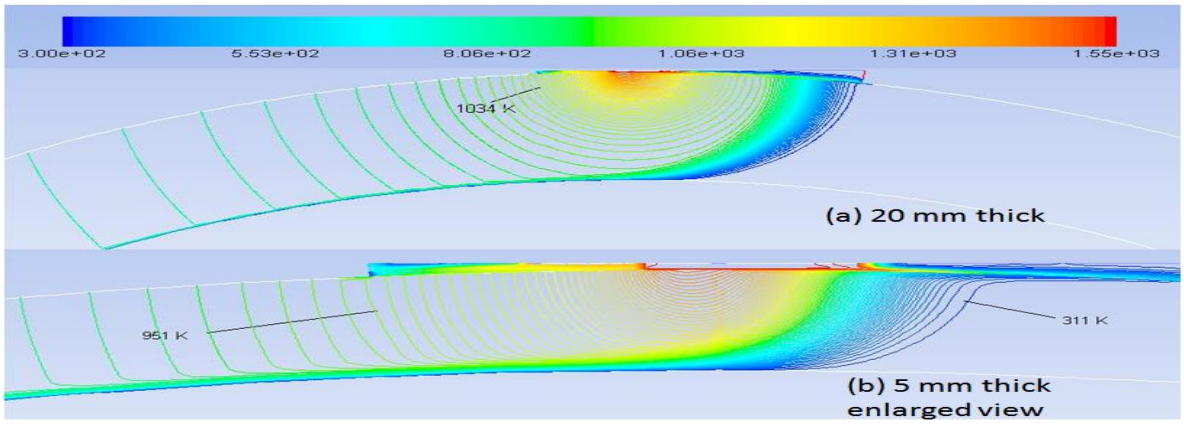


FIGURE 3. Isotherms in the wheel under the puddle (a) 20 mm (b) 5 mm enlarged

The new geometry is selected to make use of the structural stability of I-section and heat transfer enhancement by extended surface as web. Each flange is of 5 mm thick and web of 10 mm. The inside wheel surface (Fig. 2(b) is assumed constant at 300 K. The heat is convected from all other parts of the wheel and the heat transfer coefficient (219.5 W/m$^2$) calculated for the wheel outer surface [3] is employed. Fig 4 shows the isotherms in the I-section wheel under the puddle after 20 rotations. The temperature of the wheel entering the air domain is 800 K and leaving at 878 K. It is interesting to note that the temperature of the wheel entering the domain under the puddle is decreased and is less than the glass transition temperature (873 K) of the alloy. When compared to the previous cases the wheel temperature after crossing the puddle is observed to be higher. This is because of the realistic convection boundary considered for the flange inside surfaces.

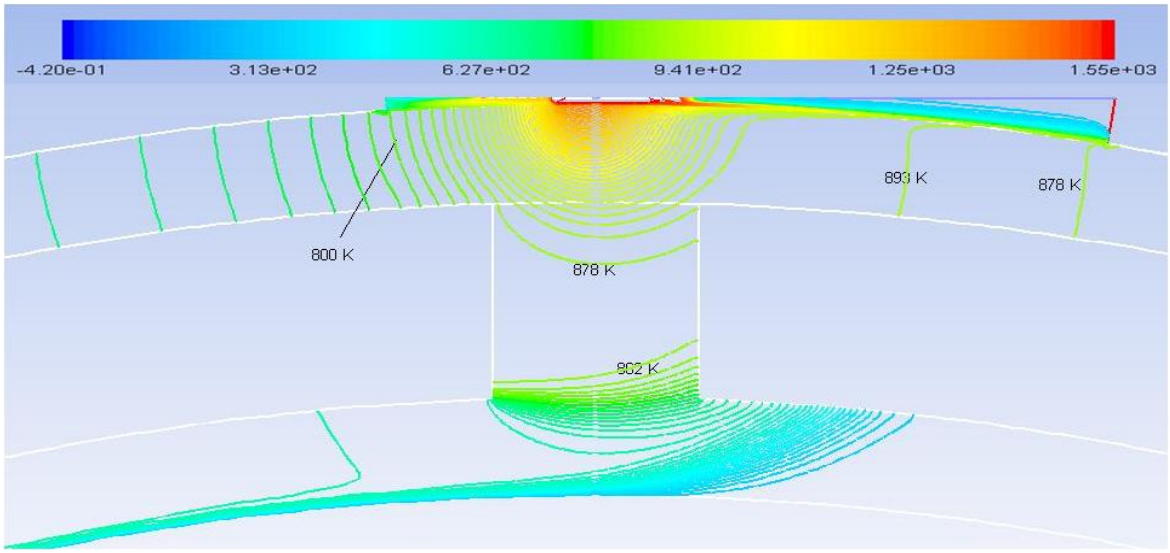


FIGURE 4. Isotherms in the wheel under the puddle for I-Section

## 4. CONCLUSIONS

Numerical models are developed to investigate the effective heat dissipation by the cooling wheel during planar flow melt spinning process. Decrease in thickness of the cooling wheel from 20 mm to 5 mm, increases heat transfer rate from the wheel. However, wheel of 20 mm thickness with I-Section further enhances heat transfer rate and reduces the wheel temperature below glass transition temperature of the alloy.

## REFERENCES

[1] Narasimhan, M.C., Flanders, N.J., U. S. Patent No: 4,142,571, 1979.

[2] Srinivas M., Majumdar B., Phanikumar G., and Akhtar D., Effect of Planar Flow Melt Spinning Parameters on Ribbon Formation in Soft Magnetic $Fe_{68.5}Si_{18.5}B_9Nb_3Cu_1$ Alloy, *Metallurgical and Materials Transactions* 42 B, 370-379, 2011.

[3] M. Sowjanya and T. Kishen Kumar Reddy, Cooling wheel features and amorphous ribbon formation during planar flow melt spinning process, *Journal of Material Processing Technology*, 214, 1861-1870, 2014.

[4] Sundararajan A. and Thomas B.G., Heat transfer during melt spinning of Al-7%Si alloy on a Cu-Be wheel, *TMS The Minerals, Metals & Materials society*, 793 – 810, 2008

[5] Liu H., Chen W., Qiu S., and Liu G., Numerical simulation of initial development of fluid flow and heat transfer in planar flow casting process, *Metallurgical and materials transactions B*, 40B, 411 – 429, 2009.

[6] Liu H., Chen W. and Liu G., Parametric investigation of interfacial heat transfer and behavior of the melt puddle in planar flow casting process by numerical simulation, *ISIJ International*, 49 No. 12 , 1895 – 1901, 2009.

[7] Karpe B. Kosec B. and Bizjak M., Modeling of heat transfer in the cooling wheel in the melt-spinning process, *Journal of achievements in materials and manufacturing engineering*, 46, 88 – 94, 2011.

[8] C.P Kothandaraman and S. Subramanyan, Heat and mass transfer data book, 6th Edition, New Age, 141, 2007.

[9] M. Sowjanya and T. Kishen Kumar Reddy, Obtaining stable puddle and thinner ribbon during planar flow melt spinning process, *Materials Today Proceeding* 4, 890-897, 2017.

Fifth International Conference on Computational Methods for Thermal Problems
THERMACOMP2018, July 9-11, 2018, Indian Institute of Science, Bangalore, INDIA
*N. Massarotti, P. Nithiarasu, Pradip Dutta and C. Ranganyakalu (Eds.)*

# CFD STUDY OF PROPELLER BLADE TEMPERATURE FOR PUSHER CONFIGURED TURBO-PROP ENGINE

Mahesh Mali[a *], Vinay C A.[b], Abhijeet Chougule[a], Sanjay Kadam[a]
[a] Department of Mechanical Engineering, Rajarambapu Institute of Technology, Sakharale, Maharashtra-415414, India
[b] National Aerospace Laboratories, Bangalore, Karnataka-560017, India
E-mail address: maheshmali7574@gmail.com, vinay.ca@nal.res.in, abhijeet.chougule@ritindia.edu, sanjay.kadam@ritindia.edu

## ABSTRACT

In this paper, aft mounted propeller blade surface temperatures during specific ground operation condition on the pusher configuration with given exhaust stub installation are analyzed. This analysis is carried out to understand the exhaust gas impingement and predict the surface temperatures before validating the compliance demonstration. It is important in pusher applications to ensure that the exposure of the propeller to the hot exhaust gas is minimized and that exhaust gas does not attach itself to the aft nacelle and cause overheating of the spinner/hub area of the propeller. An established numerical analysis approach is applied in this study, CFD analysis for flow through and around the nacelle, engine exhaust duct and the propeller is presented for ground static condition using SST, k-ω model using commercially available software ANSYS Fluent. Special emphasis was laid on developing a good quality mesh for the computational domain with a finer boundary layer mesh along the wall and maintaining a higher density mesh at critical areas. The flow characteristics derived from this CFD analysis remained unaltered during grid dependence studies. CFD results are compared with the analytical work to assess the exhaust temperature at the propeller plane for the engine ground static condition. The results obtained from CFD study have shown that the temperature distribution around the propeller plane is in agreement with analytical results. This simulation model will be used to carry out dynamic analysis considering different flight conditions with propeller rotation.

**Key Words:** *Propeller, CFD, Surface Temperature, Stub.*

## 1 INTRODUCTION

Pusher-Propeller installations have been shown to offer a number of advantages at the aircraft level in terms of cost, weight and aerodynamic considerations. For example, choice of a stub-wing mounted pusher over a wing mounted tractor propeller installation avoids the interactions of the propeller slipstream with the wing and offers the potential to enable significant portions of laminar flow to be achieved. Another major advantage is that the de-icing boots are not required because this design induces long exposure of the blades to the hot gases. A good configuration is one that minimizes the exposure of the blades to the exhaust. In general, exhaust plume characteristics are very difficult to predict, being subject to the influences of engine power, propeller swirl, and the flow field of the wing/nacelle/ aircraft. For this reason, some post design development work should be anticipated. Areas on the nacelles, stub-wings, fuselage etc. that could be prone to heating should be instrumented with temperature sensitive tape or paint and the aircraft put through all the standard flight and ground manoeuvres so that the temperature can be assessed.

The general goal was to estimate the temperature on propeller surface when the engine is running at full power and aircraft is in static condition by simulating the flow field around the nacelle and propeller using commercial CFD package ANSYS Fluent [1].

## 2 NUMERICAL STUDY

For CFD analysis, the complete engine assembly geometry i.e. nacelle, propeller and spinner assembly of Light Transport Aircraft (LTA) were considered as shown in Figure 1. The modeling was done by using CATIA V5 R20. The IGES file was imported into pre-processor before that domain is created [2]. The cylindrical domain was created for this study as that one uses the elements most efficiently with minimum distortion and eliminates edge effect at corners. The full domain is shown in figure 2. After completion of geometry cleaning the mesh was created. The unstructured tetra mesh was generated for computational analysis with patch Independent octree technique [3]. The prism layers are generated near the wall. It is a difficult task to control mesh because of the complexity of the model. 6.9 million elements were generated.

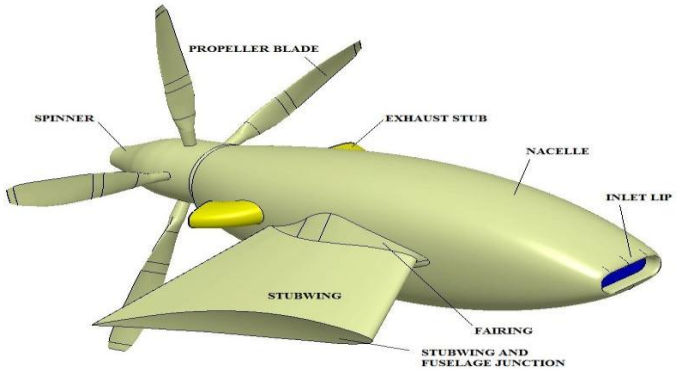


FIGURE 1. CAD-Model of Turboprop Engine

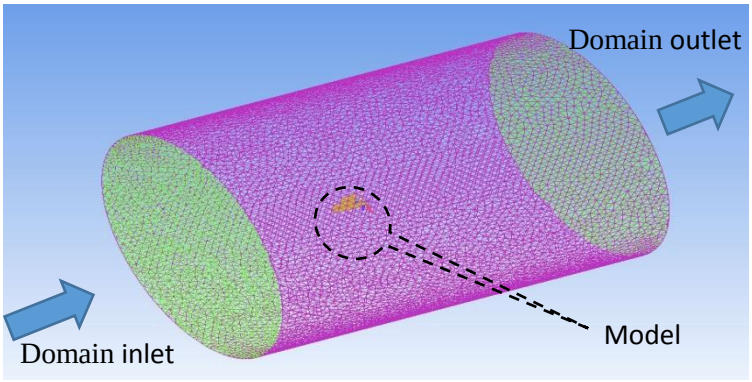


FIGURE 2. Mesh model

The proper boundary conditions were applied to all appropriate places as follows [2],

| Sr. No | Face | Type of boundary condition | Magnitude | Temperature |
|---|---|---|---|---|
| 1. | Domain Inlet | Velocity Inlet | 4 m/s | 304 K |
| 2. | Domain Outlet | Pressure Outlet | Pressure Outlet | 304 K |
| 3. | Domain Wall | Wall | - No slip condition. | 304 K |
| 5. | Stub inlets | Mass Flow Inlet | 0.5935 kg/s | 913 K |
| 6. | Blades, Spinner, etc. | Wall | - No slip condition. | - |

TABLE 1. Boundary conditions for numerical analysis.

## 3 ANALYTICAL STUDY

The Calculation was done by referring literature. For this calculation, the preliminary data is defined by CSIR-NAL. Area and Perimeter of stub at the outlet are 0.035 $m^2$ and 0.735 m respectively. Hydraulic Diameter ($D_h$) is 0.1924 m, Mass flow rate at stub outlet is 0.59 kg/s, Velocity is 28.8 m/s, Exhaust gas temperature is 640°c i.e. 913 K, ambient temperature is 34°c i.e. 307 K, therefore Mean temperature is 337°c, Distance from stub to propeller plane (H) is 0.6 m.

By taking the properties of flue gas at mean temperature the calculations are to be done. That are, Density ($\rho$) = 0.58296 $kg/m^3$, Viscosity ($\mu$) = 0.0000295002 $Ns/m^2$ or Pa.s, Thermal conductivity (k) = 0.051566 W/m.k, Pr = 0.6463.

Reynolds number,

$$Re = \frac{\rho \times V \times D}{\mu} = 109484$$

Here the flow coming from stub on to the plane, therefore Nusselt number is,

$$Nu = 0.023 \times (Re)^{0.8} \times (Pr)^{0.3}$$

$$Nu = 216.94$$

Martin developed the equation for nusselt number [3] i.e.,

$$N_{uavg} = Pr^{0.42}\frac{D}{r}\frac{1-1.1D/r}{1+0.1\left(\frac{H}{D}-6\right)D/r}F \quad \text{, when } 2000 < Re < 400000$$

For $30000<Re<120000$, $F = 0.54\ Re^{0.667}$

Put value of Nu in above equation,

r/D = 3.6

A correlation for effectiveness is given by Goldstein et al.[4] i.e.,

$$\text{Effectiveness} = 1.193(x/D)^{-0.98} \quad \text{, when } x/D \geq 3.5$$

$$= 0.3399$$

$$\text{Effectiveness} = \frac{Tref - Tamb}{Tj - Tamb}$$

Therefore, $T_{ref}$ = 239.97°c or 513.97 K is the temperature at the propeller plane.

## 4 RESULTS AND CONCLUSIONS

In the analytical study, the reference temperature ($T_{ref}$) is the temperature on the propeller plane which facing the exhaust gas flow when the surface is considered to be an adiabatic wall. $T_{ref}$ is the average temperature of particular surface. In Numerical analysis when the solution was carried out nearly 10000 iterations, the stability of residuals is found. In post processing contour of temperature at blade surface or the plane is taken and temperature profile is shown in Figures 3-4. By considering area weighted average of the blade surface which faces towards the stub, it shows the temperature of about 531.8 K. This is in close agreement with the analytical results. After analysis, it is observed that the blade appears high temperature in a static condition. From this baseline study, the methodology and model are satisfactory and the same will be used to perform dynamic analysis considering the flight envelope with propeller rotation.

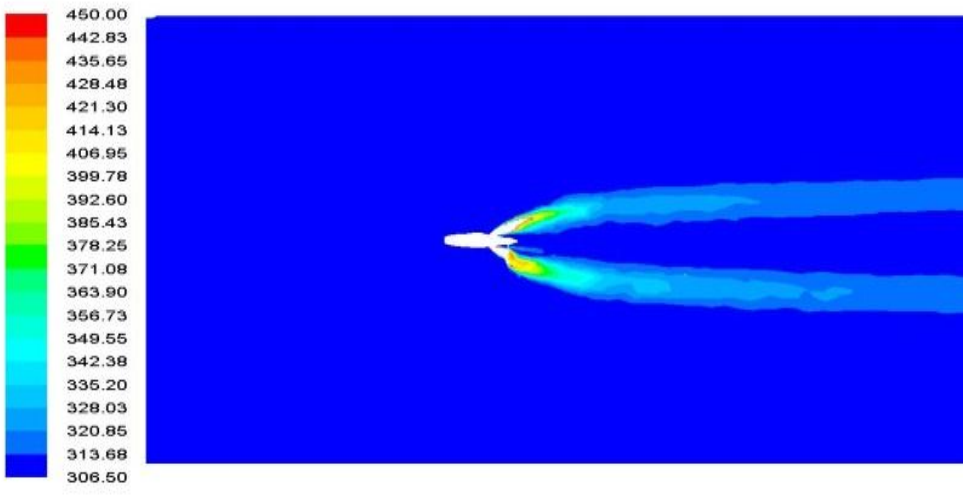


FIGURE 3. Contours of temperature for a plane

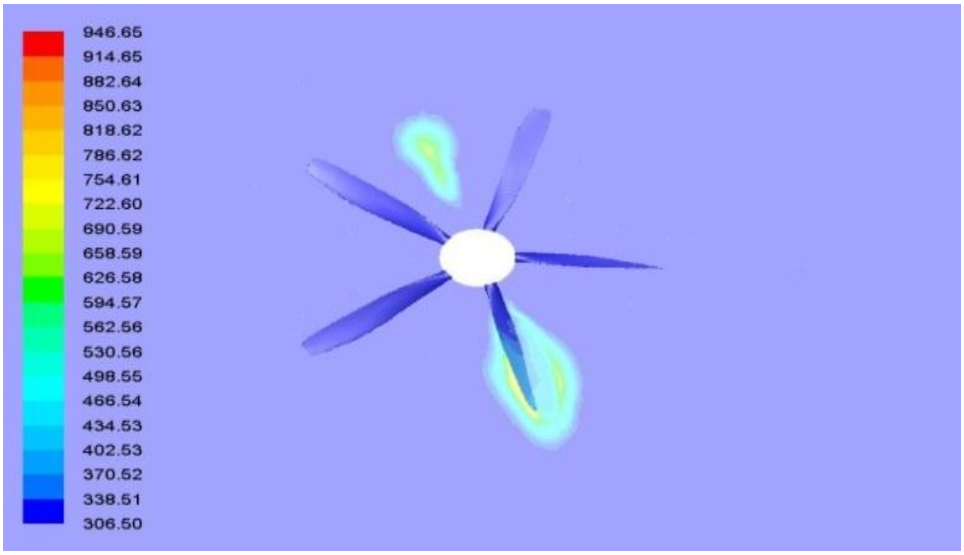


FIGURE 4. Temperature profile at propeller plane

REFERENCES

[1] Jiyuan Tu, Guan Heng Yeoh and Chaoqun Liu, Computational Fluid Dynamics: A Practical Approach, First Edition, *Elsevier*, USA, 2008.

[2] Abhijeet B. Chougule, Vinay C A., Suresh R, Pusher Configured turboprop engine oil cooler ejector performance: CFD analysis and validation, *Proceeding of the 6th International and 43rd National conference on Fluid Mechanics and Fluid Power*, 35, 2016.

[3] Abhijeet B. Chougule, Vinay C A., Saleel Ismail, CFD Analysis of Cooler Duct for Turboprop Aircraft Engine in Pusher Configuration, *International Journal of Innovative Research in Science, Engineering and Technology*, 5, 2016.

[4] Martin H., Heat and mass transfer between impinging gas jets and solid surfaces, *Advances in heat Heat Transfer*, 16, 1977.

[5] R. J. Goldstein, K. A. Sobolik, W. S. Seol, Effect of Entrainment on the Heat Transfer to a Heated Circular Air Jet Impingement on a Flat Surface, *Journal of Heat Transfer*, 112, 608-11, 1990.

# NUMERICAL ANALYSIS OF PROPELLER BLADE TEMPERATURE FOR PUSHER CONFIGURED TURBO-PROP ENGINE

Mahesh Mali[a *], Vinay C A.[b], Abhijeet Chougule[a], Sanjay Kadam[a]
[a] Department of Mechanical Engineering, Rajarambapu Institute of Technology, Sakharale, Maharashtra-415414, India
[b] National Aerospace Laboratories, Bangalore, Karnataka-560017, India
E-mail address: maheshmali7574@gmail.com, vinay.ca@nal.res.in, abhijeet.chougule@ritindia.edu, sanjay.kadam@rit.edu

ABSTRACT

In this paper, aft mounted propeller blade surface temperatures during specific ground operation condition on the pusher configuration with given exhaust stub installation are analyzed. This analysis is carried out to understand the exhaust gas impingement and predict the surface temperatures before validating the compliance demonstration. It is important in pusher applications to ensure that the exposure of the propeller to the hot exhaust gas is minimized and that exhaust gas does not attach itself to the aft nacelle and cause overheating of the spinner/hub area of the propeller. An established numerical analysis approach is applied in this study, CFD analysis for flow through and around the nacelle, engine exhaust duct and propeller is presented for ground static condition using Realizable K-epsilon model using commercially available software ANSYS Fluent. Special emphasis was put on developing a good quality mesh for the domain with a finer boundary layer along the wall and maintaining a higher density mesh at critical areas. The flow characteristics derived from this CFD analysis remained unaltered during grid dependence studies. CFD results are compared with the analytical work to assess the exhaust temperature at the propeller plane for engine ground static condition. The results obtained from CFD study have shown that the temperature distribution around the propeller plane is in agreement with practical results which has been carried out at CSIR-NAL. By considering this as a baseline study, this simulation model will be used to carry out for different flight conditions.

**Key Words:** *Propeller, CFD, Surface Temperature, Stub.*

## 1 INTRODUCTION

Pusher-Propeller installations have been shown to offer a number of advantages at the aircraft level in terms of cost, weight and aerodynamic considerations. For example, choice of a stub-wing mounted pusher over a wing mounted tractor propeller installation avoids the interactions of the propeller slipstream with the wing and offers the potential to enable significant portions of laminar flow to be achieved. Another major advantage is that the de-icing boots are not required because this design induces long exposure of the blades to the hot gases. A good configuration is one that minimizes the exposure of the blades to the exhaust. In general, exhaust plume characteristics are very difficult to predict, being subject to the influences of engine power, propeller swirl, and the flow field of the wing/nacelle/ aircraft. For this reason, some post design development work should be anticipated. Areas on the nacelles, stub-wings, fuselage etc. that could be prone to heating should be instrumented with temperature sensitive tape or paint and the aircraft put through all the standard flight and ground manoeuvres, so that the temperature can be assessed.

The general goal was to estimate the temperature on propeller surface when the engine is running at full power and aircraft is in static condition by simulating the flow field around the nacelle and propeller using commercial CFD package ANSYS Fluent [1].

## 2 NUMERICAL STUDY

For CFD analysis, the complete engine assembly geometry i.e. nacelle, propeller and spinner assembly of Light Transport Aircraft (LTA) was considered as shown in Figure 1. The modeling was done by using CATIA V5 R20. The IGES file was imported into pre-processor, before that domain is created [2]. The cylindrical domain was created for this study as that one uses the elements most efficiently with minimum distortion and eliminates edge effect at corners. The full domain is shown in figure 2. After completion of geometry cleaning, mesh was created. The unstructured tetra mesh was generated for computational analysis with patch Independent octree technique [3]. The prism layers are generated near the wall. It is difficult task to control mesh because of complexity of the model. After completion mesh nearly 20 million elements were generated.

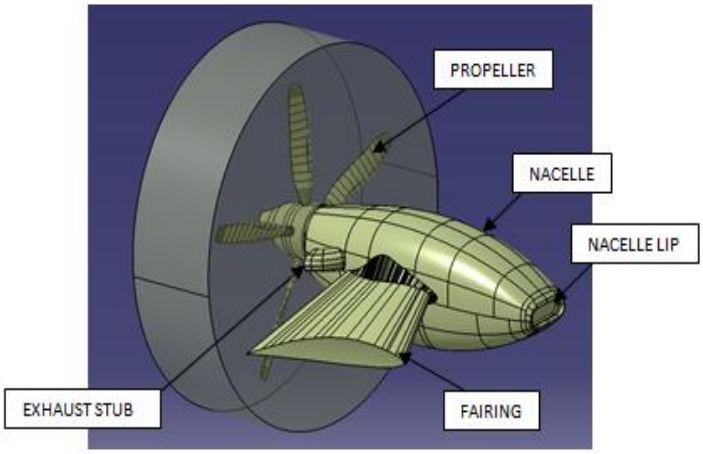


Figure 1. CAD-Model with part names

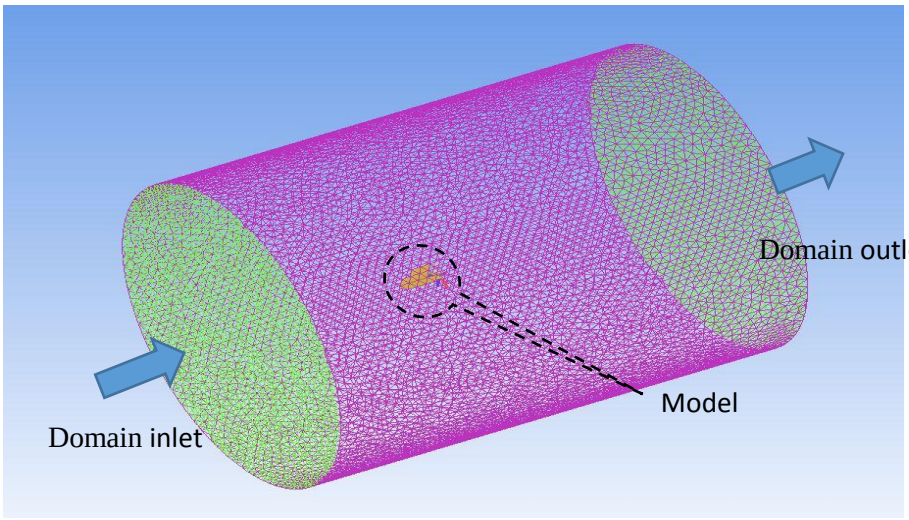


Figure 2. Mesh model

For numerical analysis following flight condition to be considered,

| Sr. No. | Flight Condition | Altitude, m (ft) | OAT, °c(K) | Speed m/s (Mach no.) |
|---|---|---|---|---|
| 1. | Ground Static Condition | 914.4 (3000) | 34 (307) | 6.8 (0.02) |

Table 1. Flight condition

The proper boundary conditions were applied to all appropriate places as follows [4],

| Sr. No | Face | Type of boundary condition | Magnitude | Temperature |
|---|---|---|---|---|
| 1. | Domain Inlet | Velocity Inlet | 6.8m/s | 307 K |
| 2. | Domain Outlet | Pressure Outlet | Pressure Outlet | 307 K |
| 3. | Domain Wall | Wall | - No slip condition. | 307 K |
| 5. | Stub inlets | Mass Flow Inlet | 0.5935 kg/s | 913 K |
| 6. | Blades, Spinner, etc. | Wall | - No slip condition. | - |

Table 2. Boundary conditions

## 3 RESULTS AND DISCUSSION

After completion of solver settings, the solution was carried out nearly 19000 iterations, when stability of residuals is found. In post processing contour of static temperature on blade surface and cut of plane was taken and temperature profile is shown in Figures 3-4. The temperature profile on blade indicates that the temperature was at middle region of blade and less at root and tip side of blade. The experimental analysis was carried out at CSIR-NAL. In this the Resistance Temperature Detectors are placed at camber side of propeller at every 110 mm distance from root to tip. The comparisons of results were plotted by graph as shown in figure 5. From graph it is observed that the numerical results of temperature are close to the practical results.

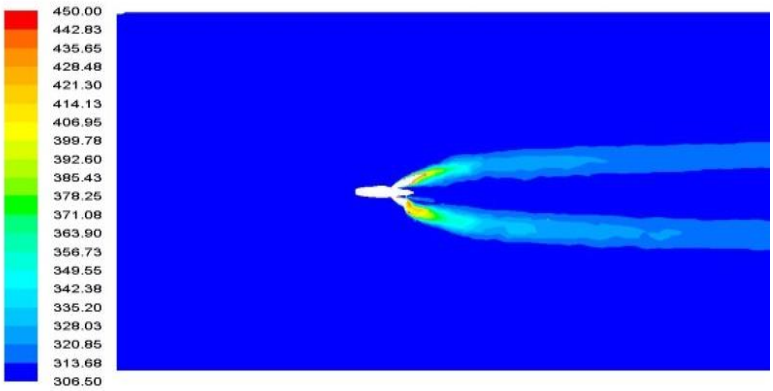


Figure 3. Contours of temperature for a plane

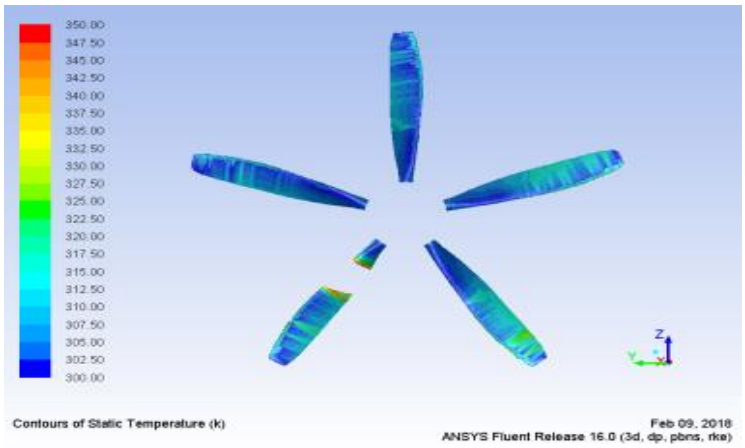


Figure 4. Temperature profile at propeller plane

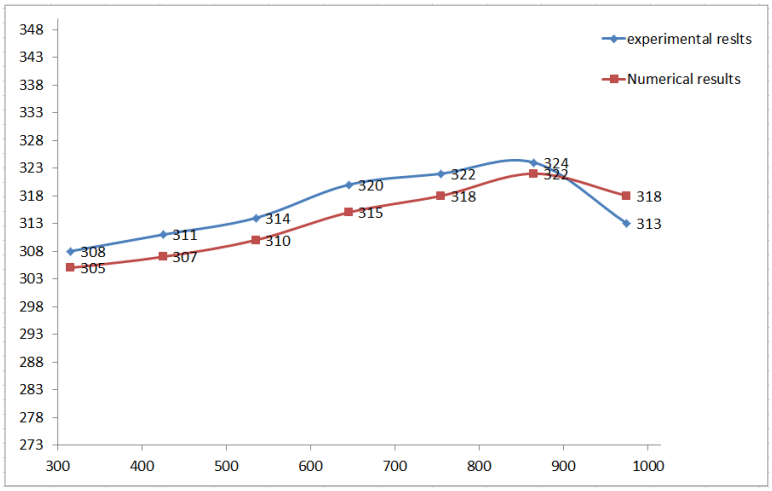


Figure 5. Result validation graph

## 4 CONCLUSION

This paper shows CFD study using ANSYS FLUENT has been successfully done for nacelle, propeller, and of LTA. In this simulation approach using Reynolds-averaged Navier-stokes computational fluid dynamics for analysis of propeller blade of pusher-propeller LTA has delivered a better understanding of temperature distribution on propeller blade surface. The simulations were carried out at ground static condition. The results obtained from CFD analysis shows an under prediction of 9.3 % when compared with the experimental results which has been carried out by CSIR-NAL and were found satisfactory. The same simulation method and model was used to do analysis for different flight conditions.

## REFERENCES

[1] Jiyuan Tu, Guan Heng Yeoh and Chaoqun Liu, Computational Fluid Dynamics: A Practical Approach, First Edition, *Elsevier*, USA, 2008.

[2] Mateusz Stajuda, Maciej Karczewski, Damian Obidowski and Krzysztof Jozwik, Development of a CFD model for propeller simulation, *Mechanics and Mechanical Engineering*, Vol. 20, No.4, PP. 579-593, 2016.

[3] Abhijeet B. Chougule, Vinay C A., Suresh R, Pusher Configured turboprop engine oil cooler ejector performance: CFD analysis and validation, *Proceeding of the 6th International and 43rd National conference on Fluid Mechanics and Fluid Power*, 35, 2016.

[4] Premkumar Pottanam Selvarajan, Senthil P. Kumar C, Elangovan Srinivasan, and Baskar Chakravarthy, Optimising Oil-Cooler Duct Position for a Pusher Type Turboprop Aircraft, *Aviation Technology, Integration, and Operations Conference, AIAA AVIATION Forum*, (AIAA 2013-4331), Los Angeles, CA, 2013.

# A LOW DISSIPATION ROE SCHEME FOR INCOMPRESSIBLE FLOW COMPUTATIONS

**Shainath Kalamkar, J. C. Mandal***
Department of Aerospace Engineering, IIT Bombay, Mumbai, India, *mandal@aero.iitb.ac.in

## ABSTRACT

In this paper, we propose a modification in Roe scheme for incompressible flows in artificial compressibility framework for minimizing numerical dissipation. The reconstructed velocity components across the interface are redefined as a function of pseudo Mach number. It modifies the velocity jumps across the cell interfaces which are responsible for the dissipation at pseudo Mach number. Three test cases are solved to demonstrate the efficacy of the method.

**Key Words:** *Roe scheme, Artificial compressibility, Numerical dissipation, Mach number.*

## 1. INTRODUCTION

Incompressible flows are encountered in a variety of engineering and scientific applications. Various numerical methods have been developed to solve incompressible flows. Methods based on artificial compressibility formulation introduced by Chorin [1] attracted researchers due to its several advantages. With this formulation it possible to use advanced numerical techniques developed for compressible flows to solve incompressible flows. This formulation allows one to solve the system of equations in a closely coupled manner. It possesses superior convergence as compared to popular pressure-based methods for incompressible flows.

Roe scheme is one of the advanced numerical methods developed for computing high-speed compressible flows. However, it has been observed that the solution of this scheme is adversely affected by undesired numerical dissipation at low Mach number. In 2008, Thornber et al. [2] demonstrated that at low Mach numbers the normal velocity jump across the cell interfaces is responsible for the undesirable numerical dissipation affecting the solution. Later, through a discrete asymptotic analysis of Roe scheme, Riper [3] reconfirmed the role of velocity jumps. Roe scheme is also widely used for solving incompressible flows in artificial compressibility formulation. In the present work, we carry out a discrete asymptotic analysis of the Roe scheme for incompressible flow to study the behaviour of numerical dissipation at low pseudo Mach number arising in artificial compressibility formulation. It has been found from the analysis that the interface velocity jumps are responsible for large numerical dissipation at low pseudo Mach number. Therefore, a modification in the velocity components is introduced in a similar manner to that suggested by Thornber et al. [2]. A few numerical test problems are solved in order to evaluate the performance of the proposed Roe scheme.

## 2. GOVERNING EQUATIONS

The compact form of two dimensional viscous incompressible flows in artificial compressibility framework is given as

$$\frac{\partial \mathbf{U}}{\partial t}+\frac{\partial \mathbf{F}}{\partial x}+\frac{\partial \mathbf{G}}{\partial y}=0$$

where $\mathbf{U} = \left[p, u, v\right]^T$, $\mathbf{F} = \mathbf{F}^c - \mathbf{F}^v$, $\mathbf{G} = \mathbf{G}^c - \mathbf{G}^v$, $\mathbf{F}^c = \left[\beta u, u^2 + p, uv\right]^T$,

$\mathbf{G}^c = \left[\beta v, uv, v^2 + p\right]^T$, $\mathbf{F}^v = \left[0, 2\nu\left(\frac{\partial u}{\partial x}\right), \nu\left(\frac{\partial v}{\partial x} + \frac{\partial u}{\partial y}\right)\right]^T$ and

$\mathbf{F}^v = \left[0, \nu\left(\frac{\partial v}{\partial x} + \frac{\partial u}{\partial y}\right), 2\nu\left(\frac{\partial v}{\partial y}\right)\right]^T$.

Here $u$, $v$, $p$, $\nu$ and $\beta$ are $x$ component of velocity, $y$ component of velocity, normalised pressure (with density), dynamic viscosity and artificial compressibility parameter respectively. Superscripts $c$ and $\nu$ denotes the inviscid and viscous flux respectively.

The semi-discretized form of the governing equation using cell centered finite volume method for a cell $i$ over an unstructured grid can be written as

$$\Omega_i \frac{d\mathbf{U}_i}{dt} + \sum_{k=1}^{K} T_{ik}^{-1}\mathbf{H}(T_{ik}\mathbf{U}_i, T_{ik}\mathbf{U}_k)dl_{ik} - \sum_{k=1}^{K}\left[\mathbf{F}^v n_x + \mathbf{G}^v n_y\right]dl_{ik} = 0$$

where $k$ = 1, 2, … $K$ ; with $K$ is the total number of cells surrounding the cell $i$ of volume $\Omega_i$. The term $T$ is the rotation matrix [4] for the edge $ik$ of length $dl_{ik}$ and $\mathbf{H}$ denotes the two state Riemann flux between cell $i$ and $k$.

## 3. FLUX CALCULATION

The inviscid flux at the cell edge $ik$ between cell $i$ and $k$ is calculated using Roe scheme as follows

$$\mathbf{H}\left(T_{ik}\mathbf{U}_i, T_{ik}\mathbf{U}_k\right) = \frac{1}{2}\left(\mathbf{F}^c\left(T_{ik}\mathbf{U}_i\right) + \mathbf{F}^c\left(T_{ik}\mathbf{U}_k\right)\right) - \frac{1}{2}\sum_{m=1}^{3}\tilde{\alpha}_m^{ik} \mid \tilde{\lambda}_m^{ik} \mid \tilde{\mathbf{K}}_m^{ik}$$

where, $\tilde{\lambda}_1^{ik} = \tilde{u}_n - \tilde{a}$, $\tilde{\lambda}_2^{ik} = \tilde{u}_n + \tilde{a}$, $\tilde{\lambda}_3^{ik} = \tilde{u}_n$ are the Eigen values of flux Jacobian $\frac{\partial\left(\mathbf{F}^c\left(T\mathbf{U}\right)\right)}{\partial\left(T\mathbf{U}\right)}$ with corresponding Eigen vectors $\tilde{\mathbf{K}}_1^{ik} = \left[1, -\frac{\tilde{a} - \tilde{u}_n}{\beta}, \tilde{v}\frac{\tilde{a} - \tilde{u}_n}{\beta\tilde{a}}\right]^T$, $\tilde{\mathbf{K}}_2^{ik} = \left[1, \frac{\tilde{a} + \tilde{u}_n}{\beta}, \tilde{v}\frac{\tilde{a} + \tilde{u}_n}{\beta\tilde{a}}\right]^T$ and $\tilde{\mathbf{K}}_3^{ik} = \left[0, 0, 1\right]^T$ respectively. Similarly, wave strengths are

$$\alpha_1^{ik} = \frac{\Delta u_1(\tilde{u}_n + \tilde{a}) - \Delta u_2\beta}{2\tilde{a}}, \alpha_2^{ik} = \frac{\Delta u_2\beta - \Delta u_1(\tilde{u}_n - \tilde{a})}{2\tilde{a}}, \alpha_3^{ik} = \Delta u_3 - \alpha_2^{ik}\tilde{u}_t\frac{\tilde{a} + \tilde{u}_n}{\beta\tilde{a}} + \alpha_1^{ik}\tilde{u}_t\frac{\tilde{u}_n - \tilde{a}}{\beta\tilde{a}}.$$

where, $\Delta u_1 = p_k - p_i$, $\Delta u_2 = \left(u_n\right)_k - \left(u_n\right)_i$ and $\Delta u_3 = \left(u_t\right)_k - \left(u_t\right)_i$. Here $u_n = un_x + vn_y$ and $u_t = vn_x - un_y$. Tilde denotes the Roe averages of the variables. In this formulation $\tilde{a} = \sqrt{\tilde{u}_n^{\,2} + \beta}$ denotes the Roe average of pseudo speed of sound.

To minimize the dissipation at low pseudo Mach number, reconstructed velocity components $u_n$ and $u_t$ are redefined as

$$\left(u_n\right)_i^C = \frac{\left(u_n\right)_i + \left(u_n\right)_k}{2} + z\frac{\left(u_n\right)_i - \left(u_n\right)_k}{2}, \qquad \left(u_t\right)_i^C = \frac{\left(u_t\right)_i + \left(u_t\right)_k}{2} + z\frac{\left(u_t\right)_i - \left(u_t\right)_k}{2}$$

$$\left(u_n\right)_k^C = \frac{\left(u_n\right)_i + \left(u_n\right)_k}{2} + z\frac{\left(u_n\right)_k - \left(u_n\right)_i}{2} \quad \text{and} \quad \left(u_t\right)_k^C = \frac{\left(u_t\right)_i + \left(u_t\right)_k}{2} + z\frac{\left(u_t\right)_k - \left(u_t\right)_i}{2}$$

where $z$ is defined as $z = min(M_{local}, 1)$ and $M_{local} = max(M_i, M_k)$ is local pseudo Mach number. Superscript $C$ denotes the modified components. The velocity components are reconstructed at the interface using solution dependent weighted least square (SDWLS) scheme.

In the present work, viscous fluxes at the every cell interface are calculated using Green-Gauss method.

## 4. RESULTS AND DISCUSSION

To validate the performance of the present formulation three types of lid driven cavity problems are solved. In all the cases no-slip boundary condition is imposed on boundaries except at the top lid where velocity in the horizontal direction (i.e. $u = 1$) is specified. Results obtained are compared with the benchmark results reported in the literature and the original Roe method.

### 4.1 *Lid driven square cavity*

A lid driven square cavity domain is discretized into 3588 triangular cells as shown in Figure 4.1(a). Simulation is performed at $\mathrm{Re} = 5000$ and results obtained are plotted in Figure 4.2(a). The results in the [5] used for the comparison are obtained on $129 \times 129$ structured grids. It is observed that the present method is able to predict the velocity variation reported in [4] compared to Roe method.

### 4.2 *Lid driven forward-step cavity*

A lid driven cavity with a forward-step is simulated on the grid with 1524 triangular cells shown in Figure 4.1(b). Results obtained for $\mathrm{Re} = 1000$ are plotted in Figure 4.2(b). The results are compared with the results reported in the [6] which are computed on $512 \times 512$ curvilinear grids. It is found that in this case also present method performs well compared to Roe method.

### 4.3 *Lid driven skew cavity*

In this case a lid driven cavity skewed at an angle 45 degrees is considered at $\mathrm{Re} = 1000$ which is discretized into 2628 triangular cells as shown in Figure 4.1(c). Here, the skewed shape of cavity creates a large portion of the domain with low pseudo Mach number. From Figure 4.2(c) it is clear that, compared to the Roe scheme the velocity profiles obtained in this case using present method are close to that found in [7] computed on $320 \times 320$ structured grids. The improvement in results obtained using present scheme clearly demonstrates the efficacy of the present formulation.

## 5. CONCLUSIONS

A simple and inexpensive way to improve the accuracy of Roe scheme for incompressible flows is presented. It is easy to implement and not restricted by any grid configuration or variable reconstruction procedure. It modifies the velocity jumps in the flux formulation to reduce the dissipation. Test cases solved concludes that this modification is useful for the accuracy improvement of the Roe scheme at low pseudo Mach number regions.

## REFERENCES

[1] A.J. Chorin, A numerical method for solving incompressible viscous flow problems, *Journal of Computational Physics*, 135, 118-125, 1997.

[2] B. Thornber, A. Mosedale, D. Drikakis, D. Youngs, R. J. R. Williams, An improved reconstruction method for compressible flows with low Mach number features, *Journal of Computational Physics*, 227. 4873-4894, 2008.

[3] F. Rieper, A low-Mach number fix for Roe's approximate Riemann solver, *Journal of Computational Physics*, 230, 5263-5287, 2011.

[4] E. F. Toro, *Riemann Solvers and Numerical Methods for Fluid Dynamics A Practical Introduction*, 2nd Edition, Springer-Verlag, 1999.

[5] K. N. Ghia, U. Ghia and C.T. Shin, High-Re solutions for incompressible flow using Navier-Stokes equations and multigrid method, *Journal of Computational Physics*, 48, 387-411,1982.

[6] C. W. Oosterlee, P. Wesseling, A. Segal and E. Brakkee. (1993). Benchmark solutions for the incompressible Navier-Stokes equations in general coordinates on staggered grids, *International Journal for Numerical Methods in Fluids*, 17,301-321, 1993.

[7] I. Demirdžić, Z. Lilek and M. Perić, Fluid flow and heat transfer test problems for non-orthogonal grids: Bench-mark solutions, *International Journal for Numerical Methods in Fluids*, 15, 329-354, 1992.

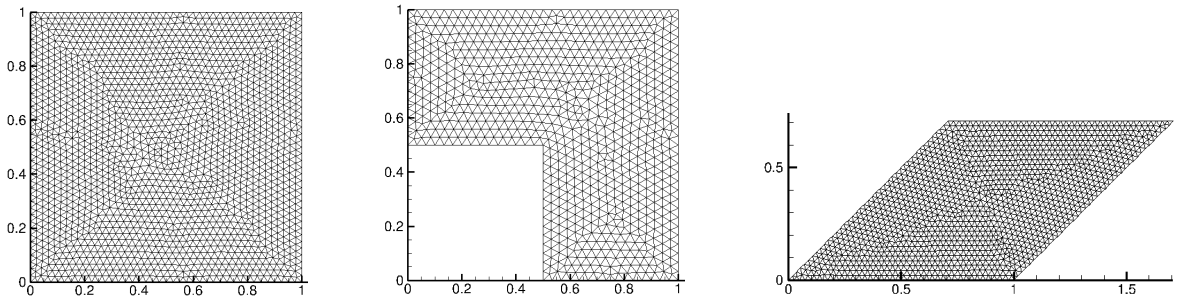

(a) (b) (c)

FIGURE 4.1 Grids used for (a) lid driven square cavity (b) lid driven forward step cavity and (c) lid driven skew cavity

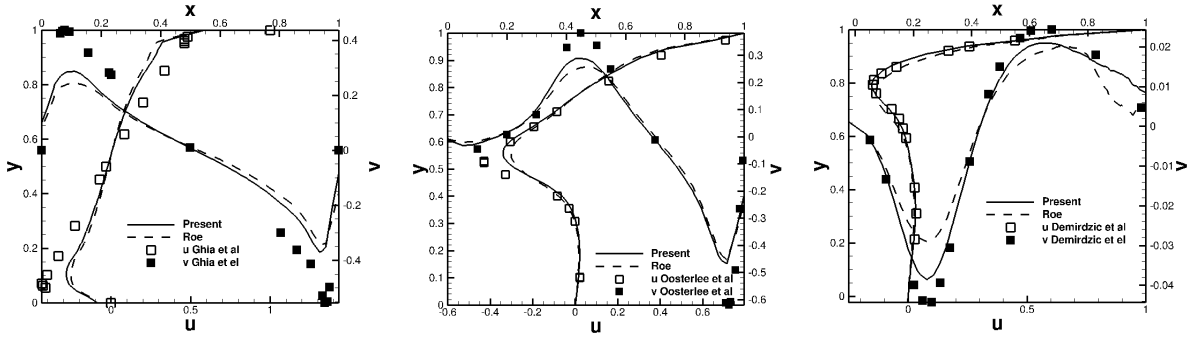


(a) (b) (c)

FIGURE 4.2 Variation of $u$ (w.r.t. $y$) and $v$ (w.r.t. $x$) velocities for (a) lid driven square cavity (b) lid driven forward-step cavity and (c) lid driven skew cavity

Fifth International Conference on Computational Methods for Thermal Problems
THERMACOMP2018, July 9-11, 2018, Indian Institute of Science, Bangalore, INDIA
*N. Massarotti, P. Nithiarasu, Pradip Dutta and C. Ranganyakalu (Eds.)*

# Effect of stratification and natural circulation on steam condensation in presence of non-condensable gases

**Somashekhar Kulkarni, Maneesh Punetha, Ajay Choudhary, Sameer Khandekar***
Department of Mechanical Engineering, Indian Institute of Technology Kanpur, 208016, India
*Corresponding Author: Tel: +91-512-259-7038, Email: samkhan@iitk.ac.in ABSTRACT

Complex thermal hydraulic phenomena inside the containment structure of Nuclear Power Plant (NPP) require detailed numerical and experimental modelling. During a severe accident, such as LOCA (Loss of Coolant Accident) due to MSLB (Main Steam Line Breakage), steam along with hydrogen dispense in the primary structure or dry well. The mixture of steam-hydrogen through wet well (where mixture get cooled to some extent) flow in the open containment space and interacts with pre-existing air. The jet interaction in the large containment space and continuous incoming heat, in the presence of several components, increases the temperature, pressure and combustible gas concentration ($H_2$, $CO_2$, etc.) inside the containment. Now, the problem arises mainly because of accumulating hydrogen and increasing heat, that demand proper hydrogen management and continuous cooling, respectively, failing which may cause severe structural damage and other long-term consequences. This study deals with the numerical modelling of spatio-temporal transport process related to stratification, natural circulation and containment wall condensation on a commercial platform Ansys CFX. The work is divided into two parts: (i) initial validations with the known experiments, (ii) analysis of the effect of stratification and natural circulation on steam condensation in a proposed Containment Thermal Hydraulic Test facility at IIT Kanpur.

**Key Words:** *containment thermal hydraulics, modelling, stratification, wall condensation.*

## 1. INTRODUCTION

Nuclear power is the one of the most viable alternative for replacing the depleting conventional power sources. However, some accidents in the past (such as Fukushima) have reduced the confidence of public on Nuclear Power Plant (NPP). This requires further reviewing of the safety standard for such power plants, and consideration of Beyond Design Basis Accidents (BDBA) which can happen in multiple unforeseen events [1].

A containment structure of NPP is huge part of the safety concern. The containment space in NPP is also a last safety barrier to the release of radioactive substances to the environment. During BDBA, a power failure may cause Loss of Coolant Accident (LOCA), which trigger large amount of hydrogen and steam generation. A rise in the pressure of reactor core may cause either Main Steam Line Breakage (MSLB) or primary structure failure. In such scenario, hot steam and other Non-Condensable Gases (NCG) may release in the outer containment environment. To avoid pressurization of the containment building, efficient cooling and proper management of combustible gases is essential [2]. Hence, this work presents a numerical study of one such situation of hot steam release and cooling activity in a model test facility. The scenario is replicated by injecting hot steam in the chamber and depressurization due to condensation at the cold wall.

In present work, a simplified mathematical model of Containment Thermal Hydraulic Test Facility (CTHTF) is developed. This mathematical model includes the effects of critical parameters such as NCG mass fraction, buoyancy driven stratification and jet interaction on heat transfer mechanism inside a model containment structure. The model is solved numerically in Ansys CFX. The study takes account of several simultaneously affecting phenomena such as jet mixing, stratification, natural circulation and wall condensation.

## 2. PROBLEM DESCRIPTION

Pressurization and subsequent depressurization by condensation of steam are studied through different tests. The test setup is capable of injection of helium and steam through inlets located at different locations and orientation. The current simulation is only restricted to axisymmetric bottom injection in vertically upward direction. These simulations have been run in the commercial package ANSYS CFX. The geometry is similar to the TOSQAN facility. Thus, the numerical solver is first validated by TOSQAN test facility shown in Fig. 1(a). The data for Test 101 (from Malet et al. [3]) is compared with the obtained results. For the validation case, a 3-D axisymmetric model of the TOSQAN facility (Fig. 1(c)) of test section (Fig. 1(b)) is modelled. Test 101 involves injection of steam from the lower inlet into the chamber. Mass flow rate of 0.167 g/s (calculated for the axisymmetric model which is 12 g/s for complete model) is injected. Other boundary conditions are given in Table 1. All other walls are kept at constant temperature of 120℃; pipe wall is insulated.

The geometry of CTHTF is modelled and is show in the figure Fig. 2(a). The test section has three condensing sections of area 130 mm ×130 mm. These condensing sections are located at different heights from the bottom. Test is conducted by injecting steam at three different volumetric Richardson number and covers the momentum dominated, mixed flow and buoyancy dominated regime. Once the test section is pressurized and reached a steady state, the injection is stopped and depressurization due to condensation takes place. The inlet and boundary conditions for the performed simulation are given in Table 2.

Table 1: Initial and boundary conditions inside the TOSQAN test facility for Test 101[3].

| Initial Conditions | | | | | Boundary Conditions | | |
|---|---|---|---|---|---|---|---|
| $X_{air}$ | $X_{H2O}$ | Temperature (℃) | Pressure (bar) | Density (kg/m$^3$) | $X_{H2O}$ at inlet | Inlet temperature (℃ ) | Density at inlet (kg/m$^3$) |
| 1 | 0 | 120 | 1 | 0.9 | 1 | 130 | 0.54 |

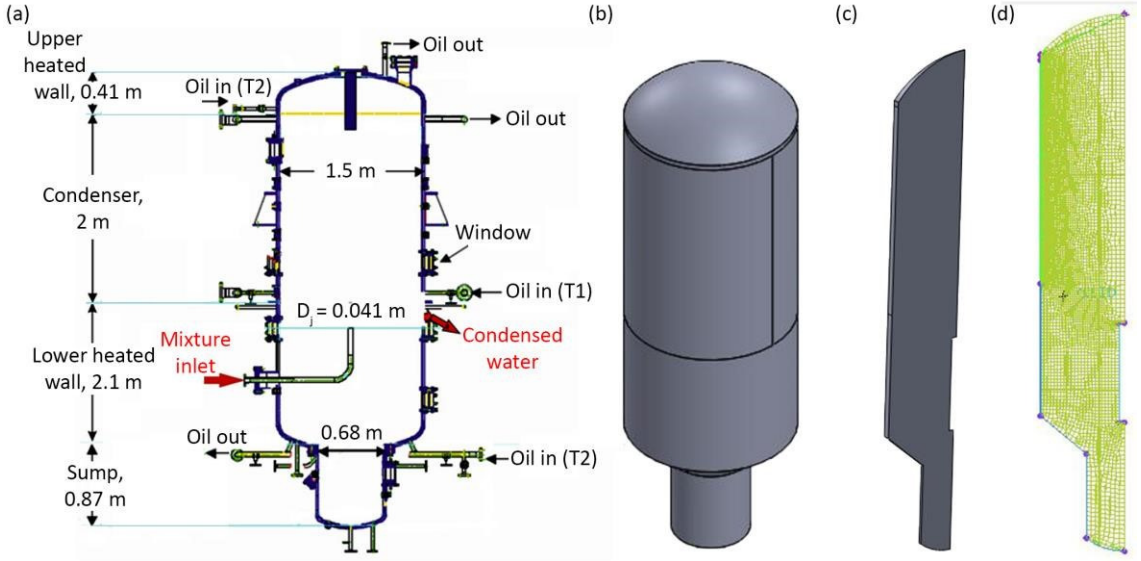


Figure 1: (a) Details of TOSQAN test facility (b) 3-D view of test section (c) 3-D axisymmetric view of test section (d) Mesh details

## 3. NUMERICAL METHOD

The solution to current problem involves solving a set of Partial Differential Equations (coupled equations of mass, momentum, energy and species transport) for which no analytical solutions exist. Hence, a numerical approach based on the Finite Volume discretization technique is adopted. Due to

the nonlinear nature of the equations, an iterative approach is used. Mixture gases are handled with Multicomponent mixture model, whereas wall condensation is taken care by Wall condensation model [4]. To achieve high accuracy and to reduce the cell count, a hexahedral dominant mesh is generated for both the validation case and the CTHTF test setup. Grid independence studies were conducted and the mesh which gave the most accurate results was chosen. The meshing is done in ICEM CFD. Cell count for the validation geometry and test setup geometry is 5771 and 418699, respectively with a mean quality of 0.87 (on a scale of 0-1 with 1 being highest). The mesh has been kept fine at critical areas such as the inlet, corners and walls. Minimum Y+ of 1 is maintained near the condensing wall of CTHTF. Time step of the transient simulation is decided by keeping in mind that CFL number should be less than 20, since an implicit solver is used [5]. The purpose of the numerical simulation is to solve for the fluid flow, heat transfer, concentration distribution as well as the level of condensation of steam.

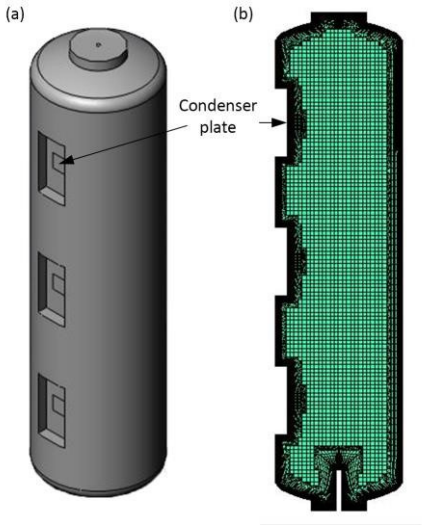


Figure 2: (a) 3-D model of CTHTF, (b) Meshing of CTHTF geometry

Table 2: Initial and boundary conditions inside the CTHTF test facility.

| Initial Conditions | | | | |
|---|---|---|---|---|
| $X_{air}$ | $X_{H2O}$ | Temperature (°C ) | Pressure (bar) | Density (kg/m$^3$) |
| 1 | 0 | 120 | 1 | 0.9 |
| **Boundary Conditions** | | | | |
| $Ri_v$ | Q (m$^3$/s) | m (g/s) | $T_{inj}$ (°C) | |
| 0.1 | 0.002221 | 2.220804 | 120 | |
| 1 | 0.000702 | 0.70228 | | |
| 10 | 0.000222 | 0.22208 | | |

## 4. RESULTS*

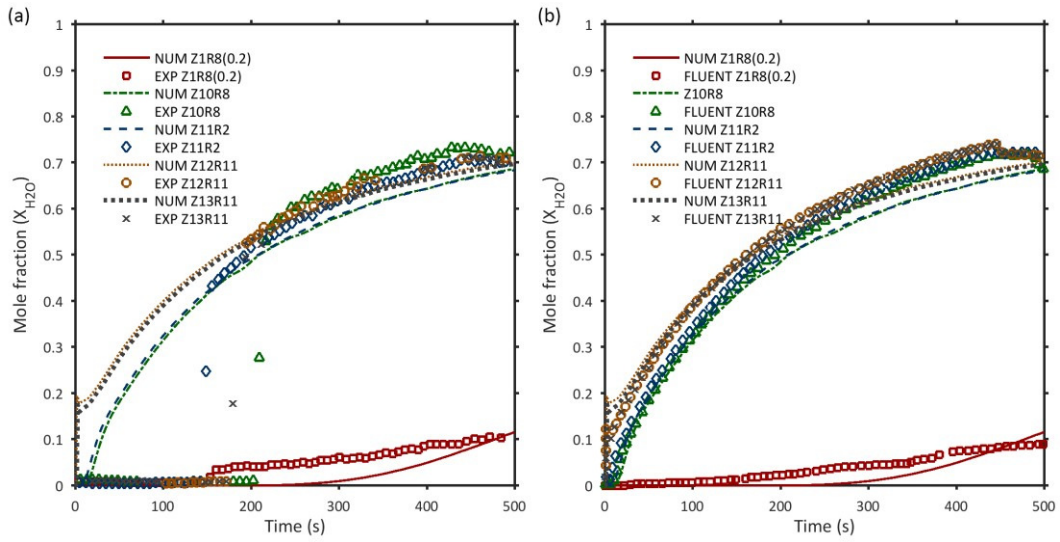


Figure 3: Comparison of current numerical results of steam injection test (a) with experiment, (b) with numerical results of Malet et al. [3]

*Detailed simulations are currently underway. Further results will be included in future.

Three regimes are simulated for the steam injection with continuous cooling via condensation heat transfer. Simulations are carried out till steady-state is achieved. This is ensured by comparing the injection mass flux with condensation mass flux, at steady state both must be equal. In all three test cases, once the steady state is achieved the injection is stopped, and the test section is allowed to depressurize. The steam mole fraction at steady state and consecutive depressurization is shown in Fig. 4. At lower $Ri_v$, the steam is well mixed in the chamber with significantly higher concentration than higher $Ri_v$ case. At higher $Ri_v$ steam will stratify, which can have an effect on condensation heat transfer.*

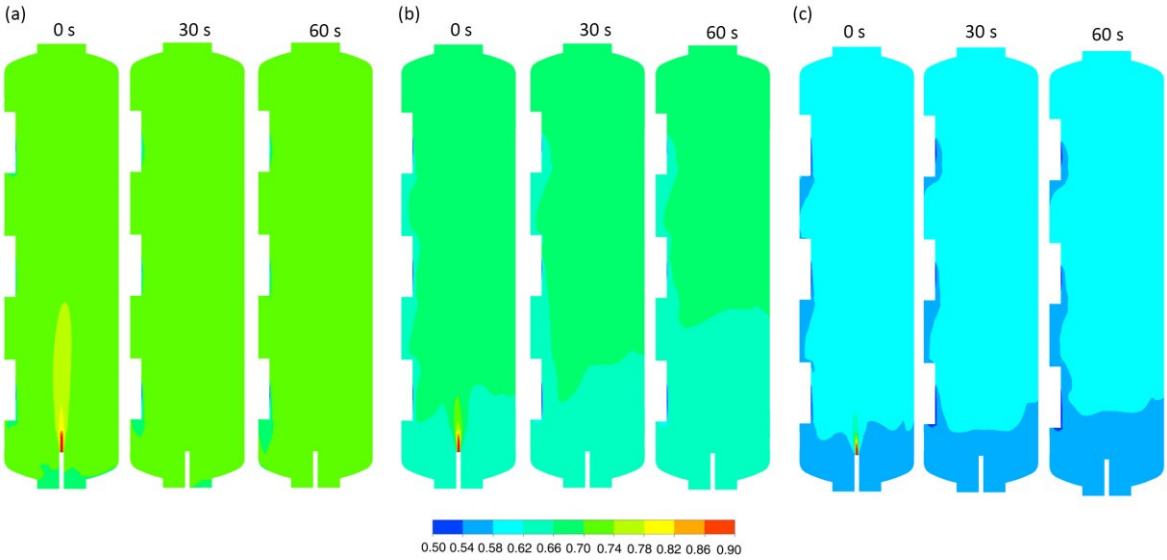


Figure 4: Steam molar fraction contour at (a) $Ri_v = 0.1$, (b) $Ri_v = 1$ and (c) $Ri_v = 10$

## 5. CONCLUSIONS

The numerical modelling of proposed Containment Thermal Hydraulic Test Facility (CTHTF) is done and a problem of steady state steam condensation and subsequent depressurization is solved in Ansys CFX. Tests are performed at three different regimes: momentum dominated, mixed flow and buoyancy dominated regimes. Buoyancy dominated and mixed flow regimes of tests show stratification of steam in the chamber, whereas in the momentum dominated tests, a well-mixed air steam mixture is available due to enhanced mixing at higher velocities. Further depressurization due to condensation will promote stratification of steam in the test chamber.

## REFERENCES

[1] Yadav MK, Khandekar S, Sharma PK. An integrated approach to steam condensation studies inside reactor containments: A review. Nuclear Engineering and Design. 2016;300:181-209.
[2] Agrawal N, Prabhakar A, Das SK. Hydrogen distribution in nuclear reactor containment during accidents and associated heat and mass transfer issues—a review. Heat Transfer Engineering. 2015;36:859-79.
[3] Malet J, Laissac R. CFD calculations of stratification build-up tests of light gas in a closed vessel under controlled boundary conditions. Computers & Fluids. 2015;107:224-41.
[4] Punetha M, Khandekar S. A CFD based modelling approach for predicting steam condensation in the presence of non-condensable gases. Nuclear Engineering and Design. 2017;324:280-96.
[5] Casey M, Wintergerste T. ERCOFTAC Special Interest Group on Quality and Trust in Industrial CFD-Best Practice Guidelines. European research community on flow, turbulence and combustion. 2000:123.

# Numerical investigation of the effect of curvature on the flow in an intermediate compressor duct

**Manish Sharma**
Research Scholar, Mechanical Engineering Department, SVNIT, Surat,
Sharma.manish726@gmail.com

**Dr. Beena Baloni**
Asst. Prof., Mechanical Engineering Department, SVNIT, Surat, pbr@med.svnit.ac.in

## ABSTRACT

Jet propulsion engines uses twin-spool compressor for requirement of high pressure ratio at design and off-design conditions. In a common twin-spool configuration the LP compressor and the HP compressor are driven by the LP turbine and HP turbine respectively. Transition ducts are to be found as a means of connecting the flow passages of the low and high pressure stages of compressors. Ducts are required because flow stability imposes that compression must be divided between two or three spools. However, optimization and high bypass ratio necessitate that the mean diameter of the compressors must be reduced, and so the interconnecting duct takes the form of an S-shape. Flow distribution within the duct depends on duct curvature, cross-sectional area variation, internal struts and the internal flow field. As flow coming out from upstream compressor it becomes very complicated especially during the operation at off-design conditions. This leads to secondary flow generation, counter-rotating vortex pairs and large pressure gradients on the bends of hub and shroud. Moreover, boundary layer separations are also occurred. It is advantageous to make the flow free from these effects. This paper incorporates a preliminary numerical investigation of pressure field, total pressure losses along the duct length, velocity field and turbulent kinetic energy distribution of a 2-D axi-symmetric duct with appropriate boundary conditions for two turbulence models. The numerical results are validated with the experimental data available in literature. Outcome of work suggests that the 2D axis symmetric flow through an S-shaped duct is complex, because of rapidly varying curvature, pressure gradient and non-uniform distribution of mass flux along the inner wall as well as outer wall and these have a significant effect on the flow behaviour within the duct. Moreover, radial adverse pressure gradient is responsible for generation of boundary layer within the s-shaped duct.

**Key Words:** Compressor, *Annular S-shaped duct, Pressure coefficient, Curvature.*

## 1. INTRODUCTION

As the annular S-shaped duct are often used between the components of a gas turbine to maintain the continuous supply of air and fuel. Compressor transition S-shaped duct is used to supply the compressed air from low pressure compressor to high pressure compressor without significant loss of the pressure ratio. S-shaped duct also ensures that the uniform flow is supplied with minimum distortion. Hence, design of an S-shaped duct plays a crucial role for achieving the maximum performance of the downstream high pressure compressor. In addition of it, Convex, concave curvature at the walls and pressure gradient in radial direction also add complexity within the duct. Curvature and pressure gradient cause development of the boundary layer along the duct walls. However, development of the boundary layer also depends on the mild or strong types of curvature.

Further, a compressor stage at the upstream of the S-shaped duct also adds more complication in terms of the inlet conditions at the duct. However, it enhances the turbulence intensity within the duct that leads the stability of the outlet flow and eventually increases the pressure recovery with small increment of the total pressure loss. Britchford et.al [1] experimentally and numerically studied the effect of the duct curvature and wakes emanating from the upstream compressor on the flow development within the duct by using LDA and five -hole probe techniques and found that the tendency of secondary flow generation and boundary layer parameters were reduced with upstream compressor stage. In additions of it, Reynolds stress model gave better capture of curvature effects as compared to k-ε model. Bailey et.al [2] experimentally investigated the effect of strut on the flow within the duct and stated that localized effect of the strut is higher however it did not significantly alter the overall performance of the duct.

## 2. Numerical Simulation

### 2.1 Geometry and Meshing

Present numerical prediction is carried out on the constant area annular S-shaped duct of the existing literature [1] with inlet passage height ($h_{in}$) of 71.1mm and axial length of 241.74mm. Detail inlet and exit geometry of the annular s-shaped duct is summarized in Table 1. In order to simulate the flow structure within the duct, 2-D geometry with similar parameters [1] is designed in GAMBIT and illustrated in Figure 1.

| | Inlet | Exit | Ratio |
|---|---|---|---|
| $x_m$ | 0.02 | 0.24174 | - |
| $r_i$ (m) | 0.2845 | 0.2110 | 0.74376 |
| $r_o$ (m) | 0.3556 | 0.3006 | 0.84505 |
| $r_m$ (m) | 0.32005 | 0.25605 | 0.80003 |
| h(m) | 0.0711 | 0.8890 | 1.25035 |
| A($m^2$) | 0.142977 | 0.143023 | 1.00 |
| HTR | 0.80006 | 0.70416 | 0.88013 |

TABLE 1.Inlet and exit s-shaped duct geometry

Numerical simulation is carried out using commercial CFD software Ansys- Fluent. Structured mesh is generated for whole assembly. Face meshes are generated with quadratic type of elements using map scheme available in Gambit. To capture accurate viscous effect near the wall Y+ >11 is selected for both of the turbulence models. Stream wise velocity of 28.3 m/s and turbulence quantities are selected as inlet boundary condition to the parallel duct in both of cases and static pressure is assumed to zero at outlet.

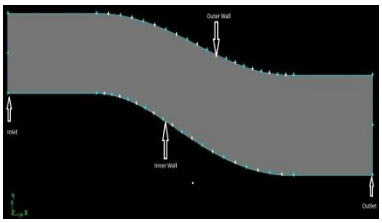


FIGURE 1. S-shaped duct

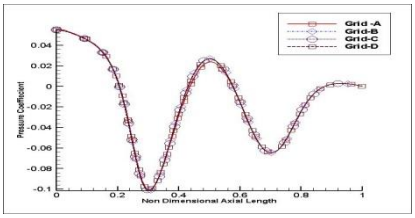


FIGURE 2. Grid independence test

### 2.2 Grid Independence Study

To make the results independent with the grid sizes, grid convergence analysis is also performed. In the present case, four different grid sized are chosen and variation of the static pressure coefficient along the duct length is selected as a sensitive parameter. For lucidity, the variation of static pressure coefficient along the duct length for four different grid sizes is presented in Figure 2. It is detected that results obtained for grid C are D are overlapping to each other for entire axial length. Hence, grid C with 192000 elements; is selected as independent grid for both of the turbulence models.

## 3. RESULTS

Since the results obtained from the numerical simulations by using two turbulence models are to be compared with existing literature, the variation of the parameters at the identical locations to literature traverse lines throughout the duct passage. In the FLUENT, it is possible to select grid lines which are almost equivalent to their respective traverse lines and locations of these lines with respect to mid-passage height are tabulated in Table 2. To make the results more significantly understandable, all parameters are presented in non-dimensional form.

| $X_m$/L | -.25 | 0.0 | 0.125 | 0.25 | 0.375 | 0.5 | 0.625 | 0.75 | 0.875 | 1.0 | 1.4 |
|---|---|---|---|---|---|---|---|---|---|---|---|

TABLE 2. Traverse lines locations

### 3.1 Predicted Contours

To describe the influence of duct curvature, axial velocity and static pressure varition along the walls are shown in Figures 3 and 4 respectively. It can be seen form the Figures that pressure is minimum at convex curvature and maximum at concave curvature due to convergent divergent nature of the wall respectively whereas, axial velocity shows opposite nature.

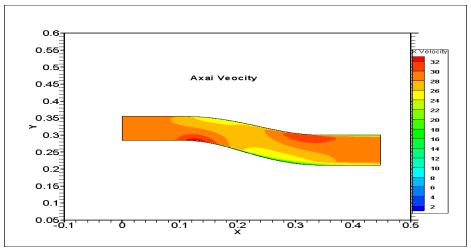


FIGURE 3. Axial velocity

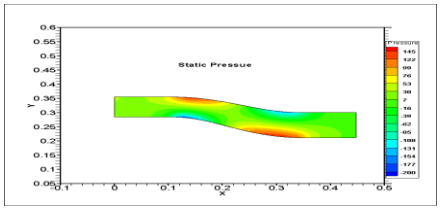


FIGURE 4. Static pressure

### 3.2 Validation of Computational Results

#### 3.2.1 Wall Static Pressure Distribution

It is well known that the development of flow within the duct is affected significantly by the pressure distribution which can be clearly understood from the Figure 5. This data is exhibited in terms of pressure coefficient ($C_p$), which is calculated using mass weighted average total and static pressures at inlet to the duct(x/L=0.0). Figure shows the variation of static pressure along the walls for predictions as well as existing literature [1].The Figure 5 indicates that there is strong pressure gradient along the inner wall compare to outer wall in all the cases. Within the first bend, pressure along the outer wall is higher than inner whereas, it is altered when it approaches to the second bend. As the consequences, along the inner wall ($C_p$), initially sinks and then advances from -0.34

to +0.22 in experimental case, -0.45 to +.20 in k-ε case and from $-0.45$ to $+0.22$ in RST case. It can also be understood that inner wall is prominent to adverse pressure gradient. In spite of it, most of portion of the outer wall is subjected to favourable pressure gradient and it varies from +0.20 to -.28 whereas, in k-ε and RST model, it is +.22 to -.36 and +.22 to -.34 respectively.

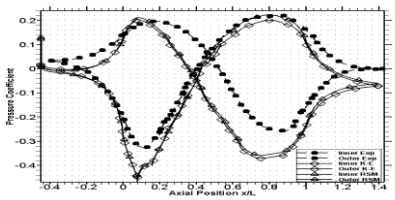


FIGURE 5. Static pressure distributions along the walls

### 3.2.2 Stream Wise Velocity

To check the accuracy of CFD predictions, the predicted stream wise velocities are to be compared with the existing literature [1]. Here, only velocity profile at x/L =-0.25 location is shown. Since, at the upstream of the duct identical inlet conditions have been applied as in the existing literature [1], predicted velocity profiles are similar to the experimental result with similar boundary layer thickness.

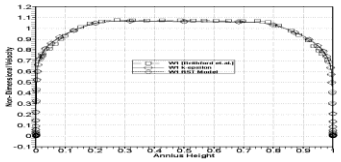


FIGURE6. Stream wise velocity at x/L=-0.25

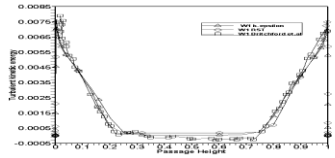


FIGURE7. Turbulent kinetic energy

It can be understood from the above figure that core region has uniform velocity and maximum velocity is also found into core region. However, near the wall, velocity is gradually varying to accommodate the effect of the boundary layer.

### 3.2.3 Turbulent Kinetic Energy

Turbulent kinetic energy in the Reynolds stress model is not obtained directly as in the eddy viscosity model. Distribution of turbulent kinetic energy shown in Figure 7, is in the non-dimensional form ($k/U_{Mean}^2$). From the Figure, it can be understood that near the wall some elevated region are found which indicate the complex behaviour of the wall. Predicted turbulent kinetic energy distributions show fairly good agreement with the existing literature [1].

## 4. CONCLUSIONS

A numerical investigation of annular S-shaped duct is carried out to examine the influence of the rapidly varying pressure gradients, non-uniform mass flux distribution and curvature of the wall. Comparison of predicted results with existing experimental data depicted good agreement for stream wise velocity, wall static pressure distribution, and turbulent kinetic energy. However, some discrepancies showed by predicted results because of not to accommodate the exact effects of the pressure gradient, non-uniform distribution of mass flux and curvature adjacent to the wall. Hence, accurate prediction of such a flow is always a challenge task for any turbulence model.

## REFERENCES

[1] K.Britchford,A.Manners,J.McGuirk, and S.Stevens, " Measurement and prediction of flow in annular s-shaped ducts," Experimental Thermal and Fluid Science,09,197-205,1994.

[2] D.Bailey,K.Britchford,J.Carrotte and S.Stevens, " Performance assessment of an annular s-shaped duct," Journal of Turbomachinary,119,149-156,1997.

[3] K.M. Britchford, "The aerodynamic behaviour of an annular s-shaped duct," Ph.D dissertation, Loughborough University, August 1998.

[4] P.Hoffmann,K.Muck and P.Bradshaw, "The effect of concave surface curvature on turbulent boundary layers," Journal of Fluid Mechanics,161,371-403,1985.

[5] H.Schlichting, Boundary Layer Theory, 7th Edition, McGraw-Hill, 1968.

[6] H.I.H. Saravanamuttoo,G.F.C Rogers and H.Cohen, Gas Turbine Theory, 5th Edition, Pearson Eduction, 2001.

[7] M.K. Gopaliya, M.Kumar, S.Kumar and S.M.Gopaliya,"Analysis of performance characteristics of s –shaped diffuser with offset," Aerosapace Science and Techanology, 11,130-135, 2007.

Fifth International Conference on Computational Methods for Thermal Problems
THERMACOMP2018, July 9-11, 2018, Indian Institute of Science, Bangalore, INDIA
*N. Massarotti, P. Nithiarasu, Pradip Dutta and C. Ranganyakalu (Eds.)*

# Design and numerical analysis of fluid flow characteristics in a non-axisymmetric convergent nozzle

**Manoj Kumar, S. K. Behera, R. K. Sahoo**
Department of Mechanical Engineering, NIT, Rourkela, Odisha, India, 769008,

E-mail:- manojbeg526@gmail.com, beherask@nitrkl.ac.in, rksahoo@nitrkl.ac.in

## ABSTRACT

This paper reports the fluid flow characteristics inside a non-axisymmetric airfoil convergent nozzle used to enhance the overall performance of a turbo-expander. The coordinates of upper ($5^{th}$ order) and lower ($3^{rd}$ order) surface of the nozzle is obtained using curve fitting method in Matlab© thereafter the computational domain has been generated in SolidWorks©. Numerical analysis has been done to visualize the flow field behavior inside the nozzle for different cryogenic fluids at a pressure ratio of two. Shear stress transport (SST) turbulence model has been used to solve the computational domain. The key feature of this implementation is to obtain subsonic velocity at the nozzle exit. The computing results show that the reduction in temperature for air is highest i.e., 14.2 K with Mach number of 0.88 at the outlet as compared to other fluids.

**Key Words:** Fluid flow, Non-axisymmetric nozzle, Turboexpander

## 1. INTRODUCTION

In the design of turbo-expander for the liquefaction of various cryogenic gases, the design of nozzle plays an important role, which affects the performance of the system. In this framework, a great interest has been concentrated in the development of non-axisymmetric convergent subsonic nozzle. Cryogenic fluids such as liquid helium, nitrogen, oxygen, hydrogen etc. are used due to its variety of applications in the fields such as, rocket propulsion and aerospace appliances, superconducting equipment, industrial applications etc. The advent of modern superconductors which will achieve superconductivity at or above liquid nitrogen temperature will increase the importance of liquid nitrogen as a refrigerant [1, 2].

The computational work to visualize the effect of nozzle pressure ratio on flow structure, shock-induced boundary layer separation inside a non-axisymmetric supersonic convergent-divergent nozzle was performed by Hasan [3]. The selection of cross-section at the exit plays a vital role to reduce the thrust loss. Researchers suggest that rectangular cross-section possess less thrust loss as compare to circular one whereas density profiles through the circular nozzle have good agreement with the experimental results as compared to that of for the rectangular or square nozzles [4, 8]. The numerical work was carried on to visualize the oscillatory flow pattern and hysteresis phenomenon for different pressure ratios between two shock structures (FSS and RSS) and its effect on annulus height, wall pressure and shear stress in axisymmetric and truncated contour nozzle [5]. The work is carried on to investigate the wall pressure, flow separation, shockwave propagation and boundary layer transient flows through 3-D planar, supersonic convergent-divergent and Laval nozzle using different subgrid models and proposed that WMLES provide best results using LES and validate it with experimental results [6, 7].

In the current paper, a non-axisymmetric convergent nozzle is designed to obtain subsonic speed at the outlet which is essential for an effective design of a turbo-expander. The design method is based on $3^{rd}$ and $5^{th}$ order curve under specified boundary condition which delivers uniform subsonic flow as well as the decrease in temperature of the fluid which is essential at low temperature. The geometry has been developed to minimize the huge amount of energy losses due to flow separation which increases the performance of the system. The demand for high-performance air and helium

liquefaction unit needs numerical analysis of flow field behavior inside major components such as nozzle to visualize the flow separation, pressure, velocity, Mach number, temperature, shock etc.

## 2. COMPUTATIONAL DOMAIN AND GOVERNING EQUATUIONS

A three-dimensional computational domain has been developed in SolidWorks© for numerical simulation is shown in the Figure [1 (a)].

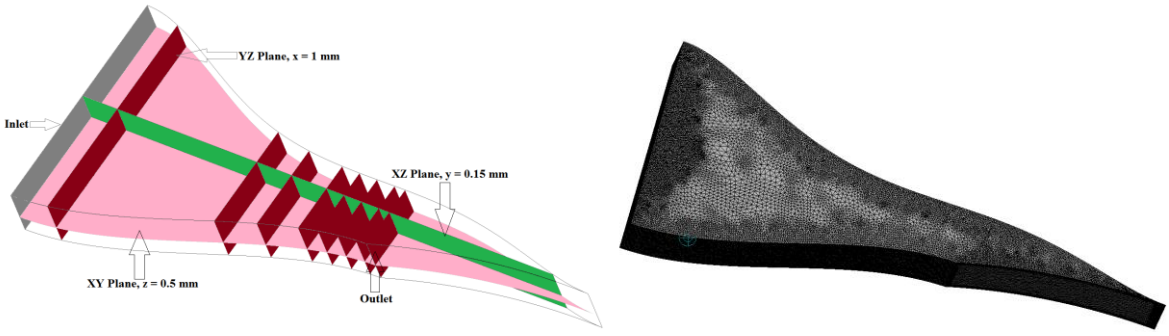


(a) (b)

Figure 1. (a) Schematic of a non-axisymmetric convergent nozzle (b) Computational mesh

Although the experiments give the exact results but it is expensive. Accurate prediction of pressure, velocity, temperature, flow separation, shock etc. inside the domain is necessary to develop an airfoil nozzle used in turbo-expander. Therefore, Computational Fluid Dynamics plays a vital role to visualize these parameters for the optimum design of the nozzle. The flow behavior, boundary layer separation etc. strongly dependent on turbulence models used for RANS simulations. In order to compute the flow field inside the nozzle, a computational mesh has been created in ANSYS© mesh which is shown in the Figure [1 (b)].

To achieve the accurate simulation results, the selection of numerical scheme is equally important as turbulence model. In the current study, the second-order upwind scheme was selected for discretization of momentum and energy equations and no-slip with adiabatic boundary condition is imposed on the wall. The flow field structure of helium, hydrogen, oxygen, and air for the pressure ratio of two are compared.

By using SST turbulence model, an efficient prediction of pressure, velocity, Mach number, static enthalpy etc. have obtained. Medium turbulence intensity of 5% is used. In the current analysis, governing equations which is used to solve the computational domain in CFX are as follows.

Continuity Equation:

$$\frac{\partial \rho}{\partial t} + \nabla.\left(\rho U\right) = 0$$

Momentum Equation:

$$\frac{\partial\left(\rho U\right)}{\partial t} + \nabla.\left(\rho U \otimes U\right) = -\nabla p + \nabla.\tau + S_M$$

Total Energy Equation:

$$\frac{\partial\left(\rho h_{tot}\right)}{\partial t} - \frac{\partial p}{\partial t} + \nabla.\left(\rho U h_{tot}\right) = \nabla.\left(\lambda \nabla T\right) + \nabla.\left(U.\tau\right) + U.S_M + S_E$$

## 3. RESULTS

The flow behavior inside a nozzle for different ideal gases (air, helium, hydrogen, and oxygen) has been reported. Generally, ideal nozzles provide uniform and parallel flow at the exit. Figure [2 (a)] represents the variation of pressure along the axial distance for different ideal gases for the pressure ratio of two. It clearly shows that the pressure variation inside the domain is from 16 bar (inlet) to 8 bar (outlet) is almost similar for all the gases but the other parameters are changed.

Figure [2 (b)] represents the Mach number and velocity profile along the axial distance. The variation of Mach number for all the fluids follows similar pattern up to 0.5 mm. Thereafter, Mach number of air increases which is 0.88 at the outlet. It is interesting to observe that the variation of Mach number for hydrogen and oxygen are almost identical but its velocity variation is different.

Figure [3 (a-d)] represents that the velocity contours of the different fluid. The velocity of air at axial distance x = 2.5 mm is approximately 35.20 m/s and continuously increases as one move towards the outlet where it is approximately 166.00 m/s with Mach number of 0.88. The velocity contours of helium at plane x = 2.5 mm the velocity is approximately 58.45 m/s and continuously increases as one move towards the outlet where it is approximately 214.65 m/s with a Mach number of 0.54. The velocity contours of hydrogen at x = 2.5 mm is approximately 78.64 m/s and continuously increases as one moves towards the outlet where it is approximately 309.00 m/s with a Mach number of 0.60. The velocity contours of oxygen at x = 2.5 mm the velocity is approximately 36.40 m/s and continuously increases as one moves towards the outlet where it is approximately 120.00 m/s with a Mach number of 0.62. It is interesting to observe that velocity of hydrogen is highest among all these gases from an inlet to outlet, whereas it is minimum for oxygen. It is also observed that the velocity increases rapidly after x = 5 mm and becomes stable at the time of impact with the turbine (outlet of the nozzle) due to which a uniform subsonic flow has been occurred. The Mach number at the outlet for helium is lowest for this nozzle.

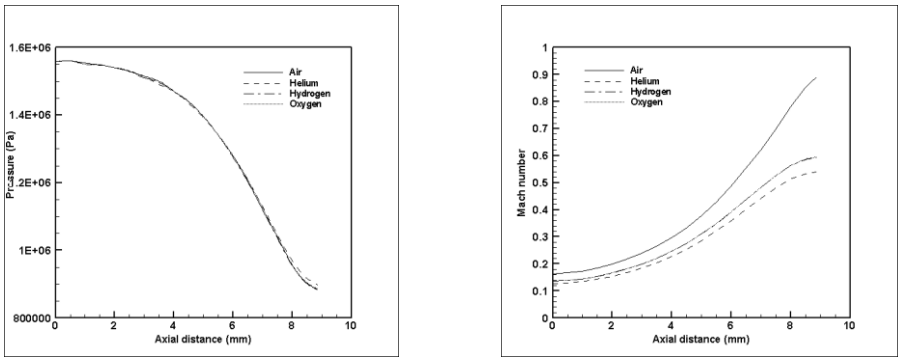


(a) (b)

Figure 2. (a) Pressure profile (b) Mach number variation from inlet to outlet

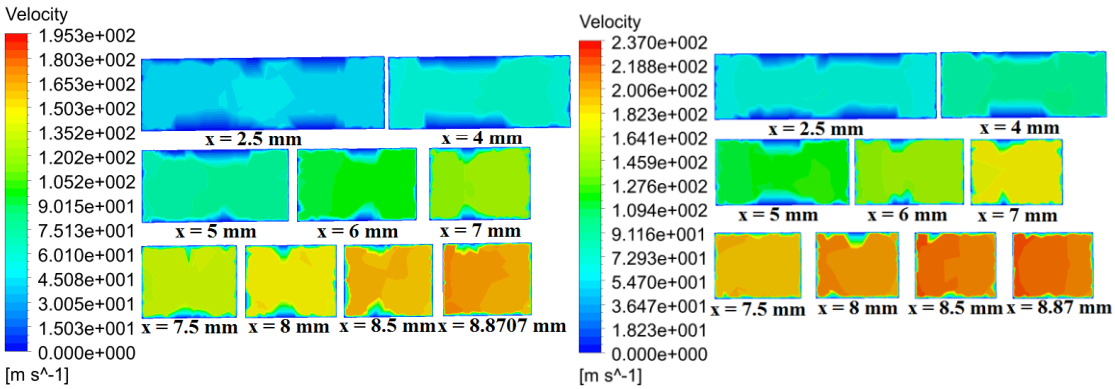


(a) (b)

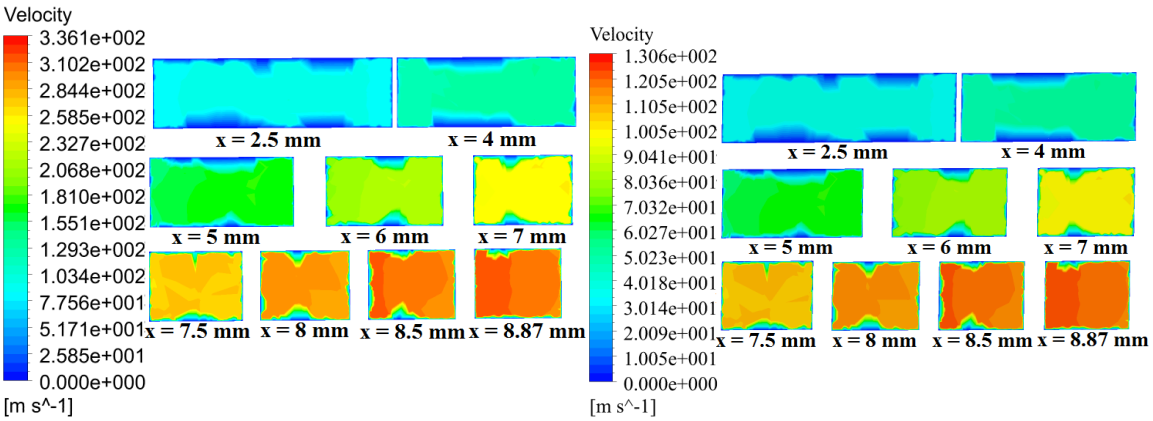


Figure 3. Velocity contour at different axial planes (a) Air (b) Helium (c) Hydrogen (d) Oxygen

Figure 3 represents the temperature contours of different fluids at different cross-sections. It shows that the temperature of the air at the outlet of the nozzle is 86.5 K which shows the decrement of 14.5 K as compared to that of an inlet. The temperature of helium at the outlet of the nozzle is 45.8 K whereas for hydrogen gas it is 46.8 K. The decrease in temperature for helium and hydrogen are 3.2 K and 4.2 K respectively as compare to that of at the inlet. It is interesting to note that the decrement in temperature for helium is greater than hydrogen by approximately 1 K. The temperature of oxygen at the outlet of the nozzle is 112.6 K, which shows the decrement of 7.4 K. This decrease in temperature is very much important at ultra-low temperature because it happens inside the nozzle which reduces the turbine work and hence increases the efficiency of turbo-expander. It is desirable for the liquefaction of gases.

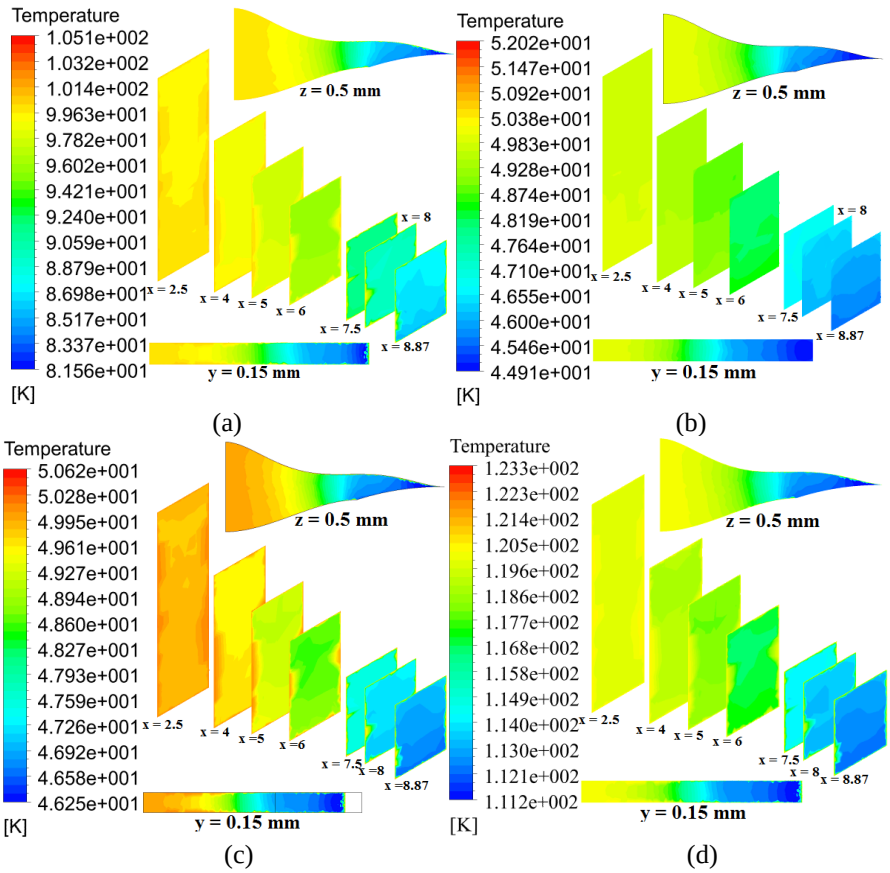


Figure 4. Temperature contours at different axial planes (a) Air (b) Helium (c) Hydrogen (d)Oxygen

## 4. CONCLUSIONS

The present work reports the design methods of the non-axisymmetric convergent nozzle and numerical simulation to visualize the flow pattern, velocity, temperature, pressure, Mach number etc. for different cryogenics fluid. Shear stress transport (SST) turbulence model is applied for all the cases and results are compared based on the simulation. Three-dimensional CFD model for turbulent fluid flow inside the convergent nozzle is simulated to visualize the fluid flow pattern as well as variation of velocity, temperature, pressure, Mach number etc. The interesting point of this study is the reduction in temperature for air is around 14.2 K with subsonic Mach number of 0.88 at the outlet of the nozzle.

## REFERENCES

[1] K. Ohira, T. Nakayama, and T. Nagai, Cavitation flow instability of subcooled liquid nitrogen in converging-diverging nozzle, Cryogenics, 52:35–44, 2012.
[2] M. Kumar, R. K. Sahoo, Development and Numerical Analysis to Visualize the Flow Pattern of Cryogenic Radial Turbine for Helium Gas, Proceedings of the 24th National and 2nd International ISHMT-ASTFE Heat and Mass Transfer Conference (IHMTC-2017), December 27-30, 2017, BITS-Pilani, Hyderabad, India
[3] A.B.N. Toufique Hasan. Characteristics of overexpanded nozzle flows in imposed oscillating condition. International Journal of Heat and Fluid Flow, 46:70-83, 2014.
[4] Marco Geron, Renato Paciorri, Francesco Nasuti, and Filippo Sabetta. Flowfield analysis of a linear clustered plug nozzle with round-to-square modules. Aerospace Science and Technology, 11:110–118, 2007.
[5] Vincent Lijo, Heuy Dong Kim, Toshiaki Setoguchi, and Shigeru Matsuo. Numerical simulation of transient flows in a rocket propulsion nozzle. International Journal of Heat and Fluid Flow, 31:409–417, 2010.
[6] J. F. Quaatz, M. Giglmaier, S. Hickel, and N. A. Adams. Large-eddy simulation of a pseudo-shock system in a Laval nozzle. International Journal of Heat and Fluid Flow, 49:108–115, 2014.
[7] A. Chaudhuri and A. Hadjadj, Numerical investigations of transient nozzle flow separation. Aerospace Science and Technology, 53:10–21, 2016.
[8] M. Kumar, S. K. Behera, A. Kumar, A Numerical Analysis of Predicting Flow Pattern Inside a Turbo-expander, Proceedings of the 6th International and 43rd National Conference on Fluid Mechanics and Fluid Power, December 15-17, 2016, MNNITA, Allahabad, U.P., India

# NUMERICAL INVESTIGATION OF THERMO-FLUID DYNAMICS IN SUBJECT-SPECIFIC HUMAN EYES USING THE GENERALIZED POROUS MEDIUM APPROACH

**Alessandro Mauro, Nicola Massarotti, Salahudeen M**

Dipartimento di Ingegneria, Università degli Studi di Napoli "Parthenope", Isola C4, Centro Direzionale di Napoli, 80143 Napoli, Italy, alessandro.mauro@uniparthenope.it, massarotti@uniparthenope.it, salahudeen.mohamed@uniparthenope.it

**Ignacio Rodríguez Uña**

Fernández-Vega Ophthalmological Institute, Department of Ophthalmology, Glaucoma Unit, Príncipe de Vergara 131, 28002, Madrid, Spain

**Mario R. Romano**

Department of Biomedical Sciences, Humanitas University, Via A. Manzoni 113, 20089, Rozzano (Milano), Italy, mario.romano.md@gmail.com

**Vito Romano**

Department of Eye and Vision Science, Institute of Ageing and Chronic Disease, University of Liverpool, Liverpool, UK

[5] Moorfields Eye Hospital, London EC1V 2PD, UK , vito.romano@gmail.com

**Perumal Nithiarasu**

Zienkiewicz Centre for Computational Engineering, College of Engineering, Swansea University,

Swansea SA2 8PP, UK, P.Nithiarasu@swansea.ac.uk

## ABSTRACT

The present work describes the application of the generalized porous medium model to the study of heat and fluid flow in healthy and glaucomatous eyes of different subject specimens, considering the presence of ocular cavities and porous tissues. The dependence of TM porosity and permeability on Intraocular Pressure (IOP) has been analysed in detail, and the differences between healthy and glaucomatous eye conditions have been highlighted. The physiological conditions of patients have been found to have a significant influence on the thermo-fluid dynamic phenomena. The influence of different eye positions (supine and standing) on thermo-fluid dynamic quantities has been also investigated: results are presented in terms of velocity, pressure, temperature, friction coefficient ($C_f$) and local Nusselt number ($Nu_L$). The results clearly indicate that porosity and permeability of Trabecular Meshwork (TM) are two important parameters that affect eye pressure distribution.

**Keywords:** *Generalised porous medium model; Eye modeling; Aqueous humor flow; Intraocular Pressure (IOP); Patient oriented*

## 1. INTRODUCTION

Glaucoma is a group of eye diseases which may result in loss of vision due to damage of the optic nerve. By the year 2020, it is estimated that there will be about 80 million people in the world affected by glaucoma.

The literature survey clearly shows a strong interest of the biomedical engineering community in numerical modelling of the anterior section of the eye. Although significant efforts have been made, the effects of both porosity and permeability of TM on AH outflow and, consequently, on IOP, on

subject-specific geometries is still lacking. These parameters play a crucial role on pressure management of an eye and thus must be properly analysed using the more available and suited comprehensive models, including non-Darcy models. Therefore, a general porous medium model that is able to take into account the effects of porosity and permeability and its interaction with porous tissues and free fluid can produce relevant information concerning AH outflow from the anterior chamber of an eye and its management of IOP.

In order to study the effects of TM porous structure on AH outflow and IOP, the authors propose here for the first time the use of the Generalised Porous Medium (GPM) model that integrates Darcy, Forcheimmer and Brinkmann models in the solution of fluid flow and heat transfer through porous media. The model is then used for the first time within a patient-oriented procedure, to solve flow and heat transfer in four different subject-specific eyes, extracted from tomographic images of healthy (HE1,HE2) and glaucomatous patients (GE1,GE2). The application of the present model allowed the authors to highlight the sensitivity of heat and mass transport phenomena occurring in human eyes to key eye parameters, such as porosity and permeability of ocular tissues and consequently, understands the differences between healthy and glaucomatous eyes. The authors aim at proving that these properties drastically affect flow and thermal fields in the AC of eyes and are strongly related to healthy and glaucomatous conditions.

## 3. MATHEMATICAL MODEL AND NUMERICAL METHODOLOGY

Laminar, incompressible fluid flow has been considered in this work for AH, in order to model its velocity and temperature inside the anterior chamber of human eyes by solving the generalised porous medium model [1,2]. Buoyancy effects have been incorporated via the Boussinesq approximation, relating density variations to temperature differences in cornea, lens and iris, obtaining a mixed convection flow regime. The conservation equations of the generalised porous medium model in indicial notation can be written as:

Continuity equation:

$$\frac{1}{\varepsilon}\frac{\partial u_i}{\partial x_i} = 0 \tag{1}$$

Momentum equation:

$$\frac{\rho_f}{\varepsilon}\left[\frac{\partial u_i}{\partial t} + \frac{\partial}{\partial x_j}\left(\frac{u_i u_j}{\varepsilon}\right)\right] = -\frac{1}{\varepsilon}\frac{\partial}{\partial x_i}\left(p_f \varepsilon\right) + \frac{\mu_e}{\varepsilon}\frac{\partial^2 u_i}{\partial x_i^2} - \frac{\mu_f u_i}{\kappa} - \frac{1.75}{\sqrt{150}}\frac{\rho_f}{\sqrt{\kappa}}\frac{|\mathrm{V}|}{\varepsilon^{3/2}}u_i + \left(\rho_{ref} - \rho_f\right) g\gamma_i \tag{2}$$

Energy equation

$$\left[\varepsilon\left(\rho c_p\right)_f - \left(1-\varepsilon\right)\left(\rho c_p\right)_s\right]\frac{\partial T}{\partial t} + \left(\rho c_p\right)_f u_i \frac{\partial T}{\partial x_i} = k\left(\frac{\partial^2 T}{\partial x_i^2}\right) \tag{3}$$

The generalised porous medium model (1-3) is very useful in problems where a porous medium interacts with a free fluid, such as the present case where ocular cavities are in contact with porous tissues. In fact, the model approaches the Navier-Stokes equations when permeability, $\kappa$, goes to infinity and porosity, $\varepsilon$, approaches unity. However, when permeability assumes a finite value and porosity is smaller than one, the model describes heat and fluid flow in porous tissues.

## 4. COMPUTATIONAL DOMAINS AND BOUNDARY CONDITIONS

The computational domain takes into account Trabecular Meshwork (TM), Schlemm's Canal (SC) and Collector Channel (CC). The small segment between lens and iris captured from the scans serves as the inlet for AH secreted by the ciliary body. Collector Channels (CC), among the AH outflow pathway, are modelled as outlets for the AH. AH is secreted by the ciliary body, which is represented in the present model by an inlet section in the anterior segment of the eye, between iris and lens, as shown in Figure 1. A nominal volumetric flow rate of 2.5 µL/min is assigned at this inlet section. The Schlemm's Canal (SC) and Collector Channels (CC) are subject to an episcleral venous pressure of 10.5 mm Hg. Lens, iris and cornea are assumed to be impermeable walls, where no slip boundary conditions are imposed. The temperature of the outer surface of cornea is set at 27°C, while the temperature of lens and iris are set to normal human body temperature of 37°C. Appropriate permeability values, depending on the health condition of human eye, are used for the porous tissue that represents the TM [3].

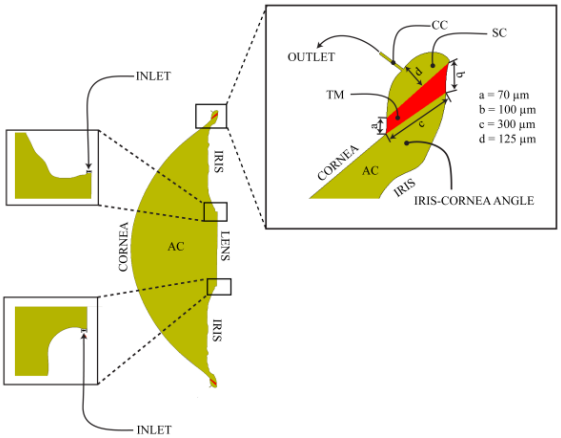


Figure 1. Computational domain of human eye model HE1.

## 4. RESULTS

In the present work, the authors have found that glaucoma eyes should be characterized by TM permeability smaller than $4 \cdot 10^{-15} \mathrm{m}^2$, and porosity values smaller than 0.08. For healthy patients, however, IOP values are usually between 9 mm Hg and 18-21 mmHg, with corresponding permeability values ranging between $8 \cdot 10^{-14} \mathrm{m}^2$ and $5 \cdot 10^{-15} \mathrm{m}^2$ with porosity values greater than 0.1. Low permeability of TM produces high resistance to the AH flow, affecting IOP valuesThe TM permeability values chosen for the four eyes have been correlated to approximately reproduce the IOP values in numerical simulation measured in clinical practice. The higher the resistance of the TM, the larger the pressure drop and, as a consequence, ophthalmologists focus their attention on the study of alternative pathways for the AH outflow from AC.

The flow in the first healthy eye HE1 has shown a more symmetric behavior compared to HE2, GE1 and GE2 in supine conditions. The asymmetry in the patient specific models of HE2, GE1 and GE2 invokes asymmetric AH circular patterns, particularly evident in supine position. It is interesting to note that, for supine position, there is a larger vortex located at the core region, characterized by higher velocity values with respect to the second smaller vortex.

The velocity magnitude distributions across horizontal and vertical sections of each eye are plotted in Figure 2. It is interesting to note that the velocity values at both horizontal and vertical sections of healthy eyes are larger than those corresponding to glaucoma eye models, for both supine and standing positions, due to the TM permeability, with a consequent influence on IOP. The higher velocity observed in healthy eyes with respect to glaucoma eyes, GE1 and GE2, is due to the lower IOP.

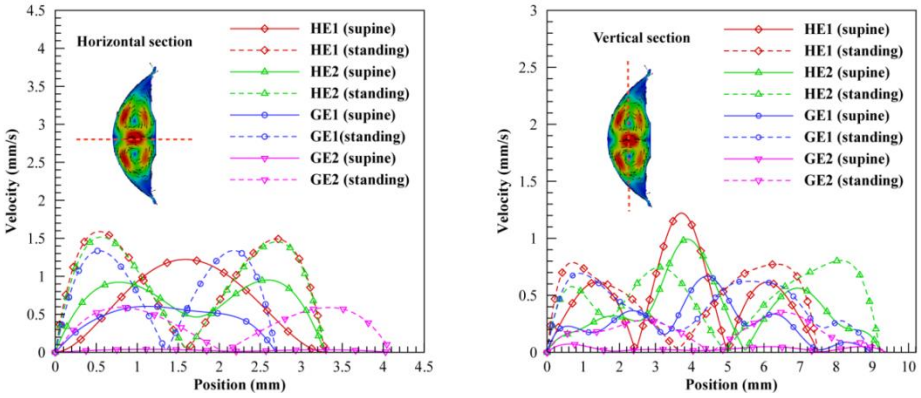


Figure 2. Velocity profile along horizontal (left) and vertical (right) section of eye for supine and standing positions for different eye models.

## 5. CONCLUSIONS

The present work describes the flow and heat transfer in four subject-specific human eyes by means of the Generalised Porous Medium (GPM) model coupled to a patient-oriented procedure. The following conclusions are drawn from the study.

1. The TM porous parameters, i.e. porosity and permeability, have a relevant role in determining the physiological conditions of the different subject specimens.
2. Glaucomatous eyes (GE1 and GE2) exhibit a lower AH velocity magnitude with respect to healthy eyes, due to higher IOP, affecting the normal biological function of the eye.
3. The heat and mass transfer phenomena are substantially different for the glaucomatous eyes when compared to the healthy eyes.

## ACKNOWLEDGMENTS

Alessandro Mauro gratefully acknowledges the local program of the University of Napoli "Parthenope" for the support to individual research.

## REFERENCES

[1] N. Massarotti, M. Ciccolella, G. Cortellessa, A. Mauro. New benchmark solutions for transient natural convection in partially porous annuli. *International Journal of Numerical Methods for Heat & Fluid Flow*, 26 (3-4), 1187-1225, 2016.

[2] A. Mauro, M. R. Romano, V. Romano, P. Nithiarasu. Suprachoroidal shunts for treatment of glaucoma: a comparison based on numerical simulations. *International Journal of Numerical Methods for Heat & Fluid Flow*. 2016. DOI 10.1108/HFF-12-2016-0508.

[3] A. Mauro, N. Massarotti, M. Salahudeen, M.R. Romano, V. Romano, P. Nithiarasu. A generalised porous medium approach to study thermo-fluid dynamics in human eyes, *Medical & Biological Engineering & Computing.* 2018. https://doi.org/10.1007/s11517-018-1813-4.

# EFFECT ON NON-UNIFORM HEATING ON HEAT TRANSFER CHARACTERISTICS IN WAVY CHANNEL

**Sumit Kumar Mehta[1], Sukumar Pati[2]**
Department of Mechanical Engineering, National Institute of Technology Silchar, Silchar-788010, India, E-mail addresses:1 sumit090391@gmail.com, 2 sukumarpati@gmail.com

## ABSTRACT

Numerical analysis has been performed to analyse the effect of non-uniform heating on heat transfer charecteristics for steady laminar flow through wavy channel. Heat transfer charecteristics has been analysed with different heat flux amplitude and phase difference of sinusoidal heat flux. We observe an intricate interplay between the amplitude and phase difference of heat flux profile on the thermal transport characteritics. The local heat transfer enhancement is highly sensitive with change in amplitude of the sinusoidal heat flux.. For zero phase difference of heat flux profile, all local minima are higher in comparesion with local minima of the corresponding reciprocal phase difference, while the decrease in local maxima is not monotonic. Decrease in amplitude of heat flux increases the average Nusselt number, while for same heat flux amplitude zero phase difference yields higher average Nusselt number.

**Key Words:** *Wavy channel, sinusoidal heat flux, Heat transfer enhancement.*

## 1. INTRODUCTION

Passive method of heat transfer using corrugation on wall is one of the effective method of heat transfer augmentation. There are so many researchers work in this area to enhance the heat transfer in wavy channel for economic design of the thermal devices like heat exchangers[1-2], solar heater [3-4] etc.

Rush et al. [5] analysed experimentally heat transfer and mixing charecteristics in wavy channel with different phase difference of wavy wall and found that mixing enhances the local heat transfer. The work of Wang and Chen [6] disclosed that average nussult number increases with increase in wave amplitude in laminar regime. Ahmed et al. [7] concluded that mixing of nanoparticle in base fluid increases the heat transfer in wavy channel and increment of volume fraction also increase the percentage of average Nusselt number enhancement. Pati et al. [8] numerically analysed the thermo-hydraulic performance of two types of wavy channel, called serpentine and raccoon. It was found that for serpentine channel have higher thermo-hydraulic performance in laminar regime.

The effects of non-uniform heating on heat transfer characteristics in wavy channel are not available in the literature. Accordingly, objective of the present work is to analyze the effect of sinosiodal heat flux on the thermal charecteristics for different heat flux amplitude and phase difference.

## 2. THEORETICAL FORMULATION

We consider two dimensional steady, incompressible, laminar flow of Newtonian fluid through the wavy channel as shown in Figure 1.The equation of the wavy wall is written in dimensionless form as:

$$s(x) = A\sin(\pi x / L) \tag{1}$$

The plain part of the channel is considered as adiabatic, while the wavy wall of the channel is imposed with sinusoidal heat flux. For numerical analysis, we consider that there is no internal heat generation and no viscous dissipation.

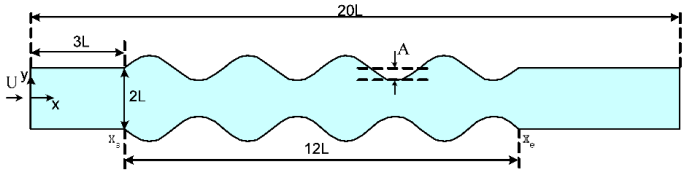


FIGURE 1. Schematic diagram of the physical model and the coordinate system

The governing transport equations are:

Continuity equation

$$\frac{\partial u}{\partial x}+\frac{\partial v}{\partial y}=0 \tag{2}$$

*x*-momentum equation

$$\rho\left[u\frac{\partial u}{\partial x}+v\frac{\partial u}{\partial y}\right]=-\frac{\partial p}{\partial x}+\mu\left(\frac{\partial^2 u}{\partial x^2}+\frac{\partial^2 u}{\partial y^2}\right) \tag{3}$$

*y*-momentum equation

$$\rho\left[u\frac{\partial v}{\partial x}+v\frac{\partial v}{\partial y}\right]=-\frac{\partial p}{\partial y}+\mu\left(\frac{\partial^2 v}{\partial x^2}+\frac{\partial^2 v}{\partial y^2}\right) \tag{4}$$

Energy equation

$$u\frac{\partial T}{\partial x}+v\frac{\partial T}{\partial y}=\frac{k}{\rho c_p}\left[\frac{\partial^2 T}{\partial x^2}+\frac{\partial^2 T}{\partial y^2}\right] \tag{5}$$

The boundary conditions used are as follows:

*At inlet*

$$u=U,\ T=T_{inlet} \tag{6}$$

*At wall*

$$u=v=0,\ \ \frac{\partial T}{\partial y}=0 \text{ for } x<3L, x>15L \tag{7}$$

$$q(x)=q_0(1+a\sin((\pi x/0.5L)+\phi)) \text{ for } 3L\le x\le 15L \tag{8}$$

*At outlet*

$$\frac{\partial T}{\partial x}=\frac{\partial u}{\partial x}=\frac{\partial v}{\partial x}=0 \tag{9}$$

The obtained temperature velocity field is synthesized by dimensionless parameter, called local Nusselt number. The local Nusselt number is found as follows:

$$Nu=\frac{q(x)L}{(T_{wall}-T_{inlet})k} \tag{10}$$

The average Nusselt number is calculated as

$$Nu_{avg}=\int_{3L}^{15L} Nuds \Big/ \int_{3L}^{15L} ds. \tag{11}$$

## 4. RESULTS

Finite element method is used to solve the governing transport equations. Relative residual criteria for convergence is set as $10^{-6}$. The number of element is taken as 85,474 after performing extensive grid independency test and maximum relative error with grid change is found less than 1%. The numerical scheme has been validated with the results of Wang and Chen [6] and the same is available in [8].

The main purpose of this work is to analyse the effect of sinusoidal heat flux on wavy channel for different heat flux amplitude and phase difference on the heat flux profile. The dimensionless amplitude of the channel is kept fixed as A/L =0.3. We consider three different amplitude of heat flux (a=0.25, 0.5 and 0.75) and two phase difference on the heat flux profile. ($\phi$=0° and 180°).

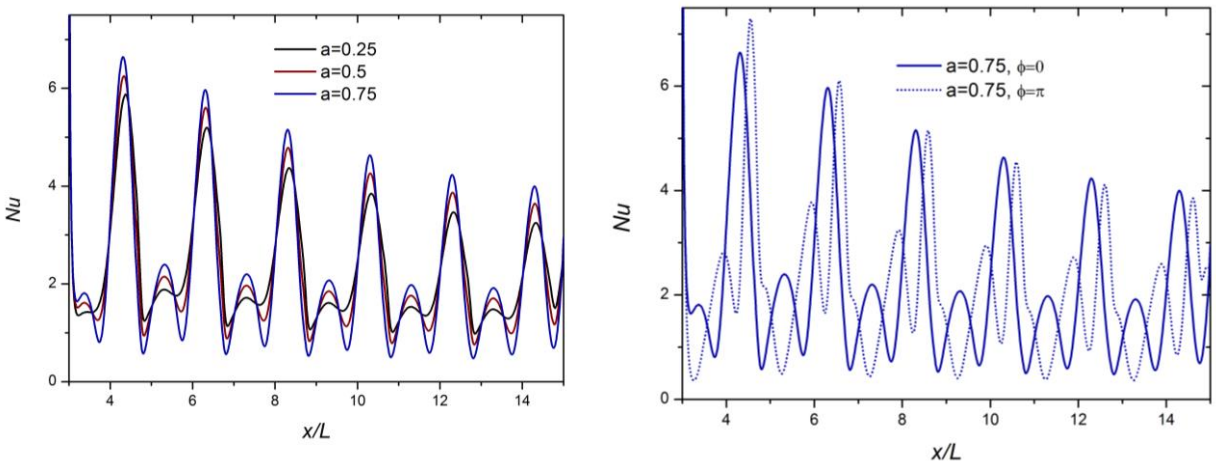


(a) (b)

FIGURE. 2 Variation of local Nusselt number at top wavy wall with (a) different heat flux amplitude a=0.25, 0.5 and 0.75, (b) phase difference (=0° and 180°) of sinusoidal heat flux for Re=300.

Figure 2(a) discloses the variation of local Nusselt number for different heat flux amplitude (a=0.25, 0.5 and 0.75) at Re=300 and $\phi$=0°. It can be seen that with increase in amplitude of heat flux profile, local maxima of Nu increases and at the time local minima also decreases. However, the decrease of local minima is more as compare to incraese in local maxima. The effect of phase difference of heat flux profile on local Nussult number is disclosed in Figure 2(b) for Re=300 and a=0.75. The local maxima for $\phi$=180° is higher for first two wavy trough in downstream direction but after third trough decreases. The local minima for $\phi$=180° is always lower than $\phi$=0° because of trapping of hot fluid for $\phi=0^0$.is lower in wavy crest as magnitude of heat flux is higher before the crest in case of $\phi$=0°.and after the crest in case of $\phi$=180°.

Figure 3 represents the combined effects of heat flux amplitude and phase difference on average Nusselt number for laminar regime (5<Re<300). With increase in amplitude average Nusselt number decreasesfor the reasons mentioned earlier. It can be observed that for any heat flux amplitude, average Nusselt number for $\phi$=0° is always higher because local minima of Nusselt number for $\phi$=0° is always higher.

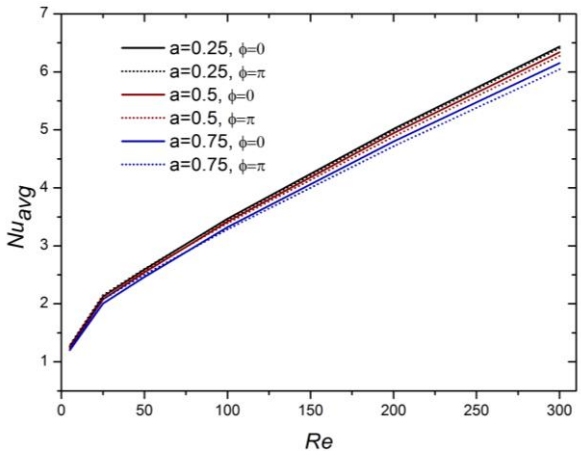


FIGURE. 3 Variation of average Nusselt number with Reynolds number for a=0.25, 0.5 and 0.75 with $\phi$ =0° and 180°

## 5. CONCLUSIONS

Numerical analysis for heat transfer analysis in wavy channel with sinusoidal heat flux has been executed. The important findings are:

- Local variation of Nusselt number is very sensible with amplitude of the heat flux. The range of local minima and maxima increases with increase in heat flux amplitude.
- The phase location of sinusoidal heat flux is significant in case of wavy channel. Average Nusselt number is higher for lower amplitude of sinusoidal heat flux and $\phi$ =0°.

## ACKNOWLEDGEMENT

The authors acknowledge TEQIP III for its support throughout the work.

## REFERENCES

[1] J.A. Esfahani, M. Akbarzadeh, S. Rashidi, M.A. Rosen, R. Ellahi, Influences of wavy wall and nanoparticles on entropy generation over heat exchanger plat, *Int. J. Heat Mass Transf.* 109 (2017) 1162–1171.

[2] Y.J. Baik, S. Jeon, B. Kim, D. Jeon, C. Byon, Heat transfer performance of wavy-channeled PCHEs and the effects of waviness factors, *Int. J. Heat Mass Transf.* 114 (2017) 809–815.

[3] J.S. Sawhney, R. Maithani, S. Chamoli, Experimental investigation of heat transfer and friction factor characteristics of solar air heater using wavy delta winglets, *Appl. Therm. Eng.* (2017).

[4] A. Priyam, P. Chand, Thermal and thermohydraulic performance of wavy finned absorber solar air heater, *Sol. Energy*. 130 (2016) 250–259.

[5] T.A. Rush, T.A. Newell, A.M. Jacobi, An experimental study of flow and heat transfer in sinusoidal wavy passages, *Int. J. Heat Mass Transf.* 42 (1999) 1541–1553.

[6] C.C. Wang, C.K. Chen, Forced convection in a wavy-wall channel, *Int. J. Heat Mass Transf.* 45 (2002) 2587–2595

[7] M.A. Ahmed, N.H. Shuaib, M.Z. Yusoff, Numerical investigations on the heat transfer enhancement in a wavy channel, using nanofluid, *Int. J. Heat Mass Transf.*55 (2012) 5891–5898.

[8] S. Pati, S.K. Mehta, A. Borah, Numerical investigation of thermo-hydraulic transport characteristics in wavy channels: Comparison between raccoon and serpentine channels, *Int. Commun. Heat Mass Transf.* 88 (2017) 171–176

# Alternative Mathematical Procedures to Solve Chemical Equilibrium Problem

**Mihir Raj and Ankit Bansal**
Mechanical and Industrial Engineering Department, IIT Roorkee,
Roorkee, Haridwar,247667,
azb162@gmail.com

## ABSTRACT

The paper reviews the existing mathematical procedures used to solve chemical equilibrium problem and suggests alternative methods. The proposed mathematical procedures are employed to solve the chemical equilibrium problem for high pressure and high temperature environment in chemical explosions. Real gas equation of state based on JCZ3 is implemented to evaluate the Gibb's free energy. The non-linear system is solved with the help of stochastic algorithms as well as optimization methods. The proposed stochastic algorithm generates a faithful random composition vector.

**Key Words:** Chemical Equilibrium, stochastic, optimization, Gibbs free energy

## 1. INTRODUCTION

In a chemical explosion from a high explosive, a detonation wave propagates through the un-reacted explosive material. Although explosions/detonations have been studied for a long time, several physical phenomena associated with their behavior still remain to be explored. In particular, the thermochemistry of non-ideal explosives and the flow-field behind the blastwave is not properly understood. The short time scales associated with the problem makes it impossible for in-situ experimental analysis. Thus, computational simulations offer a capabilityto simulate and understand the complex physics involved in detonation.

Numerical simulation is the main approach to predict the effect of explosions. The usual starting point for any investigation into a new explosive composition is the prediction of its ideal detonation velocity and Chapman-Jouget (C-J) state properties using a thermodynamic equilibrium code. Thermo-chemical codes solve thermodynamic equations to find chemical equilibrium by minimizing the Gibbs free energy. Many thermo-chemical codes such as RUBY [1], TIGER [2], CHEETAH [3], etc. have been developed to predict the performance of propellants and explosives and to evaluate formulations of new energetic materials.

## 2. THERMO-CHEMICAL ANALYSIS

The most widely used method for solving the thermo-chemical equilibrium problem is based on the principal of minimization of Gibbs free energy. The state of the art thermochemical codes apply this approach with models based on ideal gas Equation of state (EOS), as well as other more advanced real gas eos, such as BKW, JCZ3 etc. In this paper, we will employ the the ideal gas as well as JCZ3 eos to represent the Gibbs free energy of gas mixture under high temperature and pressure

conditions. A large number of codes use the method of steepest descent to perform the minimization of Gibbs free energy, and this method requires an initial estimate of the CJ state to be made. The method of steepest descent finds the closest minimum to the initial guess, but does not guarantee to find the global minimum. For highly non-ideal explosives, it is desired to have a method of minimizing the free energy which guarantees global minimum without requiring an initial estimate.

Borg et. al. proposed an alternative approach to minimizing functions based on probabilistic or stochastic methodology [4]. In this general approach, a composition is guessed and the free energy is computed. This process is continued until a pre-determined number of guesses has been achieved. At this stage the equilibrium composition is that composition amongst all the guesses that yields the lowest free energy. The stochastic method guarantee to find a global maximum/minimum, albeit the involved computation reqirement is higher than deterministic methods. Let $f$ represent the free energy of the mixture of products with given composition $X$, then the algorithm for the free energy minimization is given as:

Generate random composition, $X_1$ with constraints

Calculate $f_1(X_1)$
For a number of guesses do
    Generate random composition, $X_2$ with constraints

    Calculate $f_2$

    $$X_3 = \frac{(f_1 X_1 + f_2 X_2)}{(f_1 + f_2)}$$

    Calculate $f_3$

    if ($f_1$ = min ($f_1$, $f_2$, $f_3$))
     do nothing

    else
        if ($f_2$ = min ($f_1$, $f_2$, $f_3$))
        $X_1=X_2$
        $f_{1=}f_2$

        else
        $X_1=X_3$
        $f_{1=}f_3$

        end if
    end if
end for

The above algorithm determines the optimum equilibrium composition $X_1$. In order to apply this algorithm to the problem of determining equilibrium compositions, we need a method for generating random composition vectors $X$. The algorithm proposed by Borg et. al. has poor efficiency, as lot of random composition vectors generated in the process are rejected owing to negative values of mole fraction and sum of mole fractions not coming equal to unity. In this paper, we studied the algorithm proposed by Borg et al. and suggest improvements to acheive overall efficiency with the stochastic method. In the proposed method, the species from the list is chosen in such a way such that the rejection process is reduced. As compared to 24 rejection out of 25 random compositions in the algorithm of Borg et. al., the proposed method reduces this number to 3 out of 10. This makes the code faster and more efficient.

## 3. OPTIMIZATION METHODS

White et al. described an alternative method based on linear programming technique for minimizing the free energy. This method automatically ensures that all mole fractions remain positive during the calculation. However, the method is suitable for only those problems where the total free energy may be expressed as a linear function of the product composition vector, and with BKW (and other complex EOS) this is not the case. We will compare this method with the other method for ideal gas eos.

To employ optimization techniques with real gas eos, such as JCZ3 eos, a non-linear optimization method is required. The Sequential Quadratic Programming (SQP) is a powerful method for non-linear optimization problems. This method is suitable for CHNO explosives like steepest descent method but the convergence rate of SQP is an order higher than that of steeepest descent method. It is one of the most effective methods for nonlinearly constrained optimisation which generates steps by solving quadratic subproblems.

## 3. RESULTS

We modified the stochastic algorithm of Borg et al. for the generation of random composition vector. The method was then employed to generate random composition of gases to solve combustion of methane in air and determine the equilibrium compositions. As can be observed from Fig. 1, the modified algorithm still retains the randomness of the compositions.

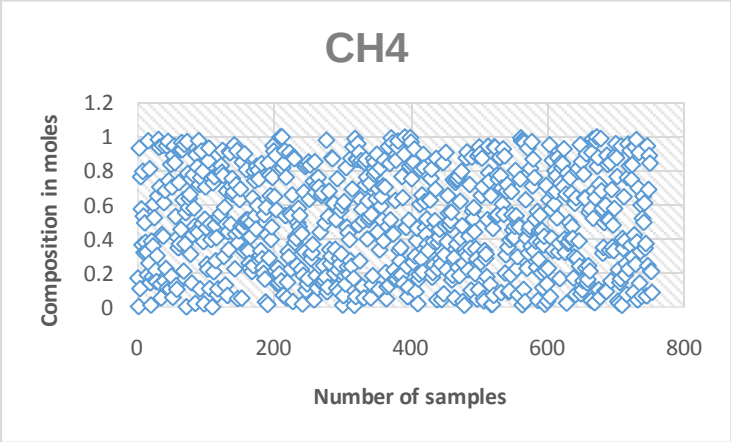

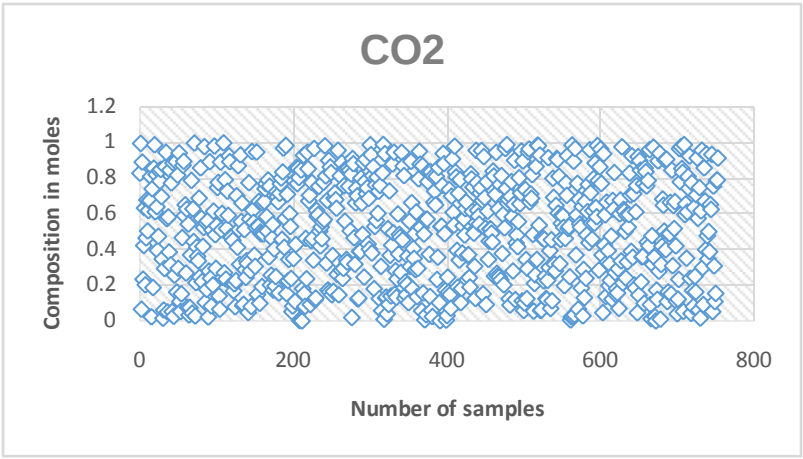


FIGURE 1 Composition vs number of samples for $CH_4$ and $CO_2$ produced by the random Composition generator

## 4. CONCLUSIONS

Alternative mathematical procedures are proposed to solve the chemical equilibrium problem for high pressure and high temperature environment in chemical explosions. Real gas equation of state based on JCZ3 is implemented to evaluate the Gibb's free energy. The non-linear system is solved with the help of stochastic algorithms as well as optimization methods. The proposed stochastic algorithm generates a faithful random composition vector.

## REFERENCES

[1] Levin H.B., Sharples R.E., Operator's manual for RUBY, Lawrenc Livermore Laboratory, Report UCRL-6815, 1962.;
[2] Cowperthwaite M., Zwisler W.H., Tiger computer program documentation, Stanford Research Institute, Publication No. Z106, 1973.;
[3] Fried L.E., CHEETAH 1.39 User's Manual, Lawrence Livermore National Laboratory, Manuscript UCRL-MA-117541 Rev. 3, 1996.
[4] R.A.J. Borg, G. Kemister and A. Jones*Chemical Equilibrium Calculations for Detonation Products* DSTO-TR-0226 Weapons Systems Division.
[5] W.H. Press, S.A. Teukolsky, W.T. Vetterling, B.P. Flannery *Numerical Recipes in C++*

Fifth International Conference on Computational Methods for Thermal Problems
THERMACOMP2018, July 9-11, 2018, Indian Institute of Science, Bangalore, INDIA
*N. Massarotti, P. Nithiarasu, Pradip Dutta and C. Ranganyakalu (Eds.)*

# COMPUTATIONAL MODELLING OF THERMAL AND FLUID FLOW PHENOMENA DURING SLM OF AZ91D ALLOY POWDER USING VOLUMETRIC HEAT SOURCE

**Ashish Kumar Mishra, Arvind Kumar***

Department of Mechanical Engineering, Indian Institute of Technology Kanpur, Kanpur – 208016, India
*arvindkr@iitk.ac.in

## ABSTRACT

A three-dimensional model using a volumetric heat source is developed to investigate the thermal and fluid flow transport during selective laser melting (SLM) of AZ91D alloy powder. The volumetric heat source is used to account for the multiple reflection and scattering of the incident laser beam in the powder bed. Transient mass, momentum and energy transport equations are solved, and the volume reduction due to the powder-liquid-solid transformation is accounted in the model. Results for temperature distribution and melt pool characteristics are presented for a single pass and multi-pass laser scanning. High values of maximum temperature are observed in both the cases. Additionally, the effect of thermal energy accumulation is observed resulting in overall increase in the domain temperature and lateral remelting in the previously deposited layers.

## 1. INTRODUCTION

AZ91D is a lightweight magnesium-aluminium-zinc alloy. Due to its excellent mechanical properties, such as very high specific strength and modulus, it can be a material of choice for aerospace and automotive industries [1, 2]. Traditionally, AZ91D alloy parts are manufactured through conventional manufacturing processes, such as casting and forming. However, additive manufacturing technologies such as selective laser melting (SLM) can further increase their use in aerospace and automotive industries due to its inherent advantages, such as greater design complexity, unique mechanical properties and finer microstructures which are not achievable through conventional manufacturing processes [3]. SLM is a powder bed fusion based metal additive manufacturing process that uses a focused laser beam to selectively melt the powder layer particles and construct a metal part in layerwise manner. The SLM process involves complex physical and thermal phenomena which govern the properties of the end product. These phenomena are controlled by the process parameters and bulk/powder material properties. Therefore, for successful production of components through SLM, selection of an optimum set of process parameters is required [4]. The experimental study of SLM of AZ91D magnesium alloy is scarce, except a few [3]. Since the experiments involve huge risk and expenses, computational modelling and simulations can be used for studying SLM of AZ91D. This approach has been used by researchers for studying SLM of other materials, such as steels [5], Ti-alloys [4] and Ni-superalloys [6]. In the current study, we have tried to extend this approach to AZ91D alloy powder. The computational model of SLM consists of transient mass, momentum and energy transport equations as well as thermal and fluid flow boundary conditions and heat source. The heat source is used to incorporate the spatial distribution of heat energy supplied by the laser beam in the model. To account for the multiple reflections and scattering of the incident laser beam due to the discrete mass distribution in the powder bed, a volumetric heat source is used. The volume reduction in the powder bed, due to the powder-liquid-solid transformation is included in the model through an algorithm based on the mass conservation. The simulations are carried out for both single pass and multiple passes of the laser beam. Results are presented for the temperature distribution and melt pool characteristics, such as maximum temperature, maximum flow velocity in the melt pool and melt pool dimensions.

## 2. MODEL DESCRIPTION

Figure 1 shows the schematic of the SLM process and the computational domain used in the study. The size of the computational domain is 1000×200×300 µm (single pass, Fig. 1b) and 1000×600×300 µm (multi-pass, Fig. 1c). The laser beam scans along the positive *x*-axis (left to right) on the top surface of the powder layer. For the multi-pass simulation, the laser beam traverses over three parallel scan paths along the *x*-axis as shown in Fig. 1c.

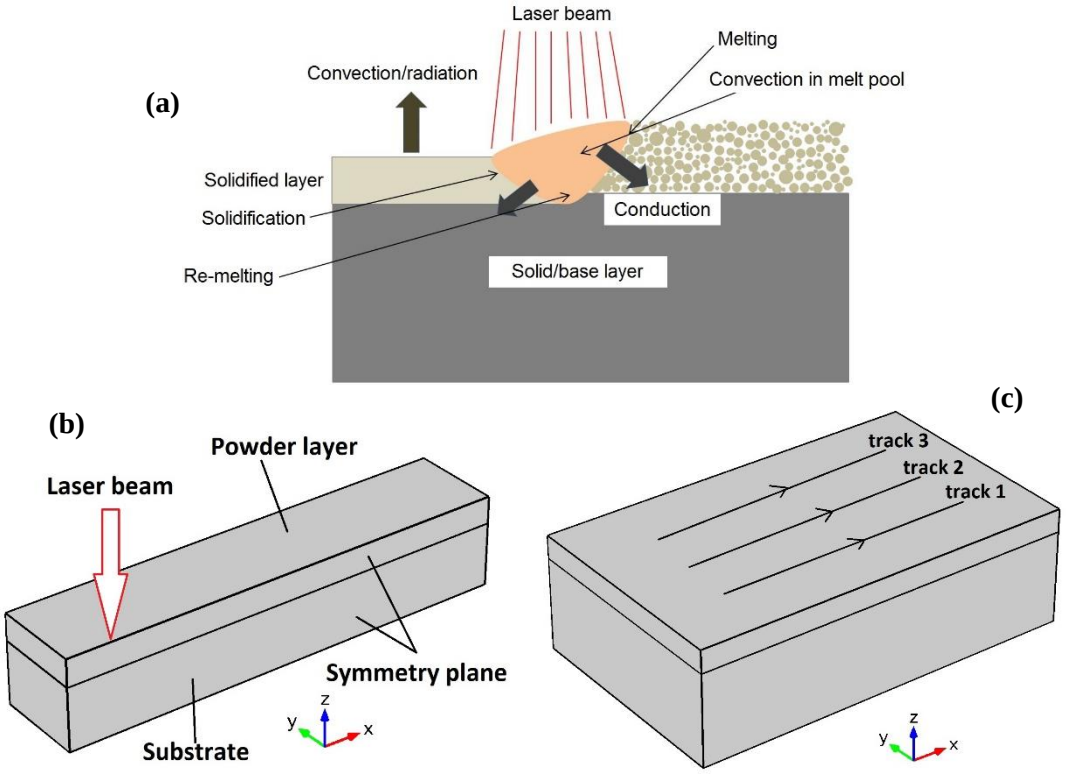


FIGURE 1. Schematic of (a) SLM process physics (b) computational domain for single pass and (c) computational domain for multiple pass scanning

The powder domain is assumed as a homogenous layer with a constant porosity of 47.5%. The governing transport equations are expressed as

*Mass conservation*
$$\nabla \cdot \rho \vec{V} = 0 \tag{1}$$

*Momentum conservation*
$$\frac{\partial(\rho \vec{V})}{\partial t} + \vec{V} \cdot \nabla(\rho \vec{V}) = -\nabla p + \nabla \cdot \left(\mu \left(\nabla \vec{V} + (\nabla \vec{V})^T\right)\right) + \vec{F} \tag{2}$$

where $\vec{F}$ is a source term, given as
$$\vec{F} = \rho_L \vec{g} \beta_T (T - T_{ref}) + \frac{A(1-f_L)^2}{B+f_L^3} \vec{V} \tag{3}$$

where the first term in RHS is the Boussinesq approximation for buoyancy force and the second term represents the mushy zone flow resistance. The variable $\vec{V}$ is the flow velocity vector of molten metal and $f_L$ is the liquid fraction, expressed as

$$f_L = \begin{cases} 0 & T < T_S \\ \frac{T-T_S}{T_L-T_S} & T_S \leq T \leq T_L \\ 1 & T > T_L \end{cases} \tag{4}$$

*Energy conservation*
$$\frac{\partial(\rho c_p T)}{\partial t} + \vec{V} \cdot \nabla(\rho c_p T) = \nabla \cdot (k \nabla T) + S_E \tag{5}$$

where $S_E$ is the source term used to include the Gaussian exponential volumetric heat source, which is used here, given as
$$q = \frac{2P}{\pi R^2 S} exp\left(-\frac{2((x-Ut)^2+y^2)}{R^2}\right) exp\left(-\frac{|z|}{S}\right) \tag{6}$$

In equation 6, *S* is called absorption depth and is taken same as the powder bed thickness in this model.

In the above conservation equations, the quantities $\rho$, $c_P$ and $k$ are given by following equations, using the solid and liquid phase properties of the AZ91D alloy.

$$\rho = (1 - f_L)\rho_P + f_L\rho_L \quad (7)$$

$$k = (1 - f_L)k_P + f_L k_L \quad (8)$$

$$c_p = \frac{1}{\rho}\{(1 - f_L)\rho_S c_{pS} + f_L\rho_L c_{pL}\} + \frac{L\partial\alpha_m}{\partial T} \quad (9)$$

$$\alpha_m = \frac{1}{2}\ \frac{(f_L\rho_L - (1-f_L)\rho_S)}{(f_L\rho_L + (1-f_L)\rho_S)} \quad (10)$$

In the powder bed, powder bed thermal conductivity and density are used instead of solid properties. These properties are given by

$$\rho_{powder} = \rho_S(1 - \varphi) \quad (11)$$

$$k_{powder} = k_S(1 - \varphi) \quad (12)$$

*Boundary conditions*

On the top surface, $$-\frac{k\partial T}{\partial z} = q - q_{conv} - q_{rad} \quad (13)$$

The Marangoni flow condition on the top surface of the melt pool, given as

$$-\mu\frac{\partial u}{\partial z} = \frac{\partial\gamma}{\partial T}\left(\frac{\partial T}{\partial x}\right) \quad ; \quad -\mu\frac{\partial v}{\partial z} = \frac{\partial\gamma}{\partial T}\left(\frac{\partial T}{\partial y}\right) \quad (14)$$

The thermal and physical properties of AZ91D are taken from reference [7].

| Parameters | Value |
|---|---|
| Layer thickness (μm) | 60 |
| Laser spot size 2*R* (μm) | 100 |
| Laser power *P* (W) | 100 |
| Scan velocity *U* (m/s) | 1 |
| Porosity ($\varphi$) | 0.475 |
| Emissivity (ε) | 0.18 |

TABLE 1. Parameters used in simulations

## 3. RESULTS

Figure 2a shows the three-dimensional view of temperature distribution in the domain and the flow field within the melt pool for single pass simulation at 100 W. The colour map shows the temperature distribution while the arrows represent the flow velocity vectors. The melt pool boundary is marked by the isothermal contour corresponding to the solidus temperature (743 K). From the results, it is obvious that during SLM high temperatures (~ $10^3$ K) and high flow velocity (1.37 m/s) are observed. However, the heating effect is limited to a small zone only and the temperature falls rapidly while moving away from the melt pool centre. An enlarged view of the melt pool is shown in Fig. 2b to clearly show the flow field directions in the melt pool. The arrows show an outwards velocity field, which is typical to the Marangoni flow in the molten metals. The values of maximum temperature, flow velocity and melt pool dimensions are listed in table 2. The melt pool is elongated and asymmetric along the scan direction (positive *x*-axis) which is due to the motion of the laser beam. The large difference between the thermal conductivities of the powder bed at the front and solidified material at the rear of the melt pool plays its role in making the melt pool asymmetric as well. The depth of the melt pool is large and considerable remelting in the bottom layer (substrate) is observed. This is in accordance with the reality where the effect of laser heating is felt till a depth much larger than the powder bed thickness. The simulation results of multiple pass scanning are presented in Figs. 2c-e, where the melt pool is shown when the laser reaches the midpoint of the track 1, 2 and 3, respectively. The results show that the temperature, as well as the melt pool, grows slightly with the increase in number of tracks scanned. The three scanning tracks are chosen such that they don't overlap with each other (interlayer gap 100 μm, beam spot radius 50 μm). Considerable lateral remelting in the previously deposited track is observed as can be seen in the Figs. 2c-e, where the melt pool extends into the previously scanned tracks as well. The remelting (lateral as

well as downwards) is desired as it ensures proper interlayer bonding, and therefore, very high-density build up.

| | |
|---|---|
| Maximum temperature | 1120 K |
| Maximum flow velocity | 1.37 m/s |
| Melt pool length | 211 µm |
| Melt pool width | 126 µm |
| Melt pool depth | 81 µm |

TABLE 2. Melt pool characteristics at 100 W

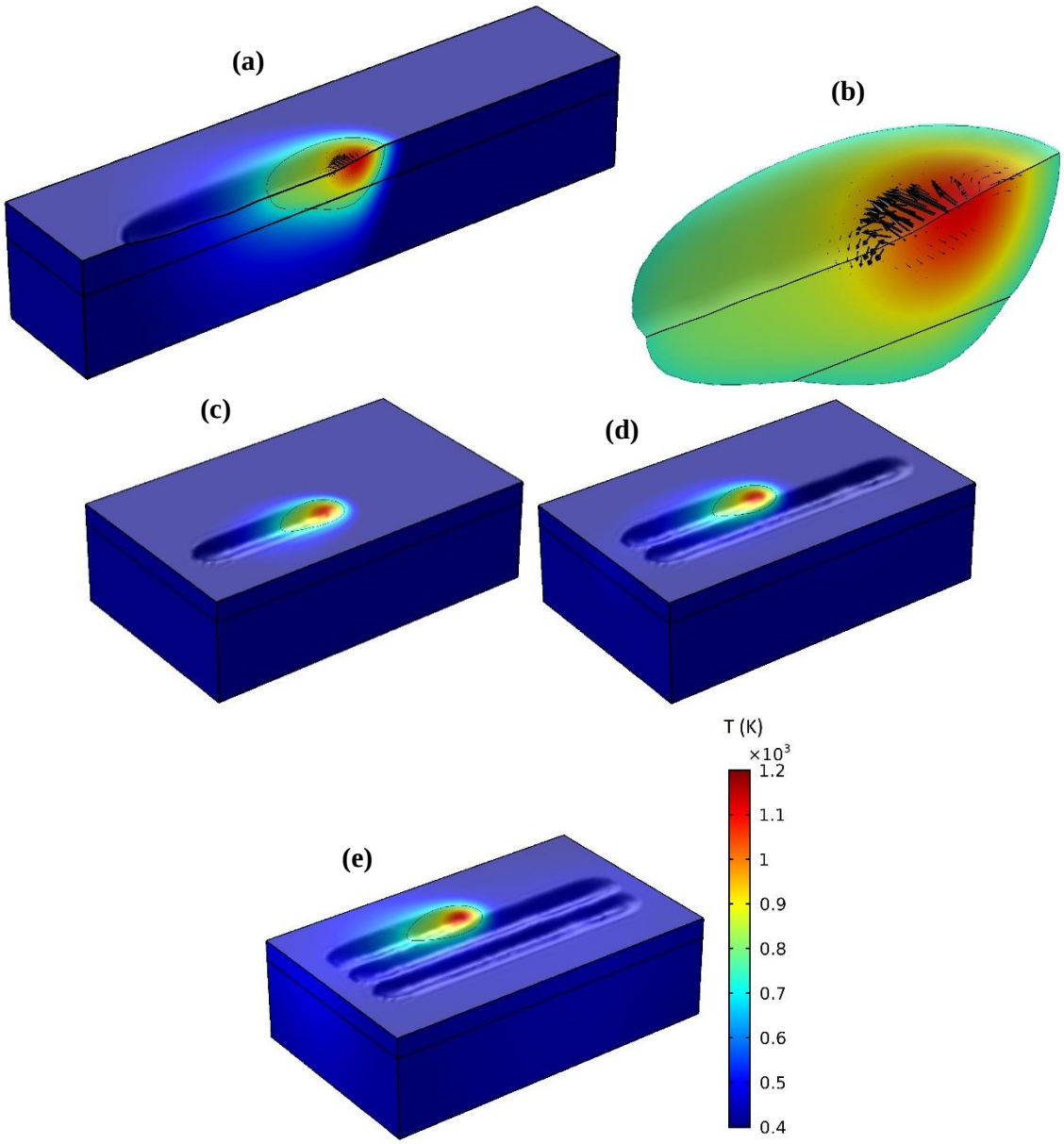


FIGURE 2. Temperature distribution and the melt pool for (a) single pass scanning, (b) enlarged view of the melt pool; Temperature distribution and the melt pool when laser reaches at the (c) midpoint of track 1 (d) midpoint of track 2 (e) midpoint of track 3.

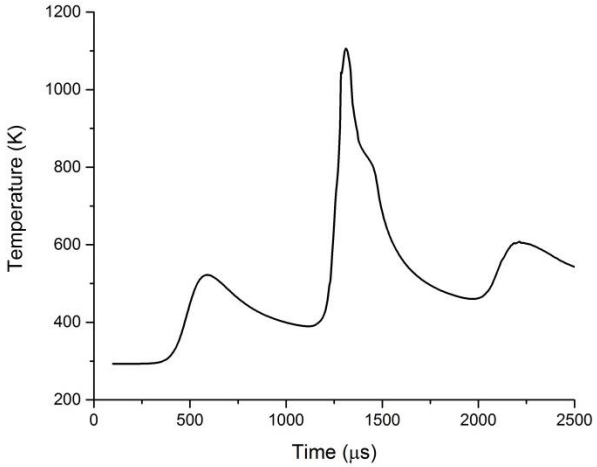


FIGURE 3. Temperature history at the midpoint of the 2nd track (500, 300, 300, μm)

Figure 3 shows the temperature history at the midpoint of the 2nd track (500, 300, 300, μm). From the plot, it can be seen that the cooling rate is very high, of the order of $10^6$ K/s. The plot shows that significant reheating occurs in a layer when the neighbouring tracks are being scanned. This may affect the microstructure and alter the mechanical properties of the deposited material. Another consequence of this reheating can be that the powder particles of the next track may get sintered together while the current track is being scanned, which will pose a problem when that track will be scanned.

## 4. CONCLUSIONS

Modelling of SLM for AZ91D magnesium alloy is attempted for the first time. High temperature ($T_{max}$ = 1120 K) and flow velocity ($|V|_{max}$ = 1.37 m/s) are observed during the process and convection drives the thermal transport in the melt pool. The melt pool size grows slightly as the consecutive tracks are scanned. Remelting is seen in downwards as well as lateral direction, which ensures proper interlayer bonding. It is observed that very high cooling rate (~ $10^6$ K/s) is involved in the process.

## REFERENCES

[1] M. Easton, A. Beer, M. Barnett, C. Davies, G. Dunlop, Y. Durandet, S. Blacket, T. Hilditch, P. Beggs, “Magnesium alloy applications in automotive structures” The Journal of The Minerals, Metals & Materials Society, vol.60 no.11, November 2008, pp. 57-62.

[2] S. Mishra, “Magnesium alloys in aerospace applications” NCAIR newsletter, vol.3 issue 2, August 2013, pp 7-9.

[3] K. Wei, M. Gao, Z. Wang, X. Zeng, “Effect of energy input on formability, microstructure and mechanical properties of selective laser melted AZ91D magnesium alloy” Material Science and Engineering A, 611 (2014), pp. 212-222.

[4] Y. Li, D. Gu, “Thermal behaviour during selective laser melting of commercially pure titanium powder: Numerical simulation and experimental study” Additive Manufacturing, 1-4 (2014), pp. 99-109.

[5] A. V. Gusarov, I. Smurov, “Modelling the interaction of laser radiation with powder bed at selective laser melting” Phys Proc., 5 (2010),pp.381–94.

[6] Y.W. Zhang, A. Faghri, C.W. Buckley, T.L. Bergman, “Three-dimensional sintering of two-component metal powders with stationary and moving laser beams”, Journal of Heat Transfer 122 (2000) pp. 150-158.

[7] H. E. Friedrich, B. L. Mordike, “Magnesium technology: Metallurgy, design data, applications" ISBN-13 978-3-540-20599-9, Springer-Verlag Berlin Heidelberg 2006.

Fifth International Conference on Computational Methods for Thermal Problems
THERMACOMP2018, July 9-11, 2018, Indian Institute of Science, Bangalore, INDIA
*N. Massarotti, P. Nithiarasu, Pradip Dutta and C. Ranganyakalu (Eds.)*

# FINITE DIFFERENCE APPROACH FOR THERMAL CONVECTION AND DYNAMO PROBLEM IN A ROTATING SPHERICAL SHELL

**Mohammad Anas, M. F. Baig**

Aligarh Muslim University, Aligarh-202002, India, mohammad.anas@zhcet.ac.in

**Fuaad P. A**

Indian Institute of Technology, Madras-600036, India, fuaadpa@gmail.com

## ABSTRACT

In this work, we present a new approach for the solution of incompressible hydrodynamic and magnetohydrodynamic (MHD) equations in a rotating spherical shell using finite difference method (FDM). The governing equations of the problem are solved in longitude/latitude spherical coordinate system $(\mathrm{r},\theta,\phi)$. The method presented here is straightforward to implement and parallelize on multi-core processors based on domain decomposition. Divergence-free magnetic field is ensured without using any separate numerical strategy thereby reducing the computational effort significantly. We validate the newly developed code for rotating thermal convection and for self-consistent dynamo problem.

**Key Words:** *Finite Difference Method, Dynamo, Thermal convection, Rotating Spherical shell*

## 1. INTRODUCTION

Magnetic field generation by earth and many celestial objects is due to the dynamo process of electrically conducting fluid. A number of self-consistent dynamo codes have been developed and many pioneer results have been reported on spatial-temporal variation of magnetic field and its occasional polarity reversal (Glatzmair & Roberts 1995; Kageyama & Sato 1995). But all the dynamo simulations performed till now, are far from the actual operating parameters. As of now, spectral methods have been the most popular choice to simulate the dynamo problems and for the development of new dynamo codes. Although high accuracy of spectral method makes it best suited for dynamo simulations at moderate parametric values, the global communication of back-and-forth transformations in real and spectral space at each time step to calculate non-linear terms in spectral method makes it computationally costly on massively parallel computers. On the other hand local method (finite difference, finite volume, finite element ) based dynamo codes are highly compatible for parallel computation architecture. The parallelization in local codes is straightforward using domain decomposition and can be easily implemented for any type of geometry. The present numerical method uses a simple numerical methodology of local discretization (finite difference) which is easy to implement and straightforward for parallel processing on multicore processors of distributed memory. In this work we present the validation of newly developed code based on FDM for the two cases: non-magnetic convection and dynamo problem in rotating spherical shells. For the non-magnetic case, quantitative validation is done with benchmark results of Christensen et al.(2001). For the magnetic case, a dynamo simulations is performed and iscompared quantitatively and qualitatively with the Jackson et al.(2014).

## 2. GOVERNING EQUATIONS AND SOLUTION METHODOLOGY

We consider a convecting, electrically conducting, incompressible fluid between radii $\mathrm{r}_i$ and $\mathrm{r}_o$ in a spherical shell. The aspect ratio is set as $\chi = r_i/r_o$= 0.35 similar to earth's interior. Gravity is decaying linearly from outer surface $\mathrm{r}_i$ to $\mathrm{r}_o$ . The shell is rotating about an z-axis with constant angular velocity. Thermal convection is modelled using the Boussinesq approximation, and electromagnetic induction make use of Maxwell equations. The non-dimensional governing equations of MHD in rotating spherical shell are

coupled Navier-Stokes, energy and magnetic induction equations along with divergence-free constraint of velocity and magnetic fields.

$$Ek(\frac{\partial \mathbf{U}}{\partial t} + \mathbf{U}\cdot\nabla\mathbf{U} - \nabla^2\mathbf{U}) = -\nabla p + \frac{Ra\ Ek}{Pr}\frac{r}{r_o}\Theta - 2\hat{e_z}\times\mathbf{U} + \frac{1}{Pm}(\nabla\times\mathbf{B})\times\mathbf{B} \tag{1}$$

$$\frac{\partial \Theta}{\partial t} + (\mathbf{U}\cdot\nabla)\Theta = \frac{1}{Pr}\nabla^2\Theta \tag{2}$$

$$\frac{\partial \mathbf{B}}{\partial t} = (\mathbf{B}\cdot\nabla)\mathbf{U} - (\mathbf{U}\cdot\nabla)\mathbf{B} + \frac{1}{Pm}\nabla^2\mathbf{B} \tag{3}$$

$$\nabla\cdot\mathbf{U} = 0 \tag{4}$$

$$\nabla\cdot\mathbf{B} = 0 \tag{5}$$

Magnetic induction equation (3) is simplied form of original equation (6)

$$\frac{\partial \mathbf{B}}{\partial t} = \nabla\times(\mathbf{U}\times\mathbf{B}) - \frac{1}{Pm}\nabla\times(\nabla\times\mathbf{B}) \tag{6}$$

Scaling of variables has been done in a similar way as reported in Christension et al.(2001). Here $\mathrm{U}$, $\mathrm{B}$ and $\Theta$ represent non-dimensional velocity, magnetic and temperature fields, respectively. Scaling results in introduction of non-dimensional control parameters: Ekman number ( $\mathrm{Ek} = \nu/\Omega D^2$ ) , Rayleigh number ( $\mathrm{Ra} = (\alpha g_o \Delta T D^3)/(\nu\kappa)$ ) , Prandtl number ( $\mathrm{Pr} = \nu/\kappa$ ) , Magnetic Prandtl number ( $\mathrm{Pm} = \nu/\eta$ ). Physical parameters $\mu$ , $\mu_0$ , $\rho$ , $\mathbf{J}$ , $\Omega$ , $\kappa$ , $\eta$ stand for dynamic viscosity, magnetic viscosity, density of fluid, Current flux ( $\nabla\times\mathbf{B}$) ), rotational velocity, thermal diffusivity and magnetic diffusivity, respectively.

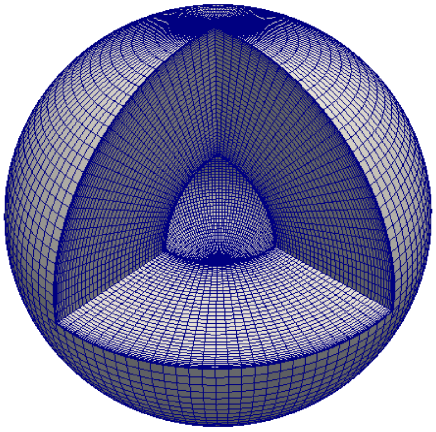

FIGURE 1: Illustration of grid system in spherical shell for finite difference method (FDM). Fine mesh is used near the inner and outer boundaries.

In our numerical solution, we use finite difference method (FDM) to solve the five governing eqns. (1-5) simultaneously on non-staggered grid. We adopt a scheme similar to simplified Marker and Cell (SMAC) proposed by Cheng and Armfield (1995). This is a two step predictor-corrector method treating all terms (Coriolis, Lorentz, etc.) explicitly except the viscous term. In solution steps, we march in time to get a provisional velocity field $\mathrm{U}^*$ in such a way that it satisfies the momentum eq.(1) using the current divergence- free velocity field. The provisional velocity field is corrected by making use of pressure field.

$$\mathbf{U}^{n+1} = \mathbf{U}^* + \beta\nabla(p^{n+1} - p^n) \tag{7}$$

where $\beta = \frac{\Delta t}{Ek}$. Taking divergence of eq. (6) and using continuity equation ( $\nabla\cdot\mathbf{U}^{n+1} = 0$ ) results in

following pressure correction Poisson equation (PCPE).

$$\nabla^2 p^* = \beta(\nabla \cdot \mathbf{U}^*) \tag{8}$$

where $\mathrm{p}^* = p^{n+1} - p^n$ is the correction pressure. The first derivative of $\mathrm{p}^*$ is set to zero at both the boundaries (inner and outer)and the PCPE (7) is solved in the interior of flow domain using an efficient iterative method named Generalized Minimal Residual Method (GMRES) developed by Saad & Schultz (1986). Similarly we solve energy eq. (8) to get temperature field $\Theta^{n+1}$ at new time step.

$$\frac{\Theta^{n+1}-\Theta^n}{\Delta t} + (\mathbf{U}^n \cdot \nabla)\Theta^n = \frac{1}{Pr}\nabla^2 \mathbf{\Theta}^{n+1} \tag{9}$$

To solve the magnetic induction equation, a similar operation is performed

$$\frac{\mathbf{B}^{n+1}-\mathbf{B}^n}{\Delta t} = (\mathbf{B}^n \cdot \nabla)\mathbf{U}^n - (\mathbf{U}^n \cdot \nabla)\mathbf{B}^n + \frac{1}{Pm}\nabla^2 \mathbf{B}^{n+1} \tag{10}$$

Taking divergence of the eq.(6) leads to the following equation

$$\frac{\partial(\nabla \cdot \mathbf{B})}{\partial t} = \nabla \cdot (\nabla \times (\mathbf{U} \times \mathbf{B})) - \frac{1}{Pm}\nabla \cdot (\nabla \times (\nabla \times \mathbf{B})) = 0 \tag{11}$$

It implies that if the initial magnetic field is divergence-free, it remains divergence free with evolution of time. Use of this property in our code reduces computational cost significantly which is one of the highlighting features of our code. We use the same boundary and initial conditions as defined by Christensen et al.(2001) for the non-magnetic cases and by Jackson et al.(2014) for the magnetic case.

## 3. VALIDATIONS

Four and six data sets, respectively are recorded for the validation of non-magnetic cases once the simulations reach a quasi-steady drifting solution. These are: Kinetic energy ($\mathrm{E}_{kin} = \frac{1}{V_s}\int_{v_s} \frac{1}{2}|\mathbf{u}|^2 dv$), magnetic energy $\mathrm{E}_{mag} = \frac{1}{V_s}\frac{1}{Ek\ Pm}\int_{v_s} \frac{1}{2}|\mathbf{B}|^2 dv$ , drift angular velocity $\omega$, Local temperature $\Theta$ , zonal velocity $\mathrm{u}_\phi$ and polar magnetic field $\mathrm{B}_\theta$.

For the validation of the non-magnetic case, a simulation is run at control parameters $\chi = 0.35, Ek = 1 \times 10^{-3}$, $Pr = 1$ and $\mathrm{Ra}{=}1{\times}10^5$ till it reaches a quasi-drifting solution. Fig. 2(a) shows kinetic energy ( $\mathrm{E}_{kin}$ ) variation with time. In Table 1, we find that the steady state values $\mathrm{E}_{kin}$, $\omega$, $\Theta$ and $u_\phi$ are in good agreement with the results reported in Christensen et al.(2001).

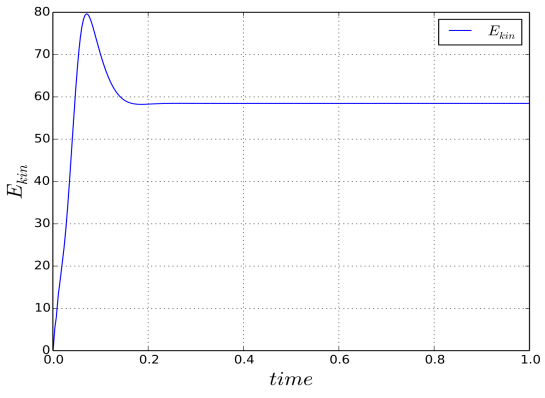


*(a)*

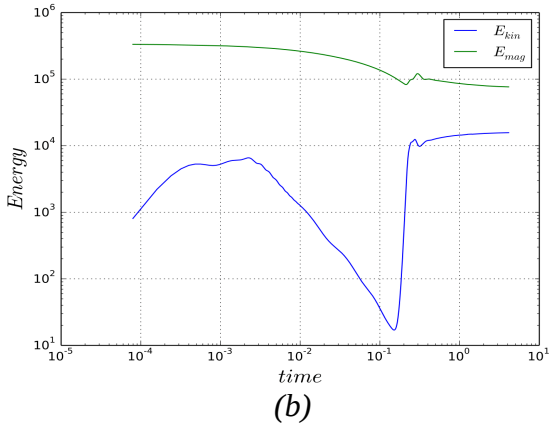


*(b)*

FIGURE 2: Fig.(a) shows time evolution of $\mathrm{E}_{kin}$ for non-magnetic case and Fig.(b) shows time evolution of $\mathrm{E}_{kin}$ and $\mathrm{E}_{mag}$ for magnetic (dynamo) case.

| | $\mathrm{E}_{kin}$ | $\Theta$ | $\mathrm{u}_{\phi}$ | $\omega$ |
|---|---|---|---|---|
| Christensen et al.(2001) | 58.35 | 0.4281 | -10.157 | 0.1824 |
| Present solver (FDM) | 58.47 | 0.4266 | -10.177 | 0.1624 |

TABLE 1. Validation of non-magnetic case with Christensen et al.(2001).

For dynamo case, we run the simulation at control parameters $\mathrm{P}_m = 5$, $\chi = 0.35, Ek = 1 \times 10^{-3}$ and $\mathrm{Ra}{=}1{\times}10^5$ till the $\mathrm{E}_{kin}$ and $\mathrm{E}_{mag}$ are observed to be converging asymptotically. The time evolution of $\mathrm{E}_{kin}$ and $\mathrm{E}_{mag}$ Fig.are very much similar as proposed in benchmark paper ( fig.1(d) in Jackson et al. (2014)). Table 3 shows the results data of present case and that of benchmark. We find that the the results are in good agreement with the proposed benchmark values. The slight deviation from the benchmark case may be due to sensitivity to grid size.

| | $\mathrm{E}_{kin}$ | $\mathrm{E}_{mag}$ | $\Theta$ | $\mathrm{u}_{\phi}$ | $\mathrm{B}_{\theta}$ | $\omega$ |
|---|---|---|---|---|---|---|
| Jackson et al.(2014) | 14846 | 80071 | 0.426 | -58.18 | 0.99 | 3.75 |
| Present solver (FDM) | 15328 | 80293 | 0.435 | -57.32 | 1.00 | 3.31 |

TABLE 2. Validation of magnetic (dynamo) case with Jackson et al.(2014).

## 4. CONCLUSIONS

In this work we have presented the solution of incompressible hydrodynamic and magnetohydrodynamic equations in a rotating spherical shell using finite difference method. We have shown the validation of the newly developed codes for the problem of thermal convection without magnetic field and for the dynamo problems with pseudo-vacuum magnetic boundary conditions using the previously reported benchmark results. The method presented is straightforward to implement and can be easily parallelized on massively parallel computers based on domain decomposition.

## REFERENCES

[1] Christensen, U. R., et al. (2001), A numerical dynamo benchmark, Phys. Earth Planet. Inter., 128, 2534.

[2] Glatzmaier, G. A., and P. H. Roberts (1995), A three-dimensional self-consistent computer simulation of a geomagnetic field reversal, Nature,377, 203209.

[3] Jackson, A. et al., 2014. A spherical shell numerical dynamo benchmark with pseu-do-vacuum magnetic boundary conditions, Geophys. J. Int.,196(2), 712-713.

Fifth International Conference on Computational Methods for Thermal Problems
THERMACOMP2018, July 9-11, 2018, Indian Institute of Science, Bangalore, INDIA
*N. Massarotti, P. Nithiarasu, Pradip Dutta and C. Ranganyakalu (Eds.)*

# CFD ANALYSIS OF COMMON HEADER PULSATING HEAT PIPE

**Bibhu Bhusan Sha, Sameer Ranjan Sahu, Manoj Kumar Moharana***
Department of Mechanical Engineering, National Institute of Technology Rourkela
Rourkela 769008 (Odisha) India
*mkmoharanam@gmail.com

## ABSTRACT

Pulsating heat pipe is a successful passive two-phase heat transfer device for space and electronic cooling. The present work is based on numerical investigation carried out for a common header pulsating heat pipe (CHPHP). CFD modeling is done using ANSYS FLUENT 18.1. The performance of the copper CHPHP of 2 mm inner diameter filled with DI water is studied by varying the heat input from 10 W − 50 W at a filling ratio of 50%. A Volume-of-Fluid (VOF) model in conjunction with continuum surface force model is applied considering the two phase flow occuring inside the device. The outcome of this study shows that an effective thermal conductivity of about 12,000 W/m-K can be achived at heat input of 50 W.

**Key Words:** *pulsating heat pipe, common header, electronic cooling, VOF.*

## 1. INTRODUCTION

Pulsating heat pipe (PHP) is a simple passive lowcost device capable of high heat flux. This may be the reason for the vast use of PHP in thermal management of electronic devices. Akachi [1] first introduced this technology, and since then this has emerged into different shape/size/configurations. A PHP is conventionally made by using a capillary tube bent into multiple turns. The capillary dimension of the PHP allows the working fluid to dustribute itself automatically into liquid slugs and vapor plugs. The heat transfer phenomena involves a series of complex process of evaporation and condensation between these two phases. The complexities occuring inside the device, thus, makes the PHP behaviour unpredicatble under various conditions. Table 1 shows the list of previous works conudcted by many reserchers both experimentally and numerically to understand the PHP behaviour.

| $D_h$ (mm) | Tube Material | No. of. Channel | Working Fluid | FR (%) | Heat Input (W) | References | |
|---|---|---|---|---|---|---|---|
| 2 | Cu | 2 | Ethanol | 60 | 14.8 -74.4 | Khandekar & Groll [2] | E |
| 2.2 | Cu | 1,2 | Ethanol, Water | 50 | 0-50 | Kim et al. [3] | E,N |
| 3 | - | 4 | Water | 10-80 | 10-65 | Pouryoussefi & Zhang [4] | N |
| 1.45 | Cu | 6 | Methanol, Water | 20-90 | 0 - 100 | Verma et al. [5] | E |
| 2 | Cu | 2 | Methanol | 60 | 10-70 | Suresh & Bhramara [6] | N |
| 2.5 | Glass | 7 | Ethanol | 50,60,70 | 38 - 110 | Sun et al. [7] | E |
| 2.75 | Cu | 9 | Water | 40,50,60 | 10 - 50 | Gamit et al. [8] | E |
| 3.8 | Glass | 1 | Water | 30-60 | 5 - 40 | Wang et al. [9] | E |
| 1.8 | Cu | 5 | Water, Ethanol | 30-80 | 5 - 70 | Shafii et al. [10] | E |

Table 1: List of operating conditions (N.B. E= Experimental Approach, N = Numerical Approach)

From the review of the literature it is revealed that all the reported work in open literature used the conventional PHP having multiple bends and turns, but consists of a closed single loop only. In this work a three loop pulsating heat pipe with common headers (CHPHP) is used to understand the thermo-hydrodynamics under varying heat load conditions.

## 2. METHODOLOGY

### 2.1 Geometry and boundary conditions

The present geometry is designed by replacing the U-turns and bends of a 3 turn conventional closed loop pulsating heat pipe (CLPHP) (see Fig. 1(a)) with common headers at both evaporator and condenser ends (see Fig. 1(b)). This geometry is described as Common header PHP (CHPHP) throughout this work. Figure 1(c) shows the boundary conditions applied on the CHPHP.

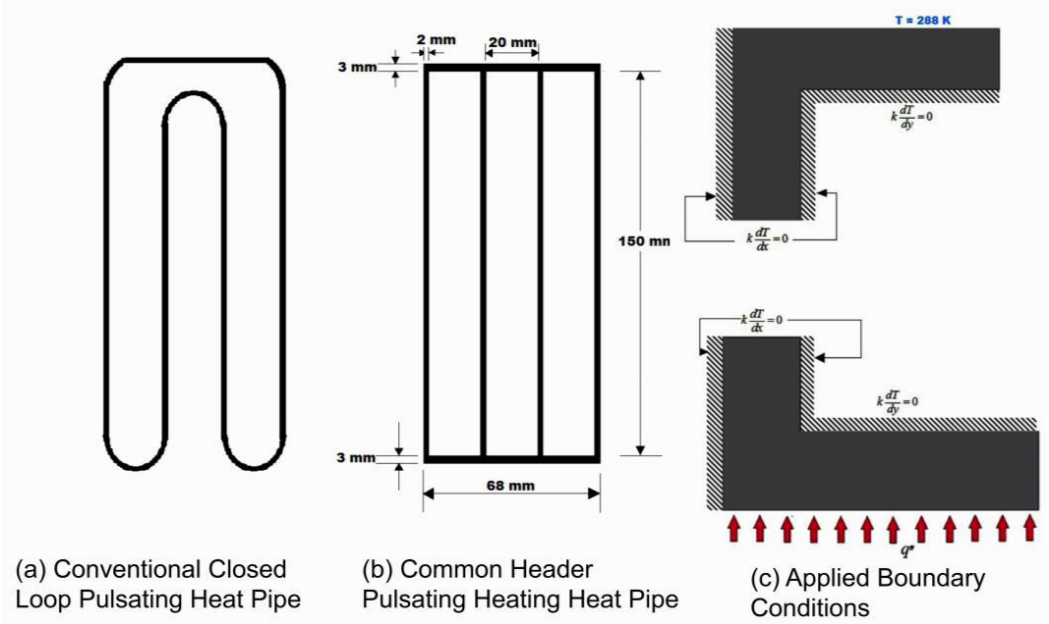


FIGURE 1. (a) Conventional CLPHP (b) Present design CHPHP (c) Boundary conditions applied to the CHPHP

### 2.2 Numerical Methodology

A two-dimensional numerical study of the CHPHP design presented in Fig 1(b) has been under taken. VOF multiphase model is applied along with a continuum surface model to account for the surface tension. DI water was taken as the working fluid having a filling ratio of 50 %. As the heat transfer process is unsteady, transient method is employed with time steps varying from $10^{-8}$ to $10^{-3}$. SIMPLE method is used for pressure-velocity coupling. For spatial discretization, PRESTO for pressure, Geo-Reconstruct for volume fraction, second order upwind for momentum and first order upwind for energy are considered. The under relaxation factors for pressure, density, momentum, vaporization mass and energy are taken as 0.3, 0.5, 0.3, 0.5 and 0.5 respectively. The viscous model is taken as laminar. Implicit body force is turned on. Gravitational acceleration of 9.81 m/s$^2$ is considered in the negative Y direction to account for gravity forces.

## 3. RESULTS

### 3.1 Model Validation

The present model is validated by simulating the experimental condition reported in Patel and Mehta [11] for water filling ratio 50%. The thermal resistance at varying heat input presented in Fig. 2 clearly indicate that the present model can predict the experimental data reported within a reasonable accuracy of 7.5% maximum.

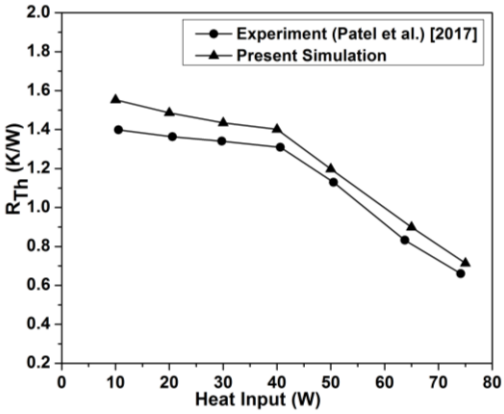


FIGURE 2. Comparison with experiment

3.2 Thermal performance of CHPHP

The model used for validation is also used for the present problem of CHPHP. The parameters of interest are (i) thermal resistance, $R_{th}$ (ii) effective thermal conductivity, $k_{eff}$ (iii) local convective heat transfer coefficient at the evaporator end, $h_{evap}$. They are defined as given below:

$$R_{th} = \frac{\bar{T}_{ef} - \bar{T}_c}{\dot{Q}},\ k_{eff} = \frac{L_t \times Q}{A_c \times \left(T_{w,evap} - T_{cold}\right)},\ h_{evap} = \frac{Q}{A_{evap} \times \Delta T_{sf}}$$

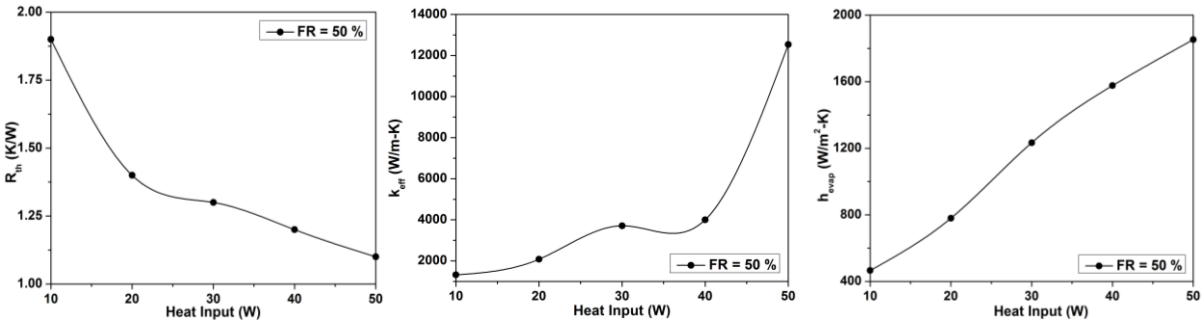


(a) (b) (c)

FIGURE 3. Thermal resistance, effective thermal conductivity and local convective heat transfer coefficient (evaporator) of CHPHP

Figure 3(a) presents variation of thermal resistance for varying heat input condition. With the increase in heat input, the working fluid gain more amount of heat and quickly change its phase and move from the hot end to the cold end. At lower heat input, the working fluid takes more time for phase change, or the pumping force developed is not sufficient to push the vapour plugs to the cold end, thus increasing its thermal resistance. The main factor responsible for heat transfer in a PHP is the sensible heat. Thus, DI water with a high specific heat can gain more sensible heat at higher input loads as compared to lower heat input loads. As can be seen in Fig. 3(b), the effective thermal conductivity increasing with increased heat input and the rate of increase in $k_{eff}$ increases at higher heat input. Also, the local convective heat transfer coefficient from evaporator side increases with increasing heat input. This can be observed in Fig. 3(c). This is also due to higher sensible heat transfer from evaporator wall to the coolant of the evaporator section at higher heat input.

## 4. CONCLUSIONS

A two-dimensional numerical study undertaken to explore the thermal performance of a three-loop common header pulsating heat pipe (CHPHP) using DI water as the working fluid. Simulation conducted at 50% filling ratio under varying heat load conditions show that it is possible to achieve an effective thermal conductivity of about 12,000 W/m-K at 50 W. With a local convective heat transfer coefficient of about 1,800 $W/m^2$-K from the evaporator side indicates that the device can receive and transfer heat to the working fluid effectively. For better thermal management of electronic devices, a higher thermal conductive device allows better heat transfer from the hot end. The CHPHP under consideration is thus found to be effective in removing heat from the hot end with a very high thermal conductivity proving its proficiency in electronic thermal management.

## REFERENCES

[1] Akachi, H. (1993). *U.S. Patent No. 5,219,020*. Washington, DC: U.S. Patent and Trademark Office.

[2] Khandekar, S., & Groll, M. (2004). An insight into thermo-hydrodynamic coupling in closed loop pulsating heat pipes. *International Journal of Thermal Sciences*, 43(1), 13-20.

[3] Kim, B., Li, L., Kim, J., & Kim, D. (2017). A study on thermal performance of parallel connected pulsating heat pipe. *Applied Thermal Engineering*, *126*, 1063-1068.

[4] Pouryoussefi, S. M., & Zhang, Y. (2017). Analysis of chaotic flow in a 2D multi-turn closed-loop pulsating heat pipe. *Applied Thermal Engineering*.

[5] Verma, B., Yadav, V. L., & Srivastava, K. K. (2013). Experimental studies on thermal performance of a pulsating heat pipe with methanol/DI water. *Journal of Electronics Cooling and Thermal Control*, *3*(1), 27-34.

[6] Suresh, J.V., Bhramara, P. (2017). CFD Analysis of multiturn pulsating heat pipe. *Materials Today: Proceedings*, *4*(2), 2701-2710.

[7] Sun, Q., Qu, J., Li, X., & Yuan, J. (2017). Experimental investigation of thermo-hydrodynamic behaviour in a closed loop oscillating heat pipe. *Experimental Thermal and Fluid Science*, *82*, 450-458.

[8] Gamit, H., More, V., Mukund, B., & Mehta, H. B. (2015). Experimental investigations on pulsating heat pipe. *Energy Procedia*, 75, 3186-3191

[9] Wang, J., Ma, H., Zhu, Q., Dong, Y., & Yue, K. (2016). Numerical and experimental investigation of pulsating heat pipes with corrugated configuration. *Applied Thermal Engineering*, 102, 158-166.

[10] Shafii, M. B., Arabnejad, S., Saboohi, Y., & Jamshidi, H. (2010). Experimental investigation of pulsating heat pipes and a proposed correlation. *Heat Transfer Engineering*, 31(10), 854-861.

[11] Patel, V. M., & Mehta, H. B. (2017). Influence of working fluids on startup mechanism and thermal performance of a closed loop pulsating heat pipe. *Applied Thermal Engineering*, 110, 1568-1577.

Fifth International Conference on Computational Methods for Thermal Problems
THERMACOMP2018, July 9-11, 2018, Indian Institute of Science, Bangalore, INDIA
*N. Massarotti, P. Nithiarasu, Pradip Dutta and C. Ranganyakalu (Eds.)*

# AN EFFICIENT ALGORITHM FOR STABILITY ANALYSIS OF TIME-PERIODIC FLOWS

**U. K. Sarkar, S. Ghosh Moulic**
Department of Mechanical Engineering, I.I.T. Kharagpur 721302, moulic@mech.iitkgp.ernet.in

## ABSTRACT

A simple, accurate and efficient numerical method is proposed for linear stability analysis of time-periodic flows. The method is based on repeated application of Richardson extrapolation to improve the accuracy of the Floquet exponents obtained by a standard time integration method using trapezoidal rule. This results in significant reduction in the computational effort required to determine the Floquet exponents to a desired level of accuracy. The growth rate of infinitesimal disturbances to time-periodically modulated plane Poiseuille flow has been determined using the proposed method, for a benchmark case. The value of the amplification rate reported is accurate to ten decimal places; the value reported in previous studies is accurate to four decimal places.

**Key Words:** *Linear stability, Time-periodic flows, Floquet theory, Spectral collocation method, Richardson extrapolation.*

## 1. INTRODUCTION

The stability of time-periodic or oscillatory flows has been an important topic of research because of its applications in different industrial and bio-medical processes. A review of the analysis of time-periodic flows involving shear instability, thermal instability, and centrifugal instability is given in [1]. In spite of its theoretical and practical importance, the literature on the stability of different prototype time-periodic flow problems is relatively scarce.

The linear stability of time-periodic flows is described by a system of partial differential equations with time-periodic coefficients. The form of the solution is given by Floquet theory. An infinitesimal disturbance to the basic state may grow or decay depending on the sign of the Floquet exponents. In previous investigations [2, 3], the governing partial differential equations are approximated by a Galerkin method using combinations of Legendre polynomials as the basis functions. The resulting system of ordinary differential equations is integrated for a full period of oscillation using the trapezoidal rule. The Floquet exponents are then computed from the eigenvalues of the monodromy matrix obtained from the time integration. To obtain accurate values of the Floquet exponents, the time integration has to be carried out using small step sizes.

In this investigation, a spectral collocation method using combinations of Chebyshev polynomials as the basis functions has been used for the spatial discretization. It is shown that with repeated application of Richardson extrapolation, the accuracy of the computed Floquet exponents can be significantly enhanced. Application of Richardson extrapolation leads to substantial reduction in the computational effort required to determine the Floquet exponents to a desired level of accuracy. Consequently, the savings in computational cost required to determine the neutral curve of linear stability can be enormous, particularly for multiparameter problems. To demonstrate the proposed method, the stability of modulated plane Poiseuille flow is considered as a test case.

## 2. PROBLEM FORMULATION

Incompressible flow of a Newtonian fluid between two horizontal parallel plates of infinite extent is considered. A Cartesian coordinate system $(\bar{x},\bar{y},\bar{z})$ is introduced in such a way that the plane $\bar{y}=0$ is parallel to the plates and located midway between the plates. The plates are separated by a distance

of $2h$ along the $\bar{y}$ axis. The basic flow is driven by a pressure gradient which has a steady component $-P_O\,\hat{i}$ and an oscillatory component $-Q_O\cos(\omega\bar{t})\,\hat{i}$, where $\hat{i}$ is the unit vector in the $\bar{x}$-direction. The governing differential equations are nondimensionalized by choosing reference scales for length, time, velocity, and pressure as, respectively, $h$, $(h/U_O)$, $U_O$, and $\rho(U_O)^2$, where $U_O=\left(h^2P_O\right)/(2\mu)$ is the maximum of the steady component of the basic state velocity, $\rho$ is the density of the fluid and $\mu$ is the dynamic viscosity. The basic state velocity and pressure may be expressed in non-dimensional form as

$$u_B(y,t)=U(y)+\Gamma W(y,t),\;\; p_B(x,t)=-\frac{2x}{Re}\left\{1+\Lambda\cos(St)\right\}, \tag{1}$$

where $U(y)=1-y^2$, $W(y,t)=Real\left[\frac{1}{i}\left\{1-\cosh\left(\beta(1+i)y\right)/\cosh\left(\beta(1+i)\right)\right\}e^{iSt}\right]$, $\Lambda=\frac{Q_O}{P_O}$, $\beta=\sqrt{(SRe)/2}$, $\Gamma=(2\Lambda)/(SRe)$, $Re=(\rho U_O\,h/\mu)$ is the Reynolds number and $S=\omega h/U_O$ is the Strouhal number.

For linear stability analysis of (1), it can be shown that Squire's theorem holds [2]. Therefore, two dimensional stability analysis is sufficient for determining the critical conditions of linear stability. The velocity and pressure for two dimensional perturbations can be written as $\boldsymbol{V}(x,y,t)=u_B(y,t)\boldsymbol{i}+u'(x,y,t)\boldsymbol{i}+v'(x,y,t)\boldsymbol{j}$ and $p(x,y,t)=p_B(x,t)+p'(x,y,t)$, where the primes denote perturbation quantities. The linearized Navier-Stokes equations admit a solution of the form, $u'=\hat{u}(y,t)exp(i\alpha x)$, $v'=\hat{v}(y,t)exp(i\alpha x)$, $p'=\hat{p}(y,t)exp(i\alpha x)$ where $\alpha$ is the non-dimensional wavenumber in the streamwise or $x$-direction. Following the standard procedure of linearized hydrodynamic stability problems, pressure terms are eliminated, and the governing equation and boundary conditions for infinitesimal two-dimensional disturbances are expressed in terms of the normal velocity component $\hat{v}(y,t)$ as given below:

$$\frac{\partial}{\partial t}\left\{\mathscr{L}(\hat{v})\right\}=\frac{1}{Re}\mathscr{L}^2(\hat{v})-i\alpha\left(u_B(y,t)\mathscr{L}(\hat{v})-\frac{\partial^2 u_B}{\partial y^2}(y,t)\hat{v}\right),\;\mathscr{L}=\frac{\partial^2}{\partial y^2}-\alpha^2 \tag{2a}$$

$$\hat{v}=0,\;\frac{\partial\hat{v}}{\partial y}=0\;\text{ at }\;y=-1,\text{ and }\;\hat{v}=0,\;\frac{\partial\hat{v}}{\partial y}=0\;\text{ at }\;y=1. \tag{2b}$$

## 3. NUMERICAL METHOD

The disturbance velocity, $\hat{v}(y,t)$, is approximated as

$$\hat{v}(y,t)=\sum_{k=0}^{K-1}a_k(t)\varphi_k(y), \tag{3}$$

where $\varphi_k(y)=\left(1-y^2\right)^2T_k(y)$ and $T_k(y)=\cos\left(k\cos^{-1}y\right)$ is the $k^{\text{th}}$ Chebyshev polynomial of the first kind [4]. Each of the basis functions, $\varphi_k(y)$, in the series (3) satisfies the boundary conditions (2b). Equation (2a) is collocated at the Gauss-Lobatto points,

$$y_j=\cos\left[\pi j/(K-1)\right],\;\; j=0,\ldots,K-1. \tag{4}$$

This leads to the following linear system of ordinary differential equations,

$$\boldsymbol{F}\frac{d\boldsymbol{a}}{dt}=\left[\boldsymbol{G}+\boldsymbol{H}(t)\right]\boldsymbol{a}, \tag{5}$$

where $\boldsymbol{a}(t)=\left[a_0(t), a_1(t), \cdots, a_{K-1}(t)\right]^T$. The matrices $\boldsymbol{F}$, $\boldsymbol{G}$, and $\boldsymbol{H}$ are obtained from the spatial discretization of the differential operators, $\mathscr{L}$, $\frac{1}{Re}\mathscr{L}^2$, and $i\alpha\left(\frac{\partial^2 u_B}{\partial y^2}-u_B\mathscr{L}\right)$, respectively. The elements of the matrices $\boldsymbol{F}$ and $\boldsymbol{G}$ are time-independent, whereas the elements of the matrix $\boldsymbol{H}$ are time-periodic, such that $\boldsymbol{H}(t)=\boldsymbol{H}(t+T)$, where $T=(2\pi)/S$ is the time-period of the basic flow. It is worth noting that the choice (4) of collocation points yields spectral accuracy or exponential convergence [4].

To determine the linear stability of the flow, the fundamental matrix, $\boldsymbol{\Phi}(t)$, satisfying

$$\boldsymbol{F}\frac{d\boldsymbol{\Phi}}{dt}=\left[\boldsymbol{G}+\boldsymbol{H}(t)\right]\boldsymbol{\Phi}(t), \tag{6}$$

and the initial condition, $\boldsymbol{\Phi}(0)=\boldsymbol{I}$, where $\boldsymbol{I}$ is the $K$ x $K$ identity matrix, is considered. According to Floquet theory, the net growth of an arbitrary disturbance over the time period $T$ is determined by the eigenvalues of the monodromy matrix $\boldsymbol{M}=\boldsymbol{\Phi}(T)$. The eigenvalues, $\mu_j$, of the $K$ x $K$ matrix $\boldsymbol{M}$, referred to as Floquet multipliers, determine the growth or decay of Floquet modes over a time period $T$; the corresponding Floquet exponents $\lambda_j$ are defined by $\mu_j=exp(\lambda_j T)$. The Floquet exponents may be ordered such that $Real(\lambda_1)\geq Real(\lambda_2)\geq\cdots\geq Real(\lambda_K)$. It follows that the basic flow is linearly stable if $Real(\lambda_1)<0$, unstable if $Real(\lambda_1)>0$, and marginally stable if $Real(\lambda_1)=0$.

The accuracy of the computed Floquet exponent, $\lambda_1(\Delta t)$, depends on the numerical integration method used to compute $\boldsymbol{M}$ and the step size, $\Delta t$, used in the numerical integration. In previous investigations [2, 3], the numerical integration is done using the trapezoidal rule which is only second-order accurate. Consequently, for accurate determination of the growth rate, the step size used in the numerical integration has to be quite small.

In this investigation, the accuracy of the computed growth rates is improved using repeated Richardson extrapolation. The system (6) is integrated numerically ($J$+1) times, from $t=0$ to $t=T$, using the trapezoidal rule with successively smaller time steps, $\Delta t_i=T/n_i$, and approximations, $\boldsymbol{M}_i$, to the monodromy matrix are determined for $i$ = 0,1, 2, ..., $J$, where $J$ is the number of times Richardson extrapolation is repeated, $n_i$ is the number of steps in the integration and $n_{i+1}=2n_i$. The eigenvalues of $\boldsymbol{M}_i$ are determined using the QZ algorithm and the corresponding amplification rates computed. If the amplification rate, $Real(\lambda_1(\Delta t_i))$, obtained using the trapezoidal rule with step size $\Delta t_i$ is denoted by $A_{i,0}$, extrapolated values of the amplification rates may be determined recursively using

$$A_{i,j}=\left\{2^{2j}\cdot A_{i,j-1}-A_{i-1,j-1}\right\}/\left(2^{2j}-1\right), \tag{7}$$

for $i$ = $j$, $j$+1,$\cdots$, $J$ and $j$ = 1, 2, 3,$\cdots$, $J$. The errors in the estimated values, $A_{i,j}$, of the amplification rates are $O\left(\left(\Delta t_{i-j}\right)^{2j+2}\right)$ [5].

## 4. RESULTS

Results have been obtained for $S=0.2694$, $\Gamma=0.25$, $Re$= 5772.22 and $\alpha$= 1.0206, and compared with available benchmark data [2, 3]. The computations have been done using $K$=80. This value of $K$ has been found to be sufficient for convergence of the series (3).

The result of repeated application of Richardson extrapolation with J = 3 are summarized in Table 1. The amplification rates presented in the third column of Table 1 have been obtained using the trapezoidal rule with 50, 100, 200 and 400 steps per cycle. A glance at the table reveals that the extrapolated value of the amplification rate converges to - 0.0053031460; the value reported in [2, 3] is - 0.0053. The values of the amplification rates predicted by the trapezoidal rule using 20000, 30000 and 40000 steps per cycle are - 0.0053031458, - 0.0053031459, and -0.0053031460 respectively. Thus, the final extrapolated value of the amplification rate obtained is as accurate as the value computed using the trapezoidal rule with 40000 steps per cycle.

| $i$ | No. of steps, $n_i$ | $A_{i,0} = Real\left(\lambda_1\left(\Delta t_i\right)\right)$ | $A_{i,1}$ (1st extrapolation) | $A_{i,2}$ (2nd extrapolation) | $A_{i,3}$ (3rd extrapolation) |
|---|---|---|---|---|---|
| 0 | 50 | -0.0052636922 | | | |
| 1 | 100 | -0.0052932345 | -0.0053030820 | | |
| 2 | 200 | -0.0053006650 | -0.0053031418 | -0.0053031458 | |
| 3 | 400 | -0.0053025256 | -0.0053031457 | -0.0053031460 | -0.0053031460 |

TABLE 1. Application of Richardson extrapolation to enhance the accuracy of the computed growth-rate of time-periodically modulated plane Poiseuille flow for $\Gamma = 0.25$, $S = 0.2694$, $Re = 5772.22$ and $\alpha$=1.0206; the growth rate reported in [2, 3] is equal to -0.0053.

## 5. CONCLUSIONS

In this study, an efficient and accurate numerical method has been proposed for linear stability analysis of isothermal and non-isothermal time-periodic flows. It has been demonstrated that repeated application of Richardson extrapolation to the growth rate data obtained by numerical integration using the trapezoidal rule enhances the accuracy significantly. For the test case of time-periodically modulated plane Poiseuille flow, application of Richardson extrapolation to the growth-rate data, obtained with 50, 100, 200 and 400 steps per cycle, could determine the growth-rate accurately to ten decimal places after the third order extrapolation. It has been found that the number of steps required to get the same accuracy using the trapezoidal rule is about 40000. Thus, application of Richardson extrapolation reduces the computational cost by a factor of about $40000 / 750$ which is approximately 53.

## REFERENCES

[1] S. H. Davis, The stability of time-periodic flows, *Annual Rev. Fluid Mechanics*, 8, 57-74, 1976.
[2] B. A. Singer, J. H. Ferziger, H. L. Reed, Numerical simulation of transition in oscillatory plane channel flow, *Journal of Fluid Mechanics*, 208, 45–66, 1989.
[3] Y. C. Chen, Stability of an oscillatory shear flow in a differentially heated vertical channel, *International Journal of Heat and Mass Transfer*, 48, 3591-3603, 2005.
[4] J. P. Boyd, *Chebyshev and Fourier Spectral method*, Dover Publications, New York, 2000.
[5] J. Stoer and R. Bulirsch, *Introduction to Numerical Analysis*, 3rd Edition, Springer, New York, 2002.

Fifth International Conference on Computational Methods for Thermal Problems
THERMACOMP2018, July 9-11, 2018, Indian Institute of Science, Bangalore, INDIA
N. Massarotti, P. Nithiarasu, Pradip Dutta and C. Ranganyakalu (Eds.)

# A COMPARISON BETWEEN MONOLITHIC AND PARTITIONED APPROACH FOR CONJUGATE HEAT TRANSFER IN AN IMMERSED BOUNDARY FRAMEWORK

Mukesh Kumar and Ganesh Natarajan
Department of Mechanical Engg., Indian Institute of Technology Guwahati, Assam, India
Corresponding author: Email: mukesh.kr@iitg.ernet.in and n.ganesh@iitg.ernet.in

## ABSTRACT

We propose both monolithic and partitioned approach to solve conjugate heat transfer in an immersed boundary framework for complex geometries. The present framework is based on the staggered/non-staggered finite volume framework for incompressible flows which is extended to handle conjugate heat transfer. The key difference in the monolithic framework is that only a single hybrid momentum equation for normal momentum and single hybrid energy equation for temperature are solved simultaneously for both fluid and solid domains. However, in partitioned approach the energy equation is solved in each sub domain and temperature of both domains are coupled using suitable boundary conditions. The equations are discretized using a second–order accurate spatial and temporal scheme, that uses three point backward differencing for time discretisation and high-resolution schemes for convective discretisation, while central differencing is adopted for the viscous terms. The resulting discretized non-linear system of equations are solved using the Newton–Krylov approach. The momentum field at the cell centroids is then reconstructed using a defect-correction algorithm. The energy conservation equation is discretized similar to the collocated framework, with a second–order convection scheme for the convective terms and implicit Euler time stepping. These equations are linearized by considering the velocity field at the latest available time step, and the resulting linear system of equations are solved using SAAMG preconditioned GMRES solver using the LiS library. The effect of immersed solids are accounted for in the governing equation using a solid fraction approach. The investigations are be carried out for conjugate heat transfer with a backward-facing flow at different ratios of solid to fluid thermal diffusivities. Studies show that both monolithic and partitioned approaches can successfully simulate conjugate heat transfer with a backward-facing flow although the former shows a faster convergence to steady state solution.

**Key Words:** *Conjugate Heat Transfer, Diffuse Interface Immersed Boundary Method, Staggered/Non-staggered.*

## 1. INTRODUCTION

The coupled heat transfer between fluid and solids is defined as conjugate heat transfer and plays a prominent role in many industrial and scientific applications, including heat exchangers, cooling of micro channels and heat transfer in reactors. The interface in the conjugate heat transfer (CHT) can be considered as fluid-fluid, fluid-solid, or solid-solid depend in on the application of the problem. The imposition of the boundary conditions like continuity and heat flux of the temperature are key issues in the overall dynamics of CHT problems and also parts a major challenge from numerical prospective. Moreover, the traditional body-fitted grid methods required a huge effort on generating separate meshes for fluid and solid domains for solving conjugate heat transfer problems and equations are solved independently in both domains with solutions are coupled through boundary condition treatment at the solid-fluid interface. In contrast, the use of immersed boundary approach allows simulations of fluid around stationary and moving bodies with complex features on a background mesh. Thus, methods based on such methodologies [1], [2], [3] have solved both fluid and solid equations on a single Cartesian grid which reduces complexity involved in solving conjugate heat transfer problems. Numerical methods that have been used to solve conjugate heat transfer can be categorized broadly into monolithic based formulation and partitioned based formulation. In a present monolithic approach, a single hybrid momentum equation and a single hybrid energy equation for temperature are solved simultaneously for both fluid and solid domains. In contrast, partitioned approaches are those where temperature equations are solved separately in each sub domain and temperature of both domains are coupled at the interface between domains using suitable boundary conditions. There are practical benefits of monolithic approach where not extra effort is required since no boundary condition at interface need to be imposed. The continuity and heat flux of temperature conditions are satisfied automatically through modified equations. But, this approach does not have the freedom to choose different time

steps for different domains. However, we can choose different time step in each sub-domain for partitioned formulation which increases the stability and accuracy of partitioned approach. On the other hand, the primary difficultly in partitioned approach is imposing boundary condition at the interface. The Dirichlet -Neumann conditions is the most suitable combination in fluid and solid domains respectively at the fluid-solid interface [3] at high thermal diffusivities ratios.

The main aim of present study is to develop and analyze monolithic and partitioned approaches to solve conjugate heat transfer problems in diffuse interface immersed boundary framework. In particular in the present monolithic approach, a single momentum equation for normal momentum and energy equation is solved in the entire computational domain. Partitioned approach is also implemented where the energy equation is solved in each sub domain and temperature of both domains are coupled at the interface between both domains. The efficacy of present approaches are demonstrated by carrying out detailed investigation of conjugate heat transfer in flow over a backward-facing steps at different thermal diffusivities ratios.

# 2. GOVERNING EQUATIONS

The governing equations for fluid flow and heat transfer which are non-dimensionalised with suitable length (L), velocity (U), and temperature (T) scales, for two dimensional incompressible flow with conjugate heat transfer can be written as,

$$\frac{\partial \rho}{\partial t} + \nabla \cdot (\rho \mathbf{u}) = 0 \tag{1}$$

$$\frac{\partial (\rho \mathbf{u})}{\partial t} + \nabla \cdot (\rho \mathbf{u}\mathbf{u}) = -\nabla p + \frac{1}{Re}(\nabla \cdot \bar{\bar{\tau}}) \tag{2}$$

$$\frac{\partial (\rho T)}{\partial t} + \nabla \cdot (\rho \mathbf{u} T) = \frac{1}{RePr}\left\{ \nabla^2 T + \frac{K_s}{K_f} \nabla^2 T \right\} \tag{3}$$

where the dimensionless numbers governing the flow are the Prandtl number $Pr = \frac{\nu}{\alpha}$, Rayleigh number $Ra = \frac{g\beta\ L^3 (T_h - T_c)}{\alpha \nu}$

# 3. NUMERICAL METHOD

The overall solution methodology is a finite–volume based projection method, extended to conjugate heat transfer, in a hybrid staggered/non–staggered framework [4]. The equations are solved in a segregated manner, similar to those of standard incompressible solvers. The key difference between the hybrid staggered/non–staggered framework employed in this study and those of collocated frameworks is that in the former we solve a single momentum equation, for the scalar normal momentum at the cell faces akin to a staggered framework, independent of the dimensionality of the problem. The calculation of convective and diffusive fluxes appearing in the equation is however carried out similar to that in collocated frameworks. The centroidal velocities required in these flux computations are recovered from the normal momentum using a reconstruction approach as described in [5]. In the present diffuse interface immersed boundary method, the boundary conditions are enforced indirectly by integrating the set of governing equations in [6] everywhere in domain. The set of global momentum and energy equations read,

- Semi-discrete form of momentum equations

$$(1-\phi_B)\left[ \frac{(\rho U)_f^* - (\rho U)_f^n}{\Delta t} + \underbrace{\frac{1}{\Omega}\Big[ \sum_{e \in E(\Omega)} \rho_e \mathbf{u}_e U_e \Delta S_e \Big] \cdot \mathbf{n}_f}_{\text{Convective flux}} - \underbrace{\frac{1}{\Omega Re}\Big[ \sum_{e \in E(\Omega)} \frac{\partial \mathbf{u}}{\partial n}\Big|_e \Delta S_e \Big] \cdot \mathbf{n}_f}_{\text{Diffusive flux}} \right] = -\frac{(1-\phi_B)}{\Omega}\left[ \frac{\delta p}{\delta n}\Big|_f \right] - \phi_B \left[ \frac{(\rho U)_f^* - (\rho U)_B}{\Delta t} \right] \tag{4}$$

- Semi-discrete form of energy equation

$$(1-\phi_B)\left[ \Omega_c \frac{(\rho T)_1^{n+1} - (\rho T)_1^n}{\Delta t} + \sum_{e \in f(\Omega_c)} (\rho T)_e U_e \Delta S_e \right] = (1-\phi_B)\frac{1}{PrRe} \sum_{e \in f(\Omega_c)} \frac{\partial T}{\partial n}\Big|_e \Delta S_e - \phi_B \left[ \frac{(\rho T)_1^{n+1} - (\rho T)^n}{\Delta t}\Omega_c - \frac{1}{PrRe}\frac{K_s}{K_f} \sum_{e \in f(\Omega_c)} \frac{\partial T}{\partial n}\Big|_e \Delta S_e \right] \tag{5}$$

where $\phi_B$ represents the solid fraction. It can be discerned a eqs. 4and 5 show that the full momentum and energy equations are recovered for $\phi_B = 0$ (outside the solid) and equations reduce to the no slip condition, $\rho U)^*_f = \rho U)_B$. Isothermal condition can be achieved when ratio of thermal conductivities ($\frac{K_s}{K_f}$) tends to zero for $\phi_B$=1 (inside the solid), $()_1 = (\rho T)_B$. But, while implementing Neumann boundary condition can be achieved when ratio of thermal conductivities ($\frac{K_s}{K_f}$) $\rightarrow \infty$ for $\phi_B$=1 (inside the solid). We identify fluid nodes as those falling outside the solid and solid nodes as those inside the body. subsequently, cells whose face have both fluid and solid nodes are marked as Immersed cells "I". The solid (S) and fluid (F) cells are categorized in a similar fashion. The volume fraction of the body in all cells are determined using a initial-cell approach. A bounding box approach reduces the cost of the identification, particularly for moving body problem and it is evident that $0 < \phi_B < 1$ for I cells, $\Phi_B = 1$ for S cells and $\phi_B = 0$ for F cells. In the partitioned approach, the energy equations are solved separately in the two domain with the fluid domain employing a temperature continuity boundary condition (Dirichlet) from solid and solid domain imposing a heat flux boundary condition (Neumann) from fluid. This Neumann-Dirichlet coupling is found to be efficient for a range of high thermal conductivity ratio.

# 4. RESULTS & DISCUSSIONS

In order to analyze the performance of the both monolithic and partitioned approaches, we consider the problem of flow over a backward-facing steps (BFS) with horizontal fluid-solid interface. The BFS is considered as a benchmark mainly due to has numerous flows features like flow separation, re-attachments and recirculation zones which have been widely studied in literature. The computational domain is divide into two regimes, fluid above the solid, and solid below with the fluid, the fluid entering through an inlet channel that is half the height of the channel, giving rise to a backward-facing step flow. The computational domain is discretized using $300 \times 100$ Cartesian mesh with bottom wall and inlet being isothermal, (bottom wall are hotter than the inlet), and the all other surfaces adiabatic. No-slip conditions are imposed for velocities on all the four walls while parabolic velocity profile imposed at the inlet and Neumann condition is imposed at the outlet of boundary. Simulations are carried out using both approaches for $Pr = 0.71$ and $Re = 800$, where Reynolds number is based on the channel height. The temperature profile at cross section $x = 3$ is shown in Fig. 1 for different thermal conductivities and a good agreement with the result of Pareschi et al. [7] is observed for the both approaches. The favourable agreement of local Nusselt number distribution along the fluid-solid interface between two different computational approach shown in Fig. 2 (a, b) with results of Pareschi et al. [7]. It makes clear that proposed both methods correctly predicted flows and heat transfer for the computation. Nevertheless, monolithic approach shows a faster rate of convergence to steady state Fig. 2(c) for the same times steps over the partitioned approach at all ratios of thermal conductivities. These studies also show that the both approaches can accurately compute the conjugate heat transfer problem in complex geometries.

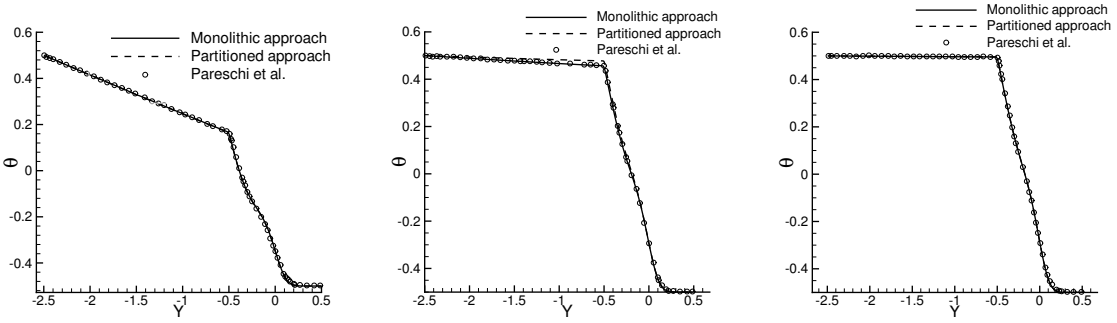


(a) $\frac{k_s}{k_f} = 10$ (b) $\frac{k_s}{k_f} = 100$ (c) $\frac{k_s}{k_f} = 1000$

Figure 1: Comparison of temperature profile at x=3 with Pareschi et al.[7] at $Re = 800$

# 5. CONCLUSIONS

A detailed numerical investigation of monolithic and partitioned approaches for numerical simulations of conjugate heat transfer in immersed boundary framework is carried out in the present work. A monolithic approach where a single hybrid momentum equation for normal momentum and single hybrid energy equation for temperature are solved simultaneously for both fluid and solid domains while in the partitioned approach energy equations are solved in a each sub domain with

REFERENCES

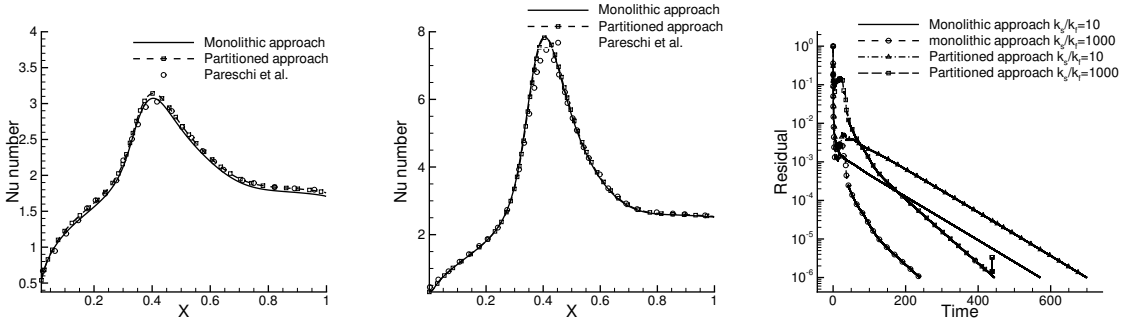


(a) $\frac{k_s}{k_f} = 10$ (b) $\frac{k_s}{k_f} = 1000$ (c)

Figure 2: (a, b) Comparison of Nusselt number profile cross the interface of solid-fluid with Pareschi et al. [7] (c) Time history of log (residual), at $Re = 800$

.

coupling using a Dirichlet- Neumann condition. The monolithic and partitioned approaches perform equally well in terms of accuracy and robustness for conjugate heat transfer in flow over a backward facing steps, although monolithic approach shows faster rate convergence than partitioned approach for the same time steps at the different ratios of thermal conductivities. However, partitioned approaches have freedom to choose different timesteps for each sub-domain which will effect the solution convergence, although, this has not explored in the present studies.

# REFERENCES

[1] W. Xie and P. DesJardin, "A level set embedded interface method for conjugate heat transfer simulations of low speed 2D flows, *Computers Fluids*, 35, 1262-1275, 2008.

[2] K. Nagendra, K. D. Tafti, and K. Viswanath, A new approach for conjugate heat transfer problems using immersed boundary method for curvilinear grid based solvers, *Journal of Computational Physics*, 267, 225–246, 2014.

[3] W. D. Henshaw, K. K. Chand, A composite grid solver for conjugate heat transfer in fluid–structure systems, *Journal of Computational Physics*, 228, 3708–3741, 2009.

[4] G. Natarajan, and F. Sotiropoulos, Adaptive finite volume incompressible Navier–Stokes solver for 3D flows with complex immersed boundaries, *Proceedings of the 62$^{nd}$ APS–DFD Annual Meeting*, November 22–24, 2009.

[5] G. Natarajan, and F. Sotiropoulos, IDeC(k): A new velocity reconstruction algorithm on arbitrarily polygonal staggered meshes, *Journal of Computational Physics*, 230, 6583–6604, 2011.

[6] D. Pan, An immersed boundary method for incompressible flows using volume of body function, *International Journal for Numerical Methods in Fluids*, 50 , 733–750, 2006.

[7] G. Pareschi, N. Frapolli, S. Chikatamarla, and I. V Karlin, Conjugate heat transfer with the entropic lattice Boltzmann method, *Phys. Rev. E*, 94, 013305, 2016.

Fifth International Conference on Computational Methods for Thermal Problems
THERMACOMP2018, July 9-11, 2018, Indian Institute of Science, Bangalore, INDIA
*N. Massarotti, P. Nithiarasu, Pradip Dutta and C. Ranganyakalu (Eds.)*

# CONVECTIVE HEAT TRANSFER AROUND A TRAPEZOIDAL CYLINDER AT VARYING INLET TURBULENT INTENSITY

**Sudhir Chandra Murmu[1]* Himadri Chattopadhyay[1]**

Department of Mechanical Engineering, Jadavpur University, Kolkata- 700032, India.

e-mail, [1]*murmusudhir@gmail.com, [1]chimadri@gmail.com

## ABSTRACT

Flow around bluff bodies have received attention of researchers over the years. In this paper, transport phenomena around a symmetrically placed trapezoidal body has been numerically investigated. The aspect ratio of the channel is varied between 4-10. The simulation is done to cover cross flow encompassing laminar and turbulent regime in the Reynolds number range upto 200,000 and inlet intensities from 5% to 40%. The flowing medium i.e., air is consider to have constant Prandtl number. The governing equations of continuity, momentum, and energy equations are solved along with transition SST Model for closure of turbulence. The effect of turbulent intensity on enhancing heat transfer from the body has been emphasized in this work.The effect of inlet turbulence level on drag coefficient is also reported.

**Key Words:** *Trapezium, heat transfer, convection; bluff body, turbulent intensity; drag coefficient.*

## 1. INTRODUCTION

Flow around a bluff body in ducts and channels has been investigated intensively by many researchers both experimentally and numerically. Relatively fewer studied deal with trapezoidal bluff body. Kahawita and Wang[1] had investigated the two dimensional numerical simulation of the Benard-von Karman hydrodynamic instability behind the trapezoidal bluff bodies studied using the spline method of the fraction steps. Venugopal et al.[2] carried out experimental investigations on the vortex flow meter with the differential wall pressure measurement method. Kondjoyan and Daudin [3] have shown the effect of free stream turbulence intensity on heat and mass transfer at a surface of circular cylinder and an elliptical cylinder. Turbulence intensity ranging from 1.5 to 40% and of Reynolds number ranging from 3,000 to 40,000 on transfer coefficients has been measured for a circular cylinder in cross-flow. Chen et al.[4] had analyzed the 2-D flow around a porous expanded trapezoidal cylinder using a finite volume method, based on the body-fitted, non-orthogonal grids and multi-block technique. Literature survey suggests that the effect of inlet fluctuation on the transport process over bluff bodies are not covered comprehensively. Only one experimental work had been done by Kondjoyan**[3]**which documents the effect of turbulent intensity on circular and elliptic cylinder and no such studies have been performed for triangular cylinder, diamond and trapezoidal cylinder.

## 2. PROBLEM FORMULATION

The present work considers the forced convection cross flow around trapezoidal cylinder as shown in figure 1. The hydraulic diameter D of the trapezoidal cylinder is the non-dimensional length. The

problem is taken as 2-D. The present work considers the forced convection cross flow around trapezoidal cylinder as shown in figure 1. The total non-dimensional length of the computational domain 50D. The ratio of the width of the cylinder to the vertical distance between the upper and lower walls, H=10D has been used in this work.

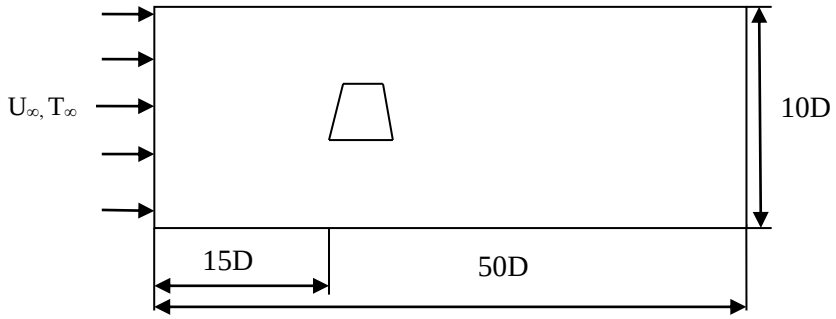


Figure 1.Computational domain for symmetrically placed trapezium

### 2.2 Boundary conditions

Fluid approaches to the cylinder with inlet velocity of $U_\infty$ and temperature of the inlet fluid is $T_\infty$ where the cylinder constant surface temperature is maintained about $T_S$ =398 K. The fluid is defined to be air with constant physical properties (Pr=0.71) with an inlet temperature of 298 K. The top and bottom walls are assumed symmetrical where the first derivative vanishes. The domain size is fixed and the fluid properties are also consider to be constant thus the variation of Reynolds number are done by changing the inlet velocity.

## 3. RESULTS

The major parameter of importance in terms of heat transfer is the Nusselt number which is defined as

$$Nu_d = \frac{hD}{k} \tag{8}$$

Where *h* is the convective heat transfer coefficient.

The viscous and pressure forces acting on the both cylinder are used to calculate the drag coefficients. The drag coefficient is given by:

$$C_d = \frac{F_d}{\frac{1}{2}\rho U_\infty{}^2 d} \tag{9}$$

where $F_d$ is the drag force acting on the cylinder.

Figure 2 show the variation of Nusselt number over the surface of the symmetrically placed trapezium at different Reynolds number. As the flow moves A to B there is sudden rise and fall of Nu due to proportional pressure variation. As the flow reaches toward B there is a slight increase in Nu but again drop in Nu value is noticed. There is uniform distribution of Nu on face BC. The Nu

value is steeply rise on the face CD in the case of Re =100,000 and 200,000 compare to the other Reynolds number. At every surface of the trapezium the Nu value is increasing with increasing Re.

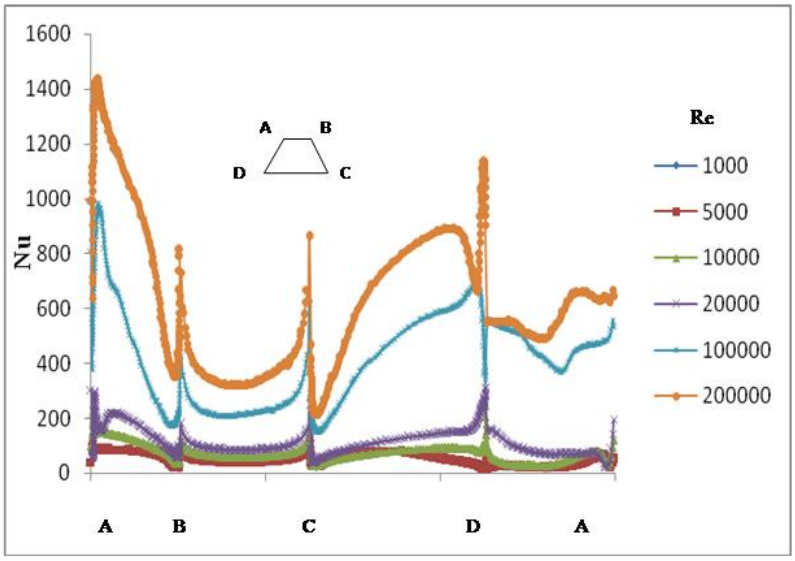


Figure 2. Variation of surface Nusselt number over the symmetrical placed trapezium at different Reynolds number(5% TI)

The figure 3 below shows the variation of Nu along the symmetrically placed trapezoidal surface at fixed Re=200,00 at different TI varying within 5 -40% TI. The graph show steep rise in Re at the vicinity of corner( A,B, C,D).This nature is observed due to increase in pressure of the flow. The surfaces of the bluff body shows much lower values of Nu as the pressure in these regions is considerably low. It is also been observed that Nu value is increase with increase the Re value.

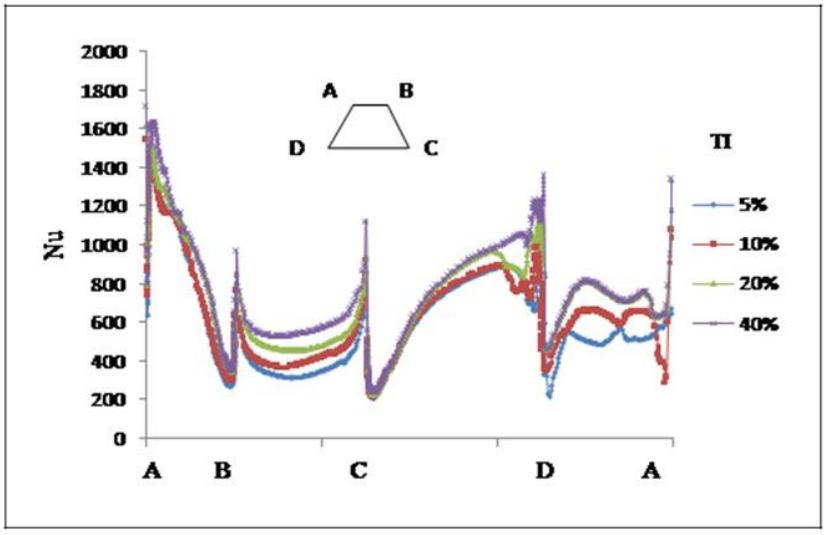


Figure 3. Variation of surface Nusselt number over the symmetrically placed trapezium at different turbulence intensity of fixed Re=200,000

The drag coefficient $C_d$ vs. Re is plot is shown in figure 4 which shows that initially there is strong descent in $C_d$ value upto Re about 1,000. Thereafter there is a gradual increase in drag coefficient while moving up to around Re 8,000 and on further increase in Re value there is also gradual decrease of $C_d$ value. It is also observed that with varying percentage of TI there is appreciable changes in $C_d$ value at all Re as observed.

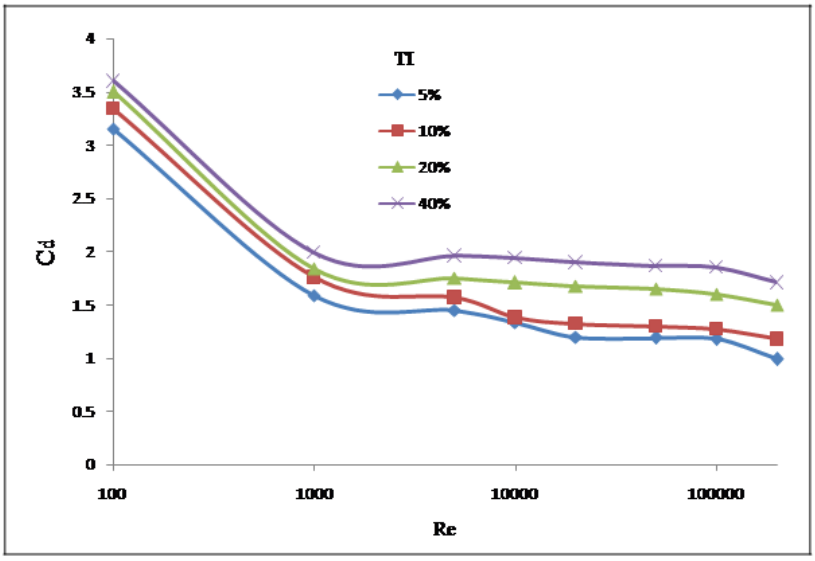


Figure 4. Variation of $C_d$ vs. Re at different TI for symmetrically placed trapezium cylinder

## 4. CONCLUSIONS

Effect of turbulent intensity on transport around the trapezium is described. Overall, the Nu value increases with increase in Re. Drag coefficient is also decrease with increasing the Re value. Drag coefficient is strongly affected by turbulence intensity.

## REFERENCES

[1] R. Kahawita, P. Wang, Numerical simulation of the wake flow behind the trapezoidal bluff bodies, *Computers and fluids*, 31, 99-112, 2002.

[2] A. Venugopal, A. Agrawal, S. V. Prabhu, Span wise correlations in the wake of a circular cylinder and a trapezoid placed inside a circular pipe", *J. of Fluids and Struct*, 54, 536– 547, 2015.

[3] A. Kondjoyan, J.D. Daudin, Effects of free stream turbulence intensity on heat and mass transfers at the surface of a circular cylinder and an elliptical cylinder, axis ratio 4, *Int. J. Heat Mass Transfer*, 10, 1735 1749, 1995

[4] O.M. Chen, T. Utnes, L.E. Holmedel, , D.M.B, Pettersen, Numerical simulation of flow around a smooth circular cylinder at very high Reynolds numbers, marine structures,. 22, 142-153, 2009.

Fifth International Conference on Computational Methods for Thermal Problems
THERMACOMP2018, July 9-11, 2018, Indian Institute of Science, Bangalore, INDIA
*N. Massarotti, P. Nithiarasu, Pradip Dutta and C. Ranganyakalu (Eds.)*

# ASYMPTOTIC APPROACH TO OBTAIN NUSSELT NUMBER CORRELATION FOR LAMINAR MIXED CONVECTION IN A VERTICAL CHANNEL

**Prasheel Nakate, Banjara Kotresha, N Gnanasekaran**
Department of Mechanical Engineering, National Institute of Technology Karnataka, Surathkal, Mangaluru-575025, prasheel.nakate123@gmail.com, bkotresha@gmail.com, gnanasekaran@nitk.edu.in

## ABSTRACT

In this paper, a general methodology is proposed for treating mixed convection problems in a vertical channel by the concept of asymptotic computational fluid dynamics (ACFD). Average Nusselt number is developed based on the limiting solutions of natural and forced convection.These correlations are then blended to find a unified composite correlation that work very well for extreme limits of mixed convection. For the purpose of demonstration, the problem of 2-D laminar, mixed convection in a vertical channel that comprises of a heater sandwiched between two aluminum plates has been used. Numerical simulations are performed with ANSYS-FLUENT to generate the required correlation. The study proposed in this work reveals that with minimum CFD solutions one can obtain a reasonably good composite correlation for the Nusselt number.

**Key Words:** *Vertical channel, ACFD, Blending, Mixed Convection, Asymptotic.*

## 1. INTRODUCTION

Until now, a lots of experimental and numerical investigations have been done to visualize the phenomenon of mixed convection in a channel or parallel plates because of its wide range of applications in various research fields such as Trombe walls, solar chimney, solar energy collectors or cooling of electronic components and many others. A Nusselt number correlation has been proposed by Kamath et al. [1] based on an experimental study for a clear vertical channel. A general approach for treating mixed convection in a lid driven cavity using ACFD has been reported by Balaji et al. [2]. A similar problem involving natural convection in asymmetrically heated vertical channel has been studied numerically as well as experimentally [3-5]. The problem being discussed here is two dimensional and its solutions can be evaluated with reasonable effort, for a range of parameters. Above approach becomes complex if many independent variables are involved. Unlike other approches this technique uses limited full solutions which are blended to obtain correltion. In past, this technique was used many times by Herwig and his co-workers [6-8]. In this case, the asymptotic solutions of limiting cases i.e., pure natural and pure forced convection are found and then systematically blended using the method first proposed by Churchill and Usagi [9] in 1972. In the present study, similar kind of approach is extended to a two dimensional mixed convection in a vertical channel having heater sandwiched between two aluminum plates.

## 2. PHYSICAL AND COMPUTATIONAL DOMAIN

In the present study, a vertical channel in which an aluminium heater plate assembly placed at the centre of the channel is considered for the numerical investigation. A heater is sandwiched between two aluminium plates and the size of the aluminium plates are 250 x 150 x 3 (all in mm). The size of the vertical channel considered for the present study is similar to the experimental setup of Kamath et al. [1] and is shown in Figure 1. From Figure 1 it is clear that the geometry is symmetrical about the Y axis, so a two dimensional computational domain is chosen which consists

of one side aluminium plate, heater, upstream and downstream of the channel as shown in Figure 2. The inlet of the channel is defined with uniform velocity boundary condition, outlet is defined with zero pressure and a uniform heat flux is applied at the heater. The side wall of the channel is assigned with no slip adiabatic condition and symmetrical part of the channel is defined with symmetry condition.

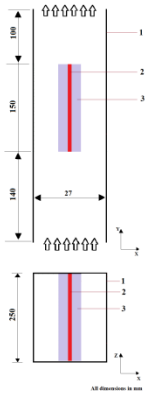

FIGURE 1. Physical domain considered for the present study 1) Wall 2) Heater 3) Aluminium plate.

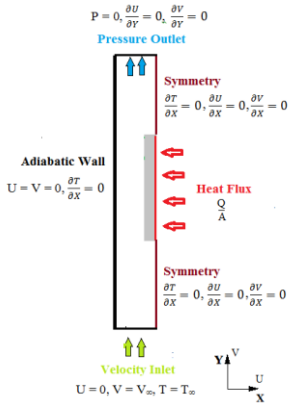


FIGURE 2. Computational domain with boundary conditions.

## 3. RESULTS

The computational domain is simulated by using commercially available ANSYS FLUENT software. The working fluid considered is air with an inlet temperature of 30°C. The velocity of the fluid varies from 0.03 to 1.6 m/s. The plate is heated initially and then transfers heat to the fluid by convection, hence the problem treated here becomes a conjugate heat transfer analysis. The gravity effect within the channel is modelled by using Boussinesq approximation. The governing equations used for solving the vertical channel are similar to pipe flow along with energy equation for solid. A second order upwind scheme are used for continuity, momentum and energy along with SIMPLE scheme for pressure velocity coupling. The convergence criterion for continuity and momentum are set to $10^{-5}$ -$10^{-4}$ and for energy it is $10^{-10}$.

Asymptotic approach is applied to obtain correlation for intermediate values from the solutions of limiting cases. Here, the idea is to correlate mixed convection happening in vertical channel with the results of natural and forced convection. The independent variable chosen for this approach is *Ri*, as its value changes from 0 to ∞, i.e., from pure forced convection limit to pure natural convection limit. For the problem under consideration, *Nu = f (Re or Gr, Pr. Ri)*. The dependency of *Pr* vanishes once the fluid is fixed. For getting solutions for limiting cases, one can define dependence of *Nu* on *Re*, *Gr* & *Ri* as follows,

For natural convection Limit: $Nu_1 = C_1 Gr^m Ri^n$ (1)

For forced convection limit: $Nu_2 = C_2 Re^p Ri^q$ (2)

For natural convection $Nu \sim Gr^{0.25}$ [10] therefore *m* can be taken as 0.25 without much error. The constants $C_1$ & *n* can be evaluated from best fitting curve for corresponding data. For natural limit, the *Nu* values are found for very low velocity by varying the heat flux.

Computed values of constants, $C_1 = 0.54$ & $n=-0.225$, Eqn. (1) becomes,

$$Nu_1 = 0.54\, Gr^{0.25} Ri^{-0.225} \quad (3)$$

Similarly, for Forced convective flows, it is found that $Nu \sim Re^{0.5}$ [10], i.e., $p=0.5$. For forced limit, the *Nu* values are found by varying velocities at the inlet of the channel. From best fitting curve, $C_2=0.56$ and $q=0.078$, So, Eqn. (2) becomes,

$$Nu_2 = 0.56\, Re^{0.5} Ri^{0.078} \tag{4}$$

Eqns. (3) and (4) are the natural and forced convections dominant regimes in the region where the effects of both natural and forced convection are expected to be significant and they have to be blended to obtain a correlation for mixed convection. It has been found that Churchill and Usagi [9] have successfully employed the blending of the limiting solutions for a variety of transfer processes. Therefore, the expression used for interpolation between these limiting cases is as follows,

$$Nu = (Nu_1^{-n} + Nu_2^{-n})^{-1/n} \tag{5}$$

Here, the exponent *n* is computed from the data of mixed convection regime and it varies for different geometries. In Eqn. (5), the right side can be interpreted as $n^{th}$ order sum of the two asymptotic solutions. This type of approach leads to a technique called "blending". It is the way of constructing correlations by using as few solutions as possible. Otherwise, to develop a correlation for mixed convection requires large amount of data from powerful computers or better experimental data. In such conditions, techniques like ACFD can be useful.

We now proceed to blend the solutions by Method given by Churchill and Usagi [9],

$$Nu_1 = 0.54\, Gr^{0.25} Ri^{-0.225} \qquad (Ri \rightarrow \infty) \tag{6}$$

$$Nu_2 = 0.56\, Re^{0.5} Ri^{0.078} \qquad (Ri \rightarrow 0) \tag{7}$$

Substituting these in Eqn. (5) and after rearrangement, we get following form,

$$\frac{0.54\, Gr^{0.25} Ri^{-0.225}}{Nu} = \left(1 + \left(\frac{0.54\, Gr^{0.25} Ri^{-0.225}}{0.56\, Re^{0.5} Ri^{0.078}}\right)^{n}\right)^{\frac{1}{n}} \tag{8}$$

Now the challenge is to evaluate the exponent *n*. It can be calculated from one full solution in mixed convection regime. For simplifying Eqn. (8), making $\left(\frac{0.54\, Gr^{0.25} Ri^{-0.225}}{0.56\, Re^{0.5} Ri^{0.078}}\right)$ term equal to 1 i.e., $0.9643\, Ri^{-0.053} = 1$. *Ri* evaluated from this equation is 0.5036. The condition for *n* is that it should be evaluated at the central value of *Ri*. The above equation is solved for $Re$=1260 and $Gr$=$7.953\times10^5$ such that *Ri* becomes close to 0.5036. The *Nu* at these conditions turns out to be 18.326. Substituting all these values in Eqn. (8).

$$\left[0.54\times (7.953\times10^5)^{0.25}\times (0.5036)^{-0.225}\right]=18.326\times (2)^{1/n} \tag{9}$$

On solving above equation $n$=26.2. Now the composite correlation for Nusselt number becomes,

$$Nu = 0.54\, Gr^{0.25} Ri^{-0.225}(1 + 0.3858\, Ri^{-1.3886})^{-0.0381} \tag{10}$$

It is pertinent to mention here that Eqn. (10) is valid as long as the flow remains laminar. Figure 3 shows the variation of Nusselt number with Richardson number (Eqn. (10)), present simulation results and experimental correlation given by Kamath et al. [1]. Figure 4 shows the parity plot between present simulation results and Eqn. (10), it is clear that the result agrees well within the limit of ±15%.

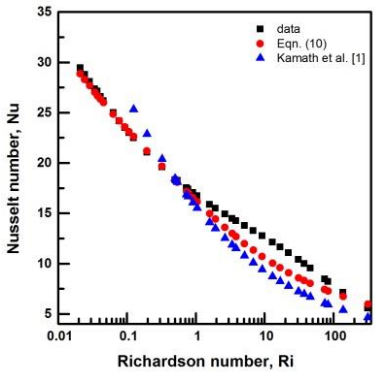


FIGURE 3. Variation of Nusselt number with Richardson number

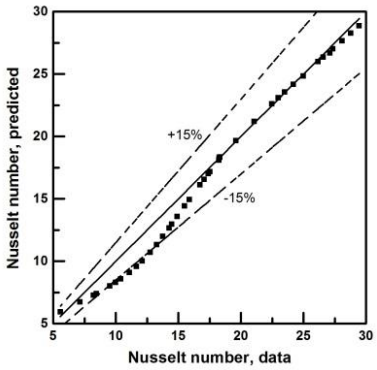


FIGURE 4. Parity plot showing the agreement between simulation data and predicted Nusselt number

## 4. CONCLUSIONS

The results obtained from this approach works well for wide range of Richardson numbers. To identify the dependent and independent parameters, dimensional analysis is necessary before applying ACFD. The main advantage of this technique is that it requires minimum number of full solutions in different regimes. As it is asymptotically correct, results can be accepted within appreciable range of errors. Due to versatile nature of this method, it is applicable for wide class of heat transfer problems.

## REFERENCES

[1] P. M. Kamath, C. Balaji, and S.P. Venkateshan, Experimental investigation of flow assisted mixed convection in high porosity foams in vertical channels, *International Journal of Heat and Mass Transfer* 54, 5231-5241, 2011.

[2] C. Balaji, M. Hölling, and H. Herwig, A general methodology for treating mixed convection problems using asymptotic computational fluid dynamics (ACFD), *International Communications in Heat and Mass Transfer* 34, 682–691, 2007.

[3] D. Ospir, C. Popa, C. Chereches, G. Polidori, and S. Fohanno, Flow visualization of natural convection in a vertical channel with asymmetric heating, *International Communications in Heat and Mass Transfer* 39, 486–493, 2012.

[4] Wu-Shung Fu, Wei-Siang Chao, Tzu-En Penga, and Chung-Gang Li, Flow downward penetration of vertical parallel plates natural convection with an asymmetrically heated wall, *International Communications in Heat and Mass Transfer* 74, 55–62, 2016.

[5] G. Desrayaud, E. Chénier, A. Joulinb, A. Bastide, B. Brangeon, J.P. Caltagironed, Y. Cherif, R. Eymard, C. Garnier, S. Giroux-Julien, Y. Harnanei, P. Joubert, N. Laaroussi, S. Lassue, P. Le Quéré, R. Li, D. Saury, A. Sergent, S. Xin, and A. Zoubir, Benchmark solutions for natural convection flows in vertical channels submitted to different open boundary conditions, *International Journal of Thermal Sciences* 72, 18-33, 2013.

[6] C.Balaji, and H. Herwig, The use of ACFD in problems involving Surface Radiation & Free Convection, *Int. Comm. Heat Mass Transfer*, Vol 30, No. 2, pp. 251-259, 2003.

[7] H. Herwig, Laminar boundary layers/asymptotic and scaling considerations, in: A. Kluwick (Ed.), Advances in Boundary Layer Theory, *Springer-Verlag, Heidelberg*, pp. 9–48, 1998.

[8] M. Hölling, and H. Herwig, Asymptotic analysis of the near wall region of turbulent natural convection flows, *Journal of Fluid Mechanics.* 541,383–397, 2005.

[9] S.W. Churchill, R. Usagi, A general expression for the correlation of rates of transfer and other phenomena, *AIChE J,* Vol 18, No. 6, 1121–1128, 1972.

[10] A. Bejan, *Heat Transfer*, John Wiley, New York, 1993.

Fifth International Conference on Computational Methods for Thermal Problems
THERMACOMP2018, July 9-11, 2018, Indian Institute of Science, Bangalore, INDIA
*N. Massarotti, P. Nithiarasu, Pradip Dutta and C. Ranganyakalu (Eds.)*

`

# EXPERIMENTAL AND NUMERICAL INVESTIGATION ON CONJUGATE EFFECTS IN DEEP PARALLEL MICROCHANNEL USING $TiO_2$ NANOFLUID FOR ELECTRONIC COOLING

**G.Narendran[1], N.Gnanasekaran[1], D.ArumugaPerumal[1,*]**
[1]Department of Mechanical Engineering, National Institute of Technology Karnataka, Surathkal, Mangalore - 575025, ***Email:*** **Perumal.iit@gmail.com,*

## ABSTRACT

The present study reports the numerical investigation of laminar forced convection based on $TiO_2$ nanofluid in a rectangular copper microchannel surrounded by Aluminium block to examine the cooling effects for increased flow rates and particle concentration. The analysis involves the use of pure fluid and $TiO_2$ nanofluid with the volume fractions of 0.01, 0.15, 0.20 and 0.25% for different flow rates. The study also examines the influence of conjugate heat transfer behavior of the microchannel using commercially available software FLUENT-15.

**Key Words:** *Conjugate heat transfer, Microchannel, Nanofluids, Forced convection.*

## 1. INTRODUCTION

The rapid advances in the field of compact electronic devices significantly altered the magnitude of operating components and also enhanced its efficiency to new level. But their processes and complexity constantly grows with increased power density; as a result heat dissipation has risen tremendously [1,2]. It is necessary to improve the effectiveness and reliability of the components by suitable selection of cooling methods to enhance the convective heat transfer in micro devices. Among the several proposed cooling solutions the most suitable for the application of high flux density is the microchannel based heat transfer. The cooling potential of Microchannel Heat Sink (MHS) in micro devices is overwhelming in the field of electronic packaging due to its high surface area to volume ratio to deliver better heat transfer solutions under higher fluxes [3]. Zang et al. [4] performed experimental study on multi layered flow passages which includes parallel, spiral and serpentine microchannels for electronic packaging. It is found that the parallel microchannel has highest mass flow rate with high heat transfer than other configurations. The influence of channel height on heat transfer and pressure drop was experimentally investigated by Manay and Sahin [5] using $TiO_2$ dispersed nanofluid. The results proved that the increase in channel height increases the pressure drop and friction factor by 18 % for the volume fraction increment of 0.25 % to 2 %.

Based on the literature, the present paper focuses heat transfer in microchannel using $TiO_2$ nanofluids for various flow rates and nanoparticle concentration. The study is carried out for flow rate in the range of 210 ml/min to 410 ml/min for increased volume fractions.

## 2. EXPERIMENTAL DESCRIPTION

The experimental set up consists of a copper rectangular microchannel surrounded with Aluminium block shown in Figure 1(a). The channel inlet is connected to the peristaltic pump to provide pulsating flow to the microchannels and the outlet is connected to the secondary heat exchanger. Thermocouples were placed in the copper channel and Aluminium block to record the temperature along the flow direction. The central part of the copper channel where 9mm diameter cartridge heater is fitted along the length of the channel for a depth of 30mm. The entire top portion of the

block is covered with Acrylic glass to avoid leakage of fluids and to visualize the fluid flow in the microchannel.

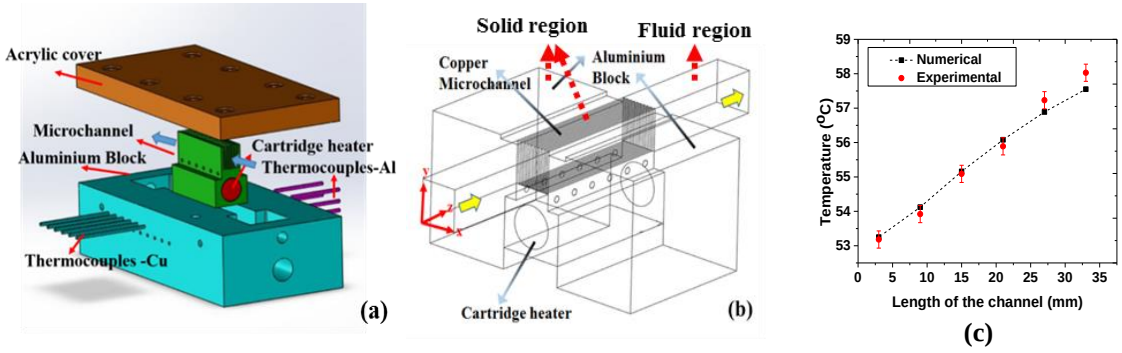


FIGURE 1. Schematic representation. (a) Exploded view of experimental components, (b) Computational domain and (c) Validation plot.

## 3. NUMERICAL METHODOLOGY

A laminar forced convection in a rectangular microchannel is considered for the present study by using commercial CFD software FLUENT-15. The schematic diagram of the computational model and its validation with experimental results is shown in Figure 1(b) and Figure 1(c). The computational model comprises two domains namely fluid and solid which corresponds to indicated fluid region and copper channel accompanied with Aluminium block. The microchannel is modeled with high thermal conductivity material copper and the flow inside the channel is assumed to three-dimensional(3-D). This model involves conjugate heat transfer simultaneously thus momentum and energy equations are solved parallel under transient condition and its governing equations are presented below.

$$\nabla . u = 0$$

$$\rho\left(\frac{\partial u}{\partial t} + u.\nabla u\right) = -\nabla p + \nabla.\left[\mu\left(\nabla u + (\nabla u)^T\right)\right]$$

$$\nabla.(\rho u h) = \nabla.(k\nabla T) + \phi; \left[\phi = \tau_{ij}\frac{\partial u_i}{\partial x_j}\right]$$

The fluid is considered as single phase, incompressible laminar without viscous dissipation of energy. Laminar fully developed flow and uniform zero pressure is assumed at the outlet. All the walls satisfy the slip condition and further details of boundary conditions are presented in Figure 2.

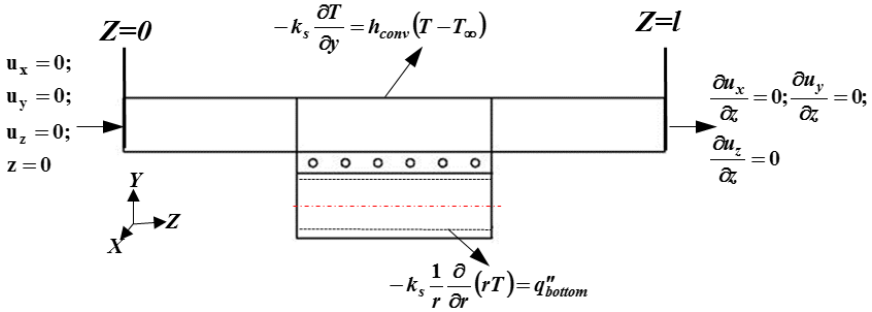


FIGURE 2. Boundary conditions

Based on the assumption there exists natural convection between top surface and the ambient. Adiabatic boundary condition is provided for the sides of the channels. Assuming the homogeneity of the cooling fluid it considered that the nanoparticle is in thermal equilibrium with the base fluid.

## 4. RESULTS

To visualize the temperature correspondence throughout the computational domain with 0.001 step time and results were presented from transient condition as follows. Figure 3 depicts the fluid temperature for two different *$TiO_2$* volume fractions at various locations for the flow rate of 210 ml/min. Temperature for $TiO_2$ 0.10% volume fraction is shown in Figure 3 (a). It has the Average outlet temperature is 39ºC. Additionally we can observe a gradual increase in fluid temperature along the length of the microchannel. Figure 3(b) demonstrates increased fluid temperature with the use of $TiO_2$ 0.25% volume fraction with 4ºC higher than of $TiO_2$- 0.10% which is purely attributed to the increased thermal conductivity of nanofluid.

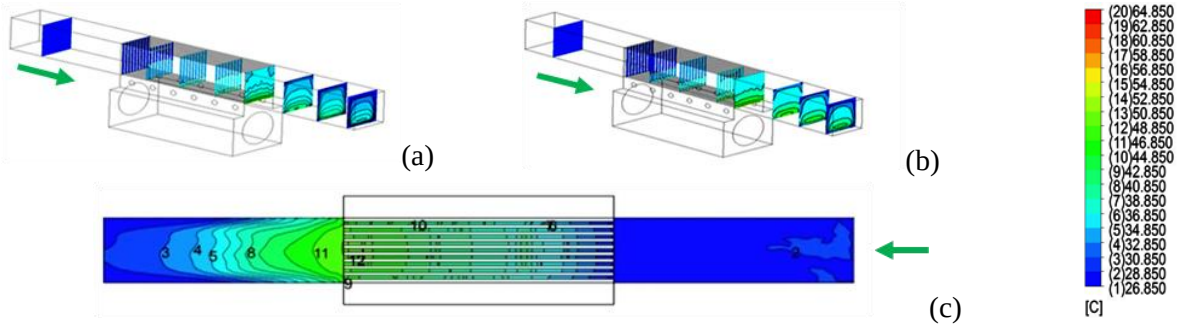


FIGURE 3. Temperature contours along the flow.(a) $TiO_2$- 0.1%, (b)$TiO_2$- 0.25% and (c) Fluid temperature distribution in the channels.

The entire temperature distribution of the fluid region is shown in Figure 3(c). It is seen that the fluid temperature in the channels increases away from the centerline channels and maximum temperature of 44ºC was seen for the last channel. The reason behind is due the increased velocity in the centerline channels and comparatively low velocity at corner channels. Figure 4 presents the summary of the temperatures at different locations for simulated parameters which includes interface temperature, microchannel tip temperature and inlet and outlet temperature of the centerline microchannels. In all these cases temperature varies from 39º C to 46º C which is shown in Figure 5(a).

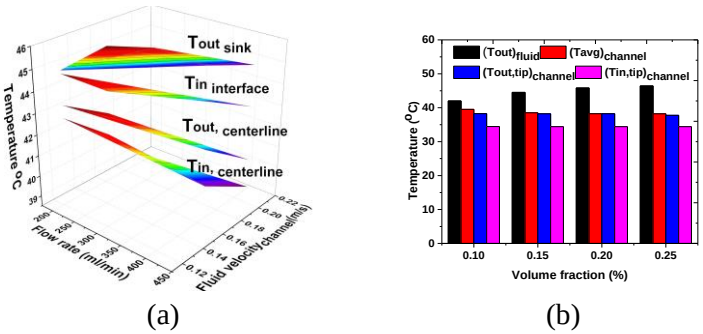


(a) (b)

FIGURE 4. Temperature Distribution in channel. (a) Flow rate and (b)Volume fraction

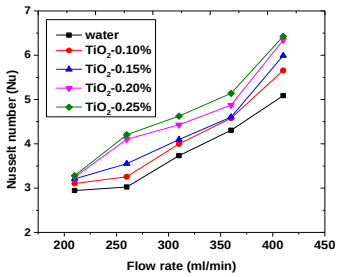


FIGURE 5. Nusselt number variation for increase in flow rate

It is found that more or less similar temperature range of 44ºC is maintained in interface for increased flow rate of 210 to 410 ml/min. the resultant fluid distribution has developed a maximum magnitude of 0.22 m/s in center line channels. However the channel average temperature remain

40ºC for all the increased ratios of particle concentration shown in Figure 5(b). In contrast the outlet fluid temperature increased by 9% for a lower flow rate of 210 ml/min. Figure 5 shows the Nusselt number variation as the function of increased flow rate. The maximum Nusselt number was obtained for 0.25% of $TiO_2$with an increment of 36% more than pure fluid which is 10.76% higher than 0.1% $TiO_2$. This enhancement is due to increased thermal conductivity combinedwith increased flow rates of the working fluids.

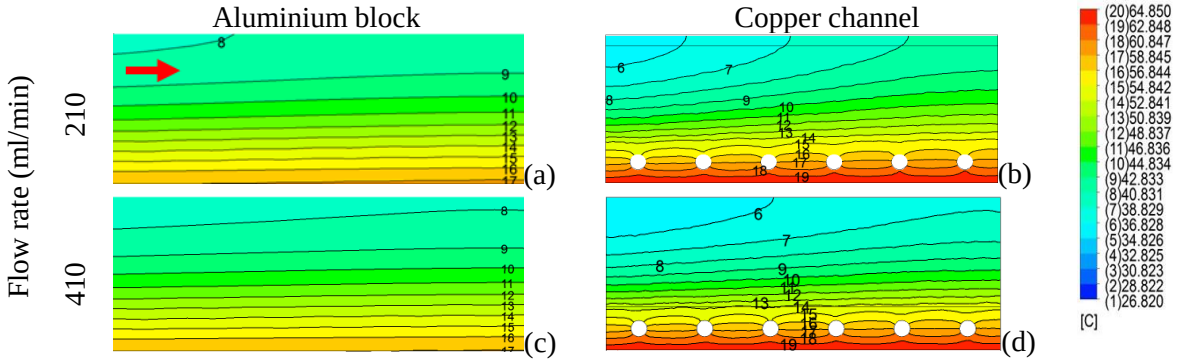


FIGURE 6.Temperature contour for 0.25%- $TiO_2$. (a,c) Near interface, (b,d) Centerline channels.

Since the microchannel is surrounded with high thermal conductive material a partial cooling effect is witnessed near the interface region of the microchannel. To understand the further penetration near interface region (i.e. 2mm away from copper and Aluminium interface, located in aluminum solid) flow rates werevaried which is shown in Figure 6 (a, c). The impact of the cooling increases along the height of the channel and the effect near the channel bed left unaltered for both the flow rates. Figure 6 (b,d) presents the reduced centerline channel temperature with maximum drop of 36ºC for the flow rate of 410 ml/min.

## 5. CONCLUSIONS

In this paper a 3-D numerical simulation on laminar forced convection in microchannels that comprises of conjugate heat transfer analysis using $TiO_2$ nanofluid has been presented. Several investigations have been conducted by varying the particle concentrations and increased flow rates. In particular the effect of heat transfer near the interface region using working fluids with increased concentration found superiour for flow rate of 210 ml/min and increased the cooling rate by 9% but for higher flow rate of 410 ml/min temperture increased by 2ºC to 3ºC near the interface region.

## ACKNOWLEDGEMENTS

Authors acknowledges the SERB - ECRA, Goverment of india for its financial support through SERB/ECR/2017/000387 fund.

## REFERENCES

[1] M. Gad-ed-Hak, The fluid mechanics of microdevices- The freeman scholar lecture, *Journal of fluid engineering*, 121, 5-33,1999.

[2] H. A. Mohammeda, G. Bhaskarana, N. H. Shuaiba, R. Saidur, Heat transfer and fluid flow characteristics in microchannels heat exchanger using nanofluids, A review, *Renewable and Sustainable energy reviews*, 15, 1502-1512, 2011.

[3] D. B. Tuckerman, R. F. Pease, High-Performance heat sinking for VLSI, *IEEE Electronic Devices letters*, 5, 126-129, 1981.

[4] L. Y. Zhang, Y. F. Zhang, J. Q. Chen, S. L. Bai, Fluid flow and heat transfer characteristics of liquid cooling microchannels in LTCC multilayered packaging substrate. *International Journal of Heat and Mass Transfer*, 84, 339-345, 2015.

[5] E. Manay, B. Sahin, The effect of microchannel height on performance of the nanofluids, International Journal of Heat and Mass Transfer, 95, 307-320, 2016.

Fifth International Conference on Computational Methods for Thermal Problems
THERMACOMP2018, July 9-11, 2018, Indian Institute of Science, Bangalore, INDIA
*N. Massarotti, P. Nithiarasu, Pradip Dutta and C. Ranganyakalu (Eds.)*

# Numerical Analysis of Flow over an Airfoil at Low Reynolds number using $\Upsilon$-$Re_\theta$ model

**Neeraj Verma**
Research Scholar, M.E.D-S.V.N.I.T-Surat, turbo.neeraj@gmail.com

**Dr. Beena D. Baloni**
Asst. Prof., M.E.D-S.V.N.I.T-Surat, pbr@med.svnit.ac.in

## ABSTRACT

A precise numerical simulation of low Reynolds number flow over an airfoil requires proper modeling and interpretation of transition physics. In the present study, a computational effort has been made, using commercial available CFD code ANSYS Fluent, towards understanding the flow behavior about an airfoil at low Reynolds number, using menter's $\Upsilon$-$Re_\theta$ model. The present work is a part of ongoing research on the flow over thick airfoil, generally used as base airfoil for small HAWT blade. An experimental analysis of the thick airfoil has to be carried out in a subsonic wind tunnel at a wind speed of 10m/s, 15m/s, 20m/s and 25m/s with a corresponding chord Reynolds number of 61324, 91986, 122648 and 153310. Therefore, prior to experiment, a numerical simulation is carried out over the given range of Reynolds number. The simulation result shows that as the angle of attack is increased, regardless of Re, the point of separation advances towards the leading edge. However at any given angle of attack, the flow separation delays with increase in Reynolds number. The simulation results also predicts the formation of separation bubble at all given Reynolds number range however, with increase in angle of attack, the separation bubble was found to contract in size.

**Key Words:** *Airfoil, laminar separation bubble, transition model (menter's $\Upsilon$-$Re_\theta$)*

## 1. INTRODUCTION

Small wind turbines are defined as the system with rotor swept area not more than 200 $m^2$ or an equivalent power of about 50kW[1]. Such type of the systems are essentially installed where the power requirement is utmost but wind resource is not necessarily available [2,3]. Small blade size and the low wind speed working condition cause the blade to operate at low Reynolds number from hub to tip[2]. Typical airfoils which were designed for high Reynolds number such as NACA airfoil series are reported to underperform under low Reynolds number conditions and hence degrade the performance of small wind turbine[4]. Hence it is crucial to use low Reynolds number airfoil for its application in small wind turbine. While developing small wind turbine, the initially aerodynamic performance of the airfoil models are experimentally investigated.

Wind tunnel measurements, at low Reynolds number, are reported to be challenging due to requirement of higher level of accuracy in equipments for correct modelling of the flow around the airfoils[5]. So in the present Paper, Prior to experimental analysis, numerical analysis, of one of the airfoil of small wind turbine blade at root section, is carried out. The airfoil intended for this purpose is a scale down model of a prototype. The prototype experiences relatively higher Reynolds number than presented above, but due to the limitation of wind tunnel maximum speed and model

blockage inside the test section, the analysis is limited to earlier mentioned Reynolds number. However, later the performance characteristics of the airfoil model will be extrapolated to higher Reynolds number. The airfoil at the root section of wind turbine blade are generally thick airfoils and are often subjected to low Reynolds numbers flow. For precise computational study of low Reynolds number flow over an airfoil requires proper modelling and interpretation of the transition physics. For that purpose, menter's $\Upsilon$-$Re_\theta$ transition model, is used to get a better understanding of the flow behaviour about such an airfoil.

## 2. NUMERICAL ANALAYSIS

Numerical simulation is carried out over a range of Reynolds number i.e, 61324, 91986, 122648 and 153310, covering a range of angle of attack from 0 degree to 20 degree. The mesh density is kept progressively coarser in the domain area were the flow gradient approaches zero. For precise simulation of the boundary layer flows, Y+, a non dimensional distance from the wall to the first node of the mesh was satisfied with the value of Y+<1.

To ensure the computed aerodynamics results independent of the grid size, a grid independency test is carried out. The FIGURE 1 and FIGURE 2 shows the computed aerodynamics coefficients (coefficient of lift and drag ) variation with total number of elements in the domain. A refined grid, with 33520 elements was adopted for numerical computation.

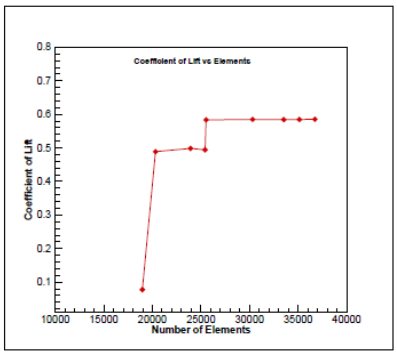


FIGURE 1. Coefficient of lift vs Number of elements

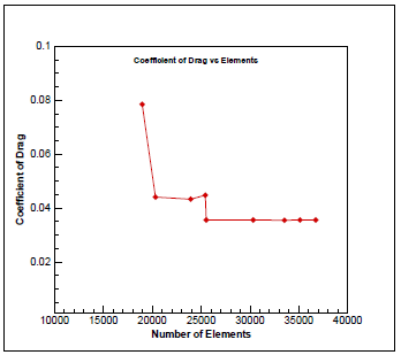


FIGURE 2. Coefficient of drag vs Number of elements

The boundary condition for inlet was taken as velocity inlet, the outlet condition was defined as pressure outlet and airfoil was set as wall type boundary condition. The turbulence intensity and length scale, at the inlet and outlet of the domain was set as 0.2% and 2m respectively. The solver was set for steady state. To solve the coupled problem between pressure momentum equations and velocity components, (SIMPLE) algorithm was employed and second order upwind spatial discretization was set in calculation. In order to maintain the accuracy the convergence criterion is set at $1 \times 10^{-5}$. The present work involves a $\Upsilon$-$Re_\theta$ transition model which incorporates the turbulence in the flow. It is a four equation turbulence model. This model is reported to have distinct advantage of associating transition modelling with experimental data[6].

## 3. RESULTS

The flow behaviour over the surface of the airfoil as acquired from ANSYS FLUENT is carefully examined and certain conclusions were drawn. The variation of the $C_l$ and $C_d$ with angle of attack

and at different Reynolds number (Re) is shown in the FIGURE 3. It was observed that coefficient of lift increases with increase in the angle of attack. Also as the Reynolds number is increased, coefficient of lift at any given angle of attack increases. At 20 degree angle of attack, coefficient of lift achieve its maximum value at the given range of angle of attack. Also $C_l$ does not vary remarkably (0.746 -0.749) at its peak value with change in Reynolds number.

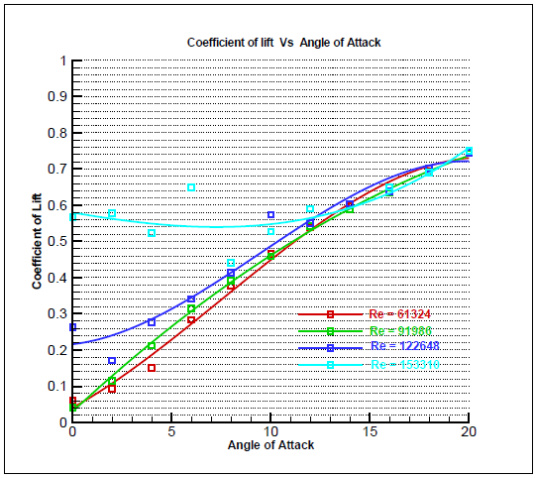


FIGURE 3. Coefficient of lift vs angle of attack

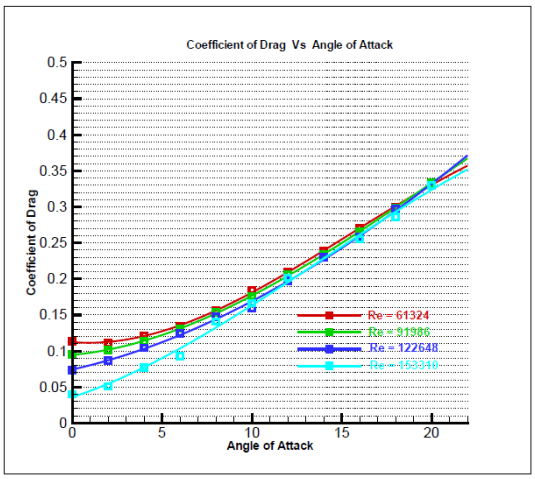


FIGURE 4. Coefficient of drag vs angle of attack

From the FIGURE 4, it can be seen that, coefficient of drag increases with increase in the angle of attack, however as the Reynolds number is increased, at a given angle of attack, the coefficient of drag decreases.

At low Reynolds number flow over an airfoil, the resistance to separation of the boundary layer is very poor, due to dominant adverse pressure gradient. As flow separates from the point of minimum pressure, due to the increase in adverse pressure at the leading edge, separation takes place. The separated flow is highly unstable, resulting in transition immediately downstream, causing the flow to become turbulent. Thereby turbulent shear stresses energies the flow to counteract the increased adverse pressure, helping the flow to reattach. Thus a zone between the separation and reattachment is formed known as Separation Bubble.

The FIGURE 5 shows the velocity vector at the bottom surface of the airfoil at a Re = 61324 and 4 degree angle of attack. The region highlighted shows the presence of a Separation Bubble.

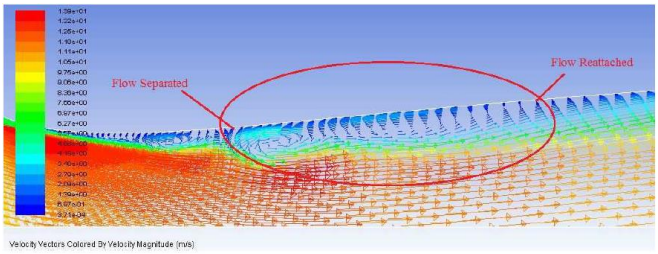


FIGURE 5. Presence of Separation Bubble

On observing the velocity vector of the flow at different angle of attack and different Reynolds number, following observations were made;

1. At Re=61324 and 0 degree angle of attack, there occurs a bubble formation extending between 30% to 40% of the chord length followed by flow separation at approximately 45% of the chord length, which reattaches at 90% of the chord length, on the top surface of the airfoil. But at higher Reynolds number (Re = 91986, 122648 and 153310) the flow remain separated. However as the angle of attack is increased, regardless of the Reynolds number, flow separation advances from approximately 30% to 15% of the chord length towards the leading edge.

2. At 0 degree angle of attack, with increasing Reynolds number, the flow separation delays from 30% to 40% of the chord length.

3. At 0 degree angle of attack, at the bottom surface of the airfoil for all Reynolds number range ( Re = 61324, 91986, 122648 and 153310), bubble formation takes place, extending from 8% to 30% of the chord length. As the angle of attack is increased the size of the bubble reduces and after 6 degree angle of attack no bubbles are noticed. Also with increase in the Reynolds number and at a given angle of attack, the bubble does not remarkably shift towards the leading edge but it reduces in size gradually.

4. There occurs no flow separation at the bottom surface of the airfoil at all Reynolds number range ( Re = 61324, 91986, 122648 and 153310) beyond 4 degree angle of attack. Bubbles formed at the bottom surface of the airfoil retains upto 6 degree angle of attack at lower Reynolds number (Re = 61324). However as the Reynolds number is increased bubble retains only upto 4 degree angle of attack.

## 4. CONCLUSIONS

This paper presents a computational effort towards understanding the flow behaviour about the airfoil at low Reynolds number for its application in small HAWT, using the menter's $\Upsilon$-$Re_\theta$ model. The flow around the airfoil experiences a separation bubble near the leading edge. The airfoil was found to be performing optimal at high Reynolds number and at low angle of attack. Thus, numerical simulation of base airfoil gives preliminary idea about the flow separation regions at airfoil surface.

## REFERENCES

[1] International standard IEC 61400-2.:Small wind Turbines,3rd edn (2013)

[2] Clausen,P.D.,Wood, D.H.:Research and Development Issues for Small Wind Turbines.Renew.Energy 16,922-927(1999)

[3] Wood,D.:Small Wind Turbines, Analysis, Design and Application.Green Energy and Technology .Springer,New Tork (2011)

[4] Shah,H.,Bhattarai,N.,Lim,C.M.,Mathew,S.:Low Reynolds number Airfoil for Small Horizontal Axis Wind Turbine blades. In:Sustainable future energy 2012 and 10th SEE forum Brunei Darussalam (2012)

[5] Genç,M.S.:Low Reynolds number Aerodynamic and Transition. InTechopen (2012).doi:10.5772/2398

[6] Menter,P.R.,Langtry.,Voker,S.:Transition modelling for general purpose CFD codes.Flow Turbul. Combust.77,277-303(2006). doi:10.1007/s10494-006-9047-1

Fifth International Conference on Computational Methods for Thermal Problems
THERMACOMP2018, July 9-11, 2018, Indian Institute of Science, Bangalore, INDIA
*N. Massarotti, P. Nithiarasu, Pradip Dutta and C. Ranganyakalu (Eds.)*

# LEVEL SET METHOD BASED STUDY ON SOLIDIFICATION DURING CASTING: EFFECT OF ADVECTION AND FILLING PROCESS

**Nihar Thakkar, Atul Sharma**
Indian Institute of Technology-Bombay, Mumbai, Maharashtra - 400076, India
15mmet26@nirmauni.ac.in, atulsharma@iitb.ac.in

**Absar Lakdawala**
Institute of Technology – Nirma University, Ahmedabad, Gujarat - 382481, India
absar.lakdawala@nirmauni.ac.in

## ABSTRACT

Present work is on numerical investigation of solidification of pure metal during casting process in a two dimensional rectangular cavity. In the present study, Dual Grid **L**evel **S**et **M**ethod (LSM) is used to capture the interface dynamics during solidification process. Finite volume based staggered grid approach is used. The evolution of the interface depends upon the method adopted to model the solidification process viz. pure diffusion, diffusion with advection, and considering residual flow due to filling prior to solidification. The three different computational model based results are compared for interface shape and isotherm patterns.

**Key Words:** *Solidification, Interface Dynamics, Natural Convection, Level Set Method.*

## 1. INTRODUCTION

The foremost aim of any casting process, is to prevent the formation of shrinkage porosity, or cavities within the cast product. The location of such defects solely depends upon the manner in which solidification is modelled. It becomes essential to have a computer simulation predicting the formation of such defects before conducting actual casting process. Various researchers model the filling and solidification process differently. For modelling the solidification problem, pure diffusion is considered as the dominant phenomena while advection is neglected by different researchers (Sutaria et al. 2012). Many of the researcher model the same considering both advection and diffusion phenomena (Im et al. 2001), (Parkitny and Sowa 2001), (Zhou et al. 2016), (Li et al. 2011). Morever, it has been evident from literature that the residual flow arising within the mould cavity at the end of filling process has a greater impact over the evolution of solidification front (Pathak et al. 2009). The location of the defects are greatly affected by filling behaviour and hence it cannot be neglected.

In the present study, unidirectional solidification solidification problem is investigated in a rectangular cavity under three conditions. In first case, the cavity is assumed to be filled with molten metal and the solidification is modelled considering only diffusion equation. The interfacial velocity is calculated using Stefan's condition applied at the interface. In the second case, advection phenomenon is also considered and the momentum equation (Navier Stokes) is solved with Boussinesq approximation as the source term to account for natural convection. In the third case, the residual flow arising at the end of filling process is taken as the initial condition to simulate the solidification process. In the third case, an attempt has been made to capture the interface dynamics that is affected by coupled residual-flow and buoyancy induced flow.

## 2. MAIN BODY

In the present study, dual grid level set method (Gada and Sharma 2009) is used and its representation is shown in Figure 1(a) and Figure 2. The physical problem considered is a pure

metal solidification problem within a rectangular cavity. The computational setup shown in Figure 1(b) is same as reported by Pathak et al. (2009). In order to have the interface evolution, level set advection equation is solved with phase change velocity as the driver, which is evaluated by applying the Stefan's condition at the interface.

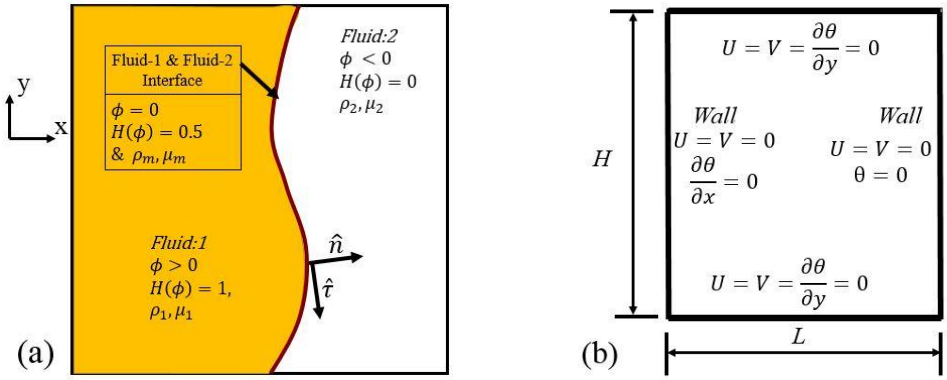


FIGURE 1. (a) Level set function for individual phase as well as solid-liquid interface (zero level set) for the solidification process. (b) Computational domain for solidification problem.

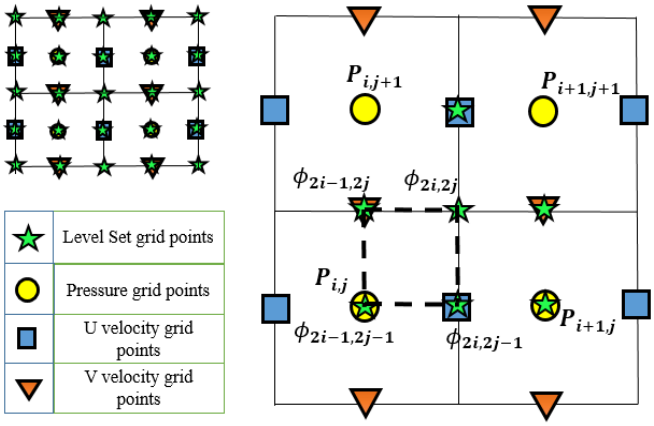


FIGURE 2. Staggered grid arrangement for flow variables with level set points defined for dual resolution.

## 3. RESULTS

Figure 3 (a1)-(a3) shows the evolution of the solidification front for the first case considering pure diffusion phenomena - 2D heat conduction equation is solved with Stefan's condition applied at the interface. The solidification front remains perfectly planar and advects with no further change in its shape. However, considering advection along with diffusion (convection), Figure 3 (b1)-(b3) shows that the interface no longer remains planar. In this case, the thermal convection results in movement of the hotter liquid to the top while the liquid metal adjacent to the interface is relatively cold and tries to settle downwards – resulting in clockwise motion of the liquid metal as seen in the figure. The clockwise convective flow of liquid metal favours the interface advection at the bottom, as the flow is along the direction of the interface advection; vice-versa at the top, resulting in a resistance for the interface advection. In the third case, considering residual flow along with the convection, Figure 3 (c1)-(c3) shows variation in the instantaneous interface as compared to the above two cases. This indicates that the residual flow tends to affect the interface advection during solidification.

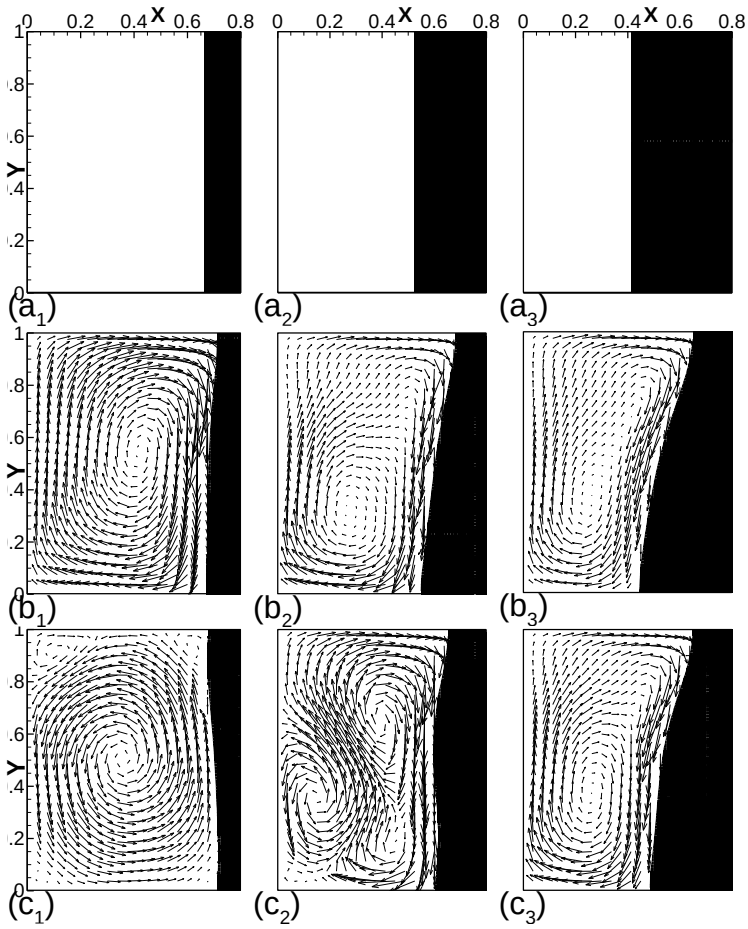


FIGURE 3. Temporal evolution of velocity vectors and interface from three computational models: (a) Stefan flow with conduction, and (b,c) two-phase flow with convection heat transfer. Initially, fluid is considered as stationary in (a,b) and corresponds to the flow field at the end of filling in (c).

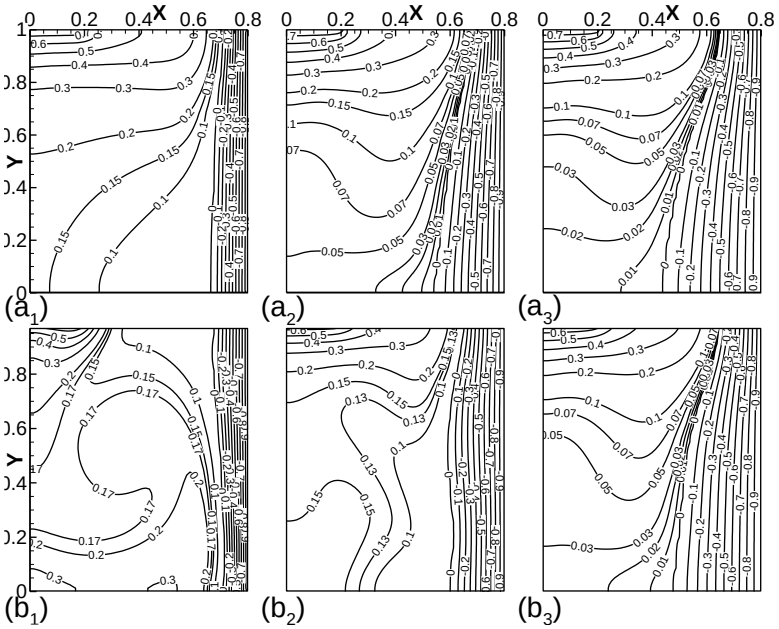


FIGURE 4. Temporal evolution of isotherms: (a1) to (a3) for two-phase flow with convection heat transfer, (b1) to (b3) for coupled filling and thermal convection.

It is interesting to note a change in the direction of flow from counter-clockwise in Figure 3(c1) to clockwise in Figure 3(c3) with the domination of buoyancy induced convective flow as compared to the residual flow obtained after filling; the transition can be seen in Figure 3(c2). The counter-clockwise movement in the residual flow is due to the in-gate position at the lower most left wall of the cavity. At the initial stage of solidification, the strength of the residual flow is higher and dominates the thermally driven flow as a result of which the interface advection is quiet slower. The residual flow opposes the thermally driven flow. However, at the later stages of the solidification, the thermally driven flow becomes dominant and a transition takes place from counter-clockwise residual flow to a thermally driven clockwise flow. The residual flow either favours the solidification phenomena or delays the same. Figure 4 (a1) to (a3) shows the isotherms for diffusion with advection case while (b1) to (b3) shows the isotherms for coupled filling and thermal convection case. The temperature gradient in later case is found to be less in the initial stages of solidification as compared the diffusion and advection case. The effect of residual flow can be visualized through the temperature distribution obtained in the initial stages of solidification.

## 4. CONCLUSION

In the present study, unidirectional solidification problem in a rectangular cavity for a pure metal is simulated. Three different cases namely pure diffusion, diffusion with advection and coupled filling and advection are considered. The effect of residual flow arising due to the filling behaviour within the mould cavity on the front evolution is studied. There is a significant change in shape of the isotherms by considering advection compared to pure diffusion case. Moreover, when the effect of residual flow is considered, the isotherms further change their shape and it becomes difficult to predict the nature of isotherms, their shape, and pattern. The filling effects cannot be neglected completely while modelling the solidification as it ultimately helps in predicting the shrinkage cavities, porosities, and hotspots.

## REFERENCES

[1] Mayur Sutaria, Vinesh H. Gada, Atul Sharma and B. Ravi, Computation of feed-paths for casting solidification using Level Set method, *Journal of Materials Processing Technology* 212, 1236-49, 2012.

[2] Ik-Tae Im, Woo-Seung Kim, Kwan-Soo Lee, A unified analysis of filling and solidification in casting with natural convection, *International Journal of Heat and Mass Transfer* 44, 1507-1515, 2001.

[3] Ryszard Parkitny and Leszek Sowa, Numerical simulation of solidification of a casting taking into account fluid flow and heat transfer phenomena. The axi-symmetrical problem, *Journal of Theoretical and Applied Mechanics* 4, 39, 2001.

[4] Jianxin Zhou, Min Wang, Yajun Yin, Xu Shen Xiang Chen, Wen Li and Dongqiao Zhang, Feed paths and Hot spots computation based on a time gradient me1thod in casting, *International Journal of Advanced Manufacturing and Technology*, 2016.

[5] Chin-Yuan Li, Suresh V. Garimella and James E. Simpson, Fixed-grid front-tracking algorithm for solidification problems, part 2: directional solidification with melt convection, *Numerical Heat Transfer, Part B: Fundamentals* 43:2,143-166, 2011.

[6] Nitin Pathak, Arvind Kumar, Anil Yadav and Pradip Dutta, Effects of mould filling on evolution of the solid-liquid interface during solidification. *Applied Thermal Engineering,* 29, 3669-3678, 2009.'

[7] Vinesh H. Gada and Atul Sharma, On a Novel Dual-Grid Level-Set Method for Two-Phase Flow Simulation, *Numerical Heat Transfer-B,* 59, 26–57, 2011.

# Investigation of All-Speed SLAU Scheme in Incompressible Limit

**Nikhil Kalkote**
PhD Student

**Aswani Assam**
PhD Student

**Nived M R**
Master Student

**Vinayak Eswaran**
Professor

Department of Mechanical and Aerospace Engineering,
Indian Institute of Technology Hyderabad, India.

## ABSTRACT

The density-based algorithms are generally used to solve high speed flows; acuuracy of these methods degrades in low-speed limit i.e. in incompressible limit due to large value of the condition number. Popular method to fix this issue is use of the preconditioning methods. Preconditioning not only maintains the accuracy in low Mach limit but also helps in accelerating the convergence by altering the characteristic speeds, which results in destructions of the time accuracy. Whereas new parameter free scheme has been suggested by Shima which solves the problem without destroying the time-accuracy. In this paper we investigate the SLAU scheme of of Shima in incompressible limit for practical applications such as aerofoils at angle of attack using our in-house developed 3-D unstructured hybrid code.

**Key Words** : *SLAU, Natural Convection, All-Speed, Unstructured Grid.*

## INTRODUCTION

Many engineering flows are characterized by low speed, so the natural choice for a solution methodology is to use pressure-based algorithms [1]. These methods not only have favorable mathematical properties but also good convergence characteristics. However, pressure-based algorithms work best for constant density, when density change is involved as in natural convection and combustion, a change in algorithms are needed. A general method dealing with such flow would be to solve for density by using a density-based method. Such methods are commonly used for high-speed (high Mach number) computations. However at low speed (low Mach number) the flow equation become stiff [2, 3, 4, 5] and schemes based on high-speed theory do not work well. A solution to this problem has been established [2, 3, 6, 5] for ideal gases and for liquids and uses preconditioning of the time-derivative to overcome the stiffness problem. This method, while directly applicable for steady-state problems, nevertheless is quite cumbersome to use, involving dual-time-stepping, for unsteady flows. An alternative is the use of the convection scheme SLAU [7, 8, 9], a well-known stable method that is time-accurate and avoids the dual-time-stepping [10] for unsteady solution. This paper discusses the implementation of the SLAU scheme on unstructured grids and then explores its capability, on problems with and without heat transfer.

## GOVERNING DIFFERENTIAL EQUATION

The integral form of the compressible Navier-Stokes equation for an arbitrary control volume $V$ with an elemental surface area $\mathrm{d}\vec{A}$ with outward unit normal $\mathbf{n} = (n_x, n_y, n_z)$ is written as:

$$\underline{\Gamma} \int \frac{\partial}{\partial t}\mathbf{Q}\mathrm{d}V + \int [\mathbf{F} - \mathbf{G}]\mathrm{d}A - \int \mathbf{S}\mathrm{d}V = 0 \tag{1}$$

where $\mathbf{Q}$ is the vector of primitive variables, $\mathbf{F}, \mathbf{G}$ are the normal components of the convective and viscous flux vectors at the elemental surface, $\mathbf{S}$ is the vector of source terms and $\Gamma$ is the transformation Jacobian of the conservative variables with respect to primitive variables at cell $p$. These quantities are given by:

$$\mathbf{F} = \begin{pmatrix} \rho V_n \\ \rho V_n u + P n_x \\ \rho V_n v + P n_y \\ \rho V_n w + P n_z \\ \rho V_n H \end{pmatrix} \mathbf{G} = \begin{pmatrix} 0 \\ n_x\tau_{xx} + n_y\tau_{xy} + n_z\tau_{xz} \\ n_x\tau_{yx} + n_y\tau_{yy} + n_z\tau_{yz} \\ n_x\tau_{zx} + n_y\tau_{zy} + n_z\tau_{zz} \\ n_x\theta_x + n_y\theta_y + n_z\theta_z \end{pmatrix} \mathbf{S} = \begin{pmatrix} 0 \\ \rho f_x \\ \rho f_y \\ \rho f_z \\ \rho(f_x u + f_y v + f_z w) + \dot{q_h} \end{pmatrix} \tag{2}$$

where $f_x$, $f_y$ and $f_z$ are external body forces per unit mass, $\dot{q_h}$ is the volumetric heating rate, $P$ is the pressure, $H$ is the total enthalpy and the primitive variable vector is

$$\mathbf{Q}^T = \begin{pmatrix} P & u & v & w & T \end{pmatrix}$$

$V_n$, $\theta_x$, $\theta_y$, $\theta_z$ and the matrix $\Gamma$ are given by [11]:

$$\begin{aligned} V_n &= n_x u + n_y v + n_z w \\ \theta_x &= u\tau_{xx} + v\tau_{xy} + w\tau_{xz} + k\frac{\partial T}{\partial x} \\ \theta_y &= u\tau_{yx} + v\tau_{yy} + w\tau_{yz} + k\frac{\partial T}{\partial y} \\ \theta_z &= u\tau_{zx} + v\tau_{zy} + w\tau_{zz} + k\frac{\partial T}{\partial z} \end{aligned} \qquad \underline{\Gamma} = \begin{bmatrix} \rho_p & 0 & 0 & 0 & \rho_T \\ u\rho_p & \rho & 0 & 0 & u\rho_T \\ v\rho_p & 0 & \rho & 0 & v\rho_T \\ w\rho_p & 0 & 0 & \rho & w\rho_T \\ H\rho_p - 1 & u\rho & v\rho & w\rho & \rho_T H + \rho C_p \end{bmatrix}$$

where subscripts (except in $C_P$) indicate differentiation with respect to the subscripting variable. The system is closed using the equation of state $P = \rho RT$.
Using the Gauss divergence theorem, equation (1) is discretized for a general multi-face cell as,

$$\underline{\Gamma}\frac{\partial}{\partial t}\mathbf{Q} + \Sigma_f \left(\mathbf{F}_f - \mathbf{G}_f\right)^{n+1} A_f - \mathbf{S}^{n+1}V = 0 \tag{3}$$

where $f$ refers to the faces of the cell. For investigating the all-speed SLAU scheme feature even for turbulence cases we use the Spallart Allmaras turbulence model, whose implementation detail can be found in [12].

## IMPLICIT TIME INTEGRATION

In the semi-discretized governing equations above, the values of the fluxes $\mathbf{F}, \mathbf{G}$ are not known at the $n+1$ level. Expanding the global residual vector $\mathbf{R}^{n+1}(\equiv \mathbf{F^{n+1}} - \mathbf{G^{n+1}} - \mathbf{S^{n+1}})$, around the known residual flux $\mathbf{R}^n$, we get

$$\mathbf{R}^{n+1} = \mathbf{R}^n + \left(\frac{\partial \mathbf{R}}{\partial \mathbf{Q}}\right)^n \Delta\mathbf{Q}^{n+1} + \text{H.O.T} \tag{4}$$

where $\Delta\mathbf{Q}^{n+1} = \mathbf{Q}^{n+1} - \mathbf{Q}^n$, and the quantity in brackets is the Jacobian. With (4), the system (3) results in:

$$\left[\frac{V_p}{\Delta t}\underline{\Gamma} + \Sigma_f \underline{J}_{f,p} A_f\right] \Delta\mathbf{Q}_p^{n+1} - \Sigma_f \underline{J}_{f,nb} \Delta\mathbf{Q}_{nb}^{n+1} = -\mathbf{R}^n \tag{5}$$

where $p, nb$ refers to centres of the cell and its neighbours, respectively, $V_p$ is the $p^{th}$ cell volume, $\underline{J}_{f,p/nb}$ is the *flux* Jacobian matrix of the discretized flux ($\mathbf{F^n} - \mathbf{G^n} - \mathbf{S^n}$) with respect to variables at the $p$ or $nb$ cell-centres. The discretized flux at face $f$ is a function of the $p^{th}$ cell value as well as the neighbouring cell values, thus the neighbouring $nb$ term appears in the equation above. Rearranging equation (5), we get

$$[\underline{I} - \Sigma_f \underline{J}_{j,nb} A_f]\Delta\mathbf{Q}^{n+1} = -\mathbf{R}^n \qquad \text{or} \qquad [\underline{A}]_{global}\Delta\mathbf{Q}^{n+1} = -\mathbf{R}^n \tag{6}$$

where

$$\underline{I} \equiv \left[\frac{V}{\Delta t}\underline{\Gamma} + \Sigma_f \underline{J}_{f,p} A_f\right] \tag{7}$$

and $\Delta\mathbf{Q}$ now includes the values at $p$ and $nb$, infact all points of the domain. The equation set (6) is solved using the symmetric Gauss-Seidal procedure [13, 4].

# RESULTS

## Results and Discussions

The compressible Navier-Stokes equations has been solved using a density-based algorithm in the framework of our in-house 3D unstructured solver. This solver was previously tested for various problems [12, 14, 15]. Here, an all speed SLAU[16] scheme is used for the convection and the Green-Gauss[11] method is used for diffusion term discretization. The convective term uses second-order discretization while the viscous term are central discretized [11]. The first-order backward Euler method is used for time-stepping [17]. Its feature of capturing flow physics in the incompressible limit will be shown below through different cases.

### Buoyancy driven cavity

We first consider the problem of the buoyancy-driven cavity, a unit square domain with its two vertical walls at different temperatures and horizontal walls insulated. This is a classical problem in natural convection which has been extensively studied and features a complex flow field depending on three parameters 1) Rayleigh number, 2) Temperature difference parameter ($\theta = (T_h - T_c)/(T_h + T_c)$), 3) aspect ratio of the domain ($L/H$).

| Parameter | Th | Tc | $\theta$ | Ra | Pr | A.R |
|---|---|---|---|---|---|---|
| Value | 1025 | 975 | 0.025 | 1000 | 0.71 | 1 |

Table 1: Parameters set in buoyancy driven cavity problem

In first step, we compare the performance of the SLAU method with the Boussinesq approximation applied to a pressure-based solver for the case detailed in Table 1. The Nusselt number obtained with the SLAU method and with Boussinesq approximation are identical as shown in Figure 1(a). Figure 1(b) compares the plot of average Nusselt number obtained by SLAU with the correlation given by Chenoweth et. al. [18]. The match is very good between the density-based algorithm and the empirical correlation. Contour plot of temperature and Mach number is shown in Figure 2. Highly incompressible flow of Ma $\approx 10^{-6}$ has been noted in Figure2(b) and successfully captured

by SLAU scheme.

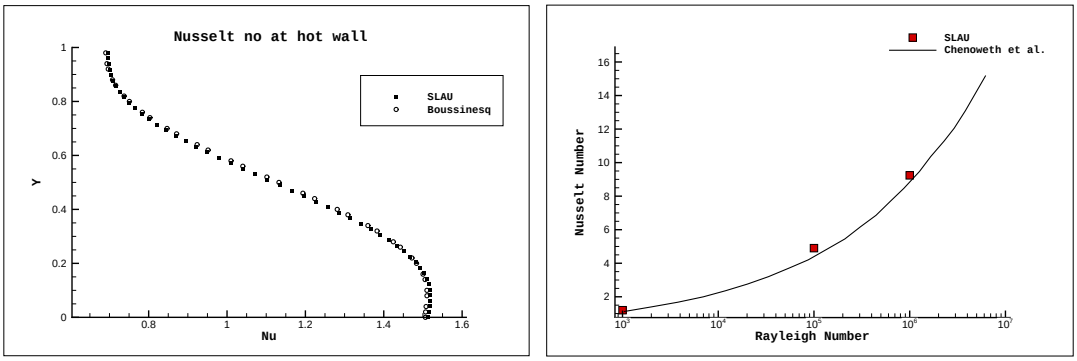


(a) Variation of Nusselt number over hot wall at Ra=1000 for buoyancy driven problem

(b) Comparison of Average Nusselt number at hot wall with empirical correlation of Chenoweth et. al. [18]

Figure 1: Buoyancy driven cavity problem

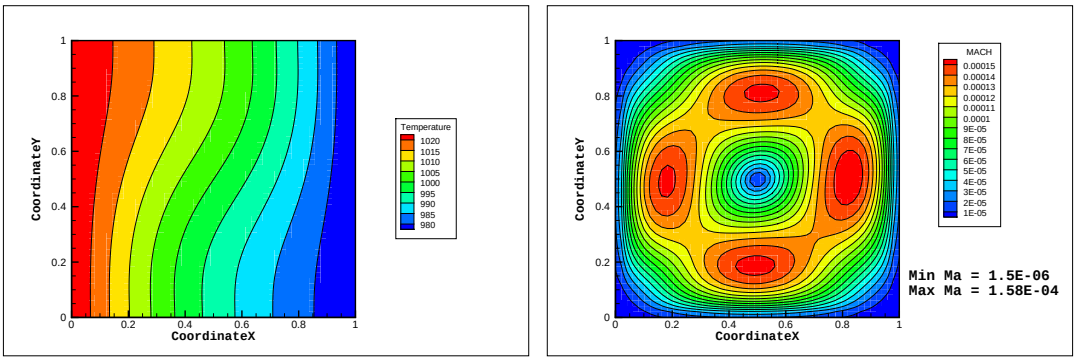


(a) Contour plot of Temperature for buoyancy driven problem at Ra=1000

(b) Contour plot of Mach number for buoyancy driven problem at Ra=1000. Highly incompressible flow Ma $\approx 10^{-6}$ has been successfully captured by SLAU scheme

Figure 2: Buoyancy driven cavity problem

### Case 2: Inviscid flow over an aerofoil

The next case considered is that of inviscid flow over a NACA 0012 airfoil with angle of attack of $2^{\circ}$. We study the external flow at a Mach Number of 0.01 at 1 atm pressure and 300 K temperature. The domain is shown in Fig. 3(a). The computational domain is taken such as to have the farfield situated at a downstream distance of five hundred times the airfoil chord length. The exit flow is given far-field boundary conditions while the airfoil wall has inviscid wall boundary conditions. The value of the pressure coefficient along the lower and upper aerofoil surfaces is compared with the reference in Fig. 3(b), showing good agreement.

### Case 3: Turbulent flow over a flat plate

The last case considered is the turbulent flow over a flat plate [20] at Ma $= 0.2$ with Reynolds number $Re = 5 \times 10^6$ and $T_\infty = 540$ R =300 K. The Reynolds number is calculated based on the half length of the plate. The flow domain and boundary conditions are shown in Fig. 4(a). The turbulent inflow boundary condition used a turbulent viscosity ratio of 3 [21]. The turbulent Prandtl number is taken to be 0.9. The main aim of this case is to verify the performance of SLAU

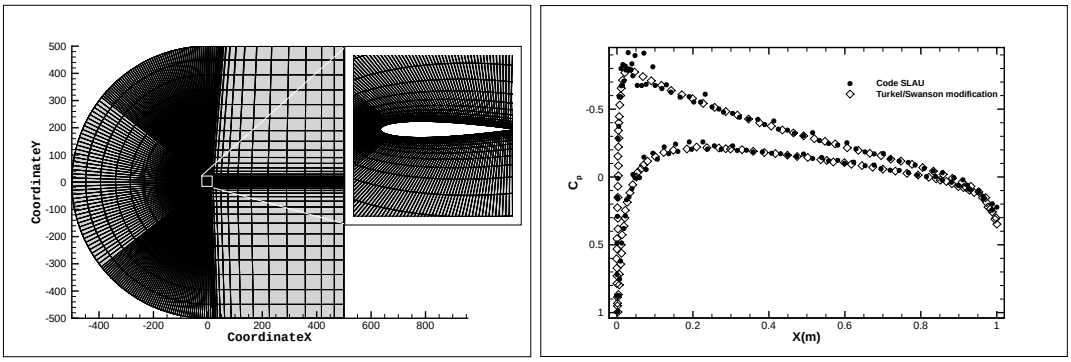


(a) Computational domain and Mesh. (b) Pressure coefficient

Figure 3: Comparison of pressure Coefficient along the wall for case 2 at M = 0.01 and $\alpha = 2.0^\circ$ with the reference solution [19].

in turbulent flow and Spalart-Allmaras model is used for turbulence. We compare the surface skin friction coefficient with those results given on the Turbulence Modeling Resource (TMR) web-page [21]. We have used a mesh having $273 \times 193$ cells.
Figure 4(b) compares the skin friction coefficient along the wall flow over a flat plate. It shows that the present results are similar to the other NASA codes results and closer to the experimental results[22]. This case shows the ability of the present solver to capture incompressible flow correctly using the SLAU scheme even with the turbulence.

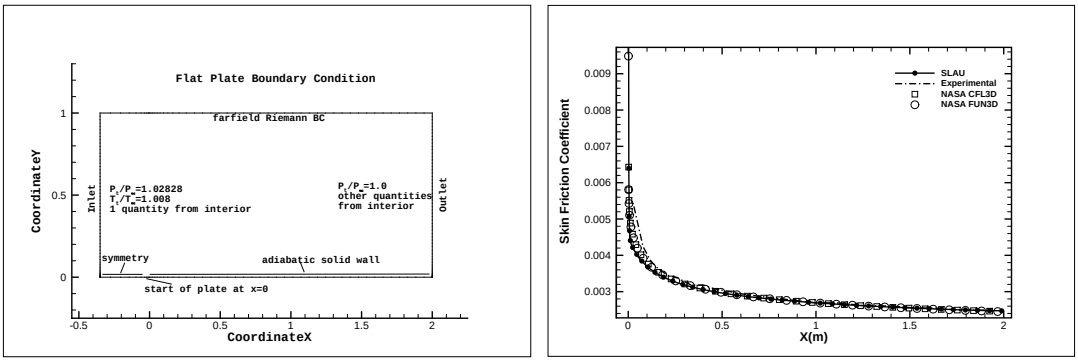


(a) Flow domain and Boundary conditions for turbulent flow over a flat plate. (b) Variation of skin friction coefficient for turbulent flow over a flat plate

Figure 4: Turbulent flow over a flat plate problem

## CONCLUSIONS

- The SLAU method has been implemented in an unstructured grid solver and validated in low Mach regime ($1.5 \times 10^{-6} - 1 \times 10^{-4}$) with heat transfer. It is shown that the SLAU scheme gives the same results as the Boussinesq approximation.
- The other two cases of inviscid flow over NACA 0012 airfoil and turbulent flow over the flat plate with inflow Mach number being small (incompressible) has also been captured using the SLAU scheme.
- It is found that the SLAU scheme works quite well (without preconditioning) for the incompressible cases implemented in a density based solver and could be used as an alternative to the preconditioning.

## References

[1] Patrick J Roache. Fundamentals of computational fluid dynamics(book). *Albuquerque, NM: Hermosa Publishers, 1998.*, 1998.

[2] Eli Turkel. Preconditioned methods for solving the incompressible and low speed compressible equations. *Journal of Computational Physics*, 72(2):277–298, 1987.

[3] Eli Turkel. Review of preconditioning methods for fluid dynamics. *Applied Numerical Mathematics*, 12(1-3):257–284, 1993.

[4] Jonathan M Weiss, Joseph P Maruszewski, and Wayne A Smith. Implicit solution of preconditioned Navier-Stokes equations using algebraic multigrid. *AIAA Journal*, 37(1):29–36, 1999.

[5] Jonathan Weiss and Wayne Smith. Preconditioning applied to variable and constant density time-accurate flows on unstructured meshes. In *Fluid Dynamics Conference*, page 2209, 1994.

[6] Y-H Choi and Charles L Merkle. The application of preconditioning in viscous flows. *Journal of Computational Physics*, 105(2):207–223, 1993.

[7] Eiji Shima and Keiichi Kitamura. On new simple low-dissipation scheme of AUSM-family for all speeds. In *47th AIAA Aerospace Sciences Meeting including the New Horizons Forum and Aerospace Exposition*, page 136, 2009.

[8] Meng-Sing Liou. A sequel to AUSM, Part II: AUSM+-up for all speeds. *Journal of Computational Physics*, 214(1):137–170, 2006.

[9] Kalyana Chakravarthy and Debasis Chakraborty. Modified SLAU2 scheme with enhanced shock stability. *Computers & Fluids*, 100:176–184, 2014.

[10] S Venkateswaran and Charles Merkle. Dual time-stepping and preconditioning for unsteady computations. In *33rd Aerospace Sciences Meeting and Exhibit*, page 78, 1995.

[11] J Blazek. *Computational fluid dynamics principles and applications*. Elsevier, Amsterdam; San Diego, 2005.

[12] Ashwani Assam, Nikhil Kalkote, Vatsalya Sharma, and Vinayak Eswaran. An Automatic Wall Treatment for Spalart-Allmaras Turbulence Model. *Journal of Fluids Engineering*, 2018.

[13] Seokkwan Yoon and Antony Jameson. Lower-upper symmetric-Gauss-Seidel method for the Euler and Navier-Stokes equations. *AIAA Journal*, 26(9):1025–1026, 1988.

[14] Nikhil Kalkote and Vinayak Eswaran. Supersonic Biplane: Cheaper, Quieter and Fuel Efficient Supersonic Travel. In *Proceedings of the 6th International and 43rd National Conference on Fluid Mechanics and Fluid Power*, Motilal Nehru National Institute of Technology Allahabad (MNNITA), 12 2016.

[15] Nikhil Kalkote and Vinayak Eswaran. Numerical Computation of Natural Convection on Unstructured Hybrid Mesh without Preconditioning. In *24th National and 2nd International ISHMT-ASTFE Heat and Mass Transfer Conference*, 2017.

[16] Eiji Shima and Keiichi Kitamura. Parameter-free simple low-dissipation AUSM-family scheme for all speeds. *AIAA journal*, 49(8):1693–1709, 2011.

[17] Nikhil Kalkote and Vinayak Eswaran. Unsteady Computations of All-Speed Flows with Modified Gear's method on Unstructured Hybrid Grid. In *24th National and 2nd International ISHMT-ASTFE Heat and Mass Transfer Conference*, BITS Pilani, Hyderabad Campus, 12 2017.

[18] DR Chenoweth and S Paolucci. Natural convection in an enclosed vertical air layer with large horizontal temperature differences. *Journal of Fluid Mechanics*, 169:173–210, 1986.

[19] Stefan Langer. Investigations of a compressible second order finite volume code towards the incompressible limit. *Computers & Fluids*, 149:119–137, 2017.

[20] Yang Zhang, Jun-Qiang Bai, and Jing-Lei Xu. A Scale-Adaptive Turbulence Model Based on the k-Equation and Recalibrated Reynolds Stress Constitutive Relation. *Journal of Fluids Engineering*, 138(6):061203, 2016.

[21] Turbulence Modeling Resource. `https://turbmodels.larc.nasa.gov/`.

[22] K. Wieghardt and W. Tillman. On the Turbulent Friction Layer for Rising Pressure. Technical Report TM-1314, NASA, 1951.

# Determination of Absorption Conditions for $LaNi_{4.7}Al_{0.3}$ Based Hydrogen Storage Device: A Numerical Investigation

**Nithin N Raju, P Muthukumar, K Malleswararao**
Department of Mechanical Engineering
Indian Institute of Technology, Guwahati, India
r.narmada@iitg.ernet.in, pmkumar@iitg.ernet.in, katamala@iitg.ernet.in

## ABSTRACT

To understand the hydriding behaviour of $LaNi_{4.7}Al_{0.3}$, a numerical model has been formulated using finite element method and solved using COMSOL Multiphysics 4.3a. In order to enhance the heat and mass transfer characteristics, embedded cooling tube (ECT) reactor configuration has been designed with optimum numbers of 55 ECT. The three dimensional model includes coupled heat and mass transfer, driving pressure gradient, diffusion of hydrogen gas and convective heat transfer. Based on numerical simulation, optimum supply pressure of 45 bar with absorption temperature ranging from 10 ºC to 30 ºC is obtained. Experimental validation corroborates the simulation model.

**Key Words:** *Metal Hydride; Thermal Modelling; Absorption; Coupled Heat and Mass Transfer; Parametric study.*

## 1. INTRODUCTION

Metal hydride based hydrogen storage devices are one of the primary focus for research in achieving hydrogen economy. Askri et al. [1] studied the reaction kinetics with different reactor designs while Veerraju and Gopal [2] presented a transient, 2-D model to predict characteristics of elliptical metal hydride tubes and tube banks. However their designs have been too complex for practical implementations. Anbarasu et al. [3] developed a mathematical model for embedded cooling tube (ECT) reactor. There is a need for design and analysis of an optimized ECT model.

## 2. NUMERICAL MODELLING

To predict and analyse the performance of metal hydride reactor with ECT, three dimensional numerical model has been developed and solved using finite element method based simulation tool COMSOL Multiphysics 4.3a. Coupled heat and mass transfer evident during hydriding reaction, driving pressure gradient between supply and hydride bed, diffusion of hydrogen gas through porous metal hydride bed, transfer of heat from bed to the heat transfer fluid (HTF) through convective heat transfer and resultant axial variation in HTF have all been captured in this numerical model. Following assumptions are considered for numerical modelling: (i) hydrogen is an ideal gas, (ii) the solid phase is isotropic and has uniform porosity, (iii) local thermal equilibrium between the hydrogen gas and metal hydride is valid, (iv) the porous filter is adiabatic, (v) the reactor is well insulated so that there is no heat loss to the surroundings and (vii) the thermo-physical properties of the hydride bed are independent of the bed temperature and supply pressure.

***Governing Equations:***

van't Hoff equation: $$\frac{P_{eq}}{P_0} = \exp\left[\frac{\Delta S}{R_u} - \frac{\Delta \mathrm{H}}{R_u T} + (\varphi_s \pm \varphi_o) \times \tan\left(\pi\left(\frac{c}{c_{end}} - \frac{1}{2}\right)\right) \pm \frac{\varphi}{2}\right] \quad (1)$$

Reaction rate equation: $$\zeta_a = c_a \exp\left(-\frac{E_a}{R_u T}\right) \ln\left(\frac{P}{P_{eq}}\right)(\rho_{ss} - \rho_t) \quad (2)$$

Mass balance equations: Hydrogen gas - $$\varepsilon \frac{\partial \rho_g}{\partial t} + \nabla.(\rho_g \vec{u}) = -\zeta_a \quad (3)$$

Metal hydride - $$(1-\varepsilon)\frac{\partial \rho_s}{\partial t} = \zeta_a \quad (4)$$

Darcy's Law: $$\vec{u} = -\left(\frac{K}{\mu_g}\right)\nabla P \quad (5);$$ Ideal Gas Eqn: $$\rho_g = \frac{P_g M_{H_2}}{R_u T} \quad (6)$$

Combined energy equation: $$(\rho C_p)_e \frac{\partial T}{\partial t} + (\rho_g C_{pg})(\vec{u}.\nabla T) = k_e \nabla^2 T + Q \quad (7)$$

Source term arises from rate of reaction: $$Q = \zeta_a \left( \frac{\Delta H}{M_g} \right) \quad (8)$$

Hydrogen storage capacity: $$wt\,\% = \frac{m_{H_2}}{m_a} = \frac{N_a M_{H_2} (c_{end} - c_{ini})}{M_a} \times 100\% \quad (9)$$

Initial conditions: $$\rho_m(r,\theta,z) = \rho_0 ; P_g(r,\theta,z) = P_s; T(r,\theta,z) = T_g(r,\theta,z) = T_f(z) = T_0 \quad (10)$$

Boundary conditions: $$P_g(r_{ip}, t) = P_s;\ \frac{\partial T}{\partial r}(r_o) = 0;\ T_{fi} = T_{cool};\ -k_e \frac{\partial T}{\partial r}(r_{ot}) = U(T - T_f) \quad (11)$$

***Geometrical Configuration:***

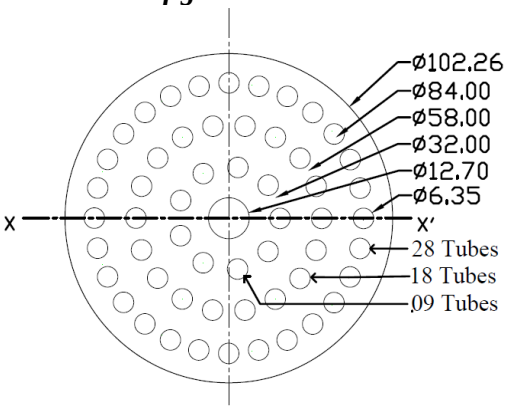


FIGURE 1. Schematic view of 55 ECT Reactor model (all dimensions are in mm)

Incorporating above problem formulation, the numerical model is developed using unique ECT configuration called 55 ECT Reactor. It contains a cylinder of inner diameter 102.26 mm. A filter of diameter of 12.7 mm is centrally placed inside the reactor. To assist in effective heat removal of bed during absorption, 55 tubes are embedded radially in a three stack structure. Each tube has an outer diameter of 6.35 mm. 9, 18 and 28 numbers of ECT are respectively distributed in circles of diameters 32 mm, 58 mm, and 84 mm, as shown in FIGURE 1.

Since the configuration is symmetrical about X-X' axis, half sectional model has been considered for the numerical simulation. Free tetrahedral mesh is used while time stepping is based on Euler Backward Difference Formula.

## 3. RESULTS AND DISCUSSION

The developed numerical model has been simulated at various operating conditions to study the effect of the parameters on its hydriding performance. Thermophysical properties of $LaNi_{4.7}Al_{0.3}$, hydrogen and the constants considered in this study [4] has been listed in TABLE 1.

| ***Properties of $LaNi_{4.7}Al_{0.3}$*** | | ***Properties of hydrogen*** | |
|---|---|---|---|
| Density of metal | 7440 kg/m$^3$ | Thermal conductivity of hydrogen | 0.127 W/m K |
| Specific heat of metal | 420 J/kg K | Specific heat of hydrogen | 14283 J/kg K |
| Thermal conductivity of metal | 5.5 W/m K | Density of hydrogen | 0.0838 kg/m$^3$ |
| Porosity | 0.5 | ***Constants used*** | |
| Effective density at saturation | 3850 kg/m$^3$ | Universal gas constant | 8.314 J/mol K |
| Effective density of solid | 3904 kg/m$^3$ | Reaction constant | 250 s$^{-1}$ |
| Hydride activation energy | 30000 J/mol $H_2$ | Slope factor | 0.3 |
| Entropy of reaction | 107.4 J/mol $H_2$ K | Constant | 0.005 |
| Enthalpy of reaction | 33820 J/mol $H_2$ | Hysteresis | 0.098 |

TABLE 1. Thermophysical properties of $LaNi_{4.7}Al_{0.3}$, hydrogen and the constants [4]

***Effect of supply pressure:***

While maintaining an absorption temperature of 25 ºC, the supply pressure has been varied from 5 bar to 15 bar, 30 bar, 45 bar and 60 bar. HTF was supplied at a volume flow rate of 35 lit/min. Variation of hydrogen storage capacity at different supply pressures have been depicted in Fig.2. At supply pressure of 5 bar, the reaction kinetics is very slow and storage capacity of 1 wt% is attained around 340 s, while complete absorption is not achieved even after 1000 s. At 1000 s, a hydrogen storage capacity of 1.3 wt% has been attained at 5 bar supply pressure. Increasing the supply pressure to 15 bar lead to 4.6% increase in storage capacity and 1.36 wt% is reached at 1000 s,

while 1.3 wt% is achieved within 380 s. Increase in supply pressure leads to larger pressure gradient between bed and supply, thereby resulting in a larger driving force. Hence, increasing the supply pressure further to 30 bar, 45 bar and 60 bar respectively resulted in duration of 230 s, 180 s and 150 s to achieve 1.3 wt%.

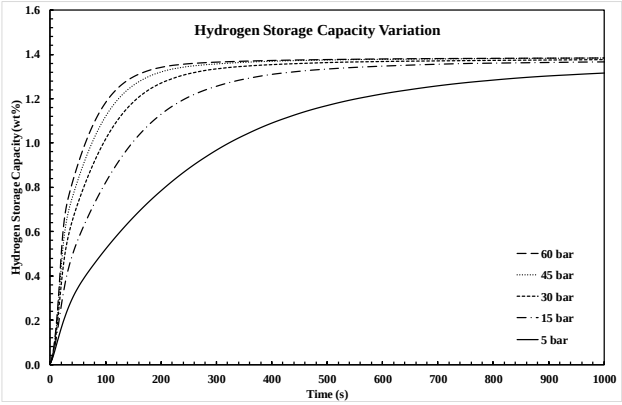


FIGURE 2. Hydrogen storage capacity variation at different supply pressures

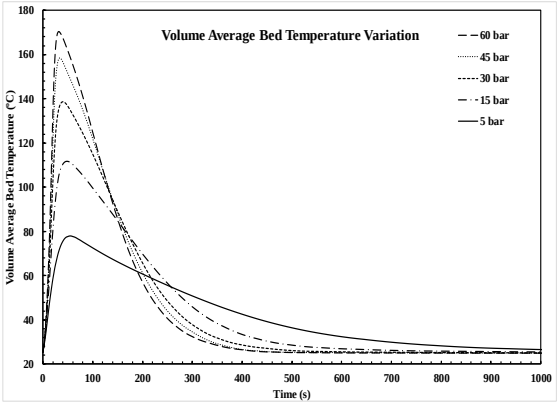


FIGURE 3. Volume average bed temperature variation at different supply pressures

It can be observed that increase of supply pressure beyond 45 bar does not influence the performance of system significantly. This behaviour is also reflected in volume average bed temperature variation at different supply pressures depicted in FIGURE 3. At supply pressure of 5 bar, the volume average bed temperature is 27 ºC even after 1000 s. However, at 15 bar supply pressure it can be observed that bed temperature of 26 ºC is attained in 700 s. This represents the duration taken by the model for achieving majority of the absorption reaction. The time duration for attaining 26 ºC reduced to 520 s, 430 s and 420 s respectively when supply pressure is increased to 30 bar, 45 bar and 60 bar. Based on the above analysis, 45 bar is suitable supply pressure for the given model.

***Effect of absorption temperature:***

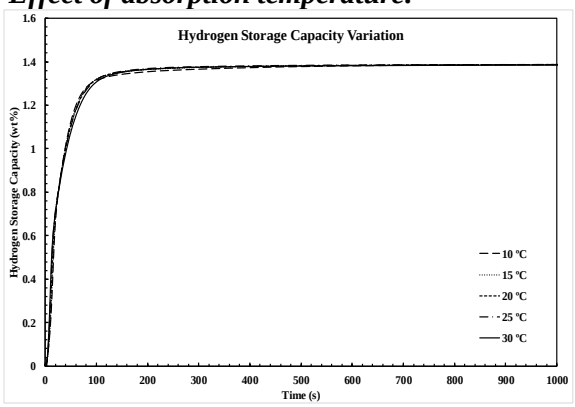


FIGURE 4. Hydrogen storage capacity variation at different absorption temperatures

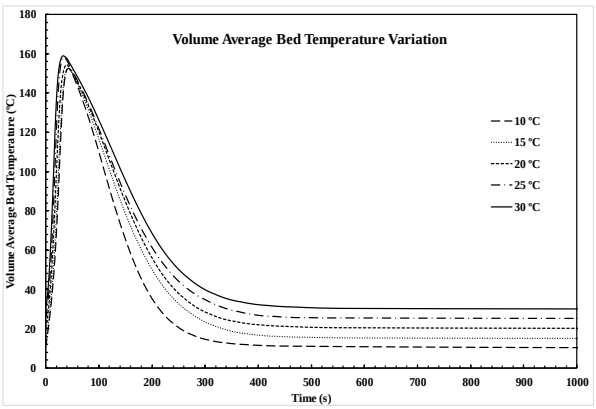


FIGURE 5. Volume average bed temperature variation at different absorption temperatures

Similar to above case, the supply pressure was maintained at 45 bar and the absorption temperature has been varied from 10 ºC to 15 ºC, 20 ºC, 25 ºC and 30 ºC with HTF flow rate of 35 lit/min. Unlike the effect of supply pressure, the effect of absortion temperature is not very prominent on the hydriding behaviour of the metal hydride as can be observed from Figs. 4 and 5. The reason for this behaviour may be due to the fact that $LaNi_{4.7}Al_{0.3}$ is a low temperature alloy. Equilibrium pressure of the alloy does not vary much in low temperature conditions. Hence, the metal hydride exhibits similar performance for the chosen absorption temperatures. However, a slight variation in volume average bed temperature can be discerned due to the influence of absorption temperature. For 30 ºC absorption condition, bed attained 32.2 ºC at 400 s, which is a difference of 2.2 ºC. The

bed temperature value for 10 ºC absorption condition at 400 s is 11.2 ºC. The difference here is 1.2 ºC signifying faster reaction kinetics. At lower absorption condition, the temperature gradient between the bed and HTF is more and hence, reaction kinetics is slightly more rapid. Overall, absorption temperature can be fixed within 10 ºC to 30 ºC temperature range.

***Experimental validation:***

In order to experimentally validate the above analysis, designed 55 ECT Reactor was fabricated and filled with 4 kg of $LaNi_{4.7}Al_{0.3}$. The material was activated successfully for absorption. Absorption experiment was carried out at 60 bar and 25 ºC. The bed temperature variation recorded by K-type thermocouple has been plotted against numerical point bed temperature variation, as represented in Fig. 6. Upon observation, it can be seen that experimental bed temperature variation corroborates the numerical trend for major part of absorption reaction. However, there is a deviation beyond 150 s due to difference in the estimation of thermophysical properties in experimental investigation. Around 55.2 g of hydrogen was absorbed at given conditions, which amounts to about 1.38 wt%.

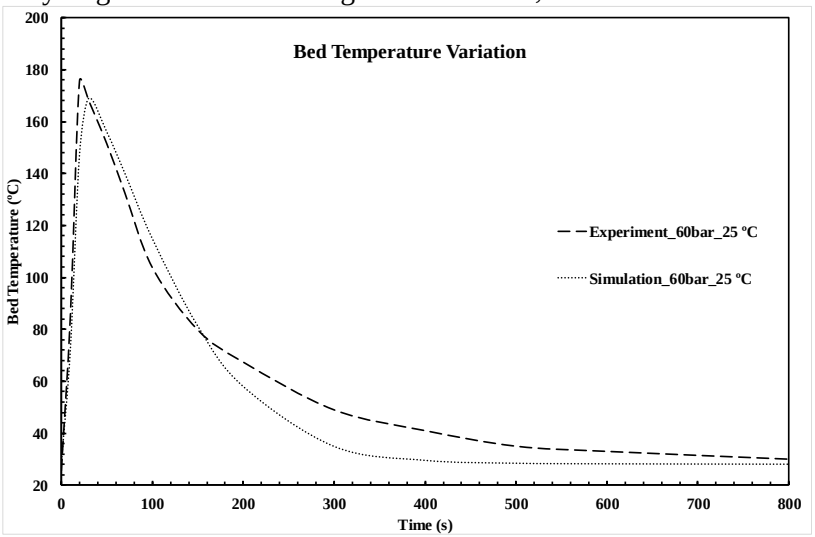


FIGURE 6. Validation of bed temperature variation

## 4. CONCLUSIONS

Three dimensional numerical model has been developed using designed 55 ECT reactor configuration and solved by finite element method using COMSOL Multiphysics 4.3a. As part of parametric investigation, supply pressure was varied from 5 bar to 15 bar, 30 bar, 45 bar and 60 bar, while HTF was fixed at 25 ºC with a flow rate of 35 lit/min. At 45 bar, maximum storage capacity of 1.38 wt% was attained in 800 s while 1.2 wt% was obtained within 125 s. Varying absorption temperature from 10 ºC to 30 ºC did not influence absorption significantly. Hence, the reactor can be operated nominally in the given absorption temperature range. Experimental investigation corroborates the numerical results. At 45 bar and 25 ºC, 55.2 g of hydrogen has been absorbed by the designed 55 ECT Reactor.

## REFERENCES

[1] Askri, F., Salah, B.M., Jemni, A., Nasrallah, S.B. (2009) Optimization of hydrogen storage in metal hydride tank, Int. J. Hydrogen Energy, 34:897-905.

[2] Veerraju, Ch., Gopal, R.M. (2010) Heat and mass transfer studies on elliptical metal hydride tubes and tube banks, Int. J. Hydrogen Energy, 34:4340-50.

[3] Anbarasu, S., Muthukumar, P. and Mishra, S.C. (2014) Thermal modelling of LmNi4.91Sn0.15 based solid state hydrogen storage device with embedded cooling tubes, Int. J. Hydrogen Energy, 39:15549-62.

[4] Hahne and Kallweit. (1998) Thermal conductivity of metal hydride materials for storage of hydrogen: Experimental investigation. Int. J. Hydrogen Energy. 23:107-14.

Fifth International Conference on Computational Methods for Thermal Problems
THERMACOMP2018, July 9-11, 2018, Indian Institute of Science, Bangalore, INDIA
*N. Massarotti, P. Nithiarasu, Pradip Dutta and C. Ranganyakalu (Eds.)*

# WALL HEAT CONDUCTION EFFECTS ON THE CONJUGATE LAMINAR FORCED CONVECTION IN CIRCULAR MICROCHANNELS

**Nonino Carlo, Savino Stefano**
Università degli Studi di Udine, DPIA,
Via delle Scienze 206, 33100 Udine, Italy
carlo.nonino@uniud.it, stefano.savino@uniud.it

## ABSTRACT

In this work, a correlation for the calculation of a suitable correction term has been derived with the aim of allowing a more accurate prediction of the length averaged Nusselt number in the laminar forced convection in thick-walled ducts where the effects of axial heat conduction in the solid material cannot be neglected. To that purpose, an in-house FEM procedure has been used to perform a parametric investigation in order to produce the set of data to be fitted.

**Key Words:** *Micro Heat Transfer, Finite Elements, Conjugate Conduction- Convection.*

## 1. INTRODUCTION

In the past twenty years, the interest of researchers for microscale heat transfer has represented the main motivation for the investigation of the complex heat transfer mechanisms that, in spite of the simple geometry, characterize the coupled convection-conduction heat transfer in microchannel entrance regions. In fact, in micro heat transfer devices the thickness of the solid walls is, in general, comparable to the characteristic transverse dimension of the flow passages. Therefore, especially when the walls are made of highly conductive material and, as is often the case in microchannel flows, the Péclét number is rather low, the effects of axial conduction cannot be neglected. However, in spite of the large number of studies on the involved heat transfer mechanisms, very few correlations are reported in the literature that allow the prediction of the local Nusselt number in simultaneously developing laminar flows in thick-walled ducts [1,2]. Moreover, to the authors' knowledge, no correlations can be found for the length averaged Nusselt number, which, in many practical situations, would be the most appropriate to use.

The present research tries to fill, at least partially, this gap of knowledge. We propose a correlation to calculate a correction term that takes the wall heat conduction effects into account. This correlation should be applied to computed length averaged Nusselt numbers in the entrance region of circular tubes with uniform heat flux boundary conditions specified at the walls, assumed to have negligible thickness. To this purpose, a parametric investigation has been carried out where the numerical simulations concern different values of tube length, Péclét number, ratio of the outer and inner diameters and ratio of solid to fluid thermal conductivities.

## 2. MATHEMATICAL AND NUMERICAL MODELS

The problem considered here consists in the steady-state laminar forced convection in the entrance region of thick-walled circular channels with uniform heat flux boundary conditions $q'' = q''_w = const$ applied to the outer surface of the ducts and adiabatic walls at the inlet and outlet sections. At the entrance of the duct, uniform values of the temperature $t = t_e = const$ and of the axial velocity component $u = u_e = \overline{u}$ are specified, $\overline{u}$ being the average axial velocity. Reference is

made to Newtonian, constant property fluids. A sketch of the geometry and of the relevant boundary conditions is shown in Figure 1.

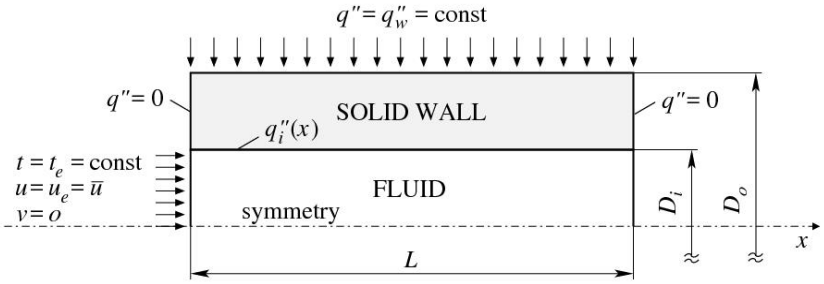


FIGURE 1. Sketch of computational domain and relevant boundary conditions.

The numerical simulations are carried out for a broad range of the relevant geometrical and thermophysical parameters using an in-house FEM code to compute both the velocity and the temperature fields. According to our approach, first the steady-state solution of the axisymmetric dimensionless form of the Navier-Stokes equations in the fluid part of the computational domain is obtained as the final stage of a pseudotransient simulation where the pressure-velocity coupling is dealt with using an improved projection algorithm previously developed by one of the authors [3]. Then the steady-state axisymmetric thermal energy equation is solved in its dimensionless form in the parts of the domain corresponding to both the flow passage and the solid wall.

The mean Nusselt number in a duct of generic length $x$ is defined as

$$\mathrm{Nu}_m(x) = \frac{1}{x}\int_0^x \mathrm{Nu}(x)\, dx \tag{1}$$

and Nu($x$) is the local Nusselt number

$$\mathrm{Nu}(x) = \frac{q''_i(x)\, D_i}{k_f [t_i(x) - t_b(x)]} \tag{2}$$

In the previous equation, $q''_i$ and $t_i(x)$ are the local heat flow rate and the solid wall temperature at the solid-fluid interface, $k_f$ is the thermal conductivity of the fluid and $t_b(x)$ is the mean bulk temperature of the fluid. The Reynolds, Prandtl and Péclét numbers are defined as $\mathrm{Re} = \rho_f \bar{u} D_i / \mu_f$, Pr = $c_f\ \mu_f / k_f$ and Pe = Re Pr, with an obvious meaning of all the symbols. Finally, the following heat conduction parameter will be used in the correlation for the correction to the length averaged Nusselt number that takes the wall heat conduction effects into account

$$M = \left(\frac{k_s}{k_f}\right)\left(\frac{D_o^2 - D_i^2}{D_i^2}\right) \tag{3}$$

## 3. RESULTS

Most of the studies on the effects of the axial heat conduction in the solid wall show that there is a reduction of the local Nusselt number compared with the corresponding no-wall-axial-conduction case [2,4]. This reduction is not uniform along the duct and depends on the wall thickness and the ratio of the solid to fluid thermal conductivities $k_s/k_f$. Figure 2(a) shows some examples of the distribution along the duct of the difference Nu($x$) – $\mathrm{Nu}_0(x)$ between the values of the local Nusselt number for thick walls and the corresponding local Nusselt number $\mathrm{Nu}_0$ for zero wall thickness, i.e., with no wall axial conduction.

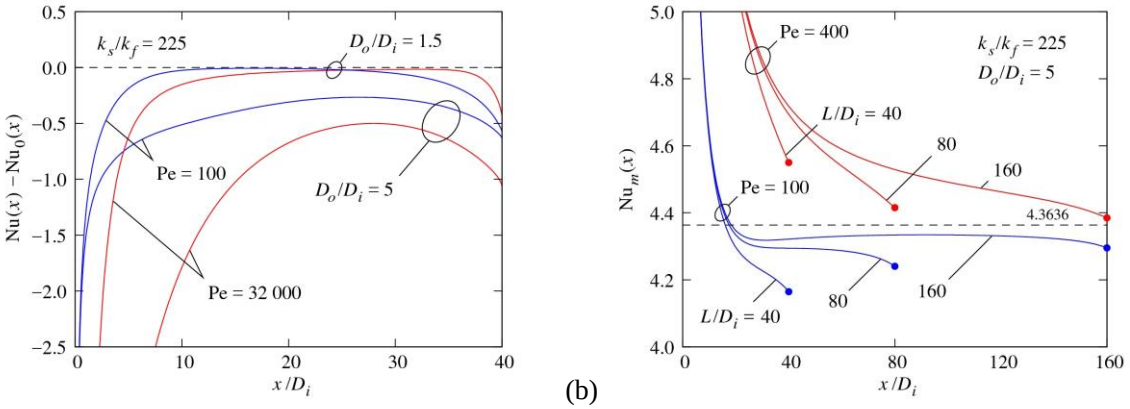


FIGURE 2. Illustrative examples: (a) differences $\mathrm{Nu}(x) - \mathrm{Nu}_0(x)$ along the duct for some combinations of the simulation parameters; (b) $\mathrm{Nu}_m(x)$ distributions for the same $D_o/D_i$ and $k_s/k_f$ and different values of Pe and $L/D_i$.

The reduction of Nu towards the outlet implies that, with a thick conductive wall, no asymptotic values can be attained, even for very long tubes. All this has relevant consequences on the approach that should be adopted in the prediction of the length average Nusselt number in a thick-walled duct of a given length. In fact, it would be incorrect to estimate the mean Nusselt number for a short duct of length $L$ as $\mathrm{Nu}_m(x{=}L)$ from a curve for $\mathrm{Nu}_m(x)$ pertaining to a longer duct for the same Pe, $D_o/D_i$ and $k_s/k_f$ because the curves for the two ducts would not coincide for $x$ close to $L$. Figure 2(b) shows some examples of $\mathrm{Nu}_m(x)$ distributions for various $L/D_i$ for flows in tubes with the same $D_o/D_i$ and $k_s/k_f$ and two values of Pe. This means that only the values corresponding to the final point of each curve (marked with a dot in the figure) and not the whole curve, are of practical interest and can be used to obtain correlations that allow the prediction of the mean Nusselt number $\mathrm{Nu}_m(L)$ in thick-walled tubes when axial heat conduction effects are not negligible.

To this purpose, a correlation has been derived for a correction $\Delta\mathrm{Nu}_m(L) = \mathrm{Nu}_m(L) - \mathrm{Nu}_{0,m}(L)$ to be applied to the value $\mathrm{Nu}_{0,m}(L)$ of the mean Nusselt number in a duct with no wall axial conduction. The parametric investigation necessary to obtain a suitable set of data required 648 numerical simulations corresponding to all the possible combinations of the following values of the relevant parameters: $L/D_i$ = 10, 20, 40, 80, 160 and 320; $D_o/D_i$ = 1.5, 2, 3 and 5; $k_s/k_f$ = 5, 75 and 225; Re = 20, 80 and 320; Pr = 5, 20 and 100. The nonuniform FEM meshes had a resolution of 57 to 85 nodes (depending on $D_o/D_i$) in the radial direction and of 99 to 991 nodes (depending on $L/D_i$) in the axial directions. The total number of nodes ranged from 5643 to 83 160. Those resolutions have been deemed adequate on the basis of preliminary grid independence tests.

The computed values of $\Delta\mathrm{Nu}_m(L)$ have been fitted using a nonlinear least-squares Marquardt-Levenberg algorithm to obtain the following correlation

$$\Delta\mathrm{Nu}_m(L) = -0.047\,\frac{(D_o/D_i)^{-0.25}\,M^{n}\,\mathrm{Pe}^{0.45}}{L/D_i + 0.023M\ \mathrm{Pe}^{-0.39}} \tag{4}$$

where $n = 0.72\ \mathrm{Pe}^{-0.06}$. The correlation allows the prediction of $\mathrm{Nu}_m(L) = \mathrm{Nu}_{0,m}(L) + \Delta\mathrm{Nu}_m(L)$ with relative percentage errors $(\mathrm{Nu}_{m,\mathrm{corr}} - \mathrm{Nu}_{m,\mathrm{num}}) / \mathrm{Nu}_{m,\mathrm{num}} \approx \pm 2.5\%$ and $(\mathrm{Nu}_{m,\mathrm{corr}} - \mathrm{Nu}_{m,\mathrm{num}}) / \Delta\mathrm{Nu}_m(L) \approx \pm 23\%$, where $\mathrm{Nu}_{m,\mathrm{corr}}$ and $\mathrm{Nu}_{m,\mathrm{num}}$ are the values of $\mathrm{Nu}_m(L)$ computed with the correlation and from the numerical solution, respectively. Since the correlation only takes into account the effects of the heat conduction in the wall, $\mathrm{Nu}_m(L)$ can be predicted by applying the correction $\Delta\mathrm{Nu}_m(L)$ to the value of $\mathrm{Nu}_{0,m}(L)$ yielded by any reliable correlation for the length averaged Nusselt number in thin-walled ducts.

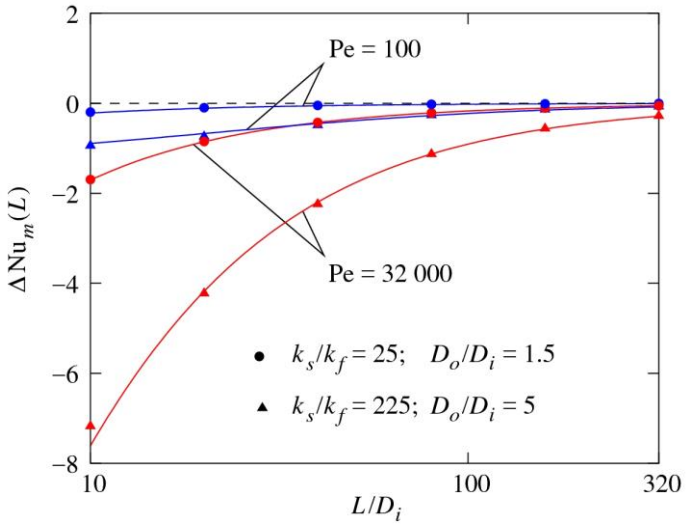


FIGURE 3. Comparison of predicted and numerical values of $\Delta Nu_m(L)$ for ($D_o/D_i$ = 1.5 ; $k_s/k_f$ = 25; Pe = 100) and ($D_o/D_i$ = 5 ; $k_s/k_f$ = 225; Pe = 32 000) and all the values of $L/D_i$ considered (solid lines: correlation; symbols: numerical results).

In Figure 3, distributions of $\Delta Nu_m(L)$ predicted using Eq.(4) and the corresponding numerical results are compared for the two extreme combinations of the simulation parameters, i.e., ($D_o/D_i$ = 1.5; $k_s/k_f$ = 25; Pe = 100) and ($D_o/D_i$ = 5; $k_s/k_f$ = 225; Pe = 32 000). As can be seen, the curves corresponding to the plot of the correlation can capture the trends of the numerical results with good accuracy. This means that, in spite of its relatively simple form, the correlation can effectively account for the complex mechanisms involved in the conjugate convection-heat conduction problem considered.

## 4. CONCLUSIONS

In this work, a correlation for the calculation of a suitable correction term has been derived with the aim of allowing a more accurate prediction of the length averaged Nusselt number in the laminar forced convection in thick-walled tubes where the effects of axial heat conduction in the solid material cannot be neglected. To that purpose, an in-house FEM procedure has been used to perform the parametric investigation in order to produce the set of data to be fitted. The proposed correlation approximates the numerical results with good accuracy.

## REFERENCES

[1] M. Rahimi and R. Mehryar, Numerical study of axial heat conduction effects on the local Nusselt number at the entrance and ending regions of a circular microchannel, *Int. J. Thermal Science*s 59, 87-94, 2012.

[2] P.I. Jagad, B.P. Puranik and A.W. Date, An iterative procedure for the evaluation of a conjugate condition in heat transfer problems, *Numerical Heat Transfer, Part A*, 61, 353-380, 2012.

[3] C. Nonino, A simple pressure stabilization for a SIMPLE-like equal-order FEM algorithm, *Numerical Heat Transfer, Part B*, 44, 61-81, 2003.

[4] C. Nonino, S. Savino, S. Del Giudice and L. Mansutti, Conjugate forced convection and heat conduction in circular microchannels, *Int. J. Heat Fluid Flow*, 30, 823-830, 2009.

Fifth International Conference on Computational Methods for Thermal Problems
THERMACOMP2018, July 9-11, 2018, Indian Institute of Science, Bangalore, INDIA
*N. Massarotti, P. Nithiarasu, Pradip Dutta and C. Ranganayakulu (Eds.)*

# RECOVERY OF FREEZING PROBES FOR THE EXPLOITATION OF GEOTHERMAL ENERGY IN URBAN ENVIRONMENT: A NUMERICAL ANALYSIS

**Filippo Cavuoto**
Studio Cavuoto, Via Bendetto Brin, 63/D2, 80142, Napoli, Italy,
f.cavuoto@studiocavuoto.com

**Nicola Massarotti, Alessandro Mauro, Gennaro Normino**
Dipartimento di Ingegneria, Università degli Studi di Napoli "Parthenope", Napoli, Italy,
Centro Direzionale, Isola C4, 80143, Napoli, Italy,
massarotti@uniparthenope.it, alessandro.mauro@uniparthenope.it, gennaro.normino@uniparthenope.it

## ABSTRACT

Geothermal energy plants allow both heating and cooling of buildings by using the ground as a renewable energy source. The present work shows the numerical results obtained for the recovery of the freezing probes used for the Artificial Ground Freezing (AGF) technique of the two tunnels between Line 1 and Line 6 of the new Metro station in Piazza Municipio, Napoli. The AGF is a consolidation technique used in geotechnical engineering. The recovered probes are connected to a geothermal heat pump. The authors propose to develop an ad hoc innovative plant, in accordance with the principles of the Industry 4.0. In particular, the authors have developed a thermo-fluid dynamic numerical model, solved by means of finite elements, in order to design an innovative energy system, recovering the freezing probes installed for the excavation of the two tunnels.

**Keywords:** *Geothermy; Low-enthalpy geothermal energy; Tunnel; Artificial Ground Freezing; Energy; Heat transfer*

## 1. INTRODUCTION

Geothermal energy can be considered as an alternative energy source for heating and cooling needs, using the ground as a renewable energy source [1]. The freezing probes used for the Artificial Ground Freezing (AGF) technique of the underground tunnels can be used as heat exchangers, avoiding additional drilling costs related to traditional geothermal probes.

In particular, the authors propose here for the first time the use of an innovative system for the exploitation of low enthalpy geothermal energy for indoor climatization needs, by recovering the freezing probes used for the Artificial Ground Freezing (AGF) technique of the two tunnels between Line 1 and Line 6 of the new Metro station in Piazza Municipio, Napoli. This system allows to obtain high energy efficiency and low environmental impact, according to the European energy policy, which aims to achieve at least 27% of the energy production from renewable sources by 2030.

## 2. EXPERIMENTAL SET-UP

The experimental set-up has been realized in the construction site of the underground station of Piazza Municipio in Napoli, Italy (Figure 1). The galleries, about 40 m long, mainly involve two layers of land, made of Neapolitan yellow tuff and pozzolana. The characteristics of the ground are reported in reference [2]. Each freezing probe is installed within a horizontal hole of 114 mm

diameter created in the ground. The stability of this hole is ensured by the presence of a stainless steel tube. The freezing probe consists of two coaxial tubes: the external one is made of stainless steel and has a diameter of 76 mm and a closed bottom. Its external surface is in contact with a cement mortar. The internal tube is made of copper and has an open bottom and a diameter of 28 mm. Through the flanges, the probes are connected to a high-density polyethylene pipe and to a horizontal wall-mounted geothermal collector, which allows the passage of the fluid coming from the distribution circuit to the inner tube of the freezing probe. The probes are connected to a power unit, called "Energy box", containing a heat pump, an inertial storage, two expansion tanks and measurement instruments.

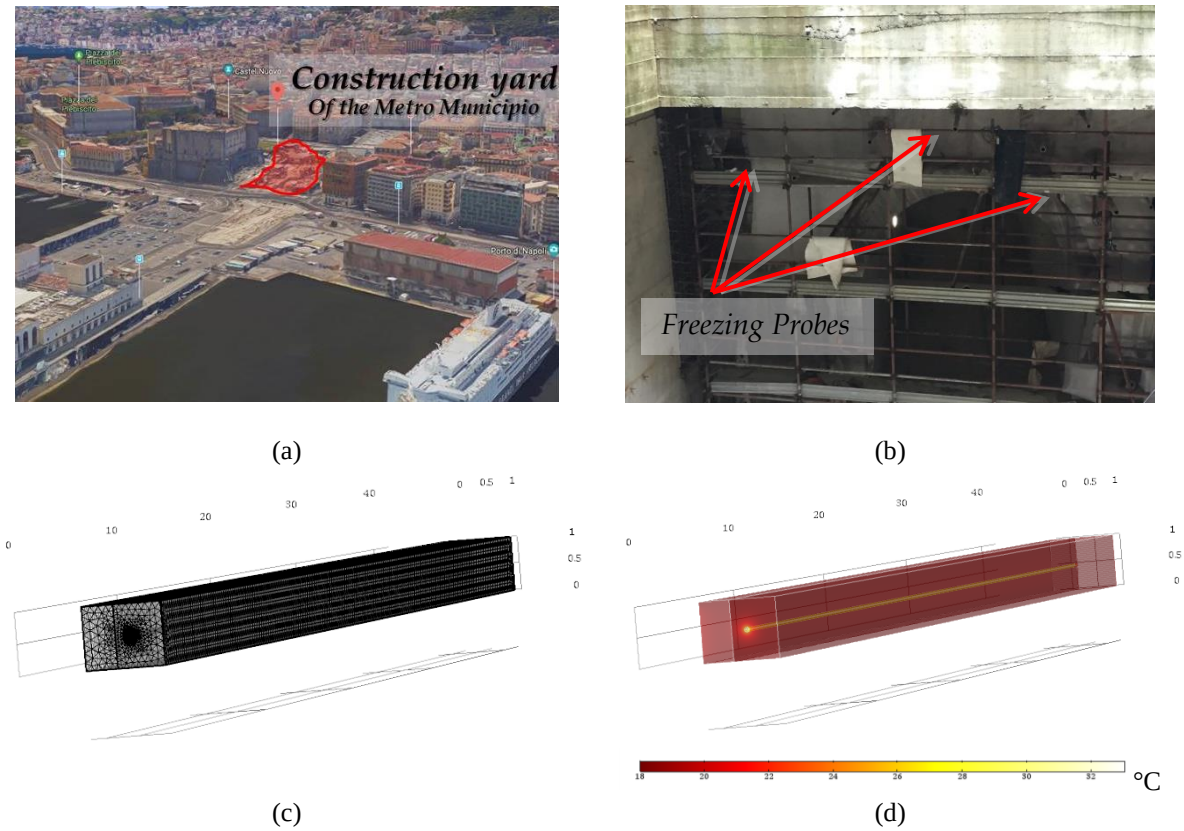


(a) (b)

(c) (d)

Figure 1. (a) Installation site of the geothermal plant; (b) details of the freezing probes; (c) mesh; (d) heat transfer in the soil.

All the pipes are hermetically sealed, to avoid possible dispersion of refrigerant fluid in the subsoil. In this work, in order to obtain the best energy performance of the system, different geometric configurations of the freezing probes have been evaluated, considering the following conditions: (i) a U-shaped HDPE probe with a diameter of 25 mm, in inside the 76 mm tube; (ii) a double-U shaped HDPE probe with a diameter of 25 mm, in inside the 76 mm tube.

## 3. MATHEMATICAL MODEL

The thermo-fluid dynamic numerical model developed by some of the authors, and validated against experimental and numerical data available in the literature [3], has been here applied to the study of the one-dimensional heat and mass transfer in the probe and the three-dimensional heat transfer in the soil for the present innovative system. Comsol Multiphysics has been used to solve the time dependent governing equations. The ground subdomain has a depth of 45 m, a width of 5.0

m and a length of 5.0 m, and can be considered sufficiently large to avoid thermal interference with the neighbouring geothermal probes.
To solve the heat and mass transfer in the soil, the following energy conservation equation has been considered:
Energy conservation equation:

$$\rho_s c_s \frac{\partial T}{\partial t} - \nabla\left(k_s \nabla T\right) + \rho c_p u \nabla T = 0 \tag{1}$$

In order to reproduce the convective heat transfer within the fluid domain, the continuity equation, the momentum equation and the energy conservation equation have been solved.

Continuity equation:

$$\frac{\partial\left(A\rho\right)}{\partial t} + \frac{\partial(A\rho u)}{\partial z} = 0 \tag{2}$$

Momentum conservation equation:

$$\frac{\partial\left(A\rho\right)}{\partial t} = -\frac{\partial p}{\partial z} - f_d \frac{\rho}{2D_k} u|u| \tag{3}$$

Energy conservation equation:

$$\frac{\partial\left(\rho_f A c_f T\right)}{\partial t} + \frac{\partial\left(\rho_f A c_f u T\right)}{\partial z} = \frac{\partial}{\partial z}\left(A k_f \frac{\partial T}{\partial z}\right) + f_d \frac{\rho}{2D_h}|u|^3 + Q_{wall} \tag{4}$$

$Q_{wall}$ (W/m) is the thermal power exchanged through the walls of the probe, has been calculated as:

$$Q_{wall} = k_T\left(T_e - T\right) \tag{5}$$

where:

$$k_T = \frac{1}{\frac{1}{A_{\text{int}} h_{\text{int}}} + \frac{1}{A_{ext} h_{ext}} + \sum_n \frac{\ln\left(\frac{r_n}{r_{n-1}}\right)}{2\pi L k_n}} \tag{6}$$

## 4. RESULTS AND DISCUSSION

The numerical results obtained are reported in Figure 2, in terms of heat transfer rate between probe and ground for each probe configuration, considering different operating conditions, i.e. varying the volumetric flow rate. In particular, the configurations of the probes considered are coaxial, U-shape and double U-shaped. The results refer to summer operating conditions (cooling): the input temperature of the inlet fluid in the probes is set to 35 °C, and the flow rate has been varied in order

to evaluate the optimal operating conditions. In the case of double U-shaped probe, the flow rate refers to one of the two probes. From the analysis of the figure, it is clear that the coaxial configuration offers the best performance in terms of heat transfer.

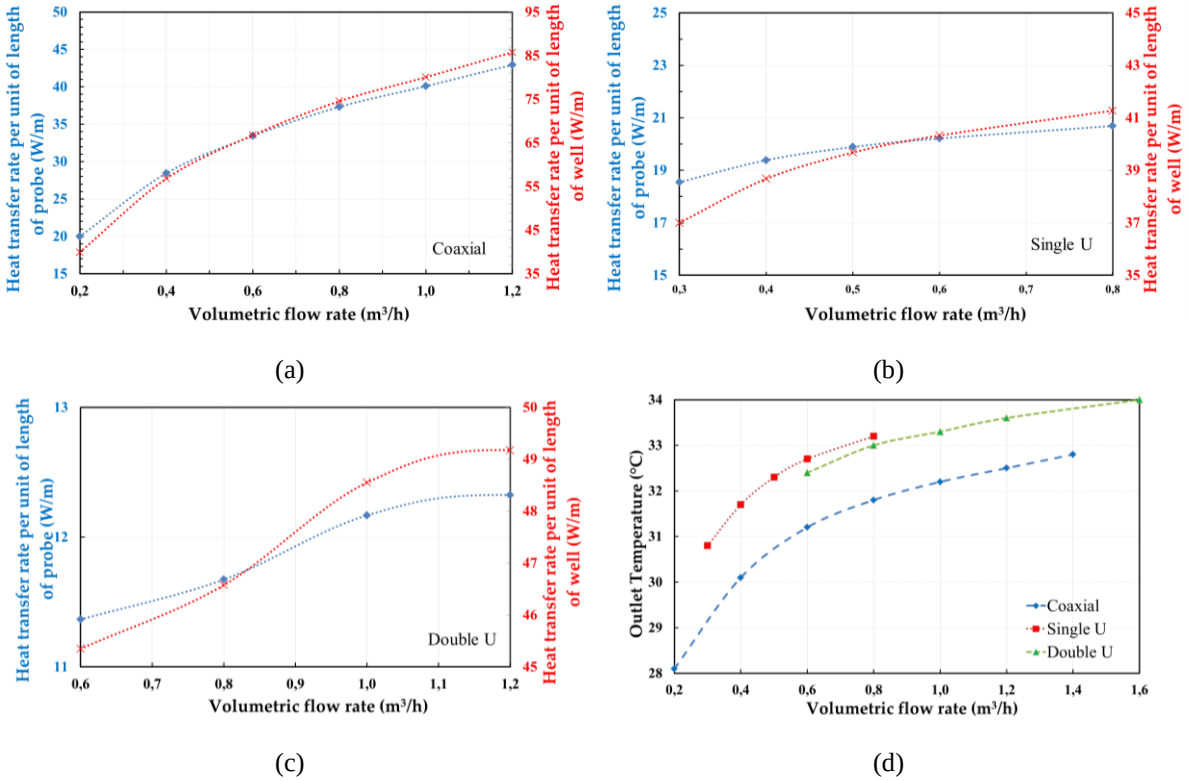


Figure 2. Heat transfer rate per unit of length of probe (left axis) and of well (right axis) for: (a) coaxial probe; (b) single U; (c) double U; and (d) temperature trend for different geometric configurations.

## 5. CONCLUSIONS

The present work reports the numerical results obtained for an innovative geothermal system developed by the authors for recovering the freezing probes employed for the Artificial Ground Freezing of the two tunnels between Line 1 and Line 6 of the new Metro station in Piazza Municipio, Napoli. The obtained results show that the coaxial probe configuration ensures the best performance in terms of heat transfer rate extracted from the soil, while the single U and double U configurations provide similar results.

## ACKNOWLEDGMENTS

The authors gratefully acknowledge the financial support of GeoGrid project PON03PE_00171_1, and both Ansaldo STS | A Hitachi Group Company and in particular Eng. Giuseppe Molisso and MetroTec Scarl for the technical support.

## REFERENCES

[1] A. Carotenuto, N. Massarotti, A. Mauro, A new methodology for numerical simulation of geothermal down-hole heat exchangers, *Applied Thermal Engineering*, 48, 225-236, 2012.

[2] M. Adinolfi, A. Mauro, R.M.S. Maiorano, N. Massarotti, S. Aversa, Thermo-mechanical behaviour of energy pile in underground railway construction site, *Proceedings of the 1st International Conference on Energy Geotechnics*, ICEGT 2016, pp. 83-88.

[3] A. Carotenuto, P. Marotta, N. Massarotti, A. Mauro, G. Normino, Energy piles for ground source heat pump applications: Comparison of heat transfer performance for different design and operating parameters, *Applied Thermal Engineering*, vol. 124, pp. 1492–1504, 2017.

Fifth International Conference on Computational Methods for Thermal Problems
THERMACOMP2018, July 9-11, 2018, Indian Institute of Science, Bangalore, INDIA
*N. Massarotti, P. Nithiarasu, Pradip Dutta and C. Ranganyakalu (Eds.)*

# A Numerical Investigation of Heat Transfer Enhancement in Nanofluids Flow in a Parallel Plate Channel Subjected to Constant Heat Flux

**Saptarshi Mandal**, **P.S. Ghoshdastidar***
Department of Mechanical Engineering,
Indian Institute of Technology Kanpur
Kanpur, U.P. 208016 INDIA
*Corresponding Author. E-Mail: psg@iitk.ac.in

ABSTRACT

This paper presents a finite-difference based numerical investigation of heat transfer in Alumina-water and Titania-water nanofluids flow between parallel plates subjected to constant equal/unequal heat fluxes, based on homogeneous and heterogeneous flow models. Stream function-Vorticity approach has been used to solve the problem. It is found that the nanofluids give rise to larger enhancement factor (the ratio of local heat transfer coefficient in nanofluid to that in base fluid) when both base fluid and nanofluid flows have equal Reynolds number. On the other hand, the enhancement factor is very small or even less than one when both base fluid and nanofluid flows have equal inlet velocity. Brownian diffusion and Thermophoresis are found to have negligible effects on the temperature profiles. On the whole, Alumina-Water nanofluid gives rise to greater enhancement in heat transfer coefficient as compared to Titania-Water nanofluid.

**Keywords:** Nanofluid, Parallel Plate Flow, Homogeneous Model, Buongiorno Model, Particle Migration, Brownian Diffusion, Thermophoresis

## 1. INTRODUCTION

Nanofluids are engineered colloids in which nanoparticles of 1-100 nm diameter are stably dispersed in a base fluid. They have abnormally high thermal conductivity and viscosity with respect to the base fluid. Three nanofluids models that are widely found in literature are: (i) Homogeneous Flow Model [1], (ii) Dispersion Model [2], and (iii) Non-homogeneous Flow Model [3]. The *homogeneous flow model* assumes that the mass, momentum and energy equations are directly applicable for the nanofluid with the thermophysical properties based on bulk weighted volume fraction of nanoparticles with no slip between base fluid and nanoparticles. The *dispersion model* says that the enhancement of heat transfer is achieved due to higher thermal conductivity and energy carried by the dispersion of nanoparticles. The *Non-homogeneous flow model* proposed by Buongiorno [3] considers slip between base fluid and nanoparticles mainly due to the two slip mechanisms such as Brownian diffusion and thermophoresis.

Although several works on heat transfer in the tube flow of nanofluids [4-6] have been found in literature, the same for parallel plates are scanty. Recently, Rossi di Schio et al. [7] used the Buongiorno model to investigate by the finite element method steady, laminar heat transfer in parallel plate flow of nanofluids with wall temperature varying linearly and periodically. The authors found that in the case of linearly varying wall temperature nanoparticle concentration influenced the temperature distribution very little. On the contrary, the periodically varying wall temperature gave rise to non-homogeneities in the nanoparticle concentration, and hence, the use of homogeneous model would not be appropriate.

## 2. OBJECTIVES

The objectives of the present work are: (a) to see the variation of enhancement factor (the ratio of heat transfer coefficient in nanofluid to that in base fluid) along the length of the channel based on the heterogeneous flow model of Buongiorno [3] in which temperature dependent viscosity and thermal conductivity are considered as

well as the homogeneous flow model of Choi [1] in which the aforesaid properties are taken as independent of temperature; and (b) to carry out a detailed parametric study with nanoparticle concentration as the variable keeping same Re (Re is based on the spacing between the walls) and same inlet velocity for both nanofluid and base fluid.

## 3. PROBLEM FORMULATION AND SOLUTION METHODOLOGY

Figure 1 shows the physical problem and the coordinate system. The velocity, temperature and nanoparticle concentration are uniform at the inlet. The flow is laminar, steady and 2D. Stream function-Vorticity approach has been used since the problem is two-dimensional and pressure calculation is not required in this study. The *False Transient Method* using pure implicit finite-difference scheme has been applied to solve the coupled governing eqs. (1) - (4) simultaneously. Constant heat flux boundary condition has been used for the energy equation. Walls are considered to be impermeable with no mass flux across the boundaries. The flow, heat and mass transfer are considered to be fully developed at the exit. While the length of the domain is taken as 1 m the gap between plates is 3 mm (0.003 m). Four different wall heat flux ratios $q''_{w2}/q''_{w1}$ such as 1.0, 1.5, 0.5 and 0 have been used ($q''_{w1} = 5000$ W/m$^2$). The diameter of the nanoparticles is considered to be 15 nm. Thermal conductivity and viscosity are calculated based on the correlations of Buongiorno [3] developed from Pak and Cho [6]. Alumina-Water and Titania-Water nanofluids with volume fractions ranging from 1% to 5%, are investigated in this study. The non-dimensional parameters and the governing equations are given below.

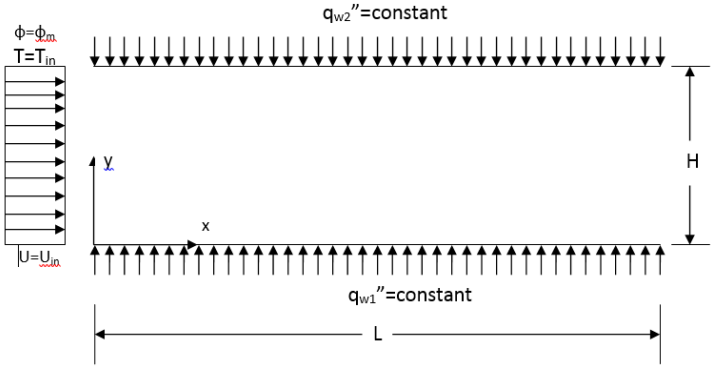


**Fig.1** The physical problem and the coordinate system

Non-dimensional parameters are defined as follows:

$$\Omega^* = \frac{\Omega H}{U_o},\ \Psi^* = \frac{\Psi}{U_o H^2},\ \theta = \frac{T - T_i}{q''_{w_1} H / \mu_{nf,o}},\ \phi^* = \frac{\phi}{\phi_m},\ x^* = \frac{x}{H},\ y^* = \frac{y}{H},\ t^* = \frac{U_o t}{H},\ V_r^* = \frac{V_r}{U_o},\ V_z^* = \frac{V_z}{U_o},\ \left(D_T/T\right)^* = \frac{D_T/T}{D_{T_o}/T_i},$$

$$D_B^* = D_B/D_{B_o},\ \mu_{nf}^* = \mu_{nf}/\mu_{nf,o},\ k_{nf}^* = k_{nf}/k_{nf,o}$$

The following non-dimensional numbers are used:

$$\mathrm{Re} = \frac{\text{Inertia Force}}{\text{Viscous Force}} = \frac{\rho_{nf,o} U_o H}{\mu_{nf,o}},\quad \mathrm{Pr} = \frac{\textit{momentum diffusivity}}{\text{thermal diffusivity}} = \frac{\nu_{nf,o}}{\alpha_{nf,o}},\ Le = \frac{\text{Thermal Diffusivity}}{\text{Brownian Diffusivity}} = \frac{k_{nf,o}}{\rho_p c_{p,p} D_{Bo} \phi_o},$$

$$Sc = \frac{\text{Momentum Diffusivity}}{\text{Brownian Diffusivity}} = \frac{\nu_{nf,o}}{D_{B_o}},\quad N_{BT} = \frac{\text{Brownian Diffusivity}}{\text{Thermophoretic Diffusivity}} = \frac{\rho_p c_{p,p} D_{B_o} \phi_o k_{nf,o}}{D_{T_o} q''_{w_1} H}$$

Brownian and thermophoretic diffusion coefficients are described as:

$$D_{Bo} = \frac{k_B T_i}{3\pi \mu_{bf} d_p},\ D_{To} = \beta \frac{\mu_{bf}}{\rho_{bf}} \phi_o \qquad \text{where } \beta = \frac{0.26 k_{bf}}{2k_{bf} + k_p}$$

**Stream function equation**

$$\frac{\partial^2 \psi^*}{\partial x^{*2}} + \frac{\partial^2 \psi^*}{\partial y^{*2}} = -\Omega^* \tag{1}$$

**Vorticity transport equation**

$$\frac{\partial \Omega^*}{\partial t^*} + u^* \frac{\partial \Omega^*}{\partial x^*} + v^* \frac{\partial \Omega^*}{\partial y^*} = \frac{\mu^*_{nf}}{\mathrm{Re}} \left( \frac{\partial^2 \Omega^*}{\partial x^{*2}} + \frac{\partial^2 \Omega^*}{\partial y^{*2}} \right) + \frac{2}{\mathrm{Re}} \left( \frac{\partial \mu^*_{nf}}{\partial x^*} \frac{\partial \Omega^*}{\partial x^*} + \frac{\partial \mu^*_{nf}}{\partial y^*} \frac{\partial \Omega^*}{\partial y^*} \right) - \frac{4}{\mathrm{Re}} \frac{\partial^2 \mu^*_{nf}}{\partial x^* \partial y^*} \frac{\partial^2 \psi^*}{\partial x^* \partial y^*} + \frac{1}{\mathrm{Re}} \left( \frac{\partial^2 \psi^*}{\partial y^{*2}} - \frac{\partial^2 \psi^*}{\partial x^{*2}} \right) \left( \frac{\partial^2 \mu^*_{nf}}{\partial x^{*2}} - \frac{\partial^2 \mu^*_{nf}}{\partial y^{*2}} \right) \tag{2}$$

**Nanoparticle continuity equation**

$$\frac{\partial \phi^*}{\partial t^*} + u^* \frac{\partial \phi^*}{\partial x^*} + v^* \frac{\partial \phi^*}{\partial y^*} = \frac{D^*_B}{\mathrm{Re}\, Sc} \left( \frac{\partial^2 \phi^*}{\partial x^{*2}} + \frac{\partial^2 \phi^*}{\partial y^{*2}} \right) + \frac{1}{\mathrm{Re}\, Sc} \left( \frac{\partial D^*_B}{\partial x^*} \frac{\partial \phi^*}{\partial x^*} + \frac{\partial D^*_B}{\partial y^*} \frac{\partial \phi^*}{\partial y^*} \right) + \frac{D^*_T}{\mathrm{Re}\, Sc N_{BT}} \left( \frac{\partial^2 \theta}{\partial x^{*2}} + \frac{\partial^2 \theta}{\partial y^{*2}} \right) + \frac{1}{\mathrm{Re}\, Sc N_{BT}} \left( \frac{\partial D^*_T}{\partial x^*} \frac{\partial \theta}{\partial x^*} + \frac{\partial D^*_T}{\partial y^*} \frac{\partial \theta}{\partial y^*} \right) \tag{3}$$

**Energy equation**

$$\frac{\partial \theta}{\partial t^*} + u^* \frac{\partial \theta}{\partial x^*} + v^* \frac{\partial \theta}{\partial y^*} = \frac{k^*_{nf}}{\mathrm{Re}\, \mathrm{Pr}} \left( \frac{\partial^2 \theta}{\partial x^{*2}} + \frac{\partial^2 \theta}{\partial y^{*2}} \right) + \frac{1}{\mathrm{Re}\, \mathrm{Pr}} \left[ \frac{\partial k^*_{nf}}{\partial x^*} \frac{\partial \theta}{\partial x^*} + \frac{\partial k^*_{nf}}{\partial y^*} \frac{\partial \theta}{\partial y^*} \right] + \frac{D^*_B}{\mathrm{Re}\, \mathrm{Pr}\, Le} \left[ \frac{\partial \phi^*}{\partial x^*} \frac{\partial \theta}{\partial x^*} + \frac{\partial \phi^*}{\partial y^*} \frac{\partial \theta}{\partial y^*} \right] + \frac{D^*_T}{\mathrm{Re}\, \mathrm{Pr}\, Le N_{BT}} \left[ \left( \frac{\partial \theta}{\partial x^*} \right)^2 + \left( \frac{\partial \theta}{\partial y^*} \right)^2 \right] \tag{4}$$

## 4. RESULTS AND DISCUSSION

Figure 2 shows the comparison of non-dimensional analytical and numerical temperature distributions at the channel exit for the wall heat flux ratio of 1.5 and inlet Re = 500, for pure fluid. Note that $T^* = (T_{w1} - T)/(T_{w1} - T_m)$, where $T_m$ is the mean fluid temperature. The slight difference between analytical and the present solution may be attributed to the consideration of temperature dependence of the thermophysical properties in the latter. Figure 3 reveals that far downstream heat transfer coefficient in alumina-water nanofluid can fall below that in base fluid thus giving rise to enhancement factors less than 1. It is also noted that Buongiorno model predicts lower enhancement in the fully developed region as compared to homogeneous model. A similar trend is also seen for titania-water nanofluid. Figure 4 demonstrates that the same nanofluid which gives rise to higher enhancement for the case of same Re (Re =1000) in both base and nanofluids flow, produces lower enhancement in the case of equal inlet velocity (0.3 m/s) in both base and nanofluids flow. This is due to the fact that if nanofluid and base fluid have to flow at the same Re, then due to higher viscosity of nanofluid it has to flow at much higher inlet velocity to achieve the same Re. For the same inlet velocity, Re for alumina-water is 268 and for titania-water it is 756. However, alumina-water always produces higher enhancement in heat transfer coefficient as compared to titania-water.

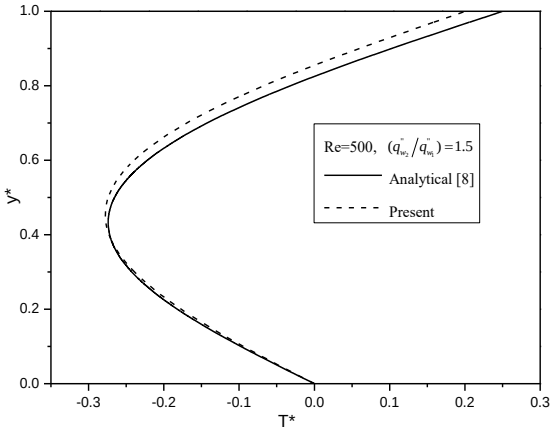


**Fig. 2** Validation of the numerical (present) with the analytical solution for pure fluid at Re=500 and wall heat flux ratio=1.5

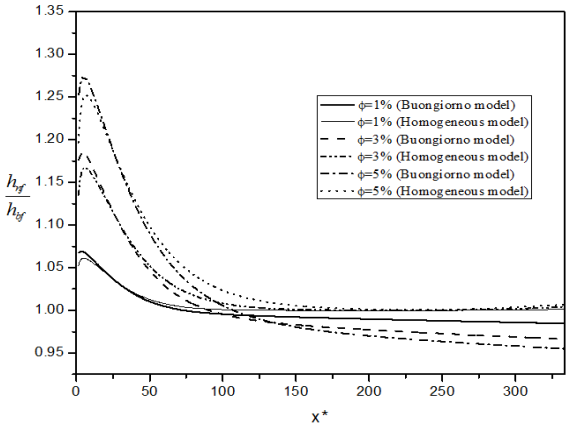


**Fig. 3** Comparison of enhancement factors for alumina-water nanofluid at Re = 100 and wall heat flux ratio = 1, based on homogeneous and Buongiorno models

Figure 5 clearly depicts the effects of thermophoresis. At the wall heat flux ratio of 0.5, since the heat flux at the upper wall is half of that at the lower wall, the nanoparticles migrate towards the upper wall causing higher viscosity near the upper wall, which result in slower motion of the alumina-water nanofluid there and subsequent reduction in heat transfer coefficient, and consequently, less percent enhancement as compared to that at the lower wall. The opposite is true for the case of wall heat flux ratio of 1.5.

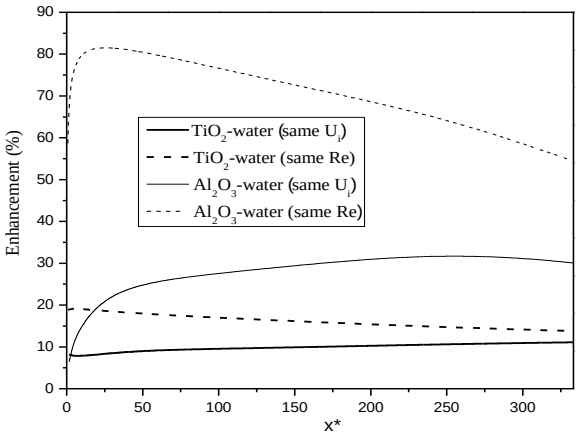


**Fig. 4** Comparison of percent enhancement in heat transfer coefficient at same inlet velocity ($U_i$=0.3 m/s) and same Reynolds number (Re=1000) for alumina-water and titania-water nanofluids at wall heat flux ratio=1

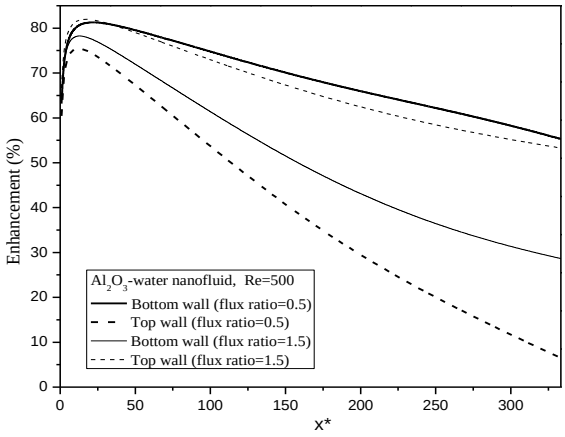


**Fig. 5** Heat transfer enhancement at the top and bottom walls at different wall heat flux ratios

## 4. CONCLUSIONS

It can be concluded from the present numerical study that the difference between the enhancement factors based on the homogeneous and heterogeneous models is marginal, enhancement in heat transfer coefficient computed from the homogeneous model being slightly higher. The nanoparticle migration effect due to Brownian diffusion and thermophoresis on the heat transfer is visible, but not significant. A nanofluid which gives higher enhancement in heat transfer coefficient for equal inlet Reynolds number for both base and nanofluids, produces much lower enhancement for the case of equal inlet velocity for both base and nanofluids.

## REFERENCES

[1] S. Choi, Enhancing thermal conductivity of fluids with nanoparticles, *Developments and Applications of Non-Newtonian Flows*, D.A. Siginer, and H.P. Wang, eds., ASME, New York, FED-Vol. 231/MD-Vol.66, 99-105, 1995.

[2] Y. Xuan, and W. Roetzel, Conceptions for heat transfer correlation of nanofluids, *International Journal of Heat and Mass Transfer*, 43, 3701-3707, 2000.

[3] J. Buongiorno, Convective transport in nanofluids, *ASME Journal of Heat Transfer*, 128, 240-250, 2006.

[4] B. C. Pak, and Y. I. Cho, Hydrodynamic and heat transfer study of dispersed fluids with submicron metallic oxide particles, *Experimental Heat Transfer*, 11,151-170, 1998.

[5] D. Wen, and Y. Ding, Experimental investigation into convective heat transfer of nanofluids at the entrance region under laminar flow conditions, *International Journal of Heat and Mass Transfer*, 47, 5181-5188, 2004.

[6] A. T. Utomo, E. B. Haghighi, A. I. T. Zavareh, M. Ghanbarpourgheravi, H. Poth, R. Khodabandeh, B. Palm, A. W. Pacek, The effect of nanoparticles on laminar heat transfer in a horizontal tube, *International Journal of Heat and Mass Transfer*, 69, 77-91, 2014.

[7] E. Rossi di Schio, M. Celli, and A. Barletta, Effects of Brownian diffusion and thermophoresis on the laminar forced convection of a nanofluid in a channel", *ASME Journal of Heat Transfer*, 136 (2), p. 022401, 2014.

[8] J. Sheela Francisca, and C. P. Tso, Viscous dissipation effects on parallel plates with constant heat flux boundary conditions, *International Communications in Heat and Mass Transfer*, 36, 249-254, 2009.

Fifth International Conference on Computational Methods for Thermal Problems
THERMACOMP2018, July 9-11, 2018, Indian Institute of Science, Bangalore, INDIA
*N. Massarotti, P. Nithiarasu, Pradip Dutta and C. Ranganyakalu (Eds.)*

# CFD Simulation of Inertance tube Pulse Tube Refrigerator with variable cross section of regenerator and pulse tube

**Pankaj Kumar, Anjuni Kujur, Amitesh Kumar, R.K. Sahoo**
Department of Mechanical Engineering, NIT, Rourkela, Odisha-769008
E-mail- pankajcryo@gmail.com, kujur.anjuni@gmail.com, kumaamitesh@nitrkl.ac.in, rksahoo@nitrkl.ac.in

## ABSTRACT

The computational fluid dynamics simulation of inertance tube pulse tube refrigerator with linear cross section and variable cross section of regenerator and pulse tube are presented in this paper. Volume of regenerator and pulse tube were kept same as linear cross section of regenerator and pulse tube for all cases. Five models with different cone angles and variable length of the convergent or divergent type regenerator and pulse tube were designed for each case. To optimize the cone angle where the performance of the inertance tube pulse tube refrigerator is maximum, two models were introduced to simulate two kinds of pulse tube refrigerator with tapered regenerator and tapered pulse tube. The linear inertance tube pulse tube refrigerator was simulated to validate with Cha et. al. model. The variable cross section regenerator inertance tube pulse tube refrigerator model and variable cross section pulse tube inertance tube pulse tube refrigerator model were simulated to find out the existence optimum cone angle for tapered regenerator and tapered pulse tube separately. The simulation results showed that convergent type of regenerator improves system performance by improving cooling power and COP of the inertance tube pulse tube refrigerator. Similarly, it is shown that divergent type pulse tube is used to improve the performance of the system.

**Key Words:** *Inertance tube pulse tube refrigerator, Tapered regenerator, Tapered pulse tube, Computational fluid dynamic simulation, Enthalpy flow theory.*

## 1. INTRODUCTION

The inertance tube pulse tube refrigerator (ITPTR) is a new development to the pulse tube refrigerator. The inertance tube pulse tube refrigerator is classified under stirling type cryocoolers. Thus the application of stirling type cryocoolers in space are under development within the temperature range from 30K to 80K. The most commonly used applications of pulse tube refrigerators are infrared sensors for surveillance, infrared sensors for aircrafts right vision, cooling sensitive detectors in satellites, and in earth observation instruments. The former stirling type pulse tube refrigerator was invented by Gifford and Longsworth [1]. The long small tube called as inertance tube is responsible for creating phase difference between pressure and mass flow rate of the working fluid. Cha et al. [2] has done two sets of computational fluid dynamics (CFD) simulation with variable dimensions of inertance tube pulse tube refrigerator components. He found that larger length-to-diameter ratio should be considered to avoid secondary circulation flow or vertices created by the working fluid. In order to improve the refrigerating efficiency and the Cooling Power of two different models in inertance tube pulse tube refrigerator have been introduced [3,4]. Now, most of the researchers focus on improving efficiency by changing dimensions and parameters of the inetance tube pulse tube refrigerator. But regenerator and pulse tube are the two important components for performance improvement of the pulse tube refrigerator. Therefore, the present work is based on a further research and computational simulation of inertance tube pulse tube refrigerator. It was found that the performance of the pulse tube refrigerator can be improved by increasing the cooling power and increasing enthalpy flow in pulse

tube at the same refrigeration temperature using tapered regenerator or tapered pulse tube with a certain cone angle in the inertance tube pulse tube refrigerator.

## 2. PROBLEM FORMULATION

Three ITPTR systems, referred to as Case1, Case2 and Case3, were simulated by using commercial fluent software, fluent15.0. A schematic of case1 ITPTR system is shown in fig.1 (a) and all the geometric dimensions are taken from Cha et al. [2] model. All the geometric dimension of different components in ITPTR system for case1 used in fig.1 (a) are taken by the cha et al. [2].

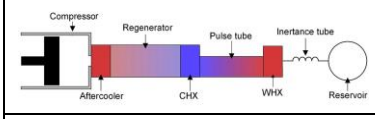


Fig.1(a).Case1 simulated ITPTR system.

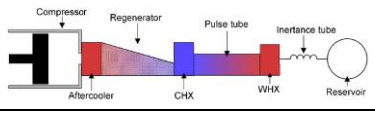


Fig.1(b). Case2 simulated ITPTR system.

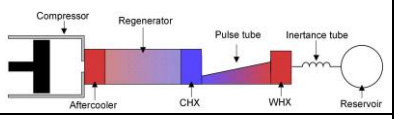


Fig.1(C). Case3 simulated ITPTR system.

The system designed as Case1 is identical to MOD1 Cha et al. model [2]. Case1 ITPTR system is simulated to validate the ITPTR system. All the component dimensions for Case2 and Case3 ITPTR system used in fig.1 (b) and (c) are listed in table 2. Case2 system is designed identical to the CFD simulation model of Liu Ying-wen [5] with the exception that Case1 includes an inertance tube (IT) instead of an orifice and a double-inlet valve. The Case3 system is designed is similar to Case2, except the regenerator and pulse tube structure and their dimensions. It is based on the computational simulation of tapered pulse tube introduced by Sang Ho Baek and his co-workers [6].

| **Study Case** | | **Case2 (Regenerator)** | **Case3 (Pulse tube)** |
|---|---|---|---|
| Mode1 | R1 (m) | 0.004 | 0.0025 |
| | R2 (m) | 0.003 | 0.001 |
| | L (m) | 7.52E-05 | 1.15E-04 |
| Mode2 | R1 (m) | 0.004 | 0.0025 |
| | R2 (m) | 0.005 | 0.003 |
| | L (m) | 4.57E-05 | 4.95E-05 |
| Mode3 | R1 (m) | 0.004 | 0.0025 |
| | R2 (m) | 0.006 | 0.0035 |
| | L (m) | 3.66E-05 | 4.13E-05 |
| Mode4 | R1 (m) | 0.004 | 0.0025 |
| | R2 (m) | 0.007 | 0.004 |
| | L (m) | 2.99E-05 | 3.49E-05 |
| Mode5 | R1 (m) | 0.004 | 0.0025 |
| | R2 (m) | 0.008 | 0.0045 |
| | L (m) | 2.49E-05 | 2.98E-05 |

Table: Tapered regenerator and tapered pulse tube dimensions (R1 and R2 is the radius of regenerator or pulse tube at their left and right end respectively, L is the length of regenerator or pulse tube)

Five different operational modes were simulated for Case1 and Case2 each, as shown in the table 1.

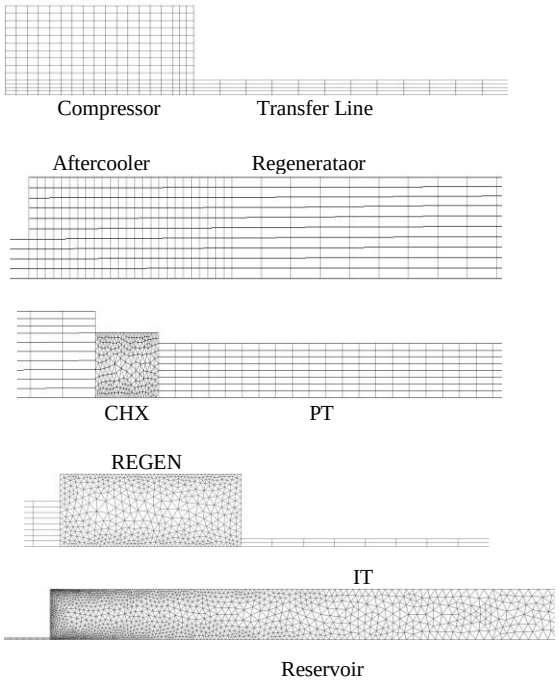


Fig.2 Nodalization of Case1 simulated system.

## 3. CFD SIMULATION

The simulation of ITPTR systems were done on a commercial package, Fluent15.0. Given assumptions were cylindrical and linear alignments of the components of ITPTR systems, axis-symmetric model, double precision, and two-dimensional flow. A simple user defined function

(UDF) written in C language was linked to the piston for piston head motion. The velocity UDF for piston head motion is modelled as:

$X = X_{amp} \times \sin(\omega t)$ ---------(1) Where $\omega$ = 213.62 rad/s, $X_{amp}$ = 4.511 × $10^{-3}$ m, and time increment $t$ = 7.3529 × 10-4 sec were assumed. Fluent has the advantage of dynamic meshing function. This function was utilized to create deformable mesh in the compressor during simulation of ITPTR systems. The exact number of nodes for Case1 ITPTR system is 4182. The ITPTR system consists of both porous and non-porous media. Thus, to get accurate results porous medium components were simulated by porous medium governing equations. The mass, momentum and energy equations solved by Fluent for compressor, tansferline, pulse tube, inertance tube and surge volume are

| | |
|---|---|
| $\frac{\partial \rho}{\partial t} + \frac{1}{r}\frac{\partial}{\partial r}(r\rho_f v_r) + \frac{\partial}{\partial x}(\rho_f v_x) = 0$ ----------(2) | $\frac{\partial}{\partial t}(\rho_f \vec{v}) + \nabla.(\rho_f \vec{v}\vec{v}) = -\nabla p + \nabla.[\bar{\bar{\tau}}]$ ----------(3) |
| $\frac{\partial}{\partial t}(\rho_f E) + \nabla.\left(\vec{v}(\rho_f E + p)\right) = \nabla.(k_{eff}\nabla T + (\bar{\bar{\tau}}.\vec{v}))$ -----(4) | |

Where

$$E = h - \frac{p}{\rho} + \frac{v^2}{2} \quad (5)$$

All properties used in the above equations represent the properties of helium. Rest of the ITPTR system components such as after cooler, regenerator, CHX and HHX are modeled as porous media. $\emptyset$ = 0.69, $\bar{\bar{\beta}}$ = 1.06 × $10^{-10}$ $m^2$, and $\bar{\bar{C}}$ = 7.609 × $10^4$ $m^{-1}$ were assumed. These parameters values are taken from Cha et al. [2]. All the simulations were done as transient and turbulent flow processes with a system initial temperature of 300K. The simulations were done till the steady periodic condition of cycle-average temperature at the cold end wall temperature of CHX.

## 4. RESULTS AND DISCUSSIONS

*1.Validation*

The variations of the cycle-average temperature at the CHX surface are shown in fig.2(a) for Case1 and Cha et al. model. The case1 ITPTR model is validated against Cha et al. simulated model. The steady state temperature at the cold end of the cold heat exchanger for Case1 is found to be 84K from the simulation.

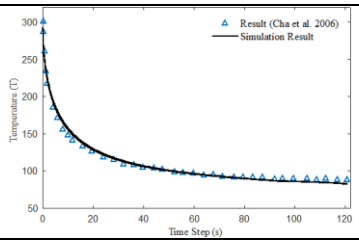


Fig.2(a). Temporal variation of cycle average CHX surface temperature for simulation Case1.

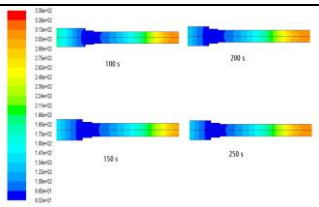


Fig.2(b). Temperature variation in pulse tube section.

From the graph, it is found that for a given geometry with same dimensions, same boundary and initial conditions the weighted average temperature variation at the CHX wall has slight deviation. Heat transport phenomenon due to oscillating pressure in the pulse tube is dependent on the flow time. Its variation changes as the flow time changes. It is most important to study the variation of pressure and temperature in pulse tube section. Temperature variation in the pulse tube section at four different times of 100 s, 150 s, 200 s and 250 s are shown in fig.2(b). The temperature variation in the pulse tube section is almost similar for four different times. Hence, from temperature and pressure variations graph, it is concluded that the temperature and pressure variations in pulse tube section are similar at given four different flow times in linear ITPTR system.

*2. Case2 simulation results and discussions*

Tapered regenerator of five different ITPTR model with different cone angles is simulated. Pressure

variation in pulse tube section at different flow times for optimized cases are shown in fig.3(a). The change of pressure in the pulse tube section is increasing as the flow time increasing.

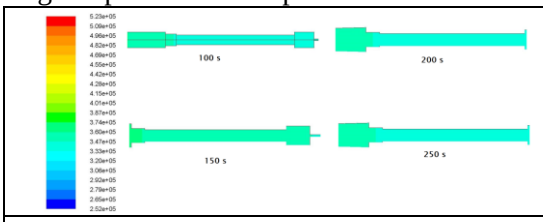


Fig.3 (a). Pressure variations in pulse tube section of Mode2 tapered regenerator ITPTR system.

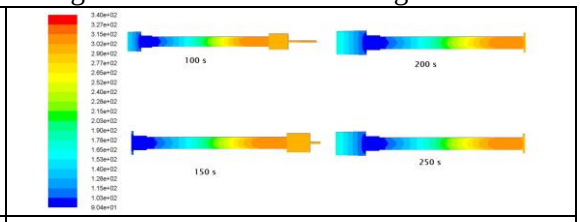


Fig.3 (b). Temperature variation in pulse tube section for Model2 tapered regenerator ITPTR system.

Temperature variations in pulse tube section at four different flow times of 100 s, 150 s, 200 s, and 250 s out of five cases the best temperature contour are shown in fig.3 (b).

The performance parameters like cooling effect, DC-mass flow rate and Coefficient of performance are plotted against the cone angle for optimized models of tapered regenerator ITPTR system. The graphs are shown in fig.4 and discussed in details.

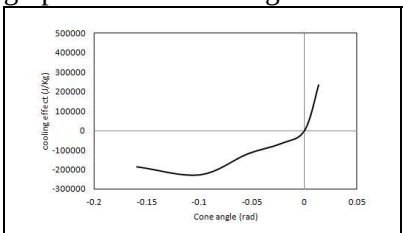


Fig.4(a). Effect of cone angle of the tapered regenerator on cooling effect.

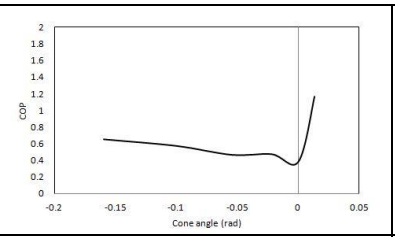


Fig.4(b). Effect of cone angle of the tapered regenerator on COP.

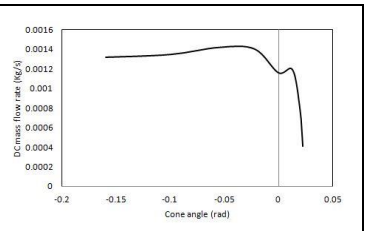


Fig.4(c). Effect of cone angle of the tapered regenerator on DC-mass flow rate.

The cooling effect is maximum at an optimum cone angle of 0.01 radian of the regenerator. The performance of the system can be increased by increasing the coefficient of performance while decreasing the DC-mass flow rate of the regenerator to enhance performance of the regenerator which increases system performance. The above graph shows a maximum COP and minimum DC-mass flow rate at an optimum cone angle. As moving towards the converging cone angle the pressure and velocity amplitude are increasing. The enthalpy flow in regenerator and pulse tube sections are shown and found that for a minimum enthalpy flow in regenerator there exists corporately higher enthalpy flow in the pulse tube section. To achieve a minimum temperature at the CHX wall there exists an optimum cone angle of the tapered regenerator. From the graph of CHX temperature against the cone angle, it is found that -0.001 radian is an optimum cone angle of tapered regenerator to achieve low temperature at the CHX wall.

3. *Case3 Simulation results and discussions*

The pressure variations in divergent type pulse tube is higher than the pressure variations in convergent type pulse tube. The results for temperature variation in pulse tube section for five different models with different cone angles are taken and compared at four different flow time of 100 s, 150 s, 200 s, and 250 s for each case. The fig.5(a) shows the temperature variations.

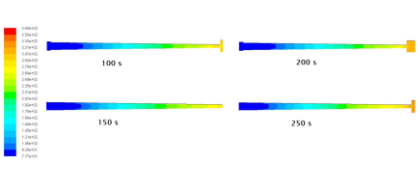


Fig.5(a). Temperature variation in pulse tube section of Mode1 tapered pulse tube ITPTR system

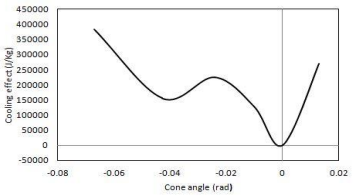


Fig.5(b). Effect of cone angle of the tapered pulse tube on cooling effect.

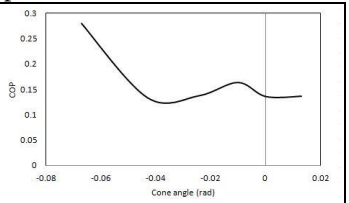


Fig.5(c). Effect of cone angle of the tapered pulse tube on COP.

From the above temperature variation figures it is seen that the temperature variation contours improve as moving from convergent to divergent type pulse tube in tapered pulse tube ITPTR system. The performance parameters like cooling effect, DC-mass flow rate and Coefficient of performance are plotted against the cone angle for five different models of tapered pulse tube ITPTR system. The graphs are shown in fig.9 and discussed in details.

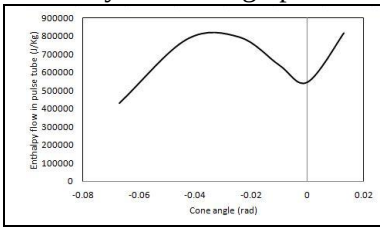


Fig.5(d). Effect of cone angle of the tapered pulse tube on enthalpy flow in pulse tube.

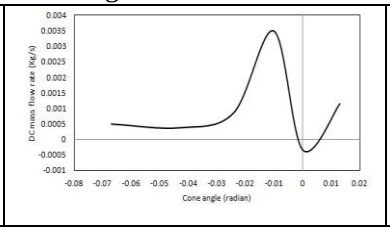


Fig.5(e). Effect of cone angle of the tapered pulse tube on DC-mass flow rate.

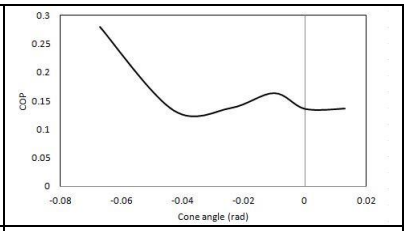


Fig.5(f). Effect of cone angle of the tapered pulse tube on COP.

The graphs show the maximum cooling effect at an approximate cone angle of -0.07 radian of the pulse tube. At that perspective, the COP is maximum and DC-mass flow rate is minimized which is reasonable. Hence, for tapered pulse tube ITPTR system – 0.07 (divergent type) will be considered as optimum angle. The enthalpy flow variation at different cone angles is shown both in regenerator and pulse tube section of tapered ITPTR system. For maximum cooling effect, the enthalpy flow in the pulse tube should be maximum while the enthalpy flow in regenerator should be minimum to neglect losses in regenerator. From the figures it can be seen that at a cone angle of -0.07 minimum enthalpy flow in regenerator and comparatively higher enthalpy flow in pulse tube than in regenerator. The pressure and velocity graph against cone angle shows that at an optimum cone angle of -0.07 (divergent type pulse tube) there exists an improved pressure and velocity amplitude. The higher pressure and velocity amplitude in pulse tube degrades the system performance. Hence, proper should be taken to design tapered pulse tube ITPTR system. The temperature variation in the CHX wall is shown in the figure above. It indicates that there exists a minimum temperature at an angle of -0.04 (divergent type) of the pulse tube. Hence to achieve minimum temperature at the cold end of cold heat exchanger a tapered pulse tube section with an optimum angle of -0.04 should be chosen.

## 5. CONCLUSION

Three different cases of ITPTR are simulated with linear and variable cross section components of regenerator and pulse tube. The losses in the regenerator could be minimized by introducing a tapered regenerator in the inertance tube type pulse tube refrigerator. The enthalpy flow in the pulse tube could be maximized by introducing tapered pulse tube in inertance tube pulse tube refrigerator. Two different type of regenerators including convergent and divergent type are considered for simulation. From the simulation results, it is found that there exists an optimum angle of tapered regenerator where all the performance parameters show maximum value. The optimum angle of the regerator in current study is 0.01 radian (convergent type regenerator). Pulse tube design at an optimum angle of -0.07 (divergent type pulse tube) shows maximum performance of the tapered pulse tube ITPTR system. At this angle, all the performance parameters have maximum value.

## 6. REFERENCES

[1] Gifford WE, Longsworth RC. Pulse tube refrigeration. Trans. ASME ser B 1964;86(1):264-8.
[2] J.S. Cha, S.M. Ghiaasiaan, P.V. Desai, J.P. Harvey, C.S. Kirkconnell. “Multi-dimentional flow effects in pulse tube refrigerators”, Cryogenics 46 (2006), pp.658-665.
[3] zhu S, Wu P, Chen z. Double inlet pulse tube refrigerator: an important improvement. Cryogenics 1990; 30:514-20.
[4] D.L.Gardnerand,G.W. Swift., “Use of inertance in orifice pulse tube refrigerators”, Cryogenics 37 (1997), pp.117-121.
[5] Liu Ying-wen, He Ya-ling. “A new tapered regenerator used for pulse tube refrigerator and its optimization”, Cryogenics 48 (2008), pp.483-491.
[6] Sang Ho Baek, Eun Soo Jeong, Sangkwon. “Two dimentional model for tapered pulse tubes”, Cryogenics 40 (2000), pp.379-385.

Fifth International Conference on Computational Methods for Thermal Problems
THERMACOMP2018, July 9-11, 2018, Indian Institute of Science, Bangalore, INDIA
*N. Massarotti, P. Nithiarasu, Pradip Dutta and C. Ranganyakalu (Eds.)*

# Comparison of Various Thermophysical Property Models of Water-$Al_2O_3$ Nanofluids

Rushabh Y. Patel [a], Niraj K. Shah [b], Anand Bhatt [c]

*Institute of Technology, Nirma University, Ahmedabad, Gujarat, India,*
*15mmet19@nirmauni.ac.in [a], niraj.shah@nirmauni.ac.in [b], anand.bhatt@nirmauni.ac.in [c]*

## ABSTRACT

*Enhancement of heat transfer is possible through many techniques. One of the technique is to improve the properties of heat transfer fluid by adding nanoparticles into it called nanofluids. To estimate heat transfer enhancement theoretically or numerically, input of effective thermophysical properties like density, dynamics viscosity, thermal conductivity and specific heat of nanofluids are required. Analytical models are used to determine these properties. Widely accepted models are available for density and specific heat whereas different models are used to estimate the effective thermal conductivity and dynamic viscosity of nanofluids. The results of effective thermal conductivity and viscosity predicted by various models differ largely. A study is required to find out appropriate models to estimate these two properties. Effective properties of the nanofluids depends upon nanoparticle and base fluid property, nanoparticle size and shape, concentration of nanoparticles and temperature. Present study compares four widely used models of thermal conductivity which are proposed by Maxwell [1], Hamilton and Crosser [2], Yu and Choi [3] and Chon et al. [4] and four dynamic viscosity models, Einstein [5], Brinkman [6], Graham [7] and Maiga et al. [8] for different parameters mentioned above and suggests the most appropriate model based on comparison of predicted and existing experimental property values. Result shows that for thermal conductivity, Chon et al. [4] model predicts better results for different particle fraction and temperature range. Yu and Choi [3] model works well for particle size smaller than 20 nm while for particle size above 25 nm Chon et al. [4] model works well. Maiga et al. [8] model works better for predicting dynamic viscosity for different particle fraction and temperature range*

**Key Words:** *Nano-fluids, Thermophysical properties, Heat transfer enhancement, Analytical models*

## 1. INTRODUCTION

In 1873, J.C. Maxwell has first introduce that mixing of micron sized particles with base fluid can increase thermal conductivity and convective heat transfer. But due to erosion, clogging, rapid sedimentation and high pressure drop it is not used practically. In 1995, Stephen U. S. Choi [9] has first coined the term Nanofluids (i.e., nanoparticle fluid suspensions) at Argonne National Laboratory of USA. Nanofluids are made by suspending nanoparticles having mean sizes below 100nm in conventional heat transfer fluids like oil, water, ethylene glycol, etc.

Nanofluids are solid-liquid composite material consisting of solid nanoparticles suspended in base fluid. All high thermal conductivity material can be used as solid nanoparticles such as metallic particles (Cu, Al, Ag, Fe, Au, etc.) and nonmetallic particles ($Al_2O_3$, CuO, $TiO_2$, SiC, carbon nanotubes, etc.). The base fluids are mostly water, oil, ethylene glycol, acetone etc.

## 2. ANALYTICAL MODELS FOR THERMOPHYSICAL PROPERTIES OF NANOFLUIDS

Thermal conductivity of nanofluids is the most important property which influence heat transfer enhancement. Many researchers have investigated effective thermal conductivity of nanofluids through experiments and based on theoretical model. But there is a variation between the theoretical and experimental results because, the thermal conductivity of nanofluids depends on various parameters such as nanofluid material properties, nanoparticle size and shape, particle concentration, fluid temperature, Brownian motion, turbulence intensification, pH value of nanofluid, etc. and the influence of each of these parameters cannot be examined individually. So, it is very difficult to taken care of all parameters in single analytical model. In the present work, four widely used and different theory based analytical models Maxwell [1], Hamilton and Crosser [2], Yu and Choi [3], Chon et al. [4] are considered to compare and find out an appropriate model under different conditions.

First thermal conductivity model was given by Maxwell [1] for solid-liquid suspension. This model is valid for low volume fraction of solid particles (< 5%).

$$\frac{k_{eff}}{k_b} = \frac{k_p + 2k_b + 2(k_p - k_b)\phi}{k_p + 2k_b - (k_p - k_b)\phi}$$

Hamilton and Crosser [2] introduced the model for non-spherical solid particles in solid-liquid suspension. For sphericity addition they introduced shape factor, n. Shape factor can be defined as n = 3/ψ, ψ is the sphericity. Sphericity can be defined as the ratio of the surface area of a sphere to the volume of the particle. For spherical particles, ψ = 1.

$$\frac{k_{eff}}{k_b} = \frac{k_p + (n-1)k_b - (n-1)(k_b - k_p)\phi}{k_p + (n-1)k_b - (k_b - k_p)\phi}$$

With some modification in Maxwell model Yu and Choi [3] introduced new thermal conductivity model by considering nanolayer thickness in account for thermal conductivity enhancement. β is a ratio of nanolayer thickness to original thickness.

$$\frac{k_{eff}}{k_b} = \frac{k_p + 2k_b + 2(k_p - k_b)(1-\beta)^3\phi}{k_p + 2k_b - (k_p - k_b)(1+\beta)^3\phi}$$

Chon et al. [4] proposed a model which includes effect of nanoparticle size, effect of temperature, effects of Brownian motion, nanoparticles volume fraction and properties of base fluids.

$$\frac{k_{eff}}{k_b} = 1 + 64.7\phi^{0.746}\left(\frac{d_{bf}}{d_p}\right)^{0.369}\left(\frac{k_p}{k_{bf}}\right)^{0.7476} Pr^{0.9955} Re^{1.2321}$$

Dynamic viscosity is an important property for heat transfer and transporting mechanism. In this section four viscosity models, Einstein [5], Brinkman [6], Graham [7] and Maiga et al. [8] model is compared and studied under different condition.

The very first model of dynamic viscosity is proposed by Einstein [5] in 1906. Two assumptions are made while deriving this model one is the volume fraction of solid particles is very less (< 2%) and second is the shape of particles is spherical.

$$\frac{\mu_{nf}}{\mu_{bf}} = 1 + 2.5\phi$$

Brinkman [6] proposed new model of viscosity by extending Einstein's model for use of higher particle concentration. He considered the effect of addition of solute molecule to an existing continuous medium of particle concentrations less than 4 %.

$$\frac{\mu_{nf}}{\mu_{bf}} = \frac{1}{(1-\phi)^{2.5}}$$

Graham [7] proposed a new model for calculating viscosity by introducing new parameters such as, particle radius and inter particle spacing. The effect of particle size is included in this model. The proposed viscosity model is given by,

$$\frac{\mu_{nf}}{\mu_{bf}} = 1 + 2.5\phi + 4.5\left(\frac{1}{\left(\frac{h}{d_p}\left(2+\frac{h}{d_p}\right)\right)(1+\frac{h}{d_p})^2}\right)$$

A new dynamic viscosity model is proposed by Maiga et al. [8]. This model is obtained by performing a least-square curve fitting of experimental data obtained by Wang et al. for water-$Al_2O_3$ nanofluid having particle concentration up to 6%. They have also proposed a model for ethylene glycol-$Al_2O_3$.

$$\frac{\mu_{nf}}{\mu_{bf}} = 1 + 7.3\phi + 123\phi^2$$

## 3. RESULTS

### 3.1 Thermal Conductivity

The effect of particle concentration on effective thermal conductivity is compared with the existing experimental results of Kyo et al. for very low particle concentration (0.01-0.3%) of water- $Al_2O_3$ of diameter (30 $\pm$ 5 nm) at temperature 21°C. As shown in Fig. 1 with increase in particle concentration thermal conductivity ratio (effective conductivity to base fluid conductivity) increases. Models other than Chon et al. [4] failed to match closely the experimental results of Kyo et al. for very low particle concentration range.

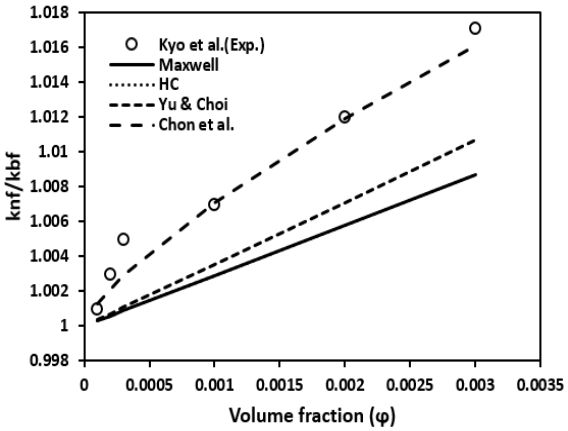


Figure 1. THERMAL CONDUCTIVITY RATIO FOR WATER-$Al_2O_3$ (30 nm) AT 21°C

Similarly thermal conductivity of nanofluids is compared with higher particle concentration, particle size and different fluid temperature.

### 3.2 Dynamic Viscosity

The effect of particle concentration on effective dynamic viscosity is compared with the existing experimental results of Kyo et al. for very low particle concentration (0.01-0.3 %) and with Nguyen et al. for concentration (0.1-0.6%) of water- $Al_2O_3$ of diameter (30 $\pm$ 5 nm) at temperature 21 °C. As shown in Fig. 2 viscosity increases with increase in particle concentration. Maiga et al. [8] model gives better results compare to other models.

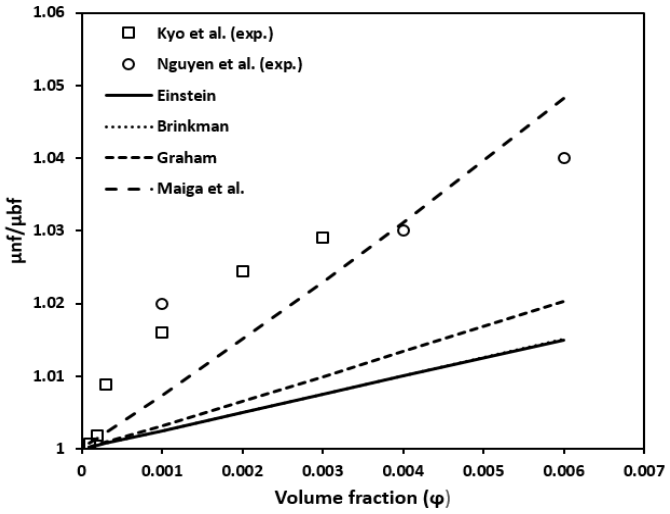


Figure 2. VISCOSITY RATIO FOR WATER-$Al_2O_3$ (0.01-0.6%)

Similarly dynamic viscosity of nanofluids is compared with higher particle concentration and different fluid temperature.

## 4. CONCLUSION

Based on this study following observations and conclusion can be drawn:

- Effective density of nanofluids can be calculated by using widely accepted model which shows excellent agreement with experimental results. For specific heat calculation, it is recommended that to used modified form of model. Because simpler form of specific heat model cannot predict correct value at high particle concentration.
- Chon et al. [4] model predicts better effective thermal conductivity value compared to other conductivity models for various particle concentration and temperature range. Whereas Yu and Choi [3] model predicts better value when particle size is less than 20 nm and for more than 25 nm size Chon et al. [4] model works better.
- For predicting effective dynamic viscosity of nanofluids, Maiga et al. [8] model gives better results compared to other models for different particle concentration. Whereas for different temperature range all models are fail to predict correct value of viscosity. Hence, research work is needed to incorporate temperature effect in viscosity model.

## REFERENCES

[1] Maxwell J. C., 1881, *A Treatise on Electricity and Magnetism*, 2nd ed., Clarendon Press, Oxford, UK.
[2] Hamilton R. L., Crosser O. K., 1962, "Thermal Conductivity of Heterogeneous Two Component Systems", Ind. Eng. Chem. Fundamen., Vol. 1(3), pp. 187–191. DOI: 10.1021/i160003a005
[3] Yu W., Choi S. U. S., 2003, "The Role of Interfacial Layers In The Enhanced Thermal of Nanofluids: A Renovated Maxwell Model", J. Nanoparticle Research, Vol. 5(167), pp. 167–171. DOI: 10.1023/A:1024438603801
[4] Chon C. H., Kihm K. D., Lee S. P, Choi S. U. S., 2005, "Empirical Correlation Finding The Role of Temperature And Particle Size for Nanofluid ($Al_2O_3$) Thermal Conductivity Enhancement", Appl. Phys. Lett., Vol. 87(15), pp. 153107 http://dx.doi.org/10.1063/1.2093936
[5] Einstein A., 1906, Eine neue Bestimmung der Molekuldimensionen, Ann. Phys., Vol. 324, pp. 289–306. doi:10.1002/andp.19063240204
[6] Brinkman H. C., 1952, "The Viscosity of Concentrated Suspensions and Solutions", J. Chem. Phys., Vol. 20, pp. 571. http://dx.doi.org/10.1063/1.1700493
[7] Graham A. L., 1981, On the viscosity of suspensions of solid spheres, Appl. Sci. Res. 37 (3-4) pp. 275–286. doi:10.1007/BF00951252
[8] Maiga S. E. B., Palm S. J., Nguyen C. T., Roy G., Galanis N., 2005, "Heat Transfer Enhancement by Using Nanofluids in Forced Convection Flows", Int. J. of Heat Fluid Flow, Vol. 26 (4), pp. 530–546. https://doi.org/10.1016/j.ijheatfluidflow.2005.02.004
[9] Choi S. U. S., 1995, "Enhancing Thermal Conductivity of Fluids with Nanoparticles", in Developments and Applications of Non-Newtonian Flows, D. A. Siginer and H. P. Wang, ASME, New York, USA FED, Vol. 231, pp. 99–105.

Fifth International Conference on Computational Methods for Thermal Problems
THERMACOMP2018, July 9-11, 2018, Indian Institute of Science, Bangalore, INDIA
*N. Massarotti, P. Nithiarasu, Pradip Dutta and C. Ranganyakalu (Eds.)*

# NON-REACTIVE IN-CYLINDER FLOW SIMULATION FOR A DIESEL ENGINE

**Pavan Prakash Duvvuri**
Combustion Research, Cummins Technical Centre India, Pune, India
Department of Energy Science and Engineering, Indian Institute of Technology Bombay, India
pavan.duvvuri@cummins.com

**Rajesh Kumar Shrivastava**
Combustion Research, Cummins Technical Centre India, Pune, India
rajesh.k.shrivastava@cummins.com

**Sheshadri Sreedhara**
Department of Mechanical Engineering, Indian Institute of Technology Bombay, India
sreedhara.s@iitb.ac.in

## ABSTRACT

Fuel injection and mixture distribution play a vital role in diesel engine combustion. With the future aimed at improved fuel economies, emissions and noise, numerical models capable of capturing spray and mixture distribution accurately assist combustion modelling and facilitate optimized performance by reducing experimental costs. The current study aims at simulating the non-reactive flow of a direct injection diesel engine. Closed cycle simulations have been performed using CONVERGE to model experimental data from the Cummins N14 optical engine at Sandia (Genzale et al., SAE 2009-01-2699). Spray and equivalence ratio from simulations have been compared with experimental optical images at different crank angles. Grid convergence has been obtained for spatial distribution of equivalence ratios. The numerical model built has been validated for change of piston bowls.

**Key Words:** *Diesel spray simulation, Numerical modelling of spray, Diesel engine*

## 1. INTRODUCTION

Direct injection diesel engine 3D-CFD combustion simulations include numerical models for mesh motion, gas flow, spray, chemical kinetics and emissions [1]. It is essential to capture the in-cylinder gas flow and spray as these result in the right distribution of equivalence ratios and temperatures which are necessary inputs to any combustion model. This non-reactive flow in turn constitutes of a number of numerical models pertaining to turbulence, spray breakup, droplet collision, spray-wall interactions, and evaporation. Non-reactive modelling becomes even more important in advanced combustion modes pertaining to low temperature combustion as predicting ignition delay for such a scenario requires accurate modelling of spray and mixing. In most diesel spray simulations, the spray is initiated at the nozzle exit and nozzle upstream flow is not generally solved due to very high computational costs. Eulerian approach for gas flow is used along with a Lagrangian representation of diesel droplets clustered in the form of parcels. Droplet breakup due to KH (Kelvin Helmholtz) and RT (Rayleigh Taylor) instabilities are accounted for. The KH instabilities result due to viscous forces due to tangential motion between two fluids and RT instabilities result due to the inertia of a denser fluid (diesel in this case) exposed to acceleration. Although near nozzle grid resolutions of the order of nozzle diameter have been observed to provide the most accurate results [2], much coarser computational grids are generally used in diesel engine combustion simulations due to computational costs. The current study aims at simulating a non-reactive flow inside a direct injection diesel engine. Published experimental data for a low

temperature late injection case of the Cummins N14 optical engine at Sandia National laboratories [3-5] has been used to validate the numerical predictions of spray penetrations and equivalence ratio distributions. Grid convergence has been achieved and the grid size hence obtained has been validated against experimental data for a change of piston bowls.

## 2. EXPERIMENTAL DATA

Experimental data from the Cummins N14 optical engine at Sandia national laboratories for a low temperature, late injection case [3-5] has been considered for the current work. Details of the experimental engine can be found in the original references and hence only a brief overview of the engine specifications and the operating conditions has been provided in Table 1.

| | |
|---|---|
| Engine | Cummins N14 |
| Bore / Stroke (mm) | 139.7 / 152.4 |
| Nozzle dia (mm) | 0.196 |
| Number of holes /spray angle | 8 / 152° |
| Speed (RPM) | 1200 |
| Injection Pressure (bar) | 1600 |
| Start of Injection (CA ATDC) | 0 |
| Fuel quantity (mg) | 56 |

TABLE 1: Engine configuration [3]

At this operating condition, visualizations of spray in [3] and equivalence ratio distributions in [4,5] have been used for validating numerical models in the current work. Lachaux et al. [3] acquired visualizations of scattering from liquid fuel and fluorescence from vapour fuel just before combustion. Genzale et al. [4,5] acquired equivalence ratio contours for a non-combusting case with Toluene as the tracer fuel at different distances from fire deck for varying bowl geometries and spray angles.

## 3. NUMERICAL SIMULATIONS

Closed cycle simulations (intake valve opening to exhaust valve closing) have been performed using CONVERGE [1], a computational fluid dynamics code for three dimensional fluid flows. Due to the symmetrical nature of the combustion geometry, a 45 degree sector grid in accordance with the 8 holes injector has been used. As the experiments replicated EGR using a force feed of nitrogen, only oxygen and nitrogen were initialized unlike a typical diesel engine condition where carbon dioxide and water vapour are also present. Discharge coefficient of 0.7 has been used for the flow through nozzle. Boundary temperatures based on finite element heat transfer simulations by Genzale et al. [5] (500K for piston, 430K for cylinder head and liner) have been used in the current study. Spray breakup has been modelled using a modified KH-RT (Kelvin Helmholtz-Rayleigh Taylor) instabilities model in which the primary breakup is due to KH instabilities and secondary breakup is due to a competition between KH and RT instabilities. Spray wall interaction has been modelled by the rebound/slide mechanism which changes the impingement regime based on the Weber number of the incoming droplet. The current study uses adaptive mesh refinement strategies which refine the grid based on velocity or temperature gradient across a cell. Near nozzle region and near surface regions have been further refined to have a cell size of one-fourth and half the grid size in bowl respectively. Due to adaptive mesh refinement, the total number of cells in the computational domain keeps changing with respect to time in accordance with the presence of steep velocity and temperature gradients. For cases with no AMR, the number of cells decreases as the computational domain becomes smaller during compression. For the cases with AMR, the number of cells increase in the presence of velocity or temperature gradients (typically injection and combustion events) as more computational cells are added. Grid convergence studies have been conducted using a range of grid sizes ranging from a near nozzle size of 1.25 mm to 0.18 mm.

## 4. RESULTS

Equivalence ratio contours for a non-combusting spray for different spray angles and bowls have been compared with the experimental data in [4,5]. Results only in the bowl region have been compared to experimental data in accordance with the optical window in the experiments. Figure 1 shows the equivalence ratio distribution for the baseline bowl and two spray angles (narrow: 124° and wide: 160°) at two planes at distances of 7 and 18 mm respectively from the firedeck at a crank angle of 12° ATDC for three near nozzle grid sizes. It can be observed that the simulated spatial distributions look very similar for 0.35 mm and 0.18 mm pointing to a grid convergence below a cell size of 0.35 mm. The coarser grid fails to show any mixture formation at the 18 mm plane for a deeper spray angle. Simulated mixture distributions for both 0.35mm and 0.18 mm grid sizes are in good agreement with experimental results.

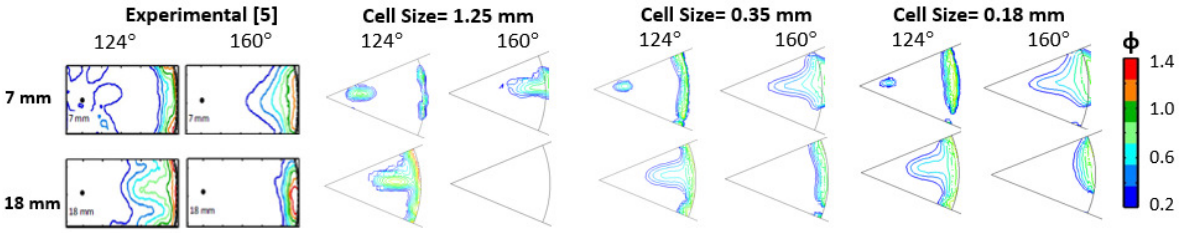


FIGURE 1. Grid convergence: Spatial distribution of equivalence ratio for two spray angles (124° and 160°) at two planes (7 and 18 mm from fire-deck)

The spray for the 0.35 mm case has been compared against experimental data obtained by Lachaux et al. [3] in Fig. 2. Blue colour in experimental plots represents scattering from liquid droplets and in simulated plots represents fuel particles. Green colour in experimental plots represents fluorescence from vapour fuel and in simulated plots represents the vapour iso-surface. The liquid length and vapour dispersion have been captured well.

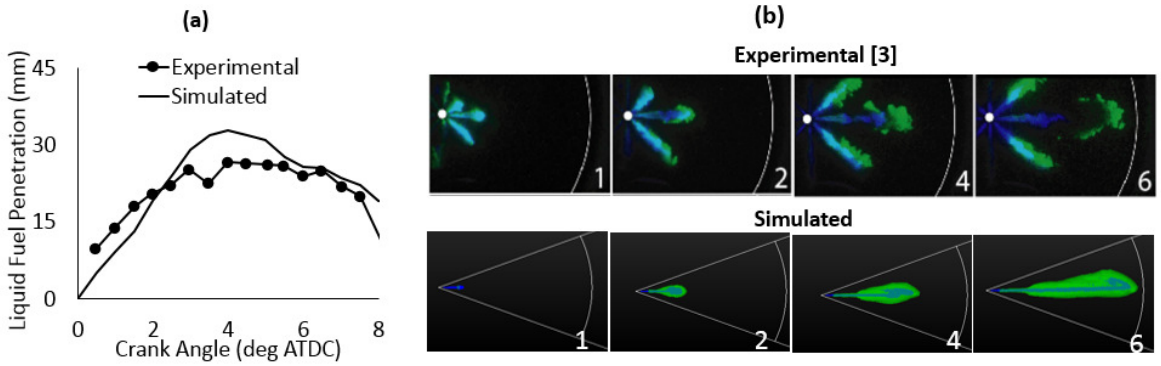


FIGURE 2: Experimental [3] and simulated spray for 0.35 mm cell size: (a) Liquid Fuel penetration; (b) Liquid (blue) and vapour (green) at different crank angle (1, 2, 4, 6 deg ATDC)

Figure 3 shows a comparison of equivalence ratios for a change in piston bowl geometry. The bowl geometries have been changed by keeping the same compression ratio and varying the bowl diameter (shown as % of bore) and depth. Results shown are for 0.35 mm grid size, at three planes at two different crank angles. It can be observed that the spatial distribution and the temporal evolution of equivalence ratio has been captured well. Based on these results, a grid size of 0.35 mm near nozzle seems to be an adequate resolution to capture spray and equivalence ratio distributions. For the current work, grid sensitivity results are in close agreement with Senecal et al. [6] who identify 0.25 mm to be an adequate grid size for spray simulations. The good agreement between experiments and simulations minimizes the numerical errors in modelling till the point of ignition and hence lays a good foundation for combustion and emissions modelling

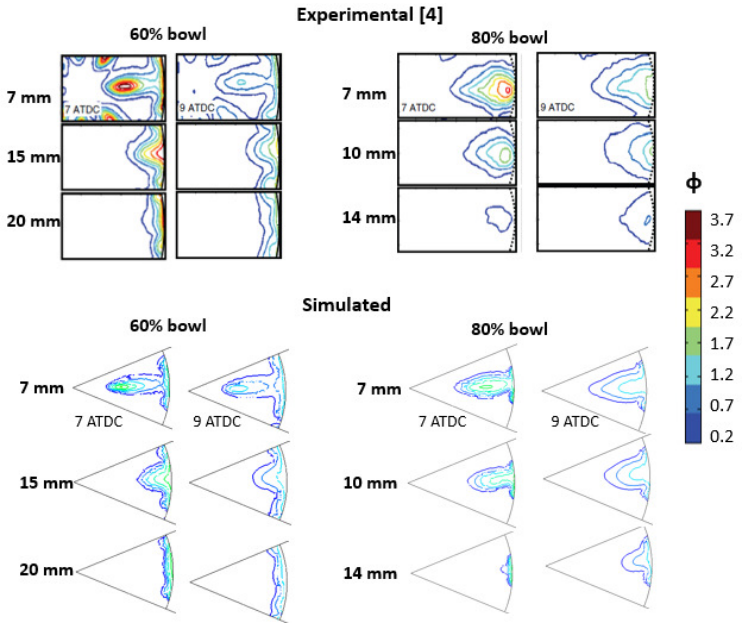


FIGURE 3: Experimental [4] and simulated equivalence ratio distribution for two piston bowls (bowl dia = 60% and 80% of bore) at three planes and two crank angles

## CONCLUSIONS

Closed cycle non-reactive simulations have been performed for a diesel engine. Spray and equivalence ratio distributions have been validated against published data for an optical engine. Equivalence ratio distributions from the model have also been validated against experimental data for different piston bowls. The results show that 0.35 mm near nozzle grid size is the adequate grid size for in-cylinder flows to predict spray and equivalence ratio distributions. Simulated spray penetration is matching well with the experimental data.

## REFERENCES

[1] K.J. Richards K.J., P.K. Senecal, and E. Pomraning, CONVERGE (v2.2), Convergent Science Inc., Madison, WI, 2014.

[2] J. Abraham, What is Adequate Resolution in the Numerical Computations of Transient Jets, *SAE* 970051, 1997.

[3] T. Lachaux, M.P.B. Musculus, S. Singh, and R.D. Reitz, Optical Diagnostics of Late-Injection Low-Temperature Combustion in a Heavy-Duty Diesel Engine, *ASME Journal of Engineering for Gas Turbines and Power*, 130(3), 032808, 2008.

[4] C.L. Genzale, R.D. Reitz, and M.P.B. Musculus, Effects of Piston Bowl Geometry on Mixture Development and Late-Injection Low-Temperature Combustion in a Heavy-Duty Diesel Engine, *SAE* 2008-01-1330, 2008.

[5] C.L. Genzale, R.D. Reitz, and M.P.B. Musculus, Optical Diagnostics and Multi-Dimensional Modeling of Spray Targeting Effects in Late-Injection Low-Temperature Diesel Combustion, *SAE* 2009-01-2699, 2009.

[6] P.K. Senecal, E. Pomraning, K.J. Richards, and S. Som, Grid-convergent spray models for internal combustion engine CFD simulations, *ASME Internal Combustion Engine Division Fall Technical Conference:* 697-710, 2012.

# ANALYSES OF THERMAL STRESSES AND STRAINS IN YTTRIA-STABILIZED ZIRCONIA (YSZ) THERMAL BARRIER COATING

**Vikram Phalke*,**
Department of Mechanical Engineering, Indian Institute of Technology Bombay, Mumbai, Maharashtra, India, vikramphalke040@gmail.com
**Milan Visaria,**
Cummins Technologies India Pvt. Ltd., Pune, Maharashtra, India, milan.visaria@cummins.com
**Shankar Krishnan,**
Department of Mechanical Engineering, Indian Institute of Technology Bombay, Mumbai, Maharashtra, India, kshankar@iitb.ac.in
**Alankar Alankar**
Department of Mechanical Engineering, Indian Institute of Technology Bombay, Mumbai, Maharashtra, India, alankar.alankar@iitb.ac.in
*Corresponding Author

## ABSTRACT

We have recently proposed application of TBCs for I.C. engines. In the present work for I.C. engines, we analyze thermal stresses in TBC and substrate that may lead to the failure of yttria stabilized zirconia (YSZ) coating due to thermal stress and strain induced during combustion in I. C. engine. Such TBCs are prone to failure at the interface between coating and substrate. We study the effect of different thermal barrier coating thickness and thermal conductivity on the thermal stresses and temperature distribution in the coating and substrate. Temperature and thermal stresses are analysed by using a 2-dimensional model in commercial finite element analysis software ABAQUS™ with temperature dependent material properties of YSZ and substrate (aluminium).

**Key Words:** *Thermal barrier coating, Yttria Stabilized Zirconia, I.C. Engine.*

## 1. INTRODUCTION

Fuel efficiency of automobile has been ever increasing driven by uncertain fuel market and strict certifications related to environment safety. Demand of increased fuel efficiency has led to redesigning of engines, hybrid and even electric automobile. The later brings challenging targets for traditional fuel based automobiles. Thus, it is obvious, as a primary and precautionary step to rethink about improvement of currently existing engine designs and related accessories. Overall such research work is focused on lowering the heat loss via better cylinder insulation. Decreased heat loss may also lead to increased pressure in combustion cell. Thus structural integrity of engine material is also of key importance.

Thermal barrier coatings are one of the options available for increasing engine efficiency by reducing heat loss. Thermal barrier coatings have traditionally been used in turbines for aerospace and power generation [1]. Such coatings have been successful in sustaining thermal gradients with relatively less cooling required for base metal [2]. However, as mentioned earlier, structure integrity of the engine and that of the coatings needs to be ensured. For all practical purposes we assume that process defects play a critical role and there is a finite life of such coating. Depending on the process used for deposition, the overall structure, noumber of inherent defects and functionality of a TBC may be different. In $ZrO_2$ - 8 wt. % $Y_2O_3$ coating, $Y_2O_3$ is in the solid solution and $ZrO_2$ is present in the form of cubic/tetragonal crystallites [3]. We, thus focus on a typical structure of coatings and the impact of thermal stress conditions on durability of the coating.

In the present work we analyze thermal stresses that may lead to the failure of YSZ coating due to thermal stresses and strain induced during combustion in I. C. Engine. We study the effect of different thermal barrier coating thickness and thermal conductivity on the thermal stresses and temperature distribution in the coating and substrate. In this work we will focus on steady state thermal cycle which is typical of single cylinder diesel based IC engine. Also, we assume that the substrate material is aluminum.

## 2. MODELING OF MECHANICAL RESPONSE

Modeling of thermo-mechanical behavior of thermal barrier coating is carried out by using commercial finite element analysis software ABAQUS™. A two dimensional heat conduction model is developed with constant temperature material properties. The material properties of the YSZ and substrate (aluminium) are as shown in Table 1.

**Table 1:** Material Properties [3]

| Material Properties | YSZ | Aluminum |
|---|---|---|
| **Density (kg/m$^3$)** | 5680 | 2770 |
| **Young's Modulus (GPa)** | 200 | 75 |
| **Thermal Conductivity (W/mk)** | 2.2 | 175 |
| **Specific Heat (J/Kg-k)** | 600 | 875 |
| **Thermal Expansion Coefficient (/k)** | 2.20E-06 | 2.00E-06 |

A thermo-mechanical coupled model with 4 nodes Quad elements (CPE4T) is used to simulate the process. The prescribed boundary conditions are as shown in Fig. 1a. The gas temperature is assigned as a sink temperature while heat transfer coefficient (HTC) is assigned on the top surface of the coating. The gas temperature and HTC variation with respect to time is as shown in Fig. 1b.

In the present work TBC is considered to be an elastic-plastic material. Uniaxial tensile stress-strain data for zirconia between 500$^o$C and 800$^o$C is used from the work of Messerchmidt et al. [4]. We consider thermal conducticity and modulus of elasticity of TBC and substrate to be temperature dependent. For the analyses of thermal and mechanical performance of TBC, we assume that steady state temperature conditions prevail. For assessing the collective effect of various material properties of TBC and coating thickness we perform a parametric study. The study is performed for one temperature cycle at steady state. Zhu et al [2] have pointed out that strain to failure determined using one temperature cycle can be used for prediction of number of thermal cycles to failure. Temperature and stress along the X-direction ($\sigma_{11}$) are recorded at the end of the cycle at the top surface, at the center of the coating and at the interface. Apart from this, the effect of $\frac{k}{t}$ on $\sigma_{11}$ is also assessed where *k* and *t* are thermal conductivity and thickness respectively of TBC. $\sigma_{11}$ is considered amongst all components of stress since it represents the effect of misfit strain between the TBC and the substrate. Since $\sigma_{11}$ may play a role in buckling and spallation of TBC, it gives

indirect measure of durability of TBC. Apart from this, a damage parameter was also tracked at the above locations. Due to only one thermal cycle, damage paramter which is a function of accumulated effect plastic strain in TBC, did not evolve to any considerable values. A detailed assessment of damage during low and high cycle fatigue will be presented in future work. Further, here we study a homogeneous elastic-plastic isotropic coating with zero roughness at the interface. The geometry of interface here does not have any characteristic waviness.

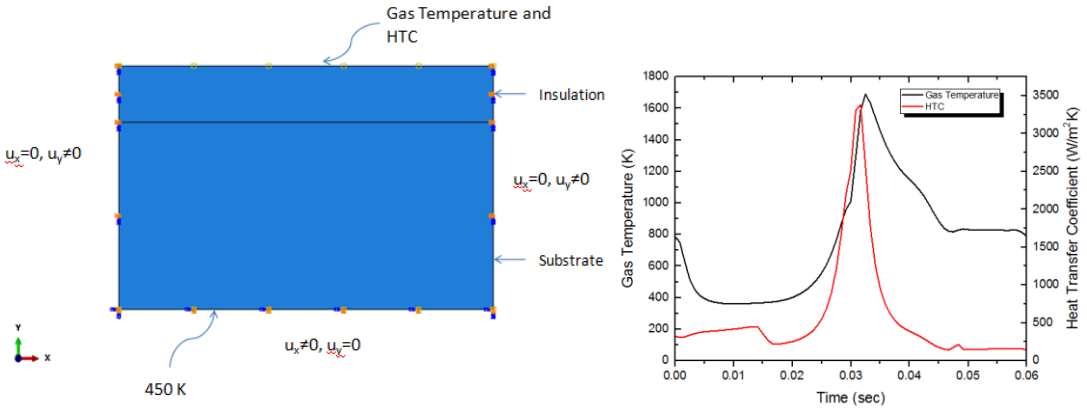


(a) (b)

Fig. 1. a) Prescribed boundary conditions b) gas temperature and heat transfer coefficient variation with respect to time

## 3. RESULTS

Fig. 2 shows the effect of coating thickness and thermal conductivity on steady state surface temperature and stress at the locations of interest. These locations are top surface of TBC, middle of TBC and TBC-substrate interface. Temperatures at middle of coating and at interface decrease as the thickness of TBC increases. The top surface of coating increases when coating thickness is increased to 0.2 mm and then decreases. Fig. 2b shows combined effect of thermal conductivity and coating thickness. For three different coating thicknesses viz. 0.1 mm, 0.2 mm and 0.3 mm thermal conductivity was decreased by 10 % and 20 % from base value as show in Table 1. In Fig. 2b stress $\sigma_{11}$ is shown as a function of aforementioned 9 combinations of $\frac{k}{t}$ so that basic assessment of durability and thermal efficiency can be performed. Compressive stress may be helpful for arresting propagation of existing cracks depending upon the orientation of local loading direction with respect to crack orientation. However in TBC coatings due to deposition process there may be existing cracks such that they may open and propagate [5,6,7] due to compressive stress $\sigma_{11}$ if the relative orientation of crack allows. Thus, one would need to avoid such in-plane compressive stresses. Such desired condition of low compressive stress at interface is seen for lower themal conductivity and greater coating thicknesses. See the $\sigma_{11}$ vs. $k/t$ curve for interface in Fig. 2b.

## 4. CONCLUSIONS

We perform a parametric study for assessing durability of a YSZ TBC. The study was performed assuming a homogenous isotropic elastic-plastic TBC. The study also assumes that the interface does not have the characteristic waviness and roughness. The effect of TBC thickness on

temperature distribution shows that the higher TBC thickness (0.3mm) gives lower temperature at three positions (top, middle and interface) as compared lower TBC thickness (0.1 mm). The desired condition of lower unidirectional compressive stress ($\sigma_{11}$) is observed to be at lower thermal conductivity ($k$) to thickness ($t$) ratio. The interesting field of further research is to implement a numerical model of damage in thermal barrier coating.

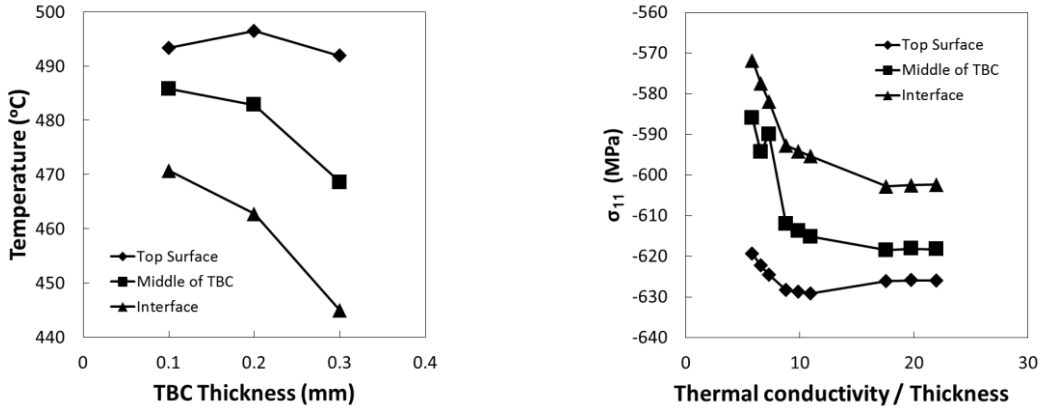


(a) (b)

Fig. 2. a) Steady state temperatures at top surface of TBC, middle of TBC and at the interface of TBC and substrate. b) Ratio of thermal conductivity and thickness of TBC ($k/t$)

## AKNOWLEDGEMENT

The authors wish to thank MHRD Uchhatar Avishkar Yojana and Cummins Technologies India Private Limited for providing the financial support for this work.

## REFERENCES

[1] T.S. Hille, A.S.J. Suiker, S. Turteltaub, Microcrack nucleation in thermal barrier coating systems, *Engineering Fracture Mechanics*, 76, 813–825, 2009.

[2] D. Zhu and R. A. Miller, Thermal fatigue testing of $ZrO_2$-$Y_2O_3$ thermal barrier coating systems using a high power $CO_2$ laser, *NASA Technical Report No. ARL-TR-1354*, 1997.

[3] A. Taibani, M. Visaria, S. Krishnan, Analysis of temperature swing thermal insulation on the performance of diesel engines. *In Proceedings of the 24th National and 2nd International ISHMT-ASTFE, Heat and Mass Transfer Conference (IHMTC-2017),* 2017.

[4] U. Messerchmidt, B. Baufeld and D. Baither, Plastic deformation of cubic zirconia crystals, Key Engineering Material, 153-154, 143-182, 1998.

[5] Y. Sun, W. Zhang, M. Tian and T.J. Wang, Thermal cycling induced crack nucleation and propagation in thermal barrier coating system, *Key Engineering Materials*, 462-463. 383-388, 2011.

[6] A.G. Evans, D.R. Mumm, J.W. Hutchinson, G.H. Meier, F.S. Pettit, Mechanisms controlling the durability of thermal barrier coatings, *Progress in Materials Science*, 46, 505-553, 2001.

[7] H. Balke, I. Hofinger, C. Häusler, H. A. Bahr, H. J. Weiß, G. Kirchhoff, Fracture mechanical damage modelling of thermal barrier coatings, *Archive of Applied Mechanic*s, 70, 193-200, 2000.

# Computational Analysis of Solar Humidifier

**Prajesh Jangale**
Department of Mechanical Engineering, Indian Institute of Technology Bombay, Mumbai**,**
Maharashtra, India, prajeshjangale@iitb.ac.in

**Shankar Krishnan*,**
Department of Mechanical Engineering, Indian Institute of Technology Bombay, Mumbai,
Maharashtra, India, kshankar@iitb.ac.in
***Corresponding Author**

ABSTRACT

Humidification-dehumidification (HDH) is a non-traditional thermal desalination cycle that operates at sub-boiling temperatures. As a decentralized water production system, HDH has number of advantages that includes low maintenance, low initial capital cost and robust operation. HDH cycle components consists of a humidifier, dehumidifier and a heat source apart from prime movers. In this work, concept of a novel solar humidifier is explored via the Volume of Fluid (VOF) computational method. Solar humidifier consists of a film of water flowing over surface subjected to solar flux and a counter flow of air within an heat and mass exchanger. As air passes through the humidifier, owing to simultaneous heat and mass transfer, the air stream gets heated as well as humidified. The VOF method allows tracking of the interface and allows accurate modelling of the humidification phenomena. A methodology has been developed to model simultaneous heat and mass exchange happening inside a humidifier. The results from the solar humidifier are compared against the traditional humidifier in which the hot water is heated externally.

**Keywords:** *solar humidifier, desalination*

## 1. INTRODUCTION

One of the most important components of a HDH desalination system is humidifier. Analysis is done for a wet-cooling tower selected as a humidifier. Wet cooling towers are classified in more detailed terms such as natural draft or induced draft, crossflow or counter flow, and splash fill or film fill. For each of these classifications, the key issue is air-water contact and its extremely important influence on the performance of wet cooling towers.

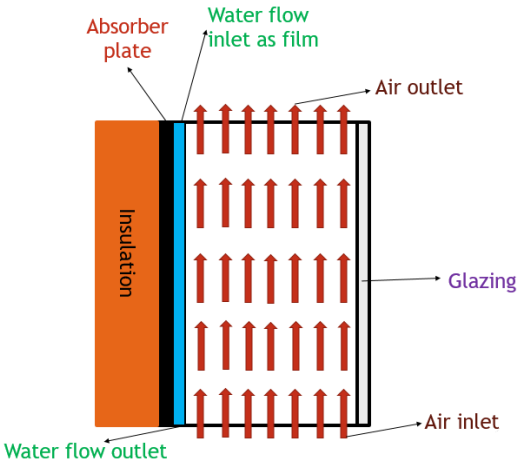


FIGURE 1. Schematic of the modelled system [2].

This figure shows a counter-flow humidifier with water forming film from the top whereas air is entering the humidifier from bottom. The absorber plate is in contact with the water film, whereas the air is flowing between glazing and water film. Water is heated along the length, while air gains moisture and heat from this water and gets heated and humidified. This heated and humidified air can be then passed into the dehumidifier where it will condense all the vapour into water at ambient. [2]

## 2. ANALYTICAL FORMULATION

In this work, a methodology has been developed to model simultaneous heat and mass exchange happening in a humidifier using the ANSYS Fluent software package [1]. A 2-dimensional system was modelled using the VOF method combined with Navier-Stokes equations as shown in Figure 1. Mass conservation, momentum conservation and energy conservation equations used are:

$$\frac{\partial(\rho u)}{\partial x}+\frac{\partial(\rho v)}{\partial y}=0$$

$$\frac{\partial(\rho u)}{\partial t}+\frac{\partial(\rho uu)}{\partial x}+\frac{\partial(\rho uv)}{\partial y}=\frac{\partial}{\partial x}\left(\mu\frac{\partial u}{\partial x}\right)+\frac{\partial}{\partial y}\left(\mu\frac{\partial u}{\partial y}\right)-\frac{\partial p}{\partial x}-\rho g$$

$$\frac{\partial(\rho v)}{\partial t}+\frac{\partial(\rho vu)}{\partial x}+\frac{\partial(\rho vv)}{\partial y}=\frac{\partial}{\partial x}\left(\mu\frac{\partial v}{\partial x}\right)+\frac{\partial}{\partial y}\left(\mu\frac{\partial v}{\partial y}\right)-\frac{\partial p}{\partial y}$$

$$\frac{\partial(\rho T)}{\partial t}+\frac{\partial(\rho uT)}{\partial x}+\frac{\partial(\rho vT)}{\partial y}=\frac{\partial}{\partial x}\left(\frac{k}{C_p}\frac{\partial T}{\partial x}\right)+\frac{\partial}{\partial y}\left(\frac{k}{C_p}\frac{\partial T}{\partial y}\right)+S_h$$

Here *u*,*v* are the *x*,*y* components of the velocity field. $\rho$ is the density, $\mu$ denoted viscosity, *p* denotes pressure field, *T* is the temperature distribution, *k* is the conductivity, $C_p$ is the specific heat and $S_h$ is the source term.

The VOF function satisfies the following equation. A fractional volume *F* was used to track the interface using the equation and *V* denotes the velocity.

$$\frac{\partial F}{\partial t}+(V.\nabla)F=0$$

Evaporation rate of water at the interface was calculated using the equations used in the Gao et al. [3] for the auxiliary equations.

$$W_z=\in_1*(P_s-P_v)*\sqrt{\frac{M}{2\pi RT_n}}$$

Here $P_s$ and $P_v$ are the saturation pressure and vapour pressure respectively. $T_n$ is the interface temperature and, *R* and *M* are universal gas constant and molecular mass. The Knudsen coefficient of evaporation $\in_1$can be calculated by following relation using the coefficient of evaporation$\in$.

$$\in_1=\frac{2\in}{2-\in}$$

The coefficient of evaporation was calculated using the following equation. Here $T_{avg}$ is the average temperature. $\rho_s$ and $\lambda$ being the density and latent heat of water. $h^*$ is the wet bulb heat transfer coefficient.

$$\in = h^* * \sqrt{\frac{2\pi R T_{avg}}{M}} * \frac{T_n}{\rho_s \lambda^2}$$

The wet bulb heat transfer coefficient was calculated using the heat transfer *h*. F = 49, b = 0.6 and *V* is velocity. Using the *h* value and specific heat of air at constant pressure $C_{pa}$, $h^*$ was calculated. *e* is a constant.

$$h^* = h * \left(1 + \frac{e\lambda}{C_{pa}}\right) \quad ; \quad h = FV^b$$

The constant *e* is given by $T_{max}$ maximum temperature between the air flow and water flow. $T_{min}$ is the saturation temperature and, $\omega_{max}$ and $\omega_{min}$ are the humidity ratio associated with them.

$$e = \frac{\omega_{max} - \omega_{min}}{T_{max} - T_{min}}$$

## 3. RESULTS

The results were obtained using the VOF method with 2-D flow transient equation. A stream of water at 0.5ms$^{-1}$ was inlet through a small opening with initial temperature of 318 K. A 1ms$^{-1}$ inlet air was let in through another opening in the counter-flow direction. A heat flux of 1000 W/m$^2$ was put across the wall along the water surface. The standard fluent properties for air and water were used. Solution method used was non-iterative time advancement with QUICK spatial discretization for momentum and energy. The water inlet and outlet was set for volume fraction of 1 and air inlet and outlet for 0 volume fraction. Using the numerical formulation above a water evaporation rate of 15.47 kg/m$^2$/s was obtained. The verification of simulation model made is shown in the following figure 2.

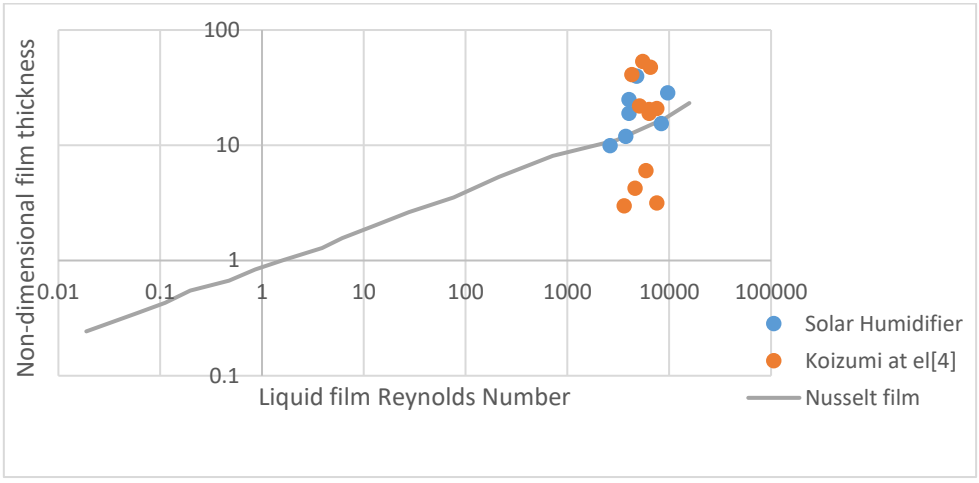


FIGURE 2a. Plot indicate the verification of simulation with falling film model Koizumi et al[4]

The outlet properties of air obtained are temperature of 317 K and humidity ratio of 6.94 g of vapour per kg of dry air. Comparing this with the traditional humidifier system using a separate flat plate collector for heating water and then using it for humidifying air in separate humidifier system, resulted in air outlet temperature as 318 K and humidity ratio of 6.41 g of vapour per kg of dry air. The contours shows the results obtained.

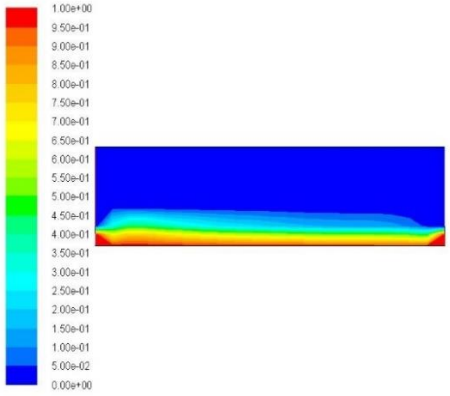


FIGURE 2a. Phase contours- (water-1)

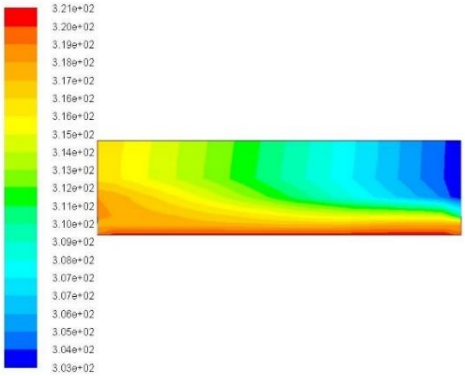


FIGURE 3b. Temperature contours (K)

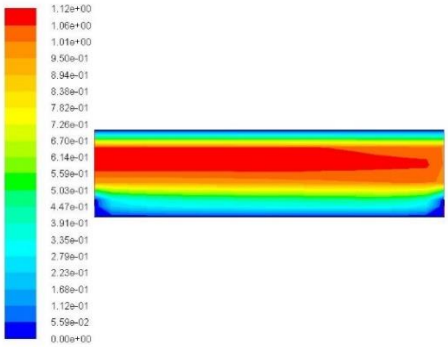


FIGURE 3c. Velocity Contours ($ms^{-1}$)

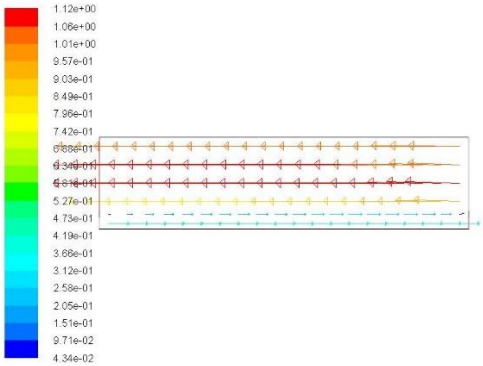


FIGURE 3d. Velocity vector field ($ms^{-1}$)

FIGURE 3: Snapshots of (a) phase contours, (b) temperature distribution, (c) velocity contours and (d) velocity vector field inside a solar humidifier.

## 4. CONCLUSIONS

A VOF based falling-film humidifier model was developed and reported. Results obtained from proposed model was compared existing analytical, numerical, and experimental data for vertical falling films. This modelling approach was used to investigate impact of a novel solar humidifier module that integrates solar heating and humidification into one device. Results are comparable with separate solar heater and humidifier components highlighting the compactness that is achieved.

## REFERNCES

[1] Using VOF Model, Release 12.1 ANSYS, Inc. 2009-09-09
[2] Vipul Ahuja, Design and development of a solar humidifier based Humidification Dehumidification Desalination system, M.Tech. Thesis.
[3] Penghui Gao, Lixi Zhang, Hefei Zhang, Performance analysis of a new type desalination unit of heat pump with humidification and dehumidification, Desalination 220, 531–537, 2008
[4] Yasuo Koizumi, Ryou Enari, Hiroyasu Ohtake, Correlations of Wave Characteristics for a Liquid Film Falling Down Along a Vertical Wall, Journal of Heat Transfer, 082901, Vol. 131, 2009

# Study of Combined Effect of Thermal Anisotropy and Forced Convection on the Growth of an Equiaxed Dendritic Crystal

**Amman Jakhar, Anirban Bhattacharya, Prasenjit Rath and Swarup Kumar Mahapatra**




***Keywords:*** *Dendrite growth, Thermal anisotropy ratio, Arm length ratio, Flow velocity, Enthalpy method.*

## Abstract

In this paper, we present a new method for the solution of the Navier-Stokes equations in porous media. The method is based on the artificial compressibility (AC) approach and is applicable to both isotropic and anisotropic porous media. The governing equations are discretized using the finite element method on unstructured meshes. The AC method is modified to account for the porous medium by introducing the permeability tensor and the porosity. The resulting system of equations is solved using a preconditioned iterative solver. The method is validated against analytical solutions for flow through a channel filled with a porous medium and against experimental data for flow through a packed bed. The results show that the method is accurate and robust for a wide range of permeability values, including highly anisotropic cases. The method is also shown to be efficient, with the computational cost scaling linearly with the number of elements.

## Introduction

The flow of fluids through porous media is of great importance in many engineering applications, such as groundwater hydrology, petroleum engineering, and chemical engineering. The governing equations for such flows are the Navier-Stokes equations modified to account for the presence of the porous medium. These equations are typically solved using the finite element method, which is well suited to handle complex geometries and boundary conditions.

The artificial compressibility method was originally developed for incompressible flows in clear fluid regions. It has been extended to porous media flows by several researchers. In this method, a pseudo-time derivative of pressure is added to the continuity equation, which allows the use of explicit time-stepping schemes. The method is attractive because it avoids the need to solve a pressure Poisson equation, which can be computationally expensive.

In this paper, we present a new formulation of the artificial compressibility method for porous media flows. The formulation is based on the work of Chorin [1] and Temam [2], and is extended to anisotropic porous media. The governing equations are discretized using the finite element method on unstructured meshes. The resulting system of equations is solved using a preconditioned iterative solver.

## Governing Equations

The governing equations for incompressible flow through a porous medium are the continuity equation and the momentum equation. The continuity equation is given by

$$\nabla \cdot \mathbf{u} = 0 \tag{1}$$

where $\mathbf{u}$ is the velocity vector. The momentum equation is given by

$$\frac{\rho}{\varepsilon}\frac{\partial \mathbf{u}}{\partial t} + \frac{\rho}{\varepsilon}(\mathbf{u}\cdot\nabla)\mathbf{u} = -\nabla p + \mu \nabla^2 \mathbf{u} - \frac{\mu}{\mathbf{K}}\mathbf{u} \tag{2}$$

where $\rho$ is the fluid density, $\varepsilon$ is the porosity, $p$ is the pressure, $\mu$ is the dynamic viscosity, and $\mathbf{K}$ is the permeability tensor. For isotropic media, $\mathbf{K} = k\mathbf{I}$, where $k$ is the scalar permeability and $\mathbf{I}$ is the identity tensor. For anisotropic media, $\mathbf{K}$ is a symmetric positive definite tensor.

The artificial compressibility method adds a pseudo-time derivative of pressure to the continuity equation:

$$\frac{1}{\beta}\frac{\partial p}{\partial \tau} + \nabla \cdot \mathbf{u} = 0 \tag{3}$$

where $\tau$ is the pseudo-time and $\beta$ is the artificial compressibility parameter. The steady-state solution is obtained when the pseudo-time derivative vanishes.

## Numerical Method

The governing equations are discretized using the finite element method on unstructured meshes. The velocity and pressure are approximated using piecewise linear basis functions. The resulting system of equations is solved using a preconditioned iterative solver. The preconditioner is based on the incomplete LU factorization with zero fill-in (ILU(0)).

The time step is chosen based on the stability criterion for explicit time-stepping schemes. The maximum time step is given by

$$\Delta t = \frac{h}{c + |\mathbf{u}|} \tag{4}$$

where $h$ is the element size and $c$ is the speed of sound in the fluid. The speed of sound is given by $c = \sqrt{\beta}$.

## Results and Discussion

The method is validated against analytical solutions for flow through a channel filled with a porous medium. The results show that the method is accurate and robust for a wide range of permeability values, including highly anisotropic cases. The method is also shown to be efficient, with the computational cost scaling linearly with the number of elements.

The method is also validated against experimental data for flow through a packed bed. The results show that the method is able to accurately predict the pressure drop and the velocity profile. The method is also shown to be robust for a wide range of Reynolds numbers.

## Conclusions

In this paper, we have presented a new formulation of the artificial compressibility method for porous media flows. The formulation is based on the work of Chorin [1] and Temam [2], and is extended to anisotropic porous media. The governing equations are discretized using the finite element method on unstructured meshes. The resulting system of equations is solved using a preconditioned iterative solver. The method is validated against analytical solutions and experimental data. The results show that the method is accurate, robust, and efficient.

d r d r r r r d r r r d r r r r r d r r r r r

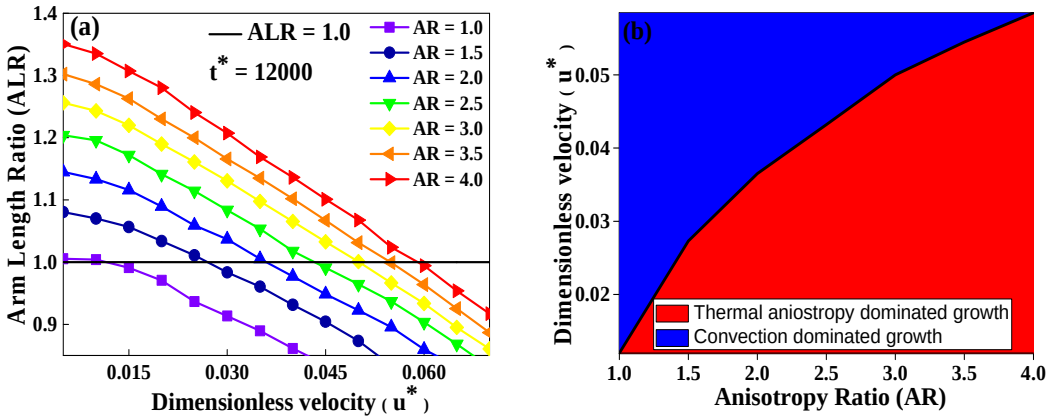


□□□ □□□ □□□□r□□□□□ □□ □□□□r□ □□□□□□□ □□□□ *ALR* □□ □□□ □□□□□□□ □□ □□□□ □□□□□□□□ *u** □□r d□□□r□□□□□r□ □□□□□□□□r□□□ r□□□ *AR* □□□□□□ □□□□ □□□□□□ □□□d □□ □□□□□□□□r □□ □□□r □r d □dr□□□ □r□□ □□ □ r□□□□□□□□□ □□□□ r□ □□□□□□□□□r□□□□ r□□□ *AR* □□r □□□□ □□□□□□□□□ *u** □□□

## □□□□□□□□□□□

□ □□□□ r□□□□□□ □d□□□□□□ □□□□d□□□□□□□d □□□□r□□r□□□□ □□□ □□□□□□□□□□□□□□□□□□□□r□ □□ □□□□□□r□□□□ □□d □□□□□□□□□□□□ □□ □□□□r□ □□□□□□ d□dr□□□ r□□ □□□□□ □□□□□ □□□□□□□□□□□□□□□□ □□□□r□ □□□ □□□□□ □□□□r□□d □□□□□ □□□□□ □□ □ □□□□ □□r□□ □□□r □□□□r□ □□ □□□□□□□□□r□□□□ r□ □□□□□□□□□□□ □□□□d □r□□□□□□ □ □□d □□ □ □□□□□□□□□□□□□□□□□□□□□□□□□□□ d□□r□ □□□□□□ □□□ d□dr□□□ □□□□□□ □□d □□□□□□□□□□□□ d□r□□□ □□□□d□□□□□□□□□□□□□□ □□□□□□□□□□□ r□□□□□□d □□r□ □□□□ □□□□□ □ □□r□ □□ □□r□□□□r□□□ □□ □d□r□□□□d□□□ □□□d□□□□□□□□□□□□□□□□ □□□□□□□□□□ □□□□□r□□□□□□□□ □□□r□□□r□□ □r□□□□□□□□□□□□□□□□□□□

Fifth International Conference on Computational Methods for Thermal Problems
THERMACOMP2018, July 9-11, 2018, Indian Institute of Science, Bangalore, INDIA
*N. Massarotti, P. Nithiarasu, Pradip Dutta and C. Ranganyakalu (Eds.)*

# PERFORMANCE EVALUATION OF LATENT HEAT BASED COOL PACK CONFIGURATION FOR THERMAL COMFORT: A NUMERICAL APPROACH

**Aniket D. Monde, Oaj Chawla, Vedant Bhuyar, Mohit Vijay, Prodyut R. Chakraborty**
Department of Mechanical Engineering IIT Jodhpur, Karwad 342037, pchakraborty@iitj.ac.in

## ABSTRACT

The PCM based heat source and heat sink devices can be effectively used for various heating and cooling applications and can store and release heat in the form of latent heat. This latent heat can be utilized for maintaining body temperature within comfort range of $33 \pm 2$ ℃. The present work focuses on developing a 2-D numerical model to evaluate the performance of PCM cool pack configuration in terms of the evolution of average skin temperature with respect to time. The numerical model is first validated with a 1-D semi-analytical for a simple PCM pack configuration. Once the model is validated, the next level of studies involves the comparison of performance analysis for different PCMs with more realistic cooling pack configuration. Optimal thermal conductivity (which can be engineered by introducing PCM-Graphite composites) is also predicted for different PCMs in order to obtain thermal comfort for a prolonged duration of 3 hrs. The studies do not include the perspiration model; however, incorporation of the skin layer within the model domain took the approach closer to the real condition.

**Key Words:** *Thermal comfort, PCM cool pack, Melting*

## 1. INTRODUCTION

Exposure to an extremely hot environment for long durations wearing thick garments such as a bulletproof jacket, military vest, and fireman apparel can cause heat-related physiological strain, enhance the thermal fatigue, reduce the working efficiency, and under the extreme condition it may even cause severe heat-shock and illness. PCMs have high heat storage capacity in the form of latent heat and can be utilized as a heat sink when the temperature variation during the process is small. Frozen PCM is put inside suitable flexible containers to form a PCM pack that is then placed in specially designed vest pockets [1]. PCM packs are suitable to control the temperature within a small range of variation for the prolonged time duration (3-5 hours) and can be reactivated (re-frozen) within much shorter time scale (15- 20 minute) to be reused. PCMs are more advantageous as it is found in the literature [2].

In the present work, duration of thermal comfort for a given configuration of PCM pack stacked between two layers of insulating materials (Polystyrene) has been studied. Since the PCM packets are kept in separate pockets, the gap between two neighbouring pockets plays a vital role in defining the hot spots on skin layer. The representative 2-D schematic diagram that includes a thin layer of skin along with PCM pack configuration within the insulation layer is shown in Fig.1.a. A 2-D diffusion based numerical model to evaluate temperature distribution within the skin layer as well as rest of the composite structure is developed. However, before obtaining the thermal analysis of the system described by Fig.1.a, validation of the numerical model is obtained with a 1-D semi-analytical model, for a much simpler configuration consisting of only one pack along with the skin layer and insulation layers. Once, the validation provided excellent agreement, the composite structure shown in Fig.1.a is analysed with the numerical model considering different PCMs.

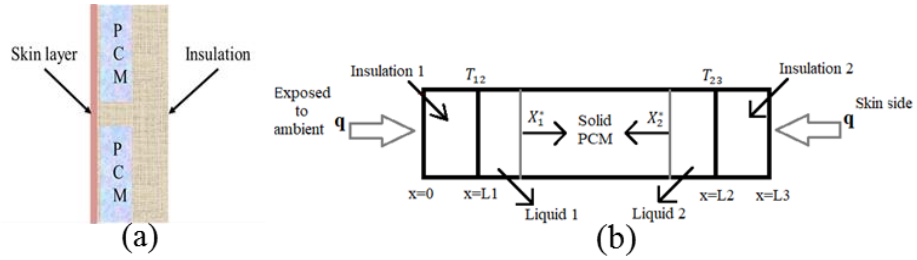


Fig.1: Schematic of (a) PCM pack adjacent to skin layer. (b) 1-D semi-analytical model

## 2. MATHEMATICAL AND NUMERICAL MODEL

The numerical model is based on volume averaged formulation [3, 4] without considering shrinkage, and is given as.:

$$\frac{\partial}{\partial t}(T) = \nabla.\left(\frac{k}{\rho c_{ps}}\nabla T\right) - \frac{\partial}{\partial t}\left(\frac{f_l h_{sl}}{c_{ps}}\right) - \frac{\partial}{\partial t}\left[f_l\left(\frac{c_{pl}}{c_{ps}} - 1\right)(T - T_m)\right] \quad (1)$$

The enthalpy updating scheme [4, 5] has been used in order to obtain the liquid/solid fractions ($f_l/f_s$) and to capture the solid-liquid interface at the melting domain. The boundary conditions are as follows: $-k\,\partial T/\partial x\,|_{x=0} = q''_{body}$, $-k\,\partial T/\partial x\,|_{x=L} = h(T_\infty - T)$. The 1D diffusion based analytical model is developed assuming material properties for each domain to be different but uniform within each domain. The 1-D heat diffusion equation is:

$$\frac{\partial T}{\partial t} = \alpha\frac{\partial^2 T}{\partial x^2} \quad (2)$$

The analytical solution of Eq. 2 for individual domain (Fig. 1b) at time step $\Delta t^{(k)}$ is:

$$T(x,t) = T_s(x) + \sum_{n=1}^{m} \exp(-\alpha\,\beta_m\,\Delta t)\;N(\beta_m, x)\,X(\beta_m, x)\,C_n \quad (3)$$

$C_n$ values are calculated from previous time step temperature distribution at $\Delta t^{(k-1)}$ [6].

| Domain | $T_s(x)$ | $N(\beta_m, x)$ | $X(\beta_m, x)$ | $\beta_m$ |
|---|---|---|---|---|
| Insulation 1 | $\frac{(T_{12} - T_a)h_r x}{k_1 + h_r L_1} + \frac{h_r T_a L_1 + k_1 T_{12}}{k_1 + h_r L_1}$ | $\frac{2\,(\beta_m^2 + \left(\frac{h_r}{k_1}\right)^2)}{L_1\left(\beta_m^2 + \left(\frac{h_r}{k_1}\right)^2\right) + \left(\frac{h_r}{k_1}\right)}$ | $\sin(\beta_m(L_1 - x))$ | $\beta_m \cot(\beta_m L) = \frac{-h_r}{k_1}$ |
| Liquid 1 | $-\frac{(T_{12} - T_m)\,(x - L_1)}{(x_1^* - L_1)} + T_{12}$ | $\frac{2}{(x_1^* - L_1)}$ | $\sin(\beta_m(x - L_1))$ | $\sin(\beta_m(x_1^* - L_1))=0$ |
| Solid PCM | $T_m$ | 0 | 0 | 0 |
| Liquid 2 | $\frac{(T_{23} - T_m)\,(x - x_2^*)}{(L_2 - x_2^*)} + T_m$ | $\frac{2}{(L_2 - x_2^*)}$ | $\sin(\beta_m(x - x_2^*))$ | $\sin(\beta_m(L_2 - x_2^*))=0$ |
| Insulation 2 | $\frac{q\,(x - L_2)}{k_3} + T_{23}$ | $\frac{2}{L_3 - L_2}$ | $\sin(\beta_m(x - L_2))$ | $\cos(\beta_m(L_3 - L_2))=0$ |

Table 1: Temperature profile for each domain

## 3. VALIDATION AND CASE STUDIES

To validate the numerical scheme, properties of savE OM 21 organic type PCM are chosen (Table 2) with an assumption as $k_s = k_l = 1W/mK$. Results obtained from numerical model for average

skin temperature with time and temperature distribution along PCM pack is compared with the analytical model. The absolute difference of 0.04 ℃ was present between both models.

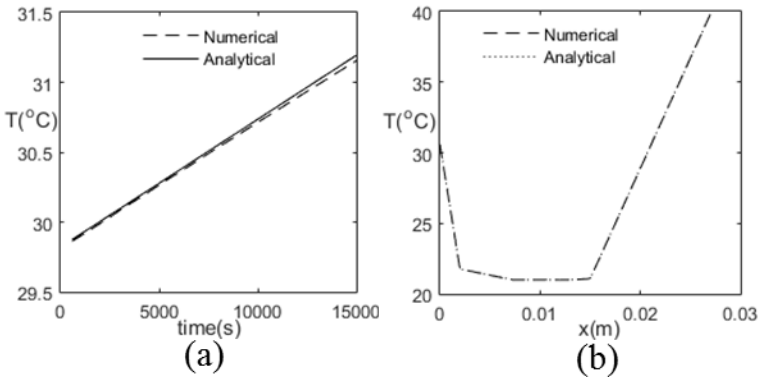


Fig.2 (a) Variation of $T_{skin}$ with time (b) Temperature profile along PCM pack @ 8400 s.

| Material | $T_{melt}$ (℃) | $\Delta H\ \left(\frac{kJ}{kg}\right)$ | $\rho\ \left(\frac{kg}{m^3}\right)$ | $k_s\ \left(\frac{W}{mk}\right)$ | $k_l\ \left(\frac{W}{mk}\right)$ | $c_{ps}\ \left(\frac{kJ}{kgK}\right)$ | $c_{pl}\ \left(\frac{kJ}{kgK}\right)$ |
|---|---|---|---|---|---|---|---|
| savE OM 21 | 21 | 250 | 924 | 0.14 | 0.21 | – | 2.6 |
| C18 Paraffin | 27.5 | 244 | 800 | 0.15 | 0.148 | – | – |
| Octadecane | 28.1 | 245 | 776 | 0.192 | 0.15 | 1.908 | 2.232 |

Table 2: Properties of chosen PCM

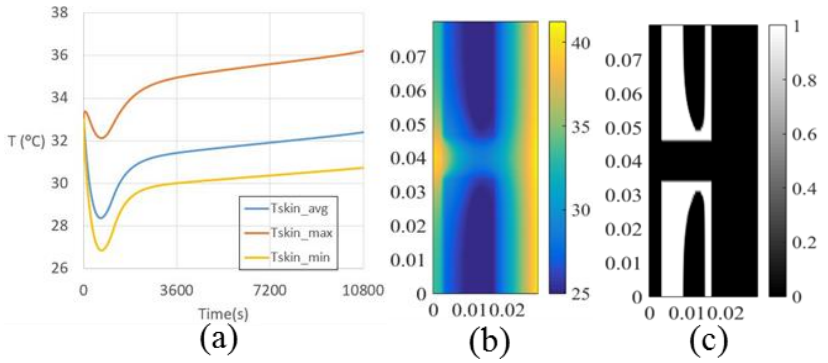


Fig.3 (a) Variation of $T_{skin\_avg}$, $T_{skin\_max}$, and $T_{skin\_min}$ with PCM savE OM21, (b) temperature distribution, (c) solid front distribution

Three different PCMs namely savE OM 21, C18 paraffin, and Octadecane are studied with melting temperatures varying from 21-28.1°C (Table 2). The properties of skin layer and insulation material (polystyrene) are chosen from Yazdi *et. al*. [7]. After the validation, comparison using different PCMs, the gap between two PCMs packs and optimal thermal conductivity for the prescribed duration of comfort (3-4 hrs) is studied. PCM pack thickness for savE OM 21, C18 paraffin and Octadecane PCM is taken to be 13, 15 and 15 mm respectively. Insulation thickness skin side is taken to be 2, 0.8 and 0.8 mm respectively. Insulation thickness on the ambient side is taken to be 12mm for all cases. The gap between PCM packs is taken to be 12, 10 and 8 mm respectively. The initial temperature of PCM is 11, 17.5 and 18.1°C respectively. The initial temperature of Insulator and skin is 20 and 33°C for all cases.

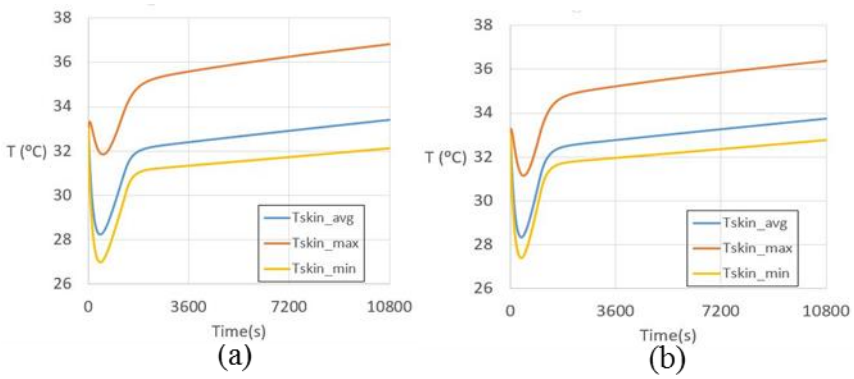


Fig.4 Variation of $T_{skin\_avg}$, $T_{skin\_max}$, and $T_{skin\_min}$ with PCM (a) C18 and, (b) Octadecane

## 4. CONCLUSIONS

(1) The conjugate heat transfer model for PCM warm packs is successfully developed and validated with the semi-analytical model. (2) Three PCM namely savE OM21, C18 paraffin and Octadecane have been studied for desired cooling effect and duration. (3) savE OM21 is found out to be most suitable in terms of comfort duration. (4) Considering 16 PCM packs (8 on the front side and 8 on the back side) with size $12\text{ cm} \times 12\text{ cm} \times 1.5\text{ cm}$) the mass of savE OM21, C18 paraffin and octadecane with enhanced thermal conductivity are found out to be 3.193, 2.765 and 2.682 kg respectively for comfort duration of more than 3 hrs. (5) The gap between the PCM packs controls the maximum skin temperature, while the thickness of insulation layer between the skin and the PCM pack regulates the minimum skin temperature.

## REFERENCES

[1] Strydom, C. H., & NB, M. (1974). The design, construction, and use of a practical ice-jacket for miners. *Journal of the Southern African Institute of Mining and Metallurgy*, 75(2), 22-27.

[2] Shim, Huensup, E. A. McCullough, and B. W. Jones. "Using phase change materials in clothing." *Textile Research Journal* 71.6 (2001): 495-502.

[3] Bennon, W. D., and F. P. Incropera. "A continuum model for momentum, heat and species transport in binary solid-liquid phase change systems—I. Model formulation." *International Journal of Heat and Mass Transfer* 30.10 (1987): 2161-2170.

[4] Chakraborty, Prodyut R. "Enthalpy porosity model for melting and solidification of pure-substances with large difference in phase specific heats." *International Communications in Heat and Mass Transfer* 81 (2017): 183-189.

[5] Brent, A. D., V. R. Voller, and K. T. J. Reid. "Enthalpy-porosity technique for modeling convection-diffusion phase change: application to the melting of a pure metal." *Numerical Heat Transfer, Part A Applications* 13.3 (1988): 297-318.

[6] Monde, Aniket D., and Prodyut R. Chakraborty. "1-D diffusion based solidification model with volumetric expansion and shrinkage effect: A semi-analytical approach." *Physics Letters A* 381.39 (2017): 3349-3354.

[7] Mokhtari Yazdi, M., M. Sheikhzadeh, and S. Borhani. "Modeling the heat transfer in a PCM cooling vest." *The Journal of The Textile Institute* 106.9 (2015): 1003-1012.

Fifth International Conference on Computational Methods for Thermal Problems
THERMACOMP2018, July 9-11, 2018, Indian Institute of Science, Bangalore, INDIA
*N. Massarotti, P. Nithiarasu, Pradip Dutta and C. Ranganyakalu (Eds.)*

# MULTI PHASE MODEL OF SEMI SOLID SLURRY GENERATION DURING COOLING SLOPE PROCESSING OF MELT TREATED AL-7SI-0.3 MG ALLOY

Prosenjit Das*[a,b], Pradip Dutta[b]

[a]Center for Advanced Materials Processing, CSIR-Central Mechanical Engg. Research Institute, Durgapur-713209, India.

[b]Department of Mechanical Engineering, Indian Institute of Science, Bangalore-560012, India.

*Email: prosenjit@cmeri.res.in

## ABSTRACT

The present paper reports development of a multiphase and multiscale volume averaging computational fluid dynamic model to simulate cooling slope slurry generation process. Novelty of the present work lies in the accurate estimation of effect of grain refiner, modifier addition on thermophysical and morphological properties of the generated semi solid slurry, which establishes potential of the present model to be implemented as a process control tool to develop engineering components using the cooling slope generated slurry. The three phases considered here are parent melt (primary phase), nearly spherical solid grains and air (secondary phases). In depth investigation is performed to understand the transport processes involved in the cooling slope slurry generation process and the findings obtained are volume fraction of constituent phases, evolution and growth of primary Al particles, viscosity distribution, temperature field, velocity field, macro and micro segregation etc. Accuracy of the present model is confirmed by performing real time experimental validation of the chosen process conditions.

**Key Words:** *Semi-solid slurry, Cooling slope, Al7Si0.3Mg alloy, Melt treatment, Multi phase model.*

## 1. INTRODUCTION

Beckermann's group [1-2], pioneered the multiphase solidification model development with their volume averaging approach to treat the liquid and solid phases as separated but highly coupled and interpenetrating continua. The approach has evolved further with Ludwig and Wu [3-4], who have studied the globular equiaxed solidification by modifying the nucleation model and heat, mass exchange terms. The present work is focussed on numerical model development of semi solid processing (SSP) of Al alloys, in case of cooling slope technique. Although there are some earlier works on numerical model development of cooling slope slurry generation, however, these models fails to establish robust processing-microstructure correlation and lacks experimental validation.

In the present numerical model, solid evolution and grain formation within the liquid melt is governed by mass, momentum, energy and species transport. The classical nucleation law and growth kinetics, given by Rappaz [5], is implemented in the present model. It is evident from the earlier work by the present research group that slope angle plays the key role to determine slurry morphology among other process variables [6]. In view of the above, the present study is focused to investigate the effect of slope angle at the onset of melt treatment in the form of individual and combined grain refiner, modifier addition on volume fractions of three different phases considered, grain evolution, grain growth, size, sphericity and distribution of solid grains, temperature field, velocity field, macro segregation, micro segregation etc.

## 2. NUMERICAL MODEL

In the present investigation, a non isothermal three phase fluid-fluid Eulerian multiphase flow model is developed to simulate the semi solid slurry preparation of Al-7Si-0.3Mg alloy, employing

cooling slope rheocasting technique. The three phases considered here are parent melt (primary phase), solidifying grains and air (secondary phases) denoted by *l*, *s* and *a*, respectively. The phases are treated as separate but interacting continua, sharing a single pressure field and characterized by their own thermo physical properties. It should be noted that air forms a definable air/liquid melt interface, i.e. free surface, due to its low density. A set of conservation equations of mass, momentum and enthalpy are solved for each of all three phases. Since, volume fractions represent the space occupied by each phase and conservation laws are solved for each phase individually, so interface tracking is not required here. Volume fractions of constituent phases are assumed to be continuous functions of space and time and their sum is equal to one. Here, although solidifying grains are actually solid but they are considered as fluid, to enhance computational efficiency. However, in case of exchange terms such as; momentum and enthalpy exchange, fluid-solid exchange model is considered for solid-liquid and solid-air interface and fluid-fluid exchange model is used for liquid-air interface, to maintain accuracy of the model. Further details on the present numerical model may be seen from our earlier published work [7].

## 3. RESULTS

### 3.1 Temperature

Comparative distribution of slurry temperature for different process conditions studied here, along the slope centreline, is shown in Fig. 1a. Moreover, Fig. 1a also shows the zoomed view of temperature distribution at slope exit. Effect of slope angle variation on slurry temperature is clearly evident from Fig. 1a. For all the melt treatment conditions lesser slope exit temperature is recorded in case of 45$^o$ slope, which is attributed to the higher melt residence time and in turn availability of higher cooling time to the melt during flow in case of 45$^o$ slope. Higher 'g' component and subsequent higher melt velocity facilitates higher slope exit slurry temperature in case of 60$^o$ slope, compared to its 45$^o$ slope counterpart. Combined addition of refining and modifying agents enhances melt cooling rate further due to tendency of modifier to decrease surface tension of the melt and causes decrease in slurry temperature.

### 3.2 Solid fraction

In the present model, immediately after the impingement of superheated melt over slope surface, solver temperature T drops below liquidus temperature of the alloy and burst nucleation occurs within the melt. Solid content serves as the key quality characteristic of semi solid slurry to determine its further processability towards component development. In case of 60$^o$ slope, approx. upto 400 mm flow length, combined melt treated slurry shows lesser solid content compared to its untreated and refined counterpart. This is may be due to the higher melt flow velocity, attained by modifier addition, and subsequent lesser growth opportunity of nucleated solids. Afterwards; enhanced progressive nucleation catches up to yield higher slope exit solid fraction in case of combined melt treated slurry (shown in Fig. 1b).

### 3.3 Grain size and degree of sphericity

Quantitative findings on microstructural morphology of the evolving primary solid particles, during melt flow along the slope, are shown in Fig. 2a and 2b. Increasing trend in grain size of primary particles is evident (Fig. 2a) for all the process conditions studied here, in line with the solid fraction evolution. Spatio-temporal increase in grain size of primary Al particles is due to the ripening and diffusion driven growth, occurs normally during solidification. For all the melt treatment conditions higher grain size values are observed in case of 45$^o$ slope compared that of slurry samples processed using 60$^o$ slope, whereas, higher melt flow velocity in case of 60$^o$ slope increases shear rate and in turn increases the shear stress undergone by the flowing melt, which results in enhanced sphericity of primary Al particles (Fig. 2b) compared to that of 45$^o$ slope.

3.4 Micro segregation

Solute rejection by the growing primary Al grains triggers micro segregation. In the present work, sudden chilling at the melt contact zone of the cooling slope facilitates nucleation of primary solid and subsequently segregation occurs at the solidification interface due to solute partitioning. Although, solute partitioning causes micro segregation only in case of a isolated control volume, however, in this study, gravity driven melt flow facilitates mass exchange among neighbour control volumes of flow front through grain movement. So, localised effect of micro segregation along the flow front, occurs due to nucleation and growth of the primary Al phase, facilitates global distribution of solutes i.e, macro segregation.

3.5 Slurry velocity and viscosity

The present study depicts the flow behaviour of semi solid slurry at the onset of gravity driven flow and gravitational acceleration facilitates uniform increase in flow velocity in the direction of melt travel along the slope. Higher velocity is recorded in case of $60^o$ slope processed slurry samples, which is rather expected. It is interesting to note that slurry viscosity values in case of $60^o$ slope processed slurry are found to be initially higher, which is due to the rapid solid formation rate in case of $60^o$ slope, since, higher velocity of melt travel in this case increases heat transfer coefficient of the melt. However, afterwards, enhanced cooling time available in case of $45^o$ slope and lesser shear rate undergone by the semi solid slurry increases its viscosity (Fig. 3a).

3.6 Comparison with experimental results

Figure 3b shows experimental validation of the particle size distribution for representative process conditions, using optical micrographs of the oil quenched slurry samples. The samples were collected successively during melt flow along the slope and subsequently image analysis is performed on the optical micrographs to validate the numerical findings of grain size and degree of sphericity.

## 4. CONCLUSIONS

The present work depicts development of an experimentally validated multiphase flow numerical model of cooling slope slurry generation process. Eulerian multi-phase flow approach is considered to investigate the effect of key process variables i.e, slope angle variations and melt treatment conditions, to identify the optimum set of process variables, to achieve desired thermo physical and morphological properties within the generated semi solid slurry. Good agreement between numerical predictions and experimental measurements confirms application potential of the present multiphase model to develop automobile, aviation components with significantly enhanced structural integrity, out of the cooling slope generated slurry, by enabling process control in the in house developed Rheo pressure die casting system.

## REFERENCES

[1] C. Beckermann, and C.Y. Wang, Equiaxed Dendritic Solidification with Convection: Part 1. Multi-Scale /-Phase Modeling, *Metall. Mater. Trans. A*, 27, 2754-2764, 1996.

[2] C. Beckermann, and C.Y. Wang, Equiaxed Dendritic Solidification with Convection: Part 2. Numerical Simulations for an Al-4wt% Cu Alloy, *Metall. Mater. Trans. A*, 27, 2765-2783, 1996.

[3] M. Wu, A. Ludwig, A. Buhring-Polaczek, M. Fehlbier, P.R. Sahm, Influence of convection and grain movement on globular equaixed solidification, *International Journal of Heat and Mass Transfer*, 46, 2819-2832, 2003.

[4] M. Wu, A. Ludwig, A Three-Phase Model for Mixed Columnar Equiaxed Solidification, *Metallurgical and Materials Transactions A*, 37, 1613-1631, 2006.

[5] M. Rappaz, Modeling of Microstructure Formation in Solidification Processes, *Int. Mater. Rev.*, 34, 93-123, 1989.

.

[6] P. Das, S.K. Samanta, H. Chattopadhyay, B.B. Sharma, P. Dutta, Eulerian two-phase flow simulation and experimental validation of semisolid slurry generation process using cooling slope. *Material Science and Technology*, 29, 83-92, 2013.

[7] P. Das, S.K. Samanta, B. Mondal, P. Dutta, Multiphase Model of Semisolid Slurry Generation and Isothermal Holding During Cooling Slope Rheoprocessing of A356 Al Alloy, *Metallurgical and Materials Transactions B*, https://doi.org/10.1007/s11663-018-1211-1.

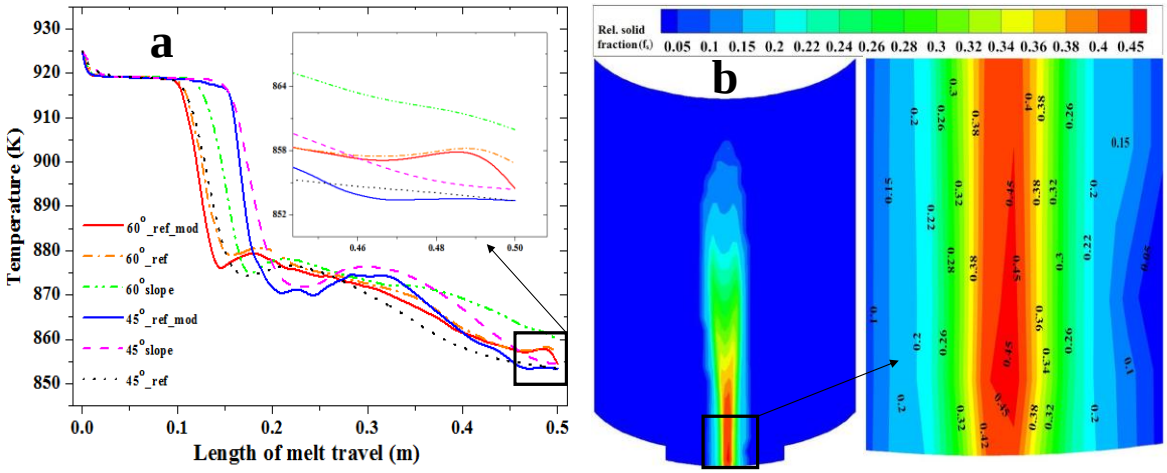


**Fig. 1:** (a) comparative distribution of slurry temperature, and (b) slope exit solid fraction.

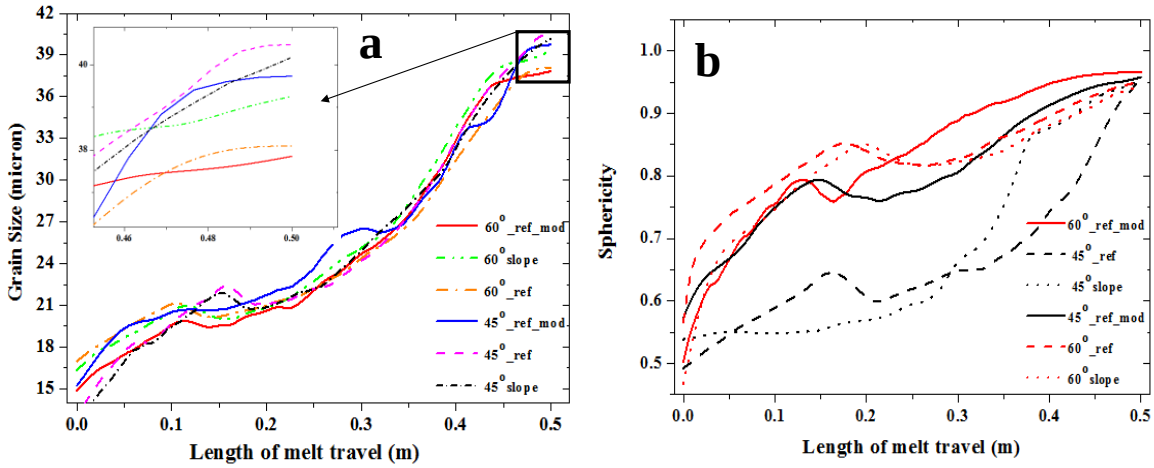


**Fig. 2:** Microstructural morphology of the primary solid particles: (a) grain size and (b) sphericity.

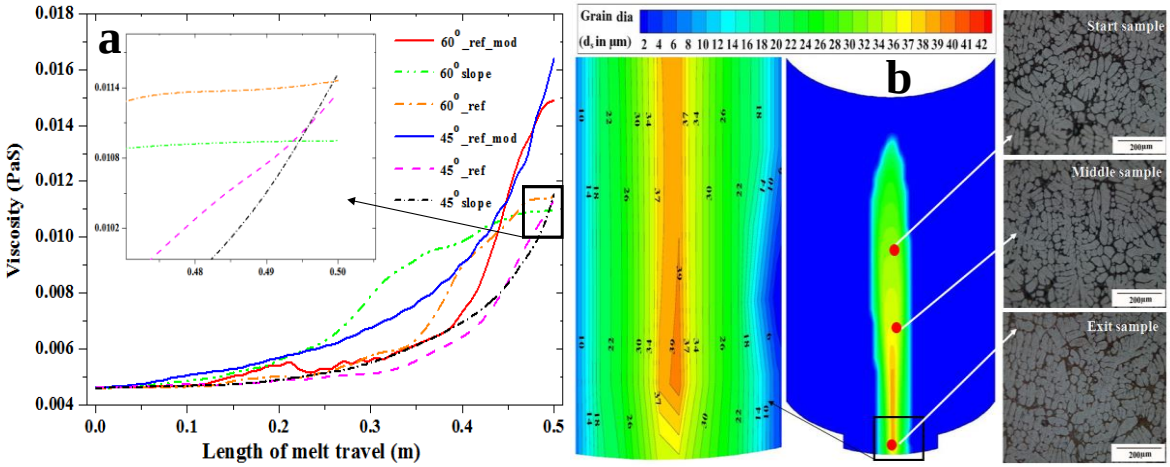


**Fig. 3:** (a) comparative slurry viscosity, and (b) grain size distribution of melt treated slurry.

Fifth International Conference on Computational Methods for Thermal Problems
THERMACOMP2018, July 9-11, 2018, Indian Institute of Science, Bangalore, INDIA
*N. Massarotti, P. Nithiarasu, Pradip Dutta and C. Ranganyakalu (Eds.)*

# COUPLED FLUID FLOW, HEAT AND MASS TRANSFER MODELLING DURING CONVECTIVE DRYING OF POTATO

**Punit Singh, Dalbir Singh and Prabal Talukdar**
IIT Delhi, Hauz Khas New Delhi-110016,

singhpunitvns@gmail.com, dalbir.drdo@gmail.com and prabal@mech.iitd.ac.in

## ABSTRACT

A 3-D conjugate numerical model for convective drying of cylindrical disk of potato sample with diameter 40 mm and height 10 mm is developed using COMSOL Multiphysics 5.3a commercial software. The present numerical model considers simultaneous heat and mass transfer inside the moist porous material as well as with the air domain. In this conjugate model, full continuity is assumed for heat and mass transfer through the food surface, to solve for temperature and concentration seamlessly across the interface. An internal evaporation is considered inside the porous material and water activity rate equation is implemented in order to determine the amount of evaporation. Thus the numerical model captures the actual physics of the problem and hence predicts the accurate drying behaviour close to experimental results. The air inlet velocities chosen for the numerical study are 2, 4 and 6 m/s and air inlet temperatures are assumed to be 40 °C, 50 °C and 60 °C.

**Key Words:** *Conjugate modelling, convective drying, heat and mass transfer, cylindrical potato disk.*

## 1. INTRODUCTION

Drying is a complex phenomenon which involve two processes. In the first process, heat transfer from the surrounding air to the surface of the moist object occurs by convection and/or radiation and from surface to the inside through conduction. In the second process, internal moisture is first transferred to the surface of the solid by diffusion and then from the surface to the surrounding air through evaporation. The various food products are dried to enhance shelf life, lower packaging cost, reduce shipping costs, enhance appearance, maintain original flavour and retain nutritional value. There are different type of drying methods such as convective drying, solar drying, freeze drying, contact drying, dielectric drying and natural air drying. Out of these drying methods, convective drying is most popularly used in commercial industries, due to its simplicity and cost effectiveness, like agricultural and food industry, building materials, bio-oil industry, paper industry, textile industry, chemical/ceramic industry, coal drying in power plants etc.

Most of the drying models in literature have been developed with simplifying assumptions. Some common assumptions are constant heat transfer coefficients at the surfaces, non-inclusion of evaporation and water activity etc. These assumptions may result in poor prediction of drying behaviour. Even though some of the models use time varying heat transfer coefficients, none of the models uses coupled modelling of the moist food material and the drying air to solve heat and mass transport simultaneously along with momentum transport in air domain. Further a full 3-D numerical model is not available for cylindrical geometries. It is required to develop a coupled model for better prediction of drying behaviour of the moist food materials. Moreover, it is also required to predict drying behaviour of cylindrical food materials as many food products are available as cylindrical slices.

The existing numerical models found in the literature have considered several other assumptions for simplification of the analysis. For example, surface evaporation and internal evaporation from the moist object has not been considered by most of the researchers. The effect of shrinkage in drying has also been less studied, except a few [1-2]. Another shortcoming that can be seen in the existing

numerical model is the decoupling of heat and moisture transfer phenomena inside the food material from the flow field around the moist object. In most of the studies flow field is solved separately to determine the boundary conditions for the heat and mass transfer problem. It could really give some more insight if a conjugate model of fluid flow around the food material and the food material can be developed. Also most of the numerical models are either 1-D or 2-D, except a few 3D model [3-4]. In case of existing decoupled models, most of the researchers used constant heat and mass transfer coefficient around the food material. But in real situation, the heat and mass transfer coefficient vary with respect to temperature gradient and the flow velocity, which implies that it will be spatially dependent. So a detailed numerical analysis by overcoming the limitations mentioned above will help to get a better insight of physics of drying.

In present work, a 3-D conjugate numerical model is developed which determines temperature and moisture distribution inside the moist food material. The model is as realistic as possible to replicate the experimental data with closest accuracy because governing equations of moist food material domain and drying air domain are simultaneously solved through continuity of flux at interfaces instead of solving flow separately and applying surface transfer coefficients. Further this model implements porosity parameter of moist food material and so the moisture dependent properties are used for the food material. Internal evaporation of moisture is also incorporated in the present model.

## 2. MODEL DESCRIPTION AND COMPUTATIONAL METHODOLOGY

Model used in the present numerical study is simulated in COMSOL Multiphysics 5.2a. Because of the symmetry of food domain and drying air domain, 1/4th part of the total domain, as shown in Figure 1, is numerically solved to save the computational cost. The dimensions of duct are 0.45 m x 0.1 m x 0.1 m. Simulations are carried out for cylindrical moist food material (D =4 cm, H = 1cm). Four studies viz. flow, heat transport, liquid species transport and vapour species transport are carried out simultaneously in drying chamber domain. For conjugate model, temperature and vapour concentration variable is taken to solve both porous and air domains of the drying chamber which maintains the continuity of heat and mass fluxes across the interfaces between moist food material and drying air.

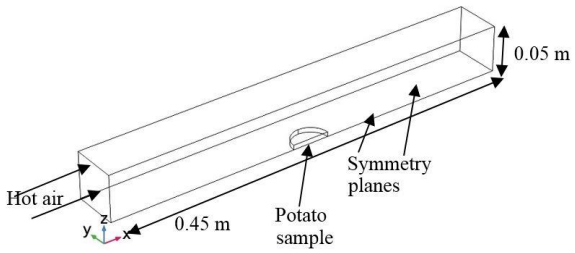


FIGURE 1. Computational domain.

A very fine unstructured mesh of tetrahedral shape is generated near the wall of the moist food object, to capture the gradients.This unstructured mesh has 2624729 domain elements. K-epsilon turbulance model is used to solve the flow fleld which can predict good results for flow over bluff body. The problem is unsteady and hence a time dependent solver is used. All phenomena are simultaneously solved in porous food material and air domains. Absolute and relative tolerances have been selected $10^{-6}$ and $10^{-4}$ respectively. A grid independence test is performed for present numerical model by varying grid sizes. For this purpose, simulations are carried out at the operating conditions: inlet air temperature of 333 K and inlet air velocity of 6 m/s. The grid independency test is performed by creating coarse, fine and finer unstructured mesh. The maximum and minimum grid size for mesh 1, 2 and 3 are 0.0030 m and 3.2e-4 m, 0.0025 m and 2.8e-4 m, and 0.0020 m and 2.2e-4 m respectively. Variation of non-dimensional moisture content with time is plotted with all three grids and it is found that all three grids are sufficiently close to each other. So, to save the computational time and to maintain better accuracy, grid 2 is selected for the present numerical model. For transient study, the

maximum time step size for the simulations performed in the COMSOL is taken as 0.01 s. The software uses adaptive time-stepping and can reduce time step till convergence criteria is satisfied.

## 3. RESULTS

Numerical model is validated with the experimental results published by Hasini et. al. [2] as shown in Figure 2. Variation of non-dimensional moisture content with time is compared for air inlet velocity of 1 m/s and air inlet temperature of 313 K. Here non-dimensional moisture content is defined as ratio of instantaneous to initial moisture content. The rectangular potato sample of size 45 x 20 x 10 mm is taken as moist material for validation purpose.

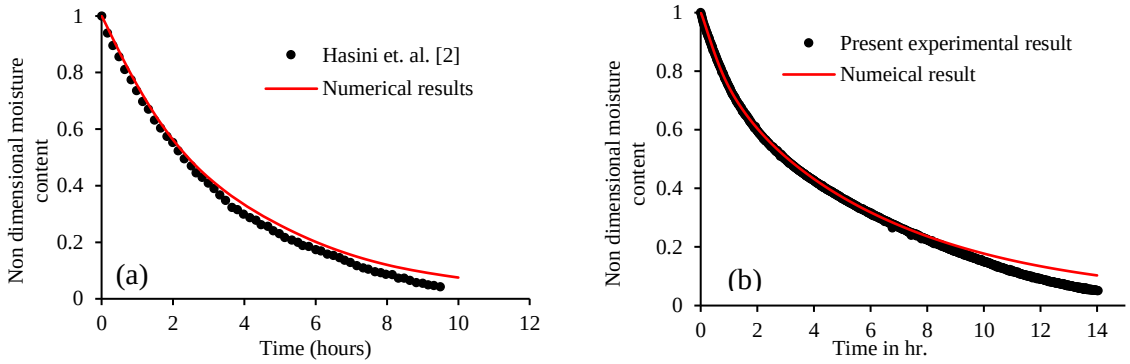


FIGURE 2. Validation of numerical results with the Hasini et. al. [2] (a) and with the present experimental results (b).

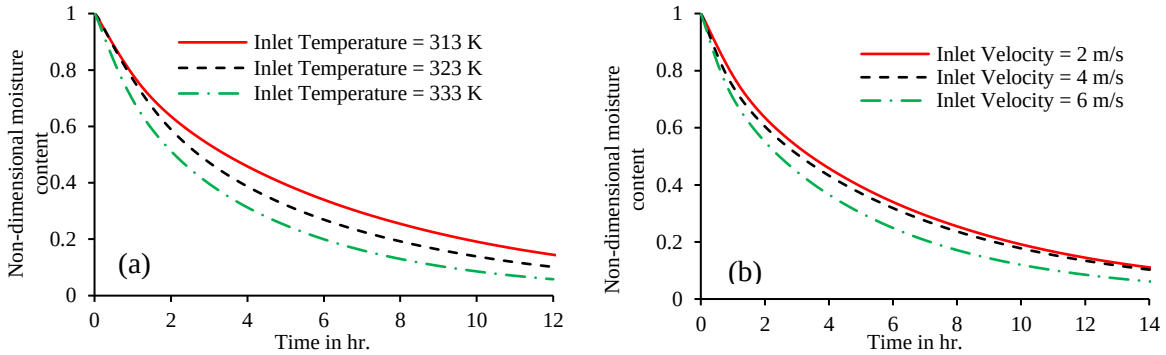


FIGURE 3. Variation of non-dimensional moisture content with drying time at air inlet temperature of 313, 323, 333 K and air velocity of 2 m/s (a) and at air inlet velocity of 2, 4 and 6 m/s and inlet temperature of 313 K (b).

The numerical model is also validated with the experimental results performed at IIT Delhi. The results are compared at air inlet velocity of 4 m/s and air inlet temperature of 313 K. The purpose of comparison of numerical results is to demonstrate that the numerical model is useful when applied for all practical conditions of convective drying. It assures that the numerical solution is valid and reliable for various conditions. Figure 3 shows the variation of non-dimensional moisture content with drying time at different air inlet temperature and at different air inlet velocities. It is found that there is noticeable influence of both air temperature and velocity on the drying rates. Moreover, the effect of temperature is more on the drying rate as compared to the effect of velocity. At higher temperature, the temperature gradient between the moist object and air is large which results in a higher diffusion rate and hence a faster drying rate.

Figure 4 shows the variation of temperature of moist potato sample with respect to time at different air inlet temperature and velocity. In Figure 4 (a), for air inlet temperature of 313 K, temperature of

potato sample rises sharply up to approximately 299 K in 12 minutes and remains almost constant for approximately for 1 hour. After that temperature rises steadily until the equilibrium reached. The similar trend is observed for other temperatures. In Figure 4 (b), as the air velocity increses the heat transfer coefficient also increases which results in increase in heat flux due to which the food material temperature rises.

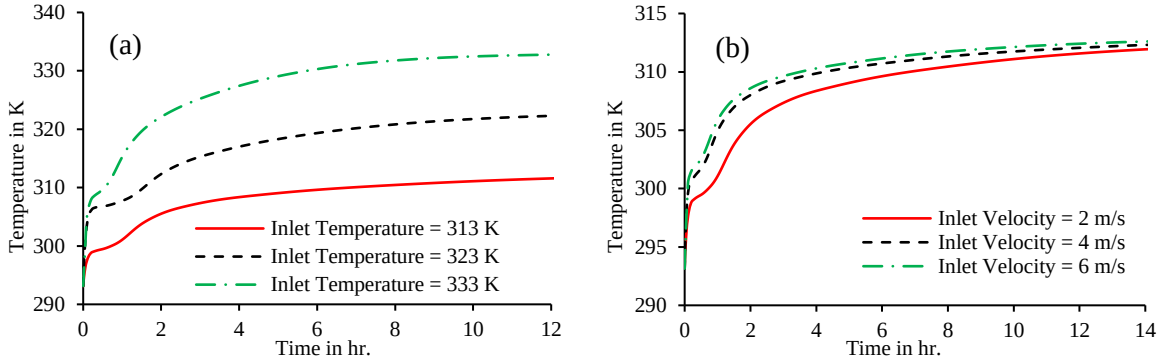


FIGURE 4. Variation of temperature with drying time at (a) air inlet temperatures of 313, 323, 333 K and air velocity of 2 m/s and (b) air inlet velocity of 2, 4, 6 m/s and inlet temperature of 313 K.

## 4. CONCLUSIONS

A 3-D conjugate numerical model is developed for convective drying of cylindrical potato disk. The numerical model simultaniously solves heat and mass transfer through the porous food material as well as in the drying air domain. The moisture content of the potato sample predicted by the numerical model is close to experimental observations under different operating conditions. The temperature and moisture distribution is determined under different operating conditions at different drying time.

## ACKNOWLEDGMENT

The authors are thankful to HRDG (Human Resource Development Group) of CSIR (Council of Scientific and Industrial Research), New Delhi for financial support through a sponsored research project.

## REFERENCES

[1] J. Irudayaraj, K. Haghighi and R. L. Stroshine, Finite element analysis of drying with application to cereal grains, Journal of agricultural engineering and research 53, 209-229, 1992.

[2] L. Hassini, S. Azzouz, R. Peczalski, A. Belghith, Estimation of potato moisture diffusivity from convective drying kinetics with correction for shrinkage, Journal of Food Engineering 79, 47–56, 2007.

[3] V.P. Chandra Mohan and Prabal Talukdar. Three dimensional numerical modeling of simultaneous heat and moisture transfer in a moist object subjected to convective drying. International Journal of Heat and Mass Transfer 53, no. 21, 4638-4650, 2010.

[4] Md. Ateeque, Ranjeet K. Mishra, V. P. Chandramohan, and Prabal Talukdar. Numerical modeling of convective drying of food with spatially dependent transfer coefficient in a turbulent flow field. International Journal of Thermal Sciences 78, 145-157, 2014.

Fifth International Conference on Computational Methods for Thermal Problems
THERMACOMP2018, July 9-11, 2018, Indian Institute of Science, Bangalore, INDIA
*N. Massarotti, P. Nithiarasu, Pradip Dutta and C. Ranganyakalu (Eds.)*

# NUMERICAL INVESTIGATION OF HEAT TRANSFER AUGMENTATION IN DUCT USING RECTANGULAR WINGLET TYPE VORTEX GENERATOR IN TURBULENT REGIME

**Rajat Dixit, Sameer Khandekar***
Department of Mechanical Engineering, Indian Institute of Technology Kanpur, 208016, India
*Corresponding Author: Tel: +91-512-259-7038, Email: samkhan@iitk.ac.in

## ABSTRACT

Requirements of light weight compact heat exchangers in power, process and aerodynamic applications have resulted in the development of specifically designed heat transfer surfaces. In some of these applications, heat transfer coefficients on the surfaces are significantly low. In order to increase heat transfer between flowing fluid and heated surface, winglet type vortex generator can be used. Heat transfer enhancement using winglets has been studied numerically for hydro-dynamically fully developed and thermally developing flow inside a square duct for Reynolds number (Re) ranging from 8000-80000. Air is used as the working fluid. Constant heat flux boundary condition is applied on the bottom wall of duct. The rest of the three walls of duct are well insulated. Low Re k-ε turbulence model is used to formulate the problem for the computational domain with well-defined initial conditions for turbulent kinetic energy and dissipation rate to account for near wall turbulence and mixing. A grid independency test for optimum mesh is also performed. Rectangular winglet is placed inside duct at the initiation of thermal entrance region with the angle of attack as controlled parameter. These winglets induce stream wise vortex shedding. Vortices disrupt the development of the thermal boundary layer and thereby enhance rate of heat transfer between the working fluid and the heated surface. Present study compares the effectiveness of these longitudinal vortex generators in the form of winglets to increase the heat transfer coefficient between heated surface and flowing fluid.

It is shown that presence of winglet induces a wake region with bulk mixing in turbulent regime thus disturbing the flow behind the vortex generator and augmenting local heat transfer. Enhancement of heat transfer is validated from the increase in bulk fluid temperature and local Nusselt number in the vicinity of the wake region. It is concluded that forced convective heat transfer can be increased significantly with increase in Reynolds number and the angle of attack of the winglet.

**Key Words:** *Heat transfer in ducts, Winglet, Vortex, Low Re k-ε model, Turbulent force convection.*

## 1. INTRODUCTION

Many methods for enhancing heat transfer of gaseous ambient have been studied for industrial applications primarily in heat exchangers. Passive augmentation methods usually offer the advantages of less complexity, lower capital cost, and higher reliability where space compactness is desired [1]. Improving the performance of these heat exchangers can have a significant impact through improvements in energy efficiency. Technique of vortex generation using winglets to enhance heat transfer has been widely offered for real life applications. Protrusions in the form of winglet can be mounted on heated surface to generate longitudinal vortices. These induced vortices, mixes the fluid near the heated plate with free stream fluid and this bulk mixing is the primary mechanism for heat transfer enhancement through vortex generation [2]. The swirling motion of fluid at different locations over heated surface along stream wise direction using winglet is desired. This swirl flow enhances the bulk fluid mixing and heat transfer.

In the present study, 3D turbulent forced convection heat transfer in a square duct configuration has been carried out for different orientation of winglet under steady state conditions. The objective of present numerical study is to compare the heat transfer enhancement with the use of winglets and can be employed to assist in designing real life experimental investigations.

## 2. PROBLEM DISCRIPTION

Hydro-dynamically fully developed and thermally developing turbulent forced convective flow with air as the working fluid inside a square duct of dimension 200 cm ($L$) and 10 cm x 10 cm cross-section is modelled. Figure 1 shows the schematic of the duct with winglet orientated at 45°. Fluid thermo-physical properties are considered at free stream temperature. Stainless steel 304 plate is used as test specimen. Winglet of cross-section 5 cm x 2 cm and thickness of 5 mm is orientated at different attack angles. Effect of presence of winglet and its orientation on plate average Nusselt number along the axial direction of flow is compared for different values of flow Reynolds number. Constant heat flux boundary condition is applied to the plate.*

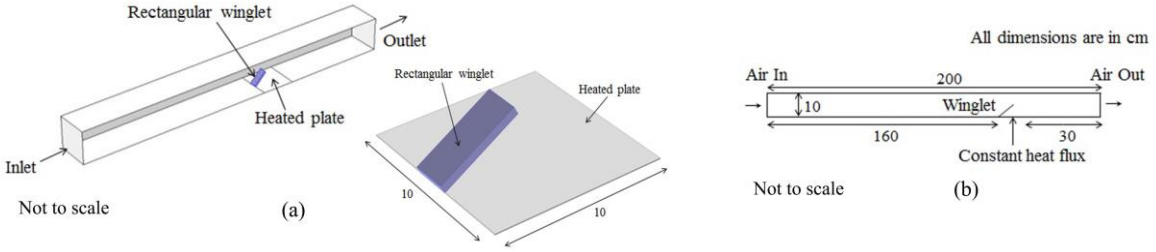


Figure 1: (a) 3D computational domain of duct with winglet in COMSOL Multiphysics®, (b) schematic diagram of computational domain in 2D cut plane.

## 3. NUMERICAL METHOD

Near wall region modelling is employed as it is important because solid walls are main source of vorticity and turbulence i.e., large variation in turbulent kinetic energy and turbulence dissipation energy. Flow separation and reattachment are strongly dependent on a correct prediction of development of turbulence near walls. Low Re k-ε turbulence model with damping function approach is incorporated to have an approximate prediction of flow near the solid walls [3]. The equations are integrated to the wall with an equilibrium condition for k and ε. Damped parameters are used to account for the behaviour of eddy viscosity. Numerical simulation is based on the solution of a coupled system of non-linear partial governing differential equations (PDEs); due to this, a numerical approach is employed based on damped Newton-Raphson method to solve the set of equations. Finite element formulation based commercial software COMSOL Multiphysics® has been used. Successive mesh refinement technique is applied for convergence and reducing residual error. A grid independency test is also performed to have an optimum mesh size for different cases. The Parallel Sparse Direct Solver (PARDISO) which is based on LU decomposition method is employed to solve a system of non-linear equations generated at each and every Newton-Raphson steps during computation. Results from numerical simulation are used to predict the flow characteristics in the vicinity of the walls. Variation of flow velocity ($u$) and wall temperature ($T$) fields in the computational domain can be visualized.

The accuracy of results obtained from COMSOL Multiphysics® can be validated by comparing the hydro-dynamically full developed turbulent velocity profile of numerical solution with that of

* Experimental validation of numerical results is ongoing using the Liquid crystal thermography technique to visualize the variation of wall temperature.

turbulent power law velocity profile [6]. Surface plots have been generated to report for the variation in wall temperature. To compare heat transfer augmentation, plate average Nusselt number is plotted along the axial direction for different cases.

## 4. RESULTS

Multiple computations have been performed at different Reynolds numbers and angle of attack of the winglet. Fully developed velocity profile obtained from the numerical solution is compared with the power law velocity profile, as depicted in Figure 2 (b). For Re = 50000, wall temperature variation over the heated surface with and without the presence of winglet is shown in Figure 3 with attack angle of winglet 30° and 45° respectively. The formation of a wake region behind the winglet disrupts the flow and enhances the bulk mixing of the fluid. As a result, the wall temperature decreases subsequently which enhances the heat transfer between the heated surface and the fluid.

Higher value of Reynolds number implies higher mass flow rate of working fluid entering in duct which increases the momentum of fluid and presence of eddies near the solid walls lead to recirculation of flow, which as a result of the presence of the winglet leads to a secondary flow. The interaction between these secondary flows with the primary flow of fluid is the main reason for bulk fluid mixing resulting in an increase in heat transfer near the heated surface. The average wall temperature change along a cross-section cut in the plane of plate along winglet width in Figure 4 (a) shows that behind the winglet there is small heated zone where temperature is high due to flow being obstructed by winglet and after that sudden drop in temperature can be seen along the axial direction due to the bulk mixing of secondary eddy flow with the primary flow. Due to this phenomenon there is an increase in the average Nusselt number of heated surface.

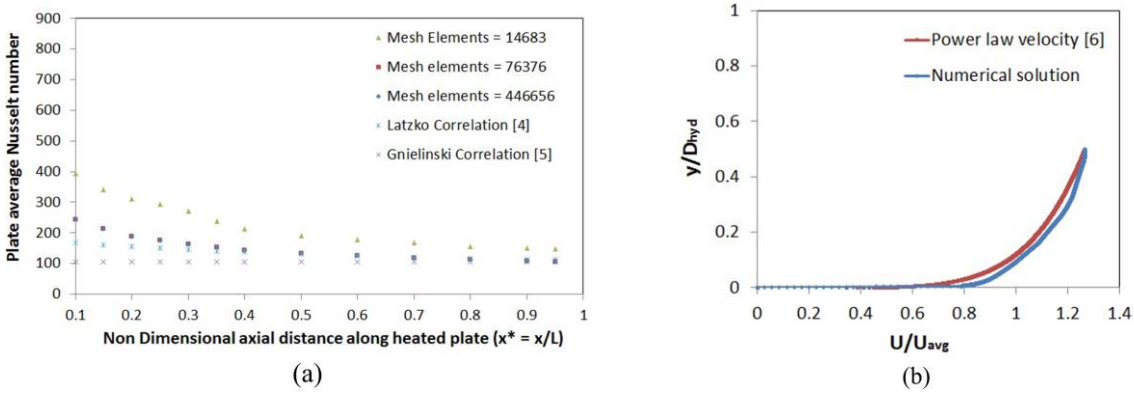


Figure 2: (a) Grid independence test for optimum mesh size at Re = 50000, (b) comparison of numerical and power law velocity profile solution for non-dimensional fully developed turbulent velocity profile.

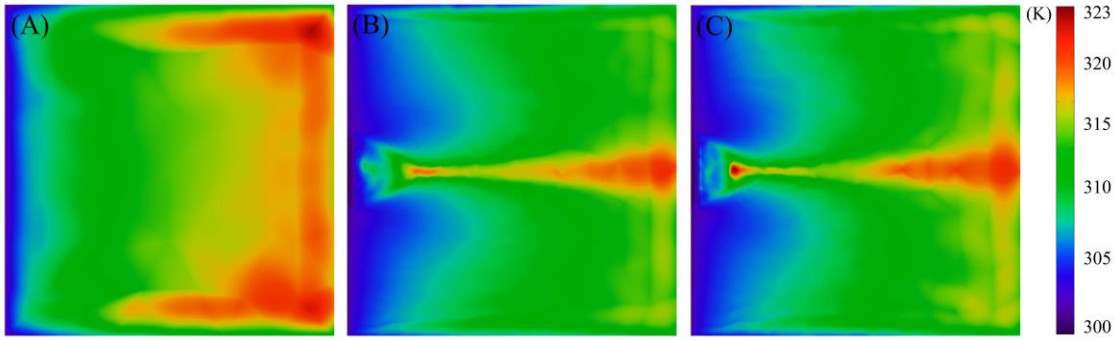


Figure 3: Temperature variation over heated surface for (A) Re = 50000 without winglet vs. winglet with attack angle (B) 30° and (C) 45° respectively.

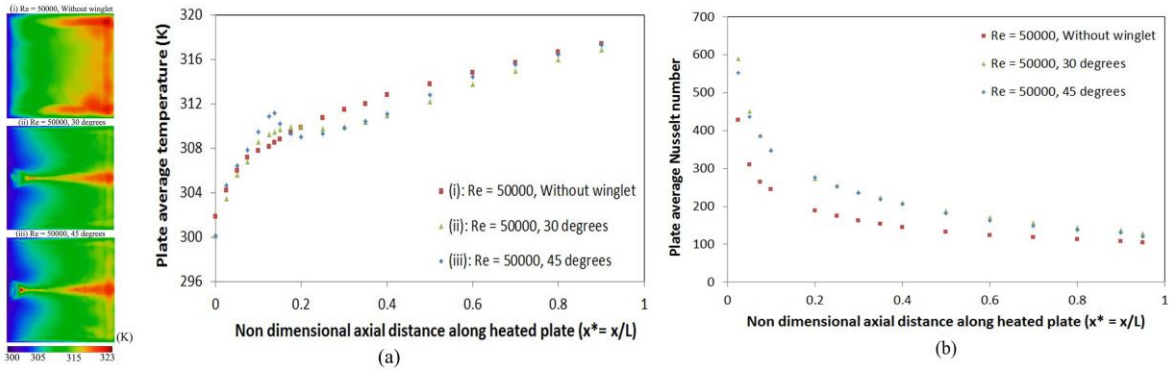


Figure 4: (a) Variation of average wall temperature over a plane cut along winglet width, (b) Plate average Nusselt number variation along the axial direction for Re = 50000 without winglet and with winglet for 30°, 45° inclination angle case.

From the above discussion, it is evident that in the vicinity of winglet there is a reduction in average wall temperature which is beneficial in enhancement of plate average Nusselt number at the desired locations, which clearly depicts the effectiveness of using winglet.

## 5. CONCLUSIONS

Augmentation of heat transfer during forced convection can be achieved by incorporating vortex generators along stream-wise direction. Results of present study shows that up to 42 percent increase in heat transfer coefficient can be achieved for different Reynolds number and attack angle of winglet as compared to the case where no winglet is used. Heat transfer increases significantly with attack angle of winglet. This shows that flow obstruction and disruption of boundary layer using vortex generators can locally enhances heat transfer at desired locations by suitably adjusting its orientation.

## REFERENCES

[1] M.C. Gentry, A.M. Jacobi, Heat Transfer Enhancement by Delta-Wing Vortex Generators on a Flat Plate: Vortex Interactions with the Boundary Layer, Exp. Therm. Fluid Sci., 14, 231-242, 1997.

[2] P. Deb, G. Biswas, N.K. Mitra, Heat transfer and flow structure in laminar and turbulent flows in a rectangular channel with longitudinal vortices, International Journal of Heat and Mass Transfer, 38, 2427-2444, 1995.

[3] C. Hrenya, S. Miller, T. Mall, J. Sinclair, Comparison of Low Reynolds number k-ε turbulence models in predicting heat transfer rates for pipe flow, International Journal of Heat and Mass Transfer, 41, 1543-1547, 1998.

[4] Boelter, L.M.K., G. Young and H. W. Iverson, Natl. Advisory Comm. Aeronaut. Tech. Note 1451, Washington D.C., 1948.

[5] F.P. Incropera, D.P. Dewitt, T.L. Bergman och A.S. Lavine, Principles of Heat and Mass Transfer, 7th Edition International Student Version, John Wiley Sons Inc, 2012.

[6] N. Afzal, Power law and log law velocity profiles in turbulent boundary-layer flow, equivalent relations at large Reynolds numbers, Acta Mech., 151, 195-216, 2001.

Fifth International Conference on Computational Methods for Thermal Problems
THERMACOMP2018, July 9-11, 2018, Indian Institute of Science, Bangalore, INDIA
*N. Massarotti, P. Nithiarasu, Pradip Dutta and C. Ranganyakalu (Eds.)*

# STUDY OF BUBBLE DYNAMICS AND FREE LIQUD SURFACE COLLAPSE DUE TO AIR INJECTION

**Sarath Raj, J.S. Jayakumar***
Department of Mechanical Engineering, Amrita Vishwa Vidyapeetham, Amritapuri, India
E-mail:- *srsnit2013@gmail.com*,*Corresponding author, E-mail:- *jsjayan@gmail.com*

## ABSTRACT

In this work, the Volume of Fluid (VOF) [1] method is used to study bubble dynamics and collapse of bubbles on free surface in a rectangular domain with single as well as double inlets. The simulation is done using open source CFD software `OpenFOAM-3.0.1`. The conservation equations for mass and momentum, which incorporates the influence of surface tension and gravity, are solved by using PIMPLE algorithm. The physical model for the simulation process is a 2D rectangular domain with a width of 50 mm and height of 100 mm. In order to study the collapsing of bubble on surface, ullage area of 15% was considered within the domain. Numerical computation was performed with multiphase solver `interFoam`. Modelling of the geometry, meshing and setting the boundary conditions were done, using OpenFOAM software. The simulation results were compared with available literature results and found that the bubble formation and dynamics are in good agreement. The behaviour of gas bubbles emanating from two adjacent orifices at different gas velocities are studied. Mixing behaviour in the bulk liquid due to bubble formation under different inlet gas velocities was also numerically investigated. The impact of surface tension of bulk liquid on collapsing of bubble on free liquid surface is investigated numerically.

**Key Words:** *Bubble dynamics, Bubble coalescence, interFoam, OpenFOAM, VOF, CFD.*

## 1. INTRODUCTION

Gas-liquid bubble columns are extensively used as reactors and multiphase contactors in chemical, biochemical, petrochemical industries and in various other engineering applications. It has numerous advantages, which can be explained in terms of higher heat-mass transfer rates, efficient inter-phase interaction, compactness, low operating and maintenance cost etc. Even though a large number of studies prevail in the literature, bubble column studies are still not well established because majority of these studies were often carried out on only one phase, i.e., either gas or liquid. However, in bubble columns the primary focus should be given to the interaction between the different phases, which are in fact mutually linked. Bubble performance is crucial in defining the fluid characteristics in bubble columns.

In the present work, the VOF [1] technique is applied in the simulation of bubbling characteristics and collapse at free liquid surface. The simulation dealt with bubble behaviour in a 2D rectangular domain with double orifice of small diameters in contrast to the single orifice simulations carried out earlier using other CFD tools. So far, no studies have been reported on bubble dynamics and collapse at free surface in a rectangular container with single or double orifices using OpenFOAM. The time for bubble detachment, average bubble diameter and the agglomeration and mixing rates of bubbles are deliberately scrutinized by utilizing computer simulations.

## 2. VALIDATION

For validating the methodology used in the present study, the work of Ma et al. (2012) [2] was considered. The comparison of bubble diameter with inlet gas velocity was investigated. It was observed that with increase in inlet gas velocity, the bubble average diameter increases, as shown in figure.1. The results of the present study are in good agreement with Ma et al. (2012) [2] and the relative error were within 5%.

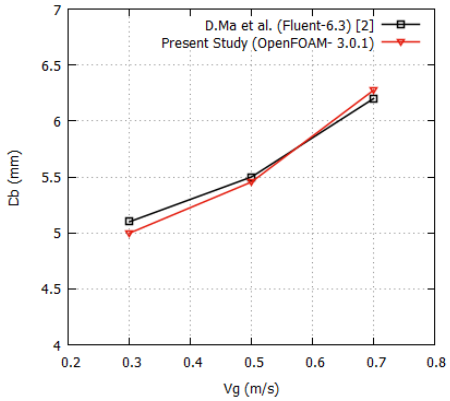


FIGURE 1. Bubble diameter vs. Inlet gas velocity, Orifice diameter Do= 0.5 mm.

## 3. ANALYSIS

In the present study, a rectangular domain of 50 mm width and 100 mm height is considered. Figures 2 (a) and 2 (b) show the rectangular domain with single and double inlet respectively.

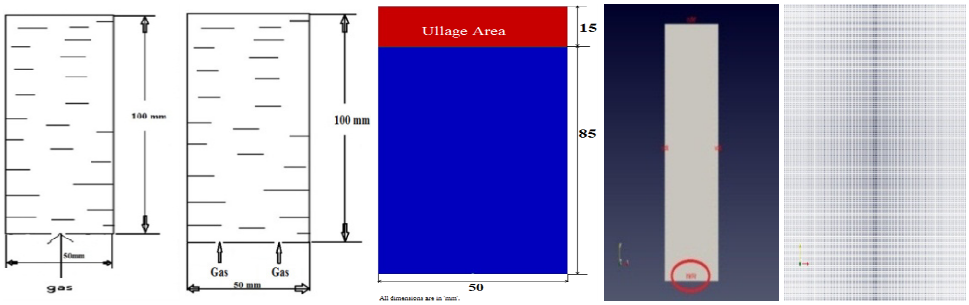


(a) (b) (c) (d) (e)

FIGURE 2. (a) Rectangular domain with single inlet. (b) Rectangular domain with double inlets. (c) Rectangular domain having ullage area with single inlet. (d) Computational model of rectangular domain. (e) Enlarged view near the inlet orifice.

The geometry depiction and dimensional details of rectangular container with 15% ullage area is shown in figure 2 (c). The grid is shown in figure 2 (d). An enlarged view of rectangular region near the orifice is shown in figure 2 (e). Finite volume method (FVM) is used for the discretization of continuity and momentum equation. PIMPLE algorithm is employed to convert PDE to a system of algebraic equations and is solved concurrently. The Piecewise Linear Interface Calculation (PLIC) method is applied here for the reconstruction of fluid interface. Numerical computations are performed with well-known multiphase solver `interFoam`. For these simulations a small time step of the order 0.1 ms is considered. The gas inlets are defined as velocity inlets. Walls are defined as no-slip. For checking the dependency of number of cells on the analysis, five ranges of cell numbers are used. The results show that a representative accuracy can be attained in bubble behaviour simulation with cell number 9.00e+05 and, the precision did not improve even if a higher cell number used [3].

## 4. RESULTS

### 4.1 Influence of inlet gas velocity on bubble behaviour without considering ullage area.

The influence of inlet gas velocity on bubble detachment time, diameter of bubble and free liquid surface deformation were numerically simulated and the results were shown in this section. Figure 3 and 4 show the bubble formation and detachment using single and double inlet when inlet gas

velocity (Vg) is 0.3 and 0.7 m/s. In which the blue part shows the liquid phase and the red portion shows the air bubble. At the initial stage the bubble develops and grows but the gas bubble neck still remains in contact with the orifice mouth. The surface tension force plays an important part in this moment. When the buoyancy force on the bubble over rules the liquid drag force, bubble get detached from the orifice and finally get deformed. The process is repeated for the consecutive bubbles. From the void fraction contours (figure.3 and 4) it can be observed that the upper first bubble get deformed in a much faster rate than the lower rising bubble. This is because of the fact that the upper first bubble flows through the dormant liquid, while the lower travels through the wake region left behind the upper leading bubble. A lower drag force is created for the lower bubble due to the wake left behind the upper bubble. Hence the relative distance between two bubbles gets decreased with time. Subsequently the bubbles get collided to form a larger bubble. The analysis reveals that the average bubble agglomeration rate for both single and double orifice cases increases with inlet gas velocity.The variation of detachment time for first and second bubble for both single and double inlet cases are shown in figure 5 (a) and 5 (b) for various inlet gas velocities. Both the graphs show a downward trend this is because of bubbles get detached from the orifice mouth with less time with the increment in inlet gas velocity.

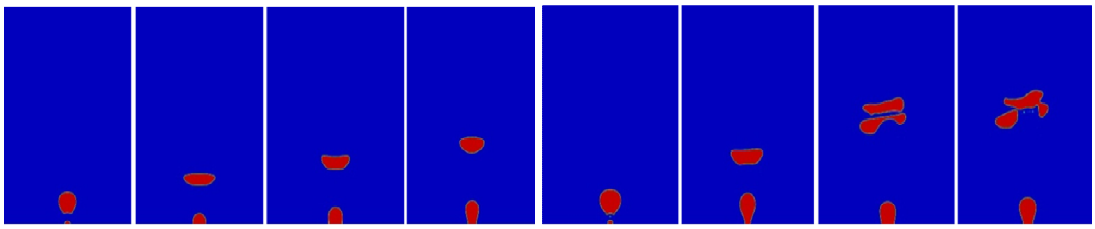


FIGURE 3.Bubble behaviour for various inlet gas velocities when Do= 0.5 mm, (a) t= 0.17s, (b)t= 0.24s, (c) t= 0.31s, (d) t= 0.38 s, (a–d) Vg= 0.3 m/s,(e) t= 0.1s,(f) t= 0.15s, (g) t= 0.22s and (h) t= 0.8s, (e)–(h) ) Vg= 0.7 m/s (Single inlet)

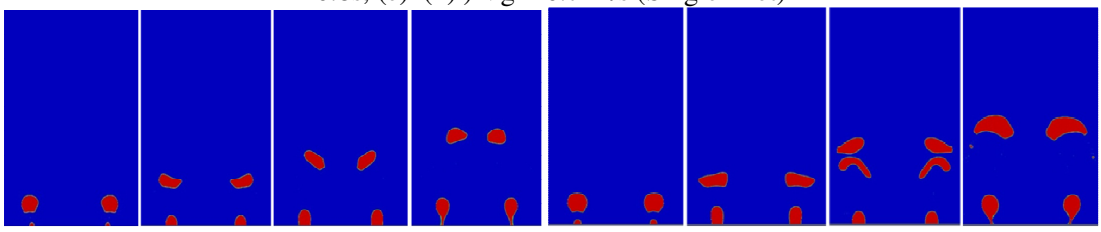


FIGURE 4.Effects of inlet gas velocity on single bubble behaviour when Do= 0.5 mm, (a) t= 0.17s, (b)t= 0.24s, (c) t= 0.31s, (d) t= 0.38 s, (a–d) Vg= 0.3 m/s, (e) t= 0.1s, (f) t= 0.15s, (g) t= 0.22s and (h) t= 0.8s, (e)–(h) Vg= 0.7 m/s (Double inlet)

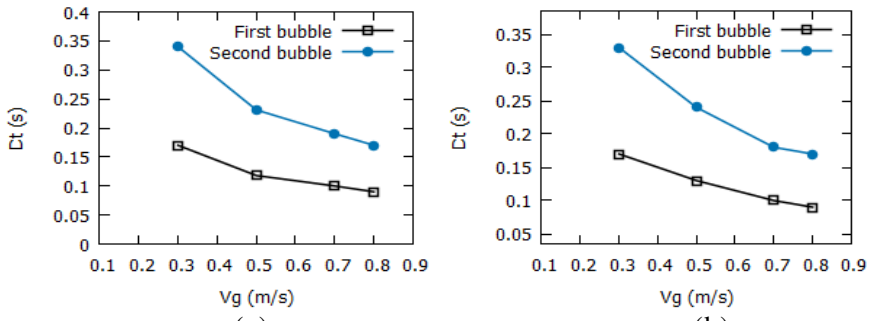


FIGURE 5. (a) Bubble detachment time for various inlet gas velocities (Single inlet). 5. (b) Bubble detachment time for various inlet gas velocities (Double inlet).

4.2 Effect of surface tension on free liquid surface collapse considering ullage area.

The impact of surface tension on free liquid surface deformation due to bubbling is shown in figure. 6 and 7. Figure.8.a and b shows the variation in bubble detachment time and bubble diameter under various values of surface tension for both single and double inlet cases. The free liquid surface deformation rate depends on bubble detachment time and bubble diameter. As the surface tension value is increased the detachment time increases and bubbles get detached from the orifice mouth at slower rate hence more amount of air is entrapped within the gas bubbles. Therefore average bubble diameter increases with increase in surface tension of bulk liquid. At higher values of surface tension, for both single and double inlet cases due to the increment in the detachment time less number of bubble are available at the top end near to the ullage area which is clear from figure.6 and 7. This leads to less turbulence effect and hence collapsing rate of free liquid decreases with increase in surface tension.

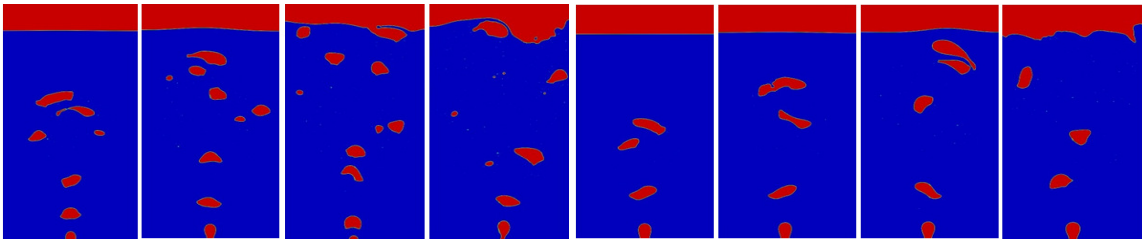

(a) (b) (c) (d) (e) (f) (g) (h)

FIGURE 6. Effect of surface tension on free liquid surface collapsing when Do= 0.5 mm, (a) t= 0.46s, (b) t= 0.56s, (c) t= 0.66s, (d) t= 0.76s. (a)-(d) Vg= 0.9 m/s, $\sigma_l$=0.0482 N/m, (e) t= 0.46s, (f) t= 0.56s, (g) t= 0.66s, (h) t= 0.76s, (e)-(h) Vg= 0.9 m/s, $\sigma_l$=0.0728 N/m. (Single Inlet)

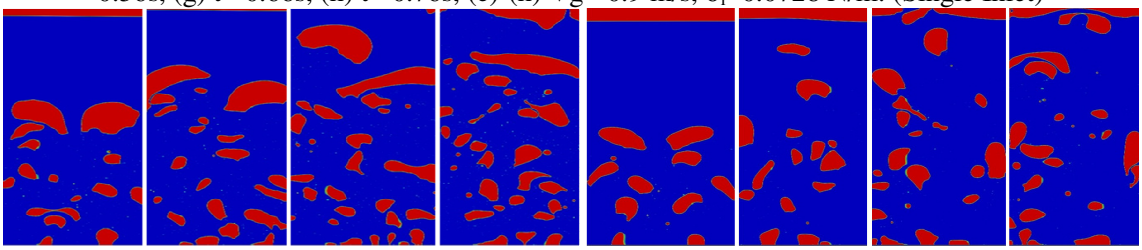

(a) (b) (c) (d) (e) (f) (g) (h)

FIGURE 7.Effect of surface tension on free liquid surface collapsing when Do= 0.5 mm, (a) t= 0.46s, (b) t= 0.56s, (c) t= 0.66s, (d) t= 0.76s. (a)-(d) Vg= 0.9 m/s, $\sigma_l$=0.0482 N/m, (e) t= 0.46s, (f) t= 0.56s, (g) t= 0.66s, (h) t= 0.76s, (e)-(h) Vg= 0.9 m/s, $\sigma_l$=0.0728 N/m (Double Inlet)

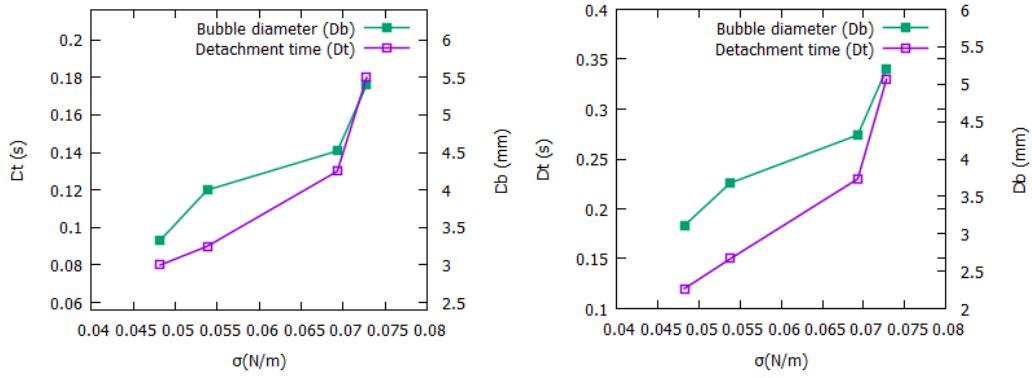


(a) (b)

FIGURE 8.a. Variation in bubble diameter and detachment time with respect to different surface tension (Single inlet). 8.b. Variation in bubble diameter and detachment time with respect to different surface tension (Double inlet).

## 5. CONCLUSIONS

Volume of Fluid (VOF) method was successfully used to numerically investigate the bubble formation, dynamics and free liquid surface deformation in a rectangular domain with single and double inlets. The numerical investigation was carried out by using the software `OpenFOAM-3.0.1`. Compared to other front tracking methods the VOF method has less computational intricacy, higher accuracy, and is easier to understand. The validation of the methodology has been done with respect to the results obtained by Ma et al. [2]. From the investigations the following conclusions are drawn. The average bubble diameter increases with increase in inlet gas velocity whereas the bubble detachment time reduces with the increment in inlet gas velocity for both single and double inlet case. The liquid surface deformation rate decreases with increase in surface tension of bulk liquid

## REFERENCES

[1] C.W Hirt, B.D. Nichols, Volume of fluid (VOF) method for the dynamics of free boundaries, *Journal of. Computational Physics*. 39, 201–225, 1981.

[2] Dou Ma, Mingyan Liu, Yonggui Zu, Can Tang, Two-dimensional volume of fluid simulation studies on single bubble formation and dynamics in bubble columns, *Chemical Engineering Science, Elsevier Science Ltd. Vol*. 72,pp. 61-77,2012.

[3] Sarath Raj, J.S. Jayakumar, Investigation of bubble dynamics with single and double gas inlet(s) in a rectangular container using OpenFOAM, *Proceedings of the 24thNational and 2ndInternational ISHMT-ASTFE Heat and Mass Transfer Conference (IHMTC-2017)*, December 27-30, 2017, BITS Pilani, Hyderabad, India.

Fifth International Conference on Computational Methods for Thermal Problems
THERMACOMP2018, July 9-11, 2018, Indian Institute of Science, Bangalore, INDIA
*N. Massarotti, P. Nithiarasu, Pradip Dutta and C. Ranganyakalu (Eds.)*

# MOLECULAR DYNAMICS SIMULATIONS FOR ESTIMATING SURFACE TENSION OF IONIC LIQUID NANO-DROPS

**Rakesh Rajegowda, Sarith P Sathian**

Department of Applied Mechanics, Indian Institute of Technology Madras, Chennai 600036, India.
Email: r.rakzz@gmail.com, sarith@iitm.ac.in

## ABSTRACT

Molecular dynamics simulations of the nano droplets of the ionic liquid 1-ethyl-3-ethylimidazolium tetrafluroborate (EMIM-$BF_4$) subjected to large external electric field were performed. It is believed that under external electric field the rearrangement of liquid molecules alters the intermolecular interactions and the forces developed influence the surface tension. With this intention we have calculated the surface tension using Irving-Kirkwood pressure tensor method. Surface tension has been estimated for various sized nano-droplets and it is observed that, there is a decrease in the values of the surface tension with a decrease in the drop size. The study also confirmed Rayleigh limit by calculating the number of surface charge present at every time step, which indeed denotes an instance of ion emission from droplet.
**Key Words:** *Surface tension, Electric field, Electrospray propulsion, Nano-drops.*

## 1. INTRODUCTION

Electro-spray propulsion thrusters are based on electrostatic acceleration of droplets and/or ions that are emitted by an electrically conducting fluid like ionic liquids through small capillaries while applying a potential difference between an extraction electrode and the capillary tube. When thrusters are operated in droplet mode maximum thrust is obtained and if it is operated in an ionic mode maximum specific impulse is obtained. The liquid interface that coming out of the capillary tube forms a conical shape due to the application of an electric field, which is called Taylor cone. Taylor [1] developed a detailed theory which opened the door of a new propulsion method. In ionic liquids positive ions near the liquid surface destabilizes the liquid surface when electric field is applied and drawn by the shear stress generated by electrostatic force. These electrostatic forces overcome the surface tension force resulting in electro hydrodynamics tip streaming. The objective of this study is to model nano-droplets and to obtain the variation of surface tension of droplet under the influence of electric field. Ionic liquids are desirable for electro-spray thrusters under vacuum conditions because of its important properties like high viscosity, wide liquid range, thermal stability, negligible vapour pressure and good electrical conductivity.

## 2. METHODOLOGY

Laplace is the one who noticed that the droplet is stabilized by a pressure difference across the interface and it is balanced by contracting force on the spherical surface. Finding surface tension based on thermodynamic analysis fail at nano-scale, as they do not give any prescription for density profile or pressure tensor in terms of intermolecular forces. The Irving-Kirkwood pressure tensor method describes a statistical approach to calculate the surface tension considering the molecular nature of liquid drop [2]. The Rayleigh limit [3] is the number of charges that a fluid drop can hold without undergoing disintegrates due to coulombic repulsion overcoming surface tension. On the application of electric field, droplets begin to reorient and the charge density of the droplet at the surface increases. Consequently the electrostatic pressure increases, which tends to increase the drop radius in the direction of the applied electric field. When electrostatic pressure is greater than

the surface pressure, coulomb repulsion exceeds the surface tension, and then the drop explodes into a jet-fission mode. The Molecular dynamics (MD) simulation are carried out using LAMMPS [4] to model the system for estimating the surface tension of ionic liquid nano-droplets. An interaction between the molecules is defined using modified AMBER force field. Studies have reported the critical electric field required for ion emissions from ionic liquid nano-droplets as 0.985 V/nm and observed the elongation of spherical drop to form the Taylor cone [1]. Surface tension is not a strong function of droplet size above the critical radius [5] and decreases with a decrease in the size of a drop.

## 3. RESULTS

The ionic liquid drop is brought to desired temperature by assigning velocities to each atom by drawing values randomly from the Maxwellian velocity distribution. The ionic liquid drop is then allowed to equilibrate at 300 K for 0.5 ns by monitoring canonical (NVT) ensemble using Nose-Hoover thermostat followed by 0.5 ns of micro-canonical (NVE) ensemble. The density profile obtained for EMIM-$BF_4$ molecules is shown in Figure 1(a) for various droplet sizes. The values plotted are time averaged from the data obtained during production run after the equilibration phase. Radial binning is performed with the help of a post processing code. The number density as function of radius is calculated by counting the number of atoms in each radial bin and subsequently the density is found. A hyperbolic tangent function is used to fit the data obtained by binning to obtain the radius of the droplet. We have used Irving-Kirkwood pressure tensor method [2] to calculate the surface tension. The normal component of pressure tensor is calculated by obtaining the pairwise forces from simulation, i.e both Van der Waals and electrostatic forces acting on surface atoms. Daily [6] calculated the surface tension of ionic liquid EMIM-$BF_4$ using MD and reported as 88.09 dyne/cm, which are almost double the values obtained from the reported experiments [7]. As expected the surface tension values thus calculated shows significant variation with different radial bin sizes, as the chain length of $EMIM^+$ itself is of around 0.5 nm. The value of the surface tension obtained using a radial bin of size 1 nm is 52.32 dyne/cm and this is in good agreement with the experimental results [7]. We repeated the procedure for 64, 80, 100, 125, 216 and 343 EMIM-$BF_4$ molecules to study the variation of surface tension with the size of the drop. Figure 1(b) shows the resulting profiles of surface tension for various droplet sizes.

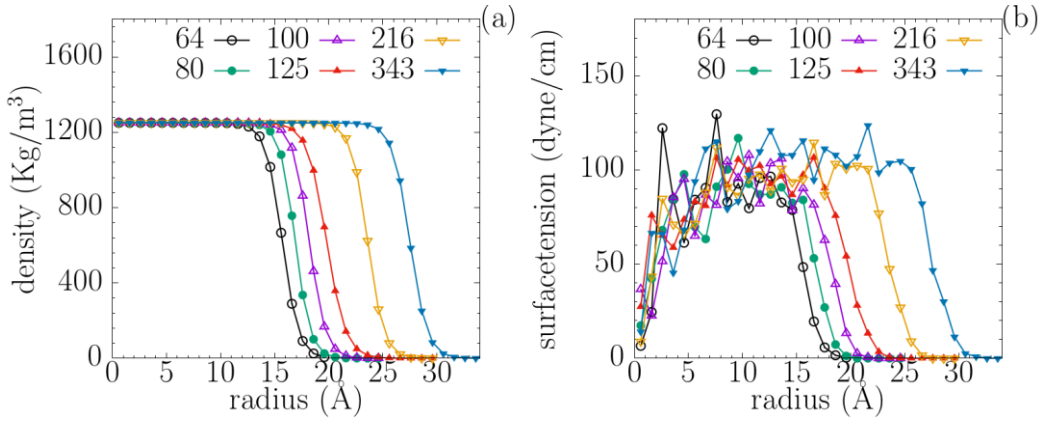


FIGURE 1. (a) The hyperbolic tangential fit of the density data and (b) Surface tension profiles for various EMIM-$BF_4$ droplet sizes. Label denotes the number of ion pairs in the droplet.

The surface tension values obtained for every drop size calculated from MD is being tabulated in Table 1. There is a gradual decrease in the value of surface tension with the decrease in droplet size. It has been reported that the droplets having radius less than 1.8 nm are not structurally stable and macroscale theoretical descriptions are not applicable [5]. From the present study it is clear that surface tension remains almost constant for those drops with radius above 1.8 nm and below this radius, surface tension decreases.

| Number of molecules | Theoretical prediction (nm) | MD calculation (nm) | Surface tension (dyne/cm) |
|---|---|---|---|
| 64 | 1.59 | 1.56 | 47.93 |
| 80 | 1.71 | 1.69 | 48.97 |
| 100 | 1.84 | 1.82 | 50.99 |
| 125 | 1.98 | 1.98 | 52.32 |
| 216 | 2.38 | 2.36 | 52.57 |
| 343 | 2.78 | 2.75 | 53.16 |

TABLE 1. The radius and surface tension of the droplet with various sizes.

As the radius of the EMIM-$BF_4$ droplet is well above critical radius value, it is further investigated under electric field. Once the system is equilibrated, electric field is applied. The critical value of the electric field, required for the emission of ions is 0.985 V/nm. Due to computational constraints we have considered comparatively higher electric field strength to accelerate the process of ion emission. Figure 2 shows the various stages of ion emission process from the droplet with time varying from 0 to 0.58 ns, after which the droplet completely dissociates at 1.4 V/nm. The procedure of ion emission from the droplet is considered as a stochastic procedure because the various simulations performed by changing the random seed for assigning the velocities during initialisation, completely changes the dynamics of the drop. Figure 2(b, c and d) shows the Taylor cone like formations at the tip of the droplets on both the end of drop in the direction of electric field applied, and in the process droplet starts loosing ion and ion clusters from the tip of the cones in both the directions. This directly depicts the process in electro-spray propulsion where ions are pulled out of the capillary tube using the electrodes by applying the potential difference. Figure 2(e and f) shows the stages of the droplet becoming unstable, oscillating and drifting in one direction since the net charge was not neutral. The droplet becomes elongated, so as to form Taylor cones and eventually undergo complete disintegration at 0.6 ns.

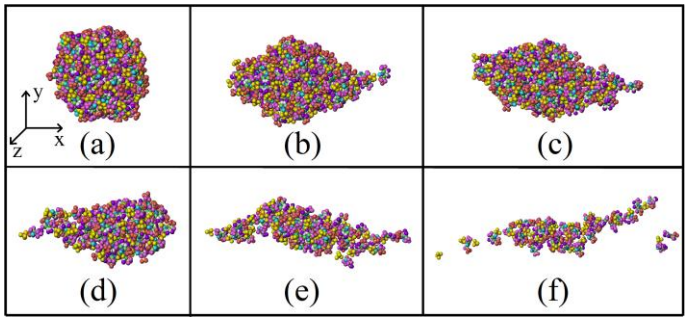


FIGURE 2. (a) 0.0, (b) 0.3, (c) 0.4, (d) 0.5, (e) 0.55 and (f) 0.58 ns after applying electric field (1.4 V/nm) to EMIM-$BF_4$ droplet in the positive *x* direction.

Figure 3(a) shows the variation of surface tension with and without electric field. The 1 ns time averaged value of surface tension without the electric field applied is obtained as 52.32 dyne/cm for EMIM-$BF_4$ droplet. On the other hand surface tension of the same droplet with electric field is determined by taking the moving average due to stochastic behaviour of the system, for very short time until only two ion emissions occur. The droplet starts deforming after this and the prediction of the surface tension become too tedious to be attempted. As soon as we apply the electric field, the droplet starts rearranging itself and orientation of the droplet is completely modified within a time period of 0.03 ns. The sudden increase in the value of the surface tension observed in the first 0.03 ns is due to the reorientation of droplet into the direction of electric field. A sudden decrease in surface tension is observed after the time period of 0.06 and 0.14 ns and this could be due to the rapid emission of ions when electric field is applied. To quantify further we used the Rayleigh limit to determine the emission of ion from the droplet. Figure 3(b) shows the change in the number of surface charge after applying electric field to EMIM-$BF_4$ droplet. The Rayleigh limit calculated as

9.25 for the droplet. The large jump observed in the number of surface charges in the first 0.03 ns is due to the reorientation of droplet in the direction of electric field and the sudden decrease in the number of charges is observed due to the emission of ions, i.e loss of surface charge as it reaches its limit. In previous reports, the emission of ion from droplet is observed when the number of surface charges reaches 90% of the predicted Rayleigh limit. In the present study, the ion emission occurred when number of surface charges reach 95% of the predicted Rayleigh limit.

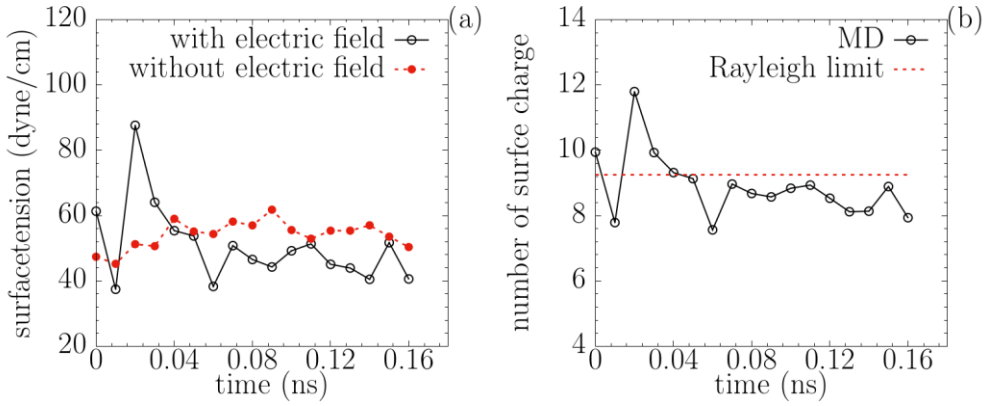


FIGURE 3. (a) Temporal evolution of surface tension with and without electric field (b) Number of surface charge after applying electric field to droplet

## 4. CONCLUSIONS

The Irving-Kirkwood pressure tensor method is used to calculate the surface tension of EMIM-$BF_4$ droplet. The equilibrium MD is performed to study the surface tension of ionic liquid droplets of various sizes. Surface tension remains constant above 1.8 nm and its value decreases below the critical radius. Observed large increase in the surface tension in the first 0.03 ns of the application of the electric field is due to the reorientation of droplet into the direction of electric field. The significant decrease in the surface tension observed could be related to the emission of ions when the electric field is applied. The Rayleigh limit is used to determine the reason and occurrence of ion emission. It is observed that the ion emission from droplet is observed when the number of surface charges reaches 95% of the theoretically predicted Rayleigh limit.

## REFERENCES

[1] G. Taylor, Disintegration of water drops in an electric field. *Proceedings of the Royal Society London A*, 280, 383-397, 1964.

[2] J. H. Irving, and J.G. Kirkwood, The statistical mechanical theory of transport process. IV. The equation of hydrodynamics. *Journal of Chemical Physics* 18, 817, 1950.

[3] Lord Rayleigh, *Philos. Mag.* 14, 184, 1882.

[4] S. Plimpton, Fast parallel algorithms for short range molecular dynamics. *Journal of Computational Physics*. 117, 1-19, 1995.

[5] A. R. Nair, and S. P. Sathian, Studies on the effect of curvature on the surface properties of nanodrops. *Journal of Molecular Liquids*, 195, 248-254, 2014.

[6] J. W. Daily, Molecular dynamics simulation of ion emission from nanodroplets of ionic liquids. *Journal of Propulsion and Power*, 24, 981-986, 2008.

[7] T. N. Krupenkin, J. A. Taylor, T. M. Schneider, and S. Yang, From rolling ball to complete wetting: The dynamic of turning of liquids on nano structured surfaces. *Langmuir*. 20, 3824-3827, 2004.

Fifth International Conference on Computational Methods for Thermal Problems
THERMACOMP2018, July 9-11, 2018, Indian Institute of Science, Bangalore, INDIA
*N. Massarotti, P. Nithiarasu, Pradip Dutta and C. Ranganyakalu (Eds.)*

# COMPUTATIONAL STUDY ON ORIENTATION BASED THERMAL LOAD BEHAVIOR OF A BUILDING IN COMPOSITE CLIMATIC ZONE OF DELHI

**Sana Fatima Ali[a], Abdus Salam Azad[b], Dibakar Rakshit[c*]**
Centre for Energy Studies, Indian Institute of Technology Delhi, India, 110016
[a]Email address: esz178538@iitd.ac.in
[b]Email address: esz148318@ces.iitd.ac.in
[*c]Email address: dibakar@iitd.ac.in
*Corresponding Author

## ABSTRACT

Worldwide use of materials, energy and water resources are greatly impacted by the construction and operation of buildings. Around 40% of the world's energy and materials are used by the building construction and operation. The chief energy consuming components in buildings are the building envelope, heating, ventilation and air conditioning equipment and energy driven devices and appliances, including lighting. The conservation of energy of all these systems can be done by implementing various measures, load management technologies and by switching to energy-efficient equipment. Analysis led design revolutionized the approach of building load management. It mainly includes the structural and fluid flow analysis of the building where energy utilization pattern is to be mitigated. The fluid flow analysis deals with computational heat transfer study of the building where before the actual construction, the pattern of heat and fluid flow can be quantified. In the present study, a single storied building, with two windows and a door, located in New Delhi, has been computationally analysed using conservation of mass, momentum and energy. The efficacy of the study lies in the estimation of solar loading to which the building is exposed. The solar loading on each surface of the building is computationally estimated for two days having worst summer condition and the worst winter condition in the month of May and December respectively. This is followed by the comparison of the results with the other observed values at the onset. These results are then used to find out the heat gained by each surface of the building and finding an optimum orientation for the building based on the winter and summer heat load. Finding an optimum orientation based on the heat load of the building can therefore help architects and designers to design the buildings for minimum or maximum heat load, based on the need of the location, thus, conserving energy using passive solar architecture.

**Key Words:** *Solar loading, Direction Optimization, Solar Air Temperature, Solar Radiation model*

## 1. INTRODUCTION

The energy audits of buildings carried out by the Bureau of Energy Efficiency (BEE) shows that buildings have around 30%-50% energy savings potential . Significant amount of energy saving is possible from changes in building construction, climate sensitive design, use of locally appropriate material, and operations [1]. In this paper, one of the methods for reducing electricity consumption in buildings has been suggested by reducing the air conditioning load. This has been achieved by optimizing the solar load on the building for maintaining thermal comfort. The variable to optimize was the orientation of the building. The main objective of the present study is to attempt minimizing the energy consumption by optimizing the orientations of the building and estimating the thermal load. The estimation of the load is done using ANSYS Workbench 15.

## 2. METHODOLOGY

A north-south facing rectangular ground floor building, with two windows and a door, in New Delhi, India (Latitude 28.70 °N, Longitude 77.10 °E) has been used for the analysis. The days for which the results have been analyzed are 16$^{th}$ May and 22$^{nd}$ December, and the time for analysis is 13:00 hours, chosen as they represent the typical worst days of summer and winter seasons, as specified in SP-41 code of BIS [2]. The building is enclosed inside an air domain as the control volume and a fine tetrahedral mesh has been generated using ANSYS Meshing. The effect of gravity with proper coordinates has been taken into consideration, along with the selection of the required models, which are Energy Equation, Realizable k-ε model, and the Solar Ray Tracing Model, for this case, along with the Discrete Ordinates Modelling. The current work has been done considering the air enveloping the building with a certain velocity, the values of which have been taken as per the respective dates and time, as taken from the weather file [3]. For the case of 16$^{th}$ May, 13:00 hours, the velocity of wind has been taken in the direction of west with a magnitude of 2.36 m/s, while for the case of 22$^{nd}$ December, 13:00 hours, the wind direction and magnitude is north and 3.64 m/s respectively. The rest of the named selection of the domain have been given the boundary condition of pressure outlet, by specifying the ambient pressure as the atmospheric pressure. The ambient temperature and the inside temperature of the building have been considered accordingly. The roof, north, south, east, and west faces of the building have been given the wall boundary condition and parameters have been set accordingly for simulating the building for finding out heat transfer values on each surface. All the three types of heat transfer, i.e., conduction, convection and radiation have been considered, with the heat transfer coefficients being specified for each of the surface of the wall. Simple scheme with second order discretization has been used for carrying out the simulations as it gives more accurate results. The convergence criteria are specified in the residual monitors, after which the solution is initialized from all zones.

## 3. RESULTS

- **Temperature and Total Surface Heat Transfer Contours**

Temperature contours of the building are shown in Figure 1, which show that the roof of the building has the highest temperature. The north and the east surfaces of the building attain very less temperatures comparatively, since at the time of consideration, these two surfaces do not receive that much radiations of the sun, as compared to the south and the west sides of the building.

Figure 2 shows the contours of total heat transfer that is taking place through the different surfaces of the building on 16$^{th}$ May at 13:00 hours. It can be seen that the maximum heat is getting transferred through the roof of the building as there is a larger temperature difference between the outside and the inside of the building, owing to the maximum temperature being attained at this surface. Similarly, contours have been obtained for the month of December. The values of the heat transfer rates at all the surfaces of the building as well as the average temperature attained by each surface for 16$^{th}$ May at 13:00 hours are shown in Table 1.

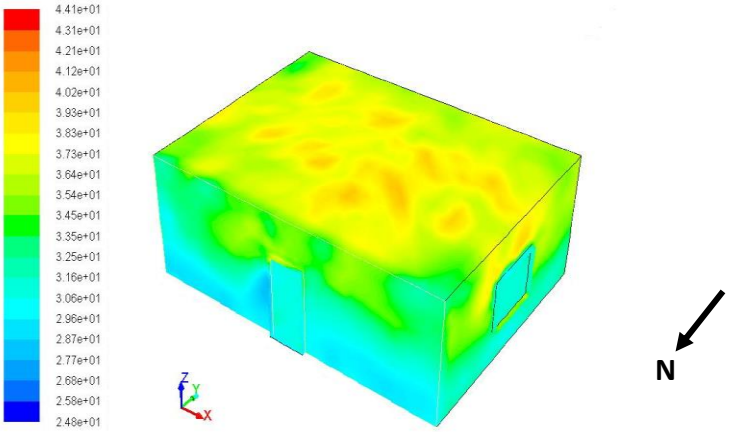


FIGURE 1: Temperature Contours (°C) (16th May)

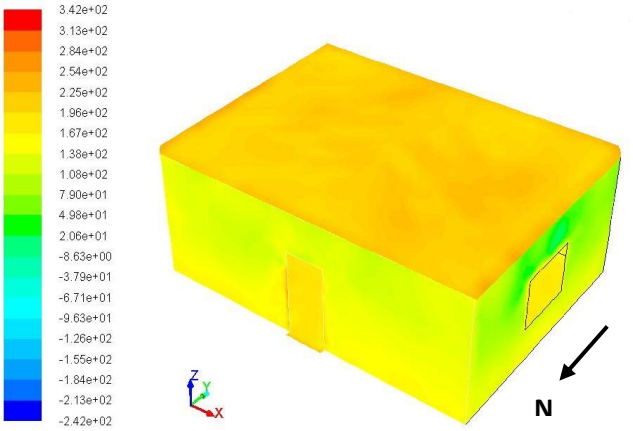


FIGURE 2: Surface Heat Transfer Contours on Roof ($W/m^2$) ($16^{th}$ May)

| | Software Values | |
|---|---|---|
| | **Temperature (ºC)** | **Total Surface Heat Transfer ($W/m^2$)** |
| **Roof** | 37.58 | 214.22 |
| **North Wall** | 32.55 | 103.55 |
| **East Wall** | 33.37 | 106.60 |
| **South Wall** | 34.75 | 109.09 |
| **West Wall** | 34.83 | 148.94 |

TABLE 1: Temperature and Total Surface Heat Transfer Values at each surface for $16^{th}$ May at 13:00 hours

- **Velocity Vectors**

Figure 3 shows the velocity vectors starting from the west direction to the east direction of the domain considered. The figure clearly shows the direction of wind flow, i.e., from west to east direction, with the higher wind speed on the west side of the building, which is nearly 2.5 m/s. When the wind comes in contact with the building surface, its speed reduces, which is seen in the figure below. Also, it can be seen that the wind diverges on coming in contact with the building and converges again but the speed of the wind gets reduced in the process.

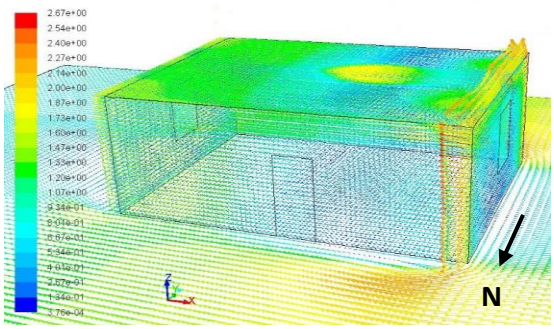


FIGURE 3: Velocity Vectors on the Building and the Domain (m/s) ($16^{th}$ May)

For the building selected, eight orientations have been chosen for analysing their effect on the heat gain of the building. Base case was taken as the building oriented in the north direction, the results of which have been shown above. The same work was carried out for the rest of the orientations and the heat load on the building for each condition was found out. SP-41 code of Bureau of Indian Standards [2] specifies that for a building located in an area of composite climate, optimum orientation is said to be the one in which the difference between the winter gain and summer gain is minimum. Same procedure was followed to find the optimum orientation. Thermal load obtained in each case of orientation, both for summers as well as winters, was plotted on a graph, which shows that the optimum orientation is achieved in the case when the building is north-oriented, which was the base case considered. Figure 4 shows the graph plotted between the thermal load obtained and the orientations in which they are achieved.

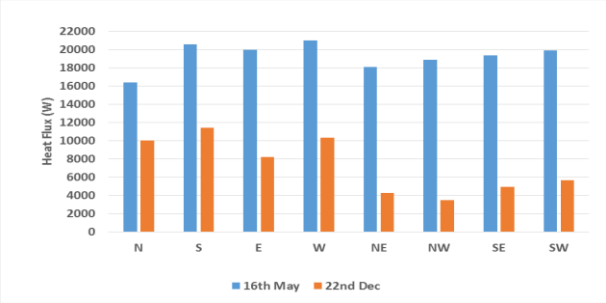


Figure 4: Graph between Thermal Load Obtained and Orientations

## 4. CONCLUSIONS

- The study has been conducted for the worst days of the summer and winter seasons, i.e., for 16$^{th}$ May and 22$^{nd}$ December respectively, for which, thermal load on the building due to incident soar radiations has been obtained. The values obtained computationally have been validated with the observed values.
- For the worst case of the summer season, the maximum heat transfer is taking place through the roof of the building, with a value of 214.22 W/m$^2$, as roof attained the maximum temperature, i.e., 37.58 °C, whereas, during the worst case of the winter season, the maximum heat transfer is taking place through the south wall of the building, with a value of 261.23 W/m$^2$, as the south wall of the building attained the maximum temperature in this case, i.e., 29.2 °C. These values obtained have been validated with the analytical results, using heat transfer equations.
- Total heat load of the building was obtained for both the days representing the worst summer and winter conditions, the values being, 16403 W and 10017 W respectively for the base case, and the difference between them was estimated.
- The same study was carried out for seven other different orientations, and the heat load on the building for each condition was found out. The results suggest that the minimum difference between the thermal loads obtained for the worst days of summer and winter was found to be for the orientation with the larger dimension of the building facing the North – South direction, having entrance in the North direction, the value being 6386 W, thus, proposing this as the optimum orientation with respect to the solar heat gain.

## REFERENCES

[1] "Energy and Buildings," Centre For Science and Environment, New Delhi, 2014.
[2] SP 41 (1987): Handbook on Functional Requirements of a Building (Other Than Industrial Buildings) (Parts 1-4), New Delhi: Bureau Of Indian Standards, 1987.
[3] Climate Design Data 2009 ASHRAE Handbook, New Delhi: ISHRAE, 2009.

Fifth International Conference on Computational Methods for Thermal Problems
THERMACOMP2018, July 9-11, 2018, Indian Institute of Science, Bangalore, INDIA
*N. Massarotti, P. Nithiarasu, Pradip Dutta and C. Ranganyakalu (Eds.)*

# HEAT TRANSFER AND PRESSURE DROP CORRELATIONS OF RECTANGULAR PERFORATED FIN SURFACE OF A COMPACT HEAT EXCHANGER

**Bala Sundar Rao Ramisetty, Ranganayakulu C**

Mechanical Engineering Dept., Bangalore Technological Institute, Bangalore - 560 035, India.
Email: balasundarrao@rediffmail.com
Aeronautical Development Agency, P.B. 1718, Vimanapura Post, Bangalore - 560017, India.
Email: chennu_r@rediffmail.com

**Ranganath G**

Mechanical Engineering Dept., Adhiyamaan College of Engineering, Hosur - 635 109, India.
Email: principal@adhiyamaan.ac.in

## ABSTRACT

Depending on the application, various types of augmented heat transfer surfaces such as wavy fins, offset strip fins, louvered fins and perforated fins are used. In this research paper the focus is on rectangular perforated fins. A numerical model has been developed for the perforated fin of plate fin heat exchanger. Perforated fin performance has been analysed with the help of computational fluid dynamics (CFD) by changing the various geometric parameters of the fin. The Colburn *j* factor and the fanning friction factor are worked out for different Reynolds numbers. These values are compared with the available literature data of Colburn *j* factor and the fanning friction factor. The correlations have been developed between Reynolds number, Colburn *j* factor and fanning friction factor by considering diameter of the perforation, fin height, fin thickness and fin spacing. The developed correlations are validated with literature data.

***Keywords:*** *Compact heat exchanger, Rectangular perforated fin, Computational fluid dynamics (CFD), Colburn j factor and fanning friction factor 'f'*

## 1. INTRODUCTION

Kays & London [1] in their elaborate discussions over the classification of heat exchangers have defined the "compact heat exchangers" as one having a heat transfer surface area more than 700 $m^2$ per $m^3$. Such compactness is achieved by providing the extended surfaces i.e. fins. Out of the various compact heat exchangers, plate fin heat exchangers are unique due to their construction and performance. They are characterized by high effectiveness, compactness and low weight. In plate fin heat exchangers, the rectangular perforated fin geometry is made by punching a pattern of spaced holes in the fin material before it is formed into flow channels. In the present study, the channels are in rectangular in shape with round perforations. Ismail et al [2] are carried out numerical study of flow patterns of compact plate fin heat exchangers and generation of design data for offset and wavy fins using CFD. Ranganayakulu [3] provided the steady and transient analysis of plate fin compact heat exchangers. Rao et al. [4] carried out numerical simulation to establish the correlations for *'f'* and *'j'* factors for rectangular plain fins.

# 2. MAIN BODY

## 2.1 NUMERICAL MODEL

The following steps are carried out in numerical analysis for data generation of Colburn *j* factor and friction fanning factor for perforated fins:

- Modeling of rectangular perforated fin
- Calculating the input values for CFD analysis
- Analyzing the modeled fin by using FLUENT 12.1
- Numerical calculation of *'j'* and *'f'* factors
- Validation of results
- Forming the correlations of *'j'* and *'f'* factors

Numerical model has been developed by considering the fin thickness (t), fin height (h), fin length (l), fin spacing (s), perforation diameter (d) and the number of perforations per inch length. The fluid path is modeled by using CFD. The fine mesh has been applied to get more accurate values and a grid independence test is carried out for the same fin. A fin is considered and the fluid travels in the punched hole space. By changing the diameter of the perforation, spacing and height, the iterations had taken and then the graphical results of static pressure and static temperature were plotted. The geometry of the perforated fin is varied continuously by using the parameter set. The wall surface and the inlet-outlet conditions are considered in the design. The fluid is selected as air. The model of rectangular perforated fin is shown in Fig. 1.

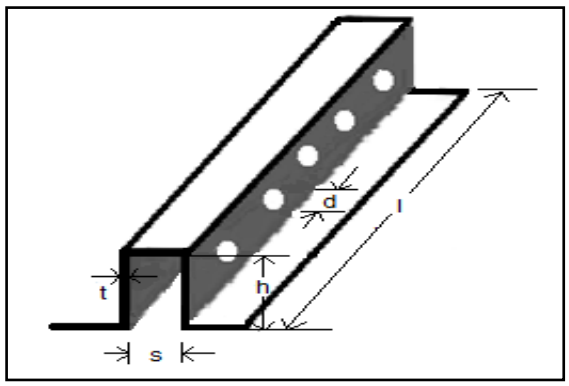


Fig. 1 Model of rectangular perforated fin

In FLUENT, the conservation equations of mass, momentum and energy are solved using the finite volume method in various heat and flow conditions. There are several turbulence models available in the code. The turbulent flow is calculated by the semi-implicit SIMPLER as mentioned in Versteeg and Malalasekara [5]. A standard κ - ε model as given in Versteeg and Malalasekara [5] with enhanced wall treatment is used to predict turbulent flow in the fin geometry.

## 2.2 PROBLEM DESCRIPTION

It will be prohibitively expensive and time consuming to fabricate heat exchanger cores and conduct experiments over reasonable ranges of all the geometric variables. In contrast, it is relatively easy and cost effective to carry out a parametric study through numerical simulation and derive acceptable correlations for use in industry. In fact plenty of research work is carried out, yet there was no unique correlation developed by anyone that can be relied upon in order to determine '*j*' and '*f*' for perforated fins. Thus, this study mainly focused to develop good correlations for rectangular perforated fins taking all the necessary parametric effects. The performance of the fins is presented for both laminar and turbulent regions of Re versus '*j*' and Re versus '*f*'. A total of 150 different fin

surfaces are modelled and CFD analysis is carried out for developing correlations. The range of geometric parameters and Reynolds numbers are considered as follows:

$d = 2$ mm (1)

$0.5 \leq h/s \leq 5$ (2)

$0.001 \leq t/s \leq 0.01$ (3)

$100 \leq Re \leq 1000$ for Laminar region (4)

$1000 < Re \leq 7500$ for Turbulent region (5)

Number of perforations per inch length = 2 (6)

## 2.3 CFD APPROACH

The computational domain of the perforated fin model is analyzed using CFD simulation tool FLUENT. The CFD analysis is carried out for different geometric parameters and Reynolds numbers. The analysis is extended out in two phases for perforated fin. In the first phase, a rectangular perforated fin is taken and characterized for '*f*' values over a range of Reynolds numbers. In the second phase, the '*j*' values are determined in the same range by switching on the energy equation.

## 2.4 VALIDATION

For the validation of the present study, rectangular perforated plain fin from Kays and London [1] has been analyzed for the following case.

- 8 mm fin height, 13.95(P) fin density and 0.152 mm fin thickness (Table 10-8)

The CFD results of rectangular perforated fin are compared with Kays & London [1] as shown in Fig. 2. The maximum variations are found to be 2 – 7% in *'f'* and 3 – 6% in *'j'* values.

# 3. RESULTS & DISCUSSION

From Fig. 2, it is observed that the *'f'* versus Re and *'j'* versus Re curves of rectangular perforated fin surfaces follow the same trends of Kays & London [1] experimental results and the CFD results are in good agreement with analytical results given by Kays & London [1] for the low and high Reynolds number region. Comparison has been made rectangular plain fin to perforated fin of fin density of 13.95. The perforated fin has higher fanning friction factor of 5 to 8% at lower Reynolds numbers and the same increases about 9 to 14% for higher Reynolds numbers and the Colburn *j* factor has higher by 3 to 6% of lower Reynolds numbers and the same increases about 7 to 9% for higher Reynolds numbers.

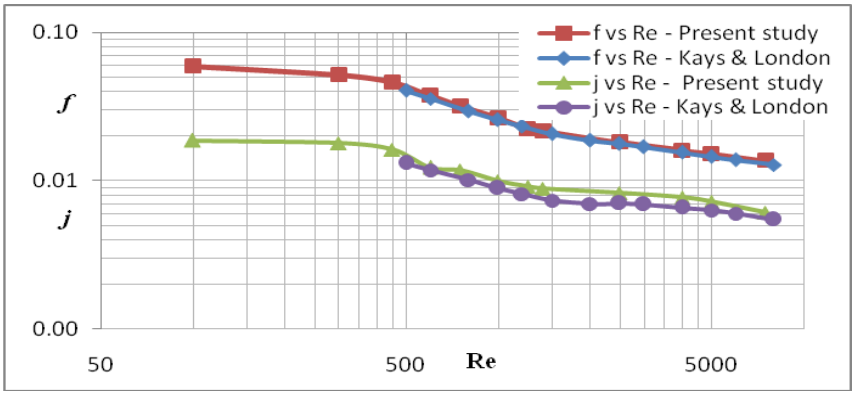


Fig. 2 Comparison of results, fanning friction factor and Colburn *j* factor versus Reynolds number, for the fin density of 13.95 and height of the fin 8 mm, with Kays & London [1]

### 3.1 CORRELATIONS FOR *'f'* AND *'j'* FACTORS

The correlations have been expressed in terms of two separate equations for the low and high Reynolds numbers along with dimensionless geometric parameters as shown in Table 1.

Table 1: *f* and *j* correlations for rectangular perforated fin surfaces

| Type of fin surface | Design data | Correlations | Range of Applicability |
|---|---|---|---|
| Rectangular Perforated fin | *f* | $0.7127(Re)^{-1.8858}(h/s)^{0.4196}(t/s)^{-1.4826}$ | 100≤Re≤1000 |
| | *f* | $0.4345(Re)^{-1.3029}(h/s)^{0.3725}(t/s)^{-1.3178}$ | 1000< Re≤7500 |
| | *j* | $0.121\ (Re)^{-2.2920}(h/s)^{2.75}(t/s)^{-1.830}$ | 100≤ Re≤1000 |
| | *j* | $11.71\ (Re)^{-2.3111}(h/s)^{2.144}(t/s)^{-1.9237}$ | 1000<Re ≤7500 |

The above correlations correctly predict 95% of the '*f*' data for laminar regions and 97% of the '*f*' data for the turbulent regions with an RMS value of 0.985. Similarly the correlations correctly predict 96% of the *'j'* data for laminar and turbulent regions with an RMS value of 0.99

## 4. CONCLUSIONS

This paper presents the heat transfer and fanning friction factor correlations for rectangular perforated fins. The expressions provided for the heat transfer coefficient and flow friction in terms of Colburn *j* factor and fanning friction factor *f* allows the computation for all values of the Reynolds number, including the laminar and turbulent regions. The generalized correlations are developed by taking geometrical parameters taken into account. These expressions are well formed in the laminar and turbulent regions, and can be considered as the standard expressions modified by correction factors. The values obtained from these correlations are in agreement with the literature data.

### NOMENCLATURE

| | | | |
|---|---|---|---|
| CFD | Computational fluid dynamics | l | Fin length, mm |
| d | Perforation diameter, mm | P | Perforated |
| FPI | Fins per inch | Re | Reynolds number, dimensionless |
| *f* | fanning friction factor, dimensionless | s | Fin spacing, mm |
| h | Fin height, mm | t | Fin thickness, mm |
| *j* | Colburn factor, dimensionless | | |

## REFERENCES

[1]. Kays WM, London AL, Compact Heat Exchangers, 1st ed. McGraw Hill, New York; 1964.
[2]. Ismail LS, Ranganayakulu C, Shah RK, Numerical study of flow patterns of compact plate-fin heat exchangers and generation of design data for offset and wavy fins, International Journal of Heat and Mass Transfer, 52, 3972–3983, 2009
[3]. C Ranganayakulu, "Steady state and transient analysis of Compact plate fin heat exchanger fins for generation of design data using CFD", International J of Numerical Methods for Heat & Fluid Flow, Vol. 26, Issue: 2, 440-460, 2016.
[4]. Rao RBS, Ranganath G, Ranganayakulu C, Development of Colburn '*j*' factor and fanning friction factor '*f*' correlations for Compact Heat Exchanger Plain fins by using CFD, Heat and Mass Transfer, 49(7), 991–1000, 2013
[5]. Versteeg HK, Malalasekera W, An introduction to computational fluid dynamics, The finite volume method, 1st ed. Prentice Hall, New York; 1995, pp: 62–146.

Fifth International Conference on Computational Methods for Thermal Problems
THERMACOMP2018, July 9-11, 2018, Indian Institute of Science, Bangalore, INDIA
*N. Massarotti, P. Nithiarasu, Pradip Dutta and C. Ranganyakalu (Eds.)*

# HEAT TRANSFER AUGMENTATION IN FERROFLUIDS IN PRESENCE OF EXTERNAL MAGNETIC FIELDS

**Ram Krishna Shah, Sameer Khandekar**
Department of Mechanical Engineering, Indian Institute of Technology Kanpur (IITK), India
Email: Ramkshah@iitk.ac.in, Samkhan@iitk.ac.in

## ABSTRACT

Heat transfer enhancement using water based ferrofluids have been studied numerically under static external magnetic fields generated by single and multiple magnetic line dipoles placed along a parallel plate channel for Reynolds number (Re) < 100 cases. Two ferrofluids having different magnetic and thermo-physical properties owing to different solid volume fractions of Iron oxide nanoparticles (IONPs) are considered for the study. The magnetization of ferrofluids and Magnetic body forces are derived in terms of Langevin function to accurately model the non-linearity of the fluid magnetization with external magnetic field. A validation study is also performed to establish the accuracy of the obtained numerical results.

It is shown that presence of non-uniform magnetic field induces a magnetic body force in ferrofluid medium thus disturbing the flow locally and augmenting the local heat transfer. This is evident from the increase in bulk fluid temperature and local Nusselt number near the location of the external magnetic field. A parametric study is performed to investigate the effect of single and multiple magnetic dipoles, solid volume fraction and Reynolds number on heat transfer enhancement. It is concluded that forced convective heat transfer can be enhanced significantly by the application of magnetic field compared to no magnetic field cases. While magnetic field strongly affects the fluid flow at Re = 25, it does not affect the flow significantly beyond Re > 75 which shows the dominance of inertial/viscous forces over magnetic forces at a given external magnetic field strength. Higher particle loading shows better results at all Reynolds number.

**Key Words:** *Heat Transfer, Ferrofluids, Nanofluids, Laminar Forced Convection.*

## 1. INTRODUCTION

Due to ever increasing demand for high heat flux management, nanofluids are one of the options being investigated for heat transfer augmentation owing to their improved thermo-physical properties (such as thermal conductivity). Magnetic nanofluids or Ferrofluids are one such type of fluids having the additional advantage of harnessing their magnetic properties as well. Ferrofluids are stable colloidal suspensions of single domain magnetic nanoparticles in a conventional working fluid such as water or in an organic solvent. The magnetic properties of ferrofluids can be used to manipulate the flow of ferrofluids [1]. When ferrofluids are exposed to an external magnetic field, magnetic nanoparticles start to align along the direction of the external field, giving rise to non-zero net magnetization. A body force gets induced in ferrofluids in non-uniform magnetic fields due to net fluid magnetization. This gives special thermo-physical properties to ferrofluids [2]. Experimental investigations performed by Philip et al. [3] observed a 300% increase in thermal conductivity of ferrofluids under magnetic field. Numerical and experimental studies performed by various investigators suggest that ferrofluids can significantly enhance heat transfer compared to pure fluids and other nanofluids under an external magnetic field. Comprehensive reviews of heat transfer applications of ferrofluids are covered in review articles published by Nkurikiyimfura et al. [4] and Bahiraei et al. [5]. An experimental investigation on laminar forced convection of ferrofluid in external magnetic fields by Asfer et al. [7] showed significant improvement in heat transfer.

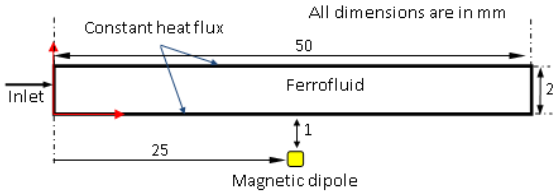


$$\vec{H}(r,\varphi) = \frac{m}{r^2}(\sin\varphi\,\hat{r} + \cos\varphi\,\hat{\varphi});\ \varphi = tan^{-1}\left(\frac{y-Y}{x-X}\right)$$

$r = \sqrt{(x-X)^2 + (y-Y)^2}$ ; H - Magnetic field strength (A/m), m - Dipole strength (A/m$^2$), $(r, \varphi)$ - Polar coordinates, (x,y) - Cartisan coordinate, (X,Y) - Dipole location

(a)

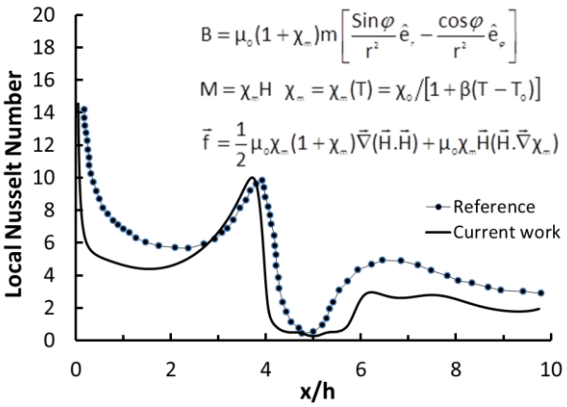


(b)

FIGURE 1: (a) Schematic of problem statement with single magnetic dipoles (Equations shown are used to simulate external magnetic field as per [6]) (b) Validation of Nusselt number of present work with previous work done by Ganguly et al. [6], (Inset) their mathematical model.

In the present work, laminar forced convection heat transfer in parallel plate configuration is studied in presence of external magnetic field generated by the magnetic dipoles. The objective of the presented study is to provide an approximate numerical investigation which can be employed to assist in designing real life experimental platforms.

## 2. PROBLEM DESCRIPTION

Steady-state laminar forced convection of water based ferrofluid is modelled as homogenous single phase fluid flow through a parallel plate channel of 50 mm length and 2 mm separation under uniform heat flux boundary condition. Figure 1(a) shows the schematic of the channel with a single magnet. Hydro-dynamically fully developed and thermally developing flow is modelled. Fluid properties such as thermo-physical and magnetic properties are considered for two commercially available ferrofluids EMG-308 (1.2% solid volume fraction) and EMG-805 (3.6% solid volume fraction) by Ferrotec® Inc. Two dimensional non-uniform localized magnetic fields are generated by simulated magnetic dipoles along the channel, following the Maxwell electromagnetic laws. Effect of single and multiple dipoles (*m*) placements of strength 0.5 Am, each placed at 1 mm distance from the plates along the flow direction, are studied for flow Reynolds numbers (Re) < 100 cases. Constant heat flux boundary condition is applied to both the walls.

## 3. NUMERICAL METHOD

Finite element formulation (FEM) based commercial software Comsol Multiphysics® has been used to solve the coupled equations of mass, momentum and energy balance for fluid flow and heat transfer, and the Maxwell equations for the magnetic field. On this platform, a fully coupled approach employing damped Newton-Raphson method is used for solving the non-linear partial differential equations. Adaptive mesh refinement technique is utilized to accurately resolve force and field gradients induced by the magnetic field in fluid medium. This feature calculates the gradient of the variables in the first step and more mesh elements are added in the regions of large gradients and all equations are solved again on this newly generated mesh structure in the next solution steps. The Parallel Sparse Direct Solver (PARDISO) which is based on LU decomposition is employed to solve the system of equations generated at each and every Newton-Raphson steps during computation. The purpose of the numerical simulation is to solve for Magnetization (*M*) in ferrofluids, Magnetic body force ($f_s$), Flow velocities (*u, v*) and Temperature (*T*) fields in the computational domain.

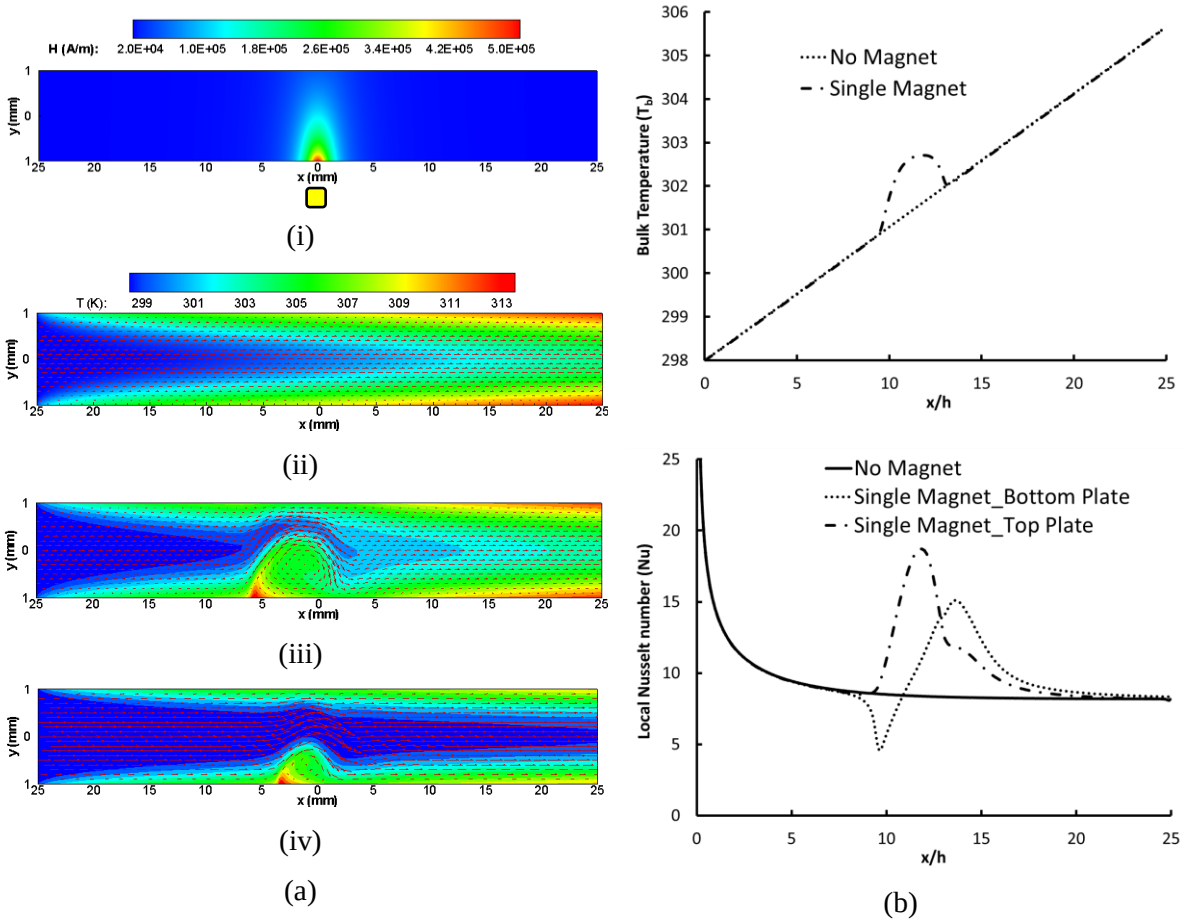


FIGURE 2: (a) (i) Distribution of magnetic field (*H*) generated by a single magnetic dipole, Velocity and Temperature profile for EMG-805 fluid flow (ii) without magnetic field (iii) with magnetic field for single magnet case at Re = 25 (iv) at Re = 75, (b) Bulk fluid temperature and Nusselt number plots for with and without magnetic field cases at Re = 25.

A validation study is performed to establish the accuracy of the obtained numerical solutions from Comsol. For this purpose, a separate mathematical model was implemented in Comsol according to modelling provided in Ganguly et al. [6]. Comsol results are then compared for validation. Quantitatively as well as qualitatively similar results for velocity and temperature fields are obtained from both the approach. In figure 1 (II), the local Nusselt number is plotted against the results of Ganguly at dipole strength of 0.58 Am showing similar comparative trend according to the present computations.

## 4. RESULTS

Magnetic field distribution due to a single line dipole and velocity and temperature profile for EMG-805 fluid at Reynolds number of 25 and 75 is shown in figure 2 (a) from (i) to (iv). It is evident from the plots that in the presence of the magnetic field, a field induced localized mixing of fluid takes places figure 2a (iii, iv) compared to no field case figure 2a (ii). This mixing of fluid significantly increases the bulk fluid temperature resulting in the enhancement of local Nusselt number as seen in figure 2 (b). This mixing of fluid is strong at Re = 25 compared to 75 showing the dominance of magnetic forces over inertial/viscous forces for low Reynolds number flow at the studied dipole strength of m 0.5 Am. Effect of the magnetic field is seen to be in the range of about ± 10 mm from the dipole location.

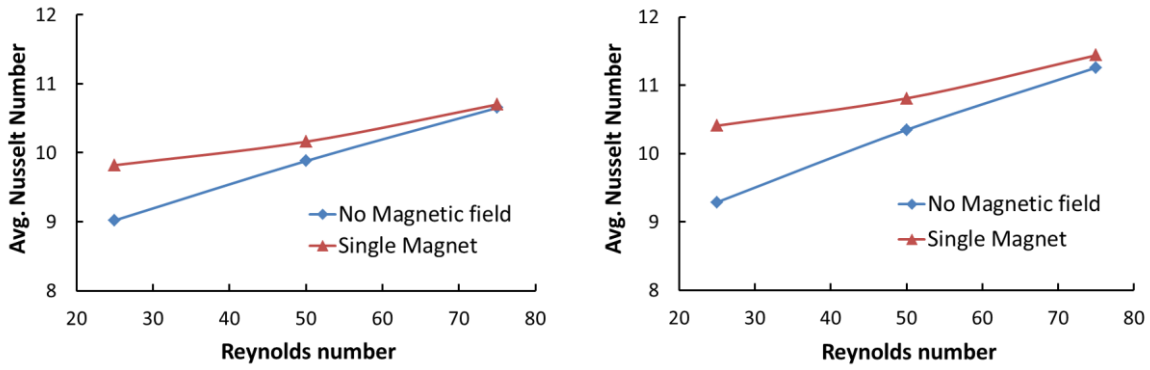


FIGURE 3: Average Nusselt number at different Re (a) EMG-308 fluid with and without magnetic field (b) EMG-805 fluid with and without magnetic field.

Average Nusselt number plots for the two ferrofluids are shown in figure 3 for single magnet case. At Re = 25, up to 15% increase in Nusselt number can be observed form the plots which decrease with Reynolds number. At Re > 75, the Nusselt numbers are almost same as in no magnetic field cases. Results shown here are only for single magnet cases. Placement of multiple magnets along the channel shows significant enhancement in heat transfer.

## 5. CONCLUSIONS

Forced convective heat transfer can be enhanced by applying external non-uniform magnetic field compared to no magnetic field case. While enhancement is higher for low Reynolds number (Re = 25, 50), flow does not get affected significantly at higher Reynolds number (Re > 100) by the magnetic field. This shows the dominance of inertial and viscous force over magnetic body force at a given external magnetic strength. Localized field induced mixing of fluid is observed in close vicinity of the dipoles, leading to disturbance in the thermal boundary layers and higher bulk fluid temperature which eventually results in an increase of the local Nusselt number. This indicates that not all cases of magnetic field application result in heat transfer enhancement. Placement of two and three magnets along the channel shows maximum improvement of 20% and 30% in heat transfer from no magnetic field cases, respectively.

## REFERENCES

[1] R.E. Rosensweig, Ferrohydrodynamics, Cambridge University Press, New York, 1985.

[2] C. Scherer and A. M. Figueiredo Neto, Ferrofluids: properties and applications, Brazilian Journal of Physics, 35, 3A, 2005.

[3] John Philip, P. D. Shima, and Baldev Raj, Enhancement of thermal conductivity in magnetite based nanofluid due to chainlike structures, Applied Physics Letter 91, 203108, 2007.

[4] I. Nkurikiyimfura, Y. Wang, and Z. Pan, Heat transfer enhancement by magnetic nanofluids: A review, Renewable and Sustainable Energy Reviews, 21, 548-561, 2013.

[5] M. Bahiraei and M. Hangi, Flow and heat transfer characteristic of magnetic nanofluids: A review, Journal of Magnetism and Magnetic Materials, 374, 125-138, 2015.

[6] R. Ganguly, S. Sen, I. K. Puri, Heat transfer augmentation using a magnetic fluid under the influence of a line dipole, Journal of Magnetism and Magnetic Materials, 271, 63-73, 2004.

[7] Asfer M, Mehta B K, Kumar A, Panigrahi P K, Khandekar S, Effect of magnetic field on laminar convective heat transfer characteristics of ferrofluid flowing through a circular stainless steel tube, International Journal of Heat and Fluid Flow, 59, 74-86, 2016.

# EXPERIMENTAL INVESTIGATION OF FORCED CONVECTION HEAT TRANSFER IN METAL FOAM-FILLED HORIZONTAL RECTANGULAR CHANNEL

**Khalid Rashid, Jophy Peter, A. Jayashree, J.C. Pisharady**
Thermal Engineering Division, LPSC, Trivandrum, Kerala, India
Khalid9835@gmail.com

## ABSTRACT

Regenerative channels with multiple ribs and variable cross sectional area are in use for thrust chamber cooling. In order to enhance the heat transfer and reduce the wall temperature of the inner shell, open cell metal foam can be inserted inside these channels. Metal foams which have very high surface area to volume ratio aids in better heat dissipation compared to other fin structures. In view of this, experiments were carried out to study the heat transfer characteristics in a horizontal rectangular channel by introducing open cell copper metal foam of 10 pores per inch (PPI) having 97% porosity. Infrared heating module is used for supplying constant heat flux on the channel bottom. The measurements include wall temperature along flow direction as well as channel inlet and outlet temperatures and pressures. This study primarily focuses on the effect of foam insert height on the channel cooling performance and relative pressure drop in the turbulent flow regime. The results of all cases are compared to that of the empty channel. It is found that the temperature of the wall is reduced by around 40% with the introduction of copper foam. However, this also results in an increase pressure drop.

For the foam-filled channel, heat transfer enhancement was found of the order of 60% to 110% due to foam height variation over the empty channel for the same Darcy velocity. Further this experimental study shows that fully filled channel is most suited for getting maximum heat transfer. Whereas partially filled channel can be utilized for increasing heat transfer without much increase in pressure drop.

**Key Words:** *Metal Foam, Channel cooling, Force convection.*

## 1. INTRODUCTION

The future demands in space exploration calls for more efficient and cost effective methods of space travel. Space agencies are presently focusing more on advanced and unconventional technologies. The conventional rocket engine technologies are extensively studied and well understood, and are also more reliable in operation. But the present space systems must be enhanced to meet the requirements for future exploration programs. Regenerative cooling system is used widely in liquid propellant rocket engines, in order to maintain the nozzle and chamber wall temperature within safe thermal limits. The need for high thrust engines has increased the cooling demands. Thus in order to withstand such high thermal loads materials with high heat transfer rates is needed. Improved high conductivity and high temperature materials are required, however even with advances in all these sectors the thrust increase in large Liquid Propellant rocket engines are ultimately governed by the limits of the cooling capacity of the cooling channel. These limits has been extended considerably with the help of transpiration cooling, injector – biasing and film cooling, but all these also adds to the overall expenditure of the mission. Increasing effectiveness of regenerative cooling is a viable option in reducing thermal loads and thus the structural margins.

The porous or open-cell foam layer has the potential to offer orders of magnitude improvement in cooling capacity. This paper documents the findings of the experimental study carried out to assess the effectiveness of foam height in the rectangular cooling channel.

## 2. EXPERIMENTAL SETUP

Experimental setup consists of a test channel made of SS321. The bottom face of the test section where IR is impinging is coated with high emissivity coating. The covering plate which is also made of SS321, is fixed to the channel using 32 nut and bolt. Rocasin sheet is provided in between to prevent leak. The heat flux is provided with help of a 2.5kW Infrared heater, whose power can be controlled using an autotransformer. Water is pumped by gear pumps as per the flow requirement. Pumping requirement is met by 2 pumps, 0-8 LPM for small flow rate and 0-20 LPM for higher flow rate. Flow is controlled using variable frequency drives which vary the motor RPM as per the requirement of flow. The flow rate is measured with flow meter [3.4-34 LPM]. The temperature and pressure at the inlet and outlet is measured using resistance temperature detectors (RTD) and pressure transducers respectively. Additionally the temperature at the channel wall is measured with the help of 13 T-type thermocouples installed on the bottom plate of the channel. The temperature and pressure readings are taken using a data acquisition system (Yokogawa MV 2000, 48 channels).

The experiment is initially conducted with no foam, since the pressure drop without foam is very low, a U- tube manometer is used with Fluroketone as the manometer fluid. After inserting the foam the pressure readings are taken from the pressure transducers fixed at both inlet and outlet. The experiment is carried out with flow rates of 1.5, 3, 5 and 7 LPM which corresponds to Reynolds number of 4475, 8900, 13500 and 17000. The heat load is varied from 500W to 2500W. The test channel consists of two rectangular flow passage, each having a cross section of 8x10 sq.mm. In order to have a developed flow at the entry of the foam inserted section, 200 mm straight flow path is provided from the inlet side for the flow to become fully developed

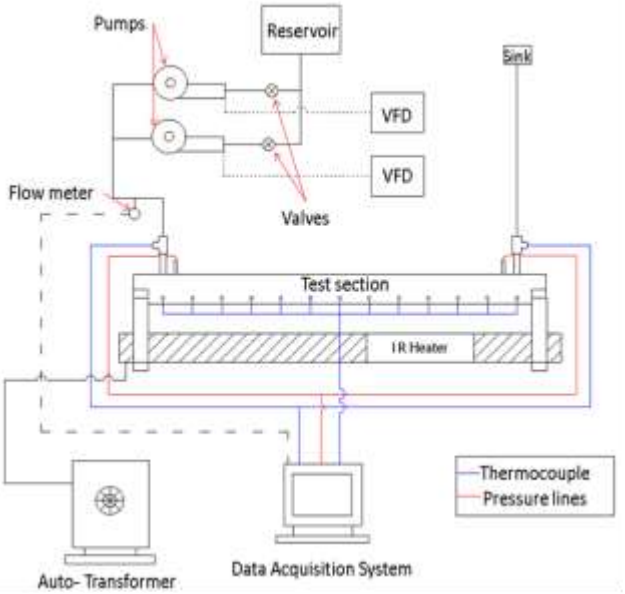


FIGURE 1: TEST SETUP SCHEMATIC

Schematic of the test setup is shown in figure 2. A total of 13 thermocouples of T-type is used to measure the temperature at the interior of channel bottom face. The holes drilled inside the channel are at first filled with non-curing high conductivity paste. The Thermocouples are inserted into

these holes and self-setting cement is applied to fix the thermocouple to the side wall surface. The inlet and outlet temperatures are measured using RTD. Excitation is provided for RTD and pressure transducers (0-3 bar) as per the equipment's requirement. Purging line is provided to remove water in the channel after the completion of each set of experiments. In order to protect the lead of IR bulb from overheating, cooling using nitrogen gas is provided.

## 3. RESULTS

In order to study the effect of metal foam insert in the rectangular cooling channel, foam height were varied from 2 mm to 10mm as shown in fig. 2. Test results are compared with the no-foam (empty channel) cooling effects and their relative pressure drop across the channel length.

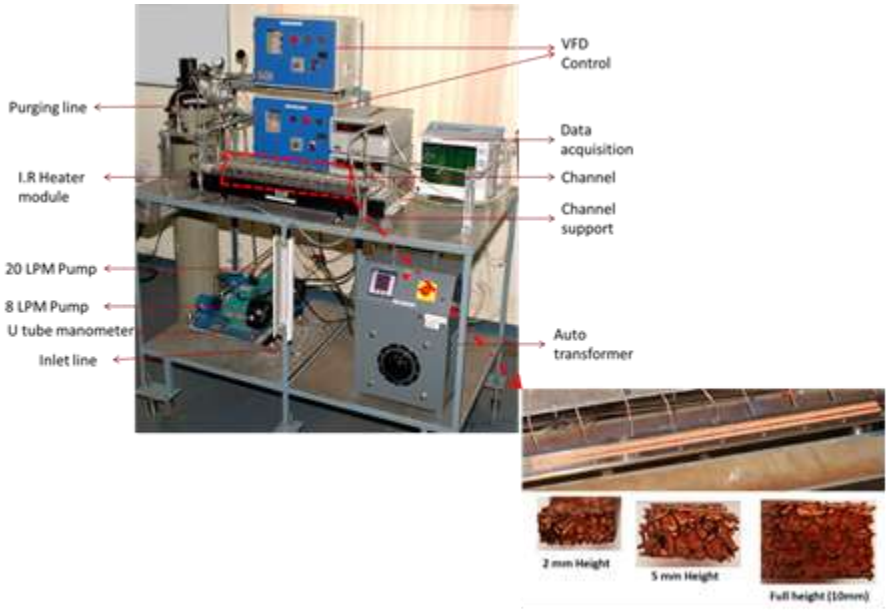


FIGURE 2: EXPERIMENTAL TEST SETUP AND TEST SECTION CONTAINING METAL FOAM

Experiments have been done to study the relative merits of metallic foam in comparison to existing no foam heat transfer surfaces. Nusselt number variation at a constant heat flux and two different flow rates are shown in fig.3.

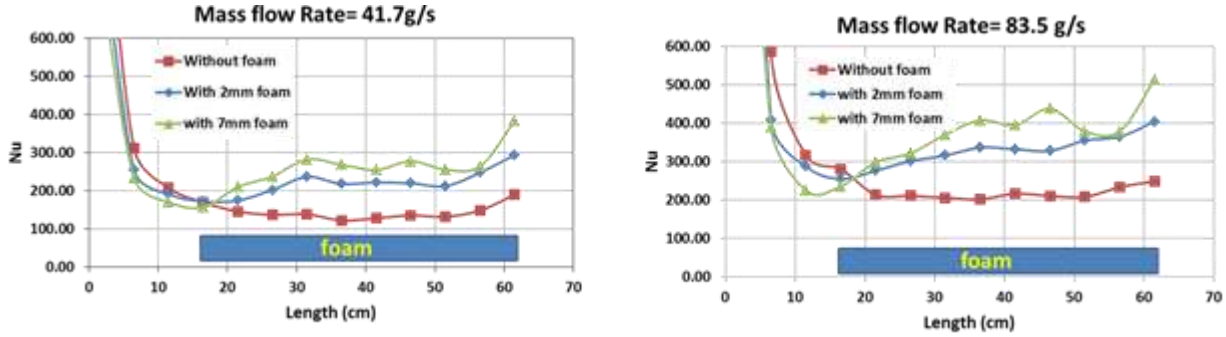


FIGURE 3: NUSSELT NO. VARIATION ACROSS CHANNEL LENGTH FOR DIFFERENT FOAM HEIGHT

The results mainly show the effect of foam insert height in the rectangular channel on the heat transfer characteristic. The metal foam in the channel increases the Nusselt number by around 60% to 110% as the foam height is increased which results in better cooling efficiency.

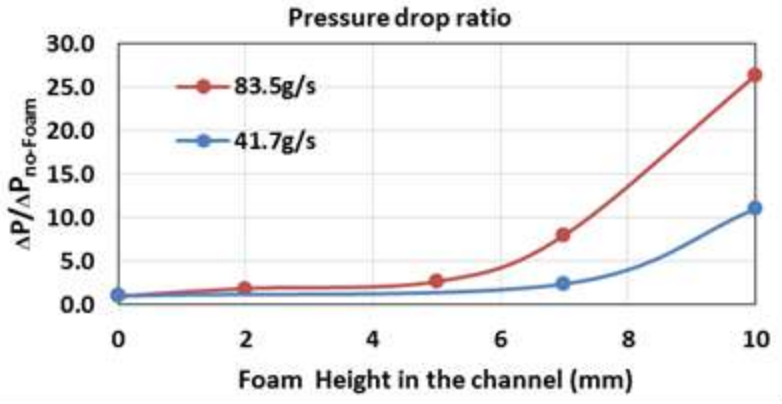


FIGURE 4: PRESSURE DROP ACROSS THE CHANNEL FOR DIFFERENT FOAM HEIGHTS

Pressure drop across the rectangular channel for two flow rates are shown in figure 4. It shows pressure drop variation for different foam thickness. It can be seen that as foam insert height is increased pressure drop is increasing with respect to no foam channel. Pressure drop increases to 25 times in case of higher flow rate for 10mm insert height while for 2mm foam height is comparatively much less.

.

## 4. CONCLUSIONS

Open-cell metal foam is considered to be a promising alternative for compact heat exchanger applications, owing to its high heat transfer surface area density, superior thermo-hydraulic characteristics, and other favorable mechanical properties. Analysis has been done to study the relative merits of porous medium in comparison to existing no foam heat transfer surfaces. The results indicate that the effect of open-cell copper foam, as porous medium, in a horizontal rectangular channel with constant wall heat flux on the heat transfer enhancement is in the range of 60% to 110% due to foam insert height variation which is rather substantial. This improvement in heat transfer comes at the expense of pressure drop in the channel. However It is beneficial to use metal foam with partially filled channel which reduces the pressure drop penalty.

Fifth International Conference on Computational Methods for Thermal Problems
THERMACOMP2018, July 9-11, 2018, Indian Institute of Science, Bangalore, INDIA
*N. Massarotti, P. Nithiarasu, Pradip Dutta and C. Ranganyakalu (Eds.)*

# COMPUTATIONAL INVESTIGATION OF MIXED CONVECTION HEAT TRANSFER FROM LAMINAR OFFSET JET AND WALL JET

**Sushil Kumar Rathore**[1]**,**
National Institute of Technology Rourkela, Rourkela-769008, isushilrathore@gmail.com,

**Aayush Pathak, Abhishek Majumdar**
Former Student, National Institute of Technology Patna, Patna-800005, ayush135151@nitp.ac.in, mazumdaraabhishek@gmail.com

**Sumanta Chaudhuri,**
School of Mechanical Engineering, Kalinga Institute of Industrial Technology (KIIT) Bhubaneswar (Deemed to be University), Bhubaneswar-751024**,** sumanta.chaudhurifme@kiit.ac.in

## ABSTRACT

Flow and heat transfer characteristics of interaction of a laminar plane offset jet with coflowing wall jet are studied at various Richardson number (Ri). The temperature of offset jet at inlet is higher than that of wall jet inlet temperature. The temperature of horizontal wall and wall jet inlet temperature are same as that of ambient temperature. The temperature of heated offset jet is varied to alter the Grashof number (Gr). The velocities of the two jets are taken equal. Study is carried out for Ri ranging from 0.0028 to 0.875 by taking Gr 1000, 10000 and 35000 for Reynolds number 200, 400 and 600. PISO algorithm based on finite volume method (FVM) is used. Power law scheme is considered for the discretization of convective terms. Boussinesq approximation is used to take into account variation in density in the buoyancy term. It is observed that mixing and heat transfer between the offset jet and wall jet increases with increase in Richardson number.

**Key Words:** *wall jet; offset jet; mixed convection; Richardson number; numerical simulation*

## 1. INTRODUCTION

A jet is a stream of fluid that is projected into ambient from a small cross-sectional area, which converts the pressure energy of fluid into kinetic energy. When more than one jet is used simultaneously in an application, it is known as multi-jets. In bounded jet, flow interacts with a wall and the interaction affects the flow of jet. The present problem consists of a lower wall jet and upper offset jet. Their interaction is studied here by taking both of them at different temperatures. Lower jet is taken at lower temperature and upper jet is taken at higher temperature. Such a situation is found in gas turbines, where a colder wall jet is used for the shielding of the turbine blades from the high temperature gases. Figure 1 shows the flow pattern for a combined offset jet and wall jet. The wall jet and the offset jet are ejected from two identical and rectangular nozzles, each one having width 12.5 mm and contained in the transverse plane (x= 0). The offset ratio is set to 3.5, this parameter is defined as OR=*H/h*, where *H* is distance between the horizontal wall (defined at y = 0) and the offset jet centre line, and h is inlet slot height [1]. A recirculation region forms just downstream of nozzle exit. Two counter rotating vortices form inside the recirculation region. Then the two jets merge together at a point known as merge point. At the merge point, both u and v velcoity components are zero [2]. The two jets combined later in the downstream direction sufficiently away from the jet inlet. Based on the literature review, it has been observed that interaction of laminar offset jet and wall jet at different temperatures in the mixed convection regime has not been studied earlier. The present study is an attempt to bridge this gap in the literature.

[1]Former Assistant Professor, National Institute of Technology Patna, Patna-800005, Bihar

## 2. MATHEMATICAL FORMULATION AND NUMERICAL SCHEME

The flow is assumed to be two-dimensional and laminar flow. The working fluid is air and its thermo-physical properties are assumed constant. The density is taken as constant in all terms (inertia and viscous terms) except the body force term using the Boussinesq approximation.

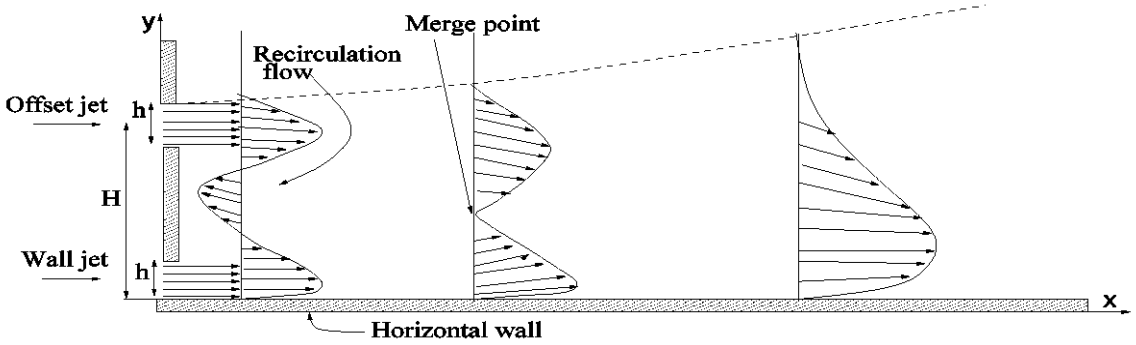


FIGURE 1. Schematic diagram of combined wall and offset jet flow

Continuity equation:

$$\frac{\partial u}{\partial x}+\frac{\partial v}{\partial y}=0 \quad \text{.....(1)}$$

x Momentum equation:

$$\frac{\partial u}{\partial t}+u\frac{\partial u}{\partial x}+v\frac{\partial u}{\partial y}=-\frac{1}{\rho}\frac{\partial P}{\partial x}+\upsilon\left(\frac{\partial^2 u}{\partial x^2}+\frac{\partial^2 u}{\partial y^2}\right) \quad \text{.....(2)}$$

y Momentum equation:

$$\frac{\partial v}{\partial t}+u\frac{\partial v}{\partial x}+v\frac{\partial v}{\partial y}=-\frac{1}{\rho}\frac{\partial P}{\partial y}+\upsilon\left(\frac{\partial^2 v}{\partial x^2}+\frac{\partial^2 v}{\partial y^2}\right)+\rho g\,\beta\,(T-T_{ref}) \quad \text{.....(3)}$$

Energy equation:

$$\frac{\partial T}{\partial t}+u\frac{\partial T}{\partial x}+v\frac{\partial T}{\partial y}=\frac{1}{\alpha}\left(\frac{\partial^2 T}{\partial x^2}+\frac{\partial^2 T}{\partial y^2}\right) \quad \text{.....(4)}$$

The unfirom velocity profile is considered at the inlet of offset jet and wall jet. The no-slip and no-penetration boundary conditions are used at the solid walls. The temperature of the wall jet is taken as 300 K. Temperature of offset jet is varied to alter Grashof number (Gr). The vertical walls are considered as adiabatic. The bottom horizontal plate is kept at a constant temperature of 300 K. The pressure outlet and pressure inlet boundary conditions are considred at the exit and top open boundary, respectively. The governing differential equations are solved based on PISO (Pressure-Implicit with Splitting of Operators) algorithm [3] in Ansys 17.2. Second order central differencing scheme is considered for the discretization of diffusive terms and power law scheme for the discretization of convective terms. Systematic grid refinement study is carried out by taking various grids viz. 50×40, 60×60, 70×60, 80×80, 100×80 and 120×80. Mesh size of 120×80 is selected for all computations after grid independence study. The domain is taken to be a rectangle having length 55×h and width 35×h.

## 3. RESULT

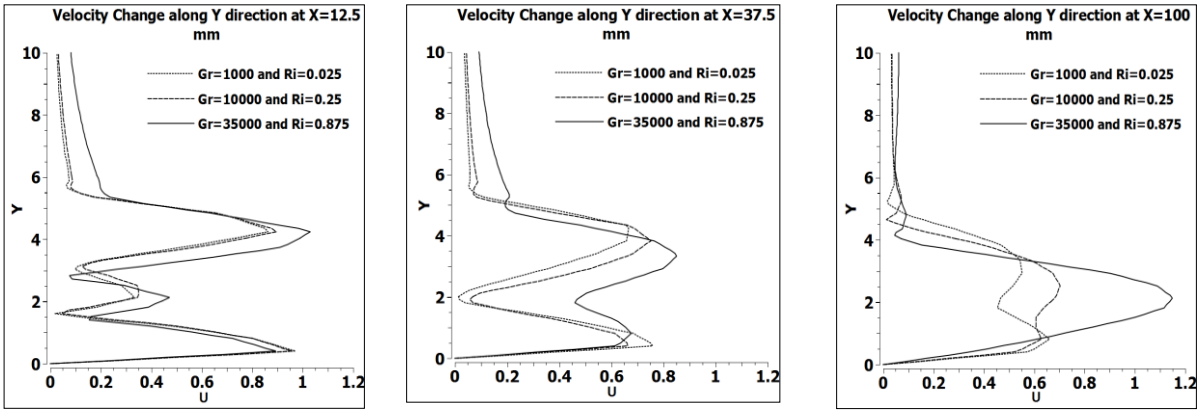


(a). x=12.5 mm (b). x=37.5 mm (c). x=100 mm

FIGURE 2. Velocity profiles for various Richardson numbers at different axial locations (Re=200)

Figure 2 shows the velocity profiles at differnt axial locations for Re 200. The Richardson number Ri is changed from 0.025 to 0.875 with increase in Gr from 1000 to 35000. The decay in velocity of wall jet is more as compared to offset jet due to the presence of wall. It is found that with an increase in Ri, the two jets merge earlier with decarse in the size of recirculation region. Due to this, the merge point and lower vortex center (LVC) shifts towards the jet inlet. The LVC has x and y coordinates as (0.0137, 0.02), (0.01094, 0.02075) and (0.003789, 0.018698) for Ri=0.025, 0.25 and 0.875, respectively. The upper vortex center (UVC) has x and y coordinates as (0.01625, 0.03750), (0.01767, 0.038) and (0.0134,0.0341) for Ri=0.025, 0.25 and 0.875, respectively. The x and y coordinates of merge point are (0.03796, 0.02475), (0.03540, 0.02560) and (0.02516, 0.02018) for Ri=0.025, 0.25 and 0.875, respectively.

Figure 3 shows the variation in non-dimensional temperature $\theta\,[=(T-T_\infty)/(T_j-T_\infty)]$ with Y (=y/h) at different x-locations for Re 200 and Gr 1000, 10000 and 35000, where $T_\infty$ is ambient temperature and $T_j$ is jet inlet temperature. It can be seen from the plot that initially temperature is higher and then it goes on decreasing as the flow proceeds in downstream direction because heat is transferred from offset jet to wall jet. The maximum temperature of offset jet at a given axial location is lower for higher value of Ri. This is due to fact that at higher Ri, buoyancey force promotes better mixing thus lower temperature. After a distance of 37.5 mm, heat transfer is so high that heat starts to penetrate deeper in the lower wall jet. It decreases the shielding effect of lower wall jet and due to it some heat even transfers to the plate. Figure 4 shows the temperature contour in the domain for Richardson number Ri=0.025 and Ri=0.875. It has been observed that in case of Ri=0.025 the heat transfers from offset jet to wall jet is low which is depicted by lower temperature values in the near wall region. However, with increase in Ri number, temperature difference between the two jets reduces and heat penetrates up to near wall region of wall jet as shown in Fig. 4(b).

## 4. CONCLUSIONS

It has been observed that as Ri increases, the converging zone becomes smaller with reduction in the size of vortex. The position of the merge point moves toward the jet inlet and thus the merging zone starts earlier with increase in Richardson number. Also, with an increase in Ri, buoyancy becomes dominant which results in better mixing and heat transfer between the two jets.

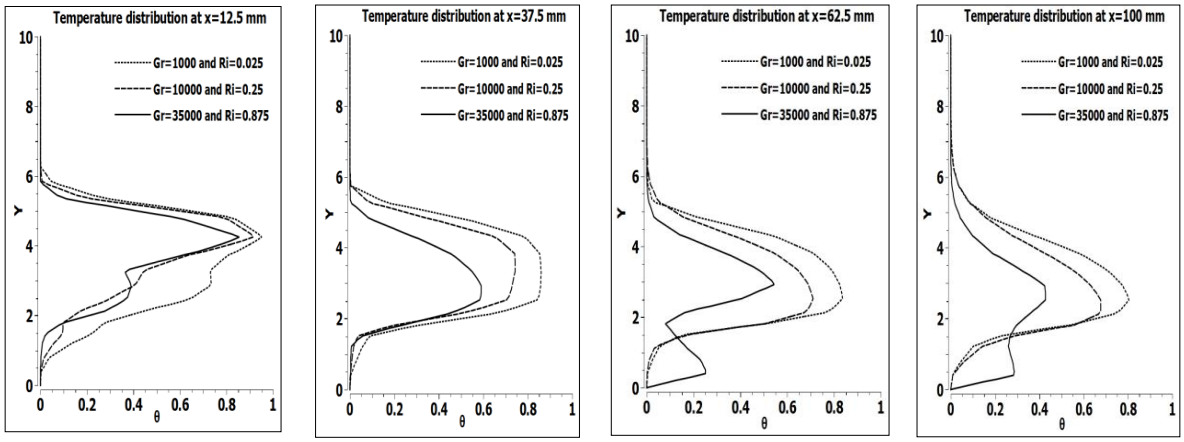


(a). x=12.5 mm (b). x=37.5 mm (c). x=62.5 mm (d). x=100 mm

FIGURE 3. Temperature profiles for various Ri at different x locations for Re=200

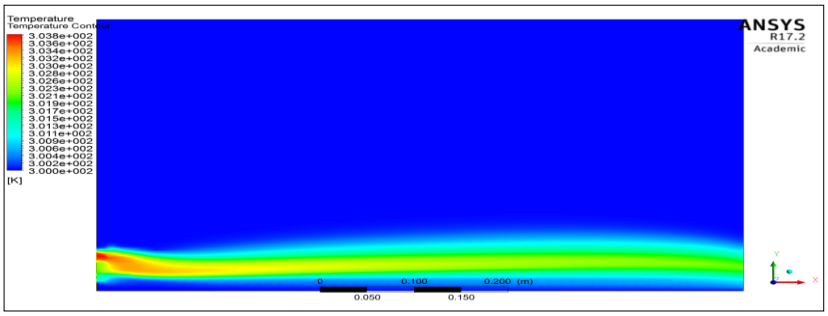


(a). Ri=0.025

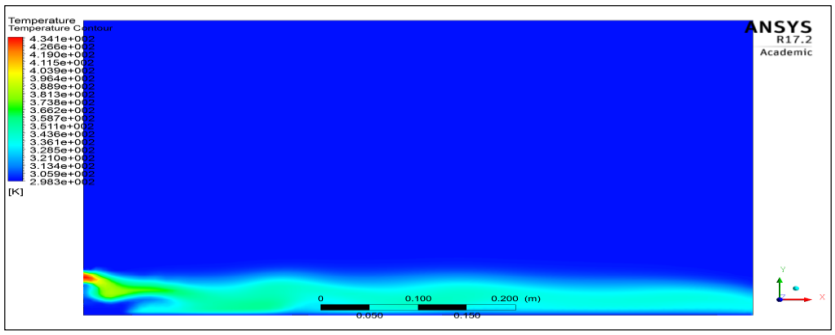


(b). Ri=0.875

FIGURE 4. Temperature contours for Ri=0.025 and 0.875

## REFERENCES

[1] P.R. Kanna and M.K. Das, Heat transfer study of two-dimensional laminar incompressible offset jet flows, *International Journal of Thermal Sciences*, 47,1620–1629, 2002.

[2] A. Kumar and M.K. Das, Study of a turbulent dual jet consisting of wall jet and an offset jet, *ASME: Journal of Fluid Engineering*, 133, 101201-1 to 101201-11, 2011.

[3] ANSYS FLUENT 12.0 Theory Guide, ANSYS Inc. (2009).

Fifth International Conference on Computational Methods for Thermal Problems
THERMACOMP2018, July 9-11, 2018, Indian Institute of Science, Bangalore, INDIA
*N. Massarotti, P. Nithiarasu, Pradip Dutta and C. Ranganyakalu (Eds.)*

# Thermal and Velocity Boundary Layer Studies in Hypersonic Flow over a Finite Thickness of Flat Plate using Conjugate Heat Transfer Analysis

**Ravi K. Peetala**
Assistant Professor, Department of Mechanical Engineering, Visvesvaraya National Institute of Technology, Nagpur-440010, India; **Email:** rkpeetala@mec.vnit.ac.in

## ABSTRACT

This paper explains about the accurate estimation of boundary layer thickness, wall skin-friction and heat-flux distributions at various wall materials using Conjugate heat transfer technique (CHT). Flow over a finite thickness flat plate has been studied successfully using loosely coupled Conjugate heat transfer (LC-CHT) technique. technique. To Analyze the significant effect of wall material on the fluid flow at moderately large time scales (~0.1sec). This effect is noticed to be dependent on thermal diffusivity of the wall material. Material with lower thermal diffusivity is found to get disturbed more keeping the fluid domain relatively undisturbed. In line with this, the material with lower diffusivity is noticed to alter the boundary layer thickness and interface properties with lesser heat penetration in itself.

**Key Words:** *Hypersonic flow, conjugate Heat Transfer, Loosely Coupled Conjugate Heat Transfer, Velocity and thermal Boundary layer.*

## 1. INTRODUCTION

Recent advances in hypersonic speed and space flight technology have focused attention on aerodynamic heating and aerodynamic drag problems. The aerodynamic heating drastically increases with increase in speed of the vehicle, aerodynamic heating is proportional to cube of velocity and drag is proportional to square of velocity [1]. Enormous changes in flow field and interface properties occurred due to the increase in vehicle speed. Small change in boundary layer significantly effects the interface properties like heat transfer and skin friction. In flow filed properties such as velocity and temperature have taken on great importance due to the influence of intense heating at the wall on the development of boundary layers. The concept of the boundary layer, introduced by Prandtl was notable for recognizing the importance of viscosity in flow at high Reynolds numbers [2]. Simulation for Thermal and velocity boundary Layer and heat transfer measurement experiments using conjugate heat transfer methodology is the central theme of this paper. Loosely coupled CHT technique is used to demonstrate this theme for hypersonic flow over finite thickness cylinder [3]. Effect of wall property variation on the fluid flow has been studied for comparatively large time scale (~0.1s) using loosely coupled CHT technique. Thermal boundary layer and velocity boundary layer thicknesses are used to understand the interaction between wall heating and hydrodynamic boundary layer. Details of the test case, boundary conditions and results are discussed in the following sections.

## 2. MATHEMATICAL FORMULATION OF CHT STUDIES

The conjugate heat transfer analysis for the hypersonic flow over a finite thickness flat plate involves solution methodology for both fluid as well as solid domain. Non-dimensional form of the two-dimensional Navier-Stokes (NS) equation is considered for the fluid flow modeling which is given as [4],

$$\frac{\partial U}{\partial t}+\frac{\partial F_i}{\partial x}+\frac{\partial G_i}{\partial y}=\frac{\partial F_v}{\partial x}+\frac{\partial G_v}{\partial y} \tag{1}$$

$$U=\begin{bmatrix}\rho\\ \rho u\\ \rho v\\ \rho E\end{bmatrix};\ F_i=\begin{bmatrix}\rho u\\ \rho u^2+p\\ \rho uv\\ \rho uH\end{bmatrix};\ G_i=\begin{bmatrix}\rho v\\ \rho uv\\ \rho v^2+p\\ \rho vH\end{bmatrix};\ F_v=\begin{bmatrix}0\\ \tau_{xx}\\ \tau_{yx}\\ u\tau_{xx}+v\tau_{xy}-\dot{q}_x\end{bmatrix};\ G_v=\begin{bmatrix}0\\ \tau_{xy}\\ \tau_{yy}\\ u\tau_{yx}+v\tau_{yy}-\dot{q}_y\end{bmatrix}$$

Where $U$ is conservative variable matrix, $F_i$ and $G_i$ are the Inviscid fluxes and $F_v$ and $G_v$ are viscous fluxes. The governing equation considered for heat transfer analysis in the solid is the two dimensional unsteady heat conduction equations, i.e.

$$\rho c\frac{\partial T}{\partial t}=\frac{\partial}{\partial x}\left[k\frac{\partial T}{\partial x}\right]+\frac{\partial}{\partial y}\left[k\frac{\partial T}{\partial y}\right] \tag{2}$$

Finite volume formulation is used to solve the dimensional form of this equation.
Integrate the above Eq.(2) over a fixed control volume in the space and with time can be represented as follows.

$$\int_t^{t+\Delta t}\int_{cv}\rho c\frac{\partial T}{\partial t}dVdt=\int_t^{t+\Delta t}\int_{cv}\frac{\partial}{\partial x}\left(k\frac{\partial T}{\partial x}\right)dVdt+\int_t^{t+\Delta t}\int_{cv}\frac{\partial}{\partial y}\left(k\frac{\partial T}{\partial y}\right)dVdt+\int_t^{t+\Delta t}\int_{cv}SdVdt \tag{3}$$

Explicit first order time stepping is used for the solid domain computations [**5**].

### 3. COMPUTATIONAL METHODOLOGY FOR CHT STUDIES

The conjugate heat transfer analysis for the hypersonic flow over a flat plate involves both fluid as well as solid domain. Typical computational domain describing the boundary conditions is given in Fig.1. The plate of length 100 mm and thickness 5 mm has been considered as the solid domain. Stretched grid is used at the interface in fluid as well as solid domains to compute the interface fluxes correctly. Mesh independence studies have been performed and the final mesh size is selected as, 300x250 for fluid domain and 300x180 for the solid domain. CHT studies are also carried out for the test conditions of free piston shock tunnel experiment. These conditions are as Mach number 9.2, pressure 690 Pa, temperature 155 K and initial wall temperature is 300 K [**6**]. The wall materials used for these studies are non-real. The properties of those materials used in the present investigations are given in Table .1. All the simulations are performed for a maximum duration of 0.1s. The major objective of this study is to analyze the effect of aerodynamic heating on fluid domain and associated change in the same with change in wall material. These computations are carried out using loosely coupled CHT technique [3,**7**]. Details of these results are mentioned in the following sections.

Table. 1: Material properties used in the simulation.

| Material | Thermal conductivity $(k)\,(\mathrm{W/m.K})$ | Density $(\rho)$ $(\mathrm{kg/m^3})$ | Specific heat $(C)$ $(\mathrm{J/kg.K})$ | Thermal diffusivity $(k/\rho C)\,(\mathrm{m^2/s})$ |
|---|---|---|---|---|
| D (Arbitrary Material I) | 204 | 1000 | 10 | $2.04\text{x}10^{-2}$ |
| E (Arbitrary Material II) | 1.46 | 1000 | 10 | $1.46\text{x}10^{-4}$ |

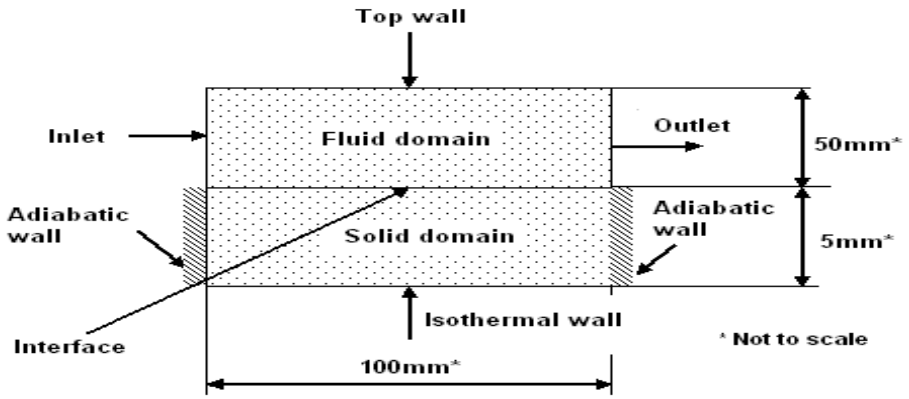


Fig. 1: Schematic diagram of computational domain for CHT analysis.

## 4. RESULTS AND DISCUSSION

The temperature and velocity profiles, at selective locations, in the fluid domain along with the temperature contour in case of material 'E', for 0.01s and 0.1s, are shown in Figs. 2 respectively. Streamwise increase in velocity boundary layer and thermal boundary layer thicknesses is evident in both the cases. Apart from this, velocity boundary layer can be seen always thinner than the thermal boundary layer. These figures clearly demonstrate the presence of large velocity and temperature gradients at the wall which decrease in the direction of flow. In line with this, higher value of heat transfer rate is expected at the leading edge of the plate in comparison with the same at downstream location. As a result of this, highest wall temperature of 1057 K for 0.01s and 1544.9 K for 0.1s are noticed at the leading edge. Thus these figures display enhancement in maximum temperature by 2.5 times for 0.01s and 4.14 times for 0.1s from its initial value (300 K). It is also evident from these figures that the heat which penetrated for ~9% of the depth of solid domain in 0.01s has disturbed 26.3 % of the solid domain in 0.1s.

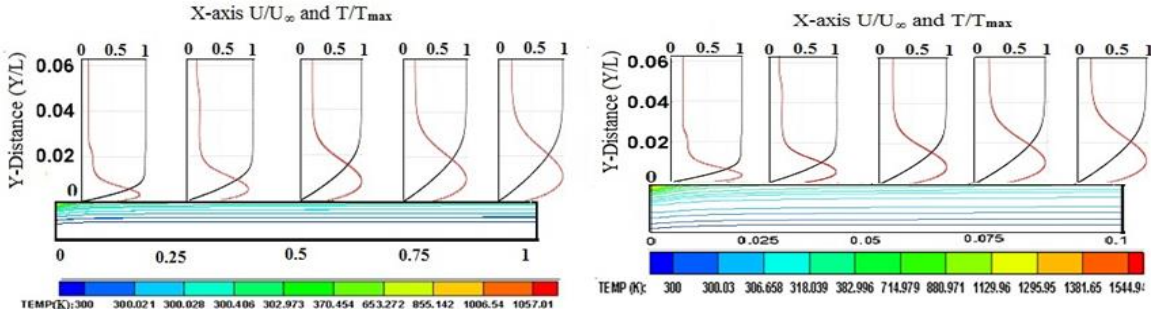


(a) (b)

Fig. 2: Temperature and velocity profile along the length and temperature contour at different time interval for wall Material E. (a) 0.01 sec; (b) 0.1 sec

The variation in temperature and velocity profiles at locations 0.01m and 0.09 m from the leading edge, for various time levels of CHT simulations, are as shown in Fig. 3 – 4. The temperature profiles shown in Fig. 3 portray inversion in trend. The temperature of the fluid increases in the normal direction to wall and attains a maximum. Upon this maximum, temperature decreases and reaches to the freestream value. Such profile is commonly experienced for isothermal cold wall conditions of conventional CFD. In the same figure, temperature profile for the adiabatic wall condition in conventional CFD shows monotonic decrease from wall temperature to the freestream value. Hence the maximum temperature

point remains at the wall for adiabatic case which is 2480 K for both the locations. The maximum temperature obtained from CHT studies for 0.01 m case is 960 K and 1024 K corresponding to 0.01s and 0.1s while the same is 850 K and 875 K for 0.09 m respectively. Thus, the maximum temperature in the thermal boundary layer at 0.01 m increases by times 2.2 initially for 0.01s and then by 2.41 times for 0.1s from its base value corresponding to isothermal simulation. The increment for the maximum temperature corresponding to same time intervals is 1.8 times and 1.91 times for 0.09 m location. Thus increase in maximum temperature is more towards the leading edge. Moreover temperature at all locations increases with time in the presence of Material 'E'. It's effect on velocity profiles is shown on Fig. 4. Besides, thicker velocity profile at any time instance, as an indication of higher boundary layer thickness at 0.09 m in comparison with the same at 0.01, is evident from those figures. The leading edge shock which is clear in the velocity profile near to the edge (Fig. 4-a) has been observed in temperature profile as well (Fig. 3-a). However shock is seen to be absent in the downstream station as shown in Fig. 4-b. As observed earlier, increase of velocity boundary layer thickness downstream of the leading edge is also clear from Fig. 4. Apart from this, inflation of the velocity profile with time is observed as its characteristic feature. This inflation can be accounted to the enhanced temperature at all locations. Such temperature increment increases the viscosity which in turn increases the boundary layer thickness. Therefore the expected increment in boundary layer thickness with time at various locations is plotted in Fig. 5-a. This figure clearly demonstrates the role of wall material 'E' in the boundary layer thickness increase which is around 29% at 0.01 m and 20% at 0.09 m from the leading edge in comparison with the conventional isothermal wall boundary condition. Similar exercise has also been performed for the wall material D. As a result of this, the thermal boundary layer thickness at various streamwise locations is plotted in Fig. 5-b for various time instances. No significant alteration in thermal boundary layer thickness is evident from this figure. Similar observation has been drawn for the velocity boundary layer thickness. Therefore material 'D' is seen to have lesser effect on the fluid flow in the duration of 0.1s. Two orders of higher thermal diffusivity in comparison with material E is the major reason for this disparity. The thermal and velocity boundary layers are plotted for all the wall conditions in Fig. 6. Here, adiabatic wall boundary condition corresponds to highest thermal and velocity boundary layer thicknesses while the minimum corresponds to the isothermal (300 K) wall boundary conditions. These figures reassert the advantage of CHT over the conventional CFD which corresponds to extreme wall boundary conditions.

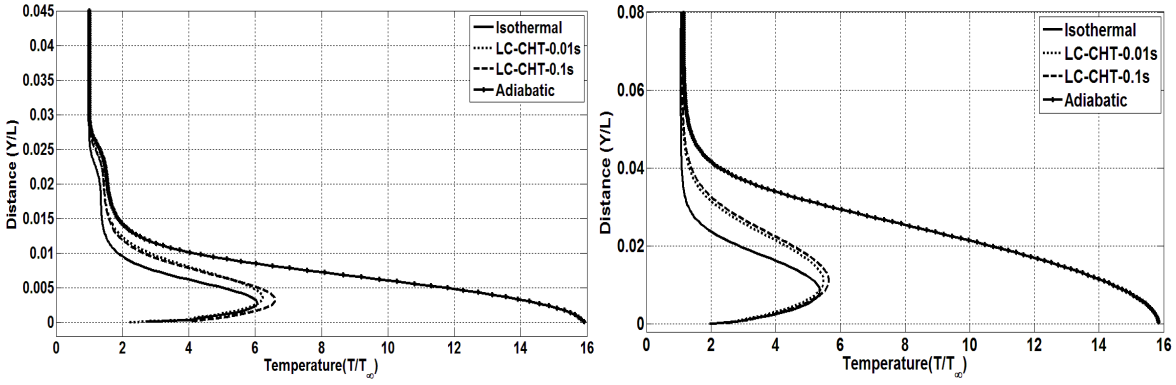


(a) (b)

Fig. 3: Temperature profile normal to the wall from leading for 'E' as wall material
(a) At x=0.01; (b) At x=0.09;

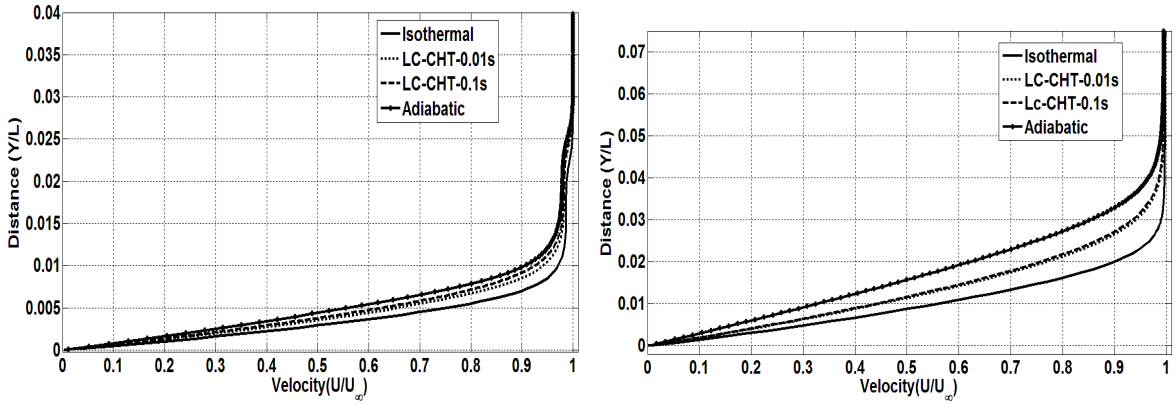


**(a)** **(b)**

Fig. 4: Velocity profile normal to the wall wall from leading for 'E' as wall material
(a) At x=0.01; (b) At x=0.09;

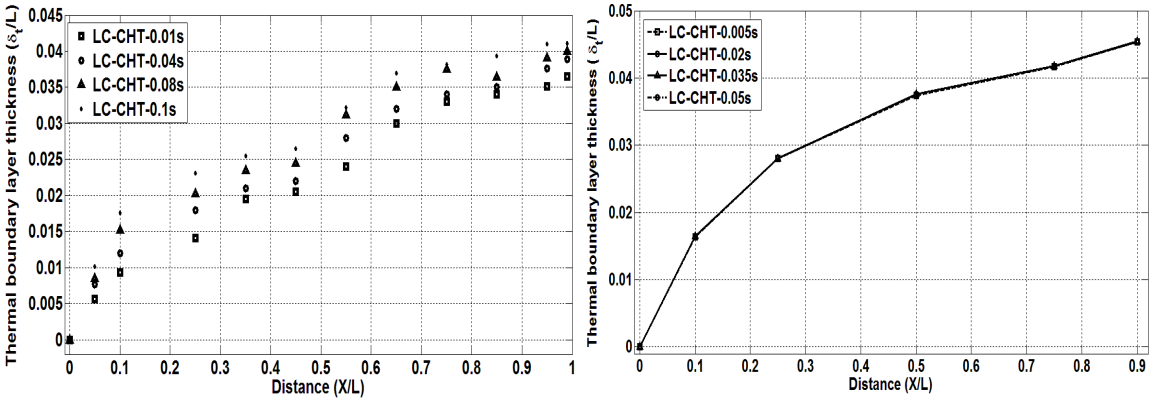


**(a)** **(b)**

Fig. 5: Thermal Boundary Layer along the flat plate at various times scales of CHT studies using different wall materials (a) Material 'E' ; (b) Material 'D'

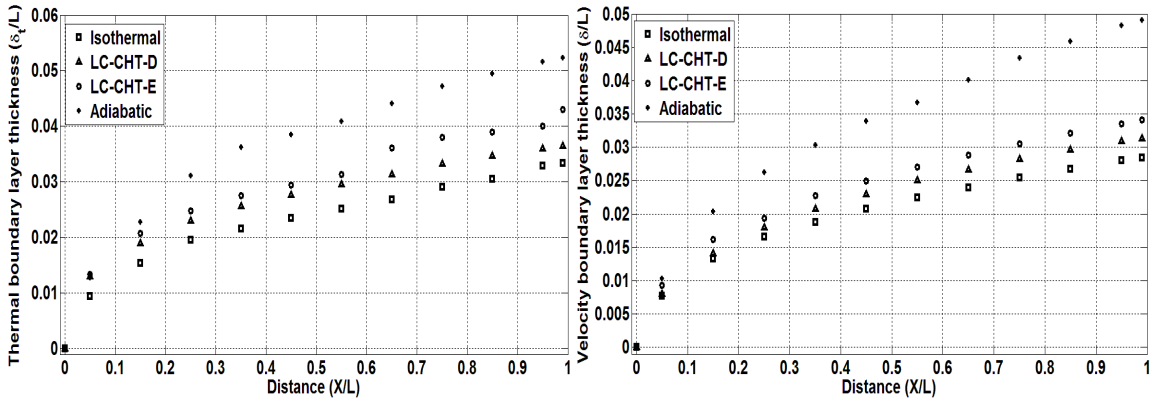


**(a)** **(b)**

Fig. 6: Thermal and velocity boundary layer thickness along the flat plate using various wall materials. (a) Thermal Boundary Layer; (b) Velocity Boundary Layer ;

The CHT based boundary layer thicknesses are seen to be placed between the extreme wall conditions. Apart from this, the thicknesses approach the adiabatic wall condition from their initial value of isothermal wall with increase in time. Boundary layer thickness is higher for material 'E' due to its lower thermal diffusivity in comparison with the material 'D'. Change in wall properties for different wall conditions at time instance of 0.1s are plotted in Fig. 7. Presence of wall material is seen to have lesser impact on the heat flux at

the leading edge which otherwise decreases slightly towards the trailing edge. Major change has been noticed in skin friction coefficient which increases in case of finite thermal conductivity. Increase in viscosity with temperature is seen to dominate the decrease in velocity gradient for increment of wall shear. Therefore higher wall shear at all locations is the result of presence of wall material.

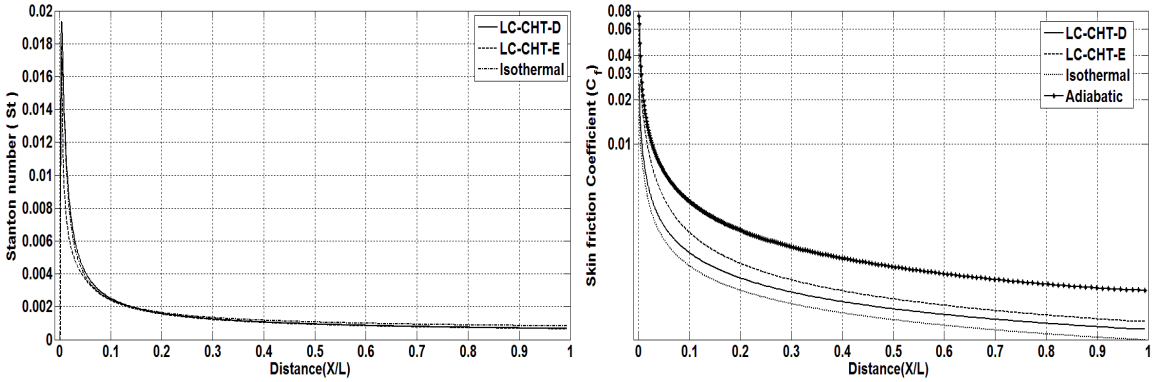


**(a)** **(b)**

Fig. 7: Stanton number and Skin friction coefficient along the length of the plate, (a) Stanton number ; (b) skin friction coefficient;

## 5. CONCLUSIONS

Flow over finite thickness flat plate has been studied successfully using loosely coupled CHT technique. Loosely coupled CHT technique on flat plate configuration showed significant effect of wall material on the fluid flow at moderately large time scales (0.1sec). This effect is noticed to be dependent on thermal diffusivity of the wall material. Material with lower thermal diffusivity is found to get disturbed more keeping the fluid domain relatively undisturbed. In line with this, the material with lower diffusivity is noticed to alter the boundary layer thickness and interface properties with lesser heat penetration in itself.

## REFERENCES

[1] Anderson J. D. Jr., "Hypersonic and High-Temperature Gas Dynamics", *AIAA Education Series; Ed: J.A. Schetz*, American Institute of Aeronautics and Astronautics, Virginia, Second Edition, 2006.

[2] White F. M., "Viscous Fluid Flow", *2nd Edn, Mc Graw-Hill. New York*, 1991.

[3] Ravi K.Peetala, Dipankar Das,Vinayak N Kulkarni and Niranjan Sahoo, Conjugate Heat Transfer Analysis for a Finite Thickness Cylinder in a Hypersonic Flow,Journal of *Asian Research: Heat Transfer (2016)*, 45(2):163-180

[4] Blazek. J., Computational Fluid Dynamics: Principles and applications, Elsevier Science Ltd, Oxford, UK, 2006.

[5] Veersteeg, H. K., and Malalasekera, W., "An introduction to computational fluid dynamics (Finite volume method)," *Longman Scientific and Technical and Wiley & sons Inc.*, New York, 1995.

[6] Mallinson, S. G., and Milthorpe J. F., "An experimental and numerical study of hypersonic study of hypersonic flat plate flow", 12th Australasian fluid mechanics conference, The University of Sydney, Australia, 1995.

[7] Niranjan Sahoo, Vinayak N Kulkarni and Ravi K. Peetala , Conjugate Heat Transfer Study in Hypersonic Flows, *Journal of the Institution of Engineers (India)*, 1:8, 2017.

# SIMULATION OF TURBULENT NATURAL CONVECTION IN ANNULAR CAVITY USING A HIGH-ORDER COMPACT FINITE-DIFFERENCE LBM

**Sai Ravi Gupta Polasanapalli, Kameswararao Anupindi**
Department of Mechanical Engineering, Indian Institute of Technology Madras, Chennai, Tamilnadu, 600036, India, kanupindi@iitm.ac.in.

## ABSTRACT

In the present work, compact finite-difference lattice Boltzmann method is extended to simulate thermal flows using double distribution approach. Fourth-order accurate spatial and temporal discretization schemes are utilized in order to accurately simulate the flow fields. The developed solver is validated by simulating natural convection in a square cavity at Rayleigh numbers $10^6$ and $10^8$. Thereafter, natural convection in a circular annulus is studied for a Rayleigh number of $10^8$. Streamlines and isotherms are used in order to visualize the results and the variation of Nusselt number and temperature profiles are studied within the cavity.

**Key Words:** *Heat Transfer, Lattice Boltzmann Method, Natural Convection.*

## 1. INTRODUCTION

Lattice Botlzmann method (LBM) has evolved as an alternative to simulate fluid flow and heat transfer problems. Several researchers has applied LBM to simulate flow through porous media, blood flows, turbulent flows and multiphase flows [1]. Classical LBM works on a two-step process consisting of streaming and collision and is limited to uniform Cartesian meshes. In order to accurately resolve the annular cavity geometry finite-difference LBM was used in the present work instead of the classical LBM. The developed solver employs fourth-order accurate compact scheme for the spatial discretization and forth-order accurate explicit Runge-Kutta method for time-integration. A double population method, employing an additional distribution function, was used in order to simulate the temperature field.

The aim of the present work is to exend the compact finite-difference LBM (CFDLBM) to simulate non-isothermal flows in complex geometries. To this end, turbulent natural convection in an annular cavity was simulated. The numerical method is presented in section 2, results obtained from the solver are discussed in section 3 and the paper is concluded in section 4.

## 2. NUMERICAL METHOD

In LBM, the governing equation is the Boltzmann equation and is discretized on a suitable lattice. Collision term in the Boltzmann equation is approximated using the single-relaxation-time Bhatnagar, Gross and Krook (BGK) approxmation. The Boltzmann equation is solved on a D2Q9 discrete lattice. The discretized governing equaiton is given as follows:

$$\frac{\partial f_\alpha}{\partial t} + e_\alpha . \nabla f = \frac{-\left(f_\alpha - f_\alpha^{eq}\right)}{\tau} \quad where \quad \alpha = 0,1,2,\ldots 8 \ .$$

Grid transformation is used to enable the solver to handle non-uniform and curvilinear meshes. Two different distribution functions, one for the flow and the other for the temperature field are used and this is known as the double distribution approach. Density distribution function f recovers the Navier-Stokes equations and the temperature distribution function g recovers the macroscopic governing equation for the temperature field. The governing equations for the distribution functions are given as follows:

$$\frac{\partial f_\alpha}{\partial t}+e_{\alpha\xi}\frac{\partial f_\alpha}{\partial \xi}+e_{\alpha\eta}\frac{\partial f_\alpha}{\partial \eta}=\frac{-\left(f_\alpha-f_\alpha^{eq}\right)}{\tau_f}+F_b \quad , \quad \frac{\partial g_\alpha}{\partial t}+e_{\alpha\xi}\frac{\partial g_\alpha}{\partial \xi}+e_{\alpha\eta}\frac{\partial g_\alpha}{\partial \eta}=\frac{-\left(g_\alpha-g_\alpha^{eq}\right)}{\tau_e}$$

where $\tau_f$, $\tau_e$ are relaxation times for denisty and temperature distributions respectively, $F_b$ is the buoyance force term and ($\xi$, $\eta$) represent the transformed coordinates. The corresponding equilibrium distribution functions can be given as:

$$f_\alpha^{eq}=w_\alpha\rho\left(1+\frac{e_\alpha.u}{c_s^2}+\frac{\left(e_\alpha.u\right)^2}{2c_s^4}-\frac{u.u}{2c_s^2}\right) \quad , \quad g_\alpha^{eq}=w_\alpha T\left(1+\frac{e_\alpha.u}{c_s^2}\right) .$$

Macroscopic properties can be calculated using the following relationships:

$$\rho=\sum_{\alpha=0}^{8}f_\alpha \quad , \quad \bar{u}=\frac{1}{\rho}\sum_{\alpha=0}^{8}e_\alpha.f_\alpha \quad , \quad T=\sum_{\alpha=0}^{8}g_\alpha .$$

The finite difference lattice Boltzmann equation used in the present work is given as follows:

$$\frac{\partial f_\alpha}{\partial t}=R\left(f_\alpha\right) \quad where \quad R\left(f_\alpha\right)=\frac{-\left(f_\alpha-f_\alpha^{eq}\right)}{\tau}-e_{\alpha\xi}\frac{\partial f_\alpha}{\partial \xi}-e_{\alpha\eta}\frac{\partial f_\alpha}{\partial \eta} .$$

Fourth-order accurate Runge-Kutta scheme is used for the time integration and fourth-order accurate compact scheme is used for the spatial discretization of $\frac{\partial f}{\partial \xi}$, $\frac{\partial f}{\partial \eta}$ terms. The same schemes are used for solving the temperature distribution function equations as well. As the central difference schemes are non-dissipative in nature, therefore in order to stabilize the solver, a sixth-order accurate compact-filter is used to remove the high frequency oscillations which may get generated due to the non-uniform grid and the boundary conditions. Filtering operation is applied every time step for both the density and the thermal distribution functions [2].

Natural convection in a square cavity was chosen as the test case in order to validate the present solver. The horizontal walls of the square cavity are insulated and the vertical walls are maintained at different uniform temperatures. Temperature gradient generated by the two vertical walls is the driving mechanism for the natural convection to take place within the cavity. Neumann temperature boundary conditions are imposed on the top and bottom walls and Dirichlet temperature boundary conditions are applied on the vertical walls at two different temperatures.

Natural convection in the annular cavity is driven by the temperature difference that exists between the inner and the outer walls. In the present study inner cylinder was maintained at a higher temperature whereas the outer cylinder was maintained at a lower temperature. No-slip velocity boundary conditions are applied on all the walls. For the temperature, Dirichlet boundary conditions are imposed on the inner and outer cylinders. In order to apply Neumann boundary conditions on the density and temperature distribution functions, one-sided fourth-order accurate finite-difference formulae were used. Distribution functions on the boundary grid are calculated using the equilibrium and the non-equilibrium distribution functions. One sided fourth-order accurate finite-

difference formula was used for approximating the non-equilibrium distribution function on the walls as given by the following equations $\frac{\partial^2 f^{non-eq}}{\partial^2 n}=0$ , $\frac{\partial^2 g^{non-eq}}{\partial^2 n}=0$ .

## 3. RESULTS

The developed solver is validated by simulating natural convection in a square cavity for two different Rayleigh numbers of $10^6$ and $10^8$. The maximum x-component of velocity on the centre vertical line and its location, maximum y-component of velocity on the central horizontal line and its location, average Nusselt number, average Nusselt number over the central vertical line and the high-temperature wall are presented in Table1. The data from the literature [3, 4, 5] was also presented in the same table together with the relative errors. Good matching of results with reference data is observed from the Table1. Schematic diagram of square cavity, isotherms and streamlines for Rayleigh numbers $10^6$ and $10^8$ and the comparison of temperature profiles along central horizontal line are shown in figure 1.

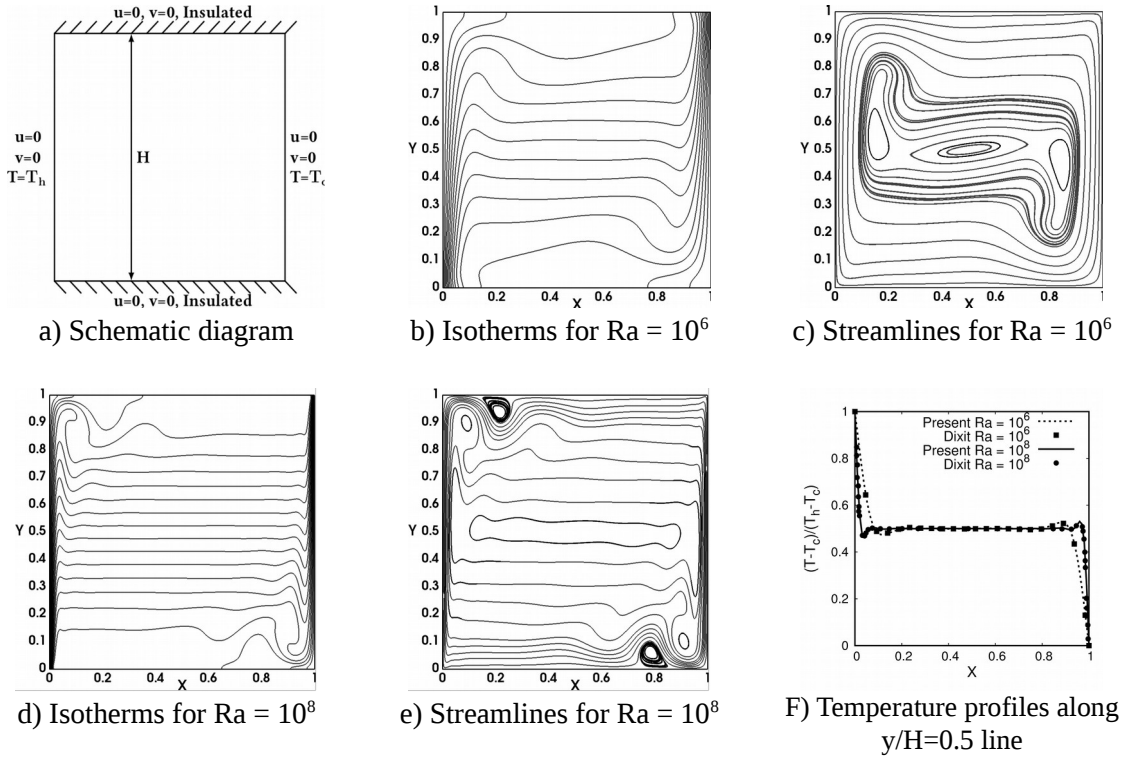


a) Schematic diagram b) Isotherms for Ra = $10^6$ c) Streamlines for Ra = $10^6$

d) Isotherms for Ra = $10^8$ e) Streamlines for Ra = $10^8$ F) Temperature profiles along y/H=0.5 line

FIGURE 1. Validation case results

| Ra | Data | $U_{max}$ | Y | $V_{max}$ | X | $\overline{Nu}$ | $Nu_{1/2}$ | $Nu_0$ |
|---|---|---|---|---|---|---|---|---|
| | Ref[2] | 64.630 | 0.850 | 219.36 | 0.0379 | 8.800 | 8.799 | 8.817 |
| $10^6$ | Present | 64.8065 | 0.8463 | 220.567 | 0.0381 | 8.8183 | 8.8172 | 8.8202 |
| | Error(%) | 0.272 | 0.435 | 0.55 | 0.528 | 0.208 | 0.207 | 0.036 |
| | Ref[3] | 321.876 | 0.928 | 2222.39 | 0.012 | | | 30.225 |
| $10^8$ | Present | 273.329 | 0.934 | 2277.55 | 0.0116 | 30.696 | 30.666 | 29.943 |
| | Error(%) | 15.0825 | 0.647 | 2.482 | 3.33 | | | 0.933 |

TABLE 1. Comparison of present results with the reference data for natural convection in a square cavity at Rayleigh numbers $10^6$ and $10^8$.

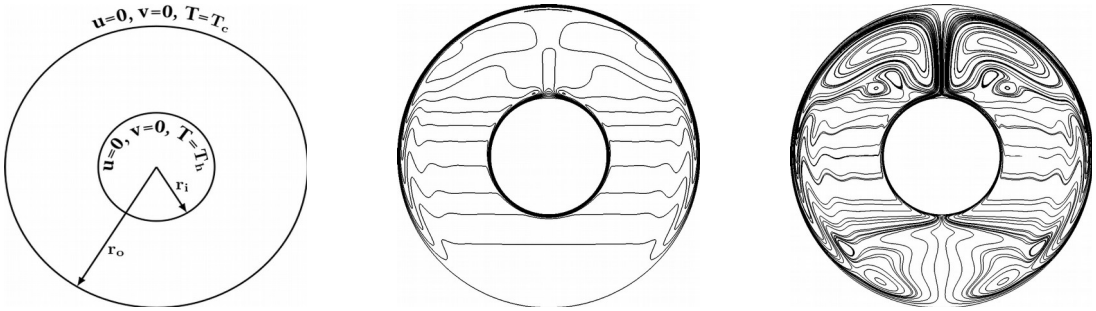


a)Schematic diagram b) Isotherms c) Streamlines

FIGURE 3: Natural convection in concentric annnular cavity for Rayleigh number Ra = $10^8$.

In the present study the ratio of the outer radius to inner radius of the cavity is taken as 2.60. Contours of isotherms and streamlines within the annular cavity at a Rayleigh number of $10^8$ are shown in figure 2. From this figure, higher flow and temperature gradients can be noted near the walls of the cavity. The velocity reaches a maximum near the upper part of the inner cylinder and a minimum velocity is observed in the bottom part of the cavity as the cold fluid settles there. Most of the fluid on the top of inner cylinder is maintained at a higher average temperature because of the presence of a thermal plume. Average Nusselt number for a Rayleigh number $10^8$ is obtained as 19.051.

## 4. CONCLUSIONS

In the present work, compact finite-difference LBM solver is extended to simulate natural convection in annular cavities. The developed solver was validated using natural convection in a square cavity at Rayleigh numbers $10^6$ and $10^8$. A good match was observed for the variation of temperature profiles and Nusselt number when compared with the reference data. The developed solver was successfully applied to simulate turbulent natural convection in a concentric annular cavity. A thermal plume was noticed on the top of the inner cylinder which is responsible for keeping the flow at a higher average-temperature in the top portion of the annulus. The present study establishes that CFDLBM can be successfully applied to simulate turbulent natural convection.

## REFERENCES

[1] Chen, S., Doolen, G.D.. Lattice Boltzmann method. Annual Review of Fluid Mechanics 1998;(Kadanoff 1986)

[2] Kazem Hejranfar and Eslam Ezzatneshan. Implementation of a high-order compact finite-difference lattice boltzmann method in generalized curvilinear coordinates. Journal of Computational Physics, 267:28–49, 2014.

[3] De Vahl Davis, G.. Natural Convection in an Enclosed Rectangular Cavity. International Journal of Heat and Mass Transfer 1968;11:1675–1693.

[4] P. Le Quéré, Accurate solutions to the square thermally driven cavity at high Rayleigh number, Comput. Fluids 20 (1991) 29–41.

[5] Dixit, H., Babu, V.. Simulation of high Rayleigh number natural convection in a square cavity using the lattice Boltzmann method. International journal of heat and mass transfer 2006;49(3):727–739

Fifth International Conference on Computational Methods for Thermal Problems
THERMACOMP2018, July 9-11, 2018, Indian Institute of Science, Bangalore, INDIA
*N. Massarotti, P. Nithiarasu, Pradip Dutta and C. Ranganyakalu (Eds.)*

# Numerical Investigation on Heat Transfer of Helical Baffles Shell and Tube Heat Exchanger

**Ravi Gugulothu, Narsimhulu Sanke**
Research Scholar, Department of Mechanical Engineering, University College of Engineering, Osmania University, Hyderabad-07, Telangana State, India, E-mail: ravi.gugulothu@gmail.com

Department of Mechanical Engineering, University College of Engineering, Osmania University, Hyderabad-07, Telangana State, India E-mail: nsanke@gmail.com

**A. V. S. S. K. S Gupta**
Department of Mechanical Engineering, JNTUH College of Engineering Hyderabad, Telangana State, India, E-mail: avs_gupta@jntuh.ac.in

## ABSTRACT

Heat exchangers are playing major role in heat and mass exchange apparatus like electrical power generation plants, oil refining, environmental protection and chemical engineering processes. Helical baffles with $40^0$ helix angle are used in shell and tube heat exchanger to enhance the heat transfer and reduce the pressure drop. New geometries have been introduced to performance enhancement and to improve reliability of heat exchangers. In this present study, shell and tube heat exchanger has been designed based on TEMA standard and thermal characteristics are observed based on different Reynolds number in shell side (ranging from 2,500 to 16,500) as well as tube side (3,000 to 22,000). The heat transfer coefficient, friction factor and overall heat transfer coefficient have been estimated for different Reynolds numbers and noticed that the heat transfer coefficient, overall heat transfer coefficients are increasing along the increase of Reynolds number and friction factor reduces by increasing Reynolds number.

**Key Words:** *Heat Exchanger, Heat Transfer, Pressure Drop, Pump Power, Reynolds Number.*

## 1. INTRODUCTION

Heat exchangers are playing major role in heat and mass exchange apparatus like electrical power generation plants, oil refining, environmental protection and chemical engineering processes. Among different types of heat exchangers shell and tube heat exchangers have been commonly used in Industries, due to the robust construction geometry as well as easy maintenance and possible upgrades. The heat transfer effectiveness can be improved by using baffles in shell and tube heat exchangers. Segmental baffles are mostly used one to support tubes and change the direction of fluid flow.

Higher pumping power is needed to offset the higher pressure drop when the segmental baffles are used in shell and tube heat exchangers under the same load. Therefore it is essential to develop a novel shell and tube heat exchanger using different baffles to have higher heat transfer efficiency and lower pressure drop. Shell and tube heat exchanger with helical baffles introduced by Lutcha and Nemcansky in May, 1990. Helical baffles serve as guide vanes for shell side flow when compared to segmental baffles. The use of continuous helical baffles in shell and tube heat exchangers can improve the performance. However, very few research works are done on shell and tube heat exchangers using continuous helical baffles. The pioneering work published is given in literature.

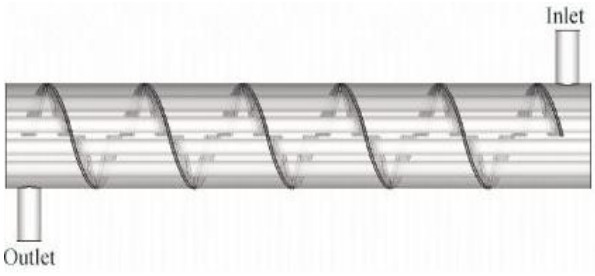


Fig 1: Shell and Tube Heat Exchanger with Helical Baffle

The heat exchangers are devices which transfers heat between two fluids which are at different temperatures. A shell and tub heat exchanger consists of a bundle of tubes enclosed within a cylindrical shell.
One fluid flows through the shell and another fluid flowing through the tubes. The fluid flow and heat transfer processes are turbulent flow and steady state. The shell and tube heat exchanger consider in the present study with helical baffles is shown in figure 1.

## 2. MAIN BODY

Master B.I et al (2006) gave the importance of heat exchangers along the worldwide applications of it. Bin Gao et al (2015) has experimentally studied on flow resistance and heat transfer of several shell and tube heat exchangers with discontinuous helical baffles of helix angles $8^0$, $12^0$, $20^0$, $30^0$ and $40^0$. Their results provide the shell and tube heat exchanger with $40^0$ helix angles is the best comprehensive performance among $8^0$,$12^0$,$20^0$,$30^0$ and $40^0$ helix angles. Cong Dong et al (2016) experimentally studied on circumferential overlap trisection helical baffles shell and tube heat exchanger with folded baffles, their results shows the heat transfer performance and comprehensive performance evaluation indexes of the circumferential overlap trisection helical baffles are much better than the segmental baffle heat exchanger.

Jian Fei Zhang et al (2009) experimentally studied the flow and heat transfer characteristics on several shell and tube heat exchangers, one with segmental baffles and helical baffles of four different helix angles like $20^0$, $30^0$, $40^0$ and $50^0$. They found that the shell and tube heat exchanger with $40^0$ helix angle shows the best performance under the same volume flow rate. Jian Fei Zhang et al (2009) carried 3D numerical simulation on shell and tube heat exchangers with three different helix angles like $30^0$, $40^0$ and $50^0$ and found that the $40^0$ helix angles shell and tube heat exchanger given best performance among all the three helix angles.

The heat exchanger has 2000 mm length and 114.3 mm, 102.10 mm of shell outer and inner diameters are chosen with 4 numbers of tubes with outer diameters are 25.4 mm, arranged in an angle of $45^0$ rotating square arrangement. From literature the optimum helix angle (β) is $40^0$ and same has been considered for the present work and thickness of the baffle is 3 mm. Hot fluid is considered in shell side at temperature of 343.15 K and cold fluid is considered in tube side at temperature of 298.15 K. In this study shell side flow rate ($\dot{Q}_S$) and tube side flow rates ($\dot{Q}_t$) are considered as 20 lpm to 60 lpm and 10 lpm to 30 lpm.

Baffle spacing (S) = $0.2 \times D_i$ or 51mm. (Whichever is greater). (1)
Tube outer diameter ($d_0$) = 25.4mm from Table RCB-4.52 (2)
$p = 1.25 \times d_0$ (3) $B_{helical} = \sqrt{2} D_i \tan(\beta)$ (4)
Number and size of tie rods: No fewer than four tie rods and not less than 9.5mm of diameter. Any baffle segment requires a minimum of three points of supports.

**Shell Side Calculation**

$\dot{m} = Q_s \times \rho_s$ (5) $A_s = 0.25\pi\left(D_i^2 - \left(N \times d_0^2\right)\right)$ (6)

$$V_s = \frac{\dot{m}_s}{\rho_s A_s} \quad (7) \qquad D_e = \frac{4\left(P_t^2 - \left(0.25\pi - d_0^2\right)\right)}{\pi d_0} \quad (8)$$

Equivalent/Effective diameter varies with the flow arrangements.

$$\mathrm{Re}_S = \frac{V_S \times D_e}{\nu} \quad (9) \qquad \mathrm{Pr}_S = \frac{\mu C_p}{k_{ShellFluid}} \quad (10)$$

For turbulent flow, Dittus-Boelter correlation is used

$$h_S = 0.023 \times \left(\frac{k_{ShellFluid}}{D_e}\right) \times (\mathrm{Re})^{0.8} \times (\mathrm{Pr})^{0.3} \quad (11) \qquad Nu_S = \frac{h_S \times D_e}{k_{ShellFluid}} \quad (12)$$

$$f_S = 0.184 \times (\mathrm{Re})^{-0.2} \quad (13) \qquad \Delta p_S = \frac{\rho \times f_S \times L_S \times V_S^2}{2 \times B} \quad (14)$$

$$Q_s = mC_{p,s}\left(T_{s,in} - T_{s,out}\right) \quad (15)$$

**Tube side calculation**

$$\dot{m}_t = \dot{Q}_t \times \rho_t \quad (16) \qquad A_t = N \times A_o \quad (17)$$

$$V_t = \frac{\dot{m}_t}{\rho_t \times A_t} \quad (18) \qquad \mathrm{Re}_t = \frac{V_t \times d_i}{\nu} \quad (19)$$

For turbulent fluid flow, from Dittus-Boelter correlation,

$$\mathrm{Pr}_t = \frac{\mu C_p}{k_{tubefluid}} \quad (20) \qquad h_t = 0.023 \times \left(\frac{k_{tubefluid}}{d_i}\right) \times (\mathrm{Re})^{0.8} \times (\mathrm{Pr})^{0.4} \quad (21)$$

The heat transfer coefficient can be calculated by the Nusselt number equation.

$$Nu_t = \frac{h_t \times d_i}{k_{tubefluid}} \quad (22) \qquad f_t = 0.184 \times (\mathrm{Re})^{-0.2} \quad (23) \qquad \Delta p_t = \frac{\rho \times f_t \times L \times V_t^2}{2 \times d_i} \quad (24)$$

$$Q_t = mC_{p,t}\left(T_{t,in} - T_{t,out}\right) \quad (25) \qquad Q = \frac{Q_s + Q_t}{2} \quad (26)$$

$$\Delta T_{\max} = T_{s,in} - T_{t,out} \quad (27) \qquad \Delta T_{\min} = T_{s,out} - T_{t,in} \quad (28)$$

$$\Delta T_{LM} = \frac{\left(\Delta T_{\max} - \Delta T_{\min}\right)}{\ln\left(\frac{\Delta T_{\max}}{\Delta T_{\min}}\right)} \quad (29) \qquad A_0 = N.\pi d_0.l_{tb} \quad (30) \qquad U = \frac{Q}{A_0 \times \Delta T_{LM}} \quad (31)$$

## 3. RESULTS

Numerical analysis of shell and tube heat exchangers using $40^0$ helical baffles are conducted in MAT Lab and results are discussing here.

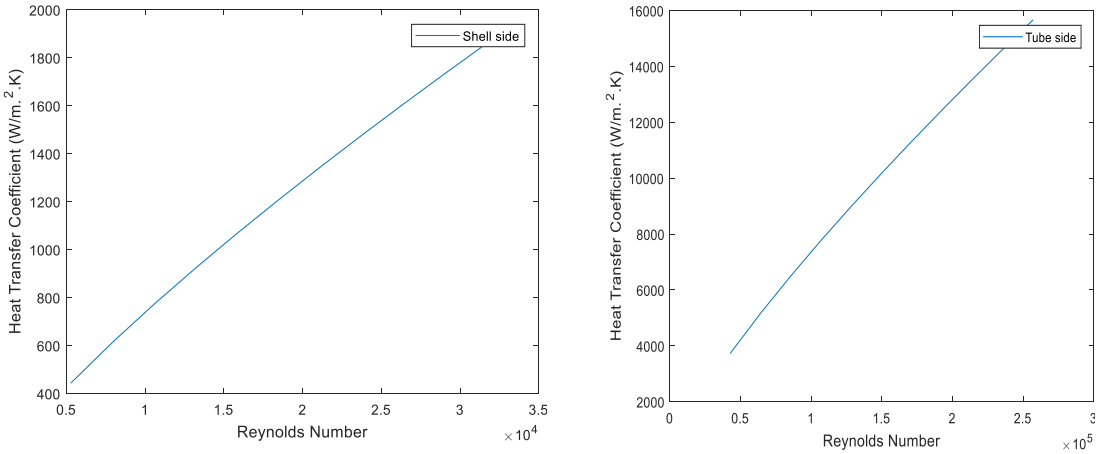


Fig 2: Reynolds number Vs Heat Transfer Coefficient (Shell side and Tube side)

Figure 2 shows the increase of heat transfer coefficient along the Reynolds number in shell side as well as tube side, due to the increase in flow rates.

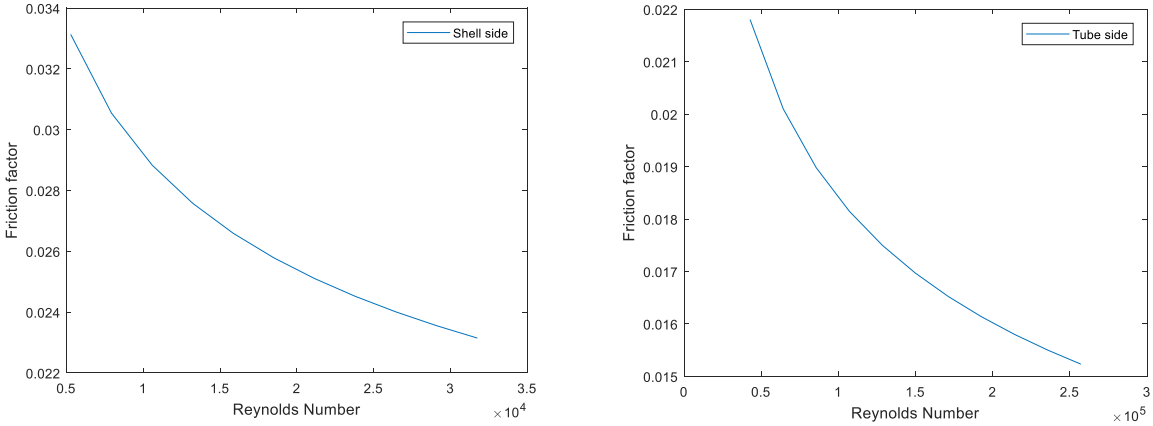


Fig 3: Reynolds number Vs Friction factor (Shell side and Tube side)

Figure 3 predicts the friction factor decreases along the increasing of Reynolds number in shell side and tube side for a helical baffled shell and tube heat exchanger. This is due to increase of mass flow rates.

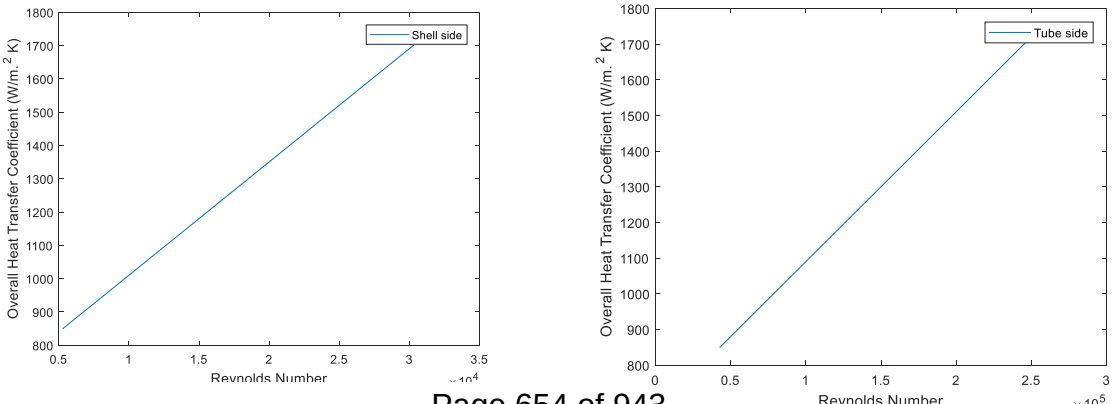

Fig 3: Reynolds number Vs Overall Heat Transfer Coefficient (Shell side and Tube side)

Figure 4 indicates the Reynolds number Vs Overall heat transfer coefficient. Overall heat transfer coefficient increases with the increasing of Reynolds number. This is happen, due to increasing of flow rates.

## 4. CONCLUSIONS

The research on shell and tube heat exchangers with helical baffles is done by many researchers and it was proved that pressure drop decreases and increases the heat transfer. For many years, various types of baffles have been used in shell and tube heat exchangers to improve the heat transfer while maintaining a reasonable pressure drop. Helical baffles are proved the suitable type of baffles for enhancing the heat transfer and reducing the pressure drop in shell and tube heat exchangers. From the pioneering work, the great significant in the improvement of heat exchangers with helical baffles and the heat transfer increases with the decreasing the helix angles and become mild after the helix angle $40^0$ for larger flow rates and $12^0$ for smaller flow rates. The friction factor decreases with the increase of Reynolds number in shell and tube heat exchangers. Heat transfer coefficient increases with the increasing of Reynolds number.

## REFERENCES

[1] Bin Gao, Qincheng Bi, Zesen Nie and Jiangbo Wu, “Experimental study of effects of baffle helix angle on shell side performance of shell and tube heat exchangers with discontinuous helical baffles”, Experimental Thermal and Fluid Science 68(2015), pp: 48-57.

[2] Cong Dong, Dongshuang Li, Youqu Zheng, Guuoneng Li, Yange Suo and Yaping Chen, “An efficient and low resistant circumferential overlap trisection helical baffle heat exchanger with folded baffles ”, Energy Conversion and Management 113 (2016), pp: 143-152.

[3] Jian Fei Zhang, Bin Li, Wen Jiang Huang, Yong Gang Lei, Ya Ling He and Wen Quan Tao, “Experimental performance comparison of shel side heat transfer for shell and tube heat exchangers with middle overlapped helical baffles and segmental baffles”, Chemical Engineering Science 64(2009), pp: 1643-1653.

[4] Jian Fei Zhang, Ya Ling He and Wen Quan Tao, “3D numerical simulation on shell and tube heat exchangers with middle overlapped helical baffles and continuous baffles-Part II: Simulation results of periodic model and comparison between continuous and non-continuous helical baffles”, International Journal of Heat and Mass Transfer 52 (2009), pp: 5381-5389.

[5] Jian Wen, Huizhu Yang, Simin Wang, Yulan Xue and Xin Tong, “Experimental investigation on performance comparison for shell and tube heat exchangers with different baffles”, International Journal of Heat and Mass Transfer 84 (2015), pp: 990-997.

[6] Lutcha J and Nemcansky J, “Performance improvement of tubular heat exchangers by helical baffles”, Chem. Eng. Res. Des, 68(1990), pp: 263-270.

[7] Master B.I, Chunangad K.S, Boxma A.J, Kral D and Stehlik P, “Most Frequently Used Heat Exchangers from Pioneering Research to Worldwide Applications”, Heat Transfer Engineering, 27(6), pp: 4-11, 2006.

[8] Peng B, Wang Q.W, Zhang C, Xie G.N, Luo L.Q, Chen Q. Y and Zeng M, “An Experimental Study of Shell and Tube Heat Exchangers With Continuous Helical Baffles”, Journal of Heat Transfer, October 2007, Vol.: 129, pp: 1425-1431.

[9] Ravi Gugulothu, Narsimhulu Sanke and A.V.S.S.K.S Gupta, “Numerical Study of flow characteristics in shell and tube heat exchangers”, Proceedings of the International Conference on Numerical Heat Transfer and Fluid Flow (NHTFF).

Fifth International Conference on Computational Methods for Thermal Problems
THERMACOMP2018, July 9-11, 2018, Indian Institute of Science, Bangalore, INDIA
*N. Massarotti, P. Nithiarasu, Pradip Dutta and C. Ranganyakalu (Eds.)*

# EFFECT OF CONTROL PLATES ON THE FLOW AND CONVECTIVE HEAT TRANSFER CHARACTERISTICS OF FLOW PAST A CIRCULAR CYLINDER

**Anuresh kumar, R. Deepakkumar*, Dhiraj D. Raut, A.V.S.S. Hemanth, G.Venkat Ritish**
National Institute of Technology, Tadepalligudam, Andhra Pradesh – 534101,
*rdeepakkumar12@gmail.com

## ABSTRACT

Vortex shedding and convective heat transfer characteristics due to control plates near the cylinder have been investigated numerically at Reynolds number 100. The control plates locations and orientation has been taken as a study parameter, the radial distance between the centroids of cylinder and control plate ($r_d$) and the angular location ($\theta$) measured from rear stagnation point decides the location of control plates. The finite volume code Ansys Fluent is used for computing the field variables. The vortex shedding forces (drag and lift), shedding frequency and Nusselt number are compared with respect to the various locations of control plates. Vortex shedding suppression is observed for the case at $\theta=90^o$, where the control plates are positioned along the main flow direction. Suppression of heat transfer is observed for the closer location of control plates.

**Key Words:** *Wake control, Vortex shedding suppression, Heat Transfer, Passive method, Control plate.*

## 1. INTRODUCTION

The study on flow past circular cylinder can be seen in various aspects such as confined or an unconfined cylinder, two or three dimensional flow, laminar or turbulent flow, creeping flow, flow separation, vortex shedding, vortex induced vibration, wake flow, vortex shedding and wake control by active and passive control methods and heat transfer enhancement studies, etc., Even though many studies have been conducted on vortex shedding and wake control, it has high scope due to its wide range of applications. Bridge piers, smoke stacks, under water structures, fin and tube heat exchanger, cooling in plastics and glass production industries, etc., are such examples.

The passive control of vortex shedding is one of the effective control methods, in which the system has less complexity and requires no external power. There are numerous works on passive control of vortex shedding. Control cylinder, splitter plate, control plates, wall confinement, cylinder surface modification (slots, wavy surface, etc.,) are such examples. Very few research work on control plate method, Zhou *et al.*[1] used control plate in the upstream of cylinder. Some of the researchers worked on splitter plate method, where the splitter plate is attached to the cylinder or placed away from the cylinder, Raghu Vamsee *et al.* [2] Jayavel and Tiwari [3]. Deepakkumar *et al.* [4], [5] and Deepakkumar and Jayavel [6] used local waviness technique for the case of wall confined cylinder. In a fin and tube heat exchanger, Deepakkumar and Jayavel [7] studied the wake heat transfer characteristics using combination of circular and elliptical tubes. This article is focussed mainly on control plate method of vortex shedding control with respective heat transfer characteristics from the unconfined cylinder. Hence, the literatures are collected related to the passive method of vortex shedding control. Due to space restriction, the detailed literatures related to passive methods are omitted here. From the previous literature, it is observed that the study on wake dynamics using control plate method has high potential scope on the fluid flow and heat transfer control. The detailed problem statement and solution methodology are discussed in section-2 and the results are discussed in section-3.

## 2. PROBLEM STATEMENT AND COMPUTATIONAL METHODOLOGY

The problem is taken in an unconfined cylinder, a two-dimensional unsteady laminar flow regime at Reynolds number 100 is considered for simulation. The possibilities of vortex shedding suppression and shedding control using two control plates located symmetrically with respect to cylinder centreline along the flow direction (Fig.1a) has been analysed for various locations of control plates. The locations of control plates are varied based on two parameters (Fig.1b). (i) the radial distance between the centroids of cylinder and control plate ($r_d$) , (ii) the angular location ($\theta$) is measured from rear stagnation point of the cylinder.

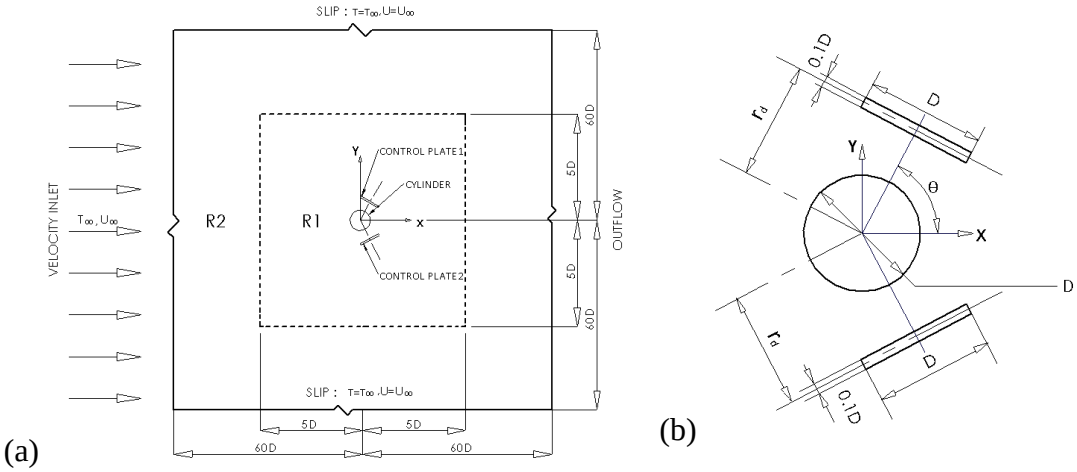


FIGURE 1. (a) Computational domain (b) details of control plates location (zoomed view)

At all locations, the control plates are positioned parallell to the tangent of the cylinder for the respective angle ($\theta$). The various angular locations ($\theta$) taken are $45^0$, $60^0$ ,$62.95^0$ ,$75^0$ and $90^0$, at each angular location, the radial distance ($r_d$) studied are 0.6D, 0.7D,0.8D ,0.9D and 1D. The various values of $\theta$ are considered based on targeting the interaction of the control plates near and around the flow separation region of the cylinder. Similarly, the $r_d$ is restricted to a maximum limit, $r_d$ = 1D, where far away location of control plates may not have significant influence on local flow control near to the cylinder. The width (w) of the control plate is taken equal to diameter of the cylinder. The thickness (t) of the control plate is 0.1 D, such that the streamlined flow around the control plate can be expected. In addition to identifying the flow characteristics due to control plates, the corresponding effect on heat transfer characteristics is also studied. For that, two cases of boundary conditions of control plates have been investigated. (i) Constant wall temperature boundary condition (CWTBC) (ii) Adiabatic boundary condition (ABC). In both cases, the cylinder is maintained at constant wall temperature boundary condition (CWTBC).

As the study is aimed on an undefined cylinder, an imaginary square computational domain of size 120Dx120D has been taken for assigning the boundary conditions of free stream fluid. The size 120Dx120D is chosen based on the work of Qu *et al.* [8]. In order to solve the continuity, momentum and energy equations the computational domain is discretized into finite number of control volumes using the grid generation code Ansys ICEMCFD. The computational domain is divided into two regions as shown in Fig. 1a. In Region-1 (R1), the gradients of pressure, velocity and temperature are high, hence fine control volumes are generated near and around the cylinder and control plates. Whereas, in Region-2 (R2), due to low gradients coarse control volumes are generated away from the cylinder. The unstructured control volume method is used for discretizing the computation domain due to the complex region between the cylinder and control plates.

The equations governing the incompressible flow with constant thermo-physical property in the computational domain can be represented by the dimensionless form of the Naviers - Stokes equations which are described as follows.

Continuity

$$\frac{\partial U}{\partial X}+\frac{\partial V}{\partial Y}=0 \qquad \text{---------- (1)}$$

X-momentum

$$\frac{\partial U}{\partial \tau}+\frac{\partial (UU)}{\partial X}+\frac{\partial (VU)}{\partial Y}=\frac{\partial P}{\partial X}+\frac{1}{\mathrm{Re}}\left(\frac{\partial^2 V}{\partial X^2}+\frac{\partial^2 V}{\partial Y^2}\right) \qquad \text{---------- (2)}$$

Y-momentum

$$\frac{\partial V}{\partial \tau}+\frac{\partial (UV)}{\partial X}+\frac{\partial (VV)}{\partial Y}=-\frac{\partial P}{\partial Y}+\frac{1}{\mathrm{Re}}\left(\frac{\partial^2 V}{\partial X^2}+\frac{\partial^2 V}{\partial Y^2}\right) \qquad \text{---------- (3)}$$

Energy equation

$$\frac{\partial \theta}{\partial \tau}+\frac{\partial (U\theta)}{\partial X}+\frac{\partial (V\theta)}{\partial Y}=\frac{1}{\mathrm{Re}\,\mathrm{Pr}}\left(\frac{\partial^2 \theta}{\partial X^2}+\frac{\partial^2 \theta}{\partial Y^2}\right) \qquad \text{---------- (4)}$$

Where,

$$U=\frac{u}{u_\infty},\quad V=\frac{v}{u_\infty},\quad \tau=\frac{tu_\infty}{D},\quad X=\frac{x}{D},\quad Y=\frac{y}{D},\quad P=\frac{p}{\rho u_\infty^2},\quad \theta=\frac{T-T_\infty}{T_W-T_\infty}$$

The code, ANSYS FLUENT is used for solving the governing equations with appropriate boundary conditions. The boundary conditions at inlet is assumed as uniform velocity U=1, V=0, $\frac{\partial P}{\partial X}=0$ and temperature θ=0, side boundaries are assumed as slip, $\frac{\partial U}{\partial Y}=0, V=0, \frac{\partial P}{\partial Y}=0$ and $\frac{\partial \theta}{\partial Y}=0$. At outlet, the outflow condition is used. The size of control volumes are chosen based on the grid independence study, the details are shown in Table 1. The parameters averaged drag coefficient ($C_D$) and Nusselt number (Nu) have been monitored for the grid independence results and validation of numerical methodology used in the present study. Based on the computational time and numerical accuracy the grid $G_3$ is taken as an optimum grid size. In validation (Table 2), the present results are closely matches with the work of Qu *et al.* [8] and Mahir and Altaç [9].

| Grid | | $G_1$ | $G_2$ | $G_3$ | $G_4$ |
|---|---|---|---|---|---|
| Maximum size of element (mm) | R1 | 5 | 2 | 1 | 0.4 |
| | R2 | 12 | 8 | 5 | 4 |
| Total elements | | 72149 | 158602 | 194422 | 453209 |
| $C_d$ (Mean) | | 1.586 | 1.513 | 1.422 | 1.44 |

TABLE 1. Details of grid independence study

| Parameter | Present work | Qu *et al.* [8] | Mahir and Altaç [9] |
|---|---|---|---|
| Cd | 1.32 | 1.317 | 1.368 |
| $Cl_{rms}$ | 0.2161 | 0.2226 | - |
| St | 0.164 | 0.1649 | 0.172 |
| Nu | 5.304 | - | 5.179 |

TABLE 2. Validation

## 3. RESULTS

The vortex shedding characteristics, drag coefficient ($C_D$), lift coefficient ($C_L$) and strouhal number and the average Nusselt number of the cylinder surface has been observed for various locations and two cases of thermal boundary conditions (CWTBC and ABC) of the control plates. In general, the cylinder heat transfer is more for adiabatic condition of control plates as compared to isothermal boundary condition, however the heat transfer is reduced as compared to cylinder without control plates. Figures 2a and 2b show the vortex shedding suppression case of θ = 90° and $r_d$ = 0.8D respectively for CWTBC and ABC. Even though the cylinders wake size is same for both the cases, the nearby hot region of control plate in CWTBC supress the heat transfer from the cylinder. The detailed results are not presented here due to space constraints.

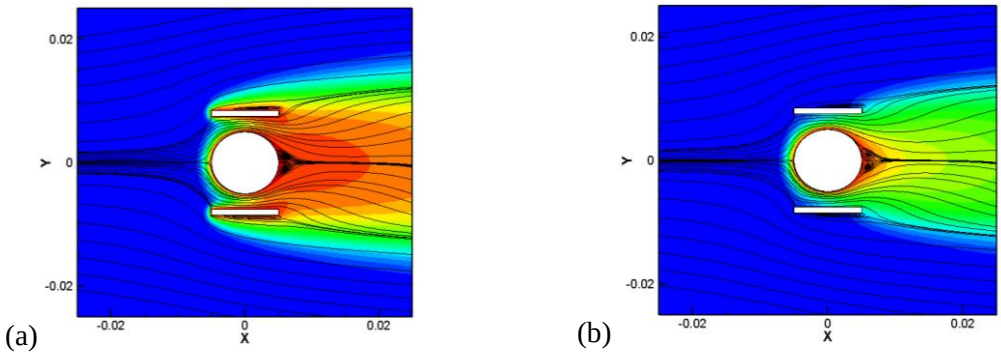


FIGURE 2. Streamline and temperature contour for θ = 90º and $r_d$ = 0.8D (a) CWTBC (b) ABC

## 4. CONCLUSIONS

Among all cases studied, suppression of shedding has been identified for the control plate location θ=90º, for all $r_d$ except $r_d$ = 0.6D and 0.7D. In all other angular locations, it fails to suppress the shedding due to the control plates acts as a bluff body, which induce the flow instability. This can be overcome by reorienting the control plate with the main flow direction. The suppression at θ=90º is due to the local deceleration of flow between cylinder and control plates delays the shedding, where the control plate act as streamlined body. The heat transfer enhancement can be expected by increasing the shedding frequency with proper location and orientation of the control plate.

## REFERENCES

[1] L. Zhou, M. Cheng and K.C. Hung, Suppression of fluid force on a square cylinder by flow control, *Journal of Fluids and Structures*, 21, 151-167, 2005.

[2] G.R. Vamsee, M. L. de Tena and Shaligram Tiwari, Effect of arrangement of inline splitter plate on flow past square cylinder, *Progress in Computational Fluid Dynamics*, 14, 277-294, 2014.

[3] S. Jayavel and Shaligram Tiwari, Effect of Vortex Generators and Integral Splitter Plate on Heat Transfer and Pressure Drop for Laminar Flow Past Channel-Confined Tube Banks *Heat Transfer Engineering*, 31, 383–394, 2010.

[4] R. Deepakkumar, S. Jayavel and Shaligram Tiwari, Cross Flow past Circular Cylinder with Waviness in Confining Walls near the Cylinder, *Journal of Applied Fluid Mechanics*, 10 (1), 183-197, 2017.

[5] R. Deepakkumar and S. Jayavel, Effect of local waviness in confining walls and its amplitude on vortex shedding control of the flow past a circular cylinder. *Ocean Engineering*, 156, 208-216, 2018.

[6] R. Deepakkumar, S. Jayavel and Shaligram Tiwari, A comparative study on effect of plain and wavy wall confinement on wake characteristics of flow past circular cylinder, *Sadhana - Academy Proceedings of Engineering Sciences*, 42 (6), 963-980, 2017.

[7] R. Deepakkumar and S. Jayavel, Air side performance of finned-tube heat exchanger with combination of circular and elliptical tubes. *Applied Thermal Engineering*, 119, 360-372, 2017.

[8] L. Qu, C.Norberg, L. Davidson, S. Huipeng, F. Wang, Quantitative numerical analysis of flow past a circular cylinder at Reynolds number between 50 and 200, *Journal of Fluids and Structures*, 39, 347-370, 2013.

[9] Necati Mahir, Zekeriya Altaç, Numerical investigation of convective heat transfer in unsteady flow past two cylinders in tandem arrangements, *International Journal of Heat and Fluid Flow* 29, 1309-1318, 2008.

# A New Interpolating MLS in MLPG Method for Heat Conduction Problem

**Rituraj Singh and Krishna Mohan Singh**

Department of Mechanical and Industrial Engineering

Indian Institute of Technology Roorkee

Roorlee-247667, India

Email: rituraj.7am@gmail.com

## ABSTRACT

A new interpolating MLS based interpolating MLPG method has been developed for steady state heat conduction problem in two dimension with Dirichlet and Neumann boundary conditions. In context of MLS approximation, a singular weight function is used in the interpolating MLS approximation. The interpolating MLS approximation possess Kronecker delta property which makes easy to impose essential boundary conditions. Three different test functions are tested, since the weight function of the interpolating MLS cannot be used as a test function in the interpolating MLPG method. The new method provides better accuracy, robustness and also saves computational time.

**Key Words:** *Heat Conduction, MLPG, Interpolating MLS*

## 1. INTRODUCTION

Meshfree methods have been well established for solving science and engineering problems [1]. MLPG method has become a popular choice among meshfree methods [2]. Moving least square (MLS) approximation is widely used in meshfree methods to generate meshfree trial functions. The MLS procedure is very complicated and it is computationally expensive as well. Imposition of Dirichlet boundary condition is a difficult task in the MLS based meshfree methods. Penalty approach is mostly used to impose essential boundary conditions (EBCs), which makes the method more complicated. Another way is to use direct interpolating method which is very easy. However, direct interpolation method is not able to exactly impose specified values on boundaries. A new interpolating moving least square approximation has been proposed which possess Kronecker delta property [3–5]. This makes it very easy to impose Dirichlet boundary condition in meshfree methods. Unlike in the MLS approximation, a singular weight function is used in the interpolating MLS approximation. It has been claimed that it improves the accuracy and computational efficiency. The moment matrix formed in the interpolating MLS is one order less than the moment matrix formed in the MLS approximation. Hence, it reduces the calculations and increases computational efficiency.

Objective of the present paper is to study the performance of the interpolating MLS approximation in MLPG method. Based on the interpolating MLS approximation an interpolating MLPG method has been developed. Three different test functions (cubic, $4^{th}$ order and Gaussian type) are used in conjunction with the interpolating MLPG method, as the singular weight function cannot be used as a test function. The interpolating MLPG method is applied to solve heat conduction problem in regular and irregular 2D domains with Dirichlet and Neumann boundary conditions. Results obtained by interpolating MLPG method are verified by analytical solution (in regular domain) and finite element solution (in irregular domain) and compared with MLS based MLPG method. Next section briefly describes MLPG formulation for the problem followed by results of numerical experiments and conclusions.

## 2. MLPG FORMULATION FOR HEAT CONDUCTION PROBLEM

Governing equation and boundary conditions for linear steady state heat conduction in 2D domain $\Omega$ bounded by the boundary $\Gamma$ are given by

$$\nabla^2 T + \frac{Q}{\kappa} = 0 \qquad \text{in } \Omega$$
$$T(\mathbf{x}) = \bar{T}(\mathbf{x}) \quad \text{for } \mathbf{x} \in \Gamma_1 \tag{1}$$
$$q(\mathbf{x}) = \bar{q}(\mathbf{x}) \quad \text{for } \mathbf{x} \in \Gamma_2$$

where $Q$ is volumetric heat generation per unit volume, $\kappa$ is thermal conductivity, $\bar{T}$ is the specified surface temperature, $\bar{q}$ is the specified heat flux, and $\Gamma_1 \cup \Gamma_2 = \Gamma$. In MLS based MLPG method, the weight function and test function are same. However, in interpolating MLPG method, the singular weight function is used in interpolating MLS approximation and a different function is used as the test function. Details regarding interpolating MLS approximation can be found in [5]. The specified values on Dirichlet boundary are placed in the final stiffness matrix for the interpolating MLPG method. Direct interpolation method is used in the MLPG method (with MLS approximation).

**Weight function**

In current work, singular weight function in the interpolating MLS is defined as [6]

$$w(\mathbf{x}, \mathbf{x_i}) = \begin{cases} d^{-\nu} & \text{if } 0 \le d \le 1 \\ 0 & \text{if } d > 1 \end{cases} \tag{2}$$

where $d = \dfrac{\|\mathbf{x} - \mathbf{x}_i\|}{r_s}$, $\nu$ is even positive integer and $r_s$ is radius of support domain.

**Test functions**

We have employed three test functions in the current work:

The cubic spline test function is defined as

$$v(\mathbf{x}, \mathbf{x_i}) = \begin{cases} \dfrac{2}{3} - 4d_i^2 + 4d_i^3 & \text{for } d_i \le \dfrac{1}{2} \\ \dfrac{4}{3} - 4d_i + 4d_i^2 - \dfrac{4}{3}d_i^3 & \text{for } \dfrac{1}{2} < d_i \le 1 \\ 0 & \text{for } d_i > 1 \end{cases} \tag{3}$$

The fourth order spline test function is defined as

$$v(\mathbf{x}, \mathbf{x_i}) = \begin{cases} 1 - 6d_i^2 + 8d_i^3 - 3d_i^4 & \text{if } 0 \le d_i \le 1 \\ 0 & \text{if } d_i > 1 \end{cases} \tag{4}$$

The Gaussian type test function is defined as

$$v(\mathbf{x}, \mathbf{x_i}) = \begin{cases} \exp\left[-\left(d_i / c_i\right)^{\gamma}\right] & 0 \le d_i \le 1 \\ 0 & d_i > 1 \end{cases} \tag{5}$$

where $c_i$ is the shape controlling factor, $d_i = \dfrac{\|\mathbf{x} - \mathbf{x}_i\|}{r_q}$, $\gamma$ is an even positive integer and $r_q$ is the radius of the local quadrature domain. BiCGSTAB solver with Jacobi preconditioner is used to solve linear system of algebraic equations. Tolerance is set equal to $10^{-8}$.

## 3. NUMERICAL EXPERIMENTS AND RESULTS

MLPG codes based on standard and interpolating MLS have been developed in C/C++. For MLPG analysis, radius of the local quadrature domain ($r_q$) is calculated by $r_q = \alpha_Q d_c$. where, $d_c$ is

characteristic distance and $\alpha_Q$ is dimensionless parameter for local domain (=0.9 in current work). The radius of the support domain is calculated by the method used in [7]. Number of nodes in the support domain (*ns*) is kept constant for every support domain. Relative percentage error is computed by $L_2$ norm. 64 gauss pints are used in quadrature domain for numerical integration. Thermal conductivity ($\kappa$) is assumed as 400 W/mK.

### 3.1 Heat conduction in 2D regular domian

The heat conduction equation is solved with unifrom grid in a unit square domian. 0º C temperature is maintained on the boundaries. Heat generation $Q$ is $10^6$ W/m$^3$. Analytical solution is taken from [8]. For quadratic basis, interpolaitng MLS provides good accuracy level for all three test functions. For linear basis only Gaussian test function works well for both approximation schemes (Table 1).

**Table 1: Relative % error for MLPG methods in 2D regular domain**

| | **Quadratic basis (*ns*=12)** | | | | | | **Linear basis (*ns*=8)** | | | | | |
|---|---|---|---|---|---|---|---|---|---|---|---|---|
| | **cubic** | | **4th order** | | **Gaussian** | | **cubic** | | **4th order** | | **Gaussian** | |
| $N\downarrow$ | IMLS | MLS | IMLS | MLS | IMLS | MLS | IMLS | MLS | IMLS | MLS | IMLS | MLS |
| $20^2$ | 0.31 | 0.48 | 0.17 | 0.33 | 0.80 | 0.36 | 47 | 19 | 40 | 8.7 | 0.23 | 1.2 |
| $75^2$ | 0.74 | 0.76 | 0.68 | 0.68 | 1.05 | 0.91 | 47 | 19 | 40 | 9.1 | 0.55 | 1.0 |
| $100^2$ | 1.0 | 1.0 | 0.92 | 0.93 | 1.22 | 1.21 | 47 | 19 | 40 | 9.1 | 0.73 | 1.15 |

### 3.2 Heat conduction in 2D comlpex shaped domian

The problem domain has been carved out of a square plate of 2m edge (Figure 1). At the centre, there is a circular hole of radius 0.5m. There are four one quarter circular hole of radius 0.5m at four corners [9]. Left edge and curved surfaces on the left side are maintained at 100º C and right edge and curved surfaces on the right side at 300º C. The periphery of centre hole is at 0º C. There is heat flow at bottom and top edge of magnitude $10^5$ W/m$^2$. The grid generated by ANSYS commercial software is imported in the MLPG codes. $d_c$ is equal to distance between computing node to the closest node.

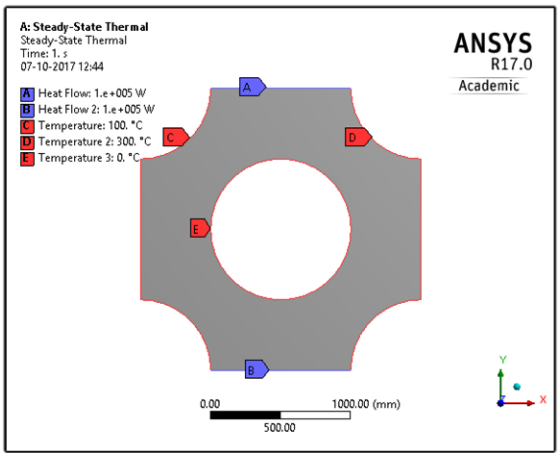


**Figure 1: Complex shaped domain**

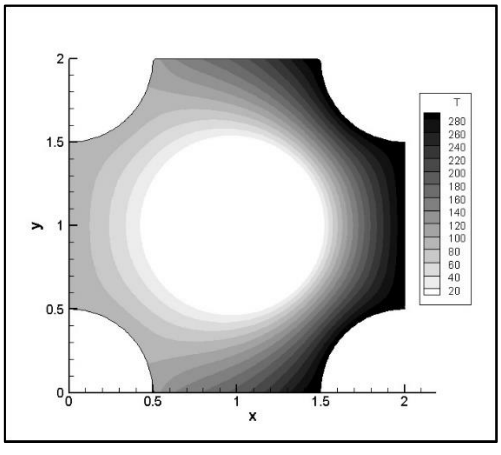


**Figure 2: MLPG solution**

Figure 2 depicts MLPG solution in 2D complex domain. Good match is found between MLPG and FE solutions. Cubic test function does not work well for quadratic and linear basis in 2D complex domain. However, Gaussian test function with optimum value of shape controlling factor is most appropriate among three chosen test functions (Table 2).

**Table 2: Relative % error for MLPG methods in 2D irregular domain**

| | **Quadratic basis (*ns*=12)** | | | | | | **Linear basis (*ns*=8)** | | | | | |
|---|---|---|---|---|---|---|---|---|---|---|---|---|
| | **cubic** | | **4th order** | | **Gaussian** | | **cubic** | | **4th order** | | **Gaussian** | |
| $N\downarrow$ | IMLS | MLS | IMLS | MLS | IMLS | MLS | IMLS | MLS | IMLS | MLS | IMLS | MLS |
| 290 | 9.3 | 9.5 | 0.52 | 1.44 | 0.45 | 0.43 | >10 | >5 | 0.56 | 1.6 | 0.56 | 1.33 |
| 6294 | 7.9 | 7.9 | 1.16 | 1.16 | 0.53 | 0.53 | >10 | >5 | 0.99 | 1.26 | 0.42 | 0.73 |
| 10899 | 7.8 | 7.8 | 1.35 | 1.34 | 0.69 | 0.69 | >10 | >5 | 1.15 | 1.5 | 0.5 | 0.84 |

## CONCLUSIONS

New interpolating MLPG method based on interpolating MLS approximation has been developed for steady state heat conduction problem. The method has been demostrated in 2D with different boundary conditions. Three diffreent test functions have been tested. It is found that all three test functions work well with quadratic basis in regular domain for both approximation. However, for linear basis only Gaussian test function works well for both approximations. In 2D complex domain, cubic test funciton does not work for quadratic and linear basis for both approximations. Gaussain test funciton seems to be more appropriate than other two test functions. Interpolating MLPG method is slightly faster than the MLS based MLPG method. Interpolating MLPG method has main advantage of easy implementing of EBCs as interpolating MLS has Kronecker delta property.

## REFERENCES


[1] T. Fries and H. Matthias, "Classification and overview of meshfree methods," *Dep. Math. Comput. Sci. Tech. Univ. Braunschweig*, 2004.

[2] J. Sladek, P. Stanak, Z.D. Han, V. Sladek, and S. N. Atluri, "Applications of the MLPG method in engineering & sciences: A review," *Comput. Model. Eng. Sci.*, 92, 423-475, 2013.

[3] R. Hong-ping, C. Yumin, and Z. Wu, "An improved boundary element-free method ( IBEFM )," 18, 4065–4073, 2009.

[4] R. Hongping, C. Yumin, and Z. Wu, "An interpolating boundary element-free method (IBEFM) for elasticity problems," *Sci. China Physics, Mech. Astron.*, 53, 758–766, 2010.

[5] H. Ren and Y. Cheng, "The interpolating element-free Galerkin (IEFG) method for two-dimensional elasticity problems," *Int. J. Appl. Mech.*, 3, 735-758, 2011.

[6] F.X. Sun, J.F. Wang, Y.M. Cheng, and A.X. Huang, "Error estimates for the interpolating moving least-squares method in n-dimensional space," *Appl. Numer. Math.*, 98, 79–105, 2015.

[7] M. Sterk and R. Trobec, "Meshless solution of a diffusion equation with parameter optimization and error analysis," *Eng. Anal. Bound. Elem.*, 32, 567-577, 2008.

[8] H.S.Carslaw. J.C.Jaeger, "Conduction of heat in solids", 2nd edition, Oxford University Press, 1959.

[9] X.Y. Gu, C.Y. Dong, T. Cheng, Y. Zhang, and Y. Bai, "The transient heat conduction MPM and GIMP applied to isotropic materials," *Eng. Anal. Bound. Elem.*, 66, 155–167, 2016.

Fifth International Conference on Computational Methods for Thermal Problems
THERMACOMP2018, July 9-11, 2018, Indian Institute of Science, Bangalore, INDIA
*N. Massarotti, P. Nithiarasu, Pradip Dutta and C. Ranganyakalu (Eds.)*

# A CONTACT CAPTURING FINITE VOLUME METHOD FOR INCOMPRESSIBILE TWO-PHASE FLOWS

**S Parameswaran, J C Mandal**
Department of Aerospace Engineering, IIT Bombay, Mumbai,
Email: j.c.mandal@gmail.com

## ABSTRACT

In this paper, a new Roe-type convective flux scheme is developed for incompressible two-phase flow equations in artificial compressibility formulation along with conservative level set method. In the present formulation the density is considered to be dependent on level set function. The efficacy of the proposed scheme is demonstrated through a Rayleigh Taylor instability test problem.

**Key Words:** *Conservative Level Set Method, Artificial Compressibility Method, Incompressible two-phase flows.*

## 1. INTRODUCTION

Capturing well resolved interface motion is crucial while simulating multiphase flow problems. Methods for solving multiphase flow problems can be broadly classified into front tracking and front capturing methods. Front capturing methods, such as, volume of fluid, level set method etc., uses an implicit function to represent the interface. This enables the front capturing methods to handle complicated interface evolution in a much easier way. In case of level set method [1], the fluid-fluid interface is represented as a predefined contour level of a smoothly varying function. Since the numerical diffusion is less affected in smooth regions, the interface will remain sharp during the course of simulation. Moreover, the smoothness also helps in accurate computation of interface curvature, which is essential for the correct estimation of surface tension forces.

In order to capture interface motion accurately, in the present work, a single system of equations is solved by combining artificial compressibility based Navier-Stokes equations and an interface advection equation in closely coupled manner. This ensures that the density field evolves along with the pressure and velocity fields at same instance of time. A conservative level set method [2] is used for advecting the interface for the following reasons. Firstly, this method has better mass conservation than the conventional level set method. Secondly, a unified finite volume framework can be used for both the system of governing equations and re-initialization equation. Finite volume framework will help in solving wide range of practical problems involving arbitrary shapes.

A novel Roe-type convective flux scheme is presented for two-phase flows, where density field is considered dependent on the level set function in the formulation of the scheme. Simplified expressions for the eigenvalues, eigenvectors and wave strengths to be used for computing the present Roe flux at the cell interfaces are reported here. With the new formulation, the present scheme is expected to have enhanced accuracy in estimating jump conditions across the shear and contact waves, which will help in accurate evolution of the material discontinuity. Several standard test problems are solved to evaluate the efficacy of the proposed scheme. However, for brevity, only one test case is reported here.

## 2. GOVERNING EQUATION AND FINITE VOLUME FORMULATION

The integral form of two dimensional unsteady Navier-Stokes equations in artificial compressibility framework with dual time stepping method can be written as,

$$\frac{\partial}{\partial \tau}\int_{\Omega} \mathbf{U}\, \mathrm{d}\Omega + I^t \frac{\partial}{\partial t}\int_{\Omega} \mathbf{U}\, \mathrm{d}\Omega + \oint_{\partial\Omega}\left[(\mathbf{F},\mathbf{G}).\mathbf{n} - (\mathbf{F}^v,\mathbf{G}^v).\mathbf{n}\right]\mathrm{d}l - \int_{\Omega}\mathbf{S}\, \mathrm{d}\Omega = 0, \text{ where,}$$

$$\mathbf{U} = \begin{Bmatrix} p/\beta \\ \rho u \\ \rho v \\ \psi \end{Bmatrix};\quad \mathbf{F} = \begin{Bmatrix} u \\ \rho u^2 + p \\ \rho uv \\ u\psi \end{Bmatrix};\quad \mathbf{G} = \begin{Bmatrix} v \\ \rho uv \\ \rho v^2 + p \\ v\psi \end{Bmatrix};\quad \mathbf{F}^v = \begin{Bmatrix} 0 \\ 2\mu\dfrac{\partial u}{\partial x} \\ \mu\left(\dfrac{\partial u}{\partial y} + \dfrac{\partial v}{\partial x}\right) \\ 0 \end{Bmatrix};\quad \mathbf{G}^v = \begin{Bmatrix} 0 \\ \mu\left(\dfrac{\partial u}{\partial y} + \dfrac{\partial v}{\partial x}\right) \\ 2\mu\dfrac{\partial v}{\partial y} \\ 0 \end{Bmatrix};\quad \mathbf{S} = \begin{Bmatrix} 0 \\ -\rho g_x \\ -\rho g_y \\ 0 \end{Bmatrix};$$

$$I^t = \begin{Bmatrix} 0 & 0 & 0 & 0 \\ 0 & 1 & 0 & 0 \\ 0 & 0 & 1 & 0 \\ 0 & 0 & 0 & 1 \end{Bmatrix};\quad \rho = \rho_2\psi + (1-\psi)\rho_1;\quad \mu = \mu_2\psi + (1-\psi)\mu_1$$

Here, $p$ is the pressure, $\rho$ is the density, $\beta$ is a constant artificial compressibility parameter, $u$ and $v$ are the velocity components along $x$ and $y$ directions respectively, $\mu$ is the dynamic viscosity, $g$ is the acceleration due to gravity, $\mathbf{n} = (n_x, n_y)$ is the outward facing normal vectors of the control volume $\Omega, \tau$ is the pseudo time and $t$ is the real time. In the above system of equations, the fourth equation for the advection of the level set function $\psi$, is added to model the two-phase flow (the contour $\psi = 0.5$ represents the interface). The density and viscosity used in the governing equations are functions of $\psi$ as shown in the above expressions. The suffixes "1" and "2" stands for dense and light fluids. Using a two dimensional cell centered finite volume method for discretizing space and a three-point implicit backward differencing method for discretizing real time derivatives, the above integral equation can be written in finite volume discretized form as,

$$\frac{\partial \overline{\mathbf{U}}_{ij}}{\partial \tau} + I^t\left[\frac{3\overline{\mathbf{U}}_{ij}^{n+1} - 4\overline{\mathbf{U}}_{ij}^{n} + \overline{\mathbf{U}}_{ij}^{n-1}}{2\Delta t}\right] + \frac{1}{\Omega_{ij}}\left[\sum_{m=1}^{4}\left[\mathbf{F}\, n_x + \mathbf{G}\, n_y\right]_m l_m - \sum_{m=1}^{4}\left[\mathbf{F}^{\mathrm{v}} n_x + \mathbf{G}^{\mathrm{v}} n_y\right]_m l_m\right] - \mathbf{S}_{ij} = 0$$

Here, $\overline{\mathbf{U}}_{ij}$ are the cell averaged values of $\mathbf{U}_{ij}$. For the above discretized equation, a three stage strong stability preserving Runge-Kutta method is used for approximating pseudo time derivatives. The source terms are computed using $g$ and cell centered density field. The velocity gradients used in the viscous fluxes are obtained using a second order accurate central differencing scheme. The convective fluxes are computed using the new Roe scheme.

The modified Roe flux at the cell interface can be written as, $\mathbf{F}_{\mathbf{n}}^{\mathrm{Roe}} = \frac{1}{2}(\mathbf{F}_{\mathbf{n}L} + \mathbf{F}_{\mathbf{n}R}) - \frac{1}{2}\sum_{\mathrm{k}=1}^{4}\tilde{\alpha}_k \mid \tilde{\lambda}^{(k)} \mid \tilde{K}^{(k)}$. Here, the flux normal to the cell interface $\mathbf{F}_{\mathbf{n}} = \mathbf{F}(T(\mathbf{U}))$, where $T$ is the matrix for rotating vectors from global to local co-ordinates at the cell interface aligned to the tangent and normal directions. The subscripts '*L*' (Left) and '*R*' (Right) represent the fluxes obtained by solution reconstruction from the interior and exterior side of the cell respectively. A weighted lease square based second order solution reconstruction scheme

[3] is used here for computing the left and right reconstructed data. Note that, after computing the fluxes one needs to rotate them back to the global co-ordinate frame before proceeding to the finite volume updation step. The eigenvalues $\tilde{\lambda}^{(k)}$ and the corresponding eigenvectors $\tilde{K}^{(k)}$ for the system of equations can be written as,

$$\tilde{\lambda}^{(1)} = \tilde{u}_n, \tilde{\lambda}^{(2)} = \tilde{u}_n, \tilde{\lambda}^{(3)} = \frac{\tilde{u}_n\left(\frac{\rho_1}{\tilde{\rho}}+1\right)+\sqrt{\tilde{u}_n\left(\frac{\rho_1}{\tilde{\rho}}+1\right)^2+4\frac{\beta}{\tilde{\rho}}}}{2}, \tilde{\lambda}^{(4)} = \frac{\tilde{u}_n\left(\frac{\rho_1}{\tilde{\rho}}+1\right)-\sqrt{\tilde{u}_n\left(\frac{\rho_1}{\tilde{\rho}}+1\right)^2+4\frac{\beta}{\tilde{\rho}}}}{2};$$

$$\tilde{K}^{(1)} = \begin{Bmatrix} 0 \\ (\rho_2-\rho_1)\tilde{u}_n \\ 0 \\ 1 \end{Bmatrix}, \tilde{K}^{(2)} = \begin{Bmatrix} 0 \\ 0 \\ 1 \\ 0 \end{Bmatrix}, \tilde{K}^{(3)} = \begin{Bmatrix} 1 \\ \frac{\tilde{\lambda}^{(3)}(\tilde{\lambda}^{(3)}\tilde{\rho}-\tilde{u}_n\rho_1)}{(\tilde{\lambda}^{(3)}-\tilde{u}_n)} \\ \frac{\tilde{\lambda}^{(3)}\tilde{\rho}\tilde{v}_n}{(\tilde{\lambda}^{(3)}-\tilde{u}_n)} \\ \frac{\tilde{\lambda}^{(3)}\tilde{\psi}}{(\tilde{\lambda}^{(3)}-\tilde{u}_n)} \end{Bmatrix}, \tilde{K}^{(4)} = \begin{Bmatrix} 1 \\ \frac{\tilde{\lambda}^{(4)}(\tilde{\lambda}^{(4)}\tilde{\rho}-\tilde{u}_n\rho_1)}{(\tilde{\lambda}^{(4)}-\tilde{u}_n)} \\ \frac{\tilde{\lambda}^{(4)}\tilde{\rho}\tilde{v}_n}{(\tilde{\lambda}^{(4)}-\tilde{u}_n)} \\ \frac{\tilde{\lambda}^{(4)}\tilde{\psi}}{(\tilde{\lambda}^{(4)}-\tilde{u}_n)} \end{Bmatrix};$$

and the wave strengths $\tilde{\alpha}_k$ are given as,

$$\tilde{\alpha}_1 = \Delta(\psi) - \tilde{\alpha}_3\left[\frac{\tilde{\lambda}^{(3)}\tilde{\psi}}{(\tilde{\lambda}^{(3)}-\tilde{u}_n)}\right] - \tilde{\alpha}_4\left[\frac{\tilde{\lambda}^{(4)}\tilde{\psi}}{(\tilde{\lambda}^{(4)}-\tilde{u}_n)}\right], \quad \tilde{\alpha}_2 = \Delta(\rho v_n) - \tilde{\alpha}_3\left[\frac{\tilde{\lambda}^{(3)}\tilde{\rho}\tilde{v}_n}{(\tilde{\lambda}^{(3)}-\tilde{u}_n)}\right] - \tilde{\alpha}_4\left[\frac{\tilde{\lambda}^{(4)}\tilde{\rho}\tilde{v}_n}{(\tilde{\lambda}^{(4)}-\tilde{u}_n)}\right],$$

$$\tilde{\alpha}_3 = \frac{1}{(\tilde{\lambda}^{(3)}-\tilde{\lambda}^{(4)})}\left[\frac{\Delta(\rho u_n)}{\tilde{\rho}} - \Delta\psi\tilde{u}_n\left(\frac{\rho_2-\rho_1}{\tilde{\rho}}\right) - \Delta P\tilde{\lambda}^{(4)}\right],$$

$$\tilde{\alpha}_4 = \frac{1}{(\tilde{\lambda}^{(4)}-\tilde{\lambda}^{(3)})}\left[\frac{\Delta(\rho u_n)}{\tilde{\rho}} - \Delta\psi\tilde{u}_n\left(\frac{\rho_2-\rho_1}{\tilde{\rho}}\right) - \Delta P\tilde{\lambda}^{(3)}\right].$$

In the above expressions $u_n = un_x + vn_y$ and $v_n = -un_y + vn_x$. The tilde symbol denotes that, they are obtained using Roe averaged state variables. The expression for the Roe averaged state variables are taken as per [4]. In the expressions for $\tilde{\alpha}_k$, the $\Delta$ symbol represents the difference between right states and left states of the variables.

## 3. RESULTS AND DISCUSSION

To demonstrate the efficacy of the proposed Roe-type convective flux scheme, a Rayleigh-Taylor instability test problem, reported in [5], is performed. The domain is discretized into 32 X 128 cells. The artificial compressibility parameter ($\beta$) is taken as 1000. The real time step ($\Delta t$) is taken as 0.01. The CFL number for the pseudo time step ($\Delta\tau$) is considered as 0.9. The $\psi = 0.5$ contours at various time levels for the present Roe scheme, the Roe scheme reported in [4] and a standard HLL scheme with fastest left and right waves as taken as $\min\{\tilde{\lambda}_L^{(4)}, \tilde{\lambda}_R^{(4)}\}$ and $\max\{\tilde{\lambda}_L^{(3)}, \tilde{\lambda}_R^{(3)}\}$ are shown in Figure (1). One can clearly observe that, for HLL scheme, due to its inability to capture contact waves, the interface evolves at a slower rate. Here the mushroom head becomes non-symmetric and get detached from the stem by t=1.2s. In case of the Roe scheme reported in [4], the mushroom head becomes conically shaped by t=0.9s and get detached from the stem by t=1.2s. However, in case of the present Roe scheme, a well developed, symmetric mushroom structure is

visible by t=0.9s and remain attached with the stem even at t=1.2s. The results from the present paper match very well with the trend reported by Puckett *et. al.* [5].

## 4. CONCLUSIONS

A new Roe-type convective flux scheme for a system of artificial compressibility based Navier-Stokes equations combined with conservative level set method is developed to solve two-phase flow problems in finite volume framework. The unique feature of the present formulation is that the density is considered to be dependent on level set function while developing the scheme. A Rayleigh Taylor instability problem is solved to study the accuracy of the proposed scheme. The results obtained for the present Roe scheme, Roe scheme reported in [4] and a standard HLL scheme are plotted and compared. It is observed that, the new Roe scheme helps in more accurate evolution of the material discontinuity.

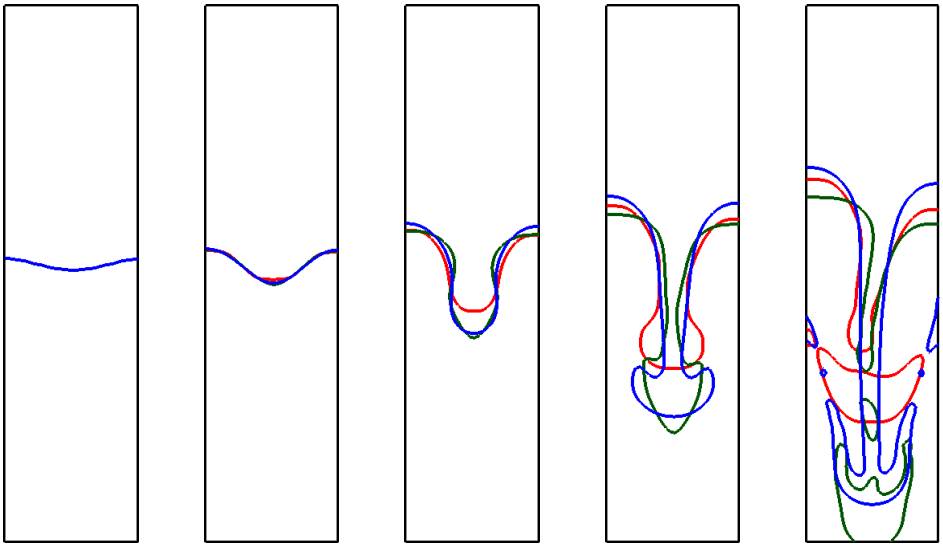

(a) t=0.0s (b) t=0.3s (c) t=0.6s (d) t=0.9s (e) t=1.2s

FIGURE 1. The $\psi = 0.5$ contours of Rayleigh-Taylor instability problem at various time levels for present Roe scheme (blue), the Roe scheme by Price and Cheng [4] (green) and HLL (red).

## REFERENCES

[1] Osher. S., and Sethian. J. A., Fronts propagating with curvature-dependent speed: Algorithms based on Hamilton-Jacobi formulations, *Journal of Computational Physics*, 79(1):12–49, 1988.

[2] Olsson. E., and Kreiss. G., A conservative level set method for two phase flow, *Journal of Computational Physics*, 210(1):225 – 246, 2005.

[3] Mandal. J. C., and Subramanian. J., On the link between weighted least-squares and limiters used in higher-order reconstructions for finite volume computations of hyperbolic equations, *Applied Numerical Mathematics*, 58(5):705 – 725, 2008.

[4] Price. W. G., Chen. Y. G., A simulation of free surface waves for incompressible two-phase flows using a curvilinear level set formulation, *International Journal for Numerical Methods in Fluids,* 51:305–30, 2006.

[5] Puckett. E. G., Almgren. A. S., Bell. J. B., Marcus. D. L., and Rider. W. J., A high- order projection method for tracking fluid interfaces in variable density incompressible flows, *Journal of Computational Physics*, 130(2):269 – 282, 1997.

Fifth International Conference on Computational Methods for Thermal Problems
THERMACOMP2018, July 9-11, 2018, Indian Institute of Science, Bangalore, INDIA
*N. Massarotti, P. Nithiarasu, Pradip Dutta and C. Ranganyakalu (Eds.)*

# NUMERICAL ANALYSIS AND OPTIMIZATION OF THERMO-HYDRAULIC PERFORMANCE IN TUBE PROVIDED WITH THIN WIRE RIB ROUGHNESS BY TAGUCHI APPROACH

**Vishal kumbhar[a] ,Sagar bhingare[b],Sanjay kadam[c],Suhas mohite[d],N.P.Gulhane[e],**

**Swapnil Gejage[f],Shubham Lidhade[g],Vinayak Jadhav[h]**

[b e g] Discipline of Mechanical Engineering,VJTI,Mumbai, 400019,India. [b] sagar.bhingare@ritindia.edu, [e] npgulhane@vjti.org.in

[a c f h] Department of mechanical Engineering,Rajarambapu Institute of Technology,Shivaji university,Sakharale,MS-415414,India. vishal.kumbhar06@gmail.com

## ABSTRACT

Presence of roughness element on the inside surface of tube enhance heat transfer and pressure drop. The present work deals with numerical investigation and optimization of thermo-hydraulic performance of artificially roughened tube. The roughness is provided in the form of thin wire ribs. The effect of geometrical parameters such as, rib angle of attack ($\alpha$ = 30°, 45°, 60°), rib height (e = 0.5mm, 1mm, 1.5mm), rib pitch (p = 50mm, 46mm, 40mm) and Reynolds number (Re = 6788, 9051, 11313) on thermo-hydraulic performance factor ($\eta$) is investigated using Taguchi approach. Nusselt number and pressure drop are considered as performance parameters to find out the thermo-hydraulic performance of artificially roughened tube. An orthogonal array of L9 ($3^4$) is considered as experimental plan. The goal of study is to obtain maximum Nusselt number and minimum pressure drop. Signal-to-noise ratios and contribution rations of each parameters is calculated. The results indicate that maximum thermo-hydraulic performance is obtain for $\alpha$ = 30°, e = 1 mm, p = 46 mm and Re = 9051

**Key Words:** *Roughness, Numerical Investigation, Optimization, Taguchi Approach, Thermo-hydraulic performance*

## 1. INTRODUCTION

The heat exchange between the two mediums is typically low due to formation of static boundary layer of fluid over the tube wall which offers higher convective resistance in the path of heat transfer. To overcome the aforesaid situation, several heat transfer enhancement techniques have been tested over the several years such as helical roughened tubes, dimpled tubes, grooved tubes, twisted tape, wire coil, circular ring. Principally all these methods are based on creation of disturbance near the wall that reduces the thermal barrier and thereby leads to higher heat transfer. As a result of the enhancement in heat transfer, the size of the heat exchange device is reduced to a large extent with the considerable improvement in its performance. Heat transfer enhancement using passive techniques was the subject of early interest. Many researchers tried to develop various correlations using different roughness and corrugations parameters.

Boelter et al. [1] in their experimental work collected data for heat transfer and pressure loss. They used strips soldered at certain angle to the flow direction in a duct. The pitch of metal strips was 25.4 mm, while height of strips as 3 mm and 10 mm respectively. They found that there was almost 200 % increase in heat transfer coefficient as compared to smooth duct with considerable increase in pressure drop. Heat transfer and frictional losses in tubes having roughness in the form of helical wire coil inserts was experimentally investigated by Sethumadhavan and Raja

Rao [2], they considered helical angles of 30°, 40°,55°, 60°, and 75° and found out that the maximum thermo-hydraulic performance was seen for helix angle of 55°. Pawan Singh Kathait, Anilkumar Patil [3] experimentally shown for roughened tubes the maximum value of thermos-hydraulic performance is obtained as 1.95 corresponding to roughened tube with pitch to height ratio 10 at Reynolds number of 7343. Pethkool et al. [4] they experimentally found that the maximum thermal performance factor is 2.33 obtained for pith ratio 0.27 and rib height ratio 0.06 also Nusselt number and friction factor are 3.10 and 2.14 times above the smooth pipe.

The Taguchi approach is one of the foremost optimization techniques which reduce overall time and experimental cost permits us to minimize the variation around the target when bringing the performance value close to target value. It also helps to determine the optimum values of the working conditions. Halit Bas and Veysel Ozceyhan [6] used Taguchi Approach in their investigation for heat transfer and pressure drop in tube assisted with twisted tape inserts. Optimum values for heat transfer and pressure drop were found to be at Reynolds number for 18,400 and 5200 respectively. Gunes et.al [7] using Taguchi approach investigated the optimum design parameters for tube with wire coil inserts. The optimum results were found to be s/D= 00357, P/D= 1, a/D= 0.0714 and Re= 19800. Taguchi approach was used by Sashin and Demir [8] in their study on rectangular channel provided with perforated pin fins, this method helped to minimize the overall cost and experimentation time. Optimum values of flow depth, fin pitch and fin thickness for heat exchanger fitted with corrugated fins were obtained using Taguchi technique by Qi [9]

Literature review shows that there are many heat transfer enhancements techniques. However little information is available regarding the determination of optimum values of roughness in the form of thin wire ribs orientated at different angle of attacks, pitch and height. The optimum values of roughness with rib height (e= 0.5mm, 1mm and 1.5mm), rib pitch (p= 50mm, 45mm and 40 mm), rib angle of attack (α= 30°, 45° and 60°) and Reynolds number (6788, 9051 and 11313) are determine for maximum Nusselt number and thermo-hydraulic performance factor and lower pressure drop using Taguchi method.

## 2. MAIN BODY

### 2.1 Numerical Analysis

All the numerical domains with length 1680 mm and diameter 28 mm of roughened tubes with are created in CATIA v5 modelling software. The numerical domains with (α=30°, 45°, 60° and e=1mm and p=50 mm) are shown in Figure 1.

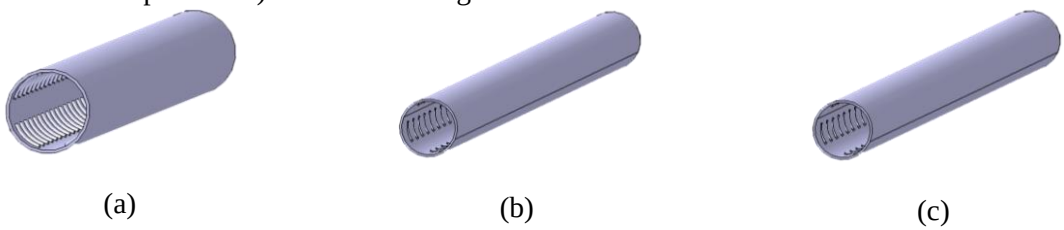

(a) (b) (c)

FIGURE 1. Numerical domain of roughened tube

The meshing of all the roughened tubes is carried out in ANSYS meshing module. Unstructured tetrahedral mesh is used to discretize all the roughened domains. Figure 2 shows the meshing of the roughened tube for 60° rib angle of attack. All the tubes were meshed in similar way. Grid independence was performed for the flow domain having rib angle of attack 30°, rib height of 1mm and rib pitch of 50mm. To obtain more accurate results the mesh near the wall of tubes and the ribbed surface is made finer. To predict the accuracy of the results obtained by simulation grids having different elements, with 863102, 1000591, 12, 49731 are used for grid independence test for Re = 9051. It was observed that there is not much change in Nusselt number for grids 1000591 and 1249731. Therefore, in order to save the computational time 1000591 grid system is considered for all the simulations. CFD code ANSYS Fluent is used to carry out all the numerical analysis for

different flow domains. The governing equations (1-6) used in numerical analysis are given as below:

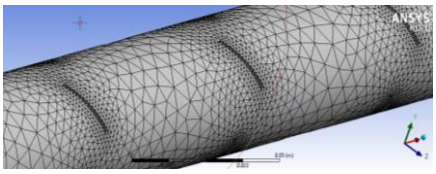

FIGURE 2. Mesh of tube with (α= 60°, e=1 mm and p= 50 mm)

Continuity Equations:

$$\frac{\partial \rho}{\partial t} + \frac{\partial(\rho u)}{\partial x} + \frac{\partial(\rho v)}{\partial y} + \frac{\partial(\rho w)}{\partial z} = 0 \quad (1)$$

Momentum Equations:

x- momentum: $$\frac{\partial(\rho u)}{\partial t} + \mathrm{div}(\rho u U) = -\frac{\partial \rho}{\partial x} + \frac{\partial_{Txx}}{\partial x} + \frac{\partial_{Tyx}}{\partial y} + \frac{\partial_{Tzx}}{\partial z} + F_x \quad (2)$$

y- momentum: $$\frac{\partial(\rho v)}{\partial t} + \mathrm{div}(\rho v U) = -\frac{\partial \rho}{\partial y} + \frac{\partial_{Txy}}{\partial x} + \frac{\partial_{Tyy}}{\partial y} + \frac{\partial_{Tzy}}{\partial z} + F_y \quad (3)$$

z- momentum: $$\frac{\partial(\rho w)}{\partial t} + \mathrm{div}(\rho w U) = -\frac{\partial \rho}{\partial z} + \frac{\partial_{Txz}}{\partial x} + \frac{\partial_{Tyz}}{\partial y} + \frac{\partial_{Tzz}}{\partial z} + F_z \quad (4)$$

Energy Equation:

$$\frac{\partial(\rho w)}{\partial t} + \mathrm{div}(\rho U T) = \mathrm{div}\left(\frac{\lambda}{C_p}\mathrm{grad}\ T\right) + S_T \quad (5)$$

The heat transfer coefficient is calculated by using the coupled method

$$tw|b = tf|b, -k\left(\frac{\partial t}{\partial \eta}\right) = ho(tw - tf) \quad (6)$$

Following assumptions are made for numerical analysis:

1. Steady-state is considered for all the numerical simulations.
2. All the thermo-physical properties of working fluid (water) assumed to be constant.
3. Heat loss to surrounding is negligible.

Present work deals with heat and fluid flow analysis through circular tube with constant wall temperature. The essential boundary conditions required for the analysis are for inlet, outlet and constant wall temperature.

### 2.2 Taguchi Method

Taguchi method consists of three design stages which are system, parameters and tolerance design. In present study the parameters design stage of Taguchi technique is used. The steps involve in Taguchi technique used in present study are as follows:

***Step 1: Identification of objective and selection of characteristics***

The objective of the present work is to determine the optimum values of design parameters in tube with thin wire rib roughness.There are 3 characteristics in Taguchi technique, higher is better, nominal is best and lower is better. In present study the first goal is to maximize the Nusselt number therefore it is higher the better. The second goal is to minimize the pressure drop hence it is lower the better problem. And finally maximize the thermo-hydraulic performance factor.

***Step 2: Selection of controllable and Noise factors and Orthogonal Array***

In present study the controllable factors are rib height (e), rib pitch (p), rib angle of attack (α) and Reynolds number (Re), while heat transfer and pressure drop are the noise factors. The controllable factor for present study is shown in Table 1. In present work, there are four factors with three levels. Hence there are 8 (4*2) degrees of freedom because of four deign parameters. In present work an orthogonal array of $L_9$ is chosen instead of $L_{27}$ to minimize the number of runs of simulation.

| Parameters | Levels | | |
|---|---|---|---|
| | 1 | 2 | 3 |
| A: Rib Height (e) | 0.5 | 1 | 1.5 |
| B: Rib Pitch (p) | 50 | 46 | 40 |
| C: Rib angle of attack (α) | 30 | 45 | 60 |
| D: Reynolds number (Re) | 6788 | 9051 | 11313 |

TABLE 1. Design parameters and their levels

***Step 3: Performing numerical simulation and analysis***

All the numerical simulations conducted as shown in experimental plan in Table 2. In present study the objective is to maximize the heat transfer or Nusselt number and minimize the pressure drop. And finally, the overall effect of heat transfer and pressure drop is taken into consideration to find the overall thermal and hydraulic performance of the use of roughened tube in terms of thermo-hydraulic performance factor suggested by Webb and Eckert [8]. Thermo-hydraulic performance is given by,

$$\eta = \frac{Nuc/Nus}{(fc/fs)^{1/3}} \quad (7)$$

| Parameters | | | | Nu | SNRA1 | ΔP | SNRA2 | η | SNRA3 |
|---|---|---|---|---|---|---|---|---|---|
| A | B | C | D | | | | | | |
| 1 | 1 | 1 | 1 | 63.18 | 36.012 | 90.57 | -39.139 | 0.978033 | -0.19293 |
| 1 | 2 | 2 | 2 | 90.62 | 39.144 | 172.6 | -44.740 | 1.181166 | 1.44622 |
| 1 | 3 | 3 | 3 | 111.64 | 40.957 | 369.65 | -51.355 | 1.154562 | 1.24834 |
| 2 | 1 | 2 | 3 | 100.10 | 40.008 | 274.69 | -48.776 | 1.09682 | 0.80271 |
| 2 | 2 | 3 | 1 | 78.67 | 37.916 | 136.63 | -42.710 | 1.010583 | 0.09144 |
| 2 | 3 | 1 | 2 | 108.55 | 40.713 | 259.56 | -48.284 | 1.268461 | 2.06554 |
| 3 | 1 | 3 | 2 | 94.58 | 39.516 | 226.34 | -47.095 | 1.021877 | 0.18798 |
| 3 | 2 | 1 | 3 | 119.62 | 41.556 | 346.65 | -50.797 | 1.139456 | 1.13395 |
| 3 | 3 | 2 | 1 | 81.55 | 38.229 | 81.5574 | -43.705 | 0.815633 | -1.77011 |

TABLE 2. Experimental plan for $L_9$ Orthogonal array and SNR values

## 3. RESULTS

The results obtained from numerical simulations are analysed in Minitab 15.0 software to determine the effect of roughness and flow parameters on heat transfer and pressure drop. Figure 3 (a) shows the effect of each roughness and flow parameter on Nusselt number. It can be observed that Nusselt number takes it maximum value at third level for parameter of rib height (e). As the height of wore increases it provides the better mixing of fluid neat to boundary layer which results in disturbance in laminar sub-layer. Also, Nusselt number is observed to be increase with decrease in pitch of roughness due to increase in turbulence intensity and increase in flow path. The maximum value of Nusselt numbers are observed for the rib angle of attack 60°. It is clear from the Figure 3 that the optimum values of parameters for maximum heat transfer are as follows: e= 1.5 mm, p=40 mm, α= 60° and Re= 11313. Hence $A_3B_3C_3D_3$ are the optimum conditions of roughness and flow parameters for maximum heat transfer according to "Larger is better" criteria for Nusselt number. The effect of roughness and flow parameters on pressure drop is shown in Figure 3 (b).

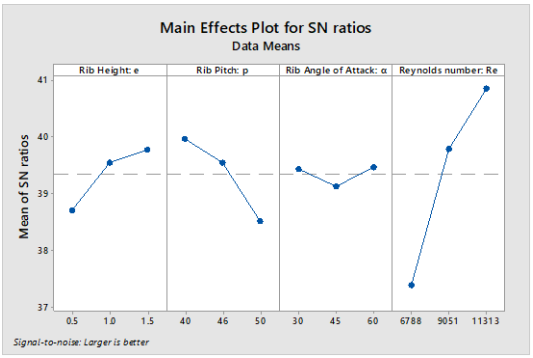


(a) Nu

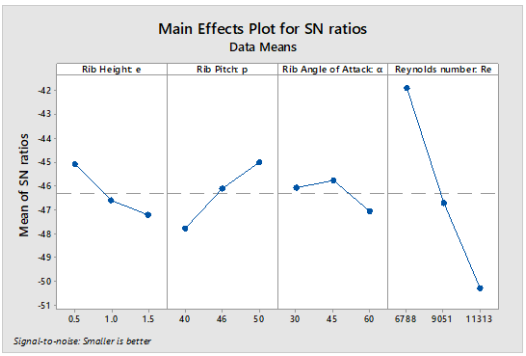


(b) ΔPD

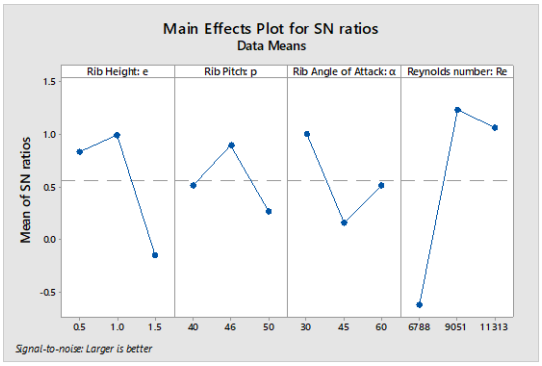


(c) η

FIGURE 3. Effect of individual roughness and flow parameters Nu, ΔPD and η

It is observed that the pressure drop decrease with decrease in rib height (e) this is due to since the height of rib increases the surface area increases and hence flow blockage increases with causes overall increase in pressure drop. Increase in pitch of roughness provides more pressure drop due to increase in turbulent intensity due to successive number of ribs placed closed to each other. The optimum values of parameters for minimum pressure drop are as follows: e= 0.5 mm, p=50 mm, α= 45° and Re= 6788. Hence $A_1B_1C_2D_1$ are the optimum conditions of roughness and flow parameters for minimum pressure drop according to "Smaller is better" criteria for pressure drop.

It is obvious that the heat transfer will increase with increase in values of roughness and flow parameters and pressure drop tends to decrease with decrease in values of roughness and flow parameters. However, it is necessary to analyse the combine effect of heat transfer and pressure drop which will provide the maximum thermo-hydraulic performance. Figure 3 (c) shows the effect of individual roughness and flow parameters on thermo-hydraulic performance factor (η).

It can be seen that the optimum values for thermo-hydraulic performance factor are e= 1 mm, p=46 mm, α= 30° and Re= 9051. Hence $A_2B_2C_1D_2$ are the optimum conditions of roughness and flow parameters for thermo-hydraulic performance according to "Higher is better" criteria for thermo-hydraulic performance factor.

The optimum conditions for heat transfer, pressure drop and thermo-hydraulic performance factor are predicted using 95% significance level as shown in Table 3. The confirmation tests are conducted at optimum conditions to check the predicted results.

| | | Parameters | | | | Nu | | ΔP | | η | |
|---|---|---|---|---|---|---|---|---|---|---|---|
| | | e | p | α | Re | Predicted | Real | Predicted | Real | Predicted | Real |
| Nu | Optimum Level | 3 | 3 | 3 | 3 | 123.70 | 125.24 | 453.79 | 455.43 | 1.001 | 0.985 |
| | Optimum value | 1.5 | 40 | 60 | 11313 | | | | | | |
| ΔP | Optimum Level | 1 | 1 | 2 | 1 | 70.80 | 72.31 | 121.79 | 124.16 | 0.955 | 0.9612 |
| | Optimum | 0.5 | 50 | 45 | 6788 | | | | | | |

| | | | | | | | | | | | |
|---|---|---|---|---|---|---|---|---|---|---|---|
| | value | | | | | | | | | | |
| η | Optimum Level | 2 | 2 | 1 | 2 | 94.41 | 96.14 | 149.89 | 152.41 | 1.11 | 1.091 |
| | Optimum value | 1 | 46 | 30 | 9051 | | | | | | |

TABLE 3. Optimum conditions and performance values for tested models

The contribution ratio of each parameters on Nusselt number, pressure drop and thermo-hydraulic performance factor is shown in Figure 4 (a-c). It can be seen that for Nusselt number the Reynolds number is the most effective parameters which contributes to overall heat transfer with 78%. Rib height (e) plays important role in pressure drop which is second most effective parameter with contribution ratio of 39%. The contribution ratio of e, p α and Re on thermo-hydraulic performance is 21.43%, 6.49%, 10.37% and 61.71% respectively.

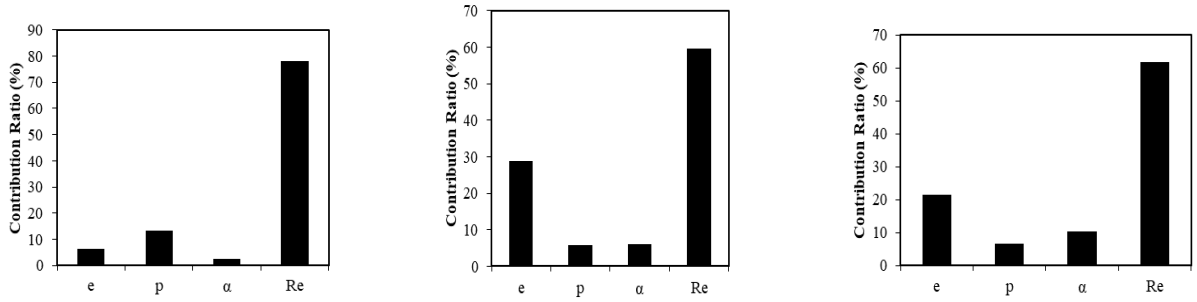


(Nu) (b) ΔPD (c) η

FIGURE 4. Contribution ratios of each parameters on Nu, ΔP and η

## 4. CONCLUSION

In present study the optimum values of roughness and flow parameters are determined using Taguchi technique for thermal and hydraulic performance for tube provided with roughness. The significant results of present work are summarized as follows:

1. Nusselt number is observed to increase with increase in roughness and flow parameters. The optimum values of parameters were obtained as e= 1.5 mm, p=40 mm, α= 60° and Re= 11313. And optimum condition of design parameters was $A_3B_3C_3D_3$.
2. Pressure drop decreases with decrease in rib height and rib pitch. The optimum values of parameters were obtained as e= 0.5 mm, p=50 mm, α= 45° and Re= 6788. Hence $A_1B_1C_2D_1$ are the optimum conditions of design parameters.
3. The optimum values of parameters for thermo-hydraulic performance factor are obtained as, e= 1 mm, p=46 mm, α= 30° and Re= 9051 with $A_2B_2C_1D_2$ as optimum design condition.
4. Amongst all the factors the Reynolds number is the most effective parameter contributing to overall thermal and hydraulic performance for roughened tube, while rib height is the second most effective parameters amongst the other.

## REFERENCES

[1] Dittus, F.W. and Boelter, L.M.K.,. Heat transfer in automobile radiators of the tubular type. *International Communications in Heat and Mass Transfer*, 12(1), pp.3-22, 1985.

[2] Sethumadhavan, R. and Rao, M.R., Turbulent flow friction and heat transfer characteristics of single-and multistart spirally enhanced tubes. *Journal of Heat Transfer*, 108(1), pp.55-61, 1986..

[3] Kathait, P.S. and Patil, A.K.,. Thermo-hydraulic performance of a heat exchanger tube with discrete corrugations. *Applied Thermal Engineering*, 66(1-2), pp.162-170, 2014.

[4] Pethkool, S., Eiamsa-Ard, S., Kwankaomeng, S. and Promvonge, P.,. Turbulent heat transfer enhancement in a heat exchanger using helically corrugated tube. *International Communications in Heat and Mass Transfer*, 38(3), pp.340-347, 2011.

[5] Chamoli, S.,. A Taguchi approach for optimization of flow and geometrical parameters in a rectangular channel roughened with V down perforated baffles. Case Studies in *Thermal Engineering, 5*, pp.59-69, 2015.

*[6]* Bas, H. and Ozceyhan, V.,. Optimization of parameters for heat transfer and pressure drop in a tube with twisted tape inserts by using Taguchi method. *Arabian Journal for Science and Engineering, 39(2), pp.1177-1186, 2014.*

[7] Gunes, S., Manay, E., Senyigit, E. and Ozceyhan, V.,. A Taguchi approach for optimization of design parameters in a tube with coiled wire inserts. *Applied thermal engineering*, 31(14-15), pp.2568-2577, 2011.

[8] Webb, R.L., Eckert, E.R.G. and Goldstein, R.,. Heat transfer and friction in tubes with repeated-rib roughness. *International Journal of Heat and Mass Transfer*, 14(4), pp.601-617, 1971.

Fifth International Conference on Computational Methods for Thermal Problems
THERMACOMP2018, July 9-11, 2018, Indian Institute of Science, Bangalore, INDIA
*N. Massarotti, P. Nithiarasu, Pradip Dutta and C. Ranganyakalu (Eds.)*

# COMPUTATIONAL MODELING OF A HIGH TEMPERATURE BLADED SOLAR RECEIVER WITH AIR AS THE HEAT TRANSFER FLUID

**Sagar Khivsara, Pradip Dutta**
Dept. Of Mechanical Engineering, Indian Institute of Science, Bangalore.
ksagar@iisc.ac.in, pradip@iisc.ac.in

**Jesus Ortega, Joshua Christian, Clifford Ho**
Sandia National Laboratories, Albuquerque, US.
jdorte@sandia.gov, jmchris@sandia.gov, ckho@sandia.gov

## ABSTRACT

Recent research has shown the potential advantages of using innovative light-trapping geometric features which are not used in conventional solar thermal tubular receivers. The studies have shown that a horizontal bladed receiver arrangement showed the best potential for increasing the effective solar absorptance by increasing the ratio of effective surface area to the aperture footprint. In this work, a detailed discussion of the Optical and Computational Fluid Dynamics (CFD) modeling of the horizontal bladed receiver developed under the Indo-US SERIIUS project is presented. Optical models using the heliostat field and the central tower facility at Sandia National Laboratories are developed to predict the actual flux map that is imposed on the receiver during on-sun testing. CFD modeling is used to predict the temperature distribution and the resulting receiver efficiencies. The simulated results using air as heat transfer fluid have also been validated experimentally. Brief details of the experimental procedure and experimental results will also be discussed where necessary for correlating with the computational models.

**Key Words:** *Solar Thermal Energy, Optical Modeling, Optical-CFD Coupling, Bladed Receiver*.

## 1. INTRODUCTION

Recent studies by the authors have involved investigation of geometric features for solar receivers which trap the radiation (incoming and emitted), resulting in increased receiver efficiencies. The analysis revealed that a horizontal bladed receiver provided the best light trapping effect, increasing the effective absorptance and reducing the radiative losses by reflection and emission. In this work, details of computational modeling of a bladed solar thermal receiver will be presented. The experiment which was performed will be discussed only briefly wherever necessary, so as to provide context of the computational model setup. The methodology developed by the authors in Ortega et. al. [1] has been used to perform the modeling in a coupled manner. The receiver model is subjected to the same process of preheating and test with flow as the on-sun tests and the heat flux input is computed by using the optical modelling methodology discussed by the authors in their previous publication [2].

## 2. GEOMETRY AND MODELING DETAILS

Optical and thermal-fluid modeling is discussed in this section in detail. The modeling was done using parameters from the optics of the heliostat field at the National Solar Thermal Test Facility (NSTTF) at Sandia National Laboratories and the air loop which was built for the on-sun experiments.

**Receiver Geometry:** The receiver design (Fig. 1) which was modeled (and tested) consists of 3 vertical panels (13 tubes per panel) at the back with 3 blades aligned at an angle of 50 degrees to the vertical. Each blade consists of two panels (9 tubes per panel). Each tube has an outer diameter of 12.7 mm and a thickness of 1.65 mm. The structural integrity of this size of tube has been discussed in detail in Ortega et al. [3]. The flow path used in the models as well as experiments is also shown in figure 1. It can be clearly seen from this figure that there are 3 distinct and similar flow paths to cool the receiver, each flow path starts with entry of fluid from the left side of the front bladed header, followed by recirculation in the bladed panel towards the back and the fluid finally entering the back panel through bottom and exit at the top.

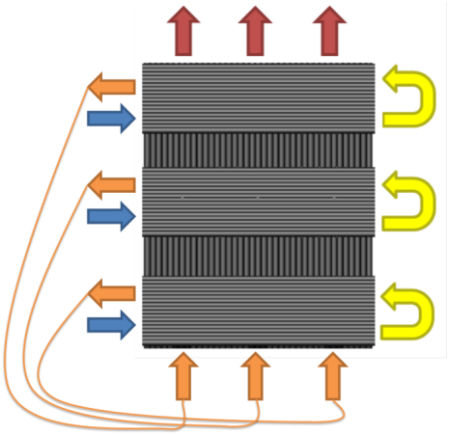

FIGURE 1. Bladed receiver design with flow path

The header was not modeled in the detailed CFD models, but the flow distribution, pressure drop, and heat transfer coefficient through the header were modeled separately to ensure that the flow distribution amongst the tubes is uniform.

**Optical Modeling:** To obtain the heat flux to be used for the thermal-fluid modeling, SolTrace, a ray-tracing based optical modeling software developed by NREL was used. The heliostat field at NSTTF was modeled in SolTrace and the receiver geometry created in Solidworks was imported in SolTrace. The typical ray intersections in SolTrace is shown in figure 2 (a).

The results obtained in SolTrace were coupled with ANSYS Fluent using a MATLAB code that generates a file which can be used as a boundary condition in ANSYS Fluent as described by Ortega et al. [1]. The preheating heat flux profiles were generated using 8-10 heliostats, while the operating heat flux profiles were obtained using 10-16 heliostats from the SolTrace model of the NSTTF for three flux levels 90, 120, 150 suns.

**CFD Modeling:** ANSYS Fluent was used for detailed investigation of the thermal fluid performance of the receiver. The CFD modeling is performed for two parts, preheating without flow and heating with air flow (with a relatively higher heat flux compared to preheating). After the preheated temperature profile is obtained, the full power heat flux profile is imposed on the receiver and air flow with receiver heating is simulated for 900 seconds, which is close to the actual on-sun heating with flow test time. Three different power levels were simulated, as in the on-sun tests, corresponding to peak fluxes of 90, 120 and 150 suns. The power imposed on the receiver surface during the 900 seconds of flow time was approximately 23 kW, 32 kW and 43 kW for the three cases, respectively. Figure 2 (b) below shows some of the important thermal boundary conditions imposed on the receiver.

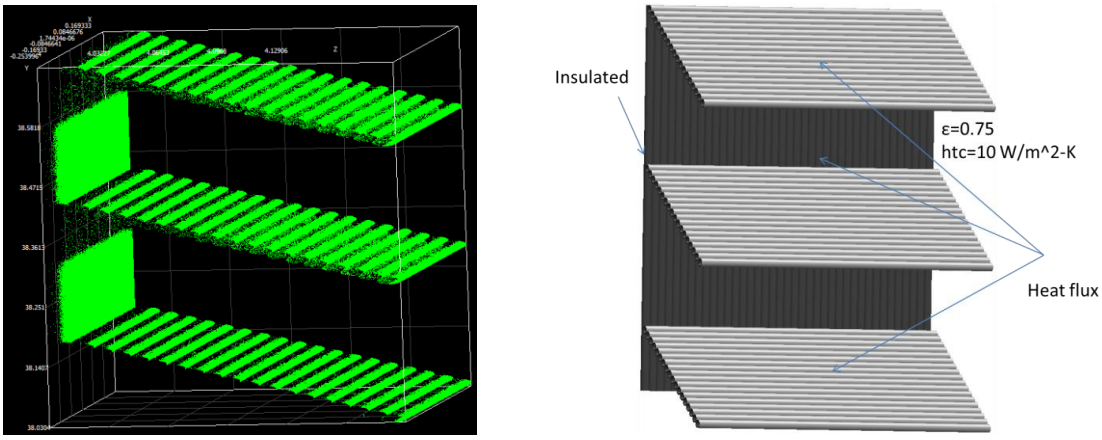


(a) (b)

FIGURE 2. (a) Typical ray intersections in SolTrace and (b) thermal boundary conditions in Fluent

The back side of the receiver was modeled as insulated and the convective and radiative heat loss was modeled using an emissivity of 0.75 and a convection heat transfer coefficient of 10 W/m$^2$-K. Recirculation boundary condition was used to connect the flow paths in the model without modeling the headers which exist in the actual receiver. Effect of gravity was considered along the axial direction of the vertical tubes. Mass flow rate of air through each flow path was 15 g/s and the pressure was slightly above atmospheric (~200 kPa). The thermo-physical properties of air, thermal conductivity, specific heat and density were modeled to take into account the variation of properties with temperature. The tube was modeled using Inconel 625 material properties and the tube thickness was modeled to evaluate the effect of conduction through the tubes. The heat flux profile was imposed as a boundary condition. Surface-to-Surface (S2S) radiation model was implemented in ANSYS Fluent to model the radiation heat exchange between tube surfaces, which can be significant due to the spatially varying temperature distribution. Turbulent flow inside the receiver tubes was modeled using the SST k-omega turbulence model with standard model constants. The SIMPLE scheme is used for the pressure-velocity coupling and second-order upwind is used for momentum and energy equation along with and first order implicit transient formulation. Standard relaxation factors from ANSYS Fluent were used and convergence for each time step was ascertained by monitoring the residuals so they dropped and remained constant. 15 monitors were setup to monitor the temperatures at 3 inlets, 3 outlets, 6 recirculation and 3 points on the receiver surface which had the thermocouples in the on-sun test.

## 3. RESULTS

Figure 3 (a) below shows a typical incident heat flux measured using the flux calibration panel adjacent to the receiver. The peak flux is about 160 suns. The same heliostat configuration used during the above measurement was simulated using SolTrace and the corresponding heat flux map from SolTrace is shown in figure 3 (b). The agreement between the simulated and measured heat flux was found satisfactory.

The receiver was subjected to three different power levels, 23 kW, 32 kW and 43 kW during subsequent tests. To achieve a higher operating temperature of the receiver, even with the low power levels and small test times due to the limitation on amount of heat transfer fluid in the bottles, the receiver was preheated slowly using few heliostats (for a duration of about an hour). Figure 4 (a) below shows a typical preheating temperature variation as measured by the thermocouple at the back of the panels during the experiment. The three plots are for three different back panels and they all overlap. The same was simulated during preheat of the modelled receiver. The flux and variation of temperature was found to be similar for the three panels.

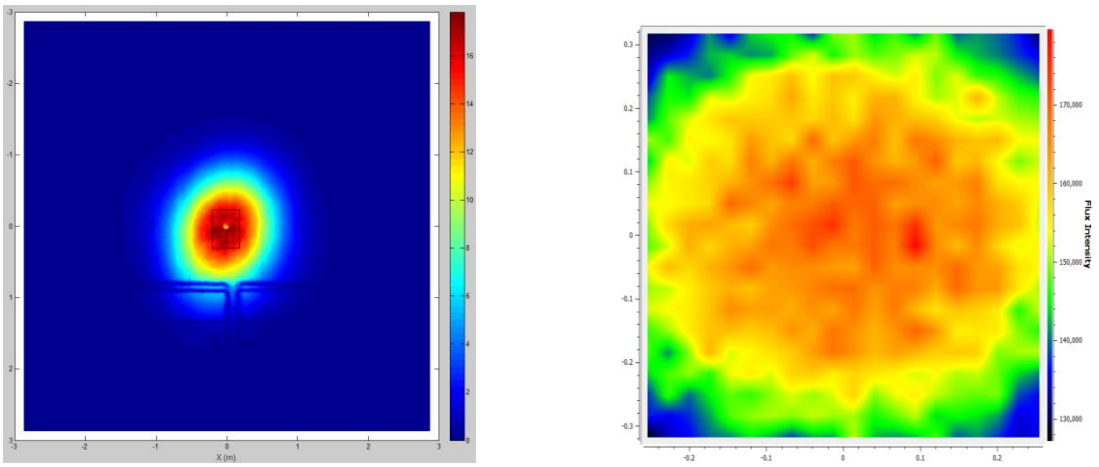

(a) (b)

FIGURE 3: Heat flux distribution with a peak flux of about 160 suns, (a) Measured, (b) Simulated

Similar to the thermocouples in experimental setup, 15 temperature monitors were setup in the CFD model to monitor the 3 inlets, 3 outlets, 6 recirculation points and 3 points on the receiver surface which had the thermocouples in the actual receiver test. Figure 4 (b) shows the temperature contour of bladed receiver for the 150 suns case at the end of 900 seconds of flow time.

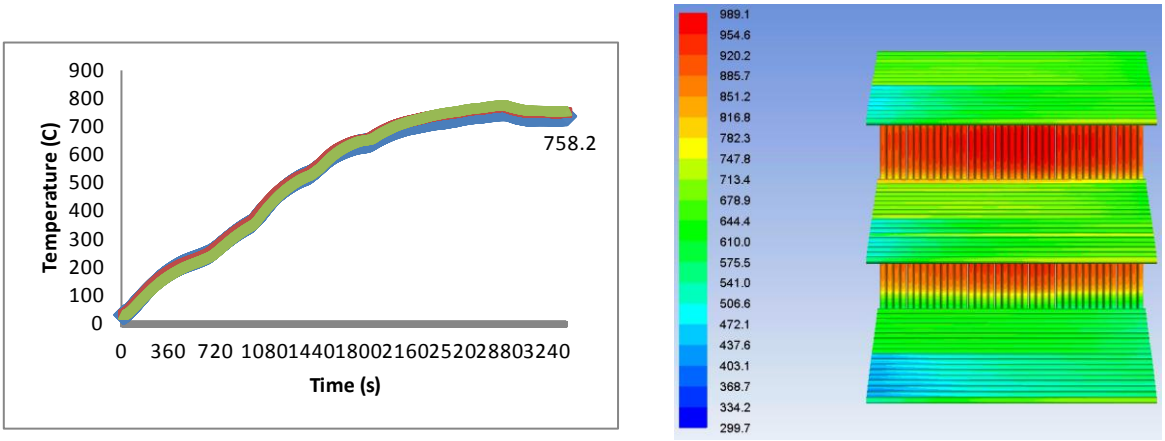


(a) (b)

FIGURE 4: (a) Temperature variation during preheat and (b) Temperature contours of bladed receiver for the 150 suns case after 900 seconds of flow time.

For the simulation, because of the nature of the recirculation boundary conditions, initially there is no fluid motion at all inside the domain during the preheating. However, as soon as the fluid flow simulation starts, a mass flow rate is imposed at the inlet. The numerical method takes time to establish the flow in the domain and hence, for the first few seconds, the preheating results in high tube temperatures (owing to no cooling due to no flow) losing heat to relatively colder fluid packets. Hence the efficiency trend is increasing initially and then stabilizes by going down. Figures 5 (a), (b) and (c) below show the transient thermal efficiency simulated during heating with flow for different power levels (and different peak concentrations) of imposed irradiation.

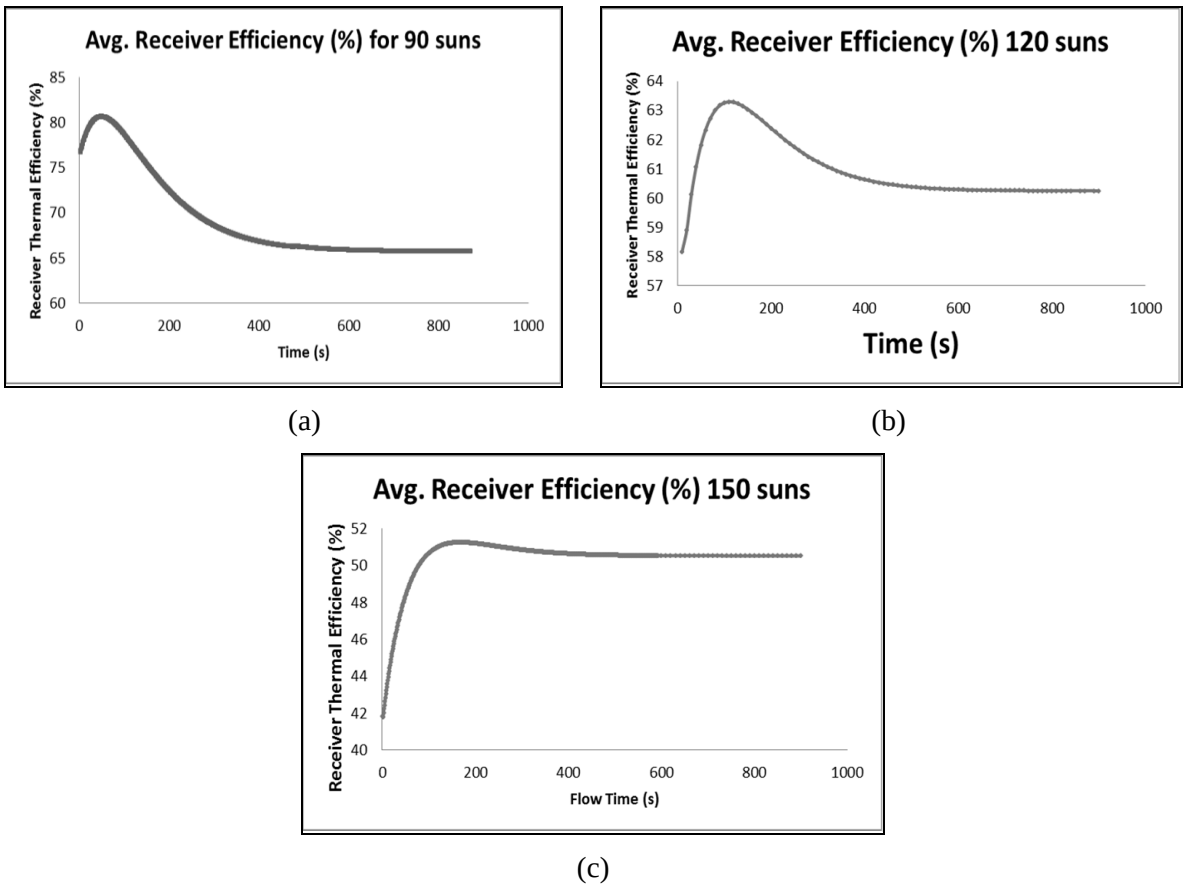


FIGURE 5: Transient thermal efficiency for different incoming power levels/peak concentrations

## 4. CONCLUSIONS

Coupled optical/thermal/fluid computational modeling of a horizontal bladed receiver is discussed in detail. The optical modeling is performed using the exact optical parameters of the heliostat field at the National Solar Thermal Test Facility (NSTTF) at Sandia National Laboratories. The receiver boundary conditions are prescribed to simulate the conditions which occur during on-sun testing which was recently performed at the solar tower at NSTTF. The flux profiles, transient temperature profiles and predicted efficiency using air as the heat transfer fluid is presented for three different power levels imposed on the receiver and the simulated results were found to match satisfactorily with the results from the experiment.

## REFERENCES

[1] Ortega, J., Khivsara, S., Christian, J., Ho, C., Yellowhair, J., & Dutta, P. (2016). Coupled modeling of a directly heated tubular solar receiver for supercritical carbon dioxide Brayton cycle: Optical and thermal-fluid evaluation. *Applied Thermal Engineering*, 109, 970-978.

[2] Ortega, J. D., Khivsara, S. D., Christian, J. M., Yellowhair, J. E., & Ho, C. K. (2015, June). Coupled optical-thermal-fluid modeling of a directly heated tubular solar receiver for supercritical CO2 Brayton cycle. *In Proceedings of the 9th International Conference on Energy Sustainability (ES2015)*, San Diego, CA, June 28th–July 2nd.

[3] Ortega, J., Khivsara, S., Christian, J., Ho, C., & Dutta, P. (2016). Coupled modeling of a directly heated tubular solar receiver for supercritical carbon dioxide Brayton cycle: Structural and creep-fatigue evaluation. *Applied Thermal Engineering*, 109, 979-987.

# AN AXISYMMETRIC COMPACT FINITE DIFFERENCE LATTICE BOLTZMANN METHOD FOR BLOOD FLOW SIMULATIONS

**M. Sakthivel and Kameswararao Anupindi**
Department of Mechanical Engineering, Indian Institute of Technology Madras, Chennai, Tamilnadu-600 036, India, kanupindi@iitm.ac.in.

## ABSTRACT

An axisymmetric lattice Boltzmann method with compact finite difference discretization is proposed and implemented to study the behaviour of the blood flow through lumen. Fourth order accurate finite difference schemes are used to discretize the discrete lattice Boltzmann equations. The solver is validated by simulating the steady flow through an axisymmetrically stenosed lumen with stenosis severities of 50% and 75%. The results show a good agreement with the data from the literature. Thereafter steady flow through an aneurysm with different width to height ratio is studied. In future the present solver will be extended to incorporate pulsatile inlet conditions as well as the ability to handle non-Newtonian fluids.

**Key Words:** *Axisymmetric, lattice Boltzmann method (LBM), blood flow, stenosis, aneurysm, compact schemes.*

## 1. INTRODUCTION

Cardiovascular diseases like aneurysm, an enlargement of the blood vessel and atherosclerosis, a local blockage in the large arteries can lead to severe health risk. The important aspect of numerical simulation of blood rheology is to predict the growth rate of the aneurysm or stenosis for diagnosis [1, 2]. Lattice Boltzmann Method (LBM) is an alternate and promising tool for simulating fluid flow and to study the physics of fluids. The key idea behind LBM is that the macroscopic dynamics of the fluid are a result of the behaviour of the group of many particles in the mesoscopic scale [3]. The standard classical LBM, however is restricted to uniform Cartesian grids and it demands the symmetry of the lattice arrangement to recover the macroscopic equations through multi-scale expansion. The shortcomings with standard LBM can be overcome by the finite difference discretization of lattice Boltzmann equation. The finite difference LBM can handle curvilinear coordinates through proper grid transformations and non-uniform body fitted meshes. Also the implementation of boundary conditions in FDLBM is straight forward [4]. The axisymmetric flow behaviour can be achieved by introducing appropriate source terms such that the resulting LBE recovers the axisymmetric macroscopic equations [5]. In the present study compact schemes are adapted, thus the spatial derivative is discretized by the fourth order implicit central difference scheme and temporal derivative term is discretized by the fourth order Runge-Kutta scheme. A sixth order low pass filter is used to damp the higher frequency errors in the solution arising because of the higher order central schemes.

## 2. AN AXISYMMETRIC LATTICE BOLTZMANN METHOD

Axisymmetric lattice Boltzmann equations with discrete axisymmetric source term is given by,

$$\frac{\partial f_\alpha(x,t)}{\partial t} + e_\alpha \cdot \nabla f_\alpha(x,t) = \frac{-1}{\tau}\left[f_\alpha(x,t) - f_\alpha^{eq}(x,t)\right] + h_\alpha\left(x + e_\alpha \delta t/2, t + \delta t/2\right) \quad (1)$$

where α denotes the number of the lattice direction which depends on the lattice type, for the D2Q9 model α = 0, 1, 2..., 8, $\mathbf{e}_\alpha$ is the lattice velocity in the α direction, $f_\alpha(\mathbf{x},t)$ is the particle distribution

function that dictates the probability of finding a particle with a velocity $\mathbf{e}_\alpha$ at a location $\mathbf{x}$=(z,r) at a particular time instant t in a particular lattice direction α, τ is the relaxation time taken by the non-equilibrium part of the particles to reach the equilibrium state represented in the equation as $f_\alpha^{eq}(\mathbf{x},t)$ [5].

The pressure based equilibrium distribution function in the incompressible flow limit is given as [4],

$$f_\alpha^{eq} = w_\alpha \left[ p + p_0 \left( \frac{e_\alpha \cdot u}{c_s^2} + \frac{(e_\alpha \cdot u)^2}{2c_s^4} - \frac{u \cdot u}{2c_s^2} \right) \right] \tag{2}$$

where $p=\rho c_s^2$, $p_0=\rho_0 c_s^2$ and $w_\alpha$ is the weighting factor. The discrete fractional source terms can be derived by Chapman-Enskog expansion of Eq 4 with a small parameter called Knudsen number, ε with atleast order of ε . After the derivation the source terms takes the form of [5],

$$h_\alpha = c_s^2 w_\alpha \left[ \theta + \frac{1}{c_s^2} \left( e_{\alpha z} H_z + e_{\alpha r} H_r \right) \right] \tag{3}$$

where,

$$\theta = -r^{-1}\rho u_r \quad , \quad H_z = r^{-1}\mu\left(\partial_r u_z + \partial_z u_r\right) - r^{-1}\rho u_r u_z \quad , \quad H_r = 2\mu r^{-1}\left(\partial_r u_r + r^{-1}u_r\right) - r^{-1}\rho u_r^2$$

The macroscopic pressure and velocity can be obtained by taking the zeroth and first moment of the local distribution function respectively [4],

$$p(x,t) = \sum_\alpha f_\alpha(x,t) \qquad p_0 u(x,t) = \sum_\alpha e_\alpha f_\alpha(x,t)$$

.

## 4. RESULTS

**Validation:** An important test case to validate the present CFDLBM model is the steady flow through a stenosed lumen which involves radial velocity and recirculation. Denoting $r_0$ as the radius of the non-stenotic part, the geometry of the stenosis is given by [6],

$$r(z) = r_0 - \frac{\beta r_0 \left[1 + \cos\left(\pi x / S_0\right)\right]}{2}, 12 - S_0 < z < S_0$$

where $2S_0$ is the length of the stenotic part and β is the severity of the stenosis. First the simulation was carried out for Re=50 with a severity of 50%. The longer post stenotic section is chosen to avoid the effect of outlet boundary. Parabolic velocity profile with a central velocity of $u_0$ and average velocity of $U_0=u_0/2$ is imposed at the inlet. The fluid accelerates due to the constricted passage, reaches a peak velocity of 3.2 times the inlet central velocity. A recirculation is created because of the separation of fluid from the wall in between the axial locations of 0.8D-0.9D. Finally the fluid completely reattaches to the wall at an axial location of 5D from the centre of the stenosis. After this location the fluid shows a jet-like laminar behaviour. The simulation results showed a very good agreement with results of Lee (2006) et al. [6] as shown in Fig.1. Next a simulation was carried for Reynolds Number of Re=500 with the severity of 75% to compare with the results of Varghese (2007) et al. [1]. From the results obtained it is found that a recirculation zone is created immediately downstream of the throat and it extends upto an axial length of 6.1D. There is negligible amount of radial velocity after this location. The fluid flow is laminar throughout the

entire length of the lumen and there is no evidence of jet breakdown. The results showed good agreement with the results of the Varghese (2007) et al. [1] as shown in Fig. 2.

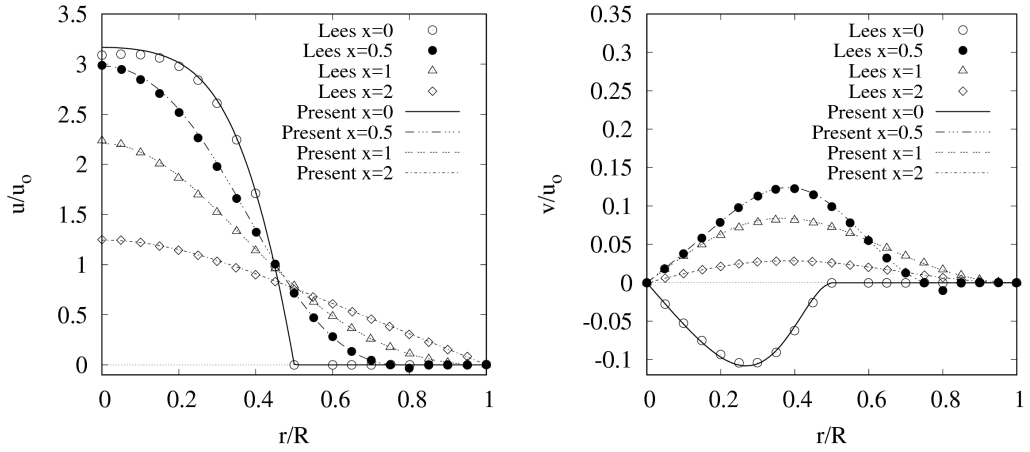


FIGURE 1. Velocity profiles at different axial locations for the stenosed lumen with severity, β=50%, for a Reynolds Number, Re=50.

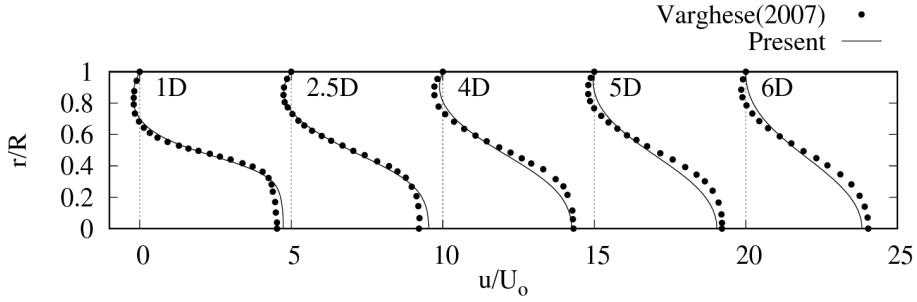


FIGURE 2. Axial velocity profiles at the different locations for the stenosed lumen with severity β=75% , for a Reynolds Number, Re=500.

These two test cases validate the present solver for the flow through an axisymmetrically constricted passage which involve radial velocity and recirculation regions.

**Simulation study:** Next the steady flow through an aneurysm is studied. The simulation is carried out for a steady flow through the blood vessel with an axisymmetric aneurysm of W=0.5 with Re=400 and Re=800 for various heights, H=0.3, H=0.5 and H=0.8. Denoting $r_0$ as the radius of the non-aneurysmal part, H as the height and W as the width, the geometry of the aneurysm is given by [2],

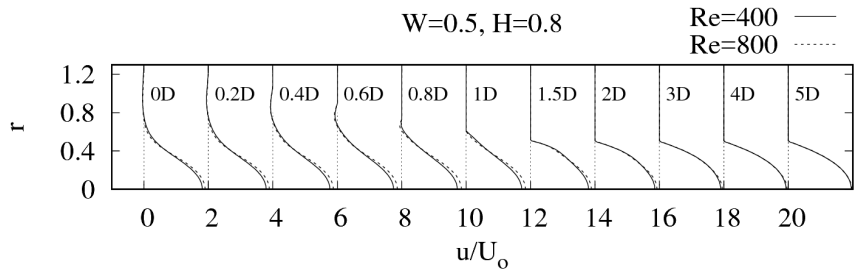


FIGURE 3. Axial velocity profiles at the different locations for the aneurysm for W=0.5, H=0.8 for different Reynolds Numbers, Re=400 and Re=800.

$$r(z) = r_0 + H \exp\left(\frac{-z^2}{2W^2}\right)$$

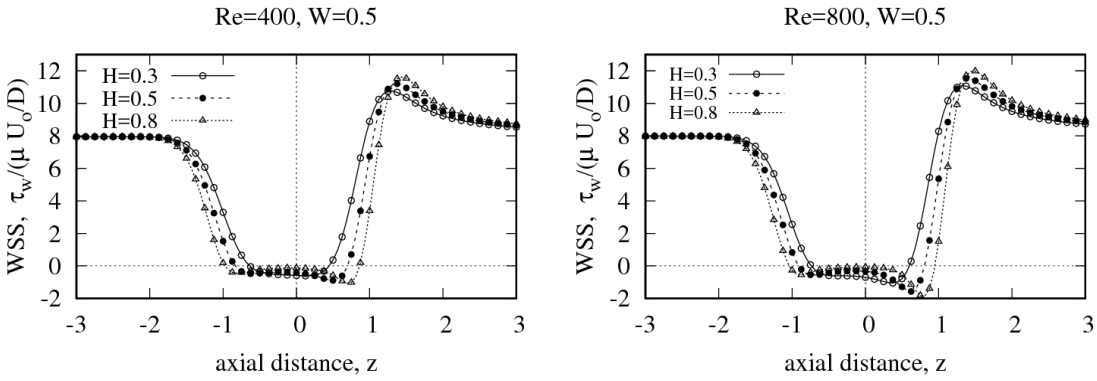


FIGURE 4.Wall shear stress distribution along the axial direction for different heights H=0.3,H=0.5 and H=0.8 for Re=400 and Re=800.

The velocity profiles at various axial locations of the aneurysm are shown in Fig. 3. The shear stress distribution along the wall of the aneurysm is shown in Fig. 4. The negative wall shear stress (WSS) indicates low velocity recirculation zone and from the figure it can be seen that as the Reynolds Number increases the recirculation zone shifts downstream and exerts a low WSS on the wall. These zones with lower shear stress are prone to expanding the aneurysm, which may lead to rupture.

## 5.CONCLUSIONS

A compact finite difference LBM with axisymmetric formulation is proposed and implemented on a D2Q9 lattice model in generalized curvilinear coordinates. The present solver is validated by simulating the steady Newtonian flow through a stenosis and and aneurysm. In future the present solver will be extended to incorporate pulsatile flow conditions as well as to handle the non-Newtonian fluids.

## REFERENCES

[1] Varghese SS, Frankel SH, Fischer PF. *Direct numerical simulation of stenotic flows. Part 1. Steady flow*. Journal of Fluid Mechanics 2007;582:281.

[2] Gopalakrishnan SS, Pier B, Biesheuvel a. *Global stability analysis of flow through a fusiform aneurysm: Steady flows*. Journal of Fluid Mechanics 2014;752:90–106..

[3] Chen S, Doolen GD. Lattice Boltzmann Method. Annual Review of Fluid Mechanics 1998;30(Kadanoff 1986):329–364..

[4] Hejranfar K, Saadat MH, Taheri S. *High-order weighted essentially nonoscillatory finite-difference formulation of the lattice boltzmann method in generalized curvilinear coordinates*. Physical Review E 2017;95(2):1–23.

[5] Srivastava S, Perlekar P, Boonkkamp JHMTT, Verma N, Toschi F. *Axisymmetric multiphase lattice Boltzmann method*. Physical Review E - Statistical, Nonlinear, and Soft Matter Physics 2013;88(1):1–14.

[6] Lee TS, Huang H, Shu C. *An Axisymmetric incompressible lattice Boltzmann model for pipe flow*. International Journal of Modern Physics C 2006;17(5):645–661.

Fifth International Conference on Computational Methods for Thermal Problems
THERMACOMP2018, July 9-11, 2018, IISC, Banglore, India
*N. Massarotti, P. Nithiarasu, Pradip Dutta and C. Ranganyakalu (Eds.)*

# A NOVEL PATIENT-ORIENTED NUMERICAL PROCEDURE FOR OCULAR DRAINAGE DEVICES

**Alessandro Mauro[1], Nicola Massarotti[1], Salahudeen M[1], Ignacio Rodríguez Uña[2], Mario R. Romano[3], Vito Romano[4,5]**

[1] Dipartimento di Ingegneria, Università degli Studi di Napoli "Parthenope", Isola C4, Centro Direzionale di Napoli, 80143 Napoli, Italy

[2] Fernández-Vega Ophthalmological Institute, Department of Ophthalmology, Glaucoma Unit, Príncipe de Vergara 131, 28002, Madrid, Spain

[3]Department of Biomedical Sciences, Humanitas University, Via A. Manzoni 113, 20089, Rozzano (Milano), Italy

[4]Department of Eye and Vision Science, Institute of Ageing and Chronic Disease, University of Liverpool, Liverpool, UK

[5]Moorfields Eye Hospital, London EC1V 2PD, UK

## ABSTRACT

A numerical investigation is presented to study heat and fluid flow inside Anterior Chamber (AC) of subject-specific human eyes, modelled with glaucoma drainage devices. The current three-dimensional eye model considers Anterior Chamber (AC), Trabecular Meshwork (TM), Schlemm's Canal (SC) and Collector Channels (CC), employing the Generalized Porous Medium (GPM) approach for modelling ocular porous tissue and cavities. The Intraocular Pressure (IOP) management inside AC of human eye is analyzed, by comparing the results obtained for four drainage devices implanted in a human eye for glaucoma treatment, i.e. ExPRESS® shunt, iStent® inject, Gold Micro Shunt® (GMS) and Silicon Shunt Device (SSD). The numerical result allows predicting the effects on heat and mass transport phenomena, i.e. Aqueous Humor (AH) drainage and IOP, deriving by the installation of these implants on human eyes of a specific patient.

**Keywords**: *Eye; Numerical modelling; glaucoma surgery; patient oriented*

## 1. INTRODUCTION

Glaucoma is a serious illness that affects human and other mammalian eyes, leading to a stage of total blindness. It is a major concern for ophthalmologists, as it is the second cause of eye vision loss after cataract. Treatment for glaucoma are targeted towards lowering IOP by means of various techniques like drug delivery techniques, laser surgery techniques, filtration surgery (such as trabeculectomy) and insertion of ocular drainage device techniques.

Insertion of Glaucoma Drainage Devices (GDD) is a surgical technique in which a non-physiological AH outflow is provided at the proximal region of conjunctiva, conventional AH outflow pathways and suprachoroidal space, in order to lower IOP. These techniques have proved to ensure prolonged efficacy for glaucoma treatment, but are basically invasive in nature. Despite the conventional surgical methods have achieved the objective of controlling IOP, the post-operative complications like hypotony, clogging of AH egress in the alternative AH outflow pathways are the major problem that motivates medical physicians for the improvisation of surgical methods. As a consequence, it is evident that there is an immense need to evaluate the possibilities of success of these invasive techniques before the surgery.

In this paper, numerical investigation of AH heat and fluid flow in the anterior section of the human eye, is carried out, taking into account the effects of porous tissues, i.e. TM, that is the main ocular

site responsible of AH outflow resistance. The patient oriented numerical procedure, developed by the authors, is used to predict the thermo-fluid dynamic phenomena in ocular tissues and cavities by implementation of GDD i.e. ExPRESS shunt, iStent inject, GMS and the novel SSD. GDD are modelled in the three-dimensional eye model to analyse their influence on IOP, velocity and heat transfer within the AC, providing a physical insight for the doctors, regarding the condition of the subject-specimen in pre-operative and post-operative cases.

## 2. MATHEMATICAL MODEL AND NUMERICAL METHODOLOGY

The laminar, incompressible AH flow and heat transfer is solved using the Generalized Porous Medium (GPM) model [1]. The flow and temperature fields are calculated taking into account also buoyancy effects, incorporated using the Boussinesq approximation, relating density differences to temperature differences among cornea, lens and iris, obtaining a mixed convection regime. The equations of the GPM model are the following:

Continuity equation:

$$\frac{1}{\varepsilon}\frac{\partial u_i}{\partial x_i} = 0 \tag{1}$$

Momentum equation:

$$\frac{\rho_f}{\varepsilon}\left[\frac{\partial u_i}{\partial t} + \frac{\partial}{\partial x_j}\left(\frac{u_i u_j}{\varepsilon}\right)\right] = -\frac{1}{\varepsilon}\frac{\partial}{\partial x_i}\left(p_f \varepsilon\right) + \frac{\mu_e}{\varepsilon}\frac{\partial^2 u_i}{\partial x_i^2} - \frac{\mu_f u_i}{\kappa} - \frac{1.75}{\sqrt{150}}\frac{\rho_f}{\sqrt{\kappa}}\frac{|\mathrm{V}|}{\varepsilon^{3/2}}u_i + \left(\rho_{ref} - \rho_f\right) g\gamma_i \tag{2}$$

Energy equation:

$$\left[\varepsilon\left(\rho c_p\right)_f - \left(1-\varepsilon\right)\left(\rho c_p\right)_s\right]\frac{\partial T}{\partial t} + \left(\rho c_p\right)_f u_i \frac{\partial T}{\partial x_i} = k\left(\frac{\partial^2 T}{\partial x_i^2}\right) \tag{3}$$

The present model is particularly useful to simulate glaucoma surgical techniques, because it allows reproducing, with the same set of equations (1-3), the flow within porous regions, drainage devices and ocular cavities. The numerical simulations are performed in an open-source finite volume solver OpenFOAM (Open Field Operation And Manipulation).

## 3. COMPUTATIONAL DOMAINS AND BOUNDARY CONDITIONS

Figure 1 shows the computational domain of human eye model. Since the extracted domain has only AC, cornea, lens and iris, the AH outflow pathways like Trabecular Meshwork (TM), Schlemm's Canal (SC), Collector Channels (CC) and also the stent implanted by the surgeon have to be modelled in the computational domain. AH is secreted by the ciliary body, and its inflow in the anterior section of the eye is reproduced in the model as an inlet between iris and lens. A nominal volumetric flow rate of 2.5 μL/min, is provided at the inlet section. Schlemm's Canal (SC) and Collector Channels (CC) are exposed to an episcleral venous pressure of 10.5 mm Hg. The outlet pressure of the stents is assigned on the basis of its location, depending on the surgical method. Lens, iris and cornea are assumed to be impermeable walls and no slip boundary conditions are imposed. The temperature of the outer surface of cornea is equal to 27°C, while lens and iris temperatures are equal to normal human body temperature of 37°C. The porous tissue, TM, needs to be properly characterized with appropriate permeability and porosity values, depending on the physiological condition of human eye. In addition, the porosity effect of ocular structure at the

outlet of suprachoroidal devices (SSD, GMS) is taken into account by imposing the permeability value equivalent to sclera.

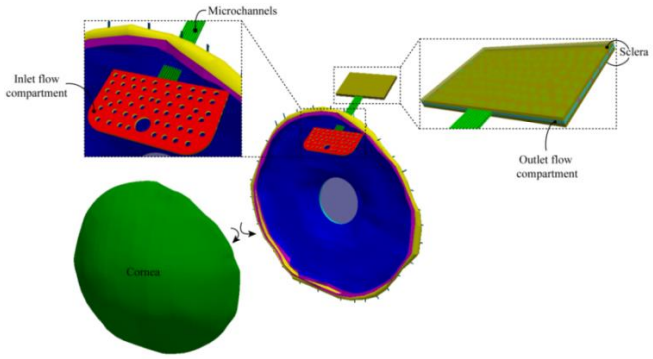


Figure 1. Computational domain of human eye model with SOLX®GMS.

## 4. RESULTS

In order to yield an unrestricted flow for the AH at the AC, a non-physiological outflow pathway is created using surgical methods, such as employment of stents. The ocular drainage devices, employed in this study, are virtually implanted in current human eye model based on its location along with TM. A reduction in IOP is observed at the AC of the eye model from the numerical analysis, after the implantation of stents, as shown in table 1.

| No. | Ocular devices implanted in human eye model | IOP inside AC (mmHg) |
|---|---|---|
| 1 | ExPRESS | 14.7 |
| 2 | iStent | 11.2 |
| 3 | GMS | 16.7 |
| 4 | SSD | 10.5 |

Table 1. IOP at AC of human eyes after implantation of different GDD.

A higher pressure drop with a flow resistance in the range of 0.708-0.710 mm Hg/ µl/min is obtained across the micro channels in GMS, while SSD has the lowest AH flow resistance. In GMS, AH enters through holes and openings of inlet flow compartment, encounters microchannels of high aspect ratio which induce a higher velocity in order to conserve the mass. In addition, the increase in AH velocity is accompanied by a higher flow resistance across the microchannels and, as a consequence, a higher pressure drop is observed. While, the smaller diameter of the primary opening along with orifices in the ExPRESS shunt induces a higher pressure drop with respect to iStent inject and SSD. The SSD has the lowest flow resistance compared to the other devices, thanks to its regular microtubular geometry. Moreover, the simplicity of design of SSD can ensure advantages in terms of flexibility in choosing different diameters [2]. Central and side lumens of iStent inject yield resistance for AH flow that amounts to 0.054-0.056 mmHg/µL/min [3]. The flow resistance across the GDD implanted in the human eye model affects the velocity at the AC as shown in Figure 2.

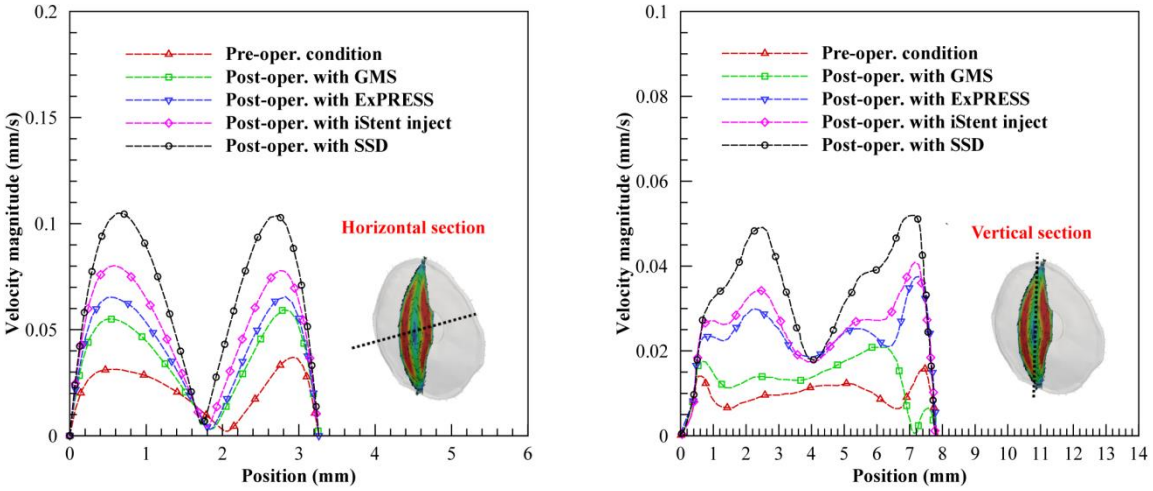


Figure 2. Velocity profiles of horizontal (left) and vertical (right) section of the human eye model in standing position for pre-operative and post-operative conditions.

## 5. CONCLUSIONS

The present paper presents a novel numerical procedure developed by the authors to reproduce the operation of glaucoma drainage devices surgically implanted in subject specific human eyes.

1. The present numerical procedure has allowed predicting the post-operative conditions of the patient: an IOP within the physiological limit (IOP<21mmHg) has been calculated in presence of virtual implantation of the four devices.
2. The three-dimensional thermo-fluid dynamic analysis carried out on the four stents implanted in the human eye model showed that the flow resistance across the stents is negligible as compared to Trabecular Meshwork (TM) resistance.
3. The variability of flow resistance across the devices affects thermo-fluid dynamic parameters and near wall quantities, such as friction coefficient and local Nusselt number at the anterior chamber of human eye model.

The authors think that this multidisciplinary approach may provide a valuable engineering support to medical doctors, providing them more useful information based on the specific patients, with consequent reduction of post-operative complications.

## ACKNOWLEDGMENTS

Alessandro Mauro gratefully acknowledges the local program of the University of Napoli "Parthenope" for the support to individual research.

## REFERENCES

[1] N. Massarotti, M. Ciccolella, G. Cortellessa, A. Mauro. New benchmark solutions for transient natural convection in partially porous annuli. *International Journal of Numerical Methods for Heat & Fluid Flow*, 26 (3-4), 1187-1225, 2016.

[2] A. Mauro, M. R. Romano, V. Romano, P. Nithiarasu. Suprachoroidal shunts for treatment of glaucoma: a comparison based on numerical simulations. *International Journal of Numerical Methods for Heat & Fluid Flow*. 2016. DOI 10.1108/HFF-12-2016-0508.

[3] Hunter, K.S., Fjieldal, T., Shandas, R., Kahook, M.Y. (2014) Characterization of micro-invasive trabecular bypass stents by ex vivo perfusion and computational flow modeling, *Clinical Ophthalmology* 2014; 8: 499–506.

Fifth International Conference on Computational Methods for Thermal Problems
THERMACOMP2018, July 9-11, 2018, Indian Institute of Science, Bangalore, INDIA
*N. Massarotti, P. Nithiarasu, Pradip Dutta and C. Ranganyakalu (Eds.)*

# Numerical analysis of heat transfer enhancement in microchannel with bioinspired surface

**Prasenjit Dey, Sandip K. Saha***
Mechanical Engineering Department, Indian Institute of Technology Bombay
Mumbai- 400076, India.
E-mail: sandip.saha@iitb.ac.in

## ABSTRACT

Numerical analysis is performed to study the influence of the bioinspired surfaces on the fluid flow and heat transfer in a microchannel. The layout of the bioinspired surface is encouraged by the fish scale geometry due to having structured micro roughness. Deionized water is selected as the working fluid, where the fluid flows through a copper microchannel of hydraulic diameter ($D_h$) of 187.5 μm with three Reynolds numbers as 250, 650 and 1050. Fish scale structures are created on the bottom surface of the channel, and a constant heat flux of 100 W/cm$^2$ is applied on the bottom surface. It is found that the bioinspired surface can enhance the convective heat transfer rate significantly compared to that of a plain channel by producing flow separation, disturbance and the vortexes in the mainstream.

**Key Words:** *Bioinspired Surface, Heat Transfer, Microchannel.*

## 1. INTRODUCTION

Rapid growth in microelectronics for delivering high performance, due to the advancement in nanotechnologies has raised severe thermal management issue. Researchers are developing various cooling technologies to dissipate high heat fluxes associated with these miniaturized electronic devices. In this context, cooling by microchannels are recognized to be one of the crucial research areas among the micro-fluidic systems because of its preeminent cooling characteristics in high power magnets, accelerator targets, material processing and manufacturing industries, advanced thermal management systems, and high computation operations in computers, etc. [1]. A very high heat transfer coefficient, which is required to remove heat quickly from a very high heat dissipating micro devices, can be achieved by using microchannel due to its higher heat transfer surface area to fluid volume ratio compared to other macroscale systems. Till date, numerous experimental and numerical studies of microchannel are accomplished since its introduction by Tuckerman and Peace [2]. Thermal boundary layer interruption, mixing between hot and cold fluids and flow separation are the potential approaches to augment the heat transfer rate in microscale [3].

Several innovative enhancement techniques were explored and reported by researchers. Regenerating the thermal boundary layer to enhance the heat transfer rate was studied numerically by Gong et al. [4] in a wavy microchannel. Combined effect of transverse micro chamber and parallel longitudinal microchannel can enhance the heat transfer rate by redeveloping the thermal boundary layer [5]. A significant enhancement in heat transfer rate can be achieved by introducing the waviness surface inside the straight microchannel [6]. The overall performance criteria of a microchannel can be enhanced by introducing porous medium which results in the reduction of pressure drop and the enhancement of the convective heat transfer rate [7, 8]. However, surface roughness plays significant role on heat transfer, which cannot be neglected if the relative roughness height is larger than 1% of the channel hydraulic diameter in microchannels [9, 10]. The effect of structured roughness or methodical flow obstacles or extended surface on the fluid flow and heat transfer in a microchannel was numerically studied by Yadav et al. [11].

Some of the structured extended surfaces are also inspired by biological surfaces (biomimetic) and applied to study the effect of these biomimetic surfaces on the two-phase flows [12,13] and

observed that the bio-inspired surfaces promote the heat transfer coefficient significantly. Therefore, the main goal of the present study is to investigate the effect of biomimetic inspired surface on single phase laminar forced convection heat transfer in microchannel.

## 2. DESCRIPTION OF PHYSICAL PROBLEM

The present microchannel is designed with biomimetic inspired bottom surface that contains fish scale geometry. The detailed geometry of the computational microchannel and considered fish scale is depicted in Fig. 1(a-b), respectively. The channel height, width and length are taken as 100 μm, 1500 μm and 0.02 m, respectively. Eight numbers of fish scales were used and they are equally spaced in the direction of flow. The geometry of the fish scale is defined by the following non-dimensional parameters: slant height ($S_f/D_h$=1.50), width ($W_f/D_h$=1.07), horizontal gap ($H_f/D_h$=1.07), vertical height ($V_f/D_h$=1.60) and inclination angle ($\alpha$ = 1° and 10°). The inflow distance between the scales ($S_p/D_h$) is also kept constant at 2.13. The numerical analysis is carried out in a commercial Finite Volume based solver ANSYS Fluent V16.

The computational domain consists of hexahedral elements where certain portion behind the fish scale is having fine mesh to adequately capture the fluid flow and heat transfer behaviour. A number of structured hexahedral mesh is also generated within the fish scale volume. After completing a detailed grid independence study, it is observed that the 9,01,500 number of cells are moderately sufficient for the numerical simulations with good accuracy and least computational time.

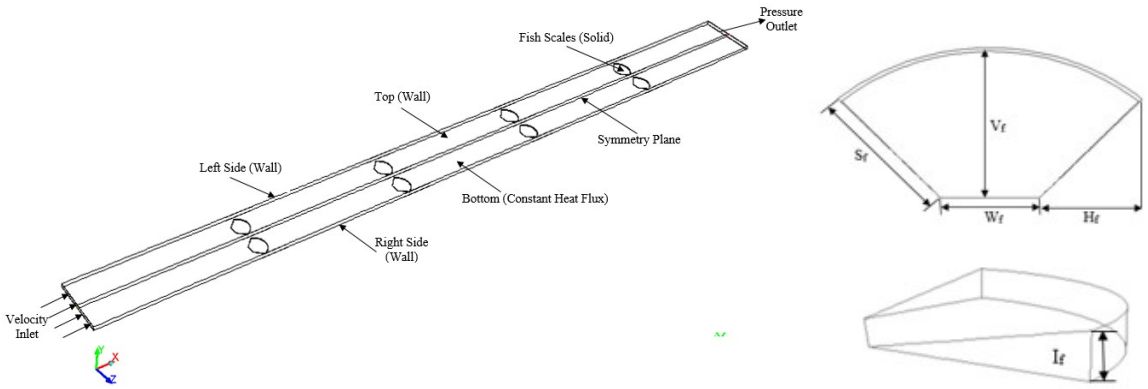


(a) (b)

FIGURE 1. (a) Schematic Diagram of the present computational model with boundary conditions and (b) Particulars of Fish scale geometry

## 3. RESULTS AND DISCUSSION

It is important to validate the present numerical model with the published numerical and experimental results. Therefore, a plain rectangular channel was considered for the validation and found that the present numerical model has a good agreement with the published data. Three different microchannels are considered; plain channel (MC_P), fish scaled channel [MC_A1 ($I_f$ = 1°) and MC_A10 ($I_f$= 10°)], keeping all other parameters as constant.

Fig. 2 shows the ratio of Nusselt number for fish scale structured and plain microchannels. Drastic enhancement in thermal performance ($Nu/Nu_0$) is noticed when the inclination angle is changed from 1° to 10°. This augmentation primarily results from the flow separation, disturbance effect and the vortices in the mainstream caused by fish scale inclination as can be observed from Fig. 3. Moreover, the effect of flow disturbance is more intense for larger inclination. This flow

disturbance in higher inclined fish scale microchannel can easily be understood from Fig. 3(b) and (c).

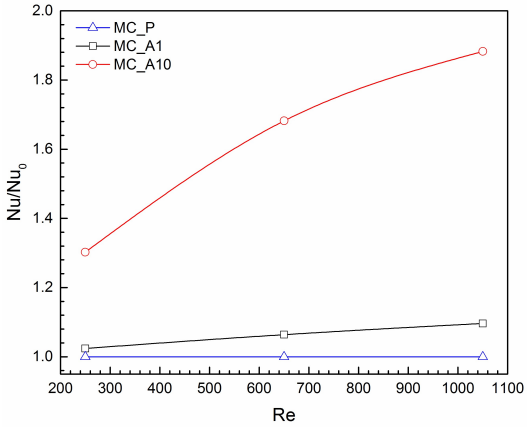


FIGURE 2: Effect of fish scale inclination angle on thermal performance.

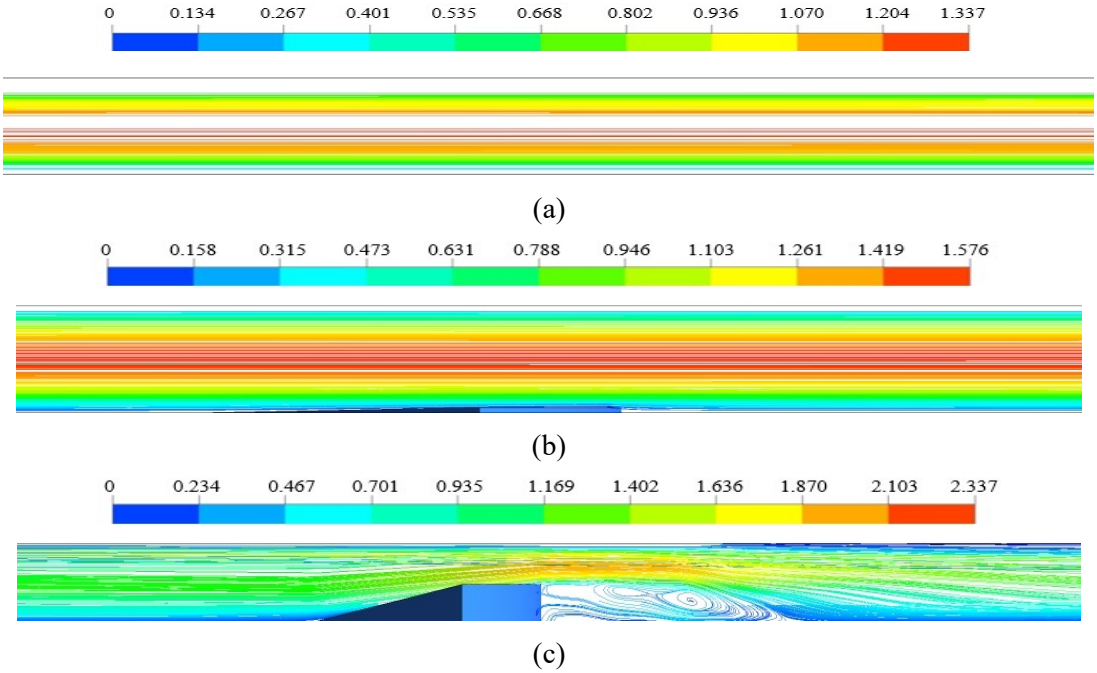


FIGURE 3: Streamline distribution in (a) MC_P (b) MC_A1 and (c) MC_A10 at *Re*=1050.

To understand the fluid flow along the stream-wise direction, streamline distributions with non-dimensional velocity contour is depicted at the cross sections for above mentioned three microchannels at $z$ = 0.375 mm for $Re$ = 1050. It is observed in Fig. 3(a) that the velocity profile remains invariable along the flow direction in the plain microchannel, however when the fish scale is introduced with an inclination angle of 1°, the velocity profile changes above the fish scale surface (Fig. 3(b)). The maximum velocity exists at the centre of the plain microchannel and remains same throughout the domain. However, as can be observed in Fig. 3(c), the velocity fluctuates significantly along the flow direction and the highest velocity is obtained at the centre of that portion of microchannel which contains fish scale structure.

More vortices are observed in the microchannel with fish scale having an inclination angle of 10° due to adverse pressure gradient which moderately improve the flow mixing and chaotic advection. This phenomenon increases heat transfer in the microchannel of fish scale of 10°.

## 4. CONCLUSIONS

A detailed numerical study is conducted to study the effect of the fish scale like geometry in a microchannel on heat transfer. It is found that the inclination angle of the present bioinspired surfaces can significantly enhance heat transfer by improving the flow mixing, and chaotic advection by introducing vortices, which increases with the inclination angle of the fish scale structure.

## REFERENCES

[1] S.K. Saha, A. Agrawal, Y. Soni, Heat transfer characterization of rhombic microchannel for H1 and H2 boundary conditions, International Journal of Thermal Sciences, 111, 223-233, 2017.

[2] D.B. Tuckerman, R.F.W. Pease, High-performance heat sinking for VLSI, IEEE Electron Device Lett., 2(5), 126-9, 1981.

[3] J.L. Xu, Y.H. Gan, D.C. Zhang, Microscale heat transfer enhancement using thermal boundary layer redeveloping concept, Int J Heat Mass Transf, 48, 1662-74, 2005.

[4] L. Gong, K. Kota, W. Tao, Y. Joshi, Parametric numerical study of flow and heat transfer in microchannels with wavy wall, Journal of Heat Transfer ASME, 133(5), 051702-10, 2011.

[5] J.L. Xu, Y.H. Gan, D.C. Zhang, X.H. Li, Microscale heat transfer enhancement using thermal boundary layer redeveloping concept, Int. J. Heat Mass Transfer, 48(9), 1662–1674, 2005.

[6] Y. Sui, P.S. Lee, C.J. Teo, An experimental study of flow friction and heat transfer in wavy microchannels with rectangular cross section, Int. J. Therm. Sci. 50, (12), 2473–2482, 2011.

[7] B.I. Pavel, A.A. Mohamad, Experimental investigation of the potential of metallic porous inserts in enhancing forced convective heat transfer, J. Heat Transfer ASME, 126, 540–545, 2004.

[8] R. Singh, A. Akbarzadeh, M. Mochizuki, Sintered porous heat sink for cooling of high-powered microprocessors for server applications, Int. J. Heat Mass Transfer, 52, 2289–2299, 2009.

[9] G.H. Tang, Z. Li, Y.L. He, C.Y. Zhao, W.Q. Tao, Experimental observations and lattice Boltzmann method study of the electroviscous effects for liquid flow in microchannels, J. Micromech. Microeng., 17, 539-550, 2007.

[10] G.H. Tang, T.B. Lu, S.X. Zhang, F.F. Wang, W.Q. Tao, Experimental investigation of non-Newtonian liquid flow in microchannels, J. Newt. Fluid Mech., 173-174, 21-29, 2012.

[11] V. Yadav, K. Baghel, R. Kumar, S.T. Kadam, Numerical investigation of heat transfer in extended surface microchannels. International Journal of Heat and Mass Transfer 93, 612-622, 2016.

[12] Q. Wang, H. Jiaju, Y. Yuying, Biomimetic capillary inspired heat pipe wicks, Journal of Bionic Engineering, 11, 469-480, 2014.

[13] E. Teodori, A. S. Moita, M. Moura, P. Pontes, A. Moreira, Y. Bai, Y. Liu, Application of Bioinspired Superhydrophobic Surfaces in Two-phase Heat Transfer Experiments, Journal of Bionic Engineering, 14(3), 506-519, 2017.

Fifth International Conference on Computational Methods for Thermal Problems
THERMACOMP2018, July 9-11, 2018, Indian Institute of Science, Bangalore, INDIA
*N. Massarotti, P. Nithiarasu, Pradip Dutta and C. Ranganyakalu (Eds.)*

# A STRATEGY TO CURE NUMERICAL SHOCK INSTABILITIES IN HLLEM RIEMANN SOLVER

**Sangeeth Simon, J.C. Mandal***
Department of Aerospace Engineering, IIT Bombay, Mumbai, India,*mandal@aero.iitb.ac.in

## ABSTRACT

Development of numerous contact and shear preserving approximate Riemann solvers for the Euler system of equations have enabled cheap and accurate computation of flows with shock waves. Unfortunately, various forms of numerical shock instability plague these schemes and manifest as distorted shock structures and erroneous post-shock field values. We present a novel strategy to cure such instabilities occurring in the popular HLL (Harten-Lax and van Leer) based HLLEM scheme. The cure works by increasing the magnitude of the HLL-type dissipation embedded within the HLLEM scheme by careful manipulation of nonlinear wavespeed estimates appearing in this dissipation vector. Some classic numerical test cases are used to demonstrate the efficacy of the modified HLLEM scheme.

**Key Words:** *Riemann solvers, Carbuncle phenomenon, Numerical shock instabilities, HLLEM*

## 1. INTRODUCTION

Computation of high-speed gasdynamical flows has benefited tremendously from the development of various Approximate Riemann solvers for the Euler system of equations. However, amongst these, only the contact and shear preserving variants are useful for computation of practically relevant flows owing to their ability to accurately resolve the linear wave fields of the Euler system. A popular example of such a scheme is the classic Roe scheme [1]. However, Roe scheme suffers from several problems like the requirement of an entropy fix, lack of positivity in near vacuum flows and requirement of the knowledge of full eigenstructure of the flux jacobians. An appealing alternative to this is the HLL based HLLEM scheme by Einfeldt et al [2] which is known to be positivity preserving, contact and shear capturing and entropy satisfying scheme which does not require the knowledge of the full eigenstructure of the flux jacobians. Unfortunately, the HLLEM scheme suffers from various forms of numerical shock instability during multidimensional simulations of flows which involves regions of strong, grid-aligned normal shocks. A classic example of such a failure is the occurrence of the Carbuncle phenomenon during the computation of a hypersonic inviscid flow over a blunt body, which is known to affect the stagnation heat transfer prediction [3]. These instabilities also manifest as oscillations in the shock profile, polluted aftershock values, growth in error norms in case of steady state problems and in extreme cases complete breakdown of the solution. In this paper, we propose a strategy to save the HLLEM scheme from such failures. Through careful modification of certain selected nonlinear wavespeed estimates appearing in the embedded HLL-type dissipation vector within the HLLEM scheme, we show that requisite numerical dissipation to prevent these instabilities can be introduced smoothly. A few classic test cases are used to demonstrate the effectiveness of this method in dealing with shock instabilities.

## 2. NUMERICAL FORMULATION

The governing equations for x-directional split inviscid compressible flow can be expressed in their conservative form as [4],

$$\frac{\partial \mathbf{U}}{\partial t} + \frac{\partial \mathbf{F}(\mathbf{U})}{\partial x} = 0$$

where $\mathbf{U}$ and $\mathbf{F}(\mathbf{U})$ are the vector of local conserved variables and grid normal fluxes at any interface given respectively as, $\mathbf{U} = \left[\rho, \rho u, \rho v, \rho E\right]^T$ and $\mathbf{F}(\mathbf{U}) = \left[\rho u, \rho u^2 + p, \rho uv, (\rho E + p)u\right]^T$. In the above experession the grid tangent fluxes are neglected in a finite volume discretization because they do not contribute to the flux across an interface. In these expressions, $\rho, u, v$, $p$ and $E$ denote local density, x-velocity, y-velocity, pressure and specific total energy. The system of equations are closed through the equation of state for ideal gas. A semi discretized form of the above equation that uses a conventional finite volume based two state approximate Riemann solver on a two dimensional quadrilateral mesh with a cell element *i* of area $|\Omega|_i$ can be written as,

$$\frac{d\mathbf{U}_i}{dt} = -\frac{1}{|\Omega|_i}\sum_{k=1}^{4}[\mathbf{F}_{Riemann}(\mathbf{U_L}, \mathbf{U_R})]\Delta s_k$$

where $\mathbf{U_L}, \mathbf{U_R}$ indicates the initial conditions of a local Riemann problem across $k^{th}$ interface of cell *i* and $\mathbf{F}_{Riemann}$ is the Riemann flux operator at the interface with face length $\Delta s_k$. The HLLEM Riemann flux due to Einfeldt et al [2] can be written as,

$$\mathbf{F}_{HLLEM} = \frac{1}{2}(\mathbf{F}_L + \mathbf{F}_R) + \mathbf{D} + \mathbf{A}$$

where $\mathbf{D} = \frac{S_R + S_L}{2(S_R - S_L)}(\mathbf{F}_L - \mathbf{F}_R) + \frac{S_L S_R}{(S_R - S_L)}(\mathbf{U}_R - \mathbf{U}_L)$ and $\mathbf{A} = \frac{S_L S_R}{S_R - S_L}(-\delta_2\tilde{\alpha}_2\mathbf{R}_2 - \delta_3\tilde{\alpha}_3\mathbf{R}_3)$

with nonlinear wavespeed estimates $S_L, S_R$ obtained using $S_{L/R} = (0, u_{L/R} \mp a_{L/R}, \tilde{u} \mp \tilde{a})_{min/max}$ where $\tilde{}$ denotes standard Roe-averaged quantities. While the term $\mathbf{D}$ denotes the HLL-type dissipation embedded within the HLLEM scheme, the term $\mathbf{A}$ denotes its antidissipation vector that enables its accuracy on contact and shear waves. Since the reason for instability in the HLLEM scheme is mostly attributed to the antidissipative terms, most authors focus on controlling the magnitude of $\mathbf{A}$ in the vicinity of shock waves to achieve shock stability [5,6]. However, improper control of the magnitude of these antidissipative terms always carries the risk of loss of accuracy on linear waves. An interesting alternative to this philosophy would be to instead focus on increasing the magnitude of $\mathbf{D}$. Hence, we propose the following modification to the HLL-type dissipation vector $\bar{\mathbf{D}}$ appearing in the HLLEM scheme,

$$\bar{\mathbf{D}} = \frac{|\overline{S_R}| - |\overline{S_L}|}{2(S_R - S_L)}(\mathbf{F}_L - \mathbf{F}_R) + \frac{|\overline{S_L}|S_R - |\overline{S_R}|S_L}{2(S_R - S_L)}(\mathbf{U}_L - \mathbf{U}_R) \text{ with } \overline{S_{L/R}} = S_{L/R} \mp \alpha\grave{o}^{L/R}.$$

The term $\grave{o}$ and $\alpha$ are some appropriately evaluated quantities (which is of the order $O(S_L, S_R)$) that are designed to affect the magnitude of $S_{L/R}$. Both $\grave{o}$ and $\alpha$ are by definition non-negative quantities. We set $\alpha$ as 3.5 [7]. At any interface $(i, j+1/2)$, $\grave{o}$ can be defined to be $\grave{o}^{L/R}_{i,j+1/2} = (1 - \omega_{i,j+1/2})|S_{L/R}|$ where $\omega_{i,j+1/2}$ is a pressure ratio based shock sensor described in [7]. The resulting modified HLLEM scheme is henceforth referred to as HLLEM-SWM-P (Selective Wave Modified using Pressure).

## 3. RESULTS

### *3.1 Hypersonic flow over a blunt body*

Most famous example of shock instability is the Carbuncle phenomenon which is observed during the steady state simulation of an inviscid hypersonic flow over a cylindrical body. The problem definition can be found in [8]. We use $320\times40$ body fitted structured quadrilateral cells with radial grid line that lies along $y=0$ perturbed in a saw-tooth profile at the order of 1e-4 to instigate the instability. First order solution is sought. The CFL for the computations were taken to be 0.5 and simulations were run for 20,000 iterations. The results showing twenty density contours equally spanning values from 1.4 to 8.5 are shown in FIGURE 1. The Carbuncle solution, represented by the distorted bow shock profile, is quite evident in case of the HLLEM scheme. However, the proposed HLLEM-SWM-P is able to compute a clean shock profile devoid of any instability.

### *3.2 Diffraction of a moving normal shock over a $90^o$ corner*

The problem of a Mach 5.09 normal shock's sudden expansion around a $90^o$ corner is another test case to ascertain the propensity of a numerical scheme to develop instability [8]. The problem is computed to second order accuracy. Simulations are run for $t=0.1561$ units with CFL of 0.4. Thirty density contours equally spanning values from 0 to 7 are shown in FIGURE 2. It is seen that the normal shock region of the diffracted shock profile is computed erroneously by the HLLEM scheme while the proposed HLLEM-SWM-P is able to avoid such spurious solution.

## 4. CONCLUSIONS

In this paper we presented a novel strategy to construct a shock stable HLLEM scheme. The method termed HLLEM-SWM-P aims to increase the overall numerical dissipation of the HLLEM scheme, in the vicinity of strong shocks, through careful manipulation of nonlinear wavespeed estimates appearing in its embedded HLL-type dissipation vector. Two standard test cases have been used to demonstrate the efficacy and robustness of this method.

## REFERENCES

[1] P. L. Roe, Approximate Riemann solvers, parameter vectors, and difference schemes, *Journal of Computational Physics*, 43, 357-72,1981.

[2] B. Einfeldt, C. D. Munz, P. L. Roe and B. Sjogreen, On Gudonov type methods near low densities, *Journal of Computational Physics*, 92, 273-95,1991.

[3] K. Kitamura, E. Shima, Y. Nakamura and P. L. Roe, Evaluation of Euler Fluxes for Hypersonic Heating Computations, *AIAA Journal*, 48, 763-76, 2010.

[4] E. F. Toro, *Riemann Solvers and Numerical Methods for Fluid Dynamics: A Practical Introduction*, 3rd Edition, Springer Berlin Heidelberg, 2009.

[5] S. H. Park and J. H. Kwon, On the dissipation mechanism of Godunov-type schemes, *Journal of Computational Physics*, 188, 524-42, 2003.

[6] W. Xie, W. Li, H. Li, Z. Tian and S. Pan, On numerical instabilities of Godunov-type schemes for strong shocks, *Journal of Computational Physics*, 350, 607-37, 2017.

[7] S. Simon. and J. C. Mandal, A cure for numerical shock instability in HLLC Riemann solver using antidiffusion control, arXiv:1803.04954, 2018.

[8] K. Huang and H. Wu and H. Yu and D. Yan, Cures for numerical shock instability in HLLC solver, *International Journal for Numerical Methods in Fluids*, 65, 1026-38, 2011.

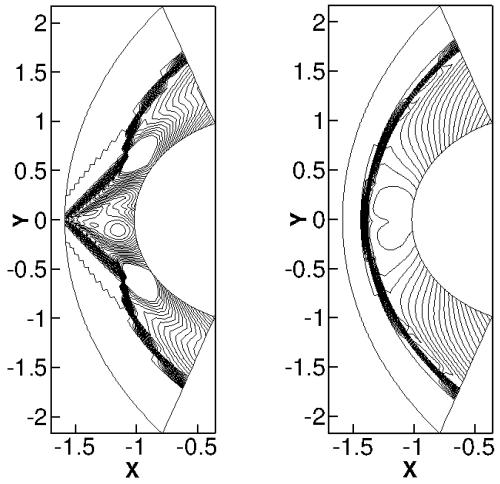


(a) (b)

FIGURE 1 Density contours for M=20 supersonic flow over a cylindrical body (a) HLLEM (b) HLLEM-SWM-P.

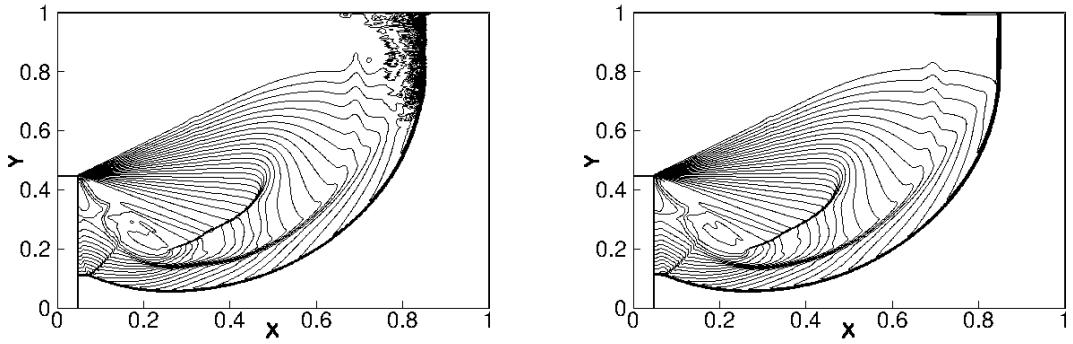


(a) (b)

FIGURE 2 Density contours for M=5.09 normal shock diffraction around a $90^o$ corner (a) HLLEM (b) HLLEM-SWM-P.

Fifth International Conference on Computational Methods for Thermal Problems
THERMACOMP2018, July 9-11, 2018, Indian Institute of Science, Bangalore, INDIA
*N. Massarotti, P. Nithiarasu, Pradip Dutta and C. Ranganyakalu (Eds.)*

# NUMERICAL STUDY OF FLUID FLOW AND HEAT TRANSFER IN COMPOUND MICROCHANNEL

**Sangram Kumar Samal, Manoj Kumar Moharana***
Department of Mechanical Engineering, National Institute of Technology Rourkela
Rourkela 769008 (Odisha) India
*mkmoharana@gmail.com

## ABSTRACT

A three-dimensional numerical study has been carried out to investigate the fluid flow and heat transfer characteristics in a compound microchannel (CMC) under conjugate heat transfer condition. A compound microchannel is one in which the channel cross-section is a combination of two shapes. In this work, the thermo-hydrodynamic performance of the compound microchannel with different cross-sections are analyzed and compared with the simple microchannel (SMC). The average Nusselt number ($Nu_{avg}$), pressure drop ($\Delta p$), thermal resistance ($R_{Th}$), and performance factor (PF) for fifteen (15) different geometric cross-sections are evaluated for flow Reynolds number, Re = 100 and applied heat flux on bottom surface of the substrate, q" = 10 W/cm$^2$. The results reveal that the compound microchannel having semicircular base (which is formed by combining square and semicircle) shows highest overall thermal performance with performance factor value of 1.34 among all the geometries considered in this study.

**Key Words:** *Compound Microchannel, Conjugate Heat Transfer, Average Nusselt Number, Performance Factor, Thermal Resistance.*

## 1. INTRODUCTION

Miniaturization of electronic components resulted in higher heat flux dissipation from the semiconductor devices. Unless these devices are maintained under some threshold temperature limits, the average life period are going to fall drastically. Therefore, thermal management of these devices is very important in controlling the operating temperature. Fluid flow through rectangular channels having hydraulic diameter less than 1 mm (referred as microchannel) is the simplest method which is commonly used for electronic cooling. Due to compact in nature, microchannel system easily fit in electronic devices in the form of heat sink or heat exchanger. Tuckerman and Pease [1] first proposed that high heat flux can be removed by using single-phase forced convection in microchannels. Since then many developments has been carried out on microchannel by considering different parameters such as shape and size of the microchannel, conjugate heat transfer, heat transfer enhancement through different means, two-phase flow etc.

It is an important aspect to study the effect of microchannel cross-sectional shape on the fluid flow and heat transfer characteristics. Peng and Peterson [2] found that the effect of geometry configuration and channel aspect ratio are very significant in the case of single-phase forced convection heat transfer through the microchannel. Moharana and Khandekar [3] numerically studied the effect of rectangular microchannel aspect ratio on its thermal performance and found that the local and the average Nusselt number over the total channel length is function of channel aspect ratio. It is found that the average Nusselt number is minimum corresponds to an aspect ratio of approximately two or slightly less than two, depending on the way the channel aspect ratio is varied. Salimpour et al. [4] found that microchannel with rectangular and elliptic cross-sections have better performance compared to microchannel with isosceles triangular cross-section. Recently Sahar et al. [5] numerically investigated the effect of hydraulic diameter and aspect ratio on the

fluid flow and heat transfer in a microchannel and found that the aspect ratio does not affect the heat transfer coefficient while the Nusselt number increases with increasing hydraulic diameter.

From the literature review, it is observed that the effect of microchannel cross-sectional shape on fluid flow and heat transfer behavior is significant. So, in this work, the thermo-hydraulic performance of a microchannel whose cross-section is the combination of two shapes (referred as compound microchannel) is investigate and compared with that of simple cross section microchannel (SMC).

## 2. PROBLEM DESCRIPTION AND MATHEMATICAL MODELLING

Figure 1(a) presents the schematic diagram of the three-dimesional computational domain of a simple microchannel (SMC) with square cross-section. The length (L), width (W) and height (H) of the computational domain are 60 mm, 1.2 mm, and 0.8 mm respectively. Simple microchannel (SMC) shapes considered in this study are square, triangular, trapezoidal and semi circular. Compound microchannel (CMC) shapes considered in this study are formed by combining square and trapezoidal with square, triangular, trapezoidal and semi-circular shapes. Cross-sectional view of simple and compound microchannels considered in this study are shown in Figure 1(b), later on referred as case 1 to 15 (read from left to right and from top to bottom). Water is used as working fluid and silicon is used as substrate material. Constant wall heat flux q" = 10 W/cm$^2$ is applied on the bottom face of the substrate while all other walls are considered as adiabatic.

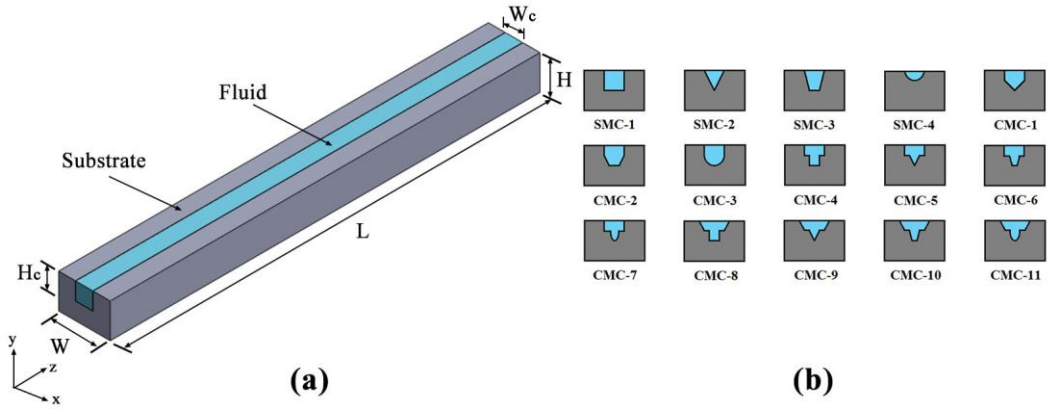


FIGURE 1. (a) Computational domain for simple microchannel (SMC) (b) Cross-sectional view of simple and compound microchannels considered in this study.

The governing equations for modelling of fluid flow and heat transfer in the microchannel are solver with the following assumptions: (i) steady laminar incompressible flow, (ii) constant thermo-physical properties for both solid and fluid, (iii) no internal heat generation in the domain, (iv) negligible heat losses due natural convection and radiation, and (v) gravitational force is negligible. The generalized governing equations for the fluid and solid domains are as follows:

Continuity equation:

$$\nabla \cdot \vec{v} = 0 \tag{1}$$

Momentum equation:

$$\rho\left(\vec{v} \cdot \nabla \vec{v}\right) = -\nabla p + \mu \nabla^2 \vec{v} \tag{2}$$

Energy equation for fluid:

$$\rho_f \left(\vec{v} \cdot \nabla T_f\right) = \frac{k_f}{C_{pf}} \nabla^2 T_f \tag{3}$$

Energy equation for solid:

$$k_s \nabla^2 T_s = 0 \tag{4}$$

Average Nusselt number ($Nu_{avg}$) over the channel length, thermal resistance ($R_{Th}$) and performance factor (PF) are evaluated using the follows expressions respectively:

$$Nu_{avg} = \frac{1}{L}\int_0^L Nu_z dz \tag{5}$$

$$R_{Th} = \frac{T_{max} - T_{min}}{Q} \tag{6}$$

$$PF = \left(\frac{Nu_{avg}}{Nu_{avg,0}}\right) \times \left(\frac{\Delta p_0}{\Delta p}\right)^{1/3} \tag{7}$$

where $Nu_z$ is the local Nusselt number along the flow direction, $\Delta p$ is the total pressure drop, $T_{max}$ is the maximum temperature at the bottom surface and $T_{min}$ is the minimum temperature which is inlet fluid temperature. $Nu_{avg,0}$ and $\Delta p_0$ are the average Nusselt number and total pressure drop for a simple microchannel with square cross-section.

## 3. RESULTS AND DISCUSSION

The parameters of interest are overall heat transfer and pressure drop due to flow of coolant. To obtain generalized outcome based on this study, the following parameters are evaluated for all the fifteen-geometrical cross-sectional shaped microchannels considered in this study and presented in Figure 2. The parameters are (i) Average Nusselt number over the channel length ($Nu_{avg}$) (ii) pressure drop (iii) thermal resistance ($R_{th}$), and (iv) performance factor (PF).

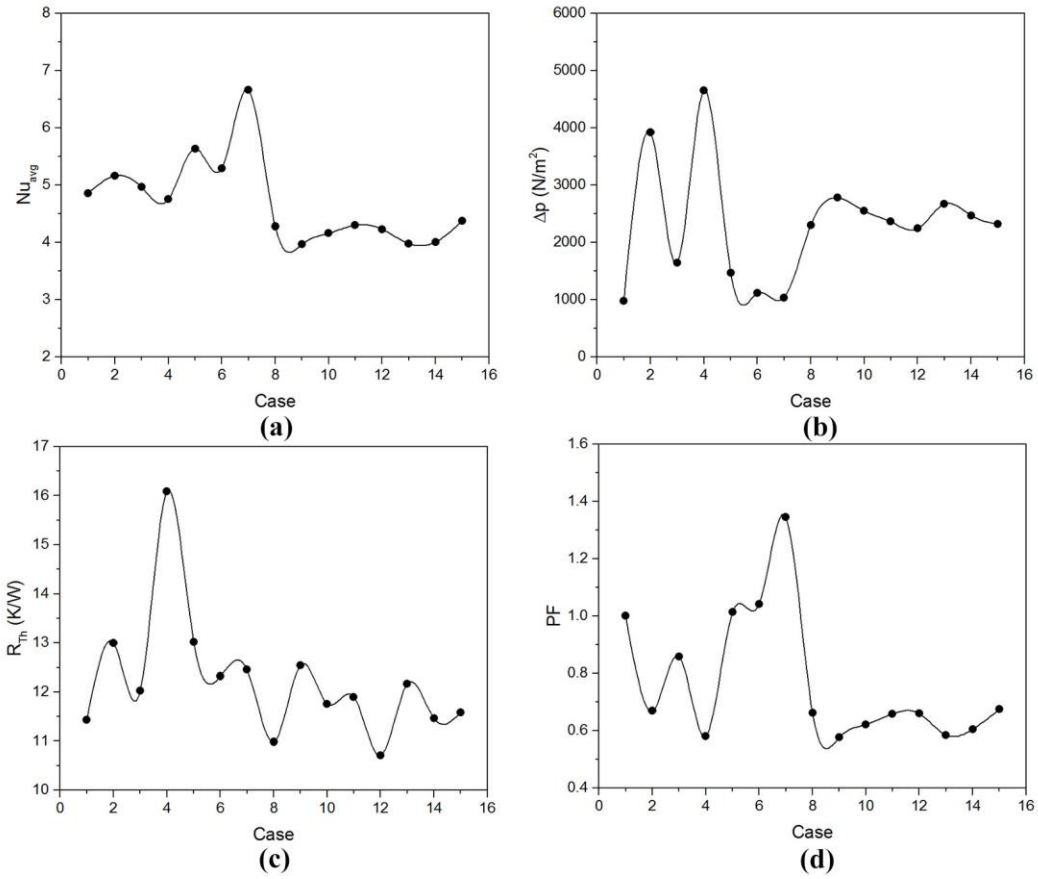


FIGURE 2. Plots of (a) average Nuseelt number ($Nu_{avg}$) (b) friction factor (f) (c) thermal reistance ($R_{Th}$) and (d) performance factor (PF) for different cases.

Figure 2(a) presents average Nusselt number ($Nu_{avg}$) for all the geometrical cases considered in this study. It can be observed in Fig. 2(a) that $Nu_{avg}$ comes out to be maximum for case 7 i.e. for the compound microchannel formed in combination with square and semi-circular (CMC-3, see Figure 1(b)). The average Nusselt Number $Nu_{avg}$ for simple microchannels i.e. case 1 to 4 is less than that of case 7. Also, the average Nusselt Number $Nu_{avg}$ for case 5 and 6 is less than that of case 7 but more than that of case 1 to 4. This is because of proximity of the geometry in case 5 and 6 with that of case 7 but due to presence of corners. The average Nusselt number ($Nu_{avg}$) value for case 8 to 15 is almost equal and minimum among others. This is due to presence of corners and sharp bends. This also reflected in pressure drop value in Fig. 2(b) where pressure drop for cases 8-15 are higher compared to other cases except case 2 and 4. Pressure drop in Fig. 2 and 4 are higher because of higher perimeter per unit area of cross section. Next, thermal resistance is calculated using Eq. (6) which reflects direct relation with maximum temperature within the solid, which will occur at the bottom surface of the solid as the minimum temperature and heat input remain constant for all cases. Thermal resistance is maximum for case 4 as it carries less fluid i.e. less convective heat transfer from the solid substrate due to its smallest hydraulic diameter.

Finally, performance factor is calculated and presented in Figure 2(d), which presents the combined effect of heat transfer enhancement and pressure drop penalty if any. Performance factor value is found to be maximum for case 7 i.e. 1.34. This is due to higher hydraulic diameter (same as simple channel hydraulic diameter) and absence of two corners. Performance factor for cases other than 5 to 7 have value less than 1 while for case 5 and 6 it is slightly greater than 1.

## 4. CONCLUSIONS

A three-dimensional numerical study has been carried out to investigate the fluid flow and heat transfer characteristics in a compound microchannel (CMC) under conjugate heat transfer condition. Based on the numerical study for thermal performance of different design compound microchannels, it is found that microchannel having semi-circular base (case 7) perform better than other design compound microchannels considered in this study. This is due to maximum average Nusselt number and minimum pressure drop among other designs considered.

## REFERENCES

[1] D.B. Tuckerman, and R.F.W. Pease, High-performance heat sinking for VLSI, *IEEE Electron Device Letters*, 2 (5), 126-129, 1981.

[2] X.F. Peng, and G.P. Peterson, Convective heat transfer and flow friction for water flow in microchannel structures, *International Journal of Heat and Mass Transfer*, 39(12), 2599-2608, 1996.

[3] M.K. Moharana, and S. Khandekar, Effect of aspect ratio of rectangular microchannels on the axial back conduction in its solid substrate, *International Journal of Microscale and Nanoscale Thermal and Fluid Transport Phenomena*, 4(3-4), 211-229, 2013.

[4] M.R. Salimpour, M. Sharifhasan, and E. Shirani, Constructal optimization of microchannel heat sinks with noncircular cross sections. *Heat Transfer Engineering*, 34(10), 863-874, 2013.

[5] A.M. Sahar, J. Wissink, M.M. Mahmoud, T.G. Karayiannis, and M.S.A. Ishak, Effect of hydraulic diameter and aspect ratio on single phase flow and heat transfer in a rectangular microchannel, *Applied Thermal Engineering*, 115, 793-814, 2017.

# NUMERICAL INVESTIGATION ON THERMO-HYDRAULIC PERFORMANCE OF TUBE WITH WIRE COIL INSERTS

**Sanjay Kadam*, Pratik Pishte**
Department of Mechanical Engineering, Rajarambapu Institute of Technology, Sakharale, Maharashtra-415414, India
**Dr. Suhas Mohite**
Department of Mechanical Engineering, Government College of Engineering Karad, Karad, Maharashtra- 415110, India
E-mail address: sanjay.kadam@ritindia.edu, pratikpishte@gmail.com, mohitess@yahoo.com

ABSTRACT

Turbulent flow creates the laminar sub layer near the wall of fluid flowing tube. This laminar sub layer is destroyed by using various techniques. Tubes with wire coil inserts enhance the heat transfer rate by destroying laminar sub layer but it also create high pressure drop which increases pumping power. The present study on numerical investigation of thermo-hydraulic performance for tube with wire coil inserts by varying various parameter of wire coil inserts. Initially the wire coil diameter of 0.5 mm, 1mm and 1.5mm at pitch 28 mm is consider for analysis at the range of Reynolds number 4526 to 11313. Wire coil diameter of 1 mm gives highest thermo-hydraulic performance than other diameter. From the various pitch to diameter ratio 0.75, 0.86, 1 and 1.11; the highest thermo-hydraulic performance is found at 0.86 pitch to diameter ratio. The maximum enhancement in thermo-hydraulic performance of 66% is observed at Reynolds number 4526 for wire coil insert tube as compared to the smooth tube under similar working conditions.

**Key Words:** *Laminar Sub layer, CFD, Thermo-Hydraulic Performance*.

## 1. INTRODUCTION

Heat transfer enhancement technique has been developed and widely applied to heat exchanger application such as automotive industries, food and process industries, thermal power plant, electronics equipments, refrigeration and air conditioning equipments etc. The passive method of heat transfer enhancement is more effective as it doesn't need external power and the simple insert manufacturing process are now available. There are various passive heat augmentation techniques available. Pipe with wire coil inserts can be used for the effective heat transfer in various applications. Heat transfer and frictional losses in tubes with helical wire coil inserts was experimentally studied by **Sethumadhavan and Raja Rao [1]** they considered helical angles of 30°, 40°,55°, 60°, and 75° and found out that the maximum thermo-hydraulic performance was seen for helix angle of 55°. **Orhan Keklikcioglu and Veysel Ozceyhan[2]** experimentally investigate the heat transfer enhancement behavior of a tube with coiled-wire inserts installed with a separation from the tube wall. In the case of a wire with s = 1 mm and P / D = 1, a heat improvement efficiency of 82% with a Reynolds number of 3429 was observed. By using these types of wire coil insertion and the laminar boundary layer can be effectively destroyed. **Garcia et al [3]** experimentally investigate the thermal hydraulic behavior for roughened tubes, wire coils and dimpled tubes. For Reynolds number lower than 200 the use of the smooth tube is recommended. For Reynolds number 200 to 2000, the employment of wire coil is more beneficial and for higher Reynolds number dimpled tubes found beneficial. **Kiml et.al [4]** numerically studied the rib-induced secondary flow effects on local circumferential heat transfer distribution inside a circular rib-roughened tube for rib angle 75°, 60°, 45° and 90°.They found highest Nusselt number at 60° rib angle. **M.T. Naik et al.[5]** studied the thermal performance of twisted tape and wire coil inserts in turbulent flow using CuO/water nanofluid. As the twist ratio decreases, the heat transfer rate increases. A maximum of 17.62% enhancement is obtained at 0.3% nanofluid at a Reynolds number of 20,000. **Jung-Yang San et**

**al[6]** experimentally investigate the heat transfer and fluid friction correlations for circular tubes with coiled-wire inserts for air and water flow**.** Nine wire coils with different wire diameters (e = 1, 1.4 and 1.8 mm) and coil pitches (p = 18, 24 and 32 mm) were selected as the inserts. Nu increase with increase in e/d & decrease in p/d.. From above literature it can be seen that the passive heat enhancement techniques like wire coil insert can be more beneficial for transfer of heat. Therefore the present numerical investigation on the thermo-hydraulic performance of wire coil inserts in tube for various wire coil diameter, wire coil pitch and Reynolds numbers.

## 2. NUMERICAL STUDY

The wire coil insert is used for the destruction of laminar sub layer. Thickness of the laminar sub-layer is given by relation [7]

$$\text{Sub-laminar thickness} = 0.03 * \text{Diameter of Pipe}$$
$$= 0.83 \text{ mm}$$

Hence the diameter of the wire coil is selected as 0.5mm, 1mm and 1.5mm. From literature review initially we selected the ratio of pitch to diameter of tube as 1. The material of the tube and wire coil is aluminum. The diameter of tube is 28 mm and tube length is 1.68 m. By considering various parameters, the numerical domains are created in Ansys DesignModeler by specifying the pitch in twist specification option under “sweep” operation.

### 2.1 MESHING:

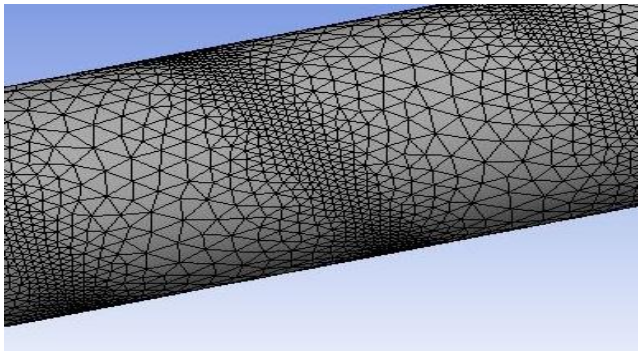

FIGURE 1. Meshing for wire coil insert tube of 1 mm wire diameter and 28 mm pitch

Unstructured tetrahedral patch independent mesh is used to discretize all the roughened domains. Figure 1 shows the meshing of the wire coil insert tube for 1 mm wire diameter and 28 mm pitch. Grid independence test is performed for all flow domain to obtain more accurate results.

### 2.2 BOUNDARY CONDITIONS:

| Sr. No | Face | Type of boundary condition | Velocity/ Pressure magnitude | Temperature |
|---|---|---|---|---|
| 1. | Inlet | Velocity Inlet | - Six different Reynolds numbers (4525, 5279, 6034, 6788, 9051, 11313) are used. | 314 K |
| 2. | Outlet | Pressure Outlet | Pressure Outlet (Atmospheric pressure) | - |
| 3. | Wall(Surface of Tube) | Constant wall temperature | - No slip condition. | 325 K |

TABLE 2. Boundary conditions for numerical analysis.

## 3.RESULTS

### 3.1 VALIDATION OF NUMERICAL MODEL

The results for smooth tube are tested by 4 different turbulence models. The results obtained by the different models are compared with the Dittus-Boelter correlation.[7]

$$Nu = 0.023\ Re^{0.8}Pr^{0.4}$$

Where, Nu is Nussult number, Re and Pr is Reynolds and Prandtl number.

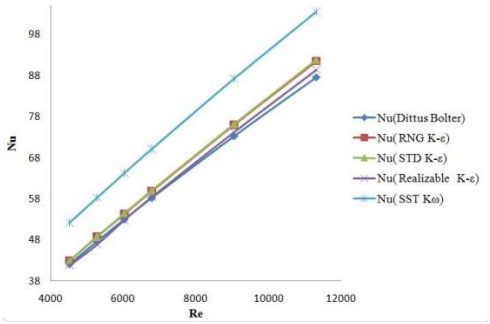


FIGURE 1. Comparison of different turbulence models against Dittus-Boelter correlation for Nusselt number for smooth tube.

The percentage deviation compared to Dittus-Boelter correlation by Realizable k- ε model is 3.39%. Therefore, for the numerical analysis of roughened tubes Realizable k- ε model is used.

### 3.2 EFFECT OF WIRE COIL DIAMETER ON THERMO-HYDRAULIC PERFORMANCE:

Thermo hydraulic performance parameter (η)[5] evaluating the thermal and hydraulic benefits of the roughened tube is defined as,

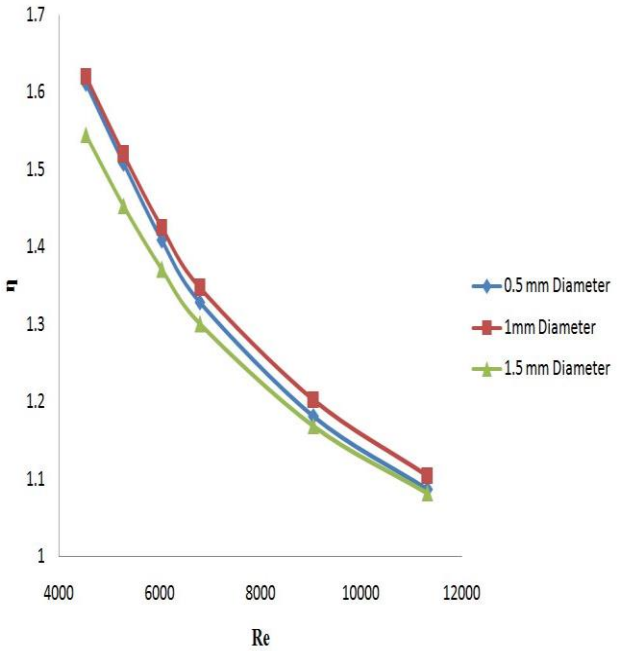


FIGURE 2. Variation of thermo-hydraulic performance parameter ($\eta$) with Reynolds number for wire coil insert tube with different wire coil diameter.

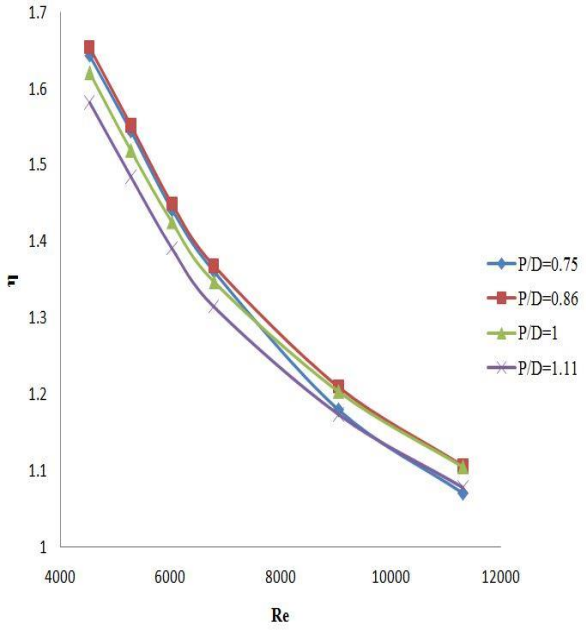


FIGURE 3. Variation of thermo-hydraulic performance parameter ($\eta$) with Reynolds number for wire coil insert tube with different wire coil pitch to diameter of tube ratio.

$$\eta = \frac{\frac{\mathrm{Nu}_{Inserts}}{\mathrm{Nu}_{Smooth}}}{\left[\frac{f_{inserts}}{f_{smooth}}\right]^{\frac{1}{3}}}$$

From figure 2, it is observed that the thermo hydraulic performance factor decreases with increase in Reynolds number. The values of thermo-hydraulic performance factor lies between 1.61-1.08, 1.62-1.11 and 1.55-1.08 for 0.5 mm, 1mm and 1.5 mm wire coil diameter respectively. Hence on the basis of thermo-hydraulic performance factor, 1 mm wire coil diameter having maximum heat transfer rate with limiting pressure drop.

3.3 EFFECT OF PITCH ON THERMO-HYDRAULIC PERFORMANCE

From figure 3, it is seen that the thermo-hydraulic performance increases with the decrease in wire coil pitch to diameter ratio up to 0.86 further decrease in pitch to diameter ratio decreases the thermo-hydraulic performance factor. This is because after 0.86 mm pitch to diameter ratio the pressure drop dominates the heat transfer and hence eventually decreases the thermo-hydraulic performance factor. The maximum value of thermo-hydraulic performance is seen at 0.86 pitch to diameter ratio. The thermo-hydraulic performance factor is 1.64-1.07, 1.66-1.11, 1.62-1.11, 1.58-1.08 for 0.75, 0.86, 1, 1.11 pitch to diameter ratio respectively. Hence on the basis of thermo-hydraulic performance factor 0.86 pitch to diameter ratio gives maximum heat transfer rate with limiting pressure drop.

## 4. CONCLUSIONS

The objective of the present work is to find the optimized roughened tube geometry by numerical analysis. The maximum enhancement in thermo-hydraulic performance of 66% is observed at Reynolds number 4525 for wire coil insert tube as compared to the smooth tube under similar working conditions.

1. Effect of wire coil diameter on heat transfer and pressure drop is studied numerically and based upon thermo-hydraulic performance factor wire coil diameter 1 mm showed better performance compared to wire coil diameter 0.5mm and 1.5 mm respectively.
2. Effect of pitch on heat transfer and pressure drop is carried out numerically and based upon thermo-hydraulic performance factor pitch to diameter ratio with 0.86 showed better performance compared to pitch to diameter ratio of 0.75, 1 and 1.11 respectively.

## REFERENCES


[1] Sethumadhavan R, Rao MR, Turbulent flow heat transfer and fluid friction in helical-wire-coil-inserted tubes, *International Journal of Heat and Mass Transfer*, 26, 1833-45, 1983.

[2] Orhan Keklikcioglu, Veysel Ozceyhan, Experimental investigation on heat transfer enhancement of a tube with coiled-wire inserts installed with a separation from the tube wall, *International Communications in Heat and Mass Transfer*, 78, 88–94, 2016.

[3] Garcia A, Solano JP, Vicente PG, Viedma A, The influence of artificial roughness shape on heat transfer enhancement: Corrugated tubes, dimpled tubes and wire coils, *Applied Thermal Engineering*, 3, 196-201, 2012.

[4] Kiml R, Magda A, Mochizuki S, Murata A, Rib-induced secondary flow effects on local circumferential heat transfer distribution inside a circular rib-roughened tube, *International journal of heat and mass transfer*, 47, 1403-12, 2004.

[5] M.T. Naik, Syed Sha Fahad,L. Syam Sundar, Manoj K. Singh, Comparative study on thermal performance of twisted tape and wire coil inserts in turbulent flow using CuO/water Nanofluid, *International Journal of Experimental Thermal and Fluid Science*, 57, 65–76, 2014.

[6] Jung-Yang San, Wen-Chieh Huang, Chang-An Chen, Experimental investigation on heat transfer and fluid friction correlations for circular tubes with coiled-wire inserts, *International Communications in Heat and Mass Transfer*, 65, 8–14, 2015.

[7] Bergman TL, Incropera FP, Fundamentals of heat and mass transfer, *John Wiley & Sons*, 2011.

Fifth International Conference on Computational Methods for Thermal Problems
THERMACOMP2018, July 9-11, 2018, Indian Institute of Science, Bangalore, INDIA
*N. Massarotti, P. Nithiarasu, Pradip Dutta and C. Ranganyakalu (Eds.)*

# Numerical investigation for convective based transient heat flux measurement with CNT based coaxial thermocouple

**Sanjeev Kumar Manjhi**[1]

Research Scholar, Indian institute of technology (ISM) Dhanbad, Jharkhand-826004, India,
sanju007mit@gamil.com

**Rakesh Kumar**[2]

Assistant Professor, Indian institute of technology (ISM) Dhanbad, Jharkhand-826004, India,
rakesh@iitism.ac.in

## ABSTRACT

Transient measurement of surface heating rates is a pretty significant activity for short duration where heat transfer rate is changing rapidly such as in the many application in the area of an aerodynamic surface, internal combustion engines, for testing wind tunnel model in impulse facilities etc. A surface heating rate is generally measured from transient temperature by using the calorimetric gauge like coaxial surface junction thermocouple. The coaxial thermocouple can be measured suitably of highly surface heat fluxes due to the response time of this type of sensors are very less (1μs). This type of reusable thermocouple fabricated easily in the house and thus it's cost effective. By using a proper one-dimensional heat conduction modelling, the surface heat fluxes are estimated from the measured temperature histories. The main aim of this numerical investigation is the effect of carbon nanotube (CNT) material on K-type and E-type coaxial thermocouple in convective heating rates.

**Key Words:** *Coaxial thermocouple, Transient temperature, Surface heat flux, CNT material.*

## 1. INTRODUCTION

Transient heat flux measurement is very significant in the time-varying heat transfer research area. In many engineering application due to rapidly fast fluctuation in heat flux, it's necessary to precise in short duration temperature measurement. Some extensive example the rapid variation of heat transfer is heat transfer at the wall of the cylinder in I.C. engine [1, 2], hypersonic shock tunnel [3, 4], Aerodynamic models [5, 6,7] etc. So it is lacked to a thermal sensor having a fast response time. Coaxial thermocouple sensors are suitable for measuring highly transient surface heat fluxes because the response times of these sensors are very small (0.1mss). These robust sensors have the flexibility of mounting them directly on the surface of any geometry. So, they have been routinely used in ground-based impulse facilities as temperature sensors where rapid changes in heat loads. [8]. Due to the extraordinary thermal conductivity, mechanical and electric properties, carbon nanotubes (CNT), it's used as additives in many structural materials. So in this investigation, the carbon nanotube is used as additives in the thermocouple material to see the effect on heat flux measurement on the K and E type of thermocouple. One dimensional coaxial thermocouple as per the definition of dimensionless thermal piercing range is given in [9] and properties (ρ, c, k) of thermocouple material. Thermocouples are divided into the various types on the basis of material used and range of temperature measurement. In this paper, numerical investigation has been carried out K-type and E-type of thermocouple. The type K (Alumel Chromel) is the most common general purpose thermocouples with the range of -200 ºC to 1350ºC and sensitivity of approximately 41 μv/ºC [10, 11]. Type E (Chromel-Constantan) has high output (68 μv/ºC), which is suited for study of production and behavior of material at very low temperature. Both thermocouples are non-magnetic. The result is obtained for K-type and

E-type coaxial thermocouple using commercial software (FLUENT 15.0) and compared (with CNT and without CNT). Numerical analysis is carried out with flow environment velocity (10 m/s), pressure (6 bar) and temperature (320 K) for thermocouple with CNT and without CNT based K-type and E-type thermocouple.

## 2. COAXIAL THERMOCOUPLE

In a traditional thermocouple, a junction is formed by combining two different type of material. Depending upon the material used, temperature measurement range varies .on this basis thermocouple is divided into various categories. The coaxial thermocouple is formed by inserting one element in another element. A very thin (0.1 mm) insulating material is used between them for tightening and avoids the electric contact between them as shown in Fig. 1

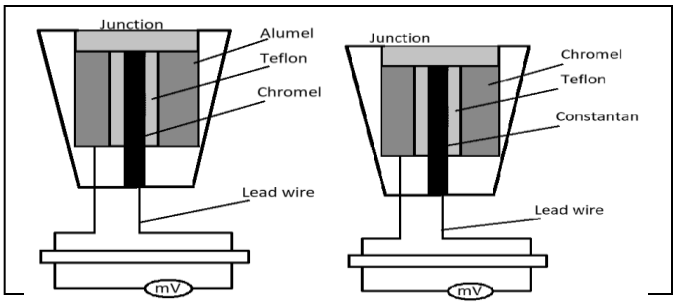


Fig.1. Schematic diagram of K and E-type coaxial thermocouple

In this type of thermocouple material, carbon nanotube is mixed in both K and E type of thermocouple and further investigation is done to show the effect on measurement of the heat flux surface by coaxial thermocouple. Properties of materials which are used in the coaxial thermocouple are shown in the table 1.

TABLE 1: THERMAL PROPERTIES OF THERMOCOUPLE MATERIALS

| Metal | Thermal Conductivity (W/mK) | Specific Heat (J/kgK) | Density ($kg/m^3$) |
|---|---|---|---|
| Alumel | 19 | 300 | 8730 |
| Chromel | 30 | 110 | 8600 |
| Constantan | 19.5 | 390 | 8900 |
| Teflon | 0.25 | 1010 | 2160 |
| CNT material | 3000 | 640 | 2600 |

## 2. NUMERICAL INVESTIGATION

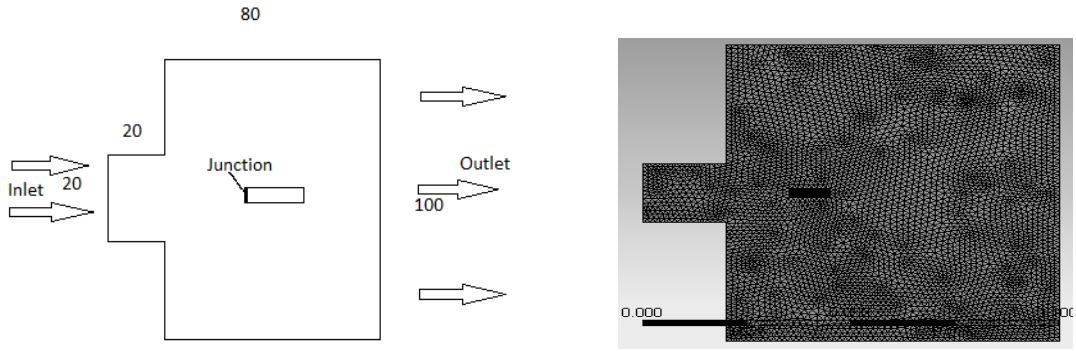


Fig.2. (a) Computational model of flow domain and (b) Computational model of mesh generation

Numerical has been done by using commercial software (FLUENT 15.0) for the different type of thermocouple. The two-dimensional geometry is formed by workbench 15.0 for investigation. The inlet boundary conditions are having velocity (10m/s), pressure (6.1 bar) and temperature (320 K) for K and E type of coaxial thermocouple. In this analysis, the second-order upwind scheme is used for better accuracy. In this simulation, the number of time step 200 for 0.01-time step size with 60 maximum of iteration. The results of both K- and E-type of coaxial thermocouples are compared by CNT based thermocouple. The temperature of the k type of thermocouple is slightly different from CNT based thermocouple. K type of thermocouple getting the fast measurement of temperature than CNT based thermocouple.

## 3. RESULTS

### 3.1. TRANSIENT TEMPERAURE ESTIMATION

The result of both K and E type of coaxial thermocouples are compared by CNT based thermocouple. The temperature of the k type of thermocouple is slightly different from CNT based thermocouple. K type of thermocouple getting fast measurement of temperature than CNT based thermocouple. The graph shows parabolic in nature in nature; it means these thermocouples are quite effective with temperature with time and efficient in the time-varying condition where heat transfer quickly changes.

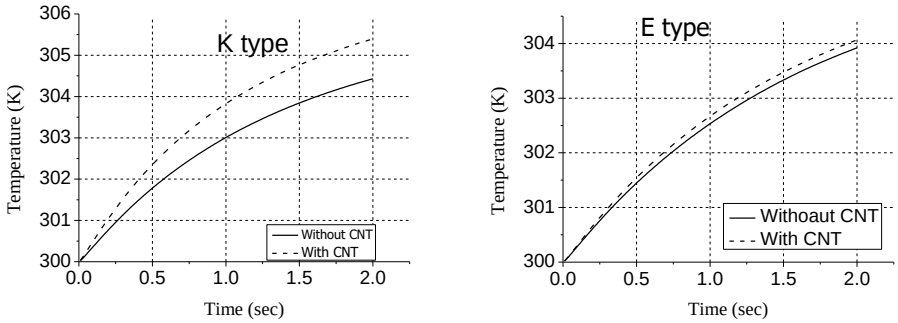


(a) (b)

Fig.3. Varitaion of temperature with respect to time

## 3.2. HEAT FLUX ESTIMATION

Measurement of transient heat flux from transient temperature histories based on one-dimensional heat conduction formulation for a semi-infinite body, according to this approach temperature measure by coaxial thermocouples into the identical temperature on the surface {Ts (t)} of the elements. The heat flux is calculated by using Duhamel's superposition integral [7] as given in Eq.

$$\dot{q}_s(t) = \frac{\beta}{\sqrt{\pi}} \int_0^t \frac{d\{T_s(t)\}}{dt} \frac{1}{\sqrt{t-\tau}} d\tau \qquad (1).$$

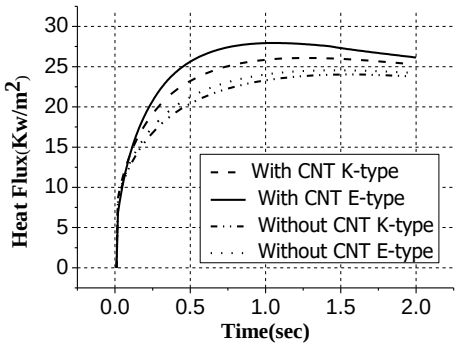


Fig.4. Surface heat flux recovered from the temperature histories for the heat transfer

## 4. CONCLUSIONS

The performance of two types of coaxial thermocouples is simulated numerically by using carbon nanotube (CNT) as additive material by using Ansys 15.0 a two-dimensional geometry has been created using Ansys fluent 15.0 for investigation of thermal behaviour on coaxial thermocouple which is based on the carbon nanotube. These numerical results compared with CNT based axial thermocouple. The effect of carbon nanotube slightly different which can be shown in the Fig. 3. It is clear from the graph that E type of coaxial thermocouple has a stronger signal and higher accuracy. Due to having thermal conductivity is high the thermal stability will be better on CNT based coaxial thermocouples.

## REFERENCES

[1] A.C. Alkidas, J.P Myers, Transient heat flux measurement in the combustion chamber of a spark- ignition engine, J. Heat transfer 104 (1) 62-6, 1982.

[2] D.J.O. Nijeweme, J.B.W. Kok, C.R. Stone, L. Wyszynski, Unsteady in cylinder heat transfer in a spark ignition engine: experiments and modeling, Proc. Inst. Mech. Eng. Part, D.J. Automobile Eng. 215, 747 760, 2001 .

[3] Reddy NM, Nagashetty K, Reddy KPJ (Review of hypersonic research investigations in the IIsc shock tunnel (HST1). Proc Indian Acad Sci SADHANA 21 (6) 741-773, 1996.

[4] Jessen. C, Vetter. M and Gronig. H , Experimental Studies in the Aachen hypersonic shock tunnel, Z. Flugwiss. Weltraumforsch. 17: 73-81, 1993.

[5] R. Sanderson, B. Sturtevant, Transient heat flux measurement using a surface thermocouple, Rev. Sci. Instrum. 73 (7), 2781-2788, 2002.

[6] Gai SL, Mudford NR, Stagnation point heat flux in hypersonic high enthalpy flow. Shock waves 2 (1):43-47, 1992.

[7] D.L.Schultz and T.V Jones (Heat Transfer measurement in short Duration Hypersonic Facilities. University of oxford Britain: AGARD NO.165, pp.47-50, 1973.

[8] R. Kumar & N. Sahoo, 2013, Dynamic Calibration of a Coaxial Thermocouples for Short Duration Transient Measurements. Asme Journal of heat transfer, 135(12), 79–84.

[9] N. Sahoo and R. Kumar, 2016. Performance assessment of thermal sensors during short-duration Convective surface heating measurements, Heat Mass Transfer, springer, 52(9), 2005-2013.

[10] Buttsworth, D. R., 2001, "Assessment of Effective Thermal Product of Surface Junction Thermocouples on Millisecond and Microsecond Time Scales," Exp. Therm. Fluid Sci., 25(6), pp. 409–429, 2001.

[11] Mohammed, H., Salleh, H., and Yusoff, Z., Design and Fabrication of Coaxial Thermocouple for Transient Heat Transfer Measurements, Int. J. Heat Mass Transfer, 35(7), pp. 853–859, 2008.

Fifth International Conference on Computational Methods for Thermal Problems
THERMACOMP2018, July 9-11, 2018, Indian Institute of Science, Bangalore, INDIA
*N. Massarotti, P. Nithiarasu, Pradip Dutta and C. Ranganyakalu (Eds.)*

# NUMERICAL STUDY TO INVESTIGATE FLOW MALDISTRIBUTION IN MINICHANNEL HEAT SINK WITH MODIFIED INLET/OUTLET ARRANGEMENT

**Sanjeev Kumar**
Research Scholar, IIT(ISM), Dhanbad, Jharkhand, India, 826004, sanjeev.kumar8696@gmail.com

**Pawan Kumar Singh**
Assistant Professor, IIT(ISM), Dhanbad, Jharkhand, India, 826004, pawan@iitism.ac.in

## ABSTRACT

In liquid cooled heat sink, uneven distribution of fluid can create zones of non-uniform cooling due to non-uniformity of flow, so it is extremely important to distribute flow equally among the channels because the uneven distribution of flow in the mini channel is a cause of the reduction in both thermal and fluid-dynamic performances of a heat sink. A computational study has been performed to investigate the thermal and hydraulic performance of minichannel heat sink. A minichannel heat sink with modified inlet/outlet arrangement has been considered in this study. Water has been used as working fluid and aluminium has been selected as a heat sink material. Flow range is varying from 0.5 LPM to 1 LPM. It has been found that the mini channel heat sink with modified inlet/outlet arrangement has uniform flow distribution and better thermal and hydraulic performance as compared to conventional mini channel heat sink.

**Key Words:** *Computational Fluid Dynamics, Heat Sink, Maldistribution, Thermal Resistance.*

## 1. INTRODUCTION

The mini-microchannel heat sink is one of the most promising devices for cooling down the miniature systems. One of the components that most firmly affect the performance of compact heat exchangers and the mini-microchannel heat sink is the uneven distribution of flow in the different parallel channels where the heat exchange has taken place. This uneven distribution of flow is called maldistribution. It is extremely important to distribute flow equally among the channels because the uneven distribution of flow in the mini-micro channel is a cause of the reduction in both thermal and fluid-dynamic performances. Recently, a large number of studies have been carried out to understand the mechanism of the flow maldistribution and its effect on hydrauulic and thermal performance of liquid cooled minichannel heat sink . Several authors have investigated single phase flow maldistribution both experimentally and numerically. Jajja et al. [1] investigated the systematic effect of heat sink geometry (by reducing fin spacing) with water as fluid on the microprocessor base temperature and found that the fin spacing has a significant effect on heat transfer. They found that the maximum base temperature can be reduced by reducing fin spacing. Liu and Yu [2] performed a numerical study on performances of mini-channel heat sinks with non-uniform inlets baffles and found that flow distribution in channels is more uniform with non-uniform inlets baffles as compared to without inlet baffles. Anbumeenakshi and Thansekhar [3] performed an experimental investigation of header shape and inlet configuration on flow maldistribution in the microchannel. They found that the flow distribution in microchannels depends significantly on the shape of the header, flow inlet configuration, and flow rate. Saeed and Kim [4] studied header design approaches for mini-channel heatsinks using analytical and numerical methods, results showed that distribution within mini-channel heatsink can be improved through proper design of the distributor and collector headers.

Literature review suggests that plenty of research has been carried out on flow maldistribution but there are very few studies which provided the cause of flow maldistribution in mini-channels heat sink using full domain simulation. In this study, a full domain simulation including inlet/outlet, fluid domain, and solid domain have been considered to understand the physics of problem and to consider the edge effect using ANSYS Fluent 16. Also it has been shown in this study how the inlet and outlet position affect the flow maldistribution.

## 2. GEOMETRY AND COMPUTATIONAL MODELING

The mini channel heat sink has been tested in this study contained 28 mini channel having hydraullic diameter 1.5 mm. Modified inlet/outlet arrangenment have been considered as shown in fig.1(c). In modified arrangement, the inlet is shifted towards left by 11.5 mm and outlet is shifted towards right by 11.5 mm from inlet and outlet position of conventional arrangement as shown in fig 1(b) respectively. Length, width, and height of channel are 45, 1 and 3 mm respectively. Width and length of heat sink are 55 and 47 mm respectively. Reactangular header has been considered for both arrangements with 10 mm width and 55 mm length which is equal to width of heat sink.

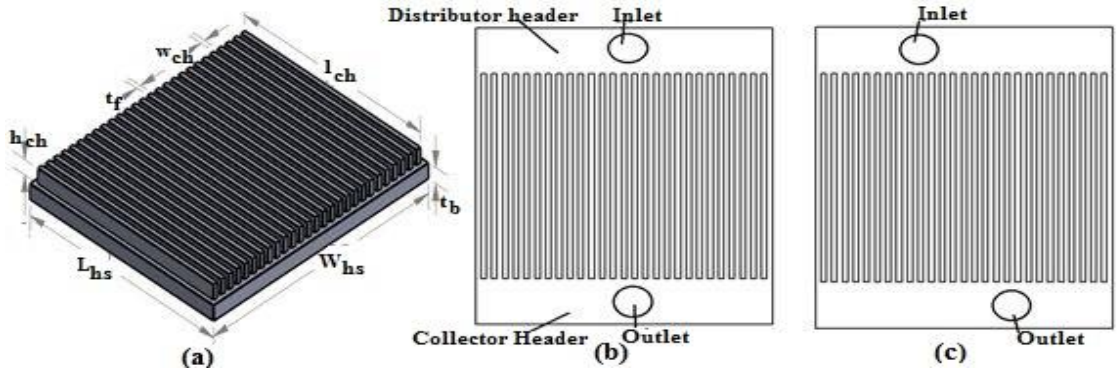


FIGURE 1. (a) Heat Sink (b) Conventional arrangement (c) Modified arrangement

## 3. GOVERNING EQUATIONS AND BOUNDARY CONDITIONS

To obtain the effect of inlet/outlet arrangement and changing volumetric flow rate on flow maldistribution and thermal performance of minichannel heat sink the following governing equations and boundary conditions are taken:

$$\nabla.\vec{V} = \mathbf{O} \tag{1}$$

$$\rho(\vec{V}.\nabla\vec{V}) = -\nabla p + \mu\nabla^2\vec{V} \tag{2}$$

$$\rho c_p(\vec{V}.\nabla T) = k_f\nabla^2 T \tag{3}$$

$$k_s\nabla^2 T = 0 \tag{4}$$

In this simulation cases, the solid aluminium is selected as the heat sink material and water is considered as the working fluid. The properties of water and solid are $\rho$ = 998.2 kg m$^{-3}$, $c_p$ = 4182 J kg$^{-1}$ K$^{-1}$, $k_f$ = 0.6 W m$^{-1}$ K$^{-1}$, $\nu$ = 1.0 ×10−6 m$^2$ s, and $k_s$ = 202.4 W m$^{-1}$ K$^{-1}$, respectively. The inlet temperature of water is set at 298 K, and the inlet velocity of water is assumed to be varied from 0.2777 to 0.5555 m s$^{-1}$, and at outlet the pressure outlet condition is applied. The Reynolds number corresponding to fluid velocity range is from 300 to 1000 and flow can be assumed laminar. The heat flux applied to the base plate of the heat sink is fixed at 20 W$cm^{-2}$ by assuming most of the electronic components generate heat flux between 10 to 50 W$cm^{-2}$. Both solid and fluid domain was discretized using ANSYS Fluent 16. Hexahedral elements with $14\times10^5$ , $44\times10^5$ ,

$70\times10^5$ and $100\times10^5$ nodes have been considered to test the grid independence of the solution. It is found that $70\times10^5$ and $100\times10^5$ nodes have almost same velocity in minichannels so $70\times10^5$ nodes have been taken for all the simulation. To ensure node to node connectivity, same approach is applied for both fluid and solid domain which minimize interpolation losses. Results of present study have been validated with experimental results of Jajja et al. [1] and numerical results of Saeed and Kim [4].

## 4. RESULTS AND DISSCUSSIONS

Flow uniformity in parallel mini channel is calculated with the help of maldistribution factor (MF) given in eq. (5).

$$MF = \sqrt{\frac{1}{N}\sum_{N=1}^{n}\left(\frac{m^k - m_{avg}}{m_{avg}}\right)^2} \tag{5}$$

Where $m_{avg} = \dfrac{\sum_{N=1}^{n} m^k}{N}$ (6)

The thermal performance of mini-channel heat sink is evaluated with the help of eq. (7)

$$R_{th} = \frac{T_{b\max} - T_{in}}{q_w W_{hs} L_{hs}} \tag{7}$$

Where $R_{th}$ is known as thermal resistance.

In both arrangements, water entered distributor header vertically upward and got out from collector header vertically downward. In conventional arrangement, the velocity in the channels those near the inlet and outlet are more due to more pressure difference results uneven distribution of flow as shown in fig 2(a). In modified arrangement, flow distribution is more uniform in minichannels due to shifting of inlet/outlet which minimize pressure difference in channels those are near the inlet/outlet as shown in fig.2 (b).

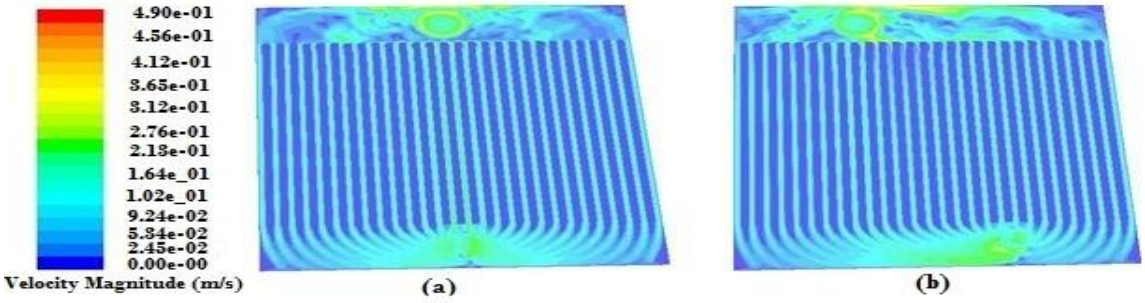


FIGURE 2. Velocity contour in parallel mini channel (a) Conventional (b) Modified

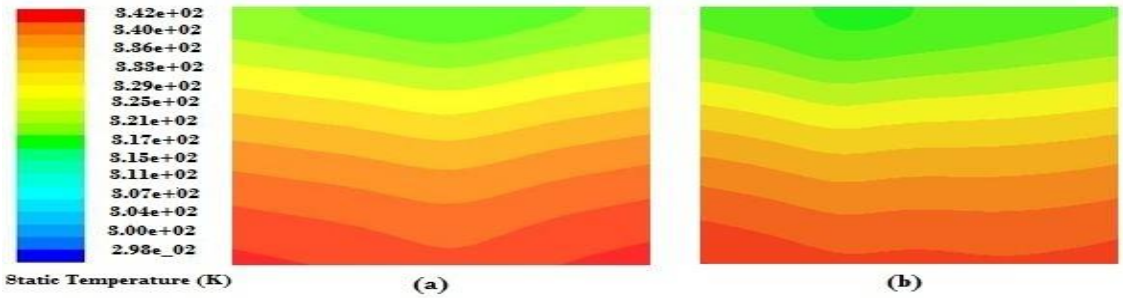


FIGURE 3. Temperature contour at the base of heat sink (a) Conventional (b) Modified

Cooling of minichannel heat sink with modified arrangement is more uniform as compared to conventional arrangement due to uniform distribution of fluid inside the parallel minichannels as shown in fig.3. Maximum base temperature of minichannel heat sink is 342K with conventional arrangement and 341K with modified arrangement at 0.5 LPM.

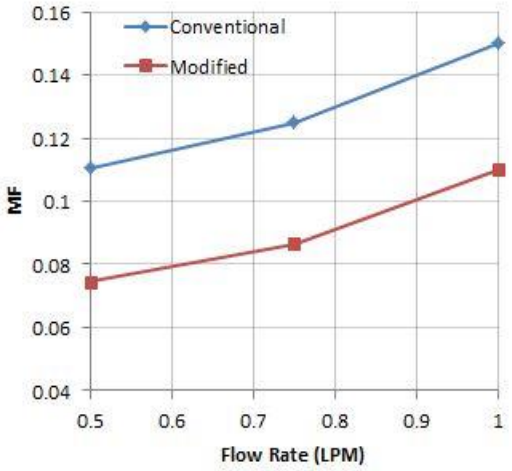


FIGURE 4. Variation of maldistribution factor with flow rate

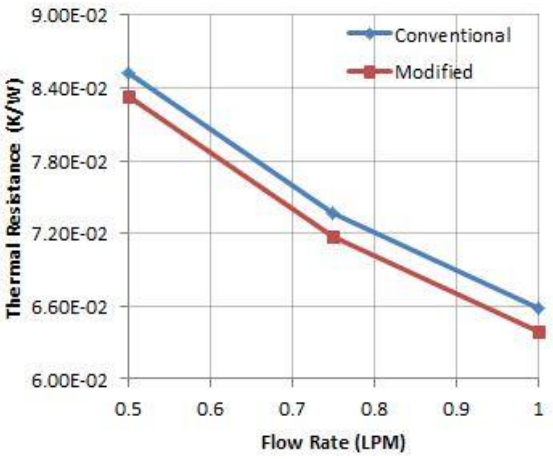


FIGURE 5. Variation of thermal resistance with flow rate

For better hydraulic and thermal performance of heat sink the value of maldistribution factor and thermal resistance should be close to zero. Maldistribution factor (MF) has been found minimum with modified arrangement and increases with volumetric flow rate as shown in fig.4. Thermal resistance has minimum value with modified arrangement and decreases with increases in volumetric flow rate as shown in fig.5.

## 5. CONCLUSIONS

Numerical investigation was performed to obtain hydraulic and thermal performance of modified mini-channel heat sink using full domain simulation in this study. It has been found that flow maldistribution can be minimized by making proper inlet/outlet arrangements. Flow maldistribution factor (MF) has lower value (0.076) with modified arrangement as compared to conventional arrangement (0.1123) at 0.5 LPM. Maldistribution factor increases with flow rate. Thermal resistance has lower value (0.0833 K/W) with modified arrangement as compared to conventional arrangement (0.0853 K/W) at 0.5 LPM. It has been found that thermal resistance decreases with increase in flow rate. The optimum position of inlet and outlet is under investigation to minimize flow maldistribution.

## REFERENCES

[1] Jajja, Saad Ayub, et al, Water cooled minichannel heat sinks for microprocessor cooling: Effect of fin spacing., *Applied Thermal Engineering*, 64, 76-82, 2014.
[2] Liu, Xiaoqin, and Jianlin Yu. "Numerical study on performances of mini-channel heat sinks with non-uniform inlets." *Applied Thermal Engineering*, 93, 856-864, 2016.
[3] Anbumeenakshi, C., and M. R. Thansekhar, Experimental investigation of header shape and inlet configuration on flow maldistribution in microchannel, *Experimental Thermal and Fluid Science*, 75, 156-161, 2016.
[4] Saeed, Muhammad, and Man-Hoe Kim, Header design approaches for mini-channel heatsinks using analytical and numerical methods. *Applied Thermal Engineering*, 110, 1500-1510, 2017.

Fifth International Conference on Computational Methods for Thermal Problems
THERMACOMP2018, July 9-11, 2018, Indian Institute of Science, Bangalore, INDIA
*N. Massarotti, P. Nithiarasu, Pradip Dutta and C. Ranganyakalu (Eds.)*

# NUMERICAL STUDY TO INVESTIGATE FLOW MALDISTRIBUTION IN MINICHANNEL HEAT SINK WITH MODIFIED INLET/OUTLET ARRANGEMENT

**Sanjeev Kumar**
Research Scholar, IIT(ISM), Dhanbad, Jharkhand, India, 826004, sanjeev.kumar8696@gmail.com

**Pawan Kumar Singh**
Assistant Professor, IIT(ISM), Dhanbad, Jharkhand, India, 826004, pawan@iitism.ac.in

## ABSTRACT

In liquid cooled heat sink, uneven distribution of fluid can create zones of non-uniform cooling due to non-uniformity of flow, so it is extremely important to distribute flow equally among the channels because the uneven distribution of flow in the mini channel is a cause of the reduction in both thermal and fluid-dynamic performances of a heat sink. A computational study has been performed to investigate the thermal and hydraulic performance of minichannel heat sink. A minichannel heat sink with modified inlet/outlet arrangement has been considered in this study. Water has been used as working fluid and aluminium has been selected as a heat sink material. Flow range is varying from 0.5 LPM to 1 LPM. It has been found that the mini channel heat sink with modified inlet/outlet arrangement has uniform flow distribution and better thermal and hydraulic performance as compared to conventional mini channel heat sink.

**Key Words:** *Computational Fluid Dynamics, Heat Sink, Maldistribution, Thermal Resistance.*

## 1. INTRODUCTION

The mini-microchannel heat sink is one of the most promising devices for cooling down the miniature systems. One of the components that most firmly affect the performance of compact heat exchangers and the mini-microchannel heat sink is the uneven distribution of flow in the different parallel channels where the heat exchange has taken place. This uneven distribution of flow is called maldistribution. It is extremely important to distribute flow equally among the channels because the uneven distribution of flow in the mini-micro channel is a cause of the reduction in both thermal and fluid-dynamic performances. Recently, a large number of studies have been carried out to understand the mechanism of the flow maldistribution and its effect on hydrauulic and thermal performance of liquid cooled minichannel heat sink . Several authors have investigated single phase flow maldistribution both experimentally and numerically. Jajja et al. [1] investigated the systematic effect of heat sink geometry (by reducing fin spacing) with water as fluid on the microprocessor base temperature and found that the fin spacing has a significant effect on heat transfer. They found that the maximum base temperature can be reduced by reducing fin spacing. Liu and Yu [2] performed a numerical study on performances of mini-channel heat sinks with non-uniform inlets baffles and found that flow distribution in channels is more uniform with non-uniform inlets baffles as compared to without inlet baffles. Anbumeenakshi and Thansekhar [3] performed an experimental investigation of header shape and inlet configuration on flow maldistribution in the microchannel. They found that the flow distribution in microchannels depends significantly on the shape of the header, flow inlet configuration, and flow rate. Saeed and Kim [4] studied header design approaches for mini-channel heatsinks using analytical and numerical methods, results showed that distribution within mini-channel heatsink can be improved through proper design of the distributor and collector headers.

Literature review suggests that plenty of research has been carried out on flow maldistribution but there are very few studies which provided the cause of flow maldistribution in mini-channels heat sink using full domain simulation. In this study, a full domain simulation including inlet/outlet, fluid domain, and solid domain have been considered to understand the physics of problem and to consider the edge effect using ANSYS Fluent 16. Also it has been shown in this study how the inlet and outlet position affect the flow maldistribution.

## 2. GEOMETRY AND COMPUTATIONAL MODELING

The mini channel heat sink has been tested in this study contained 28 mini channel having hydraullic diameter 1.5 mm. Modified inlet/outlet arrangenment have been considered as shown in fig.1(c). In modified arrangement, the inlet is shifted towards left by 11.5 mm and outlet is shifted towards right by 11.5 mm from inlet and outlet position of conventional arrangement as shown in fig 1(b) respectively. Length, width, and height of channel are 45, 1 and 3 mm respectively. Width and length of heat sink are 55 and 47 mm respectively. Reactangular header has been considered for both arrangements with 10 mm width and 55 mm length which is equal to width of heat sink.

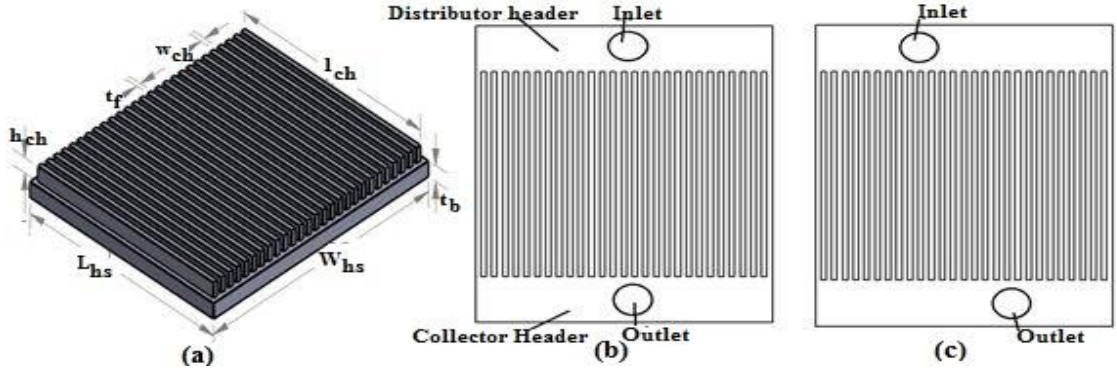


FIGURE 1. (a) Heat Sink (b) Conventional arrangement (c) Modified arrangement

## 3. GOVERNING EQUATIONS AND BOUNDARY CONDITIONS

To obtain the effect of inlet/outlet arrangement and changing volumetric flow rate on flow maldistribution and thermal performance of minichannel heat sink the following governing equations and boundary conditions are taken:

$$\nabla.\vec{V} = \mathbf{O} \tag{1}$$

$$\rho(\vec{V}.\nabla\vec{V}) = -\nabla p + \mu\nabla^2\vec{V} \tag{2}$$

$$\rho c_p(\vec{V}.\nabla T) = k_f\nabla^2 T \tag{3}$$

$$k_s\nabla^2 T = 0 \tag{4}$$

In this simulation cases, the solid aluminium is selected as the heat sink material and water is considered as the working fluid. The properties of water and solid are $\rho$ = 998.2 kg m$^{-3}$, $c_p$ = 4182 J kg$^{-1}$ K$^{-1}$, $k_f$ = 0.6 W m$^{-1}$ K$^{-1}$, $\nu$ = 1.0 ×10−6 m$^2$ s, and $k_s$ = 202.4 W m$^{-1}$ K$^{-1}$, respectively. The inlet temperature of water is set at 298 K, and the inlet velocity of water is assumed to be varied from 0.2777 to 0.5555 m s$^{-1}$, and at outlet the pressure outlet condition is applied. The Reynolds number corresponding to fluid velocity range is from 300 to 1000 and flow can be assumed laminar. The heat flux applied to the base plate of the heat sink is fixed at 20 W$cm^{-2}$ by assuming most of the electronic components generate heat flux between 10 to 50 W$cm^{-2}$. Both solid and fluid domain was discretized using ANSYS Fluent 16. Hexahedral elements with $14\times10^5$ , $44\times10^5$ ,

$70\times10^5$ and $100\times10^5$ nodes have been considered to test the grid independence of the solution. It is found that $70\times10^5$ and $100\times10^5$ nodes have almost same velocity in minichannels so $70\times10^5$ nodes have been taken for all the simulation. To ensure node to node connectivity, same approach is applied for both fluid and solid domain which minimize interpolation losses. Results of present study have been validated with experimental results of Jajja et al. [1] and numerical results of Saeed and Kim [4].

## 4. RESULTS AND DISSCUSSIONS

Flow uniformity in parallel mini channel is calculated with the help of maldistribution factor (MF) given in eq. (5).

$$MF = \sqrt{\frac{1}{N}\sum_{N=1}^{n}\left(\frac{m^k - m_{avg}}{m_{avg}}\right)^2} \tag{5}$$

Where $m_{avg} = \dfrac{\sum_{N=1}^{n} m^k}{N}$ (6)

The thermal performance of mini-channel heat sink is evaluated with the help of eq. (7)

$$R_{th} = \frac{T_{b\max} - T_{in}}{q_w W_{hs} L_{hs}} \tag{7}$$

Where $R_{th}$ is known as thermal resistance.

In both arrangements, water entered distributor header vertically upward and got out from collector header vertically downward. In conventional arrangement, the velocity in the channels those near the inlet and outlet are more due to more pressure difference results uneven distribution of flow as shown in fig 2(a). In modified arrangement, flow distribution is more uniform in minichannels due to shifting of inlet/outlet which minimize pressure difference in channels those are near the inlet/outlet as shown in fig.2 (b).

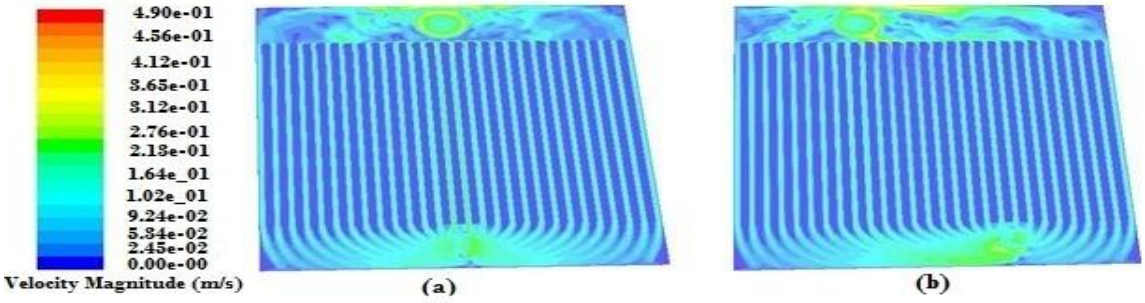


FIGURE 2. Velocity contour in parallel mini channel (a) Conventional (b) Modified

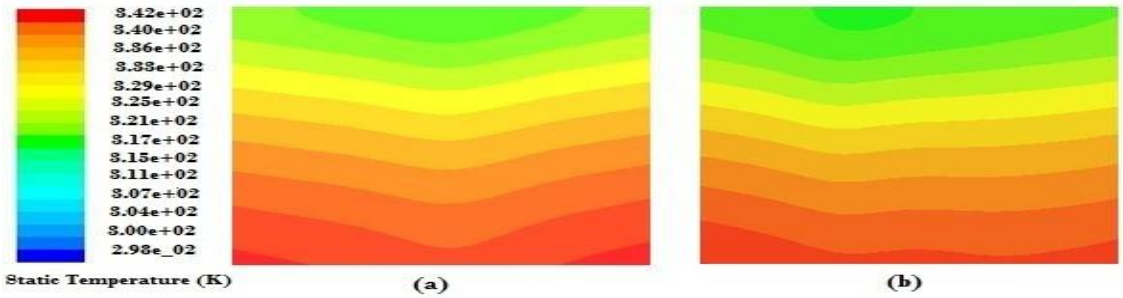


FIGURE 3. Temperature contour at the base of heat sink (a) Conventional (b) Modified

Cooling of minichannel heat sink with modified arrangement is more uniform as compared to conventional arrangement due to uniform distribution of fluid inside the parallel minichannels as shown in fig.3. Maximum base temperature of minichannel heat sink is 342K with conventional arrangement and 341K with modified arrangement at 0.5 LPM.

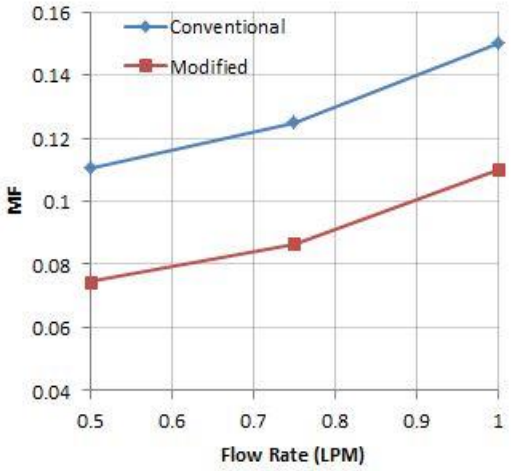


FIGURE 4. Variation of maldistribution factor with flow rate

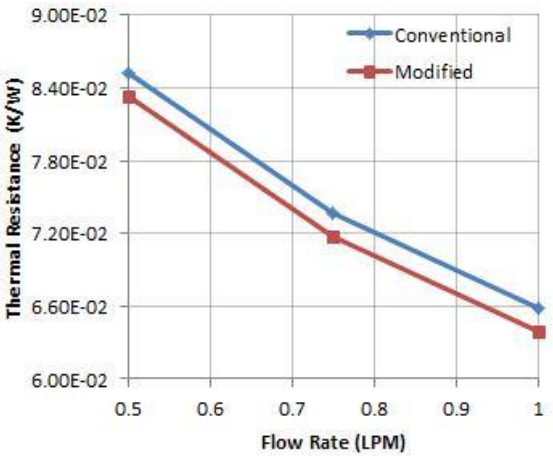


FIGURE 5. Variation of thermal resistance with flow rate

For better hydraulic and thermal performance of heat sink the value of maldistribution factor and thermal resistance should be close to zero. Maldistribution factor (MF) has been found minimum with modified arrangement and increases with volumetric flow rate as shown in fig.4. Thermal resistance has minimum value with modified arrangement and decreases with increases in volumetric flow rate as shown in fig.5.

## 5. CONCLUSIONS

Numerical investigation was performed to obtain hydraulic and thermal performance of modified mini-channel heat sink using full domain simulation in this study. It has been found that flow maldistribution can be minimized by making proper inlet/outlet arrangements. Flow maldistribution factor (MF) has lower value (0.076) with modified arrangement as compared to conventional arrangement (0.1123) at 0.5 LPM. Maldistribution factor increases with flow rate. Thermal resistance has lower value (0.0833 K/W) with modified arrangement as compared to conventional arrangement (0.0853 K/W) at 0.5 LPM. It has been found that thermal resistance decreases with increase in flow rate. The optimum position of inlet and outlet is under investigation to minimize flow maldistribution.

## REFERENCES

[1] Jajja, Saad Ayub, et al, Water cooled minichannel heat sinks for microprocessor cooling: Effect of fin spacing., *Applied Thermal Engineering*, 64, 76-82, 2014.
[2] Liu, Xiaoqin, and Jianlin Yu. "Numerical study on performances of mini-channel heat sinks with non-uniform inlets." *Applied Thermal Engineering*, 93, 856-864, 2016.
[3] Anbumeenakshi, C., and M. R. Thansekhar, Experimental investigation of header shape and inlet configuration on flow maldistribution in microchannel, *Experimental Thermal and Fluid Science*, 75, 156-161, 2016.
[4] Saeed, Muhammad, and Man-Hoe Kim, Header design approaches for mini-channel heatsinks using analytical and numerical methods. *Applied Thermal Engineering*, 110, 1500-1510, 2017.

# MODELING AND OPTIMIZATION OF CONTROLLING PARAMETERS FOR NANOFLUID BASED ULTRA-FAST-COOLING

**Santosh Kumar Nayak, Purna Chandra Mishra, Radha Kanta Sarangi**
KIIT Deemed to be University, Patia, Bhubaneswar-751024, E.mail: sknayakfme@kiit.ac.in,
E.mail: pcmishrafme@kiit.ac.in, E.mail: radha.sarangifme@kiit.ac.in

## ABSTRACT

This paper describes the optimization of process parameters governing to the heat transfer during nanofluid spray impingement cooling of hot strips. The data of each parameter were collected from the experiments conducted with various air-$TiO_2$ water based nanofluid pressure combinations and three distinct nozzle to plate distance (120 mm, 180 mm and 240 mm). The parametric optimization was carried out by using Response Surface Method (RSM) in Design Expert 8 software environments. The results show that for 0.05 wt% particle concentration and higher fluid pressure has ability of higher heat transfer rate. The ultra-fast cooling by nanofluid was found an efficient alternative cooling technique over the conventional water impingement cooling to achieve the optimal and high cooling rate.

**Key Words:** *Optimization, Controlling Parameters, Nanofluid, Ultra Fast Cooling.*

## 1. INTRODUCTION

Spray cooling plays an important role in many industrial including material processing, agricultural, electronics and microelectronics, medical, laser, aviation, steel quenching in the hot rolling mills etc. In these applications, the development of an effective thermal management system depends on issues like controlled, fast and efficient cooling performance. Aamir *et al.* [1] developed artificial neural network (ANN) models to predict spray cooling heat flux of free propane sprays. Li *et al*. [2] used response surface method for optimization of the heat transfer coefficient during gas quenching in order to obtain minimum distortion with stress. Chakraborty *et al*. [3] have investigated the performance of water based $TiO_2$ nano fluids jets impinging on the hot steel surface under laminar flow regime and found a significant improvement in cooling rate with the nano fluids having lower surface tension as compared with water. The use of nanofluids as a coolant in large thermal system and micro devices reduces the entropy generation rate with very little increase in the required pumping power [4]. The adsorption for nano particles is highly dependent on the size of the nanoparticle and is linearly correlated with the enhancement of the thermal conductivity [5]. Mitra *et al.* [6] used water -$TiO_2$ and water-MWCNT nano fluids for cooling of hot steel plate by laminar jet to study the boiling heat transfer aspects and found only marginal variation of CHF in case of nano fluids as compared to water. Several convective heat transfer studies indicates that the improvement of HTC is only due to the migration of nano particle [7].

## 2. OPTIMIZATION METHODOLOGY

*Design of Experiments*

The Box-Behnken design of response surface method (RSM) is used as it performs non-sequential experiments having fewer design points to get the experimental design matrix. Nanofluid pressure, air pressure and nozzle height are the input parameters and surface heat flux is the response. In the current investigation, the response is the surface heat flux which can be

computed by using the Equation 1 at various operating conditions. The magnitude of the outcome at different set of controlling parameters was represented in Table 1.

$$\Rightarrow Heat\ flux = q = \rho \times C_p \times t \times CR \quad (1) \quad \text{where } Cooling\ Rate = CR = \frac{\partial T}{\partial \tau} = \frac{T_1 - T_2}{\tau_2 - \tau_1}\ ^{o}\text{C/Sec}$$

| Run | Factor 1 Air Pressure (Pa)bar | Factor 2 Nanofluid Pressure(Pnf)bar | Factor 3 Concentration, %wt | Factor 4 Nozzle Height (H) mm | Response Heat Flux (q), kW/m$^2$ |
|---|---|---|---|---|---|
| 1 | 1 | 2 | 0.03 | 240 | 2217 |
| 2 | 3 | 2 | 0.05 | 180 | 3947 |
| 3 | 1 | 3 | 0.03 | 180 | 3045 |
| 4 | 3 | 2 | 0.03 | 240 | 2178 |
| 5 | 2 | 2 | 0.03 | 180 | 3276 |
| 6 | 2 | 2 | 0.05 | 240 | 3075 |
| 7 | 2 | 2 | 0.01 | 240 | 1865 |
| 8 | 1 | 2 | 0.05 | 180 | 3421 |
| 9 | 2 | 2 | 0.03 | 180 | 3104 |
| 10 | 3 | 3 | 0.03 | 180 | 3153 |
| 11 | 2 | 1 | 0.05 | 180 | 2658 |
| 12 | 2 | 2 | 0.03 | 180 | 3104 |
| 13 | 3 | 2 | 0.01 | 180 | 2669 |
| 14 | 1 | 2 | 0.01 | 180 | 2386 |
| 15 | 2 | 1 | 0.03 | 120 | 2104 |
| 16 | 2 | 3 | 0.05 | 180 | 4347 |
| 17 | 2 | 3 | 0.01 | 180 | 2822 |
| 18 | 2 | 1 | 0.03 | 240 | 2089 |
| 19 | 2 | 2 | 0.01 | 120 | 1987 |
| 20 | 2 | 2 | 0.05 | 120 | 2763 |
| 21 | 1 | 1 | 0.03 | 180 | 2456 |
| 22 | 2 | 3 | 0.03 | 240 | 3526 |
| 23 | 1 | 2 | 0.03 | 120 | 2375 |
| 24 | 3 | 2 | 0.03 | 120 | 2562 |
| 25 | 2 | 3 | 0.03 | 120 | 2851 |
| 26 | 2 | 1 | 0.01 | 180 | 1852 |
| 27 | 3 | 1 | 0.03 | 180 | 2358 |

TABLE 1. Box Behnken RSM based coded experimental design matrix

## 3. RESULTS

*Empirical Model Development Using Response Surface Method*

The Regression analysis was carried out and the quadratic model developed for heat flux from the experimental data is presented in Equation 2.

q = -3350 + 779 Pa + 105 Pnf - 4787 C + 51.6 H - 181 Pa*Pa - 119 Pnf*Pnf - 131875 C*C
- 0.1605 H*H + 52 Pa*Pnf + 3037 Pa*C - 0.94 Pa*H + 8987 Pnf*C + 2.87 Pnf*H + 90 C*H (2)

*Response Surface Analysis*

The response surface analysis of the experimental results was carried out by Design Expert 8 software. Figure 1 (a) shows the variation of heat flux with respect to air pressure and nanofluid pressure. It is observed that nanofluid pressure has more significant effect on the heat flux in comparison to air pressure. The maximum value of heat flux was achieved at high level of fluid pressure and low level of air pressure because the atomization of fluid particles is more effective at higher air pressure enables maximum blown up of the tiny nanofluid particles and reduces the heat transfer from the plate surface. Figure 1 (b) shows the variation of heat flux with respect to nanofluid pressure and nozzle height. It is observed that with increase in both the factors there is an increase in heat flux and vice-versa. As the height increases, the momentum of the fluid particle decreased due to the decreased in impact energy of the fluid particle which reduces the heat transfer from the plate surface

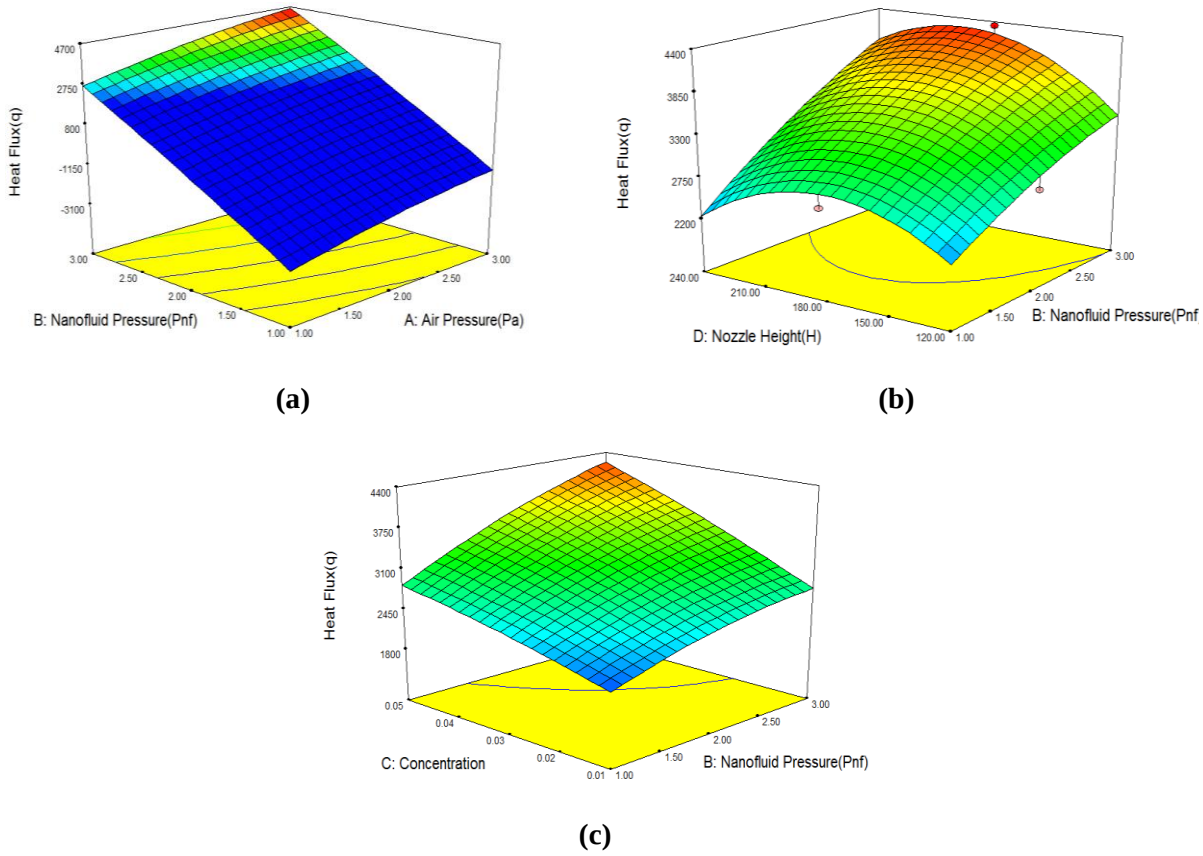


FIGURE 1. Variation of heat flux with respect to nanofluid pressure and (a) air pressure, (b) nozzle height and (c) particle concentration.

Figure 1 (c) shows the variation of heat flux with respect to nanofluid pressure and particle concentration. High particle concentration nanofluids are inadequate for spray cooling applications as they are easily accumulated on the hot surface of the specimen, as a result slow down the convective heat transfer process by reducing the number of nucleation points.

The thermal performance of spray cooling technique was enhanced with low particle concentration since most of the nano particles ricochet or washed away by afterward impinging droplets and decreased the thermal resistance at the fluid interface without formation of nano-sorption film. As the particle concentration increases, then the dynamic viscosity of the nano fluids also increases, as a result slow down the fluid flow rate. At the same time some nano particle stick to the heated surface and offers resistance to heat flow, as a consequence reduced the heat transfer rate.

From the analysis of variance, it is concluded that, the model F-value of 8.72 implies the model is significant with probability ( P) of 0.000312. The lack of fit of 0.104 implies not significant which is good for the model to fit.

*Response Surface Optimization*

The response surface optimization was performed to predict the optimal condition in which the maximum heat flux was obtained. It is being done at the Minitab 17 software interface with the help of response surface optimiser tool and the predicted outcome was given in Table 2.

| Solution | $P_{nf}$ | $P_a$ | Con. | H | q-Fit | Composite Desirability |
|---|---|---|---|---|---|---|
| 1 | 3 | 2.49495 | 0.05 | 193.939 | 4325.32 | 0.991312 |

TABLE 2. Optimized response prediction

*Experimental Validation*

Test was carried out at the predicted optimal parametric conditions, i.e. for $P_{nf}$ = 3 bar, $P_a$ = 2.4949 bar, concentration = 0.05wt% and nozzle height = 193.939 mm and the heat flux was found to be 4324.69 kW.

## 4. CONCLUSIONS

- The use of nanofluids as coolant found more effective than the conventional water for cooling applications.
- The cooling rates and surface heat flux were optimized for different parametric conditions.
- The surface-cooling rate decreased with an increased in concentration of water quenchant.
- The improvement of thermal performance only due to migration of nano particles.
- The deterioration of thermal performance was because of instability of nanofluids due to sedimentation which can produce large amount of clusters.

## REFERENCES

[1] M.A. Aamir, M.M. Awais, and A.P. Watkins, Application of artificial neural networks modeling to sprays and spray impingement heat transfer, *Atomization and Sprays*, 12, 4, 359-86, 2002.

[2] Z. Li, R.V. Grandhi, and R. Shivpuri, Optimum design of the heat-transfer coefficient during gas quenching using the response surface method, *International Journal of Machine Tools and Manufacture,* 42, 5, 549-58, 2002.

[3] S. Chakraborty, A. Chakraborty, S. Das, T. Mukherjee, D. Bhattacharjee, and R. K. Ray, Application of water based $TiO_2$ nanofluid for cooling of hot steel plate, *ISIJ international*, 50, 1, 124-27, 2010.

[4] T. Chang, and Y. Yang, Heat transfer performance of jet impingement flow boiling using $Al_2O_3$-water nanofluid, *Journal of Mechanical Science and Technology,* 28, 4, 1559-66, 2014.

[5] M. Kamalvand, and M. Karami, A linear regularity between thermal conductivity enhancement and fluid adsorption in nanofluids, *International Journal of Thermal Sciences,* 65, 189-95, 2013.

[6] S. Mitra, S.K. Saha, S. Chakraborty, and S. Das, Study on boiling heat transfer of water–$TiO_2$ and water–MWCNT nanofluids based laminar jet impingement on heated steel surface, *Applied Thermal Engineering,* 37, 353-59, 2012.

[7] Y. Xuan, and Q. Li, Heat transfer enhancement of nanofluids." *International Journal of Heat and Fluid Flow,* 21, 1, 58-64, 2000.

Fifth International Conference on Computational Methods for Thermal Problems
THERMACOMP2018, July 9-11, 2018, Indian Institute of Science, Bangalore, INDIA
*N. Massarotti, P. Nithiarasu, Pradip Dutta and C. Ranganyakalu (Eds.)*

# STUDY AND THERMAL HYDRAULIC ANALYSIS FOR STEAM GENERATOR FEED WATER PIPE BREAK FOR KKNPP USING COMPUTER CODE RELAP-5/MOD 3.2

**Sanuj Chaudhary, P.Krishna Kumar, Y.K. Pandey, H.P.Rammohan and Gautam Biswas**

Directorate of Engg-LWR, Nuclear Power Corporation of India Ltd,

Nabhikiya Urja Bhavan, Anushakti Nagar, Mumbai-400094 Email:sanujc@npcil.co.in

## ABSTRACT

Feed water break pipeline which is a design basis accident has been analysed using Thermal Hydraulic computer code RELAP-5/MOD 3.2 for Kudankulam Nuclear Power Plant (KKNPP). KKNPP has two operating VVER-1000 Reactors**.** VVER-1000 is a Pressurized Water Reactor incorporating advanced safety features including passive ones. The RELAP5/MOD3.2 computer code was developed at the Idaho National Engineering and Environmental Laboratory (INEEL) for use in analyzing transients in light water reactors. It can be used for simulating a wide variety of system transients of interest in reactor safety. The core, primary system, secondary system, feedwater train, and system controls can be simulated. RELAP5/MOD3.2 uses a one-dimensional, two fluid, nonequilibrium, six equation hydrodynamic model with a simplified capability to treat multi-dimensional flows. This model provides continuity, momentum, and energy equations for both the liquid and the vapor phases within a control volume. The energy equation contains source terms which couple the hydrodynamic model to the heat structure conduction model by a convective heat transfer formulation. The code contains special process models for critical flow, abrupt area changes, branching, crossflow junctions, pumps, accumulators, valves, core neutronics, and control systems. A counercurrent flow limitation model can also be applied at vertical junctions. Instantaneous break of pipeline before the emergency steam generator with two-side coolant outflowing both from the emergency steam generator and from the feed water collector has been considered as an initiating event. The accident results in drying of the steam generator and loss of feed water supply to the other operating steam generators and which affect the heat removal of the core.

The objective of this study is to evaluate the thermal hydraulic behavior of the core and check the capability of safety systems for event mitigation. The thermal hydraulic parameters are checked against the applicable acceptance criterion for the event.

**Key Words:** *Pipeline break, Thermal-hydraulic analysis, Nucleate boiling, Natural Circulation.*

## 1. INTRODUCTION

Kudankulam Nuclear Power Plant (KKNPP 1& 2) are 1000 MWe VVER-1000 Reactors. In order to investigate the variations in different parameters of the power plant under condition of decrease in heat removal through secondary side, steam generator feed water pipeline break was analysed. It is a Design Basis Accident (DBA) which can demonstrate the capability of safety systems to cope with such accidents. Break of steam generator feed water pipe break with coolant outflowing both from the emergency steam generator and from the feed water collector has been considered as an initiating event

The analysis has been done using system thermal hydraulics code RELAP5/MOD3.2. The RELAP5 code has been developed for transient simulations of Light Water Reactor (LWR) coolant systems during postulated accidents.

## 2. RELAP-5 MODELLING OF KKNPP-1&2 REACTORS

### 2.1 Brief Description of KKNPP-1&2 Reactors

In KKNPP-1&2 Reactors, enriched uranium (3.92% $U^{235}$) in oxide form is used as fuel with light water as moderator and coolant. KKNPP is a two circuit system namely primary and secondary circuit. Simple schematic of KKNPP-1&2 Reactor primary circuit is shown in Figure-1.

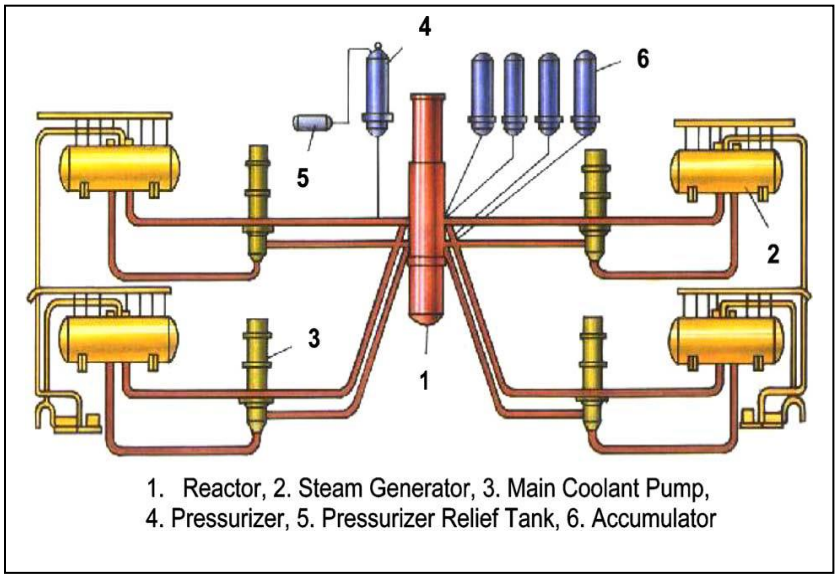


FIGURE 1. Simple schematic of KKNPP-1&2 Reactor primary circuit

The secondary circuit is a non-radioactive circuit. It consists of steam generators, main steam lines, turbine, auxiliary equipment and associated systems of de-aeration, reheating and feed water supply to the steam generators.

### 2.2. RELAP-5 Model of KKNPP-1&2

To analyze system thermal-hydraulic behavior under various accidents and transients conditions a detailed nodalization was developed for the reactor. Reactor point kinetics was also incorporated in the model with coolant temperature and fuel temperature feedback effects. Decay heat data is used from the 1979 standard data (American National Standard for Decay Heat Power in Light Water Reactors) for U-235 in light water reactors[2]. Selected enveloped cases were analysed with the developed RELAP model and the result were validated with the results of Final Safety Analysis Report for KKNPP-1.

## 3. RESULTS

Instantaneous break of pipeline of one steam generator with two-side coolant outflowing both from the emergency steam generator and from the feed water collector has been considered as an initiating event (Figure.2). The turbine trip occurs by the factor of drop of live steam pressure below 5.1 MPa in emergency SG (Figure.3). The subsequent process is accompanied with rise of the primary (Figure.4) and secondary parameters as a result of which reactor scram set point of DNBR decrease on fuel rod surface is reached (Figure.5). Loss of Nuclear power plant a.c. power is assumed 1.9 s before reactor trip conservatively resulting in trip of Reactor coolant pump (RCP). Upon completion of RCP sets coast down, coolant natural circulation is settled in primary circuit. Reduction in heat removal causes rise of the primary parameters. Failures of Steam Generator cooldown (SGECD) safety system in two loops are further assumed resulting in cooldown of only one SG in pressure maintenance mode. This leads to pressurization of the two SG's (except the emergency SG and SG with cooldown) leading to periodic actuation of these SG PSD .

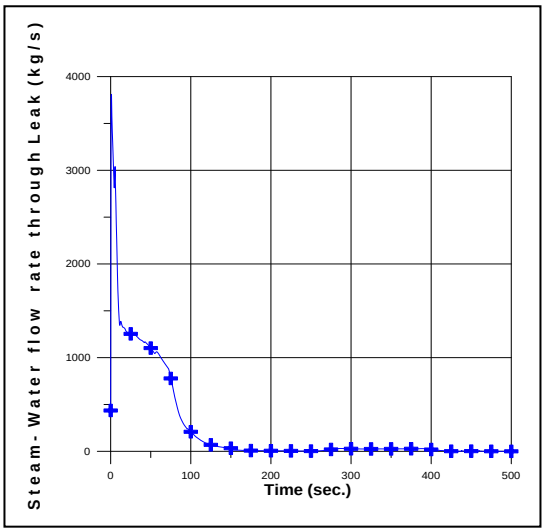


FIGURE 2. Steam-Water flowrate through leak

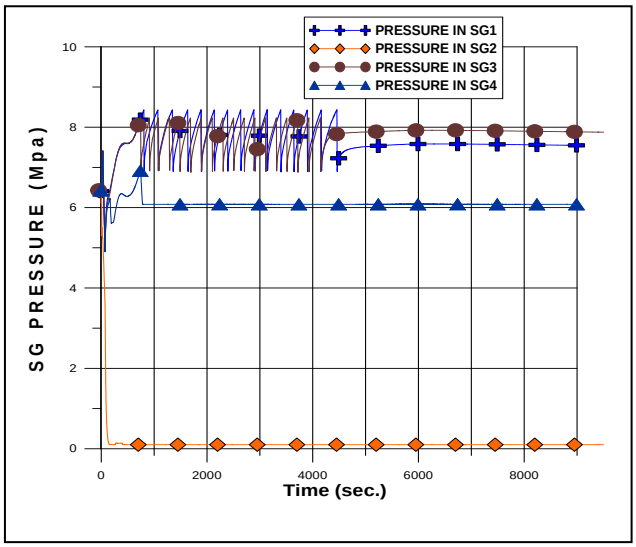


FIGURE 3. Steam Generator Pressure

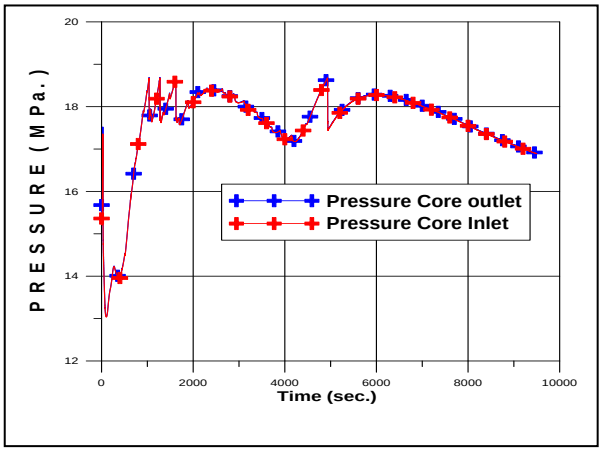


FIGURE 4. Primary Pressure

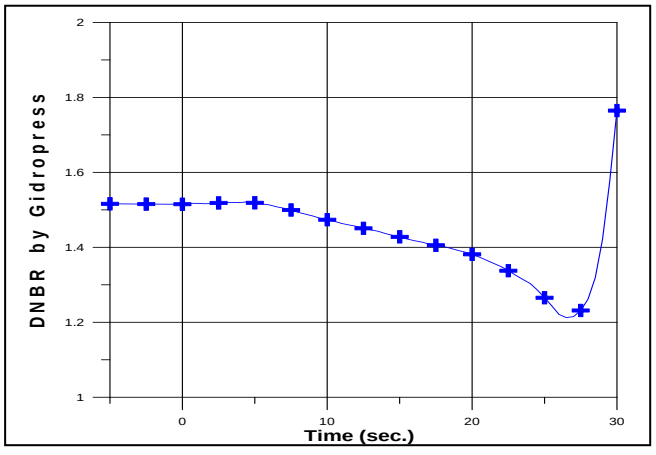


FIGURE 5. DNBR by Gidropress Correlation

## 4. CONCLUSIONS

The maximum pressure of the primary and secondary circuit reached is 18.6 MPa and 8.27 MPa respectively during the whole transient (Figure.4 & Figure.3) which is within acceptable limits based on brittle failure resistance of the reactor vessel and other components of the reactor coolant system.

The primary reactor coolant system was maintained in cooling down state during short-term and long-term periods of time by settling a stable coolant flow rate in the primary circuit due to natural circulation. Absence of DNB for all fuel rods with probability of 95% at confidence level of 95% was observed as minimum DNBR reached during the whole transient is 1.2 (Figure.5).

Maximum fuel rod claddings temperature reached is 362.0 ºC (Figure.6) which indicate absence of any fuel clad damage. Temperature of the fuel (Figure.7) did not exceed significantly during the transient thereby avoiding any local fuel melting and fuel damage. Analysis of the conditions was performed with disregard for operator's actions and showed that safety systems with taking principle of single failure into consideration are capable to overcome the accident consequences.

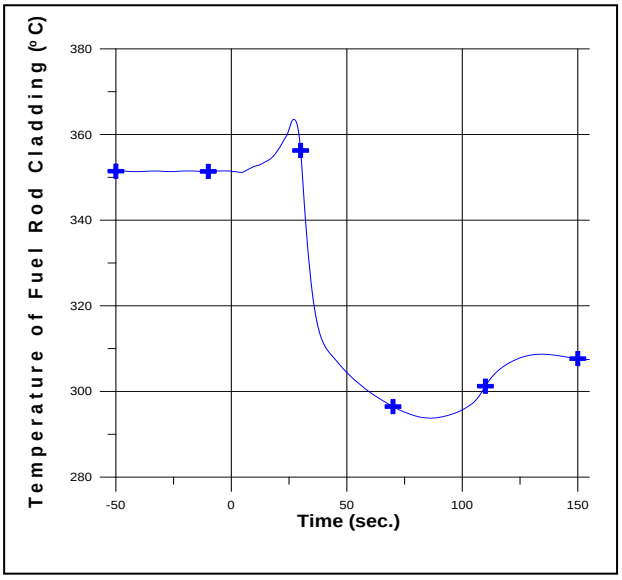


FIGURE. 6. Fuel Rod Cladding temperature

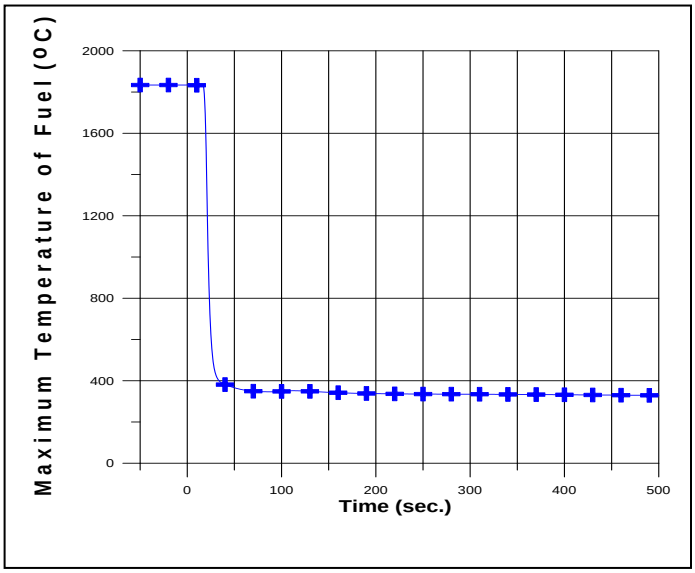


FIGURE. 7. Maximum Fuel temperature

## REFERENCES

[1] V. H. Ransom et al., *RELAP5/MOD2 Code Manual, Volume 1: Code Structure, System Models,and Solution Methods*, NUREG/CR-4312, EGG-2396, August 1985.

[2] American National Standard for Decay Heat Power in Light Water Reactors, "ANSI/ANS-5.1" (1979)."

[3] KKNPP-3&4 Preliminary Safety Analysis Report (PSAR), *Accident Analysis*, Section 15.2.8, Rev.0, August 2016.

Fifth International Conference on Computational Methods for Thermal Problems
THERMACOMP2018, July 9-11, 2018, Indian Institute of Science, Bangalore, INDIA
*N. Massarotti, P. Nithiarasu, Pradip Dutta and C. Ranganyakalu (Eds.)*

# A Numerical Investigation of Heat Transfer Enhancement in Nanofluids Flow in a Parallel Plate Channel Subjected to Constant Heat Flux

**Saptarshi Mandal**, **P.S. Ghoshdastidar***
Department of Mechanical Engineering,
Indian Institute of Technology Kanpur
Kanpur, U.P. 208016 INDIA
*Corresponding Author. E-Mail: psg@iitk.ac.in

ABSTRACT

This paper presents a finite-difference based numerical investigation of heat transfer in Alumina-water and Titania-water nanofluids flow between parallel plates subjected to constant equal/unequal heat fluxes, based on homogeneous and heterogeneous flow models. Stream function-Vorticity approach has been used to solve the problem. It is found that the nanofluids give rise to larger enhancement factor (the ratio of local heat transfer coefficient in nanofluid to that in base fluid) when both base fluid and nanofluid flows have equal Reynolds number. On the other hand, the enhancement factor is very small or even less than one when both base fluid and nanofluid flows have equal inlet velocity. Brownian diffusion and Thermophoresis are found to have negligible effects on the temperature profiles. On the whole, Alumina-Water nanofluid gives rise to greater enhancement in heat transfer coefficient as compared to Titania-Water nanofluid.

**Keywords:** Nanofluid, Parallel Plate Flow, Homogeneous Model, Buongiorno Model, Particle Migration, Brownian Diffusion, Thermophoresis

## 1. INTRODUCTION

Nanofluids are engineered colloids in which nanoparticles of 1-100 nm diameter are stably dispersed in a base fluid. They have abnormally high thermal conductivity and viscosity with respect to the base fluid. Three nanofluids models that are widely found in literature are: (i) Homogeneous Flow Model [1], (ii) Dispersion Model [2], and (iii) Non-homogeneous Flow Model [3]. The *homogeneous flow model* assumes that the mass, momentum and energy equations are directly applicable for the nanofluid with the thermophysical properties based on bulk weighted volume fraction of nanoparticles with no slip between base fluid and nanoparticles. The *dispersion model* says that the enhancement of heat transfer is achieved due to higher thermal conductivity and energy carried by the dispersion of nanoparticles. The *Non-homogeneous flow model* proposed by Buongiorno [3] considers slip between base fluid and nanoparticles mainly due to the two slip mechanisms such as Brownian diffusion and thermophoresis.

Although several works on heat transfer in the tube flow of nanofluids [4-6] have been found in literature, the same for parallel plates are scanty. Recently, Rossi di Schio et al. [7] used the Buongiorno model to investigate by the finite element method steady, laminar heat transfer in parallel plate flow of nanofluids with wall temperature varying linearly and periodically. The authors found that in the case of linearly varying wall temperature nanoparticle concentration influenced the temperature distribution very little. On the contrary, the periodically varying wall temperature gave rise to non-homogeneities in the nanoparticle concentration, and hence, the use of homogeneous model would not be appropriate.

## 2. OBJECTIVES

The objectives of the present work are: (a) to see the variation of enhancement factor (the ratio of heat transfer coefficient in nanofluid to that in base fluid) along the length of the channel based on the heterogeneous flow model of Buongiorno [3] in which temperature dependent viscosity and thermal conductivity are considered as

well as the homogeneous flow model of Choi [1] in which the aforesaid properties are taken as independent of temperature; and (b) to carry out a detailed parametric study with nanoparticle concentration as the variable keeping same Re (Re is based on the spacing between the walls) and same inlet velocity for both nanofluid and base fluid.

## 3. PROBLEM FORMULATION AND SOLUTION METHODOLOGY

Figure 1 shows the physical problem and the coordinate system. The velocity, temperature and nanoparticle concentration are uniform at the inlet. The flow is laminar, steady and 2D. Stream function-Vorticity approach has been used since the problem is two-dimensional and pressure calculation is not required in this study. The *False Transient Method* using pure implicit finite-difference scheme has been applied to solve the coupled governing eqs. (1) - (4) simultaneously. Constant heat flux boundary condition has been used for the energy equation. Walls are considered to be impermeable with no mass flux across the boundaries. The flow, heat and mass transfer are considered to be fully developed at the exit. While the length of the domain is taken as 1 m the gap between plates is 3 mm (0.003 m). Four different wall heat flux ratios $q''_{w2}/q''_{w1}$ such as 1.0, 1.5, 0.5 and 0 have been used ($q''_{w1} = 5000$ W/m$^2$). The diameter of the nanoparticles is considered to be 15 nm. Thermal conductivity and viscosity are calculated based on the correlations of Buongiorno [3] developed from Pak and Cho [6]. Alumina-Water and Titania-Water nanofluids with volume fractions ranging from 1% to 5%, are investigated in this study. The non-dimensional parameters and the governing equations are given below.

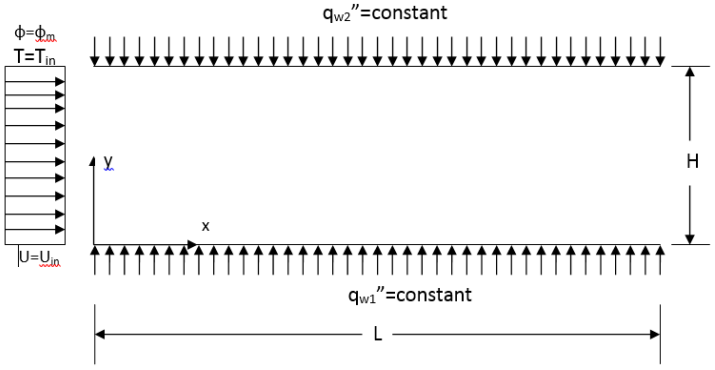


**Fig.1** The physical problem and the coordinate system

Non-dimensional parameters are defined as follows:

$$\Omega^* = \frac{\Omega H}{U_o},\ \Psi^* = \frac{\Psi}{U_o H^2},\ \theta = \frac{T - T_i}{q''_{w_1} H / \mu_{nf,o}},\ \phi^* = \frac{\phi}{\phi_m},\ x^* = \frac{x}{H},\ y^* = \frac{y}{H},\ t^* = \frac{U_o t}{H},\ V_r^* = \frac{V_r}{U_o},\ V_z^* = \frac{V_z}{U_o},\ \left(D_T/T\right)^* = \frac{D_T/T}{D_{T_o}/T_i},$$

$$D_B^* = D_B/D_{B_o},\ \mu_{nf}^* = \mu_{nf}/\mu_{nf,o},\ k_{nf}^* = k_{nf}/k_{nf,o}$$

The following non-dimensional numbers are used:

$$\mathrm{Re} = \frac{\text{Inertia Force}}{\text{Viscous Force}} = \frac{\rho_{nf,o} U_o H}{\mu_{nf,o}},\quad \mathrm{Pr} = \frac{\textit{momentum diffusivity}}{\text{thermal diffusivity}} = \frac{\nu_{nf,o}}{\alpha_{nf,o}},\ Le = \frac{\text{Thermal Diffusivity}}{\text{Brownian Diffusivity}} = \frac{k_{nf,o}}{\rho_p c_{p,p} D_{Bo} \phi_o},$$

$$Sc = \frac{\text{Momentum Diffusivity}}{\text{Brownian Diffusivity}} = \frac{\nu_{nf,o}}{D_{B_o}},\quad N_{BT} = \frac{\text{Brownian Diffusivity}}{\text{Thermophoretic Diffusivity}} = \frac{\rho_p c_{p,p} D_{B_o} \phi_o k_{nf,o}}{D_{T_o} q''_{w_1} H}$$

Brownian and thermophoretic diffusion coefficients are described as:

$$D_{Bo} = \frac{k_B T_i}{3\pi \mu_{bf} d_p},\ D_{To} = \beta \frac{\mu_{bf}}{\rho_{bf}} \phi_o \qquad \text{where } \beta = \frac{0.26 k_{bf}}{2k_{bf} + k_p}$$

**Stream function equation**

$$\frac{\partial^2 \psi^*}{\partial x^{*2}} + \frac{\partial^2 \psi^*}{\partial y^{*2}} = -\Omega^* \tag{1}$$

**Vorticity transport equation**

$$\frac{\partial \Omega^*}{\partial t^*} + u^* \frac{\partial \Omega^*}{\partial x^*} + v^* \frac{\partial \Omega^*}{\partial y^*} = \frac{\mu^*_{nf}}{\mathrm{Re}} \left( \frac{\partial^2 \Omega^*}{\partial x^{*2}} + \frac{\partial^2 \Omega^*}{\partial y^{*2}} \right) + \frac{2}{\mathrm{Re}} \left( \frac{\partial \mu^*_{nf}}{\partial x^*} \frac{\partial \Omega^*}{\partial x^*} + \frac{\partial \mu^*_{nf}}{\partial y^*} \frac{\partial \Omega^*}{\partial y^*} \right) - \frac{4}{\mathrm{Re}} \frac{\partial^2 \mu^*_{nf}}{\partial x^* \partial y^*} \frac{\partial^2 \psi^*}{\partial x^* \partial y^*} + \frac{1}{\mathrm{Re}} \left( \frac{\partial^2 \psi^*}{\partial y^{*2}} - \frac{\partial^2 \psi^*}{\partial x^{*2}} \right) \left( \frac{\partial^2 \mu^*_{nf}}{\partial x^{*2}} - \frac{\partial^2 \mu^*_{nf}}{\partial y^{*2}} \right) \tag{2}$$

**Nanoparticle continuity equation**

$$\frac{\partial \phi^*}{\partial t^*} + u^* \frac{\partial \phi^*}{\partial x^*} + v^* \frac{\partial \phi^*}{\partial y^*} = \frac{D^*_B}{\mathrm{Re}\, Sc} \left( \frac{\partial^2 \phi^*}{\partial x^{*2}} + \frac{\partial^2 \phi^*}{\partial y^{*2}} \right) + \frac{1}{\mathrm{Re}\, Sc} \left( \frac{\partial D^*_B}{\partial x^*} \frac{\partial \phi^*}{\partial x^*} + \frac{\partial D^*_B}{\partial y^*} \frac{\partial \phi^*}{\partial y^*} \right) + \frac{D^*_T}{\mathrm{Re}\, Sc N_{BT}} \left( \frac{\partial^2 \theta}{\partial x^{*2}} + \frac{\partial^2 \theta}{\partial y^{*2}} \right) + \frac{1}{\mathrm{Re}\, Sc N_{BT}} \left( \frac{\partial D^*_T}{\partial x^*} \frac{\partial \theta}{\partial x^*} + \frac{\partial D^*_T}{\partial y^*} \frac{\partial \theta}{\partial y^*} \right) \tag{3}$$

**Energy equation**

$$\frac{\partial \theta}{\partial t^*} + u^* \frac{\partial \theta}{\partial x^*} + v^* \frac{\partial \theta}{\partial y^*} = \frac{k^*_{nf}}{\mathrm{Re}\, \mathrm{Pr}} \left( \frac{\partial^2 \theta}{\partial x^{*2}} + \frac{\partial^2 \theta}{\partial y^{*2}} \right) + \frac{1}{\mathrm{Re}\, \mathrm{Pr}} \left[ \frac{\partial k^*_{nf}}{\partial x^*} \frac{\partial \theta}{\partial x^*} + \frac{\partial k^*_{nf}}{\partial y^*} \frac{\partial \theta}{\partial y^*} \right] + \frac{D^*_B}{\mathrm{Re}\, \mathrm{Pr}\, Le} \left[ \frac{\partial \phi^*}{\partial x^*} \frac{\partial \theta}{\partial x^*} + \frac{\partial \phi^*}{\partial y^*} \frac{\partial \theta}{\partial y^*} \right] + \frac{D^*_T}{\mathrm{Re}\, \mathrm{Pr}\, Le N_{BT}} \left[ \left( \frac{\partial \theta}{\partial x^*} \right)^2 + \left( \frac{\partial \theta}{\partial y^*} \right)^2 \right] \tag{4}$$

## 4. RESULTS AND DISCUSSION

Figure 2 shows the comparison of non-dimensional analytical and numerical temperature distributions at the channel exit for the wall heat flux ratio of 1.5 and inlet Re = 500, for pure fluid. Note that $T^* = (T_{w1} - T)/(T_{w1} - T_m)$, where $T_m$ is the mean fluid temperature. The slight difference between analytical and the present solution may be attributed to the consideration of temperature dependence of the thermophysical properties in the latter. Figure 3 reveals that far downstream heat transfer coefficient in alumina-water nanofluid can fall below that in base fluid thus giving rise to enhancement factors less than 1. It is also noted that Buongiorno model predicts lower enhancement in the fully developed region as compared to homogeneous model. A similar trend is also seen for titania-water nanofluid. Figure 4 demonstrates that the same nanofluid which gives rise to higher enhancement for the case of same Re (Re =1000) in both base and nanofluids flow, produces lower enhancement in the case of equal inlet velocity (0.3 m/s) in both base and nanofluids flow. This is due to the fact that if nanofluid and base fluid have to flow at the same Re, then due to higher viscosity of nanofluid it has to flow at much higher inlet velocity to achieve the same Re. For the same inlet velocity, Re for alumina-water is 268 and for titania-water it is 756. However, alumina-water always produces higher enhancement in heat transfer coefficient as compared to titania-water.

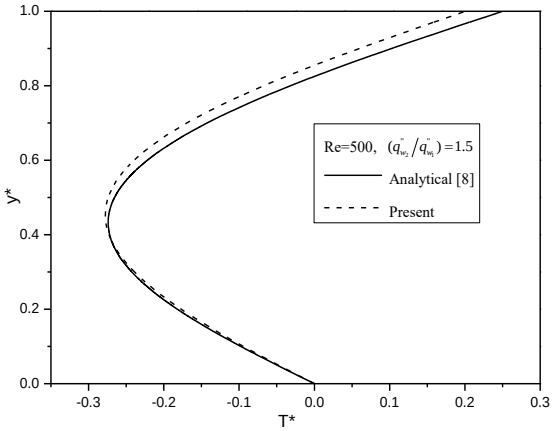


**Fig. 2** Validation of the numerical (present) with the analytical solution for pure fluid at Re=500 and wall heat flux ratio=1.5

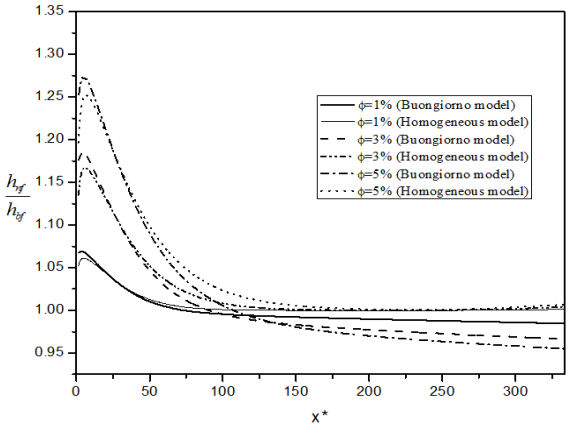


**Fig. 3** Comparison of enhancement factors for alumina-water nanofluid at Re = 100 and wall heat flux ratio = 1, based on homogeneous and Buongiorno models

Figure 5 clearly depicts the effects of thermophoresis. At the wall heat flux ratio of 0.5, since the heat flux at the upper wall is half of that at the lower wall, the nanoparticles migrate towards the upper wall causing higher viscosity near the upper wall, which result in slower motion of the alumina-water nanofluid there and subsequent reduction in heat transfer coefficient, and consequently, less percent enhancement as compared to that at the lower wall. The opposite is true for the case of wall heat flux ratio of 1.5.

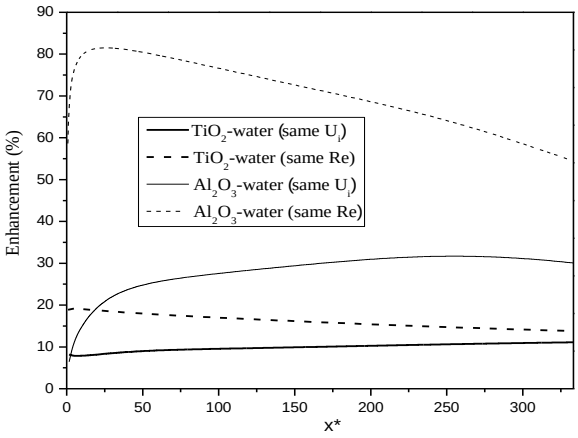


**Fig. 4** Comparison of percent enhancement in heat transfer coefficient at same inlet velocity ($U_i$=0.3 m/s) and same Reynolds number (Re=1000) for alumina-water and titania-water nanofluids at wall heat flux ratio=1

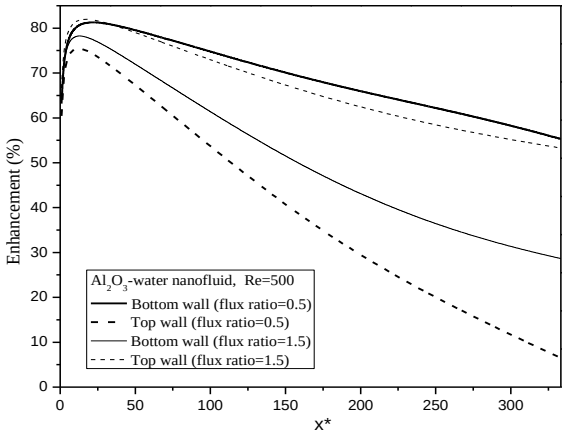


**Fig. 5** Heat transfer enhancement at the top and bottom walls at different wall heat flux ratios

## 4. CONCLUSIONS

It can be concluded from the present numerical study that the difference between the enhancement factors based on the homogeneous and heterogeneous models is marginal, enhancement in heat transfer coefficient computed from the homogeneous model being slightly higher. The nanoparticle migration effect due to Brownian diffusion and thermophoresis on the heat transfer is visible, but not significant. A nanofluid which gives higher enhancement in heat transfer coefficient for equal inlet Reynolds number for both base and nanofluids, produces much lower enhancement for the case of equal inlet velocity for both base and nanofluids.

## REFERENCES

[1] S. Choi, Enhancing thermal conductivity of fluids with nanoparticles, *Developments and Applications of Non-Newtonian Flows*, D.A. Siginer, and H.P. Wang, eds., ASME, New York, FED-Vol. 231/MD-Vol.66, 99-105, 1995.

[2] Y. Xuan, and W. Roetzel, Conceptions for heat transfer correlation of nanofluids, *International Journal of Heat and Mass Transfer*, 43, 3701-3707, 2000.

[3] J. Buongiorno, Convective transport in nanofluids, *ASME Journal of Heat Transfer*, 128, 240-250, 2006.

[4] B. C. Pak, and Y. I. Cho, Hydrodynamic and heat transfer study of dispersed fluids with submicron metallic oxide particles, *Experimental Heat Transfer*, 11,151-170, 1998.

[5] D. Wen, and Y. Ding, Experimental investigation into convective heat transfer of nanofluids at the entrance region under laminar flow conditions, *International Journal of Heat and Mass Transfer*, 47, 5181-5188, 2004.

[6] A. T. Utomo, E. B. Haghighi, A. I. T. Zavareh, M. Ghanbarpourgheravi, H. Poth, R. Khodabandeh, B. Palm, A. W. Pacek, The effect of nanoparticles on laminar heat transfer in a horizontal tube, *International Journal of Heat and Mass Transfer*, 69, 77-91, 2014.

[7] E. Rossi di Schio, M. Celli, and A. Barletta, Effects of Brownian diffusion and thermophoresis on the laminar forced convection of a nanofluid in a channel", *ASME Journal of Heat Transfer*, 136 (2), p. 022401, 2014.

[8] J. Sheela Francisca, and C. P. Tso, Viscous dissipation effects on parallel plates with constant heat flux boundary conditions, *International Communications in Heat and Mass Transfer*, 36, 249-254, 2009.

# Modeling of Boiling Heat Transfer in Microchannel for Nonuniform Heat Input

**R K Sarangi and S K Nayak**

School of Mechanical Engineering, KIIT Univeristy, Bhubaneswar, Odisha, India,
sarangi_radhakanta@yahoo.co.in sknayakfme@kiit.ac.in

## ABSTRACT

In this paper, modeling studies on two-phase forced convection in microchannels using water as the fluid medium have been reported. Model, results have been shown for homogeneous flow boiling. The governing equations have been solved to predict the boiling front, pressure drop and thermal resistance as functions of exit pressure and heat input. The model has been specially used to study the effects of non-uniform heat input along the flow direction. The results show that the nonuniform power map can have a very strong effect on the overall fluid dynamics and heat transfer.

**Key Words:** *Flow boiling, Heat transfer, Homogeneous flow model, Pressure drop, Two phase flow*

## 1. INTRODUCTION

A range of MEMS devices, such as VLSI coolers, micro-rockets, chemical reactors utilize heat transfer phenomena of liquid-gas phase change, in microchannels. The benefits of high heat transfer coefficients and high heat carrying capacity through latent heat transport come at a penalty of high pressure drop. The boiling front needs to be determined first, for predicting the pressure drop and heat transfer coefficient in flow boiling through microchannel. There is always a degree of wall super heat for boiling to start. In the present modeling, wall super heat is not considered and it is assumed that boiling starts instantly.

Pressure drop characteristics of microchannels have been investigated by various researchers. According to them, there is an early transition and magnitude of pressure drop is higher than the pressure drop predicted by Poiseuille law. In the present model, Reynolds number falls in the range of 100 hence, laminar flow is assumed and traditional Poiseuille law is used for calculating the pressure drop. Due to the presence of laminar boundary layer and perhaps a vastly bubble generation mechanism within a microchannel, its flow boiling characteristics is different Watel [1]. In the present model, considering laminar flow, heat transfer coefficient in single phase flow is calculated by constant Nusselt number relation for constant heat flux boundary condition and in two phase flow, it is calculated by correlations. The effect of non-uniform heat flux in microchannel has been investigated experimentally by Rirchey *et al*. [2] and Alam *et al*. [3]. They concluded that, in non uniform heat flux input pressure drop and heat transfer characteristics are different from uniform heat flux input. In the research work of Sarangi *et al*. [4], boiling front, wall temperature and film temperature have been investigated for homogeneous flow model in uniform heat flux input. This paper investigates, boiling heat transfer in microchannels for non-uniform heat flux in case of, homogeneous flow.

## 2. PRESSURE DROP AND HEAT TRANSFER CALCULATIONS

As the mass flow rate is small and tube hydraulic diameter is also very small, Reynolds number is always less than 100 and flow is laminar. So, pressure drop in single phase is determined by

Haygen-Poiseuille law. Two phase pressure drop is determined by following equation in homogeneous flow like Sarangi *et al*. [4].

$$\frac{dp}{dz} = \frac{f_{2\phi} m''^2}{2\rho d_{he}} + \frac{1}{A_{CH}} \frac{d}{dz}\left( \frac{m''^2 A_{CH}}{\rho} \right) \quad \ldots(1)$$

where $f_{2\Phi}$ is the two-phase friction factor, m" is the mass flux, $A_{CH}$ is the channel cross sectional area and $d_{he}$ denotes the hydraulic diameter of the channel. Due to very high pressure drops across the microchannel, the thermo-physical properties like μ and $h_{fg}$ of the fluid undergo appreciable changes. Hence, these properties need to be included in Eq. (1) as functions of pressure. The Cicchitti relation (Eq. 2) is used for evaluating the average viscosity of the liquid vapor mixture.

$$\mu_{2\phi} = x\mu_g + (1-x)\mu_f \quad \ldots(2)$$

where x is the quality of the liquid vapor mixture and the subscripts f and g denote the liquid and vapor phases respectively. Using water as the working fluid, simple curve fitting regression exercise can be conducted to obtain relations that can be used to determine these properties as functions of pressure and/or saturation temperature. This, however, complicates the equation, which no longer remains amenable to analytical solutions and has to be solved numerically using the finite difference method.

$$\frac{dp}{dz} = \frac{p_n - p_{n-1}}{dz} = \frac{1}{\frac{10^6 m^2 x_e z_n}{5.672 w^2 d^2 l} p_n^{-2} - 1}\left[ \frac{16.49 m x_e}{w d l d_{he}^{\,2}} z_n p_n^{-0.8445} + \frac{0.000357 6m}{w d d_{he}^{\,2}} p_n^{-0.2842} + \frac{10^6 m^2 x_e}{5.672 w^2 d^2 l} p_n^{-1} \right] \quad \ldots(3)$$

Equation (3) gives the pressure profile in the two-phase flow region. Here $p_n$ denotes the pressure at location $z_n$ (nth node) while w, d, l and dhe are the width, depth, length and hydraulic diameter of the microchannel respectively. If the exit quality ($x_e$) is less than 1, the entire region corresponds to saturation condition. Hence the Clausius-Clapeyron equation can be used to determine the fluid temperature profile. The intersection point of this profile with that for the single phase region gives the boiling front ($z_c$) which can then be used for calculating the total pressure drop across the channel. The above exercise also gives the temperature variation of the fluid along the channel, which, in turn is used for calculating the wall temperatures as described below.

The second part of the analysis involves the determination of heat transfer and hence wall temperature profile along the channel during flow through these microchannels. The energy equations can be written as

$$\frac{d}{dz}\left( k_w A_w \frac{dT_w}{dz} \right) - \eta h_{conv} p (T_w - T_f) - \frac{w(T_w - T_f)}{R_{conv}} + q'' w = 0 \quad \ldots(4)$$

$$m\frac{dh_f}{dz} - \eta h_{conv} p (T_w - T_f) = 0 \quad \ldots(5)$$

where $T_w$ and $T_f$ denote the wall and fluid temperatures respectively, Aw is the base area, q" is the heat flux, η is the microchannel fin efficiency and hf is the fluid enthalpy. The first term in the LHS of Eq. (4), which captures the effects of spreading in the base of the microchannel, is neglected in our analysis. For the convective heat transfer coefficient (hconv), the correlation of Kandlikar [5] for homogenous flow boiling through a tube is used.

$$h_{conv} = h_l \left[ C_1 Co^{C_2} (25 Fr_{le})^{C_5} + C_3 Bo^{C_4} F_k \right] \quad \ldots(6)$$

Here $h_l$ is the heat transfer coefficient for single phase flow given by and constants C1 – C5 can be found from standard look-up tables for water. The constant $F_k$ is a fluid dependent parameter and is

equal to 1 for water. Co, Bo and Fr are convective, boiling and Froude number respectively. The wall temperature can be found out easily using

$$T_w = T_f + \frac{q}{h_{conv}(wl + \eta 2dl)} \quad \ldots(7)$$

## 3. RESULT AND DISCUSSION

The model is extended to study the effects of non-uniform heat input along the flow direction. The heat flux was made to vary spatially along z. The results show that a nonuniform power map can have a very strong effect on the overall fluid dynamics and heat transfer. The thermal resistance for non-uniform heating can be higher or lower than the uniform heating case depending on the location of the hot spot and the boiling front. For analyzing the non uniform heat flux channels four case studies are considered. The representative plots are shown in the following figures(Fig. 2 to Fig.5) where the channel cross-section is taken as 300μm x 300μm while its length is 10 mm. The flow rate of water was 0.31ml/min and the outlet pressure was held at 1.0132 bar for all these cases. The inlet temperature of water was maintained at 70ºC. The total heat input given to the channel was 2.5 W, which was distributed non-uniformly along the length. It was assumed that 90% of the heat (2.25W) is concentrated along one third of the channel (3.33mm) while the remaining 10% (0.25W) was distributed over 6.67 mm in various combinations.

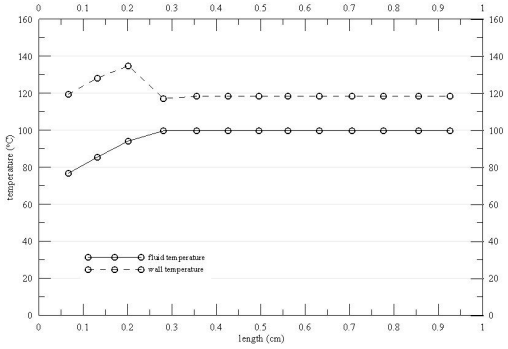


Fig. 2: Wall and film temperature variation (Uniform heating case)

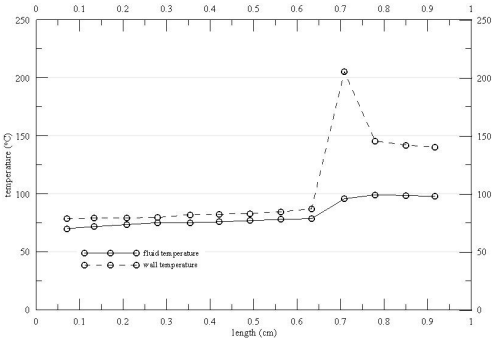


Fig. 3: Wall and film temperature variation (Hot spot towards downstream)

The maximum wall temperatures are 205.5ºC and 200.4ºC. Fig. 5 shows that the maximum wall temperature is 199ºC. Here it is important to note that even the liquid enters high heat flux region, there is no appreciable temperature rise compared to the cases of Fig.3 and Fig.4. This is because in Fig.5, the boiling starts much earlier than that of Fig.3 and Fig. 4. Also uniform heat flux case is considered in Fig.2. In Fig. 3 and Fig.4 the hot spot is located in the downstream section. Thus, the liquid enters in the low heat flux region and is already in the two-phase domain before it reaches the

hot spot. Since the heat transfer coefficient in two-phase flow is orders of magnitude higher than in single phase, the wall temperature remains within allowable limits.

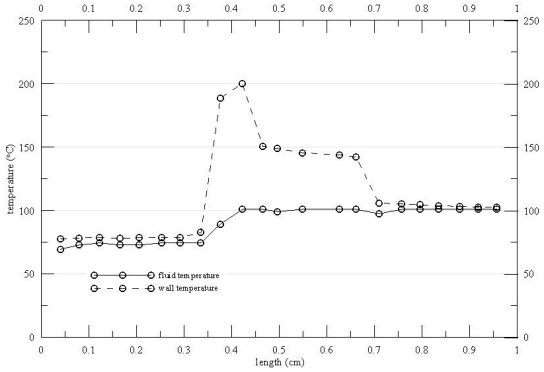


Fig. 4: Wall and film temperature variation (Hot spot at central location)

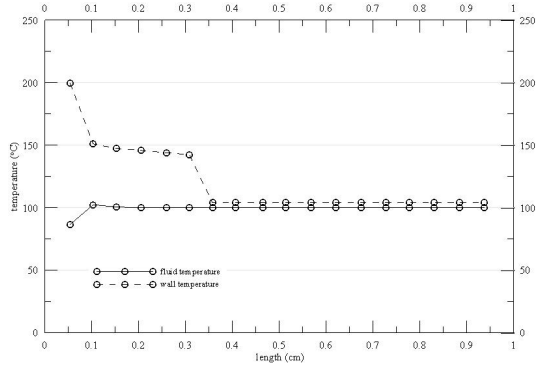


Fig. 5: Wall and film temperature variation (Hot spot towards upstream side)

## 6. CONCLUSIONS

Boiling fronts have been predicted for non uniform heat flux channels by homogeneous flow model. The results show that, the boiling front, pressure drop, wall temperature and film temperature are strong functions of heat flux distribution, mass flow rate and channel dimension. The model can be used for optimum design of channels for effective heat transfer and minimum pressure drop. Hot spots can be located by analyzing the wall temperature variations along the channel. The present numerical model can be refined for more accurate results.

## REFERENCES

[1] Watel, Review of Saturated Flow Boiling in Small Passage of Compact Heat Exchangers, *Int. Journal of Thermal Sciences*, 42,107-140, 2003.

[2]. N. S. Ritchey, A Justin, Weibel and S. V. Garimella, Local measurement of flow boiling heat transfer in an array of non-uniformly heated microchannels, *International Journal of Heat and Mass Transfer,* 71, 206–216, 2014.

[3] T. Alam, P. S. Lee, R. Christopher, Yap and L. Jin, A comparative study of flow boiling heat transfer and pressure drop characteristics in microgap and microchannel heat sink and an evaluation of microgap heat sink for hotspot mitigation, *International Journal of Heat and Mass Transfer,* 58, 335–347, 2013.

[4] R. K. Sarangi, A. Bhattacharya, R. S. Prasher, Numerical Modeling of Boiling Heat Transfer in Micro Channel, *Applied Thermal Engineering* , 29, 300-309, 2009.

[5] Kandlikar, S.G., Fundamental Issues Related to Flow Boiling in Microchannels, *Experimental Thermal and Fluid Scheme*, 26, 389-407, 2002.

Fifth International Conference on Computational Methods for Thermal Problems
THERMACOMP2018, July 9-11, 2018, Indian Institute of Science, Bangalore, INDIA
*N. Massarotti, P. Nithiarasu, Pradip Dutta and C. Ranganyakalu (Eds.)*

# EXCITATION OF A LAMINAR SEPARATION BUBBLE AND HEAT TRANSFER CHARACTERISTICS: A LARGE-EDDY SIMULATION

**H. Babu and S. Sarkar**
Department of Mechanical Engineering,
Indian Institute of Technology Kanpur,
Kanpur, 208016, India
E-mail: subra@iitk.ac.in

## ABSTRACT

In this paper, effects of inlet free-stream turbulence (*fst*) are described to highlight the physics of transition and heat transfer due to a laminar separation bubble (LSB) through Large-eddy simulations (LES). Two kinds of inlet perturbations are imposed: one with a deterministic frequency and other being a band of frequencies to manifest the *fst*. The LES resolves the instability of the shear layer and its breakdown forming large- and energetic small-scale structures, which retain their appearance far downstream. When compared with the literature, it suggests that the excitation of boundary layer (BL) and thus, history of transition are sensitive to the imposed perturbations, although time-averaged flow features are similar.

**Key Words:** *Laminar Separation Bubble, LES, Transition, Heat Transfer.*

## 1. INTRODUCTION

A laminar BL over a solid surface occasionally separates under the influence of an adverse pressure gradient or sudden change of curvature, undergoes transition due to amplification of *fst*, becomes turbulent and finally reattaches to form a LSB. Typically associated with low to moderate Reynolds number (*Re*), LSB may be observed near the leading edge of an aerofoil, on a high-lift gas turbine blade, small-scale wind turbines and on wings of small unmanned aerial vehicles. Further, LSB dictates the evolution of downstream BL adversely affecting the stall characteristics of an aerofoil. Thus, studies of such flows are of immense importance due to practical applications apart from academic interests.

Figure 1 shows the schematic of a LSB formed near the leading edge following the work of Horton (1968). First half of the bubble, referred as 'Dead-air' region, contains almost stationary fluid and is associated with an almost constant pressure distribution. Near the reattachment, the bubble contains a region of strong re-circulating flow, attributing to the 'Reverse flow vortex' and a strong pressure gradient. A number of studies [1-6] have been conducted to illustrate the transition of a LSB. Most of the studies elucidate that transition of a separated BL occurs in a similar fashion of free shear layer with high receptivity to perturbations. Amplification of certain selective frequencies of background disturbances is observed leading to the formation of Kelvin-Helmholtz (K-H) rolls and shedding of large-scale vortices in the vicinity of reattachment.

There are evidences that transition of a laminar separated BL occurred via oblique modes and Λ-vortex induced breakdown resulting in turbulent reattachment [7]. A secondary instability was seen in the second-half of the bubble with a considerable growth of three-dimensional motions and evolution of hairpins attributing to breakdown [8]. Recently, Samson and Sarkar [9] investigated the transition of separated BL over a modelled aerofoil for different *Re* and *fst*. Anand and Sarkar [10] studied effects of angle of attack (α). The shear layer was unstable through K-H instability for low *fst*, whereas, the primary K-H instability was bypassed for high *fst* and larger α.

In spite of several studies made on the excitation of a LSB, there are uncertainties in understanding transition under different flow conditions. In reality, transition mechanism includes the following features, i.e. receptivity, linear growth of disturbance and then non-linear effects followed by breakdown. Here, flow past a thick flat plate with a semi-circular leading-edge is considered, where *Re* based on inlet velocity and leading edge diameter (*D*) is 3450. The objective of the paper is to demonstrate the transition, growth of three-dimensional motions and unsteady heat-transfer for different *fst* manifested by two different kinds of imposed inlet perturbations: One with a deterministic frequency (referred by S) and other being a band of frequencies (denoted by R).

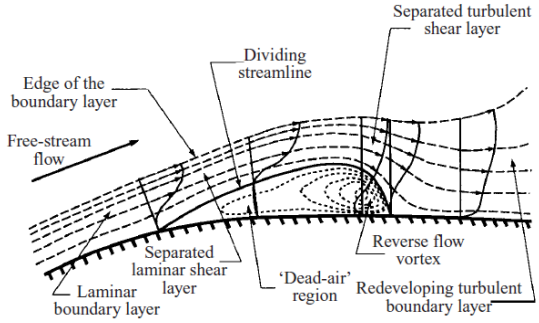


Figure 1. Mean flow structure of a laminar separation bubble.

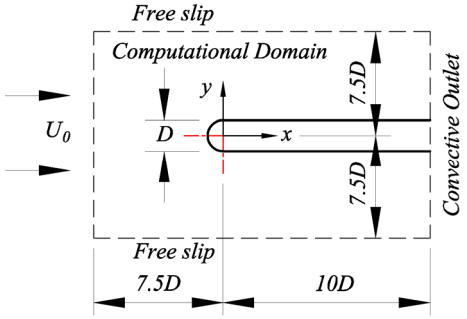


Figure 2. Schematic of the computational domain and the boundary conditions imposed.

## 2. COMPUTAIONAL DETAILS

The three-dimensional (3D) unsteady Navier-Stokes equations along with energy equation are solved for Newtonian incompressible flow in Cartesian coordinate system. A dynamic subgrid-scale (SGS) model proposed by Germano et al. [11] and modified by Lilly [12] is used to model the stress tensor and temperature flux, which represent the effect of subgrid motion on the resolved field of LES. The solver used in the present simulation has been extensively validated for variety of transitional and turbulent flows [5, 13, 14].

The schematic of the computational domain is illustrated in Fig. 2, where, the z-span used in the simulation is 2.0*D* following previous experience and the literature [8]. The length and velocity scales are normalized with respect to leading edge diameter *D* and inlet velocity $U_0$. Similarly, the temperature *T* is scaled by inlet temperature $T_0$ and surface temperature $T_b$ to obtain the non-dimensional temperature as $(T - T_0)/(T_b - T_0)$. The energy equation is solved by taking a Prandtl number of 0.7. To resolve the leading edge in Cartesian geometry, the Immersed Boundary (IB) method is used here to apply the boundary conditions, where the geometry is non-conformal to the grid [15]. The velocity and temperature field near the boundary of the body is modified at each step such that the no-slip and isothermal wall boundary conditions are satisfied. At the inlet, a uniform streamwise velocity profile is specified, while a convective boundary condition is imposed at the exit. The spanwise direction is taken to be periodic. Free-stream boundary condition is imposed at the top and bottom boundary of the computational domain.

The grid in *z*-direction is uniform, while non-uniform grid distributions are used in *x* and *y* directions with finer resolution in the vicinity of body to resolve the BL. A mesh of 364 × 300 × 64 in the streamwise, wall normal and spanwise directions was chosen after grid refinement test. The near wall resolution at $x/l$ =2, where the flow has relaxed sufficiently to a turbulent BL is $\Delta x+ \approx 16$, $\Delta y+ \approx 1$ and $\Delta z+ \approx 9$. Based on previous work [5, 13, 14], the mesh appears sufficient to resolve the transitional flow.

It is known that a separated layer is highly receptive to *fst* changing the flow characteristics and thus the bubble length. In an experiment, different levels of *fst* may be produced by placing turbulence

grids upstream of the test piece in a wind tunnel. To mimic this effect, perturbations are imposed to the wall-normal velocity on a plane at a distance 1.0*D* upstream of the leading edge. The perturbations are applied at discrete locations, which are 0.5*D* apart in y-direction following Gaussian distribution over a streamwise distance. The perturbations are varied in both time and space, where the frequency and the spanwise wavenumber are chosen to be in the unstable range for both Blasius BL and separated shear layer.

## 3. RESULTS AND DISCUSSION

Figure 3 shows the variation of time-averaged bubble length (*l*) evaluated from surface friction coefficient for different levels of turbulence (*Tu*) from the present LES. *Tu* was calculated at a point, where it becomes maximum along the wall normal direction at the point of separation. As expected *l* reduces with increase of *Tu*. But, *l* predicted with random perturbations for the same value of *Tu* is lower than that of a sinusoidal perturbations, the trend being the same. The *l* decreases from 3.9*D* to 1.6*D* for random perturbations, while it decreases from 3.9*D* to 1.8*D* for sinusoidal perturbations as *Tu* increases from 0.07% to 2.7% indicating some dependence on the nature of inlet perturbations. Following the experiment [16], the bubble length was around 2.75*D* with *Tu* ≈ 0.2%. The present LES predict a bubble length of 2.98*D* for *Tu* = 0.34% with defined imposed frequency (S2), whereas, the bubble length is 2.77*D* for *Tu* = 0.15% with R2. Now the discussion are limited to the LES results with R2 and S2.

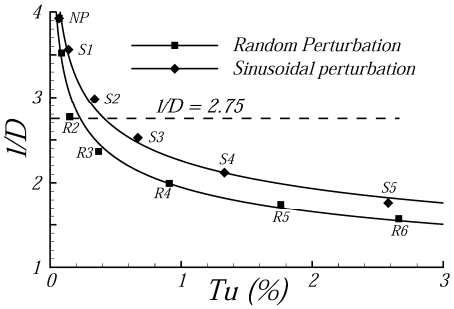


Figure 3. Variation of time averaged bubble-length (*l)* with Turbulence Intensity (*Tu*): NP denotes no imposed perturbations; S1 to S5 refer to the sinusoidal perturbations with defined frequency and R1 to R6 refer to random perturbations.

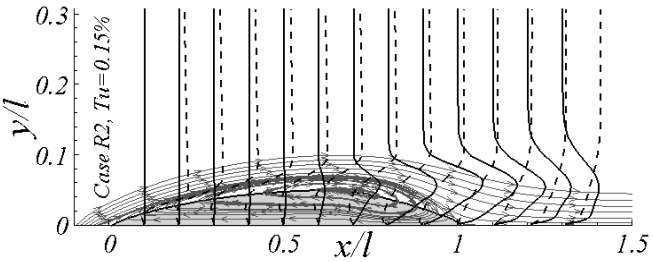


Figure 4. Profiles of $U_m$ (dotted line) and $u'_{rms}$ (solid line) superimposed over mean streamlines, indicating the development of three-dimensional motion over the separation region.

To qualitatively present the growth of 3D motion over the separation region, scaled profiles of $U_m$ and $u_{rms}$ are superimposed over contours of $U_m$ and presented in Fig. 4. The profiles are presented for the locations $x/l$ = 0.1 to 1.3 at intervals of 0.1. It is seen that the growth of $u_{rms}$ occurs in the latter half of the bubble along the outer shear layer, while it is negligibly small at the very beginning. For both R2 and S2, the maximum $u_{rms}$ occurs near the reattachment location, however there are some minor differences in $u_{rms}$ fluctuations. A double peak feature in $u_{rms}$ is seen with R2, while a single peak prevails with S2. Further downstream, the near wall turbulence slowly develops, while that in the outer shear layer is reduced. Thus, the differences in $u_{rms}$ are appreciable only in the first half of the bubble, while after reattachment the trends are similar. When compared with the experimental data of Coupland and Brierley [16], the agreement in both $U_m$ and $u_{rms}$ was good (not shown because of limited space). To illustrate the evolution of heat transfer in the separated BL, the distribution of Stanton numbers (*Sn*) is superimposed on the $C_f$ distribution (Fig. 5). A factor of $2Pr^{(2/3)}$ given by Colburn [17] is used for flow and heat transfer analogy, where Pr denotes Prandtl number. The Stanton number becomes maximum at the point where the $C_f$ is minimum, which corresponds to the breakdown of shear layer. As downstream is approached $2SnPr^{(2/3)}$ slowly drops down and approaches the value of $C_f$ illustrating an equilibrium BL.

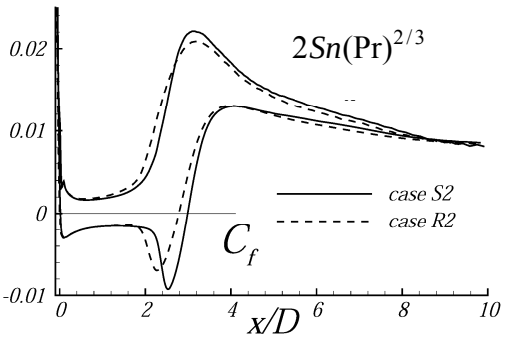


Figure 5. Streamwise variation of time-averaged skin friction coefficient ($C_f$) and Stanton number ($Sn$).

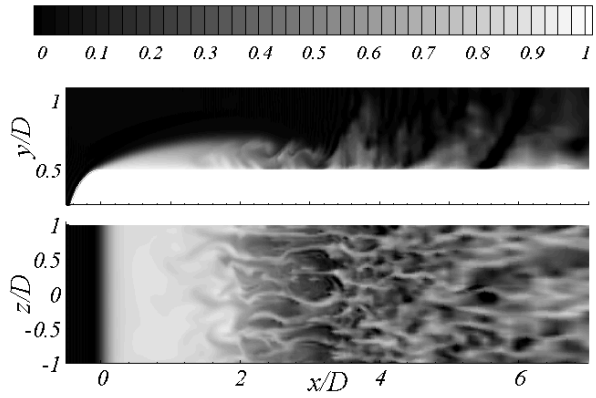


Figure 6. Details of flow structures as illustrated by the contours of instantaneous temperature for case R2 ($Tu$ = 0:15%).

Figure 6 shows the instantaneous temperature contours in the side view ($x$-$y$ plane) at mid-span and in the top view ($x$-$z$ plane) at $y$ = 0.04$D$ from top wall under R2. The contours of instantaneous temperature illustrate the internal growth mechanism of shear layer and formation of 3D flow structures. The temperature contours in the $x$-$y$ plane, illustrates that the instability of the separated shear layer is attributed to the enhanced receptivity to perturbations forming K-H rolls that break down near reattachment. 3D motions sets in downstream of $x/l$ = 0.3, followed by appearance of longitudinal streaks, which are the characteristics of transition. These streaks undergo elongation and breakdown near the reattachment forming small-scale eddies. Both the perturbations have resulted in similar effect evolving shedding of large-scale vortices that retain their identity far downstream.

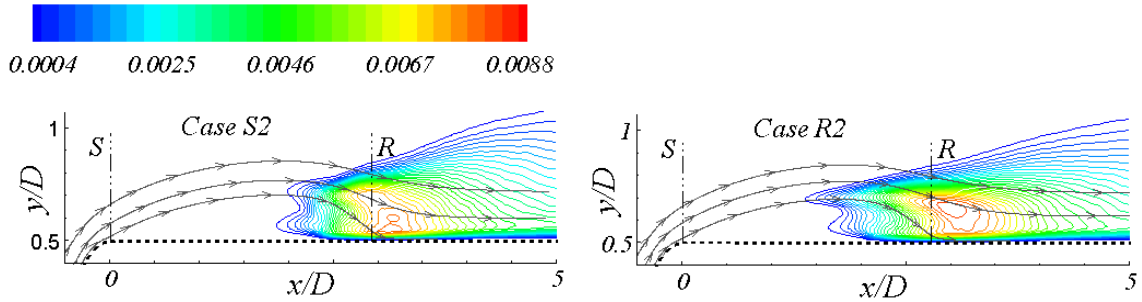


Figure 7. Contours of turbulent heat flux $\overline{v'T'}$ for case S2 and R2.

The contours of turbulent heat flux are presented in Fig. 7 for the two kinds of imposed perturbations. The flow field was allowed to evolve for fifteen primary vortex-shedding cycles and then the data were collected for statistics over the next twenty cycles. Few representative mean streamlines are shown to give an indication of the time-averaged bubble structure. The turbulence statistics on the top and bottom surfaces are symmetric and hence results are presented only for the top half. The turbulent heat flux and Reynolds stress are concentrated along the shear layer and becomes maximum in the near reattachment region. Downstream of reattachment, the peak shifts towards the wall indicating the approach to an equilibrium layer. The contours reveal the double peak nature of the turbulent heat, where the outer peak corresponds to growth in the shear layer and the inner peak refers to wall turbulence.

## 4. CONCLUSIONS

The LES resolves the instability of separation bubble and its breakdown via K-H mode resulting in large and small-scale energetic structures. It is interesting to note that the non-linear growth of

perturbations during the succession of transition is strongly influenced by the imposed inlet perturbations and its frequency. A considerable difference in first half of the bubble indicates that the transition and vortex shedding depend on the inlet disturbances. The transition and breakdown of LSB here appear more realistic with the imposed perturbations containing a band of frequencies. However, after breakdown, the time-averaged turbulence characteristics such as stresses, heat flux tensor and also integral parameters are almost indistinguishable. Further, there is a minute difference in the span-wise spacing of transition streaks in the shear layer with different inlet perturbations. Thus, transition of a LSB depends on proper inlet conditions, but after breakdown the time-averaged characteristics are not sensitive to the nature of imposed perturbations.

## REFERENCES

1. Horton, H. P., Laminar separation in two and three-dimensional incompressible flow, PhD Dissertation, University of London, 1968.
2. Watmuff, J. H., Evolution of a Wave Packet into Vortex Loops in a Laminar Separation Bubble, *J. Fluid Mech*., **397**, 119-169, 1999.
3. Robert, S. K., and Yaras, M. I., Boundary layer Transition Affected by Surface Roughness and Free-stream Turbulence, *ASME J. Fulids Eng*., **127**(3), 449-457, 2005.
4. Hain, R., Kahler, C. J., and Radespiel, R., Dynamics of Laminar Separation Bubbles at Low-Reynolds-Number Aerofoils, *J. Fluid Mech*., **630**, 129–153, 2009.
5. Sarkar. S., Identification of flow structures on a LP turbine blade due to periodic passing wakes, *ASME J. Fluids Eng.*, **130**, 061103-061103-10, 2008.
6. Spalart, P. R., and Strelets, M. K., Mechanisms of Transition and Heat Transfer in a Separation Bubble, *J. Fluid Mech*., **403**, 329-349, 2000.
7. Alam, M. and Sandham, N. D., Direct numerical simulation of short laminar separation bubbles with turbulent reattachment, *J. Fluid Mech*., **410**, 1-28, 2000.
8. Yang, Z. Y., and Voke, P. R., Large-Eddy Simulation of Boundary Layer Separation and Transition at a Change of Surface Curvature, *J. Fluid Mech*., **439**, 305–333, 2001.
9. Samson A. and Sarkar S., Effects of Free-Stream Turbulence on Transition of a Separated Boundary Layer Over the Leading-Edge of a Constant Thickness Airfoil, *ASME J. Fluids Eng*, **138** (2), 021202-021202-19, 2016.
10. Anand K. and Sarkar, S., Features of a Laminar Separated Boundary Layer near the Leading-edge of a model aerofoil for different Angles of Attack: An Experimental Study, *ASME J. Fluids Eng*, 2016.
11. Germano, M., Piomelli, U., Moin, P., Cabot, W. H., A dynamic subgrid-scale eddy viscosity model, *Physics of Fluids A*, **3**, 1760-1765, 1991.
12. Lilly, D.K., A proposed modification of the Germano subgrid-scale closure method, *Physics of Fluids A*, **4**, 633-635, 1991.
13. Sarkar, S., Babu, H., and Sadique, J., Interactions of separation bubble with oncoming wakes by LES", ASME J. Heat Transfer, **138**(2), 021703-021703-12, 2016.
14. Sarkar, S. and Sarkar Sudipto, Large-Eddy Simulation of Wake and Boundary Layer Interactions Behind a Circular Cylinder, *ASME J. Fluids Eng*, **131**, 091201, 2009.
15. Fadlun, E. A., Verzicco, R., Orlandi, P. and Mohd.-Yusof, J., Combined immersed boundary finite difference methods for three dimensional complex flow simulations, *J. Comp. Physics*, **161**, 35-60, 2000.
16. Coupland, J., Brierley, D., Transition in turbomachinery flows, Final Report, BRITE/EURAM Project AERO-CT92-0050, 1996.
17. Colburn, A. P., A method of correlating forced convection heat transfer data and a comparison with fluid friction, *Trans. of American Inst. of Chemical Eng*., **29**, 174-210, 1933.

Fifth International Conference on Computational Methods for Thermal Problems
THERMACOMP2018, July 9-11, 2018, Indian Institute of Science, Bangalore, INDIA
*N. Massarotti, P. Nithiarasu, Pradip Dutta and C. Ranganyakalu (Eds.)*

# NUMERICAL ANALYSIS OF ELECTRODE COOLING IN A STEELMAKING LADLE FURNACE

**Pradipta Kr. Das, Sandip Sarkar, Suvankar Ganguly, S K Ajmani**

Research & Development Division, Tata Steel Ltd. Jamshedpur 831001,
sandip.sarkar@tatasteel.com

## ABSTRACT

Present study investigates the thermal behaviour of Ladle Furnace (LF) electrode used commonly in a liquid steel refining. To reduce the LF electrode consumption, a cooling apparatus is provided to cool the surface of the electrode by air-water spray cooling. In a finite element based frame work, combined thermal convection, radiation simulation has been performed for complete side-surface cooling. Increased water flow rate and increased cooling time shows that the electrode will achieve temperature below minimum oxidation temperature after spray cooling period. This ensures no-oxidation loss and better electrode life.

**Key Words:** *Heat Transfer, Finite Elements, Convection.*

## 1. INTRODUCTION

Ladle refining of liquid steel is a proven technology to produce high quality steel. A ladle refining furnace is used to raise the temperature and adjust the chemical composition of molten metal. Conventionally, in a ladle furnace, arc heating by using a graphite electrode is used.Usually 40% electrode consumption is due to arcing, 5% by falling down of the tip due to thermal shock, 50% by oxidization of side surfaces and rest 5% is by other causes [1]. Therefore, it is clear from the consumption figure that significant electrode is consumed by oxidation of side surfaces. The oxidation of the surface depends upon the surface temperature provided it is exposed to ambient. The oxidation behavior for different surface temperature is shown in Figure 1. Hence oxidation of the side surface can be reduced by bringing down the side surface temperature. Aiming to that a cooling apparatus is provided to cool down the upper surface of the LF electrode. In the current practice, after arcing, the LF electrode is cooled by air-water spray cooling for few mins using water flow rate of maximum 20 lpm [2-4]. Thereafter, it is exposed to only air cooling for next 15-30 mins. The present study investigates the variation of temperature profile with time and water flow rate. Additional implications are studied to ensure reduction in electrode loss during successive time instances of complete operation.

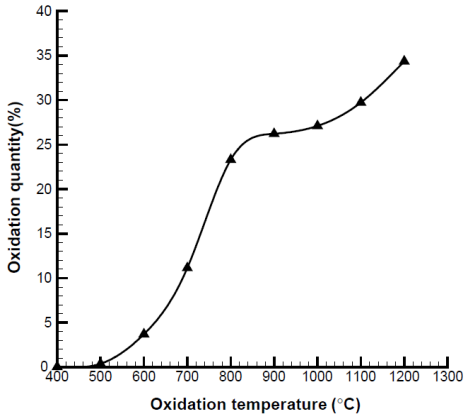


FIGURE 1. oxidation behavior of LF electrode for different surface temperature.

## 2. METHODOLOGY

**Computational domain:**

The electrode temperature profile is assumed to be axi-symmetric. Therefore the computational domain is taken as a rectangular section as shown in the Figure 2 below:

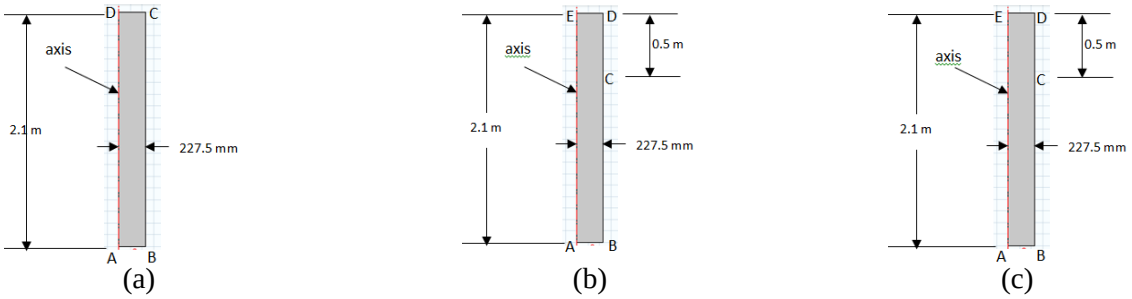


FIGURE 2. Computational domain of for (a) step 1; (b) step 2; (c) step 3.

**Governing equation:** The steady state heat transport inside the electrode is governed by purely conduction equation: $\nabla.(k\nabla T)=0$

**Boundary condition:step 1:** Along AB fixed temperature is specified: $T=2000\,^{o}C$; Along BC radiation loss is specified $q=\varepsilon\sigma\left(T^4-T_\infty{}^4\right)$; Along CD and AD insulation boundary condition is specified: $\partial T/\partial n=0$, where *n* the direction normal to the surface.

**Step 2:** In the second step, the electrode having a temperature profile achieved in step 1 is being cooled by air-water spray cooling as well as radiation loss. This unsteady cooling has been done for 300s.

**Governing equation:** The unsteady heat transport inside the electrode is given by: $\rho C_p\dfrac{\partial T}{\partial t}=\nabla.(k\nabla T)$

**Boundary condition:** Along AB and BC radiation loss is specified $q=\varepsilon\sigma\left(T^4-T_\infty{}^4\right)$; Along CD convective heat loss is specified $q=h(T-T_\infty)$ where $h=3\left(Q/A\right)^{1.5}$ W/m$^2$K. Q = water flow rate in lpm. A= the area (m$^2$) upon which spay is impinging. Along DE and EA insulation boundary condition is specified: $\partial T/\partial n=0$, where *n* the direction normal to the surface.

**Step 3:**

In this step, the electrode having a temperature profile achieved in step 2 after 300s is further cooled through ambient cooling. The cooling has been done for 30 mins.

**Governing equation:** The unsteady heat transport inside the electrode is governed by following equation. $\rho C_p\dfrac{\partial T}{\partial t}=\nabla.(k\nabla T)$

**Boundary condition:** Along AB and BC radiation loss is specified $q=\varepsilon\sigma\left(T^4-T_\infty{}^4\right)$; Along CD convective heat loss is specified $q=h(T-T_\infty)$ where heat transfer coefficient is taken as $h=20$

W/m$^2$K. Along DE and EA insulation boundary condition is specified: $\partial T/\partial n = 0$, where *n* the direction normal to the surface.

## 3. RESULTS

The temperature profile along the surface is shown below (Figure 3). Water flow rate Q is 10 lpm in this case. The results show that before spray cooling, temperature profile indicates an exponential decay having maximum temperature (2000 $^o$C) at the bottom. However, due to spray cooling the temperature of the top region of electrode get cooled with time. The temperature of bottom portion of the electrode is getting lowered by radiation loss. After 5 mins of air-water spray cooling, the maximum temperature of the electrode becomes ~1050 $^o$C.

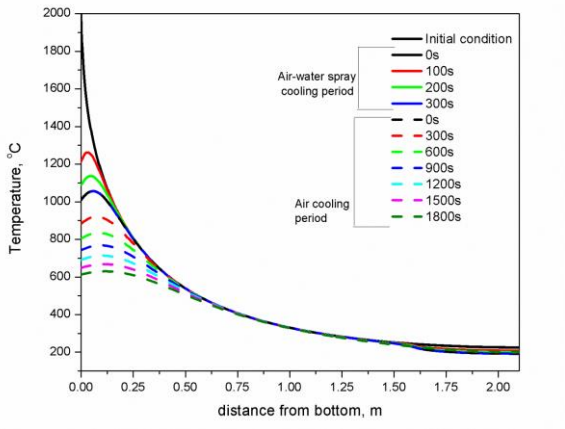


FIGURE 3. Temperature profile along the surface for different steps and time.

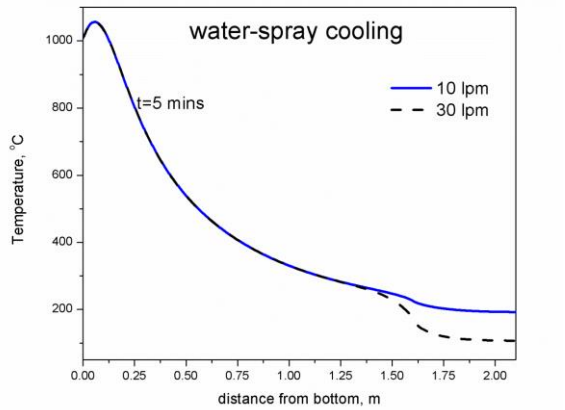


FIGURE 4: temperature profile along the surface after 5 mins of water spray cooling for different water flow rate.

Figure 4 shows the temperature profile of LF electrode surface after 5 mins of air-water spray cooling. The effect of water flow rate in cooling the bottom portion of electrode is insignificant as obtained from the numerical study. As the consumption of electrode due to oxidation is occurring for temperature > 500 (see Fig. 1), the effect of water flow rate is not at all influencing the electrode consumption. Figure 5 shows the temperature profile of electrode surface 5 mins after the closing of air-water spray. Here also we can observe that the increase in water flow rate can only influence the top region of the electrode where the temperature is below 500$^o$C (where oxidation loss is minimum).

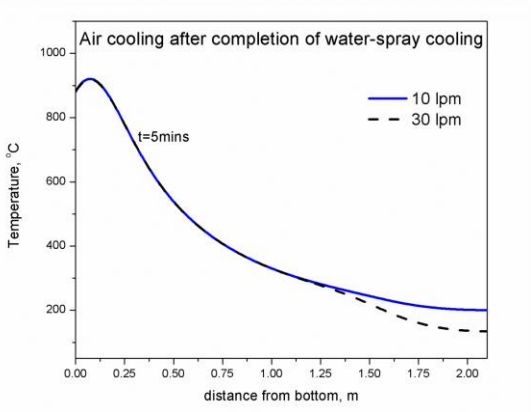


FIGURE 5: Temperature profile along the surface 5 mins after closing of water spray.

For the purpose of extending the study to the condition of both radiation loss and spray cooling from the complete side surface, a set of case-study is considered. Figure 6 shows the temperature profile for such case. As the overall cooling effect is high for this combined effect, the temperature profile shows lower values as compared to the condition specified in modeling section.

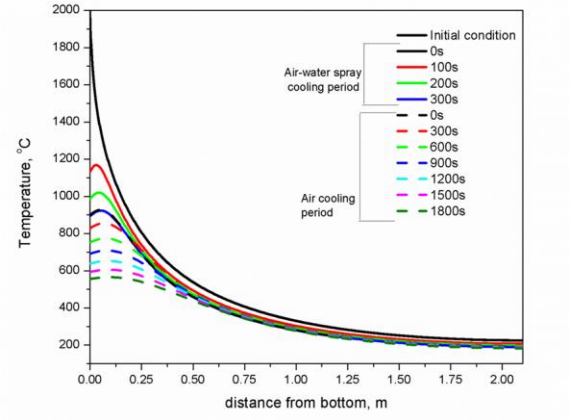


FIGURE 6: LF electrode surface temperature profile considering radiation loss and spray cooling.

## 4. CONCLUSIONS

The present numerical studies show temperature profile of LF electrode for different types of spray cooling. Although the temperature will be reduced at the top of the electrode, temperature of the oxidation prone area will not be reduced by increasing the water flow rate. The oxidation prone area i.e. the lower part of the electrode is not getting affected by spray cooling provided at the top where temperature is much less than minimum oxidation temperature.

## REFERENCES

[1] Luo Xiaowei, Robin Jean-Charles b, Yu Suyuan, Effect of temperature on graphite oxidation behavior, *Nuclear Engineering and Design*, 227, 273-280, 2004.

[2] Eigi Udo, Cooling apparatus for electric arc furnace electrodes, US patent-4,852,120, Jul 25, 1989.

Fifth International Conference on Computational Methods for Thermal Problems
THERMACOMP2018, July 9-11, 2018, Indian Institute of Science, Bangalore, INDIA
*N. Massarotti, P. Nithiarasu, Pradip Dutta and C. Ranganyakalu (Eds.)*

# ENERGY OPTIMIZATION OF A PUSHER-TYPE REHEATING FURNACE WITH COAL BURNERS USING NUMERICAL MODEL

**Saurav Chakraborty, Prabal Talukdar**
IIT Delhi, Hauz Khas New Delhi-110016, srv1406@gmail.com, prabal.talukdar@gmail.com

## ABSTRACT

Optimal energy utilisation in a reheating furnace to achieve desired thermal quality of billets inevitably needs the help of mathematical formulation and computational modelling. In view of this desired goal, a pusher type reheating furnace with axial burners injecting air-coal mixture, is simulated with the help of a computationally efficient numerical model. The effect of varying air flow velocity, coal types and geometric dimensions of the furnace on the thermal efficiency and productivity are studied along with physical reasoning. An optimal value of 37.5 m/s is identified for the flow velocity which maximises thermal efficiency and furnace productivity. Further, Steel Grade coal is found to be the better choice of coal out of the available types. A preliminary study on changing the geometric dimensions of the furnace is also carried out and a few important observations are made.

**Key Words:** *Pusher-type reheating furnace, Coal combustion, Energy optimization.*

## 1. INTRODUCTION

The reheating furnace in steel industry is used to uniformly heat the steel billets above recrystallization temperature using energy from fuel combustion. Since there is a huge investment of fuel resource utilization in reheating furnaces, which are exhaustible and sources of environmental pollution as well, there is a growing need to optimise fuel consumption, quality and productivity of steel billets. Investigation of the complex physical phenomena inside the furnace is more easily affordable with the help of numerical models because of the involvement of extremely high temperature inside the furnace which renders experimental investigation to very limited accessibility. In the past few decades, a fairly large number of numerical models have been established for different types of reheating furnaces using different types of fuel. Essentially there is thermal energy generation inside the furnace from fuel combustion, which is used to heat the moving billets to a temperature close to 1473 K before getting discharged from the furnace. The modelling of the combustion process in a turbulent flow field and the resultant heat transfer to the moving billets through radiation and convection at the surface and conduction within the billets makes the numerical model computationally very challenging and time consuming. Therefore efforts have been made to develop models of different degrees of simplicity, which are primarily oriented towards the required level of computational accuracy. Recently, the authors have developed a computationally efficient numerical model for such pusher type reheating furnace [1].

Although several numerical models have been developed till date, very little effort has been made to directly use these models in optimising the operational efficiency of the reheating furnace. As a first level of effort, one can optimise the flow parameters like air and fuel flow rates or the rate of discharge of billets, which is directly related to the productivity of the furnace. Han et al. [2] performed a study to determine the optimal residence time of slabs in a single location within a walking beam type furnace which satisfied two requirements of target temperature and uniformity of temperature distribution in the discharged slabs. A more involved analysis can be to optimise the geometric configuration of the furnace itself, which to the author's knowledge, has not yet been carried out. This is a very broad scope of study and in this work, only a few important geometrical aspects have been studied. In view of the goal described above, an effort has been made to reveal

the effects of varying different flow and geometric parameters on the thermal characteristics of the furnace which will help to determine the optimal values of the parameters for the furnace under consideration. Additionally, the study is also aimed at providing useful understanding to the thermal characteristics of other similar furnaces to help in their efficient design.

## 2. MODEL DESCRIPTION AND COMPUTATIONAL METHODOLOGY

The furnace geometry and mesh is constructed using the commercial software ANSYS ICEM CFD. The geometry of the pusher type reheating furnace, as shown in Figure 1, is complicated due to the shape of furnace wall, insertion of billets and an array of three axial circular burners through which the coal-air mixture enters into the furnace. Flue gases exit through two outlets at the bottom of the furnace towards the back end as shown in Figure 1. The billets are inserted from the back end to move in the direction opposite to the flow of hot combustion gases. The billets are carried forward through rollers intermittently and instantaneously with a residence time of 337.5s in each position, to the extreme left where they are finally pushed out of the furnace through a small discharge door in the side wall. The discharge door and the rollers are excluded from the modelling in order to keep simplicity without much loss of accuracy of the numerical modelling. The grid for the furnace is generated using multi-block structured mesh with hexahedral volume elements and quadrilateral surface elements. For the circular burners, O-grid has been created inside the blocks containing the circular surface as shown in Figure 2. The mesh consists of a total of 10,85,562 hexahedral cells, excluding the billets.

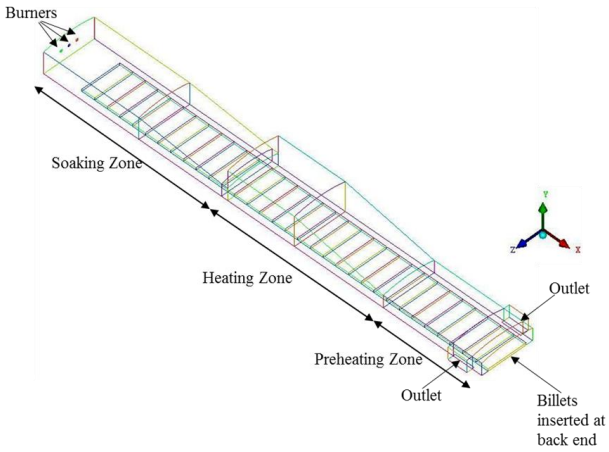


FIGURE 1: Furnace Geometry

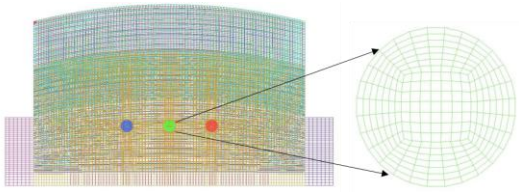

FIGURE 2: Enlarged front view of mesh

The reactive flow field in the furnace is simulated in ANSYS Fluent 15.0 and the thermal diffusion in the billets is simulated using an in-house code programmed in MATLAB R2014b. The combustion in the furnace is modelled as a 3-D steady state process with appropriate governing equations for all the different phenomena taking place simultaneously. The flow and the thermal fields are governed by the continuity, momentum and energy equations which are not mentioned here for the sake of simplicity. The turbulence is modelled using the realizable k-ε model with the standard values of model constants and Discrete Ordinates model is used for modelling radiation. The coal combustion inside the furnace is modelled using the species transport model in Fluent with a two-step global reaction mechanism for the volatile reactions in the homogeneous gaseous phase and a single step heterogeneous reaction for the char. The coal particles mixed with air are modelled using Euler-Lagrangian approach, where air is treated as continuous media in which coal particles

are dispersed. This is done using the Discrete Phase Model (DPM) in Fluent where all the details regarding the injection properties are provided. The heat transfer within the billet is only by conduction. While the billets move through the furnace, their temperature continuously change as they are exposed to variable flux conditions, which are different at different locations of the furnace. The problem is therefore, transient in nature with a time dependent flux boundary condition. The entire model is run iteratively by a two-way coupling of the results of the furnace simulation in Fluent and the simulation of the billets in MATLAB, as described in detail in the previous work [1].

## 3. RESULTS AND DISCUSSION

The results of the simulation with convergence criterion as per the previous work [1], are discussed in this section. The validation of combustion model and grid and ray independency studies, having been already carried out and shown previously [1], is skipped here. The primary goal of a furnace designer is to maximise the thermal efficiency, either by proper geometric construction of the furnace, or by controlling the flow parameters to their optimal values. Both of these are very challenging tasks because of the interplay of various physical phenomena which influence the thermal characteristics of the furnace in different ways. In an attempt to enhance the operational efficiency of the furnace, two important parameters relevant to this furnace are identified, viz., the air flow velocity through the axial burners and the type of coal used. Apart from these, the effect of changing height and zone lengths of the furnace is also studied.

The air flow velocity through the burners is varied from 30 m/s to 55 m/s, and the resultant effect on the thermal efficiency is as shown in Figure 3, revealing that the highest thermal efficiency is achieved at an injection velocity of 37.5 m/s. This is governed by the interplay of fuel stoichiometric requirement and the furnace design.

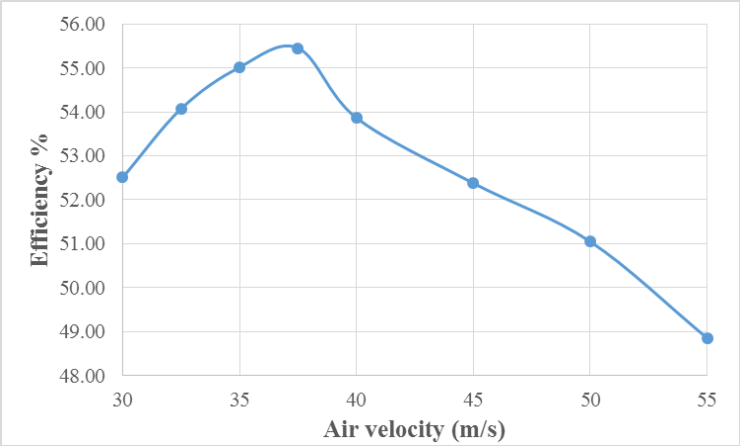


FIGURE 3. Variation of thermal efficiency with air inlet velocity

Four different types of coal are available for operating the furnace and in such situation it is always beneficial to know the most suitable fuel. The comparison of thermal efficiency for these four cases is shown in Figure 4. The Steel Grade coal is seen to clearly outperform the efficiency of Indonesian and Mixed coals which have much lesser calorific values. It also gives higher efficiency than the US coal, inspite of having slightly lower calorific value. Since high calorific value coal also requires less feed rate into the furnace, therefore the Steel Grade coal also has this additional advantage. Of course, such coals are costlier than the Indonesian and Mixed coal which have low calorific values, and to determine the best choice of fuel, a complete cost analysis can be carried out with the cost of coals, profit from billet production and the data generated from this simulation. The productivity, defined here as the potential rate of discharge of billets at a temperature of 1473 K, and specific energy consumption (SEC) of the furnace are shown in Figure 5. The highest

productivity and the lowest SEC is also obtained for the Steel Grade coal and this is also verified by trial runs in the operational industry.

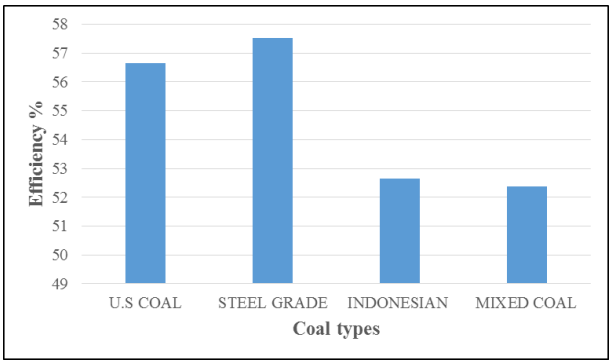


FIGURE 4. Variation of thermal efficiency with coal types

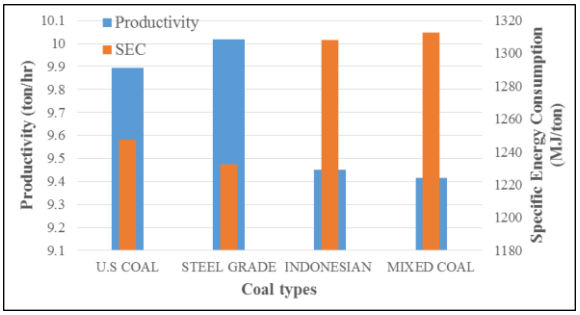


FIGURE 5. Variation of productivity and SEC with coal types

The effect of changing the height and lengths of soaking and heating zone of the furnace was studied because they are the most crucial design parameters. Interestingly, it is observed that a higher furnace efficiency is obtained by decreasing the height of the furnace as well as by decreasing the soaking zone length as shown in Figure 6. Although an optimising study will be most suitable, but for the time being this study gives some preliminary exposure to the effect of these parameters on furnace efficiency.

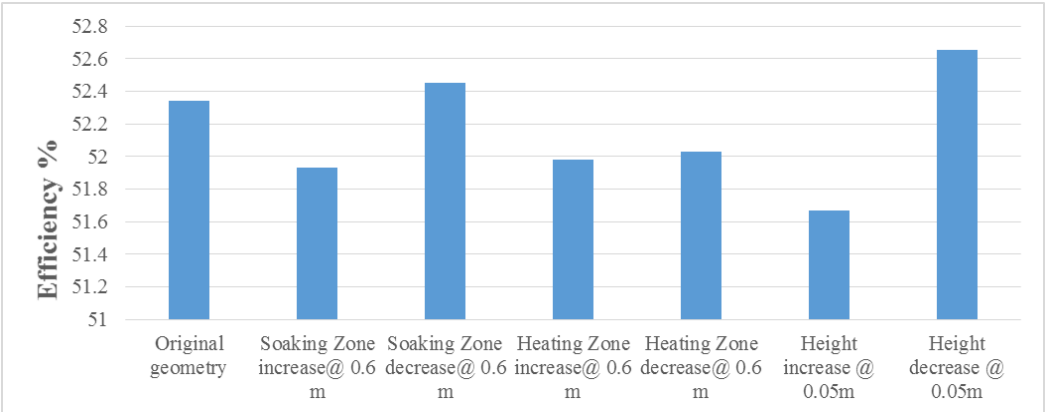


FIGURE 6. Variation of thermal efficiency for different furnace geometries

## 4. CONCLUSIONS

A pusher type reheating furnace is simulated with the help of a computationally efficient numerical method, developed in a previous work [1]. Optimal value of air flow velocity and better choice of coal type are determined. A preliminary effect on geometric design of furnace is also realized.

## REFERENCES

[1] S. Chakraborty, A. Rajora, S.P. Singh, P. Talukdar, Heat Transfer and discrete phase modelling of coal combustion in a pusher type reheating furnace, Applied Thermal Engineering 116, 66-78, 2017.

[2] S. Han, D. Chang, Optimum residence time analysis for a walking beam type reheating furnace, Int. J. Heat Mass Transfer 55, 4079–4087, 2012.

Fifth International Conference on Computational Methods for Thermal Problems
THERMACOMP2018, July 9-11, 2018, Indian Institute of Science, Bangalore, INDIA
*N. Massarotti, P. Nithiarasu, Pradip Dutta and C. Ranganyakalu (Eds.)*

# NUMERICAL ANALYSIS OF PRESSURIZED CAVITY-AIR-RECEIVER IN CONCENTRATING SOLAR POWER SYSTEM

**Sayuj Sasidharan**
Interdisciplinary Centre for Energy Research, Indian Institute of Science, Bangalore, India,
sayujs@iisc.ac.in

**Pradip Dutta**
Department of Mechanical Engineering, Indian Institute of Science, Bangalore, India,
pradip@iisc.ac.in

## ABSTRACT

Concentrating solar power system consists of an optical concentrator, receiver and power block. Solar air receiver converts concentrated solar radiation from the optical concentrator to heat and acts as a high temperature source for the power block. Presence of porous medium in the flow domain increases convective heat transfer to the fluid by providing large surface area. This study models coupled optical and thermal analysis of receiver with ceramic and steel foam/mesh as porous absorber. Ray tracing analysis of the concentrator provides energy input to the cavity receiver. Porous medium is modelled using LTNE model as temperatures of working fluid and hot solid matrix can be different. The ceramic and steel foam act as participating medium in the flow domain. Radiation transport in the flow domain is modelled using P1 approximation. The study also compares results for Local Thermal Equilibrium (LTE) and Local Thermal Non-Equilibrium (LTNE) models for the porous medium, which is assumed to be homogeneous and isotropic.

**Keywords**: *Solar receiver, optical concentrator, porous medium, LTNE, LTE.*

## 1. INTRODUCTION

Electricity generation from solar thermal power plants is expensive compared to conventional methods [1]. The primary reason for higher cost is the low conversion efficiency of the power block resulting from low source temperature. Currently, researchers are focussing on more efficient conversion using Brayton cycle with high temperature pressurized air or supercritical-$CO_2$ , which can result in significantly higher efficiency compared to that with conventional steam turbine based cycle [2]. Such operations require high source temperatures provided by appropriately designed solar receivers. Direct heating of supercritical-$CO_2$ poses challenge due to sharp variations in thermophysical properties. However, indirect heating is possible using air receiver. This study deals with the numerical analysis of cavity air receiver for indirect heating of supercritical-$CO_2$

## 2. CAVITY RECEIVER MODELLING APPROACH

Cavity receiver is considered for the current study, shown in figure 1. Porous absorber of the receiver is concentrically bounded by cylindrical cavity with one-end open while the other dome closed. Modelling the energy input to the receiver is carried out using optical analysis of the concentrator. Optical analysis of the concentrator involves ray tracing since the wavelength of solar radiation is much smaller compared to the size of the receiver. The flux map on the cavity surface obtained from the ray tracing study is used as boundary condition for the thermal analysis of the receiver. Loss modelling of the receiver accounts for radiative loss and natural convection loss from the cavity surface. Thus, coupled optical and thermal analysis would accurately model the receiver. Porous medium is modelled using a volume averaging approach.

## 2.1. RECEIVER GEOMETRY

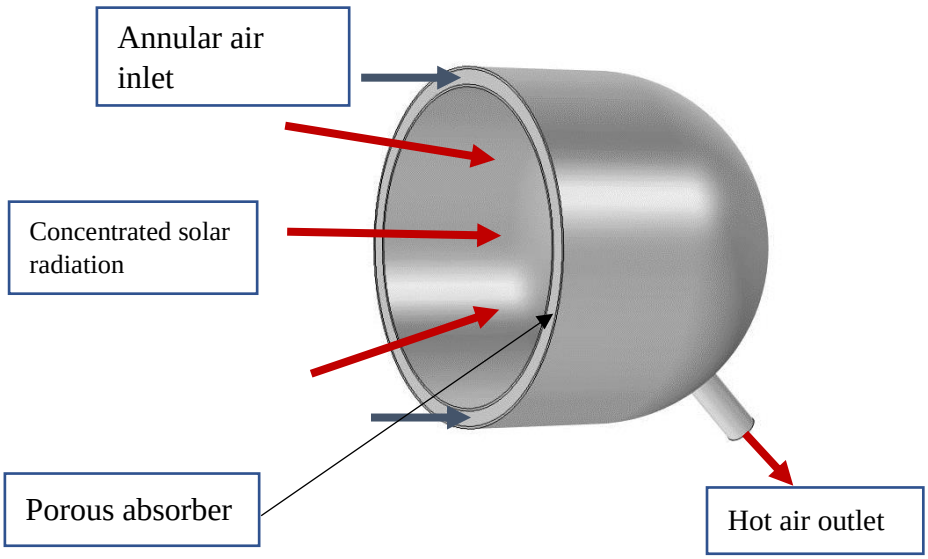


FIGURE 1. Schematic of cavity solar air receiver

## 2.2. NUMERICAL MODELLING

*Optical modelling*

Optical modelling of the concentrator is performed using Ray Optics module of COMSOL 5.3a. The geometric optics interface is used to model electromagnetic wave propagation when the wavelength of the radiation is much smaller than the smallest geometric entity in the model. Geometric optics interface computes ray trajectories for each ray by solving a set of two first order differential equations for each component of position and wave vector of the ray.

$$\frac{d\boldsymbol{k}}{dt} = -\frac{\partial \omega}{\partial q}$$

$$\frac{d\boldsymbol{q}}{dt} = \frac{\partial \omega}{\partial k}$$

where **k** is wave vector, **q** is position vector and $\omega$ is angular frequency.

The initial ray direction is specified based on solar radiation using the time and location on the Earth's surface. The rays falling on the cavity surface is used as heat flux boundary condition for the thermal analysis.

*Flow modelling*

Compressed air flow through the porous medium assumes a steady state problem with negligible viscous dissipation. Volume averaging of the porous medium provides macroscopic quantities like velocity field inside the domain that are of relevance instead of pore-scale velocities. It also helps to avoid the description of complicated internal morphology of the porous medium. Brinkman flow model is used to obtain the velocity and pressure fields since it extends the Darcy model to capture the viscous

dissipation of the kinetic energy by viscous shear. Geometric properties of the porous medium like permeability, specific surface area and porosity values were taken from [4].

$$\nabla.\mathbf{u} = \mathbf{0}$$

$$\nabla.\left[-p\mathbf{I} + \frac{\mu}{\epsilon_p}(\nabla\mathbf{u} + (\nabla\mathbf{u})^T)\right] - \left(\frac{\mu}{k}\boldsymbol{u}\right) = \mathbf{0}$$

Where $\boldsymbol{u}$ is velocity vector, p is pressure, $\mu$ is dynamic viscosity, $\epsilon_p$ is porosity, $k$ is thermal conductivity.

*Heat transfer and radiation modelling*

Conservation of energy inside the porous medium is carried out by assuming both LTE and LTNE models. LTE model assumes infinite heat transfer coefficient between the fluid and the solid matrix which is not practical. However, LTNE model assumes a finite heat transfer coefficient thus providing more realistic air temperature distribution in the domain. The interfacial heat transfer coefficient in the porous medium is obtained using a Nusselt number correlation from [3]. Solid matrix of the porous foam gets heated by conduction from the stainless-steel cavity surface. Hot solid matrix then emits radiation acting as a participating medium. Radiative modelling in the porous medium assumes P1 approximation for solving the radiative transfer equation with absorption coefficient, $\kappa$ = 220 $m^{-1}$ [5]. The energy conservation equation for solid matrix and air is given below:

Solid phase: $$\nabla.\left(\theta_p k_{\boldsymbol{s}} \boldsymbol{\nabla} \mathrm{T}_{\boldsymbol{s}}\right) + h_{\mathrm{sf}}(\mathrm{T_f} - \mathrm{T_s}) = \boldsymbol{\nabla}.\boldsymbol{q_r}$$

Where $\theta_p$is 1- $\epsilon_p$, $k_{\boldsymbol{s}}$ is solid thermal conductivity, $h_{\mathrm{sf}}$ is interstitial heat transfer coefficient, $\mathrm{T}_{\boldsymbol{s}}$ is solid temperature distribution, $\mathrm{T_f}$ is fluid temperature distribution and $\boldsymbol{q_r}$ is radiative heat flux.

Fluid phase: $$(1 - \theta_{\mathbf{p}})\rho c_p \boldsymbol{u}_{\mathrm{f}}.\nabla \mathrm{T_f} + \nabla.\mathbf{q} = \nabla.\left((1-\theta_p)k_{\mathrm{f}}\boldsymbol{\nabla}\mathrm{T_f}\right) + h_{\mathrm{sf}}(\mathrm{T}_{\boldsymbol{s}} - \mathrm{T_f})$$

Where $\rho$ is fluid density, $c_p$ is fluid heat capacity at constant pressure, $\mathbf{q}$ is conductive heat flux.

Closure equation: $$Q_s = \frac{q_{sf}}{\theta_p}(\mathrm{T_f} - \mathrm{T}_S)\ ; Q_{\mathrm{f}} = \frac{q_{sf}}{1-\theta_p}(\mathrm{T_s} - \mathrm{T_f});\ q_{sf} = \mathrm{h_{sf}} * \mathrm{a_{sf}}$$

Radiation equation: $q_r = \kappa(\mathrm{G} - 4\pi\mathrm{I}_b)$; $q_r$ obtained by solving: $\nabla.\left(\mathrm{D_{p1}}\nabla\mathrm{G}\right) + \kappa(\mathrm{G} - 4\pi\mathrm{I}_b) = 0$ where $\mathrm{D_{p1}}$ = P1 diffusion coefficient, G = incident radiation and $\mathrm{I}_b$ = blackbody radiative intensity.

## 3. RESULTS

1. Ray Tracing analysis provided accurate flux distribution corresponding to a location and time of the sun during the day. Ray trajectories from the Scheffler concentrator to the cavity surface is shown in figure 2. Flux map (figure 3) obtained shows a peak flux value of 780 kW/$m^2$ for an equivalent direct normal irradiance of 430 W/$m^2$.

2. The average air temperature obtained at the outlet is 393 K for flow rate of 0.02 kg/s. The simulation solves for local thermal non-equilibrium thermal model for porous medium air flow coupled to radiation transfer in the medium shown in figure 4.

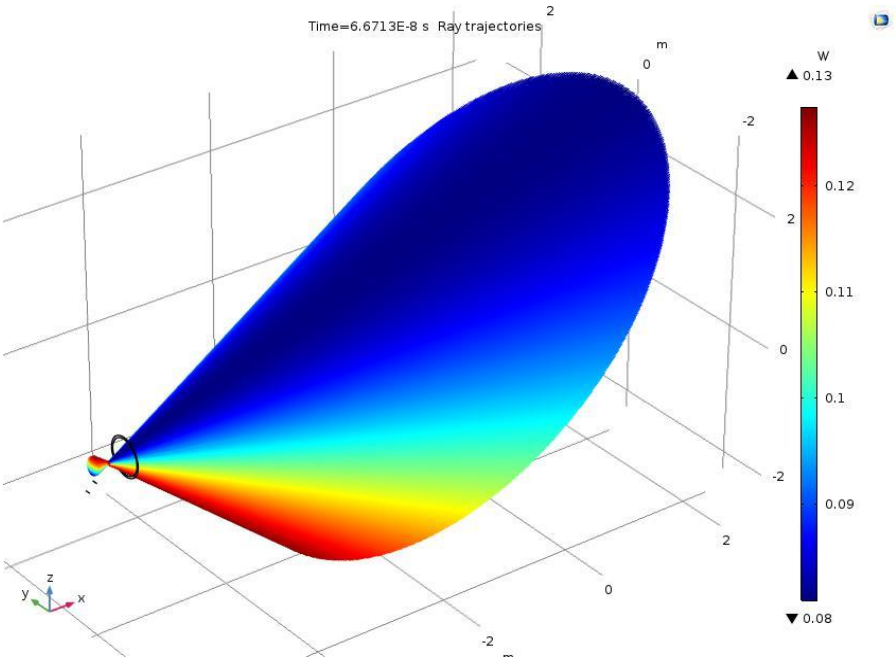


FIGURE 2. Ray tracing analysis of the Scheffler dish and the receiver

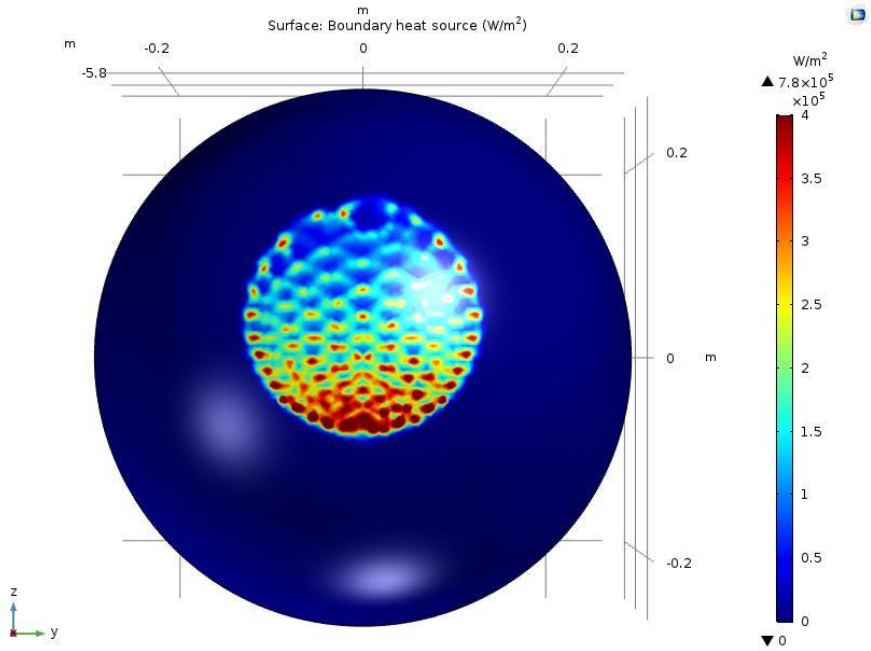


FIGURE 3. Flux map obtained on the curved cavity surface

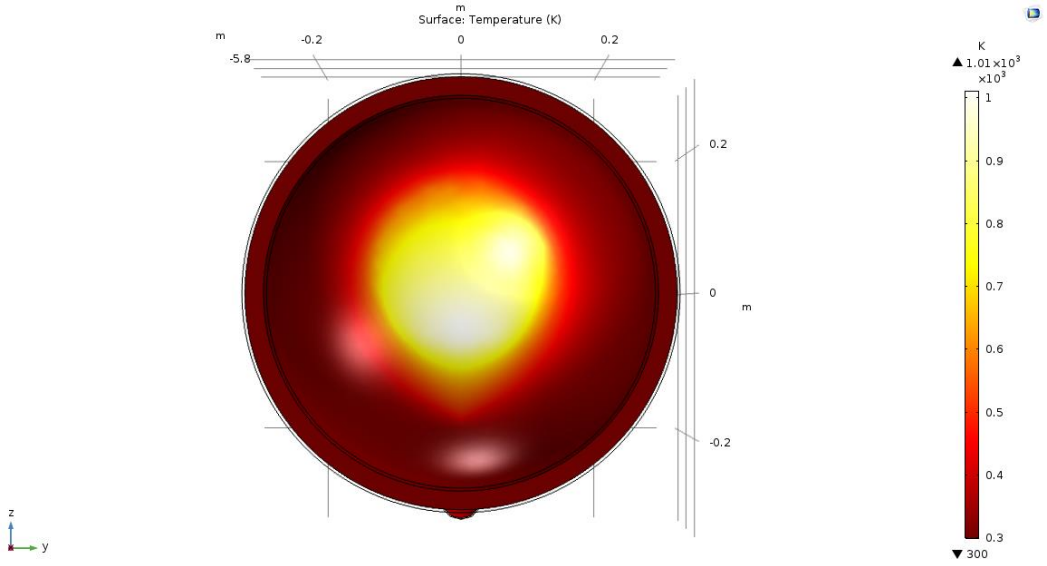


FIGURE 4. Air temperature distribution for ṁ = 0.02 kg/s with ceramic porous medium (porosity 0.8)

## 4. CONCLUSIONS

The primary concentrator used for the study, namely Scheffler dish was geometrically modelled for ray tracing analysis. Ray tracing analysis captures non-uniform flux distribution on the receiver surface as opposed to a constant flux value being used as boundary condition in the thermal analysis. LTNE modelling of the porous medium accurately captures the convective heat transfer within the porous domain compared to LTE modelling. Enhancement of convective heat transfer within the porous domain can directly affect the performance of the receiver. For a range of flow rates, the air temperature distribution was observed for a given porosity. Loss modelling of the receiver includes natural convection loss and radiative loss from the cavity surface.

## REFERENCES

[1] A. Kribus, Y. Gray, M. Grijnevich, G. Mittleman, S. Mey-Cloutier, C. Caliot, The promise and challenge of solar volumetric absorbers, *Solar Energy*, 110, 463-81, 2014.

[2] L. Irwin, Y. Le Moullec, Turbines can use $CO_2$ to cut $CO_2$, *Science*, 356,805-6, 2017.

[3] P. Poživil, S. Ackermann, A. Steinfeld, Numerical Heat Transfer Analysis of a 50 $kW_{th}$ Pressurized-Air Solar Receiver, *Journal of Solar Energy Engineering*, 137, 064504-08, 2015.

[4] S. Haussener, P. Coray, W. Lipiński, P. Wyss, A. Steinfeld, Tomography-Based Heat and Mass Transfer Characterization of Reticulated Porous Ceramics for High Temperature Processing, *Journal of Heat Transfer*, 132, 023305-14, 2010.

[5] J. Petrasch, P. Wyss, A. Steinfeld, Tomography-based Monte Carlo determination of radiative properties of reticulate porous ceramics, Journal of Quantitative Spectroscopy and Radiative Transfer, 105, 180-97, 2007.

Fifth International Conference on Computational Methods for Thermal Problems
THERMACOMP2018, July 9-11, 2018, Indian Institute of Science, Bangalore, INDIA
*N. Massarotti, P. Nithiarasu, Pradip Dutta and C. Ranganyakalu (Eds.)*

# Steady State Mathematical Modelling and Parametric Study of Ammonia based Loop Heat Pipe for Space Application

**Shail N. Shah**
Nirma University, Ahmedabad-382481, shailthermal@gmail.com

**Kamlesh K. Baraya**
SF Scientist, Indian Space Research Organisation, Ahmedabad, kkbaraya@sac.isro.gov.in

**Dr. A. M. Achari**
Associate Professor, Nirma University, madhusudan.achari@nirmauni.ac.in

## ABSTRACT

Loop Heat Pipe is a two phase passive heat transfer device. This paper is about in depth study to have modelling of LHP at varying heat loads by applying fundamentals of HMT, FM and Thermodynamics. Through figures how the fluid flow occurs within the loop has been explained. Energy Balance has been done at each section. Descriptive method to find out the SSOT (Steady State Operating Temperature) has been explained. SSC (Steady State Convergence) scheme is developed using Dev C++ and descriptive algorithm has been generated. To best of the author's knowledge hardly any detail is available in open literature about how temperature distribution along the loop is to be evaluated. Results for Ammonia based Loop Heat Pipe is obtained and compared with open literature and error is found within 5%. Parametric Study has been done to see the effect of different parameters on pressure drop and SSOT(Steady State Operating Temperature) at varying heat loads.

**Key Words:** *Loop Heat Pipe, Mathematical modelling, Operating Principle*

## 1. INTRODUCTION

2D diagram is explained with each section of Loop Heat Pipe in figure 1. The main benefit of having LHP over conventional heat pipe is higher heat load carrying capacity and long distance covered between evaporator and condenser section. The main advantage of having secondary wick and compensation chamber is to have primary wick completely saturated all the time to have it functioning for higher heat loads. Vapour formation and distribution from source to sink and back to C.C. has been shown in figure 1 via bubbles and liquid.

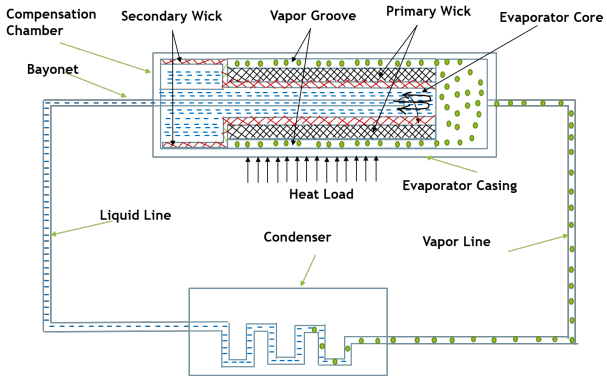


**Figure 1 : Functioning of LHP**

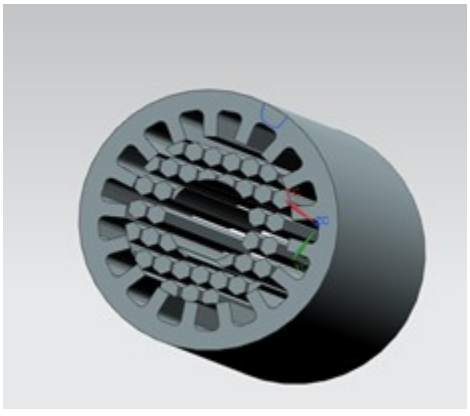

**Figure 2 : 3D view of vapour grooves and primary wick**

## 2. MAIN BODY

SSC scheme to find SSOT of LHP is explained in depth. Thermophysical properties of ammonia has been curved fitted to fifth order polynomial [8]. In SSC (Steady State Convergence) scheme equations at each section are developed and convergence is obtained by having energy balance at C.C. Descriptive algorithm has been generated for SSC (Steady State Convergence Scheme).

**Table 1 : Input Dimesnions**

| Working Fluid | Ammonia | - |
|---|---|---|
| Components | Dimensions (OD x ID x Length) | Unit |
| Evaporator | Φ 24.1/19.1 x 610 | mm |
| Compensation Chamber | Φ 69.3/68.3 x 160 | mm |
| Vapour Line | Φ 6.4/5.3 x 740 | mm |
| Vapour Line | Φ 6.4/5.3 x 970 | mm |
| Condenser | Φ 6.4/4.6 x 4650 | mm |
| Wick | Φ 19.1/9.5 x 610 | mm |
| Wick Porosity | 60% | - |
| Pore radius | 1.6 | μm |
| Wick Material Conductivity | 93 | W/mK |

- **Assumptions :**

- Vapour line is considered to be completely insulated.
- As value of superheat is very small so it is being neglected.
- As diameter of liquid and vapour line is very small compared to length of pipe, fluid is considered to be fully developed in liquid and vapour line.
- Heat transfer through wick occurs only in radial direction.
- Minor loses like effect of bends, fittings and valve are neglected in liquid and vapour line

## 3. RESULTS

Result for water based LHP with SSC scheme has been compared with [4] and result is found within 5%. Temperatures at each sections of LHP are obtained applying Clausius-Clapeyron Equation. Developed model is compared with available in open literature and is shown in fig. 3. Further parametric study has been done to see the effects of different parameters on pressure drop. Effect of sink temperature and ambient have also been studied. Fig. 3 is standard operating characteristic curve of LHP. Initially condenser works as Variable Conductance mode which leads to reduction in SSOT temperature but once condenser reaches to its fixed conductance mode, there will be rise in temperature as condenser will be working at its full load. Fig. 4 indicates Condenser outlet temperature rise with increase in heat loads. As heat load keeps on increasing it leads to increase in condenser outlet temperature depending on sink temperature and mass flow rate. Here we have used e-NTU method to find condense outlet temperature based on sink temperature which is at 6 oC.

Ambient temperature and Sink temperature plays important role on SSOT condition of LHP. Fig. 5 is study of ambient temperature on SSOT. Higher the ambient temperature higher will be heat gained by liquid from condenser outlet to C.C. inlet which will lead to increase in SSOT temperature. Vice versa for reduction in ambient temperature as it will lead to reduced C.C. inlet temperature which will reduce SSOT temperature of Loop.

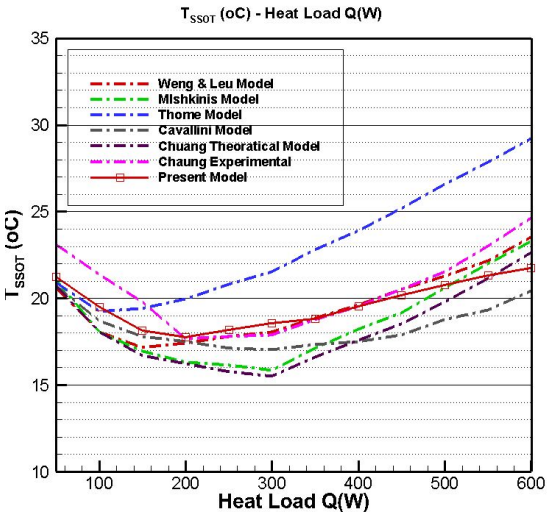


FIGURE 3. SSOT-Q for ammonia based LHP

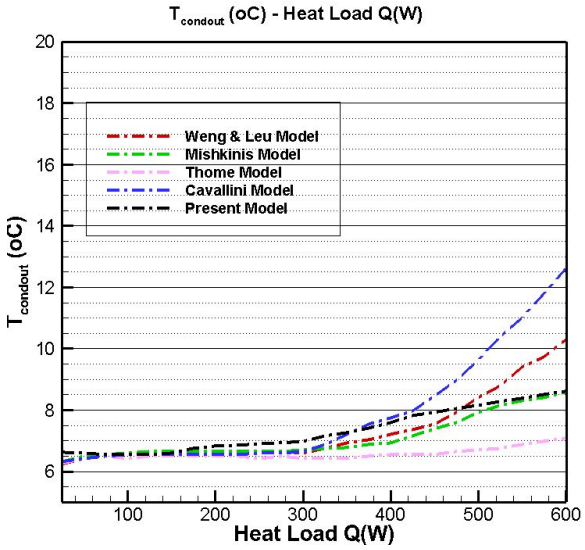


FIGURE 4. SSOT-Q for ammonia based LHP

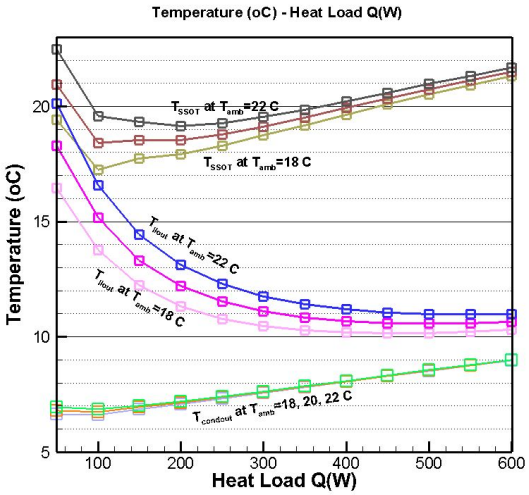


FIGURE 5. T-Q (Ambient Effect)

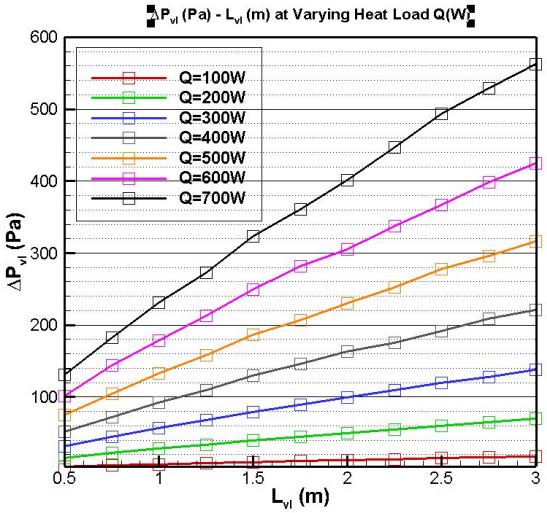


FIGURE 6. ΔPwick-Lvl at varying Q(W)

Fig. 6 is study of pressure drop across wick with Change in length of Vapour line at varying heat loads. Curve trend is inclined line. As the head load keeps on increasing the angle of inclined line keeps increasing and at higher heat load angle increases significantly as compared to lower heat loads. Figure 7 indicates effect of wick porosity on SSOT temperature of LHP. Higher the porosity higher will be heat leak from Evaporator to C.C. which will lead to higher SSOT temperature. Figure 8 is combined effect of Sink and ambient temperature. When sink temperature is below ambient, condenser can work at variable conductance and we do get standard characteristic curve. When sink temperature is below ambient temperature than it is not possible to have condenser at variable conductance and we will get inclined line with increase in temperature with heat Load.

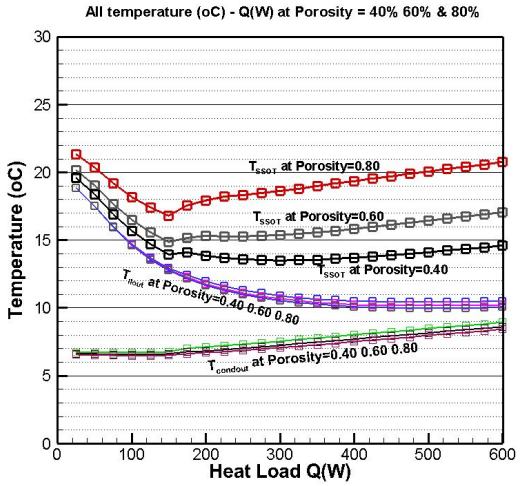


FIGURE 7. T-Q(W) at varying Wick Porosity

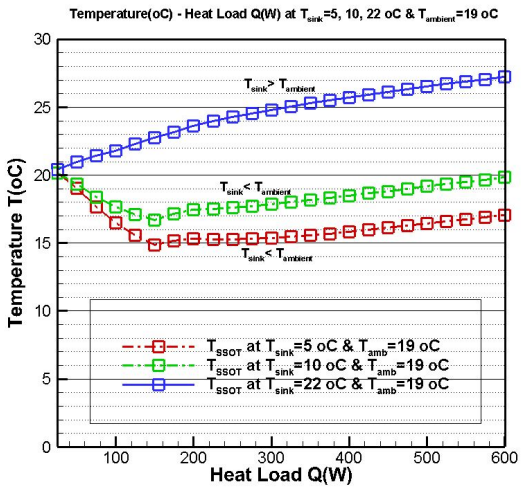


FIGURE 8. T-Q (Ambient & Sink combined Effect)

## 4. CONCLUSIONS

Functioning and fluid flow within LHP has been briefly explained. Temperature at each section of Loop has been obtained by applying SSC scheme. Standard operating curve of LHP is shown in fig. 3. Depending on condenser effectiveness condenser outlet value varies which is shown in fig. 4. Length and Diameter of vapour line plays significant role in overall pressure drop of LHP depending on which functioning of LHP is considered. Increase in wick porosity leads to increase in heat leak and that leads to increase in SSOT temperature. If sink is below ambient temperature than it will give standard characteristic curve but only inclined increase for vice versa condition.

## REFERENCES

[1] T. Kaya, T. Hoang, "Mathamatical Modelling of Loop Heat pipes and Experimental Validation," *J. Thermophys.,Heat Transfer 13(1999)*, pp. 314–320.

[2] Chuang, P. An improved steady-state model of loop heat pipes based on experimental and theoretical analyses. PhD thesis, Pennsylvania State University, 2003.

[3] Bai, L., Lin, G., Zhang, H., and Wen, D. Mathematical modeling of steady-state operation of a loop heat pipe. *Applied Thermal Engineering*, 29:2643–2654, 2009

[4] Chih-Yuan Weng,Tzong-Shyng Leu, 2015, "Two phase flow pattern based theoratical study of loop heat pipes," Appl. Therm. Eng., 98(2016), pp. 228–237.

[5] Chernysheva, M. and Maydanik, Y. Heat and mass transfer in evaporator of loop heat pipe. Journal of Thermophysics and Heat Transfer, 23(4):725–731, 2009

[6] Launay, S., Sartre, V., and Bonjour, J. Parametric analysis of loop heat pipe operation: a literature review. International Journal of Thermal Sciences, 46(7):621–636, 2007

[7] Adoni, A., Ambirajan, A., Jasvanth, V., Kumar, D., and Dutta, P. Theoretical studies of hard filling in loop heat pipes. *Journal of Thermophysics and Heat Transfer*, 24(1): 173–183, 2010.

[8] Faghri, A., 1995, Heat Pipe Science and Technology, *Taylor & Francis*, Washington, DC.

Fifth International Conference on Computational Methods for Thermal Problems
THERMACOMP2018, July 9-11, 2018, Indian Institute of Science, Bangalore, INDIA
*N. Massarotti, P. Nithiarasu, Pradip Dutta and C. Ranganyakalu (Eds.)*

# Implicit finite difference method for MHD flow of a micropolar fluid past a stretching sheet with heat transfer

B.Shankar Goud [1], M.N Rajashekar[2]

[1]*Department of Mathematics, JNTUH College of Engineering, Kukatpally, Hyderabad- 085, TS, India.*

[2]*Department of Mathematics, JNTUH College of Engineering Nachupally, Karimnagar -505501,TS, India.*

## Abstract

The problem focused in this paper can be described as numerical solution of a heat transfer to MHD flow of a micro polar fluid from a stretching sheet with suction and blowing through a porous medium. The solution is obtained with the help of implicit finite difference method known as Keller Box method. A similarity solution to governing momentum, angular momentum and energy equations is derived. The velocity and temperature profiles are studies for the effects of Prandtl number, porous medium, magnetic field and surface mass transfer. Obtained numerical results depict the increased velocity and angular velocity with higher permeability parameter and vice versa with magnetic field. Temperature is affected with permeability parameter and magnetic field. An observation is made that the higher values of the permeability parameter leads to decreased temperature. Alternatively, temperature increases with magnetic field.

**Keywords:** MHD flow, Heat transfer,Micropolar fluid, Stretching sheet,Keller box, Porous medium.

## Introduction

The purpose of this work is to explore and obtain a numerical model for the heat transfer characteristics of a magneto-micropolar fluid which is incompressible, steady and is flowing past a stretching sheet with suction and blowing through a porous medium utilising Keller Box method. Micropolar fluids are micro structured fluids with non-symmetrical stress tensor. Such fluids are also termed as polar fluids. Physically, these fluids represent randomly oriented particles suspended in a viscous medium. Continuum Mechanics classical theories tend to be inadequate to elucidate microscopic manifestations of microscopic events thereby giving rise to a new stage in the evolution of fluid dynamics. ElArabawy [1] analyzed the problem of the effect of suction/injection on the flow of a micropolar fluid past a continuously moving plate in the presence of radiation.Odda and Farhan [2] studied the effects of variable viscosity and variable thermal conductivity on heat transfer to a micro-polar fluid from a non-isothermal stretching sheet with suction and blowing.Nadeem Ahmad Sheikh [3] et.al describes MHD Flow of Micropolar Fluid over an Oscillating Vertical Plate Embedded in Porous Media with Constant Temperature and Concentration.E. M. Abo-Eldahab and A. F. Ghonaim,[4] investigated Radiation effect on heat transfer of a micropolar fluid through a porous medium. Heat and mass transfer in MHD micropolar flow over a vertical moving porous plate in a porous medium was studied by Y. J. Kim[5]. MHD stagnation flow of a micropolar fluid through a porous medium is presented by S. Nadeem [6] et.al. T.Hayat[7] et.al analized Analytic solution for MHD transient rotating flow of a second grade fluid in a porous space. B.I. Olajuwon and, J.I.

Oahimire[8] studied Unsteady free convection heat and mass transfer in an MHD micropolar fluid in the presence of thermo diffusion and thermal radiation.

The current problem under investigation has applications in large scale. They include MHD generators with neutral fluid seeding in the form of rigid micro inclusions, unclear fluids in industrial processes where fluids are a working medium. Practical engineering applications of porous media heat transfer problems are extensive in crude oil extraction, geothermal systems and ground water pollution. Hassanien [10] investigated boundary layer flow and heat transfer on continuous accelerated sheet extruded in anbambient micropolar fluid. M.A. Seddeek[11] analyzed Flow of a magneto-micropolar fluid past a continuously moving plate. P.G. Siddheshwar , U.S. Mahabaleshwar [12] analyzed an analytical solution to the MHD flow of micropolar fluid over a linear stretching sheet.

The purpose of this work is to explore and obtain a numerical model for the heat transfer characteristics of a magneto-micropolar fluid which is incompressible, steady and is flowing past a stretching sheet with suction and blowing through a porous medium utilising Keller- box method.

## Problem formulation

Here, magneto-micropolar fluid which is incompressible and steady, flowing past a horizontal stretching sheet through a porous medium and issues from a thin slit as found on polymer processing applications is taken into consideration. An assumption is made that velocity at any point on the sheet is directly proportional to its distance from the slit. Hence, we may arrive at the governing equations within boundary layer approximation.

Equation of mass: $$\frac{\partial u}{\partial x} + \frac{\partial u}{\partial y} = 0 \qquad \text{--- (1)}$$

Momentum equation: $$u\frac{\partial u}{\partial x} + v\frac{\partial u}{\partial y} = n\frac{\partial^2 u}{\partial y^2} - \left(\frac{m}{r k^*} + \frac{s B_0^2}{r}\right)u + \frac{K}{r}\frac{\partial N}{\partial y} \qquad \text{--- (2)}$$

Angular momentum equation: $$G_1\frac{\partial^2 N}{\partial y^2} = 2N + \frac{\partial u}{\partial y} \qquad \text{--- (3)}$$

Energy equation: $$u\frac{\partial T}{\partial x} + v\frac{\partial T}{\partial y} = \frac{k_f}{r c_p}\frac{\partial^2 T}{\partial y^2} + \frac{n}{c_p}\left(\frac{\partial u}{\partial y}\right)^2 \qquad \text{--- (4)}$$

The corresponding boundary conditions are:

$$\begin{aligned} &u = U_s = Bx, v = -V_w, N = 0, T = T_w, && at\ y = 0 \\ &u \to 0, \quad N \to 0 \qquad T \to T_\infty && as\ y \to \infty \end{aligned} \qquad \text{--- (5)}$$

where $u$ and $v$ are the velocity components in the $x$ and $y$ directions and also $N$ and $T$ are also microrotation and temperature component in the same direction, $\upsilon, \rho, \sigma, c_p, B_0, \mu, K$ and $G_1$ are kinetic viscosity , fluid density , electric conductivity , specific heat constant , magnetic field, dynamic viscosity, vertex viscosity and microrotation constant. $k^*, T_w, T_\infty$ and $U_s$ are the permeability and electric conductivity , specific heat constant at the plate and free stream temperature, surface velocity and also $B$ and $V_w$ are constants.

The Eqs.(2)-(5) are transform into the ordinary differential equations by using the following similarity transformations and dimensionless variables

$$h = \sqrt{\frac{B}{\nu}}y, u = Bxf'(h), n = -\sqrt{B\nu}f(h), q = \frac{T - T_\infty}{T_w - T_\infty}, N = \sqrt{\frac{B^3}{\nu}}xg(h). \quad \text{--- (6)}$$

Substituting the Eq.(6) into Eqs. (1)- (5). We get the following ordinary differential equations are

$$f''' + ff'' + Ng' - \left(M + \frac{1}{K_p}\right)f' = 0 \quad \text{--- (7)}$$

$$Gg'' - (2g + f') = 0 \quad \text{--- (8)}$$

$$q'' + Pr\left(fq' + Ec(f'')^2\right) = 0 \quad \text{--- (9)}$$

And the boundary conditions:

$$\begin{aligned} &f(0) = s, f'(0) = 1, g(0) = 0, q(0) = 1, \quad at\ h = 0 \\ &f'(\infty) = 0, g(\infty) = 0, q(\infty) = 0, \quad as\ h \to \infty \end{aligned} \quad \text{--- (10)}$$

Using equation (6) shear stress at the wall is given $\tau_w = \left((\mu + K)Bx\sqrt{\frac{B}{\nu}}f''(0)\right)$.

The local heat transfer coefficient is given by $Nu_x = \sqrt{\frac{B}{\nu}}\theta'(0)$.

Where "′" denote the diff. w. r. to $\eta$, and $N = \frac{k}{\rho\nu}$, the magnetic parameter $M = \frac{\sigma B_0^2}{B\rho}$, permeability parameter $K_p = \frac{\rho K^* B}{\mu}$, microrotation parameter $G = \frac{G_1 B}{\nu}$, Prandtl number $Pr = \frac{\rho c_p \nu}{k_f}$, Eckert number $Ec = \frac{U_s^2}{C_p(T_w - T_\infty)}$, and mass transfer parameter which is for +ve for injection and +ve for injection and –ve for –ve for surjection i.e $f_w = \frac{v_w}{\sqrt{B\nu}}$.

**Method of solution:**

The flow equations (7) – (9) represent non – linear homogeneous differential equations for which closed form solutions can't be obtained. Hence the equations (7)-(9) subject to the conditions (10) are solved numerically by using Keller- box implicit finite difference method. This method gives the accurate outcomes for the boundary layer equations. Since the physical phenomenon of the underlying problem and bounded, the computational domain is chosen sufficiently large in order to meet the infinite boundary condition. In the present case the transverse distance is fixed to 10 (i.e. η→∞). In this method the non linear differential equations are transformed into simultaneous first order equations as follows:

So the desired equation can be written as

$$f' = p, \quad \text{--- (11)}$$

$$p' = q, \quad \text{--- (12)}$$

$$g' = t, \quad \text{--- (13)}$$

$$\theta' = h, \quad \text{--- (14)}$$

$$q' + fq + p^2 + Nt - K_1 p = 0 \text{ , where } \quad K_1 = \left(M + \frac{1}{K_p}\right) \quad \text{--- (15)}$$

$$Gt' - (2g + q) = 0, \quad \text{--- (16)}$$

$$n' + Prfn + A_1(q)^2 = 0 \text{ , Where } A_1 = Pr\ Ec \quad \text{--- (17)}$$

**Results and Discussion**

The behaviour of the velocity, angular velocity and temperature profiles are studied by drawing curves for varied parametric values governing the flow. The obtained results for velocity, angular velocity, temperature are illustrated by figures 1-3. It is clear from the figures that increased velocity is achieved with higher dimensionless porous medium parameter $kp$. Additionally, by increasing the values of the porous parameter $kp$, the location of peak micro rotation is driven away from the surface.

The behaviour of temperature is observed in Fig.3 that higher $kp$ values reduce the temperature. To sum up, it can be stated that higher values of $kp$ reduce the effects of $kp$.The effect of surface mass transfer on the dimensionless velocity, angular velocity and temperature distributions are studied from figs. 4-6. In order to make the temperature distribution and velocity move uniformly within the boundary layer, suction is introduced. Angular velocity is affected in an equivalent manner with permeability and suction parameter [9]. The temperature distribution for Prandtl numbers with no surface mass transfer is shown in Fig.7. On increasing values of Prandtl number, the surface heat transfer rate increases. Also, as $Pr$ increases the thermal boundary layer decreases.

Figs. 8-10 describe the effect of magnetic field on the velocity, angular velocity and temperature distribution respectively. As magnetic parameter $M$ increases, angular velocity, velocity decreases while temperature increases. From Fig. 10, it is observed that there is a weak effect of magnetic field on temperature distribution.

The effect of permeability parameter $kp$ on the heat flux at the surface and shear stress is depicted in Table 1. Here it is observed that $-\theta'(0)$tends to increase with higher $kp$ values while $g'(0)$and $f''(0)$ decrease.

The effect of magnetic field on $f''(0)$, $g'(0)$ and $f''(0)$ are described by Table 2. It is evident that on increasing M values$f''(0)$, and $g'(0)$, attain higher values while $-\theta'(0)$ reduce.

**Conclusion**

In this paper, a discussion of magneto-micropolar fluid characteristics which is incompressible, flowing through a porous medium past a horizontal stretching sheet is made. In order to transform the governing partial differential equations into ordinary equations, we made use of a similarity transformation. The obtained equations, using implicit finite difference method known as Keller Box method are used to obtain a numerical solution.

Shear stress and Nusselt number are reduced by Suction, the opposite effect. Alternatively, the permeability has the opposite magnetic fields effect on Nusselt number

and shear stress. Angular velocity and velocity tend to increase proportionally with permeability parameter and an opposite behaviour is observed with magnetic field. To obtain this result physically, the resistance of the medium must be neglected and can be arrived at when the holes of the porous medium are very large.

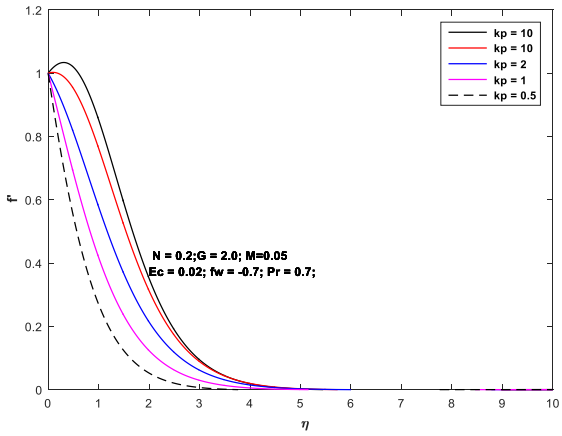


Fig.1:Effect of porous medium on velocity profiles

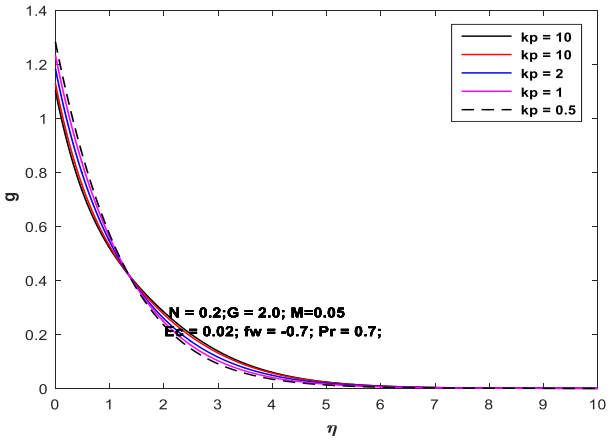


Fig.2: Effect of porous medium on angular velocity profiles

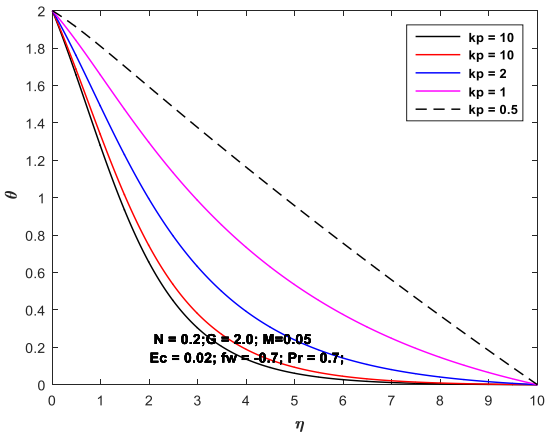


Fig.3: Effect of porous medium on Temperature profiles

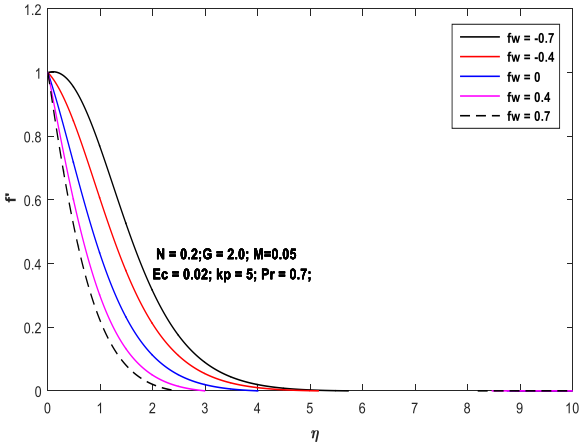


Fig.4: Effect of porous medium on velocity profiles

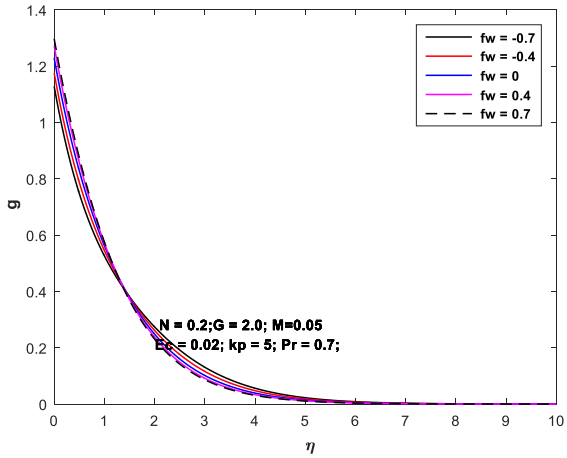


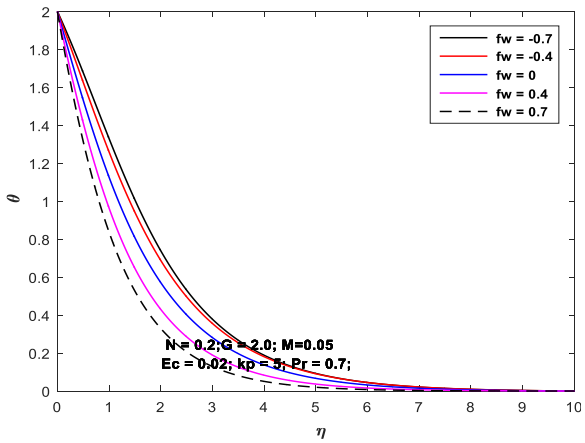

Fig.5: Effect of porous medium on angular velocity profiles

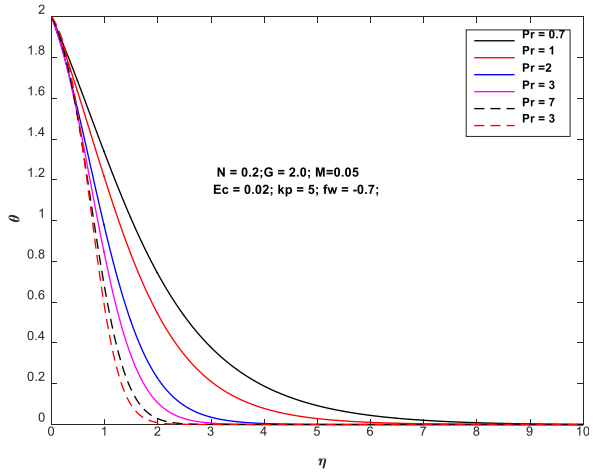


Fig.5: Effect of porous medium on Temperature profiles

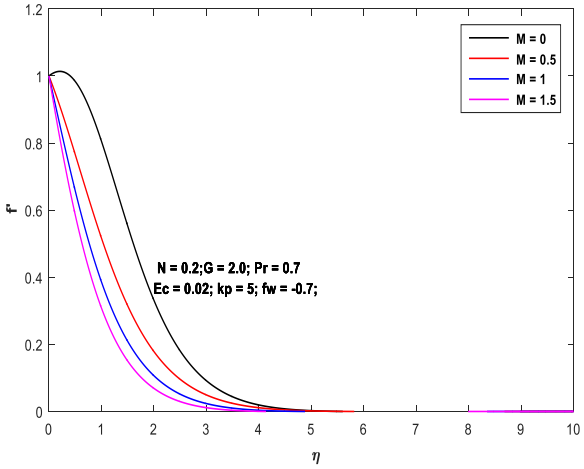


Fig.7: Effect of porous medium on Temperature profiles

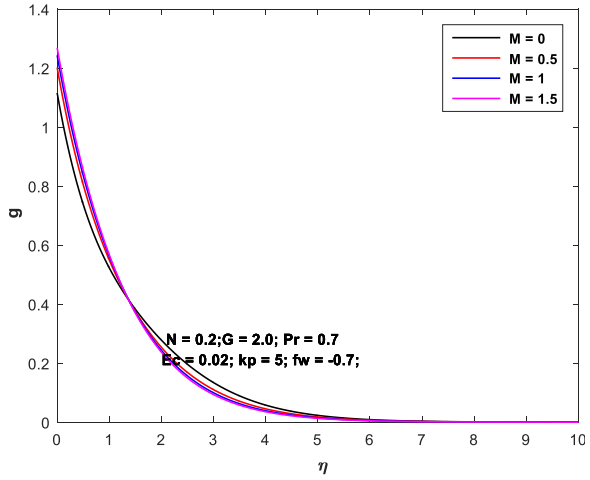


Fig.8 Effect of porous medium on velocity profiles

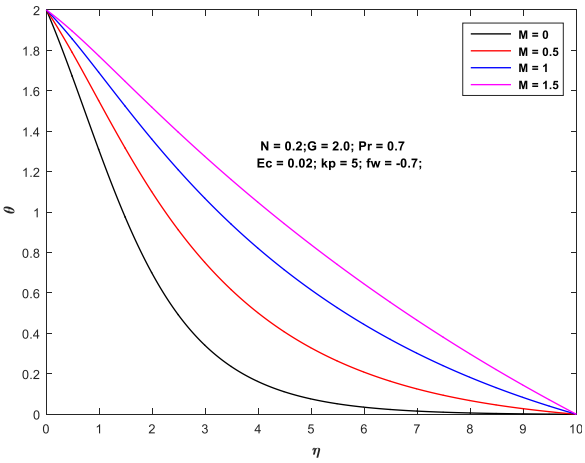


Fig.9: Effect of porous medium on angular velocity profiles

Fig.10: Effect of porous medium on temperature profiles

**Table 1**

Values of $-f"(0), g'(0) - \theta'(0)$ taking the values parameter $N = 0.0, G = 2, f_w = -0.7, M = 1, Pr = 0.7, Ec = 0.02.$

| $kp$ | $-f"(0)$ | $g'(0)$ | $-\theta'(0)$ |
|---|---|---|---|
| 15 | 1.1298 | 0.2651 | 0.1034 |
| 10 | 1.1408 | 0.2664 | 0.1021 |
| 5 | 1.7397 | 0.2701 | 0.0965 |
| 2 | 1.2694 | 0.2798 | 0.0826 |
| 1 | 1.4171 | 0.2913 | 0.0651 |
| 0.5 | 1.6804 | 0.3134 | 0.04215 |

Table 2: Values of $-f"(0), g'(0)$ and $-\theta'(0)$ taking the values parameter $N = 0.0, G = 2, f_w = -0.7, Kp = 5, Pr = 0.7, Ec = 0.02.$

| $M$ | $-f"(0)$ | $g'(0)$ | $-\theta'(0)$ |
|---|---|---|---|
| 0 | 0.8001 | 0.2223 | 0.1762 |
| 0.5 | 1.0001 | 0.2501 | 0.1.2863 |
| 1.0 | 1.7398 | 0.2701 | 0.09666 |
| 1.5 | 1.3301 | 0.2855 | 0.07849 |

REFERENCES:

1. H. A. M. El-Arabawy, Effect of suction/injection on the flow of a micropolar fluid past a continuously moving plate in the presence of radiation, *Int. J. Heat Mass Tran*., 46, pp. 1471–1477, 2003.
2. S. N. Odda, A. M. Farhan, Chebyshev finite difference method for the effects of variable viscosity and variable thermal conductivity on heat transfer to a micro-polar fluid from a nonisothermal stretching sheet with suction and blowing, *Chaos Soliton. Fract.*, 30, pp. 851–858, 2006.
3. Nadeem Ahmad Sheikh, Farhad Ali, Ilyas Khan, Muhammad Saqib, and Arshad Khan,. "MHD Flow of Micropolar Fluid over an Oscillating Vertical Plate Embedded in Porous Media with Constant Temperature and Concentration", *Mathematical Problems in Engineering,* Volume 2017, Article ID 9402964, pp.1-20, 2017.
4. E. M. Abo-Eldahab and A. F. Ghonaim, "Radiation effect on heat transfer of a micropolar fluid through a porous medium," *Applied Mathematics and Computation*, 169(1), pp. 500–510, 2005.
5. Y. J. Kim, "Heat and mass transfer in MHD micropolar flow over a vertical moving porous plate in a porous medium," *Transport in Porous Media*, 56(1), pp. 17–37, 2004.
6. S. Nadeem, M. Hussain, and M. Naz, "MHD stagnation flow of a micropolar fluid through a porous medium," *Meccanica*, 45(6), pp. 869–880, 2010.
7. T.Hayat, C. Fetecau, and M. Sajid, "Analytic solution for MHD transient rotating flow of a second grade fluid in a porous space," *Nonlinear Analysis: Real World Applications*, 9(4), pp. 1619–1627, 2008.
8. B.I. Olajuwon and, J.I. Oahimire, " Unsteady free convection heat and mass transfer in an MHD micropolar fluid in the presence of thermo diffusion and thermal radiation*", Int. J. of Pure and Applied Mathematics*, 84 (2), pp.15-37, 2013.
9. I.A. Hassanien, R.S.R. Gorla, "Heat transfer to a micropolar fluid from a non-isothermal stretching sheet with suction and blowing", *Acta Mech*. 84,pp.191-199, 1990.
10. I.A. Hassanien, "Boundary layer flow and heat transfer on continuous accelerated sheet extruded in an ambient micropolar fluid", *Int. Comm. Heat Mass Transfer* 25 pp.571–583,1998.
11. M.A. Seddeek, "Flow of a magneto-micropolar fluid past a continuously moving plate", *Phys.Lett*. A 306 (2003) 255–257.
12. P.G. Siddheshwar , U.S. Mahabaleshwar , "Analytical solution to the MHD flow of micropolar fluid over a linear stretching sheet", *Int. J. of Applied Mechanics and Engineering*, 20(2), pp.397-406, 2015.

# Analytical and Experimental Thermal Behavior of an AC-DC Convertor with Natural Convection.

**Santosh Joteppa[a], Sharath BK[b*], Venkatesha KA[c], Vinod Chippalkatti[d]**
santoshj@centumelectronics.com, sharathbk@centumelectronics.com, venkateshaka@centumelectronics.com, vinod@centumelectronics.com
**[a-d] Design and Engineering, Centum Electronics Limited, Bangalore, Karnataka, India**

**ABSTRACT:**
*Thermal design and development of highly integrated and denser power supply module, which can convert AC input voltage into multi output DC voltage is very challenging. The design will be even more challenging when the heat need to be transferred from components mounted on the PCB to the chassis under natural convection cooling. The components used for electrical design have different shape, size, and made of many different materials and finding the thermal properties of such components is next to impossible. These components again will have their own operating temperature limits and also will start degrading themselves when the components reaches their limited temperature and operated for longer duration and this will affect reliability. Hence it is necessary to verify the thermal design to identify the components temperature to limit below their operating temperatures in the design phase itself to avoid the repetitive manufacturing and testing.*

*This paper explains the methods of Thermal design, analysis and testing of an AC-DC converter with 205W output power and having multiple outputs. Thermal design verification has been carried out using computational fluid dynamics technique by considering heat dissipation of 37.92W and under natural convection. The analysis has been carried out by thermally modeling all the power dissipating components and components constructed with dissimilar materials. The design has been validated by thermally testing the AC-DC convertor in rapid temperature chamber by maintaining the ambient temperature at 65 Deg C. The results have been compared with that of the results obtained from computational fluid dynamics which gave robust and efficient thermal analysis results. This analysis result also leads to reduction of repetitive manufacturing of the product and running numerous lab experiment and time taken for redesigning.*

***Keyword:*** *Thermal analysis, electronics cooling, Computational fluid dynamics, Heat transfer, AC-DC convertor, Natural convection.*

**NOMENCLATURE**

| | | | |
|---|---|---|---|
| $T_s$ | Heat sink surface temperature, ($^0C$) | $T$ | Temperature (°C) |
| $T_\infty$ | Ambient temperature,($^0C$) | $t$ | Thickness (mm) |
| $T_{avg}$ | Average of surface and ambient temperature, ($^0C$) | $Q$ | Total heat dissipation in the converter, (W) |
| $Gr_L$ | Grashof number | $u$ | Velocity in direction of x |
| $\beta$ | volume expansion coefficient, (1/k) | $v$ | Velocity in direction of y |
| $l$ | Length of the heat sink, (m) | $w$ | Velocity in direction of y |
| $\nu$ | kinematic viscosity of the fluid, ($m^2/s$) | $\tau$ | Shear stress |
| $Pr$ | Prandtl numbers | $h_0$ | Enthalpy |
| $Ra_l$ | Rayleigh number | $K_{ej}$ | Effective thermal conductivity |
| $Nu_l$ | Nusselt Number | $f_i$ | Body force in i direction |
| $h$ | Heat transfer coefficient, ($w/m^2k$) | $\eta$ | Efficiency |
| $\Delta t$ | Temperature difference surface and ambient | Subscripts | |
| $Q_h$ | Heat Dissipation on heatsink, (W) | $jc$ | Junction to case |
| $\rho$ | Density (gm/cc) | $j$ | Junction |
| $k$ | Thermal conductivity (W/mk) | $c$ | Case |
| $C_p$ | Specific heat (J/kg-°K) | $h$ | Heatsink |
| $P$ | Pressure ($N/m^2$) | $l$ | Length of the fin |

## 1 INTRODUCTION

The trend in electronics packaging continues to be towards greater packaging density with high performance and higher power dissipation in both chip packages and printed circuit boards. As a result of this the working temperature of the package will increase and hot spots will cause high junction temperature of the devices. Generally, temperature increase in the assembly will decrease the reliability of the product so it is necessary to control the temperature of the assembly with in the limit. The most common approach of cooling is natural convection, it is a most commonly used technique for thermal management to have higher reliability.

AC-DC convertor, converts AC input voltage to DC output voltage. Alternating current is fed as input in the form of single phase or three phase to give pulsating DC. Rectifier circuits may be classified into two categories, i) half wave rectifiers and ii) full wave rectifier again this are sub-divided two into controlled and uncontrolled rectifiers. Mosfets are extensively used for changing AC to DC. In this paper AC-DC convertor has been designed for single phase AC input to convert into DC voltage, and then same DC voltage is divided to get a nine output of DC [1]. The converter consists of mainly Magnetics, transformer, diode, resistors and all these electronics components will be placed on printed circuit board (PCB).

In this paper, thermal design verification and validation of AC-DC convertor is discussed in detail. The paper also elaborates on thermal modeling of the components used in the design. The Thermal analysis is carried using computational fluid dynamics (CFD) technique for analyzing the problems involving fluid flow and heat transfer. These CFD tools will help in i) optimization of the design ii) reduce time and cost iii) many design configurations can be studied in a short time.

## 2 MECHANICAL DESIGN

Mechanical package design is very challenging in electronics systems design. These mechanical parts need to be designed to withstand thermal, environmental and vibration loads. Complete mechanical assembled converter is shown in the fig.1 The PCB need to be designed to maintain the stiffness and also to keep the PCB temperature within the limit. In this design a separate heat sink has been designed in such a way that it will have enough contact with PCB for better heat transfer through conduction and outside the fins have been designed to suit for better natural convection which mainly occurs due to buoyancy forces[2]. Determining optimal plate fin spacing of a natural convection, small-form-factor heat sink is an effective way to improve heatsink performance. The Fins spacing have been optimized to allow airflow between fins to stream as freely as possible from the heatsink base to the outer edge of heatsink fins.

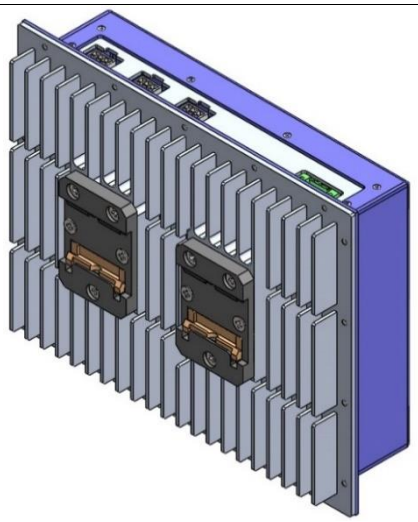

**Figure 1.** AC DC convertor assembly

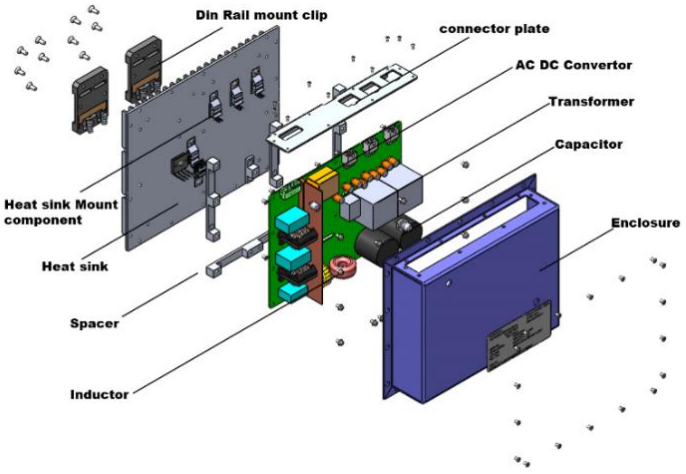


**Figure 2.** Exploded view of the AC DC convertor

The materials used for the mechanical parts design are of aluminum alloy having good thermal conductivity and light weight. PCB is designed with glass epoxy and components like transformer, inductor, capacitor, diode and resistor are placed on it and thermal vias are provided in the PCB, for better heat transfer from PCB to the heat sink. Some of the components like Mosfets and diode, which are dissipating high heat flux are directly placed on the heat sink which is shown in the fig. 2 of exploded view [3],

## 3 THERMAL DESIGN AND ANALYSIS:

### 3.1 Numerical Approach

Thermal design of AC-DC convertor is carried out under natural convection with total heat dissipation of 37.92W in that 23.77W is handled by the heat sink at ambient temperature of 65Deg C. In natural convection, where the velocity of moving air is unknown, no single velocity is analogous to the free stream velocity that can be used to characterize the flow. The Grashof number (Gr) and Rayleigh number (Ra) are used to correlate natural convection flows and heat transfer. Grashof number is as computed using air properties, which are taken at $T_{avg}$, by assuming the $T_s$, Grashof number $Gr_L$ expressed in following way,

$$Gr_l = \frac{g\beta\Delta t l^3}{\nu^2} \quad (1)$$

It is customary to correlate Rayleigh number in terms of Grashof and Prandtl numbers.

$$Ra_l = Gr_l \,\mathrm{Pr} \quad (2)$$

For the calculating the heat transfer coefficient for heat sink, Rayleigh number (Ra) obtained from equation $(2)$ was laminar flow ($10^4 \leq RaL \geq 10^9$), then Nusselt number $Nu_l$ is computed by below equation

$$Nu_l = 0.54 Ra_l^{0.25} \quad (3)$$

Heat transfer coefficient h can be calculated using following equation

$$\bar{h} = \frac{Nu_l k}{l} \quad (4)$$

$T_s$ is computed by below equation and area considered for cooling is sum of lateral fins surface and the plane surface.

$$\Delta t = \frac{Q_h}{\bar{h} A_s} \quad (5)$$

$$T_s = T_\infty + \Delta t$$

As evident, the estimated values of $T_s$ is inconsistent. To calculate appropriate value of $T_s$, Equation $(i)\ to\ (vii)$ need be solved in an iterative procedure until the value obtained temperature $T_s$ with more consistent [4].

In our case, following values are considered for calculation, $T_\infty = 65^0 C$, $A_s$=0.1399 m$^2$, $l$=0.1578m and $Q_h$=23.77W. The heat transfer coefficient obtained during calculation is 5.24 w/m$^2$k and temperature heat sink surface is 97.3Deg C.

During the design of heat sink, fin spacing plays critical role in natural convection. Since heat sink with closely spaced fins will have superior surface area for the heat transfer but a smaller heat transfer coefficient because of the extra resistance the additional fins introduce to fluid flow through the inter fin passages. On the other hand, a heat sink with widely spaced fins, will have a higher heat transfer coefficient but a smaller surface area [5]. Therefore, there must be an optimum spacing that maximizes the natural convection heat transfer. To compute the Rayleigh number (Ra), equation from (i) to (iii). The following equation is used,

$$Ra_l = Gr_l \Pr \tag{6}$$

Bar-Cohen and Rohsenow given an expression for optimum fin spacing for a vertical heat sink is,

$$S_{opt} = 2.714 \frac{l}{Ra_l^{0.25}} \tag{7}$$

To calculate the number of fin which required for the heatsink for Natural convection by ignoring fins at extreme ends,

$$n = \frac{W}{S_{opt} + t} - 1 \tag{8}$$

The number of fins for in case is calculated as 21 fins.

### 3.2 Thermal Modeling

Simulation was carried out to check that thermal design of convertor is adequate to meet the intended specification. Mechanical CAD model was prepared and Thermal analysis is done with finite volume method and all active component like transformer, diode, Mosfets and inductors which are critical from thermal point of view are modeled and heat from inactive component and PCB tracks loss are added as uniformly distributed load to PCB. It was analyzed under the natural convection, Temperature and flow behavior of converter inside the cabinet are studied in detail.

#### 3.2.1 Computational fluid dynamics

CFD expansively used in the all kind of engineering industries for different applications, which help in creating the new design model, understanding the complete behavior of the system, to identifying the design flaws (if any) and predicting advantage of optimization or new design of the system. The computational representation of the model is basically taken by the CFD solver and which is an iteratively solved for the continuity, momentum and energy [6].

The governing equation for the Steady flow (Time-independent flow), incompressible flow of viscous fluid. The equation that includes conservation of mass, momentum equation in the direction of x-, y- and z-direction and energy equation.

*Continuity Equation,*

$$\frac{\partial u}{\partial x} + \frac{\partial v}{\partial y} + \frac{\partial w}{\partial z} = 0 \tag{9}$$

*Momentum equation in X-direction,*

$$\nabla(\rho u V) = -\frac{\partial p}{\partial x} + \frac{\partial \tau_{xx}}{\partial x} + \frac{\partial \tau_{yx}}{\partial y} + \frac{\partial \tau_{zx}}{\partial z} + f_x \tag{10}$$

*Momentum equation in Y-direction,*

$$\nabla(\rho v V) = -\frac{\partial p}{\partial y} + \frac{\partial \tau_{xy}}{\partial x} + \frac{\partial \tau_{yy}}{\partial y} + \frac{\partial \tau_{zy}}{\partial z} + f_y \tag{11}$$

*Momentum equation in Z-direction,*

$$\nabla(\rho w V) = -\frac{\partial p}{\partial z} + \frac{\partial \tau_{xz}}{\partial x} + \frac{\partial \tau_{yz}}{\partial y} + \frac{\partial \tau_{zz}}{\partial z} + f_z \tag{12}$$

*Energy equation,*

$$\nabla(\rho h_0 V) = -P\nabla.V + \nabla.\left(K_{eff}\nabla T\right) + f_h \tag{13}$$

Where,

In above equation, *(u, v, w)* are the component of the fluid velocity *V* in direction of *(x, y, z)* direction; *p* is pressure; *T* is temperature, $\tau$ shear stress, $h_0$is total enthalpy and *( $f_x$, $f_y$, $f_z$)* are body force in the direction of *(x, y, z)* respectively.

#### 3.2.2 Modelling Methodology

Thermal design has to be done in such a way that the component temperature should be well below operating temperature limit specified by manufacturer and also it should meet intended electrical performance while it is operated in harsh thermal environmental. To meet this specification, the study of thermal behavior of complete electronic product is very important, so thermal modeling has to be constructed in detail to get accurate results.

*Component*

The component which are important from the thermal point of view are modelled. For the components which are having thermal resistance ($\theta_{jC}$), provided by component manufacturer are modelled using 2R network and heat dissipation are applied to particular component. [7]. for components like mosfets and diode, which are dissipating high heat flux are directly placed on the heat sink with thermal interface as shown in fig 3.

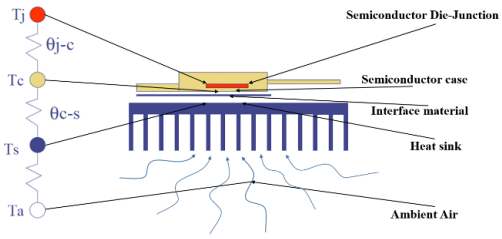


**Figure 3.** Thermal resistance model

| Sl. No | Material | Density (kg/m$^3$)X10$^3$ | Thermal Conductivity K(w/mk) | Specific heat $C_p$ (J/kg-°K) |
|---|---|---|---|---|
| 1 | Al Alloy 6061T6 | 2.7 | 167 | 896 |
| 2 | Al Alloy 5052H32 | 2.68 | 138 | 880 |
| 3 | Copper | 8.96 | 386 | 380 |
| 4 | Glass Epoxy (FR4) | 1.25 | 0.3 | 1300 |
| 5 | Kovar | 8.36 | 16.3 | 432 |
| 6 | Ferrite | 4.85 | 3.5 | 1100 |

**Table 1.** Properties of material used in analysis.

The component manufacture who does not provide the thermal resistance value, they are modelled by specifying the material properties that has been used for the contracting the component, the heat dissipation details are applied to the complete volume. Table 1 shows the material properties used for the analysis [8].

| Board dimension: LXWXH: 153.8X206.6X1.6 mm | | | |
|---|---|---|---|
| CTM8416D953 | | | |
| | | Name | Isolation in mm |
| | Solder mask top | | 0.01 |
| Layer 01 | 35µm base-copper + 35µm plating | | 0.07 |
| | 0,008" FR4 ITEQ IT-180A (IPC-4101D/99/101/126) | core | 0.2 |
| | 2 X 1080 =0.0060" Prepreg ITEQ IT-180A | prepreg | 0.15 |
| Layer 02 | 70µm base-copper | | 0.07 |
| | 0,008" FR4 ITEQ IT-180A (IPC-4101D/99/101/126) | core | 0.2 |
| Layer 03 | 70µm base-copper | | 0.07 |
| | 2 X 1080 =0.0060" Prepreg ITEQ IT-180A | prepreg | 0.15 |
| Layer 04 | 70µm base-copper | | 0.07 |
| | 0,008" FR4 ITEQ IT-180A (IPC-4101D/99/101/126) | core | 0.2 |
| Layer 05 | 70µm base-copper | | 0.07 |
| | 2 X 1080 =0.0060" Prepreg ITEQ IT-180A | prepreg | 0.15 |
| | 0,008" FR4 ITEQ IT-180A (IPC-4101D/99/101/126) | core | 0.2 |
| Layer 06 | 35µm base-copper + 35µm plating | | 0.07 |
| | Solder mask bottom | | 0.01 |
| | Total 1.6± 10% | | 1.69 |

**Table 2.** Stackup details of PCB

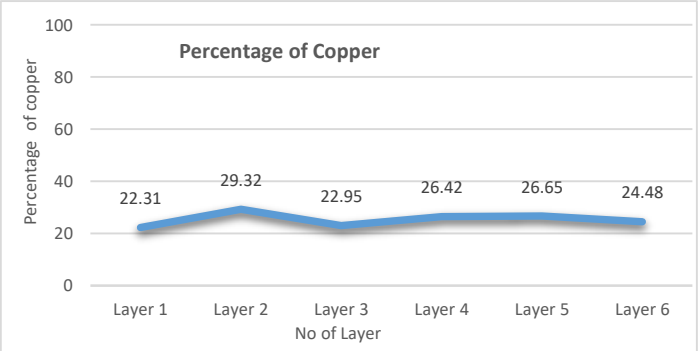


**Graph 1.** Percentage of PCB

*Printed circuit board*

PCBs are made by sandwich of many layers of copper and dielectric material glass epoxy (FR4). Electrical signal are transferred with help of copper traces in each signal layer, power plane is often used in addition to a ground plane in a multilayer circuit board, to distribute DC power to the active devices. And thermal layer are provided in the PCB with many thermal and electrical vias for better heat flow through in-plane and out-plane direction, which help in transfer of heat from low thermal conductivity PCB to the mechanical heat sink [9].

The PCB is modelled in Ansys Icepak simulation software which has inbuilt calculator for computing thermal conductivity, density in both in plane and out of plane based on geometry, thickness, number of layer and percentage of copper in each layer. PCB stackup of the converter provide in table 2 and copper percentage in each layer are mentioned in graph 1 and even software has capable to display the traces in 3D and it can show metal fractions or percentage of copper for each trace layer of a PCB. The thermal conductivity of PCB is calculated as 26.12W/mk in plane and 0.4739 W/mk out of plane. These values have been used in the analysis.

*Power dissipation*

The heat dissipation is detrained based the efficiency of system. Efficiency of the system can be defined as the electrical output to the electrical input.

$$\eta = \frac{output\ Power}{Input\ power} \qquad \& \qquad Heat\ Dissipation = \left(\frac{1}{\eta} - 1\right) output$$

All active component are modelled which are critical from thermal point of view and heat dissipation are applied to component. Other heat loss are considered as lumped heat which is uniformly distributed in the printed circuit board as given table 3.

| Sl. No | Reference | Heat Dissipation(W) |
|---|---|---|
| 1 | AD1(Bridge rectifier) | 5.4 |
| 2 | AD3(Rectifier) | 0.632 |
| 3 | CD2 (Rectifier) | 1.3 |
| 4 | DD2( Rectifier) | 1.5 |
| 5 | BD2 | 7.5 |
| 6 | FU1 | 0.5 |
| 7 | FQ3 | 0.3 |
| 8 | BTR1 | 1.655 |
| 9 | CTR1 | 2.168 |
| 10 | DTR1 | 1.561 |
| 11 | BU1 | 0.575 |
| 12 | CU1 | 0.43 |
| 13 | DU1 | 0.56 |
| 14 | AL4 | 1.5 |

| Sl. No | Reference | Heat Dissipation(W) |
|---|---|---|
| 15 | AM1 | 7.44 |
| 16 | AL1(CMI) | 0.36 |
| 17 | AL2(CMI) | 0.36 |
| 18 | AL3(DMI) | 0.18 |
| 19 | Other losses | 4 |
| | Total Power Dissipation (W) | 37.92 |

**Table 3.** Heat dissipation of the component used for the analysis.

*Grid Generation*

In this system, Mesher-HD used for creating the mesh since model consists of both CAD and primitive objects. It is very important to use the fine mesh for high temperature density region and coarse mesh is used for other region. CFD solution are mainly depend on the grid generation, hence it basic criteria for obtaining quality of mesh to obtain accurate CFD solution.

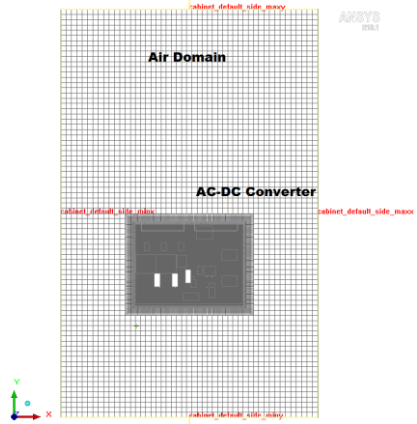


**Figure 4.** Meshed model of the cabinet with system

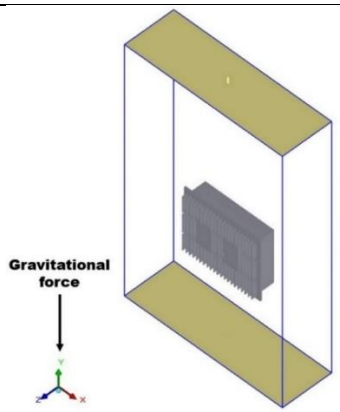


**Figure 5.** CFD model along with cabinet

Fine mesh is used in the high heat density region and coarse mesh is used for outside converter region. The above fig. 4 show the meshed region in the cabinet.

| Mesh details | | |
|---|---|---|
| Sl. No. | Description | Range |
| 1 | No. of nodes | 57,48,479 |
| 2 | No. of elements | 64,19,869 |

**Table 4.** Details of mesh in analysis.

| Mesh quality | | |
|---|---|---|
| Sl. No. | Element Quality | Range |
| 1 | Face alignment | 0.288 to 1 |
| 2 | Volume | 1e-6 to 2.06e-13 |
| 3 | Skewness | 0.07 to 1 |

**Table 5.** Mesh quality used in the analysis.

### 3.2.3 Boundary condition

Defining the accurate boundary condition will play vital role in for getting veracious CFD results. Thermal analysis is carried out in the computational domain which is approximately equal to physical space where testing and end usage operating requirement. Steady state thermal simulation was carried out by considering the natural convection at the 65 deg C ambient temperature, the four side of the cabinet are assumed as wall by maintained the temperature at 65 deg C. the gravitational force is assumed negatives Y axis direction as shown in the fig. 5, inside the cabinet air properties are assumed. Contact conductance is assumed between the Transformer & PCB, PCB & Heat sink.

### 3.2.4 Analysis Result

Steady state thermal analysis is carried out using by considering heat dissipation of 37.92W. The temperature distribution plots for the assembly are shown below, for natural convection mode of heat transfer.

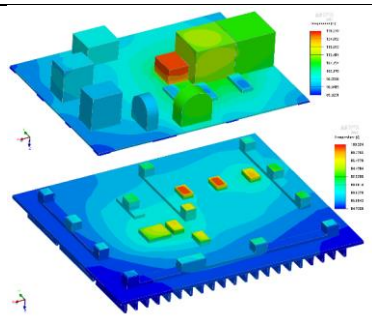

**Figure 6.** Isometric view PCB and heat sink with components.

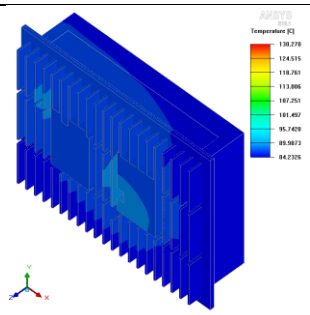

**Figure 7.**Temperature distribution in rear view of whole assembly.

The fig. 6 show the temperature distribution in the PCBA, and Heat sink with components, where maximum temperature observed in PCB assembly is 130.27 Deg C and maximum temperature observed in Heat sink assembly is 100.3 Deg C and the fig. 7 show the temperature distribution in complete mechanical housing which includes mechanical enclosure, Heat sink, PCBA with spacers.

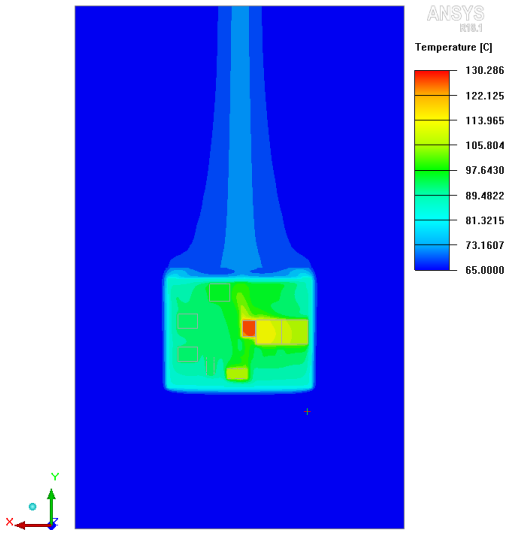


**Figure 8.** Plane cut view of cabinet at near PCB assembly

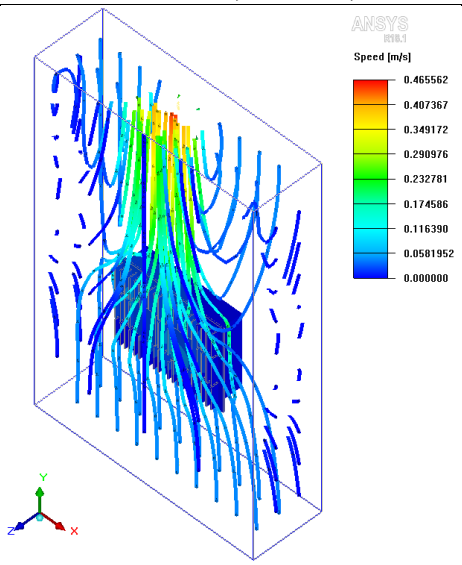


**Figure 9.** Particle trace inside the cabinet

The temperature distribution of cut sectional near to the PCB assembly and inside the cabinet ambient is maintained at 65 Deg C, temperature of ambient air is getting heated on the top surface of the package. It is noticeable from figure 8 that minimum temperature maintained is 65 °C and maximum temperature obtained is 130.27 °C that is observed in the component CTR1 transformer. In figure 9, shows the plume of hot air rising from the heated surface of the assembly due to the buoyancy force acting on the air. The maximum positive Y direction velocity driven by buoyancy is approximately equal to 0.4655m/s which is fairly reasonable for natural convection environment [10]. And thermal analysis results are tabulated in table. 8 for some of critical temperatures components in the convertor.

### 3.3 Assembling Methodology

Based on the analysis results, the converter has been manufactured and assembled. During thermal design stage, thermal interface material was considered to provide blow the transformer which is dissipating more heat so in order to remove the heat and to maintain the temperature blow the glass transition, gap pad are introduced in between the transformer and PCB to reduce air gap. The figure 10. Show the CAD model and actual assembled module.

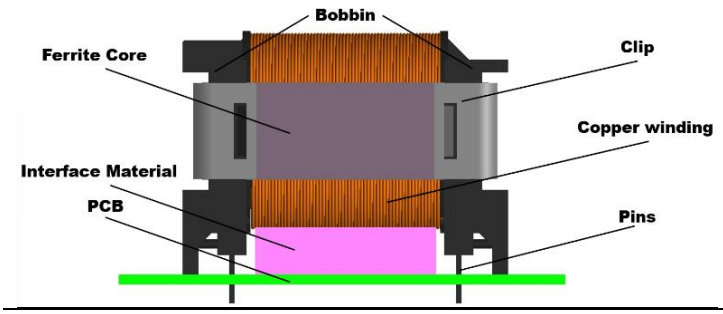


**Figure 10.** TIM considered during design phase

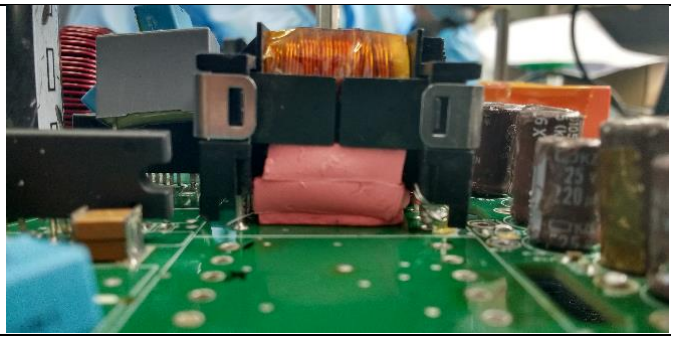

**Figure 11.** Assembling TIM beneath the Transformer

Gap pad is specifically used, since it is having good thermal conductivity and electrically insulting properties. Critical assembly producer from thermal point of view is to maintain the minimum compression ratio of the interface material to reduce the voids and air gap between the component and PCB. The above figure show assembling process of gap pad [11].

### 3.4 Thermal Testing

When manufacturing and assembly is finished, the converter has been taken for electrical performance test, when electrical performance are satisfactory then converter available for the thermal testing. Thermal testing is the one of the comprehensive risk mitigation test used during the design qualification stages. Since electronic products used for aerospace application will be exposed to repeated, harsh and extensive changes in operating temperature.

#### 3.4.1 Rapid Temperature chamber

The Rapid temperature chamber are an enclosure used to examine the effects of specified environmental conditions for electronics component and product. A rapid temperature chamber artificially replicates the conditions under which electronic product is exposed

in real time. This chamber which helps in determining effect of temperature on electrical performance and reliability of the product. Thermal cycling for qualification levels were conducted at more stressing temperature than predicted. If any malfunctioning in electrical performance due to thermal effects, which can be resolved during the qualification stage before using in the real time situation [12].

| Sl. No | Particular | Description |
|---|---|---|
| 1 | Make | COMET ENVIRONS |
| 2 | Model | 2012 |
| 3 | Temperature range | -70ºC to +180º C |
| 4 | Power Dissipation | <19 Kw |
| 5 | Work space | 750X750X750mm |

**Table 6.** Rapid temperature chamber details.

### 3.4.2 Testing approach

Thermal cycling is essential qualification test for electronics product to check the temperature of the component, which can be compared with analysis results. Temperature of electronic product will consequence in electrical performance and reliability of the product can be estimated, so it is essential to measure the accurate temperature of component.

- Base on the Thermal analysis result, temperature sensor are attached to the hotspot component and it was ensured perfect contact between the temperature sensor and component by applying potting material to sensor.

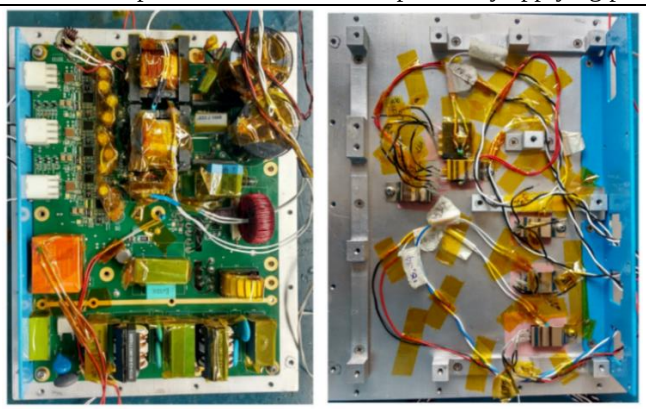

**Figure 12.** Thermistor attached to component in PCB and heat sink.

**Figure 13.** Converter inside the rapid temperature cycle chamber.

The figure 12 shows temperature sensor are attached to the PCB assembled component and heat sink mount component, where this are hot spot component and which dissipate more heat.

- The convertor is placed inside the Rapid temperature chamber with the help of L shaped bracket which is having din rail to hold the convertor. Chamber ambient temperature is maintained at 65 Deg C and monitored by hanged temperature sensor in the in air.
- Converter is subjected to Thermal cycling test, the following graph is used and the temperatures have been continuously monitored along with the electrical functionality test at each temperature extremes. At final positive extreme cycle, the temperature is monitored until the unit reaches thermal equilibrium.

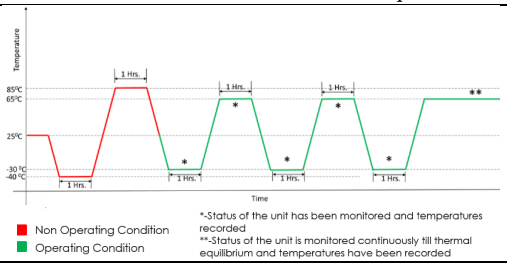


**Graph 2.** Thermal cycling profile.

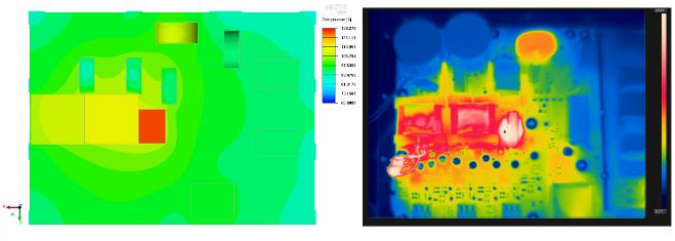

**Figure 14.** IR image and analysis image comparison

- The result obtained during the analysis are also compared with Infrared Radiation (IR) camera has been used for identifying the hotspot in the convertor at room temperature, when converter is operated with full load till the components have attained their thermal equilibrium, then plots from IR imaging have been captured. IR image is used to compare with analysis results which gives enough confidence in the analysis.

### 3.4.3 Test Result

During the thermal cycling test at positive extreme temperature of last cycle, temperature are monitored from thermistor for every five minute until it reaches thermal equilibrium. The maximum temperature obtained during the testing is 131 Deg C which is in

CTR1. For some of the important component test results are tabulated in the table 8, the results obtained during the experiment are compared with the analysis results, through this deviated of results are may be predicted. Errors can be reduced in some of the assumptions made during the analysis are fine-tuned for the future analysis. The maximum percent variation found is 7.4 which was on the component.

| Sl. No | Reference | Analysis Results | Experimental results | Error % |
|---|---|---|---|---|
| 1 | AD1(Bridge rectifier) | 95.91 | 91 | 5.12 |
| 2 | AD3(Rectifier) | 97.17 | 92 | 5.32 |
| 3 | CD2 (Rectifier) | 100.32 | 93 | 7.30 |
| 4 | BD2 | 98.41 | 95 | 3.47 |
| 5 | FU1 | 97.65 | 96 | 1.69 |
| 6 | BTR1 | 111.57 | 118 | 5.75 |
| 7 | CTR1 | 130.27 | 131 | 0.56 |
| 8 | DTR1 | 115.73 | 124 | 7.14 |
| 9 | AL4 | 107.86 | 106 | 1.72 |
| 10 | AM1 | 97.24 | 90 | 7.45 |
| 11 | PCB ( Near The CTR1) | 103.31 | 100 | 3.19 |
| 12 | DD2( Rectifier) | 100.20 | NA | |
| 13 | AL1(CMI) | 95.17 | NA | |
| 14 | AL2(CMI) | 94.61 | NA | |
| 15 | AL3(DMI) | 96.35 | NA | |

**Table 9.** Analysis and experimental results compression

## 4 SUMMARY AND CONCLUSION

An analytical and experimental investigation on thermal performance of electronics product was carried out, in which the detailed thermal design, calculation, modelling methodology for the thermal management of electronics package and thermal testing of electronic product are explained. The study is summarized as, steady state thermal analysis is carried out with power dissipation of 37.92 W under natural convection and with an ambient temperature of 65 Deg C to identify the hotspots in converter. Based on the analysis results, the unit is manufactured and assembled. Thermal testing of converter carried out in rapid temperature chamber and thermal sensors are used to measure the temperature on the components which are critical from the thermal point of view. In order to have more confidence on thermal testing, convertor hot spots are identified using thermal camera and compared with analysis results. The result of experimental are compared with that of analysis results and the maximum error found is 7%.

# Reference

[1] B. Singh, B. N. Singh, A. Chandra, K. Al-Haddad, A. Pandey, andD. P. Kothari, “A review of single-phase improved power quality AC–DC converters,”IEEE Trans. Ind. Electron., vol. 50, no. 5, pp. 962–981, Oct. 2003.

[2] Roderick K. W. Lee., Michael G., Montero and Paul K. Wright., “Design methodology for the thermal packaging of hybrid electronic mechanical products” ASME, Design Engineering Technical Conferences, DAC-48790, pp.1-10, 2003.

[3] Hossein Maleki., Ahmad K. Shamsuri., “Thermal analysis and modeling of a notebook computer battery” Elsevier Science, Journal of Power Sources, vol. 115, pp.131–136, 2003.

[4] Theodore l. Bergman., Adrienne S. Lavine., Frank P. Incropera., David P. Dewitt., “Fundamentals of Heat and MassTransfer”. Wiley, 2011.

[5] Yunus A. Cengel., “Heat Transfer: A Practical Approach” Tata McGraw-Hill Education, 2007.

[6] Manasa Sahini., Eric Kumar., Tianyi Gao., Charles Ingalz., Ali Heydari., Sun Xiaogang., “Study of Air Flow Energy within Data Center Room and Sizing of Hot Aisle Containment” IEEE 15th ITHERM Conference pp. 1453-1458, 2016.

[7] John H. Lau., and Tang Gong Yue., “Thermal Management of 3D IC Integration with TSV” IEEE Electronic Components and Technology Conference, pp.635-640, 2009.

[8] Jerry E. Sergent., Al Krum., “Thermal Management Handbook: for the electronics assembly” Tata McGraw-Hill, 1998.

[9] J.E. Greabner, Thermal Conductivity of Printed Wiring Board, Bell, 1995.

[10] ANSYS Icepak 12.1, user’s guide November, 2009.

[11] Ronald J. Warzoha., Andrew N. Smith., and Maurice Harris., “Maximum Resolution of a Probe-Based, Steady-State Thermal Interface Material Characterization Instrument” Journal of Electronic Packaging, Vol. 139, 011004 pp.1-8, 2017.

[12] Santosh Joteppa., Bhoopendrakumar Singh., Satyanarayana Prasad., Vinod S Chippalkatti., R. N. Garvalia., K. G. Domadia., R. M. Parmar., R.K. Dave., DRM Samudraiah.,“ Analysis and Experimental Verification of Space Grade Power Supply Performance under Thermo-Vacuum Environment” Scientific & Academic Publishing, International Journal of Aerospace Sciences, Vol.1(3) pp. 43-48, 2012.

Fifth International Conference on Computational Methods for Thermal Problems
THERMACOMP2018, July 9-11, 2018, Indian Institute of Science, Bangalore, INDIA
*N. Massarotti, P. Nithiarasu, Pradip Dutta and C. Ranganyakalu (Eds.)*

# NUMERICAL STUDY OF CONJUGATE HEAT TRANSFER DUE TO IMPINGEMENT OF TURBULENT SLOT JET ONTO A MOVING FLAT PLATE

**Shashikant[1], Devendra Kumar Patel[2]**
School of Mechanical Engineering, VIT Vellore, 632 014
[1]Shashikant@vit.ac.in & [2]devendrakumar.patel@vit.ac.in

## ABSTRACT

A numerical study of the conjugate heat transfer of an impinging jet with the moving flat plate has been carried out using the standard high Reynolds number two equation $k-\epsilon$ eddy viscosity model. The plate velocity has been considered in the range of $0-0.25$ with the interval of $0.05$. The Reynolds number based on the jet exit conditions and the turbulent intensity at the nozzle exit are considered $9{,}900$ and $2\%$ respectively. The nozzle-to plate distance $\left({}^{h}/_{w}\right)$ is fixed at $7.5$ for all the simulations. The constant wall temperature boundary condition has been considered at the bottom face of the moving flat plate. The influence of plate velocity on the flow field and heat transfer has been presented using the one-dimensional plot of velocity, pressure, temperature, Nusselt number, and skin friction coefficient. It is found the rate of heat transfer gets uniform with increase in the plate velocity.

**Key Words:** *Heat and Fluid flow, Conjugate Heat Transfer, Moving Plate, $k-\epsilon$ model.*

## 1. INTRODUCTION

Impinging jets are utilized to enhance the heat transfer in a broad range of engineering applications. Applications in engineering fields include fabric drying [1], furnace heating [2], turbine blade cooling [3], tempering of glass and metal sheets [4], and many others. This topic is extensively researched which has drawn the attention of several scientists. It cannot be denied that conjugate heat transfer of impinging jets still stays as one of the dynamic areas of research due to the complex nature of fluid flow. B. E. Launder and D. B. Spalding [5], Viskanta [6], and S. A. Frost et al. [7] are the few important review work present in the literature, delineating the conjugate heat transfer due to the impinging jet flow. A number of experimental [8], [9] and numerical [10], [11], [12] studies are found in the literature which deals the heat transfer between the normal impingement of jet and the flat surface. The present study concerns with conjugate heat transfer in an impinging turbulent slot jet with the moving flat plate of finite thickness. This study is helpful in estimating the cooling performance of the moving plate.

## 2. COMPUTATIONAL DOMAIN, NUMERICAL SCHEME AND METHOD OF SOLUTION

A confined single vertical jet of cold fluid is impinging onto a hot moving flat plate of finite thickness $t(=w)$ is shown in Figure 1. The channel height is considered h. The origin of Cartesian coordinate system $(0\ 0)$ considered at the bottom surface of the moving plate. The size of computational is domain is $120 \times 8.5$. The top, left and right boundary of domain is located at $X = +8.5$, $X = -60$ and $X = +60$ respectively. The confinement plate has been considered to be adiabatic. The width of the nozzle $(w)$ and magnitude of the jet exit velocity $(V_0)$ are considered as the characteristic length and characteristic velocity respectively. These values have been used to non-dimensionalize the different parameters of governing equations.

$$U = \frac{u}{V_0},\ V = \frac{v}{V_0},\ X = \frac{x}{w},\ Y = \frac{y}{w},$$

$$\theta = \frac{T-T_\infty}{\Delta T_{ref}},\ \text{where}\ \Delta T_{ref} = T - T_\infty,\ X = \frac{x}{w},\ Y = \frac{y}{w},\ P = \frac{p-p_0}{\rho {V_0}^2},$$

$$k_n = \frac{k}{{V_0}^2},\ \epsilon_n = \frac{\epsilon}{{V_0}^3/_w},\ v_{t,n} = \frac{v_t}{v},\ \propto_{t,n} = \frac{\propto_t}{\propto} \qquad (1)$$

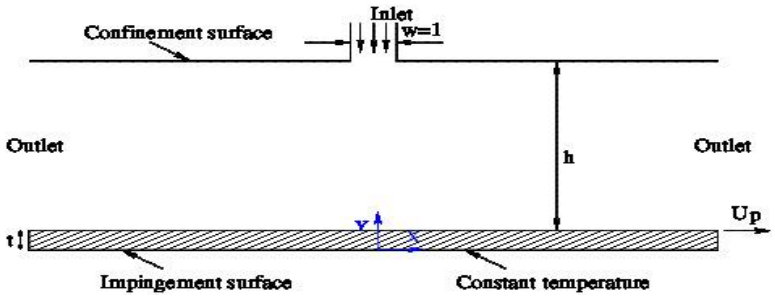


FIGURE 1. Schematic diagram of a turbulent slot jet impinging on a moving flat plate

The two-dimensional, steady, incompressible, turbulent jet flow fields have been resolved using the standard high Reynolds number two equation $k-\epsilon$ eddy viscosity model. The governing equations are discretized using finite volume approach [13]. To achieve the numerical stability, the power-law upwinding scheme and central difference scheme are used for the convective and diffusive terms respectively. The velocity and pressure equations are coupled using the SIMPLE algorithm [13]. The pseudo-transient approach [14] is used to under-relax the momentum and turbulent equations. The numerical simulation and post processing has been carried out using OpenFOAM and ParaView respectively. All the computations have been conducted in an Intel(R) Xeon(R) E5, 2.20 GHz machine on Linux platform.

## 3. VALIDATION OF NUMERICAL STUDY

The results of the present numerical study have been compared with the experimental data of Center and Solliec [9]. Figure 2 presents the comparison of variation in velocity along the jet centerline. The comparison of velocity magnitude $V_0 = \sqrt{(U^2+V^2)}$ along the horizontal line at the location of $Y = 4$ has been presented in Figure 3. It is found that, the numerical results are in good agreement with the available experimental data.

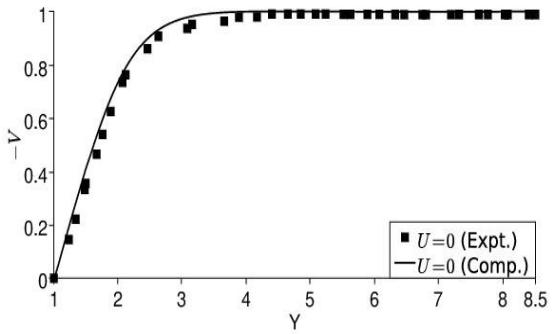


FIGURE 2. Comparison of vertical velocity along the jet centerline with the experimental data of Senter and Solliec [9] for the case $U_p = 0$

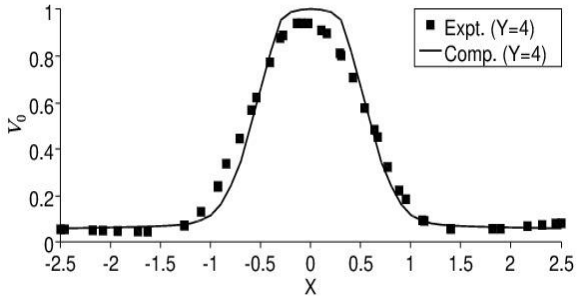


FIGURE 3. Comparison of velocity magnitude profiles at $Y = 4$ with the experimental data of Senter and Solliec [9] for the case $U_p = 0$

## 4. RESULTS

In the present numerical study, the influence of plate motion on the conjugate heat transfer has been conducted with varying the plate velocity in the range of $0 - 0.25$. The nozzle-to-plate distance $\left({}^{h}/_{w}\right)$ is fixed at 7.5 for all the simulations. The Reynolds number and the turbulent intensity at the nozzle exit are 9,900 and 2% respectively. The bottom face of impingement plate has been maintained at a constant wall temperature higher than the nozzle exit temperature.

### *4.1 Flow characteristics*

The velocity profiles over the horizontal line at different $Y$-locations 1.5, 2.5, 4.5, 6.5 and 8.5 have been presented in Figure 4. For the stationary plate impingement $U_p = 0$, the velocity profiles at different $Y$-locations are found to be symmetric about the jet axis is shown in Figure 4a. As the jet flow approaches to the flat plate from the nozzle exit, the velocity profiles of jet get wider due to the penetration of viscous effect from the surrounding stagnant fluid towards the jet. The variation in pressure $(P)$ and velocity magnitude $(V_{mag})$ along the jet centerline have been presented in Figure 5.

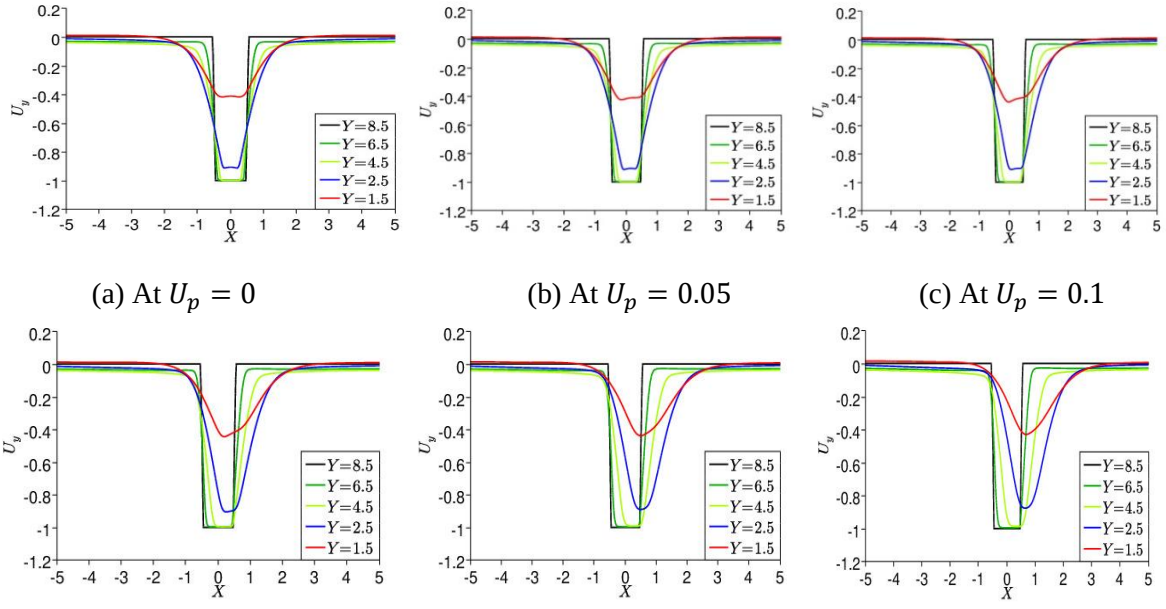


(a) At $U_p = 0$ (b) At $U_p = 0.05$ (c) At $U_p = 0.1$

(a) At $U_p = 0.15$ (b) At $U_p = 0.2$ (c) At $U_p = 0.25$

FIGURE 4. The influence of the plate velocity $(U_p)$ over the development of jet

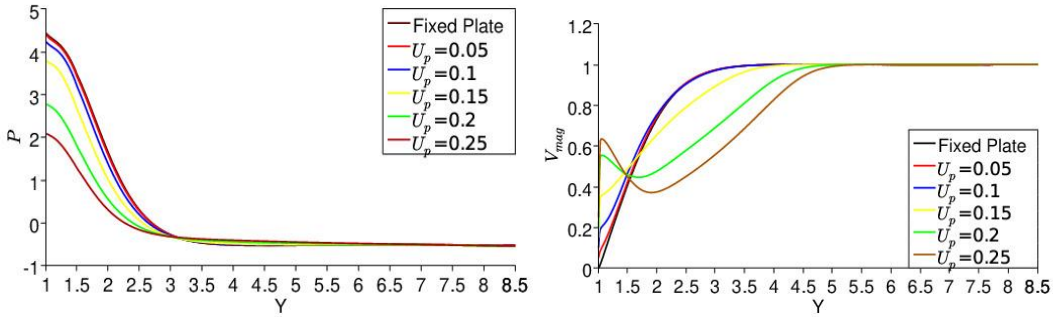


FIGURE 5. Pressure ($P$) and velocity magnitude ($V_{mag}$) along the jet centerline

*4.2 Local shear stress variation*

The distribution of skin-friction coefficient over the plate surface for the different plate velocities have been presented in Figure 6. The profile of skin-friction coefficient is found to be symmetric about the jet axis for the case of fixed plate. However, the symmetry vanishes with increase in the plate motion. The degree of skewness is increasing with increase in the plate velocity. The locations of local minimum skin-friction coefficient are found at 0, 0.15, 0.45, 0.8, 1.0 and 1.15 for the different plate velocities of 0, 0.05, 0.1, 0.15, 0.2 and 0.25 respectively. In the stagnation region, the relative velocity of the fluid is almost zero, in this region; the skin-friction coefficient shows almost zero value. The high pressure in the stagnation zone acts as a driving force, which accelerates the fluid beside of the stagnation zone. Results, the increase in the skin-friction coefficient has been observed. Further, the fluid deaccelerate due to shear force and consequently the skin-friction coefficient reduces.

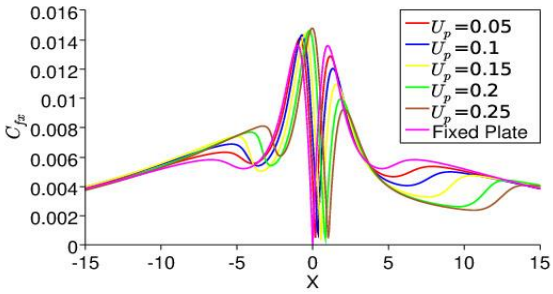


FIGURE 6. Skin-friction coefficient $(C_{f,x})$ over the plate surface for different plate velocities

*4.3 Temperature variation*

The variation in temperature profiles near to the impingement surface over the horizontal line at different $Y$-locations have been presented in Figure 7. The minimum interface temperature is found at the stagnation point. The interface temperature is minimum at the start of the thermal boundary layer and it indicates the high heat transfer rate at that location. The variation in temperature profiles gets uniform with increase in the plate speed.

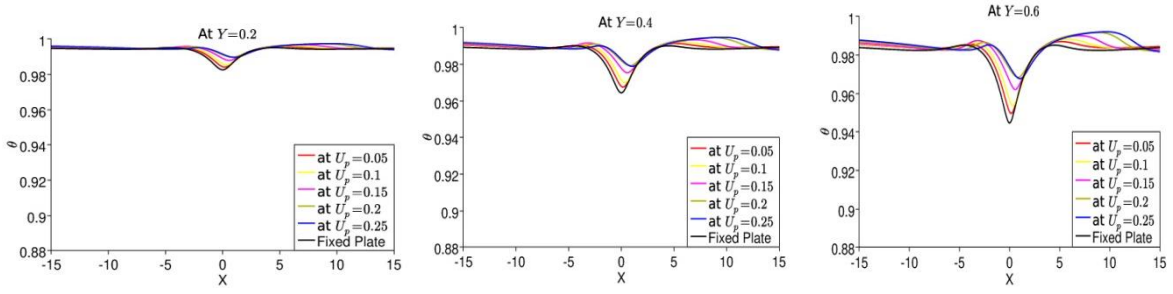


FIGURE 7. Temperature variation at Y -location for the different plate velocities

*4.4 Local Nusselt number and local heat flux variation*

The local Nusselt number and local heat flux distribution at solid-fluid interface for the different plate velocities have been presented in Figure 8. The peak value of the local Nusselt number is found at the location of minimum interface temperature. The variation in local Nusselt number is found symmetry about the jet axis for the case of $U_p = 0$, and the symmetricity vanishes with increasing the plate velocity.

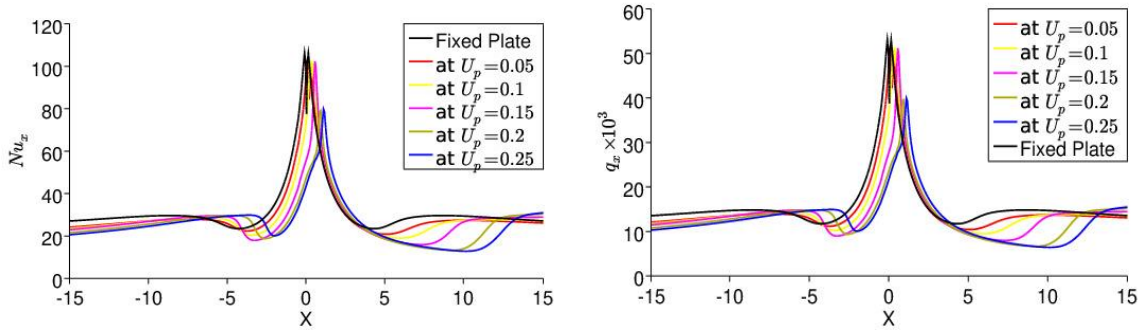


FIGURE 8. Distribution of local Nusselt number $(Nu_x)$ and local heat flux $(q_x)$

## 4. CONCLUSIONS

The numerical study of conjugate heat transfer between the flat plate and jet for the different values of the plate velocities has been conducted using the standard high Reynolds number two equation $k - \epsilon$ eddy viscosity model. In this study, the influence of plate motion on the conjugate heat transfer has been presented with varying the plate velocity in the range of $0 - 0.25$ . The constant wall temperature boundary condition has been considered at the bottom surface of the flat plate. The effects of jet impingement over the fixed plate controls the fluid flow and conjugate heat transfer behavior. When the impingement plate is subjected to motion, the shear driven flow takes the dominating role in controlling the flow and thermal fields. As the impingement plate speed increases, the difference between the average temperatures in the right part and the left part of the domain gets increases. Thereby, increasing the magnitude of the skewness in the thermal field. The distribution of the solid-fluid interface temperature, local Nusselt number and local heat flux get more uniform with increase in the plate velocity.

## ACKNOWLEDGMENTS

The authors would like to acknowledge the support for this work in terms of equipment grant from Science and Engineering Research Board, Department of Science and Technology, Government of India and wish to thank them for their help and encouragement.

## REFERENCES

[1] E. Watson, "The radial spread of a liquid jet over a horizontal plane," Journal of Fluid Mechanics, vol. 20, no. 3, pp. 481–499, 1964.

[2] J. Lienhard, "Liquid jet impingement," Annual Review of Heat Transfer, vol. 6, no. 6, 1995.

[3] W. Rohlfs, C. Ehrenpreis, H. D. Haustein, and R. Kneer, "Influence of viscous flow relaxation time on self-similarity in free-surface jet impingement," International Journal of Heat and Mass Transfer, vol. 78, pp. 435–446, 2014.

[4] N. Zuckerman and N. Lior, "Jet impingement heat transfer: physics, correlations, and numerical modeling," Advances in heat transfer, vol. 39, pp. 565–631, 2006.

[5] B. E. Launder and D. B. Spalding, "The numerical computation of turbulent flows," Computer methods in applied mechanics and engineering, vol. 3, no. 2, pp. 269–289, 1974.

[6] R. Viskanta, "Heat transfer to impinging isothermal gas and flame jets," Experimental thermal and fluid science, vol. 6, no. 2, pp. 111–134, 1993.

[7] S. Ashforth-Frost, K. Jambunathan, and C. Whitney, "Velocity and turbulence characteristics of a semiconfined orthogonally impinging slot jet" Experimental Thermal and Fluid Science, vol. 14, no. 1, pp. 60–67, 1997.

[8] R. Gardon and J. C. Akfirat, "The role of turbulence in determining the heat-transfer characteristics of impinging jets," International Journal of Heat and Mass Transfer, vol. 8, no. 10, pp. 1261–1272, 1965.

[9] J. Senter and C. Solliec, "Flow field analysis of a turbulent slot air jet impinging on a moving flat surface," International Journal of Heat and Fluid Flow, vol. 28, no. 4, pp. 708–719, 2007.

[10] H. Chattopadhyay and A. Cemal Benim, "Turbulent heat transfer over a moving surface due to impinging slot jets," Journal of Heat Transfer, vol. 133, no. 10, 2011.

[11] D. Benmouhoub and A. Mataoui, "Computation of heat transfer of a plane turbulent jet impinging a moving plate," Thermal Science, vol. 18, no. 4, pp. 1259–1271, 2014.

[12] A. M. Achari and M. K. Das, "Conjugate heat transfer study of a turbulent slot jet impinging on a moving plate," Heat and Mass Transfer, vol. 53, no. 3, pp. 1017–1035, 2017.

[13] S. Patankar, Numerical heat transfer and fluid flow. CRC press, 1980.

[14] H. K. Versteeg and W. Malalasekera, An introduction to computational fluid dynamics: the finite volume method. Pearson Education, 2007.

Fifth International Conference on Computational Methods for Thermal Problems
THERMACOMP2018, July 9-11, 2018, Indian Institute of Science, Bangalore, INDIA
*N. Massarotti, P. Nithiarasu, Pradip Dutta and C. Ranganyakalu (Eds.)*

# NUMERICAL HEAT TRANSFER ANALYSIS OF SPHERICAL AND ELLIPSOIDAL DIMPLE PLATES

**Ashif Perwez, Shreyak Shende, Rakesh Kumar**
IIT(ISM) Dhanbad, Police Line, Sardar Patel Nagar, Dhanbad, Jharkhand 826004,
ashifperwez@gmail.com, shreyakshende@mece.ism.ac.in, rakesh@iitism.ac.in.

## ABSTRACT

Flat plate with ellipsoidal and spherical dimple subjected to external flow is investigated in this numerical study. The present investigation is focused on two different geometries of dimple surfaces (spherical and ellipsoidal).Five different types of dimple arrangements and dimple intervals are investigated. Constant heat flux is applied at the bottom surface of plate and air is flown over the top surface of the plate. The velocity of air is varied from 1m/s to 5m/s. The heat transfer coefficient is determined and compared with the result of the flat plate. For staggered arrangement, the ellipsoidal dimple pitch of $S_L$=11.25mm and $S_T$=12.5 yields the highest heat transfer coefficient value which is about 9.81% better than the flat plate and the spherical dimple pitch of $S_L$=11.25mm and $S_T$=18.75mm yields the highest heat transfer coefficient value which is about 10.25% better than the flat plate.

**Keywords**: *Flat Plate, Dimple Plate, Numerical analysis, Forced Convection, ANSYS fluent.*

## 1. INTRODUCTION

In industrial process, internal heat generation may cause overheating and sometimes system failure. So, effective means of heat removing is often required. One method to increase the convective heat transfer is to manage the growth of thermal boundary layer, which can be made thinner or partially broken by flow disturbance. As the boundary layer is reduced by interruption or by patterned extended surfaces convective heat transfer can be increased. Pin fin, protruding ribs, slit fins, and vortex generators are typical methods. Heat transfer augmentation using these methods always results in pressure drop penalties that adversely affect the aerodynamics and overall efficiencies. In case of cooling of turbine blades, surface protrusions induce excessive pressure losses, thus increasing compressor loads. The separated flow field over ribs or pin fins can make a significant non-uniform cooling, which leads to thermal stress. The dimple is an effective solution to these problems. This is a method of improving heat transfer rates without significant pressure drop. Normally the dimple produces vortex flow within the hole and this augments the heat transfer. Dimples accomplish this by not protruding into the flow region and therefore not generating form drag. Because of easiness of manufacturing, dimples are also attractive as a method of heat transfer augmentation.

Afansayev [1] studied the inclusive heat transfer and pressure drop for turbulent flow with a staggered array of spherical dimples on a flat surface. Notable 30%-40% increase in heat transfer without substantial pressure losses is recorded. Lin [2] investigated the computational heat transfer in a channel with rows of a staggered hemispherical cavity. Results show that vortical structure emerges from each hole in two ways. One way is by combining and then busting from the downstream part of the cavity centre as one stream tube and in another way instead of combining, streamlines from each vertical structure flows zig-zags from cavity to cavity. Doseo Park [3] studied the Heat transfer enhancement of spherical and elliptical dimple. Results showed that heat transfer enhancement up to 6% relative to the flat plate were observed for a Reynolds number in the range of 500-1650. Katkhaw [4] studied the Heat transfer enhancement of flat plate having 45°

ellipsoidal dimpled surfaces. The result showed that for inline arrangement heat transfer coefficient increases to 21.7% as compared to smooth surfaces whereas for the staggered arrangement it is about 15.8%.

## 2. MAIN BODY

a) Geometry

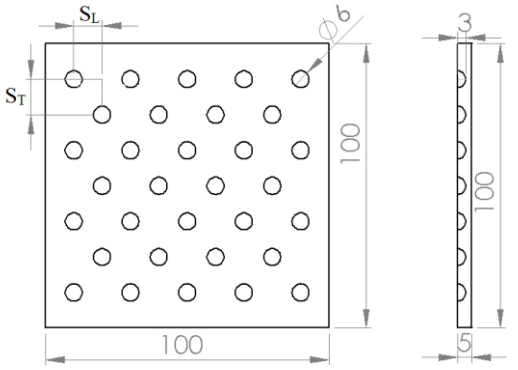


FIGURE 1. Staggered Spherical

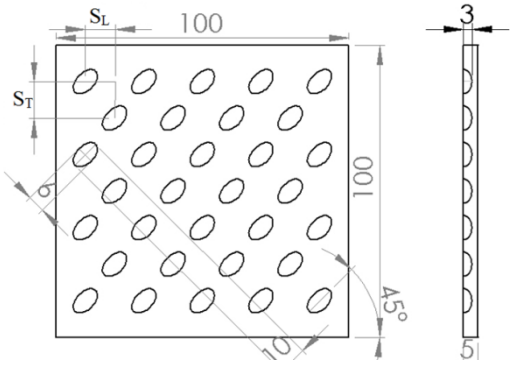


FIGURE 2. Staggered elliptical

| Case no | $S_T$ | $S_L$ | $S_T/S_L$ |
|---|---|---|---|
| 1 | 12.5 | 10 | 1.25 |
| 2 | 12.5 | 11.25 | 1.11 |
| 3 | 12.5 | 12.5 | 1.00 |
| 4 | 15 | 11.25 | 1.33 |
| 5 | 18.75 | 11.25 | 1.67 |

TABLE 1. Geometric Dimensions of dimpled surface

In this work 100×100×5mm aluminum plate is taken with dimples formed on the surface in the staggered formation. We studied two geometries i.e. spherical and elliptical as shown in fig.1 and 2. In both the cases, depth is kept the same as 3mm. In the case of elliptical dimples, the major axis is inclined at an angle of 45 degrees. The diameter of the spherical dimple is kept constant at 6mm whereas the major and minor axes of the ellipse are kept constant at 10mm and 6mm respectively. For each case, the distances $S_T$ and $S_L$ are varied as shown in table 1.

b.) Numerical Analysis

Mathematical model

Fluid flow and heat transfer in a channel can be described mathematically by using three fundamental laws 1.The Principle of Mass Conservation 2.The Principle of Momentum Conservation 3.The Principle of Energy Conservation.

Continuity Equation

$$\frac{\partial u}{\partial x}+\frac{\partial v}{\partial y}+\frac{\partial w}{\partial z}=0 \qquad (1)$$

Momentum Equations

X-Momentum

$$\rho\left(u\frac{\partial u}{\partial x}+v\frac{\partial u}{\partial y}+w\frac{\partial u}{\partial z}\right)=-\frac{\partial P}{\partial x}+\frac{\partial}{\partial x}\left(\mu\frac{\partial u}{\partial x}\right)+\frac{\partial}{\partial y}\left(\mu\frac{\partial u}{\partial y}\right)+\frac{\partial}{\partial z}\left(\mu\frac{\partial u}{\partial z}\right) \qquad (2)$$

Y-Momentum

$$\rho\left(u\frac{\partial v}{\partial x}+v\frac{\partial v}{\partial y}+w\frac{\partial w}{\partial z}\right)=-\frac{\partial P}{\partial y}+\frac{\partial}{\partial x}\left(\mu\frac{\partial v}{\partial x}\right)+\frac{\partial}{\partial y}\left(\mu\frac{\partial v}{\partial y}\right)+\frac{\partial}{\partial z}\left(\mu\frac{\partial v}{\partial z}\right) \quad (3)$$

Z-Momentum

$$\rho\left(u\frac{\partial w}{\partial x}+v\frac{\partial w}{\partial y}+w\frac{\partial w}{\partial z}\right)=-\frac{\partial P}{\partial Z}+\frac{\partial}{\partial x}\left(\mu\frac{\partial w}{\partial x}\right)+\frac{\partial}{\partial y}\left(\mu\frac{\partial w}{\partial y}\right)+\frac{\partial}{\partial z}\left(\mu\frac{\partial w}{\partial z}\right) \quad (4)$$

Energy Equation

$$\rho C_p\left(u\frac{\partial T}{\partial x}+v\frac{\partial T}{\partial y}+w\frac{\partial T}{\partial z}\right)=\frac{\partial}{\partial x}\left(k\frac{\partial T}{\partial x}\right)+\frac{\partial}{\partial y}\left(k\frac{\partial T}{\partial y}\right)+\frac{\partial}{\partial z}\left(k\frac{\partial T}{\partial z}\right) \quad (5)$$

## 3. RESULTS

There are five cases in staggered formation. For cases 1-3 we have constant $S_T$ and varied $S_L$. For cases 2, 4, 5 $S_L$ is constant and $S_T$ is varied. Velocities are changed from 1m/s to 5m/s. Fig.3 and 4, shows the temperature distribution along the ellipsoidal and spherical dimple surface. Plain surface is at a lower temperature than dimple area as seen from the contour. The lower temperature is located at the right side and gradually increases as we move from right to left this is mainly due to the air stream flowing over the spherical and ellipsoidal dimple surfaces. Dimple creates the vortex flow and hence heat transfer enhancement occurs.

Fig.5 and 6 show the variation of heat transfer coefficient vs. velocity in case of flat surfaces, staggered ellipsoidal and spherical surfaces. As the velocity increases heat transfer coefficient also increases. For ellipsoidal dimple, case 2 yields the highest heat transfer coefficient than other geometry and a flat surface. And for spherical dimple surface case 5 gives the highest heat transfer coefficient than any other case and a flat surface.

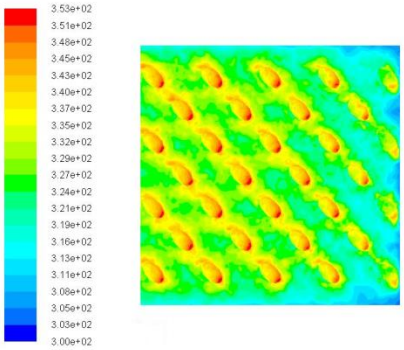


FIGURE 3. Temperature distribution of Geometry No.2 at velocity of 5m/s

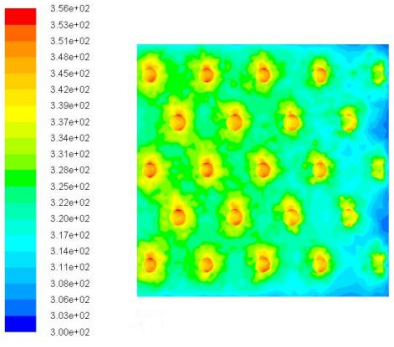


FIGURE 4. Temperature distribution of Geometry No.5 at velocity of 5m/s

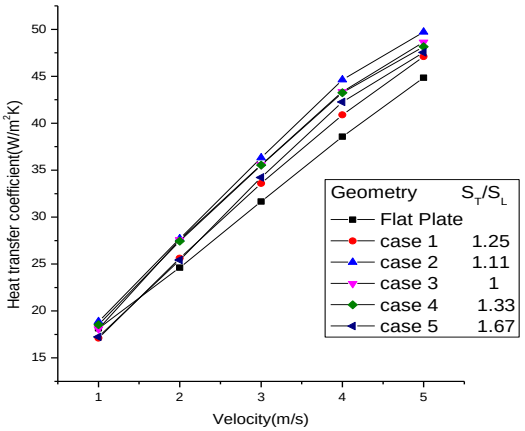


FIGURE 5. Variation of Heat Transfer Coefficient vs. Velocity for Staggered Elliptical Surface at 5m/s

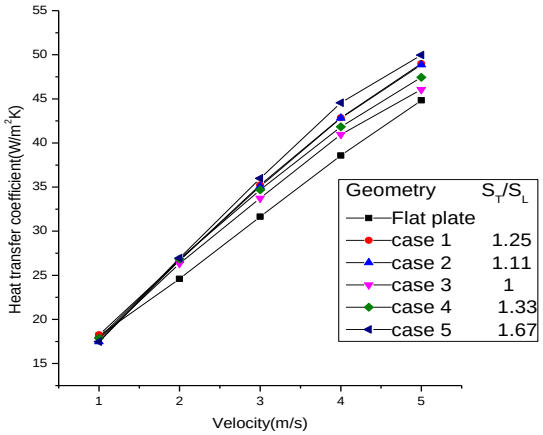


FIGURE 6. Variation of Heat Transfer Coefficient vs. Velocity for Staggered Spherical Surface at 5m/s

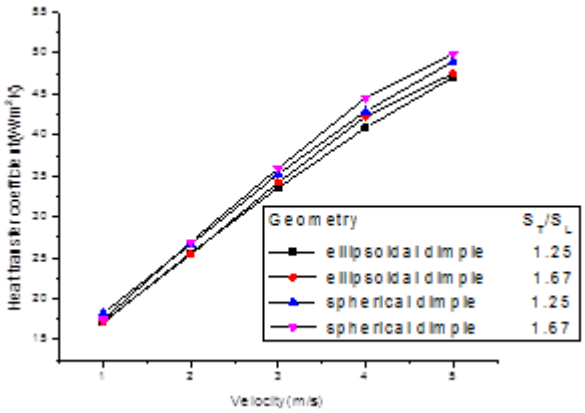


FIGURE 7. Comparison of heat transfer coefficient for staggered arrangement of Spherical and ellipsoidal dimple surface

Nomenclature

μ=dynamic viscosity [Nsm-2]
k=thermal conductivity [Wm-1K-1]
T=temperature [K]
ρ=density [kgm-3]
$S_T$=Span wise pitch [mm]
$S_L$=Stream wise pitch [mm]
h=heat transfer coefficient [Wm-2K-1]

## 4. CONCLUSIONS

The present numerical work reports the heat transfer of external air flow over the spherical and ellipsoidal dimple surface. The dimple arrangement and dimple interval are examined. For staggered arrangement, the ellipsoidal dimple pitch of $S_L$=11.25mm and $S_T$=12.5mm yields the highest heat transfer coefficient value which is about 9.81% better than the flat plate. For staggered arrangement, the spherical dimple pitch of $S_L$=11.25mm and $S_T$=18.75mm yields the highest heat transfer coefficient value which is about 10.25% better than the flat plate.

## REFERENCES

[1] Afanasyev,V. N., et al.,Turbulent Flow Friction and Heat Transfer Characteristics for Spherical Cavities, Experimental Thermal and Fluid science ,(1993),7, pp. 1-8

[2] Lin,Y.L., et al.,Computations of Flow and Heat Transfer in a Channel with Rows of Hemispherical Cavities",ASME,(1999), pp. 99-263

[3] Park D., et al.,Study of Laminar Forced Convection Heat Transfer for Dimpled Heat Sinks, Journal of thermophysics and heat transfer,22 (2008),2, pp. 262-270

[4] Katkhaw,N., et al.,Heat transfer behavior of flat plate having 45° ellipsoidal dimpled surfaces, Case Studies in Thermal Engineering,(2014), 2 , pp. 67-74

# Numerical investigation of natural convection heat transfer from a heated horizontal cylinder in copper based nano-fluid

Shubham Sharma[*] and V Sajith[#]

*Department of Mechanical Engineering, [#]School of Nano Science and Technology,

National Institute of Technology Calicut, Kerala

sharma.shubham428@gmail.com*, +91-9736420501[*]

Corresponding author: sajith@nitc.ac.in[#], +91-9446361125[#]

**ABSTRACT**

Present numerical work focuses on investigation of natural convection heat transfer from a heated horizontal cylinder in a copper based nano-fluid for volumetric concentration ranging from $\emptyset = 0\ to\ 0.06$ and for Rayleigh number range of 100 to$10^4$. Numerical model was first validated by comparing it with the results of various experimental studies and a good agreement was found between the present study and data available in literature. Variation of local and average heat transfer coefficient over the cylinder periphery is also presented. Results shows an enhancement in the heat transfer coefficient due to addition of copper oxide nanoparticle into water, which is found to be in proportional with the concentration of nano-particles in the fluid. Maximum enhancement in average heat transfer coefficient was found to be 14.49% for nano-fluid volumetric concentration of 0.06 by volume and Ra = 10000.

**Key Words:** *Natural Convection, Rayleigh number, SIMPLE scheme.*

## 1. INTRODUCTION

Convective heat transfer from heated horizontal cylinders have been in keen interest among researchers and engineers, as it has numerous engineering applications such as evacuated tube type solar collectors, condenser of domestic refrigerator, heated cylinders in paper and textile industries, fire tube boilers and many more. Natural convection from single cylinder has been studied extensively from last half century and various correlations have been formulated for determination of average Nusselt number by different researchers. V.T. Morgan [1] in 1975, reviewed large number of numerical and experimental studies and proposed a general correlation for determining the average Nusselt number with different value of Rayleigh number. Bejan et al [2] proposed a numerical model for an array of horizontal cylinders in staggered formation, with a very small computational domain without affecting the accuracy of the solution and similar modified numerical methodology has been used in the present work. Most of the reported works were focused on either air or water as working fluid medium. With the concept of nano-fluids as a possible method of enhancement of heat transfer from the fluid medium , a shift of focus of research towards nano-fluid medium has been seen in last decade. Most of studies are focused on forced convection heat transfer from the cylinder. Jalan and Shirivastav [3] used digital interferometry to study the convective heat transfer from a heated horizontal cylinder and addition of $Al_20_3$ nano-particles into the fluid medium was found to increase the heat transfer coefficient and reduction in average Nusselt number.

Most of the works were carried using air and water as a fluid medium and very less studies were focused on the heat transfer characteristics of nano-fluid. Moreover condradiction in the results i.e. enhancement as well as reduction in heat transfer characteristics was reported by the different authors with the use of nano-fluid, indicating a large gap in research in this field. The present numerical study focuses on heat transfer characteristics of the horizontal cylinder with copper based nano fluid as fluid medium. Three different concentration of copper oxide based

nano-fluids (i.e. $\emptyset = 2\%, 4\%, 6\%\ by\ volume$) were investigated at different Rayleigh numbers from 100 to $10^4$. Validation of present numerical model is provided by comparing present results with available literatures[1], [4] . ANSYS 16.0 was used for otained the solution in the present numerical problem.

## 2. MAIN BODY

Continuity equation, momentum equation and energy equation were modified by using Boussinesq approximation for two dimensional flow and the modified form of these equations can be mathematically represented as

***Continuity equation:*** $$\frac{\partial u}{\partial x} + \frac{\partial v}{\partial y} = 0 \quad (1)$$

***Momentum equation:*** *x direction* $$u\frac{\partial u}{\partial x} + v\frac{\partial u}{\partial y} = -\frac{1}{\rho_{nf}}.\frac{\partial p}{\partial x} + \vartheta_{nf}\nabla^2 u \quad (2)$$

*y direction* $$u\frac{\partial v}{\partial x} + v\frac{\partial v}{\partial y} = -\frac{1}{\rho_{nf}}.\frac{\partial p}{\partial y} + \vartheta_{nf}\nabla^2 v + g\beta(T - T_\infty) \quad (3)$$

***Energy equation:*** $$u\frac{\partial T}{\partial x} + v\frac{\partial T}{\partial y} = \alpha_{nf}\nabla^2 T \quad (4)$$

Considering the practical aspects, fluid mediums taken in present study is two phase medium, which requires complicated method for analysis of problem. The problems has been simplified by assuming it to be a single phase medium having properties equivalent to that of actual medium by using following mathematical expressions:

Effective density ($\rho_{nf}$): $$\rho_{nf} = (1 - \emptyset)\rho_f + \emptyset\rho_{np} \quad (5)$$

Effective heat capacity ($C_{nf}$) $$C_{nf} = \frac{(1-\emptyset)\rho_f C_f + \emptyset\rho_{np}C_{np}}{\rho_{nf}} \quad (6)$$

Effective dynamic viscosity ($\mu_{nf}$) $$\mu_{nf} = \frac{\mu_f}{(1-\emptyset)^{2.5}} \quad (7) \quad [5]$$

Effective expansion coefficient ($\beta_{nf}$) $$\beta_{nf} = (1 - \emptyset)\beta_{fluid} + \emptyset\beta_{sp} \quad (8)$$

Effective thermal conductivity ($K_{nf}$) $$\frac{K_{nf}}{K_f} = \frac{K_{np} + 2K_f - 2\emptyset(K_f - K_{np})}{K_{np} + 2K_f - 2\emptyset(K_f - K_{np})} \quad (9) \quad [6]$$

Cylinder surface is modelled as stationary wall with no slip condition over it and having uniform surface temperature ($T_s$). Since the flow around the cylinder surface is found to be symmetric about the vertical axis, symmetric boundary condition is provided on the vertical axis as shown in fig.1. In addition to that, another symmetric boundary condition is also provided at the right wall of computational domain, basically reduce the size of computational domain [2]. As the velocity of incoming fluid is not known as prior in buoyancy driven flows, pressure inlet boundary condition [7] is defined at the bottom of computational domain. An additional inlet was provided at the top of right wall to avoid the chimney effect in the domain [2].An exit to the flow is provided at the top of the domain on which pressure outlet boundary condition [7] is employed. Computational domain is divided into three sub-regions fig.1(b) namely as region-A, region-B and region – C. Region-A and Region-B are set to have triangular elements because they are surrounding the cylindrical surface and better conformity will be there for triangular element as compared to rectangular elements, whereas rectangular elements are chosen for Region – C . It has to be noted that maximum element density exist in the region –A (having element size ratio $\delta/D = 0.003$ ), while region-B which is less refined to region-A is having $\delta/D = 0.02$ , region-C is kept to be a bit coarse as less gradients in velocity and temperature are expected in this region. Semi-Implicit Scheme for Pressure Linked Equation (SIMPLE) scheme is used for velocity and pressure coupling and first order upwind scheme was used for

handling of convective terms in the governing equation. Convergence criteria for the residuals of continuity, momentum and energy equation is kept equal to$10^{-6}$, which is good enough to have a solution accuracy desired in present computational study. In addition to this, plotting of values of local drag coefficient as well as local surface heat fluxes is also done so as to verify the convergence of solution and average value of these two parameters is calculated in order to find the indifference in results of two grids while doing grid independence studies. During grid independence studies grid (G1) with 325876 elements was chosen as where difference in monitors falls below 0.2% when compared with a grid having 288420 elements (G2).

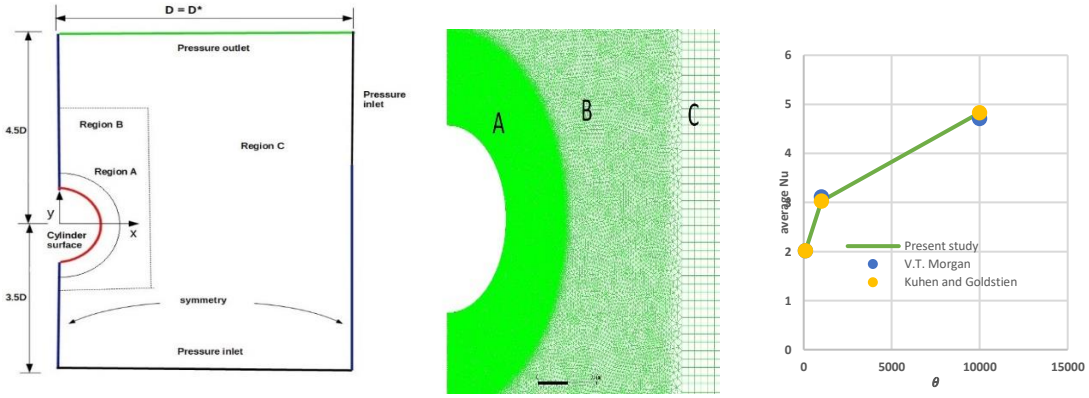


(a) (b) (c)

FIGURE1 (a) computational domain (b) computational grid (c) results of validation study with available data in literature.

## 3. RESULTS

Fig.1 (b) shows the results of validation studies for present model and available literature with air as fluid medium. Good agreement was found for present work as maximum difference in average Nusselt number values was found to be less than 5% for air as fluid medium. Variation of local heat transfer coefficient along the cylinder surface at different Rayleigh number and nano-fluid concentration is shown in fig.2. Here $\theta$ represents the angle along the surface of cylinder with respect to the bottom. At lower Rayleigh number the thermal boundary layer around the cylinder surface is thicker, while it reduces for higher values of Rayleigh number. Lower thickness of thermal boundary layer indicates high temperature gradients around the cylinder surface and hence a higher potential exist for the transfer of heat from the surface of cylinder. For a given concentration of nano-fluid at higher Rayleigh number the value of heat transfer coefficient increases and vice – versa. It can also be observed that for a particular value of Rayleigh number maximum heat transfer coefficient exist at the bottom of cylinder and minimum value occur at the top of the cylinder where formation of buoyant plume occurs and thickness of thermal boundary layer is very high thus reducing the potential for heat transfer. The effect of addition of nano-particles in the base fluid can be easily seen with increasing value of heat transfer coefficient as shown in figure (2). Addition of nano-particles in the fluid medium results in increase in effective thermal conductivity of the whole fluid medium as per the Eq.[6]. This increase in conductivity of fluid medium will cause more conduction of the heat from the cylinder surface to the ambient fluid medium, hence will result in increasing the value of heat transfer coefficient of the fluid. The increase in heat transfer coefficient is proportional to the concentration of nanoparticles in fluid medium. The minimum value of heat transfer coefficient occurs at $\emptyset = 0$ and maximum value occurs at the highest concentration (6%), in the present work for a particular value of Rayleigh number. This enhancement in heat transfer coefficient can be seen collectively in fig.2, which represents the variation of average heat transfer coefficient for different concentrations of nano-fluid and for different Rayleigh

numbers. Maximum enhancement of 14.49% for average heat transfer coefficient was found for nano-fluid concentration of 0.06 and Rayleigh number value of 10000. Thus addition of nano-fluid was found to be effective in increasing the heat transfer coefficient of fluid medium.

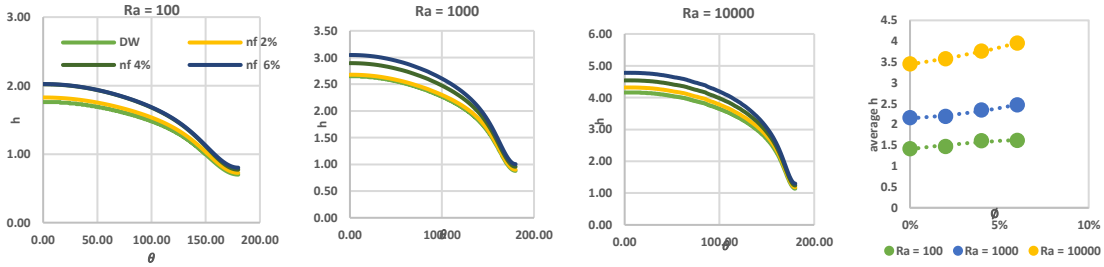


FIGURE 2. Variation of local and average heat transfer coefficient over the cylinder surface at different Rayleigh number and fluid concentrations.

## 4. CONCLUSIONS

Numerical study on natural convection heat transfer from heated horizontal cylinder for Copper based nano-fluids was studied for different concentration nano-particles ranging from (0 to 6%) and for different Rayleigh number (100 to 10000). The validation study of the present works shows good agreement with the data available in the literature. Addition of nano-particles into the fluid medium increases the convective heat transfer coefficient of fluid. Heat transfer coefficient was found to be increase with increase in Rayleigh number due to decrease in thermal boundary layer thickness. Variation of local heat transfer coefficient over the periphery of cylinder shows that maximum value of heat transfer coefficient occurs at lower stagnation point, while minimum value of heat transfer coefficient exist at upper stagnation point at top of cylinder for corresponding Rayleigh number values .A maximum of 14.49% of enhancement in average heat transfer coefficient value was found for the case $\emptyset = 0.06$ and Ra = 10000 when compared with the values of base fluid.

## REFERENCES


[1] V. T. Morgan, “The Overall Convective Heat Transfer from Smooth Circular Cylinders,” *Adv. Heat Transf.*, vol. 11, no. C, pp. 199–264, 1975.

[2] A. Bejan, A. J. Fowler, and G. Stanescu, “The optimal spacing between horizontal cylinders in a fixed volume cooled by natural convection,” *Int. J. Heat Mass Transf.*, vol. 38, no. 11, pp. 2047–2055, 1995.

[3] P. Jalan, A. Vyas, and A. Srivastava, “Nonintrusive Diagnostics of Nanofluids-Based Natural Convection Heat Transfer over a Heated Cylinder,” *J. Thermophys. Heat Transf.*, pp. 1–12, 2017.

[4] T.H. Kuehn, R.J. Goldstein, Numerical solution to the Navier-Stokes equations for laminar natural convection about a horizontal isothermal circular cylinder, Int. J. Heat Mass Transfer 23 (1980) 971–979.

[5] H. C. Brinkman, “The Viscosity of Concentrated Suspensions and Solutions,” vol. 571, pp. 1–2, 1952.

[6] J. C. M. Garnett, “Colours in Metal Glasses and in Metallic Films Article cited in :,” no. January, 1904.

[7] T. D. Canonsburg, “ANSYS Fluent Users Guide,” vol. 15317, no. November, pp. 724–746, 2013.

# AERO-THERMAL ANALYSIS OF A COMPRESSOR BLADE AT LOW REYNOLDS NUMBER THROUGH LES

S. Katiyar and S. Sarkar
Department of Mechanical Engineering
Indian Institute of Technology Kanpur
Kanpur – 208016, India
subra@iitk.ac.in

## ABSTRACT

An attempt is made to estimate the flow and heat transfer over a controlled-diffusion (C-D) compressor stator blade following the experiment of Hobson et al. [1] at low Reynolds number (*Re*) condition through Large-Eddy Simulation (LES). At low *Re*, the boundary layer on the suction surface of the blade remains laminar up to the mid-chord, where it separates, undergoes a rapid transition due to high receptivity to free-stream disturbances and then reattaches as a turbulent boundary layer. The LES resolves dynamics of vortices, their non-linear interactions and is successful to predict transitional flow and thermal field.

**Key Words:** *Compressor Cascade, Separation Bubble, Nusselt number, LES.*

## 1. INTRODUCTION

Efforts towards reduction in cost and weight of the engine have led to the development of C-D blades that provide more lift than the conventional blade. This allows the use of lesser number of blades. However, the reduction in the number of blades comes up against the problem of boundary layer separation in the aft region on the suction surface. It has been observed that the flow remains laminar over a large percentage of the blade chord till it separates from the surface at a high altitude and low flight speed. The transition of the separated boundary layer is inevitable being unconditionally unstable and the flow reattaches to the surface as a turbulent boundary layer.

In the present work, LES with dynamic subgrid-scale (SGS) model is used to predict the flow field over a C-D compressor blade at *Re* of $2.1\times10^5$ (based on the chord and the inlet velocity). Flow features and vortex dynamics have also been analysed at a very low *Re* of $0.5\times10^5$. The objective is to resolve the transitional flow due to the separation bubble on a compressor blade. Certainly RANS calculations will not provide the answer. LES can resolve the dynamics of vortices, their non-linear interactions and the flow instability.

## 2. NUMERICAL METHODS AND COMPUTAIONAL DETAILS

The filtered incompressible covariant Navier-Stokes and energy equations have been solved for the flow past a compressor cascade on a staggered mesh using a symmetry-preserving central difference scheme. A dynamic SGS model proposed by Germano et al. [2] and modified by Lilly [3] is used to model the SGS stress tensor, where the model coefficient is dynamically calculated instead of input a priori. The momentum equations are advanced in time explicitly following the second-order Adam-Bashforth scheme, except for the pressure term, which is solved by a standard projection method. The pressure equation is discrete Fourier transformed in the spanwise direction to obtain a set of decoupled equations that are solved by a multigrid technique. The solver used in the present simulation has been extensively validated for variety of transitional and turbulent flows [4-7]. A H-grid within the blade passage is developed by applying the power law to the control functions appearing in the elliptic grid-generation scheme [8], which confirms the near-wall orthogonality

along the boundaries. A mesh of 400×200×64 points is used here. The computation domain and boundary conditions are shown in Fig. 1.

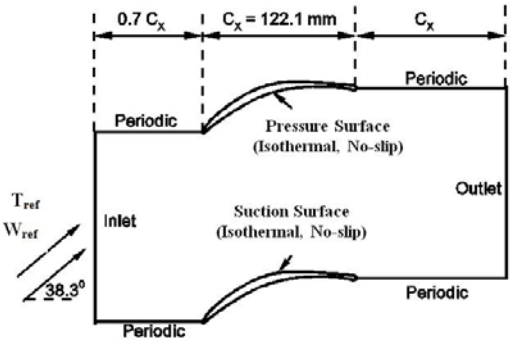


Figure 1. Computational domain and C-D compressor blade in cascade.

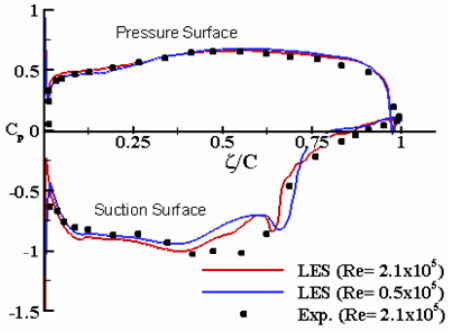


Figure 2. Mean $C_p$ distribution for different *Re*, ($C_p = (p - p_{ref})/\frac{1}{2}\rho W_{ref}^2$, $\zeta$ refers to chordwise distance, *C* chord, *p* pressure and *W* inlet velocity)

## 3. RESULTS AND DISCUSSION

Fig. 2 indicates the distribution of time-averaged surface pressure coefficient along the compressor blade and compares with that of the experiment [1] at $Re = 2.1\times10^5$. According to the experiment, the distribution of $C_p$ on the suction surface with a plateau in the mid-chord region implies the occurrence of a separation bubble. The computed $C_p$ variations agree moderately well with the experiment, however it fails to capture the extended bubble on the suction surface. With decrease in *Re*, the pressure plateau increases depicting enhancement of bubble length.

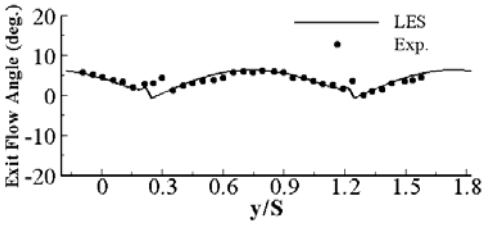


Figure 3. Flow angle at exit plane

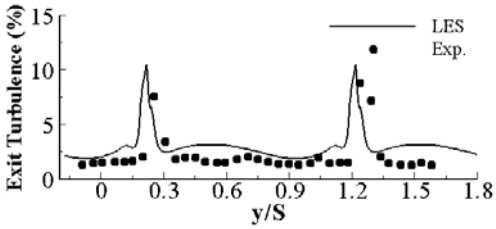


Figure 4. Turbulence level (%) at exit plane

The variations of time-averaged flow angle and turbulence intensity along the blade pitch at exit from LES data have been shown in Fig. 3 and 4 respectively, which compares well with the experiment for $Re = 2.1\times10^5$. The exit plane is taken at the downstream distance of 20% chord length from trailing edge. Further, the velocity profiles and turbulence level at different stations along the suction surface are presented in Fig 5. LES resolves the boundary layer growth fairly well on the suction surface, although discrepancies exist. The predicted turbulence level compares reasonably well with the experiment and illustrates the generation of turbulence in the separation region. Towards the trailing-edge the level of turbulence is higher in outer layer, which is characteristic of a separated boundary layer.

The flow on the suction surface of the C-D compressor blade undergoes a significant change with further decrease of *Re* to $0.5\times10^5$. A big separation bubble forms in the second half of the blade and begins to shed large-scale vortices. Time-averaged skin friction coefficients ($C_f$) for both *Re* are shown in Fig 6. The separation and reattachment points are located by zero crossing of $C_f$ plot. It is evident from $C_f$ plot that the onset of separation remain almost invariant with *Re* as found in earlier

study [9]. However, for low *Re* the reattachment point moves downward and the bubble length increases by 57%.

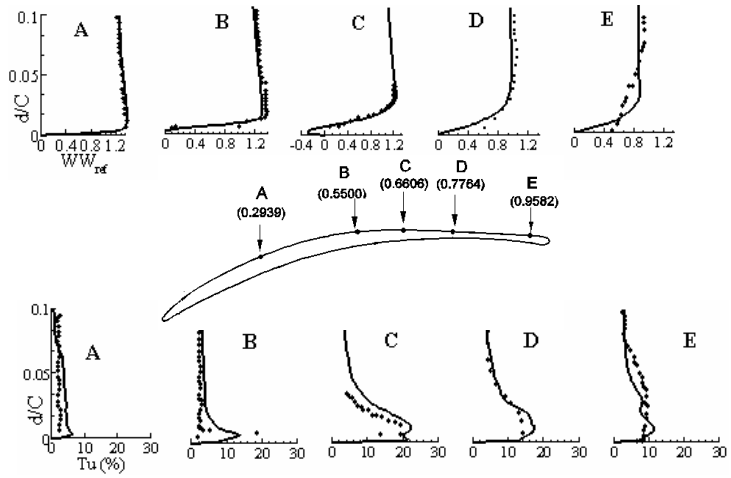


Figure 5. Velocity profile (top) and turbulence distribution (bottom) at different station (A-E) on suction surface: solid line represents the LES and symbols for the experiment [1].

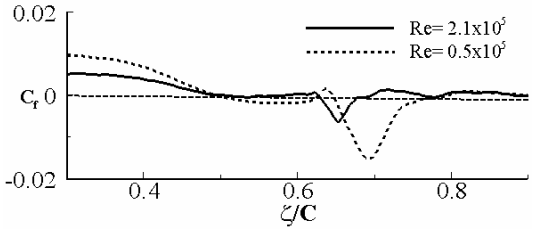


Figure 6. Time-averaged skin friction coefficient over the suction surface for different *Re*

The evolution of Nusselt number (*Nu*, based on chord) on the suction surface from LES data are presented in Fig 7 as *Re* decreases. Correlations for laminar ($Nu_L$) and turbulent ($Nu_T$) flows are also superimposed. Upstream of separation point for both *Re*, *Nu* matches with the laminar correlation justifying that the flow is laminar till it separates. Within the separation region, *Nu* increases rapidly for both cases. At high *Re*, *Nu* becomes almost close to turbulent correlation after breakdown, whereas it neither follows the laminar nor turbulent correlation at low *Re*, illustrating that flow has not attained turbulent equilibrium after reattachment.

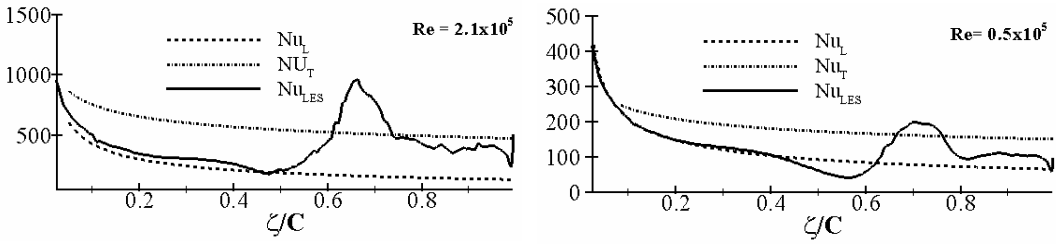


Figure 7. Time-averaged Nusselt number distribution over suction surface

Instantaneous contours of temperature are superimposed with spanwise component of vorticity for a vortex passing time $t_p$ and presented in Fig. 8 for both *Re*. These snapshots illustrate that the flow and thermal fields are in good concurrence. Development of both boundary and thermal layers are evident. The boundary layer separates near 45% of the chord length (ζ) and then rolls up forming large-scale coherent vortices. This effect is enhanced at low *Re* resulting in a highly unsteady flow.

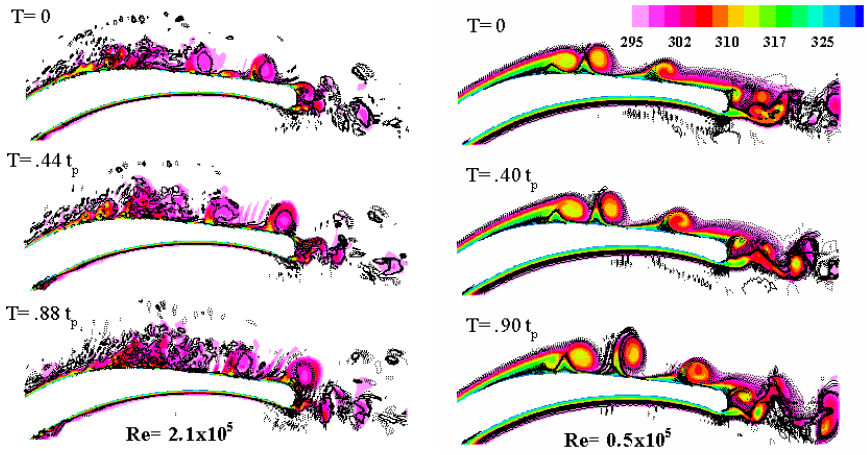


Figure 8. Instantaneous temperature (flood) and $\omega_z$ (line) for a vortex shedding cycle at different *Re*.

## 4. CONCLUSIONS

LES is used to investigate the laminar separated boundary layer and its thermal behaviour over a C-D compressor blade as *Re* decreases. At *Re* = $2.1\times10^5$, LES resolves the flow field with reasonable accuracy, however few discrepancies exist. Significant changes occur as *Re* is decreased to $0.5\times10^5$. The flow becomes highly unsteady with occurrence of larger separation bubble and shedding of large-scale vortices on the suction surface. The instantaneous temperature contours closely follow the vorticity field, illustrating a strong correlation between species and momentum transport. Distributions of *Nu* upstream of separation accords with laminar correlation for both the *Re*. At high *Re,* the variation of *Nu* after flow reattachment matches well with turbulent correlation, whereas it neither follows the laminar nor turbulent correlation at low *Re*.

## REFERENCES

[1] Hobson, G. V., Hansen, D. J., Schnorenberg, D. G. and Grove, D. V., 2001, "Effect of Reynolds Number on Separation Bubbles on Compressor Blades in Cascade", *Journal of Propulsion and Power*, **17** (1), pp. 154-162.

[2] Germano, M., Piomelli, U., Moin, P., and Cabot, W. H., 1991, "A dynamic subgrid-scale eddy viscosity model", *Phys Fluids* , A**3** (7), pp. 1760-1765.

[3] Lilly, D. K., 1992, "A proposed modification of the Germano subgrid-scale closure method", *Phys Fluids A*, **4** (3), pp. 633-635.

[4] Sarkar, S. and Voke, P. R., 2006, "Large Eddy Simulation of Unsteady Surface Pressure over a Low-Pressure Turbine Blade due to Interactions of Passing Wakes and Inflectional Boundary Layer", *J. Turbomachinery*, **128**, pp. 221-231.

[5] Sarkar, S., 2007, "The effects of passing wakes on a separating boundary layer along a low-pressure turbine blade through large-eddy simulation," *Proc. Inst. Mech. Eng.*, Part A, **221**, pp. 551-564.

[6] Sarkar, S., 2008,"Identification of flow structures on a LP turbine blade due to periodic passing wakes," *ASME J. Fluids Eng.*, **130**, 061103.

[7] Sarkar, S., 2009, "Influence of wake structure on unsteady flow in an LP turbine blade passage," *ASME J. Turbomachinery*, **131**, 041016.

[8] Hsu, K. and Lee, S. L., 1991, "A Numerical Technique for Two-Dimensional Grid Generation with Grid Control at All of the Boundaries" Journal of computational physics, 96, pp. 451-469.

[9] Samson, A. and Sarkar, S., 2016, "An Experimental Investigation of a Laminar Separation Bubble on the Leading-Edge of a modelled aerofoil for different Reynolds Numbers" *Proc IMechE Part C: J Mechanical Engineering Science*, **230**(13), pp. 2208-2224.

Fifth International Conference on Computational Methods for Thermal Problems
THERMACOMP2018, July 9-11, 2018, Indian Institute of Science, Bangalore, INDIA
*N. Massarotti, P. Nithiarasu, Pradip Dutta and C. Ranganyakalu (Eds.)*

# CONJUGATE HEAT TRANSFER ANALYSIS OF A RADIAL HEAT SINK USING OpenFOAM

**Shubham Dalvi***
shubhamdalvi74@gmail.com

**Dr. V. R. Kalamkar***
Associate Professor,vilas.kalamkar@gmail.com

*Department of Mechanical Engineering, Visvesvaraya National Institute of Technology, Nagpur

ABSTRACT

Numerical simulations were carried out to study the natural convective heat transfer in a radial heat sink which can be used for heat dissipations in circular LED's. The analysis is conducted for different values of constant heat flux which is implemented at the base of a heat sink. The effect is studied by comparing the thermal performance in each case. The conjugate heat transfer method is applied for executing the evaluation using OpenFOAM.

**Key Words:** *Radial Heat Sink, Natural Convection, Conjugate Heat Transfer, OpenFOAM.*

## 1. INTRODUCTION

Due to the enhancements in the technology related to the luminous efficiency of a LED, their market demand has increased significantly. Nevertheless, it is estimated that about 70% of the total energy consumed by an LED light is emitted as heat, creating a thermal problem. Thus, to improve the performance of LED lights, along with the lifespan of its components many researchers have suggested different geometrical configurations [1-4]. Seung et al. [1] have carried out parametric studies to compare the effects of the number of fins, long fin length, middle fin length and heat flux on the thermal resistance and average heat transfer coefficient. Furthermore, Bin Li et al. [2] investigated natural convection heat transfer in a radial heat sink with the perforated ring. And it is concluded, that the thermal resistance of the radial heat sink with optimized perforated ring reduces by 17%, additionally reducing the mass of ring by up to 37%. In this study, a radial heat sink with square fins is analysed for the case of natural convection. Moreover, a conjugate method is used for examining heat transfer interaction between the fluid and solid domain simultaneously.

## 2. MATHEMATICAL MODELLING & NUMERICAL FORMULATION

The schematic diagram of geometry is shown in Figure 1 where radial heat sink is depicted with protruded square fins. The vertical fins are radially distributed with regular interval on the horizontal heat sink. The heat sink is made of aluminum whose properties are given in Table 1 accompanied by the properties of air. The height of each fin is H = 0.0213 m where the solid base has a thickness of 0.002 m. To capture all the flow physics, the height of fluid domain is kept five times the height of the solid fin. Owing to the complex geometry, the non-uniformly distributed unstructured mesh is created in ICEM software. Firstly, a surface mesh has been generated with proper refinements near the wall (depicted in Figure 1) which is then extruded along the perpendicular direction to make volume mesh. The mesh consists of 321180 no of elements with average non- orthogonality of 5.85 and maximum skewness of 0.397. The average mesh quality was 0.936 with a minimum of 0.52 for only 0.072 % elements.

| Material | Cp | μ | K | ρ |
|---|---|---|---|---|
| Air | 1005 | 1.834e-5 | 2.643e-5 | Ideal Gas Law |
| Heat Sink | 891 | - | 202.4 | 2719 |

TABLE 1. Properties of Air and Heat Sink

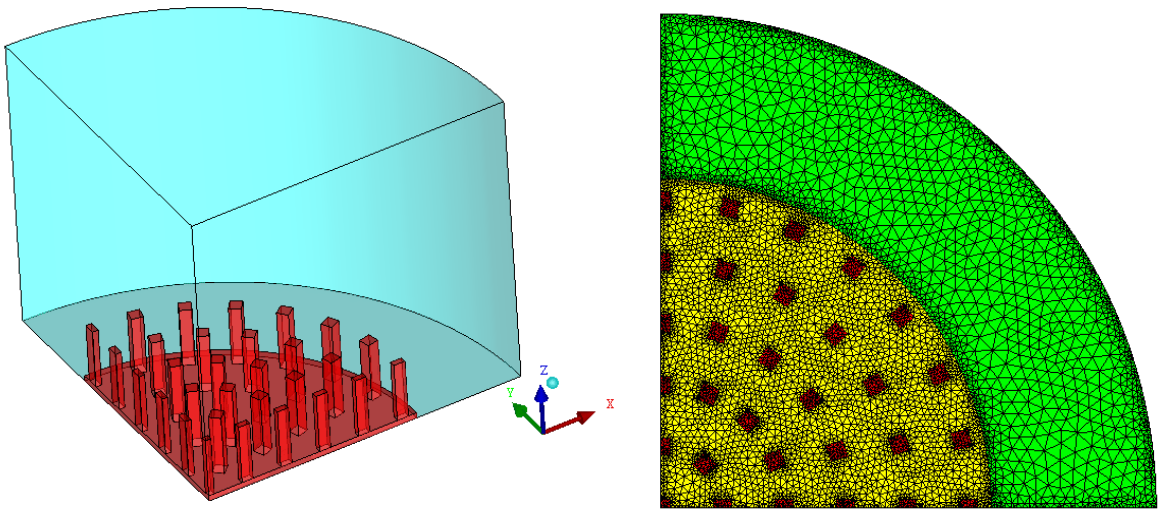


FIGURE 1. Schematic diagram of a section of Radial Heat Sink & Mesh distribution.

To simplify our analysis, following assumptions were made for completing the numerical simulations while keeping the flow physics undisturbed.
(1) The 3-Dimensional analysis is carried out presuming flow to be steady and laminar in nature.
(2) All the fluid properties except for density are considered to be independent of temperature.
(3) The density of air is calculated from the ideal gas law and the Boussinesq approximation is used to cater for its variation with respect to temperature.
(4) As the maximum temperature reached in the domain is considerably small, all the heat transfer by means of radiation is neglected.
In response to the repetitive nature of the geometry, periodic boundary conditions were imposed. A derived type of boundary condition "solidWallMixedTemperatureCoupled" is implemented at the fluid-solid interface for satisfying the conjugate approach. To reduce the computational time and the number of grids, only a quarter of the radial sink is simulated. The validation shown in Figure 2 is in good agreement with the experiments carried out by Seung et al [1] and hence our computational results can be accepted with more certainty.

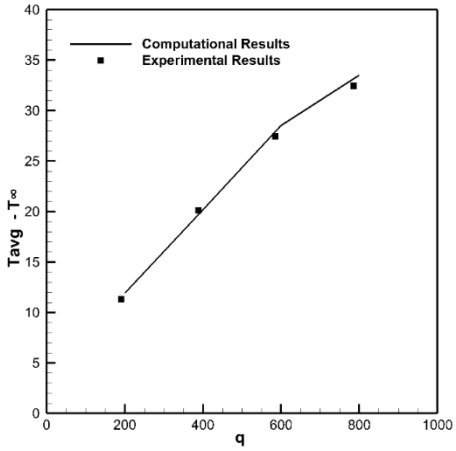


FIGURE 2. Comparison between Computational and Experimental results.

The incompressible based steady-state solver with Boussinesq approximation for performing conjugate heat transfer analysis is developed using OpenFOAM. For this, the inbuilt chtMultiRegionFoam solver has modified accordingly [3]. Being steady-state analysis, SIMPLE algorithm was used for pressure-velocity coupling.

## 3. RESULTS

The constant heat flux which is supplied at the base of heat sink gets transferred to the protruded fins via conduction, and at the air solid interface, the convection takes the charge to dissipate the heat to the surrounding. To have a better understanding of thermal behaviour, temperature contours are displayed in Figure 3 where a slice is cut in XY plane at distance of Z = 0.020 m in the Z direction. As it can be clearly seen from the Figure 4 that, as we go on increasing the amount of heat flux provided at the base of heat sink, the average temperature difference for both the fluid domain and solid domain gets increased. But the rate of increment for the solid domain is much larger as compared to that of fluid domain. This can be attributed to the high thermal conductivity of aluminium heat sink. It clearly implies that solid fins are capable of higher heat transfer rate as compared to the surrounding air for the same difference of the heat flux provided.

**q = 200 W/m2** **q = 400 W/m2**

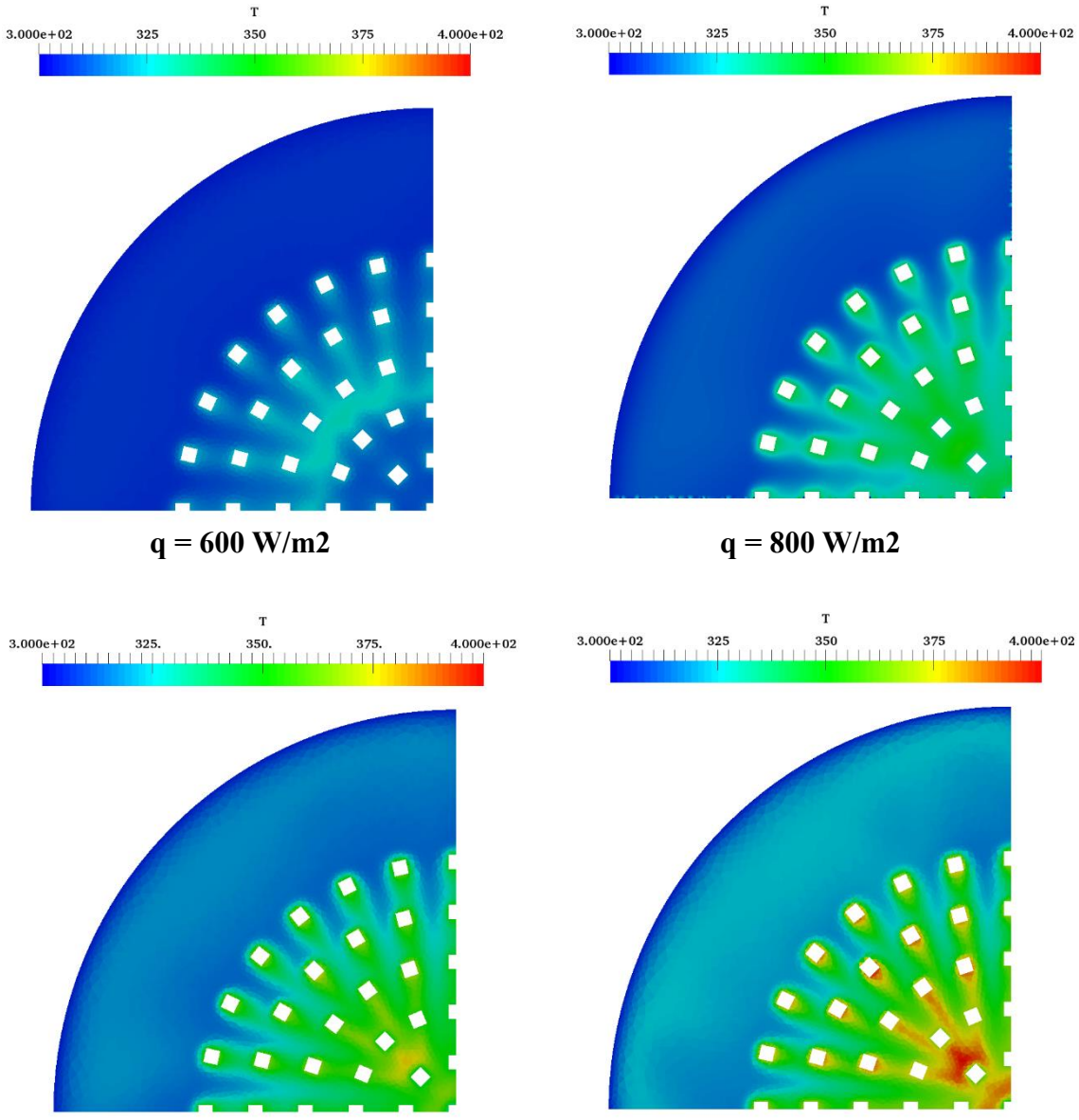


**q = 600 W/m2** **q = 800 W/m2**




FIGURE 3 Temperature Distribution along XY plane at Z = 0.020 m for different heat flux.

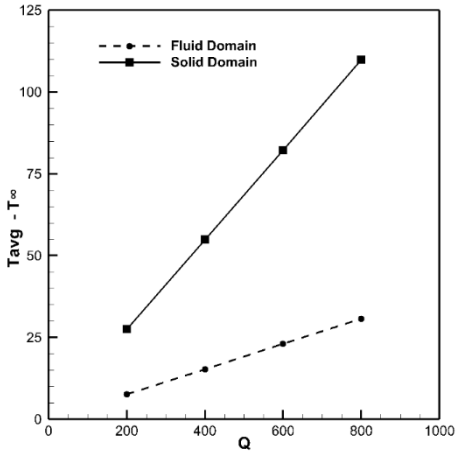


FIGURE 4. Variation of the Temperature difference with respect to the heat flux. (T∞ = 303K)

In addition to that, Figure 3 illustrates the influence of increasing heat flux on the temperature distribution of the fluid domain. As the outer periphery of the heat sink is enclosed by ambient air which is at surrounding temperature of 303K. The fins which are located at the farthest distance from the center of radial sink will have a better heat dissipation. Because of the density variation due to temperature, the hotter fluid will escape out to the upward direction which is replaced by the cold air coming from the surrounding. But as fluid flows towards the center, the heat dissipation reduces significantly. This is mainly because of the constrictions that are created by the closely spaced solid fins. Finally, it also supports the fact that, as we elevate the value of heat flux supplied, the surface temperature of the solid fins gets increased accordingly.

## 4. CONCLUSIONS

This study deals with CFD analysis of constant heat flux provided at the base of a radial heat sink trying to simulate the phenomenon similar to that of circular LED's. Four different values were used to analyse the effective thermal dissipation from a heat sink with radially distributed square fins. The numerical model is initially validated before carrying out the further investigation. It is found that as we go on increasing the heat flux, it leads to more non-uniform distribution of temperature primarily because of the uneven distribution of solid fins. This eventually leads to the formation of localised hot spot near to the centre of the heat sink.

## REFERENCES

[1] Seung-Hwan Yu, Kwan-Soo Lee, Se-Jin Yook, Optimum design of a radial heat sink under natural convection, *International Journal of Heat and Mass Transfer* 54 (2011) 2499–2505.

[2] Bin Li, Sora Jeon, Chan Byon, Investigation of natural convection heat transfer around a radial heat sink with a perforated ring, *International Journal of Heat and Mass Transfer* 97 (2016) 705–711

[3] C.D. Jones, L.F. Smith, Optimum arrangement of rectangular fins on horizontal surfaces for free-convection heat transfer, *J. Heat Transfer, Trans. ASME* 92 (1970) 6–10

[4] R.-T. Huang, W.-J. Sheu, C.-C. Wang, Orientation effect of natural convective performance of square pin fin heat sinks, *Int. J. Heat Mass Transfer* 51 (2008) 2368–2376.

[5] User Guide, OpenFOAM, The Open Source CFD Toolbox, Version 3.0.0 November 2015.

Fifth International Conference on Computational Methods for Thermal Problems
THERMACOMP2018, July 9-11, 2018, Indian Institute of Science, Bangalore, INDIA
*N. Massarotti, P. Nithiarasu, Pradip Dutta and C. Ranganyakalu (Eds.)*

# THEORETICAL INVESITIGATION OF LASER TREATMENT OF OTA'S NEVUS WITH EXTERNAL SKIN COOLING

**Shujian ZHANG, Dong LI, Bin CHEN***
State Key Laboratory of Multiphase Flow in Power Engineering, Xi'an Jiaotong University, China
chenbin@mail.xjtu.edu.cn

## ABSTRACT

Q-switched lasers are effective in the treatment of Ota' Nevus, but complications can arise after laser treatment due to high residual temperature. In this study, a four-layer skin model for Ota's Nevus was established and a local thermodynamic non-equilibrium two-temperature model was proposed to obtain skin temperature after treatment. Skin cooling was introduced to protect the skin from thermal damage. The effects of different cooling procedures were investigated. The results show that 1064nm laser has better performance than 755nm laser for deep-buried melanosomes. Cryogen Spray Cooling (CSC) is effective only in cooling the epidermis, while continuous cold air cooling can cause a larger drop in dermal temperature, which can effectively protect the dermis. For 755nm laser, -10$^{o}$C cold air cooling for 15s combining 100ms CSC can effectively protect both the epidermis and the dermis. For 1064nm laser, 100ms CSC is necessary.

**Key Words:** *Laser Dermatology, Nevus of Ota, Skin Cooling, Two-temperature Model.*

## 1. INTRODUCTION

Nevus of Ota is a pigmentary disorder consisting of blue-black or grey-brown patchy lesions that occur in areas along the first and second branches of the trigeminal nerve (FIGURE 1). It is common in Asians and Africans but rare in Caucasians. Possible etiology of this dermal pigmentary disorder is failure of melanocytes migration from the neural crest to the epidermis during foetal stage. So far, the use of 755nm Q-switched laser has been proven effective in the treatment of Ota' Nevus, but adverse reactions and complications such as bleeding during treatment, hyper-pigmentation and hypopigmentation can still arise from laser treatment, especially for Asians with high epidermal melanin concentration. External skin cooling including cryogen spray cooling (CSC) and cold air cooling, has been used in laser dermatology to protect the skin from unwanted thermal damage, but has not been introduced to the laser treatment of Ota's Nevus. The objective of this study is to investigate the effect of different cooling procedures on laser treatment of Ota's Nevus and propose an approach for skin protection from thermal damage.

FIGURE 1. Nevus of Ota [1]

* This work was financially supported by National Nature Science Foundation of China (51727811)

## 2. MATHEMETIC MODEL AND ALGORITHM

In this paper, a four-layer Nevus of Ota skin model was established that consists of a skin tissue matrix and melanosomes superposed on the matrix (FIGURE 2). The four parallel planar layers are the 60-μm thick epidermal layer and three dermal layers with thicknesses of 440μm, 1500μm and 1000μm, respectively. The dermal melanosomes are contained in the second dermal layer. Melanin content in the epidermal layer and the 2nd dermal layer is 15% and 35%, respectively.

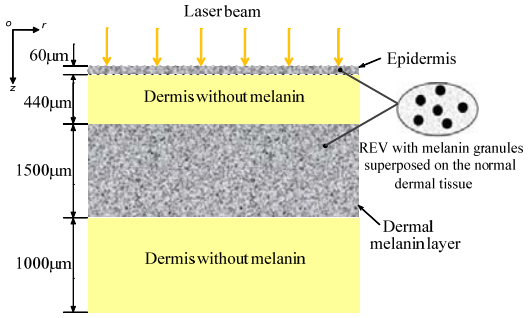


FIGURE 2. Schematic of the skin model for Nevus of Ota

The epidermal layer and the dermal melanin layer are mixtures of skin matrix and spherical melanosomes, which can be respectively treated as matrix and discrete small heat sources that fill in the voids of porous medium. Representative element volume (REV) in porous media is the smallest volume over which a measurement can be made that will yield a value representative of the whole. In FIGURE 2 it is the repeating unit cells composed of normal tissue and several melanosomes. In this case, two energy equations, one for each phase, are used to describe the heat transfer between the two phases. The metabolic and blood perfusion terms can be neglected, due to the short duration of laser pulse. Then the reduced energy equations for the description of melanosome temperature $T_m$ and tissue temperature $T_t$ are given as follows,

$$\varepsilon\rho_c c_{p,c}\frac{\partial T_c}{\partial t}=\nabla\left(\varepsilon k_c\nabla T_c\right)-h_{ct}a_{ct}\left(T_c-T_t\right)+\varepsilon Q_c \tag{1}$$

$$\left(1-\varepsilon\right)\rho_t c_{p,t}\frac{\partial T_t}{\partial t}=\nabla\left(\left(1-\varepsilon\right)k_t\nabla T_t\right)+h_{ct}a_{ct}\left(T_c-T_t\right)+\left(1-\varepsilon\right)Q_t \tag{2}$$

where $\varepsilon$ is the volumetric fraction of the melanosome, $\rho$ is density, $c_p$ is specific heat, $k$ is thermal conductivity, $h$ is heat transfer coefficient, and $a$ is the specific interfacial area. The Subscripts $m$ and $t$ represent melanin and skin tissue, respectively. $Q_m$ and $Q_t$ are energy absorbed by the melanosome and the skin tissue, which only exist during the laser pulse duration.

## 3. RESULTS

We investigated the temperature distributions of the skin matrix and melanosomes after laser radiation without cooling, with CSC and with cold air cooling, respectively. FIGURE 3. (a) shows the skin temperature distribution along the depth at the beam center immediately after 60ns of 755-nm laser irradiation. The laser irradiation energy density is 5J/cm$^2$. The threshold disruption temperatures are 70$^o$C for skin tissue and 112$^o$C for melanosomes [2] [3], respectively. As shown in FIGURE 3. (a), the temperature of epidermal melanosome reaches 128$^o$C, and both the epidermal

and the dermal temperature exceed 70°C, which may cause unwanted thermal damage to the skin. The highest temperature of dermal melanosome is 156°C, which is enough for melanosome disruption. However, the disruption can only reach a depth of 40μm. Temperature of dermal melanosome buried deeper than 1200μm remains unchanged. Therefore, when treatment is performed without cooling procedure, the skin is vulnerable to laser irradiation.

The temperature distributions of the skin tissue and melanosomes immediately after 1064nm Nd:YAG laser irradiation are plotted in FIGURE 3. (b), with pulse duration of 6ns and energy density of 8J/cm$^2$. Laser at wavelength of 1064nm with short pulse duration of 6ns introduces less thermal diffusion between the melanosomes and the skin tissue, resulting in lower tissue temperature than those in FIGURE 3. (a), thus higher energy density is required to achieve good clearance. Melanosome temperature reaches 120°C in epidermis and 145°C for dermis, both exceeds the threshold. The tissue temperatures remain below 41°C, which is safe for the normal skin tissue. It is clear that the melanosomes buried at depth of 500-2000μm have higher temperature rises compared with those in FIGURE 3. (a), which indicates that 1064nm-laser has better performance when dealing with melanosomes buried deeper in the dermis.

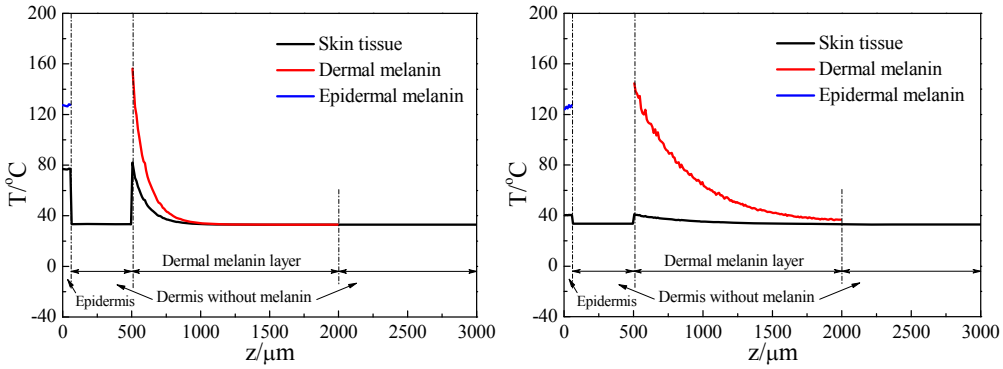


(a) 755nm (b)1064nm

FIGURE 3. Temperature distribution of the skin immediately after laser irradiation without cooling

Cryogen Spray Cooling (CSC) is effective in chilling down the epidermis. On the other hand, continuous cold air cooling can cause a larger drop in dermal temperature, which can effectively protect the dermis. When cold air at temperature of -10°C is applied for 15s, followed by 100ms of R134a (boiling point: -26.1°C) spray cooling, the temperature distribution immediately after laser irradiation within the skin is shown in FIGURE 4. (a). The wavelength of the laser is 755nm, with pulse duration of 60ns and energy density of 5J/cm$^2$. Compared to the result in FIGURE 3. (a), the highest temperature of the epidermal melanosomes and tissue are 77°C and 27°C, respectively. The dermal tissue temperature is below the threshold as well. In summary, CSC combining cold air cooling is an effective and promising way for skin protection from thermal damage in 755-nm laser treatment of Ota's Nevus.

Skin temperature distribution after 1064-nm laser irradiation with pulse duration of 6ns, energy density of 8J/cm$^2$ and R134a precooling of 100ms is plotted in FIGURE 4. (b). The highest temperature of epidermal melanosomes is 88°C, which has achieved an ideal cooling effect. Unlike 755-nm laser, 1064-nm laser does not cause a large temperature rise in the dermis, thus dermal protection is not necessary. CSC is effective to protect the skin for Nd:YAG laser.

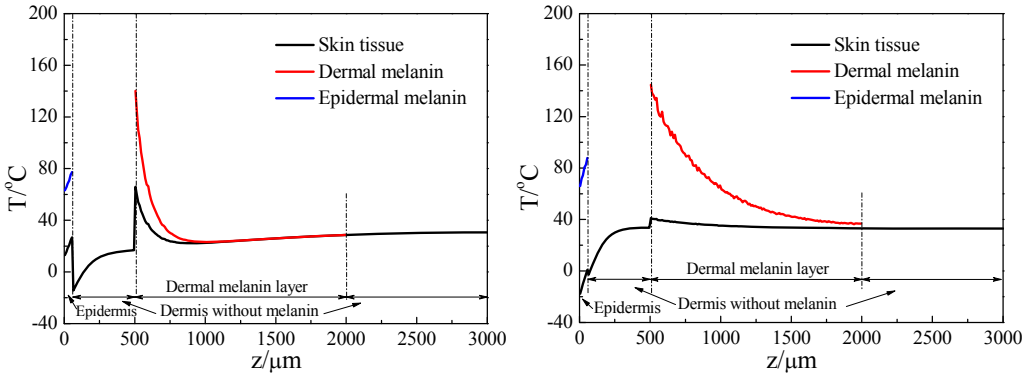


(b) 755nm with CSC combining cold air cooling (b) 1064nm with 100ms CSC

FIGURE 4. Temperature distribution of the skin immediately after laser irradiation

## 4. CONCLUSIONS

Laser treatment has become the effective therapy for Nevus of Ota, but adverse reactions and complications can arise from high residual temperature. Unfortunately, external skin cooling including cryogen spray cooling (CSC) and cold air cooling has not been introduced to the laser treatment of Ota's Nevus. In order to obtain skin temperature after laser irradiation, a four-layer Nevus of Ota skin model is established in this work. The temperature of the skin after laser treatment can be obtained with the local thermodynamic non-equilibrium two-temperature model.

We investigated the temperature distributions of the skin after 755-nm and 1064-nm laser radiation without cooling, with CSC and cold air cooling, respectively. When simulation is performed using laser beam at a wavelength of 755nm and energy density of 5J/cm$^2$, the temperatures of the tissue and epidermal melanosomes exceed their temperature thresholds without cooling procedure, which causes damage to the skin. The results show that 1064 nm-laser has better performance than 755-nm laser when dealing with melanosomes buried deeper in the dermis. CSC is effective but can only chill down the epidermis and the superficial layer of dermis. It is sufficient for skin protection in 1064-nm laser treatment. In comparison, continuous cold air cooling can cause a larger drop in dermal temperature, which can effectively protect the dermis. When 100ms of CSC combining 15s of -10$^o$C cold air cooling is implemented, temperatures of the tissue and epidermal melanosomes are below their temperature threshold. In summary, CSC combining cold air cooling is the best way for skin protection from thermal damage in 755-nm laser treatment of Ota's Nevus.

## REFERENCES

[1] Chang C J, Kou C S. Comparing the effectiveness of Q-switched Ruby laser treatment with that of Q-switched Nd:YAG laser for oculodermal melanosis (Nevus of Ota).[J]. Journal of Plastic Reconstructive & Aesthetic Surgery, 2011, 64(3):339-345.

[2] Jacques S L, Mcauliffe D J. The melanosome: threshold temperature for explosive vaporization and internal absorption coefficient during pulsed laser irradiation [J]. Photochemistry & Photobiology, 1991, 53(6):769.

[3] Dong Li, Chen B, Wang G X, et al. A New Theoretical Model of Selectively Photothermolysis to Aid Laser Treatment of Poor Responding Port Wine Stain Blood Vessels[J]. Begel House Inc, 2014.

# MODELLING AIR ENTRAPMENT DYANAMICS DURING IMPACT OF A HIGH SPEED METAL DROPLET ONTO A SOLID SUBSTRATE

**Rajesh Kumar Shukla, Alok Kumar, Arvind Kumar***

Dept. of Mechanical Engineering, Indian Institute of Technology Kanpur, Kanpur – 208016, India
*arvindkr@iitk.ac.in

## ABSTRACT

When a liquid drop impacts onto a solid surface, thin air film is generally entrapped between the droplet and the substrate at the central portion which eventually evolves into a spherical air bubble due to minimization of surface energy. This interetsing phenomenon during impact of molten metal droplet in thermal spray deposition, also involving freezing of the droplet, is not clearly understood due to opaque nature of the metal droplet. This study for the first time numerically report the air entrapment dynamics during impact of high velocity micron size molten metal droplet onto a solid substrate by considering fluid flow, heat transfer, solidification phase change, ambient air and free surface deformation. Earlier models have not considered heat transfer and phase change and focused on hydrodynamics and free surfce deformation only. The volume of fluid surface tracking method (VOF) coupled with the solidification heat transfer model within a one-domain continuum formulation is utilized. Results shows that initially a thin circular film of air was entrapped in the droplet which grew into an air bubble and eventually detached through the upper surface of the droplet creating a hole in the central portion of the droplet. It is also found that wettability of the solid surface affects the detachment of the air bubble, suggesting a method for bubble elimination in many drop-impact applications.

**Key Words:** *Metal droplet, High-speed impact, Entrapped air dynamics, Solidification, Free surface, Wettability.*

## 1. INTRODUCTION

A thermally sprayed coating is built up by impact of molten droplets onto a solid substrate. The individual droplet forms a splat through the processes of flattening, rapid solidification and cooling of the impacting droplet. Then, the splats are piled up layer by layer, forming the coating deposition. The quality of the coating is closely linked with the way the individual splatis formed. Such droplet impingement onto the substrate with a small diameter (~μm), high temperatures (~3000 K), and high velocities (~100 m/s) involves complex phenomena, such as free surface deformation, fluid dynamics, solidification, air entrapment and heat transfer. Among these the air entrapment is of great interest because of its key role in controlling the quality of droplet-substrate adhesion during the deposition process. Moreover, the air entrapment also influences the layered microstructure and bonding between the splat-substrate and splat-splat interface. Air entrapment in the droplet during its impact onto a solid subsrate has been widely reported experimentally and numerically for transparent droplets at room temperature (a review is reported in refrence [1]). Howevere, there are only a few studies for opaque molten metal droplets [2–4]. For the molten droplet case air entrapment and its dynamics is very difficult to visualize experimentally due to opaque nature of the droplet. Therefore, in this case numerical simulation becomes an effective tool for performing the investigation. Mehdi-Nejad et al. [2] modelled the motion of molten nickel droplet on a flat surface. They observed the air entrapment in the droplet and suggested the formation of central pore causesd by the air entrapment dynamics. In their simulation only hydrodynamics of droplet impact was considered, howevere, heat transfer between the splat and substrate and freezing of the droplet were ignored. It must be noted

that due to these assumptions the state-of-the-art numerical investigations of air entrapment and its dynamics are severely incomplete, and hence there is a great need to study the air entrpament dynamics by considering heat transfer and solidification in order to represent the actual conditions of the thermal spray deposition process. The current study numerically investigates the air entrapment and its dynamics during impact of a high-speed molten metal droplet onto a solid substrate by considering heat transfer and solidification. This study also seeks to observe the effect of surface wettability on the behaviour of entrapped air.

## 2. MODEL

The problem considered is shown schematically in Fig. 1. A molten molybdenum droplet with a diameter of 40 µm at an initial uniform temperature of 3083 K is impacting on a flat aluminum substrate with a velocity of 140 m/s. The thermophysical property data used in the simulations have been taken from reference [5].The model used in the current study has been discussed in detail elsewhere [3], therefore, here only the specific features of the model are mentioned. The governing equations are shown in Table 1. In the droplet impingement model transient fluid flow during the droplet impact, its subsequent spreading, heat transfer and solidification are considered using the volume of fluid surface tracking method (VOF) coupled with a solidification model within a one-domain continuum approach based on the classical mixture theory [3,6]. For computational cells which are undergoing the phase change (solidification), the solid-liquid interaction in the momentum conservation (Eq. 4) is considered using the Darcy source term *Su* [6]. Momentum conservation equation accounts for surface tension effects at the free surface using $F_{vol}$ source term which is considered by a continuum surface force model [3]. The momentum and the energy conservation equations (Eqs. 4 and 5) are coupled. The source term $S_h$ (in Eq. 5), for handling the solidification phase change, is active only for the computational cells filled with a molten droplet ($F$ = 1). In the substrate, only the conduction heat transfer is solved (Eq. 6). A thermal contact resistance value of $1.0\times10^{-8}$ m$^2$ K W$^{-1}$ is used for considering the droplet-substrate imperfect contact.

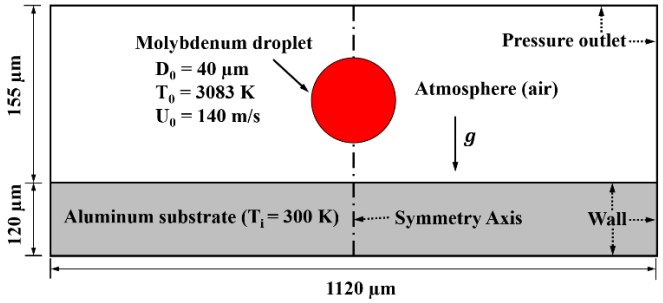


Figure 1: Computational domain

| | | |
|---|---|---|
| VOF equation | $\frac{\partial F}{\partial t} + \nabla . \vec{u} F = 0$ | (1) |
| Definition of mixture quantities for a cell in the mushy state | $f_s + f_l = 1,\ c_{eff} = F\, c_d + (1-F) c_{air}, \rho = F\rho_d + (1-F)\rho_{air}$ $k_{eff} = F\, k_d + (1-F)k_{air}, k_d = f_l k_l + (1-f_l)k_s, \mu = F\, \mu_d + (1-F)\mu_{air}$ | (2) |
| Continuity equation | $\frac{\partial \rho}{\partial t} + \nabla . (\rho \vec{u}) = 0$ | (3) |
| Momentum conservation equation | $\frac{\partial}{\partial t}(\rho \vec{u}) + \nabla . (\rho \vec{u}\vec{u}) = -\nabla p + \nabla . [\mu(\nabla \vec{u} + \nabla \vec{u}^T)] + \rho \vec{g} + F_{vol} - S\vec{u}$ $S\vec{u} = \begin{cases} \left[ C \frac{(1-f_l)^2}{f_l^3 + e} \right] \vec{u} & F = 1 \\ 0 & F < 1 \end{cases}$ | (4) |

| | | |
|---|---|---|
| Energy conservation equation | $$\frac{\partial}{\partial t}(\rho c_{eff} T) + \nabla \cdot (\rho \vec{u} c_{eff} T) = \nabla \cdot (k_{eff} \nabla T) + S_h$$ $$S_h = \begin{cases} -L\left[\frac{\partial}{\partial t}(\rho f_l) + \nabla.(\rho \vec{u} f_l)\right] & F = 1 \\ 0 & F < 1 \end{cases}$$ $$f_l = 0 \quad if\ T \le T_{solidus},$$ $$f_l = 1 \quad if\ T \ge T_{liquidus}$$ $$f_l = \frac{T - T_{solidus}}{T - T_{liquidus}} \quad if\ T_{solidus} < T < T_{liquidus}$$ | (5) |
| Substrate: Conduction heat transfer equation | $$\frac{\partial}{\partial t}(\rho_{subs} c_{subs} T) = \nabla \cdot (k_{subs} \nabla T)$$ | (6) |

Symbols:

| | | | | | |
|---|---|---|---|---|---|
| $c$ | Specific heat capacity | $L$ | Latent heat of fusion | *Subscripts* | |
| $C$ | Constant related to Darcy source term | $t$ | Time | $d$ | Droplet |
| $f$ | Weight fraction | $T$ | Temperature | *subs* | Substrate |
| $F$ | Volume of fluid function | $\vec{u}$ | Continuum velocity vector | *air* | Air |
| $F_{vol}$ | Continuum surface tension force | *Greek symbols* | | *eff* | Effective |
| $\vec{g}$ | Acceleration due to gravity vector | μ | Dynamic viscosity | *l* | Liquid |
| $k$ | Thermal conductivity | ρ | Density | *s* | Solid |

Table 1: Governing equations

## 3. RESULTS AND DISCUSSIONS

Figure 2 shows the pressure map near the imapct zone at different time while the droplet is approaching towards the substrate. Here negative time shows the time before the impact. As the droplet approaches towards the substrate, pressure rises in the air region between the droplet and substrate which can be seen from the pressure contour. The cause of the air presure rise is due to the effect of air viscosity which hindered the air escape from the thin region. Due to this pressure rise, bottom surface of the droplet gets flattened which can be clearly seen in the Fig. 5 ($t$ = -0.0087 μs). As the droplet impacts on the substrate, its pressure rises upto 6000 MPa in a short duration of time (0.028 μs, Fig. 3). After this droplet started to deform in the radial direction and pressure started to decrease.

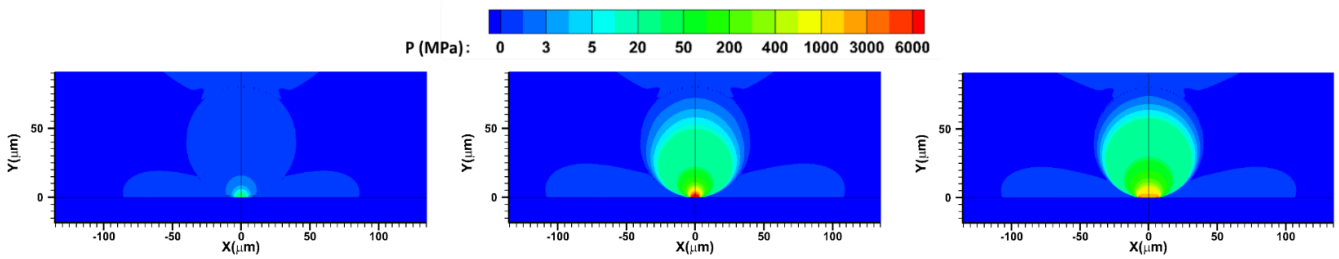


$t$ = -0.0018 μs $t$ = 0 μs $t$ = 0.0034 μs

Figure 2: Pressure maps

After the initial contact is made, air is entrapped as a thin circular film under flattened droplet bottom surafce and the substrate (Fig.5, $t$ = 0.0013 μs) which is eventually evolved to an air bubble ($t$ = 1.6107 μs) and reside at the centre, and it remained there during the subsequent flattening of the droplet. After the time $t$ = 2.3071 μs air bubble gets detached from the substrate and formed the central hole which is often seen in the actual coating deposit. Figure 5 shows the sequential images of the evolution of an entrapped air film into a buble and its detachment. It can be observed that once the entrapped air film formed, it retract very rapidly (0.0013 μs - 0.1113 μs) to minimize the surface energy. Further, the air volume contracts into a toroidal bubble at time, $t$ = 0.2913 μs.

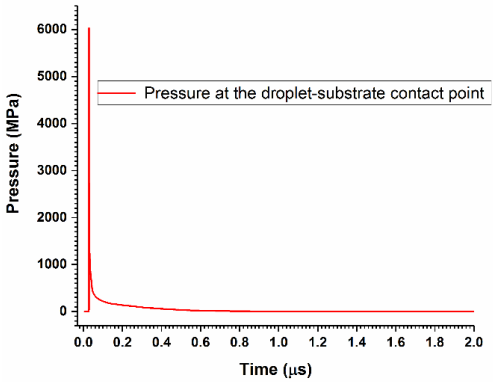


Figure 3: History of pressure variation

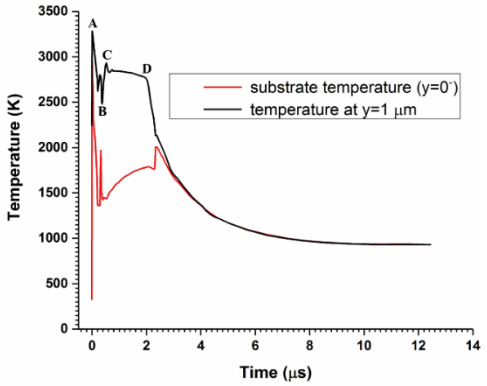


Figure 4: Temperature history at different heights from substrate

At later time, pinch-off of the liquid part that had been confined within the core of the toroidal bubble and generates a tiny secondary (daughter) droplet on the substrate (Fig. 5, $t$ = 0.3413 μs). After this time air bubble stay in this position untill the liquid thickness decreases due to droplet flattening and then air bubble detachment occurs. The effect of entrapped air dynamics is also reflected in the temperature-time profile at the bottom point of the droplet (Fig. 4) and at the top substrate point. It can be seen in the Fig. 4 that, as the droplet impact on the substrate, droplet bottom temperature shoots up to point A. More air gets collected gradually at the centre due to entrapped air dynamics and the temperature decreases to point B, this happens due to the fact that the air temperature is very low due to lower value of thermal conductivity. Consequently, small air bubbles which are approaching towards the central portion collide with each other and some part of the heated droplet comes near the considered point and hence, the temperature shoots up to point C. The accumulated bigger volume of air rests in the same state. During this period the temperature is almost constant (from point C to D) during this period the droplet layer becomes thinner and thinner due to spreading. Then afterward the accumulated air escapes into the atmosphere, as the liquid layer becomes very thin. The effect of this entrapped air dynamics is also reflected in the substrate temperature profile (Fig. 4). Effect of contact angle is also seen in the simulations with contact angle of 90º and 30 º. From Fig. 6 it can be seen that entrapped air shape is very different in both the cases (Fig. 6). For high contact angle (hydrophobic surface) the air resides at the substrate surface and gets detached as the air- droplets interface aprroaches the air bubble and droplet become thinner. For lower contact angle (hydrophilic surface) the air bubble rises upward direction in the droplet (Fig. 6, $t$ = 0.1813 μs) and detached from the liquid-air interface ($t$ = 1.7313 μs). It can be concluded that air bubble can be detached from the droplet material for the hydrophilic surfaces and it can enhance droplet-substrate adhesion quality. It can also be seen that time of air bubble detachment is very less in case of lower contact angle (hydrophilic surface) compared to high contact angle (hydrophobic surface).

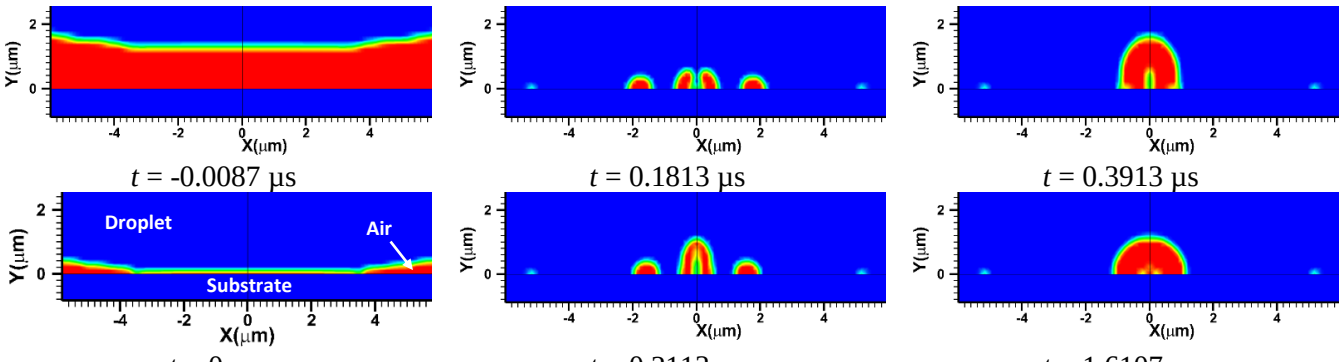


$t$ = -0.0087 μs | $t$ = 0.1813 μs | $t$ = 0.3913 μs

$t$ = 0 μs | $t$ = 0.2113 μs | $t$ = 1.6107 μs

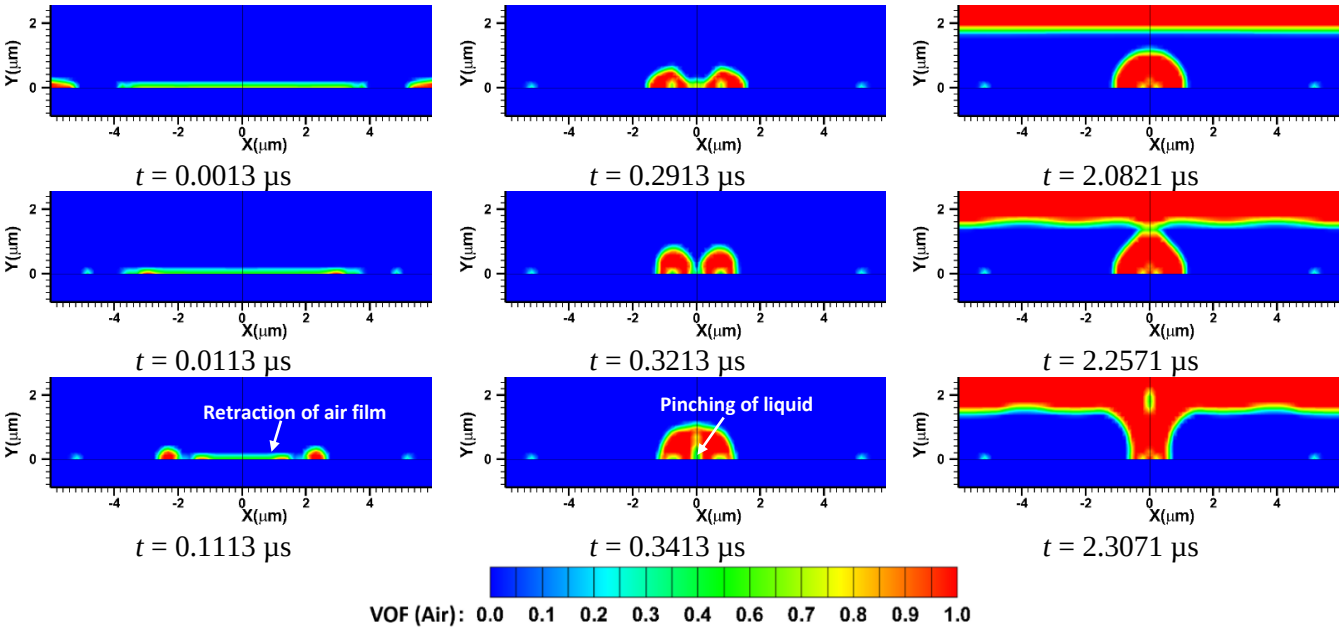


Figure 5: Evolution of shape of the entrapped air

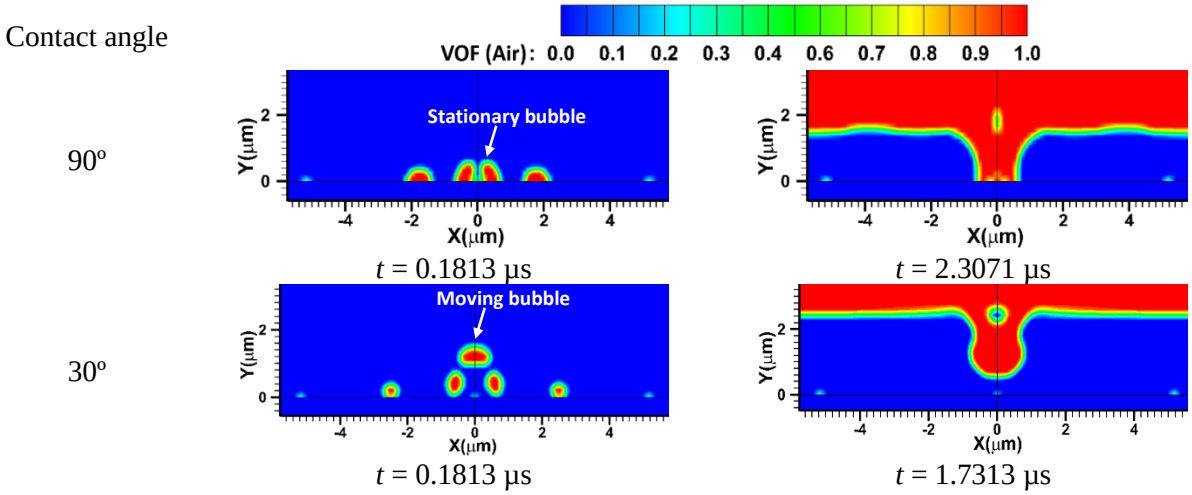


Figure 6: Effect of contact angle on entrapped air bubble

## 4. CONCLUSIONS

The presented model captures air entrapement at the central portion of the droplet during the high-speed impact of a molten metal droplet onto a substrate. It is found that initially a thin circular film of air was entrapped in the droplet which grew into an air bubble and eventually detached through the upper surface of the droplet creating a hole in the central portion of the droplet. The central hole is usually seen in the splat formed in thermal spray deposition. The current model can further provide deeper insight of the air entrapment in thermal spray coating by overcoming the technical constraints in performing the real-time experiments of high-speed imapct and freezing of opqaue molten metal droplets. For higher contact angle the air bubble tend to remain adhered to the substrate surface, whereas for lower contact angle the entrapped air bubble is not adhered to the substrate instead it rises in the droplet. This indicates that good wettability is beneficial for air bubble detachment and suggests a method for bubble elimination in many drop-impact applications.

## REFERENCES

[1] C. Josserand, S.T. Thoroddsen, Drop impact on a solid surface, Annu. Rev. Fluid Mech. 48 (2016) 365–391.
[2] V. Mehdi-Nejad, J. Mostaghimi, S. Chandra, Air bubble entrapment under an impacting droplet, Phys. Fluids. 15 (2003) 173–183.
[3] A. Kumar, S. Gu, H. Tabbara, S. Kamnis, Study of impingement of hollow $ZrO_2$ droplets onto a substrate, Surf. Coatings Technol. 220 (2013) 164–169.
[4] Y. Zhang, S. Matthews, A.T.T. Tran, M. Hyland, Effects of interfacial heat transfer, surface tension and contact angle on the formation of plasma-sprayed droplets through simulation study, Surf. Coat. Technol. 307 (2016) 807–816.
[5] S.-P. Wang, G.-X. Wang, E.F. Matthys, Melting and resolidification of a substrate in contact with a molten metal: operational maps, Int. J. Heat Mass Transf. 41 (1998) 1177–1188.
[6] S. Kamnis, S. Gu, Numerical modelling of droplet impingement, J. Phys. D. Appl. Phys. 38 (2005) 3664–3673.

Fifth International Conference on Computational Methods for Thermal Problems
ThermaComp2018, July 9-11, 2018, Indian Institute of Science, Bangalore, INDIA
*N. Massarotti, P. Nithiarasu, Pradip Dutta and C. Ranganyakalu (Eds.)*

# A MODIFIED MUSHY ZONE PERMEABILITY MODEL FOR PREDICTING MACROSEGREGATION

**Jatin Yadav**, **Abhishek G S**, and **Shyamprasad Karagadde**
Indian Institute of Technology Bombay, Mumbai, India
p17jatin@iima.ac.in, gsabhishek1@iitb.ac.in, s.karagadde@iitb.ac.in

## ABSTRACT

A-segregation is a macrosegregation pattern which emerges due to the flow of solute-rich interdendritic fluid via thermosolutal convection. This has a detremental effect on steel ingots. Thus modeling of this phenomenon through numerical simulations is an area of great interest. During modelling, the description of the mushy zone is a key aspect due to its impact on fluid flow. In the present study, a real time mushy zone permeability model has been developed using the depedence of its permeability on the local cooling rate. This model can be further developed to predict the formation and the location of other phenomena such as negative base segregation, V-segregation etc.

**KEYWORDS:** *Macrosegregation, A-segregation, Solidification Modelling*

## 1 INTRODUCTION

Since 19th century, steel ingots are being produced to serve the ever increasing demand of steel products worldwide. Understanding of the solidification behavior of such ingots is imperative to create defect free steel ingots. Time and cost intensive pouring-sectioning experiments were performed to understand the solidification process. Considerable research work [1, 2, 3] is underway to develop a numerical model that can simulate the ingot solidification accurately, still a lot of improvement is needed to achieve the desirable confidence in the results of such models.

Macrosegregation refers to the defect caused due to variation in alloy composition over a length scale varying from a few millimeters to meters.The undesirable effects on the mechanical properties due to the compositional inhomogenity make macrosegregation a highly undesirable phenomenon. Macrosegregation manifests itself in a variety of patterns such as A-segregates,V-segregates,negative base segregates etc. The A-segregates are the defects which appear in casting of large steel ingots. They are caused due to the thermo-solutal convection of solute rich liquid arising due to density difference caused due to segregation of elements such as S,P,C and Si into the liquid.Hence, the detection and elimination of A-segregates through numerical simulations of steel ingot castings can be of huge commercial and scientific benefit.

In the present study, an attempt has been made to improve the mixture continuum solidification model [4, 5] by development of mushy zone permeability model which modifies the value of mushy zone parameter ($A_{mush}$) in real time based on the cooling rate of mushy zone. Secondary dendritic arm spacing-SDAS($\lambda_2$) has been used to interlink the mushy zone parameter and the cooling rate. Further modifications to the permeability model are made to obtain more accurate predictions with regard to the location of the defect. The developed model successfully demonstrates the A-segregation phenomenon.

## 2 NUMERICAL MODEL

For simulation purposes, cylindrical ingot is treated as a 2-D axisymmetric geometry. Multi-component system in ANSYS Fluent, which implements finite-volume method couples with a continuum solidification model, has been used to solve mass, momentum, energy and species conservation equations.

The mushy zone is modeled as a porous medium through enthalpy-porosity technique in ANSYS Fluent. Mushy zone porosity appears as a sink term($S$) in the momentum conservation equation.

$$S = \frac{(1-\beta)^2}{(\beta^2+\epsilon)} A_{mush} \vec{v} \tag{1}$$

where $\beta$ is the liquid fraction, $\epsilon$ is a non-zero term to avoid division by zero and $A_{mush}$ is the mushy zone parameter which is a measure of permeability in the semi-solid regime.The solidification module in Ansys Fluent assumes a constant value of $A_{mush}$ throughout the solidification simulation. This assumption is not valid as the mush permeability is known to vary throughout solidification. The variation of the permeability constant as a function of viscosity$\mu$ and SDAS is given by the Blake-Kozeny model:

$$A_{mush} = \frac{180\mu}{\lambda_2^2} \tag{2}$$

Further, from experiments it has been established that SDAS and the cooling rate($\dot{T}$) are interrelated. M. El-Bealy et. al. developed an empirical relationship to estimate SDAS for steels containing less than 0.53 wt pct carbon as a function of the cooling rate[6]:

$$\lambda_2 = A_1 \dot{T}^{-n} 10^{-6} \tag{3}$$

where $A_1 = 148$ and $n = 0.38$. Using the Equations 2, 3, a direct relationship between $A_{mush}$and $\dot{T}$ is established.

$$A_{mush} = \frac{180\mu 10^{12}}{(A_1 \dot{T}^{-n})^2} \tag{4}$$

This variation in $A_{mush}$ is calculated only for cells which were in mushy zone ($0 < \beta < 1$).

## 3 RESULTS

An axisymmetric simulation domain of dimension 20 mm * 50 mm was setup with convection at the bottom and outer walls ($h = 35W/m^2K$) and ambient temperature($T_w = 350K$). The top face was insulated and no-slip boundary condition was applied at the walls. A mesh of size $0.25mm$ was generated. Ansys Fluent Finite-Volume solver was used to run the simulations.The SIMPLE scheme was used to solve the momentum equation and power law scheme was used to solve the scpecies and energy equations.Both solutal and thermal buoyancy effects were considered for the simulation. Scheil based solidification module was used to slove for evolution of solid fraction.The simulation was performed for medium-carbon steel. The material parameters used for the simulations are given in Table 1.

Three different cases of modeling are shown in Figure 1 with carbon concentration maps after 12 minutes of simulation. On using a fixed default value of $A_{mush}$ the model is unable to predict formation of A segregates as shown in Figure 1(a). Further on using a real time calculation of $A_{mush}$ the model can predict the formation of A-Segregates. However the exact location cannot be identified. This is shown in Figure 1(b).

On comparison with the experimental observations, it was found that on multiplying the $A_{mush}$ term by a correction factor($C_F$) of magnitude $0.2$ the model prediction matches with the experimental prediction. The result of the modified $A_{mush}$ is shown in fig 1(c). The modified version of mushy zone permeability model is given by:

$$A_{mush} = C_F \left( \frac{180\mu 10^{12}}{A_1 \dot{T}^{-n}} \right) \tag{5}$$

With the use of modified mushy zone permeability model for changing $A_{mush}$ in real time during solidification simulation, the model was successfully able to predict the location of A-segregates in the steel ingots. The A-segregate formation was successfully simulated for a representative steel However,

ingot. The comparison of the eperimental and model predictions is shown in Figure 3.The segregation of carbon along the centreline obtained by simulating the complete solidification of the ingot using modified mushy zone permeability model. This has been compared with experimental results and is shown in Figure 2. As the ingot size used for simulation is much smaller than the experimental ingot, height of both ingots has been normalized to get a uniform scale for comparison. Both the experimental and simulation results demonstrate negative segregation in the lower half and positive segregation in the upper half of the steel ingot. The percentages of segregation also match reasonably well in the top and bottom region of ingot.

| | |
|---|---|
| Liquidus Temperature | 1808 $K$ |
| Partition Coefficient | 0.324 |
| Thermal Expansion Coefficient | 1.07 x $10^{-4} K^{-1}$ |
| Solutal Expansion Coefficient | 1.4164 |
| Viscosity | 0.0042 $kgm^{-1}s^{-2}$ |
| Density | 6990 $kgm^{-3}$ |
| Specific Heat | 500 $Jkg^{-1}K^{-1}$ |
| Thermal Conductivity | 39.3 $Wm^{-1}K^{-1}$ |
| Latent Heat | 27000 $Jkg^{-1}$ |

Table 1: Material Properties used for the Simulation

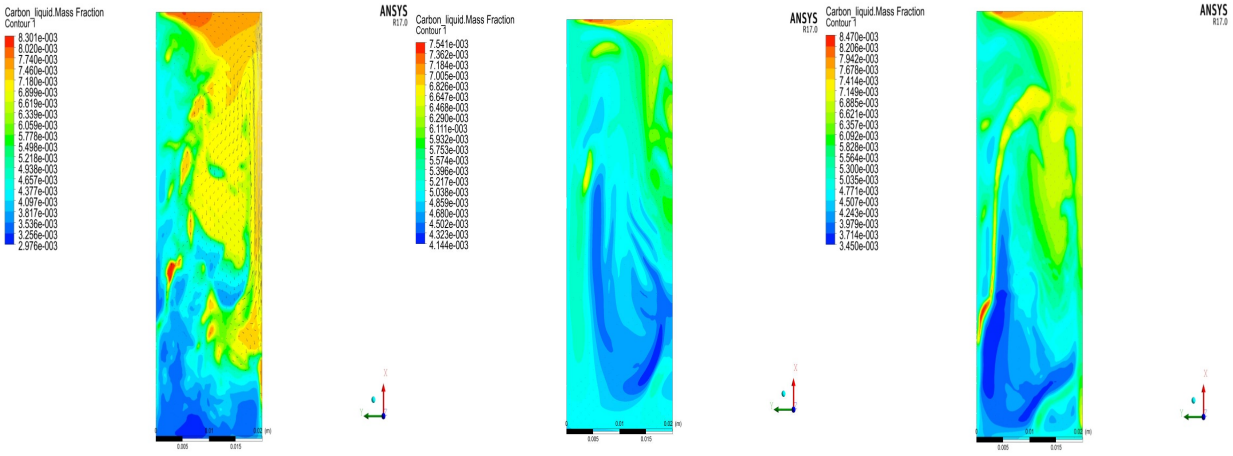


(a) (b) (c)

Figure 1: Carbon concentration maps of 50 mm * 20 mm axisymmetric domain with Co = 0.51 wt. % and 0.25 mm grid size after 12 minutes with (a) default $A_{mush} = 10^5$, (b) variable $A_{mush}$ , and (c) variable $C_F A_{mush}$

the transition from negative to positive segregation happens earlier in the case of simulation while going from bottom to top. This could be attributed to the different setup conditions, and smaller size of ingot used for simulation which makes it easier for solute to diffuse to nearby locations.

**Rayleigh number criterion for A-Segregation**

The Rayleigh number can be used as a criterion to predict the formation of A-Segregates in the ingot under a given set of conditions, (Thermal Gradient,Cooling Rate,Alloy Composition,Densitiy). M. Torabi et al. [7] developed a modified Rayleigh number-based criterion which predicted that the A-segregates would form when Rayleigh numbers were in the range of $(17 \pm 8)$. This criterion was further validated by E. J. Pickering et al.[3] by using the criteria to successfully predict formation A-segregates in two different steel ingots. The modified Rayleigh number is given by

$$Ra = 2.3810^{-6} C_o^{1.1-3.99C_o} \Delta\rho \frac{G}{\dot{T}^{1.7232}} \tag{6}$$

where $Ra$ is the Rayleigh number and $G$ is the thermal gradient.
A Rayleigh number map was obtained using Equation 6 along with the modified $A_{mush}$ term was able to pin-point the regions of formation A-segregates. It can be observed in Figure 4 that Rayleigh numbers are considerebly high($\approx 100$) in regions of A-segregates whereas at other regions it is considerebly low.

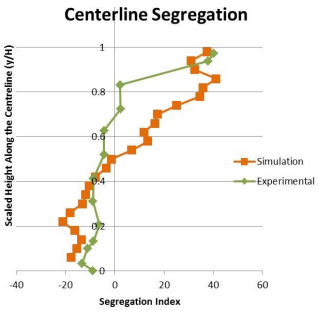


Figure 2: Experimental [8] vs Simulated Centreline segregation profile for Co = 0.51 wt% C

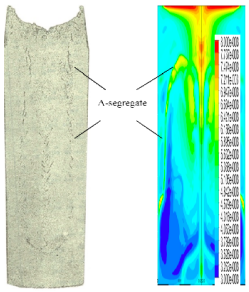


Figure 3: Comparison of Experimental [8] and Simulated solid Steel ingot

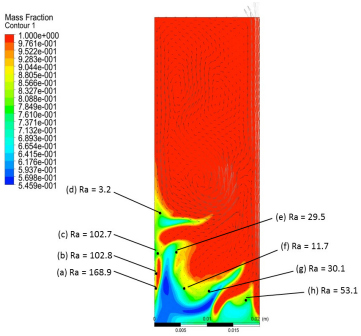


Figure 4: Rayleigh number for points (a)-(h) calculated at Time=450s and $\beta$=0.2.

## 4 CONCLUSION

In the present study, the A-Segregates formation in steel ingot was predicted through solidification simulation of a representative small steel ingot. Following points conclude the insights acquired from the study:

- A mushy zone permeability model was developed which calculated value of $A_{mush}$ in real time based on the cooling rate of mushy zone during simulation.
- A correction factor ($C_F$=0.2) was implemented in the developed permeability model so as to obtain a more accurate model prediction.
- Using the modified mushy zone permeability model, a clear manifestation of A-segregate formation was shown in Figure 3. The carbon segregation maps predicted by the model were in good agreement with the A-segregates observed in the experimental data.
- Centreline segregation comparison of scaled simulated and experimental ingots showed good qualitative match with negative segregation in bottom portion and positive segregation in top region(Figure 2).
- Rayleigh number study was performed to calculate *Ra* values at the time when A-segregates start to form. Distinctively high values obtained at locations where A-segregate is about to evolve.

A significant quantitative discrepancy still exists between the simulated and experimental data (Figure 2). Main reasons for this discrepancy can be attributed to the following: (1) Neglecting microstructural morphology that develops during solidification; (2) ignoring the solidification shrinkage; (3) simplification of geometry and boundary conditions used for steel ingot; (4) simplification of the Fe-C phase diagram; etc.; (5)Mould filling process which impacts the evolution of solidification interface through residual flows and temperature gradients has not been taken into account in the present study. To improve the accuracy of simulations, further improvements in the above mentioned areas are required.

## REFERENCES

[1] G Lesoult. Macrosegregation in steel strands and ingots: Characterisation, formation and consequences. *Materials Science and Engineering: A*, 413:19–29, 2005.

[2] Jiaqi Wang, Paixian Fu, Hongwei Liu, Dianzhong Li, and Yiyi Li. Shrinkage porosity criteria and optimized design of a 100-ton 30cr 2 ni 4 mov forging ingot. *Materials & Design*, 35:446–456, 2012.

[3] EJ Pickering, SS Al-Bermani, and J Talamantes-Silva. Application of criterion for a-segregation in steel ingots. *Materials Science and Technology*, 31(11):1313–1319, 2015.

[4] WD Bennon and FP Incropera. A continuum model for momentum, heat and species transport in binary solid-liquid phase change systems - i : Model formulation. *International Journal of Heat and Mass Transfer*, 30(10):2161–2170, 1987.

[5] PJ Prescott and FP Incropera. Convective transport phenomena and macrosegregation during solidification of a binary metal alloy: I?numerical predictions. *Journal of Heat Transfer*, 116(3):735–741, 1994.

[6] M El-Bealy and Brian G Thomas. Prediction of dendrite arm spacing for low alloy steel casting processes. *Metallurgical and materials transactions B*, 27(4):689–693, 1996.

[7] M Torabi Rad, Petr Kotas, and C Beckermann. Rayleigh number criterion for formation of a-segregates in steel castings and ingots. *Metallurgical and Materials Transactions A*, 44(9):4266–4281, 2013.

[8] $1^{st}$ report on the heterogeneity of steel ingots. *Journal Iron and Steel Institute*, 113:39.

Fifth International Conference on Computational Methods for Thermal Problems
THERMACOMP2018, July 9-11, 2018, Indian Institute of Science, Bangalore, INDIA
*N. Massarotti, P. Nithiarasu, Pradip Dutta and C. Ranganayakulu (Eds.)*

# MODELLING ELECTRO-OSMOTIC FLOW THROUGH POROUS MEDIA

**Simona Di Fraia, Nicola Massarotti, Alessandro Mauro**
Dipartimento di Ingegneria, Università degli Studi di Napoli "Parthenope", Napoli, Italy,
Centro Direzionale, Isola C4, 80143, Napoli, Italy,
simona.difraia@uniparthenope.it, massarotti@uniparthenope.it, alessandro.mauro@uniparthenope.it

**Perumal Nithiarasu**
Biomedical Engineering and Rheology Group, Zienkiewicz Centre for Computational Engineering,
Swansea University, Swansea SA2 8PP, United-Kingdom,
p.nithiarasu@swansea.ac.uk

## ABSTRACT

A numerical investigation of electro-osmotic flow in water saturated porous media is presented. The aim of the work is to analyse the effectiveness of using electro-osmosis to drive flow through water saturated porous media. Electro-osmotic flow is studied by using two sets of equations, one for the reproduction of the electro-kinetic forces, and the other to simulate fluid flow through porous media, based on the generalised model. The results show that the presence of porous media increases the range of channel width over which the electro-osmotic flow is effective, and produces higher flow rates than free channels of the same widths. The results also prove that beyond 100μm channel width, electro-osmotic flow is effective only if porous media are employed.

**Key Words:** *Electro-osmosis, Finite element, CBS, Width effect, Generalised porous medium model.*

## 1. INTRODUCTION

Electro-Osmosis (EO) is used in several applications in the fields of engineering and biology. The operation of EO driven systems is based on the interaction between solids and electrolytes. A solid surface in contact with an electrolytic solution becomes spontaneously charged. Therefore, the ions of the solution concentrate close to the charged surface, generating the so-called Electric Double Layer (EDL) [1]. The application of an external electric field makes the ions of the EDL moving, in order to restore the electro-neutrality of the system. As a consequence, the nearby ions are dragged and Electro-Osmotic Flow (EOF) is generated. As the distance from the charged surface increases, the ions concentration decreases and therefore EO effect weakens. For this reason, introducing charged porous media can potentially enhance EOF, as charged particles increase charged surfaces area and contribute to fluid flow [2, 3]. In order to investigate the effectiveness of using porous media to enhance EOF, a numerical model of EOF through porous media is proposed in this work. EOF is modelled by employing two sets of equations, one to study the electrical field, the other to model the fluid flow. In particular, the fluid flow through porous media is analysed by using the generalized porous medium model, which has been proposed in the past to study EOF in micro-channels packed with charged spherical micro-particles, by either using analytical models or Lattice Boltzmann Method (LBM) [4]. In this work, the Characteristic Based Split (CBS) algorithm and the finite element method are used to solve the generalised porous medium model [5].
The numerical model proposed is presented in Section 2, the computational domain and the boundary conditions used in the study are described in Section 3. In order to determine the evidence for effectively using porous media, a comparative study between micro-channels with and without porous media is presented in Section 4. Finally, some conclusions are given in Section 5.

## 2. MATHEMATICAL MODEL AND SOLUTION PROCEDURE

Electro-kinetic effects, responsible for EOF, are studied through a Laplace equation for external potential, $\phi$, and a Poisson-Boltzmann equation for the Electric Double Layer (EDL) potential, $\psi$. Fluid flow is modelled by using the generalised model for porous media, modified by introducing a source term in the momentum equation to take into account the electro-kinetic forces [7]. The non-dimensional form of these equations is given as follows:

| ***External potential*** | | ***EDL potential*** | | ***Continuity*** | |
|---|---|---|---|---|---|
| $\nabla^2\phi^* = 0$ | (1) | $\nabla^2\psi^* = -(\kappa L_{ref})^2 \sinh\left(\psi^*\right)$ | (2) | $\frac{1}{\beta^2}\frac{\partial p^*}{\partial t^*} = -\rho^* \frac{\partial u_i^*}{\partial x_i^*}$ | (3) |

***Momentum***

$$\frac{\rho^*}{\Phi}\left[\frac{\partial u_i^*}{\partial t^*} + \frac{1}{\Phi}\frac{\partial\left(u_j^* u_i^*\right)}{\partial x_j^*}\right] = -\frac{\partial p^*}{\partial x_i^*} + \frac{1}{\Phi \,\mathrm{Re}}\frac{\partial \tau_{ij}^*}{\partial x_i^{*2}} - \frac{1}{\mathrm{Re}\,Da}u_i^* - \frac{c_F}{Da^{1/2}}|V|u_i^* + \Phi\left(J\sinh\left(\psi^*\right) + J_{eff}\right)\left(-\frac{\partial\phi^*}{\partial x_i^*}\right) \quad (4)$$

In the EDL potential equation, $\kappa$, known as Debye-Hűckel parameter [4], is the reciprocate of the EDL thickness, which accounts for the properties of the electrolyte, and $L_{ref}$, is the reference length, assumed equal to the channel width, $W$. In the continuity equation $\beta$ is an artificial compressibility parameter [5,6], whereas in the momentum equation $\Phi$ is the porosity of the medium and $c_F$ is a non-dimensional form-drag constant. The dimensionless form of the governing equations for forced convection is obtained through the following non-dimensional scales:

$$x_i^* = \frac{x_i}{L_{ref}}; \quad \phi^* = \left(\frac{ze\phi}{k_B T}\right); \quad \psi^* = \left(\frac{ze\psi}{k_B T_{ref}}\right); \quad p^* = \frac{p - p_{ref}}{\rho_{ref} u_{ref}^2}; \quad t^* = \frac{t u_{ref}}{L_{ref}}; \quad u_i^* = \frac{u_i}{u_{ref}}; \quad \mathrm{Re} = \frac{\rho_{ref} u_{ref} L_{ref}}{\mu};$$

$$\rho^* = \frac{\rho}{\rho_{ref}}; \quad J = \left(\frac{2n_0 k_B T_{ref}}{u_{ref}^2 \rho_{ref}}\right); \quad J_{eff} = \frac{\Phi\varepsilon\varepsilon_0\zeta_p}{K}\frac{k_B T_{ref}}{ze u_{ref}^2 \rho_{ref}}\left(\frac{2I_1\left(\kappa R_p\right)}{\kappa R_p I_0\left(\kappa R_p\right)} - 1\right); \quad Da = \frac{K}{L_{ref}^2}; \quad u_{ref} = \frac{E_x\varepsilon\varepsilon_0\zeta_w}{\mu}.$$

where $z$ is the valance of the ions, $e$ is the elementary charge, $k_B$ is the Boltzmann's constant, $T$ is the temperature measured in kelvin, $\rho$ is the density, $\mu$ is the dynamic viscosity, Re is the Reynolds number, $n_0$ is the ionic number concentration in the bulk solution, $J$ and $J_{eff}$ are the non dimensional source terms, $u_{ref}$ is the reference velocity, $\varepsilon$ is the dielectric constant of the electrolyte, $\varepsilon_0$ is the permittivity of vacuum, $I_n$ is the modified Bessel function of the first type of order $n$, $R_p$ is the average pore size, $Da$ is the Darcy number, $K$ is the medium permeability, $E_x$ is the applied electrical field and $\zeta_w$ is the zeta potential of the channel walls.

It is worth noticing that the generalised model for porous media approaches the Navier-Stokes equations for free fluid when permeability, κ, goes to infinity and porosity, ε, approaches unity.

Both the Laplace and Poisson-Boltzmann equations are solved explicitly, by adding a pseudo time term which becomes negligible when a steady state solution is reached. They are temporally discretized using a forward difference approach and spatially discretized through the standard Galerkin finite element method. The solution of Laplace and Poisson-Boltzmann equations is implemented into the source term of the momentum equation. The equations of the generalised model for porous media are temporally discretized by using the Characteristic Based Split (CBS) algorithm [5,6], that consists in splitting up the solution into three steps: (i) solution of the momentum equation without considering the pressure term, therefore calculating an intermediate velocity; (ii) pressure calculation; (iii) correction of the intermediate velocity field introducing the pressur term. The Galerkin approximation is used for the spatial discretization.

## 3. COMPUTATIONAL DOMAIN AND BOUNDARY CONDITIONS

The walls are assumed to be active with a prescribed non-dimensional zeta potential and to obey no-slip velocity boundary conditions. In order to account for the effect of the charged porous medium on EDL potential distribution within the micro-channel and the possible overlap between EDL potential of particles and channel walls, a modified zeta potential, $\zeta_w^{'}$, is considered [8]:

$$\zeta_w^{'} = \zeta_p \left( 1 - \frac{2I_1\left(\kappa R_p\right)}{\kappa R_p I_0\left(\kappa R_p\right)} \right) + \zeta_w - \zeta_p \tag{5}$$

where $\zeta_p$ is the zeta potential of the porous material. An applied external potential difference between inlet and outlet is considered and the normal velocity gradients are assumed to be zero at both inlet and outlet. The computation is started with prescribed zero velocity components as initial condition. A 2D unstructured mesh refined near all channel boundaries is used, in order to capture the rapid change in both internal potential and velocity. A mesh sensitivity study has been carried out in order to obtain grid independent results.

## 4. RESULTS

A silicon micro-channel, characterized by an aspect ratio of 10, with deionized water as working fluid is considered in the present work. A porosity equal to 0.8 is assumed and the particles composing the porous medium are supposed to have a diameter equal to 16% of channel width. The zeta potential of channel walls and porous medium is assumed to be equal to -19 mV. An external electric field of 1 kV/m is applied. A range of width of the micro-channel, from 5μm to 240μm, is analysed. The profiles of internal potential and horizontal velocity at the outlet section of the channel are reported for channel widths from 5 to 150 μm in Figure 1.

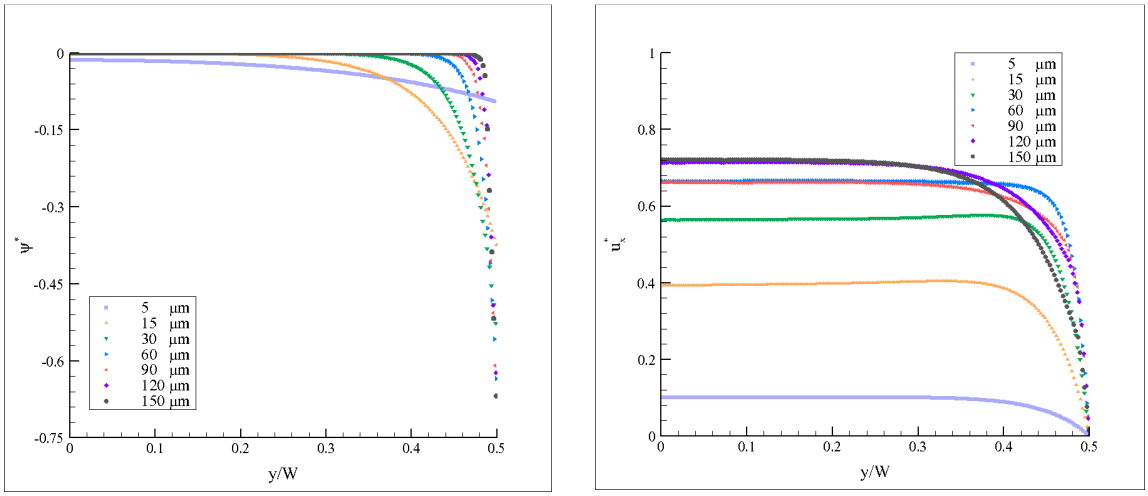


(a) Internal potential profile.

(b) Horizontal velocity profile.

FIGURE 1. Numerical results at different widths for channel packed with charged solid particles.

The internal potential reports higher gradients close to the channel walls as the channel width is increased, and goes to zero in the central region of the channel. The zeta potential imposed as boundary condition on the channel walls for internal potential varies with porosity and particle size. In the current analysis, particle diameter is proportional to channel width. Therefore, the zeta potential applied on the channel walls varies, as it can be seen in FIGURE 1a. As the channel width increases, the zeta potential and then the maximum internal potential, both considered in absolute value, increase. At smaller widths the average velocity is very low, as shown in FIGURE 1b. This is due to the modest value of zeta potential applied on the channel walls, and to the small distance

between particles, that causes higher resistance to fluid flow. The higher the channel width, the higher the average velocity. Beyond 60μm, the influence of the charge of channel walls decreases and EOF is mainly due to the charge of solid particles. As the channel width increases further, the variability of average velocity with channel width becomes negligible. The results in terms of flow rate are reported in Table 1, together with the results obtained for free channel, that are here considered for comparison. The analysis confirms the efficacy of EO to drive flow through porous media. It is worth noticing that flow rate through porous media increases in the whole range of channel widths analysed. For this reason, EO can be effectively used to drive flow through porous media independently on the scale of the system, contrary to what happens in free fluid systems, where the efficiency of EO as driving force becomes negligible as the scale of the system increases.

| Channel width (μm) | Flow rate through porous media ($\mu m^2$/min) | Flow rate in plain channel ($\mu m^2$/min) |
|---|---|---|
| 5 | $3.63 \cdot 10^{-4}$ | $2.87 \cdot 10^{-3}$ |
| 30 | $1.48 \cdot 10^{-2}$ | $2.41 \cdot 10^{-2}$ |
| 60 | $3.26 \cdot 10^{-2}$ | $4.10 \cdot 10^{-2}$ |
| 90 | $4.84 \cdot 10^{-2}$ | $4.01 \cdot 10^{-2}$ |
| 120 | $5.91 \cdot 10^{-2}$ | $1.21 \cdot 10^{-2}$ |
| 150 | $6.31 \cdot 10^{-2}$ | $2.32 \cdot 10^{-4}$ |
| 180 | $1.09 \cdot 10^{-1}$ | - |
| 210 | $1.28 \cdot 10^{-1}$ | - |
| 240 | $1.47 \cdot 10^{-1}$ | - |

TABLE 1. Flow rate at different widths.

## 5. CONCLUSIONS

The model developed by the authors has been used to evaluate the effectiveness of using electro-osmosis to drive flow through porous media. The results have shown that beyond a channel width of 100μm, the charge of particles composing the porous medium is responsible for electro-osmotic flow. This means that electro-osmosis through porous media can be employed independently of the scale of the system, contrary to what has been observed in free channels, where electro-osmotic flow decreases beyond a certain size of the channel.

## REFERENCES

[1] Probstein, R.F., *Physicochemical hydrodynamics: an introduction*. John Wiley & Sons, 2005.
[2] Di Fraia, S., Massarotti, N. and Nithiarasu, P. "Effectiveness of flow obstructions in enhancing electro-osmotic flow." Microfluidics and Nanofluidics 21.3: 46, 2017.
[3] Di Fraia, S., Massarotti, N., Mauro, A., and Nithiarasu, P. “Heat and fluid flow in electro-osmotically driven systems.” Energy Procedia, 126, 91-98, 2017.
[4] Di Fraia, S., Massarotti, N. and Nithiarasu, P. "Modelling electro-osmotic flow in porous media: a review", International Journal of Numerical Methods for Heat & Fluid Flow, https://doi.org/10.1108/HFF-11-2016-0437, 2018.
[5] Nithiarasu, P., Lewis, R.W., Seetharamu, K.N. *Fundamentals of the Finite Element Method for Heat and Mass Transfer*. Wiley, second edition, 2016.
[6] Arpino, F., Massarotti, N., Mauro, A., Nithiarasu, P., Artificial compressibility-based CBS scheme for the solution of the generalized porous medium model, Numerical Heat Transfer, Part B: Fundamentals, 55(3), pp. 196-218, 2009.
[7] Patankar NA, Hu HH, Numerical simulation of electroosmotic flow, *Analytical Chemistry*, 70(9), 1870–1881, 1998.
[8] Tang, G., Ye, P. and Tao,W. (2010), “Pressure-driven and electroosmotic Non-Newtonian flows through microporous media via Lattice Boltzmann method”, Journal of Non-Newtonian Fluid Mechanics, Vol. 165 Nos 21/22, pp. 1536-1542.

Fifth International Conference on Computational Methods for Thermal Problems
THERMACOMP2018, July 9-11, 2018, Indian Institute of Science, Bangalore, INDIA
*N. Massarotti, P. Nithiarasu, Pradip Dutta and C. Ranganyakalu (Eds.)*

# A NUMERICAL STUDY OF A BLUFF BODY STABILIZED DIFFUSION FLAME

**[1]Sombuddha Bagchi, [2]Sourav Sarkar, [4]Achintya Mukhopadhyay, [5]Swarnendu Sen**
Dept. of Mech. Engg., Jadavpur University, Kol-700032, [1]sombuddha.bagchi@gmail.com, [2]souravsarkar.iitm@gmail.com, [4]achintya.mukho@gmail.com, [5]sen.swarnendu@gmail.com

**[3]Uddalok Sen**
Dept of Mech. Engg., University of Illinois at Chicago, IL 60607, [3]uddalok.sen.us@gmail.com

## ABSTRACT

A laminar, two-dimensional flow past a cylindrical bluff body is simulated with methane injection perpendicular to the free stream flow using an unstructured grid finite volume method. The numerical simulations are carried out using a commercial CFD package ANSYS Fluent 14.5. Initially the flow is ignited and then methane is injected through the slots. The velocity of injection of methane is regulated. Comparisons are drawn between the combustion characteristics of two different velocities of methane injection and the results are studied both qualitatively and quantitatively. Both the cases of combustion are observed to be stable and the flame is anchored. The combustion occurring at injection velocity equal to the free stream velocity exhibits no visible vortex shedding while the combustion occurring at the higher injection velocity displays a substantial amount of vortex shedding with a fluctuating lift coefficient of frequency 8.485Hz.

**Key Words:** *Stabilized combustor, Flow past a cylinder, Vortex Shedding.*

## 1. INTRODUCTION

NOx emission control are principal concern of aerospace and automobile industries due to the stringency of emission control rules and regulations in recent times. Combustion at high temperature are primary source of NOx formation. Gas turbine has applications for stabilization of primary or secondary combustion due to their light weight, low cost, and simplicity. Bluff bodies are also important in scramjet, ramjet, and ground- based gas turbine flame holding. Bluff body flame stabilizer are installed in practical combustor like ramjet and turbojet afterburner. Mixing shear layer formed at the downstream of the bluff body helps to stabilize the flame. However, the flow pattern in the wake behind is complex and has different interesting flow features and it is identified as one of the classical problem of fluid mechanics. Asymmetrical Von Karman vortex shedding pattern at certain values of Reynolds number is one of the most interesting feature in flow past a cylinder situation which is of prime importance in bluff body stabilized combustors. Bagchi et al. [1-3] studied the simulation of vortex shedding behind a bluff-body flame stabilizer for unconfined flow domain. Mondal et. al [4] experimentally studied a bluff body stabilized laboratory-scale pulse combustor to investigate the effects of different parameters on combustion instability. Feng et al. [5] did a proper orthogonal decomposition of flow past a cylinder. Uddalok et al. [6] studied the transient, 2-D laminar flow past a circular cylinder with injection of methane. Raghavan et al. [7] did a considerable amount of work in flame stabilisation in a combustor having vortices generated by flame holding devices and flame–vortex interactions in separated methane–air cross flow flames established behind three bluff bodies, namely a square cylinder, an isosceles triangular cylinder and a half V-gutter, have been analysed in detail. Shijin et al. [8] presented a detailed numerical study of laminar cross-flow non-premixed methane–air flames in the presence of a square cylinder.

In our present work, a stabilized combustor is simulated and transient flow past a circular cylinder has been considered. The bluff body i.e. the cylinder has two slots perpendicular to the direction of

the flow, both of them 180º apart which is referred to as a cross-flow arrangement. At a particular velocity, methane is injected through the two slots. Here, a comparison of the flow has been done between two cases. First, the flow past a circular cylinder has been done at free stream velocity. Second, the flow past the cylinder is studied at twice the free stream velocity. The commercial CFD package ANSYS Fluent 14.5 has been used to carry out the simulations at a free stream Reynolds number of 100. To determine the frequency of vortex shedding, a Fast Fourier Transform is done for both cases.

## 2. PROBLEM GEOMETRY

A rectangular confined flow domain (200 mm x 200mm) is considered and the slotted cylinder is placed centrally within the flow domain. The maximum diameter of the cylinder is 6 mm and two diametrically opposite slots are placed perpendicular to the direction of the flow 180º apart. Schematic of geometry is presented in figure 1. The free stream Reynolds number of 100 is considered for the present study. A velocity inlet condition is specified at the inlet, pressure-outlet condition at the outlet and a fixed wall condition at the two walls. The ratio of magnitude of injection velocity of methane to that of magnitude of velocity of the free stream is denoted as ε. In this configuration, the direction of injection velocity of methane is along the positive and negative y-direction and has a value of 0.243m/s or ε=1 for the initial case. The ε is changed from 1 to 2 i.e. 0.486m/s and the effects of this variation on the combustion is observed.

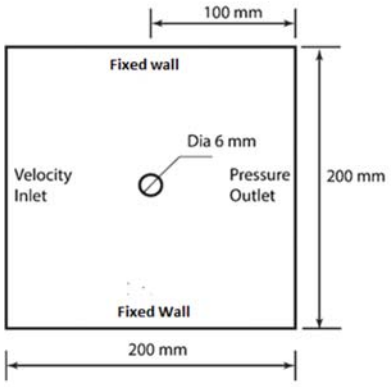


FIGURE 1: Problem Geometry

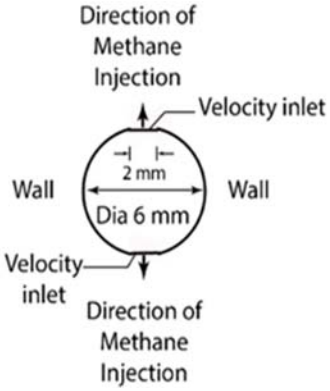


FIGURE 2: Boundary Conditions

## 3. GOVERNING EQUATIONS

For incompressible, laminar, 2-D transient flow the following governing equations has been used:

Continuity:

$$\frac{\partial \rho}{\partial t} + \nabla.(\rho \vec{V}) = 0 \qquad (1)$$

Momentum:

$\frac{\partial(\rho \vec{V})}{\partial t} + \nabla.(\rho \vec{V}\vec{V}) = -\nabla p + \nabla.\vec{\tau} + \rho\vec{g}$ (2) where p is the static pressure, $\vec{\tau}$ is the stress tensor, $\rho\vec{g}$ is the gravitational body force and $\vec{F}$ is any other external body force such as that arising from interaction with the discrete phase. The stress tensor is given by $\vec{\tau} = \mu\left[(\nabla\vec{V} + \nabla\vec{V}^T) - \frac{2}{3}(\vec{V}\, I)\right]$

Energy Equation:

$$\frac{\partial(\rho E)}{\partial t} + \nabla.\left[\vec{V}(\rho E + p)\right] = \nabla.\left[(k\,\nabla T) - \sum_j h_j J_j + \nabla.(\vec{\tau}\vec{V})\right] + S_h \qquad (3)$$

The energy is given by $E = h - \frac{p}{\rho} + \frac{V^2}{2}$ where $h = \sum_j Y_j h_j + \frac{p}{\rho}$

$h_j = \int_{T_{ref}}^{T} C_{p,j}\ dT$ The reference temperature was taken to be 298.15 K.

Species Transport Equation:

$$\frac{\partial(\rho Y_i)}{\partial t} + \nabla.\left(\rho \vec{V} Y_i\right) = -\nabla.J_i + R_i + S_i \qquad (4)$$

Where $R_i$ is a reaction source term and $S_i$ represents other source terms, which is generated from the discrete phase. For N species, generally N - 1 species equations are solved. The N $^{th}$ species mass fraction is determined by subtracting from 1. Nitrogen is taken to be the N $^{th}$ species.

$J_i$ is the diffusion flux of species i $J_i = -\rho D_{i,m} \nabla Y_i - D_{T,i} \frac{\nabla T}{T}$ (5). The Laminar finite rate model was used to calculate source term $R_i$. As gas flows are laminar in this study, laminar finite rate model is chosen. For a reversible reaction, the molar rate of generation of a species $i$ in reaction $r$ is given by the expression

$$R_i = \Gamma(\nu_i'' - \nu_i')\left[k_{f,r} \prod_{j=1}^{N} C_{j,r}^{\nu'_{j,r}} - k_{b,r} \prod_{j=1}^{N} C_{j,r}^{\nu''_{j,r}}\right] \qquad (6).$$ The rate constants are calculated as

$k_{f,r} = A_r T^{\beta_r} e^{\frac{E_r}{RT}}$

$k_{b,r} = {k_{f,r}}/{k_r}$ Where $k_r$ is the equilibrium constant of the $r^{th}$ reaction calculated from enthalpy and entropy of the species evaluated at the respective temperature and pressure. A reduced reaction mechanism with 16 species and 46 reactions was used to model chemistry of the combustion phenomena. All the other data for evaluation of the rate constants are provided through the thermodynamic and transport database files in FLUENT.

## 4. NUMERICAL SIMULATION AND VALIDATION

A finite volume based CFD code ANSYS Fluent 14.5 has been used to perform the required numerical simulations. The laminar viscous model is used as the Reynolds number of the flow is 100. The pressure based solver has been chosen as the numerical scheme, and second order implicit transient solutions are performed. A least squares cell based scheme is employed for gradient calculations. SIMPLE scheme is used for pressure-velocity coupling and QUICK scheme was used for discretization of momentum equation. The convergence criteria for continuity and momentum equations were set at $10^{-3}$.

The ANSYS Meshing package is used to create a triangle based unstructured grid. For better results and finer meshing around the central region, inflation is carried out with least element size of $10^{-7}$ m having 80 layers and a growth rate of 1.5. Grid independence study along with time independence is carried out to select the optimum mesh and time step for simulation. It is carried out by replacing the bluff body by a regular cylinder of the same diameter. The Reynolds number of the free stream is 100. Grid independence study was again carried out post combustion to validate the mesh.

This mesh and a time step size of 0.001 is considered to be optimum for simulation to reduce the computational time without any considerable loss in accuracy.

## 5. RESULTS AND DISCUSSION

The velocity, vorticity and mass fraction of methane contours of the confined flow for ε=1 and ε=2 are shown below. Negligible vortex shedding is observed for ε=1 while substantial vortex shedding is observed for ε=2.

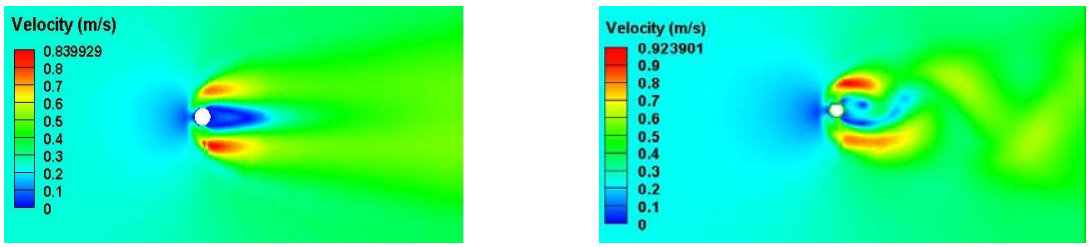


FIG. 3: Velocity contours for ε=1 (left) and velocity contours for ε=2 (right); the e=2 contours clearly illustrates the Von Karman vortex street

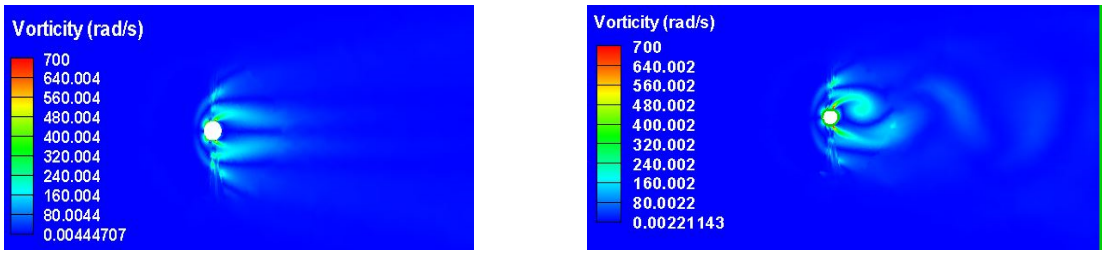


FIG. 4: Vorticity contours for ε=1(left) and vorticity contours for ε=2 (right). Vortex shedding is visible only in e=2

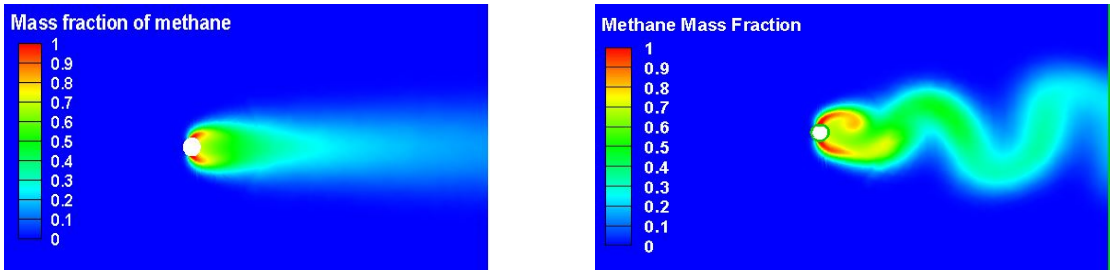


FIG. 5: Mass fraction of methane contours for e=1 (left) and mass fraction of methane contours for e=2 (right).

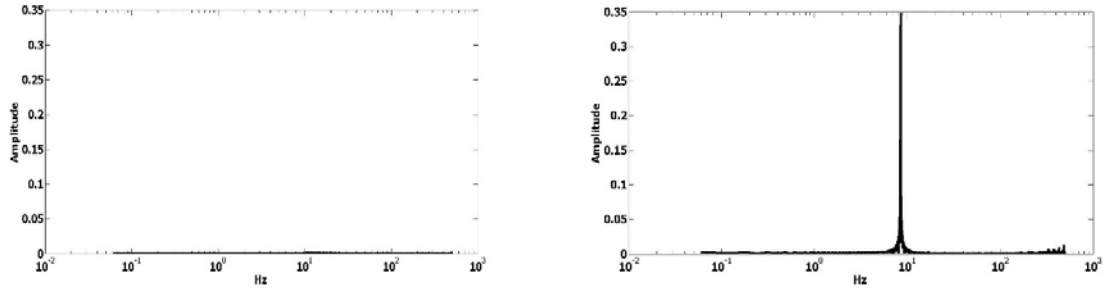


FIG. 9: FFT Plot for ε=1 (left) and FFT Plot for ε=2 (right); no dominant peak of vortex shedding frequency is observed for the initial case

From the Fast Fourier Transform Plots, the dominant peak of the temporally fluctuating lift coefficient is observed at a Strouhal number of 0.209 (8.485Hz) for ε=2.

## 6. CONCLUSION AND FUTURE SCOPE OF WORK

The flame is anchored right in front of the cylinder for both the cases. However, vortex shedding is only observed for ε=2 (2S mode). The combustion characteristics are analysed both qualitatively and quantitatively. The flame is stabilized and continues to burn without losing heat. Proper orthogonal decomposition can be performed to further analyse the flow structure of the current analysis.

## 7. REFERENCES

1. S.Bagchi, S.Sarkar, U.Sen, A. Mukhopadhyay, S.Sen, Numerical Simulation of Vortex Shedding from Bluff-Body Stabilised Flame with Cross Injection, *Journal of Basic and Applied Engineering Research*, Vol. 4, Issue 7, 561-566, 2017.

2. S. Bagchi, S.Sarkar, U.Sen, A. Mukhopadhyay, S.Sen, Numerical Investigation of Vortex Shedding from a Bluff Body Stabilised Flame with Cross Injection, *Proceedings of International Conference on Sustainable Energy and Environmental Challenges, IISc Bangalore*, 23, 250-254, 2018.

3. S. Bagchi, S.Sarkar, A.Mukhopadhyay, S.Sen, *Numerical Simulation of Vortex Shedding from Cylindrical Bluff Body Flame Stabiliser, Proceedings of First International Conference on Mechanical Engineering, Jadavpur University, Thermal Engg. Energy*, 228, 678-682, 2018.

4. S.Mondal, A.Mukhopadhyay, S.Sen, Dynamic characteristics of a laboratory scale pulse combustor, *Combustion Science and Technology*, 186 (2), 139-152, 2014.

5. L.-H. Feng, J.-J.Wang, C.Pan, Proper orthogonal decomposition analysis of vortex dynamics of a circular cylinder under synthetic jet control, *Physics of Fluids*, 23, 014106, 2011.

6. U.Sen, A.Mukhopadhyay, S.Sen, Effects of fluid injection on dynamics of flow past a circular cylinder, *European Journal of Mechanics B/Fluids*, 61,187-199, 2017.

7. P.K. Shijin, V. Raghavan, V. Babu, Numerical investigation of flame-vortex interactions in laminar cross-flow non-premixed flames in the presence of bluff bodies, *Combustion Theory and Modelling*, Volume 20, Issue 4, pp.683-706, 2016.

8. P.K. Shijin, S.S. Sundaram, V. Raghavan, V. Babu, Numerical investigation of laminar cross-flow non-premixed flames in the presence of a bluff-body, *Combustion Theory and Modelling,* Vol. 18, No. 6, 692-710, 2014.

# NUMERICAL SIMULATION OF FLOW THROUGH HELICAL HEAT EXCHANGER

**Sonawane C. R.**
Associate Professor, Mechanical Engineering Department, Symbiosis Institute of Technology, Symbiosis International University, Pune, India, E-mail: crsonawane@gmail.com

**Mandal J. C.**
Professor, Aerospace Engineering Dept, Indian Institute of Technology Bombay, Mumbai, India, E-mail : mandal@aero.iitb.ac.in

## ABSTRACT

In this paper, the three-dimensional flow through a concentric annulus heat exchanger having a helical flow passage known as helixchanger, is studied. The Harten Lax and van Leer with contact for artificial compressibility (HLLC-AC) Riemann solver is used for evaluating convective fluxes where interface values are reconstructed using solution dependent weighted least squares (SDWLS) for high resolution. Viscous fluxes are evaluated in central differencing manner. The flow-through helixchanger is simulated for various Reynolds numbers, corresponding pressure drop and average heat transfer coefficient is presented. It has been observed that, due to the helical flow path, the flow becomes naturally turbulent thereby help in increasing heat transfer.

**Key Words:** *Helical passage, helixchanger, Higher order accuracy, SDWLS, Incompressible flow, Artificial compressibility method.*

## 1. INTRODUCTION

The success of various equipment, utilizing the non-conventional solar power sources, depends on the effectiveness of heat exchanging devices utilized. The heat exchanger is expected to have high heat transfer with minimum possible flow pressure drop. In the conventional heat exchangers, the zigzag flow patterns were produced using segmental baffle arrangement. However, these segmental baffles found to produce large dead spaces with a high degree of back mixing, unfavorably affecting the rate of heat transfer by reducing the mean temperature difference [1].

The helixchanger, a helically baffled heat exchanger, helps in alleviating the principal shortcomings of the conventional design [1]. From literature [1-3] it has been observed that only shell and tube type of helixchanger is been investigated. Other combinations like pipe-in-pipe or square channel with helical baffles have not been investigated in detail. There has been no correlation for Nusselt number or velocity distribution inside helixchanger reported in literature.

In this paper, the flow and heat transfer through the pipe-in-pipe type (annulus) helixchanger, which will act as a potential generator of a solar assisted refrigerator system, is studied. The flow and heat transfer variation at various Reynolds number is presented. The flow through helical passage is complex as the flow gets mixed due to the influence of a centrifugal and Coriolis force, thus the flow becomes naturally turbulent which helps in enhancing the heat transfer.

## 2. MATHEMATICAL FORMULATION

In artificial compressibility formulation [4], utilizing the dual-time stepping approach with Spalart-Allmaras [5] one equation turbulent model, the integral form of the three-dimensional unsteady turbulent Navier-Stokes equations can be written as

$$\iint_{\Omega} \frac{\partial W}{\partial \tau} dxdy + I^{M} \iint_{\Omega} \frac{\partial W}{\partial t} dxdy + \Theta^{M} \oint_{A} \left[(E^{c} + E^{v})n_x + (F^{c} + F^{v})n_y + (G^{c} + G^{v})n_z\right] dA = \iint_{\Omega} S_0 dxdy \quad (1)$$

Eq. (1) does not exhibit any physical meaning until pseudo time steady state $\left(\frac{\partial p}{\partial \tau} = \frac{\partial u}{\partial \tau} = \frac{\partial v}{\partial \tau} = \frac{\partial w}{\partial \tau} = \frac{\partial T}{\partial \tau} = \frac{\partial \breve{v}}{\partial \tau} = 0\right)$ is reached. As the pseudo-steady state is reached, the equations are identical to the original turbulent unsteady incompressible Navier-Stokes equations. The computational domain is divided into hexahedral grids. Now, approximating the real-time derivative $\frac{\partial}{\partial t}$ by second-order implicit backward formula, the discretized form of the Navier-Stokes Eq. (1) in finite volume formulation over unstructured grid can be written for a particular cell 'i' as

$$\Omega_i^{n+1} \frac{\partial \overline{W_i}}{\partial \tau} + I^{M} \left\{\frac{3\Omega_i^{n+1}\overline{W}_i^{n+1} - 4\Omega_i^{n}\overline{W}_i^{n} + \Omega_i^{n-1}\overline{W}_i^{n-1}}{2\Delta t}\right\} + R\left(\overline{W}_i^{n+1}\right) = 0 \quad (2)$$

here, $R(\overline{W_i}) = \Theta^{M} \sum_{k=1}^{K} \left[(E^{c} + E^{v})n_x + (F^{c} + F^{v})n_y + (G^{c} + G^{v})n_z\right]_k - S_0\Omega_i \quad (3)$

Above discretization results in an ordinary differential equation (ODE) of the type

$$\Omega_i^{n+1} \frac{\partial \overline{W_i}}{\partial \tau} + R^{*}\left(\overline{W}_i^{n+1}\right) = 0 \quad (4)$$

Where $R^{*}\left(\overline{W}_i^{n+1}\right)$ is consisting of second and third term in equation (2). The ODE Eq. (4) in pseudo-time, $\tau$ is integrated using a five-stage Runge-Kutta scheme. It is to be noted that the required real-time accurate solution at time level n+1 satisfies $R^{*}\left(\overline{W}_i^{n+1}\right) = 0$ and this is found by marching Eq. (4) to a steady state in pseudo time. The fluxes at cell interface, that is, the convective fluxes are evaluated using the HLLC-AC [6, 7] upwind method whereas central differencing method based on Green-Gauss approach is used for discretizing the viscous fluxes.

## 3. SOLUTION DEPENDENT WEIGHTED LEAST SQUARE (SDWLS) GRADIENT CALCULATION

The left and right state values of any solution variable, W at the interface between two adjacent cells i and j are found using Taylor series expansion of solution variables about the cell center as

$$W_L = \bar{W}_i + (r_{int} - r_i)^{T} \nabla \bar{W}_i + \frac{1}{2}(r_{int} - r_i)^{T} H_i (r_{int} - r_i) + \cdots$$

$$W_R = \bar{W}_j + (r_{int} - r_j)^{T} \nabla \bar{W}_j + \frac{1}{2}(r_{int} - r_j)^{T} H_j (r_{int} - r_j) + \cdots \quad (5)$$

The third order scheme requires an evaluation of both first and second order derivatives of $\bar{W}$ with respect to space variable at the cell centers. Thus, quadratic reconstruction in three dimensions requires the calculation of nine derivatives

$\frac{\partial \overline{W}}{\partial x}, \frac{\partial \overline{W}}{\partial y}, \frac{\partial \overline{W}}{\partial z}, \frac{\partial^2 \overline{W}}{\partial x^2}, \frac{\partial^2 \overline{W}}{\partial y^2}, \frac{\partial^2 \overline{W}}{\partial z^2}, \frac{\partial^2 \overline{W}}{\partial x \partial y}, \frac{\partial^2 \overline{W}}{\partial y \partial z}, \frac{\partial^2 \overline{W}}{\partial z \partial x}$ at the cell centers.

A new high-resolution scheme based on solution dependent weighted least squares (SDWLS) is developed and applied to compute above-mentioned gradients for incompressible viscous flows [7]. The SDWLS method uses the neighbouring cells variable values with weights which are a function of the solution itself. The various expressions for weights can be found in [8]. For the three-dimensional case with a vertex-based stencil, depending on grids and flow conditions, the SDWLS based gradients are solved using Lapack routine DGELS. This routine uses the Householder transformation for the QR method to solve the full rank least squares problem. Detailed validation of SDWLS gradients methods can be found in [7].

## 4. NUMERICAL RESULTS AND DISCUSSION

Pipe-in-pipe heat exchanger with parallel and counter flow configurations are popular for practical applications like solar heating/cooling units, water cooled jackets, etc. In order to study the improvement in the heat transfer characteristics for shell side of a double-pipe heat exchanger, a simple configuration with one helical baffle is introduced between double pipes (i.e. at the annulus area). Figure 1 (a) shows the double pipe helixchanger under considerations used for the solar assisted refrigeration system. Due to helical baffle, provided along the pipe length, the hot water is flowing through a helical passage created between the annulus area. In order to compare the heat transfer, the annulus heat exchanger (i.e. without helical passage) is also simulated and is taken as a base for the comparison.

Figure 1(b) shows the computational domain, the helical passage between the inner and outer pipe, considered to carry out flow simulation at various Reynolds number conditions. Various boundary conditions used for the simulation are, the hot water enters through 'inlet' from the bottom side of helixchanger and leaves from the top 'outlet' as pressure outlet conditions. The outer wall and helical baffle walls are insulated whereas the inner wall ie $NH_3$-pipe rejects the heat of 100 watts to the ammonia. Based on mesh convergence study, mesh with 265557 nodes and 252000 hex mesh elements are used for all simulations. Figure 1(c) shows the mesh generated.

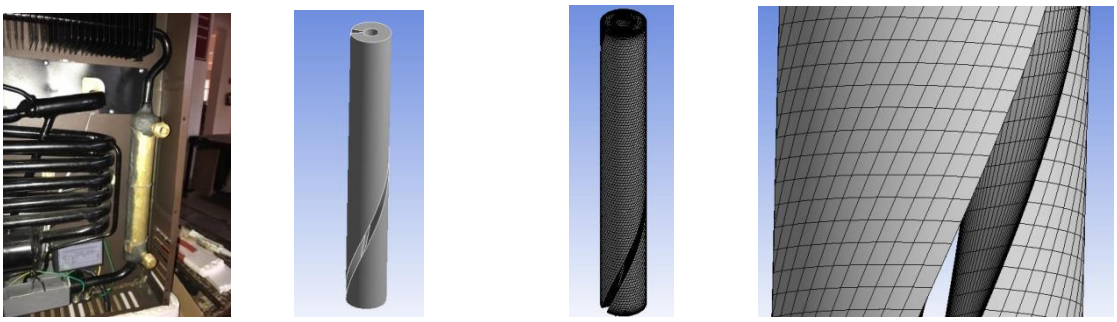

(a) Helixchanger (b)Domain used (c)Mesh generated (d) enlarged view

Figure 1: Heat exchanger details.

Table 1 shows the results obtained at various Reynolds number considered for unsteady flow computations. From the comparison of average heat transfer coefficient, at $NH_3$ inner pipe wall, it can be seen that the average heat transfer coefficient is increased by a factor of 1.93 – 2.69. The pressure drop along helixchanger axis is also increased by 3.84 – 6.1 times. The increase in heat transfer rate is mainly due to helical flow passage conditions as well as due to increased turbulence level as compared to without helical passage heat exchanger conditions.

| Sr. No. | Mass flow rate (kg/s) | Reynolds's Number (Re) | Pressure Drop | | % increase in pressure drop | Heat transfer coefficient | | % increase in heat transfer coefficient |
|---|---|---|---|---|---|---|---|---|
| | | | In straight flow | In helical flow | | In straight flow | In helical flow | |
| 1 | 0.005709 | 164.69 | 0.2698 | 1.0371 | 384.36 | 371.24 | 718.37 | 193.50 |
| 2 | 0.011417 | 329.38 | 0.5826 | 2.5677 | 440.71 | 463.88 | 955.17 | 205.91 |
| 3 | 0.022834 | 658.77 | 1.3828 | 6.8726 | 496.98 | 583.93 | 1303.81 | 223.28 |
| 4 | 0.045668 | 1317.55 | 3.4683 | 19.7151 | 568.43 | 742.07 | 1812.19 | 244.21 |
| 5 | 0.091336 | 2635.11 | 13.2412 | 60.7401 | 458.72 | 947.26 | 2549.53 | 269.15 |
| 6 | 0.182672 | 5270.22 | 32.2266 | 196.628 | 610.14 | 1598.45 | 3641.21 | 227.80 |

Table 1: Results obtained at various Reynolds number.

Figure 2 shows the temperature contours plotted at pipe outlet for various Reynolds number. It can be seen that as Reynolds number increases, the effect of centrifugal and Coriolis forces become more dominant on the thermal boundary layer developed. The maximum temperature generated at the inner pipe wall of the helixchanger is found to be increased with Reynolds number. The thickness of the boundary layer is found to be decreased along the radial direction. The mushroom-like boundary layer is observed as the Reynolds number increases.

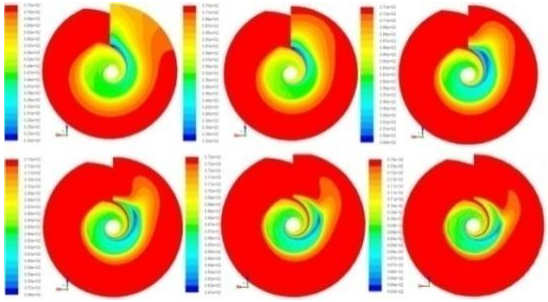

Figure 2: Temperature contours produced for various Reynolds number (Table 1).

## 5. CONCLUSIONS

In this paper, pipe-in-pipe type of heat exchanger having one complete helical passage is studied. From above studied, it can be concluded that due to helical flow scenario, the heat and fluid flow becomes naturally turbulent and the centrifugal and Coriolis forces help to transfer heat at a much higher rate resulting in increased heat transfer coefficient.

## ACKNOWLEDGEMENT

This work has been supported by Science and Engineering Research Board (SERB) – Department of Science and Technology (DST), Government of India (ECR/2017/000476).

## REFERENCES

[1] D. Kral, P. Stehlik, H. J. V. D. Ploeg and B. I. Master, Helical baffles in shell-and-tube Heat exchangers, part I: experimental verification, H*eat Transfer Engineering*, 17:1, 93-101, 1996.

[2] Ya-Ping Chen, Yan-Jun Sheng, Cong Dong, Jia-Feng Wu, Numerical simulation on flow field in circumferential overlap trisection helical baffle heat exchanger, *Applied Thermal Engineering*, 50, 1035-1043, 2013.

[3] Qiuwang Wang, Qiuyang Chen, Guidong Chen, Min Zeng, Numerical investigation on combined multiple shell-pass shell-and-tube heat exchanger with continuous helical baffles, *International Journal of Heat and Mass Transfer*, 52, 1214-1222, 2009.

[4] A. J. Chorin, Numerical solution of Navier-Stokes equations, *Math Comput*, 22, 745-762, 1968.

[5] S. R. Allmaras, P. R. Spalart, A one-equation turbulence model for aerodynamic flows, *AIAA Paper* 92-0439, 1992.

[6] J. C. Mandal, C. R. Sonawane, Simulation of moderator flow and temperature inside calandria of candu reactor using artificial compressibility method. *Heat Transfer Engineering*, 34 (14-15), 1254-1266, 2014.

[7] Sonawane C. R., Mandal J. C. and Rao S, J. *Inst. Eng. India Ser. C*, 2017. https://doi.org/10.1007/s40032-017-0390-x

[8] J. C. Mandal and J. Subramanian, On the link between weighted least-squares and limiters used in higher-order reconstructions for finite volume computations of hyperbolic equations, *Appl Numer Math*, 58(5), 705-725, 2008.

# OPTIMISATION OF VENTILATION SYSTEM BY ACTIVE DISPLACEMENT VENTILATION USING CFD

**Shujaathussian Soudagar ,Vikalp Jha**
M.Tech student ,Depatment of Aerospace Engineering,UPES deharadun,
shujaatsoudagar@gmail.com , vikalp2711@gmail.com
**Dr.Velidi VSS Gurunadh[3]**
Assistant Professor, ,Depatment of Aerospace Engineering,UPES deharadun,
GVSSVELIDI@ddn.upes.ac.in

## ABSTRACT

Computational Fluid Dynamics also commonly known as CFD is a computational tool used to predict and analyze fluid flows numerically. In HVAC Industry ,CFD is used to analyze factors that adversely affect the atmospheric environment and thermal conditions as airflow pattern, heat distribution humidity and contamination of the system (room / surrounding to be studied).It is a very important tool which gives comparative results for research and design of this system. Active Displacement Ventilation also known as ADV is a method or a process of air supply in a room, which has a potential to compete with other traditional supply methods .The paper is written with hope to review and analyse the use of Computational Fluid Dynamics in study of ADV i.e. , Active Displacement Ventilation.

**Key Words**: Heat Transfer, Finit Element, CFD, Active Displacement Ventilation. Ordinary Displacement Ventilation

## 1. INTRODUCTION

One major objective of a HVAC design engineer is to provide comfortable and healthy in an indoor environment with maximising energy saving while reducing the GHG i.e. Greenhouse gas emission from the building. Energy demand can be reduced by the use of Natural Driving Force and few smart preheating air ways .Heat from wasted air during the processes can be partially achieved by decreasing the pressure losses of the system. The design of the building which is interactive with the exterior environment would be beneficial while utilizing NDF.

ADV has a potential to be more efficient in terms of energy then various traditional methods as displacement or mixing ventilation. The concept of ADV is simple i.e. utilizing the wasted air from the warm or polluted room while maintaining the air quality and thermal comfort in the occupancy zone.

## 2. THEORY

This part will shed light over use of methodology, discussion, results and conclusion presented. We shall cover various concepts of ADV and important concepts in relation with this. Under as main focus:-

1) Indoor climate
2) Categorization of ventilation
3) Building Integrated Ventilation

1) Indoor climate

It is influenced by various physical parameters. The various categories in which indoor climate is divided into are :-

a) Thermal environment
b) Acoustic environment
c) Atmospheric environment
d) Mechanical environment
e) Actinic environment

The Atmospheric and thermal conditions are most important as considered in this paper hence are main focus.

2) Categorization Of Ventilation

Ventilation is utilized to control the indoor conditions, the principle point of HVAC is to keep individuals agreeable and beneficial to make a gainful situation for working individuals. When we talk about ventilation it is helpful to sort into two unique composes

a) Type of supply
b) By which power air is driven

We are mainly focusing on the above both in this paper as we are focused on what happens within a room. In ODV thermal forces which displaces air near the floor bottom supply to ceiling extract. On other hand mixed ventilation uses momentum causing an air mixing where the room conditions are ideally uniform with temperature and concentration of contaminant. This paper ADV also uses buoyant forces, here air was supplied high on the wall and the temperature lower than ODV.

Types of Displacement

a) Mixing Ventilation
b) Active Displacement Ventilation
c) Ordinary Displacement Ventilation

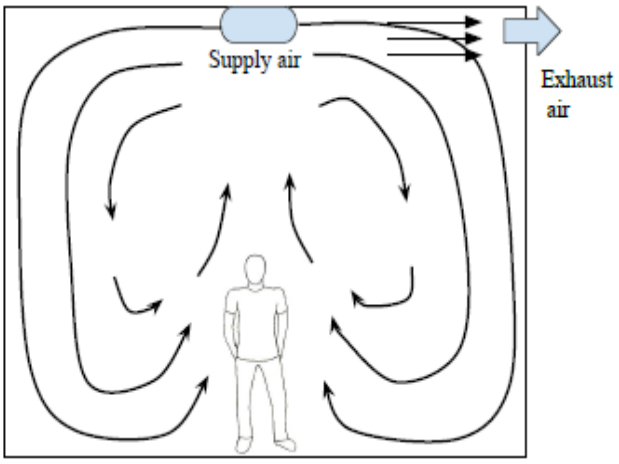


Fig 1 .Mixing Ventilation

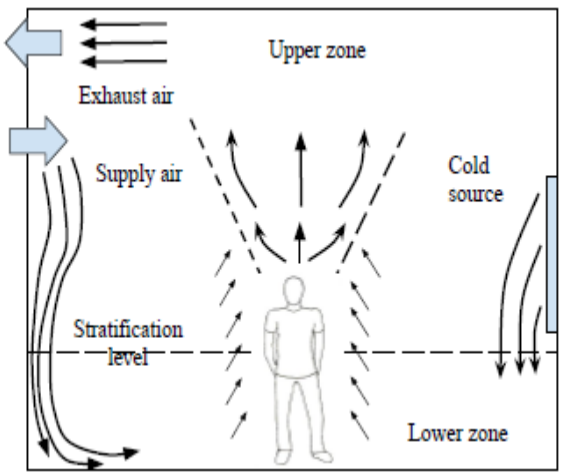


Fig 2 .Active Displacement Ventilation

3) LITERATURE REVIEW ACTIVE DISPLACEMENT VENTILATION

The diffusers are positioned on higher end of the wall and constructed for the air flowing downwards which entrains the old air in room. The supply velocity and temperature of the air are lower than room air. The main principle used for the air “LOWER ” down in the room is the thermal forces. The heat source is treated similarly to ODV where due to convective flow contaminants are pushed to polluted zone of higher parts of the room. The air supplied for ODV has the objective replacing the air form old one to new also maintain the polluted zone outside occupant zone.

An important in ADV is the way that jets stick to wall due to “Coanda Effect”. “Coanda effect” is a fluid phenomenon to attach the surface due to lower pressure on wall side. The pressure drop is due to air entrained inform surrounding. For horizontal jet near the ceiling it stays intact to the wall unless attachment forces are large as compared to gravitational force.

In design of ADV, one must keep in mind the discomfort caused by cold draught as cold air lower at velocity over recommended values. Specific solution is designed to ensure cold draught lower down in the absent zone .

## 3. METHOD.

1) Geometrical and Boundary condition

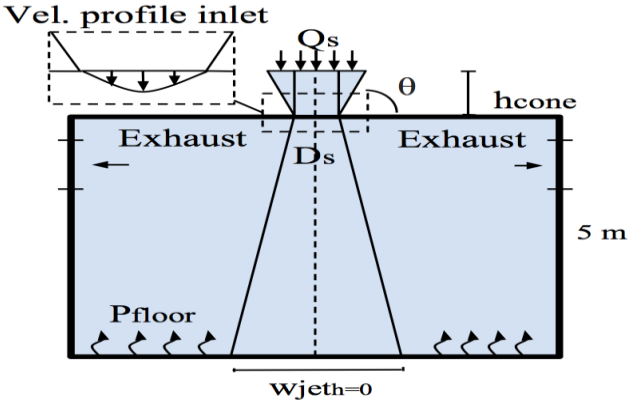


Fig 4. Model sketch

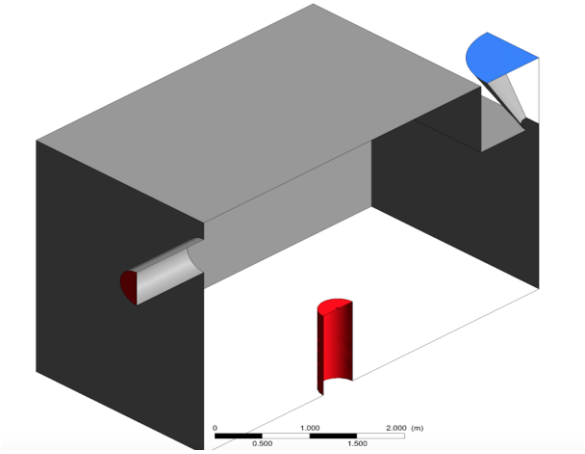

Fig 5. ANSYS model for ADV

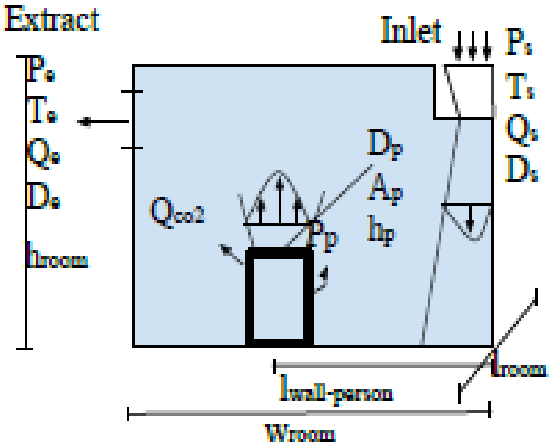


Fig 6. Model for ADV

| | |
|---|---|
| Room dimension (lxbxh) .....(m) | 5 x 5 x 5 |
| Circular inlet diameter ($d_s$) .....(m) | 0.2 |
| Circular Extract diameter ($d_e$) | 1 |
| Angle between ceiling and cone wall .....( $\theta$) | 60° |
| Height of cone ($h_c$) .....(m) | 1 |
| Temperature Inlet ($T_i$) .....(°C) | 12 |
| Temperature floor ($T_{constant}$) .....(°C) | 24 |
| Rest of wall condition | $\frac{\partial T}{\partial x} = \frac{\partial T}{\partial y} = 0$ |
| Inlet Velocity of Air ( $U_0$ ).....(m/s) | At ceiling = 0.2<br>Below = 0.004 |
| Turbulent intensity outlet | 8.89% |
| Inlet | |
| Inlet air flow ($Q_s$ ) .....(l/s) | 5,6,7 |
| Inlet velocity ($V_s$ ) ,,,,,,,,,,,,,,,,(m/s) | 0.08,0.1,0.116 |
| Inlet velocity cone ($V_{cone}$ ) ,,,,,,,,,,,,,,,,(m/s) | 0.005,0.006,0.007 |
| Turbulent intensity Inlet | 7.3 % |
| Outlet | |
| Outlet | Pressure Outlet |
| Turbulent intensity outlet | 8.89% |

| Body Condition | |
|---|---|
| Total heat .....(W) | 100 |
| Convective heat .....(W) | 0.5 x 100 = 50 |
| Radiative heat .....(W) | 50 |
| CO2 Production .....($m^3/h$) | 0.02 |
| CO2 velocity .....(m/s) | 0.003 |
| Radiation | |
| Emissivity | 1 |

Table 1. Boundary condition and dimension

## 4. RESULTS

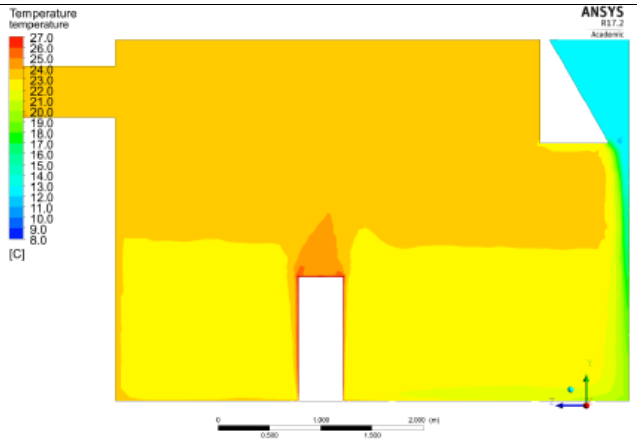


Fig.7 Temperature Contour at inlet temp.=12°C & Inlet flow=7 l/s

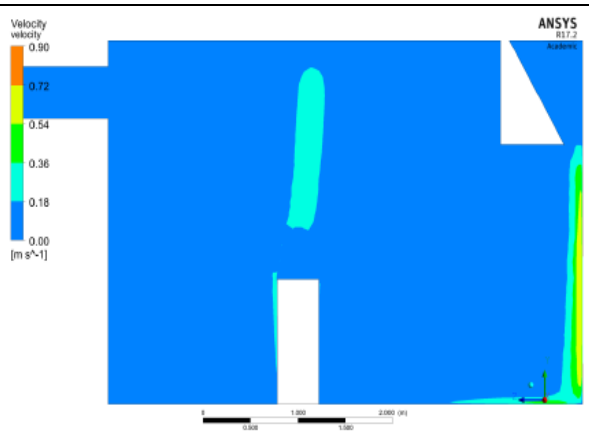


Fig.8 Velocity Contour at inlet temp.=12°C & Inlet flow=7 l/s

## 5. CONCLUSION

- The deflection obtained with empirical relation and CFD simulation is observed to be minimum. Those we conclude the empirical relation derived by E.Skaret is recommended for designing ADV along with heat and mass balance.
- The CO2 concentration is independent of inlet temperature as difference in relative temperature is same in the room
- The cold draught in occupant zone is increased if one can use inlet device having a larger area.

## REFERENCE

1. Ergonomics of the thermal environment - ISO 7730:2005.
2. Vojislav Novakovic, Jan Vincent Thue. Energy Management I Buildings. Gyldendal Norsk, 3E, 2017
3. A study of air quality in the breathing zone in a room with displacement ventilation. Department of engineering science, University of Oxford, Oxford.UK,2001.
4. 1995, Displacement ventilation system- convection flows and temperature gradients. Building and Environment, Vol.30 No.1,

Fifth International Conference on Computational Methods for Thermal Problems
THERMACOMP2018, July 9-11, 2018, Indian Institute of Science, Bangalore, INDIA
*N. Massarotti, P. Nithiarasu, Pradip Dutta and C. Ranganyakalu (Eds.)*

# ACOUSTIC ANALYSIS OF REACTING FLOWS IN AFTERBURNER

**Gurrala Srinivasa Rao**
Mechanical Engineering Department, Indian Naval Academy, Ezhimala-670310, Kerala, India
**A Shaija**
Mechanical Engineering Department, NIT, Calicut – 673601, Kerala, India

## ABSTRACT

*The exhaust gas from the turbine passes through afterburner, which is fitted at the end of the jet aircraft, for providing additional thrust when required during take-off, combat, maneuvers, emergencies and in supersonic flight of high performance aircrafts. The main components of afterburner are diffuser with struts, fuel manifold, a hollow V-gutter, liner, nozzle and casing.The disadvantage associated with the afterburner is the high frequency screech instabilities. The optimal design of the screech liner will help in mitigating these instabilities. Hence, a $60^o$ sector full scaled afterburner is modeled to find out the effectiveness of screech liner for mitigation of instabilities. The numerical calculations are performed in Ansys Fluent using SIMPLE algorithm with k-ε model for turbulence. Kerosene ($C_{12}H_{23}$) is taken as fuel and virtual injectors are specified for fuel injection. Energy equation and species transport with the Discrete Phase model is selected for computations. These results of CFD analysis are imported into ACTRAN for acoustic analysis to find out the absorption of acoustic energy by the liner in the case of reacting flows. It is observed that the absorption of acoustic energy is more in case of reacting flows with perforated liner than without liner. It is found that the perforated liner is more effective in absorbing the acoustic energy produced due to the transverse oscillations during the entire operating range.*

**Key Words:** *Afterburner, Screech, Liner, acousitc, instabitlies.*

## 1. INTRODUCTION

The military aircrafts require more thrust during take-off, combat, maneuvers, emergencies and in supersonic flight of high performance aircrafts. In order to cater the requirement of additional thrust these aero engines are provided with afterburners, which is the low-cost and light weight alternative.

Afterburners are fitted to the exit of the low pressure turbine. The main components of the afterburner are diffuser to reduce the velocity of flow, struts to reduce the vorticity, screech liner to attenuate the transverse oscillations, fuel manifolds for distribution of fuel and the flame stabilizer to provide the recirculation zone for anchoring of the flame.

The disadvantages associated with the afterburner are the development of instabilities. These high frequency instabilities will damage the aircraft. Two types of instabilities are associated with the afterburner. First, the low frequency (50-200 Hz) self-excited longitudinal amplitudes, travelling axially along the engine afterburner, called Buzz and second the high frequency (500-5000Hz) radial amplitudes, travelling in planes at right angles to the jet pipe axis and flow direction, called Screech [1].

The high frequency screech is characterized by a peculiar violence, and its onset is invariably followed by rapid mechanical failure which evinces itself in the tearing of the sheet metal, or if the screech is mild, persistent breakage of bolts or slackening the nuts. The afterburner inlet conditions at which screech occur differs widely for various afterburner designs. However, due to the operational constraints and high costs incurred during its development, combustion instability in afterburners still remains an attractive subject of research.

Computational analysis of reacting flows in the afterburner is carried out by Gurrala and Shaija [2] and found that the results are matching with the earlier computational and experimental values.

Computational analysis of fluid flow in the afterburner for various nozzle angles of $0^o$, 4° and 8° is anlayzed for the maximum speed of the aircraft by Gurrala and Shaija [3] and found that the maximum Mach number and thrust produced are observed with 8° nozzle angle.

Few research papers are also available on afterburners where the experimental and computational results have been presented. Useller [4] presented the results of various combustor chamber lengths and their effect on the combustion efficiency for full scale afterburner designs conducted by erstwhile NACA.

Analysis of reacting flows in aero-engine afterburner is also carried out by Unaune and Ganesan [5]. The numerical calculations are performed using SIMPLE algorithm and RNG k-ε model. Probability density function is used for modeling combustion. The results are obtained and analyzed for two air fuel ratios of 30 and 46.

The effectiveness of a cylindrical perforated liner with mean bias flow in its absorption of planar acoustic waves in duct has been investigated by Eldredge and Dowling [6] and shown that such a system can absorb a large fraction of incoming energy and can prevent all of the energy produced by an upstream source in certain frequency ranges from reflecting back. The effect of a liner on the resonances which occur in a cylinder has been examined by Hughes and Dowling [7] and shown that a well-designed liner may suppress resonances over a range of frequencies.

There is a need to properly analyse the fluid flow in the afterburner and the effectiveness of the liner in suppressing the instabilities. Hence the copmuptational fluid flow results obtained using fluent, by Gurrala and Shaija [2, 3] for the afterburner with 6° nozzle angle, is used for acoustic analysis. ACTRAN$^{TM}$ can be used to simulate acoustic radiation from inlet of afterburner to exit. Realistic conditions such as complex flows, temperature gradients and acoustic liners are accurately accounted by ACTRAN. This will enable us to predict the better designed afterburner for avoiding the instabilities and screech. There is an obvious advantage of time and cost savings where one can rely on the predictions.

## 3. RESULTS

The flow quantities like velocity vector, scalar fields like static density and static pressure obtained from the CFD analysis are interpolated from the CFD mech to ACTRAN mesh. The interpolation is performed by ACTRAN interpolate CFD (ACTRAN ICFD) by importing the native fluent files into ACTRAN by reading the *.cas and *.dat fluent files. ACTRAN ICFD is designed to be the only tool for interfacaing CFD codes with ACTRAN which is used to map the mean flow CFD fileds, compute aero acoustic sources and translate the time domain CFD data into the frequency domain. The output file form iCFD is used for analysis in ACTRAN mesh.

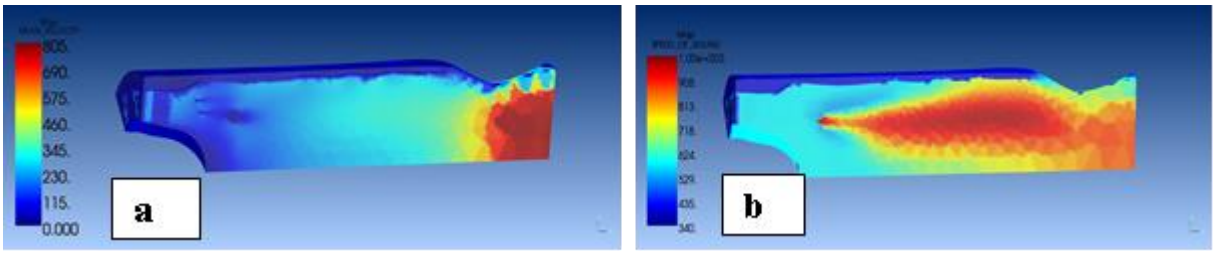


**Figure 1. Interpolated Results a – Mean Velocity, b - Speed of Sound**

The interpolated mean values of velocity and speed of sound are shown in Figures 1a and 1b. A low velocity region is observed near the V-gutter. A substantial velocity drop in diffuser section is observed. The velocity is observed very low near the walls due to shear stress opposing the motion of fluid particles. The increase in the velocity is observed from the throat of the nozzle and the maximum increase could be observed at outlet section due to heat addion and convergent nozzle. The speed of sound is seen increasing due to unsteady combustion and heat of reaction.The interpolated mean pressure, temperature and density are as per the results obtained through fluent whcih indicates that the results are properly interpolated.

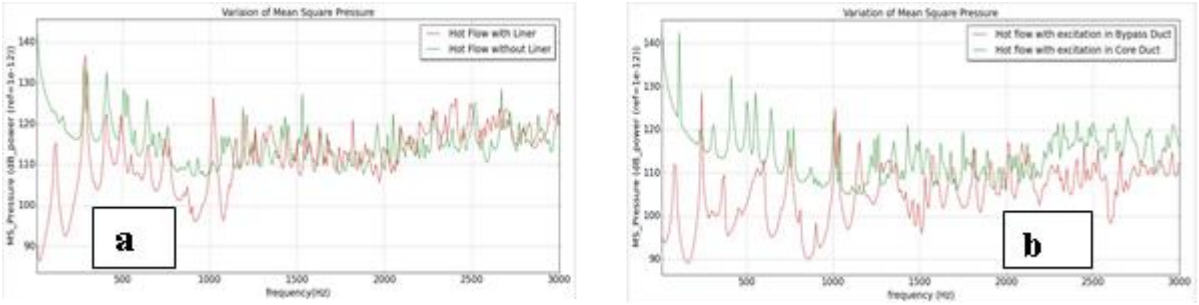


**Figure 2. Square Pressure (dB_Power) a - Hot flow with Liner and W/o Liner, b – Hot flow with excitation in core duct and bypass duct**

The root mean square pressure peaks of 115.6 dB power at 1190 Hz, 118.8 dB power at 1530 Hz, 120.2 dB power at 2670 Hz for hot flow without liner have been reduced by 10 dB when the liner is introduced in the afterbruner. It is also observed that the root mean square on average is more in case of hot flow without liner, as shown in Figure 2a.

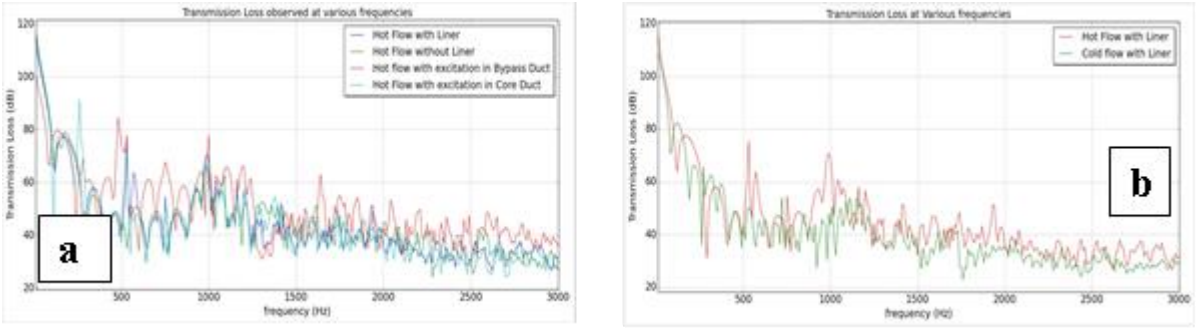


**Figure 3. Transmission Loss for a - various cases of Hot Flow, b - Hot Flow v/s Cold Flow**

The root mean square pressure peaks for hot flow with excitation in bypass duct is observed of 10 dB power less than the hot flow with excitation in core duct as shown in Figure 2b.This is attributed to the effect of exciation of bias flow through the holes of screech liner which absorbs the acoutic energy.

After getting the results from Actran, the results are plotted for analyzing the transimission loss in different cases. Transmission Loss is calculated as ratio of incident power to the transmitted power.

The transmission loss peaks for hot flow with liner are observed as 77.4 dB at 170 Hz, 75.5 dB at 530 Hz, 70.7 dB at 990 Hz and 51.2 dB at 1930 Hz, from Figure 3a. The maximum transmission loss is observed as 78.9 dB at 180 Hz, 66 dB at 990 Hz, 62.7 dB at 1090 Hz, 507 dB at 1620 Hz for hot flow without liner. The transmission loss of more than 10dB is observed in the case of hot flow (reacting flow) with liner than the flow without liner.

On the core and bypass model, the comparison of transmission loss is shown for core excitation and for bypass excitation considering only plane waves. In the case of excitation in bypass duct the transmission loss peaks are observed as 84.7 dB at 480 Hz, 78 dB at 530 Hz, 78 dB at 1000 Hz and 63 dB at 1640 Hz where as the transmission loss peaks are observed as 91.2 dB at 260 Hz, 71.7 dB at 530 Hz, 67.8 dB at 990 Hz and 58 dB at 1210 Hz. It can be seen from Figure 3a that the transmission loss is more when the excitation is only in bypass duct. This is attributed to the effect of bias flow through screech holes due to the excitation in bypass duct.

The comparison of transmission loss is also done for the two cases of afterburner including liner, with combustion (hot flow or reacting flow) and without combustion (cold flow) in Figure 3b. It is observed that the transmission loss is more in case of hot flow with liner due to the coupling effect of combustion and acoustic energy.

## 4. CONCLUSIONS

A $60^{o}$ full scaled afterburner model, with extended domain, is created and acoustic analysis is carried out after importing the resluts obatined from fluent.

It is observed that the maximum transmission loss and less mean square pressure is observed in the case of recting flow in the afterbruner (with liner) with excitation in bypass duct, due to the effect of bias flow through screech holes. Hence, these acoustic absorption results prove the effectiveness of liner in the absorption of acoustic energy. This is in agreement with the results obtained by Eldredge and Dowling [6] and Hughes and Dowling[7]. Hence the liner with best design can be selected with the help of Fluent and ACTRAN software as conducting the experiments every time is very complex and expensive.

## REFERENCES

[1] Kampa, A., Combustion Instability Screech in Gas Turbine Afterburners, PhD thesis, Department of Aerospace Engineering, Indian Institute of Science Bangalore, 2007.

[2] Gurrala Srinivasa Rao, A.Shaija, “Computational Analysis of Reacting Flows in Afterburner”, Proceedings of the Ist Internation 18th ISME Conference, ISME 18, February 23-25, 2017, NIT Warangal, Telangana.

[3] Gurrala Srinivasa Rao, A Shaija, Effect of Nozzle Angle on Mach Number of Afterburner in Jet Aircraft, Proceedings of the IEEE International Conference on Advances in Mechanical, Industrial, Automation and Management Systems (AMIAMS-2017), 3-5 February, 2017, MNNITA, Allahabad, U.P. , India. Available: http://ieeexplore.ieee.org/document/8069238/?reload=true.

[4] Useller, J.W., Effect of Combustor Length on Afterburner Combustion, Lewis Research Center-NASA, 1959.

[5] Unaune, S.V., and Ganesan, V., Analysis of reacting flows in an aero-engine afterburner using computational fluid dynamics, Indian Journal of Engineering & Material Sciences, Vol. 11, pp. 31-37, 2005.

[6] Eldredge, J.D., and Dowling, A.P., The Absorption of Axial Acoustic Waves by a Perforated Liner with Bias Flow. J. Fluid Mech., 485(2003) 307–335.

[7] Hughes, I. J. and Dowling, A. P., The absorption of sound by perforated linings, J. Fluid Mech. 218(1990) 299-335.

Fifth International Conference on Computational Methods for Thermal Problems
THERMACOMP2018, July 9-11, 2018, Indian Institute of Science, Bangalore, INDIA
*N. Massarotti, P. Nithiarasu, Pradip Dutta and C. Ranganyakalu (Eds.)*

# INVESTIGATION OF HEAT DISTRIBUTION AND THERMAL STRESS DISTRIBUTION OF PISTON

**Sudarshan Kumar, Yogesh K. Prajapati, Bhoopendra Pandey**
Department of Mechanical Engineering, National Institute of Technology Uttarakhand
Srinagar (Garhwal) 246174, India
91sudoist@gmail.com, yogesh.k@nituk.ac.in, bhoopendrapandey.101622@gmail.com

## ABSTRACT

Numerical work has been carried out to investigate the effect of different material of thermal coating layer which is applied at the piston top. Thermal coating layer is essentially considered to improve the piston life and hence the performance of internal combustion (IC) engines. An aluminium alloy (AlSi) piston compatible with modern internal combustion engines has been used in the present analysis. Partially stabilized Zirconia (PSZ) along with two other thermal coating materials have been examined for their varying thickness layer. In order to predict the piston performance, parameters such as temperature distribution and thermal stress distributions have been numerically calculated across the piston. Present problem has been solved using commercially available code ANSYS. Three-dimensional geometry of piston (of a heavy diesel engine) has been made on the workbench of the ANSYS software. Furthermore, steady-state thermal module of ANSYS has been used for the simulation purpose. To highlight the effect of coating materials, comparative results of piston with and without thermal coating have been presented. Based on the analysis it has been observed that due to the application of coating material, piston experiences reduced temperature and hence thermal stress decreases that may help to increase the life of piston.

**Key Words:** *Thermal coating, heat transfer, thermal stress, ANSYS, temperature distribution*

## 1. INTRODUCTION

It is well-known fact that piston is one of the severely heat affected parts of IC engines. It is directly exposed to the combustion process and hence experiences maximum temperature. In addition to thermal loading (temperature difference), piston encounters thrust force of combustible product. Due to thrust force on the piston, stress is developed, that is of compressive nature. It is worth mentioning that piston experiences combined loading conditions, and stress developed is combined stress. Moreover, it also reciprocates at significantly high velocity. Therefore, it should have lightweight as well as high thermal resisting property to restrict the failure. However, a piston has a large heating area and low dissipating area due to compact size. Due to high temperature of combustion, the thermal expansion on the piston takes place and followed by the expression $L(1+\alpha T)$ where $L$ is the length of the piston, $\alpha$ is the coefficient of thermal expansion, $T$ is temperature difference on the piston between two points, and $\alpha T$ represents the developed strain. As per Young's modulus of elasticity, if thermal expansion is opposed, certainly, stress will be developed that depend on the material property. Hence, the material having light weight and low Young's modulus of elasticity is desirable for piston design. Due to fixing of piston pin, there is restriction in the expansion, which causes thermal stress to be generated. The value of the thermal stress at each point is similar to that of mechanical stress, which means the thermal stress can't be ignored in the design process [1]. Several works have been done that report different techniques to minimize the thermal stress of piston. Thermal coating of the piston is one of the techniques that have been emphasized by several researchers in this field. It has been pointed out that with the application of the thermal coating layer, maximum temperature of the piston volume decreases. Furthermore, heat transfer to the piston substrate can be controlled by putting appropriate coating

material of suitable coating thickness. It also improves the critical thermal expansion temperature limit by using low thermally conductive material as a coated material [2]. Therefore, it is required to comprehend the effect of different types of coating materials on the piston. Keeping this in view, present work has been undertaken considering three different coating materials i.e. Partially stabilized zirconia (PSZ), Magnesium Partially Stabilized Zirconia (Mg-PSZ) also called Zirconates, and Yttrium Partially Stabilized Zirconia (Y-PSZ).

## 3. SOLUTION METHODOLOGY

Commercially available code ANSYS has been used for the modelling of three-dimensional geometry of the piston. In ANSYS, steady-state thermal module which is based on FEM has been used to simulate the problem. Figure 1 shows the meshed piston geometry and its enlarged view. It may be observed that very fine meshing of tetrahedral type has been generated to capture the different physical phenomenon. After doing grid independence, total number of nodes 293620 and elements 186978 have been considered for the final analysis of the problem.

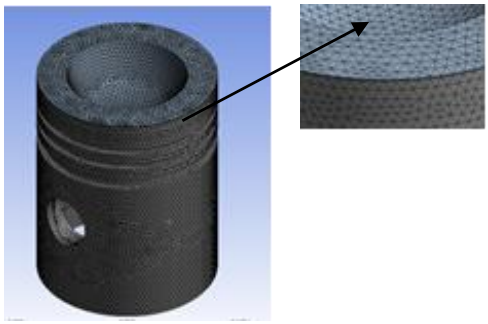

FIGURE 1. Meshing of piston and its enlarged view

| Properties | Aluminium alloy | Partially stabilized Zirconia (PSZ) | Zirconates (Mg-PSZ) | Y-PSZ |
|---|---|---|---|---|
| Density ($kg/m^3$) | 2700 | 5600 | 5600 | 5650 |
| Coefficient of thermal expansion ($K^{-1}$) | $21 \times 10^{-6}$ | $10.5 \times 10^{-6}$ | $8\times 10^{-6}$ | $10.9\times 10^{-6}$ |
| Thermal conductivity (W/m·K) | 155 | 1.68 | 0.8 | 1.4 |
| Young's Modulus($10^9 N/m^2$) | 70 | 48 | 46 | 11.25 |
| Poisson's Ratio | 0.3 | 0.2 | 0.8 | 1.4 |

TABLE 1. Material properties of piston and coating layer

The standard piston of heavy duty diesel engine made of aluminium alloy (AlSi) has been considered and dimensions are taken accordingly. Table 1 summarizes the properties of the piston material and three coated materials. Two important boundary conditions i. e. gas (surrounds the piston) temperature and convective heat transfer coefficient have been applied at different portions of the piston. Table 2 shows the respective values of boundary conditions.

| Piston parts | Gas Temperature (°C) | Convective Heat transfer coefficient ($W/m^2$) |
|---|---|---|
| Top surface of the piston | 650 | 600 |
| Piston skirt and gudgeon pin | 60 | 85 |
| Lateral surface of the piston | 300 | 230 |

TABLE 2. Boundary condition

## 4. RESULTS AND DISCUSSION

Validation of the present model has been done with the work of Vedharaj et at. [3]. Work of the Vedharaj et al. [3] has been reproduced considering the similar geometry, operating condition, and all boundary conditions. Figure 2 shows the comparison of temperature distribution.

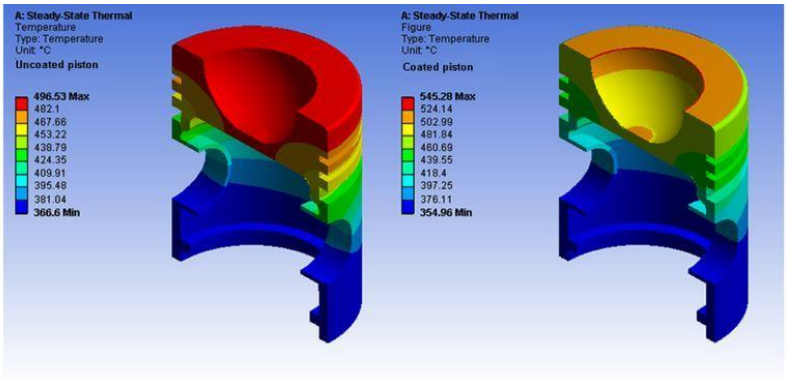


(a) Results of Vedharaj et al. [3]

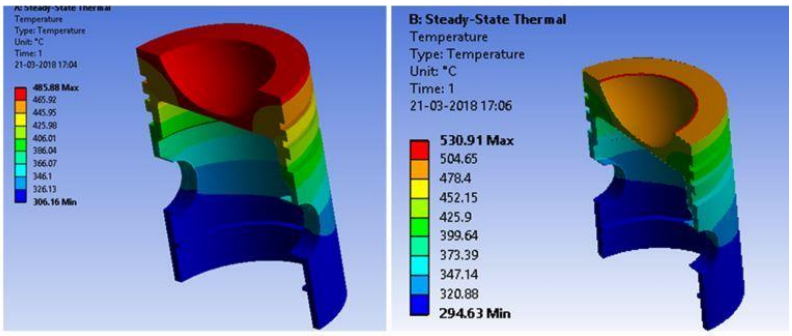


(b) Results obtained from present model

FIGURE 2. Validation of the present model with Vedharaj et al. [3]

It may be observed that the temperature distribution pattern of the present model is in good agreement with Vedharaj et al. [3] however, it underpredicts the maximum and minimum temperature range. Results of the parametric study for three different coating materials as mentioned above have been shown in figure 3 and 4. In case of PSZ coating material, the maximum temperature at the top surface of the coated piston is about 530°C and for the substrate, it is about 455°C. Similarly for Mg-PSZ maximum temperatures are about 507°C and 470°C and for Y-PSZ maximum temperatures are about 513°C and 468°C. Hence, the lowest substrate temperature is predicted for PSZ this may be attributed due to its higher thermal conductivity. Maximum stress

occurs at the piston pin in all cases. The maximum reported values of stresses for PSZ, Mg-PSZ, and Y-PSZ are 1109 MPa, 1136MPa and 1130 MPa respectively.

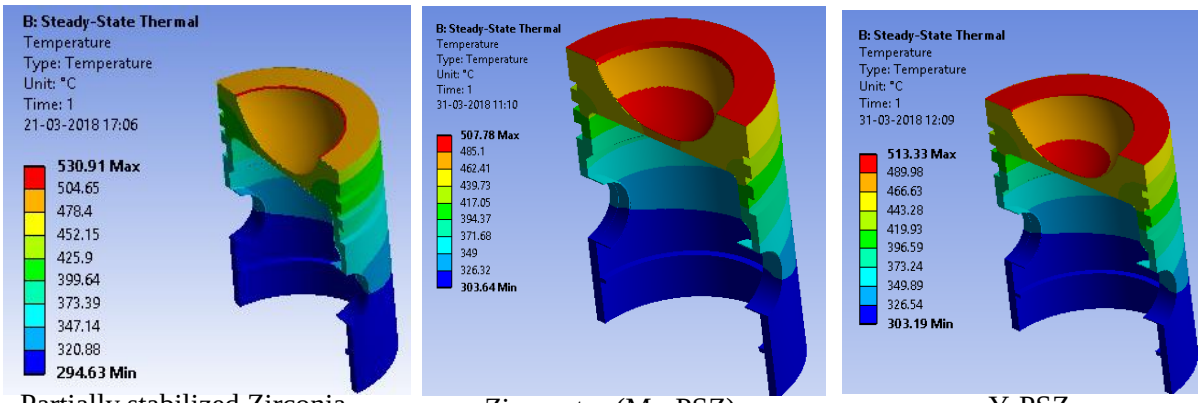


Partially stabilized Zirconia Zirconates (Mg-PSZ) Y-PSZ

FIGURE 3. Temperature distribution for three different coating materials

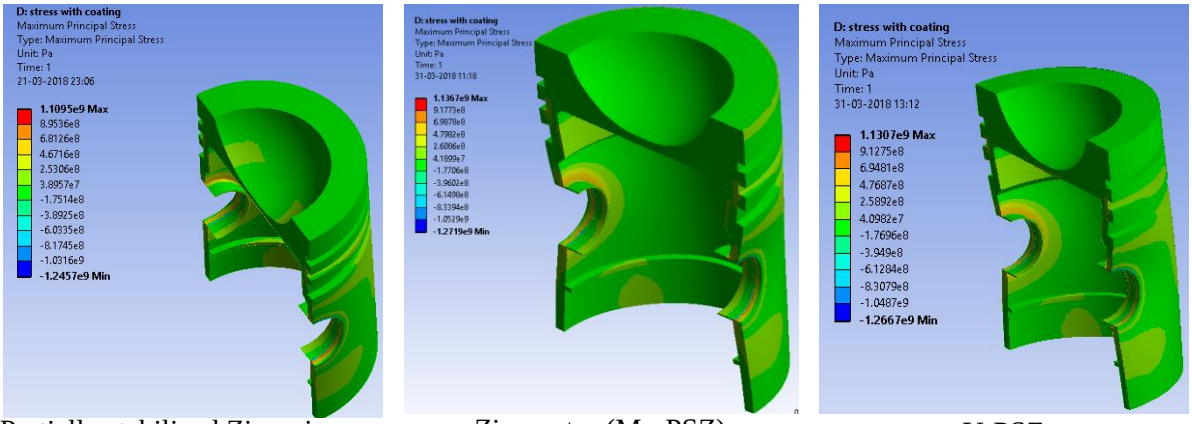


Partially stabilized Zirconia Zirconates (Mg-PSZ) Y-PSZ

FIGURE 4. Stress distribution for three different coating materials

## 4. CONCLUSIONS

Comparative results of three different thermal coating materials applied on piston top have been presented. It has been found that with the increase in thermal conductivity of coating material, the maximum temperature on the substrate part of the piston decreases. Thermal stress becomes lesser in case of the coated piston.

## REFERENCES

[1] Y. Lu, X. Zhang, P. Xiang, and D. Dong, "Analysis of thermal temperature fields and thermal stress under steady temperature field of diesel engine piston," *Appl. Therm. Eng.*, vol. 113, pp. 796–812, 2017.

[2] M. Cerit, V. Ayhan, A. Parlak, and H. Yasar, "Thermal analysis of a partially ceramic coated piston: Effect on cold start HC emission in a spark ignition engine," *Appl. Therm. Eng.*, vol. 31, no. 2–3, pp. 336–341, 2011.

[3] S. Vedharaj, R. Vallinayagam, W. M. Yang, S. K. Chou, K. J. E. Chua, and P. S. Lee, "Experimental and finite element analysis of a coated diesel engine fueled by cashew nut shell liquid biodiesel," *Exp. Therm. Fluid Sci.*, vol. 53, pp. 259–268, 2014.

# EFFECT OF PULSATILITY ON BLOOD FLOW IN A CONSTRICTED CHANNEL

**Sufia Khatoon**
Mechanical Engineering Dept., IIT Delhi, India, sufia3304@gmail.com

**Syed Fahad Anwer**
Comp. Aero. Lab, Mechanical Engineering Dept., AMU, Aligarh, sfahadanwer@zhcet.ac.in

**Nadeem Hasan**
Mechanical Engineering Dept., AMU, Aligarh, nadhasan@gmail.com

## ABSTRACT

Atherosclerosis is a chronic disease which leads to excessive deposition of lipids (cholesterol) in the artery wall. In some cases, they form a solid structure (plaque) and become calcified immediately beneath the wall surface. With time, the plaque hardens and narrows the arteries. This limits the flow of oxygen-rich blood to the organs and other body parts. Blood flow in the arteries under such diseased condition is an important field of study. In this work, we have made an attempt to study the effects of pulsatility and non-Newtonian nature of blood on physiologically important flow quantities such as velocity, vorticity and wall shear rate for blood flow in an artery. The artery has been modelled with a channel and the stenosis with a semi-circular constriction on upper wall of channel. The peak constriction is 50% of the height of the channel. An inlet pulsatile velocity which matches the physiological velocity has been supplied at the inlet. The governing Navier-Stokes equation for blood flow is solved on a structured body fitted curvilinear non-orthogonal mesh flow. Solver employed is a finite difference type of discretization. Non-Newtonian behaviour of blood is modelled as Generalized Newtonian model [1]. The physiological velocity profile at the inlet were taken from Tutty [2] who has done the study assuming blood to be Newtonian fluid. We have observed a significant difference in the values of shear rate and vorticity observed in the two cases.

**Key Words:** *Blood Flow, Newtonian model, Atherosclerosis.*

## 1. INTRODUCTION

There is indirect evidence that the developments and cause of many cardiovascular diseases are, to a great extent, related to the characteristics of blood flow, such as due to the high values of the shear stress at the wall or its variation. Hence, it is important to understand the connection between blood flow characteristics and development of cardiovascular diseases.

Understanding the phenomena of stenotic flow has proceeded from quite a good number of theoretical, computational and experimental efforts. Assuming blood flow to be steady flow, flow through an axisymmetric stenosis has been investigated extensively by Smith [3] using an analytical approach concluding that the flow patterns strongly depend on the geometry of the stenosis and the upstream Reynolds number. However, blood flow is unsteady. The cyclic nature of the heart pump creates pulsatile conditions in all arteries. Womersley [4] considered the flow of blood through a straight pipe driven by an oscillatory pressure gradient. Pressure and flow have characteristic pulsatile

shapes that vary in different parts of the arterial system. Many theoretical analysis and experimental measurements on the flow through stenosis have been performed.

## 2. PROBLEM FORMULATION

This work focusses on developing a computational methodology which studies blood flow through a blood vessel segment having a stenosis in its lumen which is modelled as a semi-circular constriction as shown in FIGURE 1. The shape of the stenosis is taken to be a semicircle with radius equal to half the width of the channel. In the computational domain a finite difference type of discretization has been used. Physiological velocity profile has been taken at the inlet. The unsteady equations, transformed in the computational domain, are marched forward in time by using a semi-explicit pressure correction scheme. The validity and performance of the entire procedure is done through some flow problems involving flows in channels.The numerical procedure developed is then applied to a constricted channel to model blood flow in an artery.

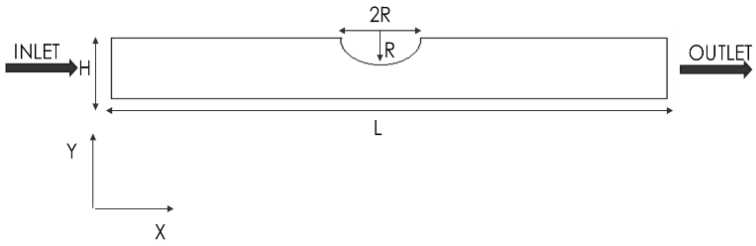


FIGURE 1. Schematic diagram of the stenosed channel

In the Generalized Newtonian model blood is described using an incompressible shear-thinning model wherein the viscosity depends on the shear rate. The model is given by:

$$\bar{\bar{T}} = \mu(\boldsymbol{A_1})\boldsymbol{A_1}$$

Where v is the velocity vector. Further the viscosity is a function of shear rate ($\dot{\gamma}$).

$$\mu(A_1) \quad = \eta_\infty \quad + (\eta_\circ - \eta_\infty)\left[\frac{1 + log(1 + \Lambda\dot{\gamma})}{1 + \Lambda\dot{\gamma}}\right]$$

For the purpose of capturing the unsteady physics of the flow we employ a semi-implicit, pressure correction type scheme, on a non-staggered structure body fitted grid mesh using a finite difference type of spatial discretization. The details of the scheme are given in [8].

## 3. RESULTS

After comparing our results with already published works of sinusoidal incoming flow which is used in theoretical and experimental studies of flow in non-uniform vessels [5-7], we have considered the effect of non-sinusoidal incoming flow, using the velocity profile given in [2]. Here, there is a double pulse, with the velocity during systole much greater than during diastole. Velocity is given by:

$V=0.251+0.290(cos\phi + 0.97cos2\phi + 0.47cos3\phi + 0.14cos4\phi)$

Where $\phi = 2\pi\tau St - 1.4142$ and St is strouhal numbers which defines the pulsatility.

The key hemodynamic variable affecting the growth of atherosclerotic plaques is the wall shear rate. We have therefore examined the difference brought about by shear-thinning behaviour on the wall shear rate, the difference in the vorticity and velocity vectors plots along the channel wall. We have taken time average of the shear rates over a cycle.

Figure 2 shows that the peak value of time average wall shear rate is higher when considering blood as a non-Newtonian fluid. However the fluctuation in shear rate decays quickly downstream of the stenosis because of the effect of higher viscosity.

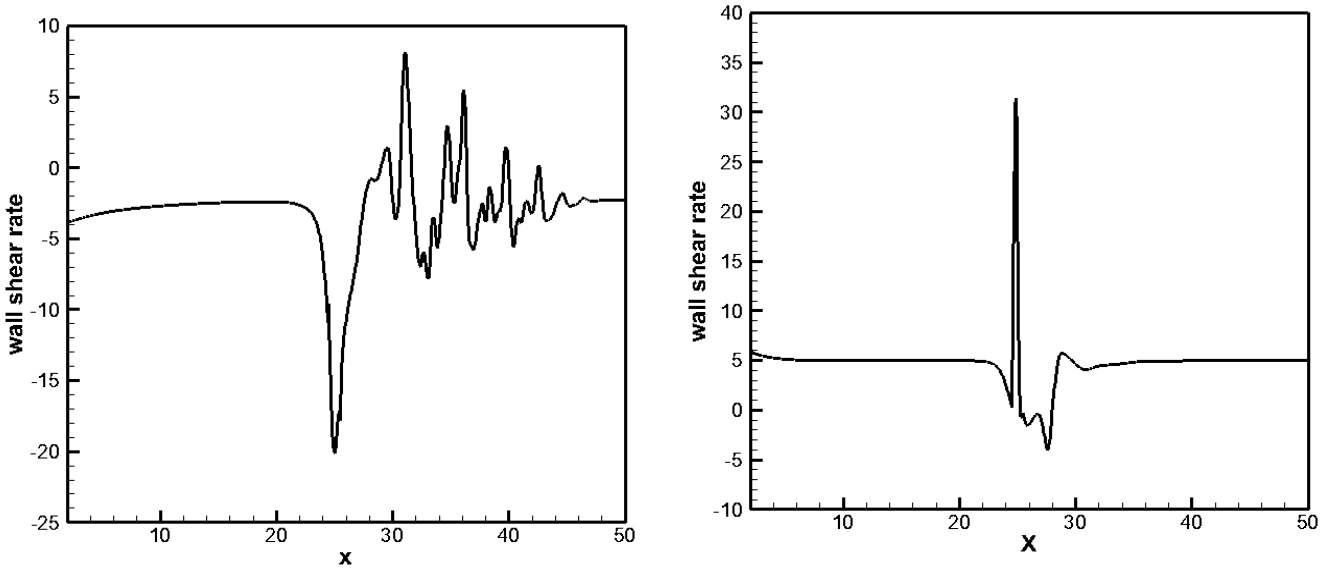


(a) (b)

FIGURE 2. Time average upper wall shear rate for non-sinusoidal flow at Re=750, St=0.024 (a) Newtonian (b) non-Newtonian

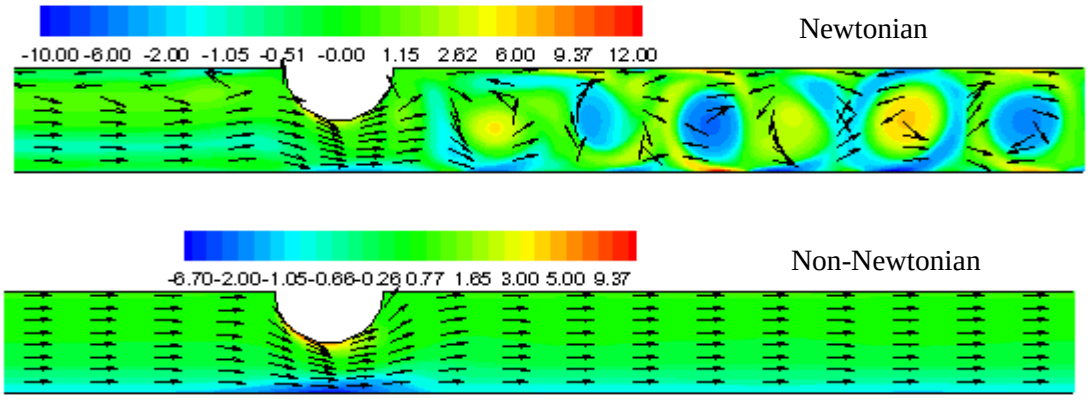


FIGURE 3. Vorticity and velocity vector plots for non-sinusoidal flow with Re=750 and St=0.024(x=22 to 32) at $\tau = 0.5$

Figure 3 shows the vorticity and velocity vectors for non-sinusoidal inflow velocity. Larger number of eddies are formed in Newtonian flows as compared to non-Newtonian flows. The peak values are formed below the constriction and in the recirculation zone in case of Newtonian flows.

## 4. CONCLUSIONS

The objective of the present study was to do numerical simulation of human arteries which should be efficient and accurate in predicting fluid dynamics generated due to the presence of a stenosis. The study done helps in predicting the changes in various flow properties which occur in stenosed arteries due to physiological inflow velocity in Newtonian and non-Newtonian fluid.

We have seen that the peak values of average wall shear rates is higher in non-Newtonian model than Newtonian. However the fluctuations in the shear rate in the post-stenotic region dampens in the non-Newtonian model due to effect of high viscosity. The vortex formed in Newtonian flow is greater than non-Newtonian flow. Since vorticity is high in low viscosity models, it suggest that the viscosity of non-Newtonian model is higher than Newtonian model which goes along with the previous studies that viscosity of blood produced by non-Newtonian models for shear rates (less than $100 s^{-1}$) is higher than that of Newtonian models.

## REFERENCES

[1] Yeleswarapu, K. K., 1996 “Evaluation of continuum models for characterizing the constitutive behavior of blood.” PhD Thesis, University of Pittsburgh.
[2] Tutty, O.R. and Pedley, T.J., 1993. “Oscillatory flow in a stepped channel”. *Journal of Fluid Mechanics*, *247*, pp. 179-204.
[3] Smith, F. T., 1979. “The separating flow through a severely constricted symmetric tube”. *Journal of Fluid Mechanics*, 90(04), pp. 725-754.
[4] Womersley, J. R. 1955. “Method for the calculation of velocity, rate of flow and viscous drag in arteries when the pressure gradient is known”. *The Journal of physiology*, 127(3), p. 553.
[5] Mittal, R., S. P. Simmons and F. Najjar. 2003. "Numerical study of pulsatile flow in a constricted channel." *Journal of Fluid Mechanics* 485 pp. 337-378.
[6] Pontrelli, G., 1998. "Pulsatile blood flow in a pipe." *Computers & fluids* 27.3 pp. 367-380.
[7] Nandakumar, N., Kirti C. S. and M. Anand. 2015 "Pulsatile flow of a shear-thinning model for blood through a two-dimensional stenosed channel." *European Journal of Mechanics-B/Fluids* 49 pp. 29-35.
[8] Anwer, S.F., Hasan and N., Sanghi, S. and Mukherjee, S., 2009. “Computation of unsteady flows with moving boundaries using body fitted curvilinear moving grids”. *Computers & Structures*, *87*(11), pp. 691-700.

Fifth International Conference on Computational Methods for Thermal Problems
THERMACOMP2018, July 9-11, 2018, Indian Institute of Science, Bangalore, INDIA
*N. Massarotti, P. Nithiarasu, Pradip Dutta and C. Ranganyakalu (Eds.)*

# Numerical analysis of heat transfer enhancement in microchannel with bioinspired surface

**Prasenjit Dey, Sandip K. Saha***
Mechanical Engineering Department, Indian Institute of Technology Bombay
Mumbai- 400076, India.
E-mail: sandip.saha@iitb.ac.in

## ABSTRACT

Numerical analysis is performed to study the influence of the bioinspired surfaces on the fluid flow and heat transfer in a microchannel. The layout of the bioinspired surface is encouraged by the fish scale geometry due to having structured micro roughness. Deionized water is selected as the working fluid, where the fluid flows through a copper microchannel of hydraulic diameter ($D_h$) of 187.5 μm with three Reynolds numbers as 250, 650 and 1050. Fish scale structures are created on the bottom surface of the channel, and a constant heat flux of 100 W/cm$^2$ is applied on the bottom surface. It is found that the bioinspired surface can enhance the convective heat transfer rate significantly compared to that of a plain channel by producing flow separation, disturbance and the vortexes in the mainstream.

**Key Words:** *Bioinspired Surface, Heat Transfer, Microchannel.*

## 1. INTRODUCTION

Rapid growth in microelectronics for delivering high performance, due to the advancement in nanotechnologies has raised severe thermal management issue. Researchers are developing various cooling technologies to dissipate high heat fluxes associated with these miniaturized electronic devices. In this context, cooling by microchannels are recognized to be one of the crucial research areas among the micro-fluidic systems because of its preeminent cooling characteristics in high power magnets, accelerator targets, material processing and manufacturing industries, advanced thermal management systems, and high computation operations in computers, etc. [1]. A very high heat transfer coefficient, which is required to remove heat quickly from a very high heat dissipating micro devices, can be achieved by using microchannel due to its higher heat transfer surface area to fluid volume ratio compared to other macroscale systems. Till date, numerous experimental and numerical studies of microchannel are accomplished since its introduction by Tuckerman and Peace [2]. Thermal boundary layer interruption, mixing between hot and cold fluids and flow separation are the potential approaches to augment the heat transfer rate in microscale [3].

Several innovative enhancement techniques were explored and reported by researchers. Regenerating the thermal boundary layer to enhance the heat transfer rate was studied numerically by Gong et al. [4] in a wavy microchannel. Combined effect of transverse micro chamber and parallel longitudinal microchannel can enhance the heat transfer rate by redeveloping the thermal boundary layer [5]. A significant enhancement in heat transfer rate can be achieved by introducing the waviness surface inside the straight microchannel [6]. The overall performance criteria of a microchannel can be enhanced by introducing porous medium which results in the reduction of pressure drop and the enhancement of the convective heat transfer rate [7, 8]. However, surface roughness plays significant role on heat transfer, which cannot be neglected if the relative roughness height is larger than 1% of the channel hydraulic diameter in microchannels [9, 10]. The effect of structured roughness or methodical flow obstacles or extended surface on the fluid flow and heat transfer in a microchannel was numerically studied by Yadav et al. [11].

Some of the structured extended surfaces are also inspired by biological surfaces (biomimetic) and applied to study the effect of these biomimetic surfaces on the two-phase flows [12,13] and

observed that the bio-inspired surfaces promote the heat transfer coefficient significantly. Therefore, the main goal of the present study is to investigate the effect of biomimetic inspired surface on single phase laminar forced convection heat transfer in microchannel.

## 2. DESCRIPTION OF PHYSICAL PROBLEM

The present microchannel is designed with biomimetic inspired bottom surface that contains fish scale geometry. The detailed geometry of the computational microchannel and considered fish scale is depicted in Fig. 1(a-b), respectively. The channel height, width and length are taken as 100 μm, 1500 μm and 0.02 m, respectively. Eight numbers of fish scales were used and they are equally spaced in the direction of flow. The geometry of the fish scale is defined by the following non-dimensional parameters: slant height ($S_f/D_h$=1.50), width ($W_f/D_h$=1.07), horizontal gap ($H_f/D_h$=1.07), vertical height ($V_f/D_h$=1.60) and inclination angle ($\alpha$ = 1° and 10°). The inflow distance between the scales ($S_p/D_h$) is also kept constant at 2.13. The numerical analysis is carried out in a commercial Finite Volume based solver ANSYS Fluent V16.

The computational domain consists of hexahedral elements where certain portion behind the fish scale is having fine mesh to adequately capture the fluid flow and heat transfer behaviour. A number of structured hexahedral mesh is also generated within the fish scale volume. After completing a detailed grid independence study, it is observed that the 9,01,500 number of cells are moderately sufficient for the numerical simulations with good accuracy and least computational time.

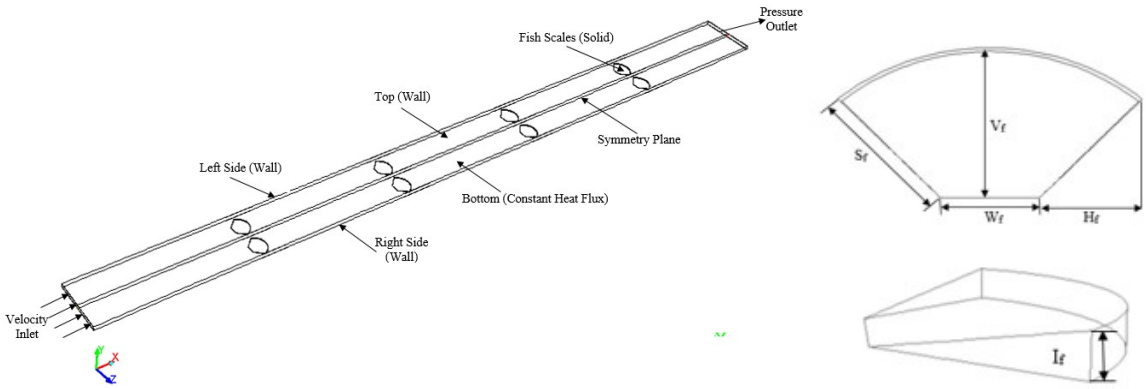


(a) (b)

FIGURE 1. (a) Schematic Diagram of the present computational model with boundary conditions and (b) Particulars of Fish scale geometry

## 3. RESULTS AND DISCUSSION

It is important to validate the present numerical model with the published numerical and experimental results. Therefore, a plain rectangular channel was considered for the validation and found that the present numerical model has a good agreement with the published data. Three different microchannels are considered; plain channel (MC_P), fish scaled channel [MC_A1 ($I_f$ = 1°) and MC_A10 ($I_f$= 10°)], keeping all other parameters as constant.

Fig. 2 shows the ratio of Nusselt number for fish scale structured and plain microchannels. Drastic enhancement in thermal performance ($Nu/Nu_0$) is noticed when the inclination angle is changed from 1° to 10°. This augmentation primarily results from the flow separation, disturbance effect and the vortices in the mainstream caused by fish scale inclination as can be observed from Fig. 3. Moreover, the effect of flow disturbance is more intense for larger inclination. This flow

disturbance in higher inclined fish scale microchannel can easily be understood from Fig. 3(b) and (c).

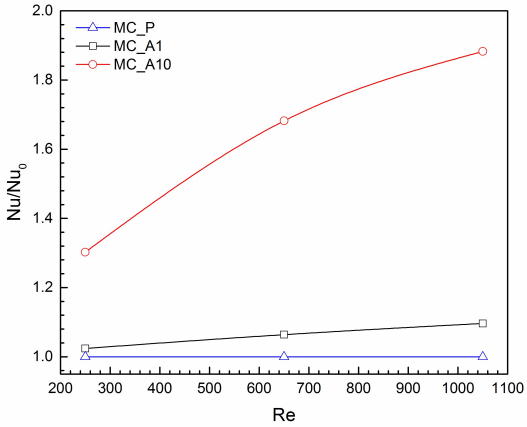


FIGURE 2: Effect of fish scale inclination angle on thermal performance.

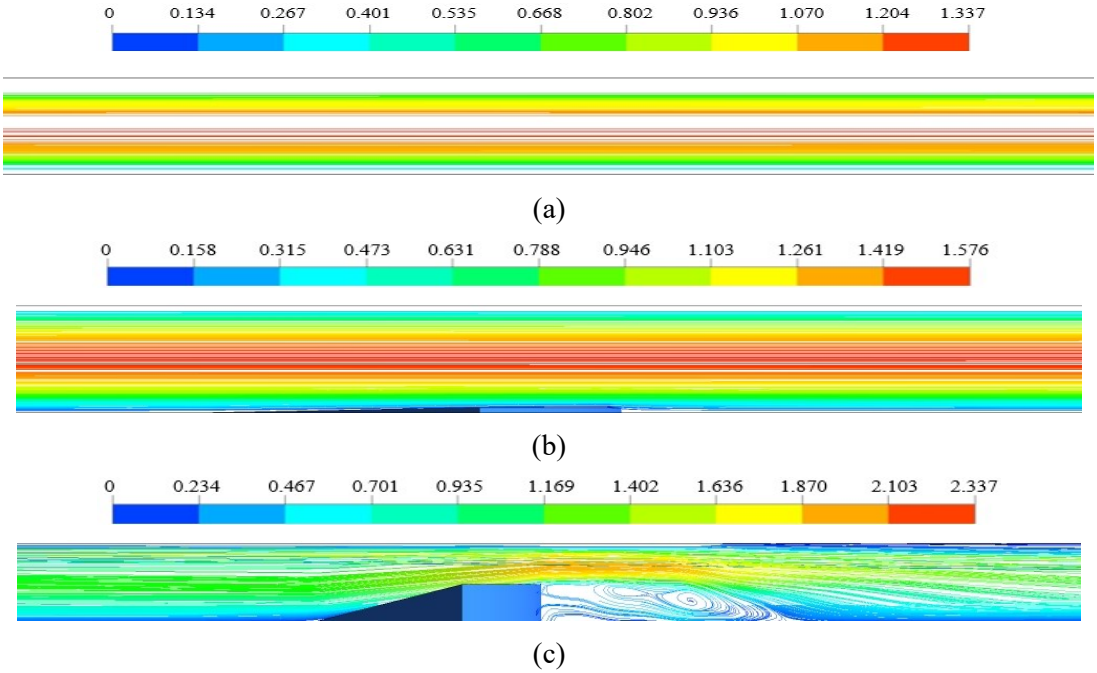


FIGURE 3: Streamline distribution in (a) MC_P (b) MC_A1 and (c) MC_A10 at *Re*=1050.

To understand the fluid flow along the stream-wise direction, streamline distributions with non-dimensional velocity contour is depicted at the cross sections for above mentioned three microchannels at $z$ = 0.375 mm for $Re$ = 1050. It is observed in Fig. 3(a) that the velocity profile remains invariable along the flow direction in the plain microchannel, however when the fish scale is introduced with an inclination angle of 1°, the velocity profile changes above the fish scale surface (Fig. 3(b)). The maximum velocity exists at the centre of the plain microchannel and remains same throughout the domain. However, as can be observed in Fig. 3(c), the velocity fluctuates significantly along the flow direction and the highest velocity is obtained at the centre of that portion of microchannel which contains fish scale structure.

More vortices are observed in the microchannel with fish scale having an inclination angle of 10° due to adverse pressure gradient which moderately improve the flow mixing and chaotic advection. This phenomenon increases heat transfer in the microchannel of fish scale of 10°.

## 4. CONCLUSIONS

A detailed numerical study is conducted to study the effect of the fish scale like geometry in a microchannel on heat transfer. It is found that the inclination angle of the present bioinspired surfaces can significantly enhance heat transfer by improving the flow mixing, and chaotic advection by introducing vortices, which increases with the inclination angle of the fish scale structure.

## REFERENCES

[1] S.K. Saha, A. Agrawal, Y. Soni, Heat transfer characterization of rhombic microchannel for H1 and H2 boundary conditions, International Journal of Thermal Sciences, 111, 223-233, 2017.

[2] D.B. Tuckerman, R.F.W. Pease, High-performance heat sinking for VLSI, IEEE Electron Device Lett., 2(5), 126-9, 1981.

[3] J.L. Xu, Y.H. Gan, D.C. Zhang, Microscale heat transfer enhancement using thermal boundary layer redeveloping concept, Int J Heat Mass Transf, 48, 1662-74, 2005.

[4] L. Gong, K. Kota, W. Tao, Y. Joshi, Parametric numerical study of flow and heat transfer in microchannels with wavy wall, Journal of Heat Transfer ASME, 133(5), 051702-10, 2011.

[5] J.L. Xu, Y.H. Gan, D.C. Zhang, X.H. Li, Microscale heat transfer enhancement using thermal boundary layer redeveloping concept, Int. J. Heat Mass Transfer, 48(9), 1662–1674, 2005.

[6] Y. Sui, P.S. Lee, C.J. Teo, An experimental study of flow friction and heat transfer in wavy microchannels with rectangular cross section, Int. J. Therm. Sci. 50, (12), 2473–2482, 2011.

[7] B.I. Pavel, A.A. Mohamad, Experimental investigation of the potential of metallic porous inserts in enhancing forced convective heat transfer, J. Heat Transfer ASME, 126, 540–545, 2004.

[8] R. Singh, A. Akbarzadeh, M. Mochizuki, Sintered porous heat sink for cooling of high-powered microprocessors for server applications, Int. J. Heat Mass Transfer, 52, 2289–2299, 2009.

[9] G.H. Tang, Z. Li, Y.L. He, C.Y. Zhao, W.Q. Tao, Experimental observations and lattice Boltzmann method study of the electroviscous effects for liquid flow in microchannels, J. Micromech. Microeng., 17, 539-550, 2007.

[10] G.H. Tang, T.B. Lu, S.X. Zhang, F.F. Wang, W.Q. Tao, Experimental investigation of non-Newtonian liquid flow in microchannels, J. Newt. Fluid Mech., 173-174, 21-29, 2012.

[11] V. Yadav, K. Baghel, R. Kumar, S.T. Kadam, Numerical investigation of heat transfer in extended surface microchannels. International Journal of Heat and Mass Transfer 93, 612-622, 2016.

[12] Q. Wang, H. Jiaju, Y. Yuying, Biomimetic capillary inspired heat pipe wicks, Journal of Bionic Engineering, 11, 469-480, 2014.

[13] E. Teodori, A. S. Moita, M. Moura, P. Pontes, A. Moreira, Y. Bai, Y. Liu, Application of Bioinspired Superhydrophobic Surfaces in Two-phase Heat Transfer Experiments, Journal of Bionic Engineering, 14(3), 506-519, 2017.

Fifth International Conference on Computational Methods for Thermal Problems
THERMACOMP2018, July 9-11, 2018, Indian Institute of Science, Bangalore, INDIA
*N. Massarotti, P. Nithiarasu, Pradip Dutta and C. Ranganyakalu (Eds.)*

# NUMERICAL INVESTIGATION ON EFFECT OF GEOMETRICAL CONFIGURATION OF ABSORBER PLATE ON HEAT TRANSFER ENHANCEMENT IN SOLAR AIR COLLECTOR

**Suman Debnath, P. R. Randive**
Department of Mechanical Engineering, NIT Silchar, Assam, Cachar, 788010,
debnath.s1990@gmail.com, kp691975@gmail.com

**Biplab Das**
Department of Mechanical Engineering, NIT Silchar, Asssam, Cachar, 788010,
biplab.2kmech@gmail.com

## ABSTRACT

Numerical investigation has been carried out to study the influence of various surface textures of absorber plate of solar air collector proposed for enhancement in heat transfer rate. The performance of the solar air collector with novel geometrical configuration of absorber plate is discussed. The influence of mass flow rate of air, glazing covers, amplitude (α) and wave length (λ) of absorber plate are numerically investigated. The investigation is carried out for the Reynolds number (Re) of range 4 × 103 to 15 × 103. Thermal performance for a range of mass flow rate of air, number of glazing covers, and for various values of amplitude and wave length of the absorber pate has been considered. Three different geometric configurations have been designed. Heat transfer and friction factor characteristic have been evaluated for a different configurations of absorber plate to determine thermo-hydraulic performance.

**Key Words:** *Energy analysis; Exergy analysis; Solar air collector; Amplitude; Wave length*

Fifth International Conference on Computational Methods for Thermal Problems
THERMACOMP2018, July 9-11, 2018, Indian Institute of Science, Bangalore, INDIA
*N. Massarotti, P. Nithiarasu, Pradip Dutta and C. Ranganyakalu (Eds.)*

# 2D CONDUCTION THROUGH HOMOGENEOUS BULK WITH HAIRLINE CRACK: INSPECTION OF CRACK IN HOMOGENEOUS BULK

**Kumar Samal, Nihar Ranjan Panda, Suman Ghosh**
Department of Mechanical Engineering, NIT Rourkela, Rourkela-769008, Odisha, India

Email: ghoshs@nitrkl.ac.in

## ABSTRACT

Due to manufacturing defects or some other reasons, cracks may be generated in a homogeneous bulk. Due to the presence of cracks, bulk may suffer from uneven stress distribution which may again propagate the existing cracks. Study of the mechanical behaviour of homogeneous bulk with the presence of crack is an essential requirement. Here, a numerical attempt is made to inspect the thermal behaviour of a homogeneous bulk with the presence of a hairline crack. A 2D rectangular homogeneous slab with a hairline crack is considered in the present study. The effect of size and position of the crack on the heat conduction through the bulk is extensively studied by varying the size and position of the crack. The 2D steady state conduction analysis are performed using Finite Volume Method (FVM). The numerical results are presented in terms of temperature distributions in the bulk as well as temperature profiles at the bottom wall and vertical mid plane. From the obtained results, it is found that the temperature distributions in the bulk as well as temperature profiles at the bottom wall and vertical mid plane are very much responsive with the position and size of the crack. Therefore, the nature and position of the crack can be inspected using the conduction analysis.

**Key Words:** *Steady state conduction, Hairline crack, Homogeneous slab, Finite Volume Method (FVM), Temperature profile at Bottom wall, Temperature profile at Vertical mid plane.*

## 1. INTRODUCTION

Due to manufacturing defects or some other reasons, cracks may present in a homogeneous bulk and consequently, the bulk may suffer from uneven stress distribution which may again propagate the existing cracks. Under thermal loadings, these manufacturing defects may spread more rapidly. As a result, the strength of the bulk may be reduced significantly and eventually causes failure of the components. Therefore, study and estimation of crack distribution in homogeneous bulk is an essential requirement. For safety, smooth, and efficient operation of the equipment in the industries, identification of crack is highly required. Identifying a crack inside a bulk medium is a challenging as well as extremely important work for researchers. Researchers have already started to investigate the above area. However, as per the authors' knowledge, not much work regarding inspection of the crack by knowing the temperature distribution on the surface of bulk is found in literature. Stationary heat conduction in an anisotropic slab containing a crack was numerically studied by Clements [1]. Clements [1] presumed an arbitrary temperature variation in one direction on each face of the slab whereas the crack surface was prescribed by specifying either heat flux or temperature. Two collinear cracks influenced by a concentrated heat source were studied by Matczyński [2]. Thermal stresses around a crack in the non-homogeneous interfacial layer between two dissimilar elastic half-planes were studied by Itou [3]. Cracks were considered as insulated surfaces by him. Using boundary element method, anisotropic heat conduction across an interface crack/defect filled with a thin interstitial medium was investigated by Shiah and Shi [4].

An attempt is made here to study the effect of presence of hairline crack on the heat conduction through a homogeneous bulk. Numerical simulations are performed by varying the size and position of the crack within the bulk and consequently, attempt is made to capture the effect of size and position on the temperature distributions in the bulk as well as on the temperature profiles at the bottom wall and vertical mid plane.

## 2.1 PROBLEM FORMULATION

A 2D rectangular homogeneous slab 'abcdef' with a hairline crack 'gh' is considered (as shown in Figure 1) for the present study. For a given set of boundary conditions, heat transfer through conduction and consequently, the temperature distribution in the slab as well as the temperature profile at the bottom wall and vertical mid plane will be significantly affected by the size and position of the crack. Therefore, the nature of the crack can be inspected by knowing the temperature profile at the bottom wall and vertical mid plane. A constant heat flux of 80 kW/m$^2$ is maintained in the portion 'bc' (heat source) of the upper wall whereas in the portion 'ab' and 'cd', constant ambient temperature of 300 K is maintained. The bottom wall is insulated. At the vertical walls ('af' and 'de'), either constant temperatures are maintained or they are insulated (as shown in Table 1). At the crack ('gh') either zero heat flux or constant temperature boundary conditions are used. For a given size and position of the crack and a given set of boundary conditions, the temperature distribution throughout the slab and the temperature variation along the bottom wall and the vertical mid plane are evaluated through steady state numerical simulation using FVM. This process is repeated for a particular set of boundary conditions (in Table 1), by varying the size and position of the crack and the corresponding temperature profile on the bottom wall and vertical mid plane (intersect the crack perpendicularly at its mid-point) are recorded.

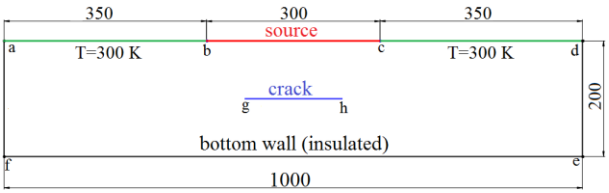


FIGURE 1. Schematic diagram of the homogeneous slab with crack (all the dimensions are in mm)

| Case | 'ab'&'cd' | 'bc' (source) | 'af'&'de' | 'gh' (crack) |
|---|---|---|---|---|
| A | 300 K | 80 kW/m$^2$ | Insulated | Insulated |
| B | 300 K | 80 kW/m$^2$ | 300 K | Insulated |
| C | 300 K | 80 kW/m$^2$ | Insulated | 300 K |
| D | 300 K | 80 kW/m$^2$ | 300 K | 300 K |

TABLE 1. Boundary conditions considered for different cases

## 2.2 METHODOLOGY

To find out the temperature distribution within the bulk or temperature profile at the bottom wall and mid vertical plane, one needs to solve the energy conservation equation along with appropriate boundary conditions for a given geometry of the bulk together with position and size of the crack. The conservation equation of energy is discretized by FVM. 2D steady state heat conduction with no heat generation is considered here to capture the temperature distribution and temperature profile. The simplified form of the governing equation is

$$\frac{\partial}{\partial x}\left[k(x,y)\frac{\partial T(x,y)}{\partial x}\right]+\frac{\partial}{\partial y}\left[k(x,y)\frac{\partial T(x,y)}{\partial y}\right]=0 \qquad (1)$$

The boundary condition of the edges (walls) which are kept at a constant temperature can be expressed as shown below in equation (2).

$$T(x,y) = \text{Specified (Constant)} \tag{2}$$

The boundary condition of the edges (walls) where, constant heat flux is maintained can be expressed as shown below in equation (3).

$$\left(-k(x,y)\frac{\partial T(x,y)}{\partial y}\right) = \text{Specified (Constant)} \tag{3}$$

For the numerical calculation using FVM, a body fitted rectangular structured grid arrangement is employed as shown in Figure 2. The grid size is decided after conducting a rigorous grid-independence test. The scaled residuals are computed at each iteration. Once all of these scaled residuals fall below a prescribed value, it is assumed that convergence is reached. A fixed value of $10^{-19}$ for the scaled energy residual is chosen as the prescribed value of convergence.

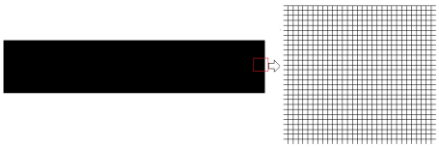

FIGURE 2. Mesh pattern employed in the present investigation

## 3. RESULTS

The grid size is decided through an exhaustive grid-independence test as shown in Figure 3a and 3b. Using the Case A from Table 1, the temperature profile in the bottom wall ('ef' in Figure 1) is plotted for all the grid size and shown in Figure 3a. The maximum temperature at the bottom wall is also plotted with grid size as shown in Figure 3b. A rectangular structured grid of size 0.001 m (from the zone where results are independent of the grid size) is selected.

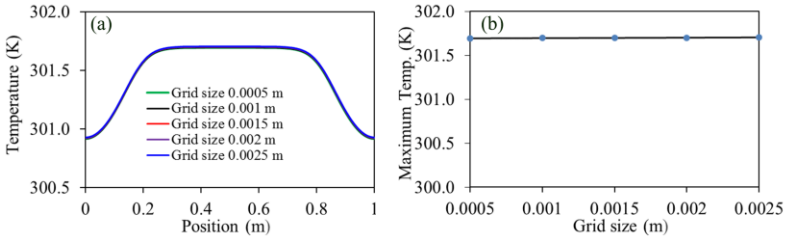


FIGURE 3. Grid independent test: (a) temperature profile at the bottom wall for different grid size, and (b) variation of maximum temperature at the bottom wall with different grid size

*3.1 Effect of Crack Size:* At first, crack at a position of 0.1 m above the bottom surface with four different size (0.2, 0.4, 0.6 and 0.8 m) are considered to study the effect of crack size on the temperature profiles and distribution. Effect of crack size on the temperature profile in the bottom wall considering Case 'A' and 'C' is shown in Figure 4a and 4b, respectively. From this figure, it is clear that temperature profile significantly varies with the crack size.

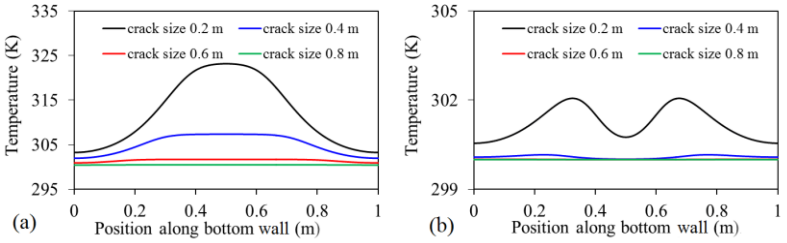


FIGURE 4. Bottom wall temperature profile considering: (a) Case 'A', and (b) Case 'C'

Considering the same case as mentioned above, the temperature profiles along the vertical mid plane are shown in Figure 5a and 5b respectively. It is clear that the boundary conditions mentioned in Case 'A' is able to distinguish the crack size whereas those mentioned in Case 'C' failed to do so.

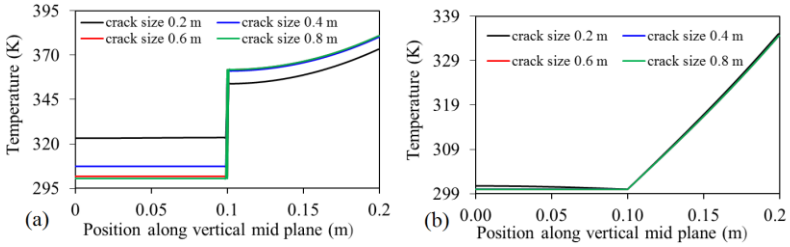


FIGURE 5. Temperature profile at the vertical mid plane: (a) Case 'A', and (b) Case 'C'

*3.2 Effect of Crack position:* Six different positions of the crack (0.05, 0.075, 0.1, 0.125, 0.15 and 0.175 m from the bottom wall) with a size of 0.6 m are considered to study the effect of crack position on the temperature profile at the bottom wall and the vertical mid plane using Case 'B'. Figure 6a and 6b show this effect of the crack position on the temperature profiles.

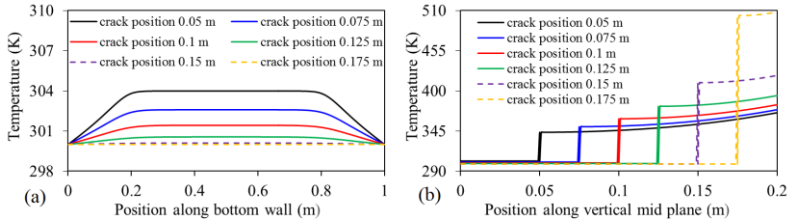


FIGURE 6. Temperature profiles at the (a) bottom wall, and the (b) vertical mid plane

## 4. CONCLUSIONS

An attempt is made to study the effect of size and position of a hairline crack in a homogeneous bulk by 2D conduction analysis using FVM. It can be concluded from the present study that temperature profiles both at the bottom wall and vertical mid plane are well responsive to the size and position of the crack when the boundary condition mentioned in Case 'A' and Case 'B' are considered. Case 'C' and 'D' are effective to capture the effect of size and position of the crack, only when temperature profiles at the bottom wall are considered (temperature profile at the vertical mid plane fails to capture the variation of size and position of the crack). At a fixed position, as the crack size increases, bottom wall temperature reduces and consequently, temperature profiles are becoming flat. Similarly, when a crack of fixed size moves towards the heat source, the amount of heat reaching the bottom wall decreases and subsequently, temperature profiles are becoming flat.

## REFERENCES

[1] D.L. Cements, Steady heat conduction in an anisotropic slab containing a crack, *International Journal of Engineering Science*, 17, 1141-49, 1979.

[2] M. Matczyński, Thermoelastic problem of two collinear cracks, *Theoretical and Applied Fracture Mechanics*, 27, 175-91, 1997.

[3] S. Itou, Thermal stresses around a crack in the nonhomogeneous interfacial layer between two dissimilar elastic half-planes, *International Journal of Solids and Structures*, 41, 923-45, 2004.

[4] Y.C. Shiah, and Y. Shi, Cements, Anisotropic heat conduction across an interface crack/defect filled with a thin interstitial medium, *Engineering Analysis with Boundary Elements*, 30, 325-37, 2006.

Fifth International Conference on Computational Methods for Thermal Problems
THERMACOMP2018, July 9-11, 2018, Indian Institute of Science, Bangalore, INDIA
*N. Massarotti, P. Nithiarasu, Pradip Dutta and C. Ranganyakalu (Eds.)*

# Numerical Analysis of Critical Heat Flux during Subcooled Boiling for a Vertically Downward Flow

**Sumanth Theeda[1], Siva Subrahmanyam Mendu[2], Rajeshwar Sripada[3], Veeredhi Vasudeva Rao[4]**

[1,2](Department of Mechanical Engineering, MVGR College of Engineering, India 535005,

theedasumanth9@gmail.com, m.sivasubrahmanyam@mvgrce.edu.in)

[3,4](University of South Africa, Johannesburg, South Africa,

rajeshwar33482@gmail.com, v_vasudevarao@yahoo.com)

## ABSTRACT

Two-phase flows are encountered in various applications in power plants, chemical plants and nuclear industry. The current day industries requirement is to operate these two-phase flow equipments over a wide range of operating conditions and is subjected to harsh environment driven by high temperature corrosive gases. This prompts for usage of expensive materials and thermal coatings to protect from tube burnout and thereby extend the life, without compromising on cost. In the context of modernization or up-gradation of the existing equipment, the transportation limits put several constraints on making the heat exchanger fatter or taller, thereby adding to the complexity. To make these heat exchangers compact without compromising on its efficiency, one should look for alternative ways. One of the ways of doing it is to increase the number of passes by routing tubes in such a way that the two-phase mixture travels downwards and upwards in a periodical manner. This brings in additional risks of premature tube burnout by reaching Critical Heat Flux limit, two-phase flow instabilities and other potential risks, especially when the flow takes place in a vertically downward direction. Critical Heat Flux (CHF) or post burnout refers to the sudden decrease in heat transfer coefficient for a surface on which evaporation or boiling occurs. Exceeding this heat flux causes the replacement of liquid adjacent to the heat transfer surface with a vapor blanket. This blanket acts as a barrier to heat flow from the heat dissipating body, resulting in possible catastrophic failure. Hence accurate estimation of CHF risk is a mandate not only from performance or life perspective, but also more important from safety perspective. Further, conducting numerous experiments to understand the flow patterns and the CHF in vertically downward two-phase flow is time consuming and expensive. All these constraints give an opportunity to leverage the numerical tools that are relatively less expensive and are quicker to estimate CHF.

The present study focuses on the numerical analysis carried in a vertically downward subcooled flow using finite volume based commercial software Fluent by ANSYS Inc. Rensselaer Polytechnic Institute (RPI) boiling model in Fluent is used to predict the void fraction and CHF in a vertically downward flow. Turbulence effects are modelled by Shear Stress Transport (SST) k-ω and k-ε models. Most of the numerical work carried till date on two-phase flows focused on flow in vertically upward direction or in horizontal direction. Hence, the numerical models are validated against the data provided in open literature for vertically upward flows. The same models are extended for vertically downward subcooled flows in present investigation and the results for upward and downward flows are compared.

**Keywords:** *Computational Fluid Dynamics, RPI Boiling Model, Vertically Downward Two-Phase Flow, Void Fraction, Critical Heat Flux.*

## 1. INTRODUCTION

Significant amount of experimental work was done on two-phase flows in last 50 years focusing on understanding the flow patterns, estimating the void fractions and determining the CHF limits for the safety. Most of the investigations in this field were primarily focused on understanding the fluid flow patterns and heat transfer in horizontal tubes, inclined tubes, and in vertical tubes with flow directed upwards and covering wide range of operating conditions. Hall & Mudawar compiled a database, which was based on previous investigators as well based on their own investigations [1, 2]. Bartolomei and Chanturiya [4] conducted the experiments with pressurized water. Their

experimental data was used for validation by many researchers. DEBORA experiments [7] also mark their importance in evaluating the CHF for R-12 refrigerant at high pressures to 2.62 MPa. Recent developments in computational facilities encouraged researchers to solve the governing equations for two-phase flows numerically. Ribeiro *et al.* [3] had adopted the experiments of Bartolomei and Chanturiya [4] and solved them numerically using commercially available FLUENT CFD code. The results were in good agreement with experimental data. Naveen and Veluswamy [6] had reported numerical solutions for Sodium boiling using FLUENT CFD code. They validated their model with Bartolomei and Chanturiya [4], and with DEBORA experiments [7]. Vyskocil and Macek [5] documented the numerical results generated using NEPTUNE_V2 CFD code and found that their results were satisfactory. They reported that NEPTUNE code was not suitable for solving low pressure cases and high heat flux cases due to numerical instabilities.

However, there were only limited investigations carried on vertically downward flows, where the buoyancy of the bubbles competes with the gravity of the liquid, resulting in the most complex flow behavior. The investigations in vertically downward flow were focused primarily on understanding the flow pattern maps and in estimating the void fractions [8]. A few investigations were focused on understanding the CHF for vertically downward flows experimentally [9, 10, 11]. To the best of the author's knowledge, hardly any numerical investigations were carried in vertically downward subcooled flows numerically. This gives an opportunity to investigate the void fraction and CHF in a vertically subcooled flow using numerical tools. This was the motivating factor for current investigations.

## 2. NUMERICAL ANALYSIS

This section briefly discusses the numerical analysis method carried for current investigations.

**Void Fraction Validation:**

The models were validated with the experimental work done by Bartolomei *et al.* [4] for the void fraction. The geometry was modelled using the Design Modeller software available in ANSYS and the analysis was carried with FLUENT. A steady-state, axi-symmetric model was considered for current simulations. The properties were assumed to be temperature dependent. Meshing was done in ICEM CFD of ANSYS Inc. Grid independent study was carried before finalizing the simulations. Turbulence effects were modelled using k-ω turbulence model. Table 1 shows the geometric and operating conditions used for current simulations.

Table 1. Geometric and operating conditions for RPI model

| **Parameter** | **Bartolomei *et al.* [4]** |
|---|---|
| **Fluid** | Pressurized Water |
| **Length of Pipe** | 2 m |
| **Inner Diameter** | 15.4 mm |
| **Heat Flux** | 570 kW/m$^2$ |
| **Mass Flux** | 900 kg/m$^2$/s |
| **Inlet Sub-cooling** | 60 K |
| **Operating Pressure** | 4.5 MPa |

### Critical Heat Flux validation for upward flow and extension to downward flow

Critical Heat Flux for upward flow was validated with the work done by Hoyer [12]. The RPI boiling model available in Fluent was used in current investigations for validation. Table 2 shows the geometric and operating conditions used in the present simulation study.

Table 2. Geometric and operating conditions for CHF model

| Parameter | Hoyer [12] |
|---|---|
| **Fluid** | Pressurized Water |
| **Length of Pipe** | 7 m |
| **Inner Diameter** | 10 mm |
| **Heat Flux** | 797 kW/m$^2$ |
| **Mass Flux** | 1495 kg/m$^2$/s |
| **Inlet Sub-cooling** | 10 K |
| **Operating Pressure** | 7.01 MPa |

## 3. RESULTS

### Void Fraction & Wall Temperature Validation for Upward Flow

The vapour void fraction prediction with numerical tool is validated with the work done by Bartolomei and Chanturiya [4][1] for vertically upward flow. Circumferential average of vapor void fraction along the length of the tube is presented. Figure 1 shows the comparison of vapor void fraction between current numerical analysis and experimental data. As it is evident, the results obtained are in good agreement with the experimental values documented by Bartolomei and Chanturiya [4].

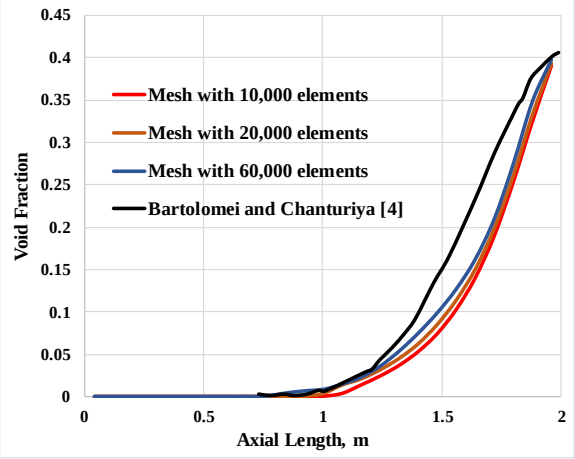


Fig. 1 Validation of vapor void fraction

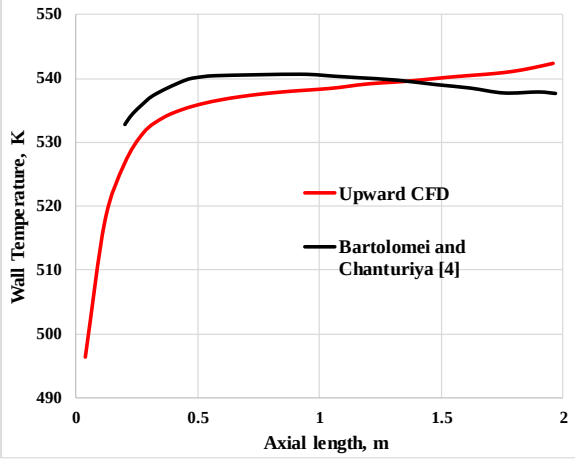


Fig.2 Validation of wall temperature

Figure 2 shows the comparison of wall temperature from current numerical analysis with the experimental data. The results show that the wall temperature prediction trends are in agreement

[1] Data taken from Riberio *et al* [3]

with the experimental data for upward flow. However, the wall temperature variations exist and is mainly due to the wall treatment procedures adopted in the turbulence modelling.

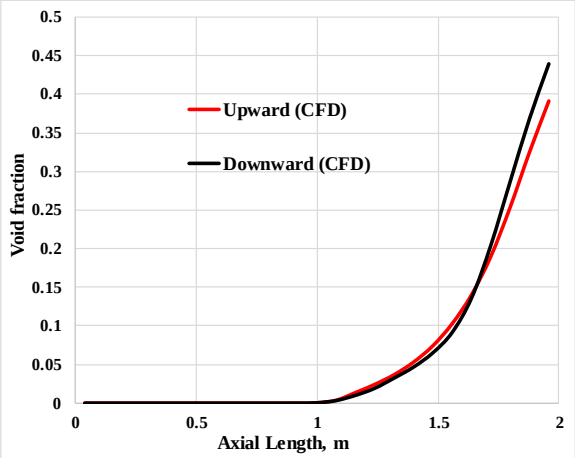


Fig. 3 Prediction of void fraction in downward flow

The validated void fraction model used for upward flow is extended to predict the void fraction for downward flow. The comparison of void fraction for upward and downward flows are shown in Fig. 3. The predicted results show that the void fraction at outlet is higher in downward flow than in upward flow, as expected and as reported most of the previous investigators.

### Critical Heat Flux

This section presents the results obtained based on CHF investigations carried using Fluent. Fig. 4(a) shows the Critical Heat Flux validation for upward flow with experimental data in open literature [12]. As it is evident, the numerical model prediction of critical heat flux defined by sudden rise in wall temperature, is in good agreement with experimental data. Figure 4(b) shows the CHF prediction for upward flow and downward flow based on the extension of validated numerical upward flow CHF model. As it is observed from Fig. 4(b), there is hardly any difference in CHF for upward flow and downward flow at high mass fluxes and at high pressures.

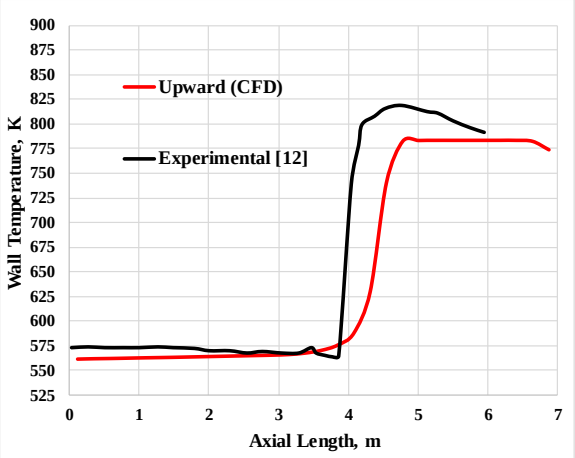


Fig. 4(a) Validation of CHF model with experiment

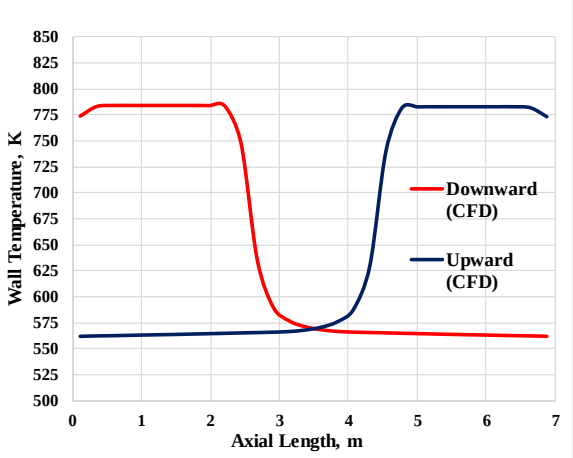


Fig. 4(b) Comparision of CHF in upward and downward flow

## 4. CONCLUSIONS

The numerical model for two-phase flow has been validated against the experimental data in open literature for void fraction, wall temperature and CHF in upward flow at high pressure. The numerical predictions are in good agreement with the experimental data for upward flow. These models are then extended to predict void fraction and CHF in a vertically downward subcooled flow. As expected, the void fraction at the outlet is higher

for downward flow compared to upward flow, where as there is no significant change in CHF for upward and downward flow at high pressure and at high mass fluxes. This indicates that the flow direction has minimal impact at high mass fluxes and at high pressures. The available numerical models for vertically upward flow could be easily extended to model vertically downward flows at high mass fluxes. Further investigations are necessary to validate the suitability of these models for vertically downward two-phase flows with low mass fluxes and at low pressures.

## 5. ACKNOWLEDGEMENT

The authors acknowledge the support provided by Jagat Paridala, Ravi Kumar Sambangi, Akash Varma Rudraraju, Venkateswar Rao Ragina from MVGR College of engineering.

## REFERENCES

[1] Hall, David D., and Issam Mudawar. "Critical heat flux (CHF) for water flow in tubes—I. Compilation and assessment of world CHF data." International Journal of Heat and Mass Transfer 43.14 (2000): 2573-2604.

[2] Hall, David D., and Issam Mudawar. "Critical heat flux (CHF) for water flow in tubes—II.: Subcooled CHF correlations." International Journal of Heat and Mass Transfer 43.14 (2000): 2605-2640.

[3] Ribeiro, Guilherme & Braz Filho, Francisco. “Assessment of Interfacial Heat Transfer Models Under Subcooled Flow Boiling.” (2017).

[4] Bartolomei, G. G., and V. M. Chanturiya. "Experimental study of true void fraction when boiling subcooled water in vertical tubes." Thermal Engineering 14.2 (1967): 123-128.

[5] Vyskocil, L., and J. Macek. "Boiling flow simulation in Neptune CFD and Fluent codes." XCFD4NRS, Grenoble, France (2008): 10-12.

[6] Raj, M. Naveen, and K. Velusamy. "CFD Simulation of Sodium Boiling in Heated Pipe using RPI Model.", Proceedings of the 2nd World Congress on Momentum, Heat and Mass Transfer (MHMT’17), Barcelona, Spain – April 6 – 8, ICMFHT, (2017).

[7] Garnier, J., E. Manon, and G. Cubizolles. "Local measurements on flow boiling of refrigerant 12 in a vertical tube." Multiphase Science and Technology 13.1&2 (2001).

[8] Bhagwat, Swanand Madhav. “Study of flow patterns and void fraction in vertical downward two phase flow”. Oklahoma State University, 2011.

[9] Ruan, S. W., G. Bartsch, and S. M. Yang. "Characteristics of the critical heat flux for downward flow in a vertical tube at low flow rate and low pressure conditions." Experimental thermal and fluid science 7.4 (1993): 296-306.

[10] Kaichiro, Mishima, Nishihara Hiedeaki, and Michiyoshi Itaru. "Boiling burnout and flow instabilities for water flowing in a round tube under atmospheric pressure." International journal of heat and mass transfer 28.6 (1985): 1115-1129.

[11] Shen, Zhi, et al. "Experimental investigation on heat transfer characteristics of smooth tube with downward flow." International Journal of Heat and Mass Transfer 68 (2014): 669-676.

[12] Hoyer, Norbert. "Calculation of dryout and post-dryout heat transfer for tube geometry." International journal of multiphase flow 24.2 (1998): 319-334.

[13] Sudo, Yukio, et al. "Experimental study of differences in DNB heat flux between upflow and downflow in vertical rectangular channel." Journal of Nuclear Science and Technology 22.8 (1985): 604-618.

[14] Mishima, Kaichiro, and Hideaki Nishihara. "Effect of channel geometry on critical heat flux for low pressure water." International journal of heat and mass transfer 30.6 (1987): 1169-1182.

# NUMERICAL STUDY OF MAGNETOHYDRODYNAMIC THREE DIMENSIONAL FLOWS AND HEAT TRANSFER OF OLDROYD-B NANOFLUID OVER A BIDIRECTIONAL STRETCHING SURFACE

**Sumit Gupta, Kalpna Sharma**
Department of Mathematics, Swami Keshvanand Institute of Technology, Management and Gramothan, Ramnagaria, email: sumit.gupta@skit.ac.in

**Third Author**
Department of Mathematics, Manipal University Jaipur, Dehmi-Kalan, Jaipur-Ajmer Expressway, Jaipur, 303007, Rajasthan, India,

ABSTRACT

In this paper, magnetohydrodynamic (MHD) three dimensional flow of Oldroyd- B nanofluid over a bidirectional stretching surface is analyzed. By using appropriate similarity transformation, the governing partial differential equations are reducing into coupled nonlinear ordinary differential equation. These nonlinear differential equations are then solved by the Differential Transform Method (DTM) combined with Padè approximation (DTM- Padè). The influence of emerging physical parameters namely, Deborah numbers $\beta_1$ and $\beta_2$, Prandtl number Pr, Brownian motion parameter $N_b$ and thermophoresis parameter $N_t$ on the fluid velocity, temperature and concentration profile are depicted through graphs. Also a comparative study between DTM and numerical method are presented by graph and other semi-analytical techniques through tables. It is noticed that DTM can overcome the earlier restriction, assumptions and limitation of traditional perturbation method. The main advantage of this method is that DTM can be applied directly to nonlinear differential equations without using linearization and round-off errors and cannot be affected by error associated to discretization.

**Key Words:** *Heat Transfer, DTM-Pade, Numerical Solution, Oldroyd B nanofluid.*

# WETTABILITY MODULATED EVAPORATION DYNAMICS OF SESSILE LIQUID DROPLETS

Sumit Kumar[1] and Suman Chakraborty[1, 2]

[1]Advanced Technology Development Centre,
Indian Institute of Technology Kharagpur, Kharagpur-721 302, West Bengal, India.
[2]Department of Mechanical Engineering,
Indian Institute of Technology Kharagpur, Kharagpur-721 302, West Bengal, India.

## ABSTRACT

In this paper, we have developed a simple and effective model to understand the evaporation dynamics of sessile droplets. The volume evolution characteristics of sessile liquid droplet in stick-slip (SS) mode is investigated on smooth surfaces with different wettability. The volume evolution of drying droplet has been presented for different receding angles. This study reveals that the droplet volume change with time on hydrophilic surface is different from the superhydrophobic surface.

**Key Words:** *droplet evaporation, stick-slip, CCR mode, CCA mode*

## 1. INTRODUCTION

In recent years, the droplet evaporation on solid surface has been a subject of very much interest not only due to its fundamental scientific importance but also of significance in a wide variety of practical applications such as DNA mapping, inkjet printing, bio-sensing, droplet based microfluidics, and hot-spot cooling [1-3]. In the last few decades, numerous work have been reported in literatures for the sessile droplets either evaporating in single CBD mode or single CCA mode [1-7]. However, the investigations on the influence of initial contact angle and the receding contact angle on the volume evolution of an evaporating sessile droplet in stick-slip mode is still remained elusive. In this paper, we report a model which predicts the volume evolution of a sessile liquid droplet in stick-slip mode. We further make a detail analysis of the evaporation behaviour of a sessile droplet in the stick-slip mode with a wide range of receding contact angles on hydrophilic and superhydrophobic surface.

## 2. THEORY

The well celebrated pure-diffusion model [4] is used in this paper to develop the volume evolution of liquid droplet drying in stick-slip mode. The droplet shape is assumed to be a spherical cap [4, 6]. The volume of sessile droplet can be obtained from

$$V = 8\pi D^3 f(\beta) \tag{1.1}$$

The evaporation rate of a sessile droplet can be expressed as

$$\frac{dV}{dt} = -\frac{\pi D^3}{8(1+\cos\beta)^2}\frac{d\beta}{dt} + \frac{1}{8}\pi D^2 \frac{(\sin^3\beta - 3\cos\beta + 2)}{\sin^3\beta}\frac{dD}{dt}, \tag{1.2}$$

Further, the volume evaporation rate of sessile liquid droplets can be obtained by the analytical solution proposed by Papov [7] and it is given as:

$$\frac{dV}{dt} = -\frac{\pi D \chi (C_S - C_\infty)}{\rho} g(\beta) \tag{1.3}$$

Where $\chi$ is the vapour diffusivity, $C_S$ is the vapor concentration at the droplet surface, $C_\infty$ is the vapor concentration of far-field air, $\rho$ is the liquid density, and $g(\beta)$ is a function of contact angle $\beta$ and is given as

$$g(\beta) = (1+\cos\beta)^2 \left\{ \tan\frac{\beta}{2} + 8\int_0^\infty \frac{\cosh^2(\beta\tau)}{\sinh(2\pi\tau)} \tanh[\tau(\pi-\beta)] \mathrm{d}\tau \right\} \tag{1.4}$$

Since the closed form of the eq. (1.3) is not possible, and therefore, numerical integration techniques has to be used to calculate $g(\beta)$. In the past decades, several approximate expressions for eq. (1.4) have been proposed [4] depending upon the application fields. Here, we have used the expression of $g(\beta)$ proposed by Picknett and Bexon [6], which is

$$g(\beta) = \frac{0.00008957 + 0.6366\beta + 0.1161\beta^2 - 0.08878\beta^3 + 0.01033\beta^4}{\sin\beta} \tag{1.5}$$

The expression for the volume evaporation rate of sessile liquid drop, after substituting the Eq. (1.5) into Eq. (1.3), can be written as follows:

$$\frac{dV}{dt} = -\frac{\pi D \chi (C_S - C_\infty) 0.00008957 + 0.6366\beta + 0.1161\beta^2 - 0.08878\beta^3 + 0.01033\beta^4}{\rho \sin\beta} \tag{1.6}$$

Under the pinned mode of a drying droplet, the contact angle decreases while base diameter remains unchanged with time. It means $D=D_0$. The comparison of Eq. (1.6) with Eq. (1.2) and then after integration, the time evolution of contact angle in CBD mode is expressed as

$$t(\beta) = \frac{\rho D_0^2}{32\chi(C_S - C_\infty)} [G(\beta_0) - G(\beta)], \tag{1.7}$$

In the equation (1.7), $\beta_0$ is the initial contact angle of the sessile liquid drop, and the function $G(\beta)$ can be presented as

$$G(\beta) = \int \frac{\sin\beta}{(0.00008957 + 0.6366\beta + 0.1161\beta^2 - 0.08878\beta^3 + 0.01033\beta^4)} d\beta. \tag{1.8}$$

The expression of base diameter evolution in CCA mode can be obtained by taking the temporal change of contact angle equal to zero, i.e. $\frac{d\beta}{dt} = 0$. The comparison of Eq. (1.6) with Eq. (1.2) and after integration, it gives the relationship between base diameter and time in constant contact angle mode, i.e.,

$$t(D) = \frac{3}{16} \frac{\rho}{(C_S - C_\infty)\chi} \frac{f(\beta_0)}{g(\beta_0)} (D_0^2 - D^2) \tag{1.9}$$

The evolutions of contact angle and base diameter of sessile drop with time in stick-slip mode (After combining the Eq. (1.7) and Eq. (1.9)) can be obtained as

$$t(\mathrm{D}) = \frac{\rho D_0^2}{32\chi(\mathrm{C}_S - \mathrm{C}_\infty)}[\mathrm{G}(\beta_0) - \mathrm{G}(\beta_{rec})] + \frac{3}{16}\frac{\rho}{\chi(\mathrm{C}_S - \mathrm{C}_\infty)}\frac{f(\beta_{rec})}{g(\beta_{rec})}(D_0^2 - \mathrm{D}^2), \quad (1.10)$$
$$\beta = \beta_{rec},\ D < D_0$$

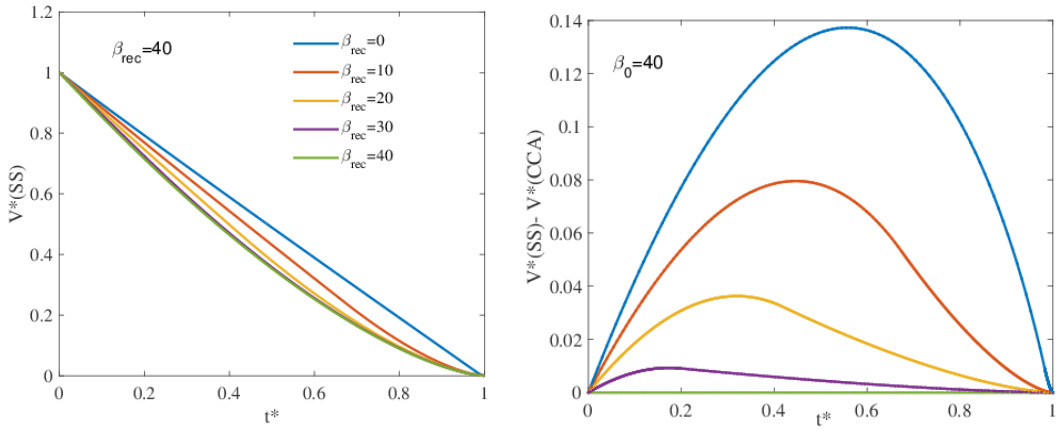


Fig. 1 The volume evolution of sessile droplet on hydrophilic surface (β=40 deg) for different receding angles ($\beta_{rec}$)

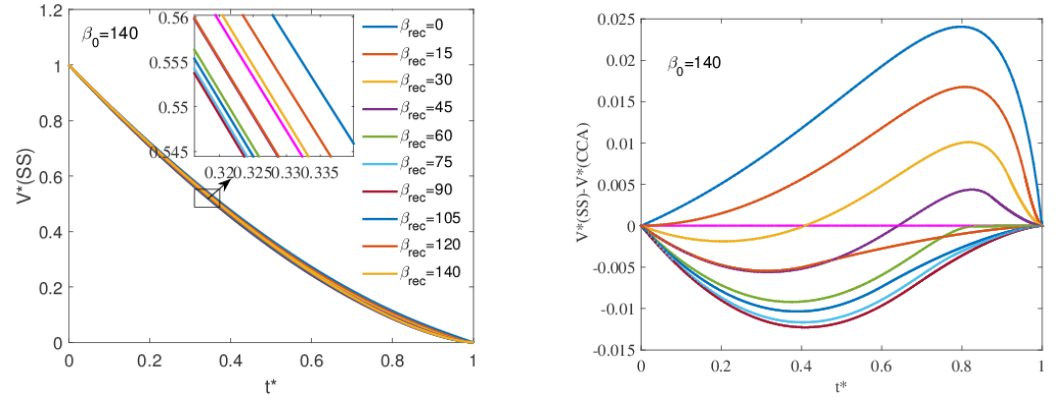


Fig. 2 The volume evolution of sessile droplet on hydrophobic surface (β =140 deg) for different receding angles ($\beta_{rec}$)

$$t(\beta) = \frac{\rho D_0^2}{32\chi(\mathrm{C}_S - \mathrm{C}_\infty)}[\mathrm{G}(\beta_0) - \mathrm{G}(\beta)],\ \beta_{rec} < \beta < \beta_0,\ D = D_0 \quad (1.11)$$

Eq. (1.1), Eq. (1.10), and Eq. (1.11) have been solved numerically to get the volume evolution of sessile liquid droplet.

## 3. RESULTS AND DISCUSSION

The Fig. 1 and the Fig. 2 show the non-dimensional volume evolution with time for hydrophilic surface and superhydrophobic surface in combined CBD-CCA mode (stick-slip mode). $V^*$(SS) and $V^*$(CCA) (Fig. 1 and Fig. 2) are non-dimensional volume in stick-slip mode and single CCA mode, respectively. The dimensional time is represented as $t^*$. This investigation reveals that the initial contact angle has a significant influence on the evaporation dynamics of droplet in SS mode. Further, it is observed that the volume evolution is constrained by the two extreme modes when droplet evaporates on hydrophilic surface (β=40 deg). However, the volume evolution is not constrained by the CBD and CCA modes for the droplet evaporating on the superhydrophobic surface (β=140 deg). During the droplet evaporation, the influence of receding angles on the hydrophilic and superhydrophobic surface are different. On the hydrophilic surface, the volume evolution of stick-slip mode departs from that of the single CBD mode and slowly reaches the CCA mode with the increasing receding angle. On the superhydrophobic surface, the influence of receding angles on the volume evolution is significantly different than that of hydrophilic surface.

## 4. CONCLUSIONS

In the present work, we report an effective and simplified model for the volume evolution of sessile liquid droplets drying in CBD-CCA (STICK-SLIP) mode. Using this model, we have investigated the temporal volume evolution of evaporating droplet in SS mode on both hydrophilic and superhydrophobic surface for a wide range of receding contact angles. The volume change of sessile liquid droplet on hydrophilic surface is constrained by the two extreme modes. However, this trend is significantly different for superhydrophobic surface. Findings reported in this work may provide some momentum in the rapid progress of the various fields such as DNA mapping, coating technologies, medical diagnostics, and microfluidics devices.

## REFERENCES

[1] N. kumari, and S. V. Garimella, Characterization of the heat transfer accompanying electrowetting or gravity-induced droplet motion, *International Journal of Heat and Mass Transfer*, 54, 4037-4050, 2011.

[2] H. K. Dhavaleswarapu, C. P. Migliaccio, S. V. Garimella, and J. Y. Murthy, *Experimental Investigation of Evaporation from Low-Contact-Angle Sessile Droplets*,26, 880-888, 2010.

[3] Q. Li, Y. T. Zhu, I. A. Kinloch, and A. H. Windle, Self-Organization of Carbon Nanotubes in Evaporating Droplets, *Journal of Physical Chemistry B*, 110, 13926-13930, 2006.

[4] D. Brutin, and V. Starov, Recent advances in droplet wetting and evaporation, Chemical Society Reviews, 47, 558-585, 2018.

[5] T. A. H. Nguyen, and A. V. Nguyen, On the Lifetime of Evaporating Sessile Droplets, *Langmuir*, 28, 1924-1930, 2012.

[6] D. Hu, and H. Wu, Volume evolution of small sessile droplets evaporating in stick-slip mode, *Physical Review E*, 93, 042805-1-9, 2016.

[7] A. M. Cazabat, and G. Guena, Evaporation of macroscopic sessile droplets, *Soft Matter*, 2591-2612, 2010.

Fifth International Conference on Computational Methods for Thermal Problems
THERMACOMP2018, July 9-11, 2018, Indian Institute of Science, Bangalore, INDIA
*N. Massarotti, P. Nithiarasu, Pradip Dutta and C. Ranganyakalu (Eds.)*

# CFD BASED COMBUSTION MODELLING FOR MITIGATING FLAME IMPINGEMENT ISSUE IN A FURNACE

**Suranjan Sarkar, Aditya Singh and Sumitra Ghosh**
Shell Technology Centre Bangalore, Shell India Markets Private Limited, Plot 7, Bangalore Hardware Park, Devanahalli Industrial Park, Bande Kodigehalli, Bengaluru, India 562149,
Suranjan.Sarkar@shell.com, Aditya.Singh@shell.com, Sumitra.Ghosh@shell.com

## ABSTRACT

A furnace in one of the Shell petrochemical complex developed hot spots due to burner flame impingement. Deep understanding and mitigation of the root cause for burner flame impingement on radiant tubes was required as hot spots posed tube integrity risk with safety ramifications. A computational fluid dynamics (CFD) study was proposed to understand the dynamics of combustion, and flue gas thermal profile in the firebox. This study was successful in identifying the causes of flame impingement and helped in validating effectiveness of proposed medium and long-term solutions to mitigate process safety and production risks involved.

**Key Words:** *CFD, Combustion, Heat Transfer, Numerical Modelling, High Performance Computing, Flame Impingement, Furnace, Process Safety, Primary air, Low NOx burners, Air staging.*

## 1. INTRODUCTION

A furnace in a Shell Petrochemical complex developed hot spots in radiant coil due to burner flame impingement. The flames were also showing patterns of lack of combustion air as firebox appeared smoky in certain operating conditions. The hot spots and impinging flames posed potential threat to production and process safety in that plant as it can cause thermal fatigue failure of radiant cell tubes resulting in a tube leak. After considering several possible causes of flame impingement, it was proposed to carry out a detailed CFD study to model and understand the dynamics of combustion and flue gas thermal profile in the firebox. The furnace is provided with low NOx burners using combustion air staging technique. While primary air helps significantly in combustion and maintaining steady flame, staging air helps in reducing NOx emissions and might have destabilizing effects on flame shapes at times. Large amount of low calorific value waste process gas is routed through dedicated staging air nozzles in the burner for incineration of hydrocarbon present in the stream. The objectives of this study were: (i) to understand flame impingement issue using CFD modelling; (ii) to study the effect of swirler, retarder, process waste-gas and staging air on flame pattern and (iii) to validate effectiveness of proposed modifications to mitigate flame impingement.

## 2. INPUTS, GEOMETRY, MODEL SET UP AND SIMULATION

The furnace has three fireboxes. In each firebox, there are four rectangular radiant cells and one burner is provided at the centre of each radiant cell. As the flame impingement issue was observed in all radiant cells, only one cell has been simulated. Both fuel gas and liquid fuel are fired in the burners. For simplicity the CFD model simulated 100% fuel gas firing in the burner considering total burner heat release and combustion air flowrate same as liquid fuel and fuel gas combination firing. This has been achieved by firing an amount of fuel gas which enables equivalent total heat liberation in the burner for combination firing. The total amount of fuel gas enters the firebox through burner throat. Table 1 shows the combustion process conditions used as inputs to the CFD model. In operations the heat flux is calculated based on the surface area of the tubes carrying the fluid. In the CFD model the

tubes are not present. Instead, they have been represented as flat walls enclosing the cell. Therefore, the heat flux into the tubes has been scaled based on the surface area of the walls and applied in CFD.

| Process Parameters | Fuel Gas | Fuel Oil | Equivalent Fuel Gas | Model: Gas through Oil Inlet | Combus-tion Air | Waste Gas |
|---|---|---|---|---|---|---|
| Pressure (barg) | 0.18 | 4.92 | 0.18 | | 0.01 | 0.05 |
| Inlet temperature (°C) | 25 | 126 | 25 | | 217 | 54 |
| Density (kg/m$^3$) | 0.44 | | | 0.44 | 1.18 | 1.06 |
| Viscosity (Pa.s) | 1.05E-5 | | | 1.05E-5 | 2.00E-5 | 1.90E-5 |
| Flowrates per burner (kg/s) | 0.14 | 0.16 | 0.26 | 0.12 | 5.04 | 3.00 |
| Heat flux, operations (kW/m$^2$) | | | | 37.99 | | |
| Scaled heat flux, CFD (kW/m$^2$) | | | | 31.44 | | |

TABLE 1. Process parameters for furnace used in CFD simulation

Figure 1 shows the geometry of a single cell used in the model. The burner is surrounded by 16 nozzles out of which 4 are process waste-gas nozzles and 12 are staging air nozzles. The height of the nozzle protruding from the bottom wall is 200 mm. The fuel oil nozzle is at the centre of the burner. The fuel gas nozzles are arranged in the annulus between fuel oil nozzle and staging air ports. Primary air enters the burner in a radially inward direction through the slots created by the 12 swirlers that produce swirl with the purpose of stabilizing the flame. The burners have a small feature called retarders which breaks larger vortices to provide stability to the flame. The four side walls of cell represent the tubes and a heat flux boundary conditions was applied. The bottom and the top walls were treated with adiabatic boundary conditions. The height of the cell is 11 m and the floor of the cell is 4.6 m x 4.6 m. The opening at the top of the furnace 1.77m x 1.77m and was assigned a pressure outlet boundary condition. All the inlets were assigned mass flow rate boundary conditions where the mass flows were taken from Table 1. There are six such retarders in the burner. The cut planes shown were used to visualize the results. Plane 1 is closer to the process waste-gas nozzles compared to Plane 2. The entire CFD model was set up in ANSYS Fluent v18.1. The flow was solved as steady incompressible turbulent flow with the mass flow rates. Temperature and pressure of the various gases were assigned at the inlet. Realizable K-epsilon model was used to model turbulence. The combustion was solved using non-premixed equilibrium chemistry combustion model. The fuel gas was assigned as the fuel, the combustion air was assigned as the oxydizer and the waste-gas was assigned as the secondary stream. The details of the non-premixed combustion modelling approach [1] was followed.

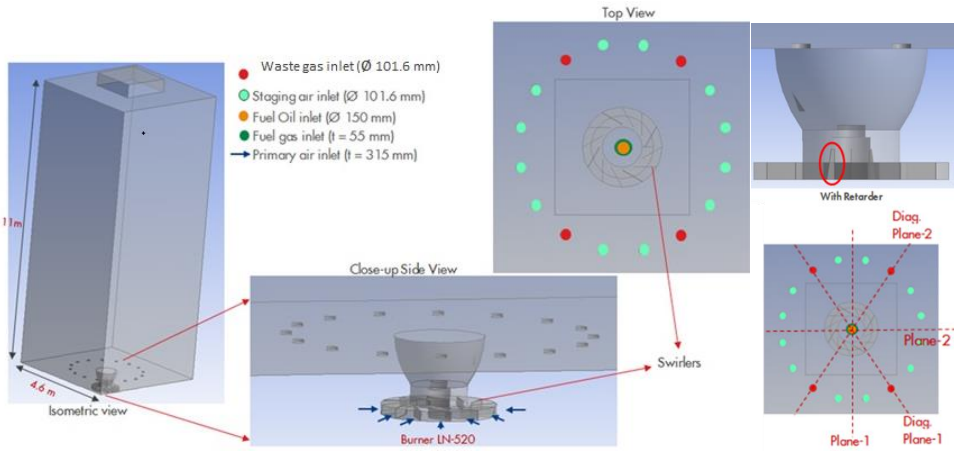


FIGURE 1. Furnace and burner geometry details with position of cut-planes for visualization

The convective, conductive and Radiation heat transfer were accounted for in the model. P1 model was used for radiation. The different cases simulated in this study were discussed in the following results section. Typical number of mesh count was in the order of 3.5 millions for the geometry considered and each simulation took approximately 3-4 days to finish using 36 cores in HPC clusters.

## 4. RESULTS

A hypothetical case was simulated first without the retarders in the burner and in presence of waste-gas. Then a case with retarders was simulated. Figure 2(a) shows the comparison of velocity contours, flow streamlines, and temperature contours with and without retarder. The velocity plume is drastically shortened and spreads on the side without the retarder. The corresponding vortex on the side shortens further in comparison to the case with retarder. This demonstrates the effectiveness of the retarder in stabilizing the flame. Without the retarder the spreading of the temperature plume is clearly visible. Another hypothetical case was simulated without waste-gas to compare and understand the effect of waste-gas on flame stability. Figure 2(b) shows the velocity contours and flow streamlines with and without waste-gas scenarios. The recirculation vortices on the sides of the furnace becomes shorter with the introduction of the waste-gas. This leads to potentially spreading the flame to the sides and leads to the bulging of the plume of velocity magnitude at a lower height. It was observed that the central inertia (flow in the core from the burner) elongates the vortices and the side inertia (flow from the off-gas nozzle) shortens it. These two flows seem to be in competition.

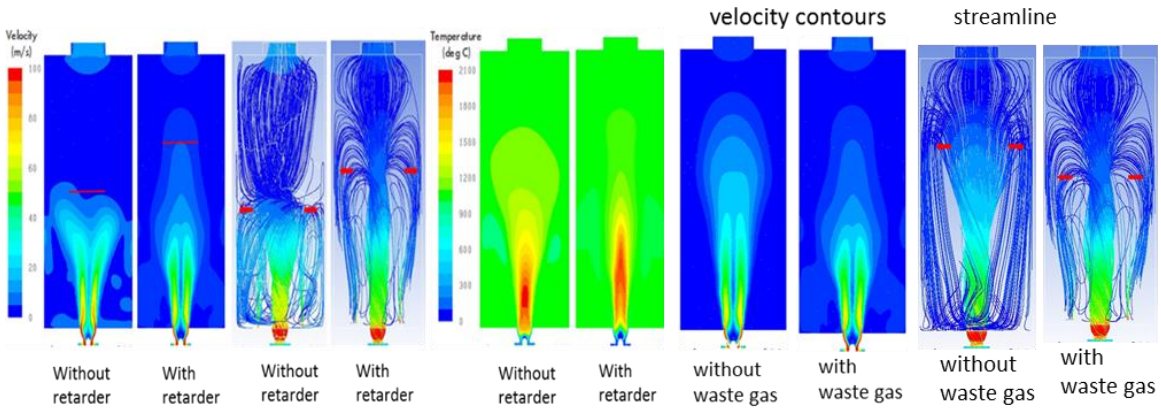


FIGURE 2. Comparison of velocity contour, flow streamlines, temperature contour: (a) with and without retarder; (b) with and without waste-gas

After studying the effect of the retarders and waste-gas, an attempt was made to understand the effect of staging air. The relative amounts of air staging can be altered in the burners by adusting staging air dampers, keeping total air flow the burner same. 14% and 28% of the total combustion air was introduced as staging air in the model. The 14% is a typical value based on plant experience. The 28% staging air rate was chosen to test sensitivity of staging air on flame instability. With introduction of 14% and 28% staging air the velocity plume shortens and spreads sidewise further compared to the case with only waste-gas (results not shown). This could be attributed to reduction in the central intertia and additional side inertia, as part of the primary air now comes out of the staging air nozzles. Since the side intertia from the waste-gas has the potential to destabilize the flame, 5 inch nozzles instead of 4 inch nozzles were tested to reduce the side inertia by reducing the velocity of the waste-gas.The velocity contours elongate and become slender with the 5 inch nozzles (results not shown). This confirms that larger nozzles would help in reducing side inertia to help stabilize the flame.

Further modification of the existing retarder was tested by increasing the width of the current retarder by 50% in anticipation of improving flame instability further. Three cases were simulated with

modified retarder and compared with corresponding original retarder case. The cases are as follows: (i) with waste-gas, 28% staging air and 4 inch nozzle; (ii) with waste-gas, 28% staging air and 5 inch nozzle; and (iii) with waste-gas, no staging air and 5 inch nozzle. Figure 3 compares the velocity contours for the three cases with original and modified retarders. For a particular nozzle size and in presence of 28% staging air, there was marginal improvement of the velocity plume with the modified retarder. Further, if the staging air was completely shut down then the plumes became much better. The case with 5 inch nozzle and modified retarder where staging air was completely shut-off, the plume was observed to be the most stable (marked in the red box as the best solution possible).

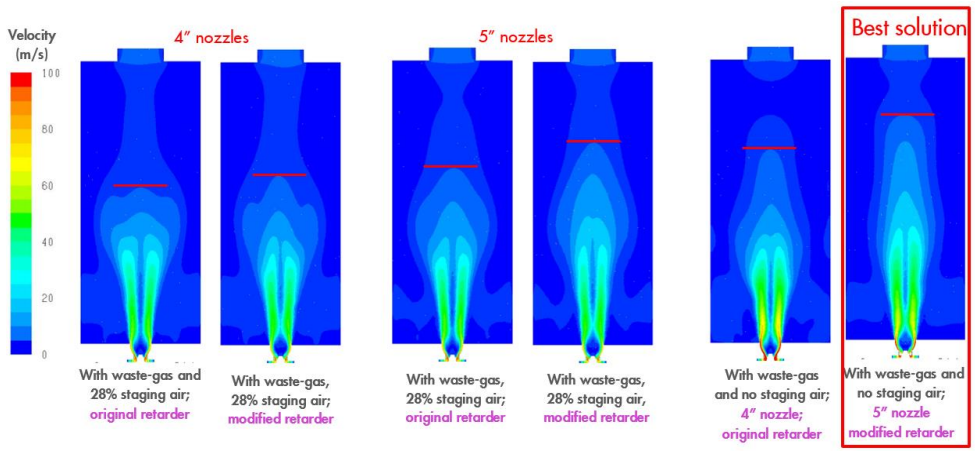


FIGURE 3. Spreading of plumes in the furnace for original and modified retarder for different nozzle sizes and staging air

## 5. CONCLUSIONS AND RECOMMENDATIONS

Based on the results from simulations, following conclusions were made: (i) retarder in the burner stabilizes the flame significantly; (ii) the central inertia (flow in the core from the burner) elongates the vortices in the cell and the side inertia (flow from the waste-gas and staging air nozzle) shortens it. The former stabilizes the flame and the latter spreads it; (iii) the risk of flame spreading increases with decrease in central inertia due to reduction in primary air (lower flowrate of total air or more staging air) and increase in the side inertia due to high velocity of waste-gas; (iv) increase in primary air flowrate is the most important lever to arrest flame spreading; (v) changing the waste-gas and staging air nozzle size from 4” to 5” helps to improve the flame by reducing the side inertia through reduction of velocity; (vi) increasing the width of the retarder makes the flame more stable. The combination of 5-inch nozzle (reduced waste-gas velocity), no staging air (no side inertia) and the modified retarder (increased central inertia) reinforces each other. As a result, it elongates the plume and reduces the bulging on the side significantly. Potential for success in overcoming flame impingement is highest if all the three options can be applied in combination.

Based on these conclusions and operational constraints in the plant, the following are recommended to alleviate the flame impingement problem (in order of priority): (i) increase the primary air flow to the extent feasible; (ii) operate with minimum possible staging air, (iii) modify retarder design (enhanced width of the retarder keeping the slopes unchanged) to reduce flame spreading and (iv) increase the waste-gas nozzle sizes from 4” to 5”.

## REFERENCES

[1] ANSYS Fluent Theory Guide 18.

Fifth International Conference on Computational Methods for Thermal Problems
THERMACOMP2018, July9-11, 2018, Indian Institute of Science, Bangalore, INDIA
*N. Massarotti, P. Nithiarasu, Pradip Dutta and C. Ranganyakalu (Eds.)*

# Investigation for the Improvement of Film Cooling Effectiveness on a High Pressure Turbine aerofoil with Shaped Film Holes

**[1]Batchu Suresh, [2]Palvadi Sai Abhilash, [3]Yagnesh Sharma N, [4]Kesavan V, [5]Kishore Prasad D**

[1]Scientist 'F', [4]Scientist 'G', [5]Scientist 'G', G.T.R.E, DRDO, Bengaluru, Karnataka, India,
[1]batchusuresh@gtre.drdo.in [4]kesavanv@gtre.drdo.in, [5]kishoreprasadd@gtre.drdo.in
[2]M. Tech (Thermal Sciences and Energy Systems), [3]Professor, Manipal Institute of Technology, Manipal, Karnataka, India, [2]saiabhilashpalvadi@gmail.com, [3]yagnesh.sharma@manipal.edu

## ABSTRACT

Modern day gas turbines are operating at gas temperatures which are close to melting temperature of the turbine aerofoil materials. It is essential to cool High Pressure Turbine (HPT) aerofoils such as Nozzle guide vane (NGV) and Rotor blades to improve their creep life to achieve safe life and reliability. Film cooling protects the blade surface from hot gas by providing a cool insulating layer between hot gas stream and the airfoil metal surface. Film cooling effectiveness is a measure of how well the metal surface is protected from the hot gas stream by the layer of cool secondary air. Cooling hole geometry is one of the key parameters which influences the film cooling coverage. Earlier aerofoils were with cylindrical holes, whereas current advanced aero engines are using shaped holes to achive higher effectiveness and better spanwise coverage. The current study is carried out with one of the shaped hole configuration namely, laid back fan shaped hole configuration on HPT turbine rotor blade without rotation. The advantage of using shaped hole over cylindrical hole is brought out in this paper. CFD analysis is carried out using FloEFD software for prediction of film cooling effectiveness for the film holes at one of the peak operating condition. The CFD analysis is validated with measured film cooling effectiveness data. The advantage of using laid back fan shaped hole is brought out from cooling effectiveness point of view. Parametric analysis is carried out for film cooling effectiveness at different blowing ratio (BR) = 1.0 to 2.5, turbulence intensity (Tu) = 5%, 7%, 9 % and fan angle ($\gamma$) = $10^{\circ}$ & $12^{\circ}$ of shaped film hole.

**Key Words:** *Blade cooling, Adiabatic film cooling effectiveness, Cylindrical holes, Laid back fan shaped holes, Blowing ratio.*

## 1. INTRODUCTION

Current gas turbines which are used for aircraft propulsion operate at high temperatures to improve the specific thrust. Increasing the turbine inlet temperatures results in increase of power output of the gas turbines but this is constrained due to materials temperature limit and the creep life of the hot end components. Hot end components like combustion chamber and turbines have to be cooled to achieve higher life and reduce the cycle maintenance cost. Generally the blade is cooled with cylindrical holes,which may not provide better flow spread due to higher exit velocity exposing the blade surface to higher gas temperature.The mixing of the coolant with the free stream is largely influenced by the velocity with which coolant is ejecting out from the hole. Exit velocity and jet lift off can be decreased by having the lower velocity with expanded exit area of shaped film holes.

Bunker [1] reviewed various factors affecting the film cooloing performance for different exit hole shapes and summarized the work carried out for different hole geometries. Michael et al. [2] studied heat transfer coefficients near the shaped film hole and found that heat transfer coefficients are lower and have better film coverage compared to cylindrical holes.The exit velocity is low and gives higher film cooling effectiveness for laidback fan shaped holes when compared to cylindrical and fans shaped holes. Colban et al. [3] studied the performance of shaped holes near the shower head region on the pressure and suction sides and found that first row of shaped holes showed jet lift off on both sides due to the curvature effect.

The current study deals with the modelling of Laid Back Fan Shaped (LBFS) holes at discrete location on the aerofoil surface and compare the film cooling effectievnss results with cylindrical holes without rotation.The advantage of using laidback shaped film holes in terms of film cooling effectiveness with reference to the coolant mass flow is highlighted.

## 2. METHODOLOGY

The computational flow domain shown in Figure.1 was modelled using SolidWorks software, meshing and analysis is carried out using FloEFD [4] commercial software. The boundary conditions are mainstream inlet pressure and temperature, coolant passage inlet pressure and temperature, mainstream outlet pressure. No slip boundary condition is given at the test section walls. The geometric model of the blade aerofoil with cylindrical film cooling holes is shown in Figure 2. CFD analysis was carried out for estimation of static pressure distribution and film cooling effectiveness over the aerofoil with the cylindrical holes on pressure surface are compared with experimental data for validation.

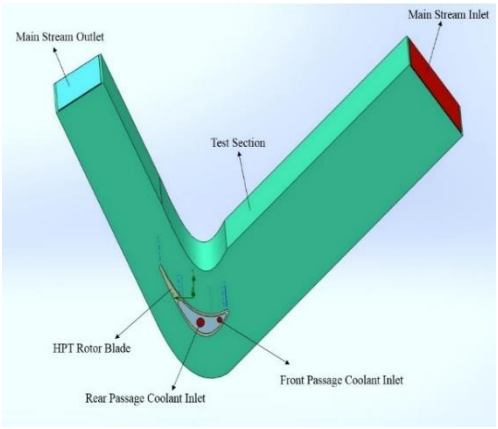


Figure 1 Computational Flow Domain

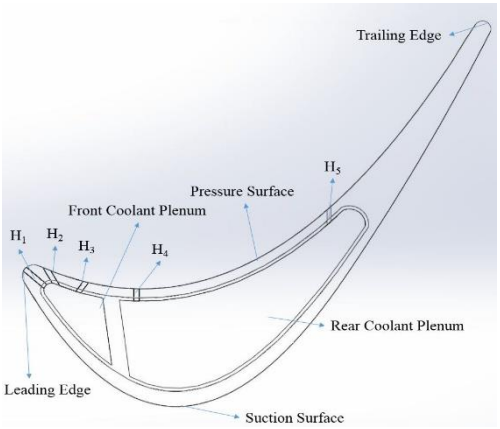


Figure 2 Aerofoil Pressure Surafce with cylindrical holes

Film Cooling Effectiveness ($\eta$) is a non-dimensional parameter which is used to define the performance of film cooling. It is defined mathematically as

$$\eta = \frac{(T_\infty - T_{aw})}{(T_\infty - T_c)} \quad (1)$$

Where $T_\infty$- Hot gas temperature, $T_{aw}$- Adiabatic wall temperature, $T_c$- Coolant temperature

Two cooling configurations are considered for the aerofoil with cylindrical and shaped holes and are shown in Figure.3 and Figure.4 respectively. Figure.3 shows aerofoil with eight rows of cylindrical holes of which five rows of holes ($H_1$,$H_2$, $H_3$, $H_6$, $H_7$) are in the leading edge region, two rows ($H_4$,$H_5$) are on the pressure side and one row ($H_8$) on the suction side of the blade. Figure.4 shows the aerofoil with cylindrical holes at the leading edge and shaped holes $SH_4$, $SH_5$ and $SH_8$ at the same locations of cylindrical holes $H_5$, $H_6$ and $H_8$. The cylindrical and laid back shaped holes are modelled using SolidWorks. There are two coolant chambers which supply coolant to the film holes, front coolant plenum supplies coolant air to the leading edge film holes and the rear plenum supplies to the pressure and suction side film holes. Grid independence study and film cooling effectiveness analysis is carried out for aerofoil with cylindrical holes for configuration shown in Figure.3. CFD analysis is carried out for the configuration shown in Figure.4 to study the film cooling effectiveness. Figure.5 shows geometry model of aerofoil with $SH_4$, $SH_5$ rows of LBFS holes. Figure.6 shows the sectional view of film cooling LBFS holes.

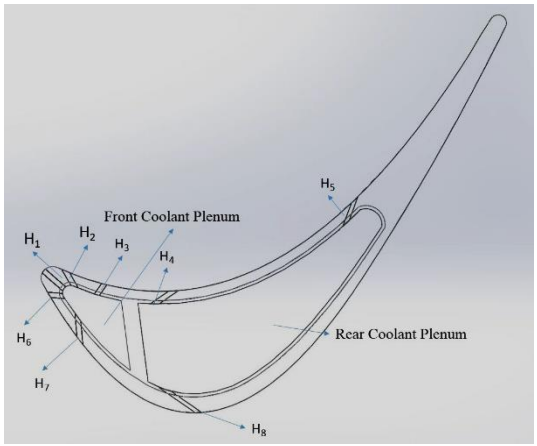


Figure 3 Aerofoil with cylindircal holes

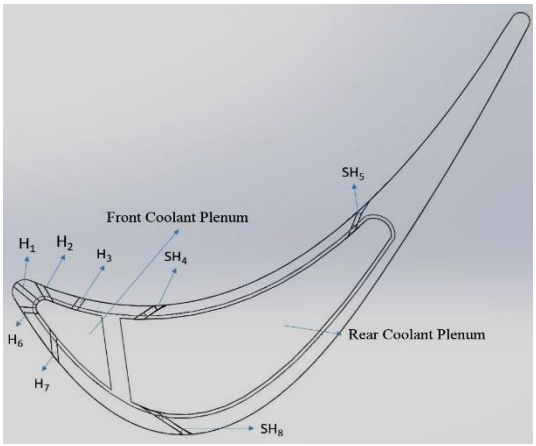


Figure 4 Aerofoil with LBFS holes

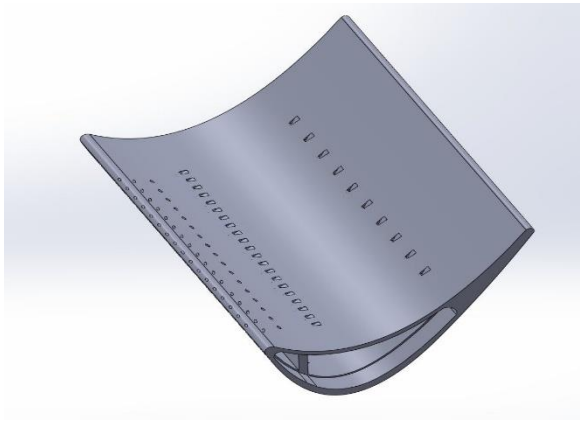

Figure 5 Aerofoil with LBFS holes

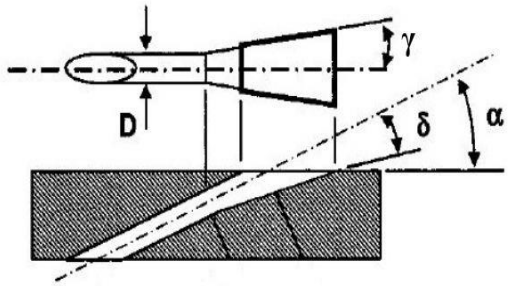


Figure 6 Sectional view of LBFS hole

Where α – Hole inclination angle, γ – Fan Angle, δ – Laid Back Angle

The geometrical features considered for analysis for LBFS holes is with laid back angle (δ) of 12°and for different fan angles.

Parametric study has to be done for the following parameters:

- Fan angle, γ = 10°, 12°.
- Main Stream Turbulence Intensity, TI = 5%, 7%, 9%
- Blowing Ratio, BR = 1.5, 2.0, 2.5

## 3. RESULTS & DISCUSSIONS

The static pressure distribution is estimated from the CFD analysis on blade aerofoil surface with clean profile i.e. without film cooling holes. The mainstream inlet total pressure and temperaure and the mainstream outlet static pressure are given as boundary condition for the analysis. The ratio of local static pressure and inlet total pressure over the blade surface is plotted with respect to ratio of axial legth to chord length. Figure.7 shows the comparision of predicted static pressure distribution with measured value and the measurements are in good agreement with the experimental data.

Static pressure is maximum is at stagnation point on the leading edge region and the lowest is observed on the suction side at throat region.

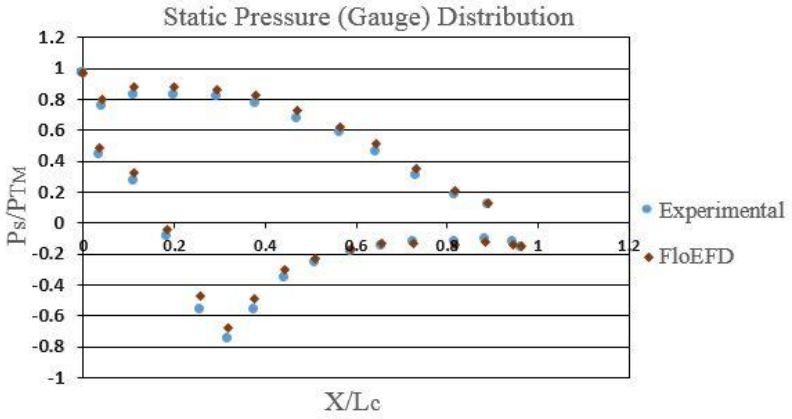


Figure 7 Comparison of measured and predcited static pressure distribution

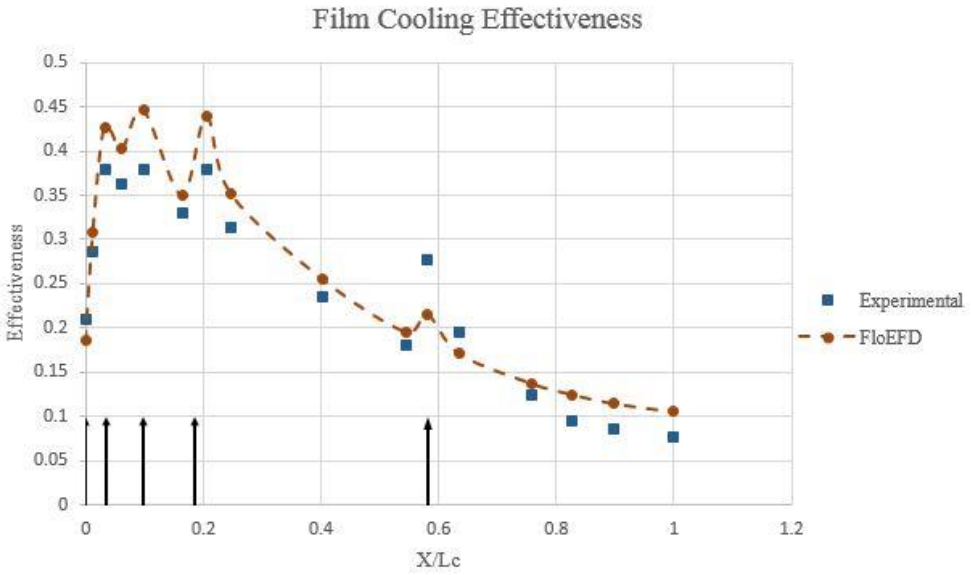


Figure 8 Comparison of measured and predcited film cooling effectiveness over a pressure surface of aerofoil.

Film cooling effectiveness is predicted with cylindrical holes on aerofoil pressure surafce. Figure.8 shows the variation of film cooling effectiveness with with non-dimensionalised chord length and axial locations of film cooling holes. CFD predictions are in good agreement with the experimental results with the maximum deviation of 19.5% at chord lenth of $X/L_c$ = 0.58. This gives us the confidence for the usage of FloEFD software for estimnating the film cooling effectuivensss for the new cooling configurations. This can be used as a design tool for optimisation cooling configurations for turbine aerofoils.

CFD analysis for the film cooling effectiveness over the aerofoil with cylindrical holes is carried out for a blowing ratio of 1.0 with a density ratio of 1.6. The aerofoil metal temperaure is non-dimensionalised with respect to maximum gas tempertaure. The non-dimensionalised temperature contour for pressure surface (PS) and suction surface (SS) is shown in Figure.9. It can be seen that coolant spread is more in the axial direction and less in the spanwise direction this is due to the high exit velocity from the cylindrical holes.

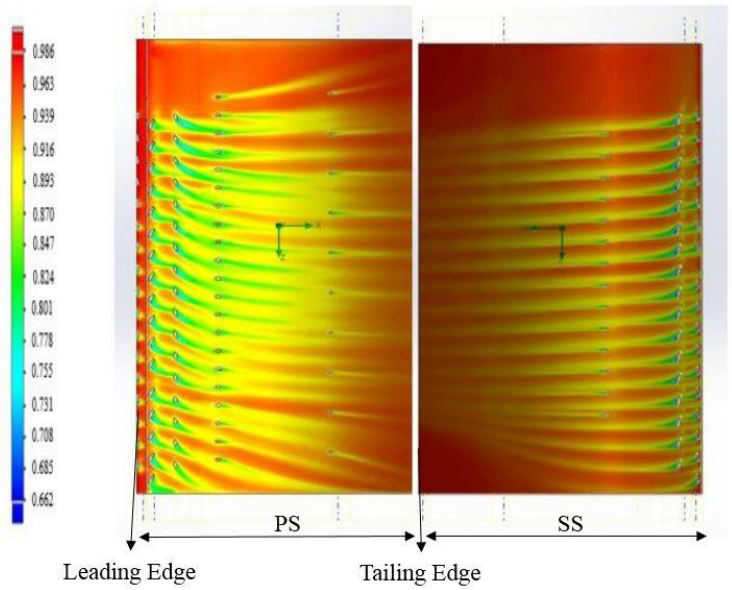


Figure 9 Non-Dimensionalized Temperature Contour for Cylindrical Holes

## 4. CONCLUSIONS

CFD is used as an analysis tool for estimating the film cooling effectiveness over a blade aerofoil with cylindrical hole and laid back fan shaped hole. Static pressure distribution and film cooling effetiveness on pressure side of an aerofoil is compared with measurements to validate the CFD code. The predictions and measurements are in good agrement. Grid independence study and CFD analysis for aerofoil with cylindrical holes for different blowing ratios is carried out. Film cooling effectiveness is compared for cylindrical and shaped hole configuration. Paramteric analysis is carried out to study the film cooling effectiveness for different blowing air ratio, turbulence intensity and fan angle. Complete results will be presented in the full manuscript.

## REFERENCES

[1] Ronald S.bunker, "A Review of Shaped Hole Turbine Film Cooling Technology", *Journal of Heat Transfer*, Vol.127, pp.441-453, 2005.

[2] Michael Gritsch, Achmed Schulz, Sigmar Wittig, "Film Cooling Holes with Expanded Exits: Near Hole Heat Transfer Coefficients", *International Journal of Heat Transfer and Fluid Flow 21*, pp. 146-155, 2001.

[3] W. Colban, K. A. Thole, M. Haendler, "Experimental and Computational Comparisons of Fan-Shaped Film Cooling on a Turbine Vane Surface", *Journal of Turbo Machinery*, Vol.129, pp.23-31, 2007.

[4] FloEFD Technical Reference, Mentor Graphics.

# NUMERICAL SIMULATION OF FLOW AND HEAT TRANSFER AROUND ELLIPTICAL CYLINDER WITH VARYING INLET TURBULENT INTENSITY

**Suvanjan Bhattacharyya, Arnab Banerjee, Mohammed Anisur Rahman, Kunal Dey**

Department of Mechanical Engineering, MCKV Institute of Engineering, Liluah, Howrah – 711204. West Bengal. India.

**Himadri Chattopadhyay**

Department of Mechanical Engineering, Jadavpur University, Kolkata – 700032. West Bengal. India.

## ABSTRACT

In this study computation is performed for an infinite elliptical cylinder, which is also the non-dimensional length scale. The computational analysis is done to cover cross flow on elliptical cylinder covering laminar and turbulent regime in the Reynolds number range of 100-100000 and turbulence intensities from 5% to 40%. Air is considered as a working fluid to have constant Prandtl number (0.707). The present study is considered to be two-dimensional. The governing equations are solved by continuity, momentum, and energy equations. Computation is performed for steady variants using Transition SST Model. The computational results are validated with well-established correlations and it shows well agreements. This work demonstrates that SST Model can effortlessly bridge all flow regimes for predicting the heat transfer. It also reports the effect of inlet turbulence intensity on augmenting heat transfer from the elliptical cylinder.

**Key Words:** *Heat Transfer, Finite Elements, Force Convection, Bluff Body, Elliptical cylinder, Turbulent Intensity.*

## 1. INTRODUCTION

The flow by the region of circular shaped cylinders has been widely studied due to its theoretical and practical consequence in engineering and scientific consequence in thermal engineering and fluid mechanics. Fluid flows are classified as external flow and internal flow, depending on whether the fluid is flowing over the surface or in the conduit. External flow generally shows a very different characteristic concerning internal flow. On the engineering application, there are a number of devices in mechanical, civil and other engineering where circular-cylindrical structures are used. Cylindrical structures are found in both alone and in a group, in the devises for heat exchangers for locomotive, cooling system for nuclear power plants, offshore structures, buildings, chimneys. Power lines, screens, grids, and cables, in both air and water as the flowing medium. In particular terms, the flow about circular cylinders shows various significant corporeal phenomena, such as division of flow, vortex shedding and also the shifting of flow from laminar to turbulence. It is the shape of the bodies which determined the form of flow and the energy transformation and flow characteristics. Therefore, designer should be careful to develop the correct shape and dimension of the body.

Any divergence from the correct shape or dimension may loss the efficiency of flow or heat exchange process. To recognize the flow and the thermal behaviors, many researchers put their efforts and few important works are reported here. Motlagh and Hashemabadi [1] performed a 2D and 3D CFD modeling of heat transfer from distinct circular cylindrical particles in four dissimilar

cases. These are infinite cylinder in cross-flow, cross-flow on fixed cylinder with dissimilar aspect ratio in a rectangular duct; axial-flow on finite cylinder and axial-flow on finite cylinder with upstream turbulence have been inspected with the commercial CFD software. All body forces have been neglected and the standard κ–ε turbulence model has been used for calculation of eddy viscosity of flow. A very good conformity involving CFD simulations and experimental results are obtained for local and overall heat transfer coefficient.

Kondjoyan and Daudin [2] have shown the consequence of free stream turbulence intensity on transfer of heat and mass at a surface of circular cylinder and an elliptical cylinder. Turbulence intensity within 1.5 to 40% and of Reynolds number ranging from 3000 to 40000 on transfer coefficients has been measured for a circular cylinder in cross-flow. Sanitjai and Goldstein [3] study the local and average heat transfer by forced convection from a circular cylinder. A Reynolds number ranging from 2000 to 90000 and Prandtl number from 0.7 to 176 has been considered. Their results are interesting for subcritical flow Scholten and Murray [4] has studied unsteady heat transfer and velocity profile of a cylinder in cross flow for Low free-stream turbulence. A method has been developed for making simultaneous measurements of time-resolved velocity, using laser Doppler anemometry, and local heat flux, using a hot film sensor, at the surface of a cylinder in cross flow. The results that they found are the magnitude of fluctuations in heat transfer at the front of the cylinder is very small. You and Kwon [5] have investigated the performances of different turbulent models for the flow simulation around a circular cylinder at a critical Reynolds number regime. The Reynolds number and turbulence intensity are considering 8.5×105, 0.7% respectively.

A literature survey shows that very little works deal with elliptical cylinder, bluff body. Hence in this work, turbulent flow and heat transfer in a channel with EC bluff body placed inside is performed with different inlet turbulent intensity.

## 2. PROBLEM FORMULATION

The present study considers the forced convection cross flow around an elliptical cylinder (EC). The non-dimensional distance between the inlet of the channel and the front surface of the EC is X =15D and the total non-dimensional length of the computational domain L = 50D following Murmu et al. [6]. The diameter of the channel is D and the hydraulic diameter is $D_h$ has been used in this study. The aspect ratio of the elliptical cylinder is 2.8 and is constant throughout the study. The problem is considered to be two-dimensional. Figure 1shows the computational domain. Air is considered as working fluid for which the Prandtl number is 0.71.

Figure 2 show the close view of the mesh of elliptical cylinder. After doing several checks for grid independence, adequate number of cells was used. The number of nodes is 85,777 and 61,956 for the case with EC and without EC respectively. Fluid approaches to the channel with inlet velocity of $U_\infty$ and temperature of the inlet fluid is $T_\infty$ where the EC constant surface temperature is maintained about $T_s$ =350K. The fluid is defined to be air with constant physical properties (Pr=0.71) with an inlet temperature of 300K.

The governing equations are discretized on a non-uniform structured grid using finite volume method and transition - SST model has been used for iteration process [7]. The velocities and pressures were predicted using semi implicit pressure linked equations (SIMPLE) scheme. The gradients for intermittency (γ), turbulent kinetic energy, specific dissipation rate, and momentum thickness used second order accurate upwind scheme. The discretized equations are then linearized using an implicit scheme and solved iteratively using Ansys Fluent 16.2, 2D double precision solver. The convergence criteria for continuity, momentum and energy are set at $10^{-4}$, $10^{-5}$, and $10^{-7}$ respectively. The convergence criterion for other four turbulence quantities was also fixed at $10^{-4}$.

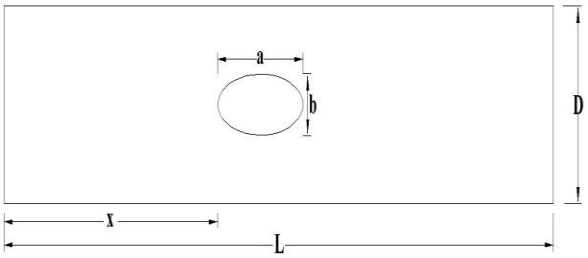


FIGURE 1. Schematic of Computational domain

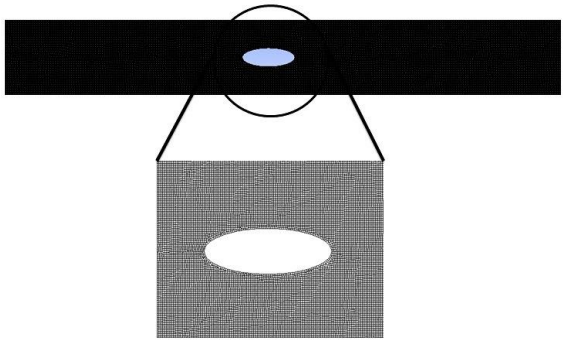

FIGURE 2. Close up view of grids of elliptical cylinder

## 3. RESULTS AND DISCUSSION

The results that obtained after the computation performed with the several Reynolds numbers are discussed in this section. The simulations are conducted for Reynolds numbers ranging from 100 to 1,00,000. The variation of average Nusselt number with the increase of Reynolds number at particular turbulence intensity is investigated and the increase in heat transfer coefficient with the increase in turbulence intensity is reported. The turbulence intensity varies from 5% to 40%.

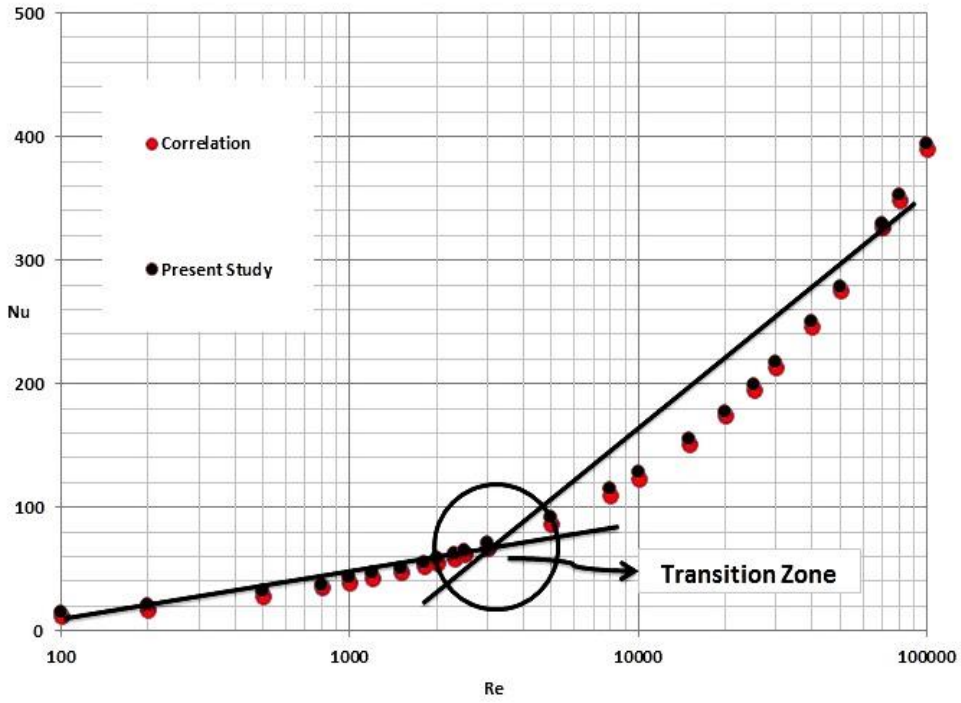


FIGURE 3.Variation of Nusselt number with Reynolds number and prediction of transitional zone

Zhukauskas [8] and Whitaker [9] correlation have been used in this study for verification of SST model simulation results for heat transfer coefficient calculation over the EC.

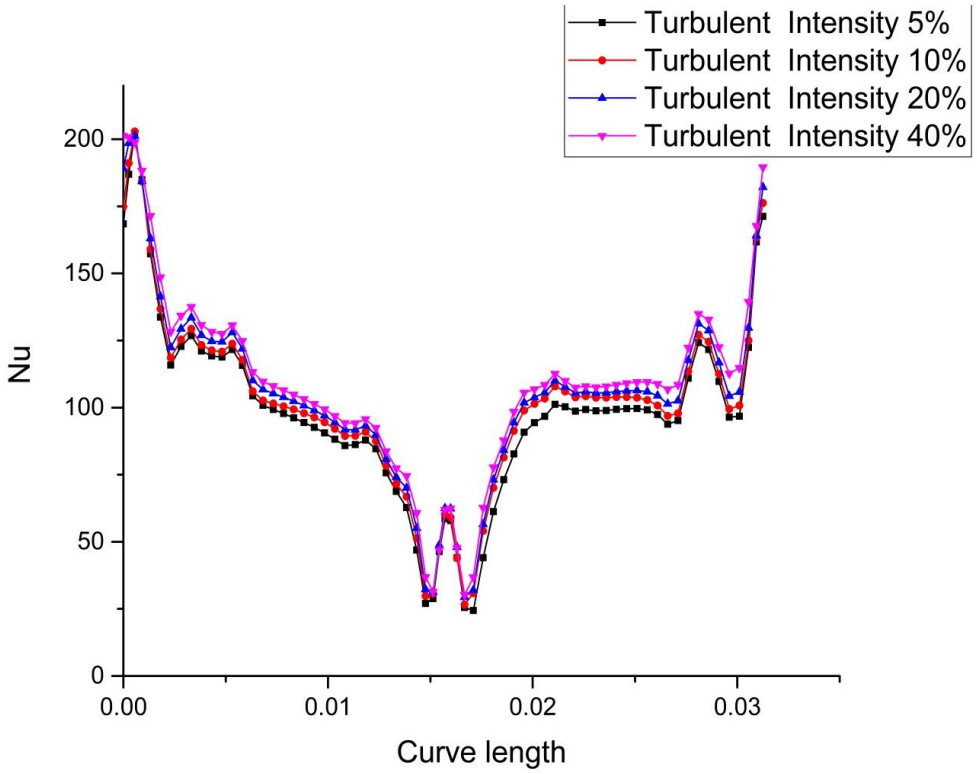


FIGURE 4. Variation of local Nusselt number at different turbulent intensity (%) over the curve length ($\theta_c$) at Reynolds number of 20,000.

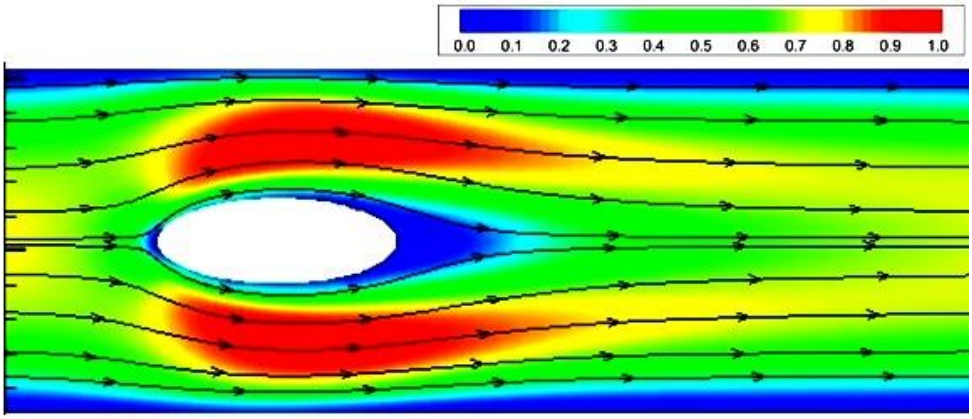


FIGURE 5. Axial velocity contour near cylinder wall at Re=1,000

Figure 3 shows the variation of Nusselt number for a fixed value of turbulence intensity of 5%.The simulation is performed for Reynolds number of 100 to 1,00,000 and the result shows good agreements with the correlation. Also, the transformation of flow field from laminar zone to turbulence zone can be visualized. From the curve it is clear that for external cross flow over a circular cylinder the transition zone is around 3,000.

The variation of local Nusselt number over the arc length at a particular Reynolds number with the increase in turbulence intensity has been shown in the Figure 4. The nature of the curve is almost

same for all the Reynolds number. From the figure it is observed that with the increase in turbulence intensity the point of separation does not change much but the value of local Nusselt number at stagnation point increases rapidly. Also, from the Figure 5 the effect of cylinder axial velocity on the flow field is observed.

## 4. CONCLUSION

In this work, a elliptical cylinder in a rectangular domain has been computed. The work predicts the steady, two dimensional incompressible flow and the thermal behaviors for a cross flow past over the cylinder numerically. It is found that Reynolds number has a significant effect on area weighted average of Nusselt number. It increases as Reynolds number increases. Turbulence intensity has an effect on local Nusselt number, with the increasing in turbulence intensity local Nusselt number increases especially at stagnation point. Value of Pressure coefficient initially decreases and then it increases monotonically with increase in Reynolds number. Transition SST model can predict the entire flow regime involving laminar turbulent and transition regime. The results from purely laminar and those from turbulent model agree well with the results from transition SST model.

## REFERENCES

[1] Ahmadi, M. A. H., Hashemabadi, S.H., 2008. "CFD based evaluation of heat transfer coefficient from cylindrical particles". International Communications in Heat and Mass Transfer, 12(35), Feb, pp. 674–680.

[2] Kondjoyan, A., Daudin, J. D., 1995. "Effects of free stream turbulence intensity on heat and mass transfers at the surface of a circular cylinder and an elliptical cylinder, axis ratio 4".Int. J. Heat Mass Transfer, 10(38), Oct, pp. 1735 1749.

[3] Sanitjai, S., Goldstein, R. J., 2004. "Forced convection heat transfer from a circular cylinder in cross flow to air and liquids". International Journal of Heat and Mass Transfer, 12(47), May, pp. 4795–4805.

[4] Scholeten, J. W., Murray, D. B., 1998. "Unsteady heat transfer and velocity of a cylinder in cross flow- I. Low free stream turbulence". Int. J. Heat Mass Transfer, 10(41), Aug, pp. 1139-1148.

[5] You, J. Y., Kwon, O. J., 2012. "Numerical assessment of turbulent models at a critical regime on unstructured meshes". Journal of Mechanical Science and Technology, 26 (5), pp. 1363~1369.

[6] Murmu, S. C., Biswas, C., Chattopadhyay, H., Sarkar, A., "Numerical simulation of flow and heat transfer around circular cylinder", Proceedings of the 23rd National Heat and Mass Transfer Conference and 1st International ISHMT-ASTFE Heat and Mass Transfer Conference IHMTC 2015, 17-20 December, 2015, Thiruvananthapuram, India.

[7] Bhattacharyya, S., Chattopadhyay, H., Benim, A.C., Simulation of Heat Transfer Enhancement in Tube Flow with Twisted Tape Insert, Progress in Computational Fluid Dynamics, an International Journal, vol. 17, no. 3, pp. 193-197, 2017.

[8] Zhukauskas, A., 1972. "Heat transfer from tubes in cross flow", in: J.P. Harnett, T.F. Irvine Jr. (Eds.), Advances in Heat Transfer. (8), Academic Press, Inc, New York.

[9] Whitaker, A., 1976. Elementary Heat Transfer Analysis, Pergamon Press, Inc, New York.

Fifth International Conference on Computational Methods for Thermal Problems
THERMACOMP2018, July 9-11, 2018, Indian Institute of Science, Bangalore, INDIA
*N. Massarotti, P. Nithiarasu, Pradip Dutta and C. Ranganyakalu (Eds.)*

# NUMERICAL MODELLING OF THERMAL ENERGY STORAGE USING PHASE CHANGE MATERIALS: ENERGY EFFICIENT BUILDINGS APPLICATION

**Swapnil S. Salvi, Kapil Garg, Vishal Bhalla**
School of Mechanical, Materials and Energy Engineering
Indian Institute of Technology Ropar
Rupnagar, Punjab, India
swapnil.salvi@iitrpr.ac.in, kapil.garg@iitrpr.ac.in, vishal.bhalla@iitrpr.ac.in

**Vikrant Khullar**
Mechanical Engineering Department
Thapar University
Patiala, Punjab, India
vikrant.khullar@thapar.edu

**Himanshu Tyagi**
School of Mechanical, Materials and Energy Engineering
Indian Institute of Technology Ropar
Rupnagar, Punjab, India
himanshu.tyagi@iitrpr.ac.in

## ABSTRACT

Due to the efficient performance in energy storage density, latent heat storage system using phase change materials is the most efficient way of storing thermal energy. It has some dominant factors like high density energy storage and nearly isothermal operations, i.e., very small temperature range for heat storage and removal. In this study, Phase change material (PCM) is assumed to be incorporated in a brick wall structure, which can improve its thermal performance. A one-dimensional numerical model on Comsol Multiphysics is developed to analyse the thermal performance of the PCM-filled brick wall unit. The numerical model and the adopted hypotheses are illustrated in detail. The comparison between temperature distributions of simple brick wall and brick wall with a PCM-layer is presented. The results using the numerical tool show that the thermal performance of the PCM-filled brick wall is efficient over the simple brick wall without PCM, as it shows the room temperature decrement of approximately 15$^{o}$C with the set of boundary conditions and parameters stated in detail in this paper.

**Key Words:** *Numerical Modelling, Thermal Energy Storage, Phase Change Material, Thermal Analysis, Energy Efficient Buildings.*

## 1. INTRODUCTION

Thermal energy storage for maintaining the ambient conditions inside the buildings is becoming increasingly important due to the surge in fossil fuel prices and environmental concerns. Different forms of thermal energy storages are sensible heat storage, latent heat storage and thermochemical storage [1]. The properties like high thermal storage density as well as the isothermal nature of the operation leads to employ phase change materials (PCMs) in latent heat storage system. New and intelligent materials, like PCM can store latent heat energy in addition to the typical sensible energy capacity, allowing to store significantly more energy as compared to conventional building materials. This kind of (latent heat type) thermal energy storage is preferred more and more in the case of buildings built with energy saving purposes.
The PCM-Brick wall system can offer some competitive advantages over the traditional brick wall [2], listed as followed:

a) The ability to save the operative fees by shifting the peak electricity demand to off-peak periods, since electricity cost is much lower at night as compared to that of the day;
b) Continuous storage of solar energy during the day, and releasing it at night, thus improvising thermal comfort level;
c) Storage of natural cooling through ventilation at night in summer, which can be released to the room air during day time, thus reducing cooling load of air conditioning.

There are various ways to incorporate the PCM into building structures which have been investigated in the literature [3], viz. direct incorporation, immersion and encapsulation. Generally the PCM included in the wall is in the form of microencapsulated particles in a thin, high molecular weight polymeric film, thus leading to prevention of any significant buoyancy effects inside the PCM layer and enhanced heat transfer [4].

In this paper, numerical modelling of a brick wall containing PCM layer in between has been done to check the effectivity of PCM layer. It has also been compared with the conventional case of simple brick wall (without PCM) experiencing similar realistic boundary conditions.

## 2. NUMERICAL MODEL FOR THERMAL ANALYSIS OF PCM IN BRICK WALLS

In this problem, brick wall is incorporated with a PCM layer in between with a specific thickness. Analysis carried out will be used to compare the results of transient temperature distributions of brick wall with Phase Change Material [PCM] experiencing solar heat gain against the results of transient temperature distributions of simple brick wall (without PCM). Phase change material selected for the thermal analysis is octadecane ($C_{18}H_{38}$) which is being used as encapsulated PCM in building structures [4], having the following properties [5][6]:-

Table 1. Properties of Octadecane.

| **Properties** | **Solid** | **Liquid** |
|---|---|---|
| Melting temperature ($T_m$) | 28 °C | |
| Latent heat of fusion ($L$) | 244 kJ/kg | |
| Density ($\rho$) | 814 kg/m$^3$ | 774 kg/m$^3$ |
| Dynamic viscosity ($\mu$) | - | 0.0039 Pa-s |
| Thermal conductivity ($k$) | 0.358 W/mK | 0.152 W/mK |
| Specific heat ($C_P$) | 2150 J/kgK | 2180 J/kgK |

Table 2. Properties of Air and Brick

| **Properties** | **Air** | **Brick** |
|---|---|---|
| Thermal Conductivity ($k$) | 0.0257 W/m-K | 0.5 W/m-K |
| Density ($\rho$) | 1.205 kg/m$^3$ | 2000 kg/m$^3$ |
| Specific Heat ($C_P$) | 1005 J/kg-K | 900 J/kg-K |

**Transient parameters for analysis:-**

Time for analysis $t$ = 24 hours
Time steps $dt$ = 0.1 hour

**Assumptions:-**

- One dimensional.
- Only conduction is considered with a heat generation term which is required for a phase transformation process.
- Free convection / gravitational effect is not considered in this problem.
- Air is assumed as a stationary medium, i.e. without convection.
- Length of wall is assumed to be infinite.

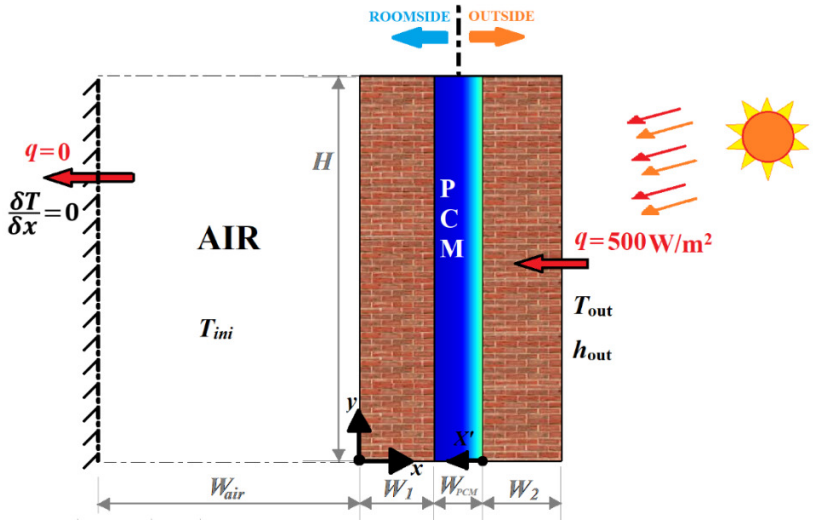


FIGURE 1 Schematic of model for thermal analysis of Brick wall with PCM

**Boundary Conditions:-**

- At $x$ = 150 mm, $q$ = 500 W/m$^2$ and $T_{out}$ = 45 °C, $h_{out}$ = 10 W/m$^2$K (i)
- At $x$ = - 150 mm, $\frac{\delta T}{\delta x} = 0$ (ii)
- At $t$ = 0 sec, $T_{ini}$ = 25 °C (iii)

**Dimensions:-**

- $W_1 = W_2$ = 60 mm [Brick wall thickness]
- $W_{air}$ = 150 mm [Air layer thickness]
- $W_{PCM}$ = 30 mm [PCM layer thickness]
- $H$ = 500 mm(Semi-infinite dimension)

Dimensions used in the problem are taken after referring some similar problems from literature[7,8].

## 3. RESULTS AND DISCUSSION

First results will be plotted depicting temperature distributions along the bricks and air passage in Fig. 2. We can observe that the phase front crosses the thickness of 30 mm in approximately 10 hours, after which all the PCM layer converts into liquid. Whereas in Fig. 3, results of temperature distributions of brick wall with PCM case is compared with the simple brick wall case. In both the cases similar boundary conditions have been taken.

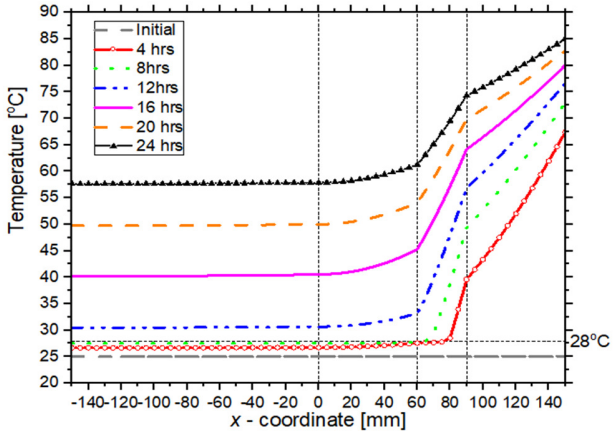


FIGURE 2 Temperature distribution for Brick wall with PCM (including Air Passage)

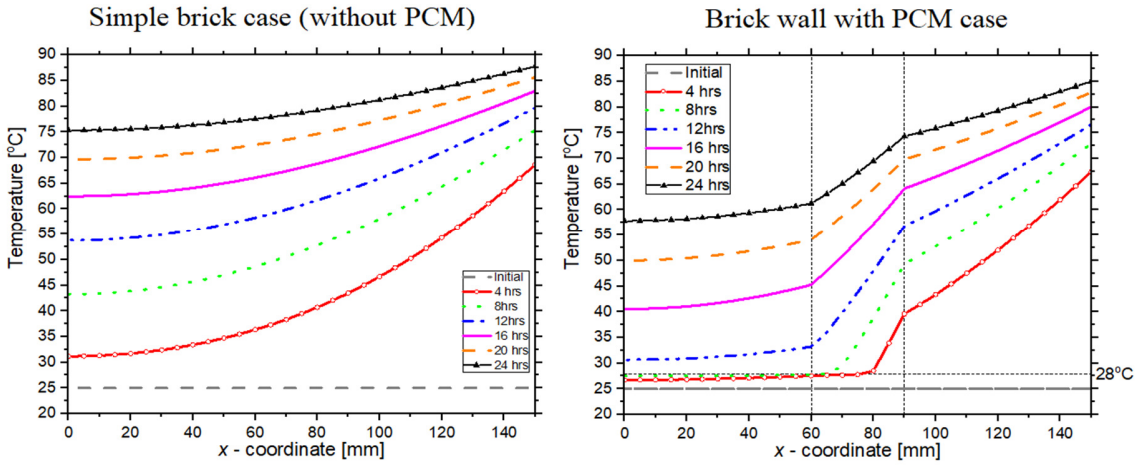


FIGURE 3 Comparison of temperature distributions (inside wall only)

## 4. CONCLUSION

The phase change material (PCM) appears to be a promising solution, since in latent form it can store and release more energy, than the sensible energy stored by most of the construction materials. From the results after designing the problem of PCM layer in brick wall, we can conclude that PCM can improve the thermal behaviour and energy efficiency of building.

The results reveal that the problem of brick wall containing PCM layer after comparing to a simple brick, change in room-side temperature can be easily observed, i.e., approximately 15 °C reduction in room temperature is achieved in the case of brick wall with PCM.

## REFERENCES

[1] Duffie, J., and Beckman, W., 2013, *Solar Engineering of Thermal Processes, 4th Ed.*

[2] Sharma, A., Tyagi, V. V., Chen, C. R., and Buddhi, D., 2009, "Review on Thermal Energy Storage with Phase Change Materials and Applications," Renew. Sustain. Energy Rev., **13**(2), pp. 318–345.

[3] Ã, Y. Z., Zhou, G., Lin, K., Zhang, Q., and Di, H., 2007, "Application of Latent Heat Thermal Energy Storage in Buildings : State-of-the-Art and Outlook," **42**, pp. 2197–2209.

[4] Khudhair, A. M., and Farid, M. M., 2004, "A Review on Energy Conservation in Building Applications with Thermal Storage by Latent Heat Using Phase Change Materials," Energy Convers. Manag., **45**(2), pp. 263–275.

[5] Hale, B. D. V, Hoover, M. M. J., Lockheed, N., Huntsville, B. D., September, E., Cha, P., Co, S., Marshall, F., Space, A., and Space, N. M., 2017, *Nasa Contractor Report Nasa Cr-51363*.

[6] Humphries, W. R., and Griggs, E. I., 1977, *A Design Handbook for Phase Change Thermal Control and Energy Storage Devices- NASA*.

[7] Vicente, R., and Silva, T., 2014, "Brick Masonry Walls with PCM Macrocapsules: An Experimental Approach," Appl. Therm. Eng., **67**(1–2), pp. 24–34.

[8] Carbonari, A., De Grassi, M., Di Perna, C., and Principi, P., 2006, "Numerical and Experimental Analyses of PCM Containing Sandwich Panels for Prefabricated Walls," Energy Build., **38**(5), pp. 472–483.

Fifth International Conference on Computational Methods for Thermal Problems
THERMACOMP2018, July 9-11, 2018, Indian Institute of Science, Bangalore, INDIA
*N. Massarotti, P. Nithiarasu, Pradip Dutta and C. Ranganyakalu (Eds.)*

# Simulation of Conjugate Heat Transfer from a Continuously Moving Horizontal Plate to Nanofluid

**Swati Singh*, P.S. Ghoshdastidar**

Department of Mechanical engineering,

Indian Institute of Technology Kanpur, Kanpur, U.P.208016. INDIA

* Corresponding Author. E-Mail: swatisi@iitk.ac.in.

## ABSTRACT

A finite-difference based numerical simulation using the homogeneous flow model has been performed to study the buoyancy-aided transient as well as steady conjugate heat transfer from a continuously moving horizontal plate to alumina-water nanofluid, as in hot extrusion. The flow and heat transfer are treated as laminar, 2D, unsteady and non-boundary layer type. Stream function-Vorticity method has been used to formulate the problem. The parameters varied are: Volume fraction of nanoparticles (1% - 5%), Richardson number (0 – 20) and Plate Velocity (0.001 m/s – 0.1 m/s). The performance criteria are given on basis of enhancement factor and effectiveness. It is observed that with increase in nanoparticle volume fraction and plate velocity, time required to cool the plate to steady state temperature is reduced. At a low plate velocity, the temperature drop in the plate is faster as compared to that at a high plate velocity. The enhancement factor increases with volume fraction of nanoparticles. On the other hand, the effectiveness drops with increase in nanoparticle concentration.

**Key Words:** *Nanofluids, Hot extrusion, Continuously moving horizontal surfaces, Conjugate heat transfer, heat transfer enhancement*

## 1. INTRODUCTION

The hot extrusion of materials, hot rolling, and continuous casting process are some of the industrial applications of continuously moving surfaces. In this paper, a numerical simulation of transient cooling by alumina-water nanofluid of an extruded plate emerging from the extrusion die is presented. Nanofluids are engineered colloids in which nanoparticles of 1-100 nm diameter are stably dispersed in a base fluid. Nanofluids have been found to show anomalous increase in thermal conductivity and viscosity with respect to base fluid with increase in volume fraction ($\phi$) of nanoparticles. The nanoparticle concentration usually does not exceed 5%.

## 2. PROBLEM FORMULATION AND SOLUTION METHODOLOGY

Figure 1 shows a continuously moving horizontal plate emerging from an extrusion slot with a velocity, U and temperature, $T_o$ into an otherwise quiescent fluid i.e. nanofluid at temperature $T_\infty$. The buoyancy force acts in a direction normal to the plate motion and opposite to the direction of gravity. The flow and heat transfer characteristics are examined on both upper and lower sides of the plate surface. Alumina-water based nanofluid has been used as the coolant. The plate material is aluminium. The plate velocity varies from 0.001-0.1 m/s. The initial plate temperature is 358 K. The temperature of quiescent fluid is 298 K. The values of Richardson number, Ri are taken as

$0 < Ri < 20$. The length, width and thickness of the computational domain are 1 m, 0.1 m and 0.01 m, respectively.

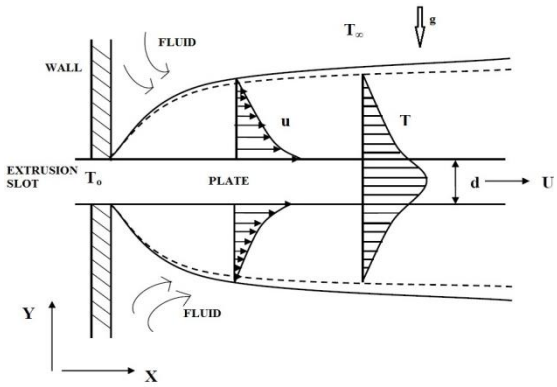


Figure1. Physical problem

The boundary layer approximations are not valid near the slot region. So the flow and heat transfer are assumed to be of non-boundary layer type and hence full elliptic governing equations are solved.

**Non-dimensionalization**

The non-dimensional parameters are as follows.

$$x^* = \frac{x}{d}, y^* = \frac{y}{d}, t^* = t\frac{U}{d}, u^* = \frac{u}{U}, v^* = \frac{v}{U}, \theta = \frac{T - T_\infty}{T_O - T_\infty}, \psi^* = \frac{\psi}{Ud}, \xi^* = \frac{\xi d}{U}, Re = \frac{Ud}{\nu_f},$$
$$Pe_p = \frac{Ud}{\alpha_p}, Pr = \frac{\nu_f}{\alpha_f}, Pe_f = Re \times \mathrm{Pr}, \; Ri = \frac{Gr}{Re^2}, Gr = \frac{g\beta(T_O - T_\infty)d^3}{\nu_f^2} \quad (1)$$

**Non-dimensional Governing Equations**

*Stream function Equation:* $$\frac{\partial^2\psi^*}{\partial x^{*2}} + \frac{\partial^2\psi^*}{\partial y^{*2}} = -\xi^* \quad (2)$$

Where, $u^* = \frac{\partial\psi^*}{\partial y^*}$ and $v^* = -\frac{\partial\psi^*}{\partial x^*}$

*Vorticity Transport Equation:* $$\frac{\partial\xi^*}{\partial t^*} + u^*\frac{\partial\xi^*}{\partial x^*} + v^*\frac{\partial\xi^*}{\partial y^*} = \frac{1}{Re}\left(\frac{\partial^2\xi^*}{\partial x^{*2}} + \frac{\partial^2\xi^*}{\partial y^{*2}}\right) + \frac{Gr}{Re^2}\left(\frac{\partial\theta}{\partial x}\right) \quad (3)$$

*Energy Equation for the Fluid:* $$\frac{\partial\theta}{\partial t^*} + u^*\frac{\partial\theta}{\partial x^*} + v^*\frac{\partial\theta}{\partial y^*} = \frac{1}{Pe_f}\left(\frac{\partial^2\theta}{\partial x^{*2}} + \frac{\partial^2\theta}{\partial y^{*2}}\right) \quad (4)$$

*Energy Equation for the Plate:* $$\frac{\partial\theta}{\partial t^*} + \frac{\partial\theta}{\partial x^*} = \frac{1}{Pe_p}\left(\frac{\partial^2\theta}{\partial x^{*2}} + \frac{\partial^2\theta}{\partial y^{*2}}\right) \quad (5)$$

The enhancement factor is defined as the ratio of average heat transfer coefficient in nanofluid to that in base fluid and the effectiveness is the ratio of average heat transfer coefficient in nanofluid to the power required to pull the plate. The nanofluid considered is assumed to be homogeneous and single phase. The property correlations as functions of bulk volume fraction ($\phi$) of nanoparticles for alumina-water have been taken from Buongiorno [1] who developed them from the experimental data of Pak and Cho [2]. Equations (2) - (5) have been solved simultaneously by pure implicit finite-difference scheme. The upwind scheme has been used. Optimum grids have been used for various parameters based on grid independence tests.

## 3. RESULTS AND DISCUSSION

The numerical results have been satisfactorily validated for pure fluid (water) against Sakiadis [3] for the case of forced convection. The Reynolds number is taken as 1119. It is seen from Fig. 2 that the validation is quite satisfactory. The small deviation arises from the fact that Sakiadis [3] solved the problem using a boundary-layer analysis whereas the present problem formulation is based on non-boundary layer considerations. The mixed convection results are compared with the experimental results of Karwe and Jaluria [4] for continuously moving vertical plate moving downward in water. Figure 3 shows a comparison of steady state variation of the numerically predicted horizontal plate centreline temperature with x* for an aluminium plate moving vertically downward in water at Re = 103 and Ri = 0.8. A reasonably good agreement between the two is observed. The deviation exists due to the fact that the solution for the present problem is obtained for continuously moving horizontal plate while the experiment was performed for a vertical plate. Figure 4 shows the transverse variation of plate temperature at x* = 0.5 m and at U = 0.01 m/s for different volume fractions of nanoparticles. It may be seen from the graph that as the nanoparticle concentration increases, the rate of heat removal from the plate also increases because of the enhanced heat transfer coefficient. Figure 5 depicts the steady state plate centreline temperature variation at $\phi$ = 0.03 for different plate velocities. The figure reveals high temperature gradients at lower plate velocities. Table 1 shows that due to increase in thermal conductivity with volume fraction of nanoparticles, the enhancement factor also increases. The effectiveness, on the other hand, drops with increase in nanoparticle volume fraction since larger power is required to pull the plate as viscous force also rises with $\phi$. Figure 6 shows that higher u-velocity near the wall region occurs due to greater buoyancy force which in turn gives rise to higher heat transfer coefficient resulting from higher temperature gradient (Fig. 7).

Table1. Comparison of enhancement factor and effectiveness at different $\phi$'s

| | **Φ** | **Enhancement factor** | **Effectiveness × $10^{-7}$ ($m^{-2}$ $K^{-1}$)** |
|---|---|---|---|
| **Base fluid** | 0.0 | 1 | 2.704 |
| **$Al_2O_3$-water** | 0.01 | 1.049 | 2.342 |
| | 0.03 | 1.146 | 1.842 |
| | 0.05 | 1.235 | 1.526 |

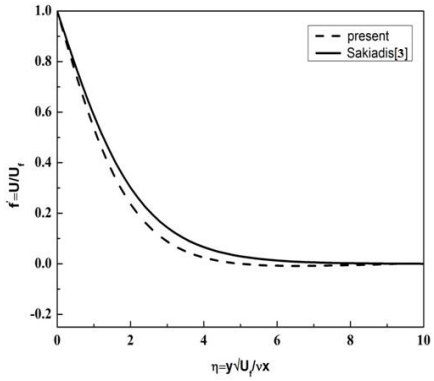


Figure 2. Comparison of u-velocity profile with the analytical solution of Sakiadis [3]

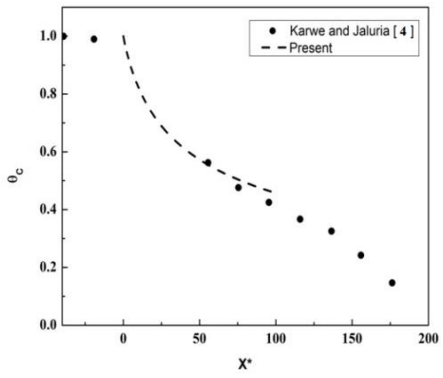


Figure 3. Comparison of experimental [4] and present results for steady state variation of plate centreline temperature with x* at Re = 103, Ri = 0.8

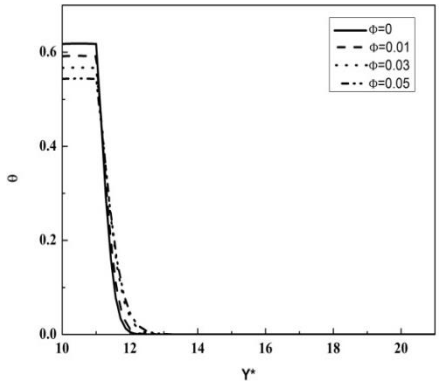


Figure 4. Transverse temperature variation in the plate and the fluid (upper half) at x*= 50 for different volume fractions of nanoparticles, $\phi$ at U = 0.01 m/s

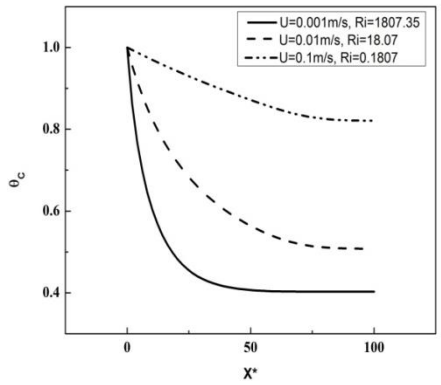


Figure 5. Centreline plate temperature variation at $\phi$ = 0.03 for different plate velocities

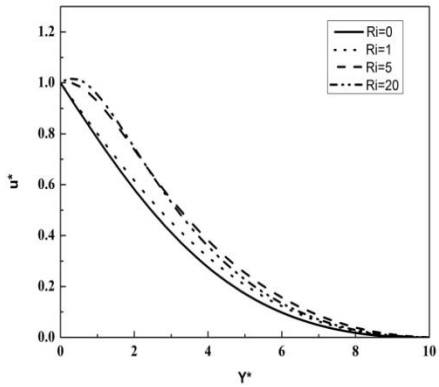


Figure 6. u-velocity profiles at x*= 50 for $\phi$ = 0.01, U = 0.001 m/s and varying Ri for the lower domain

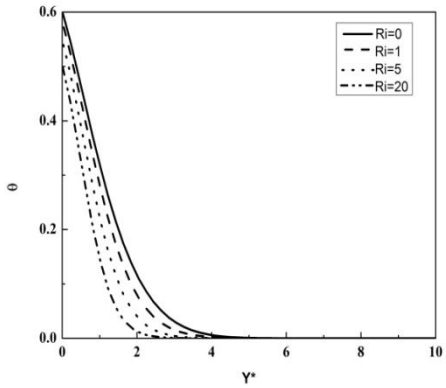


Figure 7. Temperature profiles at x* = 50 for $\phi$ = 0.01, U = 0.001m/s and varying Ri for the lower domain

## 4. CONCLUSIONS

A numerical simulation based on a non-boundary layer formulation has been performed for a continuously moving horizontal plate cooled by alumina-water nanofluid, as in hot extrusion. The results have been satisfactorily validated with earlier analytical and experiment works. The study reveals that with increase in nanoparticle concentration and plate velocity the time required to cool the plate to steady state temperature is reduced. At a low plate velocity, the temperature drop in the plate is faster than that at a high plate velocity. While the enhancement factor increases with increase in the volume fraction of nanoparticles the effectiveness falls with rise in nanoparticle concentration. The heat transfer coefficient and enhancement factor in the region below the plate are marginally lower than those above the plate.

## REFERENCES

[1] Buongiorno, J., 2006, Convective Transport in Nanofluids, *ASME J. Heat Transfer*, Vol. 128, pp. 240–250.

[2] Pak, B. C., and Cho, Y.I., 1998, Hydrodynamic and Heat Transfer Study of Dispersed Fluids with Submicron Metallic Oxide Particles, *Experimental Heat Transfer*, Vol. 11, No. 2, pp. 151-170.

[3] Sakiadis, B. C., 1961, Boundary-layer Behavior on Continuous Solid Surfaces: 2. The Boundary Layer on a Continuous Flat Surface, *AIChE Journal*, Vol. 7, No. 2, pp.221-225.

[4] Karwe, M. V., and Jaluria, Y., 1992, Experimental Investigation of Thermal Transport from a Heated Moving Plate, *Int. J. Heat Mass Transfer*, Vol. 10, No. 2, pp. 493-511.

Fifth International Conference on Computational Methods for Thermal Problems
THERMACOMP2018, July 9-11, 2018, Indian Institute of Science, Bangalore, INDIA
*N. Massarotti, P. Nithiarasu, Pradip Dutta and C. Ranganyakalu (Eds.)*

# NUMERICAL INVESTIGATION OF Bi-CGSTAB SOLVER WITH ILU(p) PRECONDITIONER

**Yogesh Thawrani, Jayakumar J. S. ***
Department of Mechanical Engineering, Amrita Vishwa Vidyapeetham, Amritapuri, India
E-mail: yogesh.thawrani@gmail.com, *Corresponding author, E-mail: jsjayan@gmail.com

## ABSTRACT

This study deals with the development of a general purpose solver that can handle any type of system of linear equations **Ax**=**b**, where **A** is a square matrix. Numerical experiments are performed using ILU(p) preconditioner with Bi-CGSTAB solver on various randomly generated matrices of order 10 to 50,000. A new pattern of ILU(p) preconditioner has been found that lead us in developing a new algorithm that requires less storage and computational time for getting the correct solution within ten iterations. The algorithm developed depends only on the order of the square matrix **A** and is independent of the type of the matrix **A**. This new algorithm which is first of its kind that can be used to solve any **Ax**=**b** kind of problem in which **A** is a square matrix.

**Key Words:** *Bi-CGSTAB solver, ILU(p) preconditioner, CSR format, Linear Algebraic equations.*

## 1. INTRODUCTION

The problem of solving large linear systems of equations occurs commonly in many scientific and engineering applications. Let us consider the linear system **Ax**=**b**, where the coefficient matrix **A**=[$a_{ij}$] is a large sparse matrix of order *n*x*n*, **b** is a given vector of order *n* and **x** is the unknown vector of order *n*. The matrix **A** may be symmetric, non-symmetric, diagonally dominant, non-diagonally dominant, or possible combination of these four. Direct methods are not good option for a system of millions or billions of unknowns because of the time and storage requirement. Iterative methods can handle such systems but are not as robust and efficient as direct methods. Despite their intrinsic appeal for very large linear systems, drawbacks in terms of efficiency and robustness hampers the acceptance of iterative methods in industrial applications. *Preconditioning* can be used to improve the efficiency and the robustness of an iterative technique. But, not all the preconditioners can be used for all kind of system of linear equations. In general, it is agreed that the construction of effective general purpose preconditioner is not possible. Some preconditioners may perform well on a wide range of problems [1].

Preconditioning is defined as the transformation of the original linear system (**Ax**=**b**) into one such system which has the same solution, but which is likely to be easier to solve using an iterative solver. An *incomplete factorization* of the original matrix **A** is one of the simplest ways of defining a preconditioner. This lead to a decomposition of the form **A**=**LU** – **R**. Here **L** is a lower triangular matrix, **U** is an upper triangular matrix and **R** is the residual or error of the factorization. For the zero fill-ins incomplete factorization known as ILU(0), **L** and **U** have the same nonzero structure as the lower and upper parts of **A** respectively. ILU(0) is rather easy and inexpensive to compute but it often leads to a crude approximation which may result in either no convergence or requiring many iterations to converge. To remedy this, several alternative incomplete factorizations have been developed. ILU(p) preconditioning allows the user to control the fill-ins provided in the preconditioner matrix (**M**) by defining the value of p. In case of more accurate ILU factorization, the pre-processing cost to compute the factors is higher but the solution converges in fewer iterations [2].

As there are lots of zero elements in a sparse matrix, if we store all these elements then the storage space taken will be very large. In order to avoid this, algorithms have been developed where the zero entries in the matrix are considered as redundant and only non-zero entries are stored, thereby minimizing the storage requirement. Out of the various storage formats, the CSR format is often more useful for performing typical computations. CSR format got the advantage of its simplicity and flexibility. CSR storage structure takes the least storage space on the disk and performs the best for the processing in comparison to other storage formats [2].

In the present work, emphasis is given for getting the solution of the system of linear equations in minimum number of iterations irrespective of the type of the coefficient matrix **A**. We have used ILU(p) preconditioner combined with Bi-CGSTAB solver. The main focus is to make a solver with high accuracy that can be used to solve any kind of **A** (i.e., dense, symmetric, non-symmetric, diagonally dominant, non-diagonally dominant or combination of the four) in lesser CPU time and requires minimum storage.

## 2. METHODOLOGY AND NUMERICAL EXPERIMENTS

The numerical experiments are performed using five different types of matrices, namely Dense, Diagonally Dominant Sparse (DDS), Diagonally Dominant Sparse Symmetric (DDSS), Non-DDS and Non-DDSS. Matlab$^R$ is used to generate the above mentioned matrices of order 10 to 50000 in a random fashion. The arrangement of the non-zero elements in the matrix is also random. The **b** vector is obtained by assuming **x** as 1 and multiplying it with matrix **A**. At the start of the iteration an initial guess of **x**=0 is given. For convergence, the iterations are continued till the residual vector falls below the tolerance of $10^{-12}$.

The c++ code is developed for Bi-CGSTAB solver with ILU(p) preconditioner. First numerical experiments are performed for the randomly generated system of linear equations in which the number of unknowns are 250, 500, and 1000. It has been found that as the fill-ins increases or p increases the chances for the convergence of the solution increases. Further numerical experiments are done with 28 randomly generated sparse system of linear equations of order 1000 and 10000.

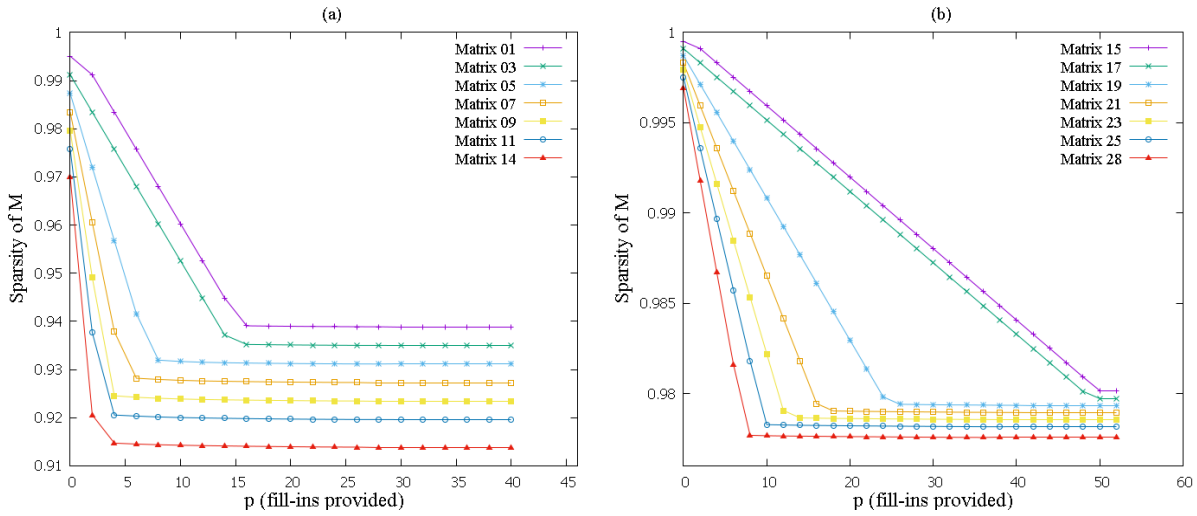


FIGURE 1. Variation of the sparsity of **M** with p (fill-ins provided) for matrices of order (a) n = 1000 and (b) n = 10000

Figure 1 shows the variation of the sparsity of the preconditioner matrix **M** with respect to p i.e., fill-ins provided. From the figure one can observe that with the increase in p the sparsity of **M** decreases up to some value of p (region 1) and after that it becomes constant (region 2). When the

value of p from region 1 is used to solve the system of equations, either the solution is not converged or has taken very large number of iterations for convergence. But, when the value of p from region 2 is used to solve the system of equations the solution has always converged within ten iterations.

From this observation, we can say that there exists a particular p which was not known earlier it is termed as optimum p ($p_{opt}$) after which the sparsity of the matrix **M** becomes constant and this **M**, when used with the solver, provides the correct solution within ten iterations. Further numerical experiments are done to find the $p_{opt}$.

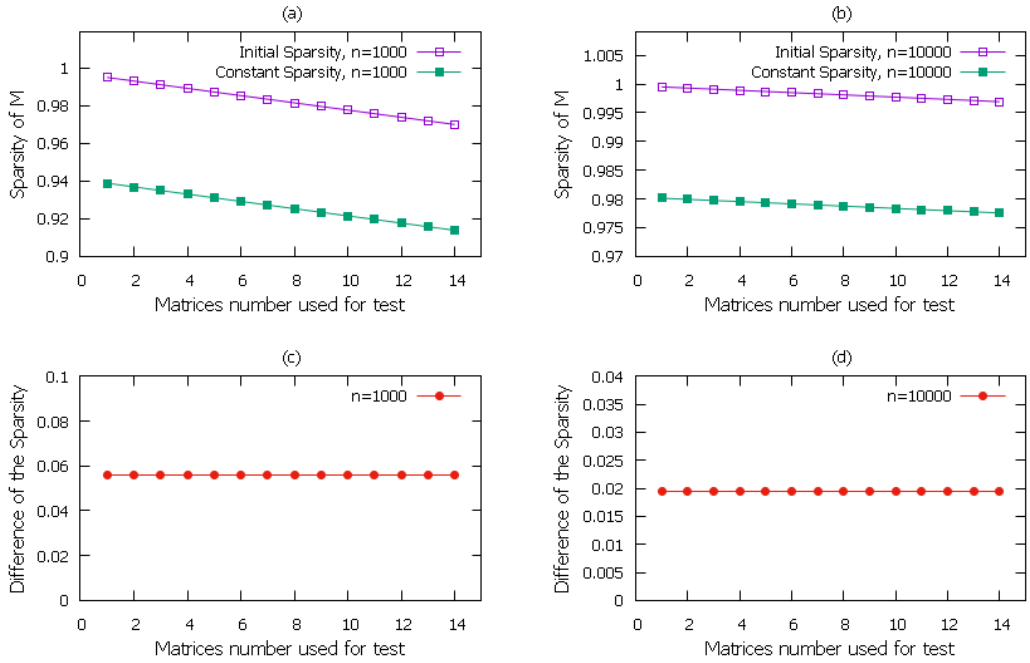


FIGURE 2. Initial sparsity of **M** and Sparsity that becomes constant after some p value for the test matrices of order (a) n=1000 and (b) n=10000. Difference between the initial sparsity of **M** and the sparsity that becomes constant after some p value for the test matrices of order (c) n=1000 and (d) n=10000.

Figure 2 (a) and 2 (b) shows variation of the initial sparsity of the matrix **M** ($Sp_M|_{initial}$) (i.e., the sparsity of the matrix **A**) and the sparsity of the matrix **M** that becomes constant after a particular value of p ($Sp_M|_{constant}$) for the test matrices of order 1000 and 10000 respectively. Figure 2 (c) and 2 (d) shows the difference between the $Sp_M|_{initial}$ and $Sp_M|_{constant}$ for the test matrices of order 1000 and 10000 respectively. The difference comes out to be constant irrespective of the type of the matrix and arrangement of the non-zero elements in the matrix. The same procedure has been carried out for the system of equations of order 10 to 50,000. Using power interpolation an equation is obtained to find the difference between the $Sp_M|_{initial}$ and $Sp_M|_{constant}$. The equation obtained is:

$$Sp_M|_{initial} - Sp_M|_{constant} = 1.365*n^{-0.462} \quad (1)$$

By trial and error method it has been found that the $p_{opt}$ can be obtained by the following relation:

$$P_{opt} = (Sp_M|_{initial} - Sp_M|_{constant}) / (Sp_M|_{initial} - Sp_M|_{p=1}) \quad (2)$$

Using the definition of the sparsity, the equation obtained for $Sp_M|_{initial} - Sp_M|_{constant}$ and making an assumption that the fill-ins provided for p=1 case is 2 times the order of the system i.e., 2n, we get the following equation for optimum p:

$$p_{opt} = 0.6825*n^{0.538} \quad (3)$$

the above equation requires only the order of the system to calculate the $p_{opt}$. Once we know the $p_{opt}$ we can also calculate the approximate number of non-zero (nz) elements present in the preconditioner matrix using the following equation:

$$nz_M = nz_A + 2n*p_{opt} \quad (4)$$

By knowing the $p_{opt}$ value the convergence of the system can be assured and by knowing the nzM, the implementation of the CSR format becomes much easier as we can predefine the positions of the fill-ins. A new algorithm has been developed using the above equations which is easy to implement in CSR format.

## 3. RESULTS

For a randomly generated sparse system of equations of order ten thousand, table 1 summarizes the result obtained from the direct method and the new algorithm developed.

TABLE 1. Comparison of the time and storage required by direct LU factorization and BiCGSTAB with ILU($p_{opt}$)

| Solver | Number of CPU core used | RAM used | Number of non-zero elements present in **A** | Memory require for storing the system **Ax**=**b** (in MB) | Number of iterations | Time taken for convergence (seconds) |
|---|---|---|---|---|---|---|
| Direct LU factorization | 32 | 128 | 97798 | 763.0157 | - | 58 |
| BiCGSTAB with ILU($p_{opt}$) | 1 | 16 | 97798 | 1.2336 | 1 | 23 |

From the table 1 we can see that there is a drastic reduction in time and storage for the new algorithm as compared to the direct LU factorization. The comparison is repeated for different randomly generated matrix. All the time we get similar result as shown in table 1.

## 4. CONCLUSIONS

In the present study, numerical experiments has been done using ILU(p) preconditioner with Bi-CGSTAB solver on various randomly generated matrices of order 10 – 50000. It has been found that ILU(p) preconditioner follows a pattern i.e., after a particular p ($p_{opt}$) the sparsity of the preconditioner matrix **M** becomes constant. **M** build using $p_{opt}$ always provides the correct solution within ten iterations (most of the time in the first iteration itself) irrespective of the coefficient matrix type and has the accuracy of $10^{-12}$. A formula has been derived for $p_{opt}$ that depends only on the order of the matrix **A**. New algorithm is developed using the $p_{opt}$ and CSR format. With this algorithm the time taken and storage for getting the solution is drastically reduced. This new algorithm is first of its kind that can be used to solve any **Ax**=**b** kind of problem in which **A** is a square matrix.

## REFERENCES

[1] Michele Benzi, Preconditioning Techniques for Large linear Systems: A survey, *Journal of Computational Physics*, 182, 418-77, 2002.

[2] Yousef Saad, *Iterative Methods for Sparse Linear Systems*, 2nd Edition, Society for Industrial and Applied Mathematics, 2003.

# STUDY ON THE EFFECTS OF PARTICLE SHAPE IN FREE MOLECULAR REGIME

**Arun Kumar Chinnappan, Rakesh Kumar**

Department of Aerospace Engineering,
Indian Institute of Technology Kanpur, India
E-mail: arun@iitk.ac.in, rkm@iitk.ac.in

**Abstract**

Shape effects of particle in free molecular regime is investigated using an in-house, three dimensional direct simulation Monte-Carlo (DSMC) solver. The solver is validated for typical shape i.e sphere with available analytical results and compared with practical particle shape i.e ellipsoidal. The sensitivity of particle shape is discussed using surface properties such as drag and heat transfer. Moreover, the variation of surface properties with respect to angle of attack is discussed.

**KEY WORDS ::** DSMC, GAS-SOLID FLOW, NON-SPHERICAL, FREE MOLECULAR REGIME

## 1 Introduction

Multiphase flows considering gas-solid have many applications in industries such as cyclone separators, sand blasting, sand storm, pollution control systems, etc. Numerous studies had been done in several years to study the gas-solid flow behavior, however it is limited to low-speed and continuum regime. Even though not many research found in high speed and free molecular regimes considering gas-solid flows, it is important to study in order to address several practical situations such as unburned fuel in solid propellant rocket nozzles, dust dispersion in lunar/planetary landings, etc. Experimental studies are quite expensive in order to mimic the low density environments as well as high speed flows. Moreover, the conventional Navier-Stokes solver is not suitable to study because of continuum failure at free molecular/transitional regime, where the characteristic length is comparable to the mean free path of the molecule. Some researchers proposed theoretical approaches to study gas-solid flows at free molecular regime notably: Gallis *et al.* [1] proposed a theoretical relation using Greens function approach to calculate drag and heat flux experienced by a particle moving in free molecular regime for monatomic gas. This approach was used to study effects of unburned solid propellants in rocket nozzle [2], predict dust emission mechanism of lunar sand particles due to plume impingement from the nozzle[3], etc. Saucer [4] derived a analytical relation to determine total heat transfer experienced by a particle in free molecular regime.

All the aforesaid research had considered particles as perfect spheres which are very convenient to model whereas, particles are non-spherical in reality. Non-spherical particle-gas flow behavior have been studied by some researchers in continuum regimes[5, 6] and addressed the complexity dealing with it. A single characteristic value (diameter) is enough to describe the behavior for spheres whereas at least two parameters are required to study even for regular non-spherical particles such as ellipsoid. Moreover, the pitching torque and lift force need to be considered if the angle of attack is non-zero.

The present work aims to study the importance of particle shape consideration in free molecular regime in aerodynamic as well as heat transfer aspects. In this work, we have used a kinetic-particle based Direct Simulation Monte-Carlo (DSMC) solver to study particle behavior in free molecular regime. This paper is arranged as follows: the brief description about DSMC method is given in Sec. 2, the numerical parameters are presented in Sec. 3. This is followed by results and discussion in Sec. 4 and conclusions in Sec. 5.

## 2 Computational Model :: The DSMC Method

The Direct Simulation Monte Carlo method (DSMC) is a particle based method proposed by G.A. Bird for the simulation of non-equilibrium gas flows [7]. This method deals with simulated molecules, each of which represents a large number of real molecules. This method governs the physics through molecular movements and collisions. Every molecule is moved with respect to their velocities and given time step. Molecular collisions are modeled probabilistically. The macroscopic parameters are calculated by time averaging the sampled data. The DSMC method does not produce direct solution to Boltzmann equation

but it evaluates the same physics as the Boltzmann equation and it has been demonstrated that this method approaches to solution of the Boltzmann equation in the limit of vanishing cell size and time step [7]. The detailed explanation about the method can be found in the references [7, 8]. The parallel in-house DSMC solver named NFS used in this work is already validated with several experimental and simulation results[9, 10]. In our solver, the Variable Hard Sphere (VHS) model is used for elastic collisions. The quantum and continuous versions of Larsen Borgnakke model are employed to model inelastic collisions.

To study this problem, the three dimensional NFS solver is used in this study with some modifications to reduce computational cost. In free molecular flows, gas-surface collision is more dominant mechanism governing the physics than gas-gas collision because the mean free path of the molecule is greater than the characteristic length (particle diameter in this case). To ensure that gas molecules are not affected by the presence of body, we have made a small modification in gas-surface interaction step in DSMC algorithm. Once a molecule hits the particle surface, the molecule velocity is unchanged instead its position will be changed randomly inside the domain. In other words, gas is not affected by the presence of body and it is quite valid in free molecular regime. However, the incident and reflected momentum/energy during gas-surface collision is sampled to calculate forces, moments and heat flux experienced by the particles. Therefore, the actual gas-surface interaction is modeled but post-reflection velocities are not assigned to the gas molecules to ensure gas properties are constant throughout the simulation.

# 3 Numerical Parameters

A 3D cubical domain is considered with a particle at the center. Argon is used as gas species. The gas density and temperature are $1.989 \times 10^{-5}\ Kg/m^3$ and 500 $K$, respectively. The bulk velocity of gas is varied based on speed ratio. Particle volume is taken as $5.236 \times 10^{-19}\ m^3$ represents a sphere of having a diameter 1 $\mu m$ and mass of the particle is $9.94 \times 10^{-16}\ Kg$. The time step is taken as $1 \times 10^{-9}\ s$, which is much smaller than the mean collision time of the gas. Periodic boundary condition is employed at all the six sides of the domain. CLL model [11] is used for gas-surface interaction with accommodation coefficient of unity.

# 4 Results and Discusion

## 4.1 Spherical Particle In Free Molecular Regime

It was found by several researchers that the particle drag and heat flux depend only on the molecular speed ratio $S$ [12, 13] in free molecular regime, where $S$ is the ratio of particle speed to the mean molecular speed of gas ($S = \frac{U}{\sqrt{2RT}}$). The analytical relation for heat transfer experienced by a spherical particle[4] is expressed in terms of thermal recovery factor $r'$ and modified Stanton number $St'$ as:

$$r' = \frac{(2S^2+1)[1+\frac{ierfc(S)}{S}] + \frac{2S^2-1}{2S^2} erf(S)}{S^2[1+\frac{ierfc(S)}{S}] + \frac{erf(S)}{2S^2}} \tag{1}$$

$$St' = \frac{S^2 + S\ ierfc(S) + \frac{erf(S)}{2}}{8S^2} \tag{2}$$

where $ierfc(S)$ is the integrated complementary error function. The analytical relation for drag coefficient of a spherical particle in the free molecular limit[12] is given by:

$$C_D = \frac{e^{S^{1/2}}}{\sqrt{\pi}S^2}(1+2S^2) + \frac{4S^4+4S^2-1}{2S^4}\ erf(S) + \frac{2\sqrt{\pi}}{3S} \tag{3}$$

In DSMC simulation, the modified Stanton number is derived from heat flux $Q$ and is given by:

$$St' = \frac{Q}{A\rho U c_p (T_r - T_w)} \frac{\gamma}{\gamma+1} \tag{4}$$

The variation of drag coefficient and modified Stanton number with respect to speed ratio for a spherical particle is plotted and compared with analytical results given by Eq. 2,3. The results obtained from 3D DSMC solver is agree well with the analytical result in all speed ratios.

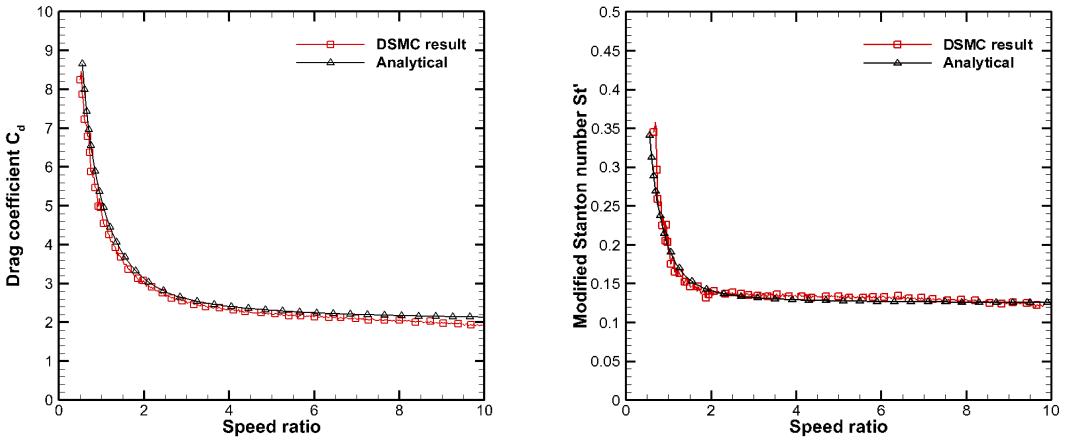


Figure 1: Comparison of DSMC results with analytical a) Drag coefficient (left) and b) Modified Stanton number (right)

## 4.2 Ellipsoidal Particle In Free Molecular Regime

To study the shape effects, we have considered an ellipsoidal particle having volume as same as sphere. In this study, there are three different ellipsoidal shapes considered having eccentricity of 0.7,0.8 and 0.9. In the first phase, the angle of attack is considered to be zero to avoid pitching torque, which arises due to particle shape. The drag coefficient and Stanton number are plotted against molecular speed ratios as shown in Fig.2. As eccentricity increases, the particle shape deviates from spherical and closes to flat plate. In other words, the contact surface area decreases as eccentricity increases since the angle of attack is zero. Therefore, less number of gas-surface collision occurs as eccentricity increases, which makes less momentum and energy imparted to the surface. This is the reason for decreasing drag coefficient and Stanton number observed in DSMC simulations as shown in Fig.2.

The difference in drag/heat flux between spherical and ellipsoidal cases is large at high speed ratios. It is observed that the variation is in the order of 50% between sphere and ellipsoidal case of eccentricity 0.9 after speed ratio 2. Similarly, the difference in Stanton number is also in the order of 50% after speed ratio 2. In our second study, we have considered ellipsoidal particle of eccentricity 0.7 and simulated for

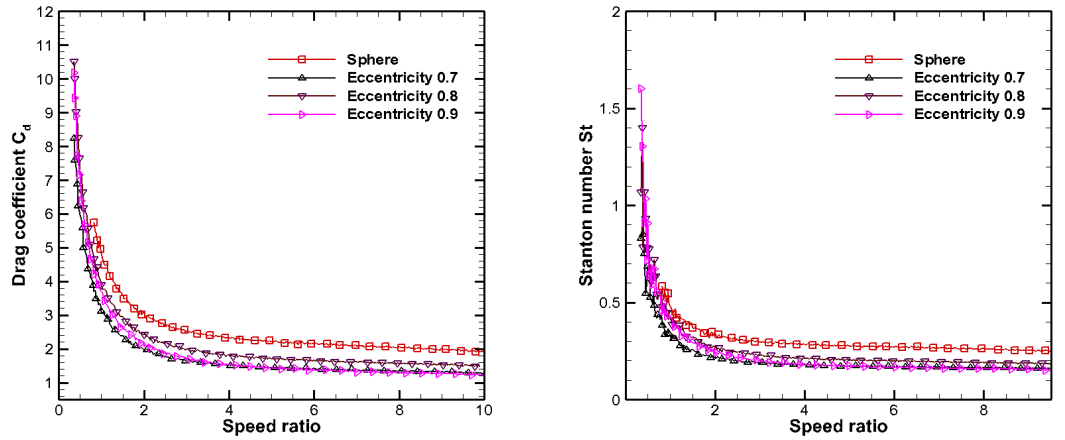


Figure 2: Comparison of spherical particle results with ellipsoidal a) Drag coefficient (left) and b) Modified Stanton number (right)

different angle of attacks as shown in Fig. 3. As angle of attack increases, the frequency of gas-granular collision increases and this leads to an increase in drag and heat flux. From the above results, we conclude that the surface properties very sensitive to the shape and its orientation to the flow.

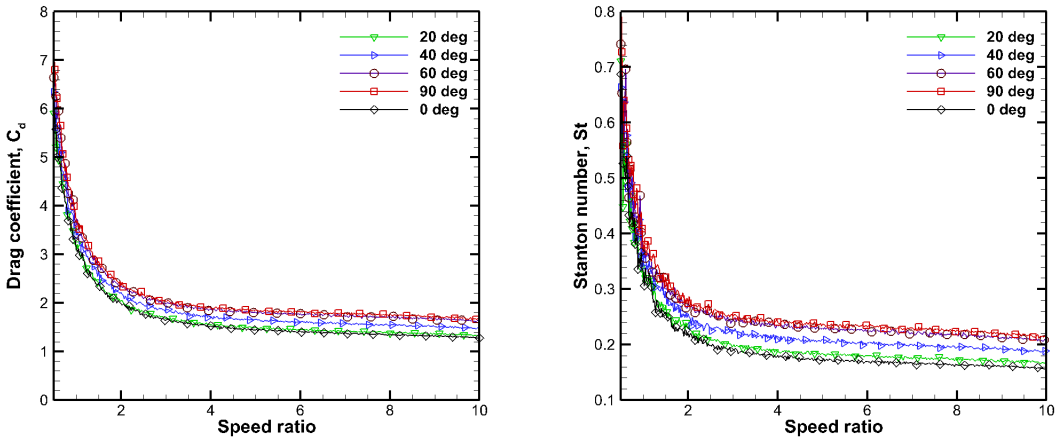


Figure 3: Variation of a) Drag coefficient (left) and b) Modified Stanton number (right) with respect to speed ratio for different angle of attack

# 5 Conclusions

Aerodynamic and heat transfer characteristics of different shaped/sized particles were studied in the DSMC framework. There was huge variation in drag and heat flux have been observed for spherical and ellipsoidal particles. Moreover, the sensitivity of angle of attack was studied in terms of drag and heat transfer. It was found that particle shape and its orientation play an important role in determining the dynamics of gas-solid flows. Furthermore studies need to be done by considering particle rotation.

## References

[1] Gallis *et al.* "An approach for simulating the transport of spherical particles in a rarefied gas flow via the direct simulation Monte Carlo method." Physics of Fluids 13.11 (2001): 3482-3492.

[2] Burt, J. M. (2006). "Monte carlo simulation of solid rocket exhaust plumes at high altitude" (Doctoral dissertation, The University of Michigan).

[3] Morris*et al.* "Approach for modeling rocket plume impingement and dust dispersal on the moon." Journal of Spacecraft and Rockets Vol. 52, No. 2 (2015), pp. 362-374

[4] Saucer *et al.* "Convective heat transfer from spheres in a free-molecule flow." Journal of the Aeronautical Sciences 18-353 (1952).

[5] Zastawny *et al.* "Derivation of drag and lift force and torque coefficients for non-spherical particles in flows." International Journal of Multiphase Flow 39 (2012): 227-239.

[6] Ouchene *et al.*"Drag, lift and torque coefficients for ellipsoidal particles: From low to moderate particle Reynolds numbers." Computers & Fluids 113 (2015): 53-64.

[7] Bird GA. "Molecular Gas Dynamics and Direct Simulation of Gas Flows." Clarendon Press, Oxford, 1994, 508.

[8] Prasanth *et al.* "Direct simulation Monte Carlo (DSMC): A numerical method for transition-regime flows-A review." Journal of the Indian Institute of Science 86.3 (2013): 169.

[9] Kumar *et al.*. "Development of a multi-species, parallel, 3D Direct Simulation Monte-Carlo solver for rarefied gas flows." Computers & Fluids 159 (2017): 204-216.

[10] Chinnappan *et al.* "Insights into flow and heat transfer aspects of hypersonic rarefied flow over a blunt body with aerospike using direct simulation Monte-Carlo approach." Aerospace Science and Technology 66 (2017): 119-128.

[11] Padilla, Jose F., and Iain D. Boyd. "Assessment of Gas-Surface Interaction Models for Computation of Rarefied Hypersonic Flow," Journal of Thermophysics and Heat Transfer 23.1 (2009): 96-105.

[12] Schaaf, S. A., & Chambr, P. L. (1961). "Flow of rarefied gases." Princeton University Press. 1962.

[13] A. K. Oppenheim, "Generalized theory of convective heat transfer in a free-molecule flow." Journal of Aeronautical Science 20-49 (1953)

# Numerical Analysis of Fluid Flow and Heat Transfer Through Multistep Channel Under The Influence of Magnetic Field

**Ranjit J Singh[a], Trushar B. Gohil[a*]**
Department of Mechanical Engineering, Visvesvaraya National Institute of Technology, Nagpur - 440010, [a]iamranjitsingh@gmail.com, [a*]trushar.gohil@gmail.com

## ABSTRACT

The numerical study of the effect of an external magnetic field on laminar, incompressible flow of an electrically conducting fluid in a multistep channel is reported. The magnetic field is applied normal to the flow direction in terms of Hartmann number (*Ha*). In liquid metal fusion blanket or in the continuous slab caster or billet caster processes, the change in the cross-section by sudden expansion or contraction affects the heat distribution, formation of flow structure and pressure drop. When the hot fluid passes through sudden expanded cross section, the uneven heat dissipation is the serious issues in the fusion blanket or casting process, causes the occurrence of crystal growth, thus to ensure proper heat dissipation and flow pattern in the sudden expanded channel, the proposed numerical study has been conducted with the help of open source CFD tool kit OpenFOAM. It is used to optimize the heat transfer and flow pattern. The application of magnetic field produces high-pressure drop by generating the Lorentz force in the reverse direction of the flow, thus the eddies formation in the sudden expansion zone is suppressed and the fluid tends to occupy the absolute area.

**Key Words:** *OpenFOAM, Magnetic field, Heat transfer, Sudden expansion*

## 1. INTRODUCTION

Magnetohydrodynamics (MHD) based fluid flows has appreciable significance to liquid metal fusion reactors blankets [1,2, 5-9], process optimization in casting of melts [10], application of magnetic field in the fusion blankets, continuous caster generates the pressure drop, which increases the pumping power and heavy magnetic load on the surfaces. The pressure drop in the channel is due to Lorentz force generated by application of magnetic field and applied in the reverse direction of fluid motion[1,2]. The solidification and melting of the metals are the salient parts of the manufacturing branch such as crystal growth. The generation of single crystals in the melts has distinctive features, particularly in the mechanical properties. Hence, several research has been focused on the production of defects-free products with single crystal [3]. The grain size and mechanical properties of the cast metal are defined by the heat transfer between cast melt and mold [4], which can be enhanced by the MHD effect.

In the fusion blankets, the entry of the electrically conducting fluid in the ducts follows the sudden expansion or contraction at the exit of the blankets [5-7]. The flows in the sudden contraction or expansion have significant effect on the mass transfer, cooling of ducts or temperature distribution along with flow redistribution, which may have the poor efficiency of the liquid metal blanket [8]. In this study, the effect of MHD on the flow structure and temperature distribution in the multistep channel is considered, and results are validated by the reference [9].

## 2. MATHEMATICAL EQUATIONS AND NUMERICAL SCHEME

The governing equations used to study the fluid flow in the multistep channel with MHD effect along with temperature distribution is obtained by incorporating the Navier-Stokes equation along with Lorentz force as source term and the electric potential equation coupled with Ohm's law of

current density. The energy equation is added in the solver to analyze the heat flow in terms of the temperature distribution. The governing equations in complete set are describes as follows:

Conservation of mass: $\nabla \cdot \vec{U} = 0$ 1

Momentum equation: $\frac{\partial \vec{U}}{\partial t} + (\vec{U} \cdot \nabla)\vec{U} = -\frac{\nabla p}{\rho} + \nu \cdot \nabla^2 \vec{U} + \frac{\vec{j} \times \vec{B}}{\rho}$ 2

Ohm's law of current density: $\vec{j} = \sigma(-\nabla \phi + \vec{U} \times \vec{B})$ 3

Conservation of current density: $\nabla \cdot \vec{j} = 0$ 4

Conservation of thermal energy: $\frac{\partial T}{\partial t} + (U \cdot \nabla)T = \nabla \cdot (\alpha \nabla T)$ 5

Poisson's equation for electric potential: $\nabla^2 \phi = \nabla \cdot (\vec{U} \times \vec{B})$ 6

Where *U, B, j, p,* $\phi$ and *T* stands for the velocity, applied magnetic field, current density, pressure, electric potential and temperature respectively. Whereas, $\rho$, $\sigma$, $\mu$ ($\rho\upsilon$), $\alpha$ denote the density (kg/m$^3$), electric conductivity (S/m), dynamic viscosity(kg/ms) and thermal diffusivity (m$^2$/s) respectively. In the present study, the value of fluid property like $\rho$ and $\sigma$ are kept constant as unity. The two non-dimensional numbers are used in this study to control the MHD effect in the fluid flow are Hartmann number ($Ha = BL\sqrt{\sigma/\rho\nu}$) and Reynolds number ($\mathrm{Re} = \rho UL/\mu$). Where Ha is the Hartmann number, which scales the ratio of electromagnetic force to viscous force. The Reynolds number (Re) anticipate the flow pattern of the fluid. Here *L* is the characteristic taken as the entry width of the channel. The surface of the channel is maintained as thermally and electrically insulating. At the inlet, the temperature is fixed at 350 K, and uniform velocity with *Re* of 1000 is fixed. The Neumann condition is applied for pressure at inlet and walls. At outlet atmospheric pressure condition is considered.

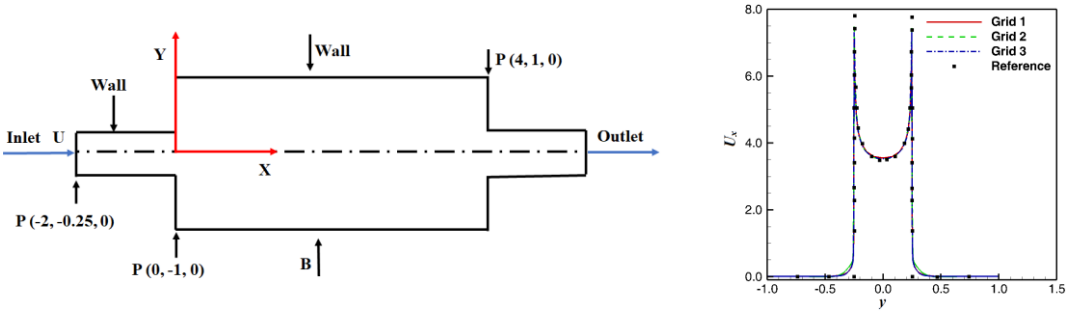


**FIGURE 1**. (left) Schematic of multistep channel, (right) Comparison of streamwise velocity at expansion point at $x = 0$ with reference [9] and grid independence test for three different grids.

## 3. RESULTS

The parameters and geometry details for validation of the MHD flow through the multistep channel is taken from the available reference [9]. Figure 1 (left) shows the detail geometrical parameters for the present test case. Figure 1 (right) shows the validation of results with reference [9] and grid independence test conducted at *Ha* = 1000 and *Re* = 1000 at the expansion ratio of 4 for three different grids. To test the standard execution of simulations, the considered grid sizes are as follows: Grid 1: (35 × 25, 50 × 95, 35 × 25), Grid 2: (70 × 50, 100 × 190, 70 × 50), Grid 3: (105 × 75, 150 × 285, 105 × 75). Based on the study, Grid 2 is used for subsequent simulations.

The numerical simulation for MHD flow through the multistep channel of expansion ratio of 4 is discussed as follows. All simulations are performed for the fixed Re of 1000 and range of Ha is 0-

1000. Figure 2 shows the streamline distribution for various *Ha*. It shows that for non-MHD case (*Ha* = 0), the jet leaves the domain without occupying the absolute area and the vortices are produced. Thus, the heat does not reach properly to the extreme corners of the channel, this implies the uneven heating or cooling effect. The variation of temperature contours and distribution at the different cross-section of the channel shown in Figure 3 and 4. The increase in the magnetic field increases the Lorentz force, which acts in the reverse direction of fluid flow is responsible for the high-pressure drop in the path of fluid flow. This drop in the pressure restricts the motion of the fluid, which tends to allow the fluid to occupy the absolute area of the channel and therefore, the formation of vortices are gone on decreasing by increasing the applied magnetic field. The formation of eddies are completely vanished, and fluids are allowed to occupy the corners of the channel beyond Ha = 100 as shown in Figure 2. As fluid occupies the complete domain the heat will flow and dissipate in the entire domain to achieve the uniform temperature, as it shown in the temperature contours and graphs. Figure 4 shows the comparison of the streamwise velocity at various Hartmann number for fixed Re = 1000, by increasing the Hartmann number the flow in the core has the different profile than the ordinary hydrodynamic profile (Ha = 0).

## 4. CONCLUSIONS

It is observed that the effect of the magnetic forces is to suppress the formation of the corner vortices and the increase in the heat transfer characteristics and proper temperature distribution. The temperature in the channel is uniform beyond the Ha = 500. At the junction point, as soon as flow approaches, flow redistributes rapidly in the broader channel following the wall profile. Thus, M-shaped profile is formed at the plane $x = 0$ for the higher Hartmann number. The application of the magnetic forces on the conducting fluid can improve the cooling efficiency of fusion blanket and quality of the final product in the casting process.

## REFERENCES

[1] A. Sterl, Numerical simulation of liquid-metal MHD flows in rectangular ducts, J. Fluid Mech, 216, 161-191, 1990.
[2] S.Y. Smolentsev, Mathematical models for magnetohydrodynamics-flows in a fusion reactor blanket, Plasma devices and operations, 7, 231-241, 1999.
[3] L. Yuanyuan, L. Dichen, Z. Kai, Static solid cooling: A new directional solidifications technique, Journal of Alloys and Compounds, 687, 674-682, 2016.
[4] M. M. Pariona, A. C. Mossi, Numerical simulation of heat transfer during the solidification of pure iron in sand and mullite molds, J. of the Braz. Soc. of Mech. Sci & Eng, 27, 399-406, 2005.
[5] C. Mistrangelo, L. Buhler, Numerical investigation of liquid metal flows in rectangular sudden expansions, Fusion Engineering and design, 82, 2176-2182, 2007.
[6] R. Reimann, L. Buhler, C. Mistrangelo, S. Molokov, Magneto-hydrodynamic issues of HCLL blanket, Fusion Engineering and design, 81, 625-629, 2006.
[7] F. Jingchao, H. Qingyun, C. Hongli, Y. Minyou, Numerical investigation of magnetohydrodynamics flow through sudden expansion pipes in liquid metal blankets, Fusion Engineering and design, 109-111, 1360-1364, 2016.
[8] S. Aleksandrova, S. Molokov, The structure of parallel layers in steady two-dimensional magnetohydrodynamic flows in sudden duct expansions and contractions, Theor. Comput. Fluid Dyn, 26, 29-35, 2012.
[9] C. Mistrangelo, Three-Dimensional MHD flow in sudden expansions, PhD thesis, University of Karlsruhe, 2006.
[10] Elco Van Vliet, Modelling solidification of an electromagnetic stirred steel flow using OpenFOAM, First Dutch OpenFOAM day, Delft University of Technology, 2010.

(a) *Ha* = 0 (b) Ha = 50

(c) *Ha* =100 (d)*Ha* = 500

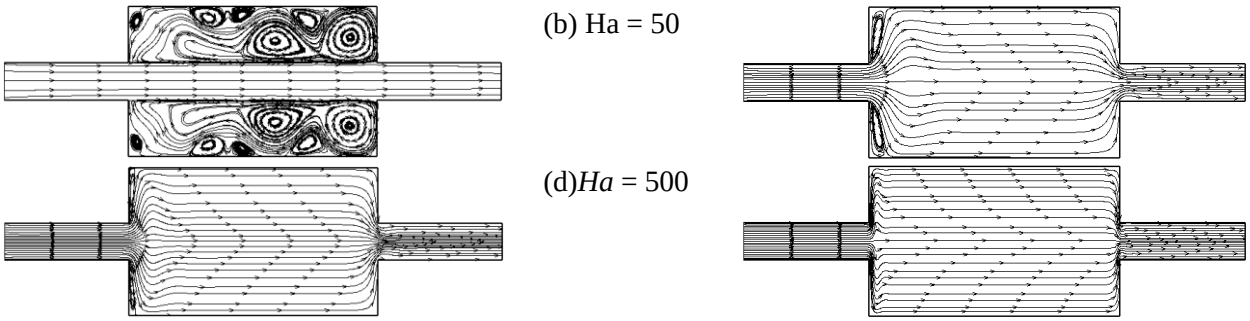

**FIGURE 2**. The streamline variation at fixed *Re* = 1000 and at different *Ha*.

(a) *Ha* = 0 (b) *Ha* = 50

(c)*Ha* =100 (d) *Ha* =500

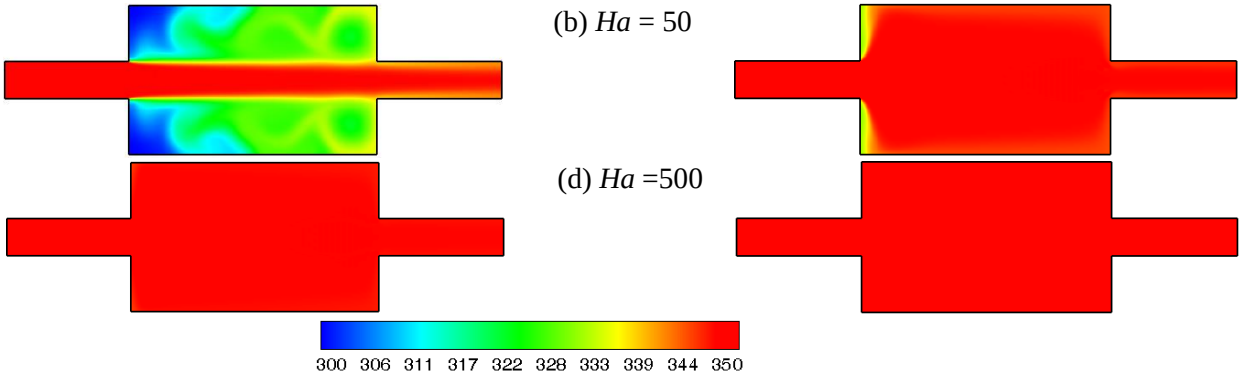


**FIGURE 3**. Temperature contours at fixed Re = 1000 and at different Ha.

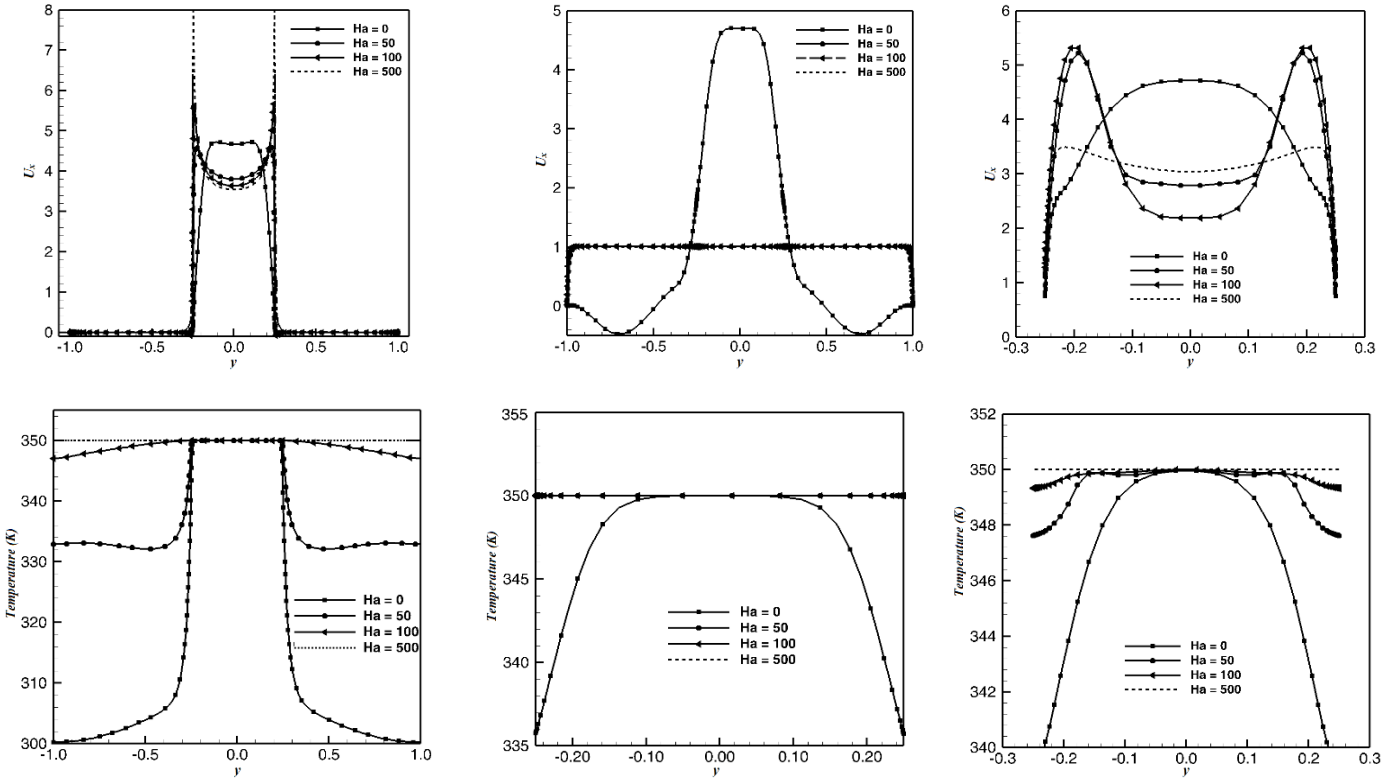


**FIGURE 4**. (Top) Streamwise velocity distribution, (Bottom) Temperature variation at fixed *Re* = 1000 and at different location, (Left) x = 0, (Middle) x = 2 and (Right) x = 4.

# THERMAL MANAGEMENT OF PHOTOVOLTAIC SYSTEM USING POROUS MEDIA

**Tushar Sathe, A.S.Dhoble, Chidanand Mangrulkar**
Department of Mechanical Engineering, Visvesvaraya National Institute of Technology, Nagpur, Maharashtra, India, tusharsathe90@gmail.com
**Sandeep Joshi**
Assistant Professor, Shri Ramdeobaba College of Engineering and Management, Nagpur, India

## ABSTRACT

Numerical analysis for the thermal management of photovoltaic (PV) systems has been carried out considering porous heat transfer medium. Effect of aluminium porous media on the temperature distribution of photovoltaic surface is analysed and compared with PV system with simple air cooling system; without porous media. PV systems are analysed at different flow rate of air and at different incoming heat flux. Effect of different fluid porosity is also analysed for the developed system. Temperature distribution on PV surface with porous heat transfer system is found to be more uniform and 14-16% reduction in PV surface temperature is observed with porous systems compared to simple air based system.

**Key Words:** *Photovoltaic (PV), Photovoltaic thermal system (PVT), porous medium*

## 1. INTRODUCTION

Photovoltaic (PV) systems have been used more widely for the generation of electricity all over the world to reduce the load on renewable resources like coal, oil, natural gases and so on. The electrical conversion efficiency of commercial PV panel is ranging from 17-25% ideally; considering standard test conditions like incoming solar radiations of 1000 $W/m^2$, AM 1.5 and PV cell temperature of $25^0$C[1]. However, the operating conditions of PV systems are not ideal always and it affects the performance of PV systems. The effect of fluctuating incoming radiations and PV cell temperature on the performance of PV systems has been studied and explored by various researchers during last 3-4 decades. It is not possible to manage incoming solar radiations for PV systems, instead; PV panel temperature can be regulated effectively. It is well known that; above $25^0$C, the efficiency of PV solar cell decreases almost 0.45% after every 1 $^0$C rise in its surface temperature. Huge research work has been carried out to manage temperature of PV panel till date: though, the commercial availability of thermal systems for the PV panel is still very limited due to few primary factors like applicability of thermal systems for specific region of world, additional cost of thermal system and use of low grade extracted thermal energy. Thermal management of concentrated PV (CPV) systems are very essential and it must be incorporated on the CPV systems but; at the same time, for rooftop PV systems, thermal regulation can cause a drastic change in its electrical performance.

Thermal management of PV systems can be carried out using various active or passive techniques. Active techniques mostly developed considering cooling mediums like air, water or nanofluid; however, passive cooling is established with fins, phase change materials or natural air cooling systems. Active and passive cooling techniques, both are much-matured techniques now and there is very less scope for further improvement considering conventional cooling medium[2].

Porous media or metal foam is emerging out as a more promising substitute for the conventional thermal management systems. Open cell metal foam are primarily used in the heat transfer applications like in heat exchangers and can also be effectively used for the thermal management of PV systems. The porosity of metal foam available in a range of 80-95%, high porosity metal foam have less weight and high heat transfer capability[3] thus, can be very useful for rooftop PV systems.

Bhattacharya and Mahajan [4] used open cell metal foam for the electronic cooling using different pore sizes and different heat sinks. Convective heat transfer coefficient was calculated and metal foam heat sink found to be more efficient than other simple fin heat sink. Dukhan and Quinones [5] analysed the effect of open cell metal foam in the solar air heater. They found that the thermal conductivity and heat transfer rate increases with the number of pores. Dixit and Ghosh [6] and Calmidi and Mahajan [7] perform experimentation on high porous metal foam and proposed an efficient model for the metal foam based fin as a heat transfer system. In this research work, numerical thermal analysis of PV system with aluminium porous medium has been carried out to enhance its electrical performance by removing excess heat.

## 2. NUMERICAL MODEL

### 2.1 Geometrical modelling, porous medium and meshing

The photovoltaic system used in this study is as shown in figure 1. Typical PV system consists of PV cell; covered with glass, sandwiched between EVA and followed by tedlar layer at the back. In the current study EVA, PV cell and tedlar is considered as a single unit and incorporated in a PV panel; as they does not contribute any strong influence on the temperature distribution.

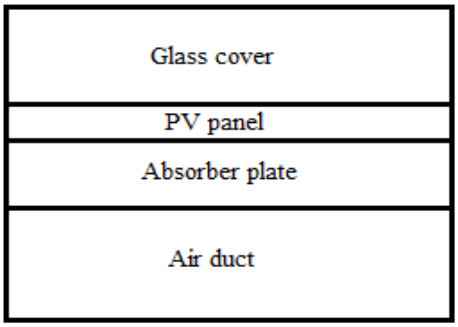


FIGURE 1. Air based PV system

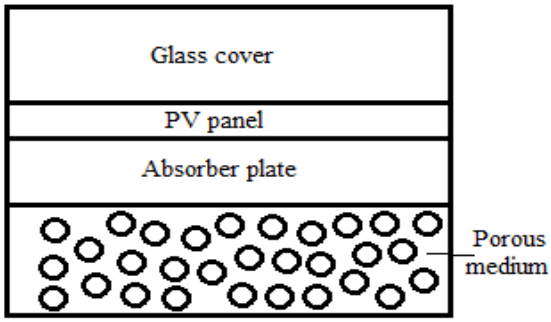


FIGURE 2. PV system with porous medium

The porous medium is included as a heat removal system considering aluminium as a solid material and air a fluid inside the pores. In the current study, porosity is varied from 80-95% as it is available in the market. The schematic diagram for the considered system is as shown in figure. 2. Equilibrium thermal model is used for the analysis without considering any viscous resistance.

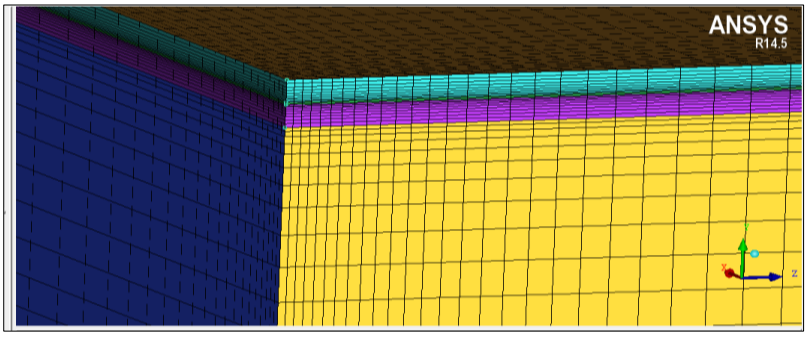


FIGURE 3. Structured mesh for the PV and thermal system

Three-dimensional geometrical model and meshing has been carried out using ANSYS ICEM commercial software as shown in figure 3. A total number of nodes computed to be 290000 with 336633 number of elements.

| System layers | Dimensions (mm) | Material | Properties | | |
|---|---|---|---|---|---|
| | | | Density ( $kg/m^3$) | Specific heat (kJ/kgK) | Thermal conductivity (W/mK) |
| Glass | 2500 x 554 x 3 | Glass | 2450 | 500 | 2 |
| PV | 2500 x 554 x 0.5 | Silicon | 2330 | 677 | 130 |
| Absorber plate | 2500 x 554 x 3 | Aluminium | 2719 | 871 | 202.4 |
| Air duct | 2500 x 554 x 50 | Wood | 700 | 2310 | 0.173 |

TABLE 1. System dimensions and properties

Table 1. Shows various dimensions of the PV and thermal systems along with material properties for various layers that to be used for numerical analysis.

2.2 Numerical analysis

Numerical analysis of the developed system has been carried out using ANSYS FLUENT. Different turbulent models are used for the analysis however, RNG k-epsilon enhanced wall treatment viscous model is used in the current study; as it exhibits close results compared to experiments results. The analysis primarily carried out using air only and without using any porous medium beneath the PV systems. The results obtained are validated with the actual field data (figure. 4) and found to be in good agreement for particular ambient conditions of Nagpur, Maharashtra, India.

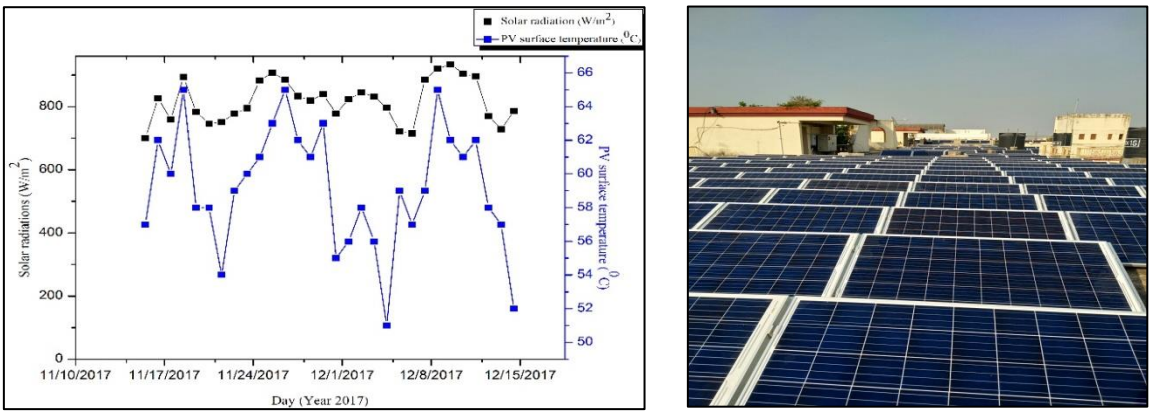


FIGURE 4. Actual field data for radiation and PV surface temperature

Figure 4 shows the temperature with respect to incoming radiations for 30 days which is obtained from the PV plant installed by TATA power at Nagpur, India.

2.3 Boundary conditions

The heat input in terms of constant heat flux is applied on the top glass layer ranging from 500 W/m2 to 1000 W/m2. The flow is laminar up to a velocity of 1.5 m/s, however, it turns into turbulent above 1.5 m/s. In the current system, only turbulent flow is considered thus the air velocity is varied from 2 to 5 m/s. Heat loss from the edges and bottom are neglected and effect of radiation losses are also not considered for the analysis to reduce the complexity of the system.

## 3. RESULTS

In the current study, the temperature distribution on the PV surface is analysed with and without considering porous medium beneath the PV system. Different input parameters are considered for the study like air velocity, incoming solar radiation and porosity. PV surface temperature with porous medium found to be more uniform and at a very low level compared to PV surface temperature

without considering the porous medium. PV surface temperature found to be decrease as the velocity of air increases in both the cases however fluid porosity has not much difference on the PV surface temperature. PV surface temperature at 3.5 m/s of air velocity and at 800 W/m2 of incoming flux is shown in fig.5.

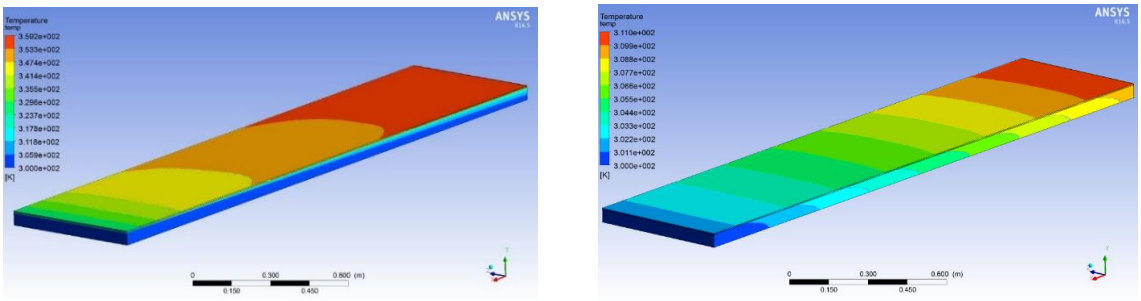

With air only With porous medium

FIGURE 5. Temperature distribution on PV surface

Figure 5 shows that the temperature distribution on the PV surface is much more uniform and lower in the porous medium compared to simple air-based system.

## 4. CONCLUSIONS

The Porous medium for the thermal management of PV system can be considered as a promising substitution for the conventional less efficient air and water-based systems. In the current study, air and porous medium based PV systems are analysed. 14-16% reduction in temperature is observed with porous medium compared to simple air based system. So, it can be concluded that the low weight, high porous medium can be the efficient solution for thermal regulation of PV systems. The conventional solid fin based system can be effectively replaced with the porous medium with the improved thermal performance along with a drastic reduction in the overall weight of the PV system array.

## REFERENCES

[1] T. M. Sathe and A. S. Dhoble, “A review on recent advancements in photovoltaic thermal techniques,” *Renew. Sustain. Energy Rev.*, vol. 76, no. October 2016, pp. 645–672, 2017.

[2] A. Ibrahim, M. Y. Othman, M. H. Ruslan, S. Mat, and K. Sopian, “Recent advances in flat plate photovoltaic / thermal ( PV / T ) solar collectors,” *Renew. Sustain. Energy Rev.*, vol. 15, no. 1, pp. 352–365, 2011.

[3] X. Han, Q. I. N. Wang, Y. Park, C. T. Joen, A. Sommers, and A. Jacobi, “A Review of Metal Foam and Metal Matrix Composites for Heat Exchangers and Heat Sinks,” vol. 33, no. 12, pp. 991–1009, 2012.

[4] A. Bhattacharya, “for Electronics Cooling in Forced Convection,” vol. 124, no. September 2002, pp. 155–163, 2017.

[5] N. Dukhan and P. D. Quinones, “Convective Heat Transfer Analysis Of Open Cell Metal Foam,” no. March 2003, pp. 15–18, 2017.

[6] T. Dixit and I. Ghosh, “An experimental study on open cell metal foam as extended heat transfer surface,” *Exp. Therm. FLUID Sci.*, vol. 77, pp. 28–37, 2016.

[7] R. L. Mahajan, “Forced Convection in High Porosity Metal Foams,” vol. 122, no. August 2000, pp. 557–565, 2017.

Fifth International Conference on Computational Methods for Thermal Problems
THERMACOMP2018, July 9-11, 2018, Indian Institute of Science, Bangalore, INDIA
*N. Massarotti, P. Nithiarasu, Pradip Dutta and C. Ranganyakalu (Eds.)*

# MODELING AND SIMULATION FOR THERMAL MANAGEMENT OF HOT SURFACES BASED ON STATE SPACE METHOD

**Manoj Ukamanal, Purna Chandra Mishra, Ashok Kumar Sahoo**
School of Mechanical Engineering, Kalinga Institute of Industrial Technology
(KIIT, Deemed to be University), Bhubaneswar-24, Odisha,

manoj.ukamanalfme@kiit.ac.in, pcmishrafme@kiit.ac.in, asahoofme@kiit.ac.in

## ABSTRACT

A Single Input Multiple Output (SIMO) control model based on state space technique for cooling of a stationary hot steel plate by jet impingement was investigated. The state space based control model was based on the thermocouple locations on the metal surface for the formulation of a semi-discrete 1-D transient heat conduction control volume problem. A general open loop plant model was incorporated for the plant validity tests. In the simulation of numerical heat transfer, the transient conduction equation has been used to show the nonlinearity of the surface temperature following a heat transfer coefficient correlation for the strain rate of air from nozzle exit. With a known temperature rate (demand) on the top surface of the plate for a single nozzle the temperatures at all the zones of steel plate thickness are evaluated by solving a set of ODEs in the MATLab and SIMULINK environments.

**Key Words:** *Jet Impingement Cooling, State Space Model, SIMO Control, Cooling Rate*.

## 1. INTRODUCTION

Quenching by jet impingement is mainly used in steel tempering, in which the rate of cooling of steel is time dependent as it is based on the flow rate of the coolant. It is necessary to study the effects of variations of the coolant flow rate so that the desired metallurgical properties of steel are obtained by following the predicted temperature or cooling profile. Chattopadhyay & Saha (2002), Shuja (2002), & Tiwari et al. (2004) did extensive work to study the jet impingement technique for cooling of stationary as well as moving steel plates. The present study is focussed on achieving accurate solutions for steady and dynamic applications. In recent researches in the field of thermal processing of materials, significant importance has been given to the heat transfer processes having full state feedback control. The goal of present study is to analyze the crucial heat transfer phenomenon to formulate new control strategies for heat transfer optimization. A control system deals with steady state as well as dynamic performances and stability of control systems in response to characteristic input signals. An open loop control is based on time-to-time calibration of input-output measurements acquired during manual setting of the controller parameters. The current study tries to anticipate the variations in temperature profile of a horizontal steel plate that are necessary by controlling the air jet velocity from the nozzle positioned in the vertical axis as shown in Fig. i.

## 2. PHYSICAL PROBLEM DESCRIPTION AND FORMULATION

A stationary rectangular steel slab was considered for cooling by air jet impingement sent from a nozzle. The desired cooling rate of the steel plate was achieved by regulating the mass flow rate of the air coming through the nozzle. Temperature sensors were attached on the top surface of the plate just below each nozzle axis to measure the surface temperatures. Since the interest is towards the temperature distribution over the thickness of the plate, we need to measure or estimate the temperature at different depths. Such a system is a Single-Input-Multiple-Output (SIMO) system from control perspective.

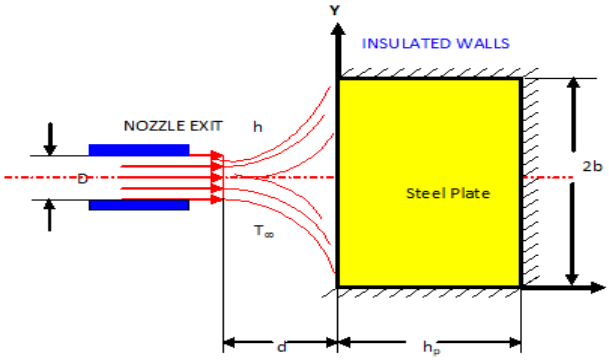


**Fig-i.** Schematic representation of nozzle arrangement for jet impingement cooling of steel plate.

Another side of the plate, opposite to the side exposed to the cooling air, is considered as insulated throughout. One-dimensional transient heat conduction model for the plate, assuming the heat transfer across the plate thickness only, was formulated. The process modeling was simplified by adopting constant property for conduction heat transfer within the plate. The local heat transfer coefficient was obtained through usage of appropriate correlations which were consistent with the approach adopted for convective heat transfer. The heat transfer of a cold laminar stagnation flow to an initially relatively hot plate is studied numerically. Fig. (ii). represents the one-dimensional (1-D) computational domain.

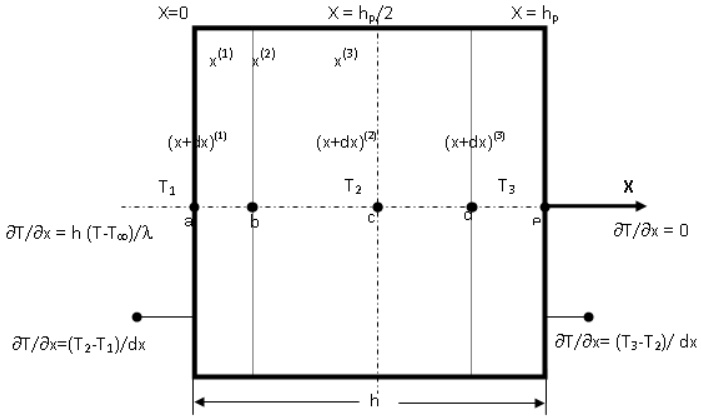


**Fig-ii.** Schematic modeling of the geometry of the plate for jet impingement cooling (Control-Volume Approach)

The heat flow is considered only in the positive x-direction i.e., left to right side of the plate as shown in Fig.(ii). Three temperature zones are considered here. i.e., ($T_1$ at x = 0, $T_2$ at hp/2 and $T_3$ at hp) and the whole plate thickness is divided into three control volumes.

1-D transient heat conduction governing energy equation can be given as:

$$\rho C \frac{\partial T}{\partial t} = \frac{\partial}{\partial x}\left[\lambda(T)\frac{\partial T}{\partial x}\right] \; ; \; 0< x<hp \qquad \text{(i)}$$

Considering the convective, initial and the insulated boundary conditions, the governing energy equation is given as:

$$h\left\{T\big|_{x=0} - T_\infty\right\} = \lambda(T)\frac{\partial T}{\partial x}\Big|_{x=0} \qquad \text{(ii)}$$

The local convective heat transfer coefficient (h) in Eq. (2) is given by Cremers et al., (2004) as:

$$h = ka^{1/2} \qquad \text{(iii)}$$

where,'k' is the constant of proportionality and 'a' is the mean strain rate in $s^{-1}$.

An implicit control volume approach is used and Eq. (i) and (ii) are descretized in space and time. These equations are solved in MATLab environment using ODE solver (ODE45), and are used to obtain the temperature profile in the plate, which is time dependent, any variation in the local convective heat transfer coefficient. The initial values for the strain rate and plate surface temperature ($T_1$) were chosen 100 $s^{-1}$ and 800K. Gradually, the strain rate was varied and the behaviour of temperature - time plots was studied. The determined strain rate (mean) is fed as the input for the system and the corresponding temperature profiles over the thickness of the plate are identified. This simulation is performed by using the f-solver for a set of nonlinear equations. The control system was mainly used to solve the inverse problem by an efficient pole placement technique to minimize any deviations from a reference temperature profile.
The governing equations can be represented in the form of an ODE set as:

$$M\dot{X} = AX + B\bar{a} \tag{iv}$$

With the known temperature rate at the surface of the plate as input to the system the state space Eq. (vii) was modified to determine the strain rate of air, initially was time invariant and then extended to time variant is as follows:

$$\hat{\dot{X}} = \hat{A}X + \hat{B}\bar{a} \tag{v}$$

Where, $\hat{A} = [M]^{-1}[A]$ and $\hat{B} = [M]^{-1}[B]$

Eq. (v) is the constraint equation of the variable that should be considered along with the control objective that is in the general formulation.

**Step-1:** The nonlinear mean dynamics equations are obtained for the plant considering the physical situations in state-space form as in Eq.(xi).

**Step-2:** Initially to ensure the validity of the plant, a forward plant test has been carried out. For this test the values of demand temperature, initial temperature at three different zones of the plates and the mean strain rate ( $\bar{a}$ ) were taken –1 K/s, 800 K and 100 $s^{-1}$ respectively. "ODE45" solver was used to solve the state space equation.

**Step-3:** On adopting both the fixed and time variant mean strain rate values the nature of demand temperature profiles with respect to each time segment has been plotted.

**Step-4:** For the feedback control test, a set of nonlinear equations were solved by using "fsolve" to assure the behaviour of state variables with respect to the determined control input.

**Step-5:** Several plots have been taken for the state variables against time so as to ensure their behaviour with respect to the prescribed strain rate.

**Step-6:** The total simulation time was divided into a number of segments, where the mean inputs ( $\bar{a}$ ) were considered fixed. A piece-wise linearization and time invariance of the nonlinear strain rate was assured in this step.

**Step-7:** From the combined plots the open loop control behaviour of the temperature profiles were studied.

## 3. RESULTS

The plate material considered in this work was plain carbon steel having constant mass density,

$\rho$ = 7850 kg/$m^3$, specific heat, C = 500 J/kg.K. The thermal conductivity K = 54 W/m.K was used based on the data presented in I.S. Code of Practice for General Construction in Steel (Second Revision). The open loop gain matrix was designed by evaluating the Eigen values of ***A*** matrix. Even-though the real parts of the Eigen values are negative but are significantly small. Thus, the stability of the system was uncertain. Adopting the traditional open loop control model in practice signifies that thermocouple locations can be used for the semi-discretization of the steel plate. In the proposed control model, only the surface temperature values are measured. The proposed control model performance is observed to be effective in eliminating the involvement of temperature sensors to be fitted at the material interiors for temperature measurement required in laboratories which were not practicable in industry. Since only $T_1$ i.e., the temperature measured from sensor

attached on the exposed surface of the steel plate is known, so taking these assumed temperatures at all the three zones, $T_2$ and $T_3$ are estimated in terms of the initial values i.e., $\dot{T}_2$ and $\dot{T}_3$ are descretized in such a manner that for each iteration three unknowns such as temperature at the interior zone of the plate ($T_2$), temperature at the insulated end of the plate ($T_3$) and the strain rate (a) are calculated. The controlled time-temperature history is depicted in Fig. (iv). It represents an agreeable performance of the control model. The convective heat transfer correlation of Eq. (iii) shows the non-linear profile of the convective heat transfer coefficient in terms of the mean strain rate away from the nozzle axis. The Eigen values of matrix A, when fed as the open loop poles, it is identified that, the temperature profile seems oscillatory (as in Fig.(iv).) because, one of the pole is negative real but very close to the imaginary plane, which calls for a feedback control of the profile for more stability.

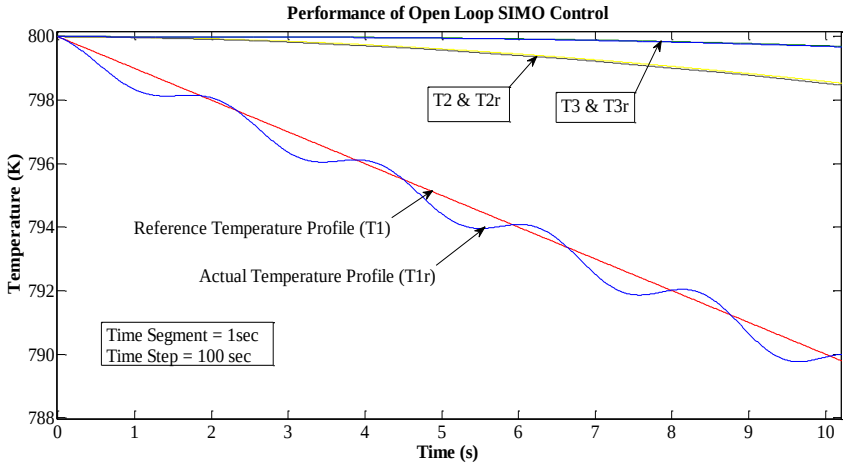


**Fig-iv.** Time Dependent Temperature History of Open-Loop SIMO control.

## 4. CONCLUSIONS

Open Loop control is found satisfactory in steel tempering by quenching air jet. This is identified by testing the plant in both the ways i.e., forward plant test and backward plant test. Low cooling rate through the steel plate makes the SIMO control model incapable for quenching by jet impingement. A simple open loop SIMO control model developed here using variable jet strain rate might become the basis to reduce the non-uniformity of the temperature distributions. This considered open-loop model might give information for simpler sensor arrangement.

## REFERENCES

[1] Chattopadhyay, H.,& Saha, S. K., (2002). Simulation of laminar slot jets impinging on a moving surface, *ASME J. Heat Transfer*, 124, 1049-1055.

[2] Cremers, M. F. G., Remie, M. J., Schreel, K. R. A. M.& H de Goey, L. P., (2004). Heat transfer mechanisms of laminar flames of Hydrogen + Oxygen, *Combustion and Flame*, 139, 39-51.

[3] Huang, C. H., & Yeh, C. -Y., (2003). An optimal control algorithm for entrance concurrent flow problems, *Int. J. Heat Mass Transfer*, 46, 1013 - 1027.

[4] Kalyon, M.& Sahin, A. Z., (2002). Application of control theory in pipe insulation, *Numerical Heat Transfer*, Part A, 41, 391-402.

[5] Tiwari, M. K., Mukhopadhyay, A., & Sanyal, D., (2004). Numerical simulation of optimal multiple-input, multiple-output control of jet impingement cooling of a glass plate, *Numerical Heat Transfer*, Part A, Applications, 46, 401-424.

Fifth International Conference on Computational Methods for Thermal Problems
THERMACOMP2018, July 9-11, 2018, Indian Institute of Science, Bangalore, INDIA
*N. Massarotti, P. Nithiarasu, Pradip Dutta and C. Ranganyakalu (Eds.)*

# NUMERICAL ANALYSIS OF THERMAL PERFORMANCE IN PIN-FIN ENHANCED MICROCHANNEL HEAT SINK

**V. P. Gaikwad[1], S. S. Mohite[2], S. S. Shinde[2], M. L. Dherange[2]**

1. Textile and Engineering Institute, Ichalkaranji, 416115, gvinayak2002@gmail.com

2. Government College of Engineering, Karad, 415124, mohitess@yahoo.com

Affiliated to Shivaji University, Kolhapur

## ABSTRACT

Enhancement of thermal performance of microchannel heat sink (MCHS) by introducing pin fins in the channels is the main objective of this study. A single microchannel with and without pin fins is studied for different flow and thermal conditions. The pin fins are introduced from the top cover instead of the conventional method of pin-fin protruding from the base of heat sink as it drastically reduces the fabrication cost. Pin fins of different heights are numerically analysed. Of the different configurations, enhanced MCHS with pin height of 1.2 mm give the best results. This is due to the fact that as clearance between base and pins increase, there is an accelerated flow in the clearance region producing more mixing of fluid and higher heat transfer performance. Effects of fluid bypassing the pins become dominant when the clearance region is further increased, resulting in lower heat transfer performance. The introduction of pin-fin increases the pressure drop; it is highest for full height pin-fin and decreases with decreased fin height. The best configuration is then studied for different flow rates. The thermal performance increases with increase in flow rate, the temperature gradient decreases by 33% for flow rate of 600 ml/min but at an increased pressure drop of 100% than the conventional MCHS.

**Key Words:** *microchannel, pin-fin, forced convection, temperature gradient*

## 1. INTRODUCTION

Recent developments in micro-electro mechanical systems and ultra large scale integrated technologies are becoming increasingly dependent upon the ability to dissipate huge amounts of heat from very small areas. This has motivated researchers to focus on the improvement of thermal and hydrodynamic performance of microchannels. After the pioneering work by Tuckerman and Pease [1], a number of researchers have made attempts to improve the performance of conventional parallel MCHS. Most of the researchers who studied pin-fin microchannels studied an array of pin-fins creating a microchannel flow area. Carlos et al. [2] developed micro pin-fin with variable fin density to generate more uniform temperature at the IC chip interface. The novel design generated thermal resistance ranging from 0.14 K/W to 0.25 K/W with a pressure drop lower than 90 kPa. Carlos et al. [3] compared online and offset micro pin-fin heat sinks with variable fin density and deduced that the offset pin-fin configuration is capable of achieving a much lower thermal resistance of 0.1 K/W. Ali Kosar and Peles [4] experimentally studied the thermal and hydraulic performance of shrouded staggered micro pin fins and compared using the correlations developed by earlier researchers. Abel et al. [5] experimentally studied pressure drop and heat transfer in a single phase micro pin fin heat sink. The measured pressure drop and temperature distribution were used to evaluate average friction factor and local averaged heat transfer coefficient and Nusselt number. They examined the previous friction factor correlations and only one was found to agree with the experimental data. John et al. [6] numerically studied a single channel of the MCHS with embedded pin-fin structures which showed lower thermal resistance compared to conventional MCHS. Thus most of the research work is in the pin-fin array. Very less work is done in the field of flow disturbance in microchannel using pin-fins.

According to forced convection mechanism theory, for a constant heat flux boundary conditions, the temperature difference between the coolant and channel wall remains constant along the flow length in the fully developed condition. Fully developed flow is one of the main reasons for this condition. So to improve the thermal performance, a mechanism to disturb the fully developed flow is needed. In this paper a new micro pin-fin configuration in a microchannel is numerically analysed. In this configuration, pin-fins are introduced into the microchannel with the help of the top acrylic cover. The size, shape and location of pin-fins are the variables against which the performance is studied.

## 2. ENHANCED MCHS DESIGN

The numerical analysis was carried out using the commercial computational fluid dynamics software ANSYS FLUENT 18.1. The computational domain consists of single channel with side walls while the pins are suspended from top cover as shown in figure 1. The pins and side walls and base of microchannel are of copper while top cover is of acrylic. The pin height $H_P$ is always less than channel height $H_c$. The numerical analysis is carried out for enhanced MCHS with different fin heights as shown in table 1 and conventional MCHS with no pin-fins. The computational domain is meshed using edge mesh with size of 20μm. The total number of elements created are 8962155. The channel and pin surfaces are treated as no-slip boundary conditions. Constant heat flux boundary condition of 65 $W/cm^2$ is applied to the bottom heater. A fully developed velocity profile corresponding to the various flow rates with inlet temperature of 300 K is applied to inlet and pressure outlet condition at outlet. The fluid is water with temperature dependent properties.

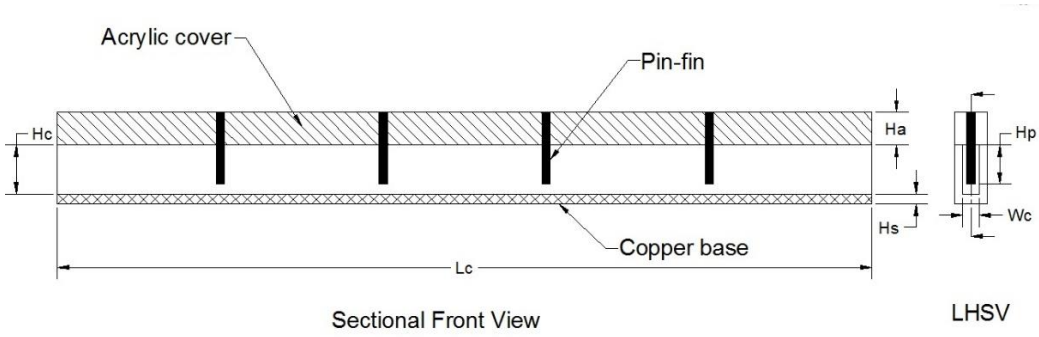


Figure 1. Pin-fin configuration in a microchannel

| Sr. No. | Channel dimension | | | pin height | $H_a$ | $H_s$ |
|---|---|---|---|---|---|---|
| | $L_c$ | $W_c$ | $H_c$ | $H_P$ | | |
| 1 | 25 | 0.5 | 1.5 | 1.5 to 1.1 | 1 | 0.3 |

TABLE 1. Dimensions of Pin-Fin in enhanced MCHS (All dimensions in mm)

## 3. RESULTS

The simulation was initially carried out to find the effect of pin height on the thermal performance. Two important parameters for checking the thermal performance are the maximum bottom heater temperature, and temperature gradient at the bottom heater which indicates the possibility of formation of hotspots and formation of thermal stresses due to lack of uniformity in temperature distribution in the electronic components being cooled. Figure 2 shows the variation of temperature along bottom heater length for different configurations. All temperature profiles show non-linear

behaviour. All enhanced MCHS show lower temperature variations than the conventional MCHS. The enhanced MCHS with pin height of 1.2 mm shows the lowest temperature variation. The temperature gradient for different configuration is given in table 2. The enhanced MCHS with $H_p$ of 1.5 mm shows the lowest temperature gradient followed by pin-fin of height of 1.2 mm. This is due to the fact that as clearance between base and pins increase, there is an accelerated flow in the clearance region producing more mixing of fluid (see figure 3) and higher heat transfer performance. Effects of fluid by-passing the pins become dominant when the clearance region is further increased, resulting in lower heat transfer performance. The introduction of pin-fin increases the pressure drop; it is highest for full height pin-fin and decreases with decreased fin height (see Table 3). This is due to the fact that as pin height reduces there is reduction in the flow disturbance. Figure 4 shows the velocity distribution of water near a single pin-fin when viewed from top. As seen in the figure the fully developed flow is disturbed which results in better mixing of fluid and better thermal performance. Simulation for enhanced MCHS with $H_p$ of 1.2 mm subjected to different flow rates is carried out and its effect on the bottom heater temperature is shown in figure 5. As the flow rate increases the temperature along the bottom heater decreases. A new heat transfer correlation (Eq.1) showing the effect of clearance between pin and base is developed to fit the present data through modifying common functional forms given by Moores and Joshi [7].

$$Nu = 0.977 \left(\frac{H_c}{H_p}\right)^{-0.06} Re^{0.85}\, Pr^{-0.75} \tag{1}$$

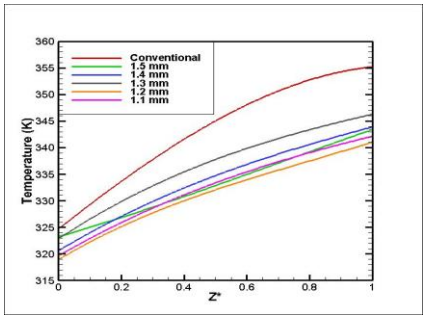


Figure 2: Bottom heater temperature for different MCHS configurations

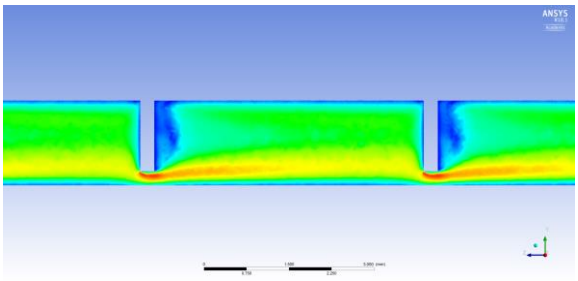

Figure 3: Velocity contour of fluid along the pin height

| $H_p$ (mm) | Conventional MCHS (without pin-fin) | Enhanced MCHS | | | | |
|---|---|---|---|---|---|---|
| | | 1.5 | 1.4 | 1.3 | 1.2 | 1.1 |
| Temp. Gradient ( $\frac{\partial T}{\partial X}$) K/mm | 1.20 | 0.80 | 0.92 | 0.91 | 0.88 | 0.89 |

TABLE 2. Temperature gradient for various configurations

| $H_P$ (mm) | Conventional (without pin-fin) | Enhanced MCHS | | | | |
|---|---|---|---|---|---|---|
| | | 1.5 | 1.4 | 1.3 | 1.2 | 1.1 |
| ΔP (kPa) | 0.51 | 1.25 | 1.26 | 1.14 | 1.04 | 0.97 |

TABLE 3. Pressure drop for various configurations

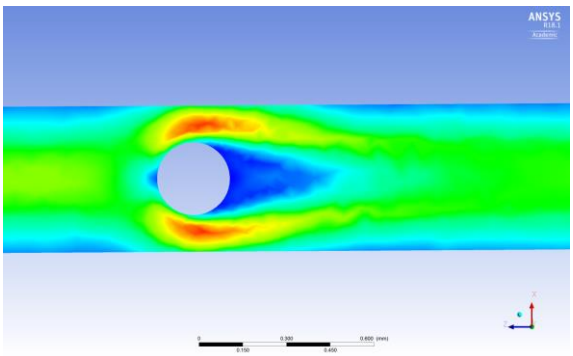


Figure 4: Velocity contour of fluid showing enhanced fluid mixing (top view)

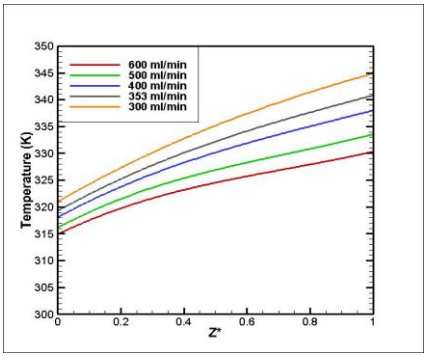


Figure 5: Bottom heater temperature for $H_p$ = 1.2 mm for different flow rates

## 4. CONCLUSIONS

A novel pin-fin configuration is studied to improve the performance of conventional MCHS.

- The enhanced MCHS with $H_p$ of 1.2 mm gives the optimum results. For the same flow rate, it has the lowest temperature along bottom heater (Average temperature difference of 12 K lower than conventional MCHS). The temperature gradient in the bottom heater reduces by 33% from 1.2 K/mm in conventional MCHS to 0.8 K/mm for $H_p$ of 1.5 mm. The pressure drop for this configuration is more by 100% than conventional MCHS.
- The pressure drop is highest for $H_p$=1.5 mm, decreases with reduction in pin-fin height for enhanced MCHS and is lowest for conventional MCHS.
- The fabrication cost of pin-fins protruding from MCHS base is huge compared to the pin-fins suspended from top cover. The improvement in thermal performance is thus at very little additional cost. A new correlation showing the effect of pin fin clearance is developed.

## REFERENCES

[1] Tuckerman, D. B., Pease, R. F.: High Performance Heat Sinking for VLSI, *IEEE Electronic Device Letters*, EDL- 2 (1981)

[2] Carlos A. R., Kandlikar S. G., Abel H-G., Numerical Analysis of Novel Micro Pin Fin Heat Sink With Variable Fin Density, *IEEE Trans. Comp. Packaging and Manu. Tech.*, Vol.2 No. 5 May 2012

[3] Carlos A. R., Kandlikar S. G., Abel H-G., Performance of Online and Offset Micro Pin Fin Heat Sink With Variable Fin Density, *IEEE Trans. Comp. Packaging and Manu. Tech.*, Vol.3 No. 1 January 2013

[4] Ali Kosar, Y. Peles, Thermal-Hydraulic Performance of MEMS Based Pin Fin Heat Sink, *J. of Heat Transfer*, Vol. 128, Feb 2006

[5] Abel Siu Ho, Weilin Qu, Frank P., Experimental Study of Pressure Drop and Heat Transfer in a Single Phase Micro Pin Fin Heat Sink, *J. of Electron Packaging*, Vol. 129, Dec. 2007

[6] John T. J., Mathew B., Hegab H., Micro Channel Heat Sink With Embedded Pin-Fin Structures, *10th AIAA/ASME Joint Thermophysics and Heat Transfer Conference*, 28 June - 1 July 2010, Chicago, Illinois

[7] K.A. Moores, Y.K. Joshi, Effect of tip clearance on the thermal and hydrodynamic performance of a shrouded pin fin array, *J. Heat Transfer* 125 (6) (2003) 999–1006.

Fifth International Conference on Computational Methods for Thermal Problems
THERMACOMP2018, July 9-11, 2018, Indian Institute of Science, Bangalore, INDIA
*N. Massarotti, P. Nithiarasu, Pradip Dutta and C. Ranganyakalu (Eds.)*

# ENHANCEMENT IN THERMAL PERFORMANCE OF MICROCHANNEL HEAT SINK FOR ELECTRONICS COOLING USING PHASE CHANGE MATERIAL

**V. P. Gaikwad[1], S. S. Mohite[2], S. S. Shinde[2], M. L. Dherange[2], Abhinandan Kumar[2]**

1. Textile and Engineering Institute, Ichalkaranji, 416115, gvinayak2002@gmail.com

2. Government College of Engineering, Karad, 415124, mohitess@yahoo.com

## ABSTRACT

Enhancement in the thermal performance of microchannel heat sink (MCHS) is numerically investigated using phase change material (PCM) as the coolant. MCHS having a width of 0.5 mm and depth of 1.5 mm is studied in detail for N-eicosane in water having volumetric concentration of 15% as coolant. The Nusselt number enhancement was found to be approximately 20%. Due to higher temperature at the bottom surface, the phase change process starts at the bottom surface and propagates upwards as the coolant moves downstream. A combination of longer thermal developing length, and phase change process of PCM results in increased Nusselt number. The average increase in pressure drop for PCM slurry is 10%. Thus use of PCM improves the performance of MCHS at the cost of slightly higher pumping power.

**Key Words**: *microchannel, phase change material, forced Convection.*

## 1. INTRODUCTION

The rapid development in electronic industry and the economic market demand for faster clock speeds in a smaller physical space has resulted in generation of very high heat flux in the electronic chips. This heat is to be removed as fast as possible or else the performance of the electronic components can deteriorate. Amongst the different approaches, the forced fluid cooling through microchannel heat sink (MCHS) is better suited for electronic cooling. Tuckerman and Pease [1] were the first to utilize the MCHS for electronic cooling. Since then huge work is done in this field, some of the work discussed below, is aimed at enhancing the performance of MCHS.

Use of Phase change materials (PCM) in cooling fluid is one way of enhancing the thermal performance of MCHS. PCM is a substance with a high heat of fusion which, by melting and solidifying at certain temperatures is capable of storing and releasing large amount of energy. PCM has low melting/freezing temperature, high specific heat, high density and high thermal conductivity. Due to these unique properties, PCM has been used as thermal energy storage device. Use of PCM as coolant has been studied by many researchers in macroscale applications but less in microscale applications. In microchannel heat sink, the PCM can be mixed with the base coolant fluid and improve the heat removing capacity of the coolant.

K. Q. Xing et al. [2] applied numerical simulation to study laminar flow and heat transfer characteristics of micro-size phase change material (Octadecane) particles suspended in water (volume fraction 0.25) passing through a micro-tube having L/D ratio of 100. Numerical results show that for volumetric fraction of 0.25, the performance index $PI_{max}$ is between1.3 to 2.0 for Reynolds number 90 and 600 respectively. S.Kuravi et al. [3] numerically investigated heat transfer performance of Nano-Encapsulated PCM (NEPCM) slurry flowing through manifold microchannels. The PCM is eicosane with Polyalphaolefin

(PAO) as base fluid having different volume concentrations of PCM. Results show that the pressure drop from inlet to outlet increases with increase in volume concentration. The heat transfer enhancement is better for narrow melting range. Kondle et al. [4] numerically compared the heat transfer behavior of pure water with N-eicosane PCM slurry under laminar flow conditions in circular and rectangular microchannels. Rectangular microchannels with fixed depth of 150 µm and different widths to get aspect ratio of 1:2, 1:4 and 1:8 were simulated. From the results it was found that the fully developed Nusselt number is highest for H1 than for H2 and T boundary conditions for all geometries. A detail literature review indicates that some researchers have studied the use of PCM in MCHS. The objective of this work is to study the effect of PCM fluid as coolant in MCHS. The selected MCHS is studied for two types of coolant, pure water and water + PCM (N-eicosane) for different heat flux and flow rates.

## 2. MICROCHANNEL GEOMETRY

The rectangular microchannel under consideration has a width of 0.5 mm and depth 1.5mm (aspect ratio D/W = 3). The total area of microchannel heat sink is 25 mm x 25 mm similar to the footprint of many electronic processors (figure 1). The width of the fins separating the microchannels is 0.5mm, thus 25 channels are housed in the heat sink. Instead of creating the entire microchannel heat sink, a periodic boundary condition is assumed to reduce the computation domain to a channel-fin pair which is further reduced to half channel-fin pair by using the planar symmetry as shown in figure 2. Numerical analysis was carried out using the computational fluid dynamics software ANSYS FLUENT 18.1.

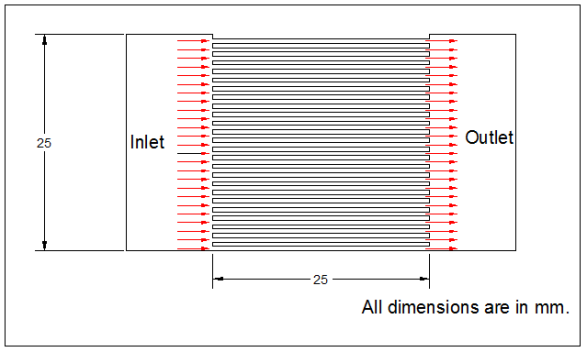


Figure 1. Top view of microchannel heat sink

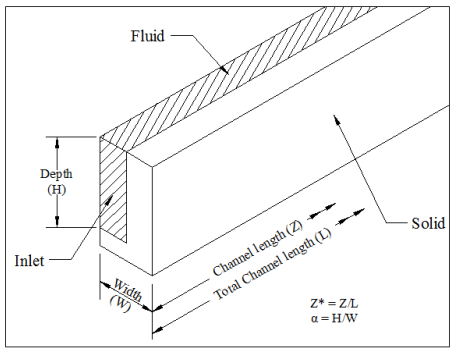


Figure 2: Details of geometric model

Two different approaches were found in literature used for modeling the complete phase change process in PCM. First approach uses a heat source term in the energy equation, while the second considers a specific heat model. Simulation of complete phase change process of PCM particles in water-PCM was based on specific heat model used in earlier research work [4]. In this model, the phase change of PCM is approximated by changing the specific heat of water-PCM within the melting temperature range of PCM. The following equations were used to determine the specific heat of water-PCM for the entire operating temperature range.

For $T < T_1$ or $T > T_2$ [4]

$$C_{p,b} = c \cdot C_{p,p} + (1 - c) \cdot C_{p,f} \quad (1)$$

For $T_1 < T < T_2$ [4]

$$C_{p,b} = (1 - c) \cdot C_{p,f} + \frac{c \cdot L_h}{(T_2 - T_1)} \quad (2)$$

where, $T_1$ and $T_2$ are the temperatures at which the phase change process starts and ends respectively. $L_h$ and c are the latent heat of fusion of the phase change material and phase change material concentration, respectively. The variation of specific heat as a function of temperature for water-PCM is incorporated in

ANSYS FLUENT software as a user defined function. Water is used as the working fluid with temperature dependent properties, and for same boundary conditions, the results were compared.

## 3. RESULTS

Results of MCHS subjected to a constant heat flux of 65 W/cm$^2$ and having pure water and water-PCM (water + PCM) as coolant for different flow rates are discussed here. The variation of Nusselt number along non-dimension length Z* (= Z/L) for different flow rates is shown in figure 3.

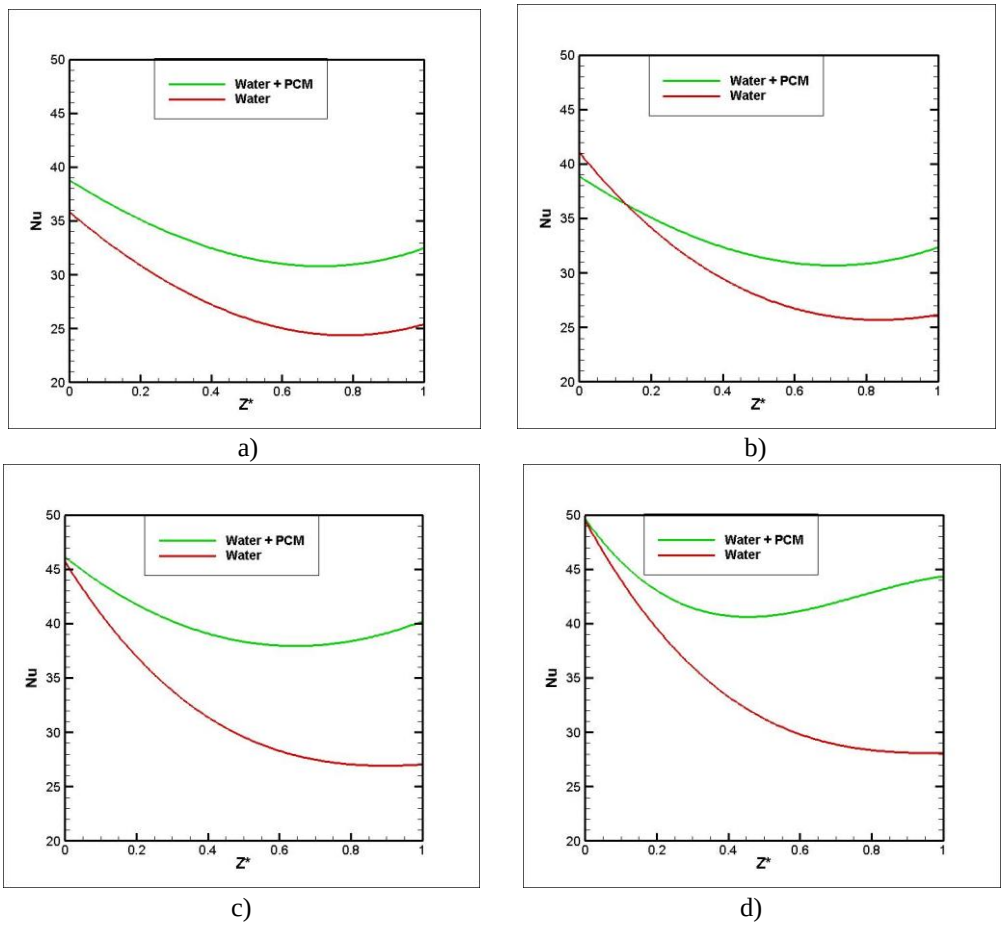


Figure 3. Comparison of Nusselt number for a flow rate of a) 300 ml/min b) 400 ml/min c) 500 ml/min d) 600 ml/min. The Nu decreases continuously along the length for water, while it drops initially but starts increasing at half channel length for bulk fluid (water-PCM).

For all flow rates, the local Nusselt number for both water cooled and water-PCM cooled MCHS is highest at the start of the channel, but it reduces continuously along channel length for water cooled MCHS, the local Nusselt number for water-PCM cooled MCHS reduces initially along the channel length but starts increasing after half the length of channel. In both cases, the local Nusselt number is highest at the start of microchannel due to the thermally developing region. It starts reducing along the length due to the formation of laminar boundary layer along the channel wall. For water-PCM cooled MCHS, the increase in local Nusselt number midway through the channel can be attributed to the onset of phase change process of the PCM in water-PCM. Due to higher temperature at the bottom surface, the phase change process starts at the bottom surface and propagates upwards along the length. A combination of

longer thermal developing length, and phase change process of PCM has resulted in increased Nusselt number.

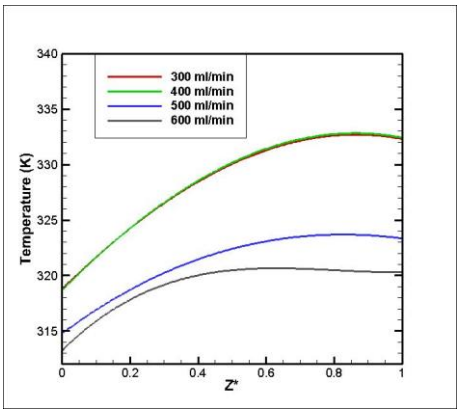


Figure 4: Temperature along bottom heater for Water-PCM cooled MCHS for different flow rates

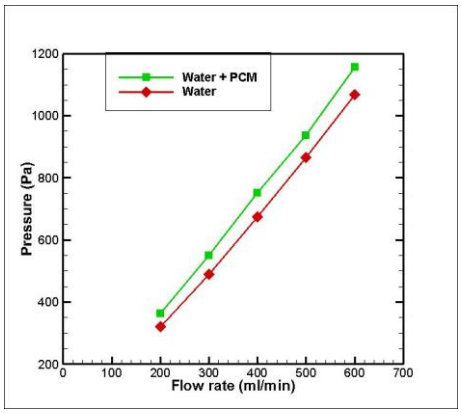


Figure 5: Pressure drop for water and water-PCM showing approximately 10% difference

The comparison of bottom heater temperature along channel length for different flow rates for water-PCM cooled MCHS shows that bottom heater temperature initially increases along the length and remains constant for the remaining length (Figure 4). The bottom heater temperature decreases as flow rate increases and is nearly constant for more than half the length for flow rate of 600 ml/min. Due to higher viscosity of PCM slurry, the pressure drop is more compared to that of pure water (Figure 5). The average increase in pressure drop for PCM slurry is approximately ten percent. Thus more pumping power is required to drive the water-PCM.

## 4. CONCLUSIONS

A numerical study is performed to find the effect of PCM as coolant on the thermal performance of MCHS for electronic cooling application.

- For the same flow rate and heat flux condition, the average Nusselt number increases by 26 percent for water-PCM cooled MCHS than for pure water.
- The maximum temperature $T_{max}$ for bottom heater is lower for water-PCM cooled MCHS by 20 percent compared to water cooled MCHS thus less possibility of formation of hotspot.
- The pressure drop within the microchannel is more by 10 percent for water-PCM than for pure water.

## REFERENCES

[1] Tuckerman, D. B., Pease, R. F.: High Performance Heat Sinking for VLSI, *IEEE Electronic Device Letters*, EDL- 2 (1981)

[2] Xing, K. Q., Tao, Y. X., and Hao, Y. L., Performance Evaluation of Liquid Flow With PCM Particles in Microchannels, *ASME J. Heat Trans.*, Vol.127, August 2005.

[3] Sarada Kuravi, Krishna M., Numerical Investigation of Flow and Heat Transfer Performance of Nano-Encapsulated Phase Change Material Slurry in Microchannels, *ASME J. Heat Trans.*, Vol. 131, June 2009.

[4] S. Kondle, J. Alvarado, C. Marsh, Laminar Flow Forced Convection Heat Transfer Behaviour of a Phase Change Material Fluid in Microchannels, *ASME J Heat Tran*, Vol. 135 / 052801-1, May 2013.

# Heating Ventilation and Air-Conditioning Analysis of a Hospital and Simulation Of An Air-conditioned Room

**Vikalp Jha, Shujaathussain Soudagar**
M.Tech student, Dept. of aerospace engineering, UPES Dehradun

**Dr. Velidi VSS Gurunadh**
Assistant professor, Dept. of aerospace engineering, UPES Dehradun

## ABSTRACT

Heating, Ventilating and Air-Conditioning plan of a commercial place, for example, a doctor's facility is itself a noteworthy test. These days making HVAC framework which can set up a sound domain and solace for individuals by having low utilization of vitality and to be practical is imperative. To investigate HVAC examination of a doctor's facility, the general highlights like, ventilation proficiency, consistency of temperature appropriation, pipe plan, and indoor air quality and to distinguish the flow of air in a room are keys to the outline conditions. The speed and temperature dispersions in a room it is possible that it is a general ward of a healing center, an I.C.U room or an Operation theater, have been figured by unraveling the essential conditions of fluid mechanics and vitality condition in unfaltering, incompressible, turbulent stream with uniform thermo-physical properties. In this paper to dissect the temperature variety and air flow over a room, we make a CFD model of a room thinking about standard information for aerating and cooling. In the past couple of years, Computational Fluid Dynamics has been assuming an indispensable part in building plan.

**Key Words:** *Air-condition system; Computational Fluid Dynamics; Temperature contours; indoor air quality; HVAC; Thermal Comfort*

## 1. INTRODUCTION

Heat Ventilation and Air Conditioning (HVAC) system has very broad fields of application such as automobiles, aerospace, commercial buildings. In all of those fields our aim is to analyze HVAC system in hospital. In Hospital, Operation Theatre, general ward room, research labs etc. all needed to have a proper ventilation system which must be reliable for condition specified in standards. In a hospital room it is necessary for maintaining proper control on Indoor Air quality and reduced bacterial contamination. There are various parameters which has vital role in consideration for analysis such as varying load conditions, infiltrations, indoor air quality and so on. Lack of positive pressure or low air velocity in ac room may cause suffocation and improper cooling where as in similar case if air flow velocity is higher it may cause turbulence so optimum air distribution and air velocity is required.
ASHRAE standard has criteria and parameters based on which, numerous HVAC businesses, healing centers and numerous business structures are outlined. These days many research is in advance for HVAC investigation since ventilating in numerous healing facility rooms are arranged yet greater improvement is required in fields of some issue, for example, bacterial pollution, uneven cooling because of turbulence in wind stream design. To defeat the turbulence we have to lessen gulf speed of air so our stream can be laminar. We can contrast and diverse gulf speed under CFD examination of an AC room. With the assistance of CFD investigation we can reproduce our information for different parameters and we can contrast it and distinctive outcomes without introducing the entire course of action actually. [2]

## 2. HVAC IN GENERAL WARD AND OPERATION THEATRE OF A HOSPITAL

In a healing facility either in Operation Theater (OT) or a general ward, aerating and cooling is valuable utilization of HVAC framework since it is examination of human solace, warm cooling and course of natural air. Legitimate ventilation and indoor air quality is required because of harmful disease. In many research it is watched that an honorable air conveyance and course with an appropriate outline of ventilating in Operation Theater or any broad ward can lessen the bacterial pollution and furthermore may cause a laminar stream for successful cooling with low power consumption. ASHRAE has standard information for appropriate cooling and human solace which is considered in this paper. In Operation Theater, turbulent wind stream causes microbial extension &there is addition in the viability of Air conveyance. Rather than turbulent stream on the off chance that we consider low speed i.e. laminar stream which can decrease the extension of bacterial contaminations [1]. This idea expresses that the laminar stream in Operation Theater is kept up by its air speed. It was reenacted by CFD apparatus and for the further examination, the stream is watched and considered inside the operation theater. According to the ASHRAE standard as examined above, required parameter for ventilating is appeared in table beneath in this paper.

| | ASHRAE[3] (for ventilation of health care facility) | ASHRAE[4] (for healthcare facility) |
|---|---|---|
| Relative Humidity (%) | 30-60 | 45-55 |
| Temperature in room ($^{o}$ C) | 20-24 | 17-27 |

TABLE 1: STANDARD DATA FOR INDOOR AIR CONDITION

Air distribution is the inactive goal of aerating and cooling in which we have to watch rate of air change every hour, air speed, and mass stream rate of air and so forth a positive weight and legitimate air course is required for human solace. One more vital parameter ought to be considered in investigation i.e. bacterial fixation. It should be lessens and it is important to scatter it at the earliest opportunity. The bacterial focus over the earth of the patient is exceedingly identified with the harming of the reason for question [5]. On the off chance that more turbulence of air is available in healing center rooms, for example, general wards and Operation Theater, there is a probability of bacterial contamination to other individuals around it so filtration of air and rate of progress of air and mass stream rate of air is need.

## 3. SIMULATION OF AN AIR-CONDITIONED ROOM

Modelling: Consider a room of 3*3*6$m^3$ volume described below. The figure is not to scale. Consider the inlet velocity to be constant over the air conditioner on wall of 3*3$m^2$ and compare it with various velocities. The pressure at the room is 1 atmosphere and flow velocity as variable for analysis. Take inside fluid as air. Consider a wall material as concrete has density of 2400 kg/m3 and thermal conductivity as 1.38 w/m-k. Heat transfer coefficient inside the room is considered as 5w/$m^2$ –k. considering the above dimension we create a geometric model to analyse. A 3D geometry is recreated in familiar for our investigation divide, taking into every single standard parameter for the real position of the inlet and outlet of cooling object. The model was re-enacted utilizing ANSYS-Fluent, for examination of HVAC framework, and all parameters, for example, temperature, speed and relative humidity were evaluate

## 4. RESULTS

A 3D model of a room is taken into examination in familiar and was acknowledged for the cross area of the space for our investigation parcel, considering the real position of the velocity inlet and the pressure outlet condition of aerate and cool. The CFD model was prepared by utilizing ANSYS-Fluent, considering the executed air conditioning framework, and various properties such as like room wall temperatures, air speed and relative humidity in environment were assessed. Consideration of major points about the concurrent impacts of the results, the new introduced air-conditioning framework can play out its commitment in keeping up the indoor parameters at ideal esteems in this hospital ward room or OT

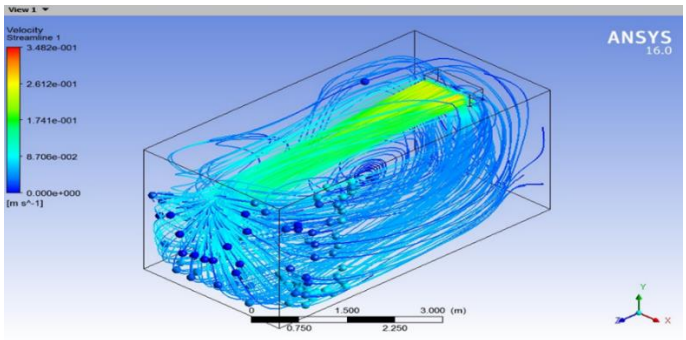


FIG1: AIR CIRCULATION IN AIR CONDITIONED ROOM

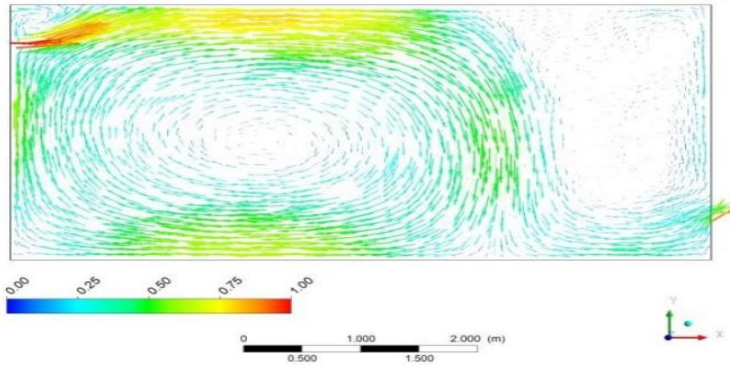


FIG 2: VELOCITY VECTOR (2D)

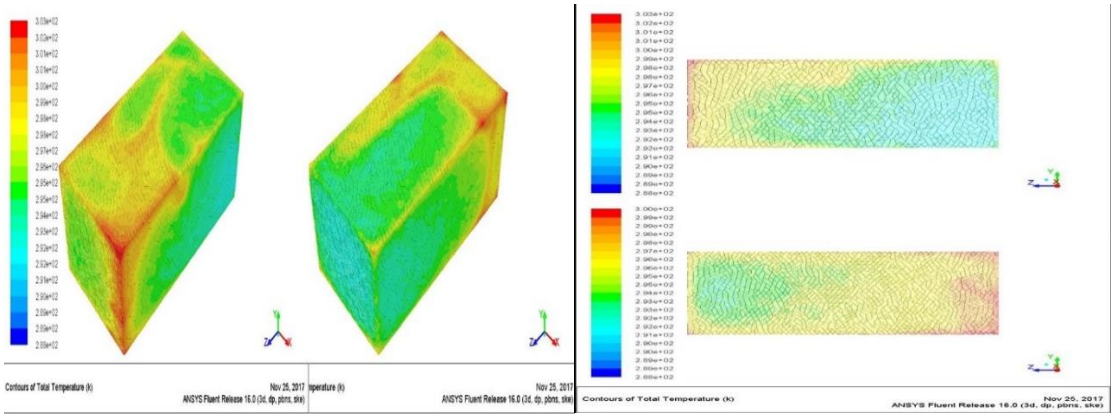

FIG3: TEMERATURE CONTOUR ACROSS ROOM FOR DIFFERENT AIR VELOCITY

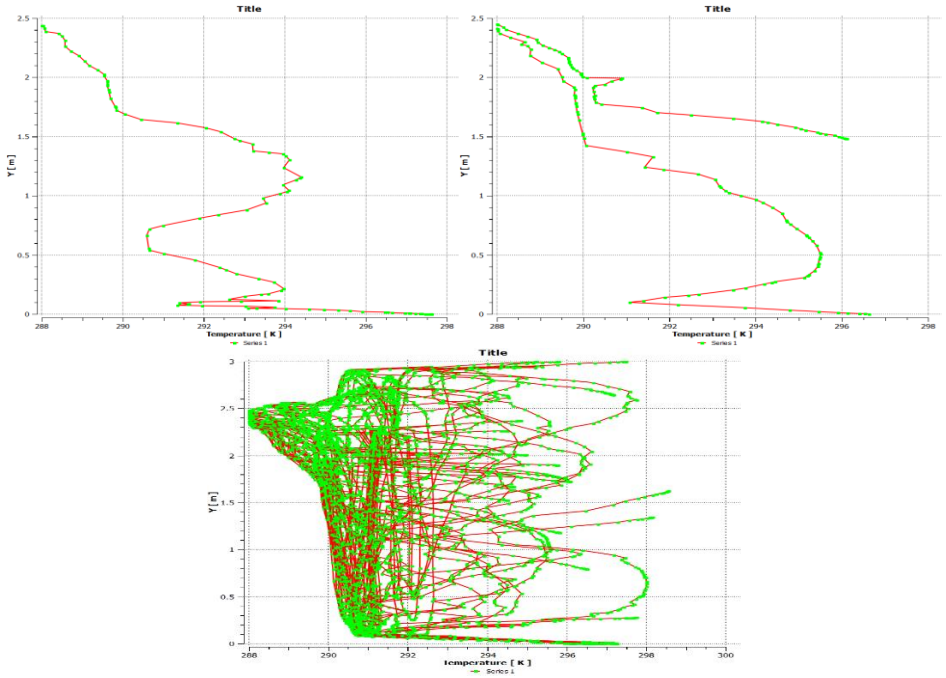


FIG 4: TEMPERATURE VARIATION ALONG VARIOUS STREAMLNES (1, 2… 50)

## 5 CONCLUSION

The examination of all procedure in CFD modelling have prompted the conclusion that exceptional change in stream design is watched for bring down speed, bring down Reynolds no. with conspicuous impact of laminar stream. For the geometry of our plan which might be either for an operation theatre or a general ward, decrement in Reynolds no. has extraordinary impact on stream design. It is observed that at for higher Reynolds no. temperature conveyance isn't uniform, which additionally gauge for higher vitality utilization because of high air speed. The essential parameter of configuration is to set up the correct temperature and relative humidity in a basic zone. The optional necessity in configuration is diminishment of bacterial sullying which is expanded by turbulence wind stream. Thus the primary aim to the HVAC build is to keep up the laminar wind current through the AC room.

## REFERENCES

[1]. “Ventilation performance in operating theatres against airborne infection: Review of research activities and practical Guidance”, Elsevier Journal of Hospital Infection by T.T. Chow and X.Y. Yang, 2004,
[2]. CFD-lectures.com by Dr. Uger Guven.
[3]. Ventilation of Health care facilities by, American Society for heating, refrigerating and air conditioning engineers Inc. Atlanta, GA, 2006 ASHRAE standards 170P.
[4]. Health care facilities from HVAC applications handbook, American Society for heating, refrigerating and air conditioning engineers Inc. Atlanta, GA,2006.
[5].M. Sandberg, T. Karimipanah and H.B. Awbi, 2000, “A comparative study of different air distribution system in a classroom”, Rommvent UK, vol. 2, pp. - 1013-1018.

# Heating Ventilation and Air-Conditioning Analysis of a Hospital and Simulation Of An Air-conditioned Room

**Vikalp Jha, Shujaathussain Soudagar**
M.Tech student, Dept. of aerospace engineering, UPES Dehradun

**Dr. Velidi VSS Gurunadh**
Assistant professor, Dept. of aerospace engineering, UPES Dehradun

## ABSTRACT

Heating, Ventilating and Air-Conditioning plan of a commercial place, for example, a doctor's facility is itself a noteworthy test. These days making HVAC framework which can set up a sound domain and solace for individuals by having low utilization of vitality and to be practical is imperative. To investigate HVAC examination of a doctor's facility, the general highlights like, ventilation proficiency, consistency of temperature appropriation, pipe plan, and indoor air quality and to distinguish the flow of air in a room are keys to the outline conditions. The speed and temperature dispersions in a room it is possible that it is a general ward of a healing center, an I.C.U room or an Operation theater, have been figured by unraveling the essential conditions of fluid mechanics and vitality condition in unfaltering, incompressible, turbulent stream with uniform thermo-physical properties. In this paper to dissect the temperature variety and air flow over a room, we make a CFD model of a room thinking about standard information for aerating and cooling. In the past couple of years, Computational Fluid Dynamics has been assuming an indispensable part in building plan.

**Key Words:** *Air-condition system; Computational Fluid Dynamics; Temperature contours; indoor air quality; HVAC; Thermal Comfort*

## 1. INTRODUCTION

Heat Ventilation and Air Conditioning (HVAC) system has very broad fields of application such as automobiles, aerospace, commercial buildings. In all of those fields our aim is to analyze HVAC system in hospital. In Hospital, Operation Theatre, general ward room, research labs etc. all needed to have a proper ventilation system which must be reliable for condition specified in standards. In a hospital room it is necessary for maintaining proper control on Indoor Air quality and reduced bacterial contamination. There are various parameters which has vital role in consideration for analysis such as varying load conditions, infiltrations, indoor air quality and so on. Lack of positive pressure or low air velocity in ac room may cause suffocation and improper cooling where as in similar case if air flow velocity is higher it may cause turbulence so optimum air distribution and air velocity is required.
ASHRAE standard has criteria and parameters based on which, numerous HVAC businesses, healing centers and numerous business structures are outlined. These days many research is in advance for HVAC investigation since ventilating in numerous healing facility rooms are arranged yet greater improvement is required in fields of some issue, for example, bacterial pollution, uneven cooling because of turbulence in wind stream design. To defeat the turbulence we have to lessen gulf speed of air so our stream can be laminar. We can contrast and diverse gulf speed under CFD examination of an AC room. With the assistance of CFD investigation we can reproduce our information for different parameters and we can contrast it and distinctive outcomes without introducing the entire course of action actually. [2]

## 2. HVAC IN GENERAL WARD AND OPERATION THEATRE OF A HOSPITAL

In a healing facility either in Operation Theater (OT) or a general ward, aerating and cooling is valuable utilization of HVAC framework since it is examination of human solace, warm cooling and course of natural air. Legitimate ventilation and indoor air quality is required because of harmful disease. In many research it is watched that an honorable air conveyance and course with an appropriate outline of ventilating in Operation Theater or any broad ward can lessen the bacterial pollution and furthermore may cause a laminar stream for successful cooling with low power consumption. ASHRAE has standard information for appropriate cooling and human solace which is considered in this paper. In Operation Theater, turbulent wind stream causes microbial extension &there is addition in the viability of Air conveyance. Rather than turbulent stream on the off chance that we consider low speed i.e. laminar stream which can decrease the extension of bacterial contaminations [1]. This idea expresses that the laminar stream in Operation Theater is kept up by its air speed. It was reenacted by CFD apparatus and for the further examination, the stream is watched and considered inside the operation theater. According to the ASHRAE standard as examined above, required parameter for ventilating is appeared in table beneath in this paper.

| | ASHRAE[3] (for ventilation of health care facility) | ASHRAE[4] (for healthcare facility) |
|---|---|---|
| Relative Humidity (%) | 30-60 | 45-55 |
| Temperature in room ($^{o}$ C) | 20-24 | 17-27 |

TABLE 1: STANDARD DATA FOR INDOOR AIR CONDITION

Air distribution is the inactive goal of aerating and cooling in which we have to watch rate of air change every hour, air speed, and mass stream rate of air and so forth a positive weight and legitimate air course is required for human solace. One more vital parameter ought to be considered in investigation i.e. bacterial fixation. It should be lessens and it is important to scatter it at the earliest opportunity. The bacterial focus over the earth of the patient is exceedingly identified with the harming of the reason for question [5]. On the off chance that more turbulence of air is available in healing center rooms, for example, general wards and Operation Theater, there is a probability of bacterial contamination to other individuals around it so filtration of air and rate of progress of air and mass stream rate of air is need.

## 3. SIMULATION OF AN AIR-CONDITIONED ROOM

Modelling: Consider a room of 3*3*6$m^3$ volume described below. The figure is not to scale. Consider the inlet velocity to be constant over the air conditioner on wall of 3*3$m^2$ and compare it with various velocities. The pressure at the room is 1 atmosphere and flow velocity as variable for analysis. Take inside fluid as air. Consider a wall material as concrete has density of 2400 kg/m3 and thermal conductivity as 1.38 w/m-k. Heat transfer coefficient inside the room is considered as 5w/$m^2$ –k. considering the above dimension we create a geometric model to analyse. A 3D geometry is recreated in familiar for our investigation divide, taking into every single standard parameter for the real position of the inlet and outlet of cooling object. The model was re-enacted utilizing ANSYS-Fluent, for examination of HVAC framework, and all parameters, for example, temperature, speed and relative humidity were evaluate

## 4. RESULTS

A 3D model of a room is taken into examination in familiar and was acknowledged for the cross area of the space for our investigation parcel, considering the real position of the velocity inlet and the pressure outlet condition of aerate and cool. The CFD model was prepared by utilizing ANSYS-Fluent, considering the executed air conditioning framework, and various properties such as like room wall temperatures, air speed and relative humidity in environment were assessed. Consideration of major points about the concurrent impacts of the results, the new introduced air-conditioning framework can play out its commitment in keeping up the indoor parameters at ideal esteems in this hospital ward room or OT

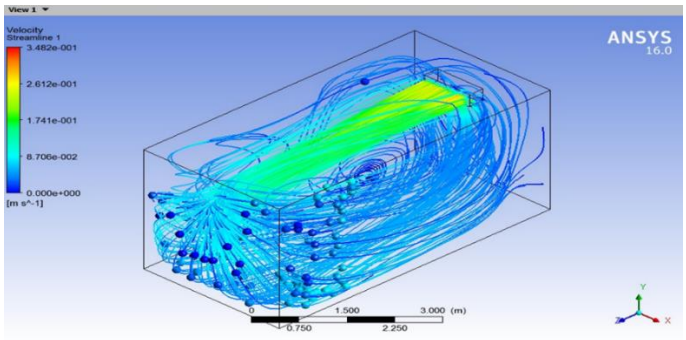


FIG1: AIR CIRCULATION IN AIR CONDITIONED ROOM

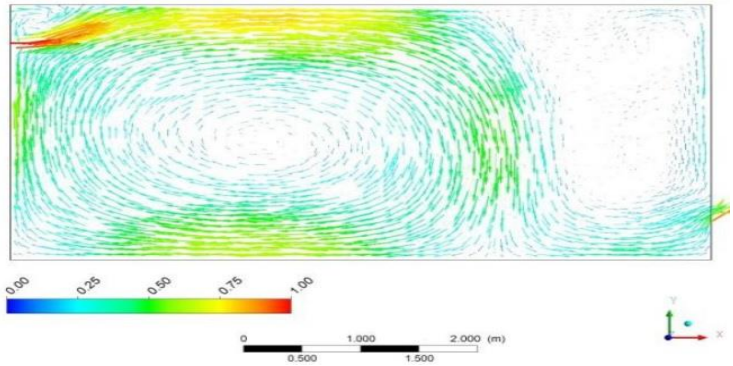


FIG 2: VELOCITY VECTOR (2D)

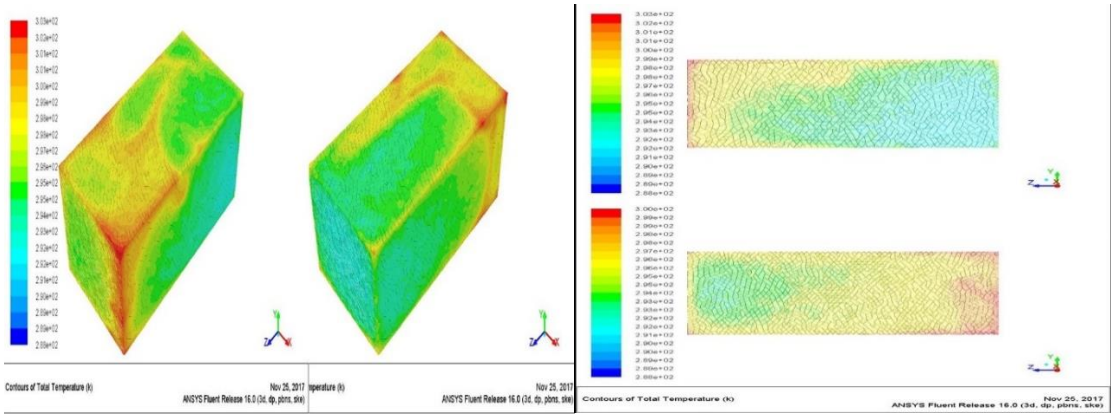

FIG3: TEMERATURE CONTOUR ACROSS ROOM FOR DIFFERENT AIR VELOCITY

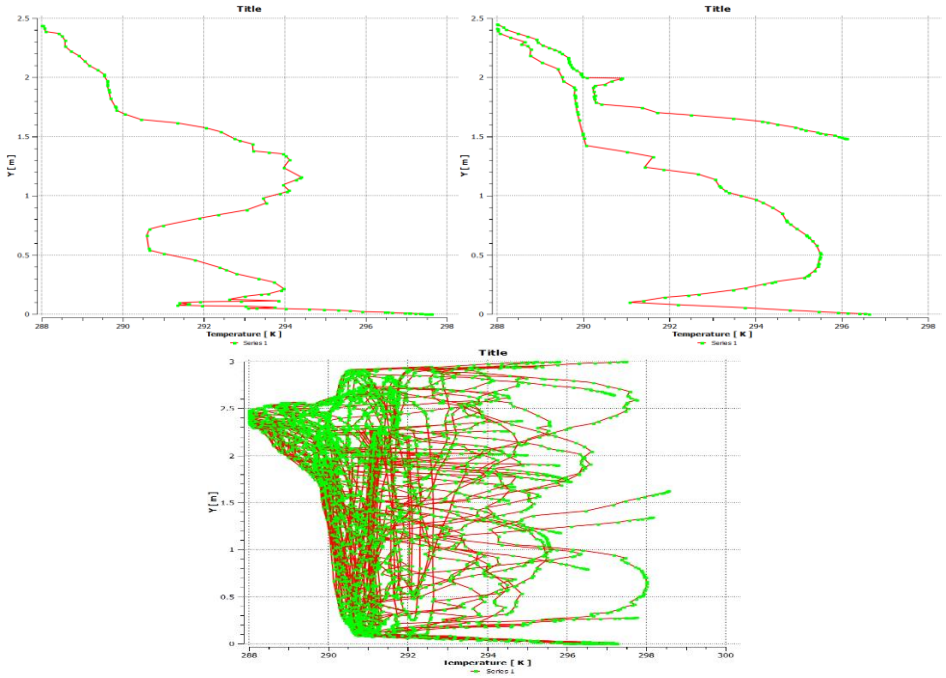


FIG 4: TEMPERATURE VARIATION ALONG VARIOUS STREAMLNES (1, 2… 50)

## 5 CONCLUSION

The examination of all procedure in CFD modelling have prompted the conclusion that exceptional change in stream design is watched for bring down speed, bring down Reynolds no. with conspicuous impact of laminar stream. For the geometry of our plan which might be either for an operation theatre or a general ward, decrement in Reynolds no. has extraordinary impact on stream design. It is observed that at for higher Reynolds no. temperature conveyance isn't uniform, which additionally gauge for higher vitality utilization because of high air speed. The essential parameter of configuration is to set up the correct temperature and relative humidity in a basic zone. The optional necessity in configuration is diminishment of bacterial sullying which is expanded by turbulence wind stream. Thus the primary aim to the HVAC build is to keep up the laminar wind current through the AC room.

## REFERENCES

[1]. “Ventilation performance in operating theatres against airborne infection: Review of research activities and practical Guidance”, Elsevier Journal of Hospital Infection by T.T. Chow and X.Y. Yang, 2004,
[2]. CFD-lectures.com by Dr. Uger Guven.
[3]. Ventilation of Health care facilities by, American Society for heating, refrigerating and air conditioning engineers Inc. Atlanta, GA, 2006 ASHRAE standards 170P.
[4]. Health care facilities from HVAC applications handbook, American Society for heating, refrigerating and air conditioning engineers Inc. Atlanta, GA,2006.
[5].M. Sandberg, T. Karimipanah and H.B. Awbi, 2000, “A comparative study of different air distribution system in a classroom”, Rommvent UK, vol. 2, pp. - 1013-1018.

Fifth International Conference on Computational Methods for Thermal Problems
THERMACOMP2018, July 9-11, 2018, Indian Institute of Science, Bangalore, INDIA
*N. Massarotti, P. Nithiarasu, Pradip Dutta and C. Ranganyakalu (Eds.)*

# ASSESSMENT OF SUITABILITY FOR HEMODYNAMIC LEVITATED CENTRIFUGAL PUMP AS LEFT VENTRICULAR ASSIST DEVICE

**Vikas Kannojiya, Arup Kumar Das,**
Department of Mechanical and Industrial Engineering, IIT Roorkee, 247667, India,
vikas.passion.singh@gmail.com, akdasfme@iitr.ac.in

**Prasanta Kumar Das**
Department of Mechanical Engineering, IIT Kharagpur, 721302, India, pkd@mech.iitkgp.ernet.in

## ABSTRACT

Cardiovascular disease such as chronic heart failure and heart attack imposes a serious threat to human life which needs a costly treatment to overcome the risk of life. The key factors responsible for heart failure are the systolic or diastolic dysfunction of a damaged ventricle. Left ventricular assist devices (LVAD) are the small mechanical pumps that are designed to execute the functions of a failed ventricle. In this work, a cost-effective, assistant device for the left ventricle of the heart having hemodynamically levitated impeller with spiral groove bearing is numerically proposed. It overcomes the inherent high weight complications as observed in the established magnetically levitated impeller. The simulation study is carried out using ANSYS CFX to check various versions of LVAD so that a novel design can be obtained for providing the optimum pressure head and blood flow rate at the cost of least shear stress. The turbulence characteristics of the blood flow through the LVAD are solved by implementing standard k-$\epsilon$ turbulence scheme. Several designs of blade profiles, blade numbers, and impeller wall roughness are tested at different operating rotational speeds to obtain a favorable and effective design. The developed LVAD could produce the required flow rate of 3-7 liters per minute against the systolic pressure head of the left ventricle ranging from 90-130 mm Hg. The backward curved blade impeller configuration is found to be the most effective design due to its uniform pressure and less shear generation, whereas the forward curved blade design showed poor performance. A centrifugal circulatory support for end-stage cardiac failure treatment is developed which is capable of delivering blood from the left ventricle to the aorta.

**Key Words:** *LVAD, Hemodynamic, Centrifugal Pump, CFD.*

## 1. INTRODUCTION

The growing global impact of cardiovascular diseases highlights the requirement of an effective treatment method. Worldwide, more than 26 million patients suffer from heart failure and the trend is increasing [1]. One of the possible reasons for a heart failure is the dysfunction of the left ventricle. The lack of heart donors makes this situation severe. In this scenario, LVAD (Left Ventricular Assist Device) is a unique solution for a number of cardiovascular diseases, which are increasing day by day [2]. It requires fine-tuning the design parameters and estimation of the optimum configuration of the engineering device before mass usage in the biological environment of the human body. Computational Fluid Dynamics (CFD) emerges to be a cost-effective tool to analyze and optimize

LVAD [3]. Several studies are going on the development of the innovative design of the pump. Many of the researchers have reported the development of magnetically levitated impeller for the prime mover of the LVAD pump [4]-[5]. However, comprising magnets in the pump will increase the weight of the pump. A lighter weight pump is highly desirable for the patient comfort.

Therefore in this study, we proposed a hemodynamically levitated centrifugal LVAD pump that will overcome the high weight concern. Several designs of the blood pump of LVAD were tested under different operating conditions by using ANSYS code CFX. An optimum design for end-stage heart failure treatment is developed in this study.

## 2. SIMULATION METHOD

The 3-D simulation study is carried out using ANSYS CFX. The geometry is created in ANSYS design modeler, which has been further discretized into 6,818,15 smaller tetrahedral elements by using ANSYS ICEM meshing tool to precisely observe the flow phenomenon. The geometry and mesh structure are provided in Figure 1. The flowing blood is considered as a Newtonian fluid having density and viscosity as 1060 kg/m$^3$ and 0.0035 Pa.s, respectively. The turbulence characteristics of the blood flow through the LVAD are solved by implementing standard k-ϵ turbulence scheme. Several designs of blades profiles, blade numbers, and impeller wall roughness are tested at different operating rotational speeds to obtain a favorable and effective design.

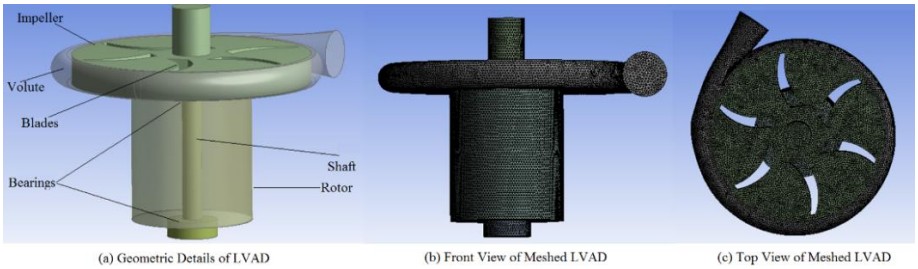


Figure 1: Details of geometry and meshing on LVAD

## 3. RESULTS

**Study on suitable blade profile**

Blade profile imparts a significant effect on the performance of the LVAD. Three different designs of the LVAD having radial, forward and backward curved blades have been simulated under variable operating conditions. Figure 2 shows the performance of all the three designs with the operating conditions. It was observed that forward blades create sufficient pressure head required as per the human physiology but due to high shear stress generation, this design is not preferred. The radial curved blades seem to be poor amongst all as it generates low-pressure head and also shear stress below the permissible limit of thrombosis that may raise the risk of thrombus formation. The thrombus formation results in the clotting of blood near the very low shear zones in the impeller, thus radial and forward curved design is not preferred. On the other hand, backward curved blades comprise the benefit of large pressure head and low shear stress and thus found to be much suitable for the blood pump.

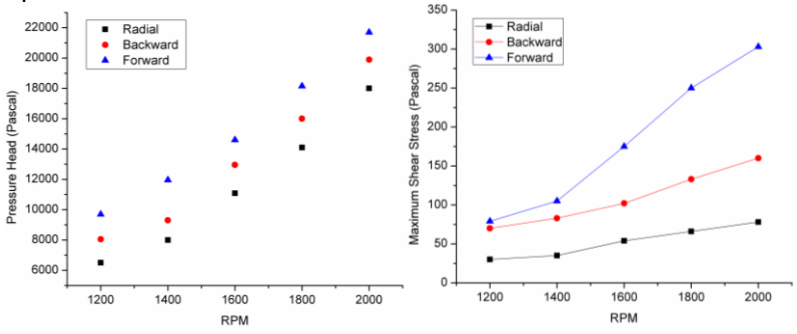

FIGURE 2: Variation of pressure and shear stress with rotational speed for different blade profiles

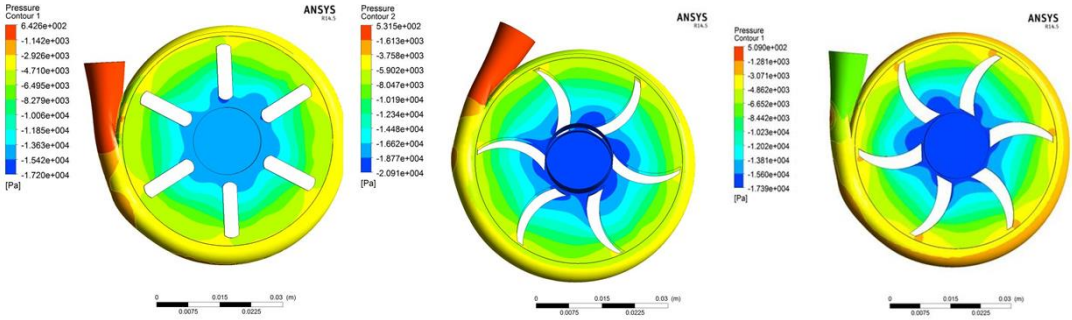


(a) Radial curved blades (b) Forward Curved Blades (c) Backward Curved Bades

FIGURE 3: Pressure distribution for radial, forward and backward curved blades

The pressure contour on the wall of LVAD pump has been plotted and represented by figure 3. It can be seen that the impeller with radial and backward curved blade has uniform pressure distribution whereas, forward curved shows large pressure variation. A region of high pressure is also noticed at the tip of backward curved blade impeller.

**Picking up optimum numbers of blade**

The effect of blade number variation on the LVAD performance has been elaborately studied by present numerical simulation. Three different designs having four, six and ten blades under variable conditions of flow rates and rotational speeds are considered for the simulation study. Figure 4 shows the variation of pressure head and maximum wall shear stress with rotational speed for different blade designs. A significant effect of the blade number on the performance of the LVAD can be observed from these graphs. The performance of six blade configuration is found to be better than the others as it generates sufficient pressure head (16000 Pascal) at the cost of least shear stress. The four and ten blades design are thus not opted as it generates considerable shear stress.

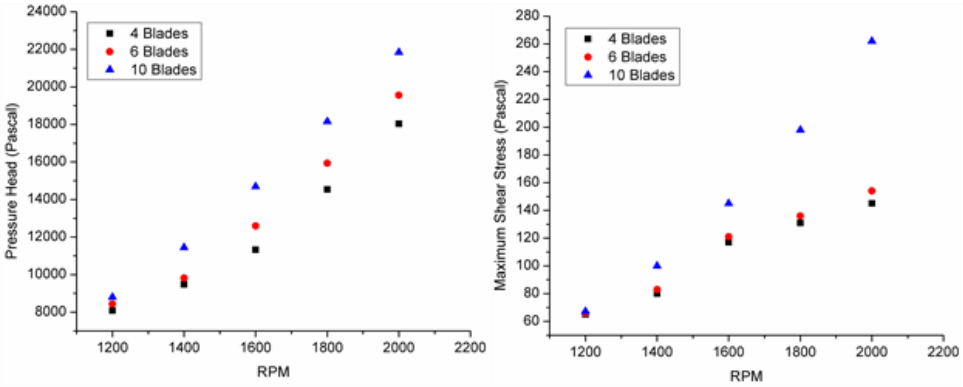


FIGURE 4: Variation of pressure and shear stress with rotational speed for different numbers of blade

**Effect of Rotational Speed**

Next, variation in rotational speed is tried as it is an important design factor. Simulations were carried out for the backward curved blade at a fixed flow rate (4 L/min) and variable RPM (1500-2400) to find out optimum rotational speeds. Figure 5 shows the variation of pressure head and wall shear

stress with different rotational speed, both the pressure head and shear stress shows increasing trend with the rise of angular velocity. The normal physiological blood pressure of human body varies between 12000 to 14000 Pascal and the optimum limit of shear stress to avoid hemolysis is 300 Pascal. The RPM ranging from 1400 to 1800 are found to be the most favorable for the blood flow inside the blood vessel.

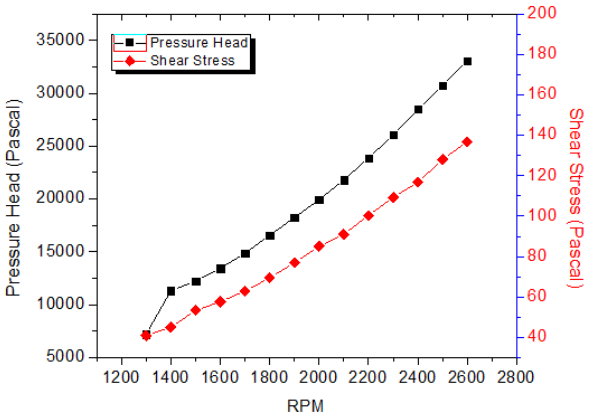


FIGURE 5: Variation of pressure head and shear stress with rotational speed for different blade profiles

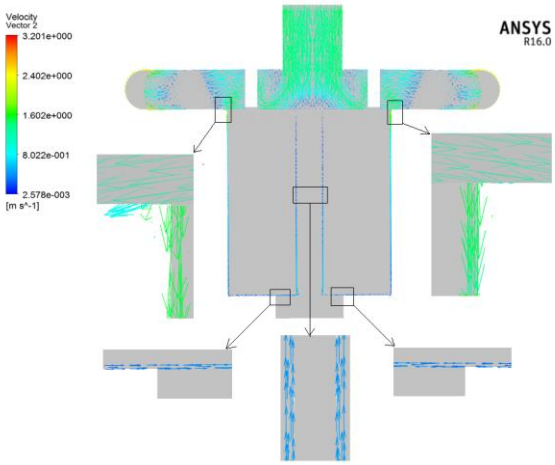


FIGURE 6: Hemodynamic Features inside optimum design of LVAD

Figure 6, provides the insight of hemodynamic features inside the optimum design of LVAD (backward facing 6 blades with 1600 rpm). A small stream of blood is directed to travel through a narrow channel of 0.04 mm as shown in the figure. The blood will again join the main flowing stream at the impeller due to the pressure difference between the impeller and channel. This blood passage helps in levitating the impeller and thereby avoids its direct contact with the rotating shaft.

## 4. CONCLUSIONS

In this study, several version of LVAD pump has been simulated and an optimum design is proposed. The impeller with backward curved blades shows the best performance as per human physiology. The impeller is hemodynamically levitated that reduces the concern of high cost and weight involved with the magnetic levitation. The blood flow behavior through the LVAD has been analyzed and the location of maximum pressure and generated shear stress is also traced. The shear stress generation at the different operating condition of the device is within the permissible limit to avoid any possibility of hemolysis. Finally, an optimum design is proposed for LVAD to be compatible for the human body.

## REFERENCES

[1] G. Savarese and L. Lund Global, Public Health Burden of Heart Failure, *Cardiac Failure Review*, 3(1):7-11, 2017.

[2] A. Ueno and Y. Tomizawa, Cardiac rehabilitation and artificial heart devices, *Journal of Artoficial Organs*, 12:90-97, 2009.

[3] G.W. Burgreen, H.M. Loree, K. Bourque et al., Computational Fuid Dynamics Analsysis of a Maglev Centrifugal Left Ventricular Assist Device, *Artificial Organs*, 28:874-880, 2004.

[4] K.X. Qian, H.Y. Yuan, P Zeng and W.M. Ru, A novel permanent maglev rotary LVAD with passive magnetic bearings, *Journal of Medical Engineering & Technology*, 29:235-237, 2005.

[5] T. Masuzawa, Magneticaly suspended motor system applied to artificial hearts and blood pumps, *Proceedings of the Isntitution of Mechanical Engineers, Part 1: Journal of Systems and Control Engineering*, 231:330-338, 2016.

# 1-D MODEL FOR FINDING GEOMETRY OF A SINGLE PHASE EJECTOR

***Vikas Kumar[1*] and Gulshan Sachdeva[2]***

[1]Department of Mechanical Engineering,
Krishna Engineering College, Ghaziabad, India
Corresponding author E-mail: vikas.burman21@gmail.com;
Contact: +91-8053644668

[2]Department of Mechanical Engineering,
National Institute of Technology, Kurukshetra, India.
E-mail: gulshan4you@gmail.com

## ABSTRACT

This paper proposed a new model to determine all the dimensions of a single phase ejector for known working conditions of evaporator, condenser and boiler conditions. The ejector is designed to operate in double choking mode. Rather than considering constant heat capacity ratio and specific heat, they are determined corresponding to the state conditions. A few novel phenomenon's of Prandtl's mixing length, Prandtl-Meyer expansion waves, Kelvin-Helmholtz instability and Baroclinic effect are introduced to calculate the mixing length, divergence angle, shape of constant area section and influence of the production of vortices within Ejector respectively. Area ratios obtained in different sections by the present model are validated with the experimental results of Huang et al. [4]. The average deviation of entrainment ratio's in comparison to Huang et al. [4] is below 2.48 %. Effect of operating conditions on geometrical parameters is also studied and discussed. It is also found that with the decrease in generator pressure, the primary nozzle divergence angle and area ratio decreases while the entrainment ratio increases slightly for the fixed condenser pressure. The nozzle exit position as well as ejector convergence angle, both increases with the increase in condenser pressure at the expense of cooling capacity.

***Keywords:*** *Jet ejector; ejector designing; entrainment ratio; refrigeration system.*

## 1. INTRODUCTION

In today's era, refrigeration and air-conditioning is an essential part of the life of the human beings. In general, the commercialized refrigeration systems are vapor compression and vapor absorption refrigeration systems. Although, VCR system has high coefficient of performance (COP) but if the thermal efficiency of the power plant and the electricity transmission losses are taken into account whilst minimizing the overall COP of the vapor compression system. Following that, another available solution is Vapor Absorption Refrigeration System (VARS). But it is bulky, complex in construction and relatively expensive. Furthermore, the maintenance cost of these systems is also high and requires waste heat at a temperature over and above 100°C. Amongst the non-conventional refrigeration systems, ejector refrigeration system is an attractive technology, utilizes low-grade energy which can be obtained from industrial waste heat or solar system at low temperature. The foremost advantages are its simple construction and low operational & maintenance cost. On the contrary, the only issue with ERS is low COP of the system and sensitivity to atmospheric temperature [2]. Consequently, to enhance the use of ERS, researchers have focused on improving COP and the working range of the system. The key part of ERS is "Ejector" which works as a mechanical compressor and increases the pressure of the refrigerant without any moving part [3]. In general, it utilizes the momentum energy of primary fluid, to entrain the secondary fluid from evaporator [1]. Generally, ejector consists four major sections named; primary nozzle, the suction chamber, constant area section and diffuser section. The potential application of the primary nozzle is used to accelerate the primary fluid coming from a generator. Consequently, the pressure of the fluid

decreases and causes a suction effect for the secondary fluid. It is obvious, vapors generated in the evaporator moves towards the suction chamber. Both start mixing with each other at constant pressure in constant area section of the system. The pressure of the mixed fluid is further raised to the condenser pressure by using diffuser section. Moreover, the performance of an ejector is mainly defined by its entrainment ratio and pressure lift ratio [2].

$$Entrainment\ ratio = \frac{Mass\ flow\ rate\ of\ secondary\ fluid}{Mass\ flow\ rate\ of\ primary\ fluid}$$

$$Pressure\ lift\ ratio = \frac{Static\ flow\ pressure\ at\ the\ ejector\ exit}{Static\ pressure\ of\ evaporator}$$

It is worth noting that many researchers have studied the performance parameters of the ejector and developed models using different refrigerants such as R113, R141b, R134a, R142b, R600a, steam, air, propane etc. to predict their behavior [4, 5, 6, 7 and 8]. Furthermore, Huang et al. [4] proposed a 1-dimensional analytical model using R141b as a refrigerant for predicting ejector performance at the critical mode of operation. Noting that, the model is based on the assumption of constant-pressure mixing of the primary and secondary fluid inside the constant pressure section. Following that, they simulated the ejector performance for obtaining the condenser pressure equal to critical back pressure by changing the area of constant pressure section. Furthermore, they verified their numerical model by conducting experiments with 11 ejectors of different geometry. Subsequently, a number of models are proposed by various researchers to simplify the method of evaluating the performance of ejectors. Moreover, Zhu et al. [9] proposed a shock circle model to analyze ejector performance with assuming non-uniform velocity distribution and uniform radial pressure. Potentially, the proposed model is simple but expressions are complex. In particular, they have changed the temperature of the secondary fluid at choked section in their simulation for ejector performance evaluation. Furthermore, Chen et al. [5] have carried out one-dimensional analysis for the prediction of ejector performance at critical and sub-critical mode. To maximize the accuracy, they have simulated the model to predict ejector performance by changing the pressure of the secondary fluid at the choked section and compared the results of their model with the experimental results using three different refrigerants. Moreover, Maghsoodi et al. [10] predicted the ejector performance using one-dimensional analysis at critical and sub-critical conditions and a maximum error of ±22 % was reported while comparing with the experimental results of Huang et al [4], Zhu et al [9] & Chen et al [5]. It is worth noting that in all these models; throat area, exit area, constant pressure section area is provided initially to predict the performance at different operating conditions. On the contrary, these models predict ejector performance with varying area ratios at different sections but do not provide the complete geometrical details such as inlet area, various angles and length of the sections etc of an ejector for the desired cooling conditions. The potential application of this article is geometry designing procedure for fixed ejector performance is proposed. All dimensions of the ejector are calculated assuming dry vapor as a working fluid.

## 2. RESULTS AND DISCUSSIONS

The present model has been validated for ejector geometry by using the same operating conditions as by Huang et al. [4]. The proposed model is set for entrainment ratio and operating conditions, for experimental data as in Huang et al. [4] to calculate the geometric dimensions of ejectors. Analysis of the results shows absolute average deviations of entrainment ratio calculated by the CFD model is very less in comparison to selected models shown in figure 2. The results shows, the importance of using specific heat's and heat capacity ratio at all section and condition instead of taking them constantly. As the area ratio calculated by the present model is more close to the experimental values as compared to theoretical values calculated by the 1-D model of Huang et al. [4] shown in figure 1. The present model is set to have the same operating conditions as Huang et al. [4] to calculate the optimized geometrical dimensions. It shows, as the generator pressure and temperature decreases, the Nozzle divergence angle also decreases. It also shows for low generator temperature and pressure, less divergence angle of the primary nozzle should be used. Figure 3 shows the effect of condenser pressure or back pressure on the Ejector convergence angle ($\alpha_1$). It shows the continuous increase in

ejector convergence angle ($\alpha_1$) with the increase in condenser pressure. Figure 4 shows the effect of condenser pressure on nozzle exit position (NXP). Nozzle exit position moves away from constant area section with an increase in condenser pressure.

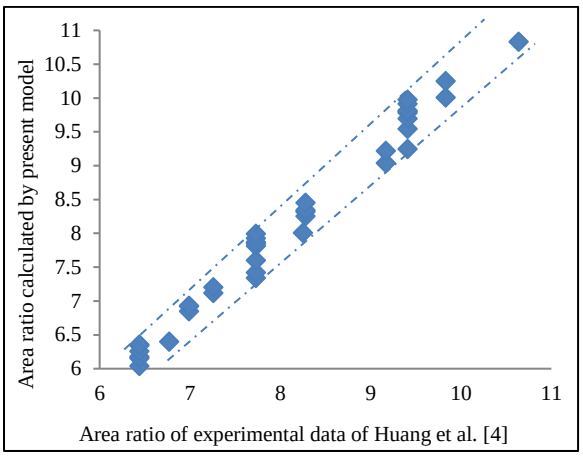


Figure - 1 Comparison between Area ratio's calculated by present model and data collected by experimental data of Huang et al. [4]

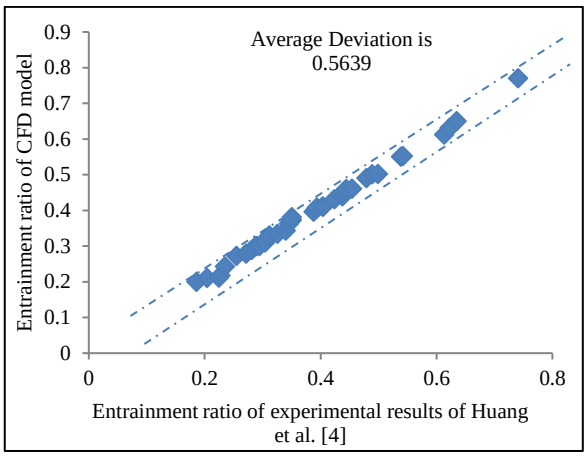


Figure - 2 Comparison between entrainment ratio of CFD model and experimental results obtained from Huang et al. [4]

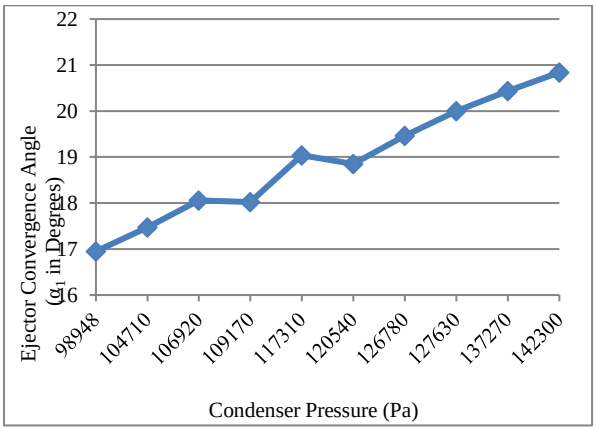


Figure - 3 Effect of Condenser pressure on Ejector convergence angle

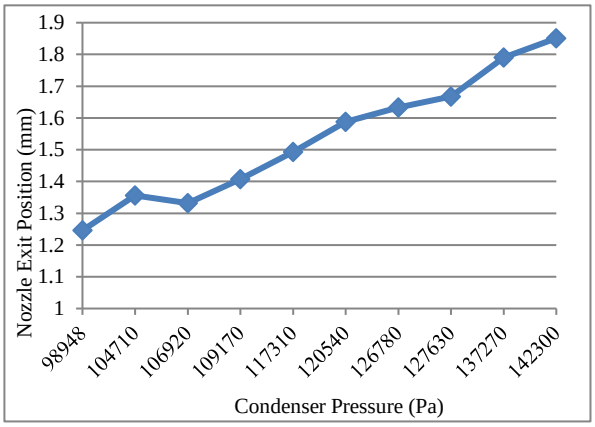


Figure - 4 Effect of condenser pressure on Nozzle Exit Position

The results also show that a larger length of constant area section is required with the decrease in generator pressure and temperature. It indicates that with the increase in generator pressure and temperature the random motion of molecules increases and requires less constant area length for the mixing. The novel concept of Kelvin-Helmholtz instability defines the shape of mixing section (i.e. in between section 4-4 and 6-6). It defines there is no roll-up of vortices and will remain extremely flat if the value critical Mach number is above 0.6. And if it less than 0.6 than there will be a spreading rate of the vortices in the mixing section. Because of the spreading of these vortices the mixing section has to design in divergence section [12]. In this case, it is found that the value of critical Mach number is above 0.6 and a constant area section for mixing of both fluids can be taken. In addition, the CFD model shows the shock is fixed at the outlet of constant pressure area regardless of condenser pressure. The shock wave may transverse towards primary nozzle as the condenser pressure increases but in this case, all geometrical dimensions are so optimized that the shock will produce at end of constant pressure area. The ejector exit divergence angle ($\alpha_2$) calculated by the model is found to be in between 2.5° to 8° and is also validated by Huang et al. [13] as they use the same. The Huang et al. [13] had used the same operating conditions and geometry as Huang et al. [4]. The ejector divergence angle ($\alpha_2$) increase with an increase in ejector exit area ($A_8$) and condenser pressure. As already

mentioned, if the pressure of both the fluids gets unequal at the primary nozzle exit than primary nozzle can have shocks and depend upon the pressure difference the primary flow may diverge or converge [9, 11]. So, for designing ejectors it is decided to have a shock free primary nozzle or equal pressure of both fluids at the nozzle exit. The value of convective Mach number calculated by the present model found above 0.6 in all results shows us the formation of vortices in between primary and secondary fluids during mixing and their effect is also considered in calculating area ratios.

## 3. CONCLUSION

The paper presents the development of a 1-D model for the calculation of all the geometrical dimension of an ejector for a fixed entrainment ratio and standard input conditions. The comparison shows the precision and adequacy of the proposed model for determining the geometrical dimensions of an ejector. The maximum difference in entrainment ratio of CFD model and experimental results of Huang et al. [4] is 12.75 %. With this validation, the 1-D model presented in this paper provides a solution for obtaining complete and accurate geometrical dimensions of an ejector for both critical and sub-critical mode of operations. The accuracy of the results is improved by using instantaneous specific heats and heat capacity ratios at the individual section, instead of taking them constantly. The present model shows a very low absolute average deviation of area ratio and entrainment ratio below -0.287 % and 2.5 % respectively. The importance of geometrical dimensions on ejector behavior has been also discussed. The novel concept of *Prandtl's mixing length* relation is utilized for calculating the minimum length required to mix both fluids (primary and secondary) properly with each other. The concept of formation of vortices in the mixing of compressible fluids is also introduced and discussed. The shapes to be designed for mixing section are also discussed and provide some qualitative data with this.

## REFERENCES

[1] Riffat SB, Jiang L and Gan G. Recent development in ejector technology; a review. International Journal of Ambient Energy, 1995; 26: 13-26.
[2] Chunnanond K and Aphornrnratana S. Ejectors: applications in refrigeration technology. Renewable and sustainable energy reviews, 2004; 8: 129-155.
[3] Gosney WB. Principle of refrigeration, Cambridge; Cambridge University Press; 1982.
[4] Huang B.J, Chang J.M, Wang C.P and Petrenko V.A. A 1-D analysis of ejector performance, International Journal of Refrigeration, 1999; 22: 354-364.
[5] Chen W, Liu M, Chong D. T, Yan J, Little A. B and Bartosiewicz Y. A –D model to predict ejector performance at critical and sub-critical operational regimes, International Journal of Refrigeration, 2013; 36: 1750 – 1761.
[6] He S, Li V and Wang* R. Z. Progress of mathematical modeling on ejectors, Renewable and sustainable energy reviews, 2009; 13: 1760-1780.
[7] Keenan JH, Neumann EP and Lustwerk F. An investigation of ejector design by analysis and experiment. ASME Journal of Applied Mech. Trans. 1950; 72: 299-309.
[8] Munday JT and Bagster DF. A new theory applied to steam jet refrigeration. Ind Eng Chem Process Des Dev, 1977; 16(4): 442-449.
[9] Yinhai Zhu, Wenjian Cai, Changyun Wen and Yanzhong Li. Shock circle model for ejector performance evaluation. Energy conversion and management, 2007; 48: 2533-2541.
[10] Maghsoodi A, Ahmadikia H. and Dadvar M. A new 1D model for supersonic ejector performance evalution at critical and sub-critical operational modes. International journal of air-conditioning and refrigeration, 2014; vol. 22, no. 1, 1430001 (9 pages).
[11] Pjush K. Kundu and Ira M. Cohen, Fluid Mechanics, second edition, Chapter – 16, Academic Press, California, USA; 1990.
[12] Lesieur M. Turbulence in Fluids, 3rd edition, Kluwer academic publishers; 1997.
[13] Huang B. J., Chang J. M., Pettenko V. A., Zhuk K. B. A solar ejector cooling system using refrigerant R141b. Solar Energy, 1998; 64:4

Fifth International Conference on Computational Methods for Thermal Problems
THERMACOMP2018, July 9-11, 2018, Indian Institute of Science, Bangalore, INDIA
*N. Massarotti, P. Nithiarasu, Pradip Dutta and C. Ranganyakalu (Eds.)*

# SINKING OF BULK SOLID PHASE CHANGE MATERIAL DUE TO CLOSE–CONTACT MELTING WITH MULTI-NANOPARTICLES

**Vikram Soni, Arvind Kumar**
Department of Mechanical Engineering, IIT Kanpur, Kanpur, India
vikrams@iitk.ac.in, arvindkr@iitk.ac.in

## ABSTRACT

In this paper, a numerical study of the sinking of bulk solid PCM (Phase Change Material) / NEPCM (Nano-enhanced Phase Change Material) due to close-contact melting is performed. A macroscopic model that uses one-domain continuum formulation is presented for the melting of PCM (Erythritol as base material) and various NEPCM composites (Erythritol with nanoparticles). The thermophysical properties of the NEPCM composite are predicted using homogeneous mixture modeling. The melting pattern of PCM and various NEPCM composites are compared. The influence on the coupled heat transfer and fluid flow behavior due to close-contact melting is described with and without nanoparticles. The numerical predictions concluded that the mono-nanoparticle (5%Cu / Erythritol) composite illustrate better thermal performance among all other multi-nanoparticles (2.5%Cu+2.5%Al / Erthyritol, 2.5%Cu+2.5%$SiO_2$ / Erthyritol and 2.5%Cu+2.5%$TiO_2$ / Erythritol) composites explored in the current study. The insights from the thermal field, velocity field and liquid fraction field thus obtained in the current study (by incorporating nanoparticles along with Erythritol as base PCM) can be used to design medium temperature range (100 $^oC$ – 150 $^oC$) waste heat recovery systems.

**Key Words:** *Solid sinking, Nanoparticles, Phase change material, Heat transfer, Convection.*

## 1. INTRODUCTION

In World Energy Outlook (WEO, 2016), it is forecasted that there will be a surge in the global energy consumption with an increase in world population from 7.3 billion in 2015 to 9.2 billion in 2040 [1]. The energy poverty due to this high energy demand can only be controlled using renewable energy resources effectively. The major prospects are biomass, hydropower, wind power and solar energy for meeting this energy scarcity. But, the reliability of such resources is still debatable due to their discontinuous supply. An appropriate solution to this limitation is to do integration with thermal energy storage (TES) devices. The latent heat based thermal energy storage systems with phase change materials are at the peak of popularity for storing energy. To explore waste heat recovery applications in the medium temperature range (100 $^oC$ – 150 $^oC$), first of all an appropriate choice of the material is essential. Recently, researcher [2-3] have proposed the studies on the non-toxicity, reliability, cyclic stability and safety of the selected organic and inorganic phase change materials. The Erythritol (sugar alcohol) is observed to be the most suitable PCM for operation in medium temperature range (100 $^oC$ – 150 $^oC$). In TES systems, mainly the heat transfer rate is restricted by the low thermal conductivity of the PCM. In order to address this issue various active or passive heat transfer enhancement techniques are being used [4-5]. Modification of the thermophysical properties of the base material to enhance heat transfer rates is one of the ways to overcome this limitation. The potential of improvement in heat transfer rate by adding nanoparticles in the PCM gives a surge to the requirement of NEPCM based TES systems for energy storage. In this paper, close-contact melting of erythritol phase change material is studied in a spherical reservoir to describe sinking effects with nano-enhancement. The insights from the current study can be used to design Erythritol based TES system with nano-enhancement for waste heat recovery in temperature range of 100 $^oC$ – 150 $^oC$.

## 2. MODELLING

A 2-D circular computational domain with internal diameter (*d*) 100.166 mm and aluminium wall of thickness 1.5 mm is considered. Considering the one domain continuum formulation [6,7], the governing equations are solved using a pressure-based finite volume method according to the SIMPLER algorithm [8]. The model is well validated with the benchmark experimental result [9]. The mesh dependency is performed and an optimised resolution is ensured using 20301 grids for numerical study. The governing equations in spherical coordinates ($r$ and $\theta$ being the radial and polar coordinates, respectively) are as following [5],

### 2.1 Governing equations

**Continuity equation**

$$\frac{1}{r^2}\frac{\partial(V_r r^2)}{\partial r}+\frac{1}{r\sin\theta}\frac{\partial(V_\theta \sin\theta)}{\partial\theta}=0 \tag{1}$$

**Energy equation**

$$\frac{\partial(c_pT)}{\partial t}+\frac{1}{r^2}\frac{\partial(V_r r^2 c_pT)}{\partial r}+\frac{1}{r\sin\theta}\frac{\partial(V_\theta \sin\theta c_pT)}{\partial\theta}=\frac{k_f}{\rho c_p}\left[\frac{1}{r^2}\frac{\partial}{\partial r}\left(r^2\frac{\partial c_pT}{\partial r}\right)+\frac{1}{r^2\sin\theta}\frac{\partial}{\partial\theta}\left(\sin\theta\frac{\partial c_pT}{\partial\theta}\right)\right]$$
$$-\frac{1}{\rho c_p}\left[\frac{\partial\Delta H}{\partial t}+\frac{1}{r^2}\frac{\partial}{\partial r}\left(r^2V_r\Delta H\right)+\frac{1}{r\sin\theta}\frac{\partial}{\partial\theta}\left(V_\theta\Delta H\sin\theta\right)\right] \tag{2a}$$

where $\Delta H$ is the latent enthalpy of the cell and defined as:

$$\begin{aligned}\Delta H &= f_l L \quad for \quad T\geq T_m\\ &= 0 \quad for \quad T<T_m\end{aligned} \tag{2b}$$

where $L$ is the latent heat of fusion and $f_l$ is the liquid fraction.

**Momentum equation in polar direction**

$$\frac{\partial(V_\theta)}{\partial t}+\frac{1}{r^2}\frac{\partial(V_r r^2V_\theta)}{\partial r}+\frac{1}{r\sin\theta}\frac{\partial(V_\theta\sin\theta V_\theta)}{\partial\theta}=-\frac{1}{\rho}\frac{1}{r}\frac{\partial p}{\partial\theta}+\frac{\mu}{\rho}\frac{2}{r^2}\frac{\partial V_r}{\partial\theta}-\frac{\mu}{\rho r^2\sin^2\theta}V_\theta-\frac{V_rV_\theta}{r}+$$
$$\frac{\mu}{\rho}\left[\frac{1}{r^2}\frac{\partial}{\partial r}\left(r^2\frac{\partial V_\theta}{\partial r}\right)+\frac{1}{r^2\sin\theta}\frac{\partial}{\partial\theta}\left(\sin\theta\frac{\partial V_\theta}{\partial\theta}\right)\right]-\frac{C(1-f_l)^2}{f_l^3+\varepsilon}V_\theta-g\beta(T-T_m)\sin\theta \tag{3}$$

**Momentum equation in radial direction**

$$\frac{\partial(V_r)}{\partial t}+\frac{1}{r^2}\frac{\partial(V_r r^2V_r)}{\partial r}+\frac{1}{r\sin\theta}\frac{\partial(V_\theta\sin\theta V_r)}{\partial\theta}=-\frac{1}{\rho}\frac{\partial p}{\partial\theta}+\frac{\mu}{\rho}\left[\frac{1}{r^2}\frac{\partial}{\partial r}\left(r^2\frac{\partial V_r}{\partial\theta}\right)+\frac{1}{r^2\sin\theta}\frac{\partial}{\partial\theta}\left(\sin\theta\frac{\partial V_r}{\partial\theta}\right)\right]$$
$$-\frac{\mu}{\rho}\frac{2}{r^2}\frac{\partial V_\theta}{\partial\theta}-\frac{\mu}{\rho}\frac{2\cot\theta}{r^2}V_\theta-\frac{\mu}{\rho}\frac{2}{r^2}V_r+\frac{V_\theta^2}{r}-\frac{C(1-f_l)^2}{f_l^3+\varepsilon}V_r-g\beta(T-T_m)\cos\theta \tag{4}$$

where $C$ is a Darcy constant which reflects the morphology of the melting front. In the current study $C$ is set to $1.0\times10^5$ kgm$^{-3}$s$^{-1}$ [4,5]. In order to avoid division by zero, a small constant $\varepsilon$ is taken as 0.0001. In the NEPCM system, the effective properties of nanofluid are considered as [10],

$$\rho_{nf}=\frac{m_f+m_{np1}+m_{np2}+....}{V_f+V_{np1}+V_{np2}+....} \qquad (\rho\beta)_{nf}=(1-\phi_{np1}-\phi_{np2}....)(\rho\beta)_f \tag{5a}$$

$$(\rho L)_{nf}=(1-\phi_{np1}-\phi_{np2}....)(\rho L)_f \qquad \mu_{nf}=\frac{\mu_f}{(1-\phi_{np1}-\phi_{np2}....)^{2.5}} \tag{5b}$$

$$(\rho c_p)_{nf}=\rho_{nf}\left(\frac{(mc_p)_f\Delta T+(mc_p)_{np1}\Delta T+(mc_p)_{np2}\Delta T....}{(m_f+m_{np1}+m_{np2}+....)\Delta T}\right)_{nf} \tag{5c}$$

$$k_{eff} = \frac{k_f\phi_f + \sum_{i=1}^{n} k_{npi}\phi_{npi}\left[F_i k_{fi}/(F_i-1)k_{fi}+k_{npi}\right]}{\phi_f + \sum_{i=1}^{n} \phi_{npi}\left[F_i k_{fi}/(F_i-1)k_{fi}+k_{npi}\right]} \text{ where } F_i = 3 \text{ (spherical shape)} \quad (5d)$$

### 2.2 Solid bulk sinking model

PCM and NEPCM sinking due to the close-contact melting of the lower surface is accounted separately using following formulation [11],

$$\tau = \left(\frac{Ste}{Pr\cdot Ar}\right)^{0.25}\left(\frac{\rho_s}{\rho}\right)\left(1.56\xi + 0.279\xi^2 + 0.261\xi^3 - 0.0686\xi^4\right) \quad (6)$$

where $\tau = Ste\cdot Fo$, $\xi = \frac{s}{d}$, $Ar$ is the Archimedes number, $Ste$ is the Stefan number, $Fo$ is Fourier number, $Pr$ is Prandtl number and $s$ is the downward distance traveled by solid in time $t$.

## 3. RESULTS

PCM and NEPCM (Erythritol as a base fluid) when subjected to hot thermal boundary conditions, melt with dissimilar rates as shown in Fig. 1. Figure 1(a) shows the temperature map and Fig. 1(b) shows the liquid fraction map with superimposed velocity streamlines (with multiple vortices) for PCM (left half) and NEPCM (right half). In the liquid fraction contours, a clear distinction of the liquid region by the orange color and the solid region is denoted by blue color.

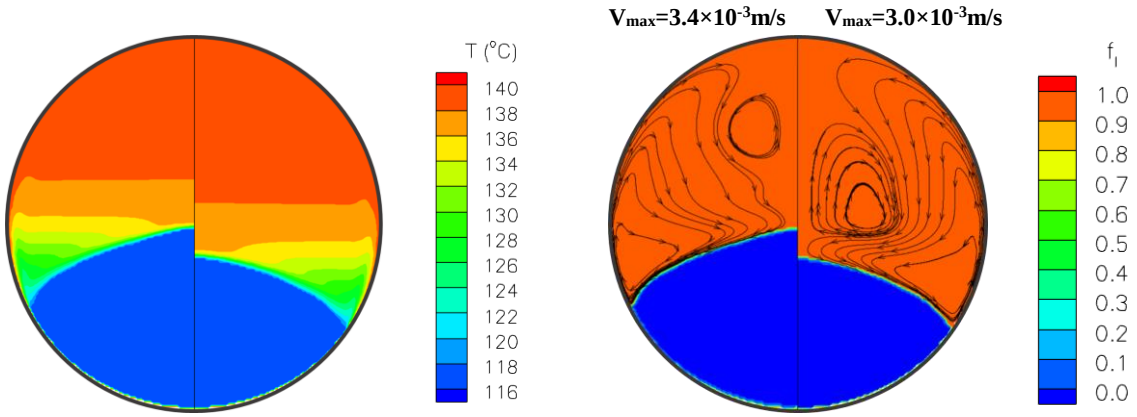


FIGURE 1. Melting at time = 1040 sec, (a) Temperature distribution (in ºC) (b) Liquid fraction distribution, for PCM (left half) and NEPCM (right half)

As the melting advances, it is observed that there is a decrease in the heat transfer rate due to the varying thermal conductivity (decrease from solid to liquid phase) of Erythritol itself during the charging process. The sinking of solid PCM cause faster close-contact melting and push melted PCM towards the top from the lower surface. The buoyancy driven flow and the simultaneous sinking of solid PCM in the reservoir ensure the formation of layers of thermally stratified regions at the upper part of the reservoir as shown in Fig. 1(a). This region possesses the higher temperature than volumetric mean averaged temperature and aid in better thermal performance. Figure 2 presents the evolution of transient liquid fraction in the reservoir. It is observed the 5% Cu / Erythritol composite has shown the earlier completion as compared to the other mixture composite (2.5%Cu+2.5%Al / Erthyritol, 2.5%Cu+2.5%$SiO_2$ / Erthyritol, and 2.5%Cu+2.5%$TiO_2$ / Erythritol), explored in the current study.

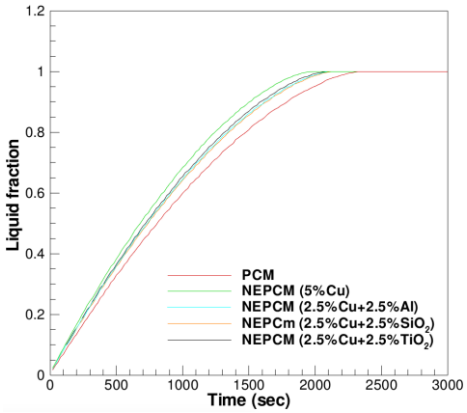


FIGURE 2. Solidified fraction of various NEPCM composites

## 4. CONCLUSIONS

The current study suggests that the varying thermal conductivity of the base fluid (Erythritol) itself reduces the heat transfer rate during charging of PCM. The buoyancy driven convection currents cause stratified thermal layers in the reservoir and aid in satisfaction of load. Multiple counter-rotating vortices formation in the reservoir is observed during the melting. The 5%Cu / Erythritol composite has shown the better performance as compared to 2.5%Cu+2.5%Al / Erthyritol, 2.5%Cu+2.5%$SiO_2$ / Erthyritol and 2.5%Cu+2.5%$TiO_2$ / Erythritol composites. Overall, the close-contact melting with nanoparticles enhance the heat transfer rate and reduce the charging cycle time. The study delineate guidelines for designing NEPCM based waste heat recovery systems.

## REFERENCES

[1] World Energy Outlook 2016, *International Energy Agency*, 2016.
[2] A. Shukla, D. Buddhi, R.L. Sawhney, Thermal Cycling Test of Few Selected Inorganic and Organic Phase Change Materials, *Renewable Energy*, 33, 2606–2614, 2008.
[3] A. Solé, H. Neumann, S. Niedermaier, I. Martorell, P. Schossig, L.F. Cabeza, Stability of Sugar Alcohols as PCM for Thermal Energy Storage, *Solar Energy Materials & Solar Cells*, 126, 125–134, 2014.
[4] S. Kashani, E. Lakzian, K. Lakzian, M. Mastiani, Numerical Analysis of Melting of Nanoenhanced Phase Change Material in Latent Heat Thermal Energy Storage System, *Thermal Science*, 18(SUPPL.2), 335–345, 2014.
[5] V. Soni, A. Kumar, V.K. Jain, Modelling of PCM Melting: Analysis of Discrepancy between Numerical and Experimental Results and Energy Storage Performance, *Energy*, 150, 190–204, 2018.
[6] W.D. Bennon, F.P. Incropera, A Continuum Model for Momentum, Heat and Species Transport in Binary Solid-Liquid Phase Change Systems-I. Model Formulation, *International Journal Heat Mass Transfer*, 30(10), 2161–2170, 1987.
[7] V.R. Voller, C. Prakash, A Fixed Grid Numerical Modelling Methodology for Convection-Diffusion Mushy Region Phase-Change Problems, *International Journal Heat Mass Transfer*, 30(8), 1709–1719, 1987.
[8] S. V. Patankar, *Numerical Heat Transfer and Fluid Flow*, Ser. computational methods Mech. Therm. Sci., 1–197, 1980.
[9] Tan, F.L., Constrained and unconstrained melting inside a sphere, *International Communications in Heat and Mass Transfer*, 35 (4), 466-475, 2008.
[10] J.C. Maxwell, *A Treatise on Electricity and Magnetism, 2nd Edition*, Oxford Univ. Press, Cambridge, 435-441, 1904.
[11] P.A. Bahrami and T.G. Wang, Analysis of gravity and conduction-driven melting in a sphere, *Journal of Heat Transfer* 109, 806–809, 1987.

# *FLOW ANALYSIS of OIL FLOW IN THE GAS TURBINE INJECTORS*

***Vimala Narayanan, Ritesh Gaur, TV Yogesh, Sc. E, Kishore Prasad D***

***Scientist, GasTurbine Research Establishment***

***Bangalore 560093***

***vimala@gtre.drdo.in***

ABSTRACT

CFD analyses were carried out using a commercially available code of NUMECA to analyse the flow in injectors of two different configurations. CFD analyses was carried out without considering the atmosphere and with atmosphere. Results are presented as the static pressure distributionand velocity contours. Experimentla tests were carried out and results will be presemted.

**Key Words:** Bearing flow analysis, CFD, Oil Brooming

## 1. INTRODUCTION

Lubricating oils perform three functions in a gas turbine engine; lubrication, cooling and cleaning. The oil generally has low viscosity to flow easily between fast rotating parts. It will have a high viscosity to avoid interference between two metals and avoid wear and tear of the components. It is necessary that the lubrication should not break down under high temperatures and pressures. Similarly, the oil must have a low pour point to flow readily when starting under extremely low temperatures.

Lubricating oil cools the moving parts by carrying the heat away from gears and bearings. It carries away thedirt, small carbon and metal particles, gum and varnish to the filters. This has become increasingly important with the higher compression ratios, engine speeds, operating temperatures, and closer tolerances between parts in newer engines.

It is necessary that the lubricating oil reaches the bearings without much spreading or broom due to mixing of jet with the surrounding rotating air. An attempt has been made to study the mixing phenomena of the jet with surrounding air in two injector geometries.

A free jet after leaving the nozzle, entrains the surrounding fluid, expands and decelerate. **Perry et al., 2007**.The total momentum which is conserved as jet momentum is transferred to the entrained fluid. It is found that when the cross-sectional area of jet is less than 1/5 than the cross section of surrounding region then jet is considered to be free jet.

**McCabe et al., 1993** has explained that the high velocity liquid jet ejecting from nozzle situated at the entrance of ejector, flows through the stagnant fluid surrounding it, maintains its identity for a substantial distance.

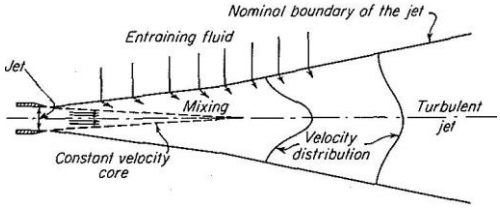


FIGURE:1. Flow of a submerged circular jet

**Eroglu et al. (1991)** measured the breakup length of round liquid jet in annular coaxial air streams. They further observed that the decreasing breakup length with increasing Weber number and they also found that liquid jet length increases by increasing Reynolds number.

First geometry is made up of a hollow cylinder closed at bottom and has one hole on the circumference of the cylinder. The second geometry consists of two co-axial cylinders where the inner cylinder is perforated.

**Grid generation**

The mesh is generated using NumecaHexpress for both the geometries. The Y+ is 1.

**Boundary conditions**

Initial Total pressure – 7 Bar; Inlet temperature - 343 K and Exit static pressure – 1bar

## 3. RESULTS

### Geometry 1 Flow Model without surrounding atmosphere

The incompressible flow mode of the 3-Dimensional flow was analysed using the commercial software. Figure 2 shows the static pressure distribution in the cross sectional view of the original injector. It is found that the static pressure is uniform in the entire length of the injector. As it ejects from the orifice the static pressure further reduces from 500000 Pascals to 150000Pa. One can observe the static pressure profile varying from 125000 at one end to 600000 Pa at the center of the injector and then reduces to 125000Paat the other end of the diameter of the injector.

Figure 3 shows the velocity magnitude contours of the fluid in the injector. It also shows the velocity magnitude along the exit plane of the injector (diameter). It can be observed that the flow in the centre of the exit plane is sharper and one sided.

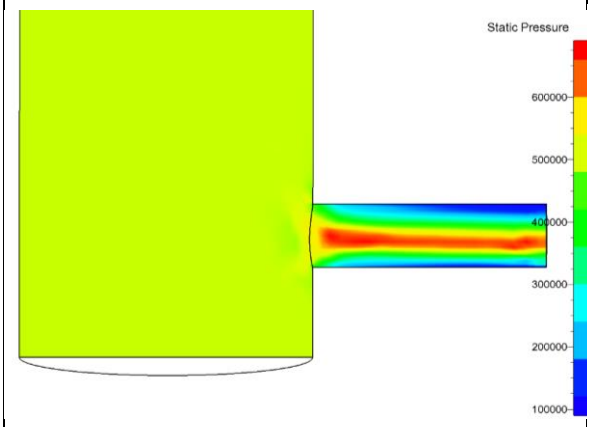


FIGURE 2. Contour of Static pressure (pascal)

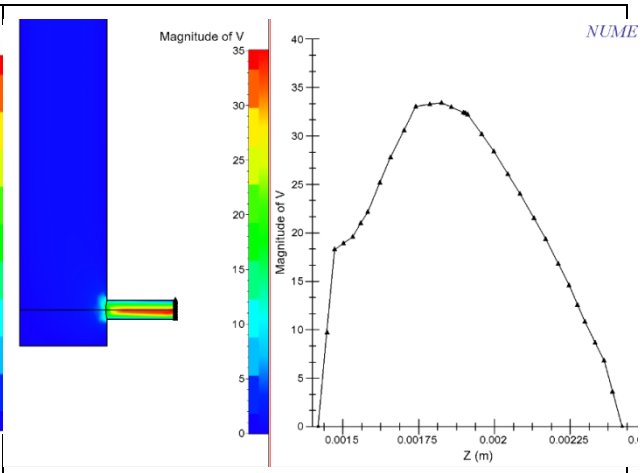


FIGURE 3. Contour of magnitude of velocity and Plot of V (m/s)

### Geometry 2 Flow Model without Atmosphere

Incompressible flow analysis for the modified injector wascarried out. The static pressure contours are shown in a part of the injector body and the nozzle in Figure 4. It can be observed that static pressure is gradually decreasing along the nozzle length. Figure 5shows the magnitude of velocity contours. The graph adjacent to the contours predicts the velocity profile prevailing at the exit plane of the injector nozzle. It can be observed that the magnitude of the peak velocity has been reduced from 32 m/s to 24 m/s but is found to be more uniform.

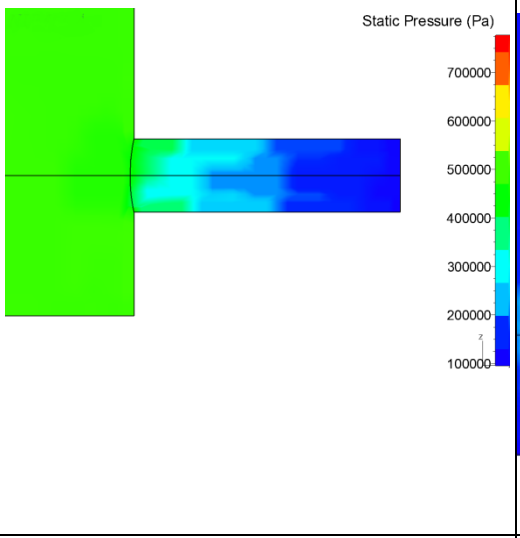


FIGURE 4. Contour of Static pressure (pascal)

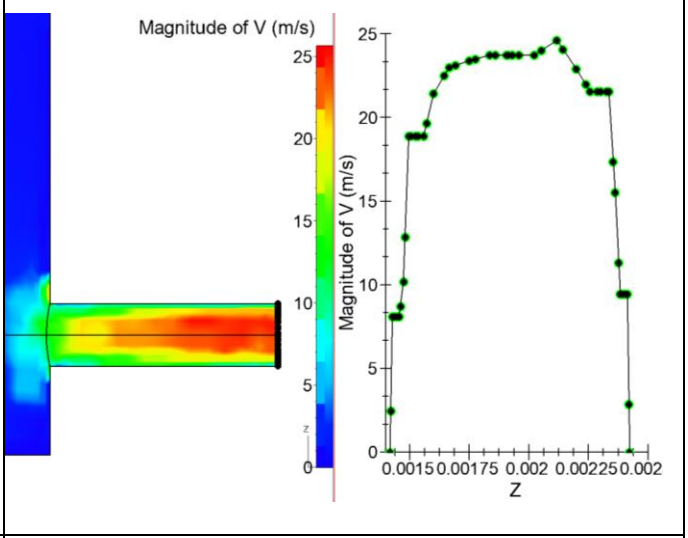


FIGURE 5. Contour of magnitude of velocity and Plot of V (m/s) vs Z (m).

Similarly analyses were carried out by modelling the surrounding atmosphere and the results are shown in Figure 6, 7, and 8.

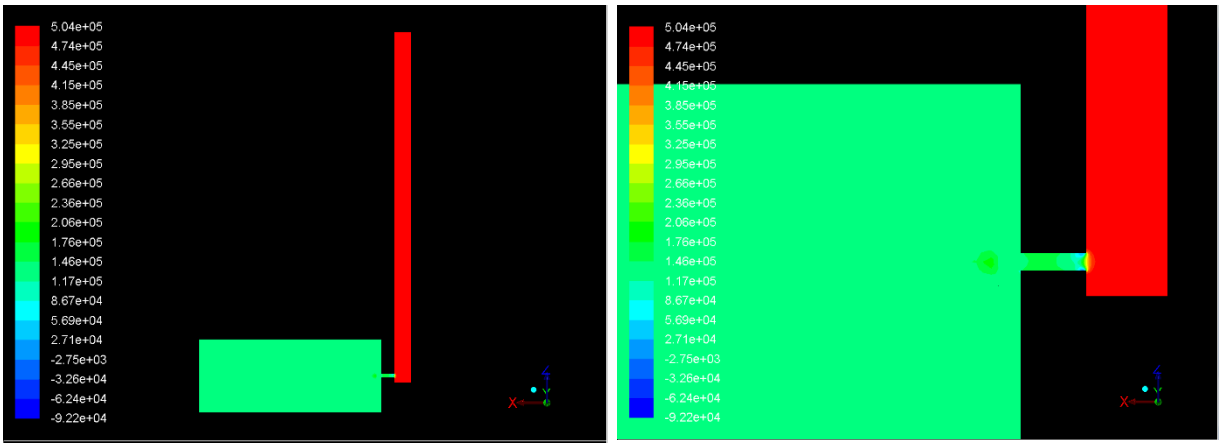


FIGURE 6. Static pressure contour of the Flow in Geometry 1 with surrounding atmosphere

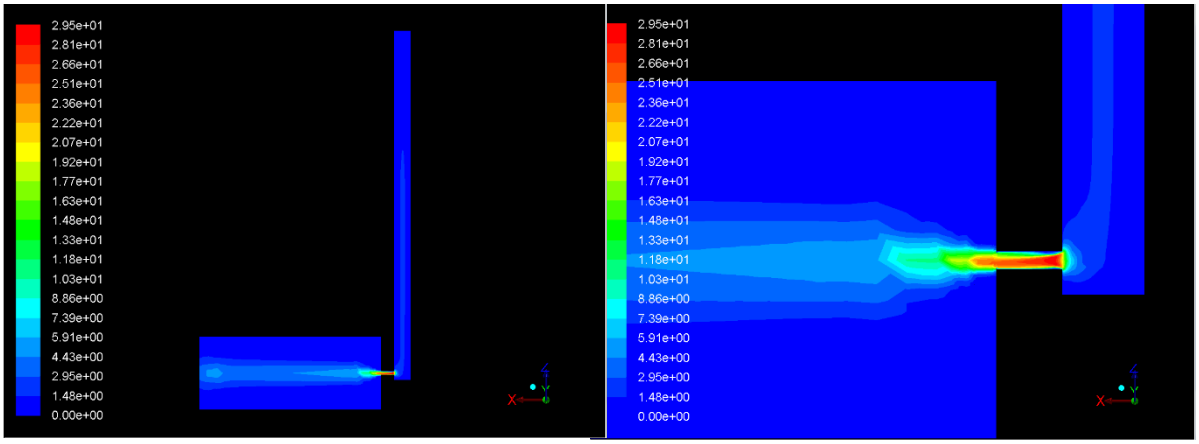


Figure: 7. Contour of Velocity magnitude (m/s)

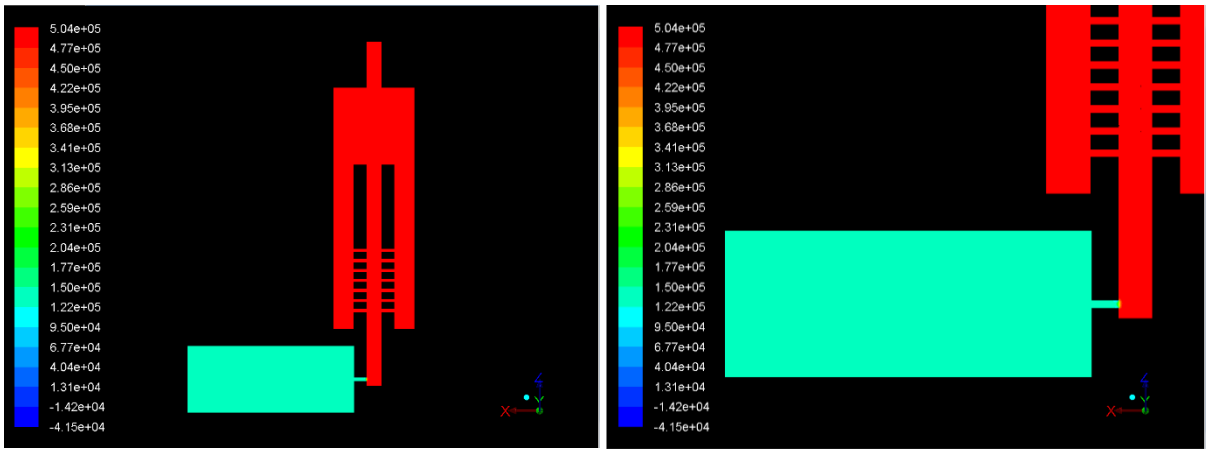


FIGURE: 8. Contour of static pressure (pascal)

## 4. CONCLUSIONS

The jet length of the both geometries of the injectors were found to be of difference when CFD analyses were carried out. When the experiments were carried out, it showed verymarginal difference.

## REFERENCES

[1] **Perry et al., 2007**.

[2] **McCabe et al., 1993**

[3] **Eroglu et al. (1991)**

Fifth International Conference on Computational Methods for Thermal Problems
THERMACOMP2018, July 9-11, 2018, Indian Institute of Science, Bangalore, INDIA
*N. Massarotti, P. Nithiarasu, Pradip Dutta and C. Ranganyakalu (Eds.)*

# NUMERICAL SIMULATION OF DOUBLE FORWARD FACING STEP WITH OBSTACLES OF DIFFERENT AXIS RATIO

**Vishnu. M**
Ph.D. Research scholar
Applied Mechanics Department
IIT Madras
Email:am15d027@smail.iitm.ac.in
**K. Arul Prakash**
Associate Professor
Applied Mechanics Department
IIT Madras
Email:arulk@iitm.ac.in

## ABSTRACT

Fluid flow and heat transfer characteristics in a double forward facing step in the presence of elliptic shaped obstacles with different axis ratios positioned before each step is numerically investigated. For the purpose, governing equations of fluid flow and heat transfer are solved in cartesian framework using an in-house code based on Streamline UPWIND/Petrov Galerkin (SUPG) finite element method.

The parametric study is carried out for various Reynolds number (Re=300,500,800 and 1000) and different axis ratios of the obstacles (AR=0.25, 0.5, 0.75, 1). It is observed that fluid flow pattern is altered due to the presence of obstacles near the steps and the reduction of the recirculation length when compared with no obstacle case.

**Key Words:** *SUPG finite element method, Double forward facing step*

## 1. INTRODUCTION

In many engineering practices flow separation and reattachment occur depending on the flow velocities and physical model under consideration. Forward facing step are usually observed in electronic cooling applications, combustion chamber, open channels and building aerodynamics.

Armaly et al. [1] presents a simulation of three dimensional laminar forced flow adjacent to backward facing step in rectangular duct to study the effect of step on flow characteristics. Yilmaz and Oztop [2] have numerically investigated the turbulent forced convection over double forward facing step and studied the effect of step lengths, step heights and Reynolds number on heat transfer and fluid flow. The main conclusion of the paper is that second step can be used to control fluid flow and heat transfer characteristics. Oztop et al. [3] have numerically studied the turbulent forced convection of double forward facing step with obstacles and studied the effect of step height, obstacle aspect ratio and Reynolds number on fluid flow and heat transfer in a double forward facing channel with rectangular obstacle before step. The main finding of the paper is that heat transfer rate increases when obstacle aspect ratio increases. Fluid flow characteristics over a forward facing channel with obstacles have received less attention in the literature.

The present work is carried out to study the effect of circular and elliptic obstacles in channel with double forward facing step to understand the variation in fluid flow pattern in the channel. For the purpose the axis ratio of the obstacle is varied and results are compared for channel flow without any obstacle. Further the cases are simulated to study the effect of Reynolds number and obstacle with various axis ratio.

## 2. MATHEMATICAL MODELING

### 2.1 Physical domain

A schematic description of the problem considered for this study is shown in FIGURE 1. The geometrical features of the domain are total length of channel L=1.6 m, step height h=0.024m, width of the channel at inlet w=0.1 m.

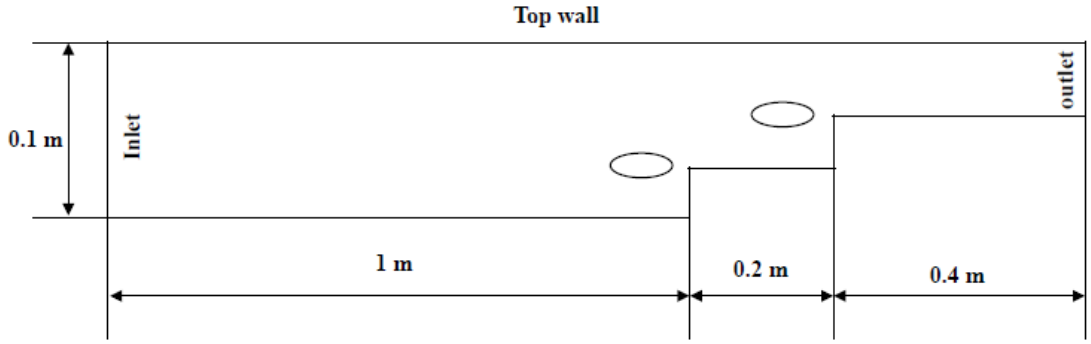


FIGURE 1. Computational domain

### 2.2 Governing equations

The fluid flow is assumed to be viscous, two dimensional, time-dependent and incompressible with constant thermo-physical properties. The effect of gravity and viscous dissipation are neglected.

The continuity and momentum equations can be expressed as follows,

$$\frac{\partial u_i}{\partial x_i} = 0 \tag{1}$$

$$\frac{\partial u_i}{\partial t} + u_j \frac{\partial u_i}{\partial x_j} = -\frac{\partial p}{\partial x_i} + \frac{1}{Re}\left\{\frac{\partial}{\partial x_i}\left(\frac{\partial u_i}{\partial x_j} + \frac{\partial u_j}{\partial x_i}\right)\right\} \tag{2}$$

### 2.3 Boundary conditions

The following boundary conditions are imposed for present domain of interest.

Along Inlet: u = 1.0, v = 0.0 and $\frac{\partial p}{\partial x} = 0$

Along Top wall: u = 0.0, v= 0.0 and $\frac{\partial p}{\partial y} = 0$

Along Bottom wall: u = 0.0, v= 0.0 and $\frac{\partial p}{\partial y} = 0$

Along Outlet: $\frac{\partial u}{\partial x} = 0$ $\frac{\partial v}{\partial x} = 0$ p = 0.0

### 2.4 Validation

The equations governing fluid flow and heat transfer are solved iteratively by using Eulerian velocity correction approach which is originally based on the projection scheme of chorin[4].The detailed

finite element formulation and validation for several benchmark cases (lid driven cavity and backward facing step) have been presented in Prakash et al.[5].

## 3. RESULTS

In the present study, fluid flow dynamics in a double forward facing step without and with obstacle for various axis ratios of obstacle (AR=0.25,0.5,0.75 and 1) and for different values of Reynolds number is analysed.

The streamlines near the steps for the different cases (Re=1000) are presented in FIGURE 2. Pressure contours for different cases are presented in FIGURE 3.

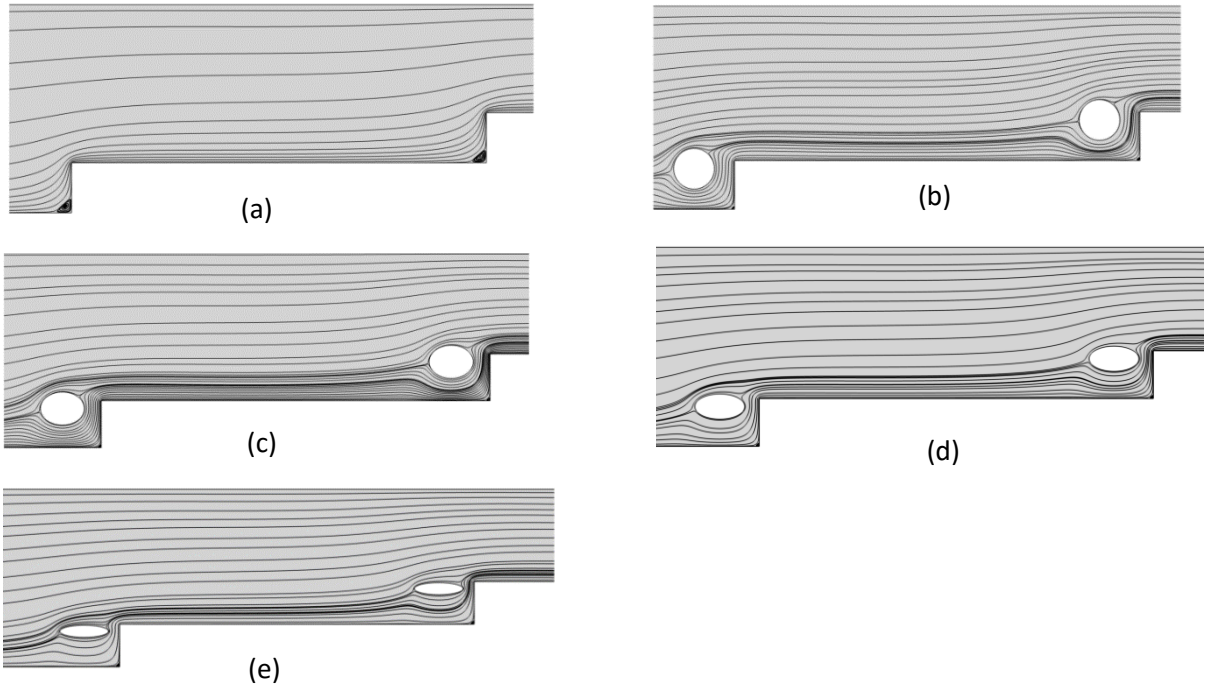


FIGURE 2. Magnified view of streamlines near the steps in Double forward facing stepped channel for Re=1000 (a) without any obstacle (b) with obstacle of AR=1(c) with obstacle of AR=0.75 (d) with obstacle of AR=0.5 (e) with obstacle of AR=0.25

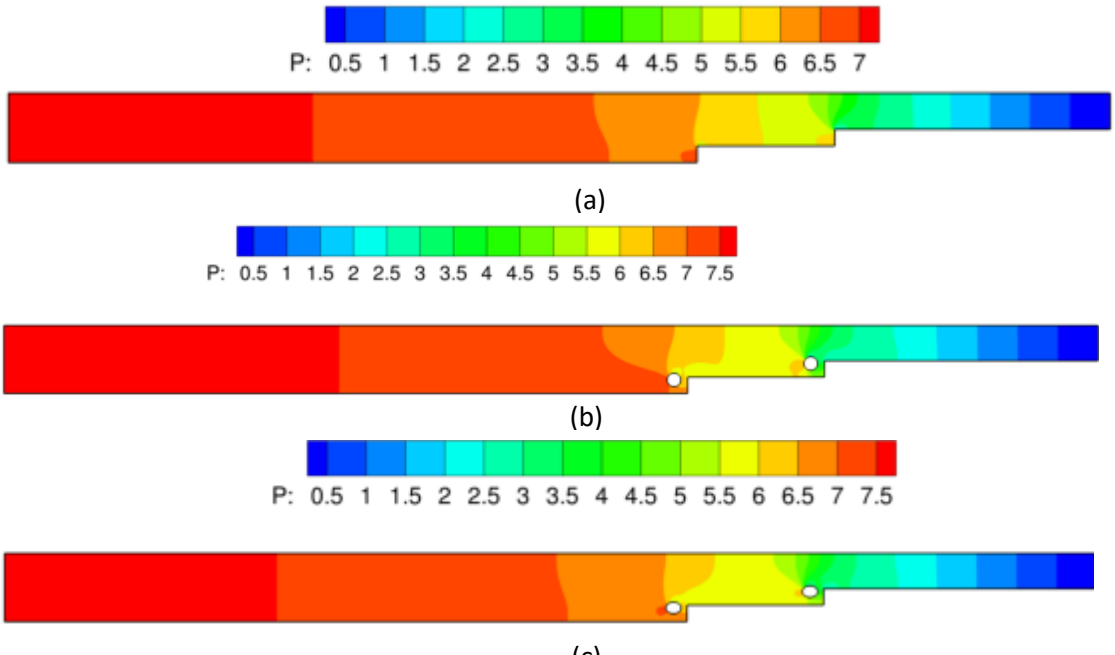

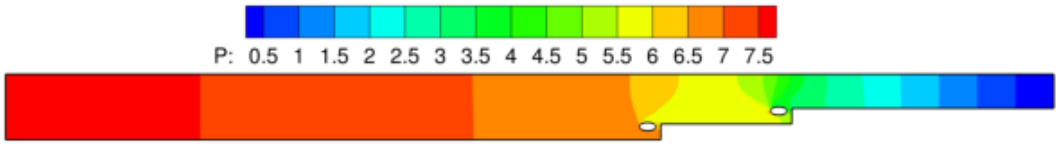


(d)

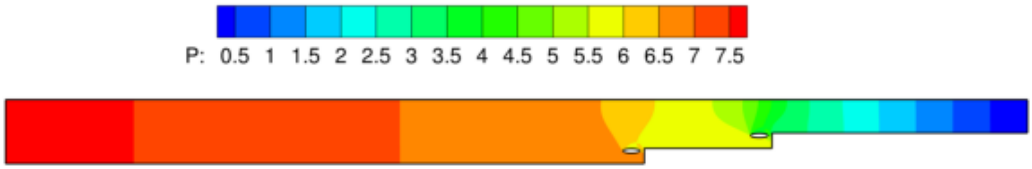


(e)

FIGURE 3. Pressure contour in Double forward facing stepped channel for Re=1000 (a) without any obstacle (b) with obstacle of AR=1(c) with obstacle of AR=0.75 (d) with obstacle of AR=0.5 (e) with obstacle of AR=0.25

## 4. CONCLUSIONS

This study presents the numerical analysis of a channel with double forward facing step with and without obstacles before the steps. The streamlines results shows that due to the presence of obstacles the recirculation length reduces. The obstacles splits the flow before the steps and one part of the flow have to pass through a much smaller area compared to case without obstacle which results in the reduction of the recirculation region. The pressure drop is more for case with obstacles and is almost same for AR=1,0.75,0.5and 0.25 cases.

## REFERENCES

[1] B. Armaly, F. Durst, J. Pereira, and B. Schonung, “Experimental and theoretical investigation of backward-facing step flow,” *J. Fluid Mech*, vol. 127, pp. 473–496, 1983.

[2] I. Yilmaz and H. F. Öztop, “Turbulence forced convection heat transfer over double forward facing step flow,” *Int. Commun. Heat Mass Transf.*, 2006.

[3] H. F. Oztop, K. S. Mushatet, and I. Yilmaz, “Analysis of turbulent flow and heat transfer over a double forward facing step with obstacles,” *Int. Commun. Heat Mass Transf.*, 2012.

[4] Chorin, A. J., 1967. "A numerical method for solving incompressible viscous flow problems". *J. of Computational physics*, 2(1), pp. 12-26.

[5] K. Arul Prakash, G. Biswas, and B. V. Rathish Kumar, “Thermal hydraulics of the spallation target module of an accelerator driven sub-critical system: A numerical study,” *Int. J. Heat Mass Transf.*, vol. 49, no. 23–24, pp. 4633–4652, 2006.

Fifth International Conference on Computational Methods for Thermal Problems
THERMACOMP2018, July9-11, 2018, Indian Institute of Science, Bangalore, INDIA
*N. Massarotti, P. Nithiarasu, Pradip Dutta and C. Ranganyakalu (Eds.)*

# COMPUTATION OF ERROR MODEL FOR THE INVERSE BIOHEAT TRANSFER PROBLEM

**Gnanasekaran N, Vishweshwara P S**
Department of Mechanical Engineering, National Institute of Technology Karnataka,Surathkal, Mangalore, 57025, Karnataka, India. E-mail addresses: ngs.iitm@gmail.com

## ABSTRACT

An inverse estimation of size and location of tumor is proposed in this paper using Bayesian framework. The forward model comprises of the Pennes equation and solved using commercial software. The forward solution of the problem is validated against the available literature and the results are found to be promising. Estimation of the size and location of the tumor is attempted based on Bayesian framework along with the Markov chain Monte Carlo method. This paper also demonstrates 2D and 3D modelling of the cancerous tissue and exploits the advantage of 2D model in the computation of MCMC method. An Approximation Error Model (AEM) is proposed in order to statistically account the model error during the estimation of the unknown parameters. The results of the AEM provide a new trend in the parametric study of cancerous tissue.

**Key Words:** *Bayesian, MCMC, Bio heat transfer, Pennes, estimation, AEM.*

## 1. INTRODUCTION

Cancer is one of the leading diseases which is causing early end of the life span of human beings. The causes of the cancer can be due to smoking, drinking, pollution, excessive mental stress, genetic, etc. Various therapies have been developed in medical field to treat the cancer which gives a sign of relief but not the ultimate solution for the cure of cancer. Apart from developing medical technologies to cure cancer, it is important to understand how cancer develops and how it affects the nearby tissues. This can be achieved by solving Pennes equation for bio heat transfer problems [1]. Several researchers worked towards the detection of tumor using Genetic algorithm [2]. Agnelli et al estimated the unknown parameters and geometrical properties of the tumor using the temperature data obtained from infrared thermography [3]. Several methods such as Lattice Boltzmann method (LBM), Finite Element Method (FEM), Finite Volume Method (FVM) are popularly used to solve the Pennes governing equation. Zhang et al used LBM method to solve 2D bio heat problems and a comparison between the numerical and analytical solutions can also be seen in [4]. Wu et al investigated the dependence of skin temperature distributions with various internal heat generation sources subjected to various physiological and environmental conditions using numerical solutions which help in knowing the physical phenomenon for various heat generation modifications [5]. Das and Mishra used inverse method to estimate the locations and size of the tumor [6].

## 2. MATHEMATICAL MODELLING

The 3-D hemispherical breast embedded with the tumor is as shown Figure 1. The dimensions of the 3-D model is as follows: hemisphere radius=10cm, tumor radius($r_t$)=1.5cm which is at a depth of 2cm from skin. Heat transferred blood perfused tissue is governed by Pennes equation which is given by

$$k\left(\frac{\partial^2 T}{\partial x^2}+\frac{\partial^2 T}{\partial y^2}\right)+\eta_b \rho_b C_{pb}(T_a - T)+Q_m+Q_s=0 \quad (1)$$

where $\rho_b, C_{pb}$ and $\eta_b$are the density and the specific heat of the blood perfusion rate of the tissue respectively. $k$is thermal conductivity, $T_a$ is the temperature of the artery in °C. The

terms $Q_m$ and $Q_s$ are the metabolic heat generation rate and distributed volumetric heat source respectively. The change in the value of $Q_m$ will manipulate the value of the property $\eta_b$. The hemispherical surface is subjected to a convective boundary condition and the core body is with a isothermal condition with $T_a$ . The above problem is solved using COMSOL multiphysics commercial software. For a healthy or normal tissue, the values of $Q_m$ and $\eta_b$ are taken to be $450Wm^{-3}$ and $0.92\times10^{-3}s^{-1}$ respectively. In presence of tumor, the values $Q_m$ and $\eta_b$ are taken to be 29000Wm$^{-3}$ and $4.5\times10^{-3}s^{-1}$ respectively. The thermophysical properties used are: $\rho_b = 1052\,kgm^{-3}, C_{pb} = 3800\,JKg^{-1}K^{-1}$. The values of $k, h$ and $T_f$ are taken as $0.5\,Wm^{-1}K^{-1}, 20\,Wm^{-2}K^{-1}$ and 20℃ respectively [6]. The initial temperature of the tissue is assumed based on the expression given as

$$T_e = T_a + \frac{Q_m + Q_s}{\eta_b \rho_b C_{pb}} \tag{2}$$

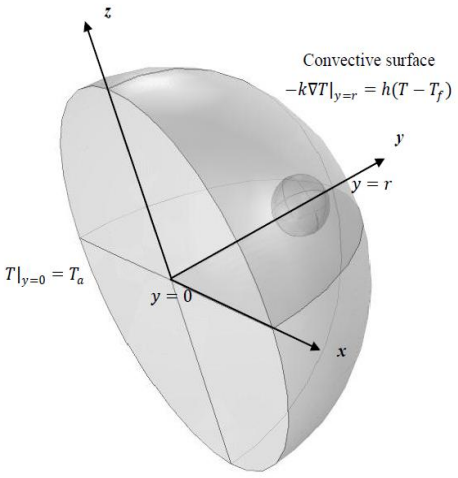


FIGURE 1. Representation of 3-D hemispherical breast with tumor.

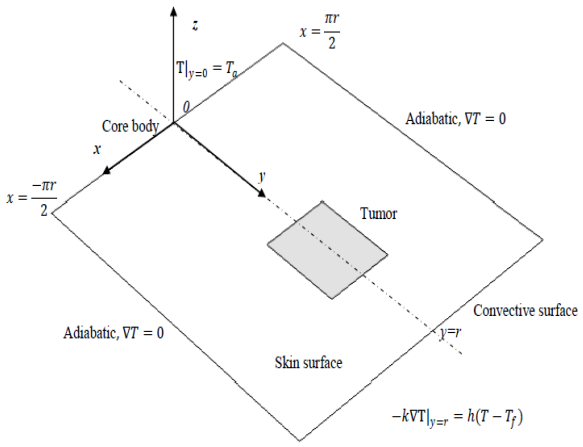


FIGURE 2. 2-D model of 3-D hemispherical breast with tumor.

## 3. APPROXIMATION ERROR MODEL

The modeling error is approximated based on statistical description in this technique. Therefore, the measurement model can be written as

$$Y = \Theta_p(P) + e \tag{3}$$

Where Θp(P) represents the solution of the forward model. In Eqn. (3), "e" represents the uncertainties in the measurement and is also assumed to be normally distributed with zero mean and known covariance matrix W. Hence, in the light of all these facts, the forward model can be written as

$$\boldsymbol{\pi(Y \mid P) = (2\pi)^{-\frac{D}{2}} \mid W \mid^{-\frac{1}{2}} \exp\{-\frac{1}{2}[Y - \Theta_p(P)]^T W^{-1}[Y - \Theta_p(P)]\}} \tag{4}$$

In Eqn.(4), D represents the total number of measurements and the forward solution is obtained from Θp(P). Let the reduced model be given as Θrp(Pr) and introducing the reduced model in to Eqn. (3), thus the resulting equation becomes

$$Y = \Theta^{r}_{p}(P^{r}) + [\Theta_{p}(P) - \Theta^{r}_{p}(P^{r})] + e \tag{5}$$

The difference between the accurate and reduced models can be given as

$$\varepsilon(P) = \Theta_{p}(P) - \Theta^{r}_{p}(P^{r}) \tag{6}$$

$$Y = \Theta^{r}_{p}(P^{r}) + \eta(P) \tag{7}$$

Where

$$\eta(P) = \varepsilon(P) + e \tag{8}$$

Assuming η(P) as normal random variable and the corresponding statistics can be computed from the knowledge of prior distribution. Now, the likelihood function is rewritten in terms of approximation error model.

$$\tilde{\pi}(\mathbf{Y} \mid \mathbf{P^{r}}) = (2\pi)^{-\frac{D}{2}} \mid \tilde{\mathbf{W}} \mid^{-\frac{1}{2}} \exp\{-\frac{1}{2}[\mathbf{Y} - \boldsymbol{\Theta}^{\mathbf{r}}_{\mathbf{p}}(\mathbf{P^{r}}) - \bar{\boldsymbol{\eta}}_{\mathbf{p^{r}}}]^{T} \tilde{\mathbf{W}}^{-1}[\mathbf{Y} - \boldsymbol{\Theta}^{\mathbf{r}}_{\mathbf{p}}(\mathbf{P^{r}}) - \bar{\boldsymbol{\eta}}_{\mathbf{p^{r}}}]\} \tag{9}$$

where

$$\bar{\boldsymbol{\eta}}_{\mathbf{p^{r}}} = \bar{\boldsymbol{\varepsilon}} + \bar{\mathbf{e}} + \boldsymbol{\Gamma}_{\boldsymbol{\eta}_{\mathbf{p^{r}}}} \boldsymbol{\Gamma}_{\mathbf{P^{r}}}^{-1}(\mathbf{P^{r}} - \boldsymbol{\mu}) \tag{10}$$

$$\tilde{\mathbf{W}} = \mathbf{W}_{\boldsymbol{\varepsilon}} + \mathbf{W} - \boldsymbol{\Gamma}_{\boldsymbol{\eta}_{\mathbf{p^{r}}}} \boldsymbol{\Gamma}_{\mathbf{P^{r}}}^{-1} \boldsymbol{\Gamma}_{\boldsymbol{\eta}_{\mathbf{p^{r}}}} \tag{11}$$

$\bar{\varepsilon}, \bar{e}$ and μ are the means of ε, e and $P^r$ respectively and $W_{\varepsilon}, \Gamma_{\eta_{p^r}}$ and $\Gamma_{P^r}^{-1}$ are the covariancematrices of ε, η and $P^r$ respectively.

Assuming the measurement uncertainties have zero mean ( $\bar{e} = 0$) and neglecting the linear dependency between η and $P^r$ , then $\Gamma_{\eta_{p^r}}$ becomes zero. Thus, Eqns.(10) and (11) are simplified to obtain Enhanced Error model.

$$\bar{\boldsymbol{\eta}}_{\mathbf{p^{r}}} \approx \bar{\boldsymbol{\varepsilon}} \tag{12}$$

$$\tilde{\mathbf{W}} \approx \mathbf{W}_{\boldsymbol{\varepsilon}} + \mathbf{W} \tag{13}$$

## 4. RESULTS

The computational time to solve 3-D hemispherical breast case was noted to be 67s. The temperature distribution along the centreline and the surface can be observed from Figures 3 and 4. The In order to reduce the computational cost, the 3-D model is represented in terms of 2-D as shown in the Figure 2. The length and width were taken to be 10cm and 31.41cm (πr) respectively. The Length of the tumor is calculated as $L_t^2 = \pi r_t^2$. For this 3D-2D case, the properties for healthy tissue used are $\eta_b = 0.92 \times 10^{-3} s^{-1}$ and $Q_m = 450 Wm^{-3}$. For tumor tissue, $\eta_b = 4.9 \times 10^{-3} s^{-1}$ and $Q_m = 29000 Wm^{-3}$. The values of $k, \rho, C_p, \rho_b$ and $C_{pb}$ are taken as

$0.42\ \mathrm{Wm^{-1}K^{-1}}, 920\ \mathrm{kgm^{-3}}$, $3000\ \mathrm{JKg^{-1}K^{-1}}$ , $1052\ \mathrm{kgm^{-3}}$ and $3800\ \mathrm{JKg^{-1}K^{-1}}$ respectively [6]. It was observed that the computational cost was reduced to 6-8 seconds. Figure 3 and 4 show the results of 2-D model agrees very well with the results of Das and Misra [6] as well as 3-D model but also helps in obtaining temperatures at lesser computational time.

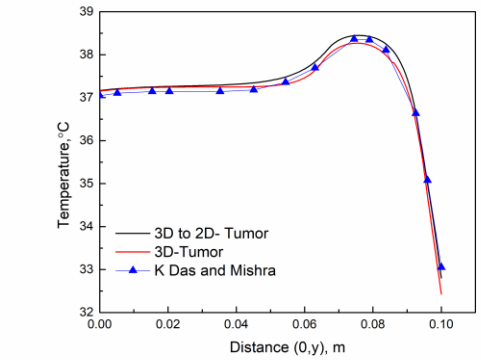


FIGURE 3. Temperature along the centreline for 2-D equivalent model w.r.t 3D with cancer tumor.

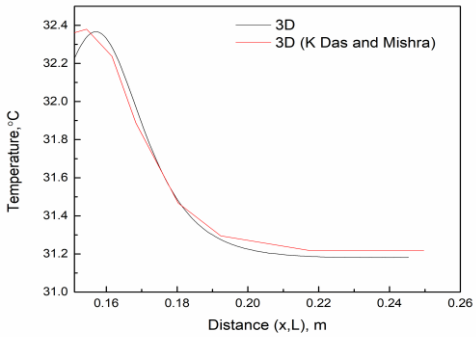


Figure 4. Temperature along the surface of the skin for 3D model with cancer tumor.

## 5. CONCLUSIONS

2D and 3D models of a cancerous tissue are considered in order to estimate the size and location of the tumour. The modelling error has been accounted in the Approximation Error Model proposed in this work. The sample space was explored using Markov Chain Monte Carlo method. The prior information was incorporated in the form of a probability distribution in the Bayesian framework. Thus, the combination of forward and inverse solutions with the help Approximation Error methodology proves to be potent tool in the field of bio heat transfer.

## REFERENCES

[1] H. H. Pennes, Analysis of Tissue and Arterial Blood Temperatures in the Resting Human Forearm, *Journal of Applied Physiology*, 1(2), 93–122, 1948.

[2] A.M. Gonçalo Filho., L.L. Nogueira, J.V.C. Silveira, M.M.S. Loureiro, F. dos Santos Loureiro Solution of the Inverse Bioheat Transfer Problem for the Detection of Tumors by Genetic Algorithms, *Computational Science and Its Applications – ICCSA 2017*, 10405,441-452, 2017.

[3] J.P. Agnelli, A.A. Barrea, C.V. Turner, Tumor location and parameter estimation by thermography, *Mathematical and Computer Modelling*, 53,(7–8), 1527-1534, 2011.

[4] H. Zhang, Lattice Boltzmann method for solving the bioheat equation, *Physics in medicine and biology*, 53,15-23,2008.

[5] Z. Wu , H.H. Liu, L. Lebanowski, Z.Liu, P.H. Zhongqi, A basic step toward understanding skin surface temperature distributions caused by internal heat sources, *Physics in medicine and biology*, 52, 5379-92, 2007.

[6] K. Das and C. S. Mishra, Non-invasive estimation of size and location of a tumor in a human breast using a curve fitting technique, *International Communications in Heat and Mass Transfer*,56 ,63-70,2014.

Fifth International Conference on Computational Methods for Thermal Problems
THERMACOMP2018, July 9-11, 2018, Indian Institute of Science, Bangalore, INDIA
*N. Massarotti, P. Nithiarasu, Pradip Dutta and C. Ranganyakalu (Eds.)*

# FINITE ELEMENT ANALYSIS OF THERMAL WAVE PROPAGATION IN THIN LAYERS

**R.Yuvaraj, Dr.D.Senthil Kumar**
Department of Mechanical Engineering, Sona College of Technology, Salem, Tamilnadu
yuvarajr@sonatech.ac.in, senthilkumard@sonatech.ac.in

## ABSTRACT

Propagation of thermal wave phenomena in thin layer is examined using Finite element approach. The finite element model is developed from Cattaneo – Vernotte heat conduction model. This model is executed by applying symmetric boundary conditions, Newmark's scheme and backward difference method to solve second order time derivatives. The results are compared with analytical solutions of same kind of problem solved by Ed Fong and Tung T.Lam [1] using superposition principle with solution structure theorems. In this study, the details of finite element modeling of parabolic equation, hyperbolic equation and thermal wave propagation of thermal waves are discussed. This finite element technique provides an alternate, simpler and convenient solutions compared to analytical solutions.

**Key Words:** *Finite Element Model, Thermal wave propagation, Hyperbolic model, Symmetric boundary.*

## 1. INTRODUCTION

In the modern nano world the application of thin layers requires a better understanding of heat transfer phenomena in strong thermal wave environments. The approaches used to describe non-Fourier heat transport is different from classical Fourier heat transport. The speed of heat propagation in a body is infinite according to the classical Fourier heat conduction law given by

$$q = -k\,\nabla T \tag{1}$$

The body will be affected by the boundary condition or initial condition at the instant. However, the speed of heat propagation in a body is always finite. Thus, to account for phenomena involving finite propagation speed of the thermal wave, a more precise heat flux model needs to be assumed to modify the Fourier heat conduction law. Cattaneo [2] and Vernotte [3] suggested independently a modified heat flux model in the form coupled with the local energy balance as

$$\tau\frac{\partial q}{\partial t} + q = -k\,\nabla T \tag{2}$$

where $q$ is the heat flux vector, $\tau$ is the relaxation time, and $k$ is the thermal conductivity. Solving hyperbolic heat conduction equation is essential and considerable effort has been focused to the study of non-Fourier heat conduction problems.

Ozisik and Tzou [4] have obtained analytical solutions for the hyperbolic heat conduction equation. Tan and Yang [5] investigated the propagation of thermal wave in thin films subjected to sudden temperature changes on its surfaces. Torii and Yang [6] studied heat transfer mechanism in thin layer with symmetrical heat source impingement on its boundaries by numerical technique based on explicit scheme. In the present investigation, a finite element model is developed to study the propagation and collision of thermal wave phenomena in nano size layers subjected to non-homogeneous boundary conditions for two cases, one is classical diffusion (Parabolic) Fourier model and another one is non-Fourier (Hyperbolic) model.

## 2. MAIN BODY

In finite element method, the given domain is divided into number of subdomains, called finite element, on each element the approximation functions of variational or weighted-residual can be constructed for the solution of the problem. The finite element method differs from the traditional Ritz, Galerkin, Least-squares, Collacation and other weighted-residual methods in the manner in which the approximation functions are constructed. The steps involved to solve finite element model is given by Reddy [7].

*Parabolic Finite Element Model:*

It is a first order derivative with respect to time, which is used for solving transient heat transfer problems. The general form of heat conduction equation is,

$$\nabla^2 T + \frac{\dot{q}}{k} = \frac{1}{\alpha}\frac{\partial T}{\partial t} \tag{3}$$

The one dimensional transient problem without heat generation can be written as,

$$\frac{\partial^2 T}{\partial x^2} = \frac{1}{\alpha}\frac{\partial T}{\partial t} \tag{4}$$

Eqn. (3) is the classical diffusion heat transfer model which governs the thermal energy transport in homogeneous solid. For convenience, the governing Eqn. (4) is non-dimensionalised by using the following terms

$$\xi = \frac{c\,x}{2\alpha},\ \eta = \frac{c^2 t}{2\alpha},\ \theta = \frac{\rho c^2 T}{q_r},\ \tau = \frac{\alpha}{c^2} \tag{5}$$

After substituting the non-dimensionalised terms from Eqn. (5) in to Eqn. (4), the governing partial differential equation for one dimensional heat conduction equation can be given in the form of dimensionless equation as

$$\frac{\partial^2 \theta}{\partial \xi^2} = 2\frac{\partial \theta}{\partial \eta} \tag{6}$$

After assembly for the mesh of finite elements,

$$[K]\{\theta\} + 2[C]\{\dot{\theta}\} = \{F\} \tag{7}$$

$$2[C]\{\theta_{n+1}\} = (2[C] - [K]\Delta\eta)\{\theta_n\} + \{F_n\}\Delta\eta \tag{8}$$

The Eqn. (8) can be used to solve the temperature at n+1$^{th}$ time for the given dimensionless time step $\Delta\eta$ by applying initial and boundary conditions. The process can be extended until the previous time step temperature and current temperature are equal. After reaching steady state temperature the process can be terminated.

*Hyperbolic Equation:*

It is a second order derivative with respect to time which is used for solving transient heat transfer through thin layer problems in which finite heat propagation takes place. In case of parabolic heat conduction by considering Fourier effects, the heat propagation is infinite. The general form of Fourier conduction equation is given in Eqn. (1).

Local energy balance equation can be written as,

$$\nabla q = -\rho c\frac{\partial T}{\partial t} \tag{9}$$

After considering and rearranging Eqn. (1), Eqn. (2) and Eqn. (9), the general form of hyperbolic heat wave equation can be written as,

$$\alpha\frac{\partial^2 T}{\partial x^2} = \tau\frac{\partial^2 T}{\partial t^2} + \frac{\partial T}{\partial t} \tag{10}$$

After substituting the non-dimensionalised terms from Eqn. (6) in to Eqn. (10), the governing partial differential equation for one dimensional hyperbolic heat conduction equation can be given in the form of dimensionless equation as

$$\frac{\partial^2\theta}{\partial\xi^2} = 2\frac{\partial\theta}{\partial\eta} + \frac{\partial^2\theta}{\partial\eta^2} \tag{11}$$

$$[K]\{\theta\} + 2[C]\{\dot{\theta}\} + [M]\{\ddot{\theta}\} = \{F\} \tag{12}$$

where, $M$ is the mass matrix and the Eqn. (12) is the dimensionless hyperbolic form of finite element model which contains a first order time derivative $\{\dot{\theta}\}$ and a second order time derivative $\{\ddot{\theta}\}$. After repeating the same procedure the $\theta_{n+1}$ can be solved by using the Newmark's scheme.

## 3. RESULTS

Consider a thin layer of length $L$ with thermal conductivity $k$, density $\rho$ and specific heat capacity $c_p$. subjected to symmetrical boundary conditions. The left and right boundary are subjected to dimensionless temperature of $T_w = 2$. The layer is discretized into $n$ number of linear elements with the following initial and boundary conditions,

Boundary conditions:

$$\theta(\xi,\eta) = 2 \quad at\ \xi = 0 \tag{16}$$

$$\theta(\xi,\eta) = 2 \quad at\ \xi = 1 \tag{17}$$

Initial conditions:

$$\theta(\xi,\eta) = 1 \quad at\ \eta = 0,\ 0 < \xi < 1 \tag{18}$$

$$\frac{\partial\theta}{\partial\eta}(\xi,\eta) = 0 \quad at\ \eta > 0,\ \xi = 0,\ \xi = 1 \tag{19}$$

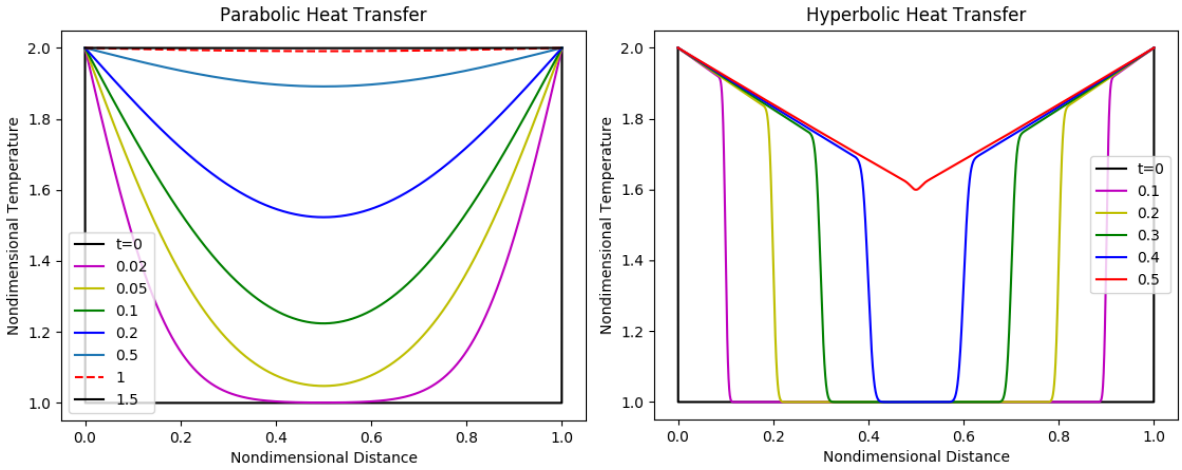


(a) (b)

FIGURE 1. Thermal wave propagation (a) Parabolic mode and (b) Hyperbolic mode

The propagation of thermal wave using parabolic model is shown in Figure 1 (a). The thin layer is initially at dimensionless temperature of 1 except the boundary and two sides of the layers are suddenly maintained symmetrically at dimensional temperature of 2 on both side of the layer. The thin layer length is taken as dimensionless length of 1. The thermal wave propagate from either sides of the layer towards the centre of the layer as shown in Figure 1 (a) at time 0.01. After propagation the heat wave from both sides meet at centre of the layer and forms a smooth temperature profile. The smooth thermal wave propagate further upward and reaches steady state at time 1.5.

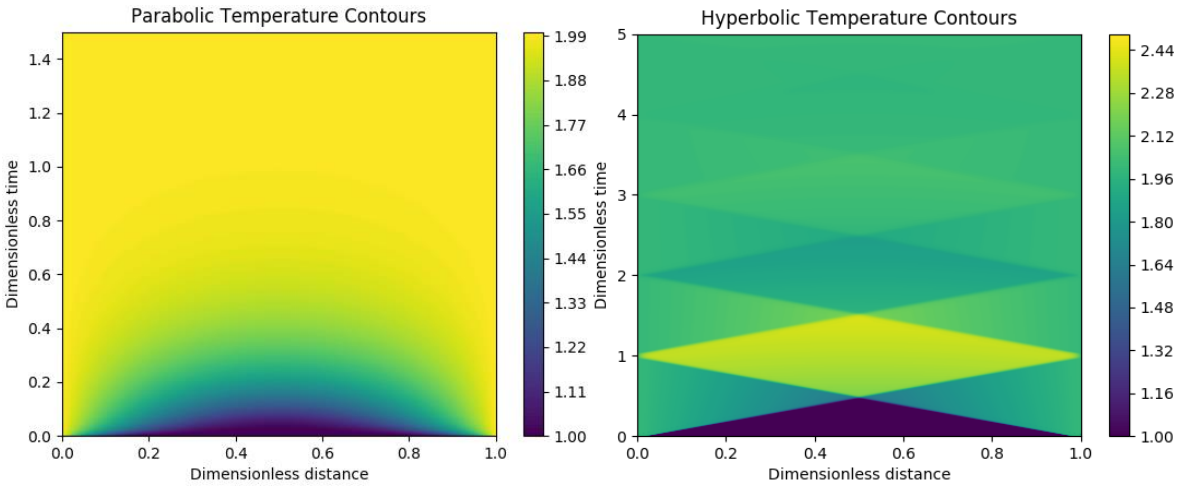


(a) (b)

FIGURE 2. Temperature contours (a) Parabolic mode and (b) Hyperbolic mode

Figure 1 (b) shows the thermal wave propagation of hyperbolic model which is totally different from the propagation happened in parabolic model. The characteristics of thermal wave propagation are examined with the help of temperature contours, for parabolic heat transfer model is shown in Figure 2 (a) and that of hyperbolic heat transfer model is shown in and Figure 2 (b) are entirely different.

## 4. CONCLUSIONS

Finite element models for parabolic and hyperbolic heat transfer are successfully developed to investigate the behavior of thermal wave propagation in a thin layer subjected to symmetric boundary conditions. The solutions obtained from the finite element model is validated with analytical solutions and made good agreement with it. The characteristics of thermal wave propagation in both parabolic and hyperbolic models are examined by plotting temperature contours. It is seen that the propagation of thermal waves in hyperbolic heat transfer model is contrast with that of parabolic model. The finite element model will provide accurate solution similar to analytical solutions, simple and fast solutions than the solutions obtained by analytical method.

## REFERENCES

[1] E. Fong and T.T. Lam, Asymmetrical collisions of thermal waves in thin films: An analytical solution, *International Journal of Thermal Sciences*, 77, 55-65, 2014.

[2] C. Cattaneo Sur une forme de l'equation de la chaleur eliminant le paradoxed'inepropagation instantanee, *C.R.Acad.Sci.*, 247, 431–433, 1958.

[3] P. Vernotte Les paradoxes de la theorie continue de l'equation de la chaleur, *C. R. Acad. Sci*., 246(22), 3154–3155, 1958.

[4] M.N. Ozisik and D.Y. Tzou, On the wave theory in heat conduction, *Journal of Heat Transfer*, 116(3), 526–535, 1994.

[5] Z.M. Tan and W.J. Yang, Heat transfer during asymmetrical collision of thermal waves in a thin film, *International Journal of Heat and Mass Transfer*, 40(17), 3999-4006, 1997.

[6] S. Torii and W.J. Yang, Heat transfer mechanisms in thin film with laser heat source, *International Journal of Heat and Mass Transfer*, 48(3-4), 537-544, 2005.

[7] J.N. Reddy, *An Introduction to the Finite Element Method*, McGraw Hill Education (India) Private Limited, New Delhi. 2015.